EURASIP Book Series on Signal Processing and Communications

Smart Antennas

State of the Art

Edited by: Thomas Kaiser, André Bourdoux, Holger Boche, Javier Rodríguez Fonollosa, Jørgen Bach Andersen, and Wolfgang Utschick

Smart Antennas—State of the Art

EURASIP Book Series on Signal Processing and Communications, Volume 3

Smart Antennas—State of the Art

Edited by: Thomas Kaiser, André Bourdoux, Holger Boche,
Javier Rodríguez Fonollosa, Jørgen Bach Andersen, and Wolfgang Utschick

Hindawi Publishing Corporation
http://www.hindawi.com

EURASIP Book Series on Signal Processing and Communications
Editor-in-Chief: K. J. Ray Liu

Hindawi Publishing Corporation
410 Park Avenue, 15th Floor, #287 pmb, New York, NY 10022, USA
Nasr City Free Zone, Cairo 11816, Egypt
Fax: +1-866-HINDAWI (USA Toll-Free)

ISBN 977-5945-09-7

Contents

Preface

It was in the summer of 2002 when the European Union launched the Sixth Framework Research Programme. One of the expected outcomes of this multibillion Euro initiative was *Structuring*, that is, tackling the fragmentation of European research on a large scale. The concept of the so-called *Network of Excellence* (NoE) was born, which was designed to strengthen scientific and technological excellence on a particular research topic. Without doubt *Smart Antennas*, which here stands for any multiantenna technique, is an important research topic in wireless communications and is characterized by severe fragmentation in Europe. Indeed, after the first steps were taken to establish a proposal, it quickly turned out that more than 100 institutions from academia and from industry were devoting much effort toward smart antenna research, so not only fragmentation but also a required critical mass of resources and of expertise were on hand. By the end of 2002, the idea of a *Network of Excellence for Smart Antenna Technology* (NESAT) took a rather concrete shape.

A series of four meetings took place up until spring 2003, where European smart antenna experts further tightened their personal links. In addition, scientists from overseas were also invited to encourage discussions of a worldwide scope. Although the NESAT proposal failed in summer 2003 because of strong competition, there was immediate commitment among the network partners to demonstrate the state-of-the-art technology in smart antennas within the framework of a comprehensive book.

This book is now in the readers' hands. It consists of six major parts, which are summarized below, and each part is split into several chapters. Most often a team of authors joining NESAT took responsibility for a single chapter, so the total number of authors is hard to count. This has made it difficult to equally thank all involved people, so we generally apologize for the absence of personal acknowledgments.

Although the first multiantenna-based products have been commercially available in wireless communications for a few months, there is no doubt that smart antennas were, are, and especially will remain a hot topic in research, even beyond this decade. Hence, a book aiming at covering the state of the art of this technology is to be seen as a *snapshot*. We hope that this book will serve as a comprehensive survey reflecting the smart antenna research in the period from 2003 to 2005.

Receiver

In this first part a collection of different receiver processing techniques and paradigms is presented, which are all based on multielement antennas. The second

chapter of this part introduces a *spatiotemporal interference rejection combining* (D. Astély and B. Ottersten) taking into account the spatial and temporal correlation of random variables at the receiver. The next chapter presents *subspace methods for space-time processing* (M. Nicoli and U. Spagnolini) which are based on the invariance of multipath parameters of the radio channel. In *multiuser MIMO channel equalization* (C. F. Mecklenbräuker et al.) a space-time matrix modulation technique is proposed, which is extended to the important cases of rank-deficient channels and multiple users. The next chapter is devoted to a new paradigm in *joint antenna combining and multiuser detection* (R. Müller and L. Cottatellucci) which relies on multistage detection and certain properties of random matrices. In *synchronization for MIMO systems* (F. Simoens et al.) the authors consider iterative algorithms for estimating the required parameters for frame synchronization and phase ambiguity resolution in MIMO systems. The following chapter deals with *turbo detection and equalization* (T. Matsumoto), which rely on an iterative channel estimation technique and a specific algorithm that takes into account the presence of unknown interference. In *architectures for reference-based and blind multilayer detection* (K.-D. Kammeyer et al.) an iterative combination of a blind source separation algorithm and a successive interference detection technique together with a reduced complexity technique for the sorted channel decomposition is proposed. Meanwhile, *uplink robust adaptive beamforming* (A. B. Gershman) presents state-of-the-art robust adaptive beamforming techniques to overcome spatial signature mismatches and received data nonstationarity in application to cellular mobile radio systems. Finally, in *robust and reduced-rank space-time decision feedback equalization* (F. A. Dietrich et al.) another approach to mitigating the troublesome effects of unreliable channel state information at the receiver is presented. At the same time a combination of the two paradigms of robustness and reduced-rank signal processing is proposed.

Channel

The second part on the radio channel deals with important aspects of the communication link between the antennas, or rather multiple antennas in a smart antenna setting. The second chapter on *propagation* (P. Vainikainen et al.) gives an update on the present state of knowledge on propagation in indoor and outdoor environments, while in the third chapter on *channel sounding measurement* (R. S. Thomä et al.) relevant channel models are described and how to measure the channel with channel sounders. Modelling the channel can be done in many ways; in *MIMO channel models* (K. Yu et al.) an overview of various methods is given. The fifth chapter *channel estimation* (G. Leus and A.-J. van der Veen) describes several ways of estimating the channel. This part concludes by finding the angular aspects of the channel in *direction-of-arrival estimation* (M. Viberg).

Transmitter

This part provides several transmitter design perspectives accommodated to different channel types, statistical variation, and knowledge. It begins with providing

a unified perspective of the design of linear transceivers for MIMO systems in the case of availability of channel state information (CSI) at both sides of the link. The chapter authored by D. P. Palomar elaborates on the design of linear precoders at the transmit side under different optimisation criteria. The third chapter considers the situation in which the transmitter has access to some limited or imperfect channel state information. Conventional space-time codes do not need any channel knowledge at the transmit side, and this is a clear advantage given the difficulties of acquiring such knowledge, but it may also be a substantial drawback since CSI, when available at the transmit side, can be used to improve performance. This chapter, authored by G. Jöngren et al., develops the concept of channel-side information-dependent codes. The fourth chapter, authored by M. Johan and W. Utschick enters into the area of nonlinear transmit processing and specifically considers Tomlinson-Harashima precoding. This technique can be understood as a generalisation in the transmit side of decision feedback equalisation in the receiver. The fifth chapter considers the optimisation the different transmission strategies in a multiuser environment. When considering optimisation of multiuser systems, objective functions can be defined based on either global or individual performance criteria. This chapter, authored by E. A. Jorswieck, motivates and analyses important representative problems of both classes. The last chapter of this part concentrates on the design of the appropriate multiplexing schemes in the presence of MIMO channel matrix ill conditioning. This chapter, authored by D. Gesbert and J. Akhtar investigates the use of constellation multiplexing in an attempt to robustify spatial multiplexing schemes.

Network Theory

In this part new theoretical results of multiantenna systems with special emphasis on network aspects are presented. In order to introduce the topic, *MIMO channel capacity* is examined (A. F. Molisch and F. Tufvesson) and validated by measurements. In the third chapter *distributed space-time coding techniques* are analyzed (S. Barbarossa et al.). In this connection a shift of paradigm in wireless communication is taking place, because here cooperation between users is not only accepted, but even favored. This makes distributed space-time coding an active research area with a number of very interesting open problems. In the fourth chapter *towards a better understanding of the quality-of-service tradeoff* (S. Stanczak and H. Boche) the geometry of feasible QoS regions is characterized. In particular, the authors investigated whether the feasible QoS region is a convex set, which is highly beneficial for resource allocation optimization. The problem of feasible QoS regions in the downlink and uplink of multiantenna systems with a given SINR is surveyed in the fifth chapter *duality theory for uplink and downlink multiuser beamforming* (H. Boche and M. Schubert). The duality between uplink and downlink, which allows to find the downlink optimum by solving an equivalent uplink problem instead, is stated and an optimization strategy for the problem of jointly optimizing beamformers and transmit power can be derived. In the sixth chapter *scheduling in multiple-antenna multiple-access channel* (H. Boche et al.) a scheduler is developed

based on network stability as one interesting criterion for optimization. To reach maximal stability a simple weighted sum of rates has to be optimized, which validates the results from the fourth chapter. As a result it is shown that the problem can be reduced to a convex problem, when the optimal successive interference cancellation (SIC) order is classified. In the appendix of this last chapter (T. Haustein) the results are implemented and experimental results are presented.

Technology

This part focuses on the real physical elements of a multiantenna transceiver and their nonidealities. Indeed, these systems operate in real life with physical components or supercomponents such as antennas, front-ends, modems, and so forth. Many of the benefits of multiantenna techniques (rate enhancements, more robust links, etc.) are dependent on the characteristics of these physical components. The scope of the part is very broad and encompasses antenna (array) design, parallel transceivers, analog transceiver nonidealities, emerging air interfaces, and prototyping issues. The second chapter *antenna design for multiantenna systems* (C. Waldschmidt et al.) addresses the impact of the antenna array on the spatial channel, the link budget, and the capacity. Modelling and design for small profile antennas are also addressed. The next chapter *radio architectures for multiple-antenna systems* (D. Evans) discusses how multiplexing techniques can be used to share a single transceiver between several antenna branches and, hence, reduce the complexity of the MIMO transceiver. In the fourth chapter *transceiver nonidealities in multiantenna systems* (A. Bourdoux and J. Liu) we look at the impact of analog transceiver nonidealities on MIMO communications. Effects such as phase noise, saturation, I-Q imbalance are addressed, and their impact is assessed, taking MIMO-OFDM as a test case. The fifth chapter *multiple antennas for 4G wireless systems* (F. Horlin et al.) considers a broader class of waveforms, combining multicarrier and direct-sequence CDMA, and analyzes the combination of these modulation/multiple access techniques with multiple antenna techniques. Finally, the last chapter *demonstrators and testbeds* (A. Burg and M. Rupp) concentrates on prototyping and provides a classification and overview of MIMO prototypes. Digital hardware issues, design methodology, and tools are discussed in detail.

Applications and Systems

This last part takes on board two aspects. On the one hand, future applications of multiantenna techniques in cellular communication systems are discussed. On the other hand, two examples for multiantenna testbeds, facilitating and validating the comprehensive design of MIMO-WLAN- and MIMO-UMTS-based systems, are explained in detail. The second chapter *smart antenna solutions for UMTS* (A. Czylwik et al.) addresses downlink beamforming with respect to system-level aspects; for example, system capacity, system coverage, and electromagnetic emission. As an extension of the second chapter, the third chapter *UMTS link-level demonstrations with smart antennas* (K. Freudenthaler et al.) shows that constraints

imposed by standardization complicate the successful exploitation of multiantenna benefits. The purpose of this chapter is to point out several low-complexity algorithmical approaches aiming for integrated circuit solutions. The fourth chapter *MIMO systems for the HSDPA FDD mode UMTS service* (A. Pagès-Zamora and M. J. Heikkilä) continues with MIMO algorithms for the high-speed downlink packet access (HSDPA) mode of UMTS. After summarizing HSDPA features relevant for applying multiantenna techniques, various MIMO-HSDPA transceiver architectures (e.g., space-time transmit diversity, vertical BLAST), and linear dispersion codes on the transmitter side and RAKE, reduced maximum likelihood and turbo space-time decoder typed receivers are discussed and evaluated by simulations with respect to fading and mobility. The next chapter *a MIMO platform for research and education* (T. Kaiser et al.) is focused on enabling the reader to set up a complete MIMO testbed of his own; it covers the basic testbed concept, an offline, hybrid, and online processing mode as well as selected network topologies. Moreover, hardware and software for BB and RF processing are highlighted; for example, module interfacing, digital signal processor (DSP) programming and field programmable gate array (FPGA) synthesis, and project and revision control software. In the final chapter *real-time prototyping of broadband MIMO WLAN systems* (M. Wouters and T. Huybrechts) a sophisticated testbed is presented with special emphasis on analog front-end impairments; for example, phase noise and amplifier nonlinearity and their cancellation. Calibration architectures and higher layer issues are addressed as well; the contribution winds up with an outlook on further developments.

Thomas Kaiser, André Bourdoux, Holger Boche, Javier Rodríguez Fonollosa,
Jørgen Bach Andersen, and Wolfgang Utschick
June 2005

Receiver

Contents

1 Introduction

Wolfgang Utschick

Technological progress has recently changed the introduction of multiple antennas at the receiver unit (Rx) of wireless access points and mobile terminals from a purely theoretical concept to a practical issue in current and future wireless communication systems. The deployment of multiple Rx antennas offers an extra spatial dimension which can be exploited by striving for diversity, multiplexing, or coherence gain in order to increase achievable information rates and reception quality. The special characteristic of multiple antennas, in addition to simply increasing the dimension of the signal space, is its relation to spatial directivity which is the linking element to the natural physical environment. Since multiple Rx antennas dramatically increase the number of parameters to be estimated and to be processed, the design of powerful and efficient receivers has become a key issue.

In this part, a collection of different receiver processing techniques and paradigms which are all based on multielement antennas is presented.

The first chapter introduces a *spatio-temporal interference rejection combining* taking not only the spatial but also the temporal correlation of random variables at the receiver into account. Such techniques are of interest in cellular systems since they require few assumptions on the structure of the interference and also can be used to suppress intersystem interference and adjacent channel interference. An understanding for when spatio-temporal interference rejection offers significant performance enhancements as compared to spatial interference rejection will be provided.

The next chapter presents *subspace methods for space-time processing* which are based on the invariance of the multipath parameters of the radio channel translated into the invariance of corresponding spatial and temporal invariant subspaces. The proposed space-time equalization techniques are considered for single or multiuser block-transmission systems and exploit the stationarity of the spatial and temporal channel subspaces over the data-blocks.

In *multiuser MIMO channel equalization*, a space-time matrix modulation technique is proposed which is then extended to the important cases of rank-deficient channels and multiple users. The proposed algorithm permits joint data detection and channel equalization without knowledge of the symbol alphabet.

Special attention is drawn to the efficient demodulation properties and to the case of time-variant MIMO multipath channels.

A further chapter is devoted to a new paradigm in *joint antenna combining and multiuser detection* which relies on multistage detection and certain properties of random matrices. It is shown how antenna combining and multiuser detection can be implemented jointly without the need for matrix multiplications or matrix inversions.

In *synchronization for MIMO systems*, the authors consider iterative algorithms for estimating the required parameters for frame synchronization and phase ambiguity resolution in MIMO systems. A special attention is drawn to algorithms which provide reliable initial conditions for the iterative techniques.

The next chapter is devoted to *turbo detection and equalization* which relies on an iterative channel estimation technique and a specific algorithm that takes into account the presence of unknown interference. It is shown that even though the equalizer's complexity can be reduced considerably, the proposed algorithms can achieve almost optimum performance.

In *architectures for reference-based and blind multilayer detection*, an iterative combination of a blind source separation algorithm and a successive interference detection technique together with a reduced complexity technique for the sorted channel decomposition is proposed. An illustrative description of the basic attempt is given.

Finally, *uplink robust adaptive beamforming* addresses the problem that in practical systems the knowledge of the user's spatial signature is likely to be unreliable. State-of-the-art robust adaptive beamforming techniques to overcome spatial signature mismatches and received data nonstationarity in application to cellular mobile radio systems are presented.

In *robust and reduced rank space-time decision feedback equalization,* another approach to mitigate the troublesome effects of unreliable channel state information at the receiver is presented. At the same time, a combination of the two paradigms of robustness and reduced rank signal processing is proposed.

Wolfgang Utschick: Institute for Circuit Theory and Signal Processing, Munich University of Technology, 80290 München, Germany

Email: utschick@tum.de

2 Spatiotemporal interference rejection combining

David Astély and Björn Ottersten

2.1. Introduction

During the last decade, the use of second-generation cellular systems such as GSM has undergone a rapid growth, and we currently see deployments of third-generation systems based on CDMA. The success of GSM and the introduction of new services, such as packet data and video telephony, motivate continuous efforts to evolve the systems and to improve performance in terms of capacity, quality, and throughput.

Receive diversity is commonly used at the base stations in cellular networks to improve the uplink performance. Relatively simple combining methods have been used to date. However, as the users eventually compete with each other for the available spectrum, interference in terms of cochannel interference (CCI), adjacent channel interference (ACI), and possibly also interference between different systems will be the limiting factor. With this in mind, more sophisticated methods, that offer interference suppression, appear attractive and to be a natural step in the evolution. Further, to improve the downlink, the use of multiple antennas at the terminal is also of relevance. The recent interest in so-called multiple-input multiple-output (MIMO) links and their potential gains in many environments may lead to the development of multiple antenna terminals. The multiple terminal receive antennas can then be used to increase the link performance with both spatial multiplexing and interference suppression depending on the operating conditions.

Herein, the problem of spatiotemporal interference rejection combining (IRC) is addressed. For burst oriented systems such as GSM, we consider the use of a vector autoregressive (VAR) model to capture both the spatial and temporal correlation of interference such as CCI and ACI. Some technical background and previous work in the area are first presented below and the underlying data model is introduced in Section 2.2. The VAR model is described and examined in Section 2.3. Two basic metrics for sequence estimation are presented in Section 2.4 in addition to reduced complexity sequence estimators. Several numerical examples are then

presented in Section 2.5 and the application to GSM is discussed in Section 2.6. Spatiotemporal IRC utilizing both spatial and temporal correlation of interference is of interest also for WCDMA. As outlined in Section 2.7, a different approach not using a VAR model may then be taken. Some concluding remarks are finally given in Section 2.8.

2.1.1. Background and some related work in the literature

In burst oriented TDMA systems such as GSM/EDGE, the modulation and the time dispersion in the radio channel introduce intersymbol interference (ISI). Even though ISI can be viewed as a form of interference, it is herein considered as a part of the signal to be detected. To handle the ISI, a maximum likelihood sequence estimator (MLSE) [1], or a suboptimum version with lower complexity, such as the delayed decision feedback sequence estimator (DDFSE) [2], is therefore assumed to be used. To cope with other forms of disturbance, such as CCI and ACI, in addition to ISI, there has been renewed interest in the approach taken in [3]. In [3], interference is modeled as a spatially and temporally colored Gaussian process, and an MLSE that takes the second-order properties of the CCI into account is derived. Some related contributions include [4, 5, 6, 7, 8, 9, 10], which utilize a Gaussian assumption for the CCI to derive an MLSE which may detect the signal in the presence of ISI and simultaneously suppress CCI. In [3, 5, 10], the sequence estimator proposed by Ungerboeck in [11] is generalized to the multiple-antenna case. The resulting structure consists of a multiple-input single-output (MISO) filter front end followed by a sequence estimator. The filter may be viewed as the concatenation of a MIMO whitening filter and a filter matched to the whitened channel. The MLSE proposed by Forney in [1], and generalized to multiple channels and multiple signals in [12], has been derived for temporally white but spatially colored noise and studied for CCI rejection, see [4, 7, 13, 8]. Forney's and Ungerboeck's formulations for sequence estimation are equivalent and a unification is presented in [14].

A suboptimum approach to handle CCI with a MISO filter and a Forney form of MLSE is proposed in [15]. Other front-end filters are considered in [16, 17]. The unified analysis of front-end filters in [18] includes a Forney form of MLSE, derivations of optimal filters of infinite length, and, based on numerical studies, guidelines on how to truncate the filters. In [19], a front-end filter for a decision feedback equalizer is used with a DDFSE for joint equalization and interference suppression.

An MLSE with spatiotemporal IRC accounts also for the temporal correlation of the interference, and in general truncation is needed, both in the front-end filter and also in the memory of the sequence estimator. A straightforward approach is to use a finite-order linear predictor and to assume that the prediction errors are temporally white and complex Gaussian. This is equivalent to using a complex Gaussian VAR model. Autoregressive modeling of interference in single-antenna spread spectrum receivers has been proposed in [20] and a VAR model is used in [21] to handle spatiotemporally correlated clutter in radar signal

processing. In the field of blind channel identification from second-order statistics, linear-prediction-based methods which exploit the simultaneous moving average, and autoregressive nature of the received signals in the multichannel setting have been proposed [22, 23, 24]. The use of a VAR model for interference rejection has also been mentioned in, for example, [16] and investigated in [25, 26]. As will be seen, with a VAR model, metrics both for Forney and Ungerboeck forms of MLSE can be derived, which is interesting since a Forney form of sequence estimator may offer alternative strategies as compared to the Ungerboeck form when the parameters are to be estimated and tracked, see [8, 14].

The prediction error filter corresponding to the VAR model introduces a finite amount of additional ISI, so that the complexity of the sequence estimator increases exponentially with the amount of temporal correlation accounted for. This motivates the use of reduced complexity sequence estimators as in [19, 27, 28]. Alternatively, a general sequence estimator such as the generalized Viterbi algorithm (GVA) [29], which includes the DDFSE as a special case, may be applied.

In direct-sequence code division multiple access (DS-CDMA) systems, such as WCDMA, RAKE receivers are typically used in time-dispersive radio channels. To incorporate spatiotemporal IRC in such a receiver structure, an alternative to the VAR model may be used. Some previous work on this can be found in, for example, [30, 31, 32]. Similar to the use of a VAR model for burst oriented TDMA systems such as GSM, we show how both spatial and temporal correlation of the interference are exploited.

Finally, we note that to handle digitally modulated interference, such as CCI, the finite alphabet property may be exploited by means of joint multiuser detection [12, 33, 34]. The approach considered herein, and referred to as interference rejection, utilizes only second-order statistics of the interference. This is in general inferior to joint detection. On the other hand, joint detection requires the knowledge of the channels of the interference and not only second-order statistics. An interference rejecting approach is also expected to be more robust if the finite alphabet assumption is invalid, for example, due to frequency offsets, or if the modulation format of the interference is unknown. Interference rejection may thus be applicable to a larger class of interfering signals, such as ACI and intersystem interference in addition to CCI, if the second-order moments of the signal of interest and the interference span sufficiently different spaces.

2.2. Data model

A discrete time model with symbol rate sampling is considered for a quasistationary scenario with time dispersive propagation. A signal of interest is transmitted with a single antenna, $N_T = 1$. The signals received by N_R antennas are modeled as

$$\mathbf{r}[n] = \sum_{l=0}^{L_1-1} \mathbf{h}_1[l] b_1[n-l] + \mathbf{j}[n], \tag{2.1}$$

where $\mathbf{r}[n]$ is an $N_R \times 1$ vector modeling the received samples, the $N_R \times 1$ vector

$\mathbf{h}_1[l]$ models the channel between the transmitter and the receive antennas for a time delay of l samples, $b_1[n]$ is the nth transmitted symbol, and $\mathbf{j}[n]$ models noise and interference on the channel. Oversampling with respect to the symbol rate can be included by treating the different sampling phases as virtual antennas. Properties of one-dimensional signal constellations such as binary phase-shift keying (BPSK), or minimum shift keying (MSK) de-rotated, can be exploited in a similar way, see [35], but this is not pursued herein.

Noise and interference are modeled as the sum of signals received from $K-1$ interfering users with single transmit antennas and additive noise,

$$\mathbf{j}[n] = \sum_{k=2}^{K} \sum_{l=0}^{L_k-1} \mathbf{h}_k[l] b_k[n-l] + \mathbf{v}[n], \tag{2.2}$$

where $\mathbf{v}[n]$ represents additive white Gaussian noise. The kth interferer transmits a sequence of symbols, $b_k[n]$, and the channel is modeled with L_k symbol spaced taps denoted $\mathbf{h}_k[l]$.

A spatiotemporal model for a number of consecutive vector samples is used. We stack $P+1$ consecutive vector samples and define the $N_{\mathrm{R}}(P+1)\times 1$ column vectors $\vec{\mathbf{r}}_P[n]$, $\vec{\mathbf{j}}_P[n]$, and $\vec{\mathbf{v}}_P[n]$ as

$$\begin{aligned}
\vec{\mathbf{r}}_P[n] &= \begin{bmatrix} \mathbf{r}^T[n] & \mathbf{r}^T[n-1] & \cdots & \mathbf{r}^T[n-P] \end{bmatrix}^T, \\
\vec{\mathbf{j}}_P[n] &= \begin{bmatrix} \mathbf{j}^T[n] & \mathbf{j}^T[n-1] & \cdots & \mathbf{j}^T[n-P] \end{bmatrix}^T, \\
\vec{\mathbf{v}}_P[n] &= \begin{bmatrix} \mathbf{v}^T[n] & \mathbf{v}^T[n-1] & \cdots & \mathbf{v}^T[n-P] \end{bmatrix}^T,
\end{aligned} \tag{2.3}$$

the $N_{\mathrm{R}}(P+1)\times(L_1+P)$ matrix $\boldsymbol{\mathcal{H}}_P$ as

$$\boldsymbol{\mathcal{H}}_P = \begin{bmatrix} \mathbf{h}_1[0] & \mathbf{h}_1[1] & \cdots & \mathbf{h}_1[L_1-1] & & \\ & \ddots & & & \ddots & \\ & & \mathbf{h}_1[0] & \mathbf{h}_1[1] & \cdots & \mathbf{h}_1[L_1-1] \end{bmatrix}, \tag{2.4}$$

and form the $(p+1)\times 1$ column vector $\vec{\mathbf{b}}_1[n;p]$ as

$$\vec{\mathbf{b}}_1[n;p] = \begin{bmatrix} b_1[n] & b_1[n-1] & \cdots & b_1[n-p] \end{bmatrix}^T. \tag{2.5}$$

Further, let $\widehat{L}$ be the maximum channel length among the interferers,

$$\widehat{L} = \max_{2\le k\le K} L_k, \tag{2.6}$$

and define the $N_{\mathrm{R}}\times(K-1)$ matrix $\mathbf{G}[n]$ as

$$\mathbf{G}[n] = \begin{bmatrix} \mathbf{h}_2[n] & \cdots & \mathbf{h}_K[n] \end{bmatrix}, \tag{2.7}$$

where $\mathbf{h}_k[l] = \mathbf{0}$ for $l \geq L_k$. The $N_R(P+1) \times (K-1)(\hat{L}+P)$ matrix $\mathcal{G}_P$ is then formed as

$$\mathcal{G}_P = \begin{bmatrix} \mathbf{G}[0] & \mathbf{G}[1] & \cdots & \mathbf{G}[\hat{L}-1] & & \\ & \ddots & & & \ddots & \\ & & \mathbf{G}[0] & \mathbf{G}[1] & \cdots & \mathbf{G}[\hat{L}-1] \end{bmatrix}, \tag{2.8}$$

and the $(p+1)(K-1) \times 1$ column vector $\vec{\mathbf{i}}[n;p]$ is defined as

$$\vec{\mathbf{i}}[n;p] = \begin{bmatrix} b_2[n] & \cdots & b_K[n] & b_2[n-1] & \cdots & b_K[n-p] \end{bmatrix}^T. \tag{2.9}$$

For model order P, we get from (2.1)

$$\vec{\mathbf{r}}_P[n] = \mathcal{H}_P \vec{\mathbf{b}}_1[n; L_1 + P - 1] + \vec{\mathbf{j}}_P[n], \tag{2.10}$$

where $\vec{\mathbf{j}}_P[n]$ can be written using (2.2) as

$$\vec{\mathbf{j}}_P[n] = \mathcal{G}_P \vec{\mathbf{i}}[n; \hat{L} + P - 1] + \vec{\mathbf{v}}_P[n]. \tag{2.11}$$

For $P = 0$, the spatiotemporal model coincides with a space-only model.

2.2.1. Why spatiotemporal interference rejection?

With an antenna array with N_R antennas, it is well known that up to $N_R - 1$ narrowband interferers may be rejected. If the interfering signals have propagated through channels with time and angle dispersion, several resolvable paths are incident on the array from each interferer. Each path requires roughly one spatial degree of freedom, and if the antenna array is large, spatial interference rejection may be sufficient. However, for a small antenna array, this may not be the case. From (2.10) and (2.11), the observations may be written as

$$\vec{\mathbf{r}}_P[n] = \mathcal{H}_P \vec{\mathbf{b}}_1[n; L_1 + P - 1] + \mathcal{G}_P \vec{\mathbf{i}}[n; \hat{L} + P - 1] + \vec{\mathbf{v}}_P[n]. \tag{2.12}$$

If the rank of $\mathcal{G}_P$ is less than $N_R(P+1)$, it is possible to form linear combinations of the spatiotemporal observations which contain no interference. Then, if the channel $\mathcal{H}_P$ is not completely in the space spanned by the columns of $\mathcal{G}_P$, these linear combinations will contain a signal part for estimating the desired data. Considering the random nature of the radio channel, the latter condition appears to be relatively mild, at least for deployments with low fading correlation. Further, a sufficient condition for $\mathcal{G}_P$ to have rank less than $N_R(P+1)$ is that $\mathcal{G}_P$ is a tall matrix, that is, the number of rows is greater than the number of columns,

$$N_R(P+1) > (K-1)(\hat{L}+P). \tag{2.13}$$

As long as $\widehat{L}$ is finite and $K - 1 < N_R$, this inequality may be satisfied with P sufficiently large. Thus, we expect large gains for spatiotemporal interference rejection ($P > 0$) as compared to space-only interference rejection ($P = 0$) in interference limited scenarios when the rank of $\mathcal{G}_0$ is N_R due to time dispersion and angular spread of the CCI. Joint space-time processing then requires fewer antennas, or channels, compared to space-only processing to achieve comparable interference rejection. Important applications include two-branch spatial or polarization diversity, for example, in mobile terminals [13].

Finally, note that the subspace for interference rejection can be determined from the second-order statistics of the interference only, and that this is done implicitly when the parameters of the VAR model introduced below in Section 2.3 are calculated. Thus, interference rejection only requires knowledge of second-order statistics, which in practice requires few assumptions on the interference and is easier to estimate than the channels and modulation formats of the interfering transmitters.

2.3. Autoregressive modeling of interference

To reject time dispersive interference with a sequence estimator which handles both ISI and temporally correlated interference, one may, as mentioned in the introduction, use Ungerboeck's formulation in [3, 10, 14]. By considering the underlying structure of the interference in (2.2), it can be seen that in the general case, the front-end filters to generate statistics for a sequence estimator as well as the memory of the sequence estimator need to be truncated, see also [18]. Herein, a different truncation approach is taken in the sense that a *measurement model* with a suitable structure is assumed. This formulation also reveals how temporally correlated CCI may be included in Forney's form of the sequence estimator.

A straightforward way to handle the temporal correlation of the interference is to use the prediction error filter associated with a Pth-order linear predictor. The order of the predictor, P, is a design parameter which also controls the additional amount of ISI introduced. By choosing the model order high enough, we also expect the prediction error filter to be able to temporally whiten any stationary process [36]. Furthermore, for an autoregressive process, the best linear predictor is of finite order. Thus, the finite-order prediction error filter is the true whitening filter of some autoregressive process. We also note that methods based on linear prediction have been developed for blind channel identification from second-order statistics. Such methods may exploit the simultaneous moving average and autoregressive nature of the signals in the multichannel case [22, 23, 24]. In fact, with zero thermal noise and finite channel lengths, the CCI in (2.2) may be modeled with a finite-order autoregressive model. Conditions for this to hold may be found in, for example, [22, 23]. One condition is that the number of interferers is strictly less than the number of antennas, $K - 1 < N_R$. Thus, in interference-limited scenarios, with negligible thermal noise, the use of an autoregressive model appears to be very suitable indeed.

It should be stressed that a VAR model for the interference and noise is an approximation which in general does not agree with the underlying signal model introduced in (2.2). However, by adjusting the model order, it may perform sufficient whitening and it integrates in a straightforward way with a sequence estimator. We therefore formulate the measurement model. The Pth-order linear predictor of $\mathbf{j}[n]$ is modeled as

$$\hat{\mathbf{j}}[n \mid n-1,\ldots,n-P] = -\sum_{p=1}^{P} \mathbf{A}_p^P \mathbf{j}[n-p], \tag{2.14}$$

and the corresponding prediction error is

$$\mathbf{e}_P[n] = \mathbf{j}[n] - \hat{\mathbf{j}}[n \mid n-1,\ldots,n-P] = \boldsymbol{\mathcal{W}}(\boldsymbol{\mathcal{A}}_P)\vec{\mathbf{j}}_P[n], \tag{2.15}$$

where the prediction error filter $\boldsymbol{\mathcal{W}}(\boldsymbol{\mathcal{A}}_P)$ is defined as

$$\boldsymbol{\mathcal{W}}(\boldsymbol{\mathcal{A}}_P) = \begin{bmatrix} \mathbf{I}_{N_R} & \mathbf{A}_1^P & \mathbf{A}_2^P & \cdots & \mathbf{A}_P^P \end{bmatrix}. \tag{2.16}$$

The covariance of the prediction error, denoted $\mathbf{Q}_P$, may then be written as

$$\mathbf{Q}_P = \mathrm{E}\left\{\mathbf{e}_P[n]\mathbf{e}_P^*[n]\right\} = \boldsymbol{\mathcal{W}}(\boldsymbol{\mathcal{A}}_P)\boldsymbol{\mathcal{R}}_P\boldsymbol{\mathcal{W}}^*(\boldsymbol{\mathcal{A}}_P), \tag{2.17}$$

where

$$\boldsymbol{\mathcal{R}}_P = \mathrm{E}\left\{\vec{\mathbf{j}}_P[n]\vec{\mathbf{j}}_P^*[n]\right\}, \tag{2.18}$$

and the expectation is evaluated with respect to the interfering data symbols modeled as independent sequences. If the coefficients of the Pth-order linear predictor are chosen so that the prediction error is orthogonal to $\mathbf{j}[n-1],\ldots,\mathbf{j}[n-P]$, then the expected squared value of any component of $\mathbf{e}_P[n]$ is minimized according to the orthogonality principle [36]. The orthogonality principle is used for the predictor of each of the N_R components of $\mathbf{e}_P[n]$, and in this way, a set of equations is obtained which may be written as

$$\mathbf{R}_{jj}[l] + \sum_{p=1}^{P} \mathbf{A}_p^P \mathbf{R}_{jj}[l-p] = \begin{cases} \mathbf{Q}_P & l = 0, \\ \mathbf{0} & 1 \le l \le P, \end{cases} \tag{2.19}$$

where

$$\mathbf{R}_{jj}[l] = \mathrm{E}\left\{\mathbf{j}[n]\mathbf{j}^*[n-l]\right\}. \tag{2.20}$$

The equations are known as the Yule-Walker equations, and for $P > 0$, they may also be written in matrix form as

$$\begin{bmatrix} \mathbf{I}_{N_R} & \mathbf{A}_1^P & \mathbf{A}_2^P & \cdots & \mathbf{A}_P^P \end{bmatrix} \boldsymbol{\mathcal{R}}_P = \begin{bmatrix} \mathbf{Q}_P & \mathbf{0}_{N_R \times PN_R} \end{bmatrix}. \tag{2.21}$$

Indeed, the solution minimizes the trace of $\mathbf{Q}_P$, the sum of the mean squared prediction errors. Furthermore, the *modeling assumption* made is that the prediction error of the Pth-order linear predictor is a *temporally white, complex Gaussian process*,

$$\mathrm{E}\left\{\mathbf{e}_P[n]\mathbf{e}_P^*[n-k]\right\} = \begin{cases} \mathbf{Q}_P & k = 0, \\ \mathbf{0} & k \neq 0. \end{cases} \tag{2.22}$$

Thus, it is assumed that the interference may be temporally whitened with a Pth-order linear predictor, and it is further assumed that the prediction errors are complex Gaussian. The Gaussian assumption is not motivated by the law of large numbers, but primarily because the solution to the sequence estimation problem is easily obtained. The choice $P = 0$ will be referred to as space-only IRC, and such a modeling assumption has been previously made to derive detectors in, for example, [4, 7, 8]. We next consider the linear predictor for some special cases.

(i) With spatially and temporally white noise, $\boldsymbol{\mathcal{R}}_P$ is a diagonal matrix, and the solution to the Yule-Walker equations is

$$\boldsymbol{\mathcal{W}}(\boldsymbol{\mathcal{A}}_P) = \left[\mathbf{I}_{N_\mathrm{R}} \quad \mathbf{0}_{N_\mathrm{R}\times PN_\mathrm{R}}\right]. \tag{2.23}$$

The solution corresponds in this case to space-only processing with maximum ratio combining.

(ii) We consider the case with negligible thermal noise, with $\vec{\mathbf{v}}_P = 0$ in (2.11). For independent temporally white symbol sequences, the linear predictor is then determined as the minimum norm solution to

$$\boldsymbol{\mathcal{W}}(\boldsymbol{\mathcal{A}}_P)\boldsymbol{\mathcal{G}}_P\boldsymbol{\mathcal{G}}_P^* = \left[\mathbf{Q}_P \quad \mathbf{0}_{N_\mathrm{R}\times PN_\mathrm{R}}\right]. \tag{2.24}$$

Suppose that the received signal is first filtered with the prediction error filter. If the covariance matrix of the filtered interference, $\mathbf{Q}_P$, is singular, then the filtered interference is confined to a subspace and may be rejected by spatial filtering in a second step. Using the structure of $\boldsymbol{\mathcal{G}}_P$ in (2.8), it can be shown that the rank of $\mathbf{Q}_P$ cannot increase with P, see [25] for details. If $\boldsymbol{\mathcal{G}}_0$ has rank less than N_R, then $\mathbf{Q}_P$ is singular for all P. Otherwise, we increase P until $\boldsymbol{\mathcal{G}}_P\boldsymbol{\mathcal{G}}_P^*$ is singular but $\boldsymbol{\mathcal{G}}_{P-1}\boldsymbol{\mathcal{G}}_{P-1}^*$ is not. Then, as shown in [25],

$$\det\left(\boldsymbol{\mathcal{G}}_P\boldsymbol{\mathcal{G}}_P^*\right) = \det\left(\mathbf{Q}_P\right)\det\left(\boldsymbol{\mathcal{G}}_{P-1}\boldsymbol{\mathcal{G}}_{P-1}^*\right), \tag{2.25}$$

from which we see that $\mathbf{Q}_P$ is low rank. Thus, for complete interference rejection in the noiseless case, P should be chosen so that $\boldsymbol{\mathcal{G}}_P\boldsymbol{\mathcal{G}}_P^*$ is singular. Note that as P is increased, $\boldsymbol{\mathcal{G}}_P$ will eventually be a tall matrix if $\hat{L}$ is finite and $K - 1 < N_\mathrm{R}$ so that $\boldsymbol{\mathcal{G}}_P\boldsymbol{\mathcal{G}}_P^*$ is singular. This agrees with the discussion in Section 2.2.1.

(iii) We finally consider the case with high signal to noise ratio (SNR) and assume that

$$\boldsymbol{\mathcal{R}}_P = \boldsymbol{\mathcal{G}}_P\boldsymbol{\mathcal{G}}_P^* + \sigma^2\mathbf{I}_{N_\mathrm{R}(P+1)}, \tag{2.26}$$

where σ^2 is the noise power, and that $\mathcal{G}_P \mathcal{G}_P^*$ has low rank. In [25], it is argued that the signal to interference and noise ratio (SINR), after filtering the received signal with the prediction error filter and whitening it with $\mathbf{Q}_P^{-1/2}$, is proportional to $1/\sigma^2$ as $\sigma^2 \to 0$ under mild conditions. Thus, the SINR grows as the noise vanishes.

For the case $K - 1 < N_R$ it is possible to reject all CCI given that the VAR model order P is chosen so that $\mathcal{G}_P \mathcal{G}_P^*$ is low rank.

2.4. Sequence estimation

Consider the received signal filtered with the prediction error filter for a VAR model of order P. By combining (2.10) and (2.15) we obtain

$$\mathbf{z}[n] = \mathcal{W}(\mathcal{A}_P)\vec{\mathbf{r}}_P[n] = \mathbf{F}_P \vec{\mathbf{b}}_1[n; L_1 + P - 1] + \mathbf{e}_P[n], \tag{2.27}$$

where the $N_R \times (L_1 + P)$ matrix $\mathbf{F}_P$ is defined as

$$\mathbf{F}_P = \mathcal{W}(\mathcal{A}_P)\mathcal{H}_P = \begin{bmatrix} \mathbf{f}[0] & \mathbf{f}[1] & \cdots & \mathbf{f}[L_1 + P - 1] \end{bmatrix}, \tag{2.28}$$

and represents the concatenated response of the prediction error filter and the channel for the signal of interest. Recall that the prediction errors, $\mathbf{e}_P[n]$, are modeled as temporally white, spatially colored complex Gaussian samples, (2.22). The underlying process is in general not a Gaussian VAR process, and the prediction error filter is therefore an approximate whitening filter. Using the assumed temporal whiteness and neglecting terms that do not depend on the transmitted data, the maximum likelihood estimate of the data sequence is

$$\{\hat{b}_1[n]\} = \arg \min_{\{b_1[n]\}} \sum_n ||\mathbf{Q}_P^{-1/2}(\mathcal{W}(\mathcal{A}_P)\vec{\mathbf{r}}_P(n) - \mathbf{F}_P \vec{\mathbf{b}}_1[n; L_1 + P - 1])||_2^2. \tag{2.29}$$

This form of sequence estimator is referred to as the Forney form after [1], see also [14]. To find the estimate, the minimization is to be carried out over all possible transmitted sequences with symbols from a finite alphabet. As is well known, the *Viterbi algorithm* with a memory of $L_1 + P - 1$ symbols can be used. With a binary symbol alphabet, the number of states in the trellis is 2^{L_1+P-1}. Thus, the complexity grows exponentially with the model order P corresponding to the amount of temporal correlation accounted for.

As shown in [10, 11, 14], the sequence estimator may also be implemented with a matched MISO space-time filter followed by an MLSE operating on a scalar signal. This form of the sequence estimator is referred to as the Ungerboeck form. It can be shown, following [14], that the sequence estimate of (2.29) may also be written as

$$\{\hat{b}_1[n]\} = \arg \max_{\{b_1[n]\}} \sum_n \mathrm{Re}\{b_1^*[n](z[n] - \mathbf{s}_P \vec{\mathbf{b}}_1[n; L_1 + P - 1])\}, \tag{2.30}$$

where $z[n]$ is obtained by filtering $\mathbf{z}[n]$ with a MISO filter as

$$z[n] = \sum_{l=0}^{L_1+P-1} \mathbf{f}^*[l]\mathbf{Q}_P^{-1}\mathbf{z}[n+l]. \tag{2.31}$$

In turn, $\mathbf{z}[n]$ is obtained by filtering the received signal with the prediction error filter, see (2.27). The statistic for the sequence estimator, $z[n]$, is thus obtained by filtering the received signal $\mathbf{r}[n]$ with a MISO filter. The $1 \times (L_1 + P)$ vector $\mathbf{s}_P$ is defined as

$$\mathbf{s}_P = \left[\frac{1}{2}s_0 \quad s_1 \quad \cdots \quad s_{L_1+P-1}\right], \tag{2.32}$$

with

$$s_k = \sum_{l=0}^{L_1+P-1-k} \mathbf{f}^*[l]\mathbf{Q}_P^{-1}\mathbf{f}[l+k]. \tag{2.33}$$

The Forney form presented in (2.29) and the Ungerboeck form in (2.30) are equivalent if the full trellis is used. However, when reduced complexity sequence estimators are used, the two forms show different performance, see also [37] and the two last examples in Section 2.5.

2.4.1. Reduced complexity sequence estimation

Performance may be significantly improved by accounting also for the temporal correlation of the interference. The cost for this is an exponential increase in complexity of the sequence estimator. Therefore, it is of interest to consider reduced complexity detectors such as the GVA of [29]. The GVA uses as state, or *label*, the last $\mu \leq L_1 + P - 1$ symbols of each survivor sequence. For simplicity, only binary alphabets are considered. There are then 2^μ states in the trellis, and in each state, $S \geq 1$ survivors are retained. The GVA can be described as follows.

(1) At time $n - 1$ there are S survivors for each of the 2^μ labels.

(2) At time n all survivors with the two possible symbols extend to form candidates. Calculate in a recursive way the metric for each candidate. These $S2^{\mu+1}$ candidates are classified according to their labels, the last μ symbols, into 2^μ *lists*.

(3) If several candidates in each list have the same last $L_1 + P - 1$ symbols, keep only the candidate with the best metric. This is known as *path merge elimination*.

(4) From each of the 2^μ lists, select the S candidates with the best metric. They will form the survivors at time n.

For $\mu = 0$, the GVA coincides with the M-algorithm [38], and for $\mu < L_1+P-1$, $S = 1$, it coincides with the DDFSE in [2]. The full MLSE implemented with the conventional Viterbi algorithm is obtained with $\mu = L_1 + P - 1$, $S = 1$. If $S > 1$, the GVA selects the S candidates with the best metric from a list with $2S$ candidates. Thus, since the M-algorithm requires ordering of the survivors, it has a higher

complexity than the DDFSE. The DDFSE only needs to find the survivor with the best metric.

We also discuss the choice of metric. For the Forney form in (2.29), the analysis of the single antenna case, $N_R = 1$, of the DDFSE in, for example, [2] shows that most of the energy must be concentrated in the first taps for best performance. It is thus desirable that the channel is minimum phase. In a fading environment, the phase of the channel varies and an alternative is to use the Ungerboeck form in (2.30) together with the DDFSE as proposed in [28, 37]. The Ungerboeck form is not dependent on the phase of the channel. On the other hand, it may be limited by ISI, which can introduce an error floor [37].

2.5. Numerical examples

Simulations were done to illustrate the performance in terms of bit error rate (BER) of space-only and spatiotemporal IRC. The first examples illustrate how performance is improved with increasing model order P at the cost of higher complexity when a full MLSE is used. Then, some further examples show that similar gains can be obtained using reduced complexity sequence estimators. Thus, noise sensitivity can be traded for interference rejecting capability by increasing P while keeping the complexity roughly the same. Herein, the cost for calculating the metric is neglected and the number of retained survivors in the trellis is used as a measure of complexity.

Data was transmitted in bursts of 200 bits. The channel was stationary during each burst but generated independently from burst to burst. The fading of the antennas was uncorrelated and the channels between a transmitter and each receive antenna had the same power delay profile with a number of symbol spaced rays with the same average strength. Temporally and spatially white Gaussian noise was added.

First, two receive antennas were used and a single cochannel interferer was present. The SNR per antenna was 10 dB and the channels were modeled with two rays, $L_1 = L_2 = 2$. The BER as a function of signal to interference ratio (SIR) per antenna is shown in Figure 2.1 using a full MLSE. There are not enough degrees of freedom to reject the time-dispersive interferer with space-only processing, $P = 0$. By increasing P, the interference may be effectively suppressed.

Recall that as the noise vanishes, the SINR after the prediction error filter grows linearly with the inverse noise power given that $K - 1 < N_R$ and that P is sufficiently large. To illustrate this, a case with two antennas and one interferer with the same SNR as the signal of interest is considered. The average BER as a function of SNR is displayed in Figure 2.2. For $P = 0$, the interference spans the entire space, and as the noise vanishes, performance is limited by CCI. For $P > 0$, the BER decreases as the noise vanishes. Performance without CCI is also included.

The two previous examples demonstrated the advantage of spatiotemporal processing over space-only processing since $\mathcal{G}_0$ spans the whole space whereas the columns of $\mathcal{G}_1$ only span a subspace. Performance also depends on the structure of the disturbance, and in the next example the number of interferers was varied.

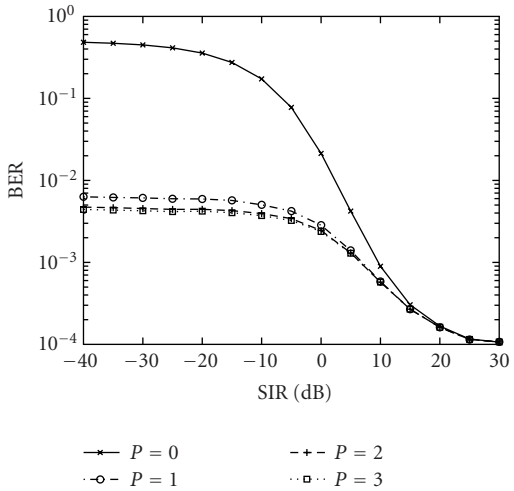

FIGURE 2.1. Two antennas and one interferer. Two uncorrelated taps of equal average power. The SNR is 10 dB. Full MLSE.

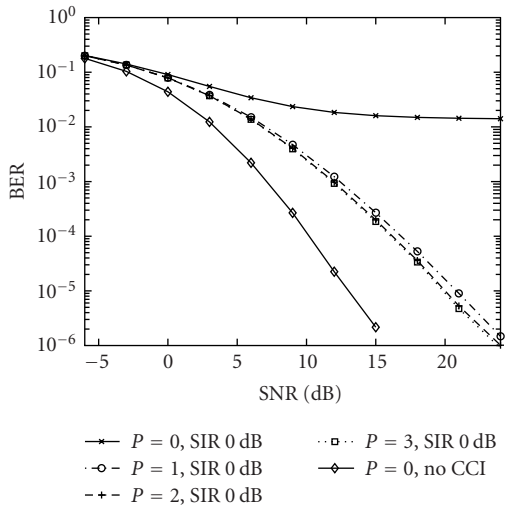

FIGURE 2.2. Two antennas, one interferer, and channels with two taps of equal power. The SIR is 0 dB. The performance with no interferer is also included. Full MLSE.

All channels were modeled with two taps, and the results are plotted in Figure 2.3 for $P = 0, 3$ and $K = 1, 2, 3$. The SNR was 20 dB for the cases with CCI. With no CCI, the SINR is equal to the SNR, and, as can be seen, spatiotemporal processing is equivalent with space-only processing. For one interferer, the interference contribution is confined to a subspace for P large enough. For two interferers of equal power, there is still gain with spatiotemporal processing, but since the interference

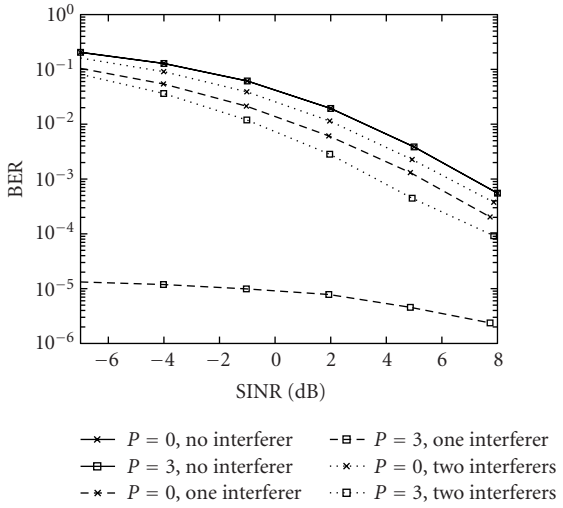

FIGURE 2.3. Two antennas, different number of interferers, and two tap channels. For the cases with interferers, the SNR is 20 dB and the SIR is varied. For the case with no interference, the SINR equals the SNR, which is varied. Full MLSE.

is not confined to a subspace no matter how large P is made, the gain is smaller than for the case with one interferer.

We now consider an example with reduced complexity sequence estimators. The signal of interest had three taps, $L_1 = 3$, and the two interferers had $L_2 = 2$ and $L_3 = 3$ taps. Four antennas were used and in Figure 2.4, the performance for different P is shown. The SIR was -10 dB and the SNR was 9 dB at each antenna. The complexity was constrained so that the sequence estimators retained four survivors except for the full MLSE with complexity increasing with P. From Figure 2.4, we see that by retaining fewer paths in the sequence estimator, spatiotemporal processing may be used to reject interference without an exponential increase in complexity. For the Forney form, it can be seen that the M-algorithm, $\mu = 0$, is preferable.

Another example with two antennas and one interferer was considered. The channels for both the signal of interest and the interferer were modeled with $L_1 = L_2 = 2$ taps. The SIR was 0 dB and the results are plotted as a function of SNR in Figure 2.5. As can be seen, the performance of the M-algorithm with the Ungerboeck metric degrades at high SNR. An explanation for this may be found in [37]; the accumulated metric will not account for anticausal ISI if the trellis is reduced. This means that ISI may limit the performance, see [37], for a remedy.

2.6. Interference rejection combining for GSM

The increasing speech and data traffic in today's GSM networks motivates the study of techniques such as IRC. The study in [39] demonstrates that the system capacity can be increased by about 50% in a tightly planned GSM network by using

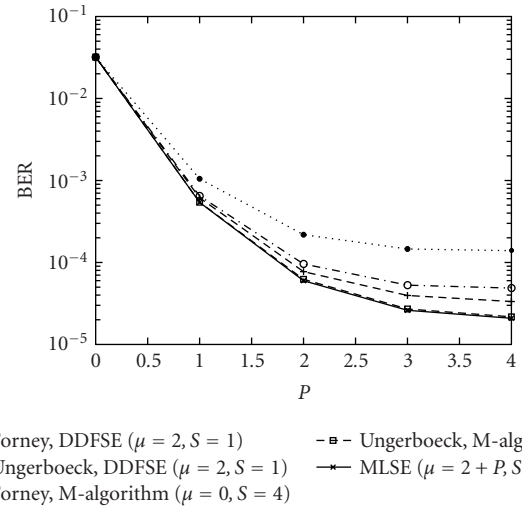

FIGURE 2.4. Four antennas, two interferers, and all algorithms retain four survivors except for the MLSE, which uses 2^{2+P} survivors. The SNR is 9 dB, the SIR is −10 dB.

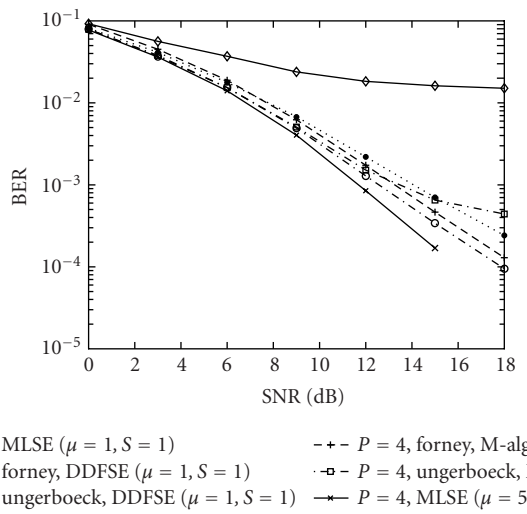

FIGURE 2.5. Two antennas and one interferer. All algorithms retain two survivors except for the $P = 4$ MLSE, which retains 32 survivors. The SIR is 0 dB.

a simple form of space-only IRC at the base stations. The gain depends to a large extent on the uplink-downlink balance of the system. If the balance is neglected and only the uplink is considered, the results indicate that the uplink capacity may be increased by up to 150%. Downlink improvements by means of IRC have also received much interest lately [40]. In fact, as outlined in [17, 40], IRC can be employed even with a single receive antenna.

For the actual implementation of spatiotemporal IRC, several aspects have to be considered. Functionality is of course required to cope with imperfections encountered in the down conversion to digital baseband such as DC and frequency offsets. Algorithms developed for white interference and noise may need to be revisited, as is done for burst synchronization in [41]. When it comes to estimating the parameters required by the sequence detector, we note that there are several challenges. Although the channel may perhaps be regarded as time-invariant during the burst, significant changes in the interference may occur during the transmission of a burst if the network is not burst synchronized. On the other hand, if the network is synchronized, the correlation between training sequences used in different cells may require some care, for example, planning as well as joint detection and estimation of the channels of the interferers.

The number of parameters to estimate grows with the chosen model order P, see also [25, 26], and estimation errors may degrade performance significantly. Iterating between parameter estimation and data detection may be an alternative. The simulation study in [42] shows that performance may be significantly improved in this way, and that performance of a linear receiver may be better than an MLSE structure, especially in the presence of estimation errors and time variations. Another possibility is to adapt the model order to the instantaneous interference scenario. Ungerboeck's formulation could be considered as a starting point since it can be trained in a different way, see also [3, 8, 14]. Another approach is to utilize the structure of the interference. This is done in [43] to improve the estimates of the parameters of the VAR model and in [44] to construct a zero-forcing front-end filter.

2.6.1. Experimental results

Data collected with a testbed for the air interface of a DCS 1800 base station was processed. A dual polarized sector antenna was mounted on the roof of a building 40 meters above ground, and the environment was suburban with 2–6 floor buildings. One mobile transmitter and one interferer were present on the air simultaneously. The angular separation between the two transmitters was small and never exceeded ten degrees. The average distance to the mobile transmitter of interest was about one kilometer, and the distance to the interferer was about 500 meters. The SNR was high, both transmitters traveled at speeds 0–50 km/h and there was typically no line-of-sight between the transmitters and the receiving dual polarized antenna.

Results from processing 20000 data bursts are shown in Figure 2.6. Both transmitters were synchronized so that the bursts overlapped completely. The 26 bit long training sequence was used to estimate the parameters required for the sequence detector. An unstructured approach was taken in the sense that $\mathbf{F}_P$ and $\mathcal{W}(\mathcal{A}_P)$ were estimated from a least squares fit and the covariance matrix of the residuals was used as an estimate of $\mathbf{Q}_P$, see also [26]. Burst synchronization was done as described in [41].

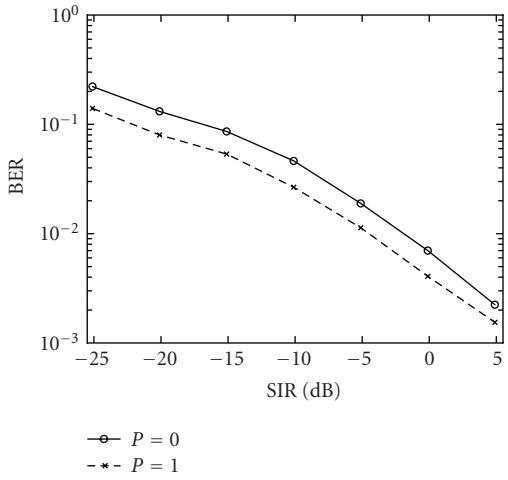

FIGURE 2.6. Experimental data, dual polarized sector antenna, $N_R = 2$, and one interferer.

As can be seen from Figure 2.6, a gain of 3–5 dB was observed at BER between 1% and 10% for spatiotemporal IRC as compared to space-only IRC. The time dispersion was probably small, and this may explain the modest gains, as compared to the very large gains demonstrated in the simulations when spatiotemporal interference rejection was compared to space-only interference rejection.

2.7. Interference rejection combining for WCDMA

Third-generation systems based on wideband code division multiple access (WCDMA) are currently being deployed around the world [45]. System performance in terms of coverage and capacity is affected by interference, and it is therefore of interest to consider advanced receiver algorithms that offer interference rejection. In addition to multiple access interference from other users operating on the same frequency band, there can be other terms of interference, referred to herein as external interference (EI). Examples of EI include ACI from adjacent carriers including the TDD mode and other communication systems as well as interference from narrowband communication systems operating in the same frequency band or causing intermodulation products. EI may in principle affect the coverage and capacity already at low loads, and it can therefore be of interest to consider interference rejection already at an early stage of system deployment.

Sequence estimators are typically used in GSM/EDGE to handle ISI, and the use of a VAR model as described in the previous sections represents a possible way to evolve such a receiver structure to include spatiotemporal IRC. The FDD mode of WCDMA is based on DS-CDMA with long aperiodic spreading codes and commonly RAKE receivers are used to handle time dispersive radio channels. The basic receiver structure thus differs from GSM/EDGE, and the approach taken herein to spatiotemporal IRC for WCDMA is therefore different as well. Common

for the two cases is that both spatial and temporal correlations of the interference are exploited in a conventional receiver structure. The present section is thus a complement to the previous sections outlining a possible approach for WCDMA.

Commonly, a RAKE receiver with a limited number of fingers is used in WCDMA. A delay is associated with each finger, and the receiver will for each finger despread the received signal by correlating it with the spreading waveform appropriately delayed [30, 31, 32, 45]. We assume that F delay estimates are used and that the signals received by all antennas are despread for each finger. The N_{R} despread samples associated with finger f for symbol n may then be modeled as

$$\mathbf{z}_f[n] = \mathbf{h}_f b[n] + \mathbf{j}_f[n], \tag{2.34}$$

where $\mathbf{h}_f$ represents the channels of finger f, $b[n]$ models the transmitted symbol, and $\mathbf{j}_f[n]$ is despread interference and noise. We define the $N_{\mathrm{R}}F \times 1$ vectors $\vec{\mathbf{z}}[n]$, $\vec{\mathbf{h}}$, and $\vec{\mathbf{j}}[n]$, as

$$\begin{aligned} \vec{\mathbf{z}}[n] &= \begin{bmatrix} \mathbf{z}_1^T[n] & \mathbf{z}_2^T[n] & \cdots & \mathbf{z}_F^T[n] \end{bmatrix}^T, \\ \vec{\mathbf{h}} &= \begin{bmatrix} \mathbf{h}_1^T & \mathbf{h}_2^T & \cdots & \mathbf{h}_F^T \end{bmatrix}^T, \\ \vec{\mathbf{j}}[n] &= \begin{bmatrix} \mathbf{j}_1^T[n] & \mathbf{j}_2^T[n] & \cdots & \mathbf{j}_F^T[n] \end{bmatrix}^T, \end{aligned} \tag{2.35}$$

and define the covariance matrix of the despread noise and interference $\boldsymbol{\mathcal{Q}}$ as

$$\boldsymbol{\mathcal{Q}} = \mathrm{E}\{\vec{\mathbf{z}}[n]\vec{\mathbf{z}}^*[n]\}. \tag{2.36}$$

The expectation is evaluated with respect to the interfering data symbols and scrambling codes which are modeled as sequences of independent QPSK symbols. Further details on this data model, including expressions for the covariance matrix and the resulting channel, may be found in [31] for the downlink with a single antenna and for the uplink with multiple antennas in [30, 32]. The RAKE receiver forms a decision variable as

$$\hat{b}[n] = \vec{\mathbf{w}}^* \vec{\mathbf{z}}[n], \tag{2.37}$$

from which the transmitted symbol and bits may be detected. The conventional RAKE receiver assumes that the despread noise and interference of different fingers is uncorrelated. Combining weights can then be expressed as

$$\vec{\mathbf{w}} = \left(\boldsymbol{\mathcal{Q}} \odot \mathbf{I}_{N_{\mathrm{R}}F}\right)^{-1} \vec{\mathbf{h}}, \tag{2.38}$$

where $\odot$ denotes the element-by-element matrix product. Further, a space-only IRC RAKE, as described in, for example, [30, 45], assumes that the covariance matrix is block diagonal. Only the spatial correlation of noise and interference is then handled. However, narrowband interference and interfering wideband signals that have propagated through multipath channels cause temporal correlation in the sense that the despread interference and noise of fingers with different delays is correlated. A RAKE receiver with spatiotemporal IRC will determine the combining weights as

$$\vec{\mathbf{w}}_{\mathrm{IRC}} = \mathcal{Q}^{-1}\vec{\mathbf{h}}. \tag{2.39}$$

As demonstrated in [30], large gains as compared to space-only interference rejection and conventional RAKE combining may be obtained for rejection of EI in the uplink, especially for cases with wideband EI when there are not enough spatial degrees of freedom. In this case, a similar behavior to that in Figure 2.1 can be observed. In the downlink, the orthogonality between the spreading codes of different channels is destroyed and the despread interference of different channels fingers is correlated in time dispersive multipath channels. Significant gains may then be obtained with a single-antenna generalized RAKE receiver as shown in [31]. Another interesting observation is that in the case of temporally correlated interference, it is advantageous to use more fingers than there are resolvable rays in the channel.

2.8. Concluding remarks

Spatiotemporal interference rejection combining for burst oriented systems such as GSM was considered, and an autoregressive model was introduced to capture both the spatial and temporal correlation of the interference. We saw that complete interference rejection is possible if the number of interferers is less than the number of antennas and the model order is chosen so that the interference is confined to a subspace in the spatiotemporal model formulated. The interference model was then incorporated into a maximum likelihood sequence estimator and two metrics were presented. Numerical examples demonstrated significant performance gains compared to space-only processing in interference-limited scenarios at the cost of an exponential increase in complexity of the sequence estimator. Therefore, reduced complexity sequence estimators were introduced, and numerical examples illustrated that noise sensitivity can be traded for improved interference rejection capabilities. Thus, spatiotemporal interference rejection can be performed with roughly the same order of complexity as space-only interference rejection. For GSM, we also showed some experimental results and discussed implementation aspects, such as estimation of the parameters for the detector, see also [42, 44].

Finally, we also outlined interference rejection combining for WCDMA. In this case, the conventional RAKE receiver may be generalized to account for spatially and temporally correlated interference.

Abbreviations

BER	Bit error rate
BPSK	Binary phase-shift keying
CDMA	Code division multiple access
DCS	Digital cellular system
DDFSE	Delayed decision-feedback sequence estimator
DS-CDMA	Direct-sequence code division multiple access
EDGE	Enhanced data for global evolution
FDD	Frequency division duplex
GSM	Global system for mobile communications
GVA	Generalized Viterbi algorithm
IRC	Interference rejection combining
ISI	Intersymbol interference
MIMO	Multi-input multi-output
MISO	Multiple-input single-output
MSK	Minimum shift keying
QPSK	Quadrature phase-shift keying
SIR	Signal-to-interference ratio
SNR	Signal-to-interference and noise ratio
TDMA	Time division multiple access
VAR	Vector autoregressive
WCDMA	Wideband code-division multiple access

Bibliography

[1] G. Forney Jr., "Maximum-likelihood sequence estimation of digital sequences in the presence of intersymbol interference," *IEEE Trans. Inform. Theory*, vol. 18, no. 3, pp. 363–378, 1972.

[2] A. Duel-Hallen and C. Heegard, "Delayed decision-feedback sequence estimation," *IEEE Trans. Commun.*, vol. 37, no. 5, pp. 428–436, 1989.

[3] J. Modestino and M. Eyuboglu, "Integrated multielement receiver structures for spatially distributed interference channels," *IEEE Trans. Inform. Theory*, vol. 32, no. 2, pp. 195–219, 1986.

[4] G. E. Bottomley and K. Jamal, "Adaptive arrays and MLSE equalization," in *IEEE 45th Vehicular Technology Conference*, vol. 1, pp. 50–54, Chicago, Ill, USA, July 1995.

[5] G. E. Bottomley, K. J. Molnar, and S. Chennakeshu, "Interference cancellation with an array processing MLSE receiver," *IEEE Trans. Veh. Technol.*, vol. 48, no. 5, pp. 1321–1331, 1999.

[6] P. Chevalier, F. Pipon, J.-J. Monot, and C. Demeure, "Smart antennas for the GSM system: experimental results for a mobile reception," in *IEEE 47th Vehicular Technology Conference*, vol. 3, pp. 1572–1576, Phoenix, Ariz, USA, May 1997.

[7] S. N. Diggavi and A. Paulraj, "Performance of multisensor adaptive MLSE in fading channels," in *IEEE 47th Vehicular Technology Conference*, vol. 3, pp. 2148–2152, Phoenix, Ariz, USA, May 1997.

[8] K. J. Molnar and G. E. Bottomley, "Adaptive array processing MLSE receivers for TDMA digital cellular/PCS communications," *IEEE J. Select. Areas Commun.*, vol. 16, no. 8, pp. 1340–1351, 1998.

[9] F. Pipon, P. Chevalier, P. Vila, and D. Pirez, "Practical implementation of a multichannel equalizer for a propagation with ISI and CCI—application to a GSM link," in *IEEE 47th Vehicular Technology Conference*, vol. 2, pp. 889–893, Phoenix, Ariz, USA, May 1997.

[10] P. Vila, F. Pipon, D. Pirez, and L. Fety, "MLSE antenna diversity equalization of a jammed frequency-selective fading channel," in *Seventh European Signal Processing Conference (EUSIPCO '94)*, pp. 1516–1519, Edinburgh, UK, September 1994.

[11] G. Ungerboeck, "Adaptive maximum-likelihood receiver for carrier-modulated data-transmission systems," *IEEE Trans. Commun.*, vol. 22, no. 5, pp. 624–636, 1974.

[12] W. van Etten, "Maximum likelihood receiver for multiple channel transmission systems," *IEEE Trans. Commun.*, vol. 24, no. 2, pp. 276–283, 1976.

[13] M. Escartin and P. A. Ranta, "Interference rejection with a small antenna array at the mobile scattering environment," in *First IEEE Signal Processing Workshop on Signal Processing Advances in Wireless Communications*, pp. 165–168, Paris, France, April 1997.

[14] G. E. Bottomley and S. Chennakeshu, "Unification of MLSE receivers and extension to time-varying channels," *IEEE Trans. Commun.*, vol. 46, no. 4, pp. 464–472, 1998.

[15] J.-W. Liang, J.-T. Chen, and A. J. Paulraj, "A two-stage hybrid approach for CCI/ISI reduction with space-time processing," *IEEE Commun. Lett.*, vol. 1, no. 6, pp. 163–165, 1997.

[16] D. T. M. Slock, "Spatio-temporal training-sequence based channel equalization and adaptive interference cancellation," in *IEEE International Conference on Acoustics, Speech, and Signal Processing (ICASSP '96)*, vol. 5, pp. 2714–2717, Atlanta, Ga, USA, May 1996.

[17] H. Trigui and D. T. M. Slock, "Cochannel interference cancellation within the current GSM standard," in *IEEE International Conference on Universal Personal Communications (ICUPC '98)*, vol. 1, pp. 511–515, Florence, Italy, October 1998.

[18] S. L. Ariyavisitakul, J. H. Winters, and I. Lee, "Optimum space-time processors with dispersive interference: unified analysis and required filter span," *IEEE Trans. Commun.*, vol. 47, no. 7, pp. 1073–1083, 1999.

[19] S. L. Ariyavisitakul, J. H. Winters, and N. R. Sollenberger, "Joint equalization and interference suppression for high data rate wireless systems," *IEEE J. Select. Areas Commun.*, vol. 18, no. 7, pp. 1214–1220, 2000.

[20] R. A. Iltis, "A GLRT-based spread-spectrum receiver for joint channel estimation and interference suppression," *IEEE Trans. Commun.*, vol. 37, no. 3, pp. 277–288, 1989.

[21] A. L. Swindlehurst and P. Stoica, "Maximum likelihood methods in radar array signal processing," *Proc. IEEE*, vol. 86, no. 2, pp. 421–441, 1998.

[22] K. Abed-Meraim, P. Loubaton, and E. Moulines, "A subspace algorithm for certain blind identification problems," *IEEE Trans. Inform. Theory*, vol. 43, no. 2, pp. 499–511, 1997.

[23] A. Gorokhov, P. Loubaton, and E. Moulines, "Second order blind equalization in multiple input multiple output FIR systems: a weighted least squares approach," in *IEEE International Conference on Acoustics, Speech, and Signal Processing (ICASSP '96)*, vol. 5, pp. 2415–2418, Atlanta, Ga, USA, May 1996.

[24] D. T. M. Slock, "Blind fractionally-spaced equalization, perfect-reconstruction filter banks and multichannel linear prediction," in *IEEE International Conference on Acoustics, Speech, and Signal Processing (ICASSP '94)*, vol. 4, pp. 585–588, Adelaide, SA, Australia, April 1994.

[25] D. Astély, *Spatial and spatio-temporal processing with antenna arrays in wireless systems*, Ph.D. thesis, Royal Institute of Technology, Stockholm, Sweden, 1999.

[26] D. Asztély and B. Ottersten, "MLSE and spatio-temporal interference rejection combining with antenna arrays," in *Ninth European Signal Processing Conference (EUSIPCO '98)*, pp. 1341–1344, Rhodes, Greece, September 1998.

[27] P. Jung, "Performance evaluation of a novel M-detector for coherent receiver antenna diversity in a GSM-type mobile radio system," *IEEE J. Select. Areas Commun.*, vol. 13, no. 1, pp. 80–88, 1995.

[28] R. Krenz and K. Wesolowski, "Comparative study of space-diversity techniques for MLSE receivers in mobile radio," *IEEE Trans. Veh. Technol.*, vol. 46, no. 3, pp. 653–663, 1997.

[29] T. Hashimoto, "A list-type reduced-constraint generalization of the Viterbi algorithm," *IEEE Trans. Inform. Theory*, vol. 33, no. 6, pp. 866–876, 1987.

[30] D. Astély and A. Artamo, "Uplink spatio-temporal interference rejection combining for WCDMA," in *Third IEEE Workshop on Signal Processing Advances in Wireless Communications (SPAWC '01)*, pp. 326–329, Taiwan, China, March 2001.

[31] G. E. Bottomley, T. Ottosson, and Y.-P. E. Wang, "A generalized RAKE receiver for interference suppression," *IEEE J. Select. Areas Commun.*, vol. 18, no. 8, pp. 1536–1545, 2000.

[32] T. F. Wong, T. M. Lok, J. S. Lehnert, and M. D. Zoltowski, "A linear receiver for direct-sequence spread-spectrum multiple-access systems with antenna arrays and blind adaptation," *IEEE Trans. Inform. Theory*, vol. 44, no. 2, pp. 659–676, 1998.

[33] S. Y. Miller and S. C. Schwartz, "Integrated spatial-temporal detectors for asynchronous Gaussian multiple-access channels," *IEEE Trans. Commun.*, vol. 43, no. 234, pp. 396–411, 1995.

[34] S. W. Wales, "Technique for cochannel interference suppression in TDMA mobile radio systems," *IEE Proceedings Communications*, vol. 142, no. 2, pp. 106–114, 1995.

[35] M. Kristensson, B. Ottersten, and D. Slock, "Blind subspace identification of a BPSK communication channel," in *Conference Record of the Thirtieth Asilomar Conference on Signals, Systems and Computers*, vol. 2, pp. 828–832, Pacific Grove, Calif, USA, November 1996.

[36] S. Haykin, *Adaptive Filter Theory*, Prentice Hall International, Englewood Cliffs, NJ, USA, 3rd edition, 1996.

[37] A. Hafeez and W. E. Stark, "Decision feedback sequence estimation for unwhitened ISI channels with applications to multiuser detection," *IEEE J. Select. Areas Commun.*, vol. 16, no. 9, pp. 1785–1795, 1998.

[38] J. Anderson and S. Mohan, "Sequential coding algorithms: A survey and cost analysis," *IEEE Trans. Commun.*, vol. 32, no. 2, pp. 169–176, 1984.

[39] S. Craig and J. Axnäs, "A system performance evaluation of 2-branch interference rejection combining," in *IEEE 56th Vehicular Technology Conference (VTC 2002-Fall)*, vol. 3, pp. 1887–1891, Vancouver, BC, Canada, September 2002.

[40] M. Austin, Ed., "SAIC and synchronized networks for increased GSM capacity," Tech. Rep., 3G Americas, Bellevue, Wash, USA, September 2003, white paper.

[41] D. Astély, A. Jakobsson, and A. L. Swindlehurst, "Burst synchronization on unknown frequency selective channels with co-channel interference using an antenna array," in *IEEE 49th Vehicular Technology Conference*, vol. 3, pp. 2363–2367, Houston, Tex, USA, May 1999.

[42] A. M. Kuzminskiy, C. Luschi, and P. Strauch, "Comparison of linear and MLSE spatio-temporal interference rejection combining with an antenna array in a GSM system," in *IEEE 51st Vehicular Technology Conference (VTC 2000-Spring)*, vol. 1, pp. 172–176, Tokyo, Japan, May 2000.

[43] G. Klang, D. Astély, and B. Ottersten, "Structured spatio-temporal interference rejection with antenna arrays," in *IEEE 49th Vehicular Technology Conference*, vol. 1, pp. 841–845, Houston, Tex, USA, May 1999.

[44] G. Klang and B. Ottersten, "Structured semi-blind interference rejection in dispersive multichannel systems," *IEEE Trans. Signal Processing*, vol. 50, no. 8, pp. 2027–2036, 2002.

[45] H. Holma and A. Toskala, Eds., *WCDMA for UMTS: Radio Access for Third Generation Mobile Communications*, John Wiley & Sons, New York, NY, USA, 2000.

David Astély: Ericsson Research, 164 80 Stockholm, Sweden

Email: david.astely@ericsson.com

Björn Ottersten: Department of Signals, Sensors and Systems, Royal Institute of Technology, 100 44 Stockholm, Sweden

Email: bjorn.ottersten@s3.kth.se

3 Subspace methods for space-time processing

M. Nicoli and U. Spagnolini

In wireless communication systems, where the space-time propagation channel is time-varying, block-by-block transmission is adopted and training symbols are inserted in each block to allow the estimation of the changing channel. The accuracy of the training-based estimate, usually performed on a block-by-block basis, is known to depend on the ratio between the number of channel unknowns and the number of pilot symbols within the block. As the reliability of channel state information is critical in space-time receivers, methods have been widely investigated in the last years to improve the channel estimate accuracy, such as parametric approaches to reduce the number of relevant channel parameters or decision-based iterative techniques to extend the training set with hard- or soft-valued data symbols. In the sequel we propose subspace-based methods that exploit both approaches and are designed for the estimation of a single-input multiple-output (SIMO) channel between a single-antenna mobile transmitter and a multiple-antenna receiver.

Two different approaches can be identified in the literature for parametric estimation of the multipath channel: structured methods for angle and delay estimation [1, 2, 3] and unstructured reduced-rank (RR) techniques [4, 5, 6, 7, 8]. Here we focus on the RR approach as it is the preferred one in terms of computational complexity and stability. RR methods parameterize the space-time channel in terms of unstructured low-rank matrices whose column space equals the subspace spanned by the spatial and/or temporal signatures of the multipath components of the channel. These subspaces, here referred to as the spatial and temporal subspaces, can be related either to instantaneous-fading parameters of the channel (short-term subspaces) or to slowly-varying features only (long-term subspaces). In the first case the channel estimate is derived by single-block processing (SB, subspace methods [4, 8]), while the second case multiblock observations are required (MB, subspace methods [9]).

The MB approach is based on the recognition that in mobile wireless systems the multipath channel is characterized by fast-varying features, such as fading amplitudes (that change from block to block), and slowly-varying parameters, such as second-order statistics of fading, delays, and angles (that can be considered as

constant over a large number of blocks). In subspace methods the quasistationarity of the above-mentioned parameters is converted into the invariance of the corresponding spatial-temporal channel subspaces. The latter are estimated from multiple blocks, while the fast-varying parameters are obtained on a block-by-block basis. As the accuracy of the estimate of the subspaces increases with the number of blocks, the parameters that affect the variance of the overall channel estimate reduces asymptotically to the fast-varying features only. This leads to a significant reduction of the number of parameters which is particularly relevant in radio environments where the angle-delay spread is small compared to the system resolution.

Further improvements of the estimate accuracy are obtained by extending the training set with hard- or soft-valued data symbols. This is feasible in iterative receivers where information symbols detected in previous iterations can be fed back to the channel estimator and used as additional known data. It is well known how soft decisions can be more effective than the hard ones, as soft information allows to account for the reliability of the estimate and thus to avoid the error propagation effects that usually arise in decision feedback. Focusing therefore on soft-iterative receivers [10] where a priori information on the information-bearing symbols are available at the channel estimator, we propose a new version of the MB subspace method that exploits both training and soft-valued data symbols. For perfect a priori information (i.e., at convergence of the iterative approach), the accuracy of the estimate is the same that would be obtained from an entire block of training symbols.

In closing this introduction, we remark that all the SB and MB subspace methods proposed in this section (either training- or decision-based) are sufficiently general to be adopted in any block-based transmission system (such as TDMA, CDMA, OFDM, or hybrid TD-CDMA, multicarrier CDMA, etc.), with single or multiple antennas at the transmitter and receiver (e.g., SISO, SIMO, or MIMO). The presentation here is carried out at first for the uplink of a TDMA SIMO system, as this is the most intuitive case. An application to time-slotted CDMA systems, such as the third-generation TD-SCDMA mobile standards [11, 12], is proposed in the final part of the section. The extension to OFDM systems can be found in [13].

3.1. System description and problem formulation

3.1.1. Signal model

We consider a block-based transmission system where a mobile terminal transmits data blocks by a single-antenna transmitter to a multiple-antenna receiver through a frequency-selective fading channel. As routinely employed, each block includes a known training sequence to be used for channel estimation purposes (Figure 3.1).

A discrete-time baseband model for the signals received within each block is derived by sampling at the symbol rate $1/T$ the output of a matched filter at each

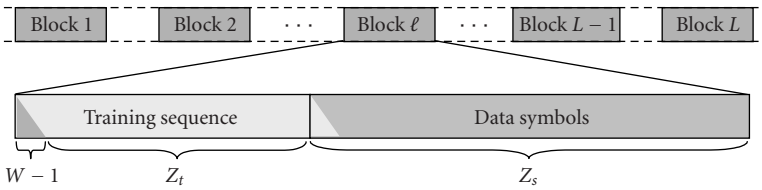

FIGURE 3.1. Block-by-block transmission system.

of the N receiving antennas. The $N \times 1$ resulting signal is

$$\mathbf{r}(i;\ell) = \mathbf{H}(\ell)\mathbf{s}(i;\ell) + \mathbf{v}(i;\ell), \tag{3.1}$$

where $\mathbf{s}(i;\ell) = [s(i;\ell) \quad s(i-1;\ell) \quad \cdots \quad s(i-W+1;\ell)]^{\mathrm{T}}$ collects W transmitted symbols, $s(i;\ell)$ denotes the ith (either training or information) complex-valued symbol within the ℓth block, chosen from a finite alphabet set. As illustrated in Figure 3.1, the sequence transmitted within the block contains $Z_{\mathrm{t}} + W - 1$ known training symbols (for $i = -W+1, \ldots, Z_{\mathrm{t}} - 1$) and Z_{s} data symbols (for $i = Z_{\mathrm{t}}, \ldots, Z_{\mathrm{s}} + Z_{\mathrm{t}} - 1$). The $N \times 1$ additive noise vector $\mathbf{v}(i;\ell) \sim \mathcal{N}_{\mathbb{C}}(\mathbf{0}, \mathbf{Q})$ is assumed to be temporally uncorrelated but spatially correlated (to account for cochannel interference) with correlation function

$$\mathrm{E}\left[\mathbf{v}(i;\ell)\mathbf{v}^{\mathrm{H}}(i-k;\ell-m)\right] = \delta(k)\delta(m)\mathbf{Q}, \tag{3.2}$$

where $\mathbf{Q}$ denotes the unknown spatial-covariance matrix. The latter is positive definite, its diagonal entries $[\mathbf{Q}]_{n,n} = \sigma_v^2$ for $n = 1, \ldots, N$ represent the noise power at each antenna element.

The $N \times W$ space-time matrix $\mathbf{H}(\ell)$ describes the discrete-time channel impulse response for the SIMO link. It accounts for the array response, the effects of path fading, the symbol waveform used for transmission, and the matched filter at the receiver. Though $\mathbf{H}(\ell)$ is generally time-varying, in many practical situations its variations within the block interval can be neglected as the block duration is selected shorter than the channel coherence time. Therefore, we can reasonably approximate $\mathbf{H}(\ell)$ as invariant within the block but varying from block to block (block-fading channel).

This section is focused on the following topics: estimation of the channels $\{\mathbf{H}(\ell)\}_{\ell=1}^{L}$ and the noise covariance matrix $\mathbf{Q}$ from the training signals received in L different blocks, by exploiting the knowledge of the transmitted symbols $\{s(i;\ell)\}$; detection of the information-bearing symbols $\{s(i;\ell)\}$ contained in the data fields of each block, by using the estimate of the channel responses. Channel estimation is performed by exploiting structural properties of the multipath propagation that are described below.

3.1.2. Algebraic structure of the channel

According to the multipath model for propagation, $\mathbf{H}(\ell)$ is modelled as the superposition of P paths, the ith path being characterized by direction of arrival ϑ_i, delay τ_i, and complex-valued amplitude $\alpha_i(\ell)$. As discussed in [9], in practical systems the variations of angles and delays stay below the receiver angular-temporal resolution for several blocks, thus the pair $\{\vartheta_i, \tau_i\}$ can be reasonably assumed as constant for $L \gg 1$ blocks (the value of L depends on the terminal speed and multipath geometry). On the other hand, the fading amplitude $\alpha_i(\ell)$ is fast varying and it randomly changes from block to block due to the terminal mobility. According to these assumptions the channel matrix can be written as

$$\mathbf{H}(\ell) = \sum_{p=1}^{P} \alpha_p(\ell)\mathbf{a}(\vartheta_p)\mathbf{g}^{\mathrm{T}}(\tau_p) = \mathbf{A}\mathbf{D}(\ell)\mathbf{G}^{\mathrm{T}}, \tag{3.3}$$

where the $W \times 1$ real-valued vector

$$\mathbf{g}(\tau_p) = \begin{bmatrix} g(-\tau_p) & g(T-\tau_p) & \cdots & g((W-1)T-\tau_p) \end{bmatrix}^{\mathrm{T}} \tag{3.4}$$

contains samples of the delayed waveform $g(\tau)$, that represents the convolution between the transmitter and receiver filters. The complex-valued vector $\mathbf{a}(\vartheta_p) = [a_1(\vartheta_p) \quad \cdots \quad a_N(\vartheta_p)]^{\mathrm{T}}$ denotes the $N \times 1$ array response to a plane-wave impinging from the direction ϑ_p. For instance, for a uniform linear array of half-wavelength-spaced omnidirectional antennas, the entries of $\mathbf{a}(\vartheta_p)$ are $a_n(\vartheta_p) = \exp(-j\pi(n-1)\sin\vartheta_p)$ [14]. By collecting the set of P temporal/spatial vectors into the temporal/spatial matrices

$$\begin{aligned} \mathbf{G} &= \begin{bmatrix} \mathbf{g}(\tau_1) & \cdots & \mathbf{g}(\tau_P) \end{bmatrix}, \\ \mathbf{A} &= \begin{bmatrix} \mathbf{a}(\vartheta_1) & \cdots & \mathbf{a}(\vartheta_P) \end{bmatrix}, \end{aligned} \tag{3.5}$$

the multipath formulation for the space-time channel matrix simplifies as indicated in the third member of (3.3), where $\mathbf{D}(\ell) = \mathrm{diag}[\alpha_1(\ell), \ldots, \alpha_P(\ell)]$ embodies the fading amplitudes. The latter are assumed to follow the WSSUS [15] model and to be uncorrelated from block to block:

$$\mathbf{C}_\alpha(m) = \mathrm{E}\left[\mathbf{D}(\ell+m)\mathbf{D}^{\mathrm{H}}(\ell)\right] = \delta(m)\,\mathrm{diag}\left[\sigma_1^2, \ldots, \sigma_P^2\right] \tag{3.6}$$

(see [9] for the generalization to correlated fading).

In order to avoid the computationally expensive estimation of the angle-delay pairs, in the following we reparameterize the channel (3.3) in terms of unstructured block-fading or stationary matrices. Let the spatial (q_{S}) and the temporal (q_{T}) diversity orders be defined as, respectively,

$$q_{\mathrm{S}} = \mathrm{rank}[\mathbf{A}] \leq N, \tag{3.7a}$$

$$q_{\mathrm{T}} = \mathrm{rank}[\mathbf{G}] \leq W. \tag{3.7b}$$

As a rule of thumb, the first rank order accounts for the number of angles that can be resolved in $\vartheta = [\vartheta_1, \ldots, \vartheta_P]$ (given the array aperture), while the second one equals the number of the resolvable delays in $\tau = [\tau_1, \ldots, \tau_P]$ (given the bandwidth of the transmitted signal). Though the number of paths can be very large, in many practical situations the diversity orders depend only on few groups of leading scatterers with moderate angle-delay spread so that it is $q_S < N$ and/or $q_T < W$. Under these reduced-rank constraints, the multipath channel matrix (3.3) can be rewritten as the combination of three full-rank matrices: the spatial and temporal stationary components $\mathbf{U}_S$ ($N \times q_S$) and $\mathbf{U}_T$ ($W \times q_T$), and the block-fading component $\mathbf{\Gamma}(\ell)$ ($q_S \times q_T$). The new channel model is

$$\mathbf{H}(\ell) = \mathbf{U}_S \mathbf{\Gamma}(\ell) \mathbf{U}_T^H. \tag{3.8}$$

Differently from $\mathbf{A}$ and $\mathbf{G}$ in (3.3), here $\mathbf{U}_S$ and $\mathbf{U}_T$ are unstructured matrices, whose column space equals the subspace spanned by the stationary spatial and temporal responses of the multipath channel, namely the *long-term spatial subspace* $\mathcal{R}[\mathbf{U}_S] = \mathcal{R}[\mathbf{A}]$ and the *long-term temporal subspace* $\mathcal{R}[\mathbf{U}_T] = \mathcal{R}[\mathbf{G}]$ for the channel matrix $\mathbf{H}(\ell)$.

An example of the parameterization (3.8) can be easily obtained from the model (3.3) by considering the singular value decompositions $\mathbf{A} = \mathbf{U}_S \mathbf{\Sigma}_S \mathbf{V}_S^H$, $\mathbf{G} = \mathbf{U}_T \mathbf{\Sigma}_T \mathbf{V}_T^H$, and by further defining $\mathbf{\Gamma}(\ell) = \mathbf{\Sigma}_S \mathbf{V}_S^H \mathbf{D}(\ell) \mathbf{V}_T \mathbf{\Sigma}_T^H$. In this case, $\mathbf{U}_S$ and $\mathbf{U}_T$ are orthonormal bases for the spatial and the temporal subspaces, respectively.

3.2. Training-based subspace methods for channel estimation

The discrete-time model (3.1) for the signals received during the training period of the ℓth block is rewritten into the standard form

$$\mathbf{R}_t(\ell) = \mathbf{H}(\ell) \mathbf{S}_t + \mathbf{V}_t(\ell), \tag{3.9}$$

by gathering the received signals into the $N \times Z_t$ matrix

$$\mathbf{R}_t(\ell) = \begin{bmatrix} \mathbf{r}(0;\ell) & \cdots & \mathbf{r}(Z_t - 1;\ell) \end{bmatrix} \tag{3.10}$$

(the first $W - 1$ samples are discarded as affected by the interference from the preceding data symbols). The $W \times Z_t$ Toeplitz matrix $\mathbf{S}_t = [\mathbf{s}(0;\ell) \quad \cdots \quad \mathbf{s}(Z_t - 1;\ell)]$ represents the convolution of the channel with the training sequence $\{s(i;\ell)\}_{i=-W+1}^{Z_t-1}$ that is assumed to be the same for all blocks. The $N \times Z_t$ matrix

$$\mathbf{V}_t(\ell) = \begin{bmatrix} \mathbf{v}(0;\ell) & \cdots & \mathbf{v}(Z_t - 1;\ell) \end{bmatrix} \tag{3.11}$$

collects the noise samples. We further assume that $Z_t > N + W$.

3.2.1. Subspace-based estimation

The problem addressed herein is the maximum likelihood estimation (MLE) of the channel matrices $\{\mathbf{H}(\ell)\}_{\ell=1}^{L}$ from the received signals $\{\mathbf{R}_{\mathrm{t}}(\ell)\}_{\ell=1}^{L}$, under the constraint (3.8), for known rank orders $\{q_{\mathrm{S}}, q_{\mathrm{T}}\}$ and unknown noise spatial covariance $\mathbf{Q}$.

For $q_{\mathrm{S}} = N$ and $q_{\mathrm{T}} = W$, the MLE reduces to the unconstrained or full-rank (FR) MLE estimate [16]

$$\mathbf{H}_{\mathrm{u}}(\ell) = \mathbf{R}_{\mathrm{t}}(\ell)\mathbf{S}_{\mathrm{t}}^{\mathrm{H}}\mathbf{C}_{\mathrm{t}}^{-1}, \quad \ell = 1, \ldots, L, \tag{3.12}$$

where $\mathbf{C}_{\mathrm{t}} = \mathbf{S}_{\mathrm{t}}\mathbf{S}_{\mathrm{t}}^{\mathrm{H}}$ is the (positive definite) correlation matrix of the training sequence. The estimate (3.12) is unbiased with covariance matrix [16]

$$\mathbf{C}_{\mathrm{u}} = \mathrm{Cov}\left[\mathbf{h}_{\mathrm{u}}(\ell)\right] = \left(\mathbf{C}_{\mathrm{t}}^{-1}\right)^{*} \otimes \mathbf{Q}, \tag{3.13}$$

where $\mathbf{h}_{\mathrm{u}}(\ell) = \mathrm{vec}[\mathbf{H}_{\mathrm{u}}(\ell)]$ is the vectorized channel estimate.

For any $q_{\mathrm{S}} \leq N$ and $q_{\mathrm{T}} \leq W$, it can be shown [17, 18] that the MLE equals asymptotically (for $Z_{\mathrm{t}} \to \infty$) the minimizer of

$$\mathcal{F} = \sum_{\ell=1}^{L} \mathrm{tr}\left[\mathbf{Q}_{\mathrm{u},L}^{-1}\left(\mathbf{H}_{\mathrm{u}}(\ell) - \mathbf{U}_{\mathrm{S}}\boldsymbol{\Gamma}(\ell)\mathbf{U}_{\mathrm{T}}^{\mathrm{H}}\right)\mathbf{C}_{\mathrm{t}}\left(\mathbf{H}_{\mathrm{u}}(\ell) - \mathbf{U}_{\mathrm{S}}\boldsymbol{\Gamma}(\ell)\mathbf{U}_{\mathrm{T}}^{\mathrm{H}}\right)^{\mathrm{H}}\right], \tag{3.14}$$

where $\mathbf{Q}_{\mathrm{u},L}$ is the unconstrained estimate (assumed to be positive definite) for the noise covariance matrix

$$\mathbf{Q}_{\mathrm{u},L} = \frac{1}{Z_{\mathrm{t}}L}\sum_{\ell=1}^{L}\left(\mathbf{R}_{\mathrm{t}}(\ell) - \mathbf{H}_{\mathrm{u}}(\ell)\mathbf{S}_{\mathrm{t}}\right)\left(\mathbf{R}_{\mathrm{t}}(\ell) - \mathbf{H}_{\mathrm{u}}(\ell)\mathbf{S}_{\mathrm{t}}\right)^{\mathrm{H}}. \tag{3.15}$$

It follows that loss function (3.14) coincides [19], apart from unimportant constant terms, with the negative log-likelihood function for the model

$$\mathbf{H}_{\mathrm{u}}(\ell) = \mathbf{U}_{\mathrm{S}}\boldsymbol{\Gamma}(\ell)\mathbf{U}_{\mathrm{T}}^{\mathrm{H}} + \Delta\mathbf{H}_{\mathrm{u}}(\ell), \quad \ell = 1, \ldots, L, \tag{3.16}$$

where the zero-mean Gaussian noise $\Delta\mathbf{H}_{\mathrm{u}}(\ell)$ is now *spatially* and *temporally* correlated, with spatial covariance $\mathbf{Q} = \mathbf{Q}_{\mathrm{u},\infty}$ and temporal covariance $\mathbf{C}_{\mathrm{t}}^{-1}$ (see (3.13)). As a consequence, the constrained MLE can be seen as a parametric reestimate from the preliminary noisy estimates $\{\mathbf{H}_{\mathrm{u}}(\ell)\}_{\ell=1}^{L}$ under the parameterization (3.8).

In the sequel, the minimization of loss function (3.14) with respect to channel parameters (3.8) is performed at first for $L = 1$ and then for $L > 1$. For single-block (SB) processing the constrained MLE coincides with the well-known reduced-rank (RR) estimate [4], while for multiblock (MB) processing the solution is the MB space-time (MB-ST) estimate [9].

In both cases, the reestimate is obtained from the preliminary estimates $\{\mathbf{H}_{\mathrm{u}}(\ell)\}_{\ell=1}^{L}$ through the following operations: (i) weighting of the unconstrained

channel estimate by the spatial and temporal factors, $\mathbf{W}_{S,L} = \mathbf{Q}_{u,L}^{-H/2}$ and $\mathbf{W}_T = \mathbf{C}_t^{1/2}$, to get

$$\tilde{\mathbf{H}}_u(\ell) = \mathbf{W}_{S,L}\mathbf{H}_u(\ell)\mathbf{W}_T^H; \tag{3.17}$$

(ii) estimation of the long-short term spatial-temporal channel subspaces from $\{\tilde{\mathbf{H}}_u(\ell)\}_{\ell=1}^L$ and projection of each channel matrix $\tilde{\mathbf{H}}_u(\ell)$ onto the estimated subspaces; (iii) inverse weighting of the projected channel matrix to get the final estimate.

It is understood that the weighting operation is simply an asymptotic whitening of the preliminary estimate error $\Delta\mathbf{h}_u(\ell) = \text{vec}[\Delta\mathbf{H}_u(\ell)]$. For $Z_t \to \infty$, it is indeed $\mathbf{W}_{S,L} \to \mathbf{Q}^{-H/2}$ and the weighted estimate error

$$\Delta\tilde{\mathbf{h}}_u(\ell) = \text{vec}\left[\mathbf{W}_{S,L}\Delta\mathbf{H}_u(\ell)\mathbf{W}_T^H\right] = \left(\mathbf{W}_T^* \otimes \mathbf{W}_{S,L}\right)\Delta\mathbf{h}_u(\ell) \longrightarrow \mathbf{C}_u^{-H/2}\Delta\mathbf{h}_u(\ell) \tag{3.18}$$

has covariance $\text{Cov}[\Delta\tilde{\mathbf{h}}_u(\ell)] \to \mathbf{I}_{NW}$.

Single-block (SB) approach. For SB processing ($L = 1$) parameterization (3.8) is equivalent to the RR constraint:

$$q = \text{rank}\left[\mathbf{H}(\ell)\right] = \min\left(q_S, q_T\right) \le \min(N, W). \tag{3.19}$$

The constrained MLE equals in this case the block-by-block RR estimate [4] that can be expressed by any of the following equivalent formulations [8, 20]

$$\hat{\mathbf{H}}_{SB}(\ell) = \mathbf{W}_{S,1}^{-1}\hat{\mathbf{\Pi}}_S(\ell)\tilde{\mathbf{H}}_u(\ell)\mathbf{W}_T^{-H} = \mathbf{W}_{S,1}^{-1}\tilde{\mathbf{H}}_u(\ell)\hat{\mathbf{\Pi}}_T(\ell)\mathbf{W}_T^{-H}, \tag{3.20}$$

where $\hat{\mathbf{\Pi}}_S(\ell)$ and $\hat{\mathbf{\Pi}}_T(\ell)$ are the projectors onto the (short term) subspaces spanned by the q leading eigenvectors of, respectively, the spatial and temporal SB sample correlations:

$$\hat{\mathbf{C}}_{S,1} = \tilde{\mathbf{H}}_u(\ell)\tilde{\mathbf{H}}_u^H(\ell), \tag{3.21a}$$

$$\hat{\mathbf{C}}_{T,1} = \tilde{\mathbf{H}}_u^H(\ell)\tilde{\mathbf{H}}_u(\ell). \tag{3.21b}$$

Efficient implementations of estimate (3.20) can be found in [20]. Extensions of the RR approach to both spatially and temporally correlated noise are proposed in [21].

Multiblock (MB) approach. The MB estimate is an extension of the RR algorithm to MB processing ($L > 1$). With respect to the block-by-block estimation, the MB approach allows the estimation of both the spatial and temporal subspaces by differentiating between the spatial (q_S) and temporal (q_T) rank orders.

The MB space-time (MB-ST) MLE is obtained by minimizing loss function (3.14) with respect to the block-independent parameters $\{\mathbf{U}_S, \mathbf{U}_T\}$ and the block-dependent terms $\{\mathbf{\Gamma}(\ell)\}_{\ell=1}^L$. The solution is [9]

$$\hat{\mathbf{H}}_{MB}(\ell) = \mathbf{W}_{S,L}^{-1}\hat{\mathbf{\Pi}}_S\tilde{\mathbf{H}}_u(\ell)\hat{\mathbf{\Pi}}_T\mathbf{W}_T^{-1} \quad \text{for } \ell = 1, 2, \ldots, L, \tag{3.22}$$

where $\widehat{\mathbf{\Pi}}_{\mathrm{S}}$ and $\widehat{\mathbf{\Pi}}_{\mathrm{T}}$ represent the projectors onto the (long term) subspaces spanned by, respectively, the q_{S} principal eigenvectors of the spatial sample correlation $\widehat{\mathbf{C}}_{\mathrm{S},L}$ and the q_{T} principal eigenvectors of the temporal sample correlation $\widehat{\mathbf{C}}_{\mathrm{T},L}$:

$$\widehat{\mathbf{C}}_{\mathrm{S},L} = \frac{1}{L}\sum_{\ell=1}^{L} \tilde{\mathbf{H}}_{\mathrm{u}}(\ell)\tilde{\mathbf{H}}_{\mathrm{u}}^{\mathrm{H}}(\ell), \tag{3.23a}$$

$$\widehat{\mathbf{C}}_{\mathrm{T},L} = \frac{1}{L}\sum_{\ell=1}^{L} \tilde{\mathbf{H}}_{\mathrm{u}}^{\mathrm{H}}(\ell)\tilde{\mathbf{H}}_{\mathrm{u}}(\ell). \tag{3.23b}$$

In dense multipath radio environments where the temporal order rises to $q_{\mathrm{T}} \simeq W$, it is convenient to neglect the temporal projection and set $\widehat{\mathbf{\Pi}}_{\mathrm{T}} = \mathbf{I}_W$ in (3.22). The resulting channel estimate exploits the stationarity of the spatial subspace only and it is referred to as MB-spatial (MB-S) estimator (see also [22]). Dually, for a large angular spread and/or a small number of antennas ($q_{\mathrm{S}} \simeq N$), it might be advisable not to use the spatial projection and set $\widehat{\mathbf{\Pi}}_{\mathrm{S}} = \mathbf{I}_N$ in (3.22). This leads to the MB-temporal (MB-T) estimator that exploits the stationarity of the temporal subspace only.

It can be easily seen that for $L = 1$, MB-ST estimate (3.22) coincides with RR or SB estimate (3.20). On the other hand, for $L \to \infty$ (but still stationary channel structural properties), it is $\mathbf{W}_{\mathrm{S},\infty} = \mathbf{Q}^{-\mathrm{H}/2}$ and the estimates $\{\widehat{\mathbf{\Pi}}_{\mathrm{S}}, \widehat{\mathbf{\Pi}}_{\mathrm{T}}\}$ tend to the projectors $\{\mathbf{\Pi}_{\mathrm{S}}, \mathbf{\Pi}_{\mathrm{T}}\}$ onto the subspaces of the weighted channel matrix

$$\tilde{\mathbf{H}}(\ell) = \mathbf{W}_{\mathrm{S},\infty}\mathbf{H}(\ell)\mathbf{W}_{\mathrm{T}}^{\mathrm{H}} = \tilde{\mathbf{A}}\mathbf{D}(\ell)\tilde{\mathbf{G}}^{\mathrm{T}}, \tag{3.24}$$

where $\tilde{\mathbf{A}} = \mathbf{W}_{\mathrm{S},\infty}\mathbf{A}$ and $\tilde{\mathbf{G}} = \mathbf{W}_{\mathrm{T}}\mathbf{G}$ are the spatial-temporal components of $\tilde{\mathbf{H}}(\ell)$. Namely, $\widehat{\mathbf{\Pi}}_{\mathrm{S}}$ tends to the projector $\mathbf{\Pi}_{\mathrm{S}}$ onto the spatial subspace $\mathcal{R}[\tilde{\mathbf{A}}]$ and $\widehat{\mathbf{\Pi}}_{\mathrm{T}}$ tends to the projector $\mathbf{\Pi}_{\mathrm{T}}$ onto the temporal subspace $\mathcal{R}[\tilde{\mathbf{G}}]$. This can be proved by simply evaluating the sample correlation matrices (3.23a)–(3.23b) for $L \to \infty$ [9]:

$$\widehat{\mathbf{C}}_{\mathrm{S},\infty} = \mathrm{E}\left[\tilde{\mathbf{H}}_{\mathrm{u}}(\ell)\tilde{\mathbf{H}}_{\mathrm{u}}^{\mathrm{H}}(\ell)\right] = \mathbf{C}_{\mathrm{S}} + W\mathbf{I}_N, \tag{3.25a}$$

$$\widehat{\mathbf{C}}_{\mathrm{T},\infty} = \mathrm{E}\left[\tilde{\mathbf{H}}_{\mathrm{u}}^{\mathrm{H}}(\ell)\tilde{\mathbf{H}}_{\mathrm{u}}(\ell)\right] = \mathbf{C}_{\mathrm{T}} + N\mathbf{I}_W. \tag{3.25b}$$

Here the spatial ($\mathbf{C}_{\mathrm{S}}$) and temporal ($\mathbf{C}_{\mathrm{T}}$) correlations for the true-weighted channel matrix $\tilde{\mathbf{H}}(\ell)$ are defined as

$$\mathbf{C}_{\mathrm{S}} = \mathrm{E}\left[\tilde{\mathbf{H}}(\ell)\tilde{\mathbf{H}}^{\mathrm{H}}(\ell)\right] = \tilde{\mathbf{A}}\mathbf{\Lambda}_{\mathrm{S}}\tilde{\mathbf{A}}^{\mathrm{H}}, \tag{3.26a}$$

$$\mathbf{C}_{\mathrm{T}} = \mathrm{E}\left[\tilde{\mathbf{H}}^{\mathrm{H}}(\ell)\tilde{\mathbf{H}}(\ell)\right] = \tilde{\mathbf{G}}\mathbf{\Lambda}_{\mathrm{T}}\tilde{\mathbf{G}}^{\mathrm{T}}. \tag{3.26b}$$

$\mathbf{\Lambda}_{\mathrm{S}} = \tilde{\mathbf{G}}^{\mathrm{T}}\tilde{\mathbf{G}} \odot \mathbf{C}_{\alpha}(0)$ and $\mathbf{\Lambda}_{\mathrm{T}} = \tilde{\mathbf{A}}^{\mathrm{H}}\tilde{\mathbf{A}} \odot \mathbf{C}_{\alpha}(0)$ are diagonal matrices, and $\odot$ denotes the element-wise product. From (3.25a) and (3.26a), it is easy to see that the subspace spanned by the q_{S} leading eigenvectors of the matrix $\widehat{\mathbf{C}}_{\mathrm{S},L}$ equals asymptotically the spatial subspace $\mathcal{R}[\mathbf{C}_{\mathrm{S}}] = \mathcal{R}[\tilde{\mathbf{A}}]$. Dually, the subspace spanned by the q_{T} leading eigenvectors of the matrix $\widehat{\mathbf{C}}_{\mathrm{T},L}$ coincides, for $L \to \infty$, with the temporal subspace $\mathcal{R}[\mathbf{C}_{\mathrm{T}}] = \mathcal{R}[\tilde{\mathbf{G}}]$.

Remarks. In real systems the rank orders (q, or both q_S and q_T) have to be estimated from the received signals. As discussed in [23], the order that minimizes the mean square error (MSE) of the estimate is a trade-off between distortion (due to under-parameterization) and noise (due to over-parameterization). Methods for optimal trade-off selection are proposed in [24] (for uncorrelated noise) and in [8] (for spatially correlated noise) by using the minimum description length (MDL) criterion [25].

An adaptive implementation of the MB methods, that allows to cancel the latency in providing the channel estimate and alleviate the computational burden, can be obtained through subspace tracking techniques [26]. The estimate of the spatial and temporal subspaces is updated on a block-by-block basis, allowing angles and delays to vary continuously (but still slowly) over the blocks [9]. In case of severe fading (i.e., for large-block duration and/or high velocity of the mobile user), a tracking of the fast-varying channel parameters is needed as well within each block interval [27].

Example 3.1. The advantage of the subspace methods with respect to the unconstrained one is illustrated by an example in Figures 3.2 and 3.3. The noise is spatially white ($\mathbf{Q} = \sigma_v^2 \mathbf{I}_N$) and the training sequence is uncorrelated ($\mathbf{C}_t = \sigma_s^2 Z_t \mathbf{I}_W$), so that the weighting terms can be neglected (as $\tilde{\mathbf{H}}_u(\ell) \propto \mathbf{H}_u(\ell)$). The multipath propagation is composed of $P = 5$ paths having $\mathbf{C}_\alpha(0) = \text{diag}[0.33, 0.25, 0.19, 0.14, 0.083]$. The path pattern is described in Figure 3.2a. Figures 3.2b and 3.2c show the power-delay-angle (PDA) diagram for the channel in the first block and the unconstrained estimate evaluated in six different blocks. As illustrated by PDA plots, the simulated angle-delay pattern is invariant over the blocks, while the fading amplitudes change from block to block.

The subspace-based channel estimates are shown in Figure 3.3. Since $\alpha_1 = \alpha_2$, $\alpha_3 = \alpha_4$, and $\tau_4 = \tau_5$, the spatial and temporal diversity orders are, respectively, $q_S = q = 3$ and $q_T = 4$. The SB and MB (for $L \to \infty$) estimates are calculated by using as rank orders $\hat{q}_S = \hat{q} = 1 \div 3$, $\hat{q}_T = 1 \div 4$. Figure 3.3 compares the PDA diagrams of all channel estimates for $\ell = 1$ and illustrates how the projection onto the short-long term spatial-temporal channel subspace reduces the estimate error with respect to the preliminary unconstrained estimate. The comparison shows that the most accurate estimate is obtained by double projection (both spatial and temporal) onto the long-term subspaces. This is proved analytically in the following.

3.2.2. Performance analysis and comparison

In the following we evaluate and compare the performance for the SB and MB subspace-based estimates with the unconstrained one under the following conditions: known q, $Z_t \to \infty$ and $L = 1$ for the SB estimate; known $\{q_S, q_T\}$ and $\{Z_t, L\} \to \infty$ for the MB estimate (performance for any L is in [8]). Notice that for $Z_t \to \infty$ it is $\mathbf{Q}_{u,L} = \mathbf{Q}$, as for known noise covariance matrix.

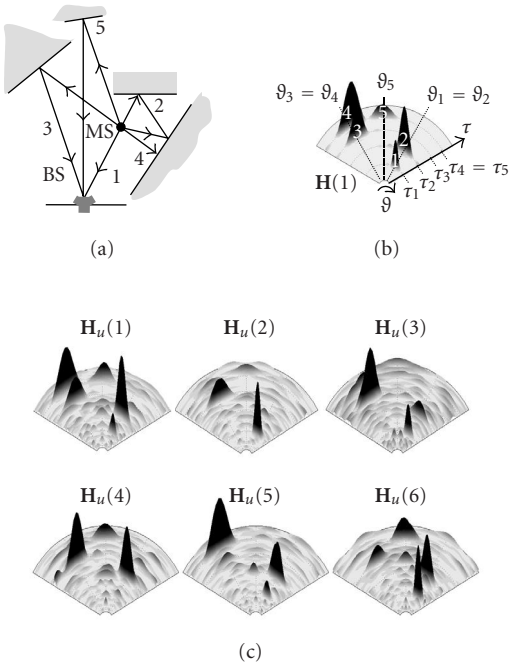

FIGURE 3.2. Example of block-by-block unconstrained estimation for a block-faded channel with stationary angle-delay pattern: (a) multipath model with $P = 5$ paths, $q_S = q = 3$ and $q_T = 4$; (b) power-delay-angle diagram for the channel in the first block; and (c) power-delay-angle diagram for the unconstrained estimate in six different blocks.

Let $\mathbf{H}_c(\ell)$ be any of the SB or MB constrained estimates, it can be shown [8, 9] that the relationship between the constrained $\Delta\mathbf{h}_c(\ell) = \text{vec}[\mathbf{H}_c(\ell) - \mathbf{H}(\ell)]$ and the unconstrained $\Delta\mathbf{h}_u(\ell) = \text{vec}[\mathbf{H}_u(\ell) - \mathbf{H}(\ell)]$ estimate error is

$$\Delta\mathbf{h}_c(\ell) = \mathbf{C}_u^{H/2}\mathbf{\Pi}\mathbf{C}_u^{-H/2}\Delta\mathbf{h}_u(\ell), \tag{3.27}$$

where $\mathbf{C}_u$ is covariance (3.13) of the unconstrained estimate and $\mathbf{\Pi}$ is a projector onto a long/short term spatial/temporal channel subspace depending on the specific constrained estimate. Namely, for the SB estimate, $\mathbf{\Pi}$ is the instantaneous-fading projector

$$\mathbf{\Pi} = \mathbf{I}_W \otimes \mathbf{\Pi}_S(\ell) + \mathbf{\Pi}_T^*(\ell) \otimes \mathbf{\Pi}_S^\perp(\ell) \tag{3.28}$$

obtained from the projector $\mathbf{\Pi}_S(\ell)$ onto the short-term spatial subspace $\mathcal{R}[\tilde{\mathbf{H}}(\ell)]$ and the projector $\mathbf{\Pi}_T(\ell)$ onto the short-term temporal subspace $\mathcal{R}[\tilde{\mathbf{H}}^H(\ell)]$. On the other hand, for the MB methods the fading is averaged over $L \to \infty$ blocks and $\mathbf{\Pi}$ is related to the long-term projectors: $\mathbf{\Pi} = \mathbf{\Pi}_T^* \otimes \mathbf{\Pi}_S$ for MB-ST; $\mathbf{\Pi} = \mathbf{I}_W \otimes \mathbf{\Pi}_S$ for MB-S; $\mathbf{\Pi} = \mathbf{\Pi}_T^* \otimes \mathbf{I}_N$ for MB-T.

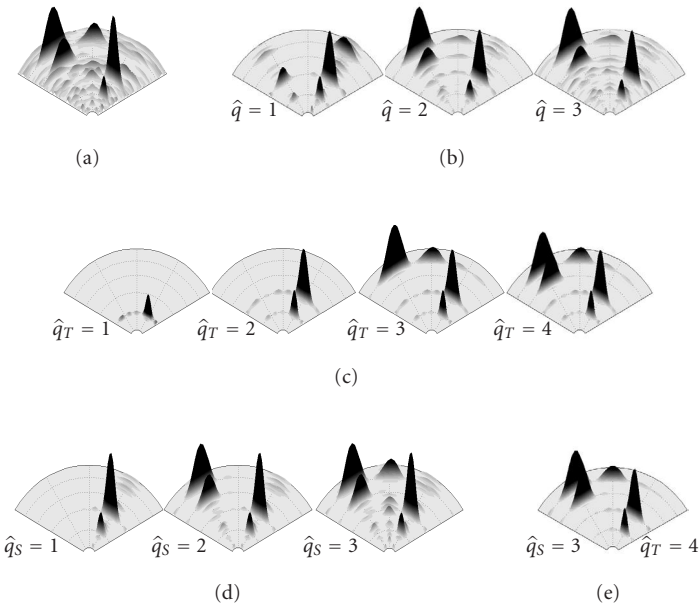

FIGURE 3.3. Comparison between the PDA of all channel estimates in the first block for the example in Figure 3.2. (a) Unconstrained estimate. (b), (c), (d) Subspace-based estimates: (b) single-block; (c) multiblock time for $\hat{q}_{\mathrm{T}} = 1, \ldots, 4$; and (d) multiblock space for $\hat{q}_{\mathrm{S}} = 1, \ldots, 3$. (e) Multiblock space-time for $\hat{q}_{\mathrm{T}} = q_{\mathrm{T}}$ and $\hat{q}_{\mathrm{S}} = q_{\mathrm{S}}$.

From (3.27), the covariance matrix of the subspace-based estimate is

$$\begin{aligned} \mathrm{Cov}\left[\mathbf{h}_{\mathrm{c}}(\ell)\right] &= \mathrm{E}\left[\Delta\mathbf{h}_{\mathrm{c}}(\ell)\Delta\mathbf{h}_{\mathrm{c}}^{\mathrm{H}}(\ell)\right] \\ &= \mathbf{C}_{\mathrm{u}}^{\mathrm{H}/2}\boldsymbol{\Pi}\mathbf{C}_{\mathrm{u}}^{-\mathrm{H}/2}\,\mathrm{Cov}\left[\mathbf{h}_{\mathrm{u}}(\ell)\right] = \mathbf{C}_{\mathrm{u}}^{\mathrm{H}/2}\boldsymbol{\Pi}\mathbf{C}_{\mathrm{u}}^{1/2}. \end{aligned} \tag{3.29}$$

As expected, the covariance of the constrained reestimate is obtained from the unconstrained estimate covariance through following operations: (i) whitening (i.e., by means of the spatial-temporal weighting factors); (ii) projection onto the long-short term spatial-temporal channel subspaces; (iii) inverse weighting. Notice that, due to the projection, the effect of the constrained re-estimation is always a reduction of the unconstrained estimate error.

This is confirmed by the asymptotic MSE of the estimate, $\mathrm{MSE} = \mathrm{E}[\|\widehat{\mathbf{H}}(\ell) - \mathbf{H}(\ell)\|^2]$, that is obtained as the trace of covariance matrix (3.29). From (3.13) and by exploiting the Kronecker product properties [28], we get the results summarized in Table 3.1 where the operator $\Phi[\cdot]$ is defined as $\Phi[\boldsymbol{\Pi}, \mathbf{C}] = \mathrm{tr}[\mathbf{C}^{\mathrm{H}/2}\boldsymbol{\Pi}\mathbf{C}^{1/2}]$. The MSE expressions simplify for spatially uncorrelated noise ($\mathbf{Q} = \sigma_v^2\mathbf{I}_N$) and training sequence with ideal correlation properties ($\mathbf{C}_{\mathrm{t}} = \sigma_s^2 Z_{\mathrm{t}}\mathbf{I}_W$), as shown in the third column in Table 3.1. In this case the MSE is linearly related to the ratio between the number of independent channel parameters to be estimated within the block and the training sequence length (Z_{t}). For instance, for the unconstrained

Table 3.1. Asymptotic MSE for training-based estimates: unconstrained estimate (FR); single-block (SB) and multiblock (MB) subspace methods.

Estimate	Correlated noise and training sequence	Uncorrelated
FR	$\Phi(\mathbf{I}_W, \mathbf{C}_{\mathrm{t}}^{-1})\Phi(\mathbf{I}_N, \mathbf{Q})$	$\frac{\sigma_v^2}{\sigma_s^2}\frac{NW}{Z_{\mathrm{t}}}$
SB	$\Phi(\mathbf{I}_W, \mathbf{C}_{\mathrm{t}}^{-1})\Phi(\mathbf{\Pi}_{\mathrm{S}}(\ell), \mathbf{Q}) + \Phi(\mathbf{\Pi}_{\mathrm{T}}(\ell), \mathbf{C}_{\mathrm{t}}^{-1})\Phi(\mathbf{\Pi}_{\mathrm{S}}^{\perp}(\ell), \mathbf{Q})$	$\frac{\sigma_v^2}{\sigma_s^2}\frac{q[N+W-q]}{Z_{\mathrm{t}}}$
MB-ST	$\Phi(\mathbf{\Pi}_{\mathrm{T}}, \mathbf{C}_{\mathrm{t}}^{-1})\Phi(\mathbf{\Pi}_{\mathrm{S}}, \mathbf{Q})$	$\frac{\sigma_n^2}{\sigma_s^2}\frac{q_{\mathrm{S}}q_{\mathrm{T}}}{Z_{\mathrm{t}}}$
MB-S	$\Phi(\mathbf{I}_W, \mathbf{C}_{\mathrm{t}}^{-1})\Phi(\mathbf{\Pi}_{\mathrm{S}}, \mathbf{Q})$	$\frac{\sigma_v^2}{\sigma_s^2}\frac{Wq_{\mathrm{S}}}{Z_{\mathrm{t}}}$
MB-T	$\Phi(\mathbf{\Pi}_{\mathrm{T}}, \mathbf{C}_{\mathrm{t}}^{-1})\Phi(\mathbf{I}_N, \mathbf{Q})$	$\frac{\sigma_v^2}{\sigma_s^2}\frac{Nq_{\mathrm{T}}}{Z_{\mathrm{t}}}$

(or FR) method, the unknowns are the NW entries of the channel matrix, while for the SB estimate (i.e., constrained to have rank equal to q), the number of unknowns is reduced to $q(N + W - q)$. On the other hand, all the MB methods have a definite advantage with respect to the SB technique, as they can estimate the invariant spatial and/or temporal subspaces with any degree of accuracy provided that L is large enough. Therefore, the MSE of the MB methods depends only on the number of parameters to be estimated on each block: $q_{\mathrm{S}}q_{\mathrm{T}}$ for MB-ST, $q_{\mathrm{S}}W$ for MB-S, and Nq_{T} for MB-T.

The following relation holds among the performances of the unconstrained and the MB-constrained estimates:

$$\mathrm{MSE}_{\mathrm{u}} \geq \left\{\mathrm{MSE}_{\text{MB-T}}, \mathrm{MSE}_{\text{MB-S}}\right\} \geq \mathrm{MSE}_{\text{MB-ST}}. \tag{3.30}$$

For the comparison between SB- and MB-constrained methods, the MSE of the SB estimate ($\mathrm{MSE}_{\mathrm{SB}}$) needs to be averaged with respect to the fading amplitudes (or, equivalently, averaged over $L \to \infty$ blocks); the following inequalities hold:

$$\mathrm{MSE}_{\mathrm{u}} \geq \mathrm{MSE}_{\mathrm{SB}} \geq \begin{cases} \mathrm{MSE}_{\text{MB-T}} & \text{for } q = q_{\mathrm{T}} \leq q_{\mathrm{S}}, \\ \mathrm{MSE}_{\text{MB-S}} & \text{for } q = q_{\mathrm{S}} \leq q_{\mathrm{T}}, \end{cases} \tag{3.31}$$

which imply also $\mathrm{MSE}_{\mathrm{SB}} \geq \mathrm{MSE}_{\text{MB-ST}}$ for any q. For the proof of the inequalities (3.30)–(3.31) see [9].

The analytical MSEs and the relationships (3.30)–(3.31) are verified by simulations in Figure 3.4. The figure compares the asymptotic MSE (lines) with the simulated MSE (markers) for different values of signal-to-noise ratio $\mathrm{SNR} = \mathrm{E}[\|\mathbf{H}(\ell)\|^2]\sigma_s^2/\sigma_v^2$ and number of blocks L. The training sequence is chosen from the UMTS-TDD standard [12] and it is composed of $Z_{\mathrm{t}} = 456$ QPSK symbols with a cyclic prefix of 56 symbols. The training signals are received in spatially correlated Gaussian noise by a ULA with $N = 8$ half-wavelength-spaced apart elements. The channel matrix is generated according to model (3.8) for $W = 15$ and

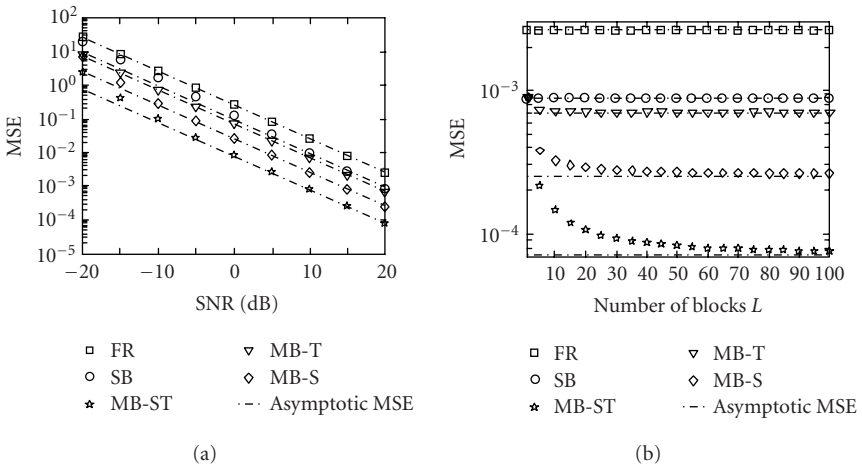

FIGURE 3.4. MSE of the SB and MB subspace-based estimates in spatially correlated noise (a) for varying SNR and $L = 40$ and (b) for varying L and SNR $= 20$ dB.

$q_S = q_T = 3$ (rank orders are known at the receiver). The MSE of the estimate is evaluated for $L = 40$ and varying SNR (Figure 3.4a), and for SNR $= 20$ dB and varying L (Figure 3.4b). The numerical analysis shows that the subspace-based methods approach the analytical MSE bound and outperform the FR estimate. Moreover the MB bound for $L \to \infty$ can be easily reached with a reasonable number of blocks (in practice, $L \geq 30$).

3.3. Decision-based subspace methods

The performance analysis in the previous section demonstrates that, for all the considered methods, the estimate accuracy is inversely related to the number of training symbols used within each block for the estimation of the channel matrix. In the following, we extend the analysis to channel estimation in soft-iterative receivers [10], where after the first iteration, a priori probabilities about the information-bearing symbols can be used at the channel estimator to extend the training set.

3.3.1. Extension to information-bearing signals

Let the $N \times Z_d$ matrix $\mathbf{R}_d(\ell) = [\mathbf{r}(Z_t + W - 1; \ell), \ldots, \mathbf{r}(Z_t + Z_s - 1; \ell)]$ collect $Z_d = Z_s - W + 1$ samples received within the ℓth data field (to simplify, the first $W - 1$ samples are discarded as they contain overlapping between training and data symbols). Model (3.9) can now be extended with the information-bearing signals

$$\mathbf{R}_d(\ell) = \mathbf{H}(\ell)\mathbf{S}_d(\ell) + \mathbf{V}_d(\ell). \tag{3.32}$$

Similarly to (3.9), here the $W \times Z_d$ Toeplitz matrix $\mathbf{S}_d(\ell)$ represents the convolution of the channel with the data sequence $\{s(i;\ell)\}_{i=Z_t}^{Z_t+Z_s-1}$, while the $N \times Z_d$ matrix $\mathbf{V}_d(\ell)$ contains the noise samples. To simplify the analysis, in the following we consider QPSK modulation, that is, $s(i;\ell) = \sigma_s(b(i;\ell;1) + jb(i;\ell;2))/\sqrt{2}$ with $b(i;\ell;z) \in \{-1,+1\}$ being the bits corresponding to the ith symbol, $z = 1,2$. The generalization to larger constellations is straightforward.

As in a soft-iterative receiver (after the first equalization and decoding of the L blocks) [29], we assume that the a priori log-likelihood ratio (LLR)

$$\lambda_1(b) = \log \frac{P[b=+1]}{P[b=-1]} \tag{3.33}$$

is available at the channel estimator for every bit $b = b(i;\ell;z)$. This soft information can be used to compute the mean value $\bar{s}(i;\ell) = \mathrm{E}[s(i;\ell)]$ and the variance $\sigma_i^2(\ell) = \mathrm{Var}[s(i;\ell)] = \sigma_s^2 - |\bar{s}(i;\ell)|^2$ for each data symbol $s(i;\ell)$, for $i = Z_t,\ldots,Z_t+Z_s-1$. Similarly to [30], the mean values $\{\bar{s}(i;\ell)\}$ can be used in addition to the training symbols to perform channel estimation as described below.

3.3.2. Subspace-based estimation

We arrange the mean values $\{\bar{s}(i;\ell)\}_{i=Z_t}^{Z_t+Z_s-1}$ into the $W \times Z_d$ matrix $\bar{\mathbf{S}}_d(\ell) = \mathrm{E}[\mathbf{S}_d(\ell)]$. The signals within the data field are modelled as

$$\mathbf{R}_d(\ell) = \mathbf{H}(\ell)\bar{\mathbf{S}}_d(\ell) + \Delta\mathbf{V}_d(\ell) + \mathbf{V}_d(\ell), \tag{3.34}$$

where the soft-valued data estimates $\bar{\mathbf{S}}_d(\ell)$ are treated as additional known training symbols, while the signals $\Delta\mathbf{V}_d(\ell) = \mathbf{H}(\ell)\Delta\mathbf{S}_d(\ell)$ generated by the data estimate errors $\Delta\mathbf{S}_d(\ell) = \mathbf{S}_d(\ell) - \bar{\mathbf{S}}_d(\ell)$ are approximated as an equivalent Gaussian noise.

Within each block a soft unconstrained estimate of the channel matrix is calculated by applying estimator (3.12) to the joint signal $\mathbf{R}(\ell) = [\mathbf{R}_t(\ell) \quad \mathbf{R}_d(\ell)]$ and by using as training data $\bar{\mathbf{S}}(\ell) = [\mathbf{S}_t\bar{\mathbf{S}}_d(\ell)]$. This yields

$$\mathbf{H}_u(\ell) = \left(\mathbf{R}_t(\ell)\mathbf{S}_t^H + \mathbf{R}_d(\ell)\bar{\mathbf{S}}_d^H(\ell)\right)\left(\mathbf{C}_t + \bar{\mathbf{C}}_d\right)^{-1}, \tag{3.35}$$

where $\bar{\mathbf{C}}_d$ is here defined as $\bar{\mathbf{C}}_d = \bar{\mathbf{S}}_d(\ell)\bar{\mathbf{S}}_d^H(\ell)$. This estimate is known to be suboptimal, but, in addition to its simplicity, it has the advantage of being unbiased and thus facilitates bootstrap and convergence in iterative receivers [31], as shown by simulation results in Section 3.4. Notice that if data symbols are independent and Z_d is large enough, $\mathbf{C}_d = \mathbf{S}_d(\ell)\mathbf{S}_d^H(\ell) \approx \sigma_s^2 Z_d \mathbf{I}_W$ and the matrix $\bar{\mathbf{C}}_d$ can be approximated as $\bar{\mathbf{C}}_d \approx \sigma_s^2 \bar{Z}_d \mathbf{I}_W$, where $\bar{Z}_d$ represents the *effective* number of known data

TABLE 3.2. Asymptotic MSE for soft-based estimates: unconstrained estimate (FR); single-block (SB) and multiblock (MB) subspace methods.

Estimate	Correlated noise and training sequence	Uncorrelated
Prior information with $0 \le \tilde{\sigma}^2 \le \sigma_s^2$		
FR	$\Phi(\mathbf{I}_W, (\mathbf{C}_\mathrm{t} + \bar{\mathbf{C}}_\mathrm{d})^{-1}) \cdot [\Phi(\mathbf{I}_N, \mathbf{Q}) + \Phi(\mathbf{I}_N, \Delta\mathbf{Q})]$	$\frac{\sigma_v^2 + \Delta\sigma_v^2}{\sigma_s^2} \frac{NW}{\bar{Z}}$
MB-ST	$\Phi(\mathbf{\Pi}_\mathrm{T}, (\mathbf{C}_\mathrm{t} + \bar{\mathbf{C}}_\mathrm{d})^{-1}) \cdot [\Phi(\mathbf{\Pi}_\mathrm{S}, \mathbf{Q}) + \Phi(\mathbf{I}_N, \Delta\mathbf{Q})]$	$\frac{\sigma_v^2 + \Delta\sigma_v^2}{\sigma_s^2} \frac{q_\mathrm{S} q_\mathrm{T}}{\bar{Z}}$
Perfect prior information ($\tilde{\sigma}^2 = 0$)		
FR	$\Phi(\mathbf{I}_W, (\mathbf{C}_\mathrm{t} + \mathbf{C}_\mathrm{d})^{-1}) \cdot \Phi(\mathbf{I}_N, \mathbf{Q})$	$\frac{\sigma_v^2}{\sigma_s^2} \frac{NW}{Z_\mathrm{t} + Z_\mathrm{d}}$
MB-ST	$\Phi(\mathbf{\Pi}_\mathrm{T}, (\mathbf{C}_\mathrm{t} + \mathbf{C}_\mathrm{d})^{-1}) \cdot \Phi(\mathbf{\Pi}_\mathrm{S}, \mathbf{Q})$	$\frac{\sigma_v^2}{\sigma_s^2} \frac{q_\mathrm{S} q_\mathrm{T}}{Z_\mathrm{t} + Z_\mathrm{d}}$

symbols that can be used in each block for channel estimation:

$$\tilde{Z}_\mathrm{d} = Z_\mathrm{d}\left(1 - \frac{\sigma_\mathrm{d}^2}{\sigma_s^2}\right), \tag{3.36}$$

$$\sigma_\mathrm{d}^2 = \frac{1}{LZ_\mathrm{d}} \sum_{i,\ell} \sigma_i^2(\ell). \tag{3.37}$$

Starting from preliminary FR estimate (3.35), a soft ST-MB estimate can be derived according to (3.22) by computing the weighting matrices $\mathbf{W}_\mathrm{S} = \mathbf{Q}_{\mathrm{u},L}^{-\mathrm{H}/2}$ and $\mathbf{W}_\mathrm{T} = (\mathbf{C}_\mathrm{t} + \bar{\mathbf{C}}_\mathrm{d})^{-\mathrm{H}/2}$ from both the training and the data signals. If the estimated symbols are unreliable (i.e., at the first iterations of the iterative processing for moderate SNR), it is $\tilde{Z}_\mathrm{d} = 0$, $\bar{\mathbf{S}}_\mathrm{d}(\ell) = 0$, and the soft MB-ST estimate coincides with the training-based one (3.22). On the other hand, for perfect a priori information (i.e., after a large enough number of iterations, provided that the iterative approach converges), it is $\tilde{Z}_\mathrm{d} = Z_\mathrm{d}$, $\bar{\mathbf{S}}_\mathrm{d}(\ell) = \mathbf{S}_\mathrm{d}(\ell)$, and therefore the soft estimate equals the training-based estimate that would be obtained from a virtual training sequence of $Z = Z_\mathrm{t} + Z_\mathrm{d}$ symbols.

3.3.3. Performance analysis and comparison

The asymptotic MSE for the soft-iterative channel estimate is evaluated in Table 3.2 by assuming the errors $\Delta s_i(\ell) = s_i(\ell) - \bar{s}_i(\ell)$ of the soft-valued data estimates as uncorrelated with zero mean and variance σ_d^2 given in (3.37). The errors are also considered uncorrelated from the noise samples $v(i;\ell)$.

We observe that the additional noise term $\Delta\mathbf{V}_\mathrm{d}(\ell)$, that affects the signals within the data fields only, is temporally uncorrelated but spatially correlated with covariance $\mathrm{Cov}[\mathrm{vec}[\Delta\mathbf{V}_\mathrm{d}(\ell)]] = \mathbf{I}_{Z_\mathrm{d}} \otimes (\sigma_\mathrm{d}^2 \mathbf{C}_\mathrm{S})$. Starting from this, it can be shown that the covariance of the unconstrained soft estimate (3.35) is obtained from the training-based one (3.13) by simply replacing $\mathbf{C}_\mathrm{t}$ with $\mathbf{C}_\mathrm{t} + \bar{\mathbf{C}}_\mathrm{d}$, and $\mathbf{Q}$ with $\mathbf{Q} + \Delta\mathbf{Q}$,

where $\Delta\mathbf{Q} = (\tilde{Z}_\mathrm{d}/\tilde{Z})\sigma_\mathrm{d}^2\mathbf{C}_\mathrm{S}$. The covariance of the subspace-based soft estimate is finally derived through the operations of weighting, projecting, and inverse weighting from the unconstrained soft estimate covariance, as in Section 3.2.2. The trace of the covariance matrices yields the MSEs summarized in the second column of Table 3.2.

The MSE expressions can be easily explained in the case of uncorrelated training sequence ($\mathbf{C}_\mathrm{t} = \sigma_s^2 Z_\mathrm{t}\mathbf{I}_W$) and spatially white noise ($\mathbf{Q} = \sigma_v^2\mathbf{I}_N$). This is shown in the third column of Table 3.2. As for the training-based methods, the MSE of the soft estimates is linearly related to the following: the ratio between the number of channel unknowns and the number $\tilde{Z} = Z_\mathrm{t} + \tilde{Z}_\mathrm{d}$ of *effective* training symbols within each block; the variance $\sigma_v^2 + \Delta\sigma_v^2$ of the *overall* noise, that is, the sum of the background noise and the noise generated by soft-decision errors, with

$$\Delta\sigma_v^2 = \frac{\mathrm{tr}[\Delta\mathbf{Q}]}{N} = \sigma_\mathrm{d}^2\frac{\tilde{Z}_\mathrm{d}}{\tilde{Z}}\frac{\mathrm{E}\left[\|\mathbf{H}(\ell)\|^2\right]}{N}. \tag{3.38}$$

Clearly, for large signal-to-noise ratio and unreliable soft data, the term due to decision errors is dominant ($\Delta\sigma_v^2 > \sigma_v^2$) and the soft-based channel estimate can be less accurate than the training-based one. Still, it has to be noticed that this extreme condition is quite unlikely when the iterative processing converges, as the signal-to-noise ratio and the data estimate variance σ_d^2 are highly correlated with each other. We finally remark that for missing prior information (i.e., at the first iteration of turbo processing), it is $\Delta\sigma_v^2 = 0$, $\sigma_\mathrm{d}^2 = 1$, $\tilde{Z} = Z_\mathrm{t}$, $\bar{\mathbf{C}}_\mathrm{d} = \mathbf{0}$, and the performance in Table 3.2 reduces to the training-based one in Table 3.1. On the other hand, for perfect prior information (i.e., close to the convergence of the iterative approach), the MSEs simplify as indicated in Table 3.2 (rows 5–7) for $\Delta\sigma_v^2 = \sigma_\mathrm{d}^2 = 0$, $\tilde{Z} = Z_\mathrm{t} + Z_\mathrm{d}$, and $\bar{\mathbf{C}}_\mathrm{d} = \mathbf{C}_\mathrm{d} = \sigma_s^2 Z_\mathrm{d}\mathbf{I}_W$.

A comparison with simulated performance is in Figure 3.5. A block transmission system is considered where $L = 20$ blocks are transmitted over a block-fading Rayleigh channel to a uniform linear antenna array of $N = 8$ elements with half-wavelength interelement spacing. The channel has temporal support $W = 16$ and it is composed of $P = 6$ paths clustered into two groups: in the first set, $\alpha_p = \pi/6$ for $p = 1, 2, 3$, and $[\tau_1, \tau_2, \tau_3] = [0, 1.2, 2.2]T$; in the second set, $\alpha_p = 0$ for $p = 4, 5, 6$ and $[\tau_4, \tau_5, \tau_6] = [7.2, 8.2, 9.2]T$. The power-delay profile is the same within each cluster: $[\sigma_1^2, \sigma_2^2, \sigma_3^2] = [\sigma_4^2, \sigma_5^2, \sigma_6^2] = [1, 0.5, 0.25]/1.75$. It follows that $q_\mathrm{S} = 2$, $q_\mathrm{T} = 6$. The noise is spatially correlated due to an interferer with direction of arrival $\vartheta = \pi/3$: $[\mathbf{Q}]_{m,\ell} = \sigma_v^2 0.9^{|\ell-m|}\exp[-i\pi(\ell - m)\sin\vartheta]$. Each block contains $Z_\mathrm{t} = 31$ training symbols (with a cyclic prefix of $W - 1$ symbols) and $Z_\mathrm{d} = 200$ information symbols. The transmitted pulse $g(t)$ is a raised cosine with roll-off factor 0.22.

Figure 3.5 compares the MSE of the soft SB and MB estimates for different values of the following: number of blocks L used in the MB estimate for the projector evaluation; number of soft-valued symbols Z_d used for channel estimation; mutual information $\mathcal{I} = \mathcal{I}[b, \lambda_1(b)]$ [32] between every bit $b = b(i; \ell; z)$ and the corresponding a priori LLR $\lambda_1(b)$ defined in (3.33). Notice that the soft FR estimate here is equivalent to the method proposed in [30]. According to [33], the

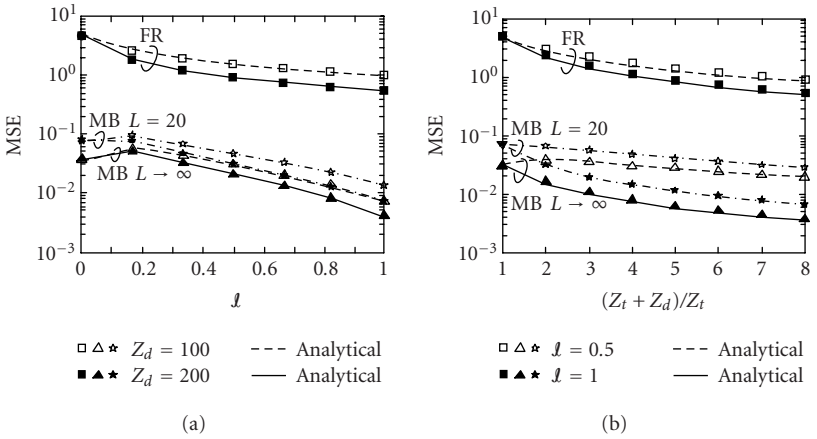

FIGURE 3.5. MSE of the soft unconstrained, and MB subspace-based estimates for varying mutual information ℓ and number of data symbols Z_d.

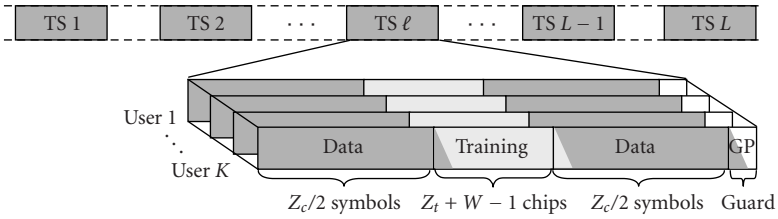

FIGURE 3.6. Block-by-block transmission in hybrid TD-CDMA systems.

a priori information $\lambda_1(b)$ is modelled as Gaussian. The signal-to-noise ratio is SNR = 12 dB. The simulated MSE values (markers) are compared with the analytical results (solid/dashed lines) of Table 3.2. It can be seen that the soft-iterative channel estimate becomes more accurate for increasing ℓ (or, equivalently, for decreasing σ_d^2), from $\ell = 0$ (i.e., estimation from training symbols only, $\sigma_d^2 = 1$) to $\ell = 1$ (i.e., estimation from the overall block of Z known symbols, $\sigma_d^2 = 0$). The maximum performance gain with respect to the training-based estimate (MSE_t) is reached for $\ell = 1$ and it is $\text{MSE}_t/\text{MSE} = Z/Z_t \approx 9$ dB as confirmed by simulations.

3.4. Subspace methods in hybrid TD-CDMA systems

The proposed SB and MB subspace methods can be also applied to communication systems dominated by multiple access interference (MAI), as block-synchronous time-slotted CDMA systems such as TD-SCDMA 3G standards [11, 12]. Block-by-block transmission is organized as illustrated in Figure 3.6.

Within the same uplink time-slot K users transmit simultaneously a block that contains a user-specific training sequence of $Z_t + W - 1$ chips and Z_c data symbols spread by a code $\mathbf{c}_k$ of length Q, for $k = 1, \ldots, K$. The discrete-time model

for the signals at the antenna array receiver is obtained as in Section 3.1.1 after chip matched filtering and sampling at the chip-rate $1/T_c$:

$$\mathbf{r}(i;\ell) = \sum_{k=1}^{K} \mathbf{H}_k(\ell)\mathbf{s}_k(i;\ell) + \mathbf{v}(i;\ell). \tag{3.39}$$

Herein i is the *chip* index within the ℓth block, the $N \times W$ channel matrix $\mathbf{H}_k(\ell)$ and the $W \times 1$ chip sequence $\mathbf{s}_k(i;\ell)$ refer to the kth user. The aim here is to evaluate the performance of a space-time receiver for model (3.39) complete with channel estimation and space-time multiuser detection (MUD) [34, 35].

Channel estimation can be performed jointly for the K users by imposing constraint (3.8) for each channel matrix $\mathbf{H}_k(\ell)$ (multiuser channel estimation). The spatial covariance of the noise is estimated from the training data as well (provided that $KW < Z_t - N$). The estimation of the channel matrices and the noise covariance is obtained by extending the subspace method described in Section 3.2.1 to multiuser model (3.39) [8]. The method can effectively cope with MAI (due to the nonorthogonality of the training sequences) and cochannel interference from neighboring cells.

After channel estimation, data detection is carried out on the data fields of each block, by using the estimates for the channel responses and the noise covariance. Even if the spreading codes are orthogonal at the transmitter, due to the frequency-selective fading channel, the information-bearing signals at the receiver are affected by both intersymbol-interference (ISI) and MAI. Block multiuser detection is needed to properly handle the interference, such as linear minimum-mean-square-error (MMSE) block MUD [36]. Since MAI and ISI are usually limited to few symbol intervals, block MUD can be carried out with a reduced block size to lower the computational complexity [37].

We first consider the uplink of a UMTS-TDD system [12] with a ULA of $N = 8$ half-wavelength-spaced elements at the receiver. Each block contains $Z_c = 122$ information symbols and a training sequence of $Z_t = 456$ chips with a cyclic prefix of length 56. Walsh-Hadamard codes of fixed length $Q = 16$ are used to spread the user data. Blocks are transmitted by QPSK modulation at the chip-rate 3.84 Mchip/s using root-raised-cosine pulse shaping at roll-off 0.22. $K = 8$ users are simultaneously active within the same cell and they have channel length $W = 45$. Perfect power control is assumed so that $\mathrm{E}[\|\mathbf{H}_k(\ell)\|^2] = 1$ for all users. The noise is spatially correlated due to $K_i = 6$ intercell interferers with equal average power, direction of arrival ϑ_k uniformly distributed within $[-\pi/3, +\pi/3]$, for $k = 1, \ldots, K_i$. The power P_k of each interfering signal is subject to Rayleigh fading and log-normal shadowing (with standard deviation 12 dB). The resulting noise spatial covariance is approximated as $[\mathbf{Q}]_{m,\ell} = \sum_{k=1}^{K_i} P_k 0.9^{|\ell-m|} \exp[-i\pi(\ell - m)\sin\vartheta_k]$ with $\sum_{k=1}^{K_i} P_k = \sigma_v^2$.

Realistic propagation environments are simulated according to the stochastic COST-259 directional channel model (COST-259 DCM) [38] that describes both the temporal and the angular dispersion of the propagation. Four macrocell radio environments are simulated according to COST-259 DCM specifications:

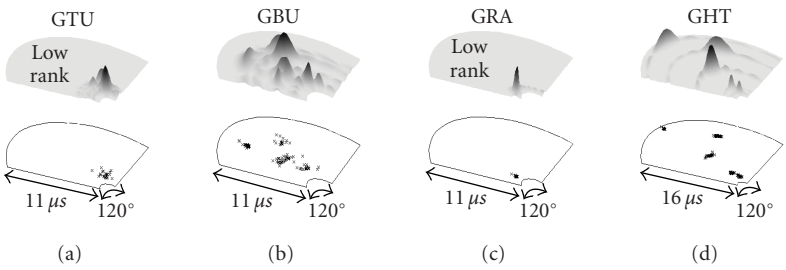

FIGURE 3.7. Power-delay-angle profile for channels generated according to COST-259 DCM propagation environments: (a) GTU, (b) GBU, (c) GRA, and (d) GHT.

generalized typical urban (GTU), generalized bad urban (GBU), generalized rural area (GRA), and generalized hill terrain (GHT). Figure 3.7 illustrates the power-delay-angle profile for a few channels generated by COST-259 model. The example shows that low-rank models are suitable for GTU and GRA environments as they are characterized by small angular-delay spread.

Figure 3.8 compares the MSE of the FR and SB-MB subspace methods for varying SNR. MB-ST estimation is carried out with $L = 30$ and adaptive selection of rank orders $\{q_S, q_T\}$ by MDL criterion (solid line with star markers). Different SB subspace estimates are obtained by using a fixed-rank order (with $q = 1, 2, 3, 4$, dashed lines) and MDL estimation of the rank order q (solid line with circle markers). Numerical results show that for low SNR the rank-1 approximation is the preferred solution (as it minimizes the number of unknowns to be estimated), while for large SNR the distortion becomes remarkable and a higher rank order is needed. The SB channel estimate with MDL selection of the rank order outperforms the fixed-rank SB estimates and the FR estimate (thick line) for all the SNR values. The minimum MSE among all the considered methods is obtained by the MB-ST subspace-based estimate with adaptive rank order.

Figure 3.9 compares the channel estimation methods in terms of BER for uncoded bits versus $E_b/N_0 = Q\sigma_s^2 \mathrm{E}[\|\mathbf{H}_k\|^2]/(2N\sigma_v^2)$. The adaptive selection of rank order by MDL criterion (circle-line for SB and star-line for MB) is again the most appropriate choice. The MB method outperforms both the FR and the SB estimates and it approaches the performance obtained with known channels. This confirms that the proposed algebraic structure is effective in reducing the channel description to the minimal number of parameters.

The performance of the soft subspace methods is evaluated by simulating a soft-iterative multiuser receiver for a convolutionally coded TD-SCDMA system similar to the UMTS-TDD low chip-rate system [11], with chip-rate 1.28 Mchip/s. The transmitter structure is shown in Figure 3.10. At the kth transmitter, $k = 1, \ldots, 4$, a sequence $\{x_k(i)\}$ of binary information symbols is encoded with the four-state convolutional code $(7, 5)_o$ with rate $R = 1/2$. Code bits are then permuted by a random interleaver of length 2814, mapped into QPSK symbols, spread by a Walsh-Hadamard code of length $Q = 4$, and arranged into $L = 16$ blocks. Each block contains $Z_c = 176$ data symbols and a training sequence of $Z_t = 128$

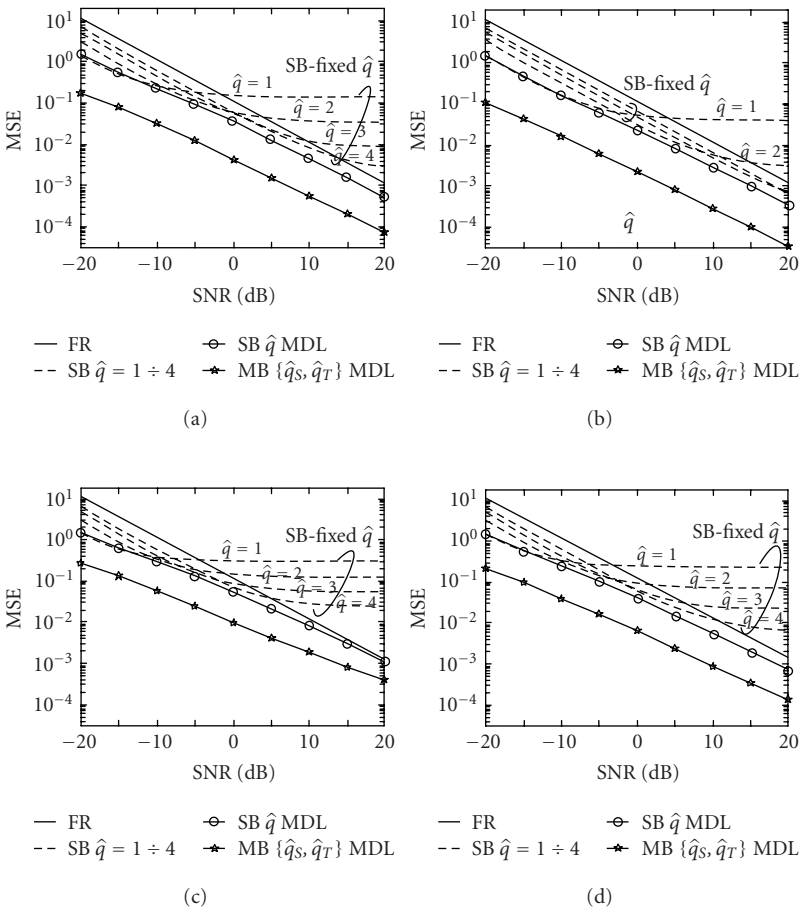

FIGURE 3.8. MSE of the unconstrained (FR) and subspace-based (SB and MB) estimates in COST-259 radio environments and spatially correlated noise. (a) GTU, (b) GRA, (c) GBU, and (d) GHT.

chips (plus a cyclic prefix of length 16). Blocks are transmitted over a Rayleigh fading three-path channel having delays $[\tau_1, \tau_2, \tau_3] = [0, 3, 6]$ microseconds, average powers $[\sigma_1^2, \sigma_2^2, \sigma_3^2] = [1/8, 1/2, 3/8]$, and directions of arrival $\vartheta_1 = \vartheta_2 = \vartheta_3$ uniformly distributed within $[-\pi/3, +\pi/3]$. The noise is spatially correlated with $K_i = 1$.

Signals are received by a ULA of $N = 4$ half-wavelength-spaced elements. The turbo receiver structure (Figure 3.11) consists of a suboptimal soft-input/soft-output (SISO) MMSE MUD with sliding window approach [39], a soft channel estimator, a set of $K = 4$ log-maximum-a-posteriori (log-MAP) SISO decoders [40] and 4 interleavers/deinterleavers. According to the turbo principle [10], channel estimation, multiuser detection, and decoding are repeated several times on the same frame of 16 received blocks with exchange of reliability information.

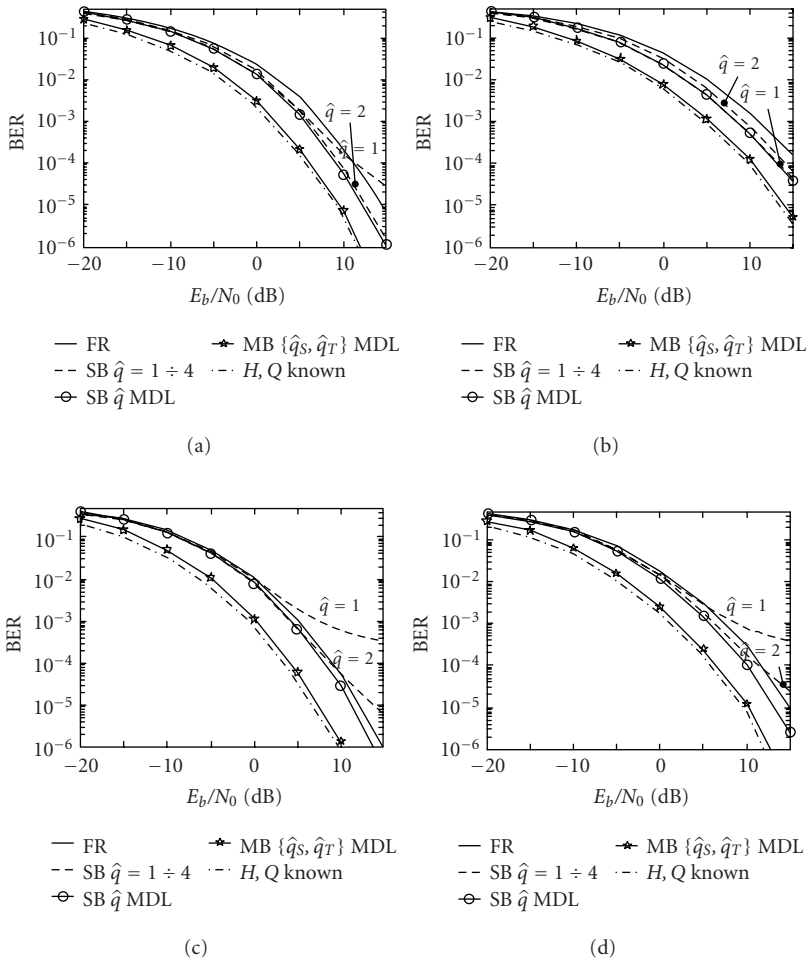

FIGURE 3.9. Performance of MMSE space-time MUD with unconstrained (FR) and subspace-based (SB and MB) channel estimation in COST-259 radio environments and spatially correlated noise. (a) GTU, (b) GRA, (c) GBU, and (d) GHT.

At each iteration, the soft channel estimator derives (as described in Section 3.3.2) new estimates $\{\widehat{\mathbf{H}}_k(\ell)\}_{\ell=1}^{L}$ for the channel matrices of all users, by exploiting both training chips and a priori LLRs $\lambda_1(b_k(i;\ell))$ for data chips. At the first iteration no a priori information is available and the channel matrices are estimated from training signals only. The estimates $\{\widehat{\mathbf{H}}_k(\ell)\}_{\ell=1}^{L}$ and the a priori LLR $\lambda_1(b_k(i;\ell))$ are fed to the SISO MUD and used to compute the extrinsic LLR for every code bit of every user. The extrinsic information is then reversed interleaved, and passed to the K channel decoders as a priori LLR $\lambda_2(b_k(i;\ell))$. Each decoder derives a refined extrinsic information that is interleaved again and fed back as new a priori LLR $\lambda_1(b_k(i;\ell))$ for further iterations. At the last iteration, the a posteriori

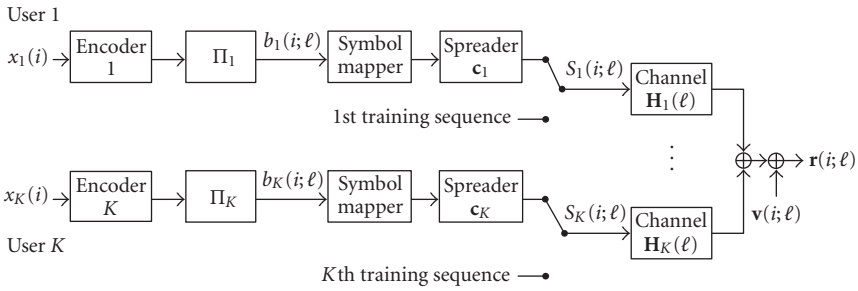

FIGURE 3.10. Transmitter structure for a coded CDMA system.

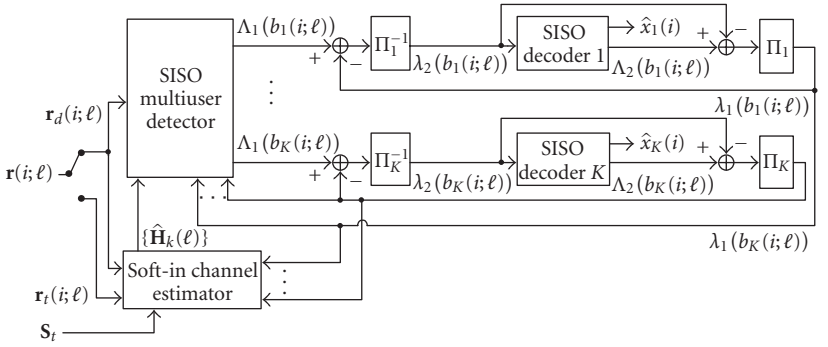

FIGURE 3.11. Soft-iterative receiver structure for a coded CDMA system.

LLRs for the information bits $x_k(i)$ are computed as well by the decoders to provide the final estimates $\hat{x}_k(i)$.

Figure 3.12 shows the BER performance of the iterative receiver for different values of $E_b/N_0 = Q\sigma_s^2 \mathrm{E}[\|\mathbf{H}_k\|^2]/(2RN\sigma_v^2)$ (defined for the coded system). The BER is evaluated at the ith turbo processing iteration for $i = 1, 2, 5$. Both the training-based (Figure 3.12a) and soft-based (Figure 3.12b) channel estimators are compared with the case of known channel. It is evident how the convergence of the iterative processing depends on the reliability of channel state information: if the training-based FR method is used, the BER is still high after 5 iterations due to channel estimate inaccuracy and the convergence is prevented. A remarkable gain in performance is reached by the training-based MB method. But the advantage of using soft information is evident: the soft MB subspace method outperforms all other estimation methods and at the 5th iteration it closely approaches the performance for known channel.

3.5. Summary

Subspace methods have been proposed for the estimation of block-fading channels in block transmission systems. The proposed methods reduce the number

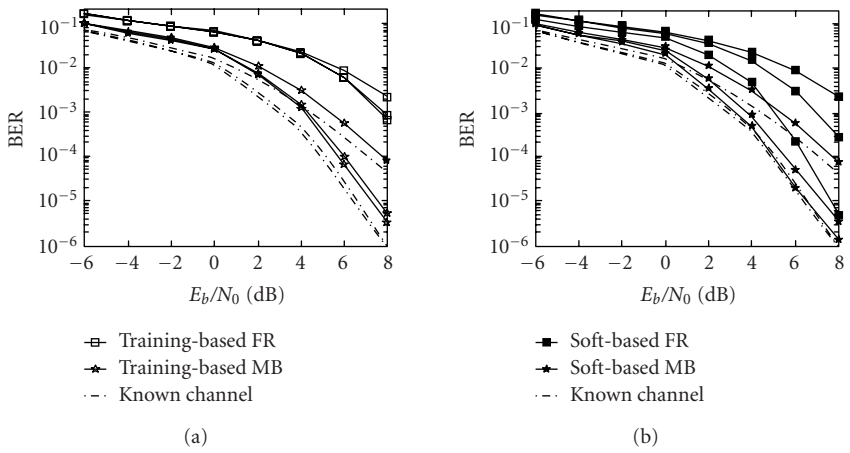

FIGURE 3.12. Performance of soft-iterative MMSE MUD receivers with FR and MB channel estimation for number of iterations $i = 1, 2, 5$: (a) training-based estimation and (b) soft-based estimation.

of relevant channel parameters by exploiting the algebraic spatial-temporal structure of the propagation and its quasistationarity over a large number of blocks. In soft-iterative receivers subspace-based estimation has been modified to incorporate soft-valued information-bearing data. Analytical and simulation results have shown the benefits of the proposed methods (either training- or data-based) on the performance of space-time receivers, even in realistic and complex multipath radio environments.

Abbreviations

BER	Bit error rate
CDMA	Code division multiple access
COST-259 DCM	COST-259 directional channel model
GBU	Generalized bad urban
GHT	Generalized hill terrian
GRA	Generalized rural area
GTU	Generalized typical urban
ISI	Intersymbol-interference
LLR	Log-likelihood ratio
MAI	Multiple access interference
MAP	Maximum a posteriori
MB	Multiblock
MB-S	MB-spatial
MB-T	MB-temporal
MB-ST	MB space-time
MDL	Minimum description length
MIMO	Multiple-input multiple-output
MLE	Maximum likelihood estimation
MMSE	Minimum mean square error

MSE	Mean square error
MUD	Multiuser detection
FR	Full-rank
OFDM	Orthogonal frequency division multiplexing
QPSK	Quaternary phase-shift keying
RR	Reduced-rank
SB	Single-block
SIMO	Single-input multiple-output
SNR	Signal-to-noise ratio
TD-CDMA	Time division-code division multiple access
TDMA	Time division multiple access
UMTS-TDD	Universal mobile telecommunication system-time division duplex
WSSUS	Wide sense stationary uncorrelated scattering
3G	3rd generation

Bibliography

[1] M. Wax and A. Leshem, "Joint estimation of time delays and directions of arrival of multiple reflections of a known signal," *IEEE Trans. Signal Processing*, vol. 45, no. 10, pp. 2477–2484, 1997.

[2] M. C. Vanderveen, A.-J. van der Veen, and A. Paulraj, "Estimation of multipath parameters in wireless communications," *IEEE Trans. Signal Processing*, vol. 46, no. 3, pp. 682–690, 1998.

[3] A. L. Swindlehurst, "Time delay and spatial signature estimation using known asynchronous signals," *IEEE Trans. Signal Processing*, vol. 46, no. 2, pp. 449–462, 1998.

[4] P. Stoica and M. Viberg, "Maximum likelihood parameter and rank estimation in reduced-rank multivariate linear regressions," *IEEE Trans. Signal Processing*, vol. 44, no. 12, pp. 3069–3078, 1996.

[5] D. Giancola, A. Sanguanini, and U. Spagnolini, "Variable rank receiver structures for low-rank space-time channels," in *IEEE 49th Vehicular Technology Conference*, vol. 1, pp. 65–69, Houston, Tex, USA, May 1999.

[6] E. Lindskog and C. Tidestav, "Reduced rank channel estimation," in *IEEE 49th Vehicular Technology Conference*, vol. 2, pp. 1126–1130, Houston, Tex, USA, May 1999.

[7] A. Dogandžić and A. Nehorai, "Finite-length MIMO equalization using canonical correlation analysis," *IEEE Trans. Signal Processing*, vol. 50, no. 4, pp. 984–989, 2002.

[8] M. Nicoli and U. Spagnolini, "Reduced-rank channel estimation for time-slotted mobile communication systems," *IEEE Trans. Signal Processing*, vol. 53, no. 3, pp. 926–944, 2005.

[9] M. Nicoli, O. Simeone, and U. Spagnolini, "Multislot estimation of fast-varying space-time communication channels," *IEEE Trans. Signal Processing*, vol. 51, no. 5, pp. 1184–1195, 2003.

[10] C. Douillard, A. Picard, P. Didier, M. Jézéquel, C. Berrou, and A. Glavieux, "Iterative correction of intersymbol interference: turbo equalization," *European Trans. Telecommunications*, vol. 6, no. 5, pp. 507–511, 1995.

[11] 3rd Generation Partnership Project (3GPP), "Technical specification group radio access network," Release 5, Series 25 (http://www.3gpp.org/).

[12] H. Holma and A. Toskala, Eds., *WCDMA for UMTS: Radio Access for Third Generation Mobile Communications*, John Wiley & Sons, New York, NY, USA, 2000.

[13] O. Simeone, Y. Bar-Ness, and U. Spagnolini, "Pilot-based channel estimation for OFDM systems by tracking the delay-subspace," *IEEE Trans. Wireless Commun.*, vol. 3, no. 1, pp. 315–325, 2004.

[14] H. L. Van Trees, *Optimum Array Processing*, Wiley-Interscience, New York, NY, USA, 2002.

[15] G. L. Stuber, *Principles of Mobile Communication*, Kluwer Academic Publishers, Norwell, Mass, USA, 1st edition, 1996.

[16] L. L. Scharf, *Statistical Signal Processing: Detection, Estimation, and Time Series Analysis*, Addison-Wesley, Reading, Mass, USA, 1991.

[17] J. Li, B. Halder, P. Stoica, and M. Viberg, "Computationally efficient angle estimation for signals with known waveforms," *IEEE Trans. Signal Processing*, vol. 43, no. 9, pp. 2154–2163, 1995.

[18] M. Viberg, P. Stoica, and B. Ottersten, "Maximum likelihood array processing in spatially correlated noise fields using parameterized signals," *IEEE Trans. Signal Processing*, vol. 45, no. 4, pp. 996–1004, 1997.

[19] A. K. Gupta and D. K. Nagar, *Matrix Variate Distributions*, vol. 104 of *Chapman & Hall/CRC Monographs and Surveys in Pure and Applied Mathematics*, Chapman & Hall/CRC, Boca Raton, Fla, USA, 2000.

[20] Y. Hua, M. Nikpour, and P. Stoica, "Optimal reduced-rank estimation and filtering," *IEEE Trans. Signal Processing*, vol. 49, no. 3, pp. 457–469, 2001.

[21] T. Gustafsson and B. D. Rao, "Statistical analysis of subspace-based estimation of reduced-rank linear regressions," *IEEE Trans. Signal Processing*, vol. 50, no. 1, pp. 151–159, 2002.

[22] P. Forster and T. Aste, "Maximum likelihood multichannel estimation under reduced rank constraint," in *IEEE International Conference on Acoustics, Speech, and Signal Processing (ICASSP '98)*, vol. 6, pp. 3317–3320, Seattle, Wash, USA, May 1998.

[23] L. L. Scharf, "The SVD and reduced rank signal processing," *Signal Process.*, vol. 25, no. 2, pp. 113–133, 1991.

[24] F. Dietrich and W. Utschick, "On the effective spatio-temporal rank of wireless communication channels," in *Proc. 13th IEEE International Symposium on Personal, Indoor and Mobile Radio Communications*, vol. 5, pp. 1982–1986, Lisbon, Portugal, September 2002.

[25] M. Wax and T. Kailath, "Detection of signals by information theoretic criteria," *IEEE Trans. Acoustics, Speech, Signal Processing*, vol. 33, no. 2, pp. 387–392, 1985.

[26] P. Strobach, "Low-rank adaptive filters," *IEEE Trans. Signal Processing*, vol. 44, no. 12, pp. 2932–2947, 1996.

[27] M. Nicoli, M. Sternad, U. Spagnolini, and A. Ahlén, "Reduced-rank channel estimation and tracking in time-slotted CDMA systems," in *IEEE International Conference on Communications (ICC '02)*, pp. 533–537, New York, NY, USA, April–May 2002.

[28] A. Graham, *Kronecker Products and Matrix Calculus: with Applications*, John Wiley & Sons, New York, NY, USA, 1981.

[29] M. Tüchler, A. C. Singer, and R. Koetter, "Minimum mean squared error equalization using a priori information," *IEEE Trans. Signal Processing*, vol. 50, no. 3, pp. 673–683, 2002.

[30] M. Tüchler, R. Otnes, and A. Schmidbauer, "Performance of soft iterative channel estimation in turbo equalization," in *IEEE International Conference on Communications (ICC '02)*, pp. 1858–1862, New York, NY, USA, April–May 2002.

[31] M. Kopbayashi, J. Boutros, and G. Caire, "Successive interference cancellation with SISO decoding and EM channel estimation," *IEEE J. Select. Areas Commun.*, vol. 19, no. 8, pp. 1450–1460, 2001.

[32] J. Proakis, *Digital Communications*, McGraw-Hill, New York, NY, USA, 3rd edition, 1995.

[33] S. ten Brink, "Convergence behavior of iteratively decoded parallel concatenated codes," *IEEE Trans. Commun.*, vol. 49, no. 10, pp. 1727–1737, 2001.

[34] S. Verdú, *Multiuser Detection*, Cambridge University Press, Cambridge, UK, 1998.

[35] X. Wang and H. V. Poor, "Space-time multiuser detection in multipath CDMA channels," *IEEE Trans. Signal Processing*, vol. 47, no. 9, pp. 2356–2374, 1999.

[36] P. Jung and J. Blanz, "Joint detection with coherent receiver antenna diversity in CDMA mobile radio systems," *IEEE Trans. Veh. Technol.*, vol. 44, no. 1, pp. 76–88, 1995.

[37] M. Beretta, A. Colamonico, M. Nicoli, V. Rampa, and U. Spagnolini, "Space-time multiuser detectors for TDD-UTRA: design and optimization," in *IEEE 54th Vehicular Technology Conference (VTC 2001-Fall)*, vol. 1, pp. 375–379, Atlantic City, NJ, USA, October 2001.

[38] L. M. Correia, Ed., *Wireless Flexible Personalised Communications: COST 259*, John Wiley & Sons, New York, NY, USA, 2001.

[39] X. Wang and H. V. Poor, "Iterative (turbo) soft interference cancellation and decoding for coded CDMA," *IEEE Trans. Commun.*, vol. 47, no. 7, pp. 1046–1061, 1999.

[40] L. Bahl, J. Cocke, F. Jelinek, and J. Raviv, "Optimal decoding of linear codes for minimizing symbol error rate," *IEEE Trans. Inform. Theory*, vol. 20, no. 2, pp. 284–287, 1974.

M. Nicoli: Dipartimento di Elettronica e Informazione, Politecnico di Milano, 32 Piazza Leonardo da Vinci, 20133 Milano, Italy

Email: nicoli@elet.polimi.it

U. Spagnolini: Dipartimento di Elettronica e Informazione, Politecnico di Milano, 32 Piazza Leonardo da Vinci, 20133 Milano, Italy

Email: spagnoli@elet.polimi.it

4 Multiuser MIMO channel equalization

Christoph F. Mecklenbräuker,
Joachim Wehinger, Thomas Zemen,
Harold Artés, and Franz Hlawatsch

In MIMO receivers, the channel state needs to be estimated for equalization, detection, and for feedback to the transmitter in case of adaptive modulation and coding. Most current iterative [1, 2, 3] and noniterative [4] schemes in the single-user MIMO case are training-based and rely on the transmission of pilot symbols. Alternatives to pilot-based algorithms are semiblind schemes which exploit, for example, the known structure of the space-time code to allow reliable channel estimation during ongoing data transmission [5, 6, 7, 8]. Channel estimation and equalization for multiuser MIMO systems involve both information-theoretic [9, 10] and signal processing aspects.

Early contributions to the field of MIMO communications assumed that the receiver has perfect channel state information. Recently there has been increased interest in the case where neither the receiver nor the transmitter knows the channel state [11, 12, 13, 14]. We consider this case in Section 4.2. In [5], a linear space-time modulation technique was proposed which allows the receiver to jointly estimate the channel and demodulate the data without prior channel knowledge at the transmitter or receiver. In Section 4.2, this modulation scheme is extended to the case of multiple users.

Section 4.3 investigates iterative equalization, detection, and interference cancellation for CDMA with random spreading. An iterative space-time receiver is considered for the uplink of a coded CDMA system. This type of receivers was studied in [15, 16, 17] for perfect channel knowledge. The extension to multipath fading channels incorporating soft decisions for improved estimation was presented in [18]. We show that such multiuser MIMO communication systems achieve low bit error rates at moderate complexity.

Section 4.4 treats equalization of time-variant MIMO multipath channels. We propose a multiuser MIMO equalizer for OFDM using a basis expansion [19, 20] with prolate spheroidal sequences to represent the time-variant mobile radio channel. The resulting blockwise estimator-equalizer fits well to OFDM receiver architectures [21, 22].

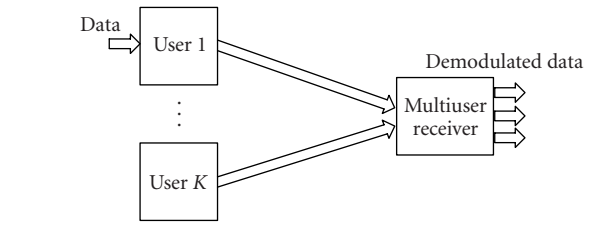

(a)

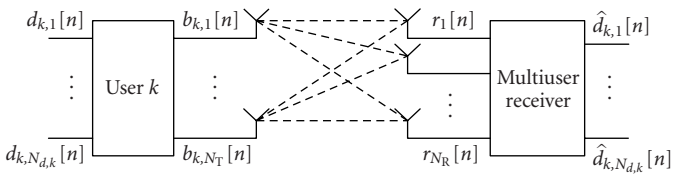

(b)

FIGURE 4.1. (a) Multiuser MIMO system model. (b) Detail for user k.

4.1. Signal and system model

We consider the multiuser MIMO signal and system model for K simultaneous users shown in Figure 4.1. In this model, the nth received sample at the qth receiver antenna element is described by

$$r_q[n] = \sum_{k=1}^{K} \sum_{p=1}^{N_T} \sum_{\ell=0}^{L-1} h_{k,p,q}[n,\ell] b_{k,p}[n-\ell] + v_q[n]. \tag{4.1}$$

The (generally time-variant) equivalent baseband MIMO channel impulse response for the kth user is denoted by $h_{k,p,q}[n,\ell]$. Here, $p = 1,\ldots,N_T$ and $q = 1,\ldots,N_R$ index the transmit and receive antenna elements, respectively. The time sample is denoted by n and ℓ is the delay index. The pth antenna element of the kth user transmits the waveform $b_{k,p}[n]$ at sample time denoted by n. The circular complex zero-mean Gaussian noise with variance σ_v^2 is denoted by $v_q[n]$. In matrix-vector notation, (4.1) is rewritten as

$$\boldsymbol{r}[n] = \sum_{k=1}^{K} \sum_{\ell=0}^{L-1} \boldsymbol{H}_k[n,\ell] \boldsymbol{b}_k[n-\ell] + \boldsymbol{v}[n], \tag{4.2}$$

where the receive vector $\boldsymbol{r}[n]$ and noise vector $\boldsymbol{v}[n]$ have N_R elements each, $\boldsymbol{H}_k[n,\ell]$ is the $N_R \times N_T$ MIMO channel impulse response matrix at sample n and lag ℓ, and the transmit sample vector $\boldsymbol{b}_k[n]$ has N_T elements.

4.2. Space-time matrix modulation and demodulation

A linear *space-time matrix modulation* technique was proposed in [5] allowing the receiver to jointly estimate the channel and demodulate the data. Prior channel state knowledge is neither required at the transmitter nor required at the receiver. Here, we extend space-time matrix modulation to multiple users. This extension is enabled by a close analogy between the rank-deficient single-user case and the multiuser case [6].

4.2.1. Review of single-user space-time matrix modulation

First, we briefly review space-time matrix modulation for the single-user case. The single-user transmission system is shown in Figure 4.1b. We consider $N_d < N_T$ input data streams $d_1[n], \ldots, d_{N_d}[n]$ with $d_l[n] \in \mathbb{C}$ (i.e., no finite-alphabet assumption is made), where n is the symbol time index. The modulator generates the transmit signal vectors $\boldsymbol{b}[n]$ of dimension N_T according to

$$\boldsymbol{b}[n] = \sum_{l=1}^{N_d} d_l[n]\boldsymbol{m}_l[n], \quad n = 0, \ldots, M-1, \tag{4.3}$$

where M is the block length and the $\boldsymbol{m}_l[n]$ are fixed sequences of *modulation vectors*. Equivalently, we have

$$\boldsymbol{B} = \sum_{l=1}^{N_d} \boldsymbol{M}_l \boldsymbol{D}_l, \tag{4.4}$$

with the $N_T \times M$ transmit signal matrix $\boldsymbol{B} \triangleq [\boldsymbol{b}[0] \cdots \boldsymbol{b}[M-1]]$, the $N_T \times M$ *modulation matrices* $\boldsymbol{M}_l \triangleq [\boldsymbol{m}_l[0] \cdots \boldsymbol{m}_l[M-1]]$, and the diagonal $M \times M$ data matrices $\boldsymbol{D}_l \triangleq \operatorname{diag}\{d_l[0], \ldots, d_l[M-1]\}$, where $l = 1, \ldots, N_d$. The modulation vectors $\boldsymbol{m}_l[n]$ (or modulation matrices $\boldsymbol{M}_l$) determine how the data is mapped to the N_T transmit antennas; they are known to the receiver.

For simplicity of exposition, we assume noiseless transmission (however, in our simulation study in Subsection 4.2.5, we will use a noisy channel). For a single-user, flat-fading, noiseless MIMO channel, (4.2) simplifies to

$$\boldsymbol{r}[n] = \boldsymbol{H}\boldsymbol{b}[n]. \tag{4.5}$$

Defining $\boldsymbol{R} \triangleq [\boldsymbol{r}[0] \cdots \boldsymbol{r}[M-1]]$ and inserting (4.4) into (4.5), we obtain

$$\boldsymbol{R} = \boldsymbol{H}\boldsymbol{B} = \boldsymbol{H} \sum_{l=1}^{N_d} \boldsymbol{M}_l \boldsymbol{D}_l. \tag{4.6}$$

From the received matrix $\boldsymbol{R}$, the receiver jointly estimates the data $d_l[n]$ and the unknown channel $\boldsymbol{H}$.

A set of modulation matrices $\{\boldsymbol{M}_1, \ldots, \boldsymbol{M}_{N_d}\}$ will be called *admissible* if the data sequences $d_l[n]$ can be uniquely reconstructed (up to a single constant factor) from the received matrix $\boldsymbol{R}$, without knowledge of $\boldsymbol{H}$. In [5], we showed that for a sufficiently large block length (typically, $M \geq \lceil (N_{\mathrm{T}}^2 - 1)/(\mathrm{rank}\{\boldsymbol{H}\} - N_d) \rceil$), an admissible set of modulation matrices exists if $N_{\mathrm{R}} \geq N_{\mathrm{T}}$ and $\mathrm{rank}\{\boldsymbol{H}\} = N_{\mathrm{T}}$, and we proposed an efficient iterative demodulation algorithm for that case. Indeed, for $N_d < N_{\mathrm{T}}$ as assumed above, the structure enforced by (4.4) corresponds to a *redundancy* of the transmit matrix $\boldsymbol{B}$ which constrains the reconstructed data such that unique reconstruction is possible.

4.2.2. Multiuser space-time matrix modulation

We now consider the multiuser case as illustrated in Figure 4.1. There are K users, each of them equipped with N_{T} transmit antennas and transmitting simultaneously to a single receiver with N_{R} receive antennas. The kth user has $N_{d,k}$ input data streams $d_{k,l}[n]$ with associated $M \times M$ diagonal data matrices $\boldsymbol{D}_{k,l} \triangleq \mathrm{diag}\{d_{k,l}[0], \ldots, d_{k,l}[M-1]\}$. By a natural extension of our space-time matrix modulation format (4.4), we construct the transmit matrix of the kth user as

$$\boldsymbol{B}_k = \sum_{l=1}^{N_{d,k}} \boldsymbol{M}_{k,l} \boldsymbol{D}_{k,l}, \tag{4.7}$$

with $N_{d,k}$ modulation matrices $\boldsymbol{M}_{k,l}$ of size $N_{\mathrm{T}} \times M$. The input-output relation of the multiuser channel is

$$\boldsymbol{R} = \sum_{k=1}^{K} \boldsymbol{H}_k \boldsymbol{B}_k, \tag{4.8}$$

where $\boldsymbol{H}_k$ and $\boldsymbol{B}_k$ are the (unknown) $N_{\mathrm{R}} \times N_{\mathrm{T}}$ channel matrix and the $N_{\mathrm{T}} \times M$ transmit matrix, respectively, associated with the kth user. Inserting (4.7) in (4.8), we obtain the overall input-output relation (which extends (4.6))

$$\boldsymbol{R} = \sum_{k=1}^{K} \boldsymbol{H}_k \sum_{l=1}^{N_{d,k}} \boldsymbol{M}_{k,l} \boldsymbol{D}_{k,l}. \tag{4.9}$$

We now reformulate this input-output relation for showing the similarity of the multiuser case to the rank-deficient single-user case. Let $\boldsymbol{\mathcal{H}} \triangleq [\boldsymbol{H}_1 \cdots \boldsymbol{H}_K]$ denote the overall channel matrix obtained by stacking the individual channel matrices of all users. Furthermore, let $\boldsymbol{\mathcal{M}}_{k,l} \triangleq \left[\boldsymbol{0}^{\mathrm{T}} \cdots \boldsymbol{0}^{\mathrm{T}} \boldsymbol{M}_{k,l}^{\mathrm{T}} \, \boldsymbol{0}^{\mathrm{T}} \cdots \boldsymbol{0}^{\mathrm{T}}\right]^{\mathrm{T}}$ denote a "zero-padded" modulation matrix of size $KN_{\mathrm{T}} \times M$ that is obtained by stacking $k-1$ zero matrices $\boldsymbol{0}$ of size $N_{\mathrm{T}} \times M$ above $\boldsymbol{M}_{k,l}$ and $K-k$ such zero matrices below $\boldsymbol{M}_{k,l}$. We rewrite (4.9) as

$$\boldsymbol{R} = \boldsymbol{\mathcal{H}} \boldsymbol{\mathcal{B}} = \boldsymbol{\mathcal{H}} \sum_{k=1}^{K} \sum_{l=1}^{N_{d,k}} \boldsymbol{\mathcal{M}}_{k,l} \boldsymbol{D}_{k,l}, \tag{4.10}$$

with $\boldsymbol{\mathcal{B}} \triangleq \sum_{k=1}^{K} \sum_{l=1}^{N_{d,k}} \boldsymbol{\mathcal{M}}_{k,l} \boldsymbol{D}_{k,l}$. Comparing with (4.6), we see that the multiuser case is equivalent to the single-user case with KN_{T} transmit antennas, N_{R} receive antennas, $N_K \triangleq \sum_{k=1}^{K} N_{d,k}$ data streams, a channel matrix $\boldsymbol{\mathcal{H}}$ of size $N_{\mathrm{R}} \times KN_{\mathrm{T}}$, and modulation matrices $\boldsymbol{\mathcal{M}}_{k,l}$ of size $KN_{\mathrm{T}} \times M$ that are nonzero only in the N_{T} rows with indices $kN_{\mathrm{T}} + 1, \ldots, (k+1)N_{\mathrm{T}}$. Typically, there will be $N_{\mathrm{R}} < KN_{\mathrm{T}}$ and thus $\mathrm{rank}\{\boldsymbol{\mathcal{H}}\} < KN_{\mathrm{T}}$ (rank-deficient case).

4.2.3. Unique reconstruction and flexible user allocation

Based on the formulation above, we can use a theorem on identifiability or unique reconstruction for rank-deficient channels [6] to prove the following statements.

Let $N_K < \mathrm{rank}\{\boldsymbol{\mathcal{H}}\}$ and $N_{d,k} < \mathrm{rank}\{\boldsymbol{H}_k\}$, that is, the total number of data streams is smaller than the rank of the composite channel and the number of data streams transmitted by any user k is smaller than the rank of that user's channel. Furthermore, assume that the block length is large enough (typically, $M \geq \lceil ((KN_{\mathrm{T}})^2 - K)/(\mathrm{rank}\{\boldsymbol{\mathcal{H}}\} - N_K) \rceil$ is sufficient but larger block lengths are advisable for faster convergence of the iterative demodulation algorithm to be proposed in Subsection 4.2.4). Then there exist sets of admissible modulation matrices $\boldsymbol{M}_{k,l}$ allowing unique reconstruction of all data streams up to a single unknown constant factor $c_k \in \mathbb{C}$ per user.

Moreover, a set of modulation matrices $\{\boldsymbol{M}_{k,l}\}$ with $k = 1, \ldots, K$ and $l = 1, \ldots, N_{d,k}$ that is admissible in the above setting is also admissible for any single $N_{\mathrm{R}} \times N_{\mathrm{T}}$ matrix $\boldsymbol{H}$ (provided that $\mathrm{rank}\{\boldsymbol{H}\}$ is sufficient for the N_K data streams), and the same is true for an arbitrary subset of $\{\boldsymbol{M}_{k,l}\}$. The latter result provides the basis for a flexible multiple-access scheme. Indeed, it means that the modulation matrices of a given admissible set $\{\boldsymbol{M}_{k,l}\}$ can be arbitrarily assigned to the individual users according to their respective data-rate requirements. In the extreme case, all N_K modulation matrices $\boldsymbol{M}_{k,l}$ could be allocated to a single user.

4.2.4. Iterative blind demodulation algorithm

Given a received matrix $\boldsymbol{R} = \boldsymbol{\mathcal{H}}\boldsymbol{\mathcal{B}}$ and assuming admissible modulation matrices $\boldsymbol{\mathcal{M}}_{k,l}$, our identifiability result implies the following. If the receiver is able to find matrices $\widehat{\boldsymbol{\mathcal{H}}}$ and $\widehat{\boldsymbol{\mathcal{B}}}$ that satisfy the two properties

(1) $\widehat{\boldsymbol{\mathcal{H}}}\widehat{\boldsymbol{\mathcal{B}}} = \boldsymbol{R}$,

(2) $\widehat{\boldsymbol{\mathcal{B}}} = \sum_{k=1}^{K} \sum_{l=1}^{N_{d,k}} \boldsymbol{\mathcal{M}}_{k,l} \hat{\boldsymbol{D}}_{k,l}$ with $\hat{\boldsymbol{D}}_{k,l}$ diagonal,

then the $\hat{\boldsymbol{D}}_{k,l}$ contain the correct data up to a single constant factor $c_k \in \mathbb{C}$ per user. This motivates an iterative blind demodulation algorithm that is primarily suited for the uplink of a multiuser wireless system because it yields the signals of all users. The ith iteration executes the following two steps.

Step 1. This step aims at enforcing property (1). That is, given $\widehat{\boldsymbol{\mathcal{B}}}_2^{(i-1)}$ as a result of Step 2 of the previous iteration (see below), we wish to find $\widehat{\boldsymbol{\mathcal{H}}}^{(i)}$ and $\widehat{\boldsymbol{\mathcal{B}}}_1^{(i)}$ such that $\widehat{\boldsymbol{\mathcal{H}}}^{(i)}\widehat{\boldsymbol{\mathcal{B}}}_1^{(i)}$ best approximates $\boldsymbol{R}$.

As a first substep, we calculate $\widehat{\boldsymbol{\mathcal{H}}}^{(i)}$ such that $\widehat{\boldsymbol{\mathcal{H}}}^{(i)}\widehat{\boldsymbol{\mathcal{B}}}_2^{(i-1)}$ best approximates $\boldsymbol{R}$ in the least-squares (LS) sense. This gives $\widehat{\boldsymbol{\mathcal{H}}}^{(i)} = \boldsymbol{R}\widehat{\boldsymbol{\mathcal{B}}}_2^{(i-1)\#}$, where $\widehat{\boldsymbol{\mathcal{B}}}_2^{(i-1)\#}$ denotes the pseudoinverse of $\widehat{\boldsymbol{\mathcal{B}}}_2^{(i-1)}$. As a second substep, we calculate $\widehat{\boldsymbol{\mathcal{B}}}_1^{(i)}$ such that $\widehat{\boldsymbol{\mathcal{H}}}^{(i)}\widehat{\boldsymbol{\mathcal{B}}}_1^{(i)}$ best approximates $\boldsymbol{R}$ in the LS sense. This gives the final result

$$\widehat{\boldsymbol{\mathcal{B}}}_1^{(i)} = \widehat{\boldsymbol{\mathcal{H}}}^{(i)\#}\boldsymbol{R} = \left(\boldsymbol{R}\widehat{\boldsymbol{\mathcal{B}}}_2^{(i-1)\#}\right)^{\#}\boldsymbol{R}. \tag{4.11}$$

Step 2. This step enforces property (2). That is, we approximate $\widehat{\boldsymbol{\mathcal{B}}}_1^{(i)}$ from Step 1 above by a matrix $\widehat{\boldsymbol{\mathcal{B}}}_2^{(i)}$ with the modulation structure of property (2), that is, $\widehat{\boldsymbol{\mathcal{B}}}_2^{(i)} = \sum_{k=1}^{K}\sum_{l=1}^{N_{d,k}} \boldsymbol{\mathcal{M}}_{k,l}\hat{\boldsymbol{D}}_{k,l}^{(i)}$. The diagonal matrices $\hat{\boldsymbol{D}}_{k,l}^{(i)}$ are chosen such that $\widehat{\boldsymbol{\mathcal{B}}}_2^{(i)}$ best approximates $\widehat{\boldsymbol{\mathcal{B}}}_1^{(i)}$ in the LS sense. It can be shown that the nonzero (diagonal) elements of $\hat{\boldsymbol{D}}_{k,l}^{(i)}$ are given by

$$\left(\hat{\boldsymbol{D}}_{k,l}^{(i)}\right)_{n,n} = \frac{1}{N_{\mathrm{T}}}\sum_{j=1}^{N_{\mathrm{T}}}\left(\widehat{\boldsymbol{\mathcal{B}}}_1^{(i)}\right)_{j,n}\left(\mathbf{C}_{\lambda(k,l)}^{(i)}\right)_{j,n}, \quad \lambda(k,l) \triangleq \sum_{\kappa=1}^{k-1} N_{d,\kappa} + l, \tag{4.12}$$

where the $\mathbf{C}_{\lambda}^{(i)}$ are matrices of size $N_{\mathrm{T}} \times M$ that are constructed as follows. Let $\boldsymbol{\mu}_{k,l}[n]$ with $n = 0,\ldots,M-1$ denote the $(n+1)$th column of $\boldsymbol{\mathcal{M}}_{k,l}$, that is, $\boldsymbol{\mathcal{M}}_{k,l} = [\boldsymbol{\mu}_{k,l}[0]\cdots\boldsymbol{\mu}_{k,l}[M-1]]$. Furthermore, for fixed n, let $\boldsymbol{M}[n]$ denote the $N_{\mathrm{T}}\times N_K$ matrix that contains the nth columns of all $\boldsymbol{\mathcal{M}}_{k,l}$ for $l = 1,\ldots,N_{d,k}$ and $k = 1,\ldots,K$, that is,

$$\boldsymbol{M}[n] \triangleq \left[\boldsymbol{\mu}_{1,1}[n]\cdots\boldsymbol{\mu}_{1,N_{d,1}}[n]\cdots\boldsymbol{\mu}_{K,1}[n]\cdots\boldsymbol{\mu}_{K,N_{d,K}}[n]\right]. \tag{4.13}$$

Then, the nth column of $\mathbf{C}_{\lambda}^{(i)}$ is defined as the λth row of the $N_K \times N_{\mathrm{T}}$ matrix $(\widehat{\boldsymbol{\mathcal{H}}}^{(i)\#}\widehat{\boldsymbol{\mathcal{H}}}^{(i)}\boldsymbol{M}[n])^{\#}$, where $\widehat{\boldsymbol{\mathcal{H}}}^{(i)}$ was calculated in Step 1 above.

This algorithm yields an estimate $\widehat{\boldsymbol{\mathcal{H}}}^{(i)}$ of the channel matrix in Step 1 and estimates $\hat{\boldsymbol{D}}_{k,l}^{(i)}$ of the data matrices in Step 2. In the noise-free case, we always observed the algorithm to converge to the correct channel and data matrices up to a single complex factor per user. Results in the presence of noise will be shown next.

4.2.5. Simulation results and discussion

We carried out both a single-user experiment and a multiuser experiment, in which we transmitted i.i.d. complex Gaussian signals $d_{k,l}[n] \in \mathbb{C}$ over channels with $N_{\mathrm{T}} = 4$ transmit antennas and $N_{\mathrm{R}} = 4$ receive antennas. The modulation matrices $\boldsymbol{\mathcal{M}}_{k,l}$ with block length $M = 100$ were constructed by taking realizations of i.i.d. Gaussian random variables as matrix entries and then orthonormalizing the corresponding columns of all $\boldsymbol{\mathcal{M}}_{k,l}$ (in our simulations, this always resulted in admissible modulation matrices). The channels were randomly generated for

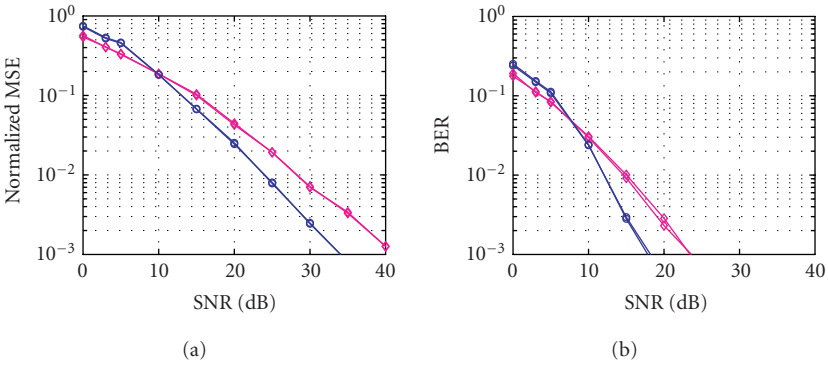

FIGURE 4.2. Performance of space-time matrix modulation and the iterative demodulation algorithm: (a) Normalized MSE versus SNR. (b) BER versus SNR. ◇—◇: Single-user case—two data streams assigned to a single user; ○—○: multiuser case—one data stream assigned to each of two different users.

each simulation run. The channel output signals were corrupted by white Gaussian noise.

In the single-user case, we transmitted $N_d = 2$ data streams. In the multiuser case, we considered $K = 2$ users with one data stream each (thus, $N_K = 2$). Figure 4.2a shows the total normalized mean square error (MSE) of the data streams reconstructed by means of our iterative blind demodulation algorithm versus the signal-to-noise ratio (SNR). We see that for high SNR, the MSE is significantly smaller when the data streams are assigned to different users than when one user transmits all data streams.

We discuss this result in the following. In the multiuser case, there are eight transmit antennas (four per user) against four in the single-user case. Thus, even though the individual users do not cooperate, the multiuser channel offers more diversity than the single-user channel. The results show that the iterative blind demodulation algorithm exploits some of this extra diversity in the multiuser case. Note that we have not exploited channel knowledge, neither at the transmitter nor at the receiver. In the multiuser case, we have to estimate twice as many unknown channel parameters as in the single-user case.

Finally, Figure 4.2b shows the corresponding bit error rate (BER) versus the SNR when a 4-QAM transmit alphabet is used instead of the Gaussian source. The iterative demodulation algorithm is followed by a quantization to the 4-QAM alphabet. It is seen that the BERs decrease more rapidly than the corresponding normalized MSEs.

Space-time matrix modulation allows to transmit data streams from multiple users over *unknown* MIMO channels. An efficient iterative receiver algorithm has been proposed which exploits the modulation structure to jointly estimate data and channels for multiple users. Unique demodulation in the noise-free case is guaranteed theoretically. Simulations demonstrate good performance of the proposed space-time matrix modulation/demodulation in the presence of noise.

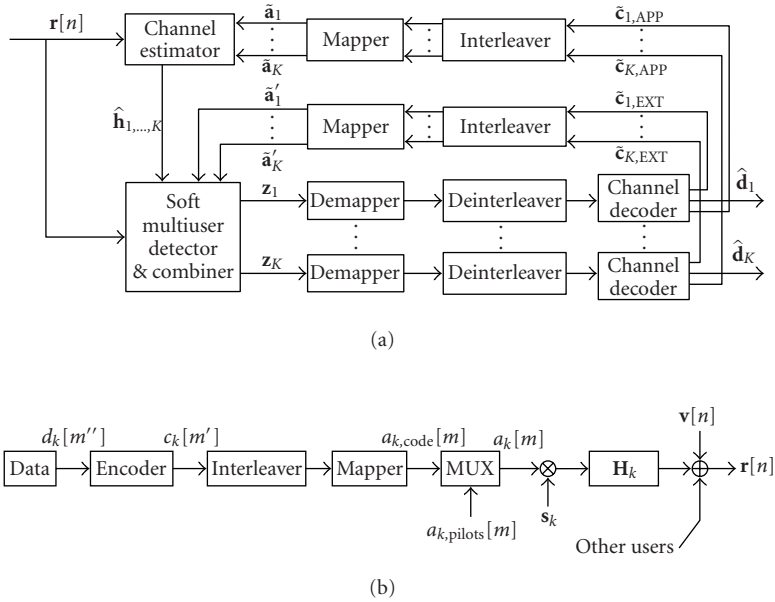

FIGURE 4.3. (a) Iterative multiuser MIMO equalization. (b) Uplink transmitter.

4.3. Iterative space-time equalization and demodulation for coded CDMA

An iterative receiver with space-time processing is considered for the uplink of a coded CDMA system. We assume that symbols are transmitted synchronously and multipath propagation is modeled with a temporal granularity of a chip duration. The receiver consists of a multiuser detector, a bank of single-user decoders, and a channel estimator; see Figure 4.3. The behavior of iterative receivers which employ ML channel estimation was reported in [23] for the special case of a single propagation path with constant amplitude. The results in this section are obtained for a receiver with N_R antenna elements. We show that such multiuser MIMO communication systems achieve low bit-error rates at moderate complexity.

4.3.1. Signal model

We assume that the propagation channel has block-fading characteristic, that is, the channel is constant over a block of M transmit symbols. Thus, $h_{k,p,q}[n,\ell]$ in the system model (4.1) does not depend on n. The first J symbols are pilots which are used for channel identification at each receiver antenna element. The subsequent $M-J$ symbols are QPSK symbols, derived from an uncoded information bit stream $d_k[m'']$ which is convolutionally encoded, randomly interleaved, and Gray mapped. The resulting M QPSK symbols $a_k[m]$ of user k are spread by the sequence $\boldsymbol{s}_k$ of dimension $N \times 1$. We reformulate (4.1) by separating the single

term for $\ell = 0$ from the remaining terms at lags $\ell > 0$:

$$r_q[n] = \sum_{k=1}^{K} \left(h_k[0] a\left[\left\lfloor \frac{n}{N} \right\rfloor \right] s_k[n \bmod N] + \sum_{\ell=1}^{L-1} h_k[\ell] a\left[\left\lfloor \frac{n-l}{N} \right\rfloor \right] s_k[(n-l) \bmod N] \right). \tag{4.14}$$

The elements of the sequence $\boldsymbol{s}_k$ are randomly drawn from the set $\{\pm 1 \pm \mathrm{j}\}/\sqrt{2N}$ such that $\|\boldsymbol{s}_k\|^2 = 1$. The uplink transmitter is shown in Figure 4.3b.

The system model (4.1) reflects the superposition of intersymbol interference (ISI) and multiple-access interference (MAI) components at the chip level n. Here, we assume that each user has a single transmit antenna, $N_\mathrm{T} = 1$, and we will thus omit the transmit antenna-element index p in the following. Note that a transmit symbol at time m is spread to a signal of length N. The channel is modeled on the chip level and has L taps such that the total receive vector affected by symbol $a[m]$ is of length $N + L - 1$. We denote this vector as

$$\boldsymbol{y}_q[m] \triangleq [r_q[(m-1)N] \cdots r_q[mN + L - 1]]^\mathrm{T}. \tag{4.15}$$

Note that $\boldsymbol{y}_q[m]$ describes a vector of temporally successive chip samples for one receive antenna, whereas $\boldsymbol{r}[n]$ in (4.1) describes a vector of chip samples at one chip instant but for all receive antennas.

The receiver consists of three processing units exchanging information on code symbols and channel estimates in an iterative manner. We will explain the individual parts in the sequel.

4.3.2. Soft multiuser detection

We implement and investigate multiuser detection with a parallel interference cancelling (PIC) unit and a subsequent single-user matched filter (SUMF) or a linear minimum mean square error (LMMSE) filter. Parallel interference cancellation is implemented using soft decisions $\tilde{a}'_k[m]$ defined in (4.29). These are obtained from the estimated *extrinsic* probabilities (EXT) of the code symbols available at the output of the channel decoder; see Figure 4.3a. See Section 4.3.4 for further details. The multiuser detector requires the signature sequences, their timing, and an estimate for the channel state to be known. The interference canceller removes MAI. ISI terms are explicitly considered in the cancellation since they can greatly influence the receiver's performance when the channel memory length L cannot be considered much smaller than N. If exact knowledge of all interfering users' symbols and the channel state were available, then the MAI could be eliminated perfectly. However, due to inaccurate channel knowledge and errors in the feedback symbols, this cannot be achieved. Usually, the process of interchanging information is done iteratively several times. The effective spreading sequence of user k at antenna element q is $\tilde{\boldsymbol{s}}_{k,q} = \boldsymbol{s}_k * \hat{\mathbf{h}}_{k,q}$ with $*$ denoting convolution and $\hat{\mathbf{h}}_{k,q}$

being the channel estimate. Stacking these vectors together leads to the effective spreading matrix $\tilde{\boldsymbol{S}}_q$ of dimension $(N+L-1)\times K$. The observation window covers ISI that is due to pre- and postcursors. The ISI length is

$$W = \left\lceil \frac{(N+L-1)}{N} \right\rceil. \tag{4.16}$$

The parallel interference canceller (PIC) calculates

$$\tilde{\boldsymbol{y}}_{k,q}[m] = \boldsymbol{y}_q[m] + \tilde{\boldsymbol{s}}_{k,q}\tilde{a}'_k[m] - \sum_{w=-W+1}^{W-1} \tilde{\boldsymbol{S}}_q[w]\tilde{\boldsymbol{a}}'[m-w]. \tag{4.17}$$

Terms indexed by $w < 0$ in the sum above correspond to ISI caused by future symbols, while terms indexed by $w > 0$ are related to preceding symbols. The matrices attributed to previous and current symbols are defined by

$$\tilde{\boldsymbol{S}}_q[w] = \begin{cases} \begin{pmatrix} \tilde{s}_{1,q}[wN] & \cdots & \tilde{s}_{K,q}[wN] \\ \tilde{s}_{1,q}[wN+1] & \cdots & \tilde{s}_{K,q}[wN+1] \\ \vdots & \ddots & \vdots \\ \tilde{s}_{1,q}[wN+\Delta-1] & \cdots & \tilde{s}_{K,q}[wN+\Delta-1] \\ \boldsymbol{0}_{wN} & \cdots & \boldsymbol{0}_{wN} \end{pmatrix} & \text{for } w > 0, \\ \tilde{\boldsymbol{S}}_q & \text{for } w = 0, \end{cases} \tag{4.18}$$

with $\Delta = (N+L-1) - WN$ and correspondingly for $w < 0$. After MAI removal, the signal is passed through a linear filter whose output is

$$z_{k,q}[m] = \boldsymbol{f}_{k,q}^{\mathrm{H}}[m]\tilde{\boldsymbol{y}}_{k,q}[m]. \tag{4.19}$$

We focus our interest on the SUMF and LMMSE filter. The latter filter is more involved due to the required matrix inversion. For certain system loads $\alpha = K/N$, the SUMF achieves the same BER as the LMMSE filter, but requires a higher number of iterations [24]. Results for both filters are shown in Figure 4.4.

The single-user matched filter is

$$\boldsymbol{f}_{k,q}[m] = \tilde{\boldsymbol{s}}_{k,q}, \tag{4.20}$$

and the LMMSE filter is defined as

$$\boldsymbol{g}_{k,q}[m] = \underset{\boldsymbol{g}}{\operatorname{argmin}}\, \mathbb{E}\left\{ \left| a_k[m] - \boldsymbol{g}^{\mathrm{H}}\tilde{\boldsymbol{y}}_{k,q}[m] \right|^2 \right\}. \tag{4.21}$$

A solution to (4.21) is found under the assumption of independent symbols $a_k[m]$ and when known symbols $a_k[m]$ are replaced by their estimates $\tilde{a}'_k[m]$ defined in

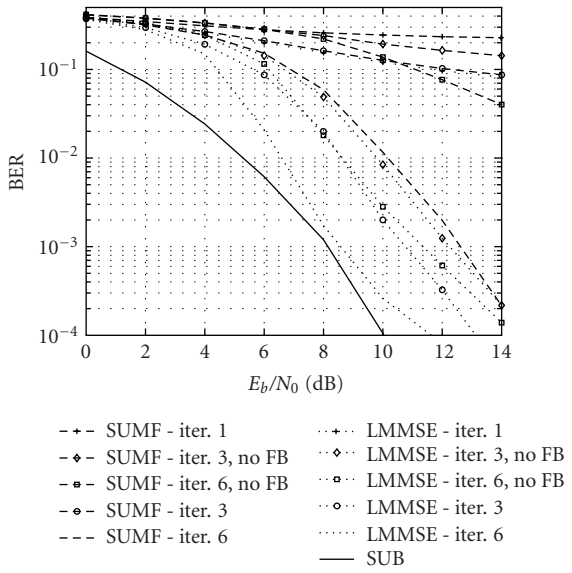

FIGURE 4.4. BER versus E_b/N_0 for the PIC-SUMF and PIC-LMMSE detectors with and without the use of soft decisions for channel estimation. The parameters are $K = 24$, $N = 16$, $L = 5$, $M = 250$, and $J = 20$.

(4.29). Then the filter becomes

$$\boldsymbol{g}_{k,q}^{\mathrm{H}}[m] = \tilde{\boldsymbol{s}}_{k,q}^{\mathrm{H}}\left(\sigma_v^2\boldsymbol{I} + \tilde{\boldsymbol{s}}_{k,q}\,|\,\tilde{a}_k'[m]\,|^2\tilde{\boldsymbol{s}}_{k,q}^{\mathrm{H}} + \sum_{w=-W+1}^{W-1}\tilde{\boldsymbol{S}}_q[w]\boldsymbol{V}[m]\tilde{\boldsymbol{S}}_q^{\mathrm{H}}[w]\right)^{-1} \tag{4.22}$$

with $\boldsymbol{V}[m]$ denoting the diagonal covariance matrix

$$\boldsymbol{V}[m] = \mathbb{E}\Big\{\big(\boldsymbol{a}[m] - \mathbb{E}\{\boldsymbol{a}[m]\}\big)\big(\boldsymbol{a}[m] - \mathbb{E}\{\boldsymbol{a}[m]\}\big)^{\mathrm{H}}\Big\}. \tag{4.23}$$

Now, we substitute $\mathbb{E}\{\boldsymbol{a}[m]\}$ by the *extrinsic* probability (EXT) $\tilde{\boldsymbol{a}}'[m]$ defined via (4.29). The resulting $\boldsymbol{V}[m]$ has diagonal elements $V_{k,k}[m] = 1 - |\tilde{a}_k'[m]|^2$. When $V_{k,k}[m]$ is computed for each symbol individually, the resulting filter is termed *conditional*. This, however, involves a matrix inversion for each symbol and every user. We follow on alternative approach and average over all code symbols in a single block to construct a $\boldsymbol{V} = \mathrm{diag}(V_{1,1}, \ldots, V_{K,K})$ which does not depend on the symbol index m. In this way, the filter needs to be computed only once for every user and iteration. The resulting filter $\boldsymbol{g}_{k,q}^{H}$ is called *unconditional* [25].

We have obtained a biased filter so far. The conditioned bias is $\beta[m] = \mathbb{E}\{z_{k,q}[m]/a_k[m]\} = \boldsymbol{g}_{k,q}^{\mathrm{H}}[m]\tilde{\boldsymbol{s}}_{k,q}[m]$. An unbiased and unconditional modification of (4.22) is $\boldsymbol{g'}_{k,q}^{\mathrm{H}} = (1/\beta)\boldsymbol{g}_{k,q}^{\mathrm{H}}$ which results in

$$\boldsymbol{g'}_{k,q}^{\mathrm{H}} = \frac{\tilde{\boldsymbol{s}}_{k,q}^{\mathrm{H}}\boldsymbol{Z}_q^{-1}}{\tilde{\boldsymbol{s}}_{k,q}^{\mathrm{H}}\boldsymbol{Z}_q^{-1}\tilde{\boldsymbol{s}}_{k,q}}, \quad \text{with } \boldsymbol{Z}_q = \sum_{w=-W+1}^{W-1}\tilde{\boldsymbol{S}}_q[w]\boldsymbol{V}\tilde{\boldsymbol{S}}_q^{\mathrm{H}}[w] + \sigma_v^2\boldsymbol{I}. \tag{4.24}$$

4.3.3. Antenna combining

The unbiased and unconditional LMMSE filter $\boldsymbol{g}'_{k,q}$ is applied to the receive vector $\tilde{\boldsymbol{y}}_{k,q}[m]$. A soft decision is obtained by maximum ratio combining (MRC) of all antennas by using the estimate $\widehat{\boldsymbol{h}}_{k,q}$ for the channel impulse response defined in (4.34):

$$z_k[m] = \frac{\sum_{q=1}^{N_R} ||\widehat{\boldsymbol{h}}_{k,q}||^2 \boldsymbol{g}'^{H}_{k,q} \tilde{\boldsymbol{y}}_{k,q}[m]}{\sum_{q=1}^{N_R} ||\widehat{\boldsymbol{h}}_{k,q}||^2}. \tag{4.25}$$

4.3.4. Decoding

The soft-decision feedback supplied to the channel and the data estimator are computed from the *a posteriori* probabilities (APP) and the *extrinsic* probabilities (EXT). A soft-input soft-output decoder for the binary convolutional code is implemented by the BCJR algorithm [26] which estimates these quantities. The decoder's input is given by the channel values $x_k[m']$ which are obtained from the $z_k[m]$ given in (4.25) through sequential demapping to a real sequence and deinterleaving (see Figure 4.3a). They are the received values for the $2(M-J)$ code bits $c_k[m']$. The conditional probability density of the multiuser detector (MUD) output values $x_k[m']$ can be modeled by a Gaussian distribution with mean $\pm\mu$ and variance v_k^2. The decision-directed estimate for the mean is $\hat{\mu} = 1/(2(M-J)) \sum_{i=0}^{2(M-J)-1} |x_k[i]|$ and for the variance is $\hat{v}_k^2 = (1/2(M-J)) \sum_{i=0}^{2(M-J)-1} |x_k[i]|^2 - \hat{\mu}$. The APP for having the value +1 as the code bit when observing the channel value $x_k[m']$ is given as $\mathrm{APP}_k[m'] = \Pr\{c_k[m'] = +1 \mid \boldsymbol{x}_k\}$, where the vector $\boldsymbol{x}_k$ contains all $x_k[m']$ of the code block. The link between the APP and the EXT is established via the relation

$$\mathrm{APP}_k[m'] \propto \mathrm{EXT}_k[m'] p(x_k[m'] \mid c_k[m'] = +1), \tag{4.26}$$

where the last term denotes the channel transition function which is assumed to be a Gaussian probability density in this section, estimated parametrically as

$$p(x_k[m'] \mid c_k[m'] = +1) \propto \exp\left(\frac{-|x_k[m'] - \hat{\mu}|^2}{\hat{v}_k^2}\right). \tag{4.27}$$

The APP values are normalized such that $\Pr\{c_k[m'] = +1|\boldsymbol{x}_k\} + \Pr\{c_k[m'] = -1|\boldsymbol{x}_k\} = 1$; the EXT values are normalized in the same way. After interleaving, these probabilities are used to obtain an estimate of the transmitted symbols. The QPSK mapping for the APPs and the EXTs is given by

$$\tilde{a}_k[J+m] = \frac{[1 - 2\,\mathrm{APP}_k[2m] + \mathrm{j}(1 - 2\,\mathrm{APP}_k[2m+1])]}{\sqrt{2}}, \tag{4.28}$$

$$\tilde{a}'_k[J+m] = \frac{[1 - 2\,\mathrm{EXT}_k[2m] + \mathrm{j}(1 - 2\,\mathrm{EXT}_k[2m+1])]}{\sqrt{2}}, \tag{4.29}$$

with $m \in \{0, \ldots, M - J - 1\}$. The symbol estimates $\tilde{a}'_k[m]$ are used in the feedback branch to the detector with PIC and SUMF/LMMSE filtering, while the soft decisions $\tilde{a}_k[m]$ are used for channel estimation as if they were additional pilot symbols.

4.3.5. Channel estimation

In a system with multiple receive antennas, all paths to the receive antennas need to be estimated. The initial estimate is based on training symbols in the preamble of the block of transmit symbols. In later iterations, the estimator is enhanced by incorporating soft decisions $\tilde{a}_k[m]$ derived from the APPs as described in (4.28).

It was shown in [27] that long spreading sequences with elements taken from the unit circle exhibit nice cross-correlation properties. These sequences are called perfect root-of-Unity sequences (PRUS) and are particularly well suited for multipath channel estimation with long delay spread. In our receiver, we choose a length of JN.

For channel estimation, we need to estimate each single propagation path and we model the signal somewhat different from (4.1):

$$\boldsymbol{y}_q = \left(\sum_{w=0}^{W-1} \boldsymbol{\mathcal{D}}_w \boldsymbol{\mathcal{A}}_w \right) \boldsymbol{h}_q + \boldsymbol{v}_q = \boldsymbol{\mathcal{U}} \boldsymbol{h}_q + \boldsymbol{v}_q, \tag{4.30}$$

where the various quantities involved are described below. The $MN \times 1$ vector $\boldsymbol{y}_q$ contains samples at the chip rate received at antenna q. The $MN \times MKL$ matrix $\boldsymbol{\mathcal{D}}_w$ is block diagonal and defined as

$$\operatorname{diag}(\underbrace{\boldsymbol{D}_w \cdots \boldsymbol{D}_w}_{M}), \quad \text{where } \boldsymbol{D}_w = [\boldsymbol{D}_{w,1} \cdots \boldsymbol{D}_{w,K}] \text{ is of dimension } N \times KL. \tag{4.31}$$

The matrix $\boldsymbol{D}_{w,k}$ is derived from the $WN \times L$ matrix

$$\boldsymbol{C}_k = \left(\begin{array}{ccccccccc}
s_k[0] & & & & & & & & \\
s_k[1] & s_k[0] & & & & & & & \\
s_k[2] & s_k[1] & s_k[0] & & & & & & \\
\vdots & \vdots & \ddots & \ddots & & & & & \\
s_k[N-1] & s_k[N-2] & s_k[N-3] & \cdots & s_k[0] & & & & \\
\hline
 & s_k[N-1] & s_k[N-2] & \cdots & s_k[1] & s_k[0] & & & \\
 & & s_k[N-1] & \cdots & s_k[2] & s_k[1] & \ddots & & \\
 & & & \ddots & \vdots & \vdots & \vdots & & \\
 & & & & & s_k[N-1] & \vdots & & \\
\hline
 & & & & & & s_k[N-1] & \ddots & \\
 & & & & & & \vdots & \ddots &
\end{array}\right). \tag{4.32}$$

Elements which are not covered by the shifted spreading sequence are zero. The matrix $\boldsymbol{D}_{w,k}$ contains the rows from $wN+1$ to $(w+1)N$ of $\boldsymbol{C}_k$. An exception is the construction of the first J matrices $\boldsymbol{D}_w$ for which the corresponding PRUSs are taken instead of the vectors $\boldsymbol{s}_k$. $\boldsymbol{\mathcal{A}}_w = [\boldsymbol{A}[0-w]\boldsymbol{A}[1-w]\cdots\ \boldsymbol{A}[M-1-w]]^{\mathrm{T}}$ is an $MKL \times KL$ vertically stacked matrix consisting of the diagonal $KL \times KL$ matrices

$$\boldsymbol{A}[m] = \operatorname{diag}\left(\boldsymbol{a}_1[m]\boldsymbol{a}_2[m]\cdots\boldsymbol{a}_K[m]\right), \quad \text{with } \boldsymbol{a}_k[m] = \tilde{a}_k[m]\mathbf{1}_L. \tag{4.33}$$

$\boldsymbol{h}_q$ is a $KL \times 1$ vector obtained by vertically stacking the $L \times 1$ chip impulse responses $\boldsymbol{h}_{k,q}$ of all users' channels, that is, $\boldsymbol{h}_q = \left[\boldsymbol{h}_{1,q}^{\mathrm{T}} \quad \boldsymbol{h}_{2,q}^{\mathrm{T}} \quad \cdots \quad \boldsymbol{h}_{K,q}^{\mathrm{T}}\right]^{\mathrm{T}}$. Finally, $\boldsymbol{v}_q$ designates an $NM \times 1$ zero-mean complex Gaussian noise vector with covariance matrix $\sigma_v^2\boldsymbol{I}_{NM}$. A least-squares (LS) estimator of $\boldsymbol{h}_q$ requires the symbols to be *known*. We replace the symbols $a_k[m]$ by their soft decisions $\tilde{a}_k[m]$ from (4.28). Using $\boldsymbol{\mathcal{U}}$ introduced in (4.30), we obtain the estimate

$$\hat{\boldsymbol{h}}_q = \left(\boldsymbol{\mathcal{U}}^{\mathrm{H}}\boldsymbol{\mathcal{U}}\right)^{-1}\boldsymbol{\mathcal{U}}^{\mathrm{H}}\boldsymbol{y}_q. \tag{4.34}$$

4.3.6. Simulation results and discussion

For illustration of the iterative space-time receiver concept, we use spreading factor $N = 16$. The encoder is a nonsystematic, nonrecursive convolutional code with rate $C_R = 1/2$ and generator polynomials $(5,7)_8$. The channel estimator uses the approximated LS approach formulated in (4.34). We assume an i.i.d. Rayleigh fading channel model with a delay spread L of 5 chips. The taps are normalized such that $\mathbb{E}\{\sum_{q=1}^{N_{\mathrm{R}}}\sum_{\ell=0}^{L-1}|h_{k,q}[\ell]|^2\} = 1$. We consider the channel impulse response to be constant during the transmission of a code block. The block length is $M = 250$ symbols out of which $J = 20$ are pilots which corresponds to 8% of the transmitted energy. To account for the energy loss due to the pilots, we define the ratio of energy per information bit and noise power spectral density as $E_b/N_0 = (1/\sigma_v^2 C_R)(M/M-J)$.

In Figure 4.4, the BER versus E_b/N_0 is shown for the PIC detectors with the SUMF and the LMMSE filter. The plot compares the difference in BER of the two detectors as well as the impact of using soft decisions to support the channel estimator. For the moment, we consider single-antenna reception in an overloaded system with load $\alpha = K/N = 1.5$. We illustrate the BER after the first, third, and sixth iterations together with single-user bound (SUB) which is defined as the BER in case of a single user in the system having perfect channel-state information. We notice that using feedback symbols in the multiuser detector and the channel estimator allows BERs of 10^{-3} after 6 iterations at an E_b/N_0 of 8.6 dB using an LMMSE filter and at 12.7 dB in case of the SUMF. The gap in E_b/N_0 between the two detectors at a BER of 10^{-3} is 4.1 dB. The LMMSE-based receiver is able to approach the SUB as close as 0.4 dB at an E_b/N_0 of 8 dB after 6 iterations. Furthermore, the results reveal that soft-decision feedback for channel estimation improves the receiver's performance considerably. When comparing the LMMSE receiver with a channel estimator using soft-decision feedback with a receiver which uses pilots

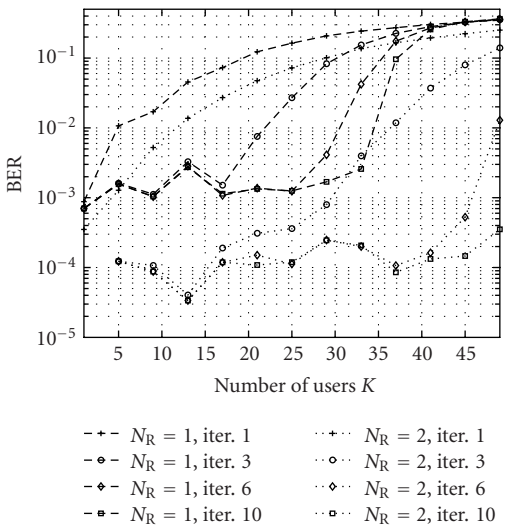

FIGURE 4.5. Achievable BER versus the number of users K for the PIC-LMMSE detector with one and two receive antennas. The parameters are $N = 16$, $L = 5$, $M = 250$, $J = 20$, and $E_b/N_0 = 8$ dB.

only for channel estimation, we observe an improvement of more than 2 dB. This improvement becomes even more pronounced in the SUMF-based receiver where a reasonable BER cannot be obtained with just 6 iterations.

Finally, Figure 4.5 shows the BER versus the number of users K in the one- and two-antenna cases. These results were obtained from simulations at an E_b/N_0 of 8 dB. For a single antenna and 10 iterations, the system serves up to 30 users while operating close to a BER of 10^{-3}. The plot shows that the number of supported users is drastically increased if two receive antennas are used. More users can be accommodated at the cost of an increased number of iterations. With two receive antennas, more than 50 users can be served in simultaneous links with a BER lower than 10^{-3} after 10 iterations. This is enabled by the reduced variability of the receiver-side signal power when employing multiple receive antennas.

We have demonstrated that an iterative receiver impressively increases the number of supported users when employing antenna diversity at the base-station receiver. These performance gains are achieved in a multipath environments when the soft-decision feedback is used for both *channel estimation* and *interference cancellation*.

4.4. Basis expansion for time-variant channel equalization

This section deals with the equalization of time-variant channels by extending the iterative receiver concept developed in Section 4.3 for block-fading channels. The variation of a wireless channel over the duration of a data block is caused by user mobility and multipath propagation. The Doppler shifts on the individual

paths depend on the user's velocity v, the carrier frequency f_C, and the scattering environment. The maximum variation in time of the wireless channel is upper bounded by the maximum (one-sided) normalized Doppler bandwidth

$$\nu_{\mathrm{Dmax}} = B_D T_S, \tag{4.35}$$

where $B_D = \nu_{\max} f_C / c_0$ is the maximum Doppler bandwidth, $\nu_{\max}$ is the maximum velocity, T_S is the symbol duration, and c_0 denotes the speed of light.

We apply orthogonal frequency-division multiplexing (OFDM) in order to transform the time-variant frequency-selective channel into a set of parallel time-variant frequency-flat channels, the so-called subcarriers. We consider time-variant channels which may vary significantly over the duration of a long block of OFDM symbols. However, for the duration of each single OFDM symbol, the channel variation is assumed small enough to be neglected. This implies a very small intercarrier interference (ICI). Each OFDM symbol is preceded by a cyclic prefix to avoid intersymbol interference (ISI).

The discrete-time sequence of channel coefficients for each frequency-flat subcarrier is bandlimited by ν_{Dmax}. It was shown by Slepian [28] that time-limited parts of bandlimited sequences span a low-dimensional subspace. A natural set of basis functions for this subspace is given by the so-called discrete prolate spheroidal sequences. A Slepian basis expansion using this subspace representation was proposed in [21] for time-variant channel equalization. It was shown in [22] that the channel estimation bias obtained with the Slepian basis expansion is smaller by one order of magnitude compared to the Fourier basis expansion (i.e., a truncated discrete Fourier transform) [20].

An iterative time-variant channel estimation scheme is developed by combining pilot symbols with soft decisions for estimating the coefficients of the Slepian basis expansion.

4.4.1. MIMO-OFDM multiuser signal model for doubly selective channels

Every user has a single $N_T = 1$ transmit antenna, the base station has N_R receive antennas. There are K users. We consider the equalization and detection problem for such a $K \times N_R$ multiuser MIMO communications system. Each user's data symbols are spread over N subcarriers by means of a user-specific spreading code. The transmission is block-oriented; a data block consists of $M - J$ OFDM data symbols and J OFDM pilot symbols.

The data symbols are chosen from a QPSK symbol constellation. The data symbols are given by $a_k[m] \in \{\pm 1 \pm \mathrm{j}\}/\sqrt{2}$ for $m \notin \mathcal{P}$ and $a_k[m] = 0$ for $m \in \mathcal{P}$, where the pilot placement is defined by the index set

$$\mathcal{P} = \left\{ \left\lfloor \frac{M}{J}\left(i + \frac{1}{2}\right) \right\rfloor \mid i = 0, \ldots, J-1 \right\}, \tag{4.36}$$

and discrete time at rate $1/T_S = 1/(PT_C)$ is denoted by m. After the spreading operation, pilot symbols $\boldsymbol{p}_k[m] \in \mathbb{C}^N$ with elements $p_k[m, e]$ are added, giving

the $N \times 1$ vectors

$$\boldsymbol{d}_k[m] = \boldsymbol{s}_k a_k[m] + \boldsymbol{p}_k[m]. \tag{4.37}$$

The elements of the pilot symbols $p_k[m,e]$ for $m \in \mathcal{P}$ and $e \in \{0,\ldots,N-1\}$ are randomly chosen from the QPSK symbol set $\{\pm 1 \pm \mathrm{j}\}/\sqrt{2N}$. For $m \notin \mathcal{P}$, we define $\boldsymbol{p}_k[m] = \boldsymbol{0}_N$. Subsequently, an N-point inverse discrete Fourier transform (DFT) is carried out and a cyclic prefix of length G is inserted. An OFDM symbol including the cyclic prefix has length $P = N + G$ chips.

The temporal channel variation for the duration of each single OFDM symbol is small which translates to small ICI [29]. For neglecting the temporal channel variation within a single OFDM symbol, ν_{Dmax} is assumed to be much smaller than the normalized subcarrier bandwidth P/N, for example, $\nu_{\mathrm{Dmax}}N/P < 0.01$. Under this assumption, we represent the time-variant MIMO channel by the $N \times 1$ vector $\boldsymbol{g}_{k,q}[m] = \sqrt{N}\boldsymbol{F}[h_{k,1,q}[mP,0],\ldots,h_{k,1,q}[mP,L-1]]^{\mathrm{T}}$. The truncated DFT matrix $\boldsymbol{F} \in \mathbb{C}^{N\times L}$ has elements $[\boldsymbol{F}]_{i,\ell} = (1/\sqrt{N})\mathrm{e}^{-\mathrm{j}2\pi i\ell/N}$ for $i \in \{0,\ldots,N-1\}$ and $\ell \in \{0,\ldots,L-1\}$. The received signal at the qth antenna element after cyclic prefix removal and DFT is

$$\boldsymbol{y}_q[m] = \sum_{k=1}^{K} \mathrm{diag}\,(\boldsymbol{g}_{k,q}[m])\boldsymbol{d}_k[m] + \boldsymbol{v}_q[m], \tag{4.38}$$

where complex additive white Gaussian noise with zero mean and covariance $\sigma_v^2\boldsymbol{I}_N$ is denoted by $\boldsymbol{v}_q[m] \in \mathbb{C}^N$ with elements $v_q[m,e]$. We define the time-variant effective spreading sequences

$$\tilde{\boldsymbol{s}}_{k,q}[m] = \mathrm{diag}\,(\boldsymbol{g}_{k,q}[m])\boldsymbol{s}_k, \tag{4.39}$$

and the time-variant effective spreading matrix $\tilde{\boldsymbol{S}}_q[m] = [\tilde{\boldsymbol{s}}_{1,q}[m],\ldots,\tilde{\boldsymbol{s}}_{K,q}[m]] \in \mathbb{C}^{N\times K}$. Using these definitions, we write the signal model for data detection as

$$\boldsymbol{y}_q[m] = \tilde{\boldsymbol{S}}_q[m]\boldsymbol{a}[m] + \boldsymbol{v}_q[m] \quad \text{for } m \notin \mathcal{P}, \tag{4.40}$$

where $\boldsymbol{a}[m] = [a_1[m],\ldots,a_K[m]]^{\mathrm{T}} \in \mathbb{C}^K$ contains the stacked data symbols for K users. Equation (4.40) is identical to the signal model for CDMA in a frequency-flat fading environment. Thus, we apply the PIC and MMSE multiuser detection algorithms defined in Section 4.3 with ISI length $W = 1$ (cf. (4.16)). However, the effective spreading sequence (4.39) is time-variant and (4.24) must be calculated for every symbol, now.

The performance of the iterative receiver crucially depends on the accuracy with which the time-variant frequency response $\boldsymbol{g}_{k,q}[m]$ is estimated, since the effective spreading sequence (4.39) directly depends on the actual channel realizations. The MIMO-OFDM signal model (4.38) describes a transmission over $N \times N_{\mathrm{R}}$ parallel frequency-flat channels. Therefore, we rewrite (4.38) as a set of

equations for every subcarrier $e \in \{0,\ldots,N-1\}$ and receive antenna $q \in \{1,\ldots,N_{\mathrm{R}}\}$:

$$y_q[m,e] = \sum_{k=1}^{K} g_{k,q}[m,e]d_{k,q}[m,e] + v_q[m,e], \tag{4.41}$$

where $d_k[m,e] = s_k[e]a_k[m] + p_k[m,e]$. The temporal variation of each subcarrier coefficient $g_{k,q}[m,e]$ is bandlimited by the normalized maximum Doppler bandwidth ν_{Dmax}. We estimate $g_{k,q}[m,e]$ for an interval with length M using the received sequence $y_q[m,e]$. Slepian [28] analyzed discrete prolate spheroidal (DPS) sequences that are maximally concentrated in a given time interval and to a given bandwidth. Thus, the properties of these DPS sequences are directly relevant to the channel estimation problem. The DPS sequences are *doubly* orthogonal over the intervals $[-\infty,\infty]$ and $[0,M-1]$. We use the DPS sequences on the index set $\{0,\ldots,M-1\}$ to define an orthogonal basis. The index-limited DPS sequences will be termed *Slepian sequences*.

4.4.2. Slepian basis expansion

The Slepian basis expansion approximates the sequence $g_{k,q}[m,e]$ by a linear combination of Slepian sequences $u_i[m]$:

$$g_{k,q}[m,e] \approx \tilde{g}_{k,q}[m,e] = \sum_{i=0}^{D-1} u_i[m]\psi_{k,q}[i,e], \tag{4.42}$$

where $m \in \{0,\ldots,M-1\}$ and $e \in \{0,\ldots,N-1\}$. The Slepian sequences $\boldsymbol{u}_i \in \mathbb{R}^M$ with elements $u_i[m]$ are defined as the eigenvectors of the matrix $\boldsymbol{C} \in \mathbb{R}^{M\times M}$ defined as $[\boldsymbol{C}]_{i,\ell} = \sin[2\pi(i-\ell)\nu_{\mathrm{Dmax}}]/(\pi(i-\ell))$, where $i,\ell = 0,1,\ldots,M-1$, that is, $\boldsymbol{C}\boldsymbol{u}_i = \lambda_i\boldsymbol{u}_i$. The approximate dimension of the time-concentrated and bandlimited signal space is $D = \lceil 2\nu_{\mathrm{Dmax}}M\rceil + 1$ [28, Section 3.3], which means that the eigenvalues λ_i rapidly decay to zero for $i > D$. In effect, (4.42) is a reduced-rank representation for time-limited parts (or snapshots) of bandlimited sequences. The mean squared error for one subcarrier is defined as (where we omit k, q, and e)

$$\mathrm{MSE}_M = \frac{1}{M}\sum_{m=0}^{M-1} \mathbb{E}\left\{ \left| g[m] - \tilde{g}[m] \right|^2 \right\}. \tag{4.43}$$

The mean squared error of the Slepian basis expansion is given by the sum of two terms $\mathrm{MSE}_M = \mathrm{bias}_M^2 + \mathrm{var}_M$. The autocorrelation of the subcarrier determines bias_M^2 and this term decreases with growing dimension D of the basis expansion. On the other hand, var_M is proportional to D and the noise variance σ_v^2 [30]. An analytic expression for bias_M^2 can be found in [19, 22]

$$\mathrm{bias}_M^2 = \frac{1}{M}\sum_{m=0}^{M-1} \int_{-1/2}^{1/2} E(m,\nu)S_{gg}(\nu)\mathrm{d}\nu, \tag{4.44}$$

where $S_{gg}(\nu)$ is the power spectral density of the subcarrier and

$$E(m,\nu) = \left| 1 - \boldsymbol{f}^{\mathrm{T}}[m]\boldsymbol{G}^{-1} \sum_{\ell=0}^{M-1} \boldsymbol{f}^{*}[\ell]\, \mathrm{e}^{-\mathrm{j}2\pi\nu(m-\ell)} \right|^2, \tag{4.45}$$

with $\boldsymbol{G} = \sum_{m=0}^{M-1} \boldsymbol{f}[m]\boldsymbol{f}^{\mathrm{H}}[m]$ and $\boldsymbol{f}[m] = [u_0[m], \ldots, u_{D-1}[m]]^{\mathrm{T}} \in \mathbb{C}^D$. The variance is independent of the selected basis, $\mathrm{var}_M \approx \sigma_v^2 D/M$. The use of the Slepian basis offers a significantly smaller square bias compared to the Fourier basis (i.e., the truncated discrete Fourier transform). This was demonstrated numerically and analytically in [21, 22].

We emphasize that the selection of a suitable Slepian basis, parameterized by M and ν_{Dmax}, exploits the band limitation of the Doppler spectrum to ν_{Dmax} only. The details of the Doppler spectrum for $|\nu| < \nu_{\mathrm{Dmax}}$ are irrelevant. Our approach therefore differs from a Karhunen-Loève transform which requires *complete* knowledge of the second-order statistics of the fading process. This approach was chosen since MIMO channel sounder measurements have shown that wireless fading channels show stationary behavior for less than 70 wavelengths in a pedestrian typical urban environment [31]. We fear that meaningful short-term fading characteristics (second-order statistics, to begin with) can hardly be acquired in a multiuser MIMO system when users move at vehicular speeds.

For the purposes of performance *analysis* for a *nominal* ensemble of channel realizations, we evaluate (4.44) for a *nominal* Doppler spectrum $S_{gg}(\nu)$.

4.4.3. Signal model for time-variant channel estimation

We insert the basis expansion (4.42) for the coefficients $g_{k,q}[m,e]$ in (4.41):

$$y_q[m,e] = \sum_{k=1}^{K} \sum_{i=0}^{D-1} u_i[m]\psi_{k,q}[i,e]d_k[m,e] + v_q[m,e]. \tag{4.46}$$

Thus, an estimate of the subcarrier coefficients $\hat{\psi}_{k,q}[i,e]$ can be obtained jointly for all K users but individually for every subcarrier e and receive antenna q. We define the stacked vector $\boldsymbol{\psi}_{e,q} = [\boldsymbol{\psi}_{e,q,0}^{\mathrm{T}}, \ldots, \boldsymbol{\psi}_{e,q,D-1}^{\mathrm{T}}]^{\mathrm{T}} \in \mathbb{C}^{KD}$ containing the basis expansion coefficients of all K users for subcarrier e, where $\boldsymbol{\psi}_{e,q,i} = [\psi_{1,q}[i,e], \ldots, \psi_{K,q}[i,e]]^{\mathrm{T}} \in \mathbb{C}^K$. Furthermore we introduce the notation $\boldsymbol{y}_{e,q} = [y_q[0,e], \ldots, y_q[M-1,e]]^{\mathrm{T}} \in \mathbb{C}^M$ for the received chip sequence for a single data block on subcarrier e. Using these definitions, we write

$$\boldsymbol{y}_{e,q} = \boldsymbol{\mathcal{D}}_e \boldsymbol{\psi}_{e,q} + \boldsymbol{v}_{e,q}, \tag{4.47}$$

where

$$\boldsymbol{\mathcal{D}}_e = [\,\mathrm{diag}\,(\boldsymbol{u}_0)\boldsymbol{D}_e, \ldots, \mathrm{diag}\,(\boldsymbol{u}_{D-1})\boldsymbol{D}_e] \in \mathbb{C}^{M\times KD}, \tag{4.48}$$

$$\boldsymbol{D}_e = \begin{bmatrix} d_1[0,e] & \cdots & d_K[0,e] \\ \vdots & \ddots & \vdots \\ d_1[M-1,e] & \cdots & d_K[M-1,e] \end{bmatrix} \in \mathbb{C}^{M\times K}, \tag{4.49}$$

contains the transmitted symbols for all K users on subcarrier e. For channel estimation, the J pilot symbols in (4.37) are used. The remaining $M - J$ symbols are not known; we replace them by soft decisions that are calculated from the APP obtained in the previous iteration. This enables a refinement of the channel estimates when the soft decisions gain reliability from these iterations. For the first iteration, the soft decisions $\tilde{a}_k[m]$ are set to zero. We define the soft-decision matrix $\tilde{\boldsymbol{D}}_e \in \mathbb{C}^{M\times K}$ according to (4.49) by replacing $d_k[m,e]$ with $\tilde{d}_k[m,e] = s_k[e]\tilde{a}_k[m] + p_k[m,e]$. Finally, we define $\tilde{\boldsymbol{\mathcal{D}}}_e \in \mathbb{C}^{M\times KD}$ according to (4.48) by replacing $\boldsymbol{D}_e$ with $\tilde{\boldsymbol{D}}_e$. Thus, $\tilde{\boldsymbol{\mathcal{D}}}_e$ contains *a priori* known pilot symbols and soft decisions for the unknown data symbols.

4.4.4. LMMSE channel estimation

We use the minimum mean square error (MMSE) criterion for estimating the basis expansion coefficients $\boldsymbol{\psi}_{e,q}$ (see [32] for the block-fading single-input single-output case):

$$\hat{\boldsymbol{\psi}}_{e,q} = \left(\tilde{\boldsymbol{\mathcal{D}}}_e^{\mathrm{H}}\boldsymbol{\Delta}^{-1}\tilde{\boldsymbol{\mathcal{D}}}_e + \boldsymbol{I}_{KD}\right)^{-1}\tilde{\boldsymbol{\mathcal{D}}}_e^{\mathrm{H}}\boldsymbol{\Delta}^{-1}\boldsymbol{y}_{e,q}, \tag{4.50}$$

where $\boldsymbol{\Delta} = \boldsymbol{\Lambda} + \sigma_v^2\boldsymbol{I}_M$. The elements of the diagonal matrix $\boldsymbol{\Lambda}$ are defined as

$$[\boldsymbol{\Lambda}]_{m,m} = \frac{1}{N}\sum_{k=1}^{K}\sum_{i=0}^{D-1} u_i^2[m]\,\mathrm{var}\,\{a_k[m]\}, \tag{4.51}$$

and the symbol variance is $\mathrm{var}\{a_k[m]\} = 1 - \tilde{a}_k^2[m]$. The rows of $\tilde{\boldsymbol{\mathcal{D}}}_e$ are scaled by the elements of the diagonal matrix $\boldsymbol{\Delta}$, taking into account the variances of the noise and of the soft decisions. After $\hat{\boldsymbol{\psi}}_{e,q}$ is evaluated for all $e \in \{0,\ldots,N-1\}$ and $q \in \{1,\ldots,N_{\mathrm{R}}\}$, an estimate for the time-variant frequency response is given by $\hat{g}_{k,q}[m,e] = \sum_{i=0}^{D-1} u_i[m]\hat{\psi}_{k,q}[i,e]$. Additional noise suppression is obtained if we exploit the correlation between the subcarriers $\hat{\boldsymbol{g}}_{k,q}[m] = \boldsymbol{F}\boldsymbol{F}^{\mathrm{H}}\hat{\boldsymbol{g}}_{k,q}[m]$. Finally, the data is detected by inserting the channel estimates $\hat{\boldsymbol{g}}_{k,q}[m]$ into (4.39).

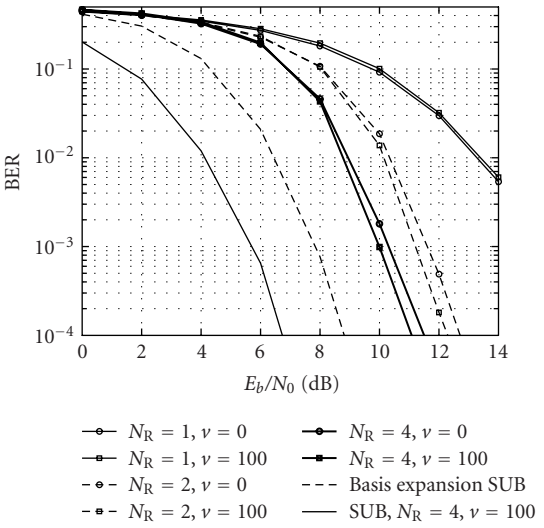

FIGURE 4.6. BER versus SNR on the uplink for multiuser MIMO-OFDM after 4 iterations and Slepian basis expansion for $D = 3$; $K = 64$ users are static ($v = 0$ km/h) or moving at $v = 100$ km/h; receiver employs $N_R = 1, 2$, or 4 antennas.

4.4.5. Simulation results and discussion

Realizations of the time-variant frequency-selective MIMO channel $h_{k,1,q}[n, \ell]$ are generated using an exponentially decaying power-delay profile (PDP) $\eta^2[\ell] = \mathrm{e}^{-\ell/4} / \sum_{\ell'=0}^{L-1} \mathrm{e}^{-\ell'/4}$, $\ell = 0, \ldots, L-1$, with essential support of $L = 15$ [33]. The time indices n and ℓ correspond to sampling at rate $1/T_C$. The PDP corresponds to a root-mean-square delay spread $T_D = 4T_C = 1$ microsecond for a chip rate of $1/T_C = 3.84 \cdot 10^6$ 1/s. The autocorrelation for every channel tap is given by $R_{h'h'}[n, \ell] = \eta^2[\ell] J_0(2\pi \nu_D P n)$ which results in the classical Jakes' spectrum. We simulate the time-variant channel using the model in [34] corrected for low velocities in [35].

The system operates at carrier frequency $f_C = 2$ GHz and the $K = 64$ users move with velocity $v \in \{0, 100\}$ km/h. This gives a Doppler bandwidth of $B_D = 190$ Hz corresponding to $\nu_D = 0.0039$. The number of subcarriers is $N = 64$ and the length of the OFDM symbol with cyclic prefix is $P = G + N = 79$. The data block consists of $M = 256$ OFDM symbols with $J = 60$ OFDM pilot symbols. The system is designed for a maximum velocity $v_{max} = 100$ km/h which results in $D = 3$ for the Slepian basis expansion. The base station uses $N_R \in \{1, 2, 4\}$ receive antennas. All simulation results are averaged over 100 independently generated data blocks.

In Figure 4.6, we illustrate the multiuser MIMO-OFDM uplink performance with iterative time-variant channel estimation based on the Slepian basis expansion in terms of bit error rate (BER) versus E_b/N_0 after 4 iterations. We also display the single-user bound (SUB) which is defined as the BER for one user and perfect

channel knowledge at the receiver, as well as the "basis expansion SUB" which is the achievable BER with a channel estimation scheme based on the Slepian basis expansion. With increasing number of coherently combined receive antennas, the channel estimation variance described by var_M becomes the limiting factor for the receiver's performance.

Simulation results show that an iterative receiver using the Slepian basis expansion for channel equalization handles a wide range of user velocities under full load. Accurate channel estimates obtained with the Slepian basis expansion with soft decisions allow to exploit the Doppler diversity. This leads to *decreased* BER at higher velocities.

Acknowledgment

This work was partly funded by **K***plus*, Infineon Technologies, and the Austrian Research Centers Seibersdorf (ARCS) through ftw. Project C3.

Abbreviations

APP	A posteriori probability
BCJR	Bahl, Cocke, Jelinek, Raviv
BER	Bit error ratio
CDMA	Code division multiple access
DFT	Discrete Fourier transform
EXT	Extrinsic probability
ICI	Intercarrier interference
ISI	Intersymbol interference
LMMSE	Linear minimum mean squared error
MAI	Multiple access interference
MAP	Maximum a posteriori
MIMO	Multiple-input multiple-output
MSE	Mean squared error
MRC	Maximum ratio combining
MUD	Multiuser detection
OFDMA	Orthogonal frequency-division multiple access
OFDM	Orthogonal frequency-division multiplexing
PDP	Power delay profile
PIC	Parallel interference cancellation
PRUS	Perfect root of unity sequence
QPSK	Quaternary phase-shift keying
SINR	Signal-to-interference-and-noise ratio
SNR	Signal-to-noise ratio
SUB	Single-user bound
SUMF	Single-user matched filter
TU	Typical urban

Bibliography

[1] J. J. Boutros, F. Boixadera, and C. Lamy, "Bit-interleaved coded modulations for multiple-input multiple-output channels," in *Proc. IEEE 6th International Symposium Spread Spectrum Techniques and Applications (ISSSTA '00)*, vol. 1, pp. 123–126, Parsippany, NJ, USA, September 2000.

[2] M. Loncar, R. Müller, T. Abe, J. Wehinger, and C. Mecklenbräuker, "Iterative equalization using soft-decoder feedback for MIMO systems in frequency selective fading," in *Proc. of URSI General Assembly 2002*, Maastricht, The Netherlands, August 2002.

[3] M. Tüchler, R. Koetter, and A. C. Singer, "Turbo equalization: principles and new results," *IEEE Trans. Commun.*, vol. 50, no. 5, pp. 754–767, 2002.

[4] Q. Sun, D. C. Cox, H. C. Huang, and A. Lozano, "Estimation of continuous flat fading MIMO channels," *IEEE Transactions on Wireless Communications*, vol. 1, no. 4, pp. 549–553, 2002.

[5] H. Artés and F. Hlawatsch, "Blind equalization of MIMO channels using deterministic precoding," in *Proc. IEEE International Conference Acoustics, Speech, Signal Processing (ICASSP '01)*, vol. 4, pp. 2153–2156, Salt Lake City, Utah, USA, May 2001.

[6] H. Artés and F. Hlawatsch, "Space-time matrix modulation: rank-deficient channels and multiuser case," in *Proc. IEEE International Conference Acoustics, Speech, Signal Processing (ICASSP '02)*, vol. 3, pp. 2225–2228, Orlando, Fla, USA, May 2002.

[7] A. Medles and D. T. M. Slock, "Semiblind channel estimation for MIMO spatial multiplexing systems," in *Proc. IEEE 54th Vehicular Technology Conference (VTC '01)*, vol. 2, pp. 1240–1244, Atlantic City, NJ, USA, October 2001.

[8] T. J. Moore, B. M. Sadler, and R. J. Kozick, "Regularity and strict identifiability in MIMO systems," *IEEE Trans. Signal Processing*, vol. 50, no. 8, pp. 1831–1842, 2002.

[9] J. Baltersee, G. Fock, and H. Meyr, "Achievable rate of MIMO channels with data-aided channel estimation and perfect interleaving," *IEEE J. Select. Areas Commun.*, vol. 19, no. 12, pp. 2358–2368, 2001.

[10] M. Medard, "The effect upon channel capacity in wireless communications of perfect and imperfect knowledge of the channel," *IEEE Trans. Inform. Theory*, vol. 46, no. 3, pp. 933–946, 2000.

[11] B. Hochwald and T. Marzetta, "Unitary space-time modulation for multiple-antenna communications in Rayleigh flat fading," *IEEE Trans. Inform. Theory*, vol. 46, no. 2, pp. 543–564, 2000.

[12] B. Hochwald and W. Sweldens, "Differential unitary space-time modulation," *IEEE Trans. Commun.*, vol. 48, no. 12, pp. 2041–2052, 2000.

[13] B. L. Hughes, "Differential space-time modulation," *IEEE Trans. Inform. Theory*, vol. 46, no. 7, pp. 2567–2578, 2000.

[14] A. L. Swindlehurst and G. Leus, "Blind and semi-blind equalization for generalized space-time block codes," *IEEE Trans. Signal Processing*, vol. 50, no. 10, pp. 2489–2498, 2002.

[15] P. D. Alexander, A. J. Grant, and M. C. Reed, "Iterative detection in code-division multiple-access with error control coding," *European Trans. Telecommunications*, vol. 9, no. 5, pp. 419–425, 1998.

[16] M. Moher, "An iterative multiuser decoder for near-capacity communications," *IEEE Trans. Commun.*, vol. 46, no. 7, pp. 870–880, 1998.

[17] X. Wang and H. V. Poor, "Iterative (turbo) soft interference cancellation and decoding for coded CDMA," *IEEE Trans. Commun.*, vol. 47, no. 7, pp. 1046–1061, 1999.

[18] J. Wehinger, R. R. Müller, M. Lončar, and C. F. Mecklenbräuker, "Performance of iterative CDMA receivers with channel estimation in multipath environments," in *Proc. 36th Asilomar Conference on Signals, Systems and Computers*, vol. 2, pp. 1439–1443, Pacific Grove, Calif, USA, November 2002.

[19] M. Niedzwiecki, *Identification of Time-Varying Processes*, John Wiley & Sons, New York, NY, USA, 2000.

[20] A. M. Sayeed, A. Sendonaris, and B. Aazhang, "Multiuser detection in fast-fading multipath environments," *IEEE J. Select. Areas Commun.*, vol. 16, no. 9, pp. 1691–1701, 1998.

[21] T. Zemen, *OFDM multi-user communication over time-variant channels*, Doctoral thesis, Vienna University of Technology, Vienna, Austria, August 2004.

[22] T. Zemen and C. F. Mecklenbräuker, "Time-variant channel estimation for MC-CDMA using prolate spheroidal sequences," to appear in *IEEE Trans. Signal Processing*, vol. 53, 2005.

[23] M. Kobayashi, J. Boutros, and G. Caire, "Successive interference cancellation with SISO decoding and EM channel estimation," *IEEE J. Select. Areas Commun.*, vol. 19, no. 8, pp. 1450–1460, 2001.
[24] J. Boutros and G. Caire, "Iterative multiuser joint decoding: unified framework and asymptotic analysis," *IEEE Trans. Inform. Theory*, vol. 48, no. 7, pp. 1772–1793, 2002.
[25] G. Caire and R. R. Müller, "The optimal received power distribution for IC-based iterative multiuser joint decoders," in *Proc. 39th Annual Allerton Conference on Communication, Control and Computing*, Monticello, IL, USA, October 2001.
[26] L. R. Bahl, J. Cocke, F. Jelinek, and J. Raviv, "Optimal decoding of linear codes for minimizing symbol error rate," *IEEE Trans. Inform. Theory*, vol. 20, no. 2, pp. 284–287, 1974.
[27] G. Caire and U. Mitra, "Structured multiuser channel estimation for block-synchronous DS/CDMA," *IEEE Trans. Commun.*, vol. 49, no. 9, pp. 1605–1617, 2001.
[28] D. Slepian, "Prolate spheroidal wave functions, Fourier analysis, and uncertainty—V: the discrete case," *Bell System Tech. J.*, vol. 57, no. 5, pp. 1371–1430, 1978.
[29] Y. Li and L. J. Cimini, "Bounds on the interchannel interference of OFDM in time-varying impairments," *IEEE Trans. Commun.*, vol. 49, no. 3, pp. 401–404, 2001.
[30] L. L. Scharf and D. W. Tufts, "Rank reduction for modeling stationary signals," *IEEE Trans. Acoustics, Speech, Signal Processing*, vol. 35, no. 3, pp. 350–355, 1987.
[31] I. Viering and H. Hofstetter, "Potential of coefficient reduction in delay, space and time based on measurements," in *Proc. 37th Conference on Information Sciences and Systems (CISS '03)*, Baltimore, Md, USA, March 2003.
[32] T. Zemen, M. Lončar, J. Wehinger, C. F. Mecklenbräuker, and R. R. Müller, "Improved channel estimation for iterative receivers," in *Proc. IEEE Global Telecommunications Conference (GLOBECOM '03)*, vol. 1, pp. 257–261, San Francisco, Calif, USA, 2003.
[33] L. M. Correia, *Wireless Flexible Personalised Communications*, Wiley, New York, NY, USA, 2001.
[34] Y. R. Zheng and C. Xiao, "Simulation models with correct statistical properties for Rayleigh fading channels," *IEEE Trans. Commun.*, vol. 51, no. 6, pp. 920–928, 2003.
[35] T. Zemen and C. F. Mecklenbräuker, "Doppler diversity in MC-CDMA using the Slepian basis expansion model," in *Proc. 12th European Signal Processing Conference (EUSIPCO '04)*, Vienna, Austria, September 2004.

Christoph F. Mecklenbräuker: Forschungszentrum Telekommunikation Wien (ftw.) Donau-City Strasse 1/3, 1220 Vienna, Austria

Email: mecklenbraeuker@ftw.at

Joachim Wehinger: Forschungszentrum Telekommunikation Wien (ftw.), Donau-City Strasse 1/3, 1220 Vienna, Austria

Email: wehinger@ftw.at

Thomas Zemen: Forschungszentrum Telekommunikation Wien (ftw.), Donau-City Strasse 1/3, 1220 Vienna, Austria

Email: zemen@ftw.at

Harold Artés: Information Systems Laboratory, Stanford University, Packard 234, 350 Serra Mall, Stanford, CA 94305-9510, USA

Email: hartes@stanford.edu

Franz Hlawatsch: Institut für Nachrichtentechnik und Hochfrequenztechnik, Technische Universität Wien, Gusshausstrasse 25/389, 1040 Vienna, Austria

Email: franz.hlawatsch@nt.tuwien.ac.at

5 Joint antenna combining and multiuser detection

Ralf Müller and Laura Cottatellucci

Smart antenna technology combined with code-division multiple-access (CDMA) is common in 3rd-generation cellular communication systems. The uplink of a cellular CDMA system where each mobile and each base station is equipped with multiple-element antennas, is exemplarily explored. Multiple reception due to multiple receive antennas and multiple reception due to symbol repetition over time—this is commonly referred to as spreading—are identified as two peculiarities of the same concept. It is shown that joint processing of antenna signals and multiuser interference is superior to a separated approach in terms of performance. Utilizing multistage detection and certain properties of random matrices, antenna combining, and multiuser detection can be implemented jointly without the need for matrix multiplications or matrix inversions. Hereby, the complexity per bit of the presented algorithms scales linearly with the number of users.

5.1. Introduction

In recent years, intense efforts have been devoted to two important lines of works: multiuser techniques for direct sequence CDMA systems and signal processing techniques in systems with antenna arrays. Multiuser receivers mitigate the crosstalk between users taking into account the structure of interference from other users. Typically, these techniques exploit the degrees of freedom given by the frequency diversity intrinsically present in CDMA systems. Antenna arrays provide spatial diversity and smart antennas make use of these degrees of freedom to enhance the system capacity. The resource pooling result, due to Hanly and Tse [1], enlightens the fact that degrees of freedom in space and frequency are interchangeable. Moreover, the total number of degrees of freedom is the product of the degrees of freedom in space and frequency. A system with spreading factor N and N_R receive antennas is in many respects equivalent to a system with a single antenna and spreading factor NN_R. This suggests the idea to treat the two effects in the same way performing antenna array processing and multiuser detection jointly. Joint processing significantly outperforms techniques that try to exploit the degrees of freedom in space and time separately. However, the optimal

algorithms for this task are known for prohibitive complexity. A joint array processing and multiuser detection approach implementable in real-time systems is offered by linear multistage detectors with asymptotic weighting: they reach an excellent trade-off between performance and complexity. In fact, they have a complexity per transmitted bit which is linear in the number of transmitting antennas and in the number of users—the same is true for a single user matched filter—and attain almost the same performance as the joint linear minimum mean-squared error receiver.

In Section 5.2, we introduce the system model. Sections 5.3 and 5.4 stress the duality between degrees of freedom in space and frequency and explain the resource pooling result. Section 5.5 shows why the separation of antenna array processing and multiuser detection is a severely suboptimum approach by means of an intuitive example. Linear multistage detectors are defined in Section 5.6. Their structure and their properties are described in Section 5.7. In Section 5.8, we introduce asymptotic weighting—this approach works excellently for systems with many users—to overcome the weight design problem which multistage detectors can suffer from. The state of the art about multistage receivers with large-systems weighting is summarized in Section 5.10.

5.2. System model

Consider the uplink (reverse link) of an asynchronous CDMA system where each of the K users is equipped with N_{T} transmitting antenna elements, and the base station receiver is equipped with N_{R} receiving antenna elements, the channel is frequency-selective with impulse responses $h_{k,p,q}(t)$, $1 \le k \le K$, $1 \le p \le N_{\mathrm{T}}$, $1 \le q \le N_{\mathrm{R}}$ and impaired by additive white Gaussian noise $v_q(t)$. Transmitting a block of M symbols and denoting the spreading sequence of user k at antenna element p and symbol-time m by $s_{k,p,m}[n]$, $0 \le n \le N-1$ and the respective data symbol by $a_{k,p}[m]$, $0 \le m \le M-1$, the signal transmitted by user k from antenna element q is given (in complex baseband notation) by

$$b_{k,p}(t) = \sum_{n=0}^{N-1} \sum_{m=0}^{M-1} \psi\left(t - nT_{\mathrm{c}} - mNT_{\mathrm{c}}\right) a_{k,p}[m] s_{k,p,m}[n] \tag{5.1}$$

with T_{c} denoting the time duration of one chip and $\psi(t)$ denoting the chip waveform. The latter combines the actual chip waveform, often a rectangular waveform, and the band-limiting influence of the pulse-shaping filter.

The received signal at antenna element q can be written in continuous time as

$$r_q(t) = \sum_{k=1}^{K} \sum_{p=1}^{N_{\mathrm{T}}} \int_{-\infty}^{+\infty} b_{k,p}(t-\tau) h_{k,p,q}(\tau) \mathrm{d}\tau + v_q(t). \tag{5.2}$$

At the receiver front end, it is passed through a chip matched filter[1] $\psi^*(-t)$ giving

$$\tilde{r}_q(t) = \int_{-\infty}^{+\infty} r_q(\tau)\psi^*(\tau - t)\mathrm{d}\tau. \tag{5.3}$$

In order to get sufficient statistics after sampling at the chip rate, the signal $\tilde{r}_q(t)$ should be passed through a bank of KN_T filters matched to the channel impulse responses $h_{k,p,q}(t)$, $1 \le k \le K$, $1 \le p \le N_\mathrm{T}$, before being sampled. Alternatively, sufficient statistics could be obtained by oversampling $\tilde{r}_q(t)$ with a rate sufficiently large to exploit the band-limitation of the chip waveform.

The first approach, matched filtering with the channel impulse response, is difficult on wireless channels due to the time-variant nature of the channel impulse response and the difficulties in channel estimation in the continuous time domain. The second approach, oversampling, is the method of choice for implementations of UMTS. For chip waveforms with roll-off factor (bandwidth extension factor) $\alpha < 1/2$, threefold oversampling is sufficient.

In the oversampled discrete-time domain, the matched filter bank can be implemented by KN_T digital filters per receive antenna, one for each user and each transmit antenna. Their output signals in chip-time n are given by

$$y_{k,p,q}[n] = \int_{-\infty}^{+\infty} \tilde{r}_q(\tau)h^*_{k,p,q}(\tau - nT_\mathrm{c})\mathrm{d}\tau \tag{5.4}$$

for user k, transmit antenna p, receive antenna q, and chip-time $1 - L \le n \le NM + L - 2$ with L denoting the length of the longest channel impulse response in chips.

The discrete-time signal representation in (5.4) is very redundant. It contains replicas of the data symbols in time due to spreading—spreading is only a repetition code with time-variant mapping of the code symbols to the signal constellation—and multiple receive antennas. The MKN_T data symbols $a_{k,p}[m]$, $1 \le k \le K$, $1 \le p \le N_\mathrm{T}$, $0 \le m \le M - 1$ are represented by the $(MN + 2L - 1)KN_\mathrm{T}N_\mathrm{R}$ received signal samples $y_{k,p,q}[n]$, $1 \le k \le K$, $1 \le p \le N_\mathrm{T}$, $1 \le q \le N_\mathrm{R}$, $1 - L \le n \le NM + L - 2$. Without loss of information, the redundant signal dimensions can be eliminated by spatial and temporal matched filtering:

$$x_{k,p}[m] = \sum_{n=1}^{N} s^*_{k,p,m}[n + mN] \sum_{q=1}^{N_\mathrm{R}} y_{k,p,q}[n + mN]. \tag{5.5}$$

Note that there is no weighting of the signals of different receive antennas in (5.5), as the correct weighting with the channel impulse responses has already taken place in (5.4).

[1] In practice, the chip matched filter is often implemented in discrete-time via oversampling.

The overall communication channel from the data symbols $a_{k,p}[m]$ to the symbol-time sufficient statistics $x_{k,p}[m]$ is a discrete-time KN_{T}-dimensional additive noise channel. It is canonically described in vector notation by

$$\mathbf{x}[m] = \sum_{\ell=-l}^{l} \mathbf{\Phi}_{\ell}[m]\mathbf{a}[\ell] + \mathbf{v}[m] \tag{5.6}$$

with $l = \lceil (L-1)/N \rceil$,

$$\mathbf{x}[m] = \begin{bmatrix} x_{1,1}[m] \\ \vdots \\ x_{K,1}[m] \\ x_{1,2}[m] \\ \vdots \\ \vdots \\ x_{K,N_{\mathrm{T}}}[m] \end{bmatrix}, \qquad \mathbf{a}[m] = \begin{bmatrix} a_{1,1}[m] \\ \vdots \\ a_{K,1}[m] \\ a_{1,2}[m] \\ \vdots \\ \vdots \\ a_{K,N_{\mathrm{T}}}[m] \end{bmatrix}, \tag{5.7}$$

where $\mathbf{\Phi}_m[\ell]$ is a matrix-valued time-variant weighting function and $\mathbf{v}[m]$ is spatially and temporally correlated Gaussian noise.

5.3. Spreading versus receive antennas

The descriptions of the multiuser MIMO channels (5.5) and (5.4) in both symbol-time and chip-time are very involved and not so illustrative. More light onto the effect of the characterizing parameters $K, N_{\mathrm{T}}, N_{\mathrm{R}}, N$ is set by the concept of resource-pooling discovered by Hanly and Tse [1]. For the purpose of explaining the concept, consider the following two simplifications: Let the autocorrelation function of the chip waveforms fulfill the Nyquist criterion and the impulse responses satisfy

$$h_{k,p,q}(t) = h_{k,p,q}\delta(t) \quad \forall k, p, q. \tag{5.8}$$

The latter condition means that the channels of all users are frequency-flat and the users are synchronized.

In discrete-time notation the simplifications introduced above result in

$$\mathbf{x}[m] = \mathbf{Q}[m]^{\mathrm{H}}\mathbf{Q}[m]\mathbf{a}[m] + \mathbf{v}[m] \tag{5.9}$$

with the $NN_{\mathrm{R}} \times KN_{\mathrm{T}}$ virtual spreading matrix

$$\mathbf{Q}[m] = \begin{bmatrix} \mathbf{S}_1[m]\mathbf{H}_{1,1} & \mathbf{S}_2[m]\mathbf{H}_{2,1} & \cdots & \mathbf{S}_{N_{\mathrm{T}}}[m]\mathbf{H}_{N_{\mathrm{T}},1} \\ \mathbf{S}_1[m]\mathbf{H}_{1,2} & \mathbf{S}_2[m]\mathbf{H}_{2,2} & \cdots & \mathbf{S}_{N_{\mathrm{T}}}[m]\mathbf{H}_{N_{\mathrm{T}},2} \\ \vdots & \vdots & \ddots & \vdots \\ \mathbf{S}_1[m]\mathbf{H}_{1,N_{\mathrm{R}}} & \mathbf{S}_2[m]\mathbf{H}_{2,N_{\mathrm{R}}} & \cdots & \mathbf{S}_{N_{\mathrm{T}}}[m]\mathbf{H}_{N_{\mathrm{T}},N_{\mathrm{R}}} \end{bmatrix} \tag{5.10}$$

composed of the $N \times K$ true spreading matrices

$$\mathbf{S}_p[m] = \begin{bmatrix} s_{1,p,m}[0] & s_{2,p,m}[0] & \cdots & s_{K,p,m}[0] \\ s_{1,p,m}[1] & s_{2,p,m}[1] & \cdots & s_{K,p,m}[1] \\ \vdots & \vdots & \ddots & \vdots \\ s_{1,p,m}[N-1] & s_{2,p,m}[N-1] & \cdots & s_{K,p,m}[N-1] \end{bmatrix} \tag{5.11}$$

depending on symbol-time m and transmit antenna p, and with the diagonal channel weight matrices $\mathbf{H}_{p,q} = \operatorname{diag}(h_{1,p,q}, h_{2,p,q}, \ldots, h_{K,p,q})$ depending on transmit and receive antenna indices p and q, and the vector-valued additive temporally white Gaussian noise $\mathbf{v}[m] \sim \mathcal{N}(\mathbf{0}, \mathbf{Q}[m]^{\mathrm{H}}\mathbf{Q}[m]\sigma^2)$.

Compared to a communication channel where only a single-element antennas is used, the structure of the mathematical formulation of the channel has not changed. The effect of multiple transmit antennas is to blow up the user dimension of the spreading matrix by a factor equal to the number of transmit antennas. The effect of multiple receive antennas is to blow up the spreading factor dimension of the spreading matrix by a factor equal to the number of receive antennas. None of these two effects is surprising: additional transmit antennas create additional data signals in the same way as additional users do, provided that the data signals at the multiple transmit antennas are statistically independent (an assumption which is violated if space-time codes are used). Additional receive antennas create replicas of the same data disturbed by independent noise samples (if the noise is spatially white) in the same way as spreading creates replicas of the same data over time which are also disturbed by independent noise samples if the noise is temporally white. Unless the expansion of the spreading matrix into a virtual spreading matrix by multiple transmit and receive antennas has a significant effect on the crosscorrelation properties of the (virtual) spreading sequences, spreading and multiple receive antennas must be seen as different peculiarities of the same concept. Transmit antennas and multiple users are then related to each other in precisely the same way.

For general spreading sequences, it is hard to investigate how much crosscorrelation properties change when a spreading matrix is blown up into a virtual spreading matrix. Obviously, if the spreading sequences are orthogonal, the virtual ones will not be. In UMTS, however, spreading sequences of different users are not orthogonal, but pseudorandom sequences. Therefore, it is more natural and of higher practical importance to consider random spreading sequences as done in the following.

5.4. Resource pooling for random spreading

Let the chips of the true spreading sequences be jointly independent and identically distributed random variables with zero mean and variance $1/N$. Let the channel weights of all users corresponding to all antenna pairs be independent random

variables. Let the channel weights belonging to the same user be identically distributed with zero mean and variance P_k. These assumptions translate into the following properties of the system.

(i) Pseudorandom spreading or scrambling sequences are used. The sequences for different transmit antennas of the same user are different—if they were not, a severe drawback in performance would occur.

(ii) The dual antenna array channels are spatially uncorrelated and without line-of-sight component.

(iii) The receiving antennas are located at the same base station, that is, there is no soft hand-off.

In addition, we will assume that the system is large, that is, there are many users $K \gg 1$ and the spreading factor $N \gg 1$ is large, but the load

$$\alpha = \frac{K}{N} \tag{5.12}$$

is fixed. The large-system assumption is accurate up to fractions of decibels in predicted performance for spreading factors of about $N = 32$ or greater.

For a channel like (5.9), many performance measures, such as channel capacity with side information and signal-to-interference-and-noise ratios of the most popular linear multiuser detectors, depend mainly or even solely on the singular values of the channel matrix and the signal-to-noise ratio. Showing that two channels have channel matrices with the same singular value distribution is therefore a strong indicator, in same cases even a proof, that the two channels are equivalent in terms of their capabilities to transport information.

In order to state the resource pooling result more precisely, we denote the singular values of any $m \times n$ matrix $\mathbf{A}$ by $\sigma_1(\mathbf{A}) \le \sigma_2(\mathbf{A}) \le \cdots \le \sigma_{\min\{m,n\}}(\mathbf{A})$ and the singular value distribution of the matrix $\mathbf{A}$ by

$$\mathrm{F}_{\mathbf{A}}(x) = \frac{1}{\min\{m,n\}} \sum_{i:\sigma_i(\mathbf{A}) \le x} 1. \tag{5.13}$$

Resource pooling. *Let the number of users K grow large for fixed load α and fixed number of transmit and receive antennas N_{T} and N_{R}, respectively, then the following singular value distributions converge with probability* 1 *to the same common singular value distribution* $\mathrm{F}_\infty(x)$,

$$\mathrm{F}_{\mathbf{Q}[m]}(x) \longrightarrow \mathrm{F}_\infty(x) \quad \forall m, \tag{5.14}$$

$$\mathrm{F}_{\tilde{\mathbf{S}}\tilde{\mathbf{H}}_p}(x) \longrightarrow \mathrm{F}_\infty(x) \quad \forall p, \tag{5.15}$$

where the $NN_{\mathrm{R}} \times KN_{\mathrm{T}}$ matrix $\tilde{\mathbf{S}}$ is composed of independent identically distributed entries with zero mean and variance $1/(NN_{\mathrm{R}})$ *and the singular value distribution of*

the diagonal matrix $\tilde{\mathbf{H}}_p$ is identical to the singular value distribution of

$$\sqrt{\sum_{q=1}^{N_R} \mathbf{H}_{p,q}^H \mathbf{H}_{p,q}}. \tag{5.16}$$

The resource pooling result[2] was proven for $N_T = 1$ under a few additional technical assumptions (the spreading sequences are Gaussian-distributed and the fading weights are uniformly bounded from above) by Hanly and Tse [1]. A generalization to arbitrary number of transmit antennas N_T and correlated fading is given in [2] and Section 5.10.

The resource pooling result states that, when going from a single-antenna CDMA system with KN_T users, spreading factor NN_R, and a fading distribution with N_Rth-order diversity to a multiple-antenna CDMA system with K users, spreading factor N, N_T transmit antennas per user, N_R receive antennas at the base station, and a fading distribution without diversity, most performance measures stay the same. This means that *receive antennas are interchangeable with the spreading factor*—if we double the number of receive antennas, we can halve the spreading factor and, therefore, save half the spectral bandwidth. It also means that *transmit antennas are interchangeable with users*. Note that unlike single-user antenna array systems, there is no need to have the number of transmit antennas scale with the number of receive antennas to have the throughput scale with the number of receive antennas. Adding users—which means adding antennas, since every user has at least one antenna—does equally well in terms of total, but not per-user throughput.

5.5. Two misconceptions

In order to exploit the potential of the resource pooling concept, the two conceptually identical tasks antenna combining and multiuser detection must be performed jointly. Sometimes a joint approach is questioned for sake of saving complexity. It is the central aim of this contribution to challenge the idea that a separate approach can be given justification. In Sections 5.6–5.8, we will show how joint antenna combining and multiuser detection can be implemented with linear complexity per bit. In this section, we aim to give an intuitive understanding of why a separate approach performs badly. For the latter purpose, we restrict ourselves to two receive antennas and translate the abstract problem of joint antenna combining and multiuser detection into the more familiar problem of equalization for analog double-sideband amplitude modulation.

Consider an analog double-sideband amplitude modulation in the equivalent complex baseband representation. Let the frequency-selective channel be as

[2]Actually, Hanly and Tse even showed a stronger result, that is, the convergence of the signal-to-interference-and-noise ratio of the linear minimum mean-squared error multiuser detector.

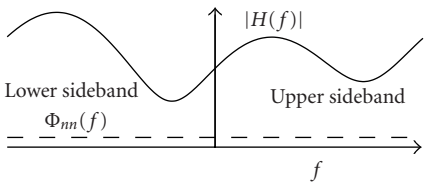

FIGURE 5.1. Example of transfer function $H(f)$ and noise power density $\Phi_{nn}(f)$ in double-sideband amplitude modulation.

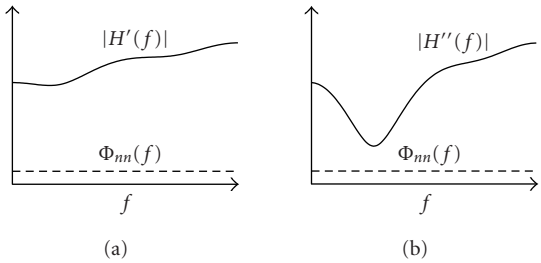

FIGURE 5.2. Transfer functions after combining the two sidebands with (a) an optimized frequency-dependent weighting versus (b) an optimized frequency-flat weighting.

shown in Figure 5.1. The two sidebands correspond to the two signals received at the two elements of the receiving antenna array. The magnitudes of the transfer functions in each sideband correspond to the singular value spectra of the first and the second block row of the virtual spreading matrix $\mathbf{Q}[m]$, these are $[\mathbf{S}_1[m]\mathbf{H}_{1,1} \cdots \mathbf{S}_{N_T}[m]\mathbf{H}_{N_T,1}]$ and $[\mathbf{S}_1[m]\mathbf{H}_{1,2} \cdots \mathbf{S}_{N_T}[m]\mathbf{H}_{N_T,2}]$. The phases of the transfer functions in each sideband correspond to the singular vectors of these two block rows.

Separating antenna combining and multiuser detection is equivalent to either ignoring the phase relations when combining the two sidebands or ignoring the existence of the other sideband when equalizing the channel. Figure 5.2 compares the resulting signals after combining the sidebands when the phase relations are taken into account versus them being not taken into account. It is not surprising that after equalization, a price in terms of a low signal-to-noise ratio within a certain frequency range has to be paid for ignoring the phase relations (cf. Figure 5.3). This figure also shows what happens when first an equalizer, which ignores the coexistence of the sidebands, is applied and then the two equalized (constant phase) signals are combined. This setting would correspond in multiantenna CDMA to the case when both receiver chains employ separate multiuser detectors and then combine the signals of the two separate antenna chains at a later stage—this approach is common in macrodiversity scenarios where the antenna elements are not colocated. The result is also not encouraging.

It seems questionable whether there remains a noticeable gain at all due to the deployment of multiple antennas, that is, two sidebands, if signals are not

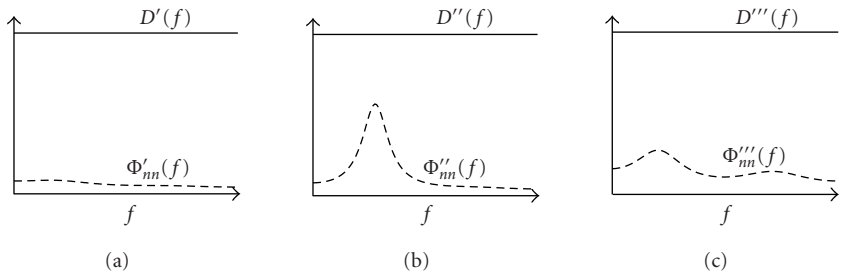

FIGURE 5.3. Noise spectral densities (a) and (b) for the two cases of Figure 5.2 after zero-forcing equalization, respectively, versus (c) an equalization-first, combining-later approach.

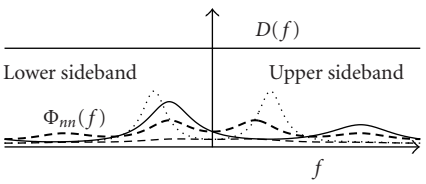

FIGURE 5.4. Noise spectral densities after reconstruction of the double-sideband signals from its single-sidebands in Figure 5.3 (dashed and dotted lines) versus direct equalization in the double-sideband (solid line).

processed jointly, since, in some cases, the mismatch of the detection procedure could outweigh the benefits of multiple reception. Figure 5.4 addresses this point. There the previous approaches to reconstruct the double sideband from the overlay of single sidebands are compared to straightforward equalization without any combining. In this case, it indeed appears that, when first combining the two sidebands separately ignoring the phase relation, the overall worst-case performance becomes inferior to no combining at all.

5.6. Linear multistage receivers

The sufficient discrete-time statistics (5.6) are fed into a receiver algorithm which aims to recover the transmitted data symbols in the presence of noise and interference. This algorithm is a detector in case of uncoded transmission providing decisions on each individual symbol. If channel coding is used, the receiver algorithm has to perform two tasks: exploit the structure of the interference (detection) and exploit the code laws (decoding). Optimally, the two tasks are performed by a jointly exhaustive search. For complexity reasons, they are often performed separately. Multiuser joint decoders are feasible only if they are implemented by successive iterations over detection and decoding.

For sake of simplicity, consider here a separate approach where the detector output is fed into a decoding unit. In order to not suffer from an unnecessary hit in performance, the decoder should be fed with soft decisions—these are (in general

nonlinear) estimates calculated from the sufficient statistics in such way that they minimize the mean-squared error to the true symbols.

The optimum nonlinear function is, in general and also in practice, a sum of at least 2^{KN_T} terms. In practice, the exponential complexity is overcome when the estimate is constrained to be a linear functional of the sufficient statistics. The best linear functional, in terms of achievable mean-squared error, for the channel in (5.9) is given by [3]

$$\mathbf{d}[m] = \left(\mathbf{Q}[m]^{\mathrm{H}}\mathbf{Q}[m] + \sigma^2\mathbf{I}\right)^{-1}\mathbf{x}[m]. \tag{5.17}$$

The need for one matrix inversion per discrete-time instant makes sure that this detector is not the method of choice in systems with many users.

In systems with many users, we can make use of the resource pooling result and the convergence of the singular values of the virtual spreading matrix $\mathbf{Q}[m]$ to some deterministic limit which is, as (5.14) shows, independent from the time index m. In order to illustrate this approach, consider the general problem of inverting a nonsingular matrix $\mathbf{R}$ with eigenvalues $0 < \lambda_1 \leq \lambda_2 \leq \cdots \leq \lambda_{K'}$. Note that any matrix annihilates its own characteristic polynomial (Cayleigh-Hamilton theorem)

$$\prod_{k=1}^{K'} \left(\mathbf{R} - \lambda_k\mathbf{I}\right) = \mathbf{0}. \tag{5.18}$$

Expanding the product and solving for the identity matrix gives

$$\mathbf{I} = \sum_{k=1}^{K'} \alpha_k\mathbf{R}^k \tag{5.19}$$

with some coefficients α_k which depend only on the eigenvalues λ_1 to $\lambda_{K'}$. Multiplying both sides of (5.19) by the inverse of $\mathbf{R}$

$$\mathbf{R}^{-1} = \sum_{k=0}^{K'-1} \alpha_{k+1}\mathbf{R}^k \tag{5.20}$$

shows how the inverse of a $K' \times K'$ matrix can be written as a $(K'-1)$th-order matrix polynomial if its eigenvalues are known.

The eigenvalues of the matrix to be inverted for the linear minimum mean-squared error (LMMSE) detector (5.17) are given by the squared singular values of the virtual spreading matrix shifted by the noise variance. Due to the resource pooling result, they are time-invariant, if the number of users is large, and so are the coefficients of the matrix polynomial in (5.20).

In practice, one would neither like to calculate the matrix polynomial up to the full order nor need to do so. In fact, the number of terms to achieve satisfactory performance for applications in LMMSE detectors is quite small (less than ten)

and does not scale with the number of users [4]. Therefore, we will choose the order of the polynomial to be $D-1$ with $D \ll K'$:

$$\mathbf{d}[m] \approx \sum_{k=0}^{D-1} \tilde{w}_k \left(\mathbf{Q}[m]^{\mathrm{H}}\mathbf{Q}[m] + \sigma^2\mathbf{I}\right)^k \mathbf{x}[m] \tag{5.21}$$

$$= \sum_{k=0}^{D-1} w_k \left(\mathbf{Q}[m]^{\mathrm{H}}\mathbf{Q}[m]\right)^k \mathbf{x}[m]. \tag{5.22}$$

This procedure to approximate the LMMSE detector was first proposed by Moshavi et al. [5].

It is not a trivial problem to choose the right coefficients w_k for an approximating polynomial with reduced order. In particular, it is not a wise choice to just use the first D coefficients of the full-order polynomial. Moshavi et al. [5] proposed to choose the coefficients in order to minimize the mean-squared error between the output of the exact LMMSE detector and its approximation. This leads to the following system of Yule-Walker equations for the choice of the coefficients:

$$\begin{bmatrix} m_1 \\ \vdots \\ m_D \end{bmatrix} = \begin{bmatrix} m_2 + \sigma^2 m_1 & \cdots & m_{D+1} + \sigma^2 m_D \\ \vdots & \ddots & \vdots \\ m_{D+1} + \sigma^2 m_D & \cdots & m_{2D} + \sigma^2 m_{2D-1} \end{bmatrix} \begin{bmatrix} w_0 \\ \vdots \\ w_{D-1} \end{bmatrix} \tag{5.23}$$

with the empirical eigenvalue moments

$$m_n = \frac{1}{K'} \sum_{k=1}^{K'} \lambda_k^n. \tag{5.24}$$

In complete analogy to the full-order polynomial, the coefficients depend only on the singular values of the virtual spreading matrix denoted by $\sqrt{\lambda_k}$, $1 \le k \le KN_{\mathrm{T}}$.

The resource pooling result states that for many users the singular value distribution (and thus all its moments) of the virtual spreading matrix for multiple-antenna systems is identical to the corresponding singular value distribution in a single antenna-system with an appropriately modified fading distribution. Thus, we can apply the same approach to find the empirical eigenvalue moments in CDMA systems with multiple antennas as in CDMA systems with single-element antennas. This approach is presented in Section 5.8. For considerations concerning asynchronous systems, the reader is referred to [6].

5.7. Block structure of receiver

Approximation (5.22) leads to the very simple implementation structure of the linear multistage receiver shown in Figure 5.5. The receiver consists of $D-1$ identical stages each of which performs a respreading of the input signals (filtering by the "virtual" spreading matrix $\mathbf{Q}[m]$) and subsequent matched filtering (filtering by $\mathbf{Q}[m]^H$).

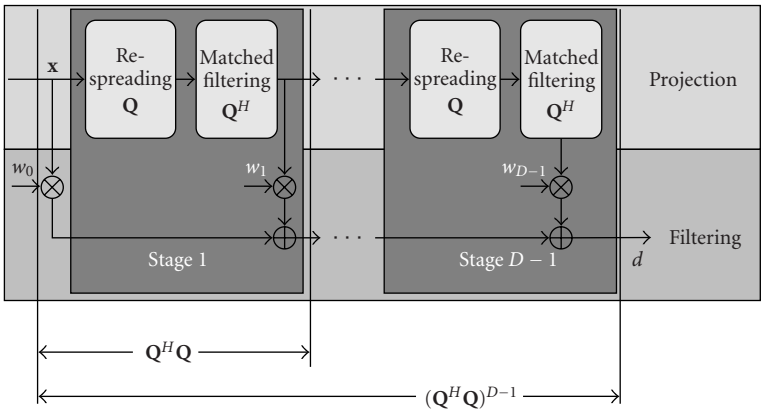

FIGURE 5.5. Linear multistage receiver structure.

Figure 5.5 suggests an alternative interpretation of the linear multistage receiver as subspace technique, an approach followed in [4]. Each stage provides the projection of the received signal onto a one-dimensional subspace. The subsequent weighting corresponds to a bank of filters working in a D-dimensional space. In contrast to other subspace methods, this technique has the following properties.

(i) It does not require tracking of the signal subspace.

(ii) It shows the surprising property that the rank D required to achieve a target SINR (e.g., within a small ϵ of the full-rank LMMSE receiver) does not scale with the system size, that is, with KN_{T} and NN_{R}. The signal space becomes larger but the dimension of the subspace needed to achieve certain performance level saturates.

(iii) A few stages are sufficient for near full-rank performance. The output SINR of the reduced rank receiver converges *exponentially fast* in the rank D towards output SINR of the full-rank receiver.

(iv) The complexity per transmitted bit of the projection module in Figure 5.5 scales in the same way with KN_{T} as the complexity of the single-user matched filter. However, the computation of the empirical eigenvalue moments has cubic complexity in KN_{T}. This drawback can be overcome using the asymptotic weighting discussed in Section 5.8.

5.8. Large-system weighting

The empirical moments m_d needed in (5.23) to calculate the weights depend on the spreading matrices $\mathbf{S}_p[m]$, $p = 1,\ldots,N_{\mathrm{T}}$ and the channel realizations. Thus, the weights have to be recomputed if one of these parameters change. In mobile communications the channel may change rapidly and the spreading matrices may vary from symbol to symbol (e.g., in the frequency-division duplex mode in UMTS). The weights have to be updated at each symbol interval or, at most, at each frame interval. When the size of the virtual spreading matrix $\mathbf{Q}[m]$ is large,

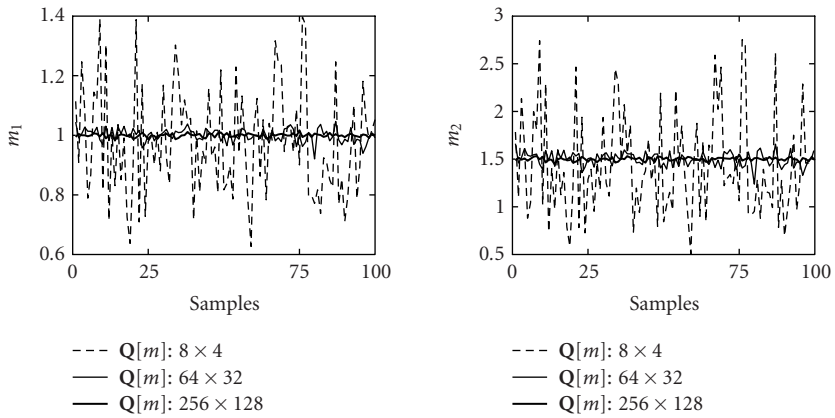

FIGURE 5.6. First two moments for 100 realizations of $\mathbf{Q}[m]$ with i.i.d. Gaussian entries.

it is computationally too demanding to determine the detector weights according to (5.23). However, it is possible to exploit a property of random matrices which allows for a significant simplification of the weight-computation. With some conditions, usually fulfilled in practice, for the virtual spreading matrix $\mathbf{Q}[m]$, all empirical moments m_d converge to deterministic limits as the system size grows large:

$$\lim_{K=\alpha N\to\infty} m_d = \mu_d. \tag{5.25}$$

The limit μ_d depends on a small set of system parameters and can be computed without much effort. Large-system weights approximate the exact weights in (5.23) by substituting the empirical moments m_d with their asymptotic limits μ_d. When the system size is sufficiently large, $m_d \approx \mu_d$ and the performance degradation due to this approximation is negligible.

We consider a simple example. Let all the entries of $\mathbf{Q}[m]$ be statistically independent and identically distributed (i.i.d.) random variables with zero mean and unitary variance. Consider matrices $\mathbf{Q}[m]$ with different sizes, but identical aspect ratios.[3] For each of them, generate 100 independent realizations. In Figure 5.6, the moments m_1 and m_2 are shown for all realizations. It is apparent that m_1 and m_2 converge to 1 and 3/2, respectively, as the size of $\mathbf{Q}[m]$ increases. The asymptotic moments μ_d depend only on the aspect ratio β and are given by

$$\mu_d = \sum_{i=0}^{d-1} \binom{d}{i}\binom{d}{i+1}\frac{\beta^i}{d}. \tag{5.26}$$

We consider now the matrix $\mathbf{Q}[m]$ with the structure defined in (5.10). Moreover, assume the following:

(i) the elements $s_{k,p,m}$ are i.i.d. with zero mean and variance $1/N$,

[3]This is the ratio of the number of columns to the number of rows of a matrix.

Initialization: let $\beta = \alpha(N_T/N_R)$, $\rho_0(x) = 1$, and $\mu_0 = \beta^{-1}$.
Recursion:
(1) define $\rho_{d+1}(x) = \beta x \sum_{s=0}^{d} \rho_s \mu_{d-s}$ and write it as polynomial in x,
(2) replace all the monomials $x, x^2, \ldots, x^{d+1}$ in the polynomial $\rho_{d+1}(x)$ by $\eta_1, \eta_2, \ldots, \eta_{d+1}$, respectively, and assign the result to μ_{d+1}.

Algorithm 5.1

(ii) the channel fading coefficients $h_{k,p,q}$ are independent across k, p, and q. Their distribution is uniform in phase over $[0, 2\pi)$ and arbitrary, but upper bounded[4] in amplitude. For a given transmitting antenna p and given user k, the fading coefficients $h_{k,p,1}, h_{k,p,2}, \ldots, h_{k,p,N_R}$ are identically distributed. The assumption of independence is verified in scenarios with rich scattering and sufficient separation between antennas. The identical distribution of the fading coefficients for a given transmitting antenna element models microdiversity scenarios, in which all the receive antenna elements are placed at the same base station.

Now, we define the powers

$$P_{k,p} = \sum_{q=1}^{N_R} |h_{k,p,q}|^2, \tag{5.27}$$

and denote with η_d the dth moment of their cumulative distribution $F_P(\pi)$, that is, $\eta_d = \int \pi^d \mathrm{d}F_P(\pi)$. The positive asymptotic moments μ_d can be determined from the moments of the powers η_d by the recursive Algorithm 5.1.

The asymptotic eigenvalue moments for $\mathbf{Q}[m]$ depend only on the aspect ratio and on the eigenvalue moments of the distribution $F_P(\pi)$. They are easily computed. The first six asymptotic eigenvalue moments are

$$\begin{aligned}
\mu_1 &= \eta_1, \\
\mu_2 &= \beta\eta_1^2 + \eta_2, \\
\mu_3 &= \beta^2\eta_1^3 + 3\beta\eta_1\eta_2 + \eta_3, \\
\mu_4 &= \beta^3\eta_1^4 + 6\beta^2\eta_1^2\eta_2 + 4\beta\eta_1\eta_3 + 2\beta\eta_2^2 + \eta_4, \\
\mu_5 &= \beta^4\eta_1^5 + 10\beta^3\eta_1^3\eta_2 + 10\beta^2\eta_1^2\eta_3 + 10\beta^2\eta_1\eta_2^2 + 5\beta\eta_1\eta_4 + 5\beta\eta_2\eta_3 + \eta_5, \\
\mu_6 &= 20\beta^3\eta_3\eta_1^3 + 3\beta\eta_3^2 + 6\beta\eta_4\eta_2 + 5\beta^2\eta_2^3 + 15\beta^4\eta_1^4\eta_2 + 6\beta\eta_5\eta_1 \\
&\quad + 15\beta^2\eta_4\eta_1^2 + 30\beta^3\eta_1^2\eta_2^2 + 30\beta^2\eta_1\eta_2\eta_3 + \beta^5\eta_1^6 + \eta_6.
\end{aligned} \tag{5.28}$$

[4]The widely used Rayleigh distribution is not upper bounded, but by physical reasons any fading coefficient is upper bounded.

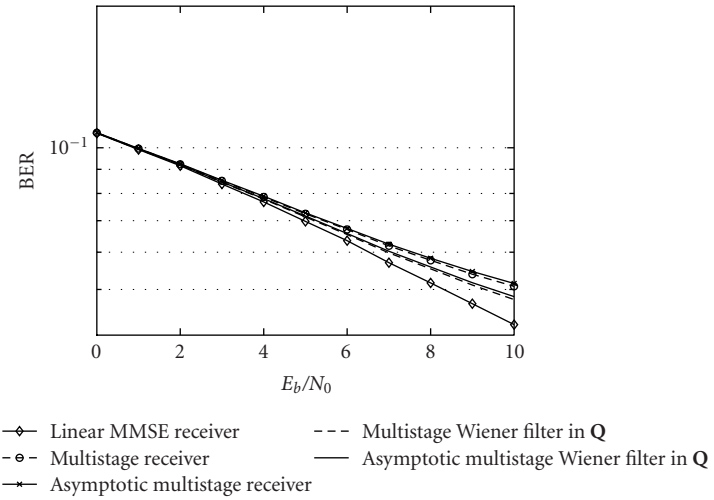

FIGURE 5.7. BER versus E_b/N_0 for $\beta = 0.5$ ($K = 64, N = 64, N_T = 2, N_R = 4, D = 5$).

5.9. Performance

In this section, we study the performance of linear multistage receivers with asymptotic weighting proposed in Section 5.8 and compare it to the exact weighting in (5.23), the large-system approximation of the multistage Wiener receiver in **Q**, described in Section 5.10, and the full-rank LMMSE receiver.

The simulation results presented in this section were obtained for uncoded transmission in flat Rayleigh fading, using $\pi/4$-offset QPSK modulation, and assuming perfect knowledge of the channel. The receivers are compared in terms of their bit error rate (BER) evaluated as a function of the normalized signal-to-noise ratio E_b/N_0 where E_b is mean energy per bit and N_0 is the one-sided noise spectral density. Figure 5.7 shows the BER versus E_b/N_0 for a five-stage detector and $\beta = 0.5$ ($K = 64$, $N = 64$, $N_T = 2$, $N_R = 4$). The performance degradation due to the large system approximation of weights is completely negligible. Figure 5.8 shows the performance improvements of the detector with large-system weighting for increasing number of stages.

5.10. Related works

The linear multistage receivers in (5.22) with weighting (5.23) belong to a wider class of receivers described by

$$\tilde{\mathbf{d}}[m] = \sum_{k=0}^{D-1} \mathbf{W}_k \left(\mathbf{Q}[m]^H \mathbf{Q}[m]\right)^k \mathbf{x}[m] \tag{5.29}$$

with $\mathbf{W}_k = \text{diag}(w_{k,1}, w_{k,2}, \ldots, w_{k,K'})$.

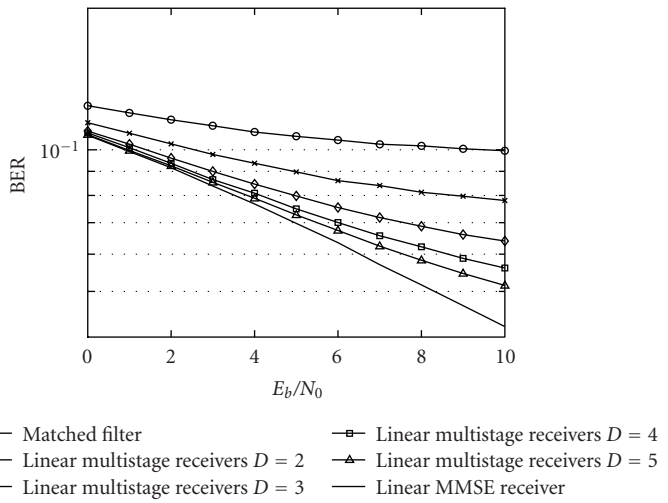

FIGURE 5.8. BER versus E_b/N_0 for $\beta = 0.5$ for $D = 2, \ldots, 5$ ($K = 64, N = 64, N_T = 2, N_R = 4$).

The weighted linear parallel interfering cancelling (W-PIC) receivers, generalized to multiple-antenna systems provide a simple example of receivers in the class described by (5.29).

A nonadaptive implementation of the multistage Wiener filters [4] is obtained from (5.29) enforcing $\mathbf{W}_d$, $d = 0, \ldots, D-1$, to minimize the mean-squared error $\mathrm{E}\{\|\tilde{\mathbf{d}}[m] - \mathbf{d}[m]\|^2\}$. Throughout, we refer to it as the *multistage Wiener filter in* $\mathbf{Q}$. This receiver was proposed and its asymptotic performance for CDMA systems in flat fading channels analyzed in [7]. Let $\mathbf{Q}_{k'}[m]$ be the matrix obtained from $\mathbf{Q}[m]$ by suppressing the virtual spreading corresponding to the signal k'. Under the conjecture[5] that, at least asymptotically, $\mathrm{E}\{\prod_k \mathbf{x}_{k'}^{\mathrm{H}}(\mathbf{Q}_{k'}^{\mathrm{H}}\mathbf{Q}_{k'})^{j_k}\mathbf{x}_{k'}\} = \prod_k \mathrm{E}\{\mathbf{x}_{k'}^{\mathrm{H}}(\mathbf{Q}_{k'}^{\mathrm{H}}\mathbf{Q}_{k'})^{j_k}\mathbf{x}_{k'}\}$ with $j_k \in \mathbb{N}$, the large-system approximation of the weights for the multistage Wiener filter for the MIMO channel model (5.9) is a straightforward extension of the results in [1, 7]. The weights for estimating the signal transmitted by antenna p of user k can be obtained from (5.23) by substituting m_d, $d = 1, \ldots, 2D$, with $\rho_d(P_{k,p})$. The multistage Wiener filter performs marginally better than the receiver discussed in Section 5.8, when applied in systems with received power imbalances among users [7] (see Figure 5.7). The two receivers coincide for equal received powers at the receiver front end [7]. However, the multistage Wiener filter in $\mathbf{Q}$ requires the inversion of equation system (5.23) for each transmitting antenna of each user. This drawback makes it less attractive for implementation. Often, an alternative linear multistage receiver is considered in literature: the *multistage Wiener filter in* $\mathbf{Q}_{k'}$. For each transmitted signal k', it is

[5]This conjecture is supported by simulations (see Figure 5.7).

given by

$$\tilde{\mathbf{d}}[m] = \sum_{k=0}^{D-1} w_k \left(\mathbf{Q}_{k'}[m]^{\mathrm{H}} \mathbf{Q}_{k'}[m]\right)^k \mathbf{x}_{k'}[m], \tag{5.30}$$

where $\mathbf{x}_{k'}[m]$ is the matched filter output corresponding to the signal k'. The weights satisfy

$$\begin{bmatrix} \tau_1 \\ \vdots \\ \tau_D \end{bmatrix} = \begin{bmatrix} \tau_2 + \sigma^2\tau_1 + \tau_1^2 & \cdots & \tau_{D+1} + \sigma^2\tau_D + \tau_1\tau_D \\ \vdots & \ddots & \vdots \\ \tau_{D+1} + \sigma^2\tau_D + \tau_D\tau_1 & \cdots & \tau_{2D} + \sigma^2\tau_{2D-1} + \tau_D^2 \end{bmatrix} \begin{bmatrix} w_0 \\ \vdots \\ w_{D-1} \end{bmatrix} \tag{5.31}$$

with $\tau_1 = P_{k,p}$ and $\tau_d = P_{k,p}\beta\mu_{d-1}$. This detector has been erroneously considered completely equivalent to the multistage Wiener filter in $\mathbf{Q}$ and widely studied since it is easier to analyze. The two receivers are equivalent from the performance point of view only. However, their implementations differ considerably. The subspace basis of the multistage Wiener filter in $\mathbf{Q}$ can be computed jointly for all the transmitted signals, as shown in Figure 5.5, and it has linear complexity order per signal. The subspace basis of the multistage Wiener filter in $\mathbf{Q}_{k'}$ has to be computed again for each transmitted signal and the filter has a quadratic complexity order per signal, as the linear MMSE receiver.

The convergence rate of the multistage receiver output SINR toward the full-rank LMMSE receiver output SINR is studied in [8]. A unified framework for the asymptotic performance analysis of multistage detectors (5.29) with any kind of weighting in CDMA systems is provided in [9]. The weighting approximation for large systems was proposed in [10] for communication over the AWGN channel. Afterwards, much effort has been devoted to extend these results to more realistic scenarios. We can distinguish two large groups: one assumes the spreading matrix to be a completely random matrix without additional constraints in order to model systems with pseudonoise scrambling sequences. The second group focuses on unitary random matrices to model systems with orthogonal spreading sequences. The extension of large-system weighting to CDMA systems in uplink with flat fading in [9] belongs to the first group. An approximation of the widely linear MMSE receiver for BPSK modulation in flat fading channels is proposed in [11]. CDMA systems in uplink with multipath fading channels are studied in [12] while the multistage Wiener filter in $\mathbf{Q}_{k'}$ for the downlink is analyzed in [13]. MMSE analysis of systems with large unitary random matrices has been introduced first in [14]. This result allows the extension of asymptotic analysis based on random matrices to OFDM and multicarrier CDMA systems. Large systems weighting for CDMA systems in downlink with multipath fading channels and unitary random spreading matrices has been proposed in [13]. In [1], the extension of the resource pooling result for scenarios with microdiversity to scenarios

with macrodiversity, in which the receive antennas are not colocated is conjectured. The resource pooling result by Hanly and Tse [1] has been generalized to CDMA systems with correlated antennas in [2]. The general result includes, as special cases, the microdiversity and macrodiversity scenarios in [1] and provides a rigorous proof for macrodiversity. In addition, it allows for arbitrary distributions of the fading coefficients including line-of-sight scenarios.

Generalized resource pooling. *Let* $\mathbf{h}_{k,p} = [h_{k,p,1}, \ldots, h_{k,p,N_R}]^T$ *be the known vector of channel coefficients between the* p*th antenna of user* k *and the receive antennas. Let* $\mathbf{h}_{k,p}$ *be a realization of an* N_R*-dimensional random column vector* $\mathbf{h}$ *such that its distribution converges almost surely as* $K \to \infty$ *to a limit distribution function* $F_{\mathbf{h}}(\mathbf{h})$ *with upper bounded support. Then, as* $N, K \to \infty$ *with* $K/N \to \alpha$ *and* N_R *and* N_T *fixed, the* SINR *at the receiver output for the* p*th antenna signal of user* k *conditioned on* $\mathbf{h}_{k,p}$ *converges almost surely to the deterministic constant*

$$\lim_{N,K\to\infty} \mathrm{SINR}_{k,p} \overset{a.s.}{=} \mathbf{h}_{k,p}^H \mathbf{C} \mathbf{h}_{k,p}, \tag{5.32}$$

where $\mathbf{C}$ *is the unique positive definite* $N_R \times N_R$ *matrix solution to the fixed point equation*

$$\mathbf{C}^{-1} = \sigma^2 \mathbf{I} + \alpha N_T \int \frac{\mathbf{h}\mathbf{h}^H}{1 + \mathbf{h}^H \mathbf{C} \mathbf{h}} \mathrm{d}F_{\mathbf{h}}(\mathbf{h}). \tag{5.33}$$

The linear multistage approach is extended to estimation of multipath fading channels for synchronous CDMA [15]. The effects of imperfect channel knowledge on the performance of linear multistage receivers is analyzed in [15].

In the previous works only synchronous systems have been considered. The impact of asynchronicity on multistage receivers for CDMA systems in flat fading channels has been studied in [6, 16]. A slightly modified version of the receiver structure in Figure 5.5 has been proposed. In contrast to the linear MMSE receiver which suffers from performance degradation due to truncation effects in asynchronous systems, the proposed implementation of multistage detectors is not affected by truncation effects [16]. Chip asynchronicity is taken into account in [6] and an algorithm to determine the large-system weighting is given.

Acknowledgment

The authors thank Stephen Hanly for clarifying some aspects of resource pooling.

Abbreviations

AWGN	Additive white Gaussian noise
BER	Bit error rate
BPSK	Binary phase-shift keying

CDMA	Code-division multiple-access
LMMSE	Linear minimum mean-squared error
MIMO	Multi-input multi-output
OFDM	Orthogonal frequency-division multiplex
QPSK	Quadrature phase-shift keying
SINR	Signal-to-interference-and-noise ratio
W-PIC	Weighted linear parallel interfering cancelling

Bibliography

[1] S. V. Hanly and D. N. C. Tse, "Resource pooling and effective bandwidths in CDMA networks with multiuser receivers and spatial diversity," *IEEE Trans. Inform. Theory*, vol. 47, no. 4, pp. 1328–1351, 2001.

[2] L. Cottatellucci and R. R. Müller, "A generalized resource pooling result for correlated antennas with applications to asynchronous CDMA," in *Proc. International Symposium on Information Theory and Its Applications*, Parma, Italy, October 2004.

[3] S. Verdú, *Multiuser Detection*, Cambridge University Press, Cambridge, UK, 1998.

[4] M. L. Honig and W. Xiao, "Performance of reduced-rank linear interference suppression," *IEEE Trans. Inform. Theory*, vol. 47, no. 5, pp. 1928–1946, 2001.

[5] S. Moshavi, E. G. Kanterakis, and D. L. Schilling, "Multistage linear receivers for DS-CDMA systems," *Int. J. Wireless Inform. Networks*, vol. 3, no. 1, pp. 1–17, 1996.

[6] L. Cottatellucci and R. R. Müller, "Multistage detectors in asynchronous CDMA systems," in *Proc. International Zurich Seminar on Communications (IZS)*, pp. 102–105, Zurich, Switzerland, February 2004.

[7] L. Cottatellucci and R. R. Müller, "Multiuser interference mitigation with multistage detectors: design and analysis for unequal powers," in *Proc. 36th Asilomar Conference on Signals, Systems and Computers*, pp. 1948–1952, Pacific Grove, Calif, USA, November 2002.

[8] P. Loubaton and W. Hachem, "Asymptotic analysis of reduced rank Wiener filters," in *Proc. IEEE Information Theory Workshop*, pp. 328–331, Paris, France, April 2003.

[9] L. Cottatellucci and R. R. Müller, "Asymptotic design and analysis of multistage detectors with unequal powers," in *Proc. IEEE Information Theory Workshop*, pp. 167–170, Bangalore, India, October 2002.

[10] R. R. Müller and S. Verdú, "Design and analysis of low-complexity interference mitigation on vector channels," *IEEE J. Select. Areas Commun.*, vol. 19, no. 8, pp. 1429–1441, 2001.

[11] A. M. Tulino and S. Verdú, "Asymptotic analysis of improved linear receivers for BPSK-CDMA subject to fading," *IEEE J. Select. Areas Commun.*, vol. 19, no. 8, pp. 1544–1555, 2001.

[12] L. Cottatellucci and R. R. Müller, "A systematic approach to multistage detectors in multipath fading channels," submitted to *IEEE Trans. Inform. Theory*.

[13] W. Hachem, "Simple polynomial detectors for CDMA downlink transmissions on frequency-selective channels," *IEEE Trans. Inform. Theory*, vol. 50, no. 1, pp. 164–171, 2004.

[14] M. Debbah, W. Hachem, P. Loubaton, and M. de Courville, "MMSE analysis of certain large isometric random precoded systems," *IEEE Trans. Inform. Theory*, vol. 49, no. 5, pp. 1293–1311, 2003.

[15] L. Cottatellucci and R. R. Müller, "Asymptotic design and analysis of multistage detectors and multistage channel estimators for multipath fading channels," in *Proc. IEEE International Symposium on Information Theory (ISIT)*, p. 243, Yokohama, Japan, June–July 2003.

[16] L. Cottatellucci, R. R. Müller, and M. Debbah, "Asymptotic design and analysis of linear detectors for asynchronous CDMA systems," in *Proc. IEEE International Symposium on Information Theory (ISIT)*, p. 509, Chicago, Ill, USA, June–July 2004.

[17] J. Evans and D. N. C. Tse, "Large system performance of linear multiuser receivers in multipath fading channels," *IEEE Trans. Inform. Theory*, vol. 46, no. 6, pp. 2059–2078, 2000.

Ralf Müller: Department of Electronics and Telecommunications, Norwegian University of Science and Technology, 7491 Trondheim, Norway

Email: mueller@iet.ntnu.no

Laura Cottatellucci: Forschungszentrum Telekommunikation Wien, 1220 Vienna, Austria

Email: cottatellucci@ftw.at

6 Synchronization for MIMO systems

Frederik Simoens, Henk Wymeersch,
Heidi Steendam, and Marc Moeneclaey

In this contribution we consider the problem of carrier and symbol synchronization in a MIMO context. We assume the transmission of frames, containing pilot symbols and coded symbols over a flat fading MIMO channel. From the likelihood function related to the above scenario, we derive iterative algorithms for estimating the carrier frequency offset, the time delay, and the channel gains. These algorithms exchange information between the detector stage and the estimator stage. In order to function properly, accurate initial estimates are required. We derive algorithms that provide these initial estimates, and compare their performance to the Cramér-Rao lower bound on the estimator error variance. The initial estimates are further refined by means of iterative algorithms. We provide performance results of a few selected iterative algorithms in terms of their estimator error variance, and compare them to the Cramér-Rao bound. Finally, the impact of the estimation algorithms on the BER performance is determined.

6.1. Introduction

Using multiple transmit and receive antennas in wireless flat-fading channels has been advocated as a means to increase capacity and mitigate fading effects [1]. In order to fully exploit the potential of high spectral efficiency, a number of coding structures for MIMO systems have been presented: they include multidimensional trellis-coded modulation [2], space-time (ST) block codes based on orthogonal design [3, 4], bit-interleaved coded modulation (BICM) [5, 6], and MIMO multilevel coding [7]. These (space-time) coded schemes assume ideal coherent detection, which means that the complex channel gains have to be estimated accurately before data detection can take place. In addition, timing estimation and carrier frequency recovery have to be carried out in order to perform optimum demodulation.

To achieve accurate synchronization without resorting to a large amount of pilot symbols, the parameter estimation algorithm should also make use of the data portion of the frame containing the coded symbols. Recently, a great effort is being devoted to develop efficient estimation techniques using soft information

from the decoding process, in order to fully exploit the code properties during estimation. In particular, the expectation-maximization (EM) algorithm [8] is becoming an attractive tool to carry out iterative joint estimation and decoding.

Most of the current technical literature in the field of estimation for MIMO channels has been focused on channel estimation. Iterative receivers with different coding schemes have been proposed using the EM algorithm for joint channel estimation and data detection in a MIMO context [9, 10, 11, 12]. The EM algorithm is utilized in [9] to perform joint noise variance and channel estimation for fast fading channels with space-time coding and MAP decoding. An MMSE channel estimator that exploits knowledge of the transmitted symbols via a modified Viterbi decoder is considered in [10, 11]. In [12], joint MIMO channel estimation and MAP ST-BICM decoding is performed. Extensions to ST-OFDM have been proposed in [13]. Rather ad hoc methods have been considered for iterative decoding and MIMO channel estimation, such as frequency selective channel estimation with decision feedback for space-time codes with Viterbi decoding [14] and MAP decoding [15].

All these channel estimation algorithms cause only a small degradation in BER performance as compared to the ideal case with known channel state information (CSI). However, the performance of these schemes may seriously degrade in the presence of synchronization errors, that is, when the estimates of the frequency offset or the symbol timing are not sufficiently accurate. In comparison with the abundant literature on (iterative) channel estimation, the literature on synchronization in a MIMO context is quite scarce: the authors of [16] investigated the performance of data-aided joint MIMO channel and frequency offset estimators, while data-aided joint time and frequency synchronization for MIMO OFDM is considered in [17].

Here we propose an iterative EM-based receiver that includes the estimation of all of the above-mentioned parameters, as was done for conventional single-input single-output channels [18, 19]. Since initial estimates are required for a number of parameters, we also show how these may be obtained using conventional data-aided (DA) or non-data-aided (NDA) algorithms.

This contribution is structured as follows. In Section 6.2 we present the MIMO system setup. As the EM algorithm is crucial to the operation of the considered receiver, Section 6.3 gives a brief general overview about how this algorithm performs ML estimation in an iterative way. In Section 6.4 the EM algorithm is applied to the MIMO system for performing synchronization and channel estimation, while in Section 6.5 we consider conventional estimation algorithms to initialize the iterative EM estimation algorithm. Simulation results are presented in Section 6.7. Finally, conclusions are drawn in Section 6.8.

6.2. System model

We consider a flat-fading MIMO transmission system with N_T transmit and N_R receive antennas. The transmitter is shown in Figure 6.1: a block of information bits is channel-encoded, bit-interleaved (denoted by Π in Figure 6.1), and mapped

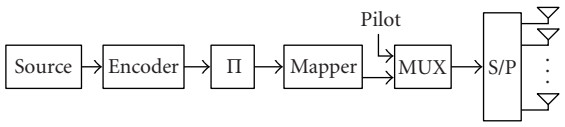

FIGURE 6.1. MIMO transmitter with channel coder and bit-interleaving.

onto a normalized M_c-point signaling constellation Ω. Pilot symbols are multiplexed with the coded symbols, and the resulting frame, consisting of MN_T symbols, is then split into N_T subblocks of length M. These subblocks are each sent over a different transmit antenna using a unit-energy square root cosine roll-off pulse $p(t)$.

The fading channel is characterized by a response matrix $\mathbf{H}$ of size $N_\mathrm{R} \times N_\mathrm{T}$: the (q, p)th component of $\mathbf{H}$ is denoted h_{qp}, and represents the channel gain from the pth transmit antenna to the qth receive antenna. We consider a block-fading channel: the channel matrix $\mathbf{H}$ is constant during a frame, but can change from one frame to the next. Assuming Rayleigh fading, the components h_{qp} are modeled as statistically independent complex-valued Gaussian random variables; their real and imaginary parts are statistically independent with zero mean and variance equal to 1/2, yielding $E[|h_{qp}|^2] = 1$. In addition, the path from the pth transmit antenna to the qth receive antenna is affected by a propagation delay (τ) and a carrier frequency offset (F), which are assumed to take on the same values for all paths; this assumption is accurate when the path delay differences are much smaller than the symbol duration, there is a common oscillator for up-converting the N_T transmitted signals, and a common oscillator for down-converting the N_R received signals. Finally, at each receive antenna the signal is corrupted by a complex-valued AWGN process; the noise processes at the different receive antennas are statistically independent. Hence, the input signal at the qth receive antenna can be written as $(q = 1, \ldots, N_\mathrm{R})$

$$y_q(t) = \sum_{m=0}^{M-1} \sum_{p=1}^{N_\mathrm{T}} h_{qp} a_m^p p(t - mT - \tau) \exp(j2\pi Ft) + v_q(t), \tag{6.1}$$

where a_m^p is the mth symbol transmitted on the pth transmit antenna, T is the symbol interval, and $v_q(t)$ is a complex-valued zero-mean AWGN process with independent real and imaginary parts, each having a power spectral density of $N_0/2$. $E_s = E[|a_m^p|^2]$ will denote the energy per transmitted symbol (which is assumed to be the same for all m and all p). Using vector notation, (6.1) becomes

$$\begin{aligned} \mathbf{y}(t) &= \mathbf{H} \exp(j2\pi Ft) \sum_{m=0}^{M-1} \mathbf{a}_m p(t - mT - \tau) + \mathbf{v}(t) \\ &\triangleq \mathbf{s}(t) + \mathbf{v}(t), \end{aligned} \tag{6.2}$$

where $\mathbf{y}(t) = [y_q(t)]_{q=1\cdots N_R}^T$ is the vector of N_R received samples, $\mathbf{a}_m = [a_m^p]_{p=1\cdots N_T}^T$ is the vector consisting of N_T symbols transmitted at the different antennas at instant m, $\mathbf{H} = [h_{qp}]_{q=1\cdots N_R,\, p=1\cdots N_T}$ is the channel matrix, $\mathbf{s}(t) = [s_q(t)]_{q=1\cdots N_R}^T$ contains the N_R useful contributions, and $\mathbf{v}(t) = [v_q(t)]_{q=1\cdots N_R}^T$ consists of the N_R complex white noise processes. We denote by $\mathbf{A}$ the $N_T \times M$ space-time matrix of transmitted symbols: $\mathbf{A} = [\mathbf{a}_0, \mathbf{a}_1, \ldots, \mathbf{a}_{M-1}]$.

The main task of the receiver is to reliably detect the transmitted symbols $\mathbf{A}$. In order to do so, however, the receiver needs accurate estimates of the channel matrix $\mathbf{H}$, the carrier frequency offset F, and the propagation delay τ. In Section 6.4 we will consider iterative estimation of these parameters based on the expectation-maximization (EM) algorithm. Section 6.3 gives a general overview of the operation of the EM algorithm and provides the basic equations to be used in Section 6.4.

6.3. ML estimation through the EM algorithm

Assume we want to estimate a parameter vector $\mathbf{b}$ from an observation $\mathbf{r}$ in the presence of a so-called nuisance vector $\mathbf{a}$, with distribution $p(\mathbf{a})$. In the context of the MIMO transmission system, $\mathbf{a}$ denotes the coded symbols, whereas $\mathbf{b}$ contains the synchronization parameters (frequency offset and symbol timing) and the channel gains. It will turn out to be convenient to decompose the time delay τ as $\tau = k_\tau T + \varepsilon_\tau$, with $-T/2 \le \varepsilon_\tau < T/2$ and k_τ integer; in these cases, the time delay is represented by two parameters, that is, the continuous parameter ε_τ and the discrete parameter k_τ. Therefore, in the following, the parameter $\mathbf{b}$ is allowed to contain both continuous and discrete parameters.

The maximum likelihood (ML) estimate of $\hat{\mathbf{b}}_{ML}$ of $\mathbf{b}$ maximizes the log-likelihood function (LLF):

$$\hat{\mathbf{b}}_{ML} = \arg\max_{\tilde{\mathbf{b}}} \{\ln p(\mathbf{r}|\tilde{\mathbf{b}})\}, \tag{6.3}$$

where

$$p(\mathbf{r}|\tilde{\mathbf{b}}) = \int_{\mathbf{a}} p(\mathbf{r}|\mathbf{a}, \tilde{\mathbf{b}})\, p(\mathbf{a})\, d\mathbf{a} \tag{6.4}$$

denotes the likelihood function. Often $p(\mathbf{r}|\tilde{\mathbf{b}})$ is very difficult to calculate. The EM algorithm is a method that iteratively solves (6.3). Defining the complete data $\mathbf{x} = [\mathbf{r}, \mathbf{a}]$, the EM algorithm breaks up in two parts: the expectation part (6.5) and the maximization part (6.6):

$$Q\left(\tilde{\mathbf{b}}, \hat{\mathbf{b}}^{(i)}\right) = \int_{\mathbf{x}} p\left(\mathbf{x}|\mathbf{r}, \hat{\mathbf{b}}^{(i)}\right) \ln p(\mathbf{x}|\tilde{\mathbf{b}})\, d\mathbf{x}, \tag{6.5}$$

$$\hat{\mathbf{b}}^{(i+1)} = \arg\max_{\tilde{\mathbf{b}}} \left\{Q\left(\tilde{\mathbf{b}}, \hat{\mathbf{b}}^{(i)}\right)\right\}. \tag{6.6}$$

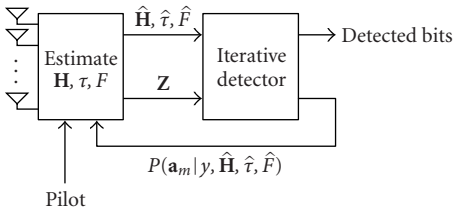

Figure 6.2. MIMO receiver with EM estimation.

It has been shown that $\hat{\mathbf{b}}^{(n)}$ converges to a stationary point of the LLF under fairly general conditions [8]. However, when the initial estimate ($\hat{\mathbf{b}}^{(0)}$) is not sufficiently close to the ML estimate or when $\mathbf{b}$ contains discrete components, the EM algorithm may converge to a local maximum or a saddle point, instead of the global maximum [20, 21]. To avoid the convergence problems associated with (finite-valued) discrete parameters, we propose the following approach [22]: let $\mathbf{b} = \{\mathbf{b}_d, \mathbf{b}_c\}$, where $\mathbf{b}_d$ and $\mathbf{b}_c$ denote the discrete and continuous components of $\mathbf{b}$, respectively. We assume that $\mathbf{b}_d$ can only take on values in a finite set B_d. We keep $\mathbf{b}_d$ fixed to some value $\tilde{\mathbf{b}}_d \in B_d$ and iteratively update only $\mathbf{b}_c$:

$$\hat{\mathbf{b}}_c^{(i+1)} = \arg\max_{\mathbf{b}_c} \{Q(\{\tilde{\mathbf{b}}_d, \tilde{\mathbf{b}}_c\}, \{\tilde{\mathbf{b}}_d, \hat{\mathbf{b}}_c^{(i)}\})\}. \tag{6.7}$$

We denote by $\hat{\mathbf{b}}_c(\tilde{\mathbf{b}}_d)$ the estimate obtained after convergence of (6.7). The final estimate of $\mathbf{b}_d$ then becomes

$$\hat{\mathbf{b}}_d = \arg\max_{\mathbf{b}_d \in B_d} \{Q(\{\tilde{\mathbf{b}}_d, \hat{\mathbf{b}}_c(\tilde{\mathbf{b}}_d)\}, \{\tilde{\mathbf{b}}_d, \hat{\mathbf{b}}_c(\tilde{\mathbf{b}}_d)\})\}, \tag{6.8}$$

while the final estimate of $\mathbf{b}_c$ is given by $\hat{\mathbf{b}}_c(\hat{\mathbf{b}}_d)$.

The EM algorithm can easily be extended to acquire the maximum a posteriori (MAP) estimate of $\mathbf{b}$, by taking the a priori distribution $p(\mathbf{b})$ into account in (6.5).

6.4. Code-aided estimation for MIMO systems

In this section, we apply the EM algorithm to the MIMO system from Section 6.2, with $\mathbf{b} \triangleq \{\mathbf{H}, F, \tau\}$ the parameters to be estimated and $\mathbf{a} \triangleq \{\mathbf{A}\}$ the nuisance parameters. The resulting receiver structure is shown in Figure 6.2. It operates by iterating between the detection stage and the estimation stage: an estimate of $\mathbf{b}$ is provided to the detector, which computes marginal posterior probabilities $P(a_m^p | \mathbf{y}, \hat{\mathbf{b}}^{(i)})$ of the coded symbols. These probabilities are then used by the estimator to update (and improve) the estimate of $\mathbf{b}$. The computation of $P(a_m^p | \mathbf{y}, \hat{\mathbf{b}}^{(i)})$ requires the presence of a MAP detector. Such a detector will be described in Section 6.4.3.

6.4.1. Expectation step

Denoting by $\mathbf{y}$ a vector representation of the received signals, obtained by expanding $\mathbf{y}(t)$ onto a suitable basis, we now make use of the EM algorithm for estimating $\mathbf{b} = \{\mathbf{H}, F, \tau\}$. The conditional LLF (conditioning is on $\mathbf{A}$) is given by

$$\ln p(\mathbf{y}|\mathbf{A},\mathbf{b}) \propto -\int_{-\infty}^{+\infty} \left(\sum_{q=1}^{N_R} |\, y_q(t) - s_q(t) \,|^2 \right) dt \tag{6.9}$$

with $s_q(t)$ denoting the useful signal at the qth receive antenna (i.e., the qth component of $\mathbf{s}(t)$ from (6.2)). It can easily be seen that

$$\sum_{q=1}^{N_R} \int_{-\infty}^{+\infty} |\, s_q(t) \,|^2 dt = \mathrm{tr}(\mathbf{H}\mathbf{A}\mathbf{A}^H\mathbf{H}^H), \tag{6.10}$$

where $\mathrm{tr}(\mathbf{X})$ denotes the trace of the square matrix $\mathbf{X}$. Similarly,

$$\sum_{q=1}^{N_R} \int_{-\infty}^{+\infty} (y_q(t) s_q^*(t)) dt = \mathrm{tr}\left(\mathbf{Z}(\tau,F)\mathbf{A}^H\mathbf{H}^H\right) \tag{6.11}$$

with $\mathbf{Z}(\tau,F)$ denoting the $N_R \times M$ matrix of matched filter outputs:

$$[\mathbf{Z}(\tau,F)]_{q,m} = \int_{-\infty}^{+\infty} y_q(t) p^*(t - mT - \tau) \exp(-2\pi F t) dt. \tag{6.12}$$

Note that the received signal $y_q(t)$ is first frequency-corrected by multiplying $y_q(t)$ with $\exp(-j2\pi Ft)$, and the resulting signal is applied to the matched filter; in Section 6.5 we will point out that the order of frequency correction and matched filtering can be reversed when $|F|T \ll 1$, yielding a considerable implementation advantage. Substituting (6.10) and (6.11) in (6.9) and dropping terms that do not depend on $\mathbf{A}$ or $\mathbf{b}$, the conditional LLF becomes

$$\ln p(\mathbf{y}|\mathbf{A},\mathbf{b}) \propto -\mathrm{tr}\left(\mathbf{H}\mathbf{A}\mathbf{A}^H\mathbf{H}^H\right) + 2\Re\left(\mathrm{tr}\left(\mathbf{Z}(\tau,F)\mathbf{A}^H\mathbf{H}^H\right)\right). \tag{6.13}$$

The E-step in the EM algorithm can be written as

$$\begin{aligned} Q(\mathbf{b}|\hat{\mathbf{b}}^{(i)}) &= E_{\mathbf{a}}[\ln p(\mathbf{y}|\mathbf{A},\mathbf{b})|\mathbf{y},\hat{\mathbf{b}}^{(i)}] \\ &= -\mathrm{tr}\left(\mathbf{H}\overline{\mathbf{A}\mathbf{A}^H}^{(i)}\mathbf{H}^H\right) + 2\Re\left(\mathrm{tr}\left(\mathbf{Z}(\tau,F)\overline{\mathbf{A}^H}^{(i)}\mathbf{H}^H\right)\right) \end{aligned} \tag{6.14}$$

with

$$\begin{aligned} \overline{\mathbf{A}\mathbf{A}^H}^{(i)} &= E_{\mathbf{a}}[\mathbf{A}\mathbf{A}^H|\mathbf{y},\hat{\mathbf{b}}^{(i)}], \\ \overline{\mathbf{A}^H}^{(i)} &= E_{\mathbf{a}}[\mathbf{A}^H|\mathbf{y},\hat{\mathbf{b}}^{(i)}]. \end{aligned} \tag{6.15}$$

Since (6.15) can be written as $E_{\mathbf{a}}[\sum \mathbf{a}_m \mathbf{a}_m^H | \mathbf{y}, \hat{\mathbf{b}}^{(i)}]$, it suffices to provide the estimator with the marginal posterior probabilities of the coded symbol vectors $P(\mathbf{a}_m | \mathbf{y}, \hat{\mathbf{b}}^{(i)})$. In Section 6.4.3, we explain how these probabilities can be computed using a MAP detector.

6.4.2. Maximization step

Substitution of (6.14) in (6.6) yields

$$\hat{\mathbf{b}}^{(i+1)} = \arg\max_{\mathbf{b}} \left\{ -\operatorname{tr}\left(\tilde{\mathbf{H}}\overline{\mathbf{A}\mathbf{A}^H}^{(i)}\tilde{\mathbf{H}}^H\right) + 2\Re\left(\operatorname{tr}\left(\mathbf{Z}(\tilde{\tau},\tilde{F})\overline{\mathbf{A}^H}^{(i)}\tilde{\mathbf{H}}^H\right)\right)\right\}. \tag{6.16}$$

The maximization problem can be solved as follows. We first note that for fixed $(\tilde{\tau}, \tilde{F})$, (6.16) can be maximized analytically with respect to $\tilde{\mathbf{H}}$, yielding

$$\hat{\mathbf{H}}^{(i+1)} = \mathbf{Z}(\tilde{\tau},\tilde{F})\overline{\mathbf{A}^H}^{(i)}\left(\overline{\mathbf{A}\mathbf{A}^H}^{(i)}\right)^{-1}. \tag{6.17}$$

Substituting (6.17) into (6.16) results in

$$(\hat{\tau}^{(i+1)}, \hat{F}^{(i+1)}) = \arg\max_{\tilde{\tau},\tilde{F}} \Re\left(\operatorname{tr}\left(\mathbf{Z}(\tilde{\tau},\tilde{F})\overline{\mathbf{A}^H}^{(i)}\left(\overline{\mathbf{A}\mathbf{A}^H}^{(i)}\right)^{-1}\overline{\mathbf{A}}\mathbf{Z}^H(\tilde{\tau},\tilde{F})\right)\right) \tag{6.18}$$

while $\hat{\mathbf{H}}^{(i+1)}$ is finally obtained by evaluating (6.17) at $(\hat{\tau}^{(i+1)}, \hat{F}^{(i+1)})$.

6.4.3. Detector operation

We now determine the marginal posterior probabilities of the coded symbol vectors, based on the received signal and the current estimates of $\mathbf{H}$, τ, and F. As the computation of the true posterior probabilities has a complexity that increases exponentially with the frame length M, we will focus on a near-optimal iterative detector, operating according to the turbo principle [6, 12]. This implies that all posterior probabilities will be factored as the product of an *a priori* probability (with subscript a) and an *extrinsic* probability (with subscript e). According to the turbo principle, the a priori probability of a certain random variable should not be used to compute its extrinsic probability.

The symbol posterior probabilities can be decomposed into

$$P(a_m^p | \mathbf{y}, \mathbf{b}) = CP_e(a_m^p)P_a(a_m^p), \tag{6.19}$$

where C is a normalization constant and the extrinsic symbol probability is given by, (for $\alpha \in \Omega$)

$$\begin{aligned} P_e(a_m^p = \alpha) &= P(\mathbf{y} | a_m^p = \alpha, \mathbf{b}) \\ &= \sum_{\mathbf{a}_m : a_m^p = \alpha} P(\mathbf{y} | \mathbf{a}_m, \mathbf{b}) \prod_{p' \neq p} P_a(a_m^{p'}) \end{aligned} \tag{6.20}$$

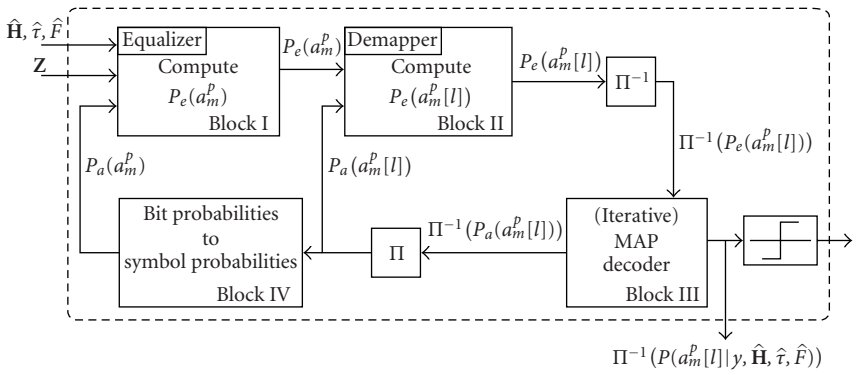

FIGURE 6.3. Iterative detector.

with

$$P(\mathbf{y}|\mathbf{a}_m, \mathbf{b}) = \frac{1}{(2\pi)^{N_R}\sigma^{2N_R}} \exp\left(-\frac{1}{2\sigma^2}\left|\mathbf{z}_m - \mathbf{H}\mathbf{a}_m\right|^2\right), \tag{6.21}$$

wherein $\mathbf{z}_m$ is the mth column of $\mathbf{Z}(\tau, F)$, $\sigma^2 = 2E_s/N_0$.

Similarly, the bit posterior probabilities are given by

$$P(a_m^p[l]|\mathbf{y}, \mathbf{b}) = C' P_e(a_m^p[l]) P_a(a_m^p[l]) \tag{6.22}$$

with C' a normalization constant and, for $\beta \in \{0, 1\}$,

$$\begin{aligned} P_e(a_m^p[l] = \beta) &= P(\mathbf{y}|a_m^p[l] = \beta, \mathbf{b}) \\ &= \sum_{\alpha \in \Omega : \alpha[l] = \beta} P_e(a_m^p = \alpha) \prod_{l' \neq l} P_a(a_m^p[l']), \end{aligned} \tag{6.23}$$

where $a_m^p[l]$ denotes the lth bit of the bit sequence mapped to the symbol a_m^p. Finally, bit a priori probabilities can be converted into symbol a priori probabilities according to

$$P_a(a_m^p) = \prod_l P_a(a_m^p[l]). \tag{6.24}$$

Note that the purpose of the interleaver is two-fold: it makes the transmitted symbols on each antenna as well as the bits within each constellation symbol essentially independent. This allows us to write expressions (6.20) and (6.23), respectively.

In order to compute all the above-mentioned probabilities, we consider a detector as shown in Figure 6.3. It consists of four main blocks.

(i) Block I is the equalizer: it converts the matched filter output samples $\mathbf{Z}$ into extrinsic symbol probabilities $(P_e(a_m^p))$ according to (6.20) and (6.21). It uses the

a priori symbol probabilities ($P_a(a_m^{p'})$) computed by block IV and the estimates of $\{\mathbf{H}, F, \tau\}$.

(ii) Block II is the demapper: it takes the extrinsic symbol probabilities ($P_e(a_m^p)$) from block I and computes extrinsic bit probabilities $P_e(a_m^p[l])$ according to (6.23). It uses the a priori bit probabilities ($P_a(a_m^p[l'])$) computed by decoder (block III).

(iii) Block III is a MAP decoder. The decoder computes from the extrinsic bit probabilities $P_e(a_m^p[l])$ the posterior bit probabilities ($P(a_m^p[l]|\mathbf{y}, \widehat{\mathbf{b}}^{(i)})$) by using the properties of the code. Taking for each bit the ratio of its posterior probability to its extrinsic probability yields the a priori probabilities $P_a(a_m^p[l])$ that are used as a priori information for block II.

(iv) Block IV converts a priori information on the bits ($P_a(a_m^p[l])$) to a priori information on the symbols ($P_a(a_m^p)$) according to (6.24). These are used by block I.

To start this iterative detector, we initialize $P_a(a_m^{p'})$ in (6.20) and $P_a(a_m^p[l'])$ in (6.23) with a uniform distribution. The combination of block II and III can be seen as a standard BICM-ID (bit-interleaved coded modulation with iterative decoding) scheme [23]. When the detector has reached convergence after a number of iterations, the computed posterior probabilities of the coded bits are assumed to be good approximations of the true posterior bit probabilities. Final decisions on the bits are made based on these probabilities.

The posterior probabilities of the coded symbol vectors are finally obtained as

$$P(\mathbf{a}_m|\mathbf{y}, \mathbf{b}) = C'' P_e(\mathbf{a}_m) P_a(\mathbf{a}_m) = C''' P(\mathbf{y}|\mathbf{a}_m, \mathbf{b}) \prod_{l,p} P_a(a_m^p[l]). \tag{6.25}$$

These symbol vector probabilities are required for the EM estimator in (6.14). In principle, the proposed EM algorithm is limited to codes for which (approximate) symbol vector MAP decoding, as outlined above, is computationally feasible. Such codes include convolutional codes, turbo codes [24, 25], LDPC [26] codes, RA (repeat-accumulate) codes [27], and so forth. In practice, the estimation algorithm can also be used with decoders that only provide hard decisions (such as convolutional Viterbi decoders), by simply replacing the posterior symbol probabilities with the hard symbol decisions resulting from the decoder; in this case the estimation becomes decision-directed.

6.5. Conventional estimation algorithms

Conventional feedforward estimation algorithms can be either data-aided (DA) or non-data-aided (NDA). DA algorithms make only use of so-called pilot symbols within the transmitted frames, while NDA estimation algorithms operate on all symbols in the frame by only exploiting the fact that the transmitted data symbols belong to a given constellation. These conventional estimation schemes do not exploit the code properties and can be used to provide initial estimates in (6.14). We will now describe how $\mathbf{H}$, τ, and F can be estimated using such algorithms.

The delay τ can be decomposed as $\tau = k_\tau T + \varepsilon_\tau$, with $-T/2 \le \varepsilon_\tau < T/2$. Some form of energy detection is assumed to roughly determine the arrival of a burst within M_τ symbol durations, hence $k_\tau \in \{0, \ldots, M_\tau - 1\}$. First, we determine a NDA estimate of ε_τ, irrespective of the values of the frequency offset F and the channel matrix $\mathbf{H}$. Then, we determine a DA estimate of the remaining parameters $\mathbf{H}$, F, and k_τ.

A simple NDA estimate of ε_τ can be obtained using the Oerder&Meyr (O&M) algorithm [28]. This algorithm is unable to distinguish between delays that differ by a multiple of the symbol interval. It therefore provides an estimate of ε_τ, but not of k_τ. The O&M estimator has originally been designed for $N_\mathrm{T} = N_\mathrm{R} = 1$, but the extension to a MIMO setup is straightforward,

$$\hat{\varepsilon}_\tau = -\frac{T_s}{2\pi} \measuredangle \left\{ \sum_k \sum_{q=1}^{N_\mathrm{R}} |z_q(kT_s)|^2 \exp\left(-j2\pi \frac{kT_s}{T} \right) \right\}, \tag{6.26}$$

where $\measuredangle\{\cdot\}$ denotes the angle of a complex number, $1/T_s$ is the sample rate (usually $T_s = T/4$), and $z_q(kT_s)$ is the matched filter output at the qth receive antenna at time kT_s when assuming $F = 0$, that is, $z_q(kT_s) = \int y_q(t) p^*(t - kT_s) dt$. This estimator does not require knowledge of $\mathbf{H}$ and F. Moreover, as we will show later, the performance of this delay estimator gives rise to a very small BER degradation. It therefore makes sense to keep this estimate of ε_τ unchanged for all EM iterations. It is important to note that when a reliable estimate of ε_τ is obtained, a significant reduction in computational complexity can be achieved: all subsequent processing may be performed at the symbol rate $1/T$ when we use the following approximation (valid for small frequency offsets, i.e., $|F|T \ll 1$):

$$\left[\mathbf{Z}(k_\tau T + \hat{\varepsilon}_\tau, F)\right]_{q,m} \approx \exp(-2\pi F m T) \int_{-\infty}^{+\infty} y_q(t) p^*(t - mT - k_\tau T - \hat{\varepsilon}_\tau) dt. \tag{6.27}$$

This leaves us with the following parameters to be estimated using a DA algorithm: $\mathbf{b} = \{\mathbf{H}, F, k_\tau\}$. We can decompose the matrices $\mathbf{A}$ and $\mathbf{Z}$ as $\mathbf{A} = [\mathbf{PC}]$ and $\mathbf{Z} = [\mathbf{Z}_P \mathbf{Z}_C]$, where the leftmost submatrices (of dimension $N_\mathrm{T} \times M_P$) correspond to the pilot symbols, and the rightmost submatrices (of dimension $N_\mathrm{T} \times M_C$) correspond to the coded symbols ($M_P + M_C = M$). DA-ML estimation of $\mathbf{b}$ is accomplished by maximizing the part of the log-likelihood function corresponding to the pilot symbols only:

$$\hat{\mathbf{b}}_\mathrm{DA} = \arg\max_{\mathbf{b}} \{\psi(\mathbf{H}, k_\tau, F)\} \tag{6.28}$$

with

$$\psi(\mathbf{H}, k_\tau, F) = -\operatorname{tr}\left(\mathbf{H}\mathbf{P}\mathbf{P}^H\mathbf{H}^H\right) + 2\Re\left(\operatorname{tr}\left(\mathbf{Z}_P(k_\tau T + \hat{\varepsilon}_\tau, F)\mathbf{P}^H\mathbf{H}^H\right)\right). \tag{6.29}$$

Similar to Section 6.4.2, this maximization problem can be solved in the following way:

$$(\hat{k}_{\tau,\mathrm{DA}}, \hat{F}_{\mathrm{DA}}) = \arg\max_{k_\tau, F} \left\| \mathbf{Z}_P(\hat{k}_{\tau,\mathrm{DA}} T + \hat{\varepsilon}_\tau, F)\mathbf{P}^H(\mathbf{P}\mathbf{P}^H)^{-1}\mathbf{P} \right\|^2, \tag{6.30}$$

$$\hat{\mathbf{H}}_{\mathrm{DA}} = \mathbf{Z}_P(\hat{k}_{\tau,\mathrm{DA}} T + \hat{\varepsilon}_\tau, \hat{F}_{\mathrm{DA}})\mathbf{P}^H(\mathbf{P}\mathbf{P}^H)^{-1}, \tag{6.31}$$

where (6.31) results from the identity $\mathrm{tr}(\mathbf{X}\mathbf{X}^H) = \|\mathbf{X}\|^2$, with $\|\cdot\|^2$ denoting the sum of the absolute squares of the matrix elements. As explained in Section 6.3, an initial estimate of the discrete parameter k_τ is not required for the EM algorithm. However, it is necessary to evaluate (6.30) for all M_τ possible values of k_τ to obtain the DA-estimates $\hat{F}_{\mathrm{DA}}$ and $\hat{\mathbf{H}}_{\mathrm{DA}}$.

As will be shown in the sequel, DA frequency offset estimation requires a large number of training symbols in order to provide an accurate estimate. To overcome this problem, we also derived an NDA frequency offset algorithm for M_c-PSK constellations. The estimate is found by averaging the low-SNR limit of $p(\mathbf{y}|\mathbf{H}, F, \mathbf{A})$ over the symbols $\mathbf{A}$ and channel matrix $\mathbf{H}$ and maximizing with respect to F:

$$\hat{F}_{\mathrm{NDA}} = \arg\max_F \left| \sum_{k,l} (\mathbf{z}_k^H \mathbf{z}_l)^{M_c} e^{-j2M\pi FT(k-l)} \right|^2, \tag{6.32}$$

where $[\mathbf{z}_m]_q = \int_{-\infty}^{+\infty} y_q(t) p^*(t - mT - \tau)dt$ and M_c denotes the constellation size.

6.6. Computational complexity

In this section, we investigate the overall computation time of the receiver, and show how it may be significantly reduced.

Denoting by T_{EM} the time to perform an update of the estimates of $\mathbf{H}$, F, and ε_τ, by M_τ the number of values that k_τ can assume, by T_{detect} the time to compute the marginal posterior symbol probabilities (given the received signal and the estimates of $\mathbf{H}$, F, ε_τ and k_τ), and by I_{EM} the number of EM iterations, the total computation time T_{tot} is given by

$$T_{\mathrm{tot}} = M_\tau I_{\mathrm{EM}}(T_{\mathrm{EM}} + T_{\mathrm{detect}}), \tag{6.33}$$

which reflects that the EM algorithm has to be run separately for each possible value of k_τ. According to Figure 6.3, the detector is iterative itself. It consists of three types of "nested" iterations:

(1) I_E iterations between the decoder and the equalizer, with each equalization stage taking time T_E,
(2) I_M iterations between the decoder and the demapper, with each demapping stage taking time T_M,
(3) I_D iterations inside the decoder (e.g., turbo codes or LDPC codes), with each iteration taking time T_D.

The resulting time for detection is given by $T_{\text{detect}} = I_E(T_E + I_M(T_M + I_D T_D))$. When performing (iterative) detection for a given EM iteration, the detector should be reinitialized by the uniform probabilities as explained in Section 6.4.3, in order to provide the posterior probabilities that correspond to the estimates related to the considered EM iteration. The above procedure in general gives rise to a total computing time T_{tot} that is excessively large. This is because for each EM iteration a sufficient number of iterations inside the detector is required for the detector to converge from reinitialization with uniform probabilities. An alternative approach is to take $I_D = I_M = I_E = 1$, and to initialize the detector with the probabilities obtained at the end of the previous EM iteration. Although this approach requires more EM iterations to approach convergence, the number of iterations (per EM iteration) inside the detector are drastically reduced, yielding a substantial reduction of the total computing time T_{tot}. In Section 6.7, we show that this reduced-complexity approach yields excellent results.

6.7. Performance results

We have carried out computer simulations for a rate 1/3 turbo-coded system with BPSK signaling for $N_{\text{T}} = 2$ transmit, $N_{\text{R}} = 3$ receive antennas setup. The considered turbo code is a parallel concatenation of two recursive systematic binary convolutional codes with octal generators $(27, 33)$ and a total frame length of 840 bits, corresponding to 420 BPSK symbols per transmit antenna. As explained in the previous section, only one mapping iteration, one equalizing iteration, and one internal decoding iteration is performed for each EM iteration (i.e., $I_D = I_M = I_E = 1$). Iterations between estimation and detection are carried out until convergence of the EM algorithm. The pilot symbols $\mathbf{P}$ are chosen randomly for each frame, with the restriction that $\mathbf{P}\mathbf{P}^H$ is nonsingular. In the remainder, we will refer to the number of pilot symbols *per transmit antenna* rather than the overall number of pilot symbols. The channel matrix $\mathbf{H}$ is generated randomly for each frame and generated according to the statistics described in Section 6.2. The delay shift k_τ is chosen uniformly within $\{0, 1, 2\}$ for each frame. The considered performance measures are the bit error rate (BER) and the mean square error (MSE) of the estimates. The BER will be compared to the BER under perfect synchronization, while the MSE will be compared to the modified Cramér-Rao bound (MCRB), which is a lower bound on the MSE of any unbiased estimator [29]. Performance will be considered as a function of SNR $= E_b/N_0$, with E_b denoting the transmitted energy per information bit. For an M_c-point signalling constellation and a rate R code, E_s and E_b are related by $E_s = E_b R \log_2 M_c$. In the following, we consider a number of scenarios, involving the estimation of a subset of parameters, assuming the remaining parameters are known. But first, we illustrate the impact of inaccurate estimation of these quantities on the BER.

6.7.1. Effect of synchronization errors

Figure 6.4 shows the effect of inaccurate estimation of the different parameters on the BER performance. We observe that even a small delay estimation error (of

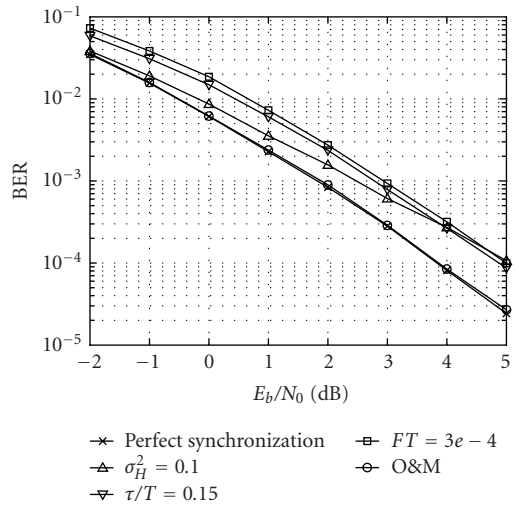

FIGURE 6.4. Performance of Oerder&Meyr timing estimation algorithm and impact of synchronization errors on the BER performance.

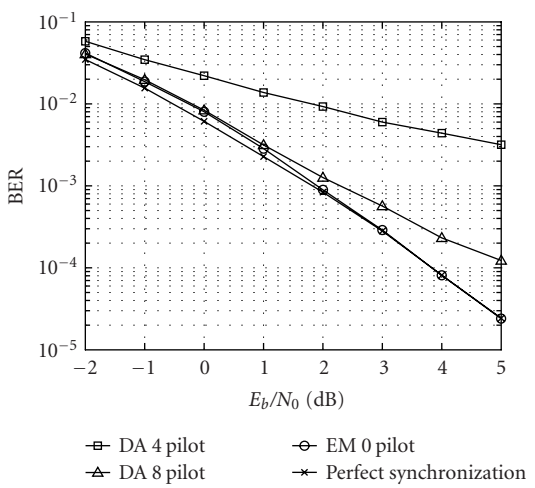

FIGURE 6.5. BER performance of pilot-assisted frame synchronization versus EM frame synchronization.

$0.15T$ at roll-off factor 0.5) can cause a significant degradation. Also, a small error on the channel taps (a complex-valued zero-mean Gaussian estimation error with variance 0.1 on the real and imaginary components) will have a severe impact on the BER, especially at high SNR. Finally, we see that even a very small frequency estimation error (of $3 \cdot 10^{-4}/T$) will cause very high BER degradations at all considered SNRs. This clearly illustrates the need to perform accurate estimation of $\mathbf{H}$, F, and τ.

6.7.2. Symbol synchronization

The O&M algorithm (6.26) provides a timing estimate ε_τ, irrespective of the other parameters. The resulting estimate causes virtually no BER degradation compared to the case where ε_τ is known (Figure 6.4). Hence there is no need to further update ε_τ during the EM iterations. This leaves us with the following parameters to estimate: frame delay k_τ, channel matrix $\mathbf{H}$, and frequency offset F.

6.7.3. Frame synchronization

We consider frame synchronization assuming knowledge of the other parameters $\mathbf{H}$ and F. Since frame synchronization involves the estimation of a *discrete* parameter k_τ, no initial estimate and thus no pilot symbols are necessary (see Section 6.4). In Figure 6.5, we compare the BER in the cases of perfect frame synchronization, DA frame synchronization, and EM frame synchronization. As shown in Figure 6.5, the EM frame synchronization without pilot symbols yields hardly any degradation compared to perfect synchronization, whereas DA frame synchronization requires more than 8 pilot symbols to achieve a comparable performance. Due to the inherent randomness of the turbo-code, time-shifted versions of a codeword are very unlikely to resemble another codeword. Hence, accurate frame synchronization is possible, based on information from the coded data symbols only.

6.7.4. Channel estimation

In contrast with frame synchronization, initial estimates are necessary for the EM estimation of the continuous parameters, that is, channel matrix $\mathbf{H}$ and frequency offset F. The DA and NDA algorithms described in Section 6.5 will be utilized to provide these estimates. As will be shown in the sequel, the performance of the EM algorithm depends on the accuracy of these initial estimates.

Figure 6.6 compares the BER performances corresponding to DA estimation and EM estimation of the channel matrix, assuming the other parameters (k_τ and F) to be perfectly known. The DA estimate makes use of 16 pilot symbols, and the EM algorithm is initialized with this DA estimate. As compared to perfect channel estimation, DA channel estimation gives rise to a BER degradation of about 2 dB, whereas the degradation is limited to about 0.5 dB for EM-based channel estimation. Considering the hypothetical situation where the EM algorithm is initialized with the correct value of the channel matrix, the corresponding BER degradation amounts to about 0.1 dB only; this illustrates the importance of the accuracy of the initial estimate. It is interesting to investigate the performance of the EM algorithm in terms of the MSE of the channel gains. In Figure 6.6, we observe that the MSE of the EM estimator (both with perfect and DA initialization) reaches the MCRB for SNRs above 2 dB. Nevertheless, a BER degradation of around 0.5 dB remains for the EM algorithm with DA initialization, while with perfect initialization this degradation is below 0.1 dB. The reason for this apparent discrepancy is

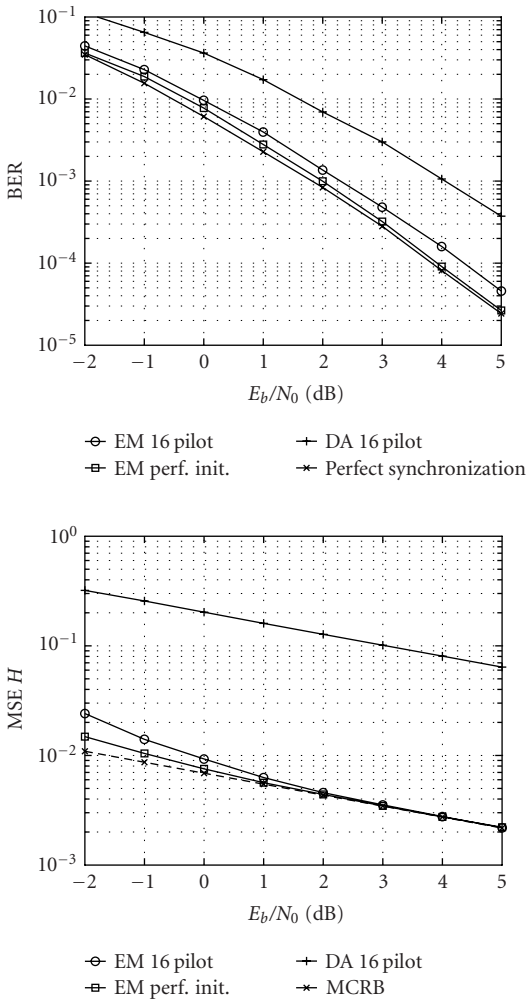

Figure 6.6. BER and MSE performance for channel estimation through EM and DA algorithms.

that occasionally poor DA initial estimates cause outliers in the EM estimation error distribution. These outliers have little impact on the variance of the estimation error distribution but may cause a noticeable BER degradation. When the initial estimates are perfect, these outliers are no longer present, resulting in very low BER degradation.

6.7.5. Frequency estimation

The frequency offset estimation performance is even more sensitive to the accuracy of the initial estimate. We will consider three different carrier frequency estimation

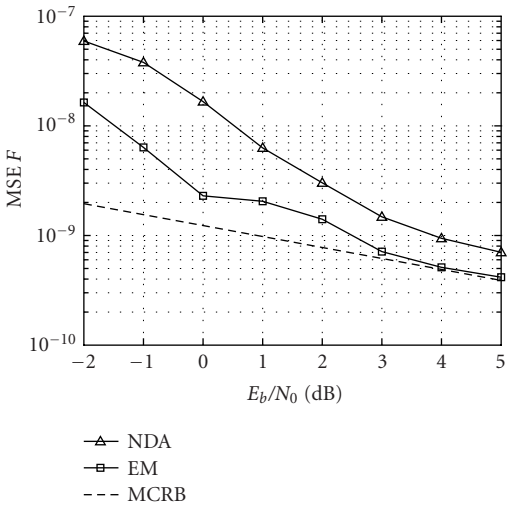

FIGURE 6.7. MSE of frequency offset estimate for NDA and EM estimation of F when all other parameters are known. Both EM and NDA algorithm use 420 symbols, and the EM algorithm is initialized with the NDA algorithm.

algorithms, assuming the other parameters (k_τ and $\mathbf{H}$) to be known: the first is DA frequency offset estimation, the second corresponds to NDA estimation, and the third one is the EM algorithm. The first and second algorithms do not exploit any knowledge about the channel matrix. The EM algorithm can be initialized with a DA or NDA-algorithm or can even be applied without initialization ($\widehat{F}^{(0)} = 0$).

Figure 6.7 shows the MSE for frequency estimation, resulting from the NDA algorithm and from the EM algorithm with NDA initialization; we note that the EM estimator reaches the MCRB for SNR above 4 dB.

Figure 6.8 considers the MSE and the BER performance resulting from DA estimation (128 pilot symbols), NDA estimation and EM estimation (with initialization $\widehat{F}^{(0)} = 0$) of the carrier frequency offset. Results are shown for $E_b/N_0 = 3$ dB, as a function of the unknown frequency offset F. While the performance corresponding to the DA and NDA algorithms does not depend on F, the EM algorithm will only work well when $(F - \widehat{F}^{(0)}) \times T \times M \ll 1$, irrespective of how $\widehat{F}^{(0)}$ is obtained. Hence EM estimation with initialization $\widehat{F}^{(0)} = 0$ severely limits the acquisition range. Within its acquisition range, the EM algorithm performs very close to the MCRB, and yields a very small BER degradation. The DA estimator requires many pilot symbols to achieve a similar performance. As compared to the EM algorithm, the NDA estimator yields an MSE that is about twice as large, but achieves nearly the same BER performance. Consequently, taking computational complexity into account, the NDA algorithm appears to be the best solution for frequency offset estimation. We should mention, however, that the performance of the NDA frequency estimation algorithm degrades for higher constellations.

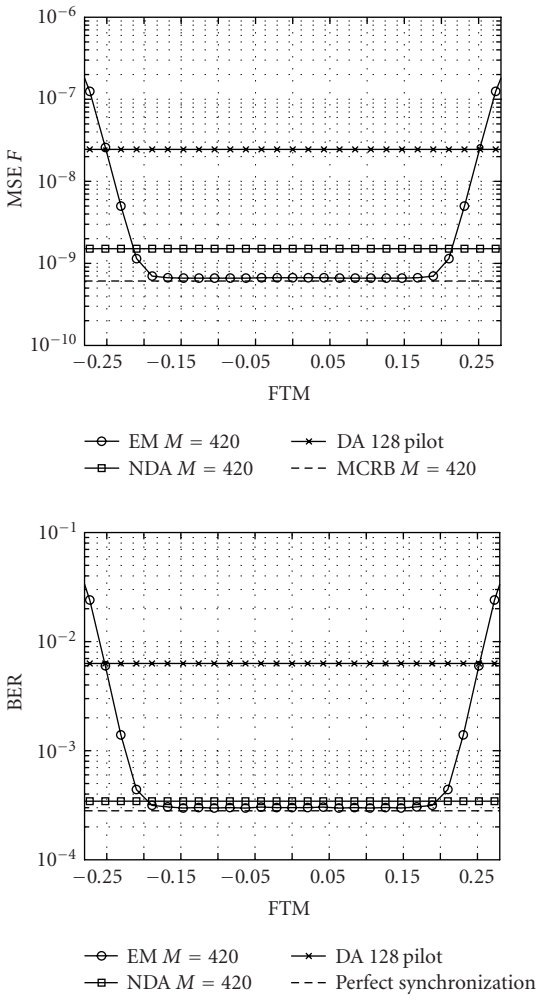

FIGURE 6.8. MSE and BER performance for frequency offset estimation using EM algorithm initialized with $\hat{F}^{(0)} = 0$ compared to NDA and DA estimation (without EM) for different values of the normalized actual frequency offset for $E_b/N_0 = 3$ dB (channel and frame synchronization are perfect).

6.7.6. Frame synchronization and channel estimation

Since a significant amount of pilot symbols is necessary to provide an accurate initial channel estimate, one could perform frame synchronization exploiting only the pilot symbols. In this case, the EM algorithm is used solely to provide an estimate of $\mathbf{H}$ and F (i.e., k_τ is excluded from the EM algorithm). Assuming F to be known, Figure 6.9 shows that the latter scheme results in only a small additional degradation (of about 0.2 dB), compared to *joint* EM frame synchronization and channel estimation. This means that by using DA frame synchronization

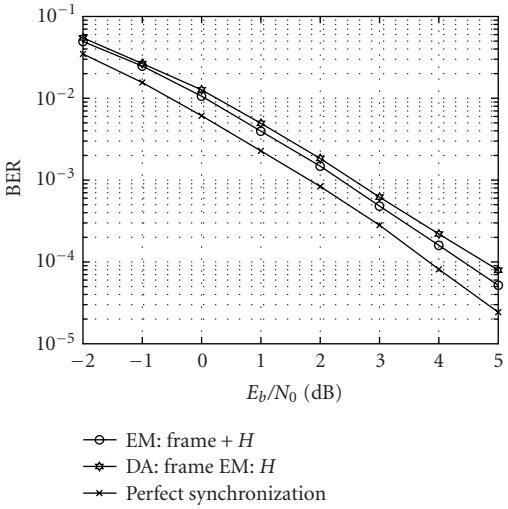

FIGURE 6.9. BER performance of joint EM frame synchronization and channel estimation versus data-aided frame synchronization and EM channel estimation. 16 Pilot symbols are used in both scenarios.

and EM-based channel estimation, a significant reduction in computational complexity can be achieved (namely, a factor M_τ in expression (6.33)) with only minor BER degradation.

6.7.7. Frame synchronization, channel estimation, and frequency estimation

Finally, we consider the joint frame synchronization, channel and frequency offset estimation. In Figure 6.10, the BER performance of the EM algorithm is illustrated for the joint frame synchronization and estimation of channel gains and frequency offset. Note that 16 pilot symbols are used to provide the initial channel estimate, while no pilot symbols are necessary for initial estimates of the frequency offset (NDA) and frame synchronization (no initialization). Estimating the channel results in a significant degradation (about 0.5 dB) compared to perfect synchronization, while frequency offset estimation and frame synchronization cause very little additional degradation.

Taking into account that NDA frequency estimation and EM frequency estimation give rise to nearly the same BER degradation (see Section 6.7.5), computational complexity can be reduced with virtually no performance loss by making an NDA frequency estimate instead of an EM frequency estimate. In addition, a further complexity reduction can be achieved by performing DA frame synchronization instead of EM frame synchronization (see Section 6.7.6). In Figure 6.10, we observe that the NDA frequency estimation with EM estimation of the other parameters results in hardly any performance degradation compared to the EM

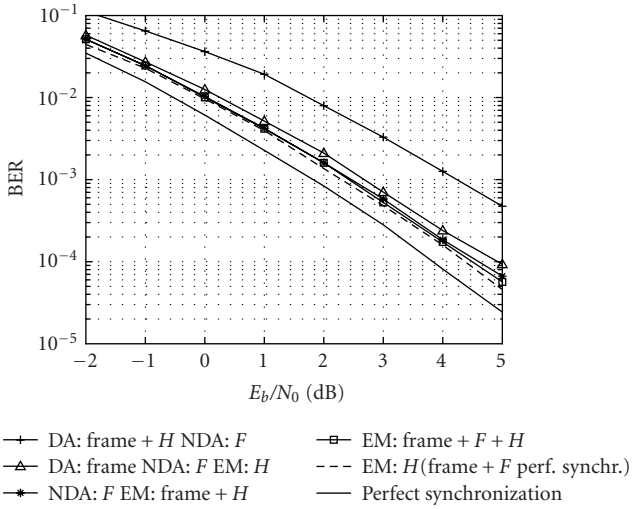

FIGURE 6.10. BER performance of conventional algorithm and EM algorithm for different scenarios: DA frame and channel estimation with NDA frequency estimation (no EM); EM channel estimation with perfect knowledge of other parameters; EM frame, frequency and channel estimation with initial NDA frequency estimate; NDA frequency estimation with EM frame synchronization and channel estimation; DA frame synchronization with NDA frequency estimation and EM channel estimation. In all scenarios, the initial channel estimate is obtained through 16 pilot symbols, which are also used for DA frame synchronization.

estimation of all parameters. On the other hand, performing DA frame synchronization instead of EM frame synchronization gives rise to an additional degradation of about 0.2 dB (which is consistent with the results from Section 6.7.6).

6.8. Conclusions and remarks

We have considered the problem of symbol synchronization, frame synchronization, frequency estimation, and channel estimation in the context of coded transmission over a flat-fading MIMO channel. We have derived iterative ML estimation algorithms that are based upon the EM algorithm; these algorithms make use of the posterior symbol probabilities that are provided by a symbol MAP detector. We have pointed out how initial estimates can be obtained from conventional DA or NDA estimation algorithms. We have shown that for the MIMO setup considered, EM estimation gives rise to a BER degradation of about 0.5 dB, as compared to the case where all parameters are known; it turns out that this degradation is caused mainly by the channel estimation errors, whereas estimation errors related to the other parameters have a much smaller impact on the BER.

The numerical complexity of the estimator can be reduced by applying the iterative EM algorithm to a subset of the parameters to be estimated, whereas the estimates of the other parameters are obtained from conventional DA or NDA algorithms. By means of computer simulations we have pointed out that involving

only frame synchronization and channel estimation in the EM algorithm, while performing NDA symbol synchronization and NDA frequency estimation, yields no noticeable BER degradation as compared to the case where all parameters are updated during the EM iterations. A further complexity reduction can be achieved by performing DA (instead of EM) frame synchronization, in which case the EM algorithm is used for channel estimation only; the DA frame synchronization gives rise to an additional degradation of about 0.2 dB.

Acknowledgments

This work has been supported by the Interuniversity Attraction Poles Programme (IAP) P5/11, Belgian Science Policy. The first author also acknowledges the support from the Institute for the Promotion of Innovation through Science and Technology in Flanders (IWT-Vlaanderen).

Abbreviations

AWGN	Additive white Gaussian noise
BER	Bit error rate
BICM	Bit-interleaved coded modulation
BPSK	Binary phase-shift keying
CSI	Channel state information
DA	Data-aided
EM	Expectation-maximization
LDPC	Low-density parity check
LLF	Log-likelihood function
MAP	Maximum a posteriori
MCRB	Modified Cramér-Rao bound
MIMO	Multiple-input multiple-output
ML	Maximum likelihood
MMSE	Minimum mean square error
MSE	Mean square error
NDA	Non data-aided
OFDM	Orthogonal frequency-division multiplexing
O&M	Oerder&Meyr
RA	Repeat-accumulate
ST	Space-time

Bibliography

[1] G. J. Foschini and M. J. Gans, "On limits of wireless communications in a fading environment when using multiple antennas," *Wireless Personal Communications*, vol. 6, no. 3, pp. 311–335, 1998.

[2] V. Tarokh, N. Seshadri, and A. R. Calderbank, "Space-time codes for high data rate wireless communication: performance criterion and code construction," *IEEE Trans. Inform. Theory*, vol. 44, no. 2, pp. 744–765, 1998.

[3] V. Tarokh, H. Jafarkhani, and A. R. Calderbank, "Space-time block codes from orthogonal designs," *IEEE Trans. Inform. Theory*, vol. 45, no. 5, pp. 1456–1467, 1999.

[4] S. M. Alamouti, "A simple transmit diversity technique for wireless communications," *IEEE J. Select. Areas Commun.*, vol. 16, no. 8, pp. 1451–1458, 1998.

[5] M. Sellathurai and S. Haykin, "Turbo-BLAST: performance evaluation in correlated Rayleigh-fading environment," *IEEE J. Select. Areas Commun.*, vol. 21, no. 3, pp. 340–349, 2003.

[6] A. Stefanov and T. M. Duman, "Turbo-coded modulation for systems with transmit and receive antenna diversity over block fading channels: system model, decoding approaches, and practical considerations," *IEEE J. Select. Areas Commun.*, vol. 19, no. 5, pp. 958–968, 2001.

[7] L. H.-J. Lampe, R. Schober, and R. F. H. Fischer, "Multilevel coding for multiple-antenna transmission," *IEEE Transactions on Wireless Communications*, vol. 3, no. 1, pp. 203–208, 2004.

[8] A. P. Dempster, N. M. Laird, and D. B. Rubin, "Maximum likelihood from incomplete data via the EM algorithm," *J. Roy. Statist. Soc. Ser. B*, vol. 39, no. 1, pp. 1–38, 1977.

[9] Z. Baranski, A. M. Haimovich, and J. Garcia-Frias, "EM-based iterative receiver for space-time coded modulation with noise variance estimation," in *Proc. IEEE Global Telecommunications Conference (GLOBECOM '02)*, vol. 1, pp. 355–359, Taipei, Taiwan, November 2002.

[10] C. Cozzo and B. L. Hughes, "Joint channel estimation and data detection in space-time communications," *IEEE Trans. Commun.*, vol. 51, no. 8, pp. 1266–1270, 2003.

[11] Y. Li, C. N. Georghiades, and G. Huang, "Iterative maximum-likelihood sequence estimation for space-time coded systems," *IEEE Trans. Commun.*, vol. 49, no. 6, pp. 948–951, 2001.

[12] J. J. Boutros, F. Boixadera, and C. Lamy, "Bit-interleaved coded modulations for multiple-input multiple-output channels," in *Proc. IEEE 6th International Symposium on Spread Spectrum Techniques and Applications*, vol. 1, pp. 123–126, Parsippany, NJ, USA, September 2000.

[13] B. Lu, X. Wang, and Y. Li, "Iterative receivers for space-time block-coded OFDM systems in dispersive fading channels," *IEEE Transactions on Wireless Communications*, vol. 1, no. 2, pp. 213–225, 2002.

[14] A. Grant, "Joint decoding and channel estimation for linear MIMO channels," in *Proc. IEEE Wireless Communications and Networking Conference (WCNC '00)*, vol. 3, pp. 1009–1012, Chicago, Ill, USA, September 2000.

[15] R. Visoz and A. O. Berthet, "Iterative decoding and channel estimation for space-time BICM over MIMO block fading multipath AWGN channel," *IEEE Trans. Commun.*, vol. 51, no. 8, pp. 1358–1367, 2003.

[16] O. Besson and P. Stoica, "On parameter estimation of MIMO flat-fading channels with frequency offsets," *IEEE Trans. Signal Processing*, vol. 51, no. 3, pp. 602–613, 2003.

[17] A. N. Mody and G. L. Stuber, "Synchronization for MIMO OFDM systems," in *Proc. IEEE Global Telecommunications Conference (GLOBECOM '01)*, vol. 1, pp. 509–513, San Antonio, Tex, USA, November 2001.

[18] N. Noels, C. Herzet, A. Dejonghe, et al., "Turbo synchronization: an EM algorithm interpretation," in *Proc. IEEE International Conference on Communications (ICC '03)*, vol. 4, pp. 2933–2937, Anchorage, Alaska, USA, May 2003.

[19] C. Herzet, V. Ramon, L. Vandendorpe, and M. Moeneclaey, "EM algorithm-based timing synchronization in turbo receivers," in *Proc. IEEE International Conference on Acoustics, Speech, and Signal Processing (ICASSP '03)*, vol. 4, pp. 612–615, Hong Kong, China, April 2003.

[20] C.-F. J. Wu, "On the convergence properties of the EM algorithm," *Ann. Statist.*, vol. 11, no. 1, pp. 95–103, 1983.

[21] P. Spasojevic and C. N. Georghiades, "On the (non) convergence of the EM algorithm for discrete parameter estimation," in *Proc. 38th Annual Allerton Conference on Communication, Control, and Computing*, Monticello, Ill, USA, October 2000.

[22] H. Wymeersch and M. Moeneclaey, "Code-aided frame synchronizers for AWGN channels," in *Proc. International Symposium on Turbo Codes & Related Topics*, Brest, France, September 2003.

[23] S. ten Brink, J. Speidel, and R.-H. Yan, "Iterative demapping and decoding for multilevel modulation," in *Proc. IEEE Global Telecommunications Conference (GLOBECOM '98)*, vol. 1, pp. 579–584, Sydney, NSW, Australia, November 1998.

[24] L. R. Bahl, J. Cocke, F. Jelinek, and J. Raviv, "Optimal decoding of linear codes for minimizing symbol error rate," *IEEE Trans. Inform. Theory*, vol. 20, no. 2, pp. 284–287, 1974.

[25] C. Berrou, A. Glavieux, and P. Thitimajshima, "Near Shannon limit error-correcting coding and decoding: turbo-codes 1," in *Proc. IEEE International Conference on Communications (ICC '93)*, vol. 2, pp. 1064–1070, Geneva, Switzerland, May 1993.

[26] D. J. C. MacKay, "Good error-correcting codes based on very sparse matrices," *IEEE Trans. Inform. Theory*, vol. 45, no. 2, pp. 399–431, 1999.

[27] D. Divsalar, H. Jin, and R. J. McEliece, "Coding theorems for "turbo-like" codes," in *Proc. 36th Annual Allerton Conference on Communication, Control, and Computing*, pp. 201–210, Monticello, Ill, USA, September 1998.

[28] M. Oerder and H. Meyr, "Digital filter and square timing recovery," *IEEE Trans. Commun.*, vol. 36, no. 5, pp. 605–612, 1988.

[29] M. Moeneclaey, "On the true and the modified Cramer-Rao bounds for the estimation of a scalar parameter in the presence of nuisance parameters," *IEEE Trans. Commun.*, vol. 46, no. 11, pp. 1536–1544, 1998.

Frederik Simoens: DIGCOM Research Group, Department of Telecommunications and Information Processing (Telin), Ghent University, 41 St. Pietersnieuwstraat, 9000 Ghent, Belgium

Email: fsimoens@telin.ugent.be

Henk Wymeersch: DIGCOM Research Group, Department of Telecommunications and Information Processing (Telin), Ghent University, 41 St. Pietersnieuwstraat, 9000 Ghent, Belgium

Email: hwymeers@telin.ugent.be

Heidi Steendam: DIGCOM Research Group, Department of Telecommunications and Information Processing (Telin), Ghent University, 41 St. Pietersnieuwstraat, 9000 Ghent, Belgium

Email: hs@telin.ugent.be

Marc Moeneclaey: DIGCOM Research Group, Department of Telecommunications and Information Processing (Telin), Ghent University, 41 St. Pietersnieuwstraat, 9000 Ghent, Belgium

Email: mm@telin.ugent.be

7 Iterative (turbo) signal processing techniques for MIMO signal detection and equalization

Tad Matsumoto

7.1. Introduction

The discovery of the turbo codes has driven research on the creation of new signal detection concepts that are, in general, referred to as the turbo approach. Recently, this approach has made a drastic change in creating signal detection techniques and algorithms such as equalization of intersymbol interference (ISI) experienced by broadband single-carrier signaling over mobile radio channels. It has long been believed that the computational complexity needed for the ISI equalization in broadband mobile communication channels is prohibitive, the belief of which is being overturned by the turbo approach.

The goal of this chapter is to provide readers with understanding of the technique based on the turbo approach. This chapter is started by an explanation that coded transmission over memory channel can be seen as a serially concatenated coded system, where the outer code is the channel code used, and the inner code the channel itself. Therefore, the turbo equalization can be viewed as a decoding technique for serially concatenated codes.

This chapter will then introduce an iterative signal detection technique, a soft canceler followed by a minimum mean square error (SC/MMSE) filter, which can be seen as a technique based on the turbo approach. The SC/MMSE concept is then applied to the equalization of relatively severe ISI experienced in broadband single-carrier signaling. It is shown that even though the SC/MMSE turbo equalizer's complexity is proportional to the third power of the total path number in the equalizer's coverage, it can achieve almost equivalent performance to that of the optimal detector based on the maximum likelihood sequence estimation (MLSE) technique. The MLSE equalizer's computational complexity increases exponentially with the equalizer's coverage, for which single-carrier signaling has long been believed to be impractical for broadband mobile communications.

This chapter then applies the SC/MMSE technique to multiple-input multiple-output (MIMO) signal detection as a reasonable expansion of the SC/MMSE turbo equalizer. The resulting device is called SC/MMSE MIMO turbo equalizer.

The SC/MMSE MIMO turbo equalizer's performance is almost equivalent to that of the MLSE single-user signal detector, even though it does not require prohibitively large computational effort.

Although the SC/MMSE equalizer does not require exponentially increasing computational complexity, its cubic order of complexity requirement may still be too large when the equalizer has to detect many signals that were transmitted from the multiple antennas in multiuser MIMO scenarios. Some approximation techniques that can further reduce the complexity without causing any significant performance loss are known. This chapter also provides the approximation techniques. This chapter then extends the SC/MMSE algorithm to the case where transmitted signals use quadrature amplitude modulation (QAM) format.

The low complexity of the SC/MMSE MIMO turbo equalizer has triggered research on single-carrier broadband MIMO uplink systems, where all users use the same time slots and the same frequency slots without relying on multicarrier or spread spectrum techniques. Obviously, single-carrier signaling is beneficial for handset terminals because when transmitting single-carrier signals highly linear amplifier is not necessary, which results in battery long lifetime. The purpose of the last section of this chapter is to estimate in-field performances of the single-carrier SC/MMSE MIMO turbo equalizer. The methodology of the link-level simulation using channel sounding field measurement data is presented. The results of the simulations are also presented to demonstrate the effectiveness of the single-carrier SC/MMSE MIMO turbo equalizer in fields.

7.2. SC/MMSE turbo equalizer

Severe signal distortion due to ISI is imposed upon received signals when broadband signal is transmitted over mobile radio channels. Furthermore, cochannel interference (CCI) is another cause of signal distortion when multiple signals are transmitted on the same frequency. The CCI scenario happens when multiple users transmit their uplink signals using the same time slots and frequency slots. Another scenario is the single-user signal transmission using multiple antennas where different sequences, that are most possibly coded sequences, are transmitted sharing the same time slots and frequency slots. Obviously, considering the mixed mode of these scenarios is a meaningful roadmap, when creating broadband mobile communication system concepts. The radio networks featuring these scenarios are categorized as MIMO systems in this chapter.

MIMO receivers have to effectively suppress ISI as well as unknown CCI that are not to be detected, while adequately detecting the multiple desired signals. Recently, the iterative technique for equalization of the signal distortion due to ISI, which is considered as an application of the turbo decoding concept, has attracted much attention [1, 2, 3]. However, when it is used in broadband MIMO channels, the computational complexity required to derive the a posteriori log-likelihood ratio (LLR) is still excessive. This is because the number of the states in the trellis diagram for the frequency-selective MIMO channels increases exponentially with the product of the number of users and their channel memory lengths.

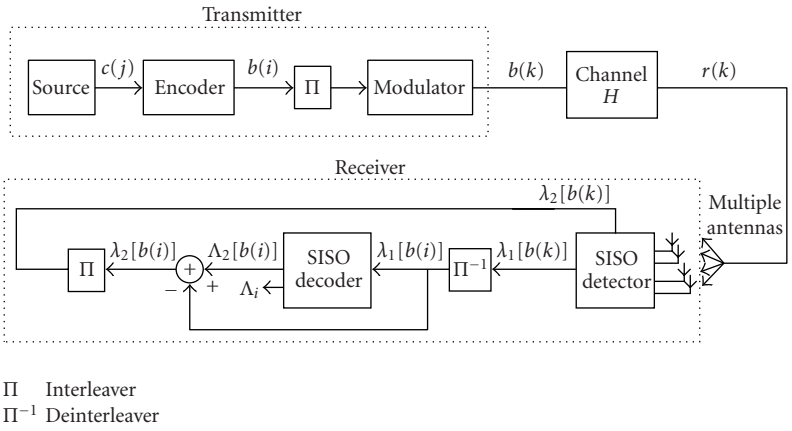

FIGURE 7.1. System block diagram for single-user single-carrier turbo equalization.

The SC/MMSE equalization algorithm was first developed by Reynolds and Wang for severe ISI channels [4] in single-user single-carrier signaling scenarios. However, it can be seen as an extension of the iterative multiuser detection algorithm originally derived for code division multiple access (CDMA) systems presented in [2]. The conceptual basis of SC/MMSE is to replicate the ISI components by using the LLR of the adjacent bits causing ISI, fed back from their channel decoder, and to subtract the soft replica from the received composite signal vector. Adaptive linear filtering is then performed to remove the interference residuals; taps of the linear filter are determined adaptively so as to minimize the mean square error (MSE) between the filter output and the signal point corresponding to the symbol of interest. The LLR of the filter output is then calculated. After deinterleaving, the LLR values of the filter output are brought to the channel decoder as extrinsic information. Soft-input soft-output (SISO) decoding of the channel code is performed by the channel decoder. The process discussed above is repeated in an iterative manner. The key point of this scheme is that it offers much lower computational complexity than turbo equalizers using trellis diagram of the channel.

In Section 7.2, the system model used is first introduced, and Reynolds and Wang's proposed single-user single-carrier SC/MMSE equalization algorithm is described in detail, assuming binary phase-shifted keying (BPSK) modulation. Several derivative techniques related to the original SC/MMSE algorithm are also introduced.

7.2.1. System model

A transmitter-receiver block diagram of the system considered in this section is depicted in Figure 7.1 [3]. The information source delivers a binary sequence $c(j)$, with j being the information bit index, to the transmitter, which is fed to

a convolutional channel encoder. It transforms the information sequence $c(j)$ into a length B block of BPSK symbols $b(i)$, with i being the coded bit index. To reduce effects of burst errors, the encoded data is reordered by an interleaver that performs a fixed random replacement in time of the coded bits in the block. After the interleaving, the coded bits are indexed by k. The coded bit sequence $b(k)$ is transmitted using the BPSK modulation format (as noted above, this subsection assumes BPSK modulation, and therefore BPSK symbols correspond to the bits coded by the encoder). The BPSK symbols $b(k)$ are transmitted over the multipath fading channel which is subjected to severe frequency selectivity. The channel output is corrupted by additive white Gaussian noise (AWGN). Due to the multipath effect, the channel introduces distortion onto the transmitted signal. Thus, the received signal, which is a sum of the multipath components, suffers from ISI.

The receiver employs M antennas that are indexed by m. A discrete-time representation of the received signal at sampling timing k is given by

$$r_m(k) = \sum_{l=0}^{L-1} h_{m,l}(k)b(k-l) + v_m(k), \tag{7.1}$$

where L is the number of propagation paths, $h_{m,l}(k)$ is the channel coefficient between transmitter and mth antenna for the lth path, $b(k)$ is the BPSK symbol transmitted at the kth symbol timing, and $v_m(k)$ is a complex AWGN process with variance σ^2.

Due to single-carrier transmission, it is reasonable to assume that the frame length is short enough compared with the fading variation speed. Therefore, it is assumed that the channel is constant over the frame, and thus symbol indexing in the channel realization is not needed. Hence, the path index l is cited in parenthesis as $h_m(l)$, $0 \le l \le L-1$, later on.

A vector presentation of the received signal $r_m(k)$ of (7.1), representing the result of space-domain sampling, is given by

$$\begin{aligned}\mathbf{r}(k) &= \begin{bmatrix} r_1(k) & r_2(k) & \cdots & r_M(k) \end{bmatrix}^T \\ &= \sum_{l=0}^{L-1} \mathbf{h}(l)b(k-l) + \mathbf{v}(k),\end{aligned} \tag{7.2}$$

where

$$\mathbf{h}(l) = \begin{bmatrix} h_1(l) & \cdots & h_M(l) \end{bmatrix}^T \tag{7.3}$$

and

$$\mathbf{v}(k) = \begin{bmatrix} v_1(k) & v_2(k) & \cdots & v_M(k) \end{bmatrix}^T \tag{7.4}$$

is the noise sample vector.

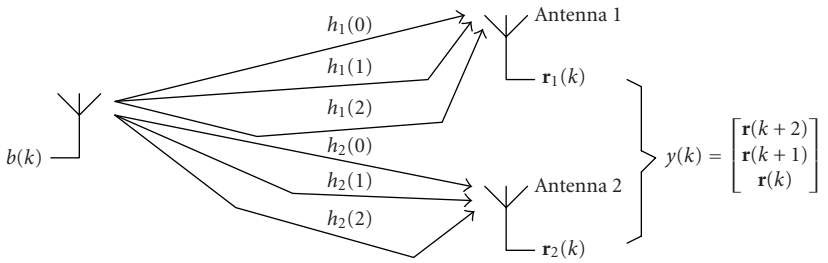

FIGURE 7.2. An example of space-time communication scenario.

After time-domain sampling on $\mathbf{r}(k)$ to capture the multipath components, the received signal vector $\mathbf{y}(k)$ can be expressed in a space-time representation as

$$\begin{aligned} y(k) &= \begin{bmatrix} \mathbf{r}^T(k+L-1) & \mathbf{r}^T(k+L-2) & \cdots & \mathbf{r}^T(k) \end{bmatrix}^T \\ &= \mathbf{H}\mathbf{b}(k) + \mathbf{V}(k), \end{aligned} \tag{7.5}$$

where

$$\mathbf{H} = \begin{bmatrix} \mathbf{h}(0) & \mathbf{h}(1) & \cdots & \mathbf{h}(L-1) & \mathbf{0} & \cdots & \mathbf{0} \\ \mathbf{0} & \ddots & & \vdots & \ddots & \ddots & \vdots \\ \vdots & \ddots & \ddots & \vdots & \ddots & \ddots & \mathbf{0} \\ \mathbf{0} & \cdots & \mathbf{0} & \mathbf{h}(0) & \mathbf{h}(1) & \cdots & \mathbf{h}(L-1) \end{bmatrix} \tag{7.6}$$

and

$$\mathbf{b}(k) = \begin{bmatrix} b(k+(L-1)) & \cdots & b(k) & b(k-1) & b(k-(L+1)) \end{bmatrix}^T \tag{7.7}$$

with

$$\mathbf{V}(k) = \begin{bmatrix} \mathbf{v}^T(k+L-1) & \mathbf{v}^T(k+L-2) & \cdots & \mathbf{v}^T(k) \end{bmatrix}^T. \tag{7.8}$$

The matrix $\mathbf{H}$ is called a "space-time channel matrix."

An example of the multipath space-time communication with one transmit and two receiver antennas is shown in Figure 7.2. In each of the transmit-to-receive antenna radio links, there are 3 path components. The space-domain sampled received signal for this example is expressed as

$$\begin{aligned} \mathbf{r}(k) &= \begin{bmatrix} h_1(0) \\ h_2(0) \end{bmatrix} b(k) + \begin{bmatrix} h_1(1) \\ h_2(1) \end{bmatrix} b(k-1) + \begin{bmatrix} h_1(2) \\ h_2(2) \end{bmatrix} b(k-2) + \mathbf{v}(k) \\ &= \mathbf{h}(0)b(k) + \mathbf{h}(1)b(k-1) + \mathbf{h}(2)b(k-2) + \mathbf{v}(k). \end{aligned} \tag{7.9}$$

After time-domain sampling over the ISI length (= 3), we have

$$\begin{aligned}\mathbf{y}(k) &= \begin{bmatrix}\mathbf{r}(k+2)\\ \mathbf{r}(k+1)\\ \mathbf{r}(k)\end{bmatrix}\\ &= \begin{bmatrix}\mathbf{h}(0) & \mathbf{h}(1) & \mathbf{h}(2) & 0 & 0\\ 0 & \mathbf{h}(0) & \mathbf{h}(1) & \mathbf{h}(2) & 0\\ 0 & 0 & \mathbf{h}(0) & \mathbf{h}(1) & \mathbf{h}(2)\end{bmatrix}\begin{bmatrix}b(k+2)\\ b(k+1)\\ b(k)\\ b(k-1)\\ b(k-2)\end{bmatrix} + \begin{bmatrix}\mathbf{v}(k+2)\\ \mathbf{v}(k+1)\\ \mathbf{v}(k)\end{bmatrix}\\ &= \mathbf{H}\mathbf{b}(k) + \mathbf{V}(k).\end{aligned} \tag{7.10}$$

7.2.2. Turbo equalization principle

Turbo equalization can be viewed as an extension of turbo decoding. Turbo coded signal contains multidimensional memory due to multiple recursive systematic codes (RSCs) that are separated in time by interleavers. A turbo decoder consists of multiple SISO decoders, corresponding to the RSCs encoders, and it produces soft decisions of the received symbols in the form of LLR, which is propagated between the decoders [5]. The RSCs may be convolutional codes or block codes, and the connection of the RSCs encoders is either parallel or serial, or in their hybrid mode.

In the case of turbo equalization, the two-dimensional memory is a result of the encoder used and ISI caused by the multipath Rayleigh fading channel. Unlike the turbo codes, the code should not necessarily be systematic. The multipath channel does not produce any "redundant" symbols, but it imposes ISI on the received signal due to the channel memory. Furthermore, the complex envelopes associated with the multipath components vary according to the mobile station's move, causing the time-varying ISI. Therefore, the space-time channel matrix $\mathbf{H}$ has to be estimated frame by frame.

Recognizing that the multipath propagation is the process taking a convolution of the symbols transmitted over each multipath component, the channel can be seen as a "convolution code," the definition of which is in the complex field. Therefore, the system is a "serially concatenated code" [6] comprised of two codes, one is the channel code used, the other the multipath channel itself. They are serially connected, and are separated by an interleaver. To "decode" the serially concatenated code, decoding techniques for serially concatenated turbo codes can be used. Such system is called "turbo equalizer."

A block diagram of communication system using single-carrier signaling with turbo equalizer is shown in Figure 7.1. The receiver presented in Figure 7.1 consists of a SISO detector and a SISO decoder that are connected by a deinterleaver and an interleaver. The inverse operation of interleaving is performed by the deinterleaver, for which the coded bit is indexed by i after deinterleaving.

For the BPSK's case, the SISO detector delivers the a posteriori LLR of a transmitted symbol "+1" and "−1," defined as

$$\Lambda_1[b(k)] = \ln \frac{\Pr[b(k) = +1|\mathbf{y}(k)]}{\Pr[b(k) = -1|\mathbf{y}(k)]}. \tag{7.11}$$

Using Bayes' rule, $\Lambda_1[b(k)]$ given by (7.11) can be rewritten as

$$\Lambda_1[b(k)] = \underbrace{\ln \frac{\Pr[\mathbf{y}(k)|b(k) = +1]}{\Pr[\mathbf{y}(k)|b(k) = -1]}}_{\lambda_1[b(k)]} + \underbrace{\ln \frac{\Pr[b(k) = +1]}{\Pr[b(k) = -1]}}_{\lambda_2^p[b(k)]}, \tag{7.12}$$

where $\lambda_2^p[b(k)]$ is the a priori LLR of the code bit $b(k)$ provided by the channel decoder in the previous iteration with p indicating the quantity obtained from the *previous* iteration. The first term $\lambda_1[b(k)]$ represents the *extrinsic information* based on the received signal $\mathbf{y}(k)$ and a priori information $\lambda_2^p[b(k')]$ of the code bits except the kth bit, that is, $k' \neq k$. After deinterleaving, $\lambda_1[b(i)]$ is fed to the SISO channel decoder, which calculates a posteriori LLR using the prior information about all possible symbols and the knowledge about the trellis structure of the code, as

$$\begin{aligned}\Lambda_2[b(i)] &= \ln \frac{\Pr[b(i) = +1|\lambda_1^p b(i')]_{i'=0}^{B-1}}{\Pr[b(i) = -1|\lambda_1^p b(i')]_{i'=0}^{B-1}} \\ &= \lambda_2[b(i)] + \lambda_1^p[b(i)],\end{aligned} \tag{7.13}$$

where B is the length of the frame. To obtain the LLR calculated by using the trellis diagram, $\lambda_1[b(i)]$ is subtracted from $\lambda_2[b(i)]$ before feeding it back as a priori information to the SISO detector through the interleaver.

The decoder also calculates the a posteriori LLR of every information bit $c(j)$, on which the final decision is made at the final iteration. At the first iteration $\lambda_1[b(k)]$ and $\lambda_2^p[b(k)]$ are statistically independent, since the ISI and the channel code put independent forms of memory. But subsequently, since both use the same information indirectly, there will be more correlation as more iterations are performed, until finally the improvement through iterations diminishes.

If the trellis diagram of the multipath channel, which can be seen as an inner code of the serially concatenated code, has to be used to calculate the a posteriori LLR $\lambda_1[b(k)]$, its computational complexity becomes prohibitive for broadband single-carrier signaling. This is because the number of the states needed to express the channel's trellis diagram increases exponentially with the number of the channel memory length $L-1$. The SC/MMSE iterative equalization technique can solve this problem by replacing the trellis-based LLR computer with soft cancelation and MMSE filtering.

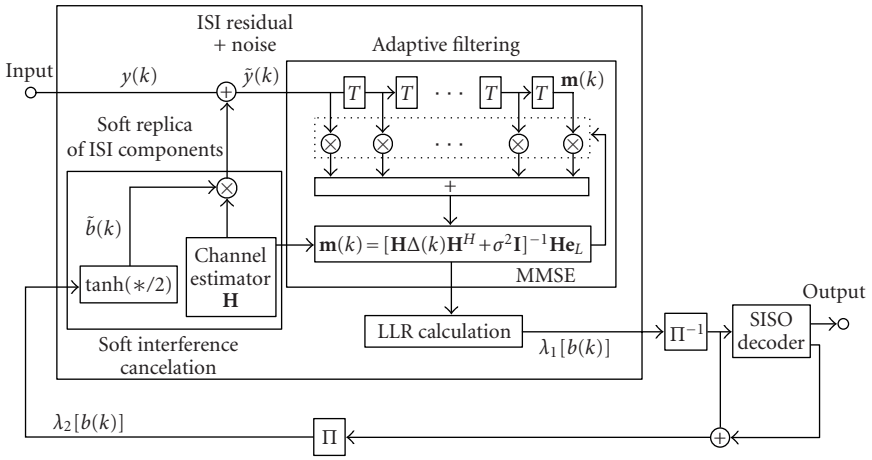

FIGURE 7.3. Block diagram of SC/MMSE signal processing.

7.2.3. SC/MMSE turbo equalization algorithm

A block diagram of the SC/MMSE iterative equalizer is shown in Figure 7.3. The principle of the SC/MMSE equalizer is that it first performs the ISI cancelation by subtracting the soft replica of ISI components from the received signal vector, and further suppresses the residual interference components by an adaptive filter. The tap coefficients of the filter are determined based on the minimum mean squared error (MMSE) criterion [4].

The soft replica is constructed from the a priori LLR $\lambda_2^p[b(k)]$ of the symbols delivered by the SISO decoder from the previous iteration. For notational simplicity, the bit index k and its corresponding bit value $b(k)$ are ignored in the following, resulting in a simpler notation:

$$\lambda_2 = \ln \frac{\mathrm{P_r}(+1)}{\mathrm{P_r}(-1)}. \tag{7.14}$$

After some mathematical manipulations we have

$$\mathrm{P_r}(-1) = \frac{1}{1 + e^{\lambda_2}}. \tag{7.15}$$

The soft estimate of symbol $\tilde{b} = \langle b \rangle$ can be calculated from the probabilities $\mathrm{P_r}(+1)$ and $\mathrm{P_r}(-1)$ as

$$\begin{aligned} \tilde{b} &= (-1) \cdot \mathrm{P_r}(-1) + 1 \cdot \mathrm{P_r}(+1) \\ &= -\mathrm{P_r}(-1) + \mathrm{P_r}(+1) \\ &= -\mathrm{P_r}(-1) + \mathrm{P_r}(-1)e^{\lambda_2} \\ &= \mathrm{P_r}(-1)\left(e^{\lambda_2} - 1\right). \end{aligned} \tag{7.16}$$

Using (7.15) and (7.16) we get

$$\tilde{b} = \frac{e^{\lambda_2} - 1}{e^{\lambda_2} + 1}. \tag{7.17}$$

Given the definition of the hyperbolic tangent function

$$\tanh(x) = \frac{e^{2x} - 1}{e^{2x} + 1} \tag{7.18}$$

it is found that the symbol estimate $\tilde{b}$ is given by

$$\tilde{b} = \tanh \frac{\lambda_2}{2}. \tag{7.19}$$

Now, we assume without loss of generality that $b(k)$ is the bit to be detected. A vector representation $\tilde{b}(k)$ of the soft estimates of the ISI-causing symbols is given as

$$\tilde{\mathbf{b}} = \left[\tilde{b}(k + (L-1)) \ \cdots \ \tilde{b}(k+1) \ 0 \ \tilde{b}(k-1) \ \cdots \ \tilde{b}(k - (L-1))\right]^T. \tag{7.20}$$

To calculate the soft replica of ISI components, $\tilde{b}(k)$ is multiplied by the estimate of the space-time channel matrix $\mathbf{H}$ provided by the channel estimator. The product is then subtracted from the received signal $\mathbf{y}(k)$ to perform soft interference cancelation for a symbol $b(k)$ as

$$\tilde{\mathbf{y}}(k) = \mathbf{y}(k) - \mathbf{H}\tilde{\mathbf{b}}(k) = \mathbf{H}(\mathbf{b}(k) - \tilde{\mathbf{b}}(k)) + \mathbf{V}(k). \tag{7.21}$$

After the soft cancelation, the remaining ISI components are further suppressed by applying a *conditional* linear MMSE filter as

$$z(k) = \mathbf{m}^H(k)\tilde{\mathbf{y}}(k), \tag{7.22}$$

where the vector $\mathbf{m}(k)$ corresponds to the filter coefficients. The term "*conditional* MMSE" indicates that the optimization due to the MMSE criterion is conditioned upon the soft feedback vector $\tilde{\mathbf{b}}(k)$. The criterion for determining vector $\mathbf{m}(k)$ is such that it minimizes the mean squared error (MSE) between symbol $b(k)$ and filter output $z(k)$ as

$$\begin{aligned} \mathbf{m}(k) &= \arg\min_m E\left\{\left|\left|b(k) - \mathbf{m}^H\tilde{\mathbf{y}}(k)\right|\right|^2\right\} \\ &= \arg\min_m \mathbf{m}^H E\{\tilde{\mathbf{y}}(k)\tilde{\mathbf{y}}(k)^H\}\mathbf{m} - 2\mathbf{m}^H E\{b(k)\tilde{\mathbf{y}}(k)\}. \end{aligned} \tag{7.23}$$

In (7.23)

$$E\{\tilde{\mathbf{y}}(k)\tilde{\mathbf{y}}^H(k)\} = \mathbf{H}\boldsymbol{\Delta}(k)\mathbf{H}^H + \sigma^2\mathbf{I} \tag{7.24}$$

and

$$E\{b(k)\tilde{\mathbf{y}}(k)\} = \mathbf{H}\mathbf{e}_L, \tag{7.25}$$

where

$$\begin{aligned}\boldsymbol{\Delta}(k) &= \operatorname{cov}\{\mathbf{b}(k) - \tilde{\mathbf{b}}(k)\} \\ &= \operatorname{diag}\{1 - \tilde{b}(k+L-1)^2, \ldots, 1 - \tilde{b}(k+1)^2, 1, \\ &\qquad 1 - \tilde{b}(k-1)^2, \ldots, 1 - \tilde{b}(k-L+1)^2\}\end{aligned} \tag{7.26}$$

and $\mathbf{e}_L$ is a length $2L-1$ vector, of which all elements are zero except the Lth element being 1. Substituting (7.24) and (7.25) into (7.23), the MSE after the MMSE filtering can be written as

$$\text{MSE} = \mathbf{m}^H(k)\left[\mathbf{H}\boldsymbol{\Delta}(k)\mathbf{H}^H + \sigma^2\mathbf{I}\right]\mathbf{m}(k) - 2\mathbf{m}^H(k)\mathbf{H}\mathbf{e}_L + 1 \tag{7.27}$$

from which the gradient with respect to $\mathbf{m}(k)$ is taken and set at zero to obtain

$$\left[\mathbf{H}\boldsymbol{\Delta}(k)\mathbf{H}^H + \sigma^2\mathbf{I}\right]\mathbf{m}(k) - \mathbf{H}\mathbf{e}_L = 0 \tag{7.28}$$

$\mathbf{m}(k)$ can then be given as

$$\mathbf{m}(k) = \left[\mathbf{H}\boldsymbol{\Delta}(k)\mathbf{H}^H + \sigma^2\mathbf{I}\right]^{-1}\mathbf{H}\mathbf{e}_L. \tag{7.29}$$

Hence, the MMSE filter output is given by

$$z(k) = \mathbf{e}_L^T\mathbf{H}^H\left[\mathbf{H}\boldsymbol{\Delta}(k)\mathbf{H}^H + \sigma^2\mathbf{I}\right]^{-1}\left[\mathbf{r}(k) - \mathbf{H}\tilde{\mathbf{b}}(k)\right]. \tag{7.30}$$

The extrinsic information of the coded bit $b(k)$ is derived from the MMSE filter output, assuming that the MMSE filter output $z(k)$ can be approximated as a Gaussian channel output having input $b(k)$, as

$$z(k) = \mu(k)b(k) + \eta(k), \tag{7.31}$$

where $\eta(k)$ is an equivalent noise sample, and

$$\mu(k) = E\{z(k)b(k)\} = \mathbf{e}_L^T\mathbf{H}^H\mathbf{m}(k) \tag{7.32}$$

with

$$v^2(k) = E\left\{|z(k)|^2\right\} - \mu^2(k) = \mathbf{e}_L^T\mathbf{H}^H\mathbf{m}(k) - \mu^2(k) = \mu(k) - \mu^2(k). \tag{7.33}$$

With this expression, the extrinsic information $\lambda_1[b(k)]$ at the MMSE filter output is given by

$$\begin{aligned}\lambda_1[b(k)] &= \ln \frac{p[z(k)|b(k)=+1]}{p[z(k)|b(k)=-1]} \\ &= -\frac{|z(k)-\mu(k)|^2}{v^2(k)} + \frac{|z(k)+\mu(k)|^2}{v^2(k)} \\ &= \frac{4\,\mathrm{Re}\{z(k)\}}{1-\mu(k)}.\end{aligned} \tag{7.34}$$

7.2.4. Asymptotic performance

At early stages of the iterations the effect of the soft interference cancelation is not significant due to the symbol estimates $\tanh\{\lambda_2^p[b(k)/2]\}$ being near zero. However, with sufficient iterations, the soft estimates become more accurate, and $\Delta(k)$ approaches $\tilde{\Delta} = \mathrm{diag}[0,\ldots,0,1,0,\ldots,0]$. With $\Delta(k) = \tilde{\Delta}$, the ISI components in the equalizer coverage can be completely canceled by the soft canceller. If this happens, since $\mathbf{H}\tilde{\Delta}\mathbf{H}^H$ becomes a rank-one matrix, the MMSE filter taps become

$$\mathbf{m}(k) \longrightarrow \mathbf{m} = \left[\mathbf{h}\mathbf{h}^H + \sigma^2\mathbf{I}\right]^{-1}\mathbf{h}, \quad \Delta(k) \longrightarrow \tilde{\Delta}, \tag{7.35}$$

where $\mathbf{h} = \mathbf{H}\mathbf{e}_L$ is the Lth column vector of the space-time channel matrix $\mathbf{H}$. Using the matrix inversion lemma,

$$\begin{aligned}\mathbf{A}^{-1} &= \left(\mathbf{C}\mathbf{D}^{-1}\mathbf{C}^H + \mathbf{B}\right)^{-1} \\ &= \mathbf{B}^{-1} - \mathbf{B}^{-1}\mathbf{C}\left(\mathbf{D} + \mathbf{C}^H\mathbf{B}^{-1}\mathbf{C}\right)^{-1}\mathbf{C}^H\mathbf{B}^{-1}\end{aligned} \tag{7.36}$$

the MMSE filter weight $\mathbf{m}$ of (7.35) becomes

$$\begin{aligned}\mathbf{m} &= \left[\frac{1}{\sigma^2} - \frac{1}{\sigma^2}\mathbf{h}\left(\frac{1}{1+\mathbf{h}^H\mathbf{h}/\sigma^2}\right)\mathbf{h}^H\frac{1}{\sigma^2}\right]\mathbf{h} \\ &= \left[\frac{1}{\sigma^2} - \frac{1}{\sigma^2}\cdot\frac{\mathbf{h}^H\mathbf{h}}{\sigma^2+\mathbf{h}^H\mathbf{h}}\right]\mathbf{h} \\ &= \alpha\mathbf{h},\end{aligned} \tag{7.37}$$

where $\alpha = 1/(\mathbf{h}^H\mathbf{h} + \sigma^2)$. Now, it is found that MMSE is equivalent to a filter matched to the channel [7], with which performance is equivalent to that of the maximum ratio combining (MRC) path diversity. Therefore, the performance of the SC/MMSE equalizer is asymptotically equivalent to the MRC bound that is also the performance limit of the MLSE equalizer. However, there is a certain point of convergence, over which the performance is not improved by further iterations. In fact, the convergence property of SC/MMSE is affected by the channel realization, and if the channel is in highly non-minimum phase mode, it cannot achieve the asymptotic performance described above.

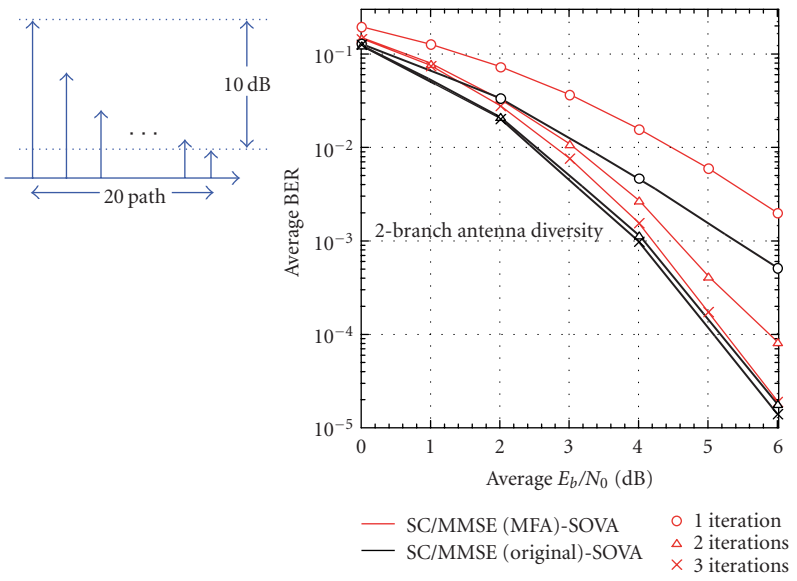

FIGURE 7.4. Performances of original SC/MMSE and its matched filter approximation (MFA) algorithms, 20-path Rayleigh fading ($f_D T_S = 1/12\,000$).

7.2.5. Performance results

Figure 7.4 shows results of simulations conducted to evaluate bit error rate (BER) performance of the SC/MMSE equalizer in a severe frequency-selective multipath fading environment. An exponentially decaying delay profile was assumed where there are 20 path components in the range from the top to 10 dB down point in the delay profile. Other simulation parameter values are summarized in the figure. The light solid lines are for the original SC/MMSE equalizer with the iteration number as a parameter, and the dark solid lines for the matched filter approximation SC/MMSE equalizer which will be derived in Section 7.4.2. It is found that SC/MMSE achieves significant iteration gain, and after 3 iterations, SC/MMSE's BER converges into its achievable asymptotic value.

7.3. SC/MMSE MIMO turbo equalization

7.3.1. Extension to MIMO

This subsection extends the single-user single-carrier SC/MMSE turbo equalization algorithm to MIMO cases [8, 9]. MIMO refers here to a situation where multiple signals are transmitted simultaneously using the same time slots and the same frequency slots. Some groups of the signals may be transmitted by some single users, each using multiple antennas, and some transmitted by multiple independent users, each using a single antenna. In the former case, each single user's

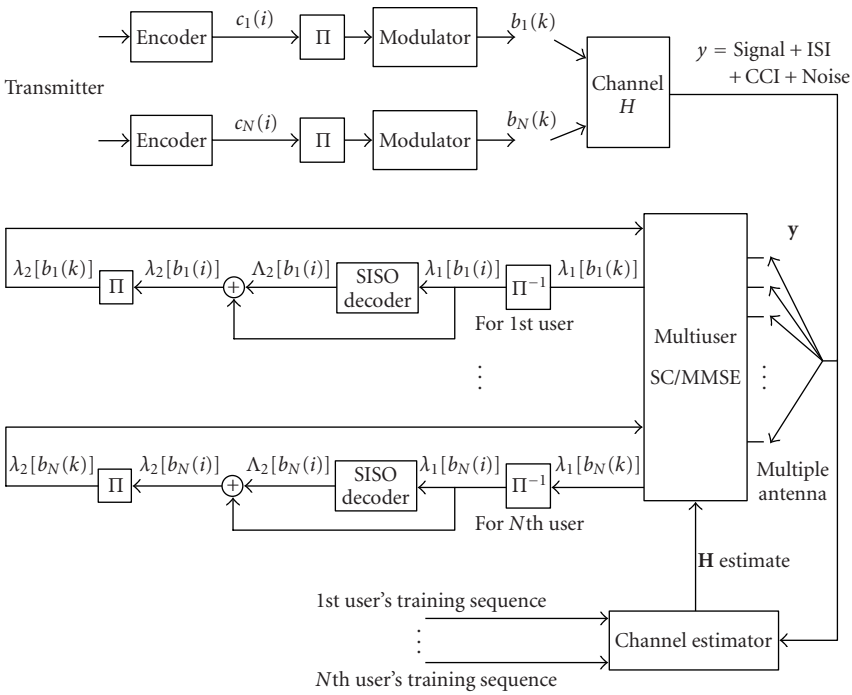

FIGURE 7.5. Single-carrier MIMO system model and block diagram of SC/MMSE MIMO turbo equalizer.

data is divided into different chains that perform encoding and interleaving separately. However, the symbol detection algorithm shown in this section can be extended easily to the case where the transmit antennas are grouped into several subgroups, in which coding and interleaving take place over the multiple antennas [10, 11].

Despite the scope of the radio network configuration described above, it is assumed later on that each antenna transmits signal of single "users" for simplicity. Now, the system has N "users," each having a single transmit antenna, and the receiver is equipped with M antennas. The receiver is comprised of a multiple user signal detector (MUSD) and SISO decoders for each user. The MUSD consists of soft interference cancellers for the N users, each followed by the MMSE filter. Since the channel model is basically the same as in the single-user case, the extended notations are shown briefly.

Figure 7.5 presents the single-carrier MIMO communication system model investigated in this section. All N users transmit their information symbols using the same time slots and frequency slots without spreading signals in the frequency domain. The information bits $c_n(i)$ with i and n denoting the bit and user indices, respectively, are encoded by each user's channel encoder. After interleaving the symbols $b_n(k)$, where k denotes the symbol index after interleaving, are modulated using the BPSK modulation format, and transmitted over frequency-selective

channels. At the receiver, the discrete-time representation of the received signal at the mth antenna can be expressed as

$$r_m(k) = \sum_{l=0}^{L-1} \sum_{n=1}^{N} h_{mn}(l) b_n(k-l) + v_m(k) \tag{7.38}$$

which is equivalent to (7.1), except that it sums up multiple users and that as noted in Section 7.2.1, the path index l is cited in parentheses as $h_{mn}(l)$ $0 \le l \le L-1$, and $1 \le n \le N$. Equation (7.38) can be rewritten in a matrix form as

$$\begin{aligned} \mathbf{r}(k) &= \begin{bmatrix} r_1(k) & r_2(k) & \cdots & r_M(k) \end{bmatrix}^T \\ &= \sum_{l=0}^{L-1} \mathbf{H}(l)\mathbf{b}(k-l) + \mathbf{v}(k), \end{aligned} \tag{7.39}$$

where

$$\begin{aligned} \mathbf{H}(l) &= \begin{bmatrix} h_{11}(l) & \cdots & h_{1N}(l) \\ \vdots & \ddots & \vdots \\ h_{M1}(l) & \cdots & h_{MN}(l) \end{bmatrix}, \\ \mathbf{b}(k) &= \begin{bmatrix} b_1(k) & b_2(k) & \cdots & b_N(k) \end{bmatrix}^T \end{aligned} \tag{7.40}$$

and

$$\mathbf{v}(k) = \begin{bmatrix} v_1(k) & v_2(k) & \cdots & v_M(k) \end{bmatrix}^T. \tag{7.41}$$

After space-domain and time-domain sampling, the space-time representation of the received signal $\mathbf{y}(k)$ is given by

$$\begin{aligned} \mathbf{y}(k) &= \begin{bmatrix} \mathbf{r}^T(k+L-1) & \mathbf{r}^T(k+L-2) & \cdots & \mathbf{r}^T(k) \end{bmatrix}^T \\ &= \mathbf{H}\mathbf{u}(k) + \mathbf{V}(k), \end{aligned} \tag{7.42}$$

where

$$\mathbf{H} = \begin{bmatrix} \mathbf{H}(0) & \cdots & \mathbf{H}(L-2) & \mathbf{H}(L-1) & 0 & \cdots & 0 \\ 0 & \mathbf{H}(0) & \ddots & \mathbf{H}(L-2) & \mathbf{H}(L-1) & \ddots & \vdots \\ \vdots & \ddots & \ddots & \vdots & \ddots & \ddots & 0 \\ 0 & \cdots & 0 & \mathbf{H}(0) & \cdots & \mathbf{H}(L-2) & \mathbf{H}(L-1) \end{bmatrix} \tag{7.43}$$

represents the temporal and spatial characteristics of the frequency-selective MIMO channel with $\mathbf{u}(k)$ and $\mathbf{V}(k)$ being

$$\mathbf{u}(k) = \begin{bmatrix} \mathbf{b}^T(k+L-1) & \cdots & \mathbf{b}^T(k) & \cdots & \mathbf{b}^T(k-L+1) \end{bmatrix}^T \tag{7.44}$$

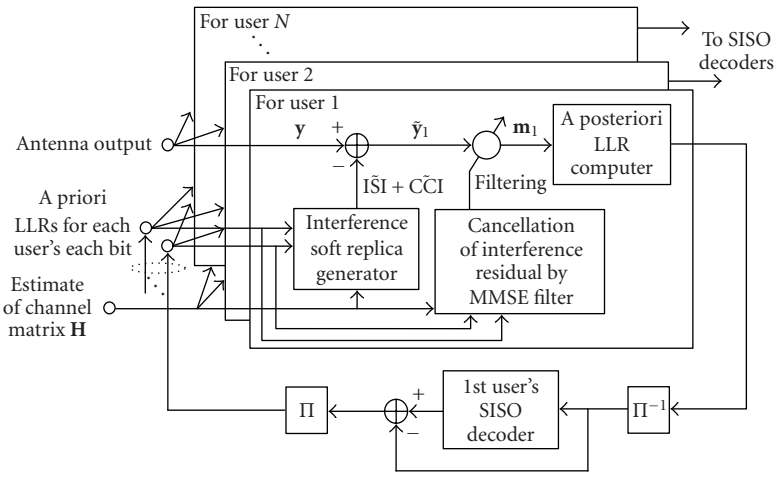

FIGURE 7.6. Block diagram of MIMO SC/MMSE signal processing.

and

$$\mathbf{V}(k) = \left[\mathbf{v}^T(k+L-1) \quad \mathbf{v}^T(k+L-2) \quad \cdots \quad \mathbf{v}^T(k)\right]^T, \tag{7.45}$$

respectively.

Since the details of the mathematical derivation of the SC/MMSE algorithm is presented in Section 7.2.3, the extension to the MIMO case is described here only briefly. The principle of MIMO SC/MMSE signal processing is illustrated in Figure 7.6. For each of the N users the SC/MMSE signal processing is conducted independently. Assume that the nth user's kth bit $b_n(k)$ is to be detected. Define $\tilde{\mathbf{u}}_n(k)$ as

$$\tilde{\mathbf{u}}_n(k) = \left[\tilde{\mathbf{b}}^T(k+L-1) \quad \cdots \quad \tilde{\mathbf{b}}^T(k) \quad \cdots \quad \tilde{\mathbf{b}}^T(k-L+1)\right]^T \tag{7.46}$$

with

$$\tilde{\mathbf{b}}(k') = \left[\tilde{b}_1(k') \;\; \tilde{b}_2(k') \;\; \cdots \;\; \tilde{b}_N(k')\right]^T, \quad k-L+1 \le k' \le k+L-1, k' \ne k \tag{7.47}$$

and

$$\tilde{\mathbf{b}}(k) = \left[\tilde{b}_1(k) \quad \cdots \quad \tilde{b}_{n-1}(k) \quad 0 \quad \tilde{b}_{n+1}(k) \quad \cdots \quad \tilde{b}_N(k)\right]^T, \tag{7.48}$$

where $\tilde{b}_n(k)$ is the soft estimate of $b_n(k)$.

The soft replicas of all ISI and CCI components $\mathbf{H}\tilde{\mathbf{u}}_n(k)$ is subtracted from the received signal vector as

$$\tilde{\mathbf{y}}_n(k) = \mathbf{y}(k) - \mathbf{H}\tilde{\mathbf{u}}_n(k). \tag{7.49}$$

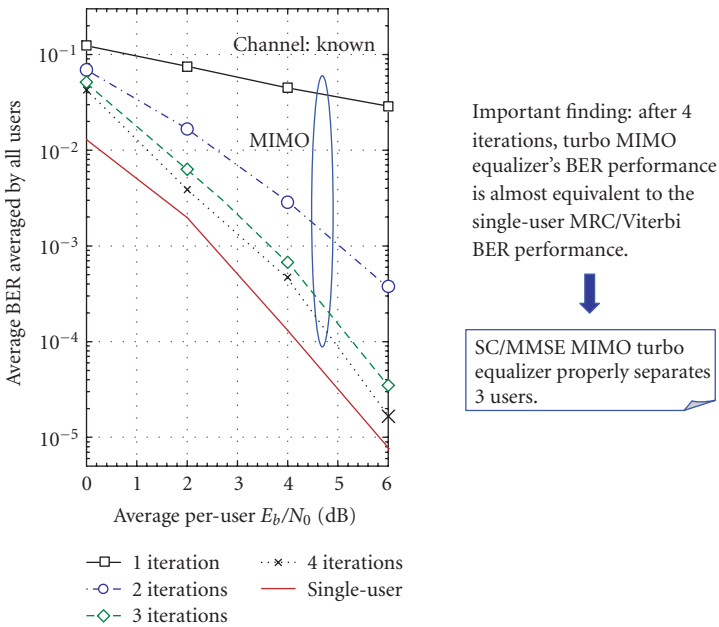

FIGURE 7.7. BER performance of SC/MMSE MIMO turbo equalizer. The scenario includes 2 antennas, 3 users each having 5 paths, MRC + Viterbi decoding, 900 symbol/frame, $f_d T_s \to 0$, $K = 3$ conventional code.

Remaining interference components are further suppressed by the MMSE filter, which also combines the multipath components of $b_n(k)$ spread in time over the ISI length L. The MMSE filter weight $\mathbf{m}_n(k)$ for the nth user's kth bit can be calculated in the same way as $\mathbf{m}(k)$ was derived by (7.29) in the single user's case. However, it requires quite a heavy computational burden to invert the covariance matrix of $\tilde{\mathbf{y}}_n(k)$. Section 7.4 investigates computationally efficient approximation methods that do not cause serious performance degradations.

After the LLR calculation by (7.34), the soft values are deinterleaved, and the *extrinsic information* is fed as input to each user's SISO decoder, which performs the SISO decoding of the channel code user by user to provide updated LLRs.

7.3.2. Performance results

Figure 7.7 shows results of simulations for the SC/MMSE MIMO equalizer performance evaluations in a 5-path frequency-selective multipath fading environment. There are 3 simultaneous users, and the receiver uses 2 antennas; each transmit-to-receive antenna radio link is comprised of 5 propagation paths having equal average power. The curve indicated by "single user" describes the single-user BER performance where the other two simultaneous users are not present, and the energy of the user's corresponding 10 path components (2×5) are MRC combined, and soft input Viterbi decoding follows for the channel code used.

Table 7.1. Complexity comparison of SISO algorithms.

Operation	Additions	Multiplications	Comparison
Log-MAP	$2^{L_c-1}(4L_c+17)-5$	$2^{L_c-1}(4L_c+2)$	$4\cdot 2^{L_c-1}-2$
Max-log-MAP	$2^{L_c-1}(4L_c+8)$	$2^{L_c-1}(4L_c+2)$	$4\cdot 2^{L_c-1}-2$
SOVA	$2^{L_c-1}(4L_c+2)$	$2^{L_c-1}(4L_c+2)$	$2\cdot 2^{L_c-1}+5L_c$

The curves indicated by MIMO show BER performance of the 3-user SC/MMSE MIMO equalizer. After 4 iterations, the decay of the MIMO performance curves is almost the same as the "single user" curve, and the difference between the two curves is less than 1 dB.

7.4. Approximations

7.4.1. Complexity of the SC/MMSE turbo equalizer

7.4.1.1. Complexity due to SISO decoder

In general, trellis-based SISO decoders require complexity order $O(M_c^{L_c-1})$, where M_c is the level of modulation and L_c is the constraint length of the code. However, there are some marginal differences in the complexities of SISO algorithms. The result of the complexity evaluation for the several well-known SISO algorithms is summarized in Table 7.1.

From Table 7.1, it can be seen that among the algorithms compared, SOVA requires the lowest computational complexity due to the lowest comparison operations. The computational burden due to comparisons is only roughly half of that required by the max-log-MAP and log-MAP algorithms.

7.4.1.2. Complexity due to SC/MMSE

The heaviest part of SC/MMSE equalizer's signal processing is the calculation of MMSE filter coefficients, since it requires inversion of the covariance matrix $(\mathbf{H}\boldsymbol{\Delta}(k)\mathbf{H}^H+\sigma^2\mathbf{I})$ of the soft canceller output. Hence, the complexity of the SC/MMSE algorithm is of a cubic order $O(L^3M^3)$, which is presented in detail in Section 7.4.4. Obviously, the larger the matrices, the heavier the computational effort needed for the matrix inversion. Even though the SC/MMSE turbo equalizer does not require exponentially increasing computational complexity, it is obvious that the complexity still becomes prohibitive when the numbers of propagation paths and receive antennas increase.

7.4.2. Matched filter approximation

As it has been shown in Section 7.2.4, the MMSE filter approaches a filter matched to the channel after sufficient iterations. In the matched filter approximation technique the MMSE filter is replaced by a matched filter even from the second

iteration onwards. Since the matrix inversion needed for the MMSE weight calculation is eliminated, the complexity can be reduced significantly.

For the first iteration, it is apparent from (7.26) that $\mathbf{\Delta}(k) = \mathbf{I}$ due to the unavailability of the symbol estimates from the SISO decoder. In this case the coefficients of the MMSE filter can be determined adaptively by using the training sequence transmitted for the estimation of the channel matrix $\mathbf{H}$. From the second iteration onwards, $\Delta(k) \neq \mathbf{I}$ and, thus, this method cannot be used.

After sufficient iterations, when the soft canceller is supposed to eliminate ISI components perfectly, equivalence between MMSE filtering $\mathbf{m}^H\tilde{\mathbf{y}}(k)$ and matched filtering, matched to the channel, is clearly seen from (7.37). Namely then, the role of the MMSE filter is to maximize the desired signal energy which can be performed by matched filtering. Hence, the matched filter $\mathbf{m} = \alpha\mathbf{h}^H$ may be used instead of (7.29) even from the second iteration onwards [7]. Since the matched filter is unique only to the channel and independent of iterations, $\mathbf{m}$ has to be determined only once.

Since the matrix inversion is no longer needed with the matched filter approximation, and since the vector-vector inner product that appears in the matrix inversion lemma only requires a square-order of complexity, the matched filter approximation can reduce the SC/MMSE complexity to $O(L^2M^2)$. BER performance of the matched filter approximation SC/MMSE equalizer in the 20-path single-user environment is shown in Figure 7.4. It is found that after 3 iterations, the matched filter approximation can achieve almost the same performance as the original SC/MMSE equalizer. The matched filter approximation SC/MMSE algorithm can easily be extended to MIMO cases [12].

7.4.3. Common covariance matrix inversion technique

Using the common covariance matrix inversion technique, the complexity can be further reduced by replacing the symbol-by-symbol interference covariance matrix by a frame-wise average. The equation for the soft cancelation, corresponding to (7.49) in Section 7.3.1, can be rewritten as

$$\tilde{\mathbf{y}}_n(k) = \mathbf{y}(k) - \mathbf{H}\tilde{\mathbf{u}}(k) + \mathbf{h}_n\tilde{b}_n(k) = \tilde{\mathbf{y}}(k) + \mathbf{h}_n\tilde{b}_n(k), \tag{7.50}$$

where

$$\tilde{\mathbf{u}}(k) = \left[\tilde{\mathbf{b}}^T(k+L-1) \quad \cdots \quad \tilde{\mathbf{b}}^T(k) \quad \cdots \quad \tilde{\mathbf{b}}^T(k-L+1)\right]^T \tag{7.51}$$

with

$$\begin{gathered}\tilde{\mathbf{b}}(k') = \left[\tilde{b}_1(k') \quad \tilde{b}_2(k') \quad \cdots \quad \tilde{b}_N(k')\right]^T, \quad k-L+1 \leq k' \leq k+L-1, \\ \tilde{\mathbf{y}}(k) = \mathbf{y}(k) - \mathbf{H}\tilde{\mathbf{u}}(k)\end{gathered} \tag{7.52}$$

and

$$\mathbf{h}_n = \mathbf{H}\mathbf{e}_{(L-1)N-n}. \tag{7.53}$$

The covariance matrix $\tilde{\mathbf{\Theta}}$ of $\tilde{\mathbf{y}}_n(k)$ is then given by

$$\mathbf{\Theta}_n(k) = \mathbf{\Theta}(k) + \mathbf{h}_n \tilde{b}_n^2(k)\mathbf{h}_n^H, \tag{7.54}$$

where

$$\mathbf{\Theta}(k) = \mathbf{H}\mathbf{\Delta}_c(k)\mathbf{H}^H + \sigma^2\mathbf{I} = E\{\tilde{\mathbf{y}}(k)\tilde{\mathbf{y}}^H(k)\} \tag{7.55}$$

is a *common* covariance matrix with a diagonal matrix $\mathbf{\Delta}_c(k)$ defined as

$$\begin{aligned}\mathbf{\Delta}_c(k) = \operatorname{diag}\{&1-\tilde{b}_1(k+L-1)^2, 1-\tilde{b}_2(k+L-1)^2,\ldots,\\ &1-\tilde{b}_N(k+L-1)^2,\ldots,1-\tilde{b}_1(k)^2,1-\tilde{b}_2(k)^2,\ldots,\\ &1-\tilde{b}_N(k)^2,\ldots,1-\tilde{b}_1(k-L+1)^2,\\ &1-\tilde{b}_2(k-L+1)^2,\ldots,1-\tilde{b}_N(k-L+1)^2\}\end{aligned} \tag{7.56}$$

which corresponds to the matrix $\mathbf{\Delta}(k)$ in the original SC/MMSE defined by (7.26) with a difference of the $\{(L-1)N+n,(L-1)N+n\}$-element being $1-\tilde{b}_n^2(k)$.

$\mathbf{\Theta}(k)$ may be approximated by a frame-wise average as

$$\mathbf{\Theta}(k) \cong \mathbf{\Theta} = \frac{1}{K}\sum_{k=1}^{K}\tilde{\mathbf{y}}(k)\tilde{\mathbf{y}}^H(k) \tag{7.57}$$

for all k and n, where K is the total sample number in a frame. This can be calculated using the matrix inversion lemma in a similar fashion as the covariance matrix is propagated in the recursive least square (RLS) algorithm. The staple equations of the RLS algorithm needed for the common covariance matrix inversion estimation method are [12]

$$\mathbf{k}(g) = \frac{\lambda^{-1}\mathbf{\Theta}(g-1)\tilde{\mathbf{y}}(g)}{1+\lambda^{-1}\tilde{\mathbf{y}}^H(g)\mathbf{\Theta}(g-1)\tilde{\mathbf{y}}(g)} \tag{7.58}$$

and

$$\mathbf{\Theta}(g) = \lambda^{-1}\mathbf{\Theta}(g-1) - \lambda^{-1}\mathbf{k}(g)\tilde{\mathbf{y}}^H(g)\mathbf{\Theta}(g-1), \tag{7.59}$$

where λ (≤ 1.0) is the forgetting factor, whose value is chosen to be close to 1.0 [13], and g is the updating index of the RLS algorithm. In many cases, the updating index g is equivalent to the symbol index k, with which $K = B$ with B being the frame length in bits. However, in the case that updating does not take place in the symbol order in the frame, or fractional sampling per symbol is performed, $g \neq k$.

Applying (7.58) and (7.59) to (7.57), the inverse matrix can be calculated by iterating

$$\boldsymbol{\Theta}^{-1}(g) = \lambda^{-1}\boldsymbol{\Theta}(g-1) - \frac{\lambda^{-2}\boldsymbol{\Theta}^{-1}\dot{\mathbf{y}}\dot{\mathbf{y}}^{H}\boldsymbol{\Theta}^{-1}(g-1)}{(1-\lambda)^{-1} + \lambda^{-1}\dot{\mathbf{y}}^{H}\boldsymbol{\Theta}^{-1}(g-1)\dot{\mathbf{y}}} \tag{7.60}$$

over the frame, where the contribution from noise is included in the residual signal as

$$\dot{\mathbf{y}} = \tilde{\mathbf{y}}(g) + \mathbf{V}(g) \tag{7.61}$$

and hence the need of estimating the noise variance is avoided. The algorithm is initialized by setting

$$\boldsymbol{\Theta}^{-1}(0) = \varepsilon^{-1}\mathbf{I}, \tag{7.62}$$

where ε is a small positive constant. Since the symbol likelihood calculation may be biased due to inaccuracy in $\boldsymbol{\Theta}(k)$, the matrix inversion lemma is normalized by $(1-\lambda)^{-1}$. Then, the calculated $\boldsymbol{\Theta}(k)$ is combined with the symbol-wise information for each user n as given in (7.54). Since the $\boldsymbol{\Theta}^{-1}(k)$ is now known, $\boldsymbol{\Theta}_n^{-1}(k)$ can be calculated again using the matrix inversion lemma as

$$\begin{aligned}\boldsymbol{\Theta}_n^{-1}(k) &= \left(\boldsymbol{\Theta}(k) + \tilde{b}_n^2\mathbf{h}_n\mathbf{h}_n^{H}\right)^{-1} \\ &= \boldsymbol{\Theta}^{-1}(k) - \boldsymbol{\Theta}^{-1}(k)\mathbf{h}_n\left(\frac{1}{\tilde{b}_n^2} + \mathbf{h}_n^{H}\boldsymbol{\Theta}^{-1}(k)\mathbf{h}_n\right)^{-1}\mathbf{h}_n^{H}\boldsymbol{\Theta}^{-1}(k).\end{aligned} \tag{7.63}$$

In MIMO systems, the calculated matrix inverse is common to all users. Hence, each equalization stage is composed of a common matrix inverter, a channel estimator, and a likelihood generator that provides the LLR for each bit of each user. This approximation requires the assumption that the channel is constant over the frame, which is, however, qualified for broadband single-carrier systems due to the short frame length. The advantage of using the time averaging technique is the possibility to evade the bit-wise matrix inverse by performing one matrix inverse lemma iteration for each received bit, the complexity of which is $O(M^2L^2)$.

Figure 7.8 shows results of simulations for the evaluation of the SC/MMSE MIMO equalizer performance based on the common covariance matrix inversion technique in a 10-path frequency-selective multipath fading environment. There are 3 simultaneous uses, and the receiver uses 3 antennas; each transmit-to-receive antenna radio link is comprised of 10 propagation paths having equal average power. Perfect knowledge about the channel is assumed. The dashed line indicates the maximum ratio combining bound of single-user BER performance where assuming that the other two simultaneous users are not present, the energy of the user's corresponding 30 path components ($= 3 \times 10$) is MRC combined and soft input Viterbi decoding follows for the channel code used.

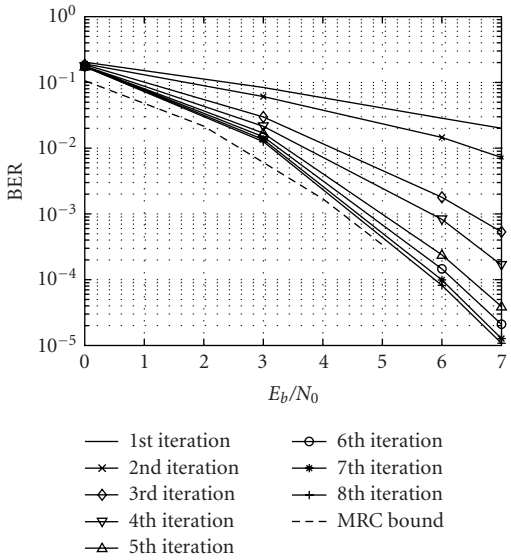

Figure 7.8. BER performance of common covariance estimation SC/MMSE MIMO turbo equalizer (w/3 users, 10-path Rayleigh fading, 3 antennas).

Table 7.2. Complexity comparison of SC/MMSE algorithms.

Operation	Additions	Multiplications	Comparison
SOVA	$2^{L-1}(4L+2M)$	$2^{L-1}(4L+2)M$	$2\cdot 2^{L-1}+5L-1$
SC/MMSE	$M^3L^3+4ML^2-4ML$	$M^3L^3+ML^2-ML+1$	–
MFA (1st iteration)	$M(3M+2)L^2$	$M(4M+1)L^2+3L+2$	–
MFA (2nd iteration)	$2M(M+3)L^2-4ML$	$2M(M+3)L^2-ML+1$	–
COM (RLS part)	$M(3ML^2+2L)+2$	$2M(3ML^2+4L)$	–
COM (each user's part)	$M(4ML^2-3L)+1$	$2M(2ML^2+L)$	–

The solid lines indicate BER performance of the 3-user SC/MMSE MIMO turbo equalizer with the common covariance estimation technique. It is found that the MRC bound can be asymptotically achieved, and after 8 iterations, the performance difference is very minor.

7.4.4. Complexity comparison

A computational complexity comparison between the original SC/MMSE algorithm, its matched filter approximation (MFA) version, and the common covariance inverse estimation (COM) version, as well as the SOVA algorithm for BPSK is depicted in Table 7.2 for a single-user case.

Figure 7.9 compares the complexities of the algorithms in terms of the number of multiplications as a function of multipath components where the number

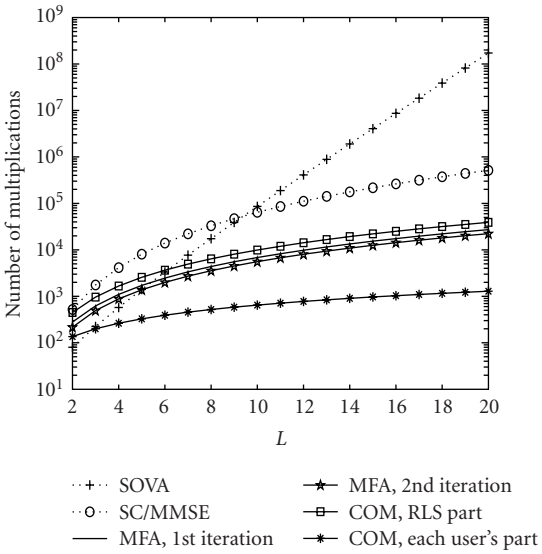

Figure 7.9. Complexity comparison in terms of multiplications.

of antennas is fixed at four. It is found that in environments with less than 10 propagation paths, the complexity of SOVA does not differ much from the complexities required by the other equalization algorithms. Actually SOVA is much simpler than the original SC/MMSE algorithm when $L < 10$. However, as L increases, the complexity of SOVA becomes prohibitive. The complexity reduction obtained by using the approximation algorithms is significant.

Comparison in terms of the number of additions versus L is presented in Figure 7.10 for the single-user case where the number of antennas is fixed at four. In the presence of only a few multipath components, the required number of additions is clearly the lowest with SOVA. In environments with more than 10 multipath components, the complexity reduction achieved by using approximation algorithms is noteworthy. However, the difference in complexity between the approximation algorithms is very minor.

7.5. Extension to generic modulation formats

Up to this point it has been assumed that the modulation format used is BPSK, but from a practical viewpoint, more spectrally efficient modulation format such as multilevel QAM has to be used. The configuration to perform equalization and SISO decoding for a standard bit-interleaved coded modulation (BICM) with arbitrary mapped QAM is introduced in this section [14].

The scenario investigated in this subsection is the same as that shown in Figure 7.5 except for the coding and modulation schemes. There are N users that are indexed by n; each transmit symbol $s_n(k)$ is generated by mapping each segment of M interleaved code bits to a 2^M-ary signal constelation S. All users are assumed to

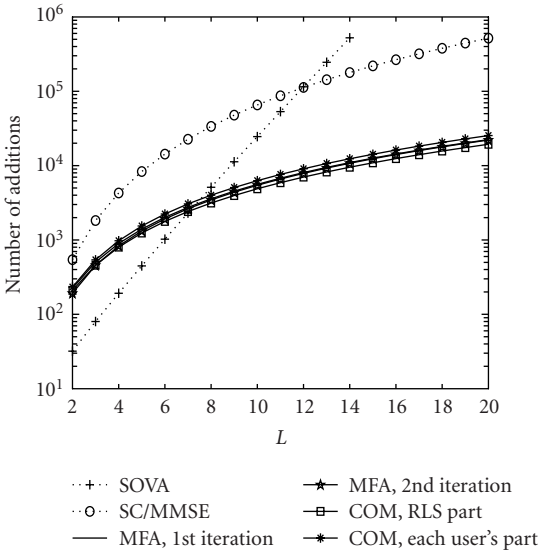

FIGURE 7.10. Complexity comparison in terms of additions.

use the same modulation format. The equalizer performs soft ISI and CCI interference cancelation, as in SC/MMSE for BPSK, for each transmitted symbol $s_n(k)$ with $n = 1 \sim N$ and $k = 0 \sim B - 1$ using a priori symbol probabilities.

The first-order and the second-order statistics of the symbols are obtained from the symbol a priori probabilities as

$$\begin{aligned} \tilde{s}_n(k) &\triangleq E\{s_n(k)\} = \sum_{s_j \in S} s_j \, \mathrm{P_a}\left(s_n(k) = s_j\right), \\ \mathrm{var}\left\{s_n(k)\right\} &\triangleq E\left\{ \left| s_n(k) \right|^2 \right\} - \left| \tilde{s}_n(k) \right|^2, \\ E\left\{ \left| s_n(k) \right|^2 \right\} &= \sum_{s_j \in S} |s_j|^2 \, \mathrm{P_a}\left(s_n(k) = s_j\right). \end{aligned} \tag{7.64}$$

The symbol a priori probability $\mathrm{P_a}(s_n(k) = s_j)$ is obtained from the corresponding bit-wise a priori LLRs, produced by the channel decoders, as

$$\mathrm{P_a}\left(s_n(k) = s_j\right) = \left(\frac{1}{2}\right)^M \prod_{m=1}^{M} \left\{ 1 - \bar{b}_{n,m}(k) \tanh \frac{\left(\lambda^j_{n,m}(k)\right)}{2} \right\}, \tag{7.65}$$

where $\bar{b}_{n,m}(k) = 1 - 2b_{n,m}(k)$ and $\lambda^j_{n,m}(k)$ is the extrinsic likelihood ratio, provided by the decoder, of the bit $b_{n,m}(k) \in (0, 1)$ in the segment that constitutes the symbol s_j. The soft canceller output is obtained in the same way as (7.50), where the

corresponding bit is replaced by symbol $s_n(k)$ as

$$\tilde{\mathbf{y}}(k) = \mathbf{y}(k) - \mathbf{H}\tilde{\mathbf{s}}(k), \tag{7.66}$$

where the vector $\tilde{\mathbf{s}}(k)$ is comprised of expected symbol values of all users and all symbols that fall within the window for the space-time sampling. To further reduce the effects of the residual interfering components, conditional MMSE filtering $\mathbf{m}_n(k)$ is used, for which the optimality criterion is

$$\mathbf{m}_n(k) = \arg\min_{m_n} E\left\{ \left| s_n(k) - \mathbf{m}_n^H\left(\tilde{\mathbf{y}}(k) + \mathbf{h}_n\tilde{s}_n(k)\right) \right|^2 \right\}, \tag{7.67}$$

where $\tilde{s}_n(k)$ is the soft estimate of $s_n(k)$. The solution to this MMSE problem is given by

$$\mathbf{m}_n(k) = \left[\mathbf{\Sigma}(k) + \left(1 - \text{var}\left\{s_n(k)\right\}\right)\mathbf{h}_n\mathbf{h}_n^H\right]^{-1}\mathbf{h}_n, \tag{7.68}$$

where $\mathbf{\Sigma}(k)$ is the covariance matrix of the residual signal in (7.66) and is given as

$$\mathbf{\Sigma}(k) = \mathbf{H}\mathbf{\Lambda}(k)\mathbf{H}^H + \sigma^2\mathbf{I}, \tag{7.69}$$

where $\mathbf{\Lambda}(k)$ is the covariance matrix of the symbol given by

$$\mathbf{\Lambda}(k) = \text{diag}\left[\text{var}\left(s_n(k)\right)\right] \tag{7.70}$$

and $\mathbf{I}$ is the size-LM identity matrix. The MMSE filter output becomes

$$z_n(k) = \alpha_n(k)\mathbf{m'}_n^H(k)\left[\tilde{\mathbf{y}}(k) + \tilde{s}_n(k)\mathbf{h}_n\right] \tag{7.71}$$

with

$$\alpha_n(k) = \left(1 + \left(1 - \text{var}\left\{s_n(k)\right\}\right)\mathbf{m'}_n^H(k)\mathbf{h}_n\right)^{-1} \tag{7.72}$$

and

$$\mathbf{m'}_n^H(k) = \mathbf{h}_n^H\mathbf{\Sigma}^{-1}(k), \tag{7.73}$$

where the matrix inversion lemma was used.

Approximating the MMSE filter output as a Gaussian channel output, as in the SC/MMSE algorithm derivation for BPSK, symbol extrinsic probabilities $\mathrm{p}(z_n(k)|s_n(k) = s_i)$ with $s_i \in S$ using an equivalent Gaussian channel assumption at the output of the MMSE filter can be calculated as

$$\mathrm{p}\left(z_n(k)|s_n(k) = s_i\right) = \frac{1}{\nu_n^2(k)\pi} \exp\left(- \frac{\left| z_n(k) - \mu_n(k)s_i \right|^2}{\nu_n^2(k)} \right) \tag{7.74}$$

for each $s_i \in S$, where $\mu_n(k)$ and $\nu_n^2(k)$ are given by

$$\mu_n(k) = \alpha_n(k)\mathbf{m}'^H_n(n)\mathbf{h}_n \tag{7.75}$$

and

$$\nu_n^2(k) = \mu_n(k) - \mu_n^2(k), \tag{7.76}$$

respectively. Now, given the symbol extrinsic probabilities by (7.74) and the a priori symbol probabilities, the bit extrinsic LLR for the nth user's channel decoder can be calculated as

$$\lambda^e_{n,m}(k) = \ln \frac{\sum_{s_j \in S^1_{n,m}} \mathrm{p}\left(z_n(k)|s_n(k) = s_i\right) \exp\left(L_a(s_i)\right)}{\sum_{s_j \in S^0_{n,m}} \mathrm{p}\left(z_n(k)|s_n(k) = s_i\right) \exp\left(L_a(s_i)\right)}, \tag{7.77}$$

where $S^1_{n,m}$ and $S^0_{n,m}$ define the subsets of S where the bit $b_{n,m}(k)$ takes the values 1 and 0, respectively. The a priori symbol probability $L_a(s_i)$ for symbol $s_i \in S$ in (7.77) is based on all bit a priori LLRs, except for that particular bit m. Note that (7.34) is the result of defining (7.77) for BPSK modulation in logarithm domain.

7.6. Field measurement data-based simulations for SC/MMSE detectors

Current advances in multidimensional channel sounding techniques [15] make it possible to evaluate performances of signal processing algorithms in realistic conditions. Channel impulse response (CIR) sequences from a transmitter to each of the multiple antenna elements can be recorded. Recorded real-time channel sounding measurement data can be used for realistic offline simulations. Since the data represents a real propagation scenario, in-field performances can be accurately evaluated by running the measurement data through the signal processing algorithms of interest. This technique provides us with significantly more realistic performance estimates than model-based simulations. Figures 7.11a and 7.11b show, for a 3-by-3 MIMO with the transmitter and receiver's antenna spacings being 1.0λ and 1.2λ, respectively, the time series of the bit errors after 4 iterations, indicated by bars [16]. The measurement took place in Ilmenau, a suburban area in Germany. Through the measurement campaign, a series of the 3-by-3 MIMO channel impulse response was recorded, and the set of data was used in offline

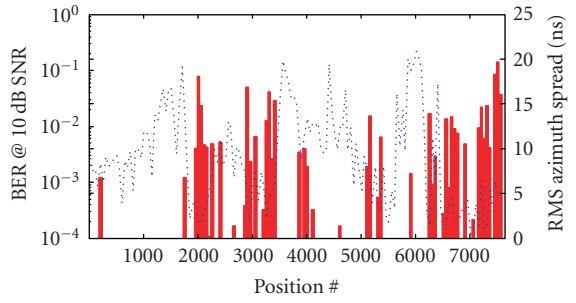

(a)

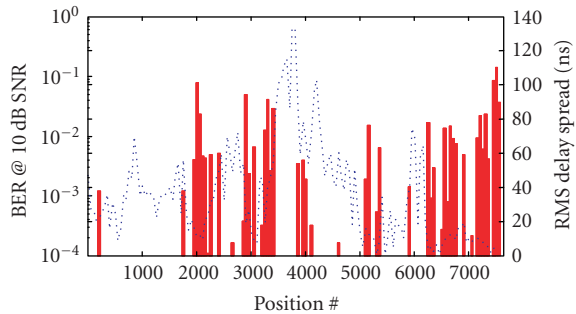

- 5.2 GHz carrier frequency
- 3×3 MIMO
- Transmit antenna spacing: 1.0λ
- Receive antenna spacing: 1.2λ
- λ: wave length
- 12 Mbps BPSK
- $K = 3$ half rate code
- Equalizer coverage: 5T
- Block random interleaver
- Max log map
- 4 iterations

(b)

FIGURE 7.11. The dotted lines in SC/MMSE BER performances versus delay and spatial spreads.

simulations to evaluate performance of the single-carrier SC/MMSE MIMO turbo equalizer. The dotted lines in Figures 7.11a and 7.11b indicate the root mean square (RMS) spatial and delay spreads, respectively. It is found that the larger the spreads in the spatial and temporal domains, the better the BER performance. This tendency agrees with the results of MIMO channel capacity analysis and measurements [17, 18].

Acknowledgments

The author of this chapter would like to express sincere appreciation to Mr. Kimmo Kansanen and Ms. Mariella Sarestoniemi of Center for Wireless Communications, University of Oulu, as well as Mr. Abe of NTT DoCoMo for their help in reviewing and editing this chapter.

Abbreviations

ISI	Intersymbol interference
SC/MMSE	Soft canceler followed by minimum mean square error
MLSE	Maximum-likelihood sequence estimation
MIMO	Multiple-input multiple-output
QAM	Quadrature amplitude modulation
CCI	Cochannel interference
LLR	Log-likelihood ratio
CDMA	Code division mutiple access
MSE	Mean square error
SISO	Soft-input soft-output
BPSK	Binary phase-shifted keying
AWGN	Additive white Gaussian noise
RSC	Recursive systematic codes
MMSE	Minimum mean squared error
MSE	Mean squared error
MRC	Maximum ratio combining
BER	Bit error rate
MUSD	Multiple user signal detector
RLS	Recursive least square
BICM	Bit-interleaved coded modulation
RMS	Root mean square

Bibliography

[1] C. Douillard, A. Picard, P. Didier, M. Jézéquel, C. Berrou, and A. Glavieux, "Iterative correction of intersymbol interference: turbo equalization," *European Trans. Telecommunications*, vol. 6, no. 5, pp. 507–511, 1995.

[2] X. Wang and H. V. Poor, "Iterative (turbo) soft interference cancellation and decoding for coded CDMA," *IEEE Trans. Commun.*, vol. 47, no. 7, pp. 1046–1061, 1999.

[3] R. Koetter, A. C. Singer, and M. Tuchler, "Turbo equalization," *IEEE Signal Processing Mag.*, vol. 21, no. 1, pp. 67–80, 2004.

[4] D. Reynolds and X. Wang, "Low-complexity turbo-equalization for diversity channels," *Signal Process.*, vol. 81, no. 5, pp. 989–995, 2001.

[5] B. Vucetic and J. Yuan, *Turbo Codes: Principles and Applications*, vol. 559 of *The Kluwer International Series in Engineering and Computer Science*, Kluwer Academic Publishers, Boston, Mass, USA, 2000.

[6] L. Hanzo, T. Liew, and B. Yeap, *Turbo Coding, Turbo Equalization, and Space-Time Coding for Transmission over Fading Channels*, John Wiley & Sons, New York, NY, USA, 2002.

[7] H. Omori, T. Asai, and T. Matsumoto, "A matched filter approximation for SC/MMSE iterative equalizers," *IEEE Commun. Lett.*, vol. 5, no. 7, pp. 310–312, 2001.

[8] T. Abe and T. Matsumoto, "Space-time turbo equalization in frequency-selective MIMO channels," *IEEE Trans. Veh. Technol.*, vol. 52, no. 3, pp. 469–475, 2003.

[9] T. Abe, S. Tomisato, and T. Matsumoto, "A MIMO turbo equalizer for frequency-selective channels with unknown interference," *IEEE Trans. Veh. Technol.*, vol. 52, no. 3, pp. 476–482, 2003.

[10] N. Veselinovic, T. Matsumoto, and M. Juntti, "Iterative receivers for STTrC-coded MIMO turbo equalization," in *The IEEE 59th Semiannual Vehicular Technology Conference (VTC 2004-Spring)*, Milan, Italy, May 2004.

[11] N. Veselinovic, T. Matsumoto, and M. Juntti, "Iterative MIMO turbo multiuser detection and equalization for STTrC-coded systems with unknown interference," *EURASIP Journal on Wireless Communications and Networking*, vol. 2004, no. 2, special issue on Multiuser MIMO Networks, pp. 309–321, 2004.

[12] K. Kansanen and T. Matsumoto, "A computationally efficient MIMO turbo-equaliser," in *The IEEE 57th Semiannual Vehicular Technology Conference (VTC 2003-Spring)*, vol. 1, pp. 277–281, Jeju, Korea, April 2003.

[13] S. Haykin, *Adaptive Filter Theory*, Prentice Hall Information and System Sciences Series. Prentice Hall International, Englewood Cliffs, NJ, USA, 2nd edition, 1991.

[14] A. Dejonghe and L. Vandendorpe, "Turbo-equalization for multilevel modulation: an efficient low-complexity scheme," in *IEEE International Conference on Communications*, vol. 3, pp. 1863–1867, New York, NY, USA, April–May 2002.

[15] R. S. Thomä, D. Hampicke, A. Richter, et al., "Identification of time-variant directional mobile radio channels," *IEEE Trans. Instrumentation and Measurement*, vol. 49, no. 2, pp. 357–364, 2000.

[16] T. Matsumoto, J. Ylitalo, and M. Juntti, "Overview and recent challenges towards multiple-input multiple-output communications systems," *IEEE Vehicular Technology Society Newsletter*, vol. 50, no. 2, pp. 4–9, 2003.

[17] U. Trautwein, T. Matsumoto, C. Schneider, and R. Thoma, "Exploring the performance of turbo MIMO equalization in real field scenarios," in *The 5th International Symposium on Wireless Personal Multimedia Communications*, vol. 2, pp. 422–426, Honolulu, Hawaii, USA, October 2002.

[18] C. Schneider, R. Thoma, U. Trautwein, and T. Matsumoto, "The dependency of turbo MIMO equalizer performance on the spatial and temporal multipath channel structure—a measurement based evaluation," in *The IEEE 57th Semiannual Vehicular Technology Conference (VTC 2003-Spring)*, vol. 2, pp. 808–812, Jeju, Korea, April 2003.

Tad Matsumoto: Center for Wireless Communications, University of Oulu, P.O. Box 4500, 90014, Oulu, Finland

Email: tadashi.matsumoto@ees2.oulu.fiw

8 Architectures for reference-based and blind multilayer detection

Karl-Dirk Kammeyer, Jürgen Rinas, and Dirk Wübben

Multilayer systems are predestinated for high-rate wireless data transmission, where the source simultaneously radiates several data streams via multiple transmit antennas. The main computational effort of transmission schemes of this type is required at the receiver for separating the superimposed information signals. We distinguish between two types of detection schemes, where the first type requires channel knowledge for the receiver and the second type performs a totally blind data estimation.

Recently, several detection algorithms have been investigated under the assumption of known channel state information at the receiver. This channel knowledge may be obtained by pilot-aided transmission and channel estimation. For these reference-aided transmission the well-known linear detection schemes are generally outperformed by successive detection schemes, namely, the V-BLAST algorithm. In order to decrease the required computational complexity of this nonlinear scheme, we will restate it by applying the QR decomposition of the channel matrix. This yields the same successive interference cancelation (SIC) detection algorithm with complexity comparable to linear detection.

A detection approach avoiding pilot symbols is given by the concept of blind source separation (BSS). BBS approaches normally lead to linear spatial filters. In order to achieve the performance of reference-based detection, an iterative combination of BSS and nonlinear SIC is proposed. Furthermore, the application of BSS is favorable in many practical cases, as the sophisticated MIMO estimation problems can be transformed to well-known solutions for SISO communication.

The performances of the discussed schemes are demonstrated by simulations as well as by measurement results.

8.1. System model

Within this chapter, we consider the single-user multiple-antenna system in Figure 8.1 with N_T transmit and $N_R \geq N_T$ receive antennas in a non-frequency-selective environment. At the transmitter, the binary information data is demultiplexed into N_T data substreams of equal length and mapped onto PSK or QAM symbols of

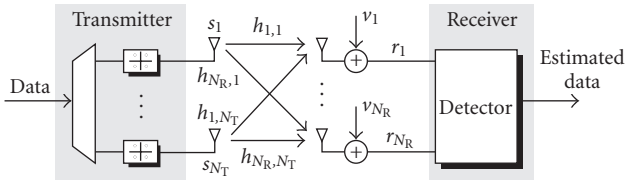

FIGURE 8.1. Model of a MIMO system with N_T transmit and N_R receive antennas.

the alphabet $\mathcal{A}$ with cardinality $|\mathcal{A}|$. These substreams are organized in frames of length M and simultaneously transmitted over the N_T antennas. Thus, the investigated scheme corresponds to the V-BLAST (vertical Bell Labs layered space-time) architecture introduced in [1, 2].

In order to describe the MIMO system, the discrete-time complex baseband model is investigated. Let $s_p[m]$ denote the symbol transmitted at time instant $1 \le m \le M$ from antenna $1 \le p \le N_T$. By defining the $N_T \times 1$ transmit signal vector $\mathbf{s}[m] = [s_1[m] \cdots s_{N_T}[m]]^T$ the corresponding $N_R \times 1$ receive signal vector $\mathbf{r}[m] = [r_1[m] \cdots r_{N_R}[m]]^T$ is given by

$$\mathbf{r}[m] = \mathbf{H}\mathbf{s}[m] + \mathbf{v}[m]. \tag{8.1}$$

In (8.1), $\mathbf{v}[m] = [v_1[m] \cdots v_{N_R}[m]]^T$ represents white Gaussian noise of variance σ_v^2 observed at the N_R receive antennas while the average transmit power of each antenna is normalized to one, that is,[1] $\mathrm{E}\{\mathbf{s}[m]\mathbf{s}^H[m']\} = \mathbf{I}_{N_T}\delta(m-m')$ and $\mathrm{E}\{\mathbf{v}[m]\mathbf{v}^H[m']\} = \sigma_v^2\mathbf{I}_{N_R}\delta(m-m')$. The $N_R \times N_T$ channel matrix $\mathbf{H} = [\mathbf{h}_1, \ldots, \mathbf{h}_{N_T}]$ with column vectors $\mathbf{h}_p$ contains uncorrelated complex Gaussian fading gains $h_{k,p}$ with unit variance. We assume that the channel matrix $\mathbf{H}$ is constant over a frame of length M and changes independently from one frame to another (*block fading channel*). As the time slots m in (8.1) are independent of each other, we will drop the time index m in the sequel resulting in

$$\mathbf{r} = \mathbf{H}\mathbf{s} + \mathbf{v}. \tag{8.2}$$

In order to investigate the maximum performance achievable, we introduce the singular value decomposition (SVD) $\mathbf{H} = \mathbf{U}\mathbf{\Sigma}\mathbf{V}^H$ of the channel matrix $\mathbf{H}$, where $\mathbf{U}$ and $\mathbf{V}$ are unitary matrices and the diagonal matrix $\mathbf{\Sigma} = \mathrm{diag}\,[\sigma_1, \ldots, \sigma_{N_T}]$ contains the singular values $\sigma_p \ge 0$ [3]. By calculating the filtered receive vector

$$\mathbf{r}' = \mathbf{U}^H\mathbf{r} = \mathbf{\Sigma}\underbrace{\mathbf{V}^H\mathbf{s}}_{\mathbf{s}'} + \underbrace{\mathbf{U}^H\mathbf{v}}_{\mathbf{v}'} = \mathbf{\Sigma}\mathbf{s}' + \mathbf{v}' \tag{8.3}$$

the MIMO system (8.2) is decomposed into N_T parallel single-input single-output

[1] δ defines the Kronecker delta with $\delta(0) = 1$ and $\delta(n) = 0$ for $n \neq 0$.

(SISO) systems

$$r'_p = \sigma_p s'_p + \nu'_p, \tag{8.4}$$

where s'_p denotes a modified transmit signal. Obviously, information can only be transmitted over those equivalent SISO channels with nonzero singular values σ_p. If the number of transmission layers exceeds the number of *strong* singular values, the performance degrades. This effect is demonstrated in Section 8.4 with respect to measurements.

Several schemes have been investigated to estimate the transmitted information at the receiver. One class of detection algorithms requires an estimate of the channel state information (CSI), whereas a second class applies higher-order statistics to separate the distinct transmit signals. In the sequel both detection principles are investigated and a hybrid scheme exploiting the advantages of each principle is proposed.

8.2. Reference-based detection algorithms

Within this section we discuss several detection schemes under the assumption of perfect channel state information at the receiver. Therefore, the achieved performances give the upper bound for the blind and non-blind schemes in the subsequent section.

8.2.1. Maximum-likelihood detection

In order to detect the transmitted information, it would be optimal to use a maximum-likelihood (ML) detector. For each time instant m this optimum ML detector searches over the whole set of transmit signals $\mathbf{s} \in \mathcal{A}^{N_T}$, and decides in favor of the transmit signal $\hat{\mathbf{s}}$ that minimizes the Euclidean distance to the receive vector $\mathbf{r}$, that is,

$$\hat{\mathbf{s}}_{\mathrm{ML}} = \arg \min_{\mathbf{s} \in \mathcal{A}^{N_T}} \|\mathbf{r} - \mathbf{H}\mathbf{s}\|^2. \tag{8.5}$$

As the computational effort for each time instant is of order $|\mathcal{A}|^{N_T}$, brute force ML detection is not feasible for larger number of transmit antennas or higher modulation schemes. As an example, for a system with $N_T = 4$ transmit antennas and 16-QAM modulation, the ML detection requires the computation of $16^4 = 65536$ Euclidean distances for each transmit vector.

A feasible alternative is the application of the sphere detector [4], which restricts the search space to a sphere around $\mathbf{r}$. However, the computational complexity is still high in comparison to simple but suboptimal linear detection or successive interference cancelation. In the sequel, we investigate these suboptimum linear and nonlinear schemes. The advantage of both strategies is that the computational overhead is only required once for each transmitted frame, so for a large frame

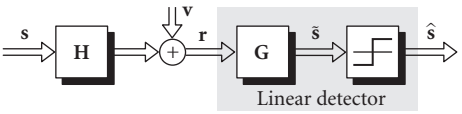

FIGURE 8.2. Block diagram of a MIMO scheme with linear detection.

length, the effort for each signal vector is very small. Furthermore, these suboptimum detection schemes may achieve near-ML performance in combination with lattice reduction, for example, see [5, 6].

8.2.2. Linear detection

The linear detector (LD) is the simplest approach for estimating the transmitted signals. The receive signal vector $\mathbf{r}$ is multiplied with a filter matrix $\mathbf{G}$, followed by a parallel decision on all layers, as shown in the block diagram in Figure 8.2.

In case of the zero-forcing (ZF) solution, the mutual interference between the layers is completely suppressed. This is accomplished by the Moore-Penrose pseudoinverse (denoted by $(\cdot)^+$) of the channel matrix

$$\mathbf{G}_{\mathrm{ZF}} = \mathbf{H}^+ = \left(\mathbf{H}^H\mathbf{H}\right)^{-1}\mathbf{H}^H, \tag{8.6}$$

where we assume that $\mathbf{H}$ has full column rank. The decision step consists of mapping each element of the filter output vector

$$\tilde{\mathbf{s}} = \mathbf{G}_{\mathrm{ZF}}\mathbf{r} = \mathbf{H}^+\mathbf{r} = \mathbf{s} + \left(\mathbf{H}^H\mathbf{H}\right)^{-1}\mathbf{H}^H\mathbf{v} \tag{8.7}$$

onto an element of the symbol alphabet $\mathcal{A}$ by an elementwise minimum distance quantization, that is, $\hat{s}_p = \mathcal{Q}_{\mathcal{A}}\{\tilde{s}_p\}$. The estimation errors of the different layers correspond to the main diagonal elements of the error covariance matrix

$$\mathbf{\Phi}_{ee,\mathrm{ZF}} = \mathrm{E}\{(\tilde{\mathbf{s}} - \mathbf{s})(\tilde{\mathbf{s}} - \mathbf{s})^H\} = \sigma_v^2\left(\mathbf{H}^H\mathbf{H}\right)^{-1}, \tag{8.8}$$

which equals the covariance matrix of the noise after the receive filter. It is obvious that small eigenvalues of $\mathbf{H}^H\mathbf{H}$ will lead to large errors due to noise amplification.

In order to improve the performance of the linear detector the noise term can be included in the design of the filter matrix $\mathbf{G}$. This is done by the minimum mean square error (MMSE) detector, where the filter

$$\mathbf{G}_{\mathrm{MMSE}} = \left(\mathbf{H}^H\mathbf{H} + \sigma_v^2\mathbf{I}_{N_{\mathrm{T}}}\right)^{-1}\mathbf{H}^H \tag{8.9}$$

represents a trade-off between noise amplification and interference suppression. The resulting filter output signal is given by

$$\tilde{\mathbf{s}} = \mathbf{G}_{\mathrm{MMSE}}\mathbf{r} = \left(\mathbf{H}^H\mathbf{H} + \sigma_v^2\mathbf{I}_{N_{\mathrm{T}}}\right)^{-1}\mathbf{H}^H\mathbf{r} \tag{8.10}$$

and the error covariance matrix is found to be

$$\mathbf{\Phi}_{ee,\mathrm{MMSE}} = \sigma_v^2 \left(\mathbf{H}^H \mathbf{H} + \sigma_v^2 \mathbf{I}_{N_\mathrm{T}}\right)^{-1}. \tag{8.11}$$

For the derivation of the nonlinear MMSE detection algorithm considered later it will be useful to point out the correspondence of the MMSE and the ZF criterion. To this end, we define an $(N_\mathrm{T} + N_\mathrm{R}) \times N_\mathrm{T}$ *extended* channel matrix[2] $\underline{\mathbf{H}}$ and an $(N_\mathrm{T} + N_\mathrm{R}) \times 1$ *extended* receive vector $\underline{\mathbf{r}}$ through [7, 8]

$$\underline{\mathbf{H}} = \begin{bmatrix} \mathbf{H} \\ \sigma_v \mathbf{I}_{N_\mathrm{T}} \end{bmatrix}, \qquad \underline{\mathbf{r}} = \begin{bmatrix} \mathbf{r} \\ \mathbf{0}_{N_\mathrm{T},1} \end{bmatrix}. \tag{8.12}$$

With these definitions we can rewrite the output of the MMSE filter (8.10) as

$$\tilde{\mathbf{s}} = \left(\begin{bmatrix} \mathbf{H}^H \sigma_v \mathbf{I}_{N_\mathrm{T}} \end{bmatrix} \begin{bmatrix} \mathbf{H} \\ \sigma_v \mathbf{I}_{N_\mathrm{T}} \end{bmatrix} \right)^{-1} \begin{bmatrix} \mathbf{H}^H \sigma_v \mathbf{I}_{N_\mathrm{T}} \end{bmatrix} \begin{bmatrix} \mathbf{r} \\ \mathbf{0}_{N_\mathrm{T},1} \end{bmatrix} \tag{8.13}$$

$$= \left(\underline{\mathbf{H}}^H \underline{\mathbf{H}}\right)^{-1} \underline{\mathbf{H}}^H \underline{\mathbf{r}} = \underline{\mathbf{H}}^+ \underline{\mathbf{r}}. \tag{8.14}$$

Furthermore, the error covariance matrix (8.11) becomes

$$\mathbf{\Phi}_{ee,\mathrm{MMSE}} = \sigma_v^2 \left(\underline{\mathbf{H}}^H \underline{\mathbf{H}}\right)^{-1}. \tag{8.15}$$

Comparing (8.14) and (8.15) to the corresponding expression for the linear zero-forcing detector in (8.7) and (8.8), the only difference is that the channel matrix $\mathbf{H}$ has been replaced by $\underline{\mathbf{H}}$. Thus, an MMSE detector can be interpreted as a ZF detector with respect to the extended system model. This simple observation will be important for incorporating the MMSE criterion into the nonlinear detection algorithm in the sequel.

8.2.3. Successive interference cancelation detection

Instead of detecting the transmitted symbols in parallel, the nonlinear successive interference cancelation (SIC) schemes detect the signals one after another. Similar to a decision-feedback equalizer, the estimated interference of already detected signals is subtracted from the receive signal $\mathbf{r}$ before detecting the remaining signals. Due to the effect of error propagation, the sequence of detecting the layers has a strong impact on the overall error performance [2].

V-BLAST algorithm. The original V-BLAST detection algorithm [2] is based on the linear zero-forcing solution (8.6), but detects the signals one after another and not in parallel. In order to achieve the best performance, it is optimal to choose always the layer with the largest *postdetection* signal-to-noise ratio (SNR), or equivalently with the smallest estimation error [2]. By rewriting the error covariance (8.8) as $\mathbf{\Phi}_{ee,\mathrm{ZF}} = \sigma_v^2 \mathbf{G}_\mathrm{ZF} \mathbf{G}_\mathrm{ZF}^H$, the pth diagonal element corresponds to $\sigma_v^2 \mathbf{g}_{(p)} \mathbf{g}_{(p)}^H$,

[2]Henceforth, *underlined* variables indicate the application of this *extended* MMSE system model.

with $\mathbf{g}_{(p)}$ denoting row p of $\mathbf{G}_{\mathrm{ZF}}$. Consequently, the smallest estimation error corresponds to the row of $\mathbf{G}_{\mathrm{ZF}}$ with minimum Euclidean norm. Assuming that row i has the smallest norm in the first detection step, the corresponding filter output signal is given by

$$\tilde{s}_i = \mathbf{g}_{(i)}\mathbf{r} = s_i + \mathbf{g}_{(i)}\mathbf{v} \tag{8.16}$$

and the estimated signal $\hat{s}_i = \mathcal{Q}_{\mathcal{A}}\{\tilde{s}_i\}$ is found by quantization. The estimated interference caused by this signal is then subtracted from the receive signal vector $\mathbf{r}$ and the ith column is removed from the channel matrix, leading to a system with only $N_{\mathrm{T}} - 1$ transmit antennas. This procedure of nulling and canceling is repeated for the reduced systems until all signals are detected.

The adaptation to the MMSE criterion was presented in several publications (e.g., [9]), where the optimal detection sequence maximizes the signal-to-interference-and-noise ratio (SINR) in each decision step. Again, this corresponds to choosing the layer with the smallest estimation error in (8.11) or (8.15). Using similar arguments as before, the layer with highest SINR corresponds to the row of $\underline{\mathbf{H}}^{+}$ with minimum norm. It is worth to note that this best layer is not necessarily associated with the row of $\mathbf{G}_{\mathrm{MMSE}}$ with minimum norm, as $\mathbf{G}_{\mathrm{MMSE}}$ is not a square root of $\mathbf{\Phi}_{ee,\mathrm{MMSE}}$ [10]. Consequently, a detector applying the ZF sorting criterion based on the Euclidean row norm of $\mathbf{G}_{\mathrm{MMSE}}$ in the MMSE case will lead to a significant performance loss.

The main drawback of the V-BLAST detection algorithm lies in the computational complexity, as it requires multiple calculations of the pseudoinverse of the channel matrix in the ZF case [11] or of the extended channel matrix in the MMSE case. Thus, several schemes with reduced complexity have been proposed, for example, [8, 12, 13, 14].

Within this section, we consider the scheme presented in [14] and extended in [8]. To this end, we restate the successive interference cancelation scheme using the QR decomposition of the channel matrix, for the ZF as well as the MMSE case. In order to efficiently achieve an optimized detection order, we will then introduce a suboptimum approach, the so-called sorted QR decomposition. Later on, we extend this simple scheme by the postsorting algorithm, yielding the perfect detection sequence and thereby the performance of the V-BLAST scheme. The main advantage of this combined scheme comes with the complexity reduction, as it only requires a fraction of the computational effort of the original V-BLAST algorithm [8, 11].

ZF-SIC with QR decomposition. It was shown in several publications, for example, [11, 14, 15, 16, 17], that the zero-forcing solution of the V-BLAST algorithm can be restated in terms of the QR decomposition of the channel matrix $\mathbf{H} = \mathbf{QR}$, where the $N_{\mathrm{R}} \times N_{\mathrm{T}}$ matrix $\mathbf{Q}$ has unitary columns and the $N_{\mathrm{T}} \times N_{\mathrm{T}}$ matrix $\mathbf{R} = (r_{i,j})_{1\le i,j\le N_{\mathrm{T}}}$ is upper triangular [3]. Multiplying the receive signal $\mathbf{r}$ with $\mathbf{Q}^{H}$ yields the sufficient statistic

$$\tilde{\mathbf{s}} = \mathbf{Q}^{H}\mathbf{r} = \mathbf{Rs} + \tilde{\mathbf{v}} \tag{8.17}$$

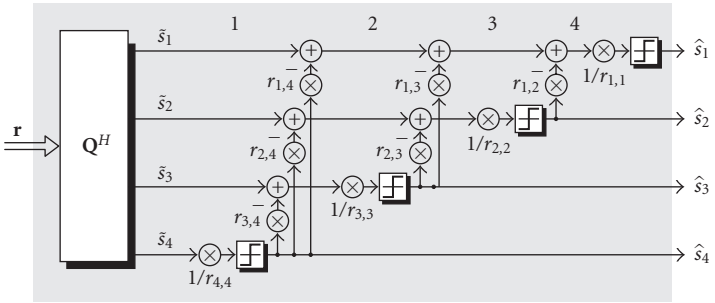

FIGURE 8.3. Block diagram of the successive interference cancelation detector for a system with $N_T = 4$ transmit antennas.

for the estimation of transmit vector $\mathbf{s}$. As $\mathbf{Q}$ is a unitary matrix, the statistical properties of the Gaussian noise term $\tilde{\mathbf{v}} = \mathbf{Q}^H\mathbf{v}$ remain unchanged and in a componentwise notation (8.17) becomes

$$\begin{bmatrix} \tilde{s}_1 \\ \tilde{s}_2 \\ \vdots \\ \tilde{s}_{N_T} \end{bmatrix} = \begin{bmatrix} r_{1,1} & r_{1,2} & \cdots & r_{1,N_T} \\ \vdots & r_{2,2} & & \vdots \\ \vdots & & \ddots & \vdots \\ \mathbf{0} & \cdots & & r_{N_T,N_T} \end{bmatrix} \begin{bmatrix} s_1 \\ s_2 \\ \vdots \\ s_{N_T} \end{bmatrix} + \begin{bmatrix} \tilde{v}_1 \\ \tilde{v}_2 \\ \vdots \\ \tilde{v}_{N_T} \end{bmatrix}. \tag{8.18}$$

Due to the upper triangular structure of $\mathbf{R}$, the pth element of $\tilde{\mathbf{s}}$ is given by

$$\tilde{s}_p = r_{p,p}s_p + \sum_{i=p+1}^{N_T} r_{p,i}s_i + \tilde{v}_p \tag{8.19}$$

and is free of interference from layers $1, \ldots, p-1$. Thus, $\tilde{s}_{N_T}$ is totally free of interference and can be used to estimate s_{N_T} after appropriate scaling with $1/r_{N_T,N_T}$. Proceeding with $\tilde{s}_{N_T-1}, \ldots, \tilde{s}_1$ and assuming correct previous decisions, the interference can be perfectly canceled in each step. Then it follows from (8.19) that the SNR of layer p is determined by the diagonal element $|r_{p,p}|^2$. For a system with $N_T = 4$ transmit antennas the successive detection and cancelation procedure is shown in Figure 8.3.

The signal spaces of the corresponding detection and interference cancelation steps are shown in Figure 8.4 (achieved with the experimental equipment described in Section 8.4). The first depicted column (step 1) corresponds to $\tilde{\mathbf{s}}$ (scaled by $r_{4,4}$ for illustration purpose), the output of the filter matrix $\mathbf{Q}^H$. Obviously layer 4 is free of interference and can be estimated, whereas the other layers are still affected by interference. The second column shows the signal space after subtracting the estimated interference, that is, step 2 in Figure 8.3. Thus, layer 3 may be detected. The succeeding steps are straightforward.

MMSE-SIC with QR decomposition. In order to extend the QR-based detection with respect to the MMSE criterion, we can exploit the similarity of linear ZF and

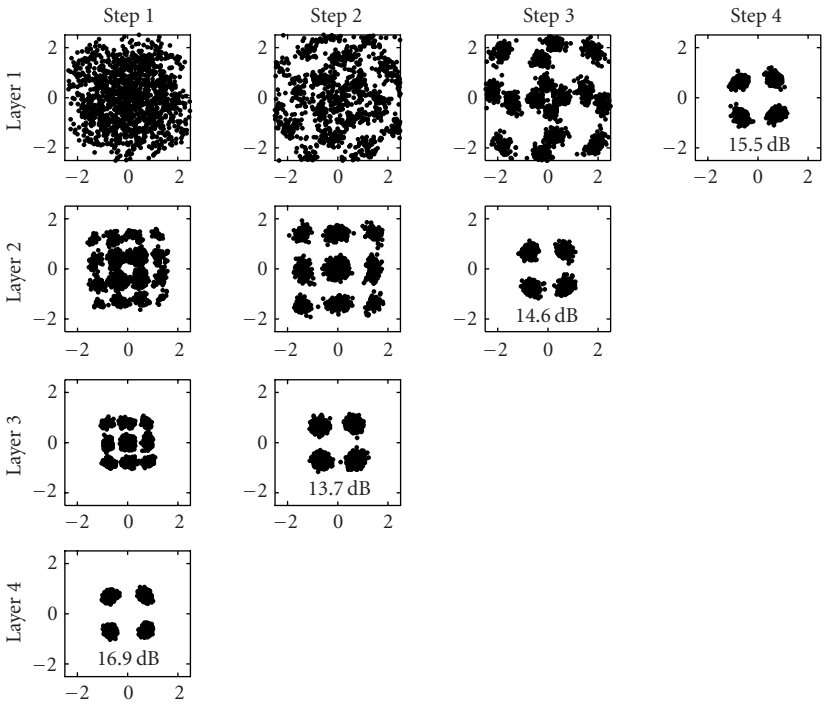

FIGURE 8.4. Signal space of each layer at the distinct steps of the successive interference cancelation for a system with $N_T = 4$ transmit antennas, $N_R = 4$ receive antennas and QPSK modulation with estimated SNR.

MMSE detection. For this purpose, we introduce the QR decomposition of the extended channel matrix (8.12)

$$\underline{\mathbf{H}} = \begin{bmatrix} \mathbf{H} \\ \sigma_v \mathbf{I}_{N_T} \end{bmatrix} = \underline{\mathbf{Q}}\underline{\mathbf{R}} = \begin{bmatrix} \mathbf{Q}_1 \\ \mathbf{Q}_2 \end{bmatrix} \underline{\mathbf{R}} = \begin{bmatrix} \mathbf{Q}_1\underline{\mathbf{R}} \\ \mathbf{Q}_2\underline{\mathbf{R}} \end{bmatrix}, \tag{8.20}$$

where the unitary $(N_T+N_R)\times N_T$ matrix $\underline{\mathbf{Q}}$ was partitioned into the $N_R \times N_T$ matrix $\mathbf{Q}_1$ and the $N_T \times N_T$ matrix $\mathbf{Q}_2$ and $\underline{\mathbf{R}} = (\underline{r}_{i,j})_{1\le i,j\le N_T}$ denotes the corresponding upper triangular matrix. Obviously,

$$\underline{\mathbf{Q}}^H\underline{\mathbf{H}} = \mathbf{Q}_1^H\mathbf{H} + \sigma_v\mathbf{Q}_2^H = \underline{\mathbf{R}} \tag{8.21}$$

holds and from the relation $\sigma_v\mathbf{I}_{N_T} = \mathbf{Q}_2\underline{\mathbf{R}}$ in (8.20), it follows that

$$\underline{\mathbf{R}}^{-1} = \frac{1}{\sigma_v}\mathbf{Q}_2, \tag{8.22}$$

that is, the inverse $\underline{\mathbf{R}}^{-1}$ is a by-product of the QR decomposition and $\mathbf{Q}_2$ is an upper triangular matrix. This relation will be useful for the postsorting algorithm

proposed later on. Using (8.21), the filtered receive vector becomes

$$\tilde{\mathbf{s}} = \underline{\mathbf{Q}}^H \underline{\mathbf{r}} = \mathbf{Q}_1^H \mathbf{r} = \underline{\mathbf{R}}\mathbf{s} - \sigma_v \mathbf{Q}_2^H \mathbf{s} + \mathbf{Q}_1^H \mathbf{v}. \tag{8.23}$$

The second term on the right-hand side of (8.23) including the lower triangular matrix $\mathbf{Q}_2^H$ constitutes the remaining interference that cannot be removed by the successive interference cancelation procedure. This points out the trade-off between noise amplification and interference suppression.

As mentioned in the discussion of the V-BLAST algorithm, the order of detection is crucial due to error propagation. Within the QR-based SIC the detection order can be changed by permuting the columns of $\underline{\mathbf{H}}$ and the corresponding elements in $\mathbf{s}$. The optimum detection sequence now maximizes the signal-to-interference-and-noise ratio (SINR) for each layer, leading to a minimum estimation error for the corresponding detection step. The estimation errors of the different layers in the first detection step correspond to the diagonal elements of the error covariance matrix (8.15)

$$\mathbf{\Phi}_{ee,\mathrm{MMSE}} = \sigma_v^2 \left(\underline{\mathbf{H}}^H \underline{\mathbf{H}}\right)^{-1} = \sigma_v^2 \underline{\mathbf{R}}^{-1} \underline{\mathbf{R}}^{-H}. \tag{8.24}$$

The estimation error for layer p after perfect interference cancelation is given by $\sigma_v^2/|\underline{r}_{p,p}|^2$. Thus, it is optimal to choose the permutation of $\underline{\mathbf{H}}$ that maximizes $|\underline{r}_{p,p}|$ in each detection step, that is, in the order $N_\mathrm{T}, \ldots, 1$. The algorithm proposed in the next paragraph determines an improved detection sequence within a single *sorted* QR decomposition and thereby significantly reduces the computational complexity in comparison to the V-BLAST algorithm.

Sorted QR decomposition (SQRD). In order to obtain the optimal detection order, first $|\underline{r}_{N_\mathrm{T},N_\mathrm{T}}|$ has to be maximized over all possible permutations of the columns of the extended channel matrix $\underline{\mathbf{H}}$, followed by $|\underline{r}_{N_\mathrm{T}-1,N_\mathrm{T}-1}|$, and so on. Unfortunately, using standard algorithms for the QR decomposition, the diagonal elements of $\underline{\mathbf{R}}$ are calculated just in the opposite order, starting with $\underline{r}_{1,1}$. This makes finding the optimal order of detection a difficult task.

A heuristic approach of arranging the order of detection within the QR decomposition for the ZF detection was presented in [11, 14] and extended to the MMSE criterion in [8, 16]. This sorted QR decomposition algorithm is basically an extension to the modified Gram-Schmidt procedure by reordering the columns of the channel matrix prior to each orthogonalization step. The fundamental idea is based on the fact that the determinant of the Gram matrix $\underline{\mathbf{H}}^H \underline{\mathbf{H}}$, that is, the squared volume of the parallelepiped spanned by $\underline{\mathbf{H}}$, is invariant to column exchanges [3]. Since this determinant can be rewritten as

$$\det\left(\underline{\mathbf{H}}^H \underline{\mathbf{H}}\right) = \det\left(\underline{\mathbf{R}}^H \underline{\mathbf{R}}\right) = \prod_{p=1}^{N_\mathrm{T}} \left|\underline{r}_{p,p}\right|^2 = \mathrm{const}, \tag{8.25}$$

the product $\underline{r}_{1,1} \cdot \ldots \cdot \underline{r}_{N_\mathrm{T},N_\mathrm{T}}$ is also independent of the chosen column order. Thus, the basic idea is to exchange the columns to *minimize* the diagonal elements $\underline{r}_{p,p}$

(1) $\underline{\mathbf{R}} = \mathbf{0}, \underline{\mathbf{Q}} = \underline{\mathbf{H}}, \mathbf{p} = [1 \cdots N_T]$
(2) for $i = 1, \ldots, N_T$
(3) $\quad \mathbf{norm}(i) = \|\underline{\mathbf{Q}}(:, i)\|^2$
(4) end
(5) for $i = 1, \ldots, N_T$
(6) $\quad k_i = \arg\min \mathbf{norm}(i, \ldots, N_T)$
(7) $\quad$ exchange columns i and k_i in
$\quad\quad \underline{\mathbf{R}}$, $\mathbf{p}$, $\mathbf{norm}$ and in the first
$\quad\quad N_R + i - 1$ rows of $\underline{\mathbf{Q}}$
(8) $\quad \underline{\mathbf{R}}(i, i) = \sqrt{\mathbf{norm}(i)}$
(9) $\quad \underline{\mathbf{Q}}(:, i) = \underline{\mathbf{Q}}(:, i)/\underline{\mathbf{R}}(i, i)$
(10) $\quad$ for $k = i + 1, \ldots, N_T$
(11) $\quad\quad \underline{\mathbf{R}}(i, k) = \underline{\mathbf{Q}}(:, i)^H \underline{\mathbf{Q}}(:, k)$
(12) $\quad\quad \underline{\mathbf{Q}}(:, k) := \underline{\mathbf{Q}}(:, k) - \underline{\mathbf{R}}(i, k)\underline{\mathbf{Q}}(:, i)$
(13) $\quad\quad \mathbf{norm}(k) := \mathbf{norm}(k) - \underline{\mathbf{R}}(i, k)^2$
(14) $\quad$ end
(15) end

Algorithm 8.1. Pseudocode of MMSE-SQRD-algorithm.

in the order of their calculation, that is, in the sequence $\underline{r}_{1,1}, \ldots, \underline{r}_{N_T,N_T}$. As the product is constant, small $\underline{r}_{p,p}$ in the upper left part should lead to large elements in the lower right part of $\underline{\mathbf{R}}$.

Now, $\underline{r}_{1,1}$ is simply the norm of the column vector $\underline{\mathbf{h}}_1$, so the first optimization in the SQRD algorithm consists merely of permuting the column of $\underline{\mathbf{H}}$ with minimum norm to this position. During the following orthogonalization of the vectors $\underline{\mathbf{h}}_2, \ldots, \underline{\mathbf{h}}_{N_T}$ with respect to the normalized vector $\underline{\mathbf{h}}_1$, the first row of $\underline{\mathbf{R}}$ is obtained. Next, $\underline{r}_{2,2}$ is determined in a similar fashion from the remaining $N_T - 1$ orthogonalized vectors, and so forth. Thus, the extended channel matrix $\underline{\mathbf{H}}$ is successively transformed into the matrix $\underline{\mathbf{Q}}$ associated with the desired ordering, while the corresponding $\underline{\mathbf{R}}$ is calculated row by row. Note that the column norms have to be calculated only once in the beginning and can be easily updated afterwards. Hence, the computational overhead due to sorting is negligible. An in-place description of the whole MMSE-SQRD algorithm is given in[3] Algorithm 8.1, with vector $\mathbf{p}$ denoting the permutation of the columns of $\mathbf{H}$.

The reordering steps (lines (6) and (7) within the algorithm) require only a very small computational overhead compared to an unsorted QR decomposition [8]. However, the SQRD ordering strategy does not always lead to the perfect detection sequence, but in many cases of interest the performance degradation is small compared to the reduced complexity. Furthermore, whenever SQRD fails to find the optimal order, the postsorting algorithm described in the sequel assures the optimal sorting and thereby achieves the same performance as V-BLAST.

[3] $\mathbf{A}(a : b, c : d)$ denotes the submatrix of $\mathbf{A}$ with elements from rows $a, \ldots, b$ and columns $c, \ldots, d$.

Postsorting algorithm (PSA). In this section we briefly present the postsorting algorithm (PSA) introduced in [8]. In order to motivate the PSA, the structure of the error covariance matrix in case of optimal sorting is investigated in more detail. Due to the relation $\mathbf{Q}_2 = \sigma_v \underline{\mathbf{R}}^{-1}$ introduced in (8.22) the error covariance matrix (8.24) is given by

$$\mathbf{\Phi}_{ee,\mathrm{MMSE}} = \mathbf{Q}_2 \mathbf{Q}_2^H, \tag{8.26}$$

that is, $\mathbf{Q}_2$ is a square root of $\mathbf{\Phi}_{ee,\mathrm{MMSE}}$ [7]. Thus, the pth diagonal element of $\mathbf{\Phi}_{ee,\mathrm{MMSE}}$ is proportional to the norm of the pth row of $\mathbf{Q}_2$. Recalling the optimal ordering criterion, the last row of $\mathbf{Q}_2$ must have minimum norm of all rows. Assume that this condition is fulfiled, then the last row of the upper left $N_\mathrm{T}-1 \times N_\mathrm{T}-1$ submatrix of $\mathbf{Q}_2$ must have minimum norm of all rows of this submatrix. In case of the correct sorting this condition is accomplished by all upper left submatrices.

Now assume that this condition is not fulfiled for the matrix $\mathbf{Q}_2$. Then the row with minimum norm and the last row (as well as the corresponding elements of $\mathbf{p}$) need to be exchanged at the expense of destroying the upper triangular structure. However, by right multiplying the permuted version of $\mathbf{Q}_2$ with a proper unitary $N_\mathrm{T} \times N_\mathrm{T}$ Householder reflection matrix[4] $\mathbf{\Theta}$, a block triangular matrix is achieved. Finally, $\mathbf{Q}_1$ has to be updated to $\mathbf{Q}_1\mathbf{\Theta}$. Instead of permuting columns of $\underline{\mathbf{R}}$ and left multiplying with $\mathbf{\Theta}^H$ in each step, we can alternatively invert $\mathbf{Q}_2$ at the end of the PSA, due to the relation $\underline{\mathbf{R}} = 1/\sigma_v \mathbf{Q}_2^{-1}$. These ordering and reflection steps are then iterated for the upper left $(N_\mathrm{T} - 1) \times (N_\mathrm{T} - 1)$ submatrix of the such modified matrix $\mathbf{Q}_2$ and the first $N_\mathrm{T} - 1$ columns of the new matrix $\mathbf{Q}_1$, resulting in the QR decomposition of the optimally ordered channel matrix $\underline{\mathbf{H}}$. The whole postsorting algorithm is given in Algorithm 8.2.

Thus, a two-step decomposition and reordering procedure is achieved. This scheme finds the optimum detection sequence in the sense of V-BLAST and therefore leads to the same performance. However, the computational complexity of the whole detection process reduces to a fraction of the V-BLAST complexity and is comparable to the effort of linear detection [8].

Performance evaluation. In order to compare the different detection schemes we investigate the achieved bit error rates (BER) for a system with $N_\mathrm{T} = 4$, $N_\mathrm{R} = 4$, and QPSK modulation. E_b denotes the average energy per information bit arriving at the receiver, thus $E_b/N_0 = N_\mathrm{R}/(\log_2(|\mathcal{A}|)\sigma_v^2)$ holds. (Due to this normalization the antenna gain is canceled out.)

Figure 8.5a shows the performance of various ZF detection algorithms and the BER of ML detection. As expected, the successive detection algorithms outperform the linear ZF detector. The impact of an optimized detection order becomes

[4]The Householder matrix for a $1 \times n$ *row* vector $\mathbf{a}$ with complex elements is given by $\mathbf{\Theta} = \mathbf{I}_n - (1 + \xi)\mathbf{u}^H\mathbf{u}$ with the definitions $\mathbf{u} = (\mathbf{a} - \|\mathbf{a}\|\mathbf{e}_n)/\|\mathbf{a} - \|\mathbf{a}\|\mathbf{e}_n\|$, $\mathbf{e}_n = [\mathbf{0}_{1,n-1}1]$ and $\xi = \mathbf{u}\mathbf{a}^H/\mathbf{a}\mathbf{u}^H$. The multiplication of $\mathbf{a}$ with $\mathbf{\Theta}$ results in a vector consisting of $n - 1$ zero elements and one element equal to the norm of $\mathbf{a}$, that is, $\mathbf{a}\mathbf{\Theta} = [\mathbf{0}_{1,n-1}\|\mathbf{a}\|]$ holds.

(1) $k_{\min} = N_T$
(2) for $i = N_T, \ldots, 2$
(3) for $\ell = 1, \ldots, i$
(4) $\mathbf{error}(\ell) = \|\mathbf{Q}_2(\ell, 1 : i)\|^2$
(5) end
(6) $k_i = \arg\min \mathbf{error}(1, \ldots, i)$
(7) $k_{\min} := \min(k_{\min}, k_i)$
(8) if $k_i < i$
(9) exchange rows i and k_i in $\mathbf{Q}_2$
and columns i and k_i in $\mathbf{p}$
(10) end
(11) if $k_{\min} < i$
(12) calculate $\mathbf{\Theta}$ such that elements
of $\mathbf{Q}_2(i, k_{\min} : i - 1)$ become zero
(13) $\mathbf{Q}_2(1 : i, k_{\min} : i) := \mathbf{Q}_2(1 : i, k_{\min} : i)\mathbf{\Theta}$
(14) $\mathbf{Q}_1(:, k_{\min} : i) := \mathbf{Q}_1(:, k_{\min} : i)\mathbf{\Theta}$
(15) end
(16) end
(17) $\underline{\mathbf{R}} = 1/\sigma_v \mathbf{Q}_2^{-1}$

Algorithm 8.2. Pseudocode of MMSE-PSA-algorithm.

obvious by comparing the unsorted SIC, SQRD-SIC, and SQRD-PSA-SIC (or equivalently V-BLAST). As SQRD-SIC does not always find the optimum detection order it results in a performance gap of about 1 dB for a BER of 10^{-3} compared to SQRD-PSA-SIC. However, this degradation reduces for an increasing number of receive antennas, for example, for a system with $N_R = 6$ the difference is only 0.5 dB for a BER of 10^{-5} [11].

For the same system, Figure 8.5b shows the performance of the MMSE detection schemes. Comparing these results with the ZF schemes, a remarkable performance improvement can be observed. Furthermore, the SQRD-SIC achieves the same performance as the optimally sorted SQRD-PSA-SIC up to $E_b/N_0 = 10$ dB. In many cases of interest, the SQRD approach would be the first choice for implementation due to the reduced complexity. However, the combination of SQRD and PSA yields optimum SIC performance with a minimum of computational complexity [8].

8.3. Blind source separation

Blind source separation (BSS) is a general problem in multisensor multiantenna systems and aims at separating data streams from a mixture of signals that stem from statistical independent sources. There are many applications for this problem ranging from audio processing to medical applications and communications. In

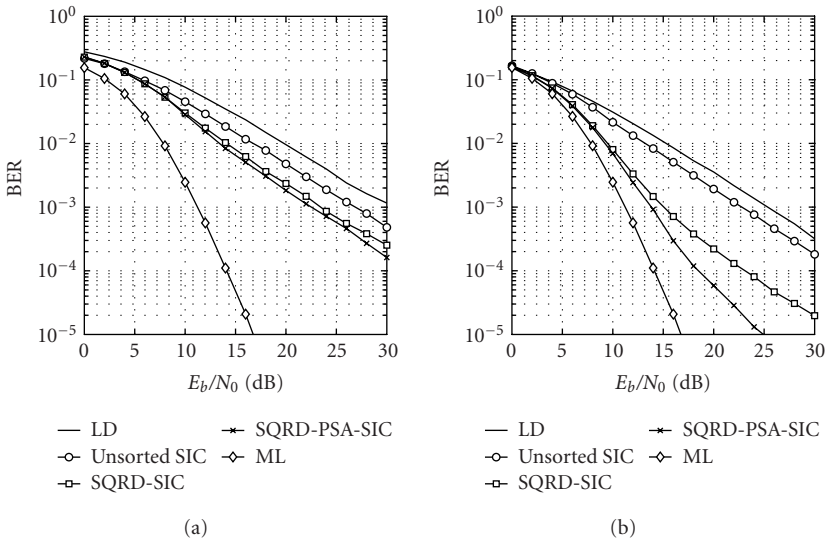

FIGURE 8.5. Bit error rate of (a) ZF and (b) MMSE detection of a system with $N_T = 4$ antennas and $N_R = 4$ antennas, uncoded QPSK symbols.

this section applications to current MIMO communication systems are presented. The investigated algorithms are termed blind, because the channel matrix **H** is not known and no additional pilot symbols are used to separate the data streams.

8.3.1. Linear separation

For the instantaneous (nonconvolutive) channel model

$$\mathbf{r} = \mathbf{H}\mathbf{s} + \mathbf{v} \tag{8.27}$$

of linear separation, the problem can be stated as follows. Blindly find a matrix **G** to be multiplied from the left-hand side onto **r** so that the statistically independent data streams **s** can be recovered. This leads to a linear detection of the data streams.

Possible approaches to this BSS problem. In general there are three types of information that can be utilized to solve the blind source separation problem [18]:

(i) *non-Gaussianity* of the source signals. This property is explicitly utilized in all higher-order statistics-(HOS-)based algorithms and will be explained later on in this text;

(ii) the different *coloring of the source signals*. This property can normally not be exploited in a communication context, because communication signals are designed to utilize a given bandwidth as good as possible and therefore the signals are mostly white. This type of information is used in the second order blind identification (SOBI) type of algorithms [19, 20];

(iii) *instationarity of the source signals* (or channel). This can be applied to audio and communication signals but requires fading or frequency-selective channels. This can also be utilized in SOBI-like approaches [19, 20].

The general idea of the HOS-based source separation algorithms will be described in this section in an illustrative way. We search for an $N_T \times N_R$ equalization matrix $\mathbf{G}$ that exploits the fact that the signal streams contained in the vector of the extracted signals

$$\mathbf{e} = \mathbf{G}\mathbf{r} \tag{8.28}$$

are statistically independent. The general definition of statistical independence is that the joint probability density function (pdf) is the product of the marginal densities[5]

$$p(e_1, e_2) = p(e_1) \cdot p(e_2). \tag{8.29}$$

In order to obtain simple algorithms from this abstract formulation, we need to apply some approximations. The simplest (first- and second-order) approach to this problem is to apply this multiplication property not to pdfs but to expectation values

$$\mathrm{E}\{e_1 \cdot e_2\} = \mathrm{E}\{e_1\} \cdot \mathrm{E}\{e_2\}. \tag{8.30}$$

Because in most practical cases communication signals have a mean value of zero, we can simplify this expression to

$$\mathrm{E}\{e_1 \cdot e_2\} = 0. \tag{8.31}$$

This can be interpreted as follows. The separation problem is split into two steps to determine the equalization matrix $\mathbf{G} = \mathbf{B}^H\mathbf{W}$. A first approximation towards a blind source separation is the decorrelation of the output signals with matrix $\mathbf{W}$. This computation step is also known as sphering, whitening, standardization, or principle component analysis. With the decorrelation the separation problem is not yet solved! The second step is to determine the unitary matrix $\mathbf{B}$. This can be accomplished using different algorithms and will be explained below.

The whitening matrix

$$\mathbf{W} = \mathbf{D}^{-1/2}\mathbf{U}^H \tag{8.32}$$

is calculated by taking the eigenvalue decomposition (EVD) $\mathbf{\Phi}_{rr} = \mathrm{E}\{\mathbf{r}\mathbf{r}^H\} = \mathbf{U}\mathbf{D}\mathbf{U}^H$ of the covariance of the received signals $\mathbf{r}$. Consequently, the decorrelated

[5] In this section we use a simplified notation, where we do not distinguish between random variables and their realizations.

signals can be obtained by

$$\mathbf{z} = \mathbf{W}\mathbf{r}, \quad \mathbf{\Phi}_{zz} = \mathrm{E}\{\mathbf{z}\mathbf{z}^H\} = \mathbf{I}_{N_\mathrm{T}}. \tag{8.33}$$

This procedure can be used in a similar way to limit $\mathbf{z}$ to the dominant subspace directions (corresponding to the greatest eigenvalues) in order to reduce the number of dimensions and the noise influence [21].

Since the decorrelation will lead to orthogonality but not statistical independence, we have to search for further degrees of freedom. One remaining degree of freedom is an $N_\mathrm{T} \times N_\mathrm{T}$ unitary matrix $\mathbf{B}$, if we do not want to destroy the spatial orthogonality of $\mathbf{z}$, that is,

$$\mathbf{I} \stackrel{!}{=} \mathrm{E}\{\mathbf{B}^H\mathbf{z}\mathbf{z}^H\mathbf{B}\} = \mathbf{B}^H\mathrm{E}\{\mathbf{z}\mathbf{z}^H\}\mathbf{B} = \mathbf{B}^H\mathbf{B}. \tag{8.34}$$

The basic criterion to determine $\mathbf{B}$ is the maximization of the kurtosis of a separated signal stream. The kurtosis is a fourth-order (auto-)cumulant

$$\mathrm{kurt}\{e\} = \mathrm{E}\{|e|^4\} - \mathrm{E}\{ee^*\}\mathrm{E}\{ee^*\} - \mathrm{E}\{ee\}\mathrm{E}\{e^*e^*\} - \mathrm{E}\{ee^*\}\mathrm{E}\{e^*e\} \tag{8.35}$$

that can be interpreted as a fourth-order moment minus the Gaussian parts of the distribution, so that its value is zero for Gaussian distributed signals. A mixture of many independent signals (as it is provided by the MIMO channel) will lead to a Gaussian distribution due to the central limit theorem of statistics. Therefore the non-Gaussianity in terms of the kurtosis is one possible criterion that is utilized in the two algorithms that are briefly explained below.[6]

JADE. The joint approximate diagonalization of eigenmatrices (JADE) algorithm [21] is one common batch procedure that solves the separation problem. The first step of this algorithm is to decorrelate the input streams as shown in (8.33). The final separation is done by additionally utilizing fourth-order information. Therefore, the JADE algorithm maximizes some elements of the cumulant matrix $\mathrm{cum}(e_i^\star, e_i, e_j^\star, e_l)$[7] obtained from the extracted signals $\mathbf{e}$ defined in (8.28)

$$\max_{\mathbf{B}} \sum_{i,j,l=1}^{N_\mathrm{T}} |\,\mathrm{cum}\,(e_i^\star, e_i, e_j^\star, e_l)\,|^2. \tag{8.36}$$

This optimization problem is solved by an eigenvalue decomposition of the cumulant matrix and a joint diagonalization of the dominant cumulant eigenvectors rearranged as matrices. This diagonalization is done by a Jacobi-like procedure

[6] Compared to this illustrative explanation of BSS algorithms more mathematical ones can be found in specialized textbooks [20, 22, 23] or in [24].

[7] $\mathrm{cum}(e_i^\star, e_i, e_j^\star, e_l)$ is a fourth-order cross-cumulant of the extracted signals e_p. Cumulants can be interpreted as higher-order moments minus their Gaussian parts of the distribution. For further details see [25].

using Givens rotations and leads to the unitary $N_T \times N_T$ matrix $\mathbf{B}$ and the independent data streams

$$\mathbf{e} = \underbrace{\mathbf{B}^H \mathbf{W}}_{\mathbf{G}} \mathbf{r} = \mathbf{B}^H \mathbf{z}. \tag{8.37}$$

For details see [21]. A similar approach that needs less computational effort is the SSARS algorithm presented in [26].

FastICA. The FastICA algorithm is organized in a different way [10, 27] compared with the JADE algorithm. The basic idea of this algorithm is to apply a blind source extraction (BSE) for each component separately and to prevent the same signal from being extracted multiple times. It starts with the whitening of the received data as presented in (8.33).

In order to extract signal number p out of the whitened mixture $\mathbf{z}$, a randomly initialized extraction vector $\mathbf{b}_p$—a column vector of the $N_T \times N_T$ matrix $\mathbf{B}$—is generated. In order to preserve the signals to remain uncorrelated, $\mathbf{B}$ has again to be a unitary matrix. Therefore, $\mathbf{b}_p$ is constrained to form an orthonormal basis using the knowledge of the vectors $\mathbf{b}_1 \cdots \mathbf{b}_{p-1}$ obtained in previous iterations. To reach this goal matrix,

$$\mathbf{B}_p = [\mathbf{b}_1, \mathbf{b}_2, \ldots, \mathbf{b}_p] \tag{8.38}$$

containing the extraction vectors of the former iterations is built. The randomly initialized vector $\mathbf{b}_p$ is orthogonalized with respect to the space spanned by $\mathbf{B}_{p-1}$

$$\mathbf{b}'_p = \mathbf{b}_p - \mathbf{B}_{p-1}\mathbf{B}^H_{p-1}\mathbf{b}_p \tag{8.39}$$

and normalized to a length of one

$$\mathbf{b}''_p = \frac{\mathbf{b}'_p}{||\mathbf{b}'_p||}. \tag{8.40}$$

In order to determine $\mathbf{b}_p$ we choose the maximization of the kurtosis of a single signal as the criterion

$$\max_{\mathbf{b}_p} J_{\text{FastICA},p}(e_p) = \max_{\mathbf{b}_p} \text{kurt}\left\{ |e_p|^4 \right\} = \max_{\mathbf{b}_p} \text{kurt}\left\{ |\mathbf{b}_p^H \mathbf{z}|^4 \right\}. \tag{8.41}$$

This can be solved using a fixed-point iteration including the additional constraints (8.39) and (8.40) [10]. The resulting signal streams $\mathbf{e}$ can be extracted by multiplying the received signal with the matrix of all collected extraction vectors $\mathbf{B} = \mathbf{B}_{N_T}$ according to (8.37).

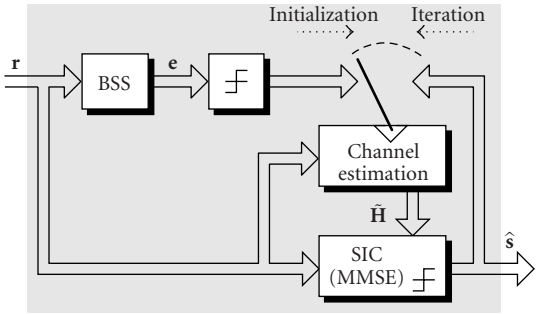

FIGURE 8.6. Block diagram of hybrid BSS detection.

Symbol decision. The algorithms presented in the previous sections only provide statistically independent data streams **e**. Therefore the signal streams can be rotated by an arbitrary phase factor—modeled by the diagonal matrix $\mathbf{\Psi} = \text{diag}\,[\psi_1, \ldots, \psi_{N_T}]$—and can be permuted by a matrix **P**. In general the permutation problem cannot be solved without additional addressing in the data streams or other side information, but the phase problem can be tackled by utilizing knowledge of the symbol alphabet. If QPSK is used as a modulation form, the phase can be estimated up to a discrete phase or quadrant ambiguity $\hat{\mathbf{\Psi}} = \text{diag}\,[\hat{\psi}_1, \ldots, \hat{\psi}_p, \ldots, \hat{\psi}_{N_T}]$, $\hat{\psi}_p \in \{0, \pi/2, \pi, (3/2)\pi\}$, which can be corrected by

$$e_{p,\text{derot}}[m] = e_p[m] \cdot e^{-j(1/4)\arg\{-\sum_{m'=1}^{M} e_p^4[m']\}} \quad \forall\, p \in 1, \ldots, N_T. \tag{8.42}$$

The remaining discrete ambiguity $\hat{\mathbf{\Psi}}$ can be removed by differential modulation forms or rotational invariant coding. But a decision of the pure symbols **s** is only possible with a remaining discrete ambiguity.

8.3.2. Hybrid BSS detector

The blind algorithms presented in the previous section approximate only linear spatial filters in order to separate the data streams. This reaches only a fractional amount of the performance reached by iterative detection algorithms as can be seen in Figure 8.5 for the nonblind case.

In this section we improve the detection performance by applying a cancelation scheme. This utilizes the finite symbol alphabet that was only used marginally up to now and results in a hybrid scheme that is initialized using a linear detection and iteratively improved using a symbol detection in order to obtain a totally blind scheme up to the point of the final symbol decision.[8]

We propose a system as depicted in Figure 8.6. We start with coarsely decided symbols $\hat{\mathbf{s}}$ that were obtained using a blind separation method (e.g., JADE) and

[8]This scheme can also be applied in semiblind setups using very few pilot symbols.

phase correction (8.42) described above.[9] Using this data we produce a first channel estimate $\tilde{\mathbf{H}}$. This channel estimate is used to detect the symbols once more using the MMSE-SIC as presented in Section 8.2.3. Using the output of the SIC detector for an improved channel estimation in combination with a further detection of the data will iteratively lead to better results.

The whole detection scheme remains blind, since this detection loop is blindly initialized and the SIC algorithm only decides symbol positions with quadrant ambiguities $\hat{s}_1, \ldots, \hat{s}_{N_T}$. It has to be proven that despite these ambiguities the iterations work properly. Therefore we assume that the matrix of estimated symbols $\hat{\mathbf{S}} = [\hat{\mathbf{s}}[1], \hat{\mathbf{s}}[2], \ldots, \hat{\mathbf{s}}[M]]$ achieved by the blind source separation is given by

$$\hat{\mathbf{S}} = \mathcal{Q}_{\mathcal{A}}\{\hat{\mathbf{\Psi}}\mathbf{P}\mathbf{S}\}. \tag{8.43}$$

In (8.43), $\mathbf{S} = [\mathbf{s}[1], \mathbf{s}[2] \cdots \mathbf{s}[M]]$ is the matrix of transmitted symbols, $\mathbf{P}$ is a permutation matrix, and $\hat{\mathbf{\Psi}}$ defines the diagonal matrix modeling the discrete quadrant ambiguities.

In order to use these BSS decision results $\hat{\mathbf{S}}$ for a first channel estimation we calculate

$$\tilde{\mathbf{H}} = \mathbf{R} \cdot \hat{\mathbf{S}}^{+} \tag{8.44}$$

using the matrix of the received symbols $\mathbf{R} = [\mathbf{r}[1], \mathbf{r}[2] \cdots \mathbf{r}[M]]$. After inserting (8.43) and assuming only a few decision errors, we can simplify the channel estimation [28] to

$$\tilde{\mathbf{H}} = \mathbf{H} \cdot \mathbf{P}^{H}\hat{\mathbf{\Psi}}^{H}. \tag{8.45}$$

This leads to an estimation $\tilde{\mathbf{H}}$ of the channel matrix $\mathbf{H}$ in a permuted form, where every column contains a quadrant ambiguity.

If we use the estimated channel matrix $\tilde{\mathbf{H}}$ again for the detection, we should find the data streams permuted and rotated in the same way as in (8.43). To show that this channel estimation leads to the same permutation and rotation, a simple linear detection is used:

$$\begin{aligned}\hat{\mathbf{S}} &= \mathcal{Q}_{\mathcal{A}}\{(\mathbf{H} \cdot \mathbf{P}^{H}\hat{\mathbf{\Psi}}^{H})^{+}\mathbf{R}\} = \mathcal{Q}_{\mathcal{A}}\{\hat{\mathbf{\Psi}}\mathbf{P}\mathbf{H}^{+} \cdot (\mathbf{H}\mathbf{S} + \mathbf{V})\} \\ &\approx \mathcal{Q}_{\mathcal{A}}\{\hat{\mathbf{\Psi}}\mathbf{P}\mathbf{H}^{+} \cdot \mathbf{H}\mathbf{S}\} = \mathcal{Q}_{\mathcal{A}}\{\hat{\mathbf{\Psi}}\mathbf{P}\mathbf{S}\}.\end{aligned} \tag{8.46}$$

[9] We need to start with a coarse data decision and cannot rely on the separation matrices $\mathbf{B}$ and $\mathbf{W}$ since these matrices do perform well for separation but do not include a correct amplitude estimation of the signals and therefore every cancelation scheme will fail without a first data decision.

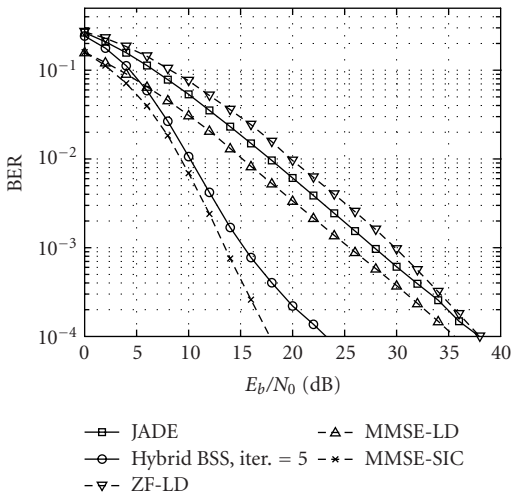

FIGURE 8.7. BER of hybrid BSS detector, $N_T = N_R = 4$, QPSK.

Therefore iterating between detection and channel estimation in a blind way leads to a stable solution of $\tilde{\mathbf{H}}$ with permutation and quadrant ambiguity.

If we apply this channel estimation in the SIC algorithm we get symbols $\hat{\mathbf{s}}$ (Figure 8.6) with the corresponding discrete quadrant ambiguities $\hat{\Psi}$, but this does not influence our further detection and cancelation process, as long as we only want to decide symbols from the alphabet $\mathcal{A}$.

To summarize, we found an iterative estimation and detection scheme that utilizes the finite symbol alphabet and remains completely blind.

Performance of the proposed iterative scheme. In order to show the feasibility of our detection approach we present some BER results of the blind source separation and the hybrid approach (Figure 8.6). As an initialization we exemplary use the output of the JADE algorithm.

Figure 8.7 depicts the results of our simulations. Beside the reference curves of the MMSE and zero-forcing linear detection the MMSE-SIC detection with ideal known channel matrix was introduced as a further reference. The performance of the blind JADE algorithm is between the ZF- and the MMSE-linear detection.

Using the proposed iterative scheme we can observe a gain of about 10 dB at a bit error rate of 10^{-3} (hybrid BSS, iterations = 5) compared to the classical source separation using the JADE algorithm only. For this improvement we need only 5 iterations of detection and channel estimation. We nearly reach the curve of the SIC algorithm with perfectly known channel matrix $\mathbf{H}$.[10] We have to emphasize that the whole detection scheme remains blind since no reference data is used in order to gain the symbol decisions.

[10]We can even decrease the gap to the detection with ideally known channel matrix if we increase the length M of the data block.

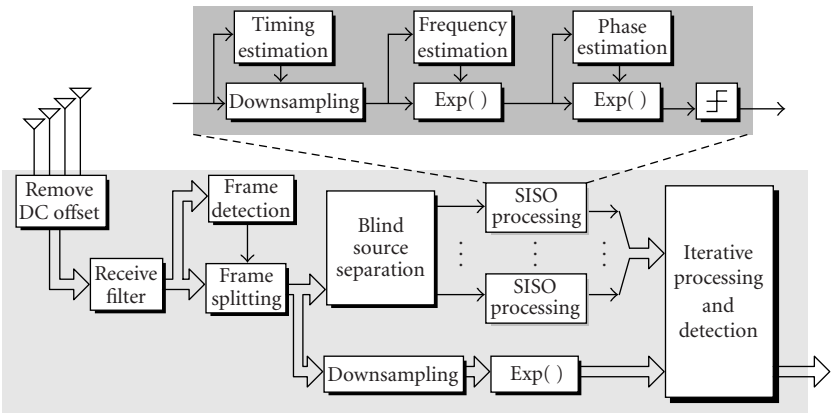

FIGURE 8.8. Receiver setup in case of hybrid blind source separation.

8.4. Experimental results—measurements

In this section some experiments of transmissions using reference-based and blind schemes are presented. As a MIMO demonstrator we used our multiple-antenna system for ISM-band transmission (MASI). This system can be applied to realize MIMO systems of up to 8 transmit and 8 receive antennas [29]. The transmission experiments are executed in real time while the processing is done offline using an interface to Matlab.

Figure 8.8 depicts the receiver setup considering exemplarily a source-separation-based transmission system. To realize transmissions, some practical problems have to be solved. First of all the DC offset caused by the direct conversion front end of the receiver has to be removed. A coarse frame detection based on a power estimation is carried out. Timing and frequency estimation have to be realized before the symbol rate processing can be accomplished.

In order to show the feasibility of the proposed approaches, the MIMO system with $N_T = 4$ antennas, and $N_R = 4$ antennas, and QPSK signals is considered. The presented measurements are carried out with a sampling frequency of $f_s = 50$ MHz. With an oversampling of $w = 8$ we can consider the transmission channel as nearly flat. The distance between transmitter and receiver was spanning two office rooms.

8.4.1. Reference-based SIC detection

For the proposed scheme we investigate two examples for reference-based transmissions. Figure 8.9 shows the eigenvalues λ_p of $\mathbf{H}^H\mathbf{H}$ ($\lambda_p = \sigma_p^2$ with σ_p denoting the singular value of $\mathbf{H}$) and the signal spaces at the slicer inputs, corresponding to Figure 8.4. Since four eigenvalues contribute to the signal transmission, the slicer input signals correspond to the modulation alphabet leading to a sufficient signal detection.

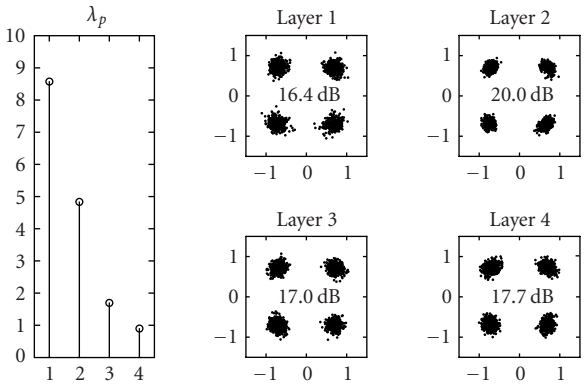

FIGURE 8.9. Eigenvalue profile and signal space diagrams for good channel condition.

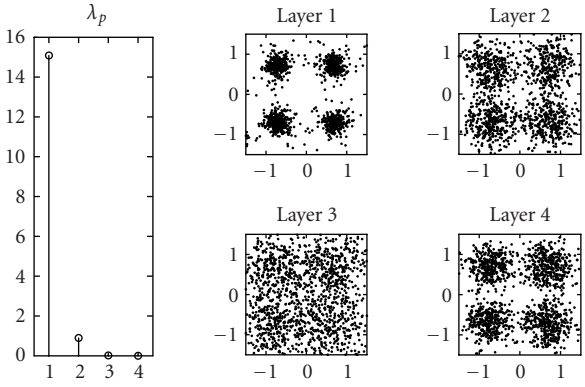

FIGURE 8.10. Eigenvalue profile and signal space diagrams for bad channel conditions.

Figure 8.10 shows a second measurement in the same office environment with slightly changed positions. In contrast to the first example, only two strong eigenvalues contribute to the transmission. The third and fourth eigenvalues are almost zero and the detection process fails.

8.4.2. Hybrid BSS detection with iterative refinement

In this section, we show the performance of the *hybrid blind source-separation-based detector* by some measurements. The setup used is depicted in Figure 8.8. To separate the independent components, the BSS algorithm is directly applied to the oversampled signal. For this step we choose the JADE [21] algorithm as a spatial separation approach. The separation leads to data streams which are processed in the classical way like in single-antenna systems. This is a considerable advantage, since well-known algorithms (e.g., for timing and for frequency synchronization) can be applied for the separated layers of MIMO systems. We synchronize to the

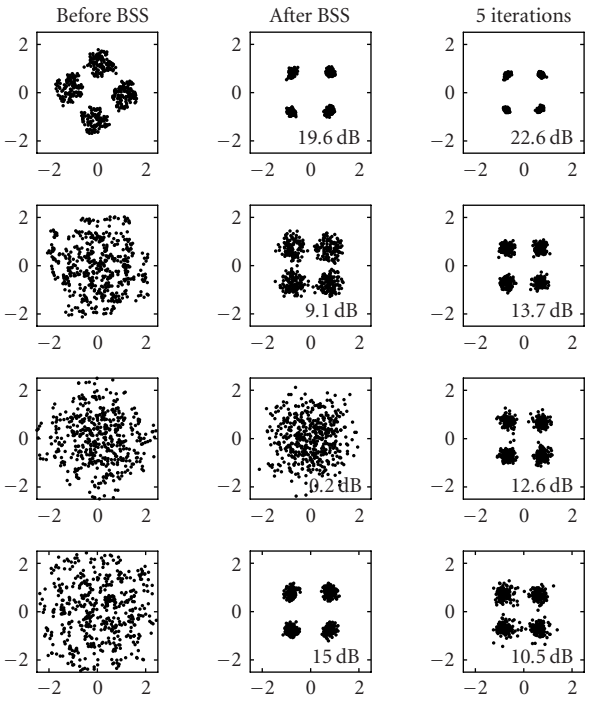

FIGURE 8.11. Signal constellations before and after blind source separation and after 5 iterations, together with blindly estimated SNR.

symbol timing using the method presented in [30]. In order to determine the carrier frequency offset we apply a non-linearity and frequency estimation.

Figure 8.11 depicts the signal constellation at symbol rate before separation, after separation, and after 5 iterations of the scheme presented in Figure 8.6. We have included estimations of the SNR of the symbol constellation before the decision devices [31]. In Figure 8.11 one of the signal constellations after BSS consists of noise only. Using the proposed iteration scheme with SIC detection and iterative channel estimation, even this constellation can be resolved to QPSK. Denote that the overall SNR has been improved.

8.5. Conclusions

Within this contribution, architectures for reference-based and blind detection of multilayer systems have been investigated. In case of known channel state information at the receiver a computational efficient detection algorithm has been proposed. Without any channel state information, we proposed a hybrid combination of blind source separation with successive interference cancelation. To ensure the feasibility of the distinct approaches, real-world transmissions have been carried out. It has been shown that the measurements correspond to the predicted

theoretical results. The feasibility of the proposed schemes have been shown in an indoor office scenario.

Abbreviations

BER	Bit error rate
BSE	Blind source extraction
BSS	Blind source separation
CSI	Channel state information
EVD	Eigenvalue decomposition
HOS	Higher-order statistics
JADE	Joint approximate diagonalization of eigenmatrices
LD	Linear detector
MASI	Multiple-antenna system for ISM-band transmission
MIMO	Multi-input multi-output
ML	Maximum likelihood
MSE	Minimum mean square error
MMSE-SIC	Minimum mean square error-successive interference cancelation
PSA	Postsorting algorithm
SIC	Successive interference cancelation
SINR	Signal-interference-and-noise ratio
SISO	Single-input single-output
SNR	Signal-to-noise ratio
SOBI	Second-order blind identification
SQRD	Sorted QR decomposition
SVD	Singular value decomposition
V-BLAST	Vertical Bell Labs Layered Space-Time
ZF	Zero forcing
ZF-SIC	Zero-forcing successive interference cancelation

Bibliography

[1] G. J. Foschini, "Layered space-time architecture for wireless communication in a fading environment when using multiple antennas," *Bell Labs. Tech. J.*, vol. 1, no. 2, pp. 41–59, 1996.

[2] P. W. Wolniansky, G. J. Foschini, G. D. Golden, and R. A. Valenzuela, "V-BLAST: an architecture for realizing very high data rates over the rich-scattering wireless channel," in *Proc. International Symposium on Signals, Systems, and Electronics (ISSSE '98)*, pp. 295–300, Pisa, Italy, September 1998.

[3] G. Strang, *Linear Algebra and Its Applications*, Harcourt Brace Jovanovich College Publishers, Orlando, Fla, USA, 3rd edition, 1988.

[4] E. Agrell, T. Eriksson, A. Vardy, and K. Zeger, "Closest point search in lattices," *IEEE Trans. Inform. Theory*, vol. 48, no. 8, pp. 2201–2214, 2002.

[5] C. Windpassinger and R. F. H. Fischer, "Low-complexity near-maximum-likelihood detection and precoding for MIMO systems using lattice reduction," in *Proc. IEEE Information Theory Workshop (ITW '03)*, pp. 345–348, Paris, France, March 2003.

[6] D. Wübben, R. Böhnke, V. Kühn, and K.-D. Kammeyer, "Near-maximum-likelihood detection of MIMO systems using MMSE-based lattice reduction," in *Proc. IEEE International Conference on Communications (ICC '04)*, Paris, France, June 2004.

[7] B. Hassibi, "An efficient square-root algorithm for BLAST," in *Proc. IEEE International Conference on Acoustics, Speech, and Signal Processing (ICASSP '00)*, vol. 2, pp. II737–II740, Istanbul, Turkey, June 2000.
[8] D. Wübben, R. Böhnke, V. Kühn, and K.-D. Kammeyer, "MMSE extension of V-BLAST based on sorted QR decomposition," in *Proc. IEEE 58th Vehicular Technology Conference (VTC '03)*, vol. 1, pp. 508–512, Orlando, Fla, USA, October 2003.
[9] A. Benjebbour, H. Murata, and S. Yoshida, "Comparison of ordered successive receivers for space-time transmission," in *Proc. IEEE VTS 54th Vehicular Technology Conference (VTC '01)*, vol. 4, pp. 2053–2057, Atlantic City, NJ, USA, October 2001.
[10] E. Bingham and A. Hyvärinen, "A fast fixed-point algorithm for independent component analysis of complex valued signals," *Int. J. Neural Syst.*, vol. 10, no. 1, pp. 1–8, 2000.
[11] D. Wübben, J. Rinas, R. Böhnke, V. Kühn, and K.-D. Kammeyer, "Efficient algorithm for detecting layered space-time codes," in *Proc. 4th International ITG Conference on Source and Channel Coding*, pp. 399–405, Berlin, Germany, January 2002.
[12] G. J. Foschini, G. D. Golden, A. Valenzuela, and P. W. Wolniansky, "Simplified processing for high spectral efficiency wireless communication employing multi-element arrays," *IEEE J. Select. Areas Commun.*, vol. 17, no. 11, pp. 1841–1852, 1999.
[13] D. W. Waters and J. R. Barry, "Noise-predictive decision feedback detection for multiple-input multiple-output channels," in *Proc. IEEE International Symposium on Advances in Wireless Communications (ISWC '02)*, Victoria, British Columbia, Canada, September 2002.
[14] D. Wübben, R. Böhnke, J. Rinas, V. Kühn, and K.-D. Kammeyer, "Efficient algorithm for decoding layered space-time codes," *IEE Electronics Letters*, vol. 37, no. 22, pp. 1348–1350, 2001.
[15] E. Biglieri, G. Taricco, and A. Tulino, "Decoding space-time codes with BLAST architectures," *IEEE Trans. Signal Processing*, vol. 50, no. 10, pp. 2547–2551, 2002.
[16] R. Böhnke, D. Wübben, V. V. Kühn, and K.-D. Kammeyer, "Reduced complexity MMSE detection for BLAST architectures," in *Proc. IEEE Global Telecommunications Conference (GLOBECOM '03)*, vol. 4, pp. 2258–2262, San Francisco, Calif, USA, December 2003.
[17] G. Ginis and J. M. Cioffi, "On the relation between V-BLAST and the GDFE," *IEEE Commun. Lett.*, vol. 5, no. 9, pp. 364–366, 2001.
[18] J.-F. Cardoso, "The three easy routes to independent component analysis; contrasts and geometry," in *Proc. Idaho Counseling Association (ICA '01)*, San Diego, Calif, USA, December 2001.
[19] A. Belouchrani, K. Abed-Meraim, J.-F. Cardoso, and E. Moulines, "A blind source separation technique using second-order statistics," *IEEE Trans. Signal Processing*, vol. 45, no. 2, pp. 434–444, 1997.
[20] A. Cichocki and S. Amari, *Adaptive Blind Signal and Image Processing*, Wiley, New York, NY, USA, 2002.
[21] J.-F. Cardoso and A. Souloumiac, "Blind beamforming for non-Gaussian signals," *IEE Proceedings F, Radar and Signal Processing*, vol. 140, no. 6, pp. 362–370, 1993.
[22] S. Haykin, Ed., *Unsupervised Adaptive Filtering, Volume 1, Blind Source Separation*, Adaptive and Learning Systems for Signal Processing, Communications and Control. Wiley Interscience, New York, NY, USA, 2000.
[23] A. Hyvärinen, J. Karhunen, and E. Oja, *Independent Component Analysis*, Wiley, New York, 2001.
[24] F. Herrmann and A. K. Nandi, "Blind separation of linear instantaneous mixtures using closed-form estimators," *Signal Processing*, vol. 81, no. 7, pp. 1537–1556, 2001.
[25] A. Stuart and K. Ord, *Kendall's Advanced Theory of Statistics—Volume I: Distribution Theory*, Wiley, New York, NY, USA, 6th edition, 1994.
[26] M. Feng and K.-D. Kammeyer, "Blind source separation for communication signals using antenna arrays," in *Proc. IEEE International Conference on Personal Wireless Communications (ICUPC '98)*, vol. 1, pp. 665–669, Florence, Italy, October 1998.
[27] A. Hyvärinen and E. Oja, "A fast fixed-point algorithm for independent component analysis," *Neural Computation*, vol. 9, no. 7, pp. 1483–1492, 1997.
[28] J. Rinas and K.-D. Kammeyer, "Comparison of blind source separation methods based on iterative algorithms," in *Proc. 5th International ITG Conference on Source and Channel Coding (SCC '04)*, Erlangen, Germany, January 2004.

[29] J. Rinas, R. Seeger, L. Brötje, S. Vogeler, T. Haase, and K.-D. Kammeyer, "A multiple antenna system for ISM-band transmission," *EURASIP J. Appl. Signal Process.*, vol. 2004, no. 9, pp. 1407–1419, 2004.
[30] S. J. Lee, "A new non-data-aided feedforward symbol timing estimator using two samples per symbol," *IEEE Commun. Lett.*, vol. 6, no. 5, pp. 205–207, 2002.
[31] R. Matzner, "An SNR estimation algorithm for complex baseband signals using higher order statistics," *Facta Universitatis: Electronics and Energetics*, vol. 6, no. 1, pp. 41–52, 1993.
[32] J. Rinas and K.-D. Kammeyer, "MIMO measurements of communication signals and application of blind source separation," in *Proc. 3rd IEEE International Symposium on Signal Processing and Information Technology (ISSPIT '03)*, pp. 94–97, Darmstadt, Germany, December 2003.

Karl-Dirk Kammeyer: Department of Communications Engineering, Universität Bremen, P.O. Box 33 04 40, 28334 Bremen, Germany
Email: kammeyer@ant.uni-breman.de

Jürgen Rinas: Department of Communications Engineering, Universität Bremen, P.O. Box 33 04 40, 28334 Bremen, Germany
Email: rinas@ant.uni-bremen.de

Dirk Wübben: Department of Communications Engineering, Universität Bremen, P.O. Box 33 04 40, 28334 Bremen, Germany
Email: wuebben@ant.uni-bremen.de

9 Uplink robust adaptive beamforming

Alex B. Gershman

9.1. Introduction

One of recent promising approaches to increase the capacity and performance of cellular mobile radio systems is to employ smart antennas (multisensor arrays) at base stations (BSs) [1, 2, 3]. Based on this approach, the spatial division multiple access (SDMA) technology recently became one of the key concepts of the third and higher generations of mobile communication systems. In particular, uplink (receive) adaptive beamforming techniques using multisensor BS arrays have been shown to be able to efficiently mitigate the cochannel (multiaccess) interference and greatly improve the system characteristics in terms of capacity, performance, and coverage [2, 3, 4, 5, 6, 7].

Although smart antennas for mobile radio systems is a relatively new trend in wireless communications, adaptive array beamforming is a universal approach that has a long and rich history of interdisciplinary theoretical research and practical applications, mainly in radar and sonar communities [8, 9, 10, 11, 12, 13, 14, 15, 16, 17, 18].

Over the last three decades, the theory of adaptive receive beamforming has been well developed and a variety of advanced algorithms has been proposed, see [10, 13, 14, 15, 16, 18] and references therein. However, in application to cellular mobile radio scenarios, most of these techniques are based on the assumption of an accurate knowledge of the uplink propagation channel (spatial signature of the user-of-interest). Moreover, these methods usually make use of several restrictive assumptions on the environment and mobile user sources. As a result, these techniques can become severely degraded in practical scenarios when the exploited assumptions on the environment, antenna array and/or sources may be wrong or inaccurate [19, 20, 21]. For example, in mobile communications such performance degradation of BS uplink adaptive beamformers may be caused by mismatches between the presumed and actual user spatial signatures (or, more generally, between the presumed and actual antenna array responses to mobile user signals) which can take place because of the signal fading and scattering phenomena, user

mobility and channel variability, finite duration of training intervals and outdated training, multiuser interference, and other effects [22, 23, 24]. Therefore, robust approaches to adaptive beamforming are of great interest and demand in such cases [19, 20, 21].

In this section, we provide an overview of the field of robust receive adaptive beamforming in the context of cellular mobile radio systems with flat fading. First of all, the main types of robustness required in uplink BS adaptive beamforming are considered. Then, we discuss the existing robust solutions to the uplink adaptive beamforming problem with a special emphasis on a recently emerged powerful class of robust adaptive beamformers based on worst-case performance optimization.

9.2. Main types of robustness

The basic idea of uplink adaptive beamforming in cellular wireless communication systems with flat fading can be understood in the following simple way. Each sensor of the BS antenna array has an adjustable weight coefficient. These coefficients are used by the BS beamformer to place the main beam of its beampattern towards the user-of-interest[1] while rejecting the cochannel interferers (which may originate from the same cell or from other cells) by placing adaptively formed beampattern nulls towards them. Note that in real-world scenarios, the desired signal and interference wavefronts (spatial signatures) are not necessarily plane waves, and, therefore, the terminology "placing the main beam and nulls" should be understood as maximally matching the weight vector to the desired user wavefront, while making this vector nearly orthogonal to the wavefronts of interfering users. To optimally match the main beam to the desired user, the BS adaptive beamformer requires an accurate knowledge of its spatial signature (which in the slow fading case characterizes the uplink channel between the desired user and the BS).

The traditional approach to the design of receive adaptive beamformers assumes that no components of the desired user signal are present in the data snapshots that are used to compute and/or update the beamformer weight vector [10, 13]. In such a case, adaptive beamforming is known to be quite robust against errors in the spatial signature of the desired user and limited sample size, and multiple rapidly converging algorithms are available [10, 13, 14, 15, 16, 18]. Although the assumption of signal-free snapshots may be relevant in certain specific applications (e.g., in radar), in wireless communications the interference and noise observations are always "contaminated" by the desired signal component. Even in the ideal case where the spatial signature of the desired user is accurately known at the BS, the presence of the desired signal components in the array snapshots dramatically reduces the convergence rates of uplink adaptive beamforming algorithms relative to the signal-free array data case [19, 25].

[1] In what follows, we refer to this user-of-interest as the *desired user*.

In practical scenarios, adaptive beamforming techniques may degrade in their performance even more severely because of possible mismatches between the nominal (presumed) and actual spatial signature of the desired user. Traditional adaptive array algorithms are known to be very sensitive even to small errors of such type [19, 21]. An easy explanation of this fact is that in the presence of such errors an adaptive beamformer tends to "interpret" the desired signal components in array observations as interference and to suppress these components by means of adaptive nulling instead of optimally combining them [19, 25]. This effect is commonly referred to as *signal self-nulling* [21].

The above-mentioned spatial signature errors can frequently occur in practice because of an imperfect knowledge of the uplink channel of the desired user. Indeed, the spatial signature of this user can be estimated either by means of training sequences [26] or blindly [27, 28]. When training-based spatial signature estimation techniques are used, the quality of the resulting estimates can be seriously affected by limited duration and number of training intervals as well as by multiuser interference, user mobility, and channel variability [29]. As a matter of fact, the percentage of training symbols in the transmitted data stream is usually strictly limited by system bandwidth efficiency requirements. Hence, in the case of limited training and in the presence of fast channel variations and rapidly moving users, the quality of training-based spatial signature estimates can either be insufficiently good originally or can become outdated soon after the training interval. In the blind case, no training sequences are used but the quality of spatial signature estimates is highly dependent on how fast the channel varies in time and how high is the received power of the user-of-interest as compared to the powers of interfering cochannel users [27, 28]. Therefore, in practice, the spatial signature of the desired user may be known imprecisely and robust approaches to uplink adaptive beamforming are required [21].

Another reason for performance degradation of receive adaptive beamforming techniques in mobile communications scenarios is the potential nonstationarity of the array data that are used to compute the beamformer weights and to null out the interference. Similarly to the above-mentioned desired user mismatch effect, this phenomenon can be caused by a highly nonstationary behavior of the propagation channel and by a fast motion of cochannel interfering users [30, 31, 32]. Such a nonstationarity restricts the beamformer sample size and this may lead to a severe performance degradation [19, 25].

One negative effect of such nonstationarity on the performance of adaptive arrays is that in the presence of rapidly moving interfering users, the array weights may not be able to adapt fast enough to compensate for the interferer motion. As a result, interfering users may be located most of time outside the areas of the adaptive beampattern nulls and, therefore, leak to the output of adaptive beamformer through the beampattern sidelobes [30, 31, 32, 33]. This phenomenon is usually referred to as *interference undernulling*. In such cases, cancellation of multiaccess interference may be insufficient and robust adaptive beamforming techniques are required to improve the performance [19].

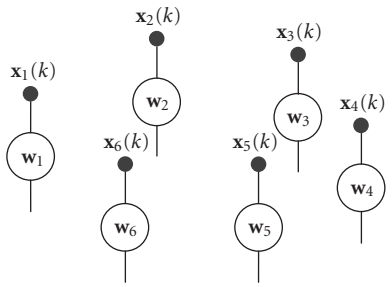

FIGURE 9.1. Basic scheme of a narrowband adaptive beamformer.

9.3. Background on adaptive beamforming

The basic scheme of a narrowband adaptive beamformer is illustrated in Figure 9.1 using a specific example of six-element circular array.[2] The beamformer output is given by

$$y(k) = \mathbf{w}^H \mathbf{x}(k), \tag{9.1}$$

where k is the time index, $\mathbf{x}(k) = [x_1(k), \ldots, x_M(k)]^T$ is the $M \times 1$ complex array snapshot vector, $\mathbf{w} = [w_1, \ldots, w_M]^T$ is the $M \times 1$ complex vector of beamformer weights, M is the number of array sensors, and $(\cdot)^T$ and $(\cdot)^H$ stand for the transpose and Hermitian transpose, respectively. The snapshot vector is given by

$$\mathbf{x}(k) = \mathbf{s}_s(k) + \mathbf{i}(k) + \mathbf{n}(k), \tag{9.2}$$

where $\mathbf{s}_s(k)$, $\mathbf{i}(k)$, and $\mathbf{n}(k)$ are the statistically independent components of the desired user signal, multiaccess interference, and sensor noise, respectively. In the case of slow fading, the vector $\mathbf{s}_s(k)$ can be modeled as

$$\mathbf{s}_s(k) = s(k)\mathbf{a}_s, \tag{9.3}$$

where $s(k)$ is the complex waveform of the desired user and $\mathbf{a}_s$ is its $M \times 1$ spatial signature which specifies the user wavefront. In this case, (9.2) can be rewritten as

$$\mathbf{x}(k) = s(k)\mathbf{a}_s + \mathbf{i}(k) + \mathbf{n}(k). \tag{9.4}$$

The optimal weight vector can be found by means of maximizing the signal-to-interference-plus-noise ratio (SINR) [13]

$$\text{SINR} = \frac{\mathbf{w}^H \mathbf{R}_s \mathbf{w}}{\mathbf{w}^H \mathbf{R}_{i+n} \mathbf{w}}, \tag{9.5}$$

[2]Note that circular arrays are considered among the best BS array configurations for next generations of cellular mobile radio systems [34].

where

$$\begin{aligned} \mathbf{R}_{\mathrm{s}} &= \mathrm{E}\left\{\mathbf{s}_{\mathrm{s}}(k)\mathbf{s}_{\mathrm{s}}^{H}(k)\right\}, \\ \mathbf{R}_{\mathrm{i+n}} &= \mathrm{E}\left\{\left(\mathbf{i}(k)+\mathbf{n}(k)\right)\left(\mathbf{i}(k)+\mathbf{n}(k)\right)^{H}\right\} \end{aligned} \tag{9.6}$$

are the so-called $M \times M$ signal and interference-plus-noise covariance matrices, respectively, and $\mathrm{E}\{\cdot\}$ denotes the statistical expectation. Generally, matrix $\mathbf{R}_{\mathrm{s}}$ can have an arbitrary rank depending on how fast the signal fading is, that is, $1 \leq \mathrm{rank}\{\mathbf{R}_{\mathrm{s}}\} \leq M$. A typical example when the rank of $\mathbf{R}_{\mathrm{s}}$ is greater than one is the case of rural and suburban environments with a high BS, where one of the major problems is the fast fading due to local scattering in the vicinity of the mobile [24, 35].

If the fading of the desired user signal is slow, then

$$\mathbf{R}_{\mathrm{s}} = \sigma_{\mathrm{s}}^{2}\mathbf{a}_{\mathrm{s}}\mathbf{a}_{\mathrm{s}}^{H}, \tag{9.7}$$

where $\sigma_{\mathrm{s}}^{2} = \mathrm{E}\{|s(k)|^{2}\}$. In this case, $\mathrm{rank}\{\mathbf{R}_{\mathrm{s}}\} = 1$ and (9.5) becomes

$$\mathrm{SINR} = \frac{\sigma_{\mathrm{s}}^{2}\left|\mathbf{w}^{H}\mathbf{a}_{\mathrm{s}}\right|^{2}}{\mathbf{w}^{H}\mathbf{R}_{\mathrm{i+n}}\mathbf{w}}. \tag{9.8}$$

To obtain the optimal weight vector, one should maximize the SINR in (9.5). This optimization problem is equivalent to maintaining the distortionless array response to the desired signal while minimizing the output interference-plus-noise power [35]:

$$\min_{\mathbf{w}} \mathbf{w}^{H}\mathbf{R}_{\mathrm{i+n}}\mathbf{w} \quad \text{subject to } \mathbf{w}^{H}\mathbf{R}_{\mathrm{s}}\mathbf{w} = 1. \tag{9.9}$$

In the rank-one signal case, this problem can be rewritten in a more familiar form [13, 18]

$$\min_{\mathbf{w}} \mathbf{w}^{H}\mathbf{R}_{\mathrm{i+n}}\mathbf{w} \quad \text{subject to } \mathbf{w}^{H}\mathbf{a}_{\mathrm{s}} = 1. \tag{9.10}$$

This approach is usually referred to as the minimum variance distortionless response (MVDR) beamforming. The solution to (9.9) is given by the following generalized eigenvalue problem (see [19, 21] and references therein):

$$\mathbf{R}_{\mathrm{i+n}}\mathbf{w} = \lambda\mathbf{R}_{\mathrm{s}}\mathbf{w}, \tag{9.11}$$

where λ is a generalized eigenvalue. From the positive semidefinitness of $\mathbf{R}_{\mathrm{i+n}}$ and $\mathbf{R}_{\mathrm{s}}$, it can be shown that all generalized eigenvalues that may correspond to (9.11) are nonnegative real numbers [21].

The solution to (9.9) is the generalized eigenvector corresponding to the *smallest* generalized eigenvalue of the matrix pencil $\{\mathbf{R}_{\mathrm{i+n}}, \mathbf{R}_{\mathrm{s}}\}$ and the optimal weight

vector can be explicitly written as [21]

$$\mathbf{w}_{\text{opt}} = \mathcal{P}\{\mathbf{R}_{\text{i+n}}^{-1}\mathbf{R}_{\text{s}}\}, \tag{9.12}$$

where $\mathcal{P}\{\cdot\}$ is the operator which gives the *principal eigenvector* of a matrix. Clearly, the resulting weight vector should be normalized to satisfy the constraint $\mathbf{w}_{\text{opt}}^H\mathbf{R}_{\text{s}}\mathbf{w}_{\text{opt}} = 1$ in (9.9). However, it is obvious that the multiplication of the weight vector by any nonzero constant does not affect the output SINR (9.5). Hence, such a normalization is immaterial.

In the rank-one signal source case, (9.12) can be simplified as

$$\mathbf{w}_{\text{opt}} = \mathcal{P}\{\mathbf{R}_{\text{i+n}}^{-1}\mathbf{a}_{\text{s}}\mathbf{a}_{\text{s}}^H\} = \alpha\mathbf{R}_{\text{i+n}}^{-1}\mathbf{a}_{\text{s}}, \tag{9.13}$$

where the constant α can be obtained from the MVDR constraint $\mathbf{w}_{\text{opt}}^H\mathbf{a}_{\text{s}} = 1$ in (9.10) and is equal to $\alpha = \mathbf{a}_{\text{s}}^H\mathbf{R}_{\text{i+n}}^{-1}\mathbf{a}_{\text{s}}^{-1}$ [10, 13]. However, as noted before, this constant does not affect the array output SINR and, therefore, it is immaterial and will be omitted.

In practical applications, the true matrix $\mathbf{R}_{\text{i+n}}$ is unavailable but can be estimated. Therefore, its estimate should be used in optimization problems (9.9) and (9.10) instead of the true value. For example, the sample covariance matrix [10, 13]

$$\hat{\mathbf{R}} = \frac{1}{N}\sum_{n=1}^{N}\mathbf{x}(n)\mathbf{x}^H(n) \tag{9.14}$$

can be used instead of $\mathbf{R}_{\text{i+n}}$. Here, N is the number of snapshots available. Replacing $\mathbf{R}_{\text{i+n}}$ by $\hat{\mathbf{R}}$ in (9.9) and (9.10) yields the following sample matrix inverse (SMI) beamformers [10, 13, 21]:

$$\begin{aligned}\mathbf{w}_{\text{SMI}} &= \mathcal{P}\{\hat{\mathbf{R}}^{-1}\mathbf{R}_{\text{s}}\},\\ \mathbf{w}_{\text{SMI}} &= \hat{\mathbf{R}}^{-1}\mathbf{a}_{\text{s}}.\end{aligned} \tag{9.15}$$

Beamformer (9.15) is the well-known technique proposed in [10], while (9.15) represents its straightforward extension to the higher-rank case where rank$\{\mathbf{R}_{\text{s}}\}>1$. The use of the sample covariance matrix $\hat{\mathbf{R}}$ instead of the interference-plus-noise covariance matrix $\mathbf{R}_{\text{i+n}}$ in (9.15) is known to affect the performance dramatically if the desired signal component is present in the data snapshots that are used to compute $\hat{\mathbf{R}}$.

9.4. Robust beamforming

The main objective of this section is to consider techniques that can improve the robustness of uplink adaptive beamforming and are applicable to scenarios with *arbitrary* spatial signature errors, small sample size, and nonstationary array data (moving cochannel interferers). We do not consider here a broad class of methods

using either point or derivative constraints to improve robustness against look direction errors [13] because these methods are restricted by the idealistic plane wavefront assumption and, therefore, they do not provide sufficient robustness against other types of mismatches (which may be caused, e.g., by signal fading).

One of the most popular and most powerful approaches to robust adaptive beamforming in the cases of arbitrary spatial signature errors and small sample size is the *diagonal loading* method [20, 36]. Its key idea is to *regularize* the solution for the weight vector [36] by adding the quadratic penalty term to the objective function in (9.9):

$$\min_{\mathbf{w}} \mathbf{w}^H \hat{\mathbf{R}} \mathbf{w} + \gamma \mathbf{w}^H \mathbf{w} \quad \text{subject to } \mathbf{w}^H \mathbf{R}_s \mathbf{w} = 1, \tag{9.16}$$

where γ is a fixed loading factor. This solution is usually called the loaded SMI (LSMI) beamformer whose weight vector can be written as [35]

$$\mathbf{w}_{\text{LSMI}} = \mathcal{P}\{(\hat{\mathbf{R}} + \gamma \mathbf{I})^{-1} \mathbf{R}_s\}, \tag{9.17}$$

where $\mathbf{I}$ is the identity matrix. If $\text{rank}\{\mathbf{R}_s\} = 1$, then (9.17) simplifies to [20, 36]

$$\mathbf{w}_{\text{LSMI}} = (\hat{\mathbf{R}} + \gamma \mathbf{I})^{-1} \mathbf{a}_s. \tag{9.18}$$

From expressions (9.17) and (9.18), we see that adding the new term $\gamma \mathbf{w}^H \mathbf{w}$ to the objective function in (9.16) is equivalent to *loading* the diagonal of the sample covariance matrix $\hat{\mathbf{R}}$ by the constant γ. Clearly, such an operation will guarantee that the matrix $\hat{\mathbf{R}} + \gamma \mathbf{I}$ is invertible even in the case when $\hat{\mathbf{R}}$ is singular. However, the diagonal loading operation provides other useful properties and, in particular, improves the beamformer robustness against spatial signature errors.

It is well known that diagonal loading can improve the performance of the SMI approach in scenarios with an arbitrary signal array response mismatch [19, 20]. However, the main drawback of this method is that there is no easy and reliable way of choosing the parameter γ. In [20], the so-called *white noise gain constraint* has been used to choose γ. Unfortunately, there is no simple relationship between the white noise gain parameter κ and the diagonal loading parameter γ.

A much simpler (and more practical) way of choosing γ is to estimate the noise power from the few smallest eigenvalues of the sample covariance matrix and then to choose a fixed γ of the same or higher order of magnitude. However, it is well known that the optimal choice of the diagonal loading factor depends on the power of the desired signal and, hence, such a way of obtaining γ is not always reliable and may cause a substantial performance degradation of the LSMI algorithm [21].

Another popular approach to robust adaptive beamforming in the case of arbitrary spatial signature errors and small sample size is the so-called eigenspace-based beamformer [25, 37]. This approach is only applicable to the slow fading class of scenarios with $\text{rank}\{\mathbf{R}_s\} = 1$. The key idea of this method is to use, instead

of the presumed spatial signature $\mathbf{a}_s$, its projection onto the sample signal-plus-interference subspace. The eigendecomposition of (9.14) can be written as

$$\hat{\mathbf{R}} = \hat{\mathbf{E}}\hat{\mathbf{\Lambda}}\hat{\mathbf{E}}^H + \hat{\mathbf{G}}\hat{\mathbf{\Gamma}}\hat{\mathbf{G}}^H, \tag{9.19}$$

where the $M \times (L+1)$ matrix $\hat{\mathbf{E}}$ contains the $L+1$ signal-plus-interference subspace eigenvectors of $\hat{\mathbf{R}}$, and the $(L+1) \times (L+1)$ diagonal matrix $\hat{\mathbf{\Lambda}}$ contains the corresponding eigenvalues of this matrix. Similarly, the $M \times (M-L-1)$ matrix $\hat{\mathbf{G}}$ contains the $M-L-1$ noise-subspace eigenvectors of $\hat{\mathbf{R}}$, while the $(M-L-1) \times (M-L-1)$ diagonal matrix $\hat{\mathbf{\Gamma}}$ is built from the corresponding eigenvalues. The number of interfering users L (which can be interpreted mathematically as the rank of the interference subspace) has to be known. The weight vector of the eigenspace-based beamformer can be computed as [37]

$$\mathbf{w}_{\text{eig}} = \hat{\mathbf{R}}^{-1}\mathbf{P}_{\hat{\mathbf{E}}}\mathbf{a}_s, \tag{9.20}$$

where $\mathbf{P}_{\hat{\mathbf{E}}} = \hat{\mathbf{E}}(\hat{\mathbf{E}}^H\hat{\mathbf{E}})^{-1}\hat{\mathbf{E}}^H = \hat{\mathbf{E}}\hat{\mathbf{E}}^H$ is the orthogonal projection matrix onto the estimated $(L+1)$-dimensional signal-plus-interference subspace. According to (9.20), the eigenspace-based beamformer "improves" the spatial signature $\mathbf{a}_s$ by projecting it onto this subspace. It can be shown that weight vector (9.20) can be rewritten in another alternative form [37]

$$\mathbf{w}_{\text{eig}} = \hat{\mathbf{E}}\hat{\mathbf{\Lambda}}^{-1}\hat{\mathbf{E}}^H\mathbf{a}_s. \tag{9.21}$$

When used in "adequate" scenarios with $L \ll M$, the eigenspace-based beamformer is known to be one of the most robust techniques applicable to arbitrary spatial signature mismatch case [21]. However, a very serious shortcoming of this approach is that it is not applicable to situations where the number of rank-one interfering sources remains uncertain or is comparable to the number of the BS array sensors (as in the cases of rapidly moving and spatially spread cochannel interferers). This makes it very difficult to use the eigenspace-based beamformer in cellular communications scenarios where the dimension of the signal-plus-interference subspace may be uncertain and high.

In situations with nonstationary training data, numerous advanced methods have been developed to mitigate performance degradation of adaptive beamformers. To preserve the adaptive array performance with a high mobility of interferers, several authors used the idea of artificially broadening the adaptive beampattern nulls in unknown interferer directions [30, 31, 32, 33].

The first way to broaden the adaptive beampattern nulls uses the so-called covariance matrix tapering (MT) procedure [31, 32]. The essence of this technique is to replace $\hat{\mathbf{R}}$ in the SMI or LSMI beamformer by the tapered covariance matrix

$$\hat{\mathbf{R}}_{\text{T}} = \hat{\mathbf{R}} \odot \mathbf{T}, \tag{9.22}$$

where $\odot$ is the Schur-Hadamard matrix product, and $\mathbf{T}$ is the $M \times M$ taper matrix. Particular types of matrix tapers are discussed in [31, 32].

Another alternative approach to broaden the adaptive beampattern nulls uses the so-called data-dependent constraints (DDCs) to broaden the adaptive beampattern nulls [30, 33]. The essence of this approach is to replace the sample covariance matrix in the SMI or LSMI beamformer by the following modified sample covariance matrix:

$$\hat{\mathbf{R}}_{\mathrm{DDC}} = \hat{\mathbf{R}} + \zeta \mathbf{B}\hat{\mathbf{R}}\mathbf{B}, \tag{9.23}$$

where $\mathbf{B}$ is the known real-valued diagonal matrix of sensor coordinates and the parameter ζ determines the tradeoff between the null depth and width. The optimal value of ζ is independent of the environmental parameters, but can be easily determined based on the array parameters only [30].

Although it has been shown in [30, 31, 32] that both the MT- and DDC-based adaptive beamformers substantially improve the robustness against slow and moderate interferer mobility, both these methods can fail when applied to scenario with rapidly moving interferers.

All techniques discussed above use *ad hoc* approaches to incorporate robustness into adaptive beamforming schemes. Recently, more theoretically rigorous techniques have been proposed that obtain robust beamforming solutions by means of the optimization of the *worst-case performance* of adaptive beamformers [35, 38, 39].

First of all, we consider the most general situation of fast fading and discuss the robust beamformer that has been recently derived in [35]. Following this work, we take into account that in practical situations, both the signal and interference-plus-noise covariance matrices are known with some errors. In particular, the errors of the signal covariance matrix are caused by a limited duration and number of training intervals, channel variations, fast motion of the desired user, and multiaccess interference during the training period. The errors in the interference-plus-noise covariance matrix are caused by finite number of snapshots in (9.14), by fast channel variations and interferer motion, and by the presence of the desired signal component in the snapshots that are used in (9.14). Hence, there is always a certain mismatch between the *actual* and *presumed* values of the matrices $\mathbf{R}_{\mathrm{s}}$ and $\mathbf{R}_{\mathrm{i+n}}$. This yields

$$\tilde{\mathbf{R}}_{\mathrm{s}} = \mathbf{R}_{\mathrm{s}} + \boldsymbol{\Delta}_1, \qquad \tilde{\mathbf{R}}_{\mathrm{i+n}} = \mathbf{R}_{\mathrm{i+n}} + \boldsymbol{\Delta}_2, \tag{9.24}$$

where $\mathbf{R}_{\mathrm{s}}$ and $\mathbf{R}_{\mathrm{i+n}}$ are the presumed signal and interference-plus-noise covariance matrices, respectively, whereas $\tilde{\mathbf{R}}_{\mathrm{s}}$ and $\tilde{\mathbf{R}}_{\mathrm{i+n}}$ are their actual values. Here, $\boldsymbol{\Delta}_1$ and $\boldsymbol{\Delta}_2$ are the unknown matrix *mismatches*.

In the presence of the mismatches $\boldsymbol{\Delta}_1$ and $\boldsymbol{\Delta}_2$, equation (9.5) for the output SINR should be rewritten as

$$\mathrm{SINR} = \frac{\mathbf{w}^H \tilde{\mathbf{R}}_{\mathrm{s}} \mathbf{w}}{\mathbf{w}^H \tilde{\mathbf{R}}_{\mathrm{i+n}} \mathbf{w}}. \tag{9.25}$$

In [35], it was assumed that the norms of the mismatch matrices $\mathbf{\Delta}_1$ and $\mathbf{\Delta}_2$ can be bounded by some known constants

$$||\mathbf{\Delta}_1|| \leq \varepsilon, \qquad ||\mathbf{\Delta}_2|| \leq \gamma. \tag{9.26}$$

To provide robustness against possible norm-bounded mismatches (9.26), it has been proposed in [35] to find the beamformer weight vector by means of maximizing the worst-case output SINR, that is, via solving the following optimization problem [35]:

$$\max_{\mathbf{w}} \min_{\mathbf{\Delta}_1,\mathbf{\Delta}_2} \frac{\mathbf{w}^H(\mathbf{R}_s + \mathbf{\Delta}_1)\mathbf{w}}{\mathbf{w}^H(\mathbf{R}_{i+n} + \mathbf{\Delta}_2)\mathbf{w}} \quad \forall ||\mathbf{\Delta}_1|| \leq \varepsilon,\ ||\mathbf{\Delta}_2|| \leq \gamma. \tag{9.27}$$

It has been shown in [35] that the solution to robust MVDR problem (9.27) can be written as

$$\mathbf{w}_{\text{rob}} = \mathcal{P}\left\{(\mathbf{R}_{i+n} + \gamma\mathbf{I})^{-1}(\mathbf{R}_s - \varepsilon\mathbf{I})\right\}. \tag{9.28}$$

In practice, the matrix $\mathbf{R}_{i+n}$ is unavailable and the sample covariance matrix $\hat{\mathbf{R}}$ is normally used instead of $\mathbf{R}_{i+n}$. Hence, the sample version of robust beamformer (9.28) is given by [35]

$$\mathbf{w}_{\text{rob}} = \mathcal{P}\{(\hat{\mathbf{R}} + \gamma\mathbf{I})^{-1}(\mathbf{R}_s - \varepsilon\mathbf{I})\}. \tag{9.29}$$

In the rank-one (slow fading) case, absorbing σ_s^2 in ε (i.e., assuming without loss of generality that $\sigma_s^2 = 1$), equation (9.29) can be simplified as

$$\mathbf{w}_{\text{rob}} = \mathcal{P}\{(\hat{\mathbf{R}} + \gamma\mathbf{I})^{-1}(\mathbf{a}_s\mathbf{a}_s^H - \varepsilon\mathbf{I})\}. \tag{9.30}$$

From (9.29) it is clear that the worst-case performance optimization approach leads to a sort of generalized diagonal loading using both the *negative* and *positive* loading factors, where the negative loading is applied to the presumed covariance matrix of the desired signal, while the positive loading is applied to the sample covariance matrix.

Assuming $\varepsilon = 0$, we have that (9.29) simplifies to (9.17), that is, we obtain the conventional LSMI algorithm. Note that robust beamformer (9.29) offers a reliable yet essentially simpler way of choosing the parameters γ and ε as compared to the way of choosing γ in the diagonal loading method based on the white noise gain constraint. Indeed, the parameters γ and ε in (9.29) are optimally matched to the assumed amount on uncertainties in the signal and interference-plus-noise covariance matrices. Note that in practical communication scenarios, it is relatively easy to obtain approximate values of the parameters γ and ε based on some preliminary (coarse) knowledge of the type of propagation channel considered. This knowledge can be obtained either through channel measurement campaigns

or through numerical channel modelling, and can then be exploited to obtain approximate values of the upper bounds of mismatches (9.26) that are typical for this particular channel.

An interesting feature of robust beamformer (9.29) has been established in [35], where it has been shown that (9.29) can also be interpreted as a new generalization of the LSMI beamformer with positive-only diagonal loading whose amount is *adaptive* rather than *fixed*.

It is noteworthy that beamformer (9.29) does not take into account that the actual signal covariance matrix $\tilde{\mathbf{R}}_s$ must be nonnegative definite [21]. Although by ignoring the aforementioned constraint we simply strengthen the worst case and this does not affect the performance of (9.29) in most of typical scenarios [35], it is interesting to develop a more adequate formulation of the robust beamforming problem that can take into account this constraint. For the slow fading case, such problem has been recently considered in [38]. In this case, the spatial signature mismatch

$$\mathbf{e} = \tilde{\mathbf{a}}_s - \mathbf{a}_s \tag{9.31}$$

can be considered instead of the signal covariance matrix mismatch $\boldsymbol{\Delta}_1$ of (9.24). Here, $\tilde{\mathbf{a}}_s$ and $\mathbf{a}_s$ are the actual and presumed spatial signatures, respectively. It is assumed in [38] that the norm of the mismatch vector is bounded as

$$\|\mathbf{e}\| \leq \epsilon, \tag{9.32}$$

where the constant ϵ is known. The idea proposed in [38] is to add robustness to the MVDR beamforming problem by means of imposing the worst-case distortionless response constraint which should be satisfied for all mismatched spatial signature vectors. With such a constraint, the robust MVDR beamformer can be obtained by solving the following constrained minimization problem [38]:

$$\min_{\mathbf{w}} \mathbf{w}^H \hat{\mathbf{R}} \mathbf{w} \quad \text{subject to } \left| \mathbf{w}^H (\mathbf{a}_s + \mathbf{e}) \right| \geq 1 \quad \forall \|\mathbf{e}\| \leq \epsilon. \tag{9.33}$$

It has been shown in [38] that problem (9.33) can be converted to

$$\min_{\mathbf{w}} \mathbf{w}^H \hat{\mathbf{R}} \mathbf{w} \quad \text{subject to } \mathbf{w}^H \mathbf{a}_s \geq \epsilon \|\mathbf{w}\| + 1, \tag{9.34}$$

and that the constraint in (9.34) is satisfied with equality. Note that although problems (9.33) and (9.34) are mathematically equivalent, problem (9.33) is computationally intractable, whereas (9.34) belongs to the class of convex second-order cone programming (SOCP) problems which can be easily solved using standard and highly efficient interior point method software with the complexity $O(M^3)$ [38]. Another way to solve this problem is to use Newton-type algorithms. Several techniques of the latter type to solve problem (9.34) and some its extensions have been recently proposed in [39, 40, 41] (all with complexities $O(M^3)$).

Several extensions of the techniques of [35, 38] have been recently developed. In [39], the beamformer of [38] has been extended to the case of ellipsoidal (anisotropic) uncertainty. In [40], a new covariance fitting-based interpretation of the robust MVDR beamformer of [38] and of its anisotropic extension of [39] has been developed.[3] The authors of [41, 42] have extended the approaches of [35] and [38] to robust multiuser detection problems. The authors of [35, 43] presented efficient online implementations of the worst-case robust adaptive algorithms of [35, 38] with the complexity $O(M^2)$.

In [44], the approach of [38] is extended to the case where, apart from the spatial signature mismatch, there is a nonstationarity of the array data (which, in turn, may be caused by the nonstationarity of multiaccess interference and propagation channel). The approach of [44] suggests, instead of modelling uncertainty in the interference-plus-noise covariance matrix (as in (9.24)), to model such an uncertainty by means of adding it directly to the data matrix $\mathbf{X} = [\mathbf{x}(1), \ldots, \mathbf{x}(N)]$. Note that the sample covariance matrix can be expressed as

$$\hat{\mathbf{R}} = \frac{1}{N}\mathbf{X}\mathbf{X}^H. \tag{9.35}$$

To take into account the nonstationarity of the array data, the mismatch matrix

$$\boldsymbol{\Delta} = \tilde{\mathbf{X}} - \mathbf{X} \tag{9.36}$$

can be introduced [44], where $\tilde{\mathbf{X}}$ and $\mathbf{X}$ are, respectively, the actual and presumed data matrices at the time when the beamformer is applied to detect the desired user. Note that the presumed matrix $\mathbf{X}$ simply corresponds to the data acquired by the beamformer prior to applying it to some particular snapshot. Because of nonstationarity effects, the data samples in $\mathbf{X}$ can become irrelevant at the time when the beamformer is applied (when the actual, yet unknown, data matrix is $\tilde{\mathbf{X}}$). In such cases, the actual sample covariance matrix can be written as

$$\hat{\tilde{\mathbf{R}}} = \frac{1}{N}\tilde{\mathbf{X}}\tilde{\mathbf{X}}^H = \frac{1}{N}(\mathbf{X} + \boldsymbol{\Delta})(\mathbf{X} + \boldsymbol{\Delta})^H. \tag{9.37}$$

According to (9.37), the matrix $\hat{\tilde{\mathbf{R}}}$ is guaranteed to be Hermitian and nonnegative definite.

To combine the robustness against interference nonstationarity and spatial signature errors, the authors of [44] use ideas similar to that of [38], that is, they assume that the norms of both the spatial signature mismatch $\mathbf{e}$ and the data matrix mismatch $\boldsymbol{\Delta}$ are bounded by some known constants as

$$\|\mathbf{e}\| \leq \epsilon, \qquad \|\boldsymbol{\Delta}\| \leq \eta. \tag{9.38}$$

[3] In [40], the robust MVDR beamformer of [38, 39] is referred to as the *robust Capon beamformer*.

Then, the robust formulation of the MVDR beamforming problem can be written in the following form [44]:

$$\min_{\mathbf{w}} \max_{\|\boldsymbol{\Delta}\| \le \eta} \left|\left|(\mathbf{X}+\boldsymbol{\Delta})^H \mathbf{w}\right|\right| \quad \text{subject to } \left|\mathbf{w}^H(\mathbf{a}_s+\mathbf{e})\right| \ge 1 \quad \forall \|\mathbf{e}\| \le \epsilon. \tag{9.39}$$

This problem represents a further extension of (9.33) with additional worst-case robustness against nonstationary received data. The essence of (9.39) is to minimize the beamformer output power in the scenario with the worst-case data nonstationarity subject to the constraint which maintains distortionless response for the worst-case spatial signature mismatch.

Problem (9.39) can be converted to [44]

$$\min_{\mathbf{w}} \left|\left|\mathbf{X}^H \mathbf{w}\right|\right| + \eta \|\mathbf{w}\| \quad \text{subject to } \mathbf{w}^H \mathbf{a}_s \ge \epsilon \|\mathbf{w}\| + 1, \tag{9.40}$$

which represents an extended version of (9.34). Problem (9.40) also belongs to the class of convex SOCP problems and can be efficiently solved using standard interior point methods.

In [21, 35, 38, 44], the worst-case robust MVDR beamformers (9.29), (9.34), and (9.40) have been compared with the earlier traditional ad hoc robust beamformers (such as the LSMI and eigenspace-based beamformers as well as different modifications of MT-based beamformers) by means of numerous simulations involving typical wireless communications scenarios with different types of fading (coherent and incoherent local scattering, etc.) and with different types of data nonstationarity/multiaccess interferer mobility. The results of these simulations show that the worst-case beamformers consistently enjoy a substantially improved robustness relative to the traditional ad hoc adaptive beamformers. Therefore, the worst-case adaptive beamformers are excellent candidates for uplink BS beamforming algorithms for cellular mobile radio systems [45, 46].

9.5. Summary

In this chapter, an overview of the state-of-the-art robust adaptive beamforming in the presence of array response mismatches and received data nonstationarity has been provided in application to cellular mobile radio systems with flat fading. A recently emerged approach to robust adaptive beamforming based on the worst-case performance optimization has been addressed in detail. Its advantages relative to the earlier ad hoc approaches to robust adaptive beamforming have been discussed.

Acknowledgment

The author is on leave from the Department of Electrical and Computer Engineering, McMaster University, Ontario, Canada.

Abbreviations

BS	Base station
DDC	Data-dependent constraints
LSMI	Loaded SMI
MT	Matrix tapering
MVDR	Minimum variance distortionless response
SDMA	Spatial division multiple access
SINR	Signal-to-interference-plus-noise ratio
SMI	Sample matrix inverse
SOCP	Second-order cone programming

Bibliography

[1] L. C. Godara, "Applications of antenna arrays to mobile communications. I. Performance improvement, feasibility, and system considerations," *Proc. IEEE*, vol. 85, no. 7, pp. 1031–1060, 1997.
[2] L. C. Godara, "Applications of antenna arrays to mobile communications. II. Beam-forming and direction-of-arrival considerations," *Proc. IEEE*, vol. 85, no. 8, pp. 1195–1245, 1997.
[3] T. S. Rappaport, Ed., *Smart Antennas: Adaptive Arrays, Algorithms, and Wireless Position Location*, IEEE Press, New York, NY, USA, 1998.
[4] J. Winters, "Spread spectrum in a four-phase communication system employing adaptive antennas," *IEEE Trans. Commun.*, vol. 30, no. 5, pp. 929–936, 1982.
[5] J. Winters, "Optimum combining in digital mobile radio with cochannel interference," *IEEE J. Select. Areas Commun.*, vol. 2, no. 4, pp. 528–539, 1984.
[6] J. Razavilar, F. Rashid-Farrokhi, and K. J. R. Liu, "Traffic improvements in wireless communication networks using antenna arrays," *IEEE J. Select. Areas Commun.*, vol. 18, no. 3, pp. 458–471, 2000.
[7] S. Kapoor, D. J. Marchok, and Y.-F. Huang, "Adaptive interference suppression in multiuser wireless OFDM systems using antenna arrays," *IEEE Trans. Signal Processing*, vol. 47, no. 12, pp. 3381–3391, 1999.
[8] B. Widrow, P. E. Mantey, L. J. Griffiths, and B. B. Goode, "Adaptive antenna systems," *Proc. IEEE*, vol. 55, no. 12, pp. 2143–2159, 1967.
[9] H. Cox, "Resolving power and sensitivity to mismatch of optimum array processors," *J. Acoust. Soc. Amer.*, vol. 54, no. 3, pp. 771–785, 1973.
[10] I. S. Reed, J. D. Mallett, and L. E. Brennan, "Rapid convergence rate in adaptive arrays," *IEEE Trans. Aerosp. Electron. Syst.*, vol. 10, pp. 853–863, 1974.
[11] L. E. Brennan, J. D. Mallett, and I. S. Reed, "Adaptive arrays in airborne MTI radar," *IEEE Trans. Antennas Propagat.*, vol. 24, no. 5, pp. 607–615, 1976.
[12] S. P. Applebaum, "Adaptive arrays," *IEEE Trans. Antennas Propagat.*, vol. 24, no. 5, pp. 585–598, 1976.
[13] R. A. Monzingo and T. W. Miller, *Introduction to Adaptive Arrays*, John Wiley & Sons, New York, NY, USA, 1980.
[14] L. J. Griffiths and C. W. Jim, "An alternative approach to linearly constrained adaptive beamforming," *IEEE Trans. Antennas Propagat.*, vol. 30, no. 1, pp. 27–34, 1982.
[15] E. K. L. Hung and R. M. Turner, "A fast beamforming algorithm for large arrays," *IEEE Trans. Aerosp. Electron. Syst.*, vol. 19, no. 4, pp. 598–607, 1983.
[16] R. T. Compton Jr., *Adaptive Antennas: Concepts and Performance*, Prentice Hall, Englewood Cliffs, NJ, USA, 1988.
[17] S. S. Haykin, J. Litva, and T. J. Shepherd, Eds., *Radar Array Processing*, Springer, New York, NY, USA, 1992.
[18] H. L. Van Trees, *Optimum Array Processing*, Wiley-Interscience, New York, NY, USA, 2002.
[19] A. B. Gershman, "Robust adaptive beamforming in sensor arrays," *Int. J. Electron. Commun. (AEU)*, vol. 53, no. 6, pp. 305–314, 1999.

[20] H. Cox, R. Zeskind, and M. Owen, "Robust adaptive beamforming," *IEEE Trans. Acoustics, Speech, Signal Processing*, vol. 35, no. 10, pp. 1365–1376, 1987.

[21] A. B. Gershman, "Robustness issues in adaptive beamforming and high-resolution direction finding," in *High-Resolution and Robust Signal Processing*, Y. Hua, A. B. Gershman, and Q. Cheng, Eds., pp. 63–110, Marcel Dekker, New York, NY, USA, 2003.

[22] J. Salz and J. H. Winters, "Effect of fading correlation on adaptive arrays in digital mobile radio," *IEEE Trans. Veh. Technol.*, vol. 43, no. 4, pp. 1049–1057, 1994.

[23] A. M. Wyglinski and S. D. Blostein, "On uplink CDMA cell capacity: mutual coupling and scattering effects on beamforming," *IEEE Trans. Veh. Technol.*, vol. 52, no. 2, pp. 289–304, 2003.

[24] K. I. Pedersen, P. E. Mogensen, and B. H. Fleury, "A stochastic model of the temporal and azimuthal dispersion seen at the base station in outdoor propagation environments," *IEEE Trans. Veh. Technol.*, vol. 49, no. 2, pp. 437–447, 2000.

[25] D. D. Feldman and L. J. Griffiths, "A projection approach for robust adaptive beamforming," *IEEE Trans. Signal Processing*, vol. 42, no. 4, pp. 867–876, 1994.

[26] B. Hassibi and B. M. Hochwald, "How much training is needed in multiple-antenna wireless links?," *IEEE Trans. Inform. Theory*, vol. 49, no. 4, pp. 951–963, 2003.

[27] N. D. Sidiropoulos, G. B. Giannakis, and R. Bro, "Blind PARAFAC receivers for DS-CDMA systems," *IEEE Trans. Signal Processing*, vol. 48, no. 3, pp. 810–823, 2000.

[28] Y. Rong, S. A. Vorobyov, A. B. Gershman, and N. D. Sidiropoulos, "Blind spatial signature estimation via time-varying user power loading and parallel factor analysis," *IEEE Trans. Signal Processing*, vol. 53, pp. 1697–1710, 2005, (also see *Proc. VTC '03*, Orlando, FL, USA, October 2003).

[29] E. Baccarelli and M. Biagi, "Power-allocation policy and optimized design of multiple-antenna systems with imperfect channel estimation," *IEEE Trans. Veh. Technol.*, vol. 53, no. 1, pp. 136–145, 2004.

[30] A. B. Gershman, U. Nickel, and J. F. Böhme, "Adaptive beamforming algorithms with robustness against jammer motion," *IEEE Trans. Signal Processing*, vol. 45, no. 7, pp. 1878–1885, 1997.

[31] J. Riba, J. Goldberg, and G. Vazquez, "Robust beamforming for interference rejection in mobile communications," *IEEE Trans. Signal Processing*, vol. 45, no. 1, pp. 271–275, 1997.

[32] J. R. Guerci, "Theory and application of covariance matrix tapers for robust adaptive beamforming," *IEEE Trans. Signal Processing*, vol. 47, no. 4, pp. 977–985, 1999.

[33] A. B. Gershman, G. V. Serebryakov, and J. F. Böhme, "Constrained Hung-Turner adaptive beamforming algorithm with additional robustness to wideband and moving jammers," *IEEE Trans. Antennas Propagat.*, vol. 44, no. 3, pp. 361–367, 1996.

[34] I. Bogdan and C. Comsa, "Analysis of circular arrays as smart antennas for cellular networks," in *Proc. International Symposium on Signals, Circuits and Systems (SCS '03)*, pp. 525–528, Iasi, Romania, July 2003.

[35] S. Shahbazpanahi, A. B. Gershman, Z.-Q. Luo, and K. M. Wong, "Robust adaptive beamforming for general-rank signal models," *IEEE Trans. Signal Processing*, vol. 51, no. 9, pp. 2257–2269, 2003.

[36] Y. I. Abramovich, "Controlled method for adaptive optimization of filters using the criterion of maximum SNR," *Radio Engineering and Electronic Physics*, vol. 26, no. 3, pp. 87–95, 1981.

[37] L. Chang and C.-C. Yeh, "Performance of DMI and eigenspace-based beamformers," *IEEE Trans. Antennas Propagat.*, vol. 40, no. 11, pp. 1336–1347, 1992.

[38] S. A. Vorobyov, A. B. Gershman, and Z.-Q. Luo, "Robust adaptive beamforming using worst-case performance optimization: a solution to the signal mismatch problem," *IEEE Trans. Signal Processing*, vol. 51, no. 2, pp. 313–324, 2003.

[39] R. Lorenz and S. P. Boyd, "Robust minimum variance beamforming," *IEEE Trans. Signal Processing*, vol. 53, no. 5, pp. 1684–1696, 2005.

[40] J. Li, P. Stoica, and Z. Wang, "On robust Capon beamforming and diagonal loading," *IEEE Trans. Signal Processing*, vol. 51, no. 7, pp. 1702–1715, 2003.

[41] K. Zarifi, S. Shahbazpanahi, A. B. Gershman, and Z.-Q. Luo, "Robust blind multiuser detection based on the worst-case performance optimization of the MMSE receiver," *IEEE Trans. Signal Processing*, vol. 53, no. 1, pp. 295–305, 2005.

[42] S. Shahbazpanahi and A. B. Gershman, "Robust blind multiuser detection for synchronous CDMA systems using worst-case performance optimization," *IEEE Trans. Wireless Communications*, vol. 3, no. 6, pp. 2232–2245, 2004.

[43] A. El-Keyi, T. Kirubarajan, and A. B. Gershman, "Robust adaptive beamforming based on the Kalman filter," to appear in *IEEE Trans. Signal Processing*.

[44] S. A. Vorobyov, A. B. Gershman, Z.-Q. Luo, and N. Ma, "Adaptive beamforming with joint robustness against mismatched signal steering vector and interference nonstationarity," *IEEE Signal Processing Lett.*, vol. 11, no. 2, pp. 108–111, 2004.

[45] L. Häring, A. B. Gershman, T. Scholand, and T. Kaiser, "Robust beamforming in application to smart antennas for TD-SCDMA communications," in *Proc. Second Joint Symp. on Opto- and Microelectronic Devices and Circuits*, pp. 279–282, Stuttgart, Germany, March 2002.

[46] T. Kaiser, A. B. Gershman, and A. Czylwik, "Smart antennas using robust adaptive beamforming," in *Proc. 6th Wireless World Research Forum*, London, UK, June 2002.

Alex B. Gershman: Department of Communication Systems, Institute of Telecommunications, Darmstadt University of Technology, Merckstrasse 25, 64283 Darmstadt, Germany

Email: gershman@ieee.org

10 Robust and reduced-rank space-time decision feedback equalization

Frank A. Dietrich, Guido Dietl, Michael Joham, and Wolfgang Utschick

10.1. Introduction

The decision feedback equalizer (DFE) is known as a popular choice for channel equalization to obtain a good performance-complexity trade-off. Originally, it was proposed to equalize single-input single-output (SISO) communication links, where the DFE feedforward filter was IIR [1, 2]. Although an IIR filter was assumed in the design, it has to be approximated by an FIR filter for implementation to obtain a causal system, which is a suboptimum approach. Thus, we restrict the *feedforward filter* to be *FIR* for the optimization *beforehand* as in [3, 4]. We consider a frequency selective MIMO channel, which models a single-user link with spatially multiplexed data streams or, alternatively, multiuser single-input multiple-output links (also known as multiuser detection). In contrast to a DFE for MIMO systems with an optimization of the detection order for the data streams, as in Bell Laboratories Layered Space-Time (BLAST) equalizer [5] or parallel interference cancellation [6], the space-time (ST) DFE applied here only feeds back preceding symbols and minimizes interstream interference in the feedforward filter. The optimization is performed minimizing the mean square error (MSE) of the symbol vector before the decision device assuming that the symbols feedback are perfectly known.

The standard DFE optimization assumes error-free knowledge of the channel parameters. Relying on a finite number of training symbols to estimate the channel, this assumption is not valid in practice. Moreover, the ST-DFE is more sensitive to channel estimation errors than linear equalizers. Thus, methods from robust optimization should be applied to reduce its sensitivity, which take into account the size and structure of the parameter errors.

Worst-case optimization, that is, minimizing the maximum possible mean square error for the given error model, is the standard approach (e.g., [7, 8]). In this case, the error model is given by bounds on the channel parameters, for example, assuming bounded errors in the Euclidean norm. The min-max approaches have the disadvantage that the free parameters describing the set of errors, for

example, the bounded norm, have to be chosen heuristically. For example, the estimation error is often assumed Gaussian-distributed given first- and second-order moments; as the error is not bounded in this case, it may be bounded heuristically depending on the standard deviation of the error. Additionally, it is difficult to define a worst case on the physical layer in a communication link, as the worst case is commonly handled by higher layers.

An alternative paradigm, which we apply to the ST-DFE in Section 10.4, is known from *static stochastic programming* [9]. Assuming a stochastic error model with known first- and second-order statistics, the traditional MSE cost function becomes a random variable. Taking the expectation of the cost function with respect to the parameters, we minimize the expected MSE knowing the error statistics. Thus, we measure the performance on average, which is a common approach in wireless communications with a time-varying scenario, and achieve a robustness on average.

Both approaches were compared for equalization of SISO channels in [10] for a fixed channel and bounded error, showing that the stochastic approach is less conservative. Stochastic programming was also applied to linear preequalization in [11]. Finally, a robust ST-DFE based on the H^∞ approach is introduced in [12].

Our robust ST-DFE is a generalization of the work in [10] with application to mobile communication. The solution is obtained explicitly with the same order of complexity as the standard solution. Note that the min-max solution is typically of higher complexity and often not obtained explicitly, but with iterative methods [7]. The parameters of the error model depend on system parameters and the channel statistics. Thus, no heuristic parameter choice is necessary and an adaptation to error size and structure is possible. In the nominal case, that is, no parameter errors, the latter aspect ensures the same performance as the standard (nonrobust) design. Certainly, in practice the first- and second-order error statistics need to be estimated, which should be possible with sufficient accuracy as they change more slowly than the channel coefficients.

Feeding back only preceding detected symbols without the need of a spatial ordering already reduces the design complexity considerably. Further reduction in complexity can be achieved with a *reduced-rank implementation* [13, 14] of the feedforward filter. An approximation in the *Krylov subspace* is known to provide a performance advantage with similar complexity compared to other reduced-rank approaches [15, 16, 17]. Previously, a Krylov-based implementation of the DFE for SISO channels was given in [18]. We introduce the Krylov subspace-based reduced-rank implementation of the standard ST-DFE and its robust version (Section 10.5).

After introducing the MIMO system model for data and pilot channel in Section 10.2 the standard optimization for the ST-DFE, which includes a latency time optimization, and its solution is given in Section 10.3. The error model, robust optimization criterion and its solution, as well as a detailed interpretation of the robust ST-DFE cost function, which is related to Tikhonov regularization, and its solution is presented in Section 10.4. The Krylov subspace-based reduced-rank implementation is motivated and described in Section 10.5, which includes a

simple low-complexity choice of the latency time. Performance results in terms of uncoded bit error rate (BER) show significant gains of the robust design for spatially correlated channels (Section 10.6). Considerable rank reduction and, thus, complexity reduction is possible with only a small loss in performance. It is also shown, that latency time optimization should be a key component of every DFE. Finally, the advantages of the robust ST-DFE in case of outdated channel knowledge is discussed.

Notation. The operators $\mathrm{E}[\cdot]$, $\mathrm{E}_{\mathbf{a}}[\cdot]$, $(\cdot)^{\mathrm{T}}$, $(\cdot)^{\mathrm{H}}$, and "$\otimes$" stand for a general expectation, expectation with respect to $\mathbf{a}$, transpose, Hermitian transpose, and Kronecker product, respectively. $\mathbf{I}_N$ is the $N \times N$ identity matrix and $\mathbf{0}_{M\times N}$ the $M \times N$ zero matrix.

10.2. System model

Data symbols $\mathbf{b}[n] \in \mathbb{B}^{N_{\mathrm{T}}}$ from a set of QAM symbols $\mathbb{B}$ with zero mean are transmitted from N_{T} antennas via a frequency selective MIMO channel $\mathbf{H}[n] = \sum_{\ell=0}^{L-1} \mathbf{H}_\ell \delta[n-\ell] \in \mathbb{C}^{N_{\mathrm{R}}\times N_{\mathrm{T}}}$ of length L. The q, pth element of $\mathbf{H}[n]$ is $h_{p,q}[n]$. The received signal vector of N_{R} antennas is (Figure 10.1)

$$\mathbf{r}[n] = \mathbf{H}[n] * \mathbf{b}[n] + \mathbf{v}[n] \in \mathbb{C}^{N_{\mathrm{R}}}, \tag{10.1}$$

where $\mathbf{v}[n] \sim \mathcal{N}_{\mathbb{C}}(\mathbf{0}, \mathbf{C}_{\mathbf{v}})$ is additive temporally white complex Gaussian noise with covariance matrix $\mathbf{C}_{\mathbf{v}} = \mathrm{E}[\mathbf{v}[n]\mathbf{v}[n]^{\mathrm{H}}] \in \mathbb{C}^{N_{\mathrm{R}}\times N_{\mathrm{R}}}$.

Pilot channel. N_{p} pilot symbols $\mathbf{b}_{\mathrm{p}}[n] \in \mathbb{B}^{N_{\mathrm{T}}}$ with $n \in \{2-L, \ldots, N_{\mathrm{p}}\}$ are time-multiplexed and include $L-1$ guard symbols. The received pilot sequence

$$\mathbf{r}_{\mathrm{p}}[n] = \mathbf{H}[n] * \mathbf{b}_{\mathrm{p}}[n] + \mathbf{v}_{\mathrm{p}}[n] \in \mathbb{C}^{N_{\mathrm{R}}} \tag{10.2}$$

can be rewritten as

$$\mathbf{R}_{\mathrm{p}} = [\mathbf{H}_0, \ldots, \mathbf{H}_{L-1}]\mathbf{B}'_{\mathrm{p}} + \mathbf{V}_{\mathrm{p}} \in \mathbb{C}^{N_{\mathrm{R}}\times N_{\mathrm{p}}} \tag{10.3}$$

with N_{p} received samples $\mathbf{R}_{\mathrm{p}} = [\mathbf{r}_{\mathrm{p}}[1], \ldots, \mathbf{r}_{\mathrm{p}}[N_{\mathrm{p}}]]$ ($\mathbf{V}_{\mathrm{p}}$ defined equivalently), and block Toeplitz $\mathbf{B}'_{\mathrm{p}} \in \mathbb{C}^{N_{\mathrm{T}}L\times N_{\mathrm{p}}}$ with first block row $[\mathbf{b}_{\mathrm{p}}[1], \ldots, \mathbf{b}_{\mathrm{p}}[N_{\mathrm{p}}]]$ and first column $[\mathbf{b}_{\mathrm{p}}^{\mathrm{T}}[1], \ldots, \mathbf{b}_{\mathrm{p}}^{\mathrm{T}}[2-L]]^{\mathrm{T}}$. Using $\mathrm{vec}(\mathbf{ABC}) = (\mathbf{C}^{\mathrm{T}} \otimes \mathbf{A})\,\mathrm{vec}(\mathbf{B})$, it reads as

$$\mathbf{r}_{\mathrm{p}} = \mathrm{vec}\,(\mathbf{R}_{\mathrm{p}}) = \mathbf{B}_{\mathrm{p}}\mathbf{h} + \mathbf{v}_{\mathrm{p}} \in \mathbb{C}^{N_{\mathrm{R}}N_{\mathrm{p}}} \tag{10.4}$$

with $\mathbf{B}_{\mathrm{p}} = \mathbf{B}'^{,\mathrm{T}}_{\mathrm{p}} \otimes \mathbf{I}_{N_{\mathrm{R}}}$. All channel coefficients are summarized in

$$\mathbf{h} = \mathrm{vec}\,([\mathbf{H}_0, \ldots, \mathbf{H}_{L-1}]) \in \mathbb{C}^{N_{\mathrm{R}}N_{\mathrm{T}}L}. \tag{10.5}$$

The additive noise $\mathbf{v}_{\mathrm{p}}[n]$ is distributed as $\mathcal{N}_{\mathbb{C}}(\mathbf{0}, \mathbf{C}_{\mathbf{v}})$.

The channel is assumed to be i.i.d. block fading and complex Gaussian $\mathbf{h} \sim \mathcal{N}_{\mathbb{C}}(\boldsymbol{\mu}_{\mathbf{h}}, \mathbf{C}_{\mathbf{h}})$ with mean $\boldsymbol{\mu}_{\mathbf{h}} = \mathrm{E}[\mathbf{h}]$ and covariance $\mathbf{C}_{\mathbf{h}} = \mathrm{E}[(\mathbf{h} - \boldsymbol{\mu}_{\mathbf{h}})(\mathbf{h} - \boldsymbol{\mu}_{\mathbf{h}})^{\mathrm{H}}]$.

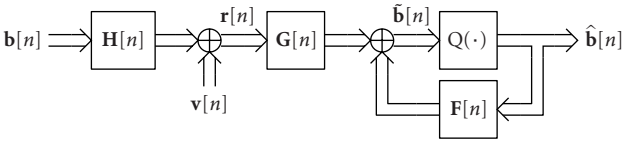

FIGURE 10.1. MIMO system with space-time decision feedback equalizer.

10.3. Standard space-time decision feedback equalization

After the received signal $\mathbf{r}[n] \in \mathbb{C}^{N_R}$ has been passed through the FIR matrix feedforward filter of length G (Figure 10.1)

$$\mathbf{G}[n] = \sum_{g=0}^{G-1} \mathbf{G}_g \delta[n-g] \in \mathbb{C}^{N_T \times N_R}, \tag{10.6}$$

the interference of the already detected symbols is removed by adding the output of the feedback filter of length $F = L + G - \nu - 2$,

$$\mathbf{F}[n] = \sum_{f=1}^{F} \mathbf{F}_f \delta[n-f] \in \mathbb{C}^{N_T \times N_T}, \tag{10.7}$$

to form the input $\tilde{\mathbf{b}}[n] \in \mathbb{C}^{N_T}$ of the element-wise nearest-neighbor quantizer $Q(\cdot)$ (see Figure 10.1), whose desired value is $\mathbf{b}[n-\nu]$ with the latency time ν, that is, a symbol is detected ν symbol times after it has been transmitted. Note that $\mathbf{F}_f = \mathbf{0}_{N_T \times N_T}$ for $f < 1$, since only already detected symbols can be fed back. Similarly, $\mathbf{F}_f = \mathbf{0}_{N_T \times N_T}$ for $f > F$, as the symbols with delays greater than F do not contribute interference to $\tilde{\mathbf{b}}[n]$.

In vector-matrix notation, the quantizer input reads as

$$\tilde{\mathbf{b}}[n] = \mathbf{G}\mathbf{H}\bar{\mathbf{b}}[n] + \mathbf{F}\mathbf{S}^{(\nu)}\bar{\mathbf{b}}[n] + \mathbf{G}\bar{\mathbf{v}}[n], \tag{10.8}$$

where we made the popular assumption for DFE that the decisions are correct, that is, $\hat{\mathbf{b}}[n] = \mathbf{b}[n-\nu]$. We put the matrix coefficients of the feedforward filter and the feedback filter into

$$\begin{aligned} \mathbf{G} &= [\mathbf{G}_0, \ldots, \mathbf{G}_{G-1}] \in \mathbb{C}^{N_T \times N_R G}, \\ \mathbf{F} &= [\mathbf{F}_1, \ldots, \mathbf{F}_F] \in \mathbb{C}^{N_T \times N_T F}, \end{aligned} \tag{10.9}$$

respectively. The block Toeplitz channel matrix is defined as

$$\mathbf{H} = \sum_{\ell=0}^{L-1} \underbrace{[\mathbf{0}_{G\times\ell}, \mathbf{I}_G, \mathbf{0}_{G\times L-\ell-1}]}_{\mathbf{\Sigma}_\ell} \otimes \mathbf{H}_\ell \in \mathbb{C}^{N_R G \times N_T (L+G-1)}. \tag{10.10}$$

The symbols and the noise are collected in

$$\begin{aligned}\bar{\mathbf{b}}[n] &= \left[\mathbf{b}^{\mathrm{T}}[n],\ldots,\mathbf{b}^{\mathrm{T}}[n-L-G+2]\right]^{\mathrm{T}} \in \mathbb{C}^{N_{\mathrm{T}}(L+G-1)},\\ \bar{\mathbf{v}}[n] &= \left[\mathbf{v}^{\mathrm{T}}[n],\ldots,\mathbf{v}^{\mathrm{T}}[n-G+1]\right]^{\mathrm{T}} \in \mathbb{C}^{N_{\mathrm{R}}G},\end{aligned} \tag{10.11}$$

respectively. For conciseness, we introduced the matrix

$$\mathbf{S}^{(\nu)} = \left[\mathbf{0}_{N_{\mathrm{T}}F\times N_{\mathrm{T}}(\nu+1)}, \mathbf{I}_{N_{\mathrm{T}}F}\right] \in \{0,1\}^{N_{\mathrm{T}}F\times N_{\mathrm{T}}(L+G-1)}, \tag{10.12}$$

which selects the last $N_{\mathrm{T}}F$ elements from a $N_{\mathrm{T}}(L+G-1)$-dimensional column vector. Note that the desired value for the estimate $\tilde{\mathbf{b}}[n]$ is

$$\mathbf{b}[n-\nu] = \mathbf{E}_{\nu+1}\bar{\mathbf{b}}[n] \quad \text{with } \mathbf{E}_{\nu+1} = \mathbf{e}_{\nu+1}^{\mathrm{T}} \otimes \mathbf{I}_{N_{\mathrm{T}}}, \tag{10.13}$$

where $\mathbf{e}_{\nu+1} \in \{0,1\}^{L+G-1}$ denotes the $(\nu+1)$th column of the identity matrix $\mathbf{I}_{L+G-1}$. Thus, the latency time ν is element of the set $\{0,\ldots,L+G-2\}$.

The MMSE-ST-DFE filters can be found by minimizing the MSE

$$\sigma^2_{\varepsilon,\mathrm{S}}\left(\{\mathbf{G},\mathbf{F},\nu\},\mathbf{h},\mathcal{M}_{\mathrm{S}}\right) = \mathrm{E}\left[\left|\left|\mathbf{b}[n-\nu]-\tilde{\mathbf{b}}[n]\right|\right|_2^2\right], \tag{10.14}$$

that is,

$$\left\{\mathbf{G}_{\mathrm{S}},\mathbf{F}_{\mathrm{S}},\nu_{\mathrm{S}}\right\} = \underset{\{\mathbf{G},\mathbf{F},\nu\}}{\arg\min}\, \sigma^2_{\varepsilon,\mathrm{S}}\left(\{\mathbf{G},\mathbf{F},\nu\},\mathbf{h},\mathcal{M}_{\mathrm{S}}\right), \tag{10.15}$$

with model parameters $\mathcal{M}_{\mathrm{S}} = \{\sigma_b^2, \mathbf{C}_{\bar{\mathbf{v}}}\}$ assumed known. For uncorrelated symbols, that is, $\mathbf{C}_{\bar{\mathbf{b}}} = \mathrm{E}[\bar{\mathbf{b}}[n]\bar{\mathbf{b}}^{\mathrm{H}}[n]] = \sigma_b^2\mathbf{I}_{N_{\mathrm{T}}(L+G-1)}$, the solution depending on latency time ν can be expressed as

$$\mathbf{G}_{\mathrm{S}} = \mathbf{E}_{\nu+1}\mathbf{H}^{\mathrm{H}}\left(\mathbf{H}\boldsymbol{\Pi}^{(\nu)}\mathbf{H}^{\mathrm{H}} + \sigma_b^{-2}\mathbf{C}_{\bar{\mathbf{v}}}\right)^{-1} = \mathbf{B}_{\mathrm{S}}\mathbf{A}_{\mathrm{S}}^{-1}, \tag{10.16}$$

$$\mathbf{F}_{\mathrm{S}} = -\mathbf{G}_{\mathrm{S}}\mathbf{H}\mathbf{S}^{(\nu),\mathrm{T}}, \tag{10.17}$$

with the projection matrix

$$\boldsymbol{\Pi}^{(\nu)} = \mathbf{I}_{N_{\mathrm{T}}(L+G-1)} - \mathbf{S}^{(\nu),\mathrm{T}}\mathbf{S}^{(\nu)} \tag{10.18}$$

setting the last $N_{\mathrm{T}}F$ columns of a matrix to zero, when applied from the right. Plugging this result into the cost function of (10.15), leads to the latency time optimization:

$$\nu_{\mathrm{S}} = \underset{\nu\in\{0,\ldots,L+G-2\}}{\arg\max}\ \mathrm{tr}\left(\mathbf{E}_{\nu+1}\mathbf{H}^{\mathrm{H}}\left(\mathbf{H}\boldsymbol{\Pi}^{(\nu)}\mathbf{H}^{\mathrm{H}} + \sigma_b^{-2}\mathbf{C}_{\bar{\mathbf{v}}}\right)^{-1}\mathbf{H}\mathbf{E}_{\nu+1}^{\mathrm{T}}\right). \tag{10.19}$$

As the matrix $\mathbf{H}\boldsymbol{\Pi}^{(\nu)}\mathbf{H}^{\mathrm{H}} + \sigma_b^{-2}\mathbf{C}_{\bar{\mathbf{v}}}$ depends on the latency time ν, the inverse has to be computed for every value of ν. Hence, the complexity to compute the MMSE-ST-DFE filters with optimum latency time ν_{S} is $\mathrm{O}(N_{\mathrm{R}}^3G^3(L+G))$.

10.4. Robust design

10.4.1. Model for parameter errors

Errors in the estimated channel parameters present the most significant source for performance degradation. To enable the robust design of the DFE, a suitable model for these errors is needed. We choose a *stochastic model* for the error $\boldsymbol{\Theta}$ with mean $\mathrm{E}[\boldsymbol{\Theta}]$ and covariance matrix $\mathbf{C}_{\boldsymbol{\Theta}} = \mathrm{E}[(\boldsymbol{\Theta} - \mathrm{E}[\boldsymbol{\Theta}])(\boldsymbol{\Theta} - \mathrm{E}[\boldsymbol{\Theta}])^{\mathrm{H}}]$, where no assumptions about the distribution of $\boldsymbol{\Theta}$ are made. The error is defined as

$$\boldsymbol{\Theta} = \mathbf{H} - \widehat{\mathbf{H}}. \tag{10.20}$$

If $\mathbf{H}$ and $\widehat{\mathbf{H}}$ are zero mean, the error $\boldsymbol{\Theta}$ is zero mean with $\mathrm{E}[\boldsymbol{\Theta}] = \mathbf{0}$. See below for conditions on $\widehat{\mathbf{H}}$ being zero mean.

Exploiting the block Toeplitz structure of $\boldsymbol{\Theta} = \sum_{\ell=0}^{L-1} \boldsymbol{\Sigma}_\ell \otimes \boldsymbol{\Theta}_\ell$ (cf. (10.10)) with $\boldsymbol{\Sigma}_\ell = [\mathbf{0}_{G\times\ell}, \mathbf{I}_G, \mathbf{0}_{G\times L-\ell-1}]$, the covariance matrix can be written as

$$\begin{aligned}\mathbf{C}_{\boldsymbol{\Theta}} &= \sum_{\ell=0}^{L-1}\sum_{\ell'=0}^{L-1} \boldsymbol{\Sigma}_\ell \boldsymbol{\Sigma}_{\ell'}^{\mathrm{T}} \otimes \mathrm{E}\left[\boldsymbol{\Theta}_\ell \boldsymbol{\Theta}_{\ell'}^{\mathrm{H}}\right] \\ &= \sum_{\ell=0}^{L-1}\sum_{\ell'=0}^{L-1} \boldsymbol{\Sigma}_\ell \boldsymbol{\Sigma}_{\ell'}^{\mathrm{T}} \otimes \left(\sum_{p=1}^{N_{\mathrm{T}}} \mathrm{E}\left[\boldsymbol{\theta}_p[\ell]\boldsymbol{\theta}_p[\ell']^{\mathrm{H}}\right] \right).\end{aligned} \tag{10.21}$$

Here, $\boldsymbol{\theta}_p[\ell] = [\theta_{p,1}[\ell], \ldots, \theta_{p,N_{\mathrm{R}}}[\ell]]^{\mathrm{T}}$ is the pth column of the estimation error $\boldsymbol{\Theta}_\ell$ in $\widehat{\mathbf{H}}_\ell$, that is, the ℓth channel tap of the pth transmitter.

If $\boldsymbol{\mu}_{\mathbf{h}} = \mathbf{0}$, the parameters in $\mathbf{H}$ can be estimated in general with an estimator $\mathbf{W}$ as $\widehat{\mathbf{h}} = \mathbf{W}\mathbf{r}_{\mathrm{p}}$. The error in the channel estimate $\widehat{\mathbf{h}}$ is defined equivalently to (10.20) by $\mathbf{h} = \widehat{\mathbf{h}} + \boldsymbol{\theta}$. From (10.21) we observe that $\mathbf{C}_{\boldsymbol{\Theta}}$ depends on subblocks of the error covariance matrix $\mathbf{C}_{\boldsymbol{\theta}}$ of the error $\boldsymbol{\theta}$.

As an example, we consider the linear minimum mean square error (LMMSE) channel estimator, which is equal to the conditional mean estimator since $\mathbf{h}$ is assumed to be Gaussian-distributed [19]:

$$\mathbf{W} = \arg\min_{\mathbf{W}'} \mathrm{E}\left[\left|\left|\mathbf{h} - \mathbf{W}'\mathbf{r}_{\mathrm{p}}\right|\right|_2^2\right] \in \mathbb{C}^{N_{\mathrm{R}}N_{\mathrm{T}}L\times N_{\mathrm{R}}N_{\mathrm{p}}}. \tag{10.22}$$

With $\mathbf{C}_{\mathbf{v}_{\mathrm{p}}} = \mathrm{E}[\mathbf{v}_{\mathrm{p}}\mathbf{v}_{\mathrm{p}}^{\mathrm{H}}]$, the LMMSE channel estimator reads as

$$\mathbf{W} = \mathbf{C}_{\mathbf{h}}\mathbf{B}_{\mathrm{p}}^{\mathrm{H}}\left(\mathbf{B}_{\mathrm{p}}\mathbf{C}_{\mathbf{h}}\mathbf{B}_{\mathrm{p}}^{\mathrm{H}} + \mathbf{C}_{\mathbf{v}_{\mathrm{p}}}\right)^{-1}. \tag{10.23}$$

From $\boldsymbol{\mu}_{\mathbf{h}} = \mathbf{0}$ as assumed above and $\boldsymbol{\mu}_{\mathbf{v}_{\mathrm{p}}} = \mathbf{0}$, that is, $\mathrm{E}[\mathbf{r}_{\mathrm{p}}] = \mathbf{0}$ (cf. (10.4)), it follows that $\boldsymbol{\mu}_{\boldsymbol{\theta}} = \mathbf{0}$. Hence, the error covariance matrix for the LMMSE estimate $\widehat{\mathbf{h}}$ is

$$\mathbf{C}_{\boldsymbol{\theta}} = \mathrm{E}\left[\boldsymbol{\theta}\boldsymbol{\theta}^{\mathrm{H}}\right] = \mathbf{C}_{\mathbf{h}} - \mathbf{W}\mathbf{B}_{\mathrm{p}}\mathbf{C}_{\mathbf{h}}. \tag{10.24}$$

It depends on the a priori information about the channel $\mathbf{C_h}$, which describes all slowly varying channel properties such as angles of arrival/departure, power delay profile, and path loss. Note that the LMMSE estimator optimally exploits—minimizing the MSE—the slowly varying channel properties, which significantly improves MSE performance in scenarios with high mobility, for example, compared to maximum likelihood estimators [20].

10.4.2. Robust optimization

The standard DFE optimization (10.15) assumes that the channel parameters are perfectly known and the estimated channel parameters $\hat{\mathbf{h}}$ are applied to the solution (10.17) as if they were error-free. Optimizing the DFE parameters based on an error model presents a problem formulation closer to reality.

A robust optimization based on the paradigm from *static stochastic programming* [9] aims at minimizing the expected MSE of the data symbols given the error model (10.20) and (10.21). Thus, it defines a *robustness on average* instead of a robustness in the worst case as in the min-max approach (e.g., [7, 8, 21]).

For a given estimate $\hat{\mathbf{H}}$, the current realization of the channel $\mathbf{H}$ is a random variable from the perspective of the equalizer. Thus, the standard cost function in (10.14) now is a random variable, too. Robustness on average is obtained taking the expected value of the cost function with respect to the parameter errors $\boldsymbol{\theta}$. Therefore, assuming zero mean errors $\boldsymbol{\Theta}$ the *robust cost function* is given by

$$\begin{aligned}\sigma^2_{\varepsilon,\mathrm{R}}(\{\mathbf{G},\mathbf{F},\nu\},\hat{\mathbf{h}},\mathcal{M}_\mathrm{R}) &= \mathrm{E}_{\boldsymbol{\theta}}\left[\sigma^2_{\varepsilon,\mathrm{S}}(\{\mathbf{G},\mathbf{F},\nu\},\hat{\mathbf{h}}+\boldsymbol{\theta},\mathcal{M}_\mathrm{S})\right]\\ &= \sigma^2_{\varepsilon,\mathrm{S}}(\{\mathbf{G},\mathbf{F},\nu\},\hat{\mathbf{h}},\mathcal{M}_\mathrm{S}) + \sigma^2_b\,\mathrm{trace}\left(\mathbf{G}\mathbf{C}_{\boldsymbol{\Theta}}\mathbf{G}^\mathrm{H}\right),\end{aligned} \tag{10.25}$$

which is the standard design criterion plus an additional penalty term on the norm of the feedforward filter $\mathbf{G}$. The *robust optimization problem* is

$$\{\mathbf{G}_\mathrm{R},\mathbf{F}_\mathrm{R},\nu_\mathrm{R}\} = \arg\min_{\{\mathbf{G},\mathbf{F},\nu\}} \sigma^2_{\varepsilon,\mathrm{R}}(\{\mathbf{G},\mathbf{F},\nu\},\hat{\mathbf{h}},\mathcal{M}_\mathrm{R}) \tag{10.26}$$

with model parameters $\mathcal{M}_\mathrm{R} = \{\mathcal{M}_\mathrm{S},\mathbf{C}_{\boldsymbol{\Theta}}\}$ including average size and structure of the errors in $\hat{\mathbf{H}}$. The *solution* is given by

$$\mathbf{G}_\mathrm{R} = \mathbf{E}_{\nu_\mathrm{R}+1}\hat{\mathbf{H}}^\mathrm{H}\left(\hat{\mathbf{H}}\boldsymbol{\Pi}^{(\nu_\mathrm{R})}\hat{\mathbf{H}}^\mathrm{H} + \sigma_b^{-2}\mathbf{C}_{\tilde{\mathbf{v}}} + \mathbf{C}_{\boldsymbol{\Theta}}\right)^{-1} = \mathbf{B}_\mathrm{R}\mathbf{A}_\mathrm{R}^{-1}, \tag{10.27}$$

$$\mathbf{F}_\mathrm{R} = -\mathbf{G}_\mathrm{R}\hat{\mathbf{H}}\mathbf{S}^{(\nu_\mathrm{R}),\mathrm{T}}, \tag{10.28}$$

where $\hat{\mathbf{H}}$ depends on $\hat{\mathbf{h}}$ (10.10). Thus, the robust solution is obtained from the solution of the standard design with the following substitutions:

$$\mathbf{C}_{\tilde{\mathbf{v}}} \longleftarrow \mathbf{C}_{\tilde{\mathbf{v}}} + \sigma_b^2\mathbf{C}_{\boldsymbol{\Theta}}, \qquad \mathbf{H} \longleftarrow \hat{\mathbf{H}}. \tag{10.29}$$

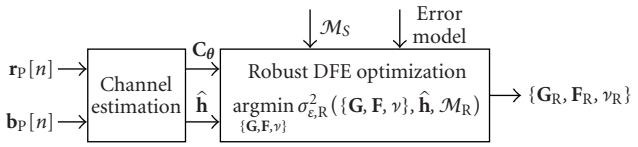

FIGURE 10.2. For a robust equalizer design the channel estimator communicates the expected size and structure of estimation errors via the error covariance matrix $\mathbf{C}_{\boldsymbol{\theta}}$. The model parameters $\mathcal{M}_R = \{\mathcal{M}_S, \mathbf{C}_{\boldsymbol{\Theta}}\}$ of the resulting robust equalizer optimization include the parameters of the error model.

The optimum latency time results from standard optimization (10.19) with the same substitutions. This simple rule illustrates that the robust design treats channel estimation error as an *additional noise source*, that is, a *structured loading* of the inverse in (10.27).

Obviously, the complexity of the robust solution is of the same order as standard solution (10.17) and (10.19). Additional computations, that is, matrix multiplications and additions, are needed for computing the error covariance matrix $\mathbf{C}_{\boldsymbol{\Theta}}$ (cf. (10.21) and (10.24)).

10.4.3. Interpretation

The robust optimization of the DFE creates an *interface* between channel estimation and equalization: the channel estimator communicates the expected size and structure of the error via the error covariance matrix $\mathbf{C}_{\boldsymbol{\theta}}$ and—in case of nonzero mean errors—the mean $\mathrm{E}[\boldsymbol{\theta}]$ (Figure 10.2). To see how this knowledge influences DFE optimization and to understand the performance improvements, we first interpret robust optimization (10.26) in more detail and then investigate the new structure of solution (10.28).

The robust behavior of the solution is controlled by the second term in the robust cost function (10.25), which can be rewritten as

$$\rho(\mathbf{G}) = \sigma_b^2 \operatorname{trace}\left(\mathbf{G}\mathbf{C}_{\boldsymbol{\Theta}}\mathbf{G}^{\mathrm{H}}\right) = \sigma_b^2 \sum_{i=1}^{N_R G} \lambda_{\Theta,i} \|\mathbf{g}'_i\|_2^2 \tag{10.30}$$

using the eigenvalue decomposition of the error covariance matrix $\mathbf{C}_{\boldsymbol{\Theta}} = \mathbf{U}_\Theta \boldsymbol{\Lambda}_\Theta \mathbf{U}_\Theta^{\mathrm{H}}$ with diagonal matrix of eigenvalues $\boldsymbol{\Lambda}_\Theta = \operatorname{diag}(\lambda_{\Theta,1}, \ldots, \lambda_{\Theta,N_R G})$. This term may be interpreted as a Tikhonov *regularization* of the feedforward filter [22, 23], which is a common method to solve ill-posed problems and *decrease the sensitivity* of an optimization problem to parameter errors. We consider the simple case of $\mathbf{C}_{\boldsymbol{\Theta}} = \sigma_\theta^2 \mathbf{I}_{GN_R}$, where we have $\rho(\mathbf{G}) = \sigma_b^2 \sigma_\theta^2 \|\mathbf{G}\|_{\mathrm{F}}^2$. Here, while minimizing the MSE, $\mathbf{G}$ is also chosen with a smaller Frobenius norm. A smaller filter norm decreases the sensitivity of the cost function to errors in $\hat{\mathbf{H}}$, since the errors $\boldsymbol{\Theta}$ are amplified by $\mathbf{G}$ in (10.14). (Note that the average MSE degradation for the standard ST-DFE based on estimates $\hat{\mathbf{H}}$ is also given by $\rho(\mathbf{G})$.) This leads to a smaller performance degradation in case of errors. For a general $\mathbf{C}_{\boldsymbol{\Theta}}$ with arbitrary structure, (10.30) is the sum of the weighted Euclidean norms of the columns of $\mathbf{G}' = \mathbf{G}\mathbf{U}_\Theta = [\mathbf{g}'_1, \ldots, \mathbf{g}'_{N_R G}]$.

The subspace of the column space of $\mathbf{G}'$ with high uncertainty in the channel parameters (large $\lambda_{\Theta,i}$) is regularized more than subspaces with small errors. Moreover, the cost function may be seen as a scalarization with equal weight of a vector optimization problem [22] with the MSE in (10.15) and $\rho(\mathbf{G})$ (10.30) as two objectives to be minimized.

Traditional robust optimization, for example, min-max optimization [21], shows a worse performance in the error-free case and a smaller sensitivity with respect to parameter errors compared to the standard (nominal) design (e.g., (10.15)) resulting in a better performance in case of significant errors. The stochastic approach presented here allows an optimum (nonheuristic) *adaptation* to the average error structure, which is important in wireless communications with a wide range of different scenarios.

Now we consider the signal $\tilde{\mathbf{b}}[n]$ before quantizer (10.8) with standard solution (10.17) of the feedback filter $\mathbf{F}[n]$, where $\hat{\mathbf{H}}$ is substituted for $\mathbf{H}$:

$$\begin{aligned}\tilde{\mathbf{b}}[n] &= \mathbf{G}\mathbf{H}\bar{\mathbf{b}}[n] - \mathbf{G}\hat{\mathbf{H}}\mathbf{S}^{(\nu),\mathrm{T}}\mathbf{S}^{(\nu)}\bar{\mathbf{b}}[n] + \mathbf{G}\bar{\mathbf{v}}[n] \\ &= \mathbf{G}\{(\mathbf{H} - \hat{\mathbf{H}}\mathbf{S}^{(\nu),\mathrm{T}}\mathbf{S}^{(\nu)})\bar{\mathbf{b}}[n] + \bar{\mathbf{v}}[n]\} \\ &= \mathbf{G}\{\mathbf{H}_\Theta\bar{\mathbf{b}}[n] + \bar{\mathbf{v}}[n]\} = \mathbf{G}\mathbf{r}_\Theta[n],\end{aligned} \tag{10.31}$$

which can be interpreted as equalization of the received signal $\mathbf{r}_\Theta$ from an equivalent channel $\mathbf{H}_\Theta = \mathbf{H}\boldsymbol{\Pi}^{(\nu)} + \boldsymbol{\Theta}\mathbf{S}^{(\nu),\mathrm{T}}\mathbf{S}^{(\nu)}$ in case of channel estimation errors. The first $N_\mathrm{T}(\nu+1)$ columns of $\mathbf{H}_\Theta$ represent the interference to be suppressed by the feedforward filter $\mathbf{G}$ in standard problem formulation (10.17). Interference created from the remaining F columns of $\mathbf{H}$ should be canceled by the feedback filter $\mathbf{F}[n]$, which cannot accomplish its task (even in presence of perfect decisions available for feedback) due to the channel estimation errors $\boldsymbol{\Theta}$. The influence of the remaining interference due to imperfect cancellation via $\mathbf{F}[n]$ is described by the last F columns in $\mathbf{H}_\Theta$. To equalize the linear model with $\mathbf{H}_\Theta$ (10.31), we could design $\mathbf{G}$ as a Wiener filter minimizing the MSE. If we had perfect knowledge about $\mathbf{H}_\Theta$, that is, about the channel and the channel estimation errors, the covariance matrix of the receive signal $\mathbf{r}_\Theta[n]$ needed for the MMSE design of $\mathbf{G}$ would be

$$\mathbf{C}_{\mathbf{r}_\Theta} = \sigma_b^2\mathbf{H}_\Theta\mathbf{H}_\Theta^\mathrm{H} + \mathbf{C}_{\tilde{\mathbf{v}}} = \sigma_b^2\mathbf{H}\boldsymbol{\Pi}^{(\nu)}\mathbf{H}^\mathrm{H} + \sigma_b^2\boldsymbol{\Theta}\mathbf{S}^{(\nu),\mathrm{T}}\mathbf{S}^{(\nu)}\boldsymbol{\Theta}^\mathrm{H} + \mathbf{C}_{\tilde{\mathbf{v}}} \tag{10.32}$$

with $\mathbf{H} = \hat{\mathbf{H}} + \boldsymbol{\Theta}$ (10.20). Since $\mathbf{H}_\Theta$ is not available, one may use an approximation based on the knowledge of correlations in $\mathbf{r}_\Theta[n]$ on average:

$$\begin{aligned}\mathrm{E}_{\boldsymbol{\theta}}\left[\mathbf{C}_{\mathbf{r}_\Theta}\,\middle|_{\mathbf{H}=\hat{\mathbf{H}}+\boldsymbol{\Theta}}\right] &= \sigma_b^2\hat{\mathbf{H}}\boldsymbol{\Pi}^{(\nu)}\hat{\mathbf{H}}^\mathrm{H} + \mathbf{C}_{\tilde{\mathbf{v}}} + \sigma_b^2\,\mathrm{E}\left[\boldsymbol{\Theta}\boldsymbol{\Pi}^{(\nu)}\boldsymbol{\Theta}^\mathrm{H}\right] \\ &\quad + \sigma_b^2\,\mathrm{E}\left[\boldsymbol{\Theta}\mathbf{S}^{(\nu),\mathrm{T}}\mathbf{S}^{(\nu)}\boldsymbol{\Theta}^\mathrm{H}\right] \\ &= \sigma_b^2\hat{\mathbf{H}}\boldsymbol{\Pi}^{(\nu)}\hat{\mathbf{H}}^\mathrm{H} + \sigma_b^2\,\mathrm{E}\left[\boldsymbol{\Theta}\boldsymbol{\Theta}^\mathrm{H}\right] + \mathbf{C}_{\tilde{\mathbf{v}}},\end{aligned} \tag{10.33}$$

where the last expression is identical to $\mathbf{A}_\mathrm{R}$ in $\mathbf{G}_\mathrm{R}$ (10.28) up to factor σ_b^2.

Thus, the robust feedforward filter $\mathbf{G}_{\mathrm{R}}$ has two *important properties*: (1) it is of *smaller norm* to decrease the sensitivity towards errors in $\widehat{\mathbf{H}}$ (10.30) and (2) it takes into account *remaining interference* due to imperfect interference cancellation by the feedback as a result of channel estimation errors. This interference is only *considered on average* and can be further suppressed by $\mathbf{G}_{\mathrm{R}}$ if $\mathbf{C}_{\boldsymbol{\Theta}}$ exhibits sufficiently rich structure.

10.5. Krylov subspace-based reduced-rank implementation

10.5.1. Reduced-rank feedforward and feedback filters

The main idea of reduced-rank processing (e.g., [13]) is to replace the original feedforward filter $\mathbf{G} \in \mathbb{C}^{N_{\mathrm{T}} \times N_{\mathrm{R}} G}$ in optimizations (10.15) and (10.25) by a prefilter matrix $\mathbf{T}^{(D)} \in \mathbb{C}^{D \times N_{\mathrm{R}} G}$, $D < N_{\mathrm{R}} G$, followed by a reduced-dimension filter $\mathbf{G}_D \in \mathbb{C}^{N_{\mathrm{T}} \times D}$, that is, $\mathbf{G} = \mathbf{G}_D \mathbf{T}^{(D)}$. The resulting problem reads as

$$\left\{\mathbf{G}_{\mathrm{S/R}}^{(D)}, \mathbf{F}_{\mathrm{S/R}}^{(D)}\right\} = \underset{\{\mathbf{G}_D, \mathbf{F}\}}{\arg\min}\, \sigma^2_{\varepsilon,\mathrm{S/R}}\left(\{\mathbf{G}_D \mathbf{T}^{(D)}, \mathbf{F}, \nu\}, \widehat{\mathbf{h}}, \mathcal{M}_{\mathrm{S/R}}\right), \tag{10.34}$$

and has the solution

$$\begin{aligned} \mathbf{G}_{\mathrm{S/R}}^{(D)} &= \mathbf{B}_{\mathrm{S/R}} \mathbf{T}^{(D),\mathrm{H}} \left(\mathbf{T}^{(D)} \mathbf{A}_{\mathrm{S/R}} \mathbf{T}^{(D),\mathrm{H}}\right)^{-1} \mathbf{T}^{(D)}, \\ \mathbf{F}_{\mathrm{S}}^{(D)} &= -\mathbf{G}_{\mathrm{S}}^{(D)} \mathbf{H} \mathbf{S}^{(\nu),\mathrm{T}}, \qquad \mathbf{F}_{\mathrm{R}}^{(D)} = -\mathbf{G}_{\mathrm{R}}^{(D)} \widehat{\mathbf{H}} \mathbf{S}^{(\nu),\mathrm{T}}. \end{aligned} \tag{10.35}$$

The reduction in computational complexity is mainly based on the selection of the prefilter matrix $\mathbf{T}^{(D)}$. It is chosen such that its computation is less intense than the inversion of the original $N_{\mathrm{R}} G \times N_{\mathrm{R}} G$ matrix $\mathbf{A}_{\mathrm{S/R}}$. Note that it will turn out that the inversion of the resulting $D \times D$ matrix $\mathbf{T}^{(D)} \mathbf{A}_{\mathrm{S/R}} \mathbf{T}^{(D),\mathrm{H}}$ is negligible due to its structure.

The prefilter matrix of the principal component method [24], for instance, is composed by the principal eigenvectors of the matrix $\mathbf{A}_{\mathrm{S/R}}$, that is, the eigenvectors corresponding to the largest eigenvalues. Thus, the matrix $\mathbf{T}^{(D)} \mathbf{A}_{\mathrm{S/R}} \mathbf{T}^{(D),\mathrm{H}}$ is easy to invert since it is diagonal and the resulting complexity is $\mathrm{O}(D N_{\mathrm{R}}^2 G^2)$ since it is only based on the computation of the D principal eigenvectors.

Nevertheless, it was shown (e.g., [25]) that eigenspace-based prefilter matrices are generally suboptimum. Thus, in the following, we restrict ourselves to prefilters where the conjugate transpose row vectors are basis vectors of the D-dimensional *Krylov subspace* [26]

$$\mathcal{K}_{\mathrm{S/R}}^{(D)} = \mathrm{span}\left[\mathbf{B}_{\mathrm{S/R}}^{\mathrm{H}}, \mathbf{A}_{\mathrm{S/R}} \mathbf{B}_{\mathrm{S/R}}^{\mathrm{H}}, \ldots, \mathbf{A}_{\mathrm{S/R}}^{d-1} \mathbf{B}_{\mathrm{S/R}}^{\mathrm{H}}\right], \tag{10.36}$$

with $D = d N_{\mathrm{T}}$, $d \in \mathbb{N}$, that is, the rank is restricted to be an integer multiple of the

$\{[\mathbf{t}_1, \mathbf{t}_2, \ldots, \mathbf{t}_M], \mathbf{R}\} \leftarrow \mathrm{QR}(\mathbf{B}_{\mathrm{S/R}}^{\mathrm{H}})$
2: *for* $i \in \{M, M+1, \ldots, D-1\}$ *do*
  $k \leftarrow i - M + 1$
4: $\mathbf{v} \leftarrow \mathbf{A}_{\mathrm{S/R}} \mathbf{t}_k$
  for $\ell \in \{i - 2M + 1, i - 2M + 2, \ldots, i\} \cap \mathbb{N}$ *do*
6: $h_{\ell,k} \leftarrow \mathbf{t}_\ell^{\mathrm{H}} \mathbf{v}$
  $\mathbf{v} \leftarrow \mathbf{v} - h_{\ell,k} \mathbf{t}_\ell$
8: *end for*
  $h_{i+1,k} \leftarrow \|\mathbf{v}\|_2$
10: $\mathbf{t}_{i+1} \leftarrow \mathbf{v}/h_{i+1,k}$
end for
12: $\mathbf{T}^{(D),\mathrm{H}} \leftarrow [\mathbf{t}_1, \mathbf{t}_2, \ldots, \mathbf{t}_D] \in \mathbb{C}^{N \times D}$

Algorithm 10.1. Lanczos-Ruhe computation of the prefilter matrix.

number of transmit antennas N_{T}. The *block Lanczos algorithm* [27, 28] is a method to compute an orthonormal basis of $\mathcal{K}_{\mathrm{S/R}}^{(D)}$, that is,

$$\mathbf{T}^{(D)} = \left[\mathbf{T}_1, \mathbf{T}_2, \ldots, \mathbf{T}_d\right]^{\mathrm{H}} \in \mathbb{C}^{D \times N_{\mathrm{R}} G}, \tag{10.37}$$

given $\mathbf{A}_{\mathrm{S/R}}$ to be Hermitian which is true in our applications. The fundamental part of the block Lanczos algorithm is the *classical Gram-Schmidt orthogonalization* step

$$\{\mathbf{T}_\ell, \mathbf{R}_\ell\} = \mathrm{QR}\left(\mathbf{A}_{\mathrm{S/R}} \mathbf{T}_{\ell-1} - \sum_{i=\ell-2}^{\ell-1} \mathbf{T}_i (\mathbf{T}_i^{\mathrm{H}} \mathbf{A}_{\mathrm{S/R}} \mathbf{T}_{\ell-1})\right) \tag{10.38}$$

which is used for the recursive calculation of $\mathbf{T}_\ell \in \mathbb{C}^{N_{\mathrm{R}} G \times N_{\mathrm{T}}}$. The recursion formula is initialized with $\mathbf{T}_1$ obtained from the initial QR factorization $\{\mathbf{T}_1, \mathbf{R}_1\} = \mathrm{QR}(\mathbf{B}_{\mathrm{S/R}}^{\mathrm{H}})$. The computation of $\mathbf{T}^{(D)}$ by Gram-Schmidt orthogonalization guarantees that the transformed $D \times D$ matrix $\mathbf{T}^{(D)} \mathbf{A}_{\mathrm{S/R}} \mathbf{T}^{(D),\mathrm{H}}$ has *block tridiagonal structure*, that is, a matrix with $N_{\mathrm{T}} \times N_{\mathrm{T}}$ nonzero blocks in the main block diagonal and the two adjacent block subdiagonals.

Note that the block Lanczos algorithm is strongly related to the *multistage matrix Wiener filter* [15, 16] (MSMWF) which is a matrix-valued extension of the *multistage Wiener filter* [17]. Nevertheless, the corresponding prefilter matrix of the general MSMWF does not necessarily have orthonormal rows.

The main problem of the block Lanczos algorithm is the fact that the rank D has to be an integer multiple of N_{T}. This restriction prevents the rank to be optimally selected in the case where it is not an integer multiple of N_{T}. Ruhe [15, 29] derived a version of the Lanczos algorithm which is summarized in Algorithm 10.1 where the rank D can be any integer between 0 and $N_{\mathrm{R}} G$.

In each iteration step, the matrix-vector multiplication $\mathbf{A}_{\mathrm{S/R}} \mathbf{t}_k$ in Line 4 of Algorithm 10.1 defines the computational complexity which is $\mathrm{O}(N_{\mathrm{R}}^2 G^2)$ since the remaining operations have only linear order. The iteration is performed $D - N_{\mathrm{T}}$

times, thus, the computational complexity of the Lanczos-Ruhe algorithm is $O((D - N_T)N_R^2G^2)$ since the complexity of the QR factorization of $\mathbf{B}_{S/R}$ in the first line is negligible. Due to the block tridiagonal structure of $\mathbf{T}^{(D)}\mathbf{A}_{S/R}\mathbf{T}^{(D),H}$, the computational complexity of its inversion is $O(N_TN_R^2G^2)$ and the resulting complexity of the Krylov subspace-based reduced-rank implementation of the MMSE-ST-DFE is $O(DN_R^2G^2)$, thus, equal to the complexity of the eigenspace-based principal component method.

10.5.2. Quasioptimal latency time

The optimization problem for the latency time in the reduced-rank case is given by the following equation:

$$\nu_{S/R}^{(D)} = \underset{\nu\in\{0,\ldots,L+G-2\}}{\arg\max} \operatorname{tr}\left(\mathbf{B}_{S/R}^H\mathbf{T}^{(D),H}\left(\mathbf{T}^{(D)}\mathbf{A}_{S/R}\mathbf{T}^{(D),H}\right)^{-1}\mathbf{T}^{(D)}\mathbf{B}_{S/R}\right). \tag{10.39}$$

Since the prefilter matrix $\mathbf{T}^{(D)}$ depends on the latency time ν, it has to be recomputed for every possible $\nu \in \{0,\ldots,L+G-2\}$. Hence, the computational complexity of the reduced-rank implementation including latency time optimization is $O(DN_R^2G^2(L+G))$, that is, of cubic order concerning the filter length G.

To avoid the additional computational burden of the latency time optimization, a quasioptimal choice of ν is taken. Remember that the matrix $\mathbf{H}\boldsymbol{\Pi}^{(\nu)}\mathbf{H}^H$ in $\mathbf{A}_{S/R}$ has a maximal possible rank of

$$\operatorname{rank}\left(\mathbf{H}\boldsymbol{\Pi}^{(\nu)}\mathbf{H}^H\right) = \min\left((\nu+1)N_T, N_RG\right), \tag{10.40}$$

that is, it is rank-deficient for special choices of ν. For a given D, the latency time can be chosen such that D is equal to $\operatorname{rank}(\mathbf{H}\boldsymbol{\Pi}^{(\nu)}\mathbf{H}^H)$ if D is an integer multiple of N_T. If this is not the case, it turns out that the heuristic choice

$$\nu_{S/R,\text{sub}}^{(D)} = \min\left(\left\lceil\frac{D}{N_T}\right\rceil, G\right) - 1, \tag{10.41}$$

which is based on the results of Figure 10.5, yields a good performance of the proposed reduced-rank methods. Note that $\nu_{S/R,\text{sub}}^{(D)}$ is a fixed latency time that is independent of the actual channel, and it is smaller than G to assure that the equalizer filter includes the energy of all channel taps. This turns out to be a good choice for medium and large ranks D.

10.6. Performance

Monte Carlo simulations for the mean uncoded bit error rate (BER) are shown for the following parameters: 16-QAM modulation, $N_R = 8$ receive antennas in a uniform linear array with half-wavelength interelement spacing, $N_T = 6$ transmitters, channel length $L = 4$, filter length $G = 9$, and $N_p = 30$ QPSK pilot symbols. The BER is averaged over 1000 i.i.d. Rayleigh fading blocks each with

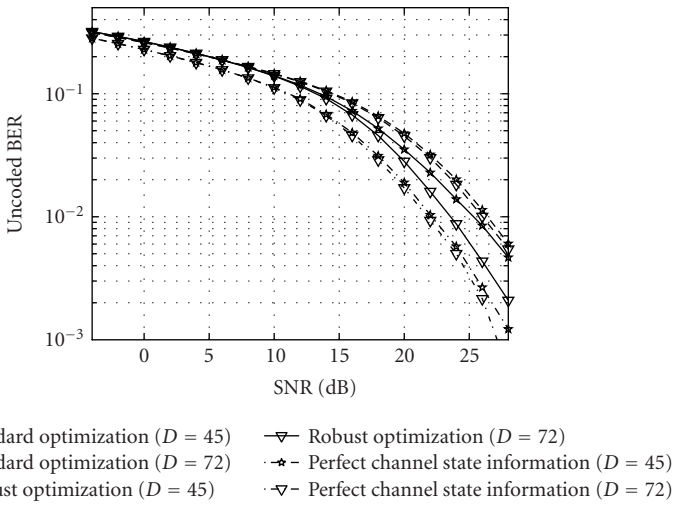

FIGURE 10.3. BER versus SNR of the MMSE-ST-DFE for Scenario 1.

500 symbols for every transmitter. The channels between the N_T transmitters are uncorrelated and angles of arrival at the receiver are Laplace-distributed (angular spread of 10°) [30]. The power delay profile is exponential with rate of decay 1 microsecond (symbol rate 1.28 MHz as in [31]). Latency time optimization is performed as described in (10.19), (10.29), and Section 10.5. For channel estimation the LMMSE estimator in (10.23) is used. Moreover, full knowledge of the second-order channel and noise statistics is assumed. For the reduced-rank implementation we apply the *Lanczos-Ruhe* Algorithm 10.1.

Scenario 1. The *channel* remains *constant* during reception of the pilot sequence and data. The SNR loss due to imperfect channel estimation of the standard design is 4.2 dB at a BER of 10^{-2} (Figure 10.3). The robust design gains 2.4 dB compared to a standard design. The improvement is due to the robust DFE's knowledge about size and—most importantly—structure of the estimation error. In our scenario the rich structure in $\mathbf{C}_{\boldsymbol{\Theta}}$ is mainly due to the channel correlations. For a rank of $D = 45$, which is 62.5% of the full-rank $N_R G = 72$, the complexity reduction is achieved with only a small loss in performance of 0.4 dB for the standard design and for perfect channel state information (CSI) (Figure 10.3). At an BER of 10^{-2} the reduced-rank implementation of the robust DFE with $D = 45$ looses 1.6 dB to its full-rank version, as important information about the error is included into the additional loading in the inverse of $\mathbf{G}_R$ (10.28), which is considered as noise by the reduced-rank algorithm. Thus, there is a trade-off between complexity and robustness, and a larger rank D should be chosen for similar performance.

Figure 10.4 shows the *sensitivity* of the *reduced-rank* DFE implementation with respect to selection of the rank D with a fixed suboptimum choice for the latency time as described in Section 10.5. To achieve the same BER as the standard

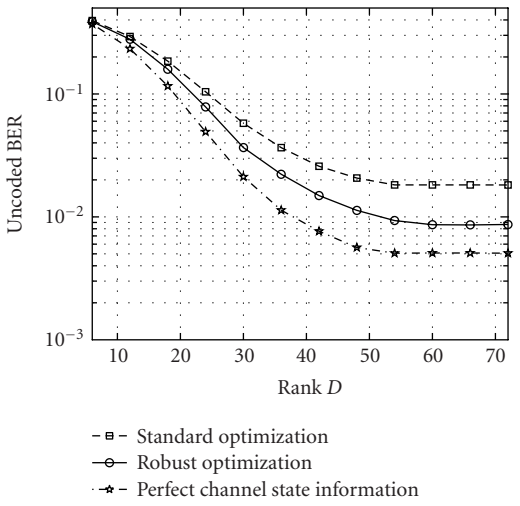

FIGURE 10.4. BER versus rank D for Scenario 1 at an SNR of 24 dB.

design, the rank of the robust DFE may be reduced further to save complexity. Generally, it can be stated that among the reduced-rank approaches, the choice of the Krylov subspace results in the smallest choice of D for a given performance level [15].

The strong dependency of the DFE performance on the *latency time* v is illustrated in Figure 10.5 for the case of perfect CSI and for all possible choices of a fixed v at an SNR of 24 dB. Latency time optimization is crucial for achieving the performance gains expected from a DFE compared to a linear equalizer due to the high sensitivity of the BER with respect to latency time. Similar conclusions hold for imperfect CSI and a standard/robust design. Furthermore, Figure 10.5 empirically justifies the rule for choosing the latency time in case of a reduced-rank implementation as introduced in Section 10.5. A latency time larger than $G-1=8$ cannot occur due to the structure of $\mathbf{H}$, that is, a small received signal power from symbols corresponding to delays v larger than $G-1$. The suboptimum choice of latency time (10.41) can be verified with this example.

Scenario 2. *A delay* of 300 symbols between pilot sequence and application of the ST-DFE to equalize the channel is assumed, which is a rough model for equalizing the channel at the end of the data block. Here, the temporally correlated channel has a maximum Doppler frequency of $5 \cdot 10^{-5}$ (Jakes Doppler spectrum) normalized to the symbol period. Note that the error covariance matrix $\mathbf{C}_{\Theta}$ now also depends on the temporal correlation coefficient of the channel.

Due to the delayed channel estimate, the standard DFE design suffers a tremendous performance degradation and the BER saturates at a high level (Figure 10.6). The *error floor* is significantly reduced by the robust design. Again for a reduced-rank implementation with $D = 45$, there is only a small performance

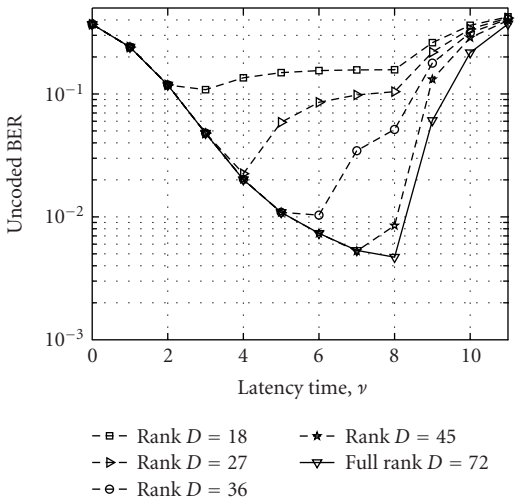

FIGURE 10.5. BER versus fixed latency time ν in case of perfect channel state information (CSI) for Scenario 1 at an SNR of 24 dB.

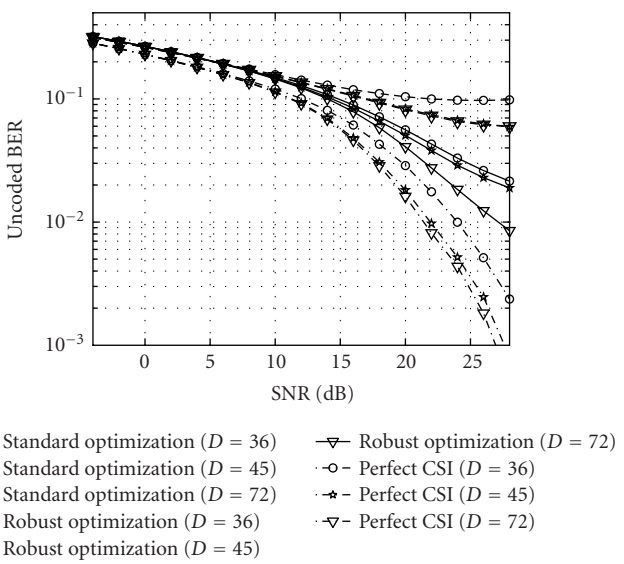

FIGURE 10.6. BER versus SNR for delayed channel estimates for Scenario 2.

degradation in case of full CSI and the standard design. But for the robust design, the performance loss due to rank reduction is more pronounced, as useful information contained in the error covariance matrix $\mathbf{C}_\Theta$ is neglected to reduce the complexity. For a rank $D = 36$, that is, 50% of the full rank, the additional performance loss is smaller for the robust design than the standard solutions.

Abbreviations

BER	Bit error rate
BLAST	Bell Laboratories Layered Space-Time
CSI	Channel state information
DFE	Decision feedback equalizer
FIR	Finite impulse response
IIR	Infinite impulse response
LMMSE	Linear minimum mean square error
MIMO	Multi-input multi-output
MMSE-ST-DFE	Minimum mean square error space-time decision feedback equalizer
MSE	Minimum square error
MSMWF	Multistage matrix Wiener filter
QAM	Quadrature amplitude modulation
QPSK	Quadrature phase-shift keying
SISO	Single-input single-output
SNR	Signal-to-noise ratio
ST-DFE	Space-time decision feedback equalizer

Bibliography

[1] M. E. Austin, "Decision-feedback equalization for digital communication over dispersive channels," Tech. Rep. 437, M.I.T. Lincoln Laboratory, Lexington, Mass, USA, 1967.

[2] P. Monsen, "Feedback equalization for fading dispersive channels," *IEEE Trans. Inform. Theory*, vol. 17, no. 1, pp. 56–64, 1971.

[3] N. Al-Dhahir and A. H. Sayed, "The finite-length multi-input multi-output MMSE-DFE," *IEEE Trans. Signal Processing*, vol. 48, no. 10, pp. 2921–2936, 2000.

[4] A. Lozano and C. Papadias, "Layered space-time receivers for frequency-selective wireless channels," *IEEE Trans. Commun.*, vol. 50, no. 1, pp. 65–73, 2002.

[5] G. J. Foschini, G. D. Golden, R. A. Valenzuela, and P. W. Wolniansky, "Simplified processing for high spectral efficiency wireless communication employing multi-element arrays," *IEEE J. Select. Areas Commun.*, vol. 17, no. 11, pp. 1841–1852, 1999.

[6] S. Verdú, *Multiuser Detection*, Cambridge University Press, Cambridge, UK, 1998.

[7] L. El Ghaoui and H. Lebret, "Robust solutions to least-squares problems with uncertain data," *SIAM J. Matrix Anal. Appl.*, vol. 18, no. 4, pp. 1035–1064, 1997.

[8] S. Shahbazpanahi, A. B. Gershman, Z.-Q. Luo, and K. M. Wong, "Robust adaptive beamforming for general-rank signal models," vol. 51, no. 9, pp. 2257–2269, 2003.

[9] A. Prékopa, *Stochastic Programming*, vol. 324 of *Mathematics and Its Applications*, Kluwer Academic Publishers, Dordrecht, The Netherlands, 1995.

[10] J. Dahl, L. Vandenberghe, and B. H. Fleury, "Robust least-squares estimators based on semidefinite programming," in *Proc. 36rd Asilomar Conference on Signals, Systems and Computers*, pp. 1787–1791, Pacific Grove, Calif, USA, November 2002.

[11] F. A. Dietrich, R. Hunger, M. Joham, and W. Utschick, "Robust transmit Wiener filter for time division duplex systems," in *Proc. 3rd IEEE International Symposium on Signal Processing and Information Technology (ISSPIT '03)*, pp. 415–418, Darmstadt, Germany, December 2003.

[12] A. T. Erdogan, B. Hassibi, and T. Kailath, "MIMO decision feedback equalization from an H^{∞} perspective," *IEEE Trans. Signal Processing*, vol. 52, no. 3, pp. 734–745, 2004.

[13] G. Dietl and W. Utschick, "On reduced-rank approaches to matrix Wiener filters in MIMO systems," in *Proc. 3rd IEEE International Symposium on Signal Processing and Information Technology (ISSPIT '03)*, pp. 82–85, Darmstadt, Germany, December 2003.

[14] M. Honig and M. K. Tsatsanis, "Adaptive techniques for multiuser CDMA receivers," *IEEE Signal Processing Mag.*, vol. 17, no. 3, pp. 49–61, 2000.

[15] G. Dietl, P. Breun, and W. Utschick, "Block Krylov methods in time-dispersive MIMO systems," in *IEEE International Conference on Communications (ICC '04)*, pp. 2683–2688, Paris, France, June 2004.
[16] J. S. Goldstein, I. S. Reed, D. E. Dudgeon, and J. R. Guerci, "A multistage matrix Wiener filter for subspace detection," in *IEEE Information Theory Workshop on Detection, Estimation, Classification and Imaging (DECI '99)*, Santa Fe, NM, USA, February 1999.
[17] J. S. Goldstein, I. S. Reed, and L. L. Scharf, "A multistage representation of the Wiener filter based on orthogonal projections," *IEEE Trans. Inform. Theory*, vol. 44, no. 7, pp. 2943–2959, 1998.
[18] G. Dietl, C. Mensing, W. Utschick, J. A. Nossek, and M. D. Zoltowski, "Multi-stage MMSE decision feedback equalization for EDGE," in *Proc. IEEE International Conference on Acoustics, Speech, and Signal Processing (ICASSP '03)*, vol. 4, pp. 509–512, Hong Kong, April 2003.
[19] S. M. Kay, *Fundamentals of Statistical Signal Processing: Estimation Theory*, Prentice Hall, Upper Saddle River, NJ, USA, 1st edition, 1993.
[20] F. A. Dietrich and W. Utschick, "Pilot assisted channel estimation based on second order statistics," *IEEE Trans. Signal Processing*, vol. 53, no. 3, pp. 1178–1193, 2005.
[21] S. A. Kassam and H. V. Poor, "Robust techniques for signal processing: a survey," *Proc. IEEE*, vol. 73, no. 3, pp. 433–481, 1985.
[22] S. Boyd and L. Vandenberghe, *Convex Optimization*, Cambridge University Press, Cambridge, UK, 2004.
[23] A. N. Tikhonov and V. Y. Arsenin, *Solutions of Ill-Posed Problems*, V. H. Winston & Sons, Washington, DC, USA, 1977.
[24] H. Hotelling, "Analysis of a complex of statistical variables into principal components," *Journal of Educational Psychology*, vol. 24, no. 6/7, pp. 417–441, 498–520, 1933.
[25] G. Dietl, M. D. Zoltowski, and M. Joham, "Reduced-rank equalization for EDGE via conjugate gradient implementation of multi-stage nested Wiener filter," in *IEEE 54th Vehicular Technology Conference (VTC 2001-Fall)*, vol. 3, pp. 1912–1916, Atlantic City, NJ, USA, October 2001.
[26] Y. Saad, *Iterative Methods for Sparse Linear Systems*, Society for Industrial and Applied Mathematics, Philadelphia, Pa, USA, 2nd edition, 2003.
[27] G. H. Golub and R. Underwood, "The block Lanczos method for computing eigenvalues," in *Mathematical Software, III*, number 39 in Publ. Math. Res. Center, pp. 361–377, Academic Press, New York, NY, USA, 1977.
[28] C. Lanczos, "An iteration method for the solution of the eigenvalue problem of linear differential and integral operators," *J. Research Nat. Bur. Standards*, vol. 45, no. 4, pp. 255–282, 1950.
[29] A. Ruhe, "Implementation aspects of band Lanczos algorithms for computation of eigenvalues of large sparse symmetric matrices," *Math. Comp.*, vol. 33, no. 146, pp. 680–687, 1979.
[30] P. E. Mogensen, K. I. Pedersen, B. Fleury, et al., "TSUNAMI II: 2D-channel characteristics," Tech. Rep., Aalborg University, Aalborg, Denmark, 1997.
[31] Third Generation Partnership Project (3GPP), http://www.3gpp.org/.

Frank A. Dietrich: Institute for Circuit Theory and Signal Processing, Munich University of Technology, 80290 München, Germany

Email: dietrich@tum.de

Guido Dietl: Institute for Circuit Theory and Signal Processing, Munich University of Technology, 80290 München, Germany

Email: dietl@tum.de

Michael Joham: Institute for Circuit Theory and Signal Processing, Munich University of Technology, 80290 München, Germany

Email: joham@tum.de

Wolfgang Utschick: Institute for Circuit Theory and Signal Processing, Munich University of Technology, 80290 München, Germany

Email: utschick@tum.de

Channel

Contents

11 Introduction

J. Bach Andersen

The radio channel in a multiuser, multiple-antenna wireless network in a complicated dynamic environment is possibly one of the most challenging channels to be dealt with by modern communication technologies. The environment defies in most cases a deterministic solution of Maxwell's equations, so a statistical description is necessary. Consider the following multitude of parameters of interest.

(i) The number of rays or paths at each end of the link.
(ii) The magnitude of each path.
(iii) The delay of each path.
(iv) The polarization of each path.
(v) The angles of arrival and departure.
(vi) The transformation from the in-the-air paths to the circuit ports, considering the mutual coupling between antenna elements.
(vii) The time variation due to the user movements and movements in the environment.
(viii) The statistical description of all the above, including mean values, variances, correlations, and so forth.
(ix) Turning the above into accurate yet simple channel models to be used for link and network simulations.

It is no wonder that it requires a multitude of experts to cover all aspects of the channel, and it is fortunate that in this chapter we find an updated description of most of these aspects.

Measurement of the channel is a very important aspect giving the reality check and the basis for the physical understanding of the propagation phenomena. Thomä et al. (Chapter 1) give first a theoretical model of the double-directional channel of interest for MIMO systems and discuss the various sounding principles used in practice today, including the important calibration techniques. Various antenna structures are discussed highlighting the need for full polarimetric measurement of the channel. By using a novel general array model, it is possible to separate the antenna from the environment, indicating that the propagation results may be used for different antenna structures than originally used in the measurements, that is, antenna-independent channel models.

Propagation measurements are applied in Chapter 2 by Vainikainen et al. to give an updated description of propagation phenomena in both indoor and outdoor environments. An important new insight is obtained by the cluster analysis for the outdoor environment, where array measurements indicate a rather small number of clusters dictated by the geometry and building layout. Most propagation studies are related to the lower microwave frequencies, but in the section also some indoor results for 60 GHz are shown.

Most engineering developments of wireless systems are prepared by simulation of the complete link, where the channel model is an important part. The development of MIMO systems has meant that a new area of channel models has been introduced. We are now interested in modeling matrices connecting the antennas on the transmit side with those on the receive side. Channel models of MIMO systems are the subject of Chapter 3 by Yu et al., highly influenced by the results of measurements. In some situations, the matrix channel may with a good approximation be determined by the correlations between the antenna elements at each end, not knowing the correlations of all the internal paths, the so-called Kronecker model. Channel modeling is also treated by standardization bodies, in order to compare systems on a fair basis. Thus channel modeling is a lively area, expected to continue when new frequencies and bandwidths are introduced.

In a practical communication system at any given time, the channel is unknown and must be estimated in order for the receiver to work properly. In some cases it could also be relevant to send back information to the transmitter, enabling complete channel knowledge to be obtained, at least until the channel has changed again. Channel estimation is the subject of Chapter 4 by Leus and van der Veen, where a number of algorithms are discussed together with some simulation results. Both training-based and semiblind results are treated, including some new trends in this important area.

This part concludes with Chapter 5 by Viberg on direction-of-arrival (DOA) estimation, an area also touched upon in some of the previous sections. DOA will include in principle both azimuth and elevation angles, as well as the corresponding angles of departure from the transmitter. DOA is important for the understanding of the propagation phenomena, and also for finding the clustering in angle, and the statistical angular spread, relevant for the functioning of antenna arrays in arbitrary environments. The question is often how accurate the estimation should be, and the section discusses various schemes from conventional beamforming to least-square methods and subspace methods of varying complexity.

J. Bach Andersen: Department of Communication Technology, Institute of Electronic Systems, Aalborg University, 9220 Aalborg, Denmark

Email: jba@kom.auc.dk

12 Propagation

P. Vainikainen, J. Kivinen, X. Zhao, and H. El-Sallabi

12.1. Introduction

Significant development of propagation measurement systems has taken place since the mid 90s. Earlier it was typically possible to measure only the power as a function of location (or time) and possibly the power delay profile of the channel in the case of wideband channel sounders. The power division between orthogonal polarizations had to be determined with two separate measurements. The development of channel sounders employing antenna arrays made it possible to determine also the directional information first at one end [1, 2] and, a few years ago, also at both [3, 4] ends of the link with MIMO configurations having more than 20×20 antennas. The use of several receive and transmit antennas enabled also the determination of the instantaneous complex polarization matrix. In the best systems these properties could be obtained with quite fast sampling rate enabling measurements over long continuous routes with less than half a wavelength sampling distance. These experiments have given significant new information for the development of multidimensional propagation channel models. They can also be used to obtain realistic estimates on the available capacity of the new radio system configurations like MIMO.

Furthermore, the directional measurements provide new information on the phenomena governing the propagation. In the earlier measurements covering only a few domains the result often consisted of joint responses of several phenomena without the opportunity to separate them. The interesting new results of these multidimensional measurements has been, for example, the short-term stability of the distinguished significant propagation paths or clusters as a function of location and also the small number of such clusters in an urban environment [5].

Another approach to studying MIMO propagation channels is electromagnetic (EM) simulations. Here the investigation of physical propagation mechanisms and their accurate and effective modeling gives new opportunities for extensive MIMO system studies [6, 7, 8].

12.2. Basic propagation mechanisms for mobile communications

12.2.1. Propagation in free space

The free space path loss with wavelength λ at distance d_0 in the far field of the antennas with gains G_1 and G_2 is given by

$$PL_0(d_0) = -G_1 - G_2 + 20\log\left(\frac{4\pi d_0}{\lambda}\right). \tag{12.1}$$

Equation (12.1) can be used for separate rays, when the first Fresnel zone is free from obstructions.

12.2.2. Ray theory

In the ray theory, it is approximated that the energy propagates between antennas inside ellipsoid-shaped tubes, defined by the first Fresnel zone. The phase difference between the straight line and the line via the equivalent source on the surface of the tube is 180°. According to the theory, only obstacles inside the tube may affect the energy.

12.2.3. Refraction, reflection, and transmission in the boundary of dielectric media

In the following equations, we assume that the wave can be regarded as a plane wave, which holds for materials with relatively low loss. So the field in point r is given by

$$E(r) = E_0 \cdot e^{-j\mathbf{k}\cdot\mathbf{r}}, \tag{12.2}$$

where $\mathbf{k}$ is the wave vector. The boundaries are assumed smooth compared to wavelength, and uniform inside the first Fresnel zone.

12.2.3.1. Refraction

The energy can propagate behind wedge-like obstacles, through both refraction and diffraction. It can be easily calculated from Snell's law that refraction behind 90° corners requires $\varepsilon_r < 2$. Therefore, refraction is an untypical propagation mechanism in man-made environments, but significant in nature (e.g., refraction in atmosphere).

12.2.3.2. Reflection

For a dielectric medium with relative dielectric permittivity $\varepsilon_r = \varepsilon_r' - j\varepsilon_r''$, the Fresnel reflection coefficients $r_\perp$ and $r_\parallel$ for perpendicular and parallel polarizations, respectively, for a plane wave in the boundary of dielectric media are well known from textbooks.

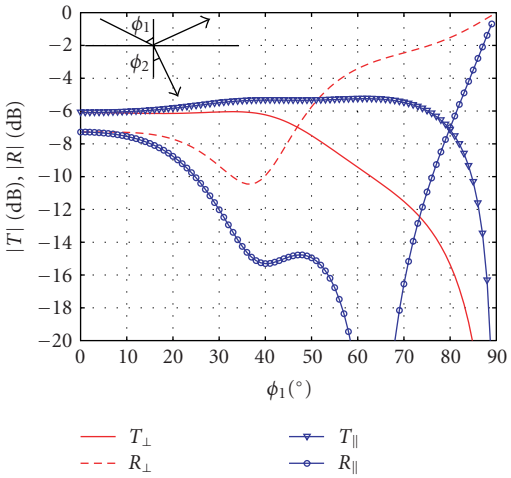

FIGURE 12.1. Transmission and reflection coefficients of a dielectric layer, thickness 13 cm, $\varepsilon_r = 4.1 - j0.15$, $f = 5.3$ GHz.

12.2.3.3. Transmission

Transmission through homogeneous layers-signal flow diagram analysis. For a layer with thickness d of homogeneous dielectric medium the field transmission coefficient is, for example,

$$T = \frac{(1 - r^2) \cdot e^{-j\delta}}{1 - r^2 e^{-j2\delta}}, \tag{12.3}$$

where r can be either a parallel or perpendicular field reflection coefficient, and

$$\delta = \frac{2\pi d\left(\sqrt{\varepsilon_r}\right)}{\lambda \cdot \cos\phi_2}, \tag{12.4}$$

where ϕ_2 is the direction of propagation inside the dielectric layer with respect to the normal of the boundary. The real part of δ is the electrical length of the path of the wave inside of the dielectric medium. The field reflection coefficient including the multiple reflections inside the layer is

$$R = \frac{r(1 - e^{j2\delta})}{1 - r^2 e^{-j2\delta}}. \tag{12.5}$$

Equations as (12.3) and (12.5) for an arbitrary number of dielectric layers can be derived using signal flow diagram analysis. In Figure 12.1, transmission (12.3) and reflection (12.5) of a brick wall with thickness 13 cm and $\varepsilon_r = 4.1 - j0.15$ are shown at 5.3 GHz. A transmission coefficient changes only slightly when $\phi = 0 - 50^\circ$. The reflection coefficients are different for the two polarizations: in the vicinity of Brewster's angle, $R_\parallel \approx 0$.

Table 12.1. Wall losses in different references (d = thickness, L = attenuation, ε_r = relative dielectric permittivity).

f (GHz)	Material	ε_r	d (cm)	L	Method	Reference
5.3	Brick	$4.1 - j0.15$	13	5 dB	Meas + sim (homogeneous layer)	[10]
0.9	Concrete+ metal grid	$7 - j0.3$	20	3.5 dB (mean)	FEM simulation (mean)	[11]
1.8	Concrete+ metal grid	$7 - j0.3$	20	6 dB (mean)	FEM simulation (mean)	[11]
1.8	Concrete+ metal grid	$7 - j0.3$	20	6.5 dB (mean)	MTL simulation (mean)	[12]
57.5	Concrete	$6.5 - j0.43$	5	46 dB	Meas + sim (homogeneous layer)	[13]

The difference between $R_{\parallel}$ and $R_{\perp}$ leads to uncorrelated fading of vertical and horizontal polarizations. Therefore, the polarization diversity is an effective diversity technique, not requiring spacing between antennas as the spatial diversity, and orthogonal polarizations will potentially be used in MIMO systems. If dominant propagation mechanism to an NLOS corridor is reflection from vertical walls, VP propagates better (e.g., [9], VP signal was several dBs higher) due to the higher reflection coefficient.

In the most common building materials, such as concrete, the dielectric permittivity ε_r changes smoothly as a function of frequency in the frequency range 2–60 GHz (e.g., Table 12.1). Therefore, the frequency dependency of wall transmission can be approximated straightforward: the average field transmission loss is proportional to $e^{1/\lambda}$.

Transmission through inhomogeneous layers. The building walls are generally inhomogeneous. Walls often consist of periodic layers. It is calculated, applying modal transmission-line method in [12], that, in such case, separate waves with different propagation directions are found. In [11] finite-element techniques are used in calculating the wave propagation through reinforced-concrete walls. In such approach, the plane wave approximation is not required, and calculations are not restricted to low-loss materials.

12.2.4. Diffraction

Diffraction occurs when the radio path between the transmitter and the receiver is obstructed by a surface that has sharp irregularities (e.g., edges). In mobile communication environments, the primary diffracting obstacles, which perturb the propagating fields are buildings. The majority of contemporary structures are comprised of a number of faces intersecting at straight edges of finite lengths. Thus, corners can be considered as wedges and diffraction theory can be applied. Diffraction formulas are well established for perfectly conducting (PC) infinite

wedges [14, 15], for absorbing wedges (AW), and for impedance-surface wedges [16]. The PC diffraction coefficients are accurate when dealing with diffraction phenomena arising from metallic objects. However, many important applications, such as in mobile communications, involve large dielectric structures with losses. In this case, the assumption of PC boundary conditions results in a lack of accuracy in predicting the actual electromagnetic field. On the other hand, the impedance-surface diffraction formulas are rather cumbersome to use for propagation prediction in mobile communications. Thus, the difficulty of using the rigorous solutions for propagation prediction forces simplifications to be made. Some existing diffraction coefficients modify the PC-UTD diffraction coefficient in order to make it applicable to dielectric wedges with losses. For a normal-incident plane wave, there is a general form of the PC-UTD-based diffraction coefficient that includes the existing solutions as special cases of it. The general form can be expressed as

$$D = \Gamma_1 D^{(1)} + \Gamma_2 D^{(2)} + \Gamma_3 D^{(3)} + \Gamma_4 D^{(4)}. \tag{12.6}$$

Detailed descriptions of the variables that appear in (12.6) are given in [14, 15]. Different definitions of multiplication factors Γ_i ($i = 1, \ldots, 4$) of each term in (12.6) result in different diffraction coefficients that appear in literature. For $\Gamma_{1,2,3,4} = 1$, and $\Gamma_{1,2} = 1$, $\Gamma_{3,4} = -1$, we obtain the PC-UTD diffraction coefficient for perpendicular and parallel polarizations [14, 15], respectively. Luebbers in [17], based on work of Burnside [18], introduced a heuristic modification to the PC-UTD diffraction coefficient to be applicable to dielectric wedges with finite conductivity. In [17], Luebbers kept $\Gamma_{1,2} = 1$ and heuristically set $\Gamma_{3,4} = R_{0,n}^{\parallel,\perp}$, where $R_{0,n}^{\parallel,\perp}$ is the plane-wave Fresnel reflection coefficient for o-face (i.e., $\phi = 0$) and n-face (i.e., $\phi = n\pi$) of the wedge with parallel ($\parallel$) and perpendicular ($\perp$) polarizations. He conjectured that this approach would yield a reliable estimate for the diffraction coefficient, particularly, around the incidence and reflection shadow boundaries. Some improvements in Luebbers' solution have been proposed in [19] based on redefining the reflection angles at which $R_{0,n}$ are calculated. Furthermore, Holm in [20] heuristically modified the PC-UTD diffraction coefficient by changing the factors $\Gamma_{1,2}$ and keeping the modification introduced by Luebbers for $\Gamma_{3,4}$. In particular, when the source illuminates the o-face, Holm set $\Gamma_1 = R_0^{\parallel,\perp} \cdot R_n^{\parallel,\perp}$ and kept $\Gamma_2 = 1$ and when the source illuminates the n-face, he modified $\Gamma_2 = R_0^{\parallel,\perp} \cdot R_n^{\parallel,\perp}$ and kept $\Gamma_1 = 1$ with some changes in the definition of the reflection angle. An improvement to Holm's solution is given in [21] for the case when the source illuminates one side of the diffracting surface. Recently, a new heuristic diffraction coefficient for lossy dielectric wedges at normal incidence is proposed in [21]. In [21], $\Gamma_{1,2} = 1$ and $\Gamma_{3,4}$ are given by new definitions of the multiplication factors. The $\Gamma_{3,4}$ are given by a modified reflection coefficient that was inferred from suitable formulation of Maliuzhinets' solution. The proposed modified reflection coefficient establishes a relationship between the incidence electric field and that at the observation point when both are parallel or perpendicular to

the plane of incidence and observation point. It is given by

$$\Re^{\parallel,\perp} = \frac{(1,\varepsilon)\tau - \sqrt{\varepsilon - 1 + \tau^2}}{(1,\varepsilon)\tau + \sqrt{\varepsilon - 1 + \tau^2}}, \tag{12.7}$$

where

$$\tau = 2\sin\left(\frac{\phi}{2}\right)\sin\left(\frac{\phi'}{2}\right), \tag{12.8}$$

where ε is the surface permittivity, ϕ' and ϕ are the incident and diffracted angles. In [22], a diffraction coefficient that combines both the improved version of Holm similar to that given in [23] and the new heuristic coefficient given in [22] is proposed. It results in an accurate diffraction coefficient for different values of wedge angles and different incident angles whether the source can illuminate one face or both sides of diffracting surface, and different diffraction regions. The accuracy is valid for both parallel and perpendicular polarizations. It is as computationally efficient as other heuristic solutions.

Examples of the calculated diffraction coefficients are shown in Figure 12.2. One sees clearly how diffraction loss increases as a function of frequency.

12.2.5. Scattering

Rough surface causes scattering into the nonspecular directions and reduction of energy in the specular direction. The influence of rough surface depends on the degree of roughness. The longer the wavelength and the smaller the grazing angle, the weaker the effect of surface irregularities. The importance of roughness has been determined by measurements [24]. In some scenarios, the roughness is so significant that no coherent part is retransmitted toward the receiver. If the diffuse reflection is isotropic, then the intensity in any direction varies as the cosine to the angle between that direction and the normal to the surface. The influence of the surface can be described by a simple cosine relation called Lambert's cosine law. In urban propagation, diffuse scattering can be considered as originating from building wall surfaces. In order to model diffuse scattering in an urban environment, a sort of effectiveness is associated with each building wall. This takes into account the real surface roughness, wall discontinuities, small object effects, and so forth [25]. The scattering contribution of each wall is computed from the distance of each wall and its orientation with respect to the transmitter and the receiver using a formula which depends on a few scattering parameters. Diffuse scattering has been modeled according to the *effective roughness approach* expressed with an integral approach for close-by objects described in [25], or with a simplified approach for far-away objects, which is important for wideband prediction [26]. The latter is expressed as

$$E_S^2 = K_0^2 S^2 \frac{\text{Area} \cdot \cos\theta_i \cos\theta_s}{\pi} \cdot \frac{1}{r_i^2 r_s^2}. \tag{12.9}$$

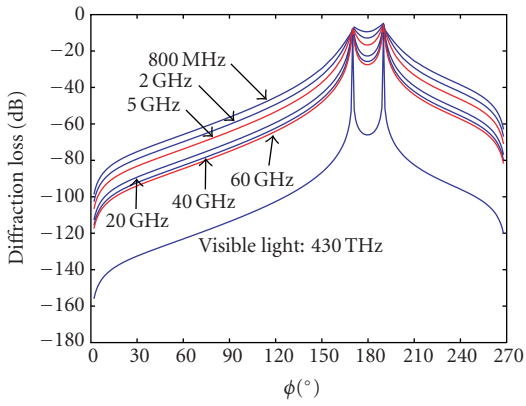

(a)

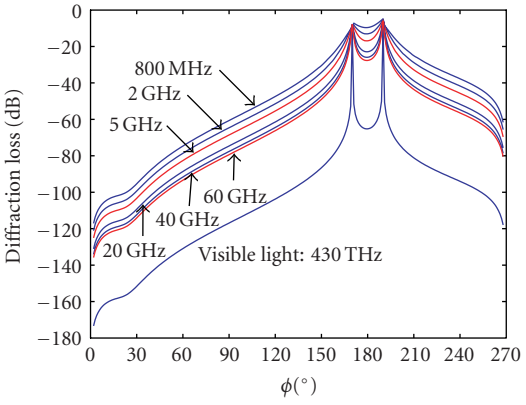

(b)

FIGURE 12.2. Frequency response of diffraction (perpendicular polarization). $S_1 = 40$ m, $S_2 = 10$ m, $\phi' = 10^\circ$. (a) $\varepsilon_r = 6.14 - j0.30$, (b) $\varepsilon_r = 4.0 - j0.10$.

The parameters in (12.9) are defined in [26]. In order to investigate what role the diffuse scattering mechanism plays over other mechanisms, the work in [27] makes comparison between measurement results and ray tracing with and without diffuse scattering. The measurement campaign was carried out in downtown of Helsinki, Finland, as shown in Figure 12.3. Figure 12.4 shows a comparison of conventional ray tracing (i.e., reflection and diffraction mechanisms are included without diffuse scattering) and a version where scattering is included. The comparison shows acceptable agreement between ray tracing including diffuse scattering and over-rooftop propagation and measurements. It can be seen clearly that the inclusion of diffuse scattering has improved the prediction of rms delay spread

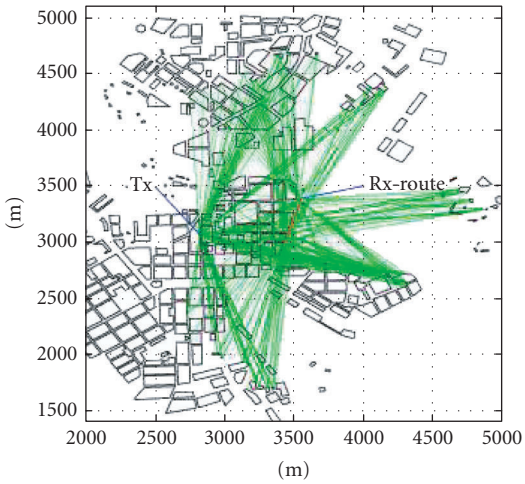

FIGURE 12.3. Sample of different rays with inclusion of diffuse scattering.

when compared to conventional full 3D ray tracing. From this comparison, we are able to understand the importance of the role of the diffuse scattering.

12.3. Characteristics of the propagation channel for different scenarios

12.3.1. Indoor propagation

12.3.1.1. Propagation mechanisms

It is seen that when frequency gets higher, the transmission loss dependency on the wavelength $e^{1/\lambda}$ causes that transmission becomes a less important mechanism and reflection, diffraction, and scattering start to dominate the propagation to NLOS (see, e.g., [10, 28]). The transmission through walls and windows varies in different buildings, new buildings often have thin walls but windows may not be transparent. Another important mechanism is waveguiding—the wave propagates by reflection from wall to wall, thus the path loss exponent is usually less than 2. The waveguiding can be observed especially in corridors. Multiple reflections happen in rooms and corridors, which causes that azimuth spread of the signal is wide in NLOS situations in hard wall environments. Elevation spread is generally modeled using Laplacian distribution [29]. The elevation spread can also be high in NLOS, if distance of Rx and Tx is not much larger than the room height, and if the transmitter antenna has wide radiation pattern in elevation plane [30, 31]. This is seen in SISO measurements so that the average Doppler spectrum is flat [30]. High angular spread causes that the correlation distance is short, only fraction of the wavelength [30, 32]. At 5 GHz, signal components with 3 to 5 bounces can be observed with significant amplitude in hard wall office environments. Thus, there

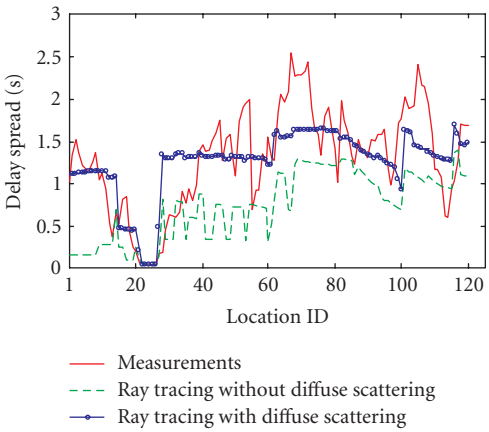

FIGURE 12.4. Comparison of measured delay spread with that from ray tracing with and without diffuse scattering.

are many paths and the indoor environments provide potentially high MIMO capacity with a relatively small antenna distance, which is comparable to Rayleigh curves (e.g., see [33, 34, 35]). However, a keyhole effect is found in long corridors and tunnels [36], where the higher-order modes of guided waves are attenuated, thus limiting the rank of the channel matrix.

12.3.1.2. Statistical parameters

The propagation characteristics of different environments are often given by the log-distance model

$$PL(d) = PL_0(d_0) + 10n\log\left(\frac{d}{d_0}\right) + X_\sigma, \tag{12.10}$$

where n is the path loss exponent, X_σ is a zero-mean lognormally distributed random variable, and d_0 is the free space path loss PL_0 distance (often d_0 equals 1 meter for comparability). The physical interpretation of $n = 1$ is a guided wave in one plane, $n = 2$ corresponds to a free space path loss, and $n = 4$ corresponds to a situation, where low antenna heights cause the first Fresnel zone to be obstructed. The values of n and σ can be extracted straightforward from the measurements (Table 12.2).

Parameters like path loss exponent and delay spread (Table 12.3) give insight into the behavior of the radio channel. For an adaptive antenna or MIMO link-level design, the spatial properties of the signal are important. The angles of departure Ω_t and arrival Ω_r have to be defined [3]. Statistics of angular spreads in an indoor environment are given in Table 12.4. The cluster angles refer to the model presented in [37].

Table 12.2. Values for parameters of log-distance model.

Class	f (GHz)	d_0	Distance	n	σ (dB)	Environment	Method	Reference
LOS	5.3	1	3–100	1.3–1.5	2–4.7	Corridors and walls	WCS	[30]
	1.5	1	4–70	< 2	—	Hallway	Pulse	[37]
	2.25	—	1–15	1.5	—	—	VNA	[38]
	5.25	—	1–15	1.7	—	—	VNA	[38]
	17.25	—	1–15	1.6	—	—	VNA	[38]
NLOS	5.3	1	5–200	1.9–4.8	2.7–5.6	—	WCS	[30]
	0.9	—	—	4.84	—	Det	RT	[39]
	1.8	—	—	6.08	—	Det	RT	[39]
	2.5	—	—	6.62	—	Det	RT	[39]
	5.2	—	—	6.99	—	Det	RT	[39]
	1.5	1	4–70	3	—	—	Pulse	[37]
Different floors	5.3	1	5–30	5.7–6.5	—	—	WCS	[30]

Table 12.3. Values for delay spreads.

Class	f (GHz)	Distance	σ_τ (ns)	Value given	Method	Reference
LOS	5.3	3–100	20–120	CDF 90%	WCS	[30]
	0.492–0.862	4–13	6–20	Min-max	VNA	[40]
	0.9	—	16	CDF 90%	Pulse	[41]
	2.25	1–15	34.5–49.0	Mean	VNA	[38]
	5.25	1–15	14.4–15.7	Mean	VNA	[38]
	17.25	1–15	11.0–26.9	Mean	VNA	[38]
NLOS	5.3	5–200	30–180	CDF 90%	WCS	[30]
	1.5	4–70	43	CDF 90%	—	[37]
	0.9	—	28	CDF 90% school	Pulse	[41]
	0.9	—	120	CDF 90% factory	Pulse	[41]
	2.25	1–15	34.5–49	Mean	VNA	[38]
	5.25	1–15	14–15.7	Mean	VNA	[38]
	17.25	1–15	11–27	Mean	VNA	[38]

12.3.2. Microcellular propagation

The coverage area of a microcell is generally less than 1 km and the height of base station antenna is usually lower than the heights of surroundings. Therefore, microcells can enhance the efficiency of frequency reuse and also increase the user density. For the designing of future radio communication systems, microcellular radio wave propagation characteristics are quite important to be investigated.

12.3.2.1. Path loss

In this section, the semiempirical path loss models are introduced using simple linear regression on measured data. The frequencies of concern here are around 1.8 and 5.3 GHz. The results are summarized in Table 12.5.

Table 12.4. Angular statistics for indoor environment.

	Mean cluster angle		Ray angle within cluster				
f (GHz)	ϕ	θ	ϕ	θ	Method	Comment	Reference
7	Uniform	—	Lapacian $\sigma = 22° - 26°$	—	Rotating antenna	Two buildings	[42]
2.154	Uniform	Double-sided exponential $\sigma^+ = 9.4°$ $\sigma^- = 6.9°$	—	—	Spherical array	—	[31]

Table 12.5. Parameters for path loss models.

	Urban					Suburban					
Class	BS (cm)		n	PL_0 (dB)	Std (dB)	BS (m)	n	PL_0 (dB)	Std (dB)	Frequency (GHz)	Reference
	4		1.4	58.6	3.7	5	2.5	38.0	4.9	5.3	[43]
	5.5		1.9	43.0	3.7					1.8	[44]
	7.5		1.71	49.1	3.6						
L	8.5		1.34	53.83	3.3					5.3	[43]
O	9.5		1.36	54.8	3.6					1.8	[44]
S	10.5		1.43	52.8	4.2					5.3	[43]
	11.5		1.84	46.4	5.2						
	12.0		2.50	35.8	2.9						
	12.5		1.70	49.0	5.6						
	45		3.50	16.7	4.6						
	3.2	zz/tr	3.7		4.5	3.2	4.0		4.8	1.9	[45] Oakland, Sunset
		zz/lat	4.3		5.5		2.7		7.4		
		Stair	5.2		2.5		5.3		6.1		
	4		2.80	50.6	4.4					5.3	[43]
	5.5		3.21								[44]
N	7.5		3.10								
L	8.5		2.41								
O	8.7	zz/tr	3.0		4.5	8.7	3.7		6.4	1.9	[45] Oakland, Sunset
S		zz/lat	3.7		6.6		2.3		7.0		
		Stair	4.9		3.9		4.3		5.1		
	9.5		3.27							1.8	[43]
	10.5		3.36								
	11.5		3.44								
	12.0		4.50	20.0	1.7	12	3.4	25.6	2.8	5.3	[43]
	12.5		3.58							1.8	[44]
	13.4	zz/tr	3.3		5.4	13.4	3.9		8.5	1.9	[45] Oakland, Sunset
		zz/lat	3.8		6.8		3.5		7.9		
		Stair	4.3		3.3		4.1		5.5		
	45		5.8	–16.9	2.8					5.3	[43]

The measured routes in [44] include the LOS streets, parallel and perpendicular streets. The BS station height varied from 5.5 to 12.5 meters shown in Table 12.5. In LOS measurements, the path loss exponents were in the range

1.3–2.0. The minimum exponent was found in the narrow street canyon due to guided wave effects. In the NLOS measurements, the exponents were in the range 2.4–3.3. The maximum path loss exponent was 3.3 in the NLOS measurements with the highest BS. The path loss exponents were more than 5.1 in the narrow street after the break point. However, in the wider street it was 2.6. The conclusion is that the changes in antenna heights did not have significant effect on the path loss provided that the BS antenna is mounted below the average rooftop of surrounding buildings.

In wide streets the power decay factors were found to be close to free space. In [46], path loss models were developed using measured data for urban block streets with low-rise, high-rise, and low-plus-high-rise buildings. The models were many related geometrical parameters such as heights of BS and MS, distance of break point, and so on. In [43], path loss models were developed using wideband measured data at 5.3 GHz for urban, suburban, and rural environments with measured distance from 30–300 m. The BS antennas in urban environments were placed at three different heights of 4, 12, and 45 m above ground level letting the BS in street canyon lower than the average height of surrounding rooftops, and over rooftops, respectively. The BS heights were 5 and 12 m for suburban measurements in street canyon and lower than rooftops, respectively. The path loss exponents (1.4–3.5 for LOS, and 2.8–5.8 for NLOS) were higher with increasing BS antenna heights in urban environments. When mobile terminal was turning a building corner, more than 25 dB attenuation was found from LOS to NLOS situations. Compared to the urban path loss models in [44], the BS antenna heights were changed much, so the antenna heights have important effects on path loss models. In [45], path loss models are available for three types of NLOS routes, namely, zigzag (zz) transverse (tr), zigzag lateral (la), and also stair routes. It is seen that stair streets have largest exponents, and zigzag transverse streets lowest exponents.

12.3.2.2. Delay spread and coherence bandwidth

Multipath propagation causes delay dispersion for wideband radio channels. The mean excess delay is the first central moment of the power delay profile (PDP) while the rms delay spread (the second moment of the PDP) is the standard deviation of the excess delays. The rms delay spread is the most important modeling parameter which is connected to the capacity and the bit error rate (BER) of a specific communication system and the complexity of a receiver. Results in [45] (see Table 12.6) show that the error floor is approximately proportional to the square of the normalized rms delay spread, namely, the BER is equal to $K \cdot (S/T)^2$, where the proportionality constant K depends on the modulation format, the filtering at the transmitter and receiver, and the sampling time, S is the rms delay spread and T is the symbol duration. The measured values for mean excess delay and rms delay spread at 5.3 GHz are available in Table 12.6. In [47], peer-to-peer channel measurement campaigns at 1.92 GHz were performed in a campus, the rms delay spreads were 17–219 nanoseconds, 26–45 nanoseconds, and 27–43 nanoseconds for outdoor-outdoor, indoor-indoor, and outdoor-indoor, respectively.

Table 12.6. Measured mean excess delay and rms delay spread at 5.3 GHz.

Tx height (m)			Urban	Suburban	Rural
Mean excess delay (ns)	LOS		38 (4) 42 (12) 102 (45)	36 (5)	29 (55)
	NLOS		70 (4)	68 (12)	
RMS delay spread (ns)	Mean	LOS	44 (4) 41 (12) 88 (45)	25 (5)	22 (55)
		NLOS	44 (4)	66 (12)	
	Media n	LOS	25 (4) 31 (12) 86 (45)	13 (5)	15 (55)
		NLOS	37 (4)	63 (12)	
	CDF < 99%	LOS	93 (4) 64 (12) 120 (45)	57 (5)	44 (55)
		NLOS	63 (4)	105 (12)	

Frequency-selective fading can be characterized by coherence bandwidth which is the frequency separation for which the channel autocorrelation coefficient reduces to 0.7 (or 0.9 or 0.5) by definition. The coherence bandwidth is inversely proportional to the rms delay spread and is a measure of the channel frequency selectivity. When the coherence bandwidth is comparable to or less than the signal bandwidth, the channel is said to be frequency selective. Therefore, the coherence bandwidth is not only related to the radio channel itself, but also to the signal bandwidth. For reference [43], the measurement campaigns have been simply described in Section 1. It was found that in urban environments the coherence bandwidth went down with increased BS antenna heights. The coherence bandwidth at 0.7 was within 1.2–11.5 MHz for LOS outdoor environments. The signal bandwidth and carrier frequency were 30 MHz and 5.3 GHz, respectively. The coherence bandwidth can be derived by using the Fourier transformation to the normalized PDP.

12.3.2.3. Number of significant paths

The number of multipaths can be got by counting the peaks of the PDPs after cutting noise. The number of multipaths was proven to have the best fit into Poisson's and Gao's distributions [2]. Poisson's and Gao's distributions are $P(N) = (\eta^{N_T-N}/(N_T - N)!) \cdot e^{-\eta}$ and $P(N) = C_{N_T}^{N}(\eta^{N_T-N}/(1+\eta)^{N_T})$, respectively. In the expressions, N is variable and C means combination. N_T is the maximum number of paths that the mobile can receive. The parameters η and N_T can be fitted by the measured data. The mean numbers of paths $[N]$ are η and $N_T/(1+\eta)$ for Poisson's and Gao's distributions, respectively. The fitted parameters are available

Table 12.7. Distributions of number of paths for outdoor environments.

Distribution characteristics		Urban				Suburban		Rural
		Tx 4 m		Tx 12 m	Tx 45 m	Tx 12 m		Tx 55 m
		LOS	NLOS	LOS	LOS	LOS	NLOS	LOS
η	Poisson	2.8	4.2	3.3	6.0	1.2	4.5	1.8
	Gao	4.7	4.5	3.5	2.7	9.0	3.3	4.0
N_T		16	21	14	22	13	20	9
$[N]$	Poisson	2.8	4.2	3.3	6.0	1.2	4.5	1.8
	Gao	2.8	3.8	3.2	6.0	1.3	4.7	1.8
	Experimental	3.4	4.2	3.5	6.2	2.4	5.0	1.7

in Table 12.7. It is shown that both Poisson's and Gao's PDFs have good agreement with experimental values. However, Gao's PDF has been noticed to give better fit than Poisson's distribution especially at high probability values. The maximum path number that the mobile can receive is around 20, but the probability is very small for the path number greater than 15 when 20 dB dynamic range was chosen for noise cutting.

The number of paths can be expected to be larger if the high resolution methods such as ESPRIT (estimation of signal parameters via rotational invariance techniques) [48] and the SAGE (space-alternating generalized expectation maximization) [49] are applied.

12.3.3. Urban macrocellular propagation

12.3.3.1. Introduction

One of the most important propagation environments for modern mobile communications systems is the urban area. It is also interesting in the radio wave propagation research point of view due to its complexity. The main features governing propagation in the urban areas are

(i) propagation over and around buildings and shadowing due to this;
(ii) reflections and scattering of buildings;
(iii) street canyon propagation;
(iv) other typical characteristics of cities: squares, parks, trees, water.

Traditionally, urban propagation has been characterized with Okumura-Hata or Walfisch-Ikegami models for path loss and different delay domain models like those used in the standard testing of GSM or UMTS cellular systems. The challenge has lately been to get the necessary information to estimate the opportunities to utilize modern intelligent antenna techniques in urban areas to provide high-capacity wireless communications services for this important user environment. For this, directional measurements are needed and those have been conducted by several groups [50, 51]. These have given significant new insight in the urban radio wave propagation and supported the development of propagation models and further communications systems.

12.3.3.2. Path loss

The average path loss in urban areas has been studied extensively during the years. Recent work has provided additional information on the propagation at the new mobile system frequencies like 2 and 5 GHz ranges. The results show that the path loss follows generally the well-known models created earlier.

12.3.3.3. Delay domain

High-capacity mobile systems have significant bandwidth compared with the correlation bandwidth in urban environments. Thus it is important to study the delay domain properties in the campaigns mentioned above. The bandwidths of several tens of MHz have been used. The rms delay spread may vary significantly in urban environments depending on the topology of the city. High-rise downtown areas or water may cause far-away clusters in the delay domain.

12.3.3.4. Angular domain

From the point of view of adaptive antennas the most interesting research area is the angular characteristics of the urban propagation. The buildings are practically nontransparent at the frequencies of new mobile systems (except for propagation into buildings) and thus the propagation is governed by the reflections, diffractions, and scattering of the buildings. In the urban outdoor environments, this seems to lead to the situation where clear clustering of propagation paths in the angular domain takes place at both the BS and MS [50, 52] due mainly to the street canyons. The existence of the clusters and their temporal behavior has been studied, for example, in [52, 53]. This clear clustering changes the traditional view of propagation modeling based on fairly uniform azimuth distribution like scatterer rings. The number of significant clusters in small macrocells seems to be less than 10 and the Ricean K factor typically 1–10 dB, with an average around 5–6 dB. Also the angular dispersion of the clusters is fairly small [52], see Figure 12.5. The results indicate that the clusters can be modeled, for example, with only a few subrays, which provides the opportunity to create fairly simple propagation models also for the complicated antenna structures that seem to increase significantly the complexity of traditional link-level channel models.

12.3.4. Large- and small-scale fading

In Section 12.3.2.1, the linear least square error method was used in path loss fitting. Path loss is actually the mean propagation loss. In addition to path loss, the received signal exhibits fluctuations which are called fading. Fading can be divided into large- and small-scale categories. Large-scale fading represents the long-term variation of the received power level, while small-scale fading represents short-term variation. Large-scale fading is caused by shadowing effects and is determined by the local mean of received power. The window length of the local mean depends

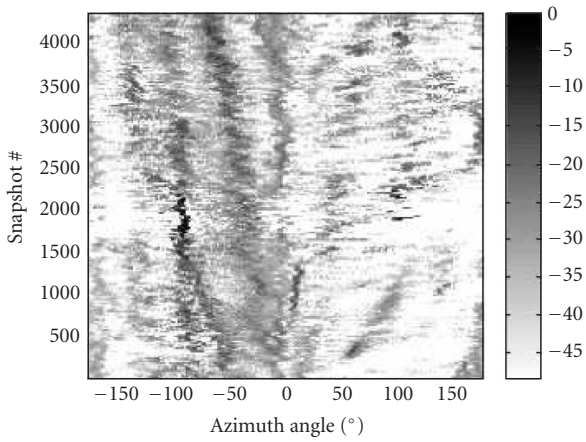

(a)

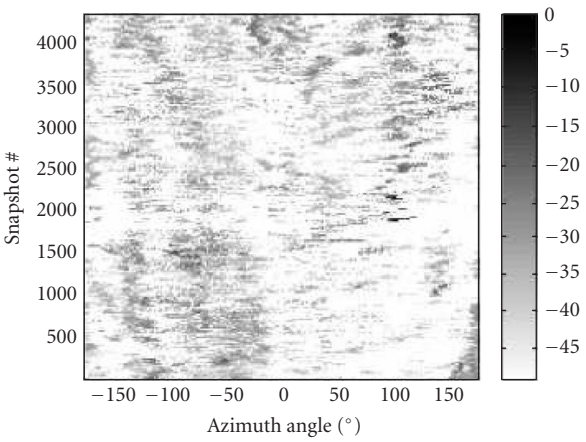

(b)

FIGURE 12.5. Azimuth plot of (a) the original DoA data, (b) residual DoA data after removal of the clusters from the measurement on the street.

on frequency, for example 20λ is used at 5 GHz and 5λ at 900 MHz. The probability density function (PDF) of large-scale received power follows lognormal distribution. The small-scale fluctuation is caused by the superposition of a large number of independent scattered components in which the in-phase and quadrature components can be assumed to be independent zero-mean Gaussian processes. Then the PDF of small-scale received power follows Rayleigh distribution. Therefore, the joint distribution for large- and small-scale received power can be assumed to be Suzuki distribution [54], which is the combination of Rayleigh and lognormal distributions. However, Suzuki distribution has not been widely applied because

of its complicated mathematical form. Some new research results were shown in [55, 56]. The received power obeys double-Rayleigh distribution, and the PDF can be expressed as

$$p_z(z) = 2K_0\left(2\sqrt{z}\right), \tag{12.11}$$

where $z = xy$ and x,y follow the Rayleigh distribution. More generally the multiple-Rayleigh distribution was discussed in [56]. The complex amplitude of the received signal propagated through a universal scattering environment can be expressed as

$$H = K + H_1 + \alpha H_2 H_3 + \beta H_4 H_5 H_6 + \cdots, \tag{12.12}$$

where K corresponds to a possible Ricean factor, H_i follow complex Gaussian distributions (Rayleigh in amplitude), and α and β are constants which can be obtained by fitting to the measured amplitude. Very good agreement is shown in Figure 12.6b for measured power and multiple-Rayleigh distributions. Also in [56], it was shown that multiple-Rayleigh and Suzuki distributions have excellent agreement when they are fitted into measured data.

12.3.5. Multipath dispersion in different domains

A channel may vary as a function of time, frequency, and space $h(t, f, r)$. There are three Fourier transform pairs that assist in the propagation channel analysis. They are frequency $(f) \leftrightarrow$ delay (τ); time $(t) \leftrightarrow$ Doppler frequency (ω), and position $(r) \leftrightarrow$ wave number (k) pairs which gave three possible spectral domains: delay, Doppler, and wave number domains [57]. To accommodate all the random dependences of a channel, it is possible to define a joint power spectrum density (PSD) as a function of Doppler, delay, and wave number $H(\omega, \tau, k)$, and $h(t, f, r) \leftrightarrow H(\omega, \tau, r)$ again is a Fourier pair. The Wiener-Khintchine theorem for WSSUS processes then leads to the Fourier transform relationship between autocorrelation function and PSD: $R(\Delta t, \Delta f, \Delta r) \leftrightarrow S(\omega, \tau, k)$. For the Fourier pair, it is seen that time-selective fading due to scatterer or mobile terminal moving results in a Doppler spread. Time-selective fading can be characterized by coherence time, which is approximately inversely proportional to Doppler spread. The coherence time is a measure of how fast the channel changes in time. The wave number spread (further is angular spread) can cause spatial-selective fading which is characterized by the coherence distance. The coherence distance is inversely proportional to the angular spread [58]. As is described in Section 12.2 delay spread causes frequency-selective fading as the channel acts as a tapped delay line filter. Relationships between numerous dependences are given on a nice transform map in [57]. The WSSUS condition is quite important in channel modeling. If we assume channel IR is expressed as $h(\tau, t)$ in which the spatial dependence is dropped for clarity, then WSS means the autocorrelation function in time $R(\tau, \Delta t) = \langle h(\tau, t)h^*(\tau, t + \Delta t)\rangle$ depends only on the lag Δt, where $\langle\rangle$ means ensemble average. The US means that the scatterers contributing to the delay spread

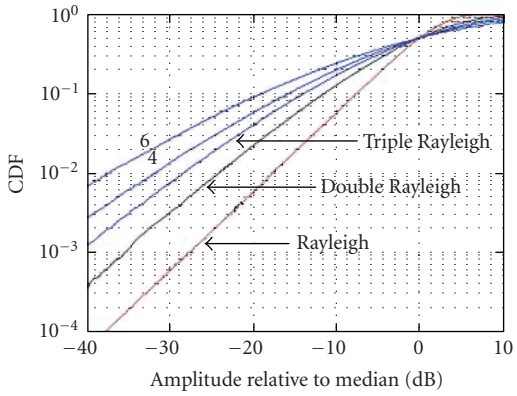

(a)

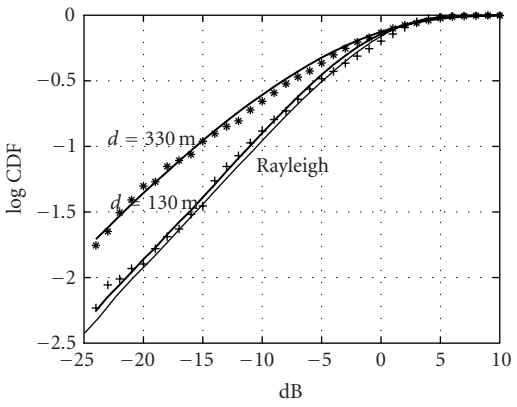

(b)

FIGURE 12.6. (a) Simulation results for multiple-Rayleigh power distributions. (b) Theoretical multiple-Rayleigh power distributions and measured results in a forest.

in the channel have independent fading, for example, $\langle h(\tau_1, t)h^*(\tau_2, t)\rangle = 0$ if $\tau_1 \neq \tau_2$. It is seen that if we assume ergodicity of a channel, the WSS assumption can be automatically fulfilled. The US assumption is well fulfilled only in macrocells. In indoor environments or certain special other environments (streets, tunnels), it is obvious that the scatterers are correlated. Still, WSSUS is assumed for most system computations because non-WSSUS models are too complicated. In a measurement over real routes, one should first divide the measured snapshots into subsets, where each subset contains, for example, 100 IRs depending on the wavelength and environment. The basic criterion is to estimate the size of the stationarity area. Then, the mean PDP, Doppler, and correlation functions [59, 30] are defined inside each of these subsets and finally the average properties of the route are obtained by using the results obtained from all the subsets.

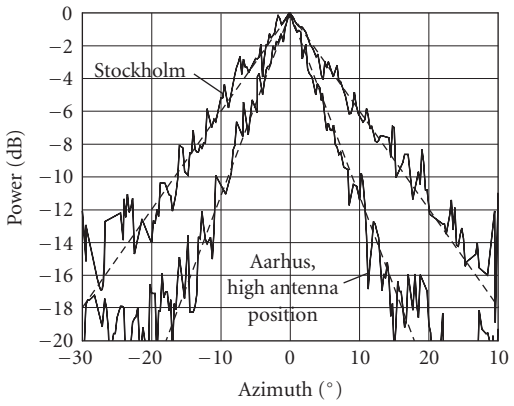

FIGURE 12.7. Example of estimated PAS obtained in Aarhus and Stockholm.

12.3.6. Power angular spectrum (macro-, micro-, and indoor)

The power angular spectra (PAS) in both the azimuth and elevation plane are quite important for the optimization of antenna array topology and combining algorithms for adaptive MIMO systems. The PAS measurements at BS by using a planar array for urban macrocells were performed in [60]. Figure 12.7 shows two examples of estimated PAS in azimuth plane from measurements in Aarhus, Denmark, and Stockholm, Sweden. The azimuth 0° corresponds to the azimuth towards the MS. In both cases the incident power is highly concentrated around 0° even through the measurements that are obtained in NLOS situation. Furthermore, it can be observed that the Laplacian function matches the PAS quite well. The PAS in Figure 12.8 from different clusters was also observed in [60] which again follows Laplacian distribution for a specific cluster.

More recent outdoor to indoor PAS measurement results are available in [61]. Several statistical models were used to fit into the incoming power at the mobile terminal in both the azimuth and elevation planes. It is seen that the statistical model in [62] matches the measured data best. The indoor measurement results [63] again show Laplacian PAS in the azimuth plane.

The measurements using a spherical array [64] for indoor and urban microcells show that the PAS in the azimuth plane is not uniform, several important clusters were observed. The elevation PAS was confined in the interval $\lfloor -20°, 20° \rfloor$. The mean power distribution in the elevation plane follows double-sided exponential distribution Figure 12.9 shows the measured power-azimuth and power-elevation spectra from an urban microcell and an indoor route.

12.3.7. Propagation studies at 60 GHz

The 60 GHz frequency range has been proposed for future broadband wireless systems in indoor and short-range outdoor environments. Based on measurements

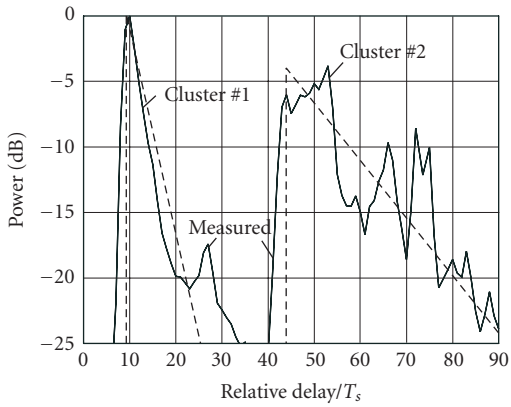

(a)

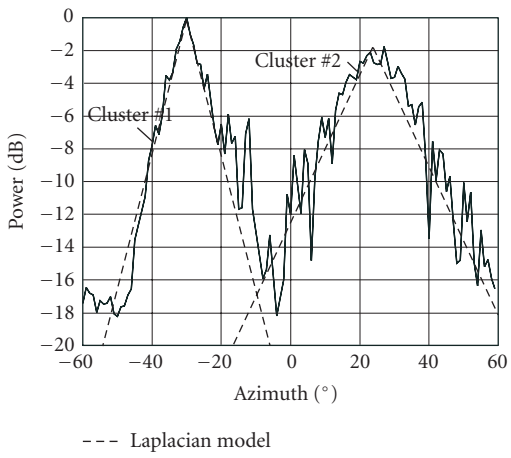

(b)

FIGURE 12.8. Example of a PAS obtained in Stockholm for different clusters.

carried out in indoor environments, the propagation mechanisms were studied in [28, 65]. For LOS applications [28, 65], free-space propagation and reflections are the dominant propagation mechanisms. LOS component and first-order reflected waves contribute a majority of received signal power. Strong multipath components can result from strong reflectors, such as glass windows, metallic furniture or blackboard. When they are present, the reflected wave can be comparable to the LOS component. When there are no strong reflectors in the propagation environment, the reflected multipath components are at least 10 dB below the LOS

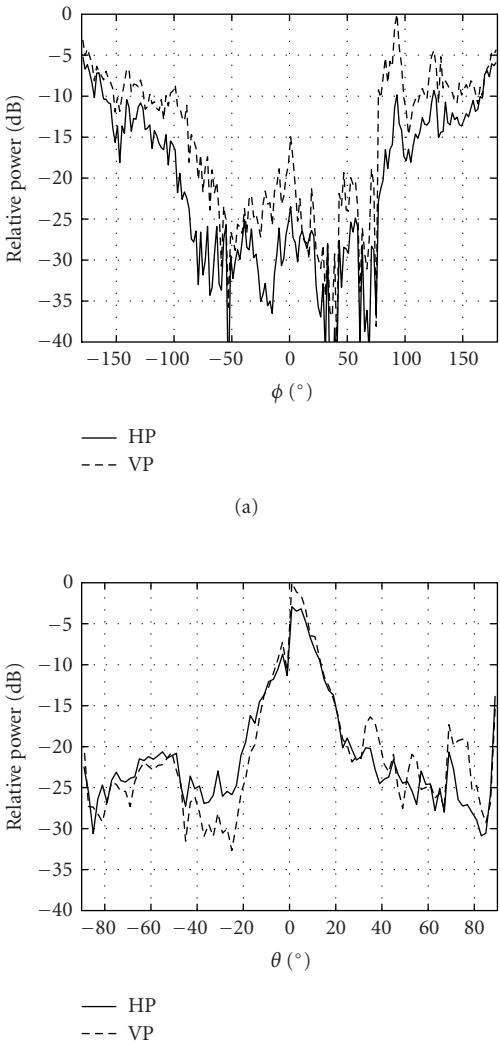

FIGURE 12.9. Measured PAS at mobile station. (a) Azimuth plane in an urban route. (b) Elevation plane in an indoor route.

component. For NLOS applications [28, 65], transmission loss through walls is quite high, depending on wall structure and thickness. This can be seen from the DoA measurements performed from a hallway into a room in [28], the measurement layout is shown in Figure 12.10a.

From the measured power angular profiles shown in Figure 12.10b, it is seen that in NLOS cases diffraction is still the dominant propagation mechanism. This

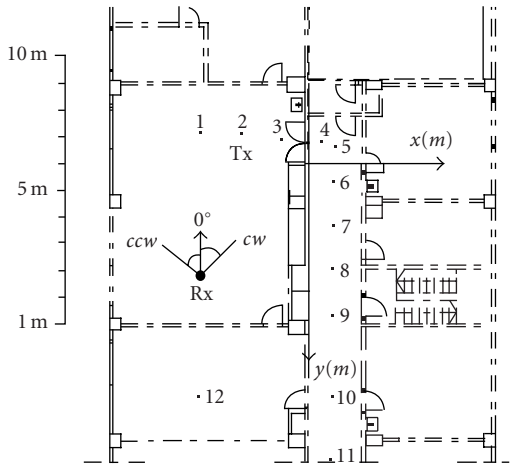

(a)

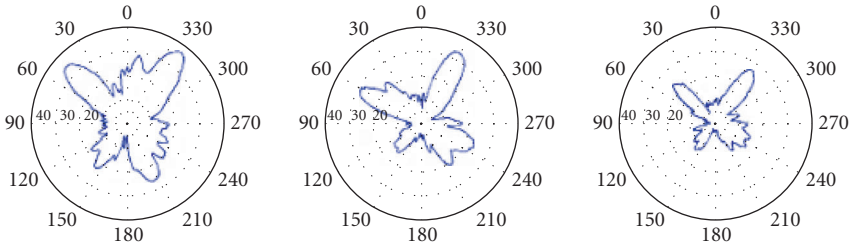

(6) (7) (8)

(b) (c) (d)

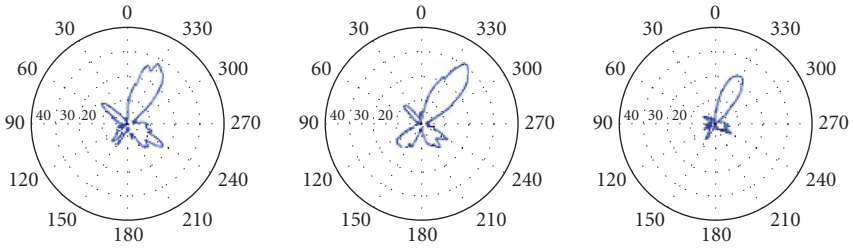

(9) (10) (11)

(e) (f) (g)

Figure 12.10. (a) Locations for 60 GHz DoA measurements, (b)–(g) PAPs at locations (6)–(11).

can also be demonstrated by theoretical calculations using Maliuzhinets' diffraction coefficient [6] (see Section 12.2.4). For indoor environments, the typical materials are brick, concrete, glass, and wood, which are dry and medium dry materials, so their permittivity does not change much with frequency. For the dry materials provided in [66], the permittivities have fairly flat frequency responses, especially for the real part. Also the imaginary parts change only moderately for dry building materials and for dry ground between 100 MHz and 200 GHz. The material "conductivities" increase significantly with increasing frequencies for 0.1–200 GHz, but this is of course only due to the erroneous use of conductivity to describe the actually dielectric losses of these materials. In Figures 12.2a and 12.2b, right angle lossy wedges were considered with complex permittivities $\varepsilon_r = 6.14 - j0.30$ and $\varepsilon_r = 4.0 - j0.10$, respectively. They are the measured values for concrete and brick at 60 GHz [67, 68]. It is seen that, compared with 5 GHz, the diffraction loss is 10 dB higher at 60 GHz (when the same permittivity is used at both frequencies). So diffraction is still dominant at 60 GHz for NLOS cases as predicted by measurements [28]. As a rough estimation, the diffraction loss for visible light would be very large.

Measurement results in [69] show that the use of directive antennas at the terminal can reduce delay spread and mitigate the effect of multipath propagation. The use of circular polarization instead of linear polarization can further reduce delay spread by about 50%. Therefore, the combined use of directive antenna and circular polarization is a good way to reduce delay spread and enhance the data transmission rate.

12.3.8. Tapped delay line channel models for wideband MIMO and SISO radio channels

Tapped delay line (TDL) channel models are of importance for simulations of mobile radio channels, and also for the design of RAKE receivers and equalizers of future radio communication systems. A typical TDL should include the tap amplitudes and excess delays, tap amplitude distributions, and tap Doppler spectra [30, 70, 71]. For MIMO radio channels, a spatial tap correlation matrix is also necessary to evaluate and simulate the correlation properties of the multiple channels between the two arrays [71]. A TDL model is based on the corresponding power delay profile (PDP). For example, in [30, 70], excess delays of the taps can be derived using the powers as weighting factors. However, for a dense-sparse tap model in [67], the time resolution (T_c) of a measurement system was chosen as the spacing for the dense taps which have 80% power contribution, while $2T_c$ spacing was chosen for the sparse taps. Many tapped delay line models [30, 59, 71] show that tap amplitudes follow Rayleigh and Ricean distributions in most cases. Tap Doppler spectra are found to be "horned," "narrow," "flat" and so forth based on the measurement environments. Tap correlation is higher for the first taps than for the later taps.

12.3.9. Capacity of MIMO channels

Normally it is assumed that the propagation channel is at least known to receiver. If the channel is also known to transmitter, capacity can be higher by using water-filling method to assign different powers to the subchannels. Of course unequal powers is a problem in diversity systems [58]. For a channel unknown to transmitter, the same power is sent over the M antennas, and the array transmit gain is not realized, only diversity gain is [62]. The eigenvalues of the transfer matrix $\mathbf{H}$ are the (relative) received power of the subchannels. For frequency-flat (narrowband) fading channel, we can calculate the capacity by using the well-known Shannon formula. For the case of frequency-selective (wideband) fading, we have to evaluate the capacity by integrating over all the frequencies [72].

Generally, the SIMO capacity is higher than MISO capacity when the channel is unknown to the transmitter. Otherwise, they are the same. The largest MIMO capacity can be obtained for rich multipath Rayleigh channel (i.i.d.) when the channel is known to both transmitter and receiver. Channel capacity when the channel is unknown to both transmitter and receiver is an area of ongoing research [58].

In analyzing the capacity of fading channels two commonly used statistics are the ergodic capacity and outage capacity. The ergodic capacity is the ensemble average of the information rate over the distribution of the elements of the channel matrix. Outage analysis quantifies the level of performance that is guaranteed with a certain level of reliability, for example, we define the q% outage capacity $C_{\text{out},q}$ as the information rate that is guaranteed for $(100 - q)$% of the channel realizations. Ricean fading, fading correlation, XPD degeneracy, and element polarization influence on MIMO capacity. Higher fading correlations of the channels can cause lower capacity; capacity is lower with increasing Ricean factor. High XPD enhances MIMO channel capacity at high SNR. Keyhole channel degeneracy significantly degrades MIMO capacity [57, 58]. The keyhole channel was found in the measurements in [62], however, real keyhole channel has not been found in practical measurements [35, 73]. It was anticipated in [73] that the keyhole effect due to real-world waveguides like tunnels and corridors will usually be very weak and difficult to be measured. In typical cellular frequencies, such waveguides are heavily overmoded and thus will not lead to severe rank reductions. Effect of element polarization on the capacity of a MIMO channel was discussed in [74] based on indoor measurements. The conclusion is that both vertical and horizontal polarizations have similar behaviors. There is an advantage in using both polarizations because their capacity stays approximately constant with distance while the capacity of a single polarization system decreases.

12.4. Conclusions

As mentioned in the introduction, there has been significant increase in especially experimental but in many cases also theoretical or computational information on the complex multipath propagation experienced in mobile communications. This

forms a very important or actually necessary basis for the development of radio systems trying to utilize optimally this complex medium for information transfer.

Abbreviations

3D	Three-dimensional
AW	Absorbing wedges
BER	Bit error rate
BS	Base station
CDF	Cumulative distribution function
DoA	Direction of arrival
EM	Electromagnetic
ESPRIT	Estimation of signal parameters via rotational invariance techniques
FEM	Finate element method
freq.	Frequency
GSM	Global system for mobile communication
i.i.d.	Independent and identically distributed
IR	Impulse response
IRs	Impulse responses
LOS	Line of sight
MIMO	Multiple-input multiple-output
MISO	Multiple-input single-output
MS	Mobile station
MTL	Modal transmission line
NLOS	Non-line-of-sight
PAS	Power angular spectra
PC	Personal computer
PC-UTD	Perfectly conducting uniform geometrical theory of diffraction
PDF	Probability density function
PDP	Power delay profile
PSD	Power spectral density
ref.	Reference
RMS	Root mean square
RT	Ray tracing
Rx	Receiver
SAGE	Space alternating generalized expectation maximization
SIMO	Single-input multiple-output
SISO	Single-input single-output
SNR	Signal-to-noise ratio
std	Standard deviation
TDL	Tapped delay line
tr	Transverse
Tx	Transmitter
UMTS	Universal Mobile Telecommunication System
US	Uncorrelated scattering
VNA	Vector network analyzer
VP	Vertical polarization
WCS	Wideband channel sounder
WSS	Wide-sense stationary
WSSUS	Wide sense stationary uncorrelated scattering

XPD	Cross-polarization discrimination
zz	Zigzag
zz/la	Zigzag lateral
zz/tr	Zigzag transverse

Bibliography

[1] K. Kalliola, H. Laitinen, L. I. Vaskelainen, and P. Vainikainen, "Real-time 3-D spatial-temporal dual-polarized measurement of wideband radio channel at mobile station," *IEEE Trans. Instrum. Meas.*, vol. 49, no. 2, pp. 439–448, 2000.

[2] R. S. Thoma, D. Hampicke, A. Richter, et al., "Identification of time-variant directional mobile radio channels," *IEEE Trans. Instrum. Meas.*, vol. 49, no. 2, pp. 357–364, 2000.

[3] J. Kivinen, P. Suvikunnas, D. Perez, C. Herrero, K. Kalliola, and P. Vainikainen, "Characterization system for MIMO channels," in *Proc. 4th International Symposium on Wireless Personal Multimedia Communications (WPMC '01)*, pp. 159–162, Aalborg, Denmark, September 2001.

[4] M. J. Gans, N. Amitay, Y. S. Yeh, et al., "Outdoor BLAST measurement system at 2.44 GHz: calibration and initial results," *IEEE J. Select. Areas Commun.*, vol. 20, no. 3, pp. 570–583, 2002.

[5] L. Vuokko, P. Vainikainen, and J.-I. Takada, "Clusterization of measured direction-of-arrival data in an urban macrocellular environment," in *Proc. 14th IEEE International Symposium on Personal, Indoor and Mobile Radio Communications (PIMRC '03)*, vol. 2, pp. 1222–1226, Beijing, China, September 2003.

[6] X. Zhao, I. Rekanos, and P. Vainikainen, "A recommended maliuzhinets diffraction coefficient for right angle lossy wedges," in *Proc. 5th European Personal Mobile Communications Conference (EPMCC '03)*, pp. 195–198, Glasgow, UK, April 2003.

[7] H. El-Sallabi and P. Vainikainen, "Improvement in a heuristic UTD diffraction coefficient for prediction of radio wave propagation," in *Proc. IEEE 57th Semiannual Vehicular Technology Conference (VTC 2003-Spring)*, vol. 2, pp. 788–792, Jeju, South Korea, April 2003.

[8] H. El-Sallabi and P. Vainikainen, "Radio wave propagation in perpendicular streets of urban street grid for microcellular communications. Part I: channel modeling," *Progress in Electromagnetic Research*, vol. 40, pp. 229–254, 2003.

[9] J. Kivinen and P. Vainikainen, "Wideband propagation measurements in corridors at 5.3 GHz," in *Proc. IEEE 5th International Symposium on Spread Spectrum Techniques and Applications (ISSSTA '98)*, vol. 2, pp. 512–516, Sun City, South Africa, September 1998.

[10] J. Kivinen, X. Zhao, and P. Vainikainen, "Wideband indoor radio channel measurements with direction of arrival estimations in the 5 GHz band," in *Proc. IEEE 50th Vehicular Technology Conference (VTC 1999-Fall)*, vol. 4, pp. 2308–2312, Amsterdam, The Netherlands, September 1999.

[11] E. Richalot, M. Bonilla, M.-F. Wong, V. Fouad-Hanna, H. Baudrand, and J. Wiart, "Electromagnetic propagation into reinforced-concrete walls," *IEEE Trans. Microwave Theory Tech.*, vol. 48, no. 3, pp. 357–366, 2000.

[12] S. V. Savov and M. H. A. J. Herben, "Application of the modal transmission-line method to radiowave propagation through building walls," *IEE Proceedings Science, Measurement and Technology*, vol. 149, no. 5, pp. 258–261, 2002.

[13] K. Sato, T. Manabe, J. Polivka, T. Ihara, Y. Kasashima, and K. Yamaki, "Measurement of the complex refractive index of concrete at 57.5 GHz," *IEEE Trans. Antennas Propagat.*, vol. 44, no. 1, pp. 35–40, 1996.

[14] D. A. McNamara, C. W. I. Pistorius, and J. A. G. Malherbe, *Introduction to the Uniform Geometrical Theory of Diffraction*, Artech House, Boston, Mass, USA, 1990.

[15] R. G. Kouyoumjian and P. H. Pathak, "A uniform geometrical theory of diffraction for an edge in a perfectly conducting surface," *Proc. IEEE*, vol. 62, pp. 1448–1461, 1974.

[16] G. D. Maliuzhinets, "Excitation, reflection and emission of surface waves from a wedge with given face impedances," *Sov. Phys. Dokl.*, vol. 3, no. 4, pp. 752–755, 1958.

[17] R. J. Luebbers, "Finite conductivity uniform GTD versus knife edge diffraction in prediction of propagation path loss," *IEEE Trans. Antennas Propagat.*, vol. 32, no. 1, pp. 70–76, 1984.

[18] W. D. Burnside and K. W. Burgener, "High frequency scattering by a thin lossless dielectric slab," *IEEE Trans. Antennas Propagat.*, vol. 31, no. 1, pp. 104–110, 1983.
[19] K. A. Remley, H. R. Anderson, and A. Weisshar, "Improving the accuracy of ray-tracing techniques for indoor propagation modeling," *IEEE Trans. Veh. Technol.*, vol. 49, no. 6, pp. 2350–2358, 2000.
[20] P. D. Holm, "A new heuristic UTD diffraction coefficient for nonperfectly conducting wedges," *IEEE Trans. Antennas Propagat.*, vol. 48, no. 8, pp. 1211–1219, 2000.
[21] H. M. El-Sallabi, I. T. Rekanos, and P. Vainikainen, "A new heuristic diffraction coefficient for lossy dielectric wedges at normal incidence," *IEEE Antennas and Wireless Propagation Letters*, vol. 1, no. 8, pp. 165–168, 2002.
[22] H. M. El-Sallabi and P. Vainikainen, "Improvement in diffraction coefficient for non-perfectly conducting wedges," to appear in *IEEE Trans. Antennas Propagat.*, September 2005.
[23] H. M. El-Sallabi and P. Vainikainen, "Improvement in heuristic UTD diffraction coefficient," *IEE Electronics Letters*, vol. 39, no. 1, pp. 10–12, 2003.
[24] O. Landron, M. J. Feuerstein, and T. S. Rappaport, "A comparison of theoretical and empirical reflection coefficients for typical exterior wall surfaces in mobile radio environment," *IEEE Trans. Antennas Propagat.*, vol. 44, no. 3, pp. 341–351, 1996.
[25] V. Degli-Esposti, "A diffuse scattering model for urban propagation prediction," *IEEE Trans. Antennas Propagat.*, vol. 49, no. 7, pp. 1111–1113, 2001.
[26] V. Degli-Esposti and H. L. Bertoni, "Evaluation of the role of diffuse scattering in urban microcellular propagation," in *Proc. IEEE 50th Vehicular Technology Conference (VTC 1999-Fall)*, vol. 3, pp. 1392–1396, Amsterdam, The Netherlands, September 1999.
[27] V. Degli-Esposti, H. M. El-Sallabi, D. Guiducci, et al., "Analysis and simulation of the diffuse scattering phenomenon in urban environment," in *Proc. 27th General Assembly of the International Union of Radio Science (URSI 2002)*, August 2002.
[28] S. Geng, J. Kivinen, and P. Vainikainen, "Measurement and analysis of indoor radio channels at 60 GHz," in *Millimetre Wave Technology and Applications: Circuits, Systems, and Measurement Techniques*, Espoo, Finland, May 2003.
[29] J. B. Andersen and K. I. Pedersen, "Angle-of-arrival statistics for low resolution antennas," *IEEE Trans. Antennas Propagat.*, vol. 50, no. 3, pp. 391–395, 2002.
[30] J. Kivinen, X. Zhao, and P. Vainikainen, "Empirical characterization of wideband indoor radio channel at 5.3 GHz," *IEEE Trans. Antennas Propagat.*, vol. 49, no. 8, pp. 1192–1203, 2001.
[31] K. Kalliola, K. Sulonen, H. Laitinen, O. Kivekas, J. Krogerus, and P. Vainikainen, "Angular power distribution and mean effective gain of mobile antenna in different propagation environments," *IEEE Trans. Veh. Technol.*, vol. 51, no. 5, pp. 823–838, 2002.
[32] V. Degli-Esposti, G. Lombardi, C. Passerini, and G. Riva, "Wide-band measurement and ray-tracing simulation of the 1900-MHz indoor propagation channel: comparison criteria and results," *IEEE Trans. Antennas Propagat.*, vol. 49, no. 7, pp. 1101–1110, 2001.
[33] K. Sulonen, P. Suvikunnas, J. Vuokko, L. Kivinen, and P. Vainikainen, "Comparison of MIMO antenna configurations in picocell and microcell environments," *IEEE J. Select. Areas Commun.*, vol. 21, no. 5, pp. 703–712, 2003.
[34] K. Sulonen, P. Suvikunnas, J. Kivinen, L. Vuokko, and P. Vainikainen, "Study of different mechanisms providing gain in MIMO systems," in *Proc. IEEE 58th Vehicular Technology Conference (VTC 2003-Fall)*, vol. 1, pp. 352–356, October 2003.
[35] J. P. Kermoal, L. Schumacher, K. I. Pedersen, P. E. Mogensen, and F. Frederiksen, "A stochastic MIMO radio channel model with experimental validation," *IEEE J. Select. Areas Commun.*, vol. 20, no. 6, pp. 1211–1226, 2002.
[36] M. Lienard, P. Degauque, J. Baudet, and D. Degardin, "Investigation on MIMO channels in subway tunnels," *IEEE J. Select. Areas Commun.*, vol. 21, no. 3, pp. 332–339, 2003.
[37] A. Saleh and R. Valenzuela, "A statistical model for indoor multipath propagation," *IEEE J. Select. Areas Commun.*, vol. 5, no. 2, pp. 128–137, 1987.
[38] P. Nobles, D. Ashworth, and F. Halsall, "Propagation measurements in an indoor radio environment at 2, 5 and 17 GHz," in *Proc. IEE Colloquium on High Bit Rate UHF/SHF Channel Sounders - Technology and Measurement*, pp. 41–46, London, UK, December 1993.

[39] T. Zwick, C. Fischer, and W. Wiesbeck, "A stochastic channel model including path directions for indoor environments," *IEEE Journal on Selected Areas in Communications*, vol. 20, no. 6, pp. 1178–1198, 2002.

[40] M. Varela and M. Sanchez, "RMS delay and coherence bandwidth measurements in indoor radio channels in the UHF band," *IEEE Trans. Veh. Technol.*, vol. 50, no. 2, pp. 515–525, 2001.

[41] G. A. Dimitrakopoulos and C. N. Capsalis, "Statistical modeling of RMS-delay spread under multipath fading conditions in local areas," *IEEE Trans. Veh. Technol.*, vol. 49, no. 5, pp. 1522–1528, 2000.

[42] Q. H. Spencer, B. D. Jeffs, M. A. Jensen, and A. L. Swindlehurst, "Modeling the statistical time and angle of arrival characteristics of an indoor multipath channel," *IEEE J. Select. Areas Commun.*, vol. 18, no. 3, pp. 347–360, 2000.

[43] X. Zhao, J. Kivinen, P. Vainikainen, and K. Skog, "Propagation characteristics for wideband outdoor mobile communications at 5.3 GHz," *IEEE J. Select. Areas Commun.*, vol. 20, no. 3, pp. 507–514, 2002.

[44] N. Papadakis, A. G. Kanatas, and P. Constantinou, "Microcellular propagation measurements and simulation at 1.8 GHz in urban radio environment," *IEEE Trans. Veh. Technol.*, vol. 47, no. 3, pp. 1012–1026, 1998.

[45] H. H. Xia, H. L. Bertoni, L. R. Maciel, A. Lindsay-Stewart, and R. Rowe, "Microcellular propagation characteristics for personal communications in urban and suburban environments," *IEEE Trans. Veh. Technol.*, vol. 43, no. 3, pp. 743–752, 1994.

[46] D. Har, H. Xia, and H. L. Bertoni, "Path-loss prediction model for microcells," *IEEE Trans. Veh. Technol.*, vol. 48, no. 5, pp. 1453–1462, 1999.

[47] A. F. Molisch, *Wideband Wireless Digital Communications*, Prentice Hall, Englewood Cliffs, NJ, USA, 2001.

[48] M. Haardt, *Efficient one-, two-, and multidimensional high-resolution array signal processing*, Ph.D. thesis, Technology University of Munich, Shaker Verlag, Aachen, Germany, 1996.

[49] J. A. Fessler and A. O. Hero, "Space-alternating generalized expectation-maximization algorithm," *IEEE Trans. Signal Processing*, vol. 42, no. 10, pp. 2664–2677, 1994.

[50] J. Laurila, K. Kalliola, M. Toeltsch, K. Hugl, P. Vainikainen, and E. Bonek, "Wide band 3D characterization of mobile radio channels in urban environment," *IEEE Trans. Antennas Propagat.*, vol. 50, no. 2, pp. 233–243, 2002.

[51] A. Kuchar, J.-P. Rossi, and E. Bonek, "Directional macro-cell channel characterization from urban measurements," *IEEE Trans. Antennas Propagat.*, vol. 48, no. 2, pp. 137–146, 2000.

[52] L. Vuokko, P. Vainikainen, and J. Takada, *Experimental Study of Clusters in Urban Macrocellular Environments*, COST273 Temporary Document, TD(03)176, Prague, Czech Republic, 2003.

[53] K. Kalliola, H. Laitinen, P. Vainikainen, M. Toeltsch, J. Laurila, and E. Bonek, "3-D double-directional radio channel characterization for urban macrocellular applications," *IEEE Trans. Antennas Propagat.*, vol. 51, no. 11, pp. 3122–3133, 2003.

[54] H. Suzuki, "A statistical model for urban radio propagation," *IEEE Trans. Commun.*, vol. 25, no. 7, pp. 673–680, 1977.

[55] V. Erceg, S. J. Fortune, J. Ling, A. J. Rustako, and R. A. Valenzuela Jr., "Comparisons of a computer-based propagation prediction tool with experimental data collected in urban microcellular environments," *IEEE J. Select. Areas Commun.*, vol. 15, no. 4, pp. 677–684, 1997.

[56] J. B. Andersen, "Amplitude distribution revisited," COST273, 2002.

[57] G. D. Durgin, *Space-Time Wireless Channels*, T. S. Rappaport, Ed., Prentice Hall, Englewood Cliffs, NJ, USA, 2003.

[58] A. Paulraj, R. Nabar, and D. Gore, *Introduction to Space-Time Wireless Communications*, Cambridge University press, Cambridge, UK, 2003.

[59] X. Zhao, J. Kivinen, P. Vainikainen, and K. Skog, "Characterization of Doppler spectra for mobile communications at 5.3 GHz," *IEEE Trans. Veh. Technol.*, vol. 52, no. 1, pp. 14–23, 2003.

[60] K. I. Pedersen, P. E. Mogensen, and B. H. Fleury, "A stochastic model of the temporal and azimuthal dispersion seen at the base station in outdoor propagation environments," *IEEE Trans. Veh. Technol.*, vol. 49, no. 2, pp. 437–447, 2000.

[61] M. B. Knudsen and G. F. Pedersen, "Spherical outdoor to indoor power spectrum model at the mobile terminal," *IEEE J. Select. Areas Commun.*, vol. 20, no. 6, pp. 1156–1169, 2002.
[62] J. B. Andersen and K. I. Pedersen, "Angle-of-arrival statistics for low resolution antennas," *IEEE Trans. Antennas Propagat.*, vol. 50, no. 3, pp. 391–395, 2002.
[63] C.-C. Chong, C.-M. Tan, D. I. Laurenson, S. McLaughlin, M. A. Beach, and A. R. Nix, "A new statistical wideband spatio-temporal channel model for 5-GHz band WLAN systems," *IEEE J. Select. Areas Commun.*, vol. 21, no. 2, pp. 139–150, 2003.
[64] L. M. Correia, Ed., *Wireless Flexible Personalised Communications*, Wiley, 2001.
[65] H. Xu, V. Kukshya, and T. S. Rappaport, "Spatial and temporal characteristics of 60-GHz indoor channels," *IEEE J. Select. Areas Commun.*, vol. 20, no. 3, pp. 620–630, 2002.
[66] "Electrical characteristics of the surface of the earth," *Recommendation ITU-R*, pp. 527–3, 1992.
[67] J. Lähteenmäki, *Indoor radio propagation measurements and modeling at 900 MHz, 1.8 GHz and 60 GHz*, Lic. thesis, Helsinki University of Technology, Espoo, Finland, 1994.
[68] L. M. Correia and P. O. Frances, "Estimation of materials characteristics from power measurements at 60 GHz," in *Proc. 5th IEEE International Symposium on Personal, Indoor and Mobile Radio Communications (PIMRC '94)*, vol. 2, pp. 510–513, The Hague, The Netherlands, September 1994.
[69] T. Manabe, Y. Miura, and T. Ihara, "Effects of antenna directivity and polarization on indoor multipath propagation characteristics at 60 GHz," *IEEE J. Select. Areas Commun.*, vol. 14, no. 3, pp. 441–448, 1996.
[70] W. Mohr, "Modeling of wideband mobile radio channels based on propagation measurements," in *Proc. 6th IEEE International Symposium on Personal, Indoor and Mobile Radio Communications (PIMRC '95)*, vol. 2, pp. 397–401, Toronto, Canada, September 1995.
[71] X. Zhao, V. Kolmonen, S. Geng, et al., "Tapped delay line channel models for indoor MIMO radio channels at 5 GHz," in *Proc. 34th European Microwave Conference (EuMC '04)*, vol. 2, pp. 397–401, Amsterdam, The Netherlands, October 2004.
[72] A. F. Molisch, M. Steinbauer, M. Toeltsch, E. Bonek, and R. S. Thoma, "Capacity of MIMO systems based on measured wireless channels," *IEEE J. Select. Areas Commun.*, vol. 20, no. 3, pp. 561–569, 2001.
[73] P. Almers, F. Tufvesson, and A. F. Molisch, "Measurement of keyhole effect in a wireless multiple-input multiple-output (MIMO) channel," *IEEE Commun. Lett.*, vol. 7, no. 8, pp. 373–375, 2003.
[74] P. Kyritsi and D. C. Cox, "Effect of element polarization on the capacity of a MIMO system," in *Proc. IEEE Wireless Communications and Networking Conference (WCNC '02)*, vol. 2, pp. 892–896, Orlando, Fla, USA, March 2002.
[75] M. Steinbauer, A. Molisch, and E. Bonek, "The double-directional radio channel," *IEEE Antennas Propagat. Mag.*, vol. 43, no. 4, pp. 51–63, 2001.

P. Vainikainen: IDC SMARAD Radio Laboratory, Helsinki University of Technology, P.O. Box 3000, FI-02015 TKK, Espoo, Finland

Email: pvainika@cc.hut.fi

J. Kivinen: IDC SMARAD Radio Laboratory, Helsinki University of Technology, P.O. Box 3000, FI-02015 TKK, Espoo, Finland

Email: jarmo.kivinen@tkk.fi

X. Zhao: IDC SMARAD Radio Laboratory, Helsinki University of Technology, P.O. Box 3000, FI-02015 TKK, Espoo, Finland

Email: xiongwen.zhao@elektrobit.com

H. El-Sallabi: IDC SMARAD Radio Laboratory, Helsinki University of Technology, P.O. Box 3000, FI-02015 TKK, Espoo, Finland

Email: hsallabi@cc.hut.fi

13 Multidimensional high-resolution channel sounding measurement

Reiner S. Thomä, Markus Landmann, Andreas Richter, and Uwe Trautwein

13.1. Introduction

The design of future mobile radio networks (beyond 3G) requires research towards new air interfaces which are characterized by the highest bandwidth efficiency and unprecedented flexibility. It is commonly understood that radio systems equipped with multiple antennas at both the mobile station (MS) and the base station (BS) have a huge potential to increase the available capacity for high bit rate wireless links, which results from a simultaneous transmission of multiple data streams from different antenna elements [1]. This multiantenna technique is called multiple-input multiple-output (MIMO) and can optimally exploit the spatial diversity of the multiple propagation paths existing in a rich scattering environment. Conceptually, the multipath propagation of the radio channel gives rise to different spatio-temporal signatures for the different transmit data streams, which permits a receiver equipped with multiple antennas to separate those data streams from the received signal mixture, that are otherwise not orthogonal in any of the conventional communication signal dimensions, that is, by time, frequency, or code. Keeping this in mind, it is not really surprising that the performance of a MIMO system will strongly depend on the radio channel conditions. A key question for a system design and implementation is therefore do we find practically feasible schemes that are sufficiently robust for this task? Or somewhat related, which specific features are required for a practical MIMO system to work reliably under a wealth of various propagation conditions?

Hence, a thorough investigation of the multidimensional wave propagation mechanisms is a prerequisite for understanding the spatial and temporal structure of the channel transfer matrix, and, thus, for optimum design and realistic performance evaluation of multiple-antenna systems. There are many attempts to simulate the input-output behavior of the channel. The physically motivated approach is based on electromagnetic wave propagation analysis and uses a ray-optical model. In case of ray tracing or ray launching, a detailed database describing the propagation environment is required. Other models, although ray-based

as well, use statistical assumptions on the geometrical distribution of scatterers (e.g., COST 259). There are also completely statistical models trying to reproduce the input/output behavior in a statistical sense by formal assumptions of correlation coefficients and distributions resulting at the transmit antenna and receive antenna ports disregarding the geometrical distribution of the scatterers. A lack of nongeometric models is that they are inherently specific for a certain antenna characteristic. For antenna-independent modeling (which allows antenna deembedding and embedding) it seems that geometry-based models are a must [2, 3].

Since the complexity of wave reflection, scattering, diffraction, and so forth in real propagation environments can never be completely reproduced by electromagnetic simulation and because of the strong simplifications of the statistical approaches, all models have to be verified and parameterized by propagation measurements. Moreover, channel models can be deduced directly from measurements in real propagation environments by estimating the geometric path parameters from the recorded data [4]. Given a ray-optical path model, the parameters of a suitably defined propagation path model are direction of arrival (DoA) at the receiver array, direction of departure (DoD) at the transmitter array, time delay of arrival (TDoA), Doppler shift, and the complex, polarimetric path weight matrix.

A multidimensional channel sounder is a measuring device that allows the observation of the time-varying multipath channel impulse response (CIR) in its relevant multiple dimensions. These dimensions may be temporal and spatial in nature and must contain enough information on all model parameters described above. To this end, we need a broadband excitation signal to "sound" the channel in the frequency range of interest and antenna arrays, which excite or sense the wave field in a properly defined spatial aperture. A sounder system typically consists of a mobile transmitter (Tx) which plays the role of the mobile station (MS) and a fixed receiver (Rx) in place of the base station (BS). Since the channel is reciprocal, it makes no difference if the results are interpreted as uplink or as downlink, respectively. The receiver may also be moving if we consider a peer-to-peer communication between two mobile platforms. Both excitation and recording must be repetitive with a period short enough in order to make the temporal variation statistics according to Doppler shift and small-scale fading visible. Moreover, the data recording must be continuous along a precisely defined trajectory to reproduce large-scale channel parameter variation. This all is called real-time MIMO channel sounding and it makes the measured data usable for simulating the MIMO transceiver performance including link- and system-level aspects.

Figure 13.1 highlights the double-directional structure of the multipath channel. Specifically, double-directional measurements that include joint DoA/DoD estimation allow the separation of the directional dependent influence of the measurement antennas from the channel measurements which is a prerequisite of antenna-independent channel characterization.

The antenna array arrangement is of crucial importance to represent a certain system scenario. This applies to the typical BS or access point (AP) location in a cellular- or WLAN-specific deployment scenario. The MS antenna array location should resemble the characteristic user roaming behavior. This may include almost

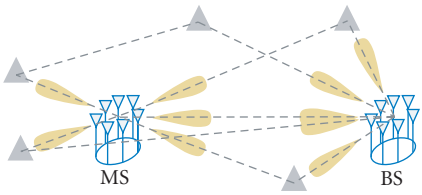

Figure 13.1. Double-directional DoD/DoA structure of a multipath channel.

stationary user terminals but also high-mobility user platforms such as cars, aircrafts, or trains. For ad hoc and multihop networking, the situation changes completely since there is no dedicated BS. Instead, both sides of the link have to represent the terminal morphology and mobility. This influences the antenna array architecture, which consists of the array size and shape and of the number, orientation as well as of the characteristics of the individual antenna elements. Both BS and AP, for example, may have a limited angular viewing sector. The MS, acting as the user, should have a full angular coverage in order to represent arbitrary user antenna orientation. Moreover, advanced network-specific scenarios such as multiple users including known and unknown interference, cooperative downlinks from multiple BS or AP, multihop networking and relaying, and so forth have to be emulated by the measurement setup. Only if the measurement scenario is properly defined, the recorded CIR data can be used for realistic link- and system-level simulation. The advantages of this measurement-based offline approach in comparison with the prototype hardware demonstration are higher flexibility, lower costs, and an improved perception of the transceiver's operation. The latter is primarily due to more effective analysis techniques that allow the observed transceiver performance to be traced back to the actual time-variant space-time structure and physical propagation phenomena.

Even more specific design roles for antenna arrays apply if we have high-resolution estimation of the ray-optical multipath model in mind. The channel response can, in general, be observed only within a limited aperture volume that is somewhat related to the array size, frequency bandwidth, and temporal observation window. This strictly limits the achievable parameter resolution and accuracy in terms of DoA/DoD, TDoA, and Doppler, respectively, when classical nonparametric estimation algorithms are applied. Therefore, high-resolution parameter estimation algorithms have to be envisaged to enhance the resolution by fitting an appropriate data model to the measured data. In this case, the resolution is only limited by the signal to noise ratio (SNR), antenna and device imperfections, calibration quality, and the limited validity of the data model. The resolution performance mainly depends on the antenna array architecture and its manufacturing quality, which includes low electromagnetic coupling, high electrical and mechanical stability and precise calibration. In the context of high-resolution channel parameter estimation, also the definition of the data model is crucial for parameter estimation. It has to be accurate enough to represent the

reality of wave propagation and the influence of the measurement device. On the other hand, it must not be finicky detailed since the amount of information gathered by the sounder is always limited and may not be sufficient to estimate all model parameters. A proper choice of the model structure and dimension can dramatically reduce the algorithmic complexity and enhance the accuracy and resolution as well as the reliability of the results. There are always compromises and simplifications, such as the narrowband assumption which presumes frequency-independent propagation mechanisms and antenna arrays, which are smaller than the spatial resolution of the sounding signal.

The rest of this chapter is organized as follows. Section 13.2 introduces the advanced data model for high-resolution parameter estimation which includes specular and diffuse scattered components. Section 13.3 describes the main design features of a typical real-time MIMO channel sounder architecture. Sections 13.4 and 13.5 describe the aspects of high-resolution antenna array design and calibration, and also the Cramér-Rao lower bound (CRLB) of the angular parameter estimation variance is derived and calculated directly from the antenna array calibration data. Section 13.6 summarizes the maximum likelihood (ML) framework as it is used for high-resolution channel parameter estimation. In Section 13.7, some aspects of sounding data usage for realistic link-level performance evaluation are outlined. Conclusions are given in Section 13.8.

13.2. The data model

The most widely accepted data model for high-resolution channel parameter estimation is based on a ray-optical understanding of the propagation phenomena. Propagation paths are modeled by planar, narrowband wavefronts. This is motivated by the idea of specular reflections at smooth surfaces. To model the influence of receiver noise, a white noise component is usually added. However, it is well known that wave propagation phenomena may also comprise diffusely scattered components [5]. Its contribution varies depending on the complexity of the propagation environment. It can be almost negligible in macrocell LOS scenarios and can even dominate in complicated propagation environments such as factory halls. Whereas the electromagnetic background of diffuse scattering is already well understood and there are also various attempts to include diffuse scattered components into geometric channel models [6], its influence is widely neglected in high-resolution parameter estimation from sounding measurements. However, this may have a very detrimental effect on the performance of the parameter estimation procedure.

Therefore, we introduce a data model comprising two components that can be handled separately throughout the estimation procedure [7, 8]. The first part is considered as deterministic and results from a limited number of specular-like reflections. We also call it the structural part of the model since is has clear geometric interpretation. The second part is observed as a dense diffuse part that is stochastic in nature and cannot be resolved by the measurement device. It results from distributed diffuse scattering as it occurs in a complicated, multipath

rich environment. For example, a sounder having a measurement bandwidth of 120 MHz [9, 10] gives us excellent possibilities to resolve a number of specular components, even though the spatial resolution is only about 2.5 m, which corresponds to 43 wavelengths at 5.2 GHz. Hence, in a "microscopic" sense we can expect quite a big number of superimposed diffused components in an observed delay bin. We call this "dense multipath model." The resulting CIR part is therefore adequately modeled by a complex circular normal distribution. It might be argued that diffuse components can be neglected in the presence of specular paths. This is however not consistent with our experience [11]. An explanation could be that specular paths can contribute to the received power only for very distinct angular constellations. On the other hand, diffused power has the chance to reach the receiver within a large (almost continuous) variety of propagation angles supposing that there is a big number of widely distributed scatterers. Note that modeling of diffuse scattering for the purposes of parameter estimation does not need to model the individual scatterers. Rather we need a model that describes the superimposed contributions to the observed data at the receiver.

In the discrete angular delay-Doppler domain the specular part is described by a superposition of K R-dimensional Dirac deltas weighted by a 2×2 complex polarimetric path weight matrix with its components $\gamma_{xy,k}$, where the indices x, y indicate polarization in azimuthal and elevation direction at Tx and Rx, respectively. The R structural parameters are DoD φ_T, ϑ_T (azimuth and elevation), TDoA τ, Doppler shift α, and DoA φ_R, ϑ_R:

$$\begin{aligned}\mathbf{H}_\delta(\alpha, \tau, \vartheta_R, \varphi_R, \vartheta_T, \varphi_T) &= \sum_{k=1}^{K} \begin{bmatrix} \gamma_{\vartheta\vartheta,k} & \gamma_{\varphi\vartheta,k} \\ \gamma_{\vartheta\varphi,k} & \gamma_{\varphi\varphi,k} \end{bmatrix} \{\delta(\alpha - \alpha_k)\delta(\tau - \tau_k) \\ &\quad \cdot \delta(\varphi_R - \varphi_{R_k})\delta(\vartheta_R - \vartheta_{R_k})\delta(\varphi_T - \varphi_{T_k})\delta(\vartheta_T - \vartheta_{T_k})\}\end{aligned} \tag{13.1}$$

with its Fourier transformed counterpart

$$\begin{aligned}\mathbf{H}_e(t, f, s_R, l_R, s_T, l_T) = \sum_{k=1}^{K} \Bigg\{ &\begin{bmatrix} \gamma_{\vartheta\vartheta,k} & \gamma_{\varphi\vartheta,k} \\ \gamma_{\vartheta\varphi,k} & \gamma_{\varphi\varphi,k} \end{bmatrix} e^{-j2\pi t\alpha_k} e^{-j2\pi f\tau_k} \\ &\cdot e^{-j2\pi s_R\varphi_{R_k}} e^{-j2\pi s_T\varphi_{T_k}} e^{-j2\pi l_T\vartheta_{T_k}} e^{-j2\pi l_T\vartheta_{T_k}} \Bigg\}.\end{aligned} \tag{13.2}$$

The last equation shows that the estimation of the structural parameters is essentially a multidimensional harmonic retrieval problem. Whereas the Doppler shift α and TDoA τ are clearly related to the observed aperture variables t and f in time and frequency, the Fourier transform of the DoA/DoD parameters is not directly related to the physical antenna array aperture. For this, we would need a further geometrical transformation which will depend on the specific array architecture. We omit this transformation step here since it can be completely avoided if we

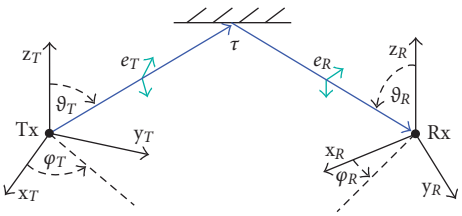

Figure 13.2. Multidimensional specular path data model.

rely on a proper antenna calibration procedure. We call the Fourier transform of the angular antenna domain the effective aperture distribution function (EADF). Hence, its dimensions $s_{T/R}$, $l_{T/R}$ are not uniquely defined in a physical sense but are somewhat related to the geometrical dimensions of the respective antenna array.

A geometrical definition of the specular path data model (13.1) is explained in Figure 13.2. For the sake of simplicity, the DoA/DoD definitions are independent and related to the local coordinate systems of the respective Tx/Rx arrays. Note that this model has to be considered as instantaneous which means it is specific for a single time instant and may be slowly changing with time when the objects of the scenario are moving. This variation of the structural parameters and their geometric coupling is currently not explicitly included in this model. The Doppler shift parameter may need some specific explanation since a Doppler shift implies that the path length changes. Phase changes on the individual propagation paths can be resolved for varying antenna distances of at least a small number of wavelengths. However, the respective change in delay can normally not be resolved in TDoA or DoA/DoD. Consequently, also the Doppler shift parameter can be considered as local and is also subjected to change slowly with time.

Unfortunately, the data model of (13.1) and (13.2) is not directly applicable for parameter estimation. For this we need a more concise vector/matrix notation. The condensed parameter vector $\boldsymbol{\Theta}_k$ contains 14 real-valued unknowns describing the six structural parameters and four complex path weight parameters of any propagation path. The observable channel response $\mathbf{s}(\boldsymbol{\Theta}_k)$ in the multidimensional aperture domain is defined by the limited observation time, finite bandwidth, and finite (effective) antenna apertures:

$$\begin{aligned}\mathbf{s}(\boldsymbol{\Theta}_k) = {} & \gamma_{\vartheta\vartheta,k} \cdot \mathbf{G}_{\vartheta\vartheta}\mathbf{a}(\boldsymbol{\mu}_k) + \gamma_{\vartheta\varphi,k} \cdot \mathbf{G}_{\vartheta\varphi}\mathbf{a}(\boldsymbol{\mu}_k) \\ & + \gamma_{\varphi\vartheta,k} \cdot \mathbf{G}_{\varphi\vartheta}\mathbf{a}(\boldsymbol{\mu}_k) + \gamma_{\varphi\varphi,k} \cdot \mathbf{G}_{\varphi\varphi}\mathbf{a}(\boldsymbol{\mu}_k).\end{aligned} \tag{13.3}$$

We arrange the sampled channel response in vectors as $\mathbf{a}(\mu_k) = \mathbf{a}(\mu_k^{(R)}) \otimes \mathbf{a}(\mu_k^{(R-1)}) \otimes \cdots \otimes \mathbf{a}(\mu_k^{(1)})$, whereby the $\mathbf{a}(\mu_k^{(i)})$ are complex exponentials resulting from Fourier transform of (13.1) and the $\mu_k^{(i)}$ are the normalized structural path parameters which are related to their physical counterparts by a unique projection $\mu^{(1)} = f(\alpha)$, $\mu^{(2)} = f(\tau)$, $\mu^{(3)} = f(\varphi_T)$, $\mu^{(4)} = f(\vartheta_T)$, $\mu^{(5)} = f(\varphi_R)$, $\mu^{(6)} = f(\vartheta_R)$ and a proper normalization to the respective aperture size, for example, frequency

bandwidth in case of $\mu^{(2)}$. The linear projector matrices $\mathbf{G}_{xy}$ describe the measurement systems response, which is composed of the Kronecker products of the frequency, Doppler, and spatial responses, respectively. Whereas the frequency response is represented by a diagonal matrix and the Doppler response is simply an identity matrix, the spatial response is described by the effective aperture distribution function (EADF) of the antenna arrays. The EADF has been found to be a very powerful method to describe the antenna array behavior for parameter estimation and calibration purposes. The calculation of the EADF from calibration measurements is explained in more detail in Section 13.5.

Resulting from many observations of measured channel responses, an exponential decaying data model is defined to represent the dense multipath components in the delay (correlation) domain $\psi(\tau)$ with its corresponding frequency response $\Psi(f)$ [8]. The parameter vector $\mathbf{\Theta}_{dds}$ is composed of the parameters β_d, τ_d, α_d, which are the normalized coherence bandwidth, LOS delay, and maximum power, respectively:

$$\begin{aligned} \psi_x(\tau) = E\{|x(\tau)|^2\} &= \begin{cases} 0, & \tau < \tau_d, \\ \alpha_1 \cdot \dfrac{1}{2}, & \tau = \tau_d, \\ \alpha_1 \cdot e^{-\beta_d(\tau-\tau_d)}, & \tau > \tau_d, \end{cases} \\ &\quad \mathcal{F} \updownarrow \\ \Psi_x(f) &= \frac{\alpha_1}{\beta_d + j2\pi f} \cdot e^{-j2\pi f \tau_d}. \end{aligned} \tag{13.4}$$

At the first glance, this model implies infinite bandwidth. However, the data are observed only within the finite sounder bandwidth. This is actually a very important issue since it warrants the dense multipath model as discussed above. This modeling approach requires that the contribution to any delay bin consist of a superposition of a reasonable number of diffuse components. That can be justified only by a limited bandwidth. The finite bandwidth influence and additional stationary noise component α_0 are also shown in Figure 13.3.

13.3. MIMO channel sounding techniques

From a historical perspective, the first sounding experiments have been carried out by using single-tone CW signals. This was sufficient as long as only the narrowband channel behavior was of interest. Single-tone CW sounding, however, gives us no information to resolve path time delays. For that, we need a frequency-domain bandwidth, which is roughly the inverse of the desired delay resolution. Sequential sounding at a number of different frequencies is the easiest approach to achieve a very high delay resolution as standard vector network analyzer techniques can be applied. The drawback is the resulting huge measurement time, which precludes mobile measurement. The only way out is to keep the environment fixed during one series of frequency sampling measurements. This actually has its equivalent in sequential sampling of the antenna array geometry and

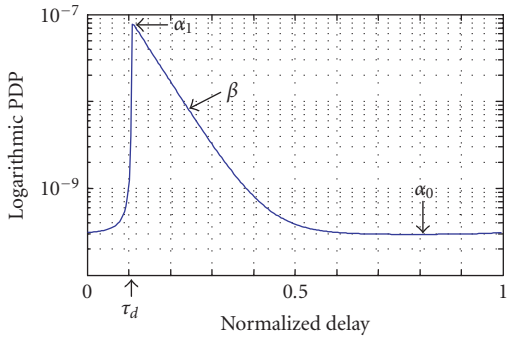

FIGURE 13.3. Dense multipath distribution model in the time delay domain.

may be considered as an equivalent to the synthetic antenna aperture approach in the frequency domain. Sustained measurement along some longer trajectory is clearly prohibitive. Network analyzer application also requires a cable connection between Tx and Rx sites.

Short duration repetitive pulses together with envelope detectors have been used in early broadband real-time sounding experiments. The main drawback of this method is the high peak-to-mean power ratio at the transmitter needed for sufficiently high SNR. Furthermore, only power delay profiles can be measured. To achieve the maximum signal to noise ratio at the receiver, excitation signals are required that have a low crest factor. The crest factor is given by the ratio of the peak value of the signal to its root mean square (rms) amplitude. Minimum crest factor signals are distinguished by a flat magnitude envelope in the time domain. At the same time, they must have a constant spectrum, which leads to a short autocorrelation function. This pulse compression approach is well known from spread spectrum technology and makes these signals very useful for real-time identification of time-delay systems since all frequencies are instantaneously excited and a considerable SNR processing gain is achieved in the time domain by correlation processing.

Pulse compression requires noise-like structured signals. Periodic pseudorandom excitation signals are of special importance since they are deterministic and can be processed in integer periods. The time period must be at least as long as the maximum path excess time delay $\tau_{\max}$ to avoid TDoA ambiguities. With a maximum delay-Doppler spreading factor $S = \tau_{\max} B_{\max}$ of a typical mobile radio channel well below 0.01, the period of the received time-variant channel response signal is still almost the same as of the excitation signal. This presumes that the minimum signal period time is chosen. Then the channel output can be transformed to the frequency domain by DFT/FFT processing without any significant leakage variance.

Probably, the most well-known examples of those excitation signals are periodic pseudo-random binary signals (PRBS). PRBS can be very easily generated by a shift register since only digital circuits are required. This allows to generate very

broadband excitation signals, even suitable for ultra-wideband sounding [12]. Another advantage of PRBS is that they can be repeated in the receiver with a slightly slower clock rate. This is applied in the classical swept time-delay cross-correlation sounder implementation [13]. This "sliding correlation" sounder requires only slow AD converters. The disadvantage of this principle, working sequentially in delay, is again the long measurement time which prohibits real-time operations.

The power spectrum of PRBS has the typical sinc "2-shape." For system identification purposes it can only be used up to a frequency of about $0.4 f_c$, whereby f_c is the clock rate [14]. Since the spectrum decays only slowly, a very high sampling rate or a suitable antialiasing filter at the receiver is required to avoid aliasing. Moreover, the system under test is excited in a frequency band which is not used. This effectively throws away transmit power. Moreover, most experimental transmit spectrum permissions given by regulation authorities will require strictly band-limited spectra. Then the signal must be filtered at the transmitter to a finite bandwidth. Any filtering and phase slope modification, however, will increase the crest factor of the PRBS, which is supposed to be unity in the ideal case. This again increases the susceptibility to nonlinear distortions.

A much more flexible excitation signal concept is known as the "periodic multisine signal." This approach is well known from frequency-domain system identification in measurement engineering [14]. In communication engineering terms this signal may be called a multicarrier spread spectrum signal (MCSSS). The MCSSS is defined by its complex Fourier coefficients $X(\mu f_0)$:

$$x(nt_0) = \sum_{\mu=0}^{N-1} X(\mu f_0) e^{j2\pi\mu/N}, \tag{13.5}$$

with $t_p = Nt_0 = 1/f_0$. Once designed in the frequency domain, the corresponding time-domain waveform $x(nt_0)$ is stored in an arbitrary waveform generator memory and periodically repeated at the Tx. So it possesses all the advantages which are discussed above for periodic signals. The difference in comparison to PRBS is that phases and magnitudes of $X(\mu f_0)$ can be arbitrarily chosen in order to optimize the system performance. As an example, in Figure 13.4 an MCSSS excitation signal with uniform power spectrum is shown. The phases of the Fourier coefficients are chosen to minimize the crest factor of the signal waveform. Although a quadratic phase slope typically results in a crest factor below 2, numerical optimization can even further reduce the crest factor to about 1.4. Another advantage of this signal design flexibility is that also analog hardware phase distortion (e.g., from the filters) and even nonlinear distortion (from the power amplifier) can eventually be mitigated. This means that a predefined ideal transmit signal is iteratively predistorted throughout a calibration procedure whereby the real output signal is measured and optimized.

Regarding the overall spectral shape, the main advantage of MCSSS is its "brickwall-type" shape, which allows concentrating the signal energy exactly to the band of interest. This can even be multiple bands when spectral magnitudes

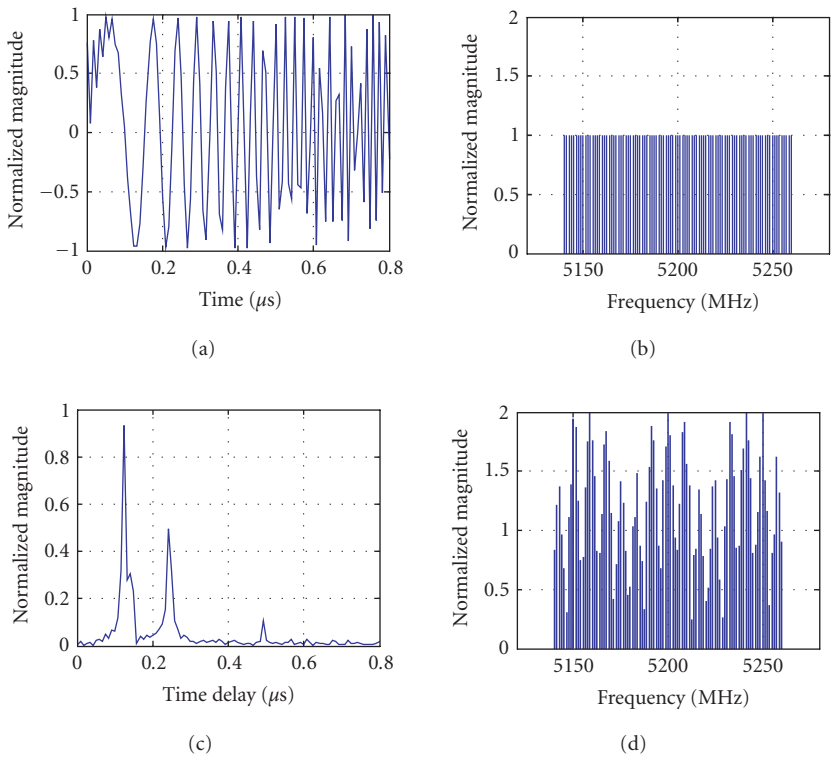

FIGURE 13.4. Broadband multicarrier spread spectrum signal (MCSSS) in the time and frequency domain: (a) Tx waveform, (b) Tx spectrum, (c) estimated CIR, and (d) received signal spectrum.

are set to zero. One example application is FDD sounding which means that the sounder simultaneously excites both the uplink and the downlink band. To meet the UTRA FDD specifications, for example, we need a total bandwidth of more than 200 MHz. Note that the desired full flexibility of the excitation signal requires quadrature up conversion at the transmitter.

At the receiver side the signal is filtered, down converted, and demodulated by a quadrature demodulator. An efficient architecture is based on low-IF analog down conversion, IF sampling, and final digital down conversion. In case of 240 MHz bandwidth, 160 MHz IF frequency and 640 MHz ADC sampling rate are adequate. For real-time processing Nyquist sampling at the receiver in most cases is a must. One integer period of the received time-variant channel response $y(t, nt_0)$ signal is sampled and transformed to the frequency domain by FFT processing. The final quadrature down conversion is accomplished by cyclic FFT shifting of the result which finally gives the baseband representation $Y(t, \mu f_0)$ of the received signal. In case of multipath transmission, frequency-selective fading as shown, for example, in Figure 13.4d shapes the power spectrum of the received signal. An

estimate of the time-variant channel frequency response is calculated from input-output cross-correlation as

$$H(t,\mu f_0) = \frac{Y(t,\mu f_0)X^*(\mu f_0)}{|X(\mu f_0)|^2} = \frac{Y(t,\mu f_0)}{X(\mu f_0)}. \tag{13.6}$$

The uniform shape of the excitation signal spectrum and its low crest factor at the transmitter maximizes the SNR. With integer period data acquisition there is no additional estimation variance resulting from leakage noise [14]. Therefore, the required data acquisition time is minimal and the estimation variance is as small as possible. With Nyquist sampling at the receiver, the highest possible measurement repetition rate for a channel with a maximum excess time delay $\tau_{\max}$ can be achieved, which is $1/\tau_{\max}$. The lower limit is given by the Doppler bandwidth $B_{\max}$. It results from the Nyquist sampling criterion of the fast fading channel response. However, since the delay-Doppler spreading factor $S = \tau_{\max} \cdot B_{\max}$ of a typical mobile radio channel is well below 0.01, there are large gaps allowed between successive measured channel response functions without sacrificing the Nyquist criterion. Normally, there is no need to measure faster since intermediate CIRs (which may be required for link-level simulation) can always be calculated by band-limited interpolation. Nevertheless, faster measurement speed may be desirable if further noise reduction by synchronous averaging of a temporal sequence $y(t, nt_0)$ is aimed. Only if the averaging window approaches or exceeds $1/B_{\max}$ this would act as a Doppler lowpass filter and potentially would suppress fast fading.

Figure 13.4 shows also the impulse response which would result from inverse Fourier transform of $H(t,\mu f_0)$. Calculating the impulse response in this way requires a tapering window function in the frequency domain, which effectively throws away measured data and, hence, reduces SNR and limits the resolution. A better choice is to use $H(t,\mu f_0)$ as an observation vector in the frequency domain for high-resolution TDoA parameter estimation described in Section 13.6. $H(t,\mu f_0)$ represents the sum-of-exponentials model describing the delay spectrum. A second frequency-domain dimension can be constructed from time-limited sections of the observed sequence $H(t,\mu f_0)$ with the sum of exponentials in t describing the Doppler spectrum. The two-dimensional Fourier transform approximates the joint delay-Doppler frequency response. A single-input single-output (SISO) sounder just relies on this principle.

A MIMO channel sounder measures the channel response matrix between all M_{Tx} antennas at the transmit side and all M_{Rx} antennas at the receiver side. This could be carried out by applying a parallel multiple-channel transmitter and receiver. However, truely parallel systems are not only extremely expensive, they are also inflexible (when considering changing the number of antenna channels) and susceptible to phase drift errors. Also a parallel operation of the transmitter channels would cause specific problems since the M_{Tx} transmitted signals have to be separated at the receiver. An alternative sounder architecture is based on switched antenna access. A switched antenna sounder contains only one physical

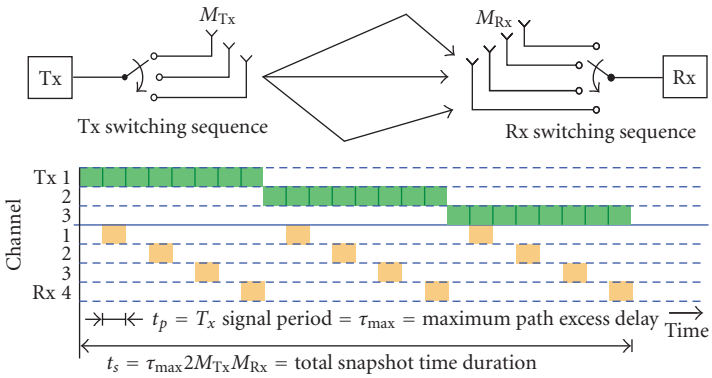

FIGURE 13.5. MIMO sounder switching time frame.

transmitter and receiver channel. Only the antennas and the switching channels are parallel. This reduces the sensitivity to channel imbalance.

Figure 13.5 shows the switching time frame of a sequential MIMO sounder using antenna arrays at both sides of the link [13]. Any rectangular block in the figure represents one period of the transmit/receive signal. Synchronous switching at the Rx and Tx is required in order to clearly assign the received signal periods to any input-output combination of the channel matrix. Timing and switching frame synchronization is established during an initial synchronization process prior to measurement data recording and must be maintained over the complete measurement time even in the case of a remote operation of Tx and Rx. This is accomplished by rubidium reference oscillators at both Rx and Tx. The total snapshot time length is now given by $t_s = 2\tau_{max} M_{Tx} M_{Rx}$, where M_{Tx} and M_{Rx} are the number of antennas at the Tx and the Rx sites, respectively. The factor of two comes from the one blank period, which is inserted at the receiver after every period acting as a guard interval to avoid switching transients. Similar to OFDM, this CIR estimation principle relies on a periodic signal model for excitation and reception. Therefore, the guard interval has to cope with the channel and the device response. For some signal processing operations based upon the recorded data, it may be a disadvantage that the antenna channels are not sampled at strictly the same time instant. If the maximum Doppler bandwidth for real-time sounding is less than $1/t_s$, the antenna channels can be individually interpolated resulting in MIMO channel responses with aligned sampling time for all channels.

Further considerations concerning the hardware operation of the sounder system refer to the Tx/Rx synchronization in the remote operation mode and to calibration, transmit power, and link budget issues. Only a short overview of the most important topics will be given here.

The remote operation means that there is no synchronization link applied between Tx and Rx. Initial synchronization is accomplished by a back-to-back calibration procedure. Hereby the overall device frequency response is measured and stored for equalization purposes. Also the frequency references are synchronized.

The synchronization has to be maintained throughout the whole measurement cycle. Separate rubidium reference sources at both Tx and Rx are required and the local oscillator (LO) signals have to be generated at both sides. This makes a sounder fundamentally different from a standard network analyzer and asks for specific considerations. For DoA/DoD estimation a full coherent operation is necessary during the snapshot period t_s. If Doppler estimation is aimed at or if a sequence of snapshots is to be averaged for SNR enhancement, the coherent operation period must extend to multiples of t_s. This sets the limits for phase noise parts having a coherence time below this time interval. However, the time period between two calibration measurements may easily take some hours if field measurements are considered. In this case some drift of the references cannot be avoided even if rubidium sources are used. This can normally be accepted as long as the reference offset is markedly smaller than the specified Doppler bandwidth. A small reference-frequency offset would be measured as a respective Doppler shift. Note that in case of synthetic antenna aperture measurements and for antenna array calibration a much longer coherent operation period will be necessary, which may require a direct Tx/Rx synchronization by cable.

Calibration has to include the absolute device power gain as well. This is also achieved throughout the back-to-back calibration when operating the transmitter with its nominal output power to a reference attenuator. Nevertheless, antenna-independent path loss estimation is however only possible if the antennas are calibrated with respect to absolute gain and if the DoA/DoDs of the polarimetric wave components at the antennas are known. This means that both the DoA and DoD have to be estimated. Otherwise, the antenna influence cannot be separated from the measurements and the path attenuation can only be given including the influence of the specific antennas used throughout the measurement.

Further issues are related to automatic gain control (AGC). AGC at the receiver has to ensure maximum signal level throughout the receiver chain from the antenna to the ADC input. At the same time it has to avoid overloading. The receiver should have a switched AGC in well-defined calibrated steps which should cover at least a range of 50–60 dB. The AGC setting has to be implemented on basis of instantaneous peak value estimation. To avoid uncontrolled transients, the AGC timing control must be synchronized to the MIMO switching time frame described in Figure 13.5. For very accurate angle-of-arrival estimation, the same AGC setting should be used for all antennas of the arrays. The best results are achieved if the complex frequency responses of all AGC steps are individually calibrated (including the complex frequency response which may vary because of changing electrical length).

Regarding the arrangement of antenna switches and amplifiers there is always a tradeoff in sensitivity and phase stability. Individual low-noise amplifiers (LNA) at Rx antennas and/or individual power amplifiers (PA) at the Tx are mostly inadequate because of the increase in phase drift between antenna channels. However, if there is only a single PA at the Tx, the corresponding antenna switch has to handle the full output power which may exceed 2–10 W for broadband bad urban measurements. At the Rx, the switch attenuation adds to the receiver noise figure.

Future steps in real-time MIMO sounding will include usage of multiple sounding transmitters and/or receivers to emulate system-specific scenarios and interference situations. Two transmitters and one receiver, for example, can be operated in a coordinated way whereby the transmitters are switched on/off in a staggered temporal sequence. This allows quasi-simultaneous measurement of two spatially distributed links. These links can represent a multiuser scenario as seen from a base station. Also two base stations can be emulated to represent soft handover scenarios and a cooperative downlink operation from spatially distributed access points. Moreover, a dual-hop link as a part of a multihop or ad hoc network or just a relay extension can be investigated. Future sounder RF interfaces will be able to handle dual-band up and down converters to emulate tandem air interfaces which will operate in completely different frequency bands. For an ultra-wideband (UWB) operation, sounders will be developed, having a real-time bandwidth of some GHz, for example, from 3 to 11 GHz. The hardware of these sounders will be extremely demanding and requires integrated SiGe technology [12]. This relates also to very broadband sounding at mm-wave frequencies, for example, at 60 GHz. To achieve enough spatial resolution for indoor scenarios, the bandwidth has to be enhanced up to some GHz. The very high frequency will put extreme demands on phase noise if DoA/DoD has to be estimated. A UWB operation, however, will shift the angle resolution paradigm from phase difference estimation to time-delay estimation which allows wider antenna distances and, thus, compensates loss in accuracy because of phasa noise..

13.4. Antenna array architecture

The spatial dimension of the channel response is accessed by antenna arrays. This mainly relates to "true" arrays but can also include synthetic aperture arrays. Those arrays consist of a sequentially sampled spatial aperture where only one antenna (or a subset) of the respective array is physically deployed. The angular resolution capability of any array depends on the effective aperture size as seen from the respective wave direction. So the spatial arrangement of the antenna elements has a major influence.

A sophisticated antenna architecture design is required to achieve high DoD/DoA resolution. This has to go along with mechanically and electrically stable construction and precise calibration. Since there is always a tradeoff between various specifications including resolution, measurement time, availability, and costs, there is a wide variety of useful antenna array architectures. In the sequel, we summarize some design considerations.

(i) Planar antenna arrays such as uniform linear arrays (ULA) or uniform rectangular arrays (URA) always have a limited viewing angle and inherent forward/backward ambiguity. They are useful to represent a base station's (BS) view to the channel. Moreover, there is a nonlinear transformation from the geometrical DoA/DoD to the respective normalized structural parameters $\mu_k^{(i)}$. Consequently, the effective array aperture depends on the DoA/DoD and the resolution capability is not uniform. Circular antenna arrays, on the other hand, have a full field of view.

They can be used to represent the mobile station (MS). Their angular resolution capability is uniform.

(ii) Double-directional estimation requires arrays at both sides of the link and MIMO operation of the sounder. For cellular system consideration, a combination of planar and circular arrays is adequate, whereas for ad hoc peer-to-peer networks identical circular arrays are most preferable.

(iii) Mainly for microcell and picocell scenarios, estimation of the elevation is aspired in addition to the azimuth. This requires application of uniform rectangular, cylindrical, or spherical arrays. However, three-dimensional wave analysis (which includes azimuth and elevation) is not only necessary to deduce three-dimensional propagation models. It is also required for the removal of the influence of the complex beam pattern of the measurement antennas from the data by a suitable calibration procedure if there are incoming waves with nonzero elevation. Moreover, this must also include polarization resolution.

(iv) Spherical antenna arrays may be applied for full azimuth and elevation coverage. However, there exists no geometric solution to arrange more than 20 patch antenna elements on a spherical surface with identical interelement distances. Therefore, nonuniform interelement distances and various relative polarization orientations of adjacent elements will complicate the design of spherical arrays. Moreover, optimization of the interelement distance for circular and spherical arrays (or of the array diameter in case of a fixed number of antenna elements, resp.) is required to minimize the sidelobes of the angular correlation function to reduce the probability of outliers in the iterative parameters search. This typically leads to interelement distances, something smaller than half of the wavelength.

(v) Full polarimetric analysis of the radio channel requires not only polarimetric reception but also polarimetric excitation of the channel. This is even true for omnidirectional excitation where we need a two-port antenna which launches both orthogonal polarized waves with omnidirectional characteristics and, thus, doubles the required sounder output ports.

(vi) High and reliable resolution in terms of separation capability of closely spaced paths and low probability of outliers requires an antenna architecture which offers a minimum of antenna array aperture size in the respective spatial dimension, including a minimum number of antenna elements, low antenna element coupling, and precise calibration. This has also to include the antenna switches and feeder cables.

(vii) The characteristics of the antenna elements depend on the basic element design (dipoles, patches, slots, etc.). It has a strong influence on high-resolution performance, estimation ambiguities, probability of outliers and polarization resolution capability, gain, bandwidth, and so forth. For example, the directivity of the antenna elements is a means to mitigate the inherent forward/backward ambiguity of ULA and URA.

(viii) For the later relation of recorded data to the respective propagation scenario, video cameras should be included into the antenna module. The optical viewing field of the cameras should correspond to the electromagnetic viewing field of the antennas. Also GPS position recording, electronic compass, and

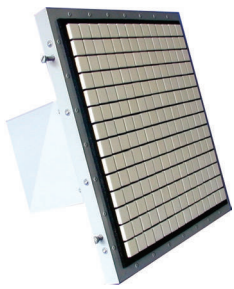

FIGURE 13.6. Uniform rectangular patch array (URA 8×8) [9, 15].

(a) (b)

FIGURE 13.7. (a) Circular dipole array (UCA32) and (b) stacked polarimetric uniform circular patch array (SPUCPA 4×24) [9, 15].

inclination sensors help to precisely document the measurement setup. Furthermore, a laser pointer should be mounted at the array to support angular adjustment.

The following figures show examples of high-resolution antennas. The URA in Figure 13.6 comprises 8×8 vertical polarized patch elements. Three peripheral dummy rows and columns are included to mitigate the fringing field effect, which distorts the beam patterns. The module also includes a 64×1 switch, LNA, and filter. It can be used for joint azimuth and elevation estimation within bore side viewing sector of 120° and 60°, respectively. The uniform circular array (UCA) in Figure 13.7a consists of 32 sleeve antennas, which do not require a ground plane. Here, a 2 W power switch is included to support the application as a transmit antenna. The usage is essentially restricted to azimuth estimation only since there is no vertical aperture available for low-elevation paths (which are most important for mobile radio application). The stacked polarimetric uniform circular path array (SPUCPA) in Figure 13.7b is a very sophisticated array. It comprises 4 stacked rings of 24 polarimetric patches. So it has 192 output ports in total. The switch is arranged inside of the cylindrical body of the array. This architecture gives a maximum resolution in azimuth for low-elevation paths and good resolution in elevation within $\pm 30°$.

13.5. Resolution limits and antenna array calibration

In (13.3), we have introduced the measurement system response. In this section we will concentrate on the part which results from the antenna arrays. The antenna response is described by the complex polarimetric beam patterns $\mathbf{b}(\Omega_k)$ of all elements, which result from vertical and horizontal polarized excitation. In an early design step, these beam patterns can be calculated from electromagnetic field simulation. Once the array is realized, the response has to be measured in a well defined propagation environment which should be an anechoic chamber. Recording the complete spherical beam pattern requires precise rotation of the array around a suitable defined pivot point located in the phase reference center of the array and excellent phase stability of the setup throughout the measurement cycle, which can take some hours. The measured beam patterns are discrete in azimuth $\varphi = (-\pi \cdots \Delta\varphi \cdots \pi - \Delta\varphi)$ and elevation $\vartheta = (0 \cdots \Delta\vartheta \cdots \pi)$. Due to the periodicity of the beam patterns in 2π the DFT transforms $\mathbf{b}(\varphi, \vartheta)$ to the EADF domain $\mathbf{g}(f_1, f_2)$ without any leakage error. This is at least true for the azimuth. For the elevation special considerations are necessary since the elevation can hardly be measured over the full angular period of 2π due to practical mechanical reasons. Moreover, the spherical Fourier transform has some numerical problems near the poles of the sphere. The beam pattern $\mathbf{b}(\varphi, \vartheta, m)$ of the antenna m is stored in the matrix $\mathbf{B}_{\mathrm{p}m}^{[N_1 \times N_2]}$ (the superscript denotes the dimension of the matrix). The EADF matrix is calculated by a two-dimensional Fourier transform by applying the Fourier matrices $\mathbf{F}_{1/2}$:

$$\mathbf{G}_m^{[N_{a1} \times N_{a2}]} = \frac{1}{\sqrt{N_1 \cdot N_2}} \mathbf{F}_1^{N_{a1} \times N_1} \cdot \mathbf{B}_{\mathrm{p}m} \cdot \mathbf{F}_2^{N_2 \times N_{a2}}. \tag{13.7}$$

The advantage of the EADF concept is threefold. (i) It allows a considerable data compression since it is distinguished by a limited support area as shown in Figure 13.8b. This is a direct consequence of the physical meaning of the antenna aperture. (ii) It provides a means to calculate the complex array response for arbitrary angles. (iii) It allows a simple analytic calculation of the beam pattern derivatives with respect to the angular parameters. This is used for the ML parameter estimation as described in Section 13.6. In this section it is used to define the fundamental limit of the achievable variance of the estimated DoA/DoD parameters in terms of the Cramér-Rao lower bound (CRLB). The matrix of the first-order derivatives of the K path parameters is given by the Jacobian matrix

$$\mathbf{D}(\boldsymbol{\Theta}) = \frac{\partial \mathbf{s}(\boldsymbol{\Theta})}{\partial \boldsymbol{\Theta}^T} \left[\frac{\partial \mathbf{s}(\boldsymbol{\Theta})}{\partial \boldsymbol{\Theta}_1} \cdots \frac{\partial \mathbf{s}(\boldsymbol{\Theta})}{\partial \boldsymbol{\Theta}_K} \right]. \tag{13.8}$$

With this result the Fisher information matrix (FIM) can be expressed in the form

$$\mathbf{J}(\boldsymbol{\Theta}) = 2 \cdot \mathrm{Re}\left\{ \mathbf{D}(\boldsymbol{\Theta})^H \cdot \mathbf{R}_{nn}^{-1} \cdot \mathbf{D}(\boldsymbol{\Theta}) \right\}, \tag{13.9}$$

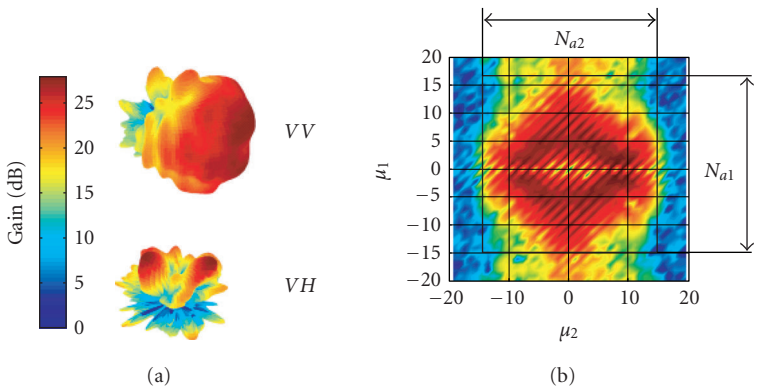

FIGURE 13.8. (a) Polarimetric beam pattern (φ) for azimuthal (φ) and elevation (ϑ) excitation and (b) corresponding EADF $\varphi\varphi$ for one element of the SPUCPA in Figure 13.7.

whereby $\mathbf{R}_{nn} = E\{\mathbf{n} \cdot \mathbf{n}^H\} = \sigma^2 \cdot \mathbf{I}$ is the noise covariance matrix. The diagonal elements of the inverse FIM represent the CRLB of the K parameters estimates, that is,

$$\text{CRLB}(\boldsymbol{\Theta}) = \mathbf{J}^{-1}(\boldsymbol{\Theta}). \tag{13.10}$$

The nondiagonal elements of the inverse FIM denote the mutual information between two parameters. If nondiagonal elements are zero, the respective parameter estimates are uncoupled or independent. In general, the data model is optimally parameterized if the FIM is diagonal. The investigation and exploitation of the FIM structure is essential to design a robust and efficient parameter estimator.

The FIM is also diagonal in case of the single impinging path scenario, which is analyzed in the following example. It is again related to the SPUCPA in Figure 13.7b. In Figure 13.9 the CRLB of the azimuth angle is compared to the variance which is achieved by an experiment. For any true azimuth/elevation pair φ, ϑ within the coverage sector of the SPUCPA the azimuth was estimated by an ML procedure. This experiment was repeated 64 times. The noise level for CRLB calculation was adjusted to match the observed device noise level, which was held constant according to an SNR in the main beam direction ($\vartheta = 90^\circ$) of 17–18 dB.

The result drastically changes in case of a coherent two-path scenario. Two paths are said to be coherent if their weights have an almost constant phase difference during the available observation window. Then the FIM predicts a strong dependency between the resulting estimates especially when the two paths are closely separated in the angular domain (closer than the Rayleigh resolution of the array). This can easily be explained by the field pattern, which results from the superposition of the two waves. There occur stationary spatial regions of constructive and destructive interference, which eventually causes a more or less ill-posed parameter estimation problem. It can be observed that the resulting degradation depends on the phase difference between the two path weights. In the test scenario

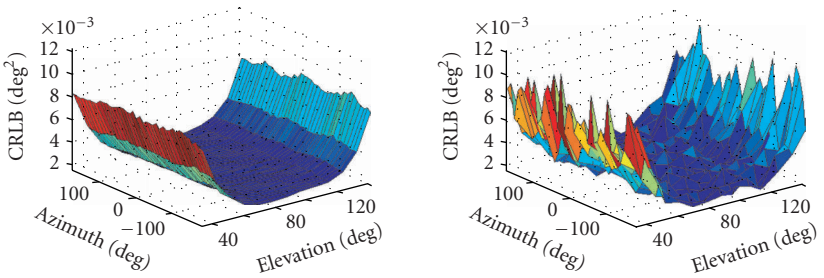

FIGURE 13.9. (a) CRLB and (b) estimated variance of estimated azimuth DoA versus the true azimuth and elevation direction range.

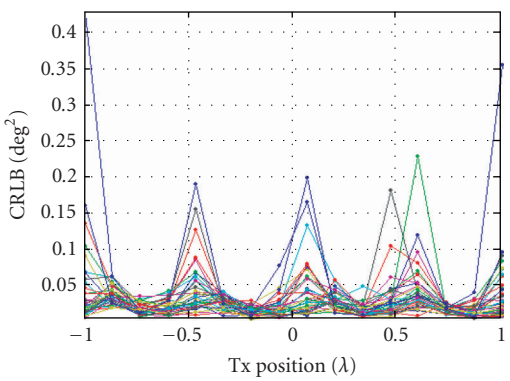

FIGURE 13.10. CRLB of the of estimated azimuth DoA in a coherent two-path scenario versus relative Tx positions.

two paths where emulated by two Tx antennas located in the horizontal plane ($\vartheta = 90°$) and at the same distance to the SPUCPA. The angular separation in azimuth and elevation was 5°, which results in a spatial field pattern period that is by far larger than the active SPUCPA aperture size. One transmit antenna was moved step by step forward and backward along the line-of-sight direction in the range of two wavelengths ($-\lambda \cdots \lambda$), thus introducing a specific phase difference between both paths.

Figure 13.10 shows the resulting CRLB in the horizontal plane. The different curves correspond to certain true Tx bearing angles in azimuth. There are clearly indicated distinct maxima for certain relative Tx positions which differ by half a wavelength. This goes along with a change in the resulting field pattern from minimum to maximum. It becomes also obvious that the array does not behave uniformly in azimuth. The reason may be the influence of the tree-like structure of the antenna switches that may result in a slight variation of the SNR over the whole azimuth range.

13.6. Maximum likelihood parameter estimation

Various algorithms have been proposed for high-resolution multidimensional parameter estimation in channel sounding including the multidimensional unitary estimation of signal parameters via rotational invariance techniques (ESPRIT) algorithm [16], and an application of the space-alternating generalized-expectation maximization (SAGE) method [17], which is essentially an expectation-maximization-(EM-) based simplified maximum likelihood (ML) parameter estimation procedure [18]. The algorithm proposed in [17] can also be understood as an application of the alternating projection algorithm [19], since the multidimensional search is broken down into sequential one-dimensional coordinate-wise searches. Both classes of the algorithm are subjected to different model assumptions and underlying conceptual restrictions including applicability to certain antenna array architectures, calculation time in terms of convergence speed and statistical efficiency. It is well known that ESPRIT is an unbiased DoA/DoD estimator only if the antenna arrays used for the measurements show the so-called shift-invariant structure. This is the case for uniform linear and planar arrays (ULA, URA) and circular uniform beam arrays (CUBA) [16]. For other usual antenna array architectures including uniform circular arrays (UCA), and uniform circular patch arrays (UCPA) or the respective spherical arrays, ESPRIT application to DoA/DoD estimation is not possible or will at least result in biased estimates. Other drawbacks may arise if we ask for a statistically efficient estimator and/or for the parameter estimation in a more complicated context such as colored measurement noise, nonideal antenna array characteristics, and so forth. Maximum likelihood parameter estimation procedures are in general more flexible to cope with these requirements. For example, the SAGE approach has been applied for a large variety of antenna array architectures. The drawback is its inefficiency and slow convergence rate if closely spaced coherent propagation paths exist in the multipath propagation scenario. Clearly, since we have only one transmitting source, all received paths have to be considered as coherent. This may result in a strong coupling of estimation results (as indicated in the FIM structure). In this case, a gradient-based multidimensional ML channel parameter estimation framework outperforms independent parameter search strategies such as SAGE [7].

With the stationary measurement noise $\mathbf{n}$ and the dense multipath and specular components $\mathbf{d}$ and $\mathbf{s}$, respectively, the total observed signal vector $\mathbf{x}$ is modeled as follows:

$$\mathbf{x} = \mathbf{n} + \mathbf{d}(\boldsymbol{\Theta}_{dds}) + \sum_{k=1}^{K} \mathbf{s}(\boldsymbol{\Theta}_k) = \mathbf{nd}(\boldsymbol{\Theta}_{dds}) + \mathbf{s}(\boldsymbol{\Theta}_{sp}) \tag{13.11}$$

having a conditional probability density of

$$\mathrm{pdf}(\mathbf{x}|\boldsymbol{\Theta}_{sp}, \boldsymbol{\Theta}_{dds}) = \frac{1}{\pi^M \det(\mathbf{R}(\boldsymbol{\Theta}_{dds}))} e^{-(\mathbf{x}-\mathbf{s}(\boldsymbol{\Theta}_{dds}))^H \mathbf{R}(\boldsymbol{\Theta}_{dds})^{-1} \cdot (\mathbf{x}-\mathbf{s}(\boldsymbol{\Theta}_{sp}))}. \tag{13.12}$$

The related log-likelihood function is

$$L(\mathbf{x};\boldsymbol{\Theta}_{sp},\boldsymbol{\Theta}_{dds}) = -M\cdot\ln(\pi) - \ln\left(\det\left(\mathbf{R}(\boldsymbol{\Theta}_{dds})\right)\right) - \left(\mathbf{x}-\mathbf{s}(\boldsymbol{\Theta}_{dds})\right)^{H}\cdot\mathbf{R}(\boldsymbol{\Theta}_{dds})^{-1}\cdot\left(\mathbf{x}-\mathbf{s}(\boldsymbol{\Theta}_{sp})\right). \tag{13.13}$$

Because of the Gaussian nature of the probability density, the maximization of (13.13) with respect to $\boldsymbol{\Theta}_{sp}$ is essentially a nonlinear weighted least squares problem. Since an exhaustive search in the multidimensional parameter space is not feasible, we are proposing an iterative search framework which is based on both gradient methods and sequential parameter update. This procedure proceeds snapshot by snapshot and takes advantage as much as possible of typical channel behavior that is known a priori from propagation physics and from experimental experience. So the estimated parameter set of every snapshot is taken as the initial estimate for the next one. This is of specific importance for the $\boldsymbol{\Theta}_{dds}$ vector since the statistic parameters of the dense multipath change only slowly as long as the "average environment" does not change completely. The K parameter vectors $\boldsymbol{\Theta}_k$, on the other hand, change much faster since they directly comprise geometric parameters. Moreover, existing paths can temporarily be shadowed or definitely disappear and new paths can suddenly show up. Therefore, we can take advantage of tracking existing paths. However, at the same time we have to search for new paths. This way the model order K is adaptively controlled throughout the sequence of snapshots. A considerable simplification of the search procedure may be possible according to the expectation-maximization (EM) principle if the parameters are independent in their influence. Since the parameter sets $\boldsymbol{\Theta}_{sp}$ and $\boldsymbol{\Theta}_{dds}$ are obviously independent, we can use alternating search procedures to maximize (13.13) with respect to $\boldsymbol{\Theta}_{sp}$ and $\boldsymbol{\Theta}_{dds}$. This way we successively remove the estimated deterministic specular paths from the observed data. For estimation of the parameters $\boldsymbol{\Theta}_{dds}$, a Gauss-Newton algorithm is applied. This gives us also a parametric representation of the covariance matrix $\mathbf{R}(\boldsymbol{\Theta}_{dds})$. The knowledge of $\mathbf{R}(\boldsymbol{\Theta}_{dds})$ is essential also for the estimation of specular parameters $\boldsymbol{\Theta}_{sp}$ since it provides appropriate weighting of the observed data according to the nonlinear weighted least squares problem:

$$\hat{\boldsymbol{\Theta}}_{sp} = \arg\min_{\boldsymbol{\Theta}_{sp}} \left(\mathbf{x}-\mathbf{s}(\hat{\boldsymbol{\Theta}}_{sp})\right)^{H}\cdot\mathbf{R}(\hat{\boldsymbol{\Theta}}_{dds})^{-1}\cdot\left(\mathbf{x}-\mathbf{s}(\boldsymbol{\Theta}_{sp})\right). \tag{13.14}$$

The global search for new paths (which has to be carried not only at the beginning of the sequence but continuously step by step) is carried out by a modified SAGE procedure. Rather than a random assumption for unknown parameters, we use some kind of noncoherent combining of independent observations to reduce the parameter dimension. To explain the strategy, we discuss an example. Suppose the channel impulse response has been measured using a 10-element ULA at one link end. At first, we treat the 10 individual channel impulse responses as independent realizations of the same process and maximize the log-likelihood function with respect to the time delay. A noncoherent combining procedure avoids

any assumption on unknown DoA in this step. In the next step, we keep the estimated time delay fixed and maximize (13.14) with respect to DoA. This reduces the maximization problem to two concatenated one-dimensional problems. Any arbitrary assumption of the DoA in the example would implicitly realize coherent combining which potentially disregards paths impinging from other angles by beamforming. This kind of noncoherent handling of data dimensions related to unknown parameters (e.g., DoA) gives us a higher probability to detect the relevant parameters which is the time delay in the example.

The problem of local search is completely different. We found that for closely spaced coherent paths the coordinate-wise search strategy has serious disadvantages because of its slow convergence rate which is not only time consuming but may also end in erroneous estimates when using a quantized parameter database [7]. This problem is related to the strong coupling of the respective parameter estimates as indicated in the FIM. Since it is well known that the ML function is, under mild restrictions, quadratic at its maximum (in the local "attractor area"), a conjugate gradient search promises much better convergence performance when the parameters are coupled in their influence to the minimization of (13.13). From the variety of available procedures for nonlinear optimization, we are using the Levenberg-Marquardt algorithm because of its robustness. To calculate the optimum step size and direction for parameter change these algorithms require the gradient, the Jacobian matrix, and the Hessian matrix of the log-likelihood function at the actual point in the parameter space. Fortunately enough, with the algebraic data model based on (13.3) the derivatives are easily available. This is especially true for the EADF model of the antenna arrays. The approximation of the Hessian as it is used in the Gauss-Newton/Levenberg-Marquardt algorithm is essentially an estimate of the Fisher information matrix (FIM). This provides us with the required information on both the variance and on the mutual dependency of the parameter estimates.

The following examples demonstrate the performance of the RIMAX algorithm which is an efficient implementation of the proposed ML parameter estimation framework [7, 8, 20]. The simulation results in Figures 13.11 and 13.12 compare the convergence behavior of the gradient-based ML search to the parameter-wise search of the SAGE in a noise-free, closely spaced coherent path scenario. In this case, the paths differ only in DoA and are separated by 5° in angle of arrival which is closer than the Rayleigh resolution of the array. The path magnitudes are equal and the phase difference is zero in Figure 13.11 and 180° in Figure 13.12. Although these constellations may be considered as worst-case situations, they frequently occur in a practical propagation scenario since path length difference has to change only by 2.5 cm to move from one worst-case situation to the other. The antenna array was a 24-element circular patch array. Only matched vertical polarization was considered. The two figures depict the iteration steps which are plotted on the cost function surface. Note that both constellations cause completely different cost function surfaces which are characterized by shaped, narrow valleys. The parameter-wise search of the SAGE forces very small zigzag steps in the direction of the individual parameters which can be seen most clearly in Figure 13.12. In both

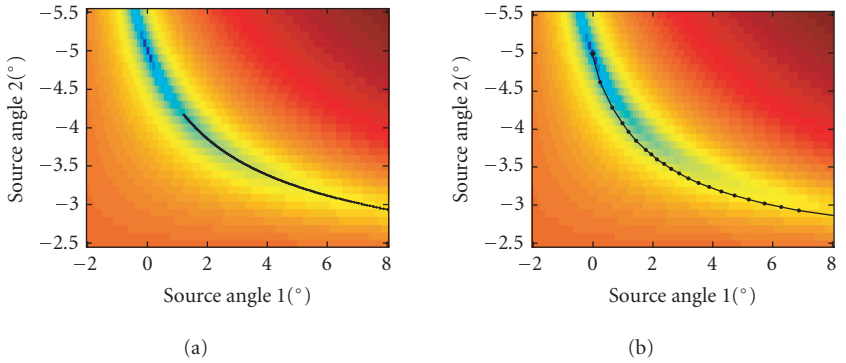

FIGURE 13.11. Convergence behavior of (a) the SAGE algorithm as compared to (b) the gradient-based RIMAX algorithm in case of two coherent paths (angular separation 5°; 0° phase difference).

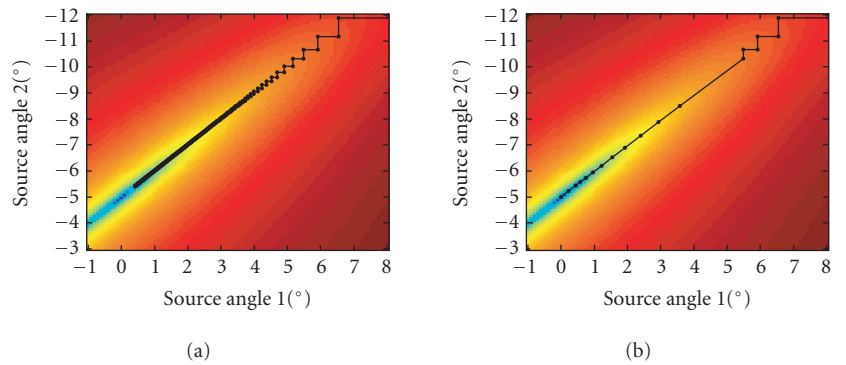

FIGURE 13.12. Convergence behavior of (a) the SAGE algorithm as compared to (b) the gradient-based RIMAX algorithm in case of two coherent paths (angular separation 5°; 180° phase difference).

cases, final convergence is not even achieved within 2000 iterations of the SAGE procedure whereas the gradient search needs only 26 and 13 steps, respectively, to reach the solution. Figure 13.12b also indicates the initial SAGE steps before starting the final gradient steps. The example shows that quantization of the data model would be detrimental since very small steps are required by the SAGE in order to achieve some progress. Moreover, data model quantization is not directly related to the desired parameter quantization. Actually, much finer steps are often required. Figure 13.13 further compares coordinate-wise (alternating) and gradient-based optimization in terms of the number of iterations versus the angular separation of two coherent paths. It becomes clear that especially for paths which are closer than Rayleigh resolution (which means that we have to apply high resolution instead of Fourier methods) the number of the required iterations becomes prohibitive.

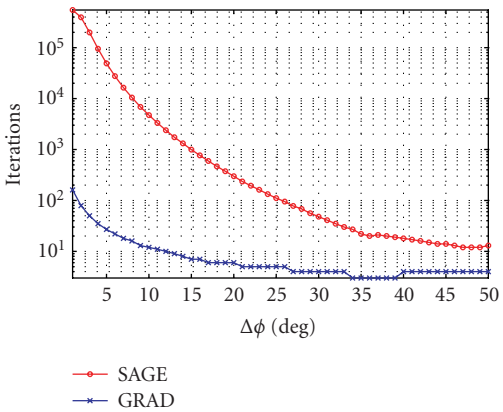

FIGURE 13.13. Convergence rate of the SAGE algorithm in comparison to a gradient-based ML algorithm (GRAD) (number of iterations versus angular separation of two coherent paths).

The example in Figure 13.14 shows the estimation results in the delay domain (power delay profile (PDP)). It was calculated from measured data in a street microcell scenario. The specular path weight magnitudes are indicated by blue dots. The reconstruction of the power delay profile within the measurement bandwidth is given by the blue curve. The green curve is the difference between the reconstructed and the measured power delay profile, thus it is an instantaneous realization of the dense multipath scattering components (*dds*). The expectation of the same part (which is estimated from the data) is given by the red triangular curve. The vertical red lines indicate the relative variances of the specular path weight estimates as they are calculated from the FIM. Most reliable paths are indicated by a variance contribution that directly follows the dense multipath slope. Noise enhancement is indicated by red points above this slope (see, e.g., at 2800 nanoseconds). The outliers around 3050 and 3350 nanoseconds are caused by line splitting, which is characterized by two very closely spaced, excessively strong paths with opposite signs. Although those paths may very well approximate a small bin of a band-limited CIR, there is clear evidence of a wrong estimate since the relative variance is greater than 1. As a consequence, one of those paths has to be omitted. A repeated estimation step will then lead to a more accurate estimate of the remaining path. Line splitting is a typical situation which occurs when the model is underdetermined. Since the proposed procedure clearly indicates and corrects this error it can be applied as a part of robust iterative model order controlling.

The described parameter estimation framework is very flexible and can be extended step by step. Further steps include enhanced estimation procedures, a more accurate data model and reduced numerical complexity. There are various possibilities. For example, the information delivered by the Fisher information matrix can be used to identify coupled parameter clusters. Then a grouping of parameters can be applied to restrict the gradient search to the coupled sets of path parameters. Independent parameters can be more easily estimated by the SAGE

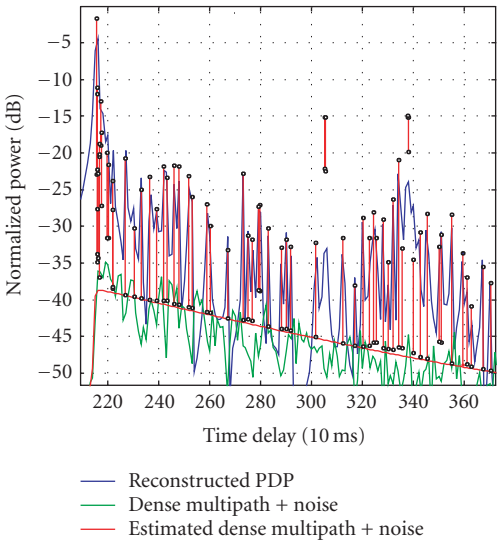

Figure 13.14. CIR measurement example and parameter estimates.

procedure. A further extension of the procedure should include enhanced parameter tracking. From a visual inspection of a temporal sequence of CIRs it becomes clear that some paths stay stable over a longer time. They can be more accurately estimated if more sophisticated path tracking is applied.

13.7. Measurement-based MIMO system performance evaluation

Initially, channel sounders were only applied to investigate wave propagation phenomena. From those results a lot of ideas have evolved for the design of channel models and even for the definition of reference models that became part of the existing cellular or WLAN standards. Moreover, quantitative results were achieved to parameterize these models for certain well-defined canonical radio environments. Mostly, standard scenarios were investigated that are related to existing wireless system generations. The large variety of system solutions and deployment scenarios of the next generation asks for novel measurement setups. One example is indicated in Figure 13.15. It is related to a public access situation in a high-speed user scenario. The figure describes an access point which serves public road transportation. Also car-to-car propagation is indicated. Models and measurement results for these scenarios are still rarely available. Other examples are public access areas in airport and train stations, factory hall environments, vehicle access in tunnels, access inside of cars or trains, and so forth. This list could be extended almost arbitrarily since very specific propagation conditions may apply for which standard models and assumptions are not applicable.

Figure 13.15. High-speed public access scenario.

A further trend is that novel system and network aspects have to be considered. This may include a coordinated downlink operation from multiple base stations, widely distributed multiple antennas, ad hoc, multihop systems and relay extensions, tandem air interfaces, and so forth. For system-specific evaluations most of all interference scenarios seem to be of interest.

A real-time channel sounder with its huge memory capacity and flexibility in using various antenna arrays can be considered as a valuable component of a rapid prototyping system when developing these new physical layer and network principles. The recorded channel data can be directly used to simulate the link behavior under very realistic propagation situations. Figure 13.16 gives a short glance to the data handling. The recoded channel matrix with its elements $h_{\nu\mu}(l)$ is adopted in its main dimensions to the required system specification. This perhaps includes bandwidth, delay window, and also the transmitter and receiver filters $g_T(t)$ and $g_R(t)$. Then the data stream is processed on the waveform or symbol level by fast convolution. It may be argued that this would result in overoptimized systems for the stored scenarios that will fail in many others. However, we believe that MIMO system performance evaluation requires a balanced mix of a deterministic modeling approach for a number of representative scenarios and the frequently favored stochastic modeling approaches. Only this allows identifying the relevant factors influencing the transceiver performance. The recorded data can be used for comparing even completely different transceiver architectures with exact reproducibility. The causality of certain performance effects can be traced back to the instantaneous channel conditions. It has been shown that the amount of the recorded data is enough even to simulate bit loading procedures, adaptive modulation, and incremental coding strategies at the transmitter, which are implicitly controlled by specific ARQ schemes [21].

It has already been stressed that the antenna configuration is of exceptional relevance for MIMO systems. The described method of direct use of recorded data for transceiver simulations lacks the flexibility to incorporate arbitrary antenna properties after the measurements have been completed. When arrays with a large number of antenna elements are used (which may be the case when high-resolution DoA/DoD estimation is considered), then there is still a great deal of

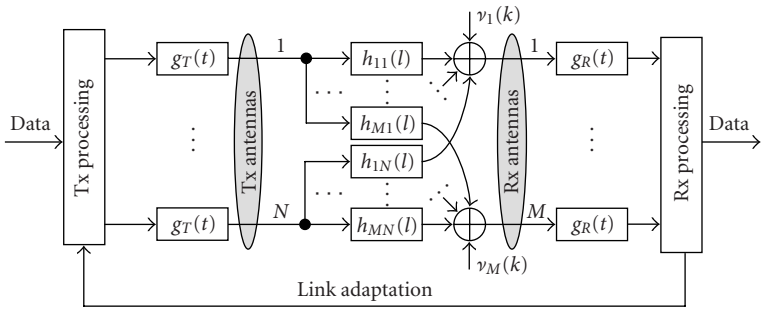

FIGURE 13.16. System model for MIMO transmission.

flexibility for simulations when we use different subsets of the antennas. This gives us also the chance to interpret and compare the MIMO link simulation results (e.g., in terms of bit error rates) to the DoA/DoD propagation structure of the channel. In any case, the individual antenna element characteristics of the measurement array are considered to be part of the channel.

An extended approach has been described in [4]. It is called measurement-based parametric channel modeling (MBPCM). It relies on the parameter estimation procedure described in the previous section. This method also belongs to the category of deterministic channel models since it takes the geometrical information on the propagation scenario from the measurement. It is essentially a two-step procedure with a parameter estimation step and a follow-up synthesis step. The parameter estimation, if properly carried out, gives an antenna-independent channel model (within well-defined limits which are determined by the measurement antennas used). The synthesis step gives us the flexibility to include a variety of antenna array architectures into the simulation and allows statistical simulation in terms of fast fading.

13.8. Conclusion

Multidimensional channel sounding for MIMO propagation analysis requires highly sophistic antenna design, calibration, and high-resolution parameter estimation. We proposed an ML channel parameter estimation framework which comprises estimation of the multidimensional specular paths parameters and of the delay distribution of dense multipath contributions which clearly outperforms existing procedures in terms of applicability, flexibility, robustness, and convergence. The estimator provides additional reliability information of the estimated parameters and uses a novel general antenna array model, the so-called EADF. Further enhancements may include enhanced path tracking and directional, respectively, spatial modeling of dense multipath components. High-resolution multidimensional channel parameter estimation is prerequisite to create antenna-independent channel models. Real-time MIMO channel sounding results can be used to obtain realistic link-level performances of transceiver algorithms. However, a

high amount of measurements will still be required to cover the variety of relevant deployment and system scenarios of future mobile radio networks.

Abbreviations

AGC	Automatic gain control
AP	Access point
BS	Base station
CIR	Channel impulse response
CRLB	Cramér-Rao lower bound
CUBA	Circular uniform beam arrays
DFT	Discrete Fourier transform
DoA	Direction of arrival
DoD	Direction of departure
EADF	Effective antenna aperture distribution function
ESPRIT	Estimation of signal parameters via rotational invariance techniques
FDD	Frequency division duplex
FIM	Fisher information matrix
FFT	Fast Fourier transform
GPS	Global positioning satellite
LNA	Low-noise amplifiers
LO	Local oscillator
LOS	Line of sight
MBPCM	Measurement-based parametric channel modeling
MC-SSS	Multicarrier spread spectrum signal
MIMO	Multiple-input multiple-output
PDP	Power delay profile
ML	Maximum likelihood
MS	Mobile station
OFDM	Orthogonal frequency division modulation
PA	Power amplifier
PRBS	Periodic pseudorandom binary signals
RMS	Root mean square
Rx	Receiver
SAGE	Space-alternating generalized expectation-maximization
SISO	Single-input single-output
SNR	Signal to noise ratio
TDoA	Time delay of arrival
Tx	Transmitter
UCA	Utility communications architecture
UCPA	Uniform circular patch arrays
ULA	Uniform linear arrays
URA	Uniform rectangular arrays
UTRA FDD	UMTS terrestrial radio access frequency division duplex
UWB	Ultra-wideband
WLAN	Wireless local area network

Bibliography

[1] G. J. Foschini and M. J. Gans, "On limits of wireless personal communications in a fading environment when using multiple antennas," *Wireless Personal Communications*, vol. 6, no. 3, pp. 311–335, 1998.

[2] A. F. Molisch, "A generic model for MIMO wireless propagation channels in macro- and microcells," *IEEE Trans. Signal Processing*, vol. 52, no. 1, pp. 61–71, 2004.

[3] M. Steinbauer, A. F. Molisch, and E. Bonek, "The double-directional radio channel," *IEEE Antennas Propagat. Mag.*, vol. 43, no. 4, pp. 51–63, 2001.

[4] R. Thomä, D. Hampicke, M. Landmann, A. Richter, and S. Sommerkorn, "Measurement-based parametric channel modelling (MBPCM)," in *Proc. International Conference on Electromagnetics in Advanced Applications (ICEAA '03)*, pp. 779–782, Torino, Italy, September 2003.

[5] R. Vaughan and J. Bach Andersen, *Channels, Propagation and Antennas for Mobile Communications*, vol. 50 of *Electromagnetic Waves Book Series*, Institution of Electrical Engineers (IEE), London, UK, 2003.

[6] V. Degli-Esposti, D. Guiducci, A. de'Marsi, P. Azzi, and F. Fuschini, "An advanced field prediction model including diffuse scattering," *IEEE Trans. Antennas Propagat.*, vol. 52, no. 7, pp. 1717–1728, 2004.

[7] A. Richter, M. Landmann, and R. S. Thomä, "A gradient based method for maximum likelihood channel parameter estimation from multidimensional channel sounding measurement," in *Proc. 27th URSI General Assembly*, Maastricht, Netherlands, August 2002.

[8] R. Thomä, M. Landmann, and A. Richter, "RIMAX—a maximum likelihood framework for parameter estimation in multidimensional channel sounding," in *2004 International Symposium on Antennas and Propagation*, pp. 53–56, Sendai, Japan, August 2004.

[9] www.channelsounder.de.

[10] R. S. Thomä, D. Hampicke, A. Richter, G. Sommerkorn, and U. Trautwein, "MIMO vector channel sounder measurement for smart antenna system evaluation," *European Trans. Telecommunications*, vol. 12, no. 5, pp. 427–438, 2001.

[11] A. Richter, C. Schneider, M. Landmann, and R. Thomä, "Parameter estimation results of specular and dense multi-path components in micro- and macro-cell scenarios," in *Proc. 7th International Symposium on Wireless Personal Multimedia Communication (WPMC '04)*, pp. V2–90–94, Abano Terme, Italy, September 2004.

[12] R. Zetik, R. Thomä, and J. Sachs, "Ultra-wideband real-time channel sounder and directional channel parameter estimation," in *Proc. International Symposium on Electromagnetic Theory (URSI '04)*, pp. 709–711, Pisa, Italy, May 2004.

[13] J. D. Parsons, *The Mobile Radio Propagation Channel*, John Wiley & Sons, New York, NY, USA, 2000.

[14] R. Pintelon and J. Schoukens, *System Identification: A Frequency Domain Approach*, Wiley-IEEE Press, Piscataway, NJ, USA, 2001.

[15] www.irk-dresden.de.

[16] M. Haardt, R. S. Thomä, and A. Richter, "Multidimensional high-resolution parameter estimation with applications to channel sounding," in *High-Resolution and Robust Signal Processing*, Y. Hua, A. Gershman, and Q. Chen, Eds., pp. 255–338, Marcel Dekker, New York, NY, USA, 2003.

[17] B. H. Fleury, M. Tschudin, R. Heddergott, D. Dahlhaus, and K. Ingeman Pedersen, "Channel parameter estimation in mobile radio environments using the SAGE algorithm," *IEEE J. Select. Areas Commun.*, vol. 17, no. 3, pp. 434–450, 1999.

[18] J. A. Fessler and A. O. Hero, "Space-alternating generalized expectation-maximization algorithm," *IEEE Trans. Signal Processing*, vol. 42, no. 10, pp. 2664–2677, 1994.

[19] I. Ziskind and M. Wax, "Maximum likelihood localization of multiple sources by alternating projection," *IEEE Trans. Acoustics, Speech, Signal Processing*, vol. 36, no. 10, pp. 1553–1560, 1988.

[20] A. Richter, M. Landmann, and R. S. Thomä, "Maximum likelihood channel parameter estimation from multidimensional channel sounding measurements," in *Proc. 57th IEEE Semiannual Technology Conference (VTC '03)*, vol. 2, pp. 1056–1060, Jeju, Korea, April 2003.

[21] C. Schneider, M. Großmann, K. Kansanen, T. Matsumoto, and R. Thomä, "Measurement based throughput performance evaluation of antenna variable modulation for broadband turbo MIMO transmission," in *Proc. 7th International Symposium on Wireless Personal Multimedia Communication (WPMC '04)*, pp. V2–85–89, Abano Terme, Italy, September 2004.

[22] U. Trautwein, T. Matsumoto, C. Schneider, and R. Thomä, "Exploring the performance of turbo MIMO equalization in real field scenarios," in *Proc. 5th International Symposium on Wireless Personal Multimedia Communications (WPMC '02)*, vol. 2, pp. 422–426, Honolulu, Hawaii, October 2002.

Reiner S. Thomä: Department of Electrical Engineering and Information Technology, Technical University Ilmenau, 98684 Ilmenau, Germany

Email: reiner.thomae@tu-ilmenau.de

Markus Landmann: Department of Electrical Engineering and Information Technology, Technical University Ilmenau, 98684 Ilmenau, Germany

Email: markus.landmann@tu-ilmenau.de

Andreas Richter: Signal Processing Laboratory, Helsinki University of Technology, FI-02015 HUT, Finland

Email: arichter@wooster.hut.fi

Uwe Trautwein: Technisch-Wissenschaftliche Software aus Ilmenau (TeWiSoft GmbH), 98693 Ilmenau, Ehrenbergstr. 11, Germany

Email: uwe.trautwein@tewisoft.de

14 MIMO channel models

Kai Yu, Mats Bengtsson, and Björn Ottersten

14.1. Introduction

In recent years, the use of multiple transmitters and receivers in a wireless communication link has attracted much attention. If deployed in an environment providing sufficiently rich scattering, the link can support extremely high data rates. As reported in [1, 2], the capacity of multiple-input multiple-output (MIMO) systems has the potential to increase linearly with the number of spatial subchannels. This has been demonstrated in [3] on the Bell Labs Layered Space-Time (BLAST) architecture.

Since then, different techniques have been proposed to exploit the potential of MIMO systems, including spatial multiplexing and space-time coding. We distinguish between spatial multiplexing schemes which transmit over spatial subchannels, often in conjunction with an outer channel code, and space-time coding techniques which attempt to provide joint coding and diversity gain through appropriate code design. By transmitting through parallel spatial subchannels and exploiting the channel state information (CSI) at the receiver, spatial multiplexing systems can provide high data rates. With CSI available at the transmitter as well, channel capacity can be achieved using a linear transformation at the transmitter and a linear receiver that converts the channel into a set of parallel independent scalar channels, combined with so-called water filling to allocate the power to each spatial subchannel [2, 4]. When CSI is not available at the transmitter, spatial multiplexing schemes can still be formulated to achieve high throughput [3], often at the expense of a more complex receiver structure. On the other hand, space-time coding introduces redundancy in time and space to achieve coding and diversity gain at the receiver without any CSI at the transmitter. Two main kinds of space-time code structures have been developed, namely space-time block codes [5, 6] and space-time trellis codes [7]. Using CSI (even approximative) at the transmitter, the performance of space-time coding schemes can be further improved [8, 9].

To design high-performance MIMO wireless systems, it is necessary to compare the performance of different MIMO techniques, modulation schemes, tune

design parameters, and so forth, and predict system performance. This should be done in a fair and realistic way. Hence, MIMO channel models that can accurately describe the propagation channels are of great importance. Channel models aiming for high accuracy tend to be complex but are of critical use for simulation purposes. In addition, we would like to stress the importance of low-complexity channel models that attempt to capture certain channel characteristics in a simple manner at the expense of accuracy. These models may be used to gain insight and allow analysis, and are useful in the communication system design process. Due to the limited space in this chapter, it is not possible to give a complete description of all reported MIMO channel modeling work. Instead, we give two examples of MIMO models, one well suited for simulation purposes and one well suited for MIMO system analysis and design. In addition, we briefly describe recent MIMO channel modeling within some industrial standardization bodies.

This chapter is organized as follows. We start with a general overview of different channel modeling techniques and then briefly review different MIMO channel models. After that, we discuss two typical MIMO channel models in more detail, namely the Kronecker-structure-based MIMO channel model and a generic geometry-based MIMO channel model with physical parameters. MIMO channel modeling works within the IEEE 802.11n and 3GPP/3GPP2 are briefly described. The chapter ends with some conclusions.

14.2. Channel modeling techniques

14.2.1. SISO channel modeling techniques

To model traditional wireless single-input single-output (SISO) channels accurately, three main propagation effects must be considered, namely, the large-scale path loss, the shadow fading, and the small-scale fading [10, 11]. The large-scale path loss predicts the average received power for a given transmit-receive distance. It is well known that the average received power decreases exponentially with the distance [11]. However, for a fixed transmit-receive distance, the path loss can vary significantly from location to location, due to shadowing. This so-called shadow fading (large-scale fading) is mostly modeled statistically by a lognormal distribution [10, 11]. When multiple reflected waves reach the receiver, they can add constructively or destructively. The amplitude variations due to small-scale movements (order of a wavelength) of the transmitter/receiver or of the surrounding environment are called small-scale fading.

Different distributions have been reported from theoretical analysis and from measurements to describe the statistics of the real-valued amplitude. Among them, three different distributions are most commonly used, the Rayleigh distribution for the non-line-of-sight (NLOS) scenarios, the Ricean distribution for the line-of-sight (LOS) scenarios, and the Nakagami distribution, which provides more degrees of flexibility to fit the model to the measured data. Another important aspect is to use the Doppler spectrum to measure the movement of the transmitter and receiver, and the variation of the local environment.

Wideband channel modeling can be done either in the time domain or in the frequency domain. In the time domain, one of the most commonly used channel models is the tapped-delay-line model

$$h(\tau) = \sum_{l=1}^{L} a_l \delta\left[\tau - (l-1)\Delta\tau\right], \tag{14.1}$$

where a_l is the complex tap amplitude, $\delta(\cdot)$ is the Dirac delta function, L is the number of taps, $\Delta\tau$ is the time spacing between neighboring taps, and τ is the time delay. The average power for each tap, $\mathrm{E}[a_l a_l^*]$, can be determined from the power delay spectrum, where $(\cdot)^*$ denotes complex conjugate. The absolute value of the tap amplitude, $|a_l|$, is modeled by the Rayleigh or lognormal distribution [10] and the RMS delay spread is widely used to characterize the dispersion of the channel. In the frequency domain, the SISO channel can be modeled as an autoregressive (AR) process where the poles of this AR process are calculated from the measured channel realizations [10, 12]. The frequency response of the channel can be obtained as the output from the filter driven by white noise.

All the above models describe the statistical properties of SISO wireless channels, hence they are called statistical channel models. Another group of models are called deterministic channel models [10]. These models try to calculate the radio propagation conditions according to the physical layout of the environment. This, however, is not possible for most applications since it requires too much computational power and too many details about the environment. To lower the computational complexity, the ray-tracing algorithm has been proposed as a simplified solution, see [10] for more details about ray tracing.

14.2.2. MIMO channel modeling techniques

Using antenna arrays at both the transmitter and the receiver makes the problem more complicated. Simply modeling each link (i.e., from one transmit antenna element to one receive antenna element) as a SISO channel and assuming they are independent and identically distributed (IID) is fairly common as a simplifying assumption in many theoretical papers. However, as seen in practical measurements [13, 14, 15, 16], this assumption is rarely true. Hence, we need to take into account the spatial correlation between different links at both ends when modeling MIMO wireless channels.

As will be shown below, it is easy to generate a MIMO channel with a specified correlation structure between the single links [17, 18]. Since a complex Gaussian random vector is completely specified by its first- and second-order moments [19], this approach is relevant in scenarios with Rayleigh fading. The MIMO channel correlation matrix is usually obtained from measurements, which means the influence from the measurement setup (e.g., antenna heights, antenna element patterns, etc.) cannot be separated from the channel itself using this MIMO channel modeling technique. These kinds of models are called nonphysical MIMO channel models.

Another popular approach is to construct a realistic geometric scattering environment and calculate the MIMO channel matrix as a sum of the contributions from different rays. The distribution of the scatterers depends on some important physical parameters, such as angle of arrival (AOA), angle of departure (AOD), and time of arrival (TOA). Therefore models using this approach are called physical MIMO channel models. The statistics of these parameters can either be obtained from the field measurements [20, 21] or be postulated as some well-known distributions with simple geometry [22, 23, 24]. Using the physical parameters makes it possible to separate the MIMO channel and the measurement setup. However, finding the correct statistics of the parameters is a difficult, if not impossible [25], task.

Finally, deterministic channel modeling may be used also to obtain MIMO channel realizations. In [26], for example, a ray-tracing simulator has been used to simulate MIMO channels.

14.3. Review of MIMO channel models

Many statistical MIMO channel models have been reported in the past few years. As mentioned previously, they can be categorized into nonphysical MIMO channel models and physical MIMO channel models. Below, we briefly review these two classes of models. A more detailed review of some MIMO channel models can be found in [27].

From now on, unless otherwise stated, we assume that the system has M transmit antennas and N receive antennas. In general, the baseband input-output relationship can be written as

$$\mathbf{y}(\tau) = \mathbf{H}(\tau) * \mathbf{s}(\tau) + \mathbf{n}(\tau), \tag{14.2}$$

where $\mathbf{H}(\tau)$ is the wideband MIMO channel impulse response matrix, $\mathbf{s}(\tau)$ is the transmitted signal, $\mathbf{y}(\tau)$ is the received signal, $\mathbf{n}(\tau)$ is additive white Gaussian noise (AWGN), and "$*$" denotes convolution. When the system bandwidth is so small that the channel becomes narrowband, (14.2) is simplified to $\mathbf{y} = \mathbf{H}\mathbf{s} + \mathbf{n}$, where $\mathbf{H}$ is the $N \times M$ narrowband MIMO channel matrix.

14.3.1. Nonphysical MIMO channel models

The simplest (nontrivial) nonphysical MIMO channel model is the IID MIMO channel model, which assumes that the elements of the MIMO channel matrix are IID zero mean complex Gaussian. It has been widely used in many published papers due to its simplicity and tractability for analysis and design. For instance, this model has been used to analyze the capacity of MIMO channels in [1].

The IID MIMO channel model does not take into account the spatial correlation between MIMO channel links, which has been demonstrated in many MIMO channel measurements [13, 14, 15, 16]. One way to solve this problem is to introduce the MIMO channel correlation matrix $\mathbf{R}_H$, defined as $\mathbf{R}_H = \mathrm{E}[\mathrm{vec}(\mathbf{H})\mathrm{vec}^H(\mathbf{H})]$,

where $\text{vec}(\cdot)$ is the vec operator and $(\cdot)^H$ denotes complex conjugate transpose. When the channel is zero mean, complex Gaussian, the MIMO channel matrix $\mathbf{H}$ can be modeled as

$$\text{vec}(\mathbf{H}) = \mathbf{R}_H^{1/2}\,\text{vec}(\mathbf{G}), \tag{14.3}$$

where $\mathbf{G}$ is a stochastic $N \times M$ matrix with IID $\mathcal{CN}(0,1)$ elements and $(\cdot)^{1/2}$ is any matrix square root such that $\mathbf{R}^{1/2}(\mathbf{R}^{1/2})^H = \mathbf{R}$.

The above model requires full knowledge of the spatial correlation between every pair of channel links. Recently, it has been reported in [17, 18] that for indoor NLOS environments, the MIMO channel correlation matrix $\mathbf{R}_H$ can be approximated as a Kronecker product of the correlation matrix at the transmitter $\mathbf{R}_{\mathbf{Tx}}$ and the correlation matrix at the receiver $\mathbf{R}_{\mathbf{Rx}}$. Furthermore, for wideband MIMO channels, this Kronecker structure can be extended to each channel tap [18]. More details concerning the Kronecker-structure-based MIMO channel models will be discussed later.

14.3.2. Physical MIMO channel models

In [22], a narrowband one-ring model has been presented in order to study the correlation and the capacity of MIMO systems. The model assumes that the base station (BS) is elevated and therefore has no scatterers around it, while the mobile station (MS) is surrounded by scatterers. This assumption is true in many outdoor scenarios, at least in macrocells where the base station is mounted on a mast or elevated above the roof tops. In [22], the effective scatterers are assumed uniformly positioned on a ring, hence the name one-ring model. Each effective scatterer is associated with a random phase shift, which is uniformly distributed over $[-\pi, \pi)$. Each ray is reflected once by a scatterer and reaches the receiver with equal power. The MIMO channel coefficients are then calculated through geometric considerations of the path lengths. When the angular spread of the scatterers is small, some approximations can be used to study the correlation between different MIMO channel elements.

For an environment when both the BS and the MS are surrounded by scatterers, the use of the so-called two-ring model, that is, assuming there exist rings of scatterers around both the BS and the MS, has been suggested in [28]. The MIMO channel coefficients can be obtained using the same approach as used in the one-ring model. The channel, however, will not be complex Gaussian in general due to the double reflections of each ray.

A model related to the one-ring model is introduced in [24]. Closed-form expressions for the spatial correlation of MIMO channel coefficients are derived assuming different powers for different scatterers and using the von Mises probability density function (PDF) to describe the angular PDF of the scatterers at the MS. The model also includes Doppler spread and a LOS component. Assuming that the gain and the phase shift for a given scatterer are the same for rays coming from different antenna elements, and using the von Mises PDF for the scatterers

at both the transmitter and the receiver, the two-ring model has been extended in [29] to obtain closed-form expressions of the spatial correlation.

Under certain scenarios, even though the correlation matrix at both the transmitter and receiver are of high rank, the MIMO channel may still be of low rank. Such channels are called "pinhole" or "keyhole" channels [23, 30] and have been observed from channel measurements conducted in a controlled (and constructed) environment [31]. The "pinhole" phenomenon can be explained by the distributed scattering model [23], where scatterers exist at both the transmit side and the receive side. Considering the scatterers at the receive side as a virtual array, it is argued in [23] that the channel matrix can be written as

$$\mathbf{H} = \frac{1}{\sqrt{S}}\mathbf{R}_{\mathrm{Rx}}^{1/2}\mathbf{G}_r\mathbf{R}_S^{1/2}\mathbf{G}_t\mathbf{R}_{\mathrm{Tx}}^{T/2}, \tag{14.4}$$

where $1/\sqrt{S}$ is a normalization factor, $(\cdot)^T$ denotes transpose, and $\mathbf{G}_t$ and $\mathbf{G}_r$ are two random matrices with IID zero-mean complex Gaussian elements. Therefore, the rank of the channel is controlled by the three correlation matrices $\mathbf{R_{Tx}}$, $\mathbf{R_{Rx}}$, and $\mathbf{R_S}$ seen from the transmitter, the receiver, and the virtual array, respectively. If $\mathbf{R_S}$ is of low rank, the MIMO channel will always be of low rank no matter what $\mathbf{R_{Tx}}$ and $\mathbf{R_{Rx}}$ are. It is also worth mentioning that the amplitudes of "pinhole" channels are not Rayleigh distributed [23, 32].

A wideband geometry-based channel model for outdoor macrocells has been reported in [33]. The model assumes that for a fixed tap, the scatterers are located on an ellipsoid, where the BS and the MS are the foci of the ellipsoid. A LOS component can be added to the first tap. To model the local scattering effect, a ring of scatterers has been generated around the MS. A disc around the BS is defined as the scatterer-free area (similar to one-ring model). Based on the power delay profile and a predetermined scatterer density, the number of scatterers can be determined. Using a ray-tracing-based technique, MIMO channel realizations can be obtained. This model takes into account the range dependency and is especially useful to simulate the effect of range as well as other parameters [33].

All the above physical MIMO channel models are based on some postulated distribution of the scatterers and a simple geometry. Other similar models include [34], where a 3D MIMO channel model is derived, and [35], where a physical model is proposed using electromagnetic (EM) theory.

Another group of physical channel models is based on physical parameters extracted from measurements. In [20], an indoor MIMO channel model has been reported using the fact that the scattered signals arrive in clusters [36]. The MIMO channel matrix is calculated using the directional impulse response, which is a sum of the contributions from different rays. The amplitude of the cluster is Rayleigh distributed and the expected cluster power decreases exponentially with the TOA. Within each cluster, each individual ray is complex Gaussian distributed and the average ray power is given by the associated cluster power. In the model, the ray AOA and AOD are Laplacian distributed, based on observations in [37].

Within the European research initiative COST 259, a directional channel model [38] has been developed. First, the double-directional channel impulse response is obtained as a sum of the contributions from different scatterers. The nondirectional channel impulse response can then be obtained by incorporating the specific antenna patterns at the transmitter and the receiver. To simulate MIMO channels for different environments, a three-level approach has been proposed [38]. The top level is the cell type that includes macrocells, microcells, and picocells. The second level includes a number of radio environments. Within each radio environment, the propagation scenarios (third level) have been identified. The global parameters (GPs) defined in the second level consist of a set of PDFs and/or statistical moments that characterize a specific radio environment. These statistics are obtained from various field measurements [38]. In the third level, the local parameters (LPs) are used to describe the impinging waves and the LPs are determined by the GPs defined in the second level.

The above physical MIMO channel models, however, are not general enough to include a wide variety of propagation effects, such as double scattering, waveguiding, and so forth. In [21, 39], a generic MIMO channel model has been proposed for outdoor macrocells and microcells, which includes a LOS component, single scattering, double scattering, far clusters, waveguiding, roof-edge diffraction, and large-scale variations. We will discuss this model in more detail later.

14.4. Two typical MIMO channel models

Below, a more detailed description of two typical MIMO channel models is provided. The first model is based on the Kronecker structure of the channel correlation matrix $\mathbf{R}_H$. It can be further divided into a narrowband MIMO channel model [17, 18] and a wideband MIMO channel model [18], depending on the system bandwidth. The second model being discussed is a generic MIMO channel model [21], which is based on geometry and some physical parameters.

14.4.1. The Kronecker-structure-based MIMO channel model

It is well accepted that in most NLOS environments, the wireless channel between the transmitter and the receiver is well modeled as zero mean complex Gaussian, that is, the real-valued amplitude is Rayleigh distributed and the phase is uniformly distributed over $[-\pi, \pi]$. For a complex Gaussian channel, it is enough to use its first- and second-order moments to fully describe the channel [19]. Therefore, the correlation between the elements of the MIMO channel matrix has been widely investigated [22, 24, 29]. By using the MIMO channel correlation matrix $\mathbf{R}_H$, the MIMO channel can be modeled as (14.3).

Kronecker structure. In scenarios with sufficiently rich multipath scattering, it is reasonable to assume spatial stationarity, that is, that the correlation between the fading signals received at two antenna elements only depends on the element distance but not on the exact location, at least for small dislocations. Then, the

correlation matrix of the signals as seen from the receive side will be the same, no matter which of the transmit elements is used, so we can define a receive side correlation matrix as

$$\mathbf{R}_{\mathrm{Rx}} = \frac{1}{M}\,\mathrm{E}\left[\mathbf{H}\mathbf{H}^{H}\right]. \tag{14.5}$$

Similarly, the transmit-side correlation matrix is defined as

$$\mathbf{R}_{\mathrm{Tx}} = \frac{1}{N}\,\mathrm{E}\left[\left(\mathbf{H}^{H}\mathbf{H}\right)^{T}\right]. \tag{14.6}$$

In [22], it is conjectured that the MIMO channel correlation matrix $\mathbf{R}_H$ is equal to the Kronecker product of the correlation matrices $\mathbf{R}_{\mathrm{Tx}}$ and $\mathbf{R}_{\mathrm{Rx}}$ at the transmitter and the receiver, that is,

$$\mathbf{R}_H = \mathbf{R}_{\mathrm{Tx}} \otimes \mathbf{R}_{\mathrm{Rx}}, \tag{14.7}$$

where $\otimes$ denotes the Kronecker product. In other words, the correlation between any two pairs of transmit-receive elements is the product of the correlations as seen from the transmit and receive sides, respectively. To avoid an additional multiplicative constant in (14.7), the MIMO channel matrix $\mathbf{H}$ used in the above equations is normalized such that

$$\mathrm{E}\left(\|\mathbf{H}\|_F^2\right) = NM, \tag{14.8}$$

where $\|\cdot\|_F$ is the Frobenius norm and $\mathrm{E}(\cdot)$ denotes the expected value.

To verify the above conjecture, indoor MIMO channel measurements were carried out by the University of Bristol, within the European Union's IST (Information Society Technology) Program, SATURN (Smart Antenna Technology in Universal bRoadband wireless Networks) Project [18, 40, 41]. The measurements were conducted at 5.2 GHz, with 120 MHz bandwidth. Both the LOS scenarios and the NLOS scenarios were measured. At the transmit side, an 8-element omnidirectional uniform linear array (ULA) was used, while the receiver used an 8-element ULA with 120° beamwidth. The interelement distance was half wavelength at both the transmitter and the receiver. The channel impulse responses were estimated and saved in the frequency domain. More details about the measurements can be found in [18, 42].

Using the data measured in the NLOS scenarios, the correlation matrices $\hat{\mathbf{R}}_H$, $\hat{\mathbf{R}}_{\mathrm{Tx}}$, and $\hat{\mathbf{R}}_{\mathrm{Rx}}$ were estimated, where $\widehat{(\cdot)}$ denotes the sample estimates. To measure the error of the Kronecker structure (14.7), the narrowband relative model error Ψ was defined as [18]

$$\Psi(\mathbf{A},\mathbf{B}) = \frac{\|\mathbf{A}-\mathbf{B}\|_F}{\|\mathbf{A}\|_F}. \tag{14.9}$$

TABLE 14.1. Narrowband model errors $\Psi(\hat{\mathbf{R}}_H, \hat{\mathbf{R}}_{\text{Tx}} \otimes \hat{\mathbf{R}}_{\text{Rx}})$.

Data set	2×2 setup	3×3 setup
Tx11	3.87%	7.57%
Tx12	3.18%	7.33%
Tx13	0.86%	4.79%
Tx14	2.95%	7.68%
Tx15	2.13%	4.94%

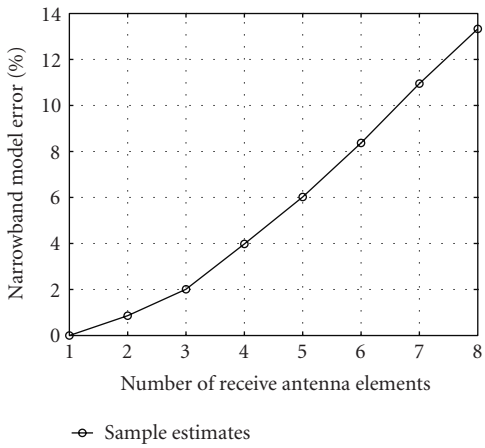

FIGURE 14.1. Narrowband model errors with 2 transmit antenna elements and 1–8 receive antenna elements (Tx13-Rx3) [18]@2004 IEEE.

Table 14.1 lists the narrowband model errors $\Psi(\hat{\mathbf{R}}_H, \hat{\mathbf{R}}_{\text{Tx}} \otimes \hat{\mathbf{R}}_{\text{Rx}})$ for 2×2 and 3×3 systems. It was shown that for 5 measured data sets, the narrowband model error is well below 10% for the measured NLOS scenarios. Furthermore, the narrowband model error increases when the number of transmit/receive antenna elements goes up. This is further illustrated in Figure 14.1, where the number of transmit antenna elements is fixed as 2 and the number of receive antenna elements increases from 1 to 8.

From the above results, it is concluded that for moderate array sizes and indoor NLOS scenarios, the MIMO channel correlation matrix can be well approximated by the Kronecker product of the correlation matrices seen from both ends.

For wideband MIMO channels, it has been found in [18, 41] that the Kronecker structure can be extended to each channel tap, that is,

$$\mathbf{R}_H^l = \mathbf{R}_{\text{Tx}}^l \otimes \mathbf{R}_{\text{Rx}}^l, \tag{14.10}$$

where for the lth tap, the MIMO channel correlation matrix $\mathbf{R}_H^l$, the transmit correlation matrix $\mathbf{R}_{\text{Tx}}^l$, and the receive correlation matrix $\mathbf{R}_{\text{Tx}}^l$ are defined similarly as in the narrowband case.

TABLE 14.2. Narrowband model errors of the optimal factorization $\Psi(\hat{\mathbf{R}}_H, \mathbf{X} \otimes \mathbf{Y})$.

Data set	2×2 setup	3×3 setup
Tx11	3.76%	7.26%
Tx12	3.05%	6.64%
Tx13	0.76%	4.52%
Tx14	2.61%	7.00%
Tx15	2.10%	4.65%

Kronecker mode decomposition. To be able to judge if the model errors estimated from the measurement data actually can be considered small, it is interesting to compare them to the errors of the best possible match between the estimated $\hat{\mathbf{R}}_H$ and any Kronecker product. In [18, 40], a least-squares Kronecker factorization method has been proposed to factorize $\hat{\mathbf{R}}_H$ optimally into two positive semidefinite Hermitian matrices $\mathbf{X}$ and $\mathbf{Y}$, that is,

$$\arg\min_{\mathbf{X},\mathbf{Y}} \left|\left|\mathbf{R}_H - \mathbf{X} \otimes \mathbf{Y}\right|\right|_F. \tag{14.11}$$

This problem can be solved by rearranging the elements of $\mathbf{R}_H$ and $\mathbf{X} \otimes \mathbf{Y}$ simultaneously, so that the original problem reduces to a least-squares rank-one approximation problem [40, 43]. Using the singular value decomposition, the optimal solution for $\mathbf{X}$ and $\mathbf{Y}$ can be obtained [18, 40].

Using the least-squares Kronecker factorization, the corresponding narrowband model errors $\Psi(\hat{\mathbf{R}}_H, \mathbf{X} \otimes \mathbf{Y})$ are listed in Table 14.2. Comparing the narrowband model errors listed in Tables 14.1 and 14.2, it is obvious that the difference between the model errors obtained using the sample estimates and the model errors obtained using the least-squares Kronecker factorization method indeed can be considered small. Therefore, the sample estimates $\hat{\mathbf{R}}_{\text{Tx}}$ and $\hat{\mathbf{R}}_{\text{Rx}}$ factorize the MIMO channel correlation matrix $\hat{\mathbf{R}}_H$ almost optimally.

Generalizing the idea of the Kronecker model, [44] shows that the correlation matrix of any MIMO channel can be expressed as a sum of Kronecker products of Hermitian matrices, that is,

$$\mathbf{R}_H = \sum_{k=1}^{K^2} \sigma_k \mathbf{W}_k \otimes \mathbf{V}_k, \tag{14.12}$$

where $K = \min(M, N)$, σ_k are the Kronecker mode values which are real and positive. In this so-called Kronecker mode decomposition [44], the Kronecker modes $\mathbf{W}_k$ and $\mathbf{V}_k$ are Hermitian matrices of size $M \times M$ and $N \times N$, respectively. Note that in general, $\mathbf{W}_k$ and $\mathbf{V}_k$ can have negative eigenvalues and therefore are indefinite [44]. The principal Kronecker modes $\mathbf{W}_1$ and $\mathbf{V}_1$, however, are always positive semidefinite.

By comparing (14.11) and (14.12), the least-squares Kronecker factorization can be seen as an optimal approximation of the MIMO channel correlation matrix $\mathbf{R}_H$ using the principal Kronecker modes $\mathbf{W}_1$ and $\mathbf{V}_1$ [44].

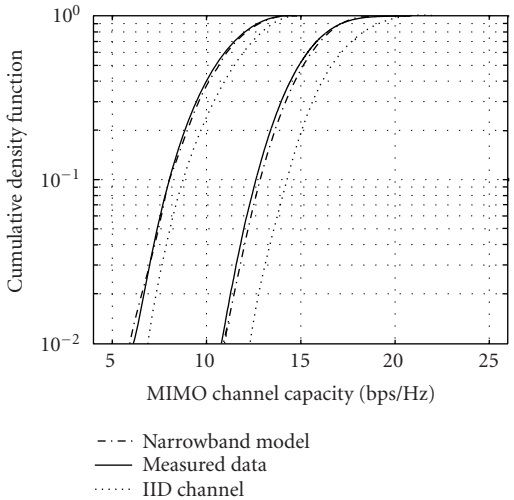

FIGURE 14.2. CDF of narrowband channel capacity from the measured data, narrowband channel model, and IID MIMO channel. Power is equally allocated to the transmit elements and the SNR at the receiver is 20 dB (Tx13-Rx3) [18]@2004 IEEE.

Narrowband and wideband channel models. Given that the MIMO channel is zero mean complex Gaussian and that the Kronecker structure of the MIMO channel correlation matrix (14.7) holds, it is easy to show that the narrowband MIMO channel model (14.3) can be rewritten as [22, 40, 45]

$$\mathbf{H} = \left(\mathbf{R}_{\mathrm{Rx}}\right)^{1/2}\mathbf{G}\left(\mathbf{R}_{\mathrm{Tx}}\right)^{T/2}, \tag{14.13}$$

where $\mathbf{G}$ is an $N \times M$ matrix with IID $\mathcal{CN}(0,1)$ elements.

To validate this narrowband MIMO channel model, 1000 MIMO channel realizations were generated according to (14.13). Figure 14.2 shows the MIMO channel capacity obtained from the measured channel data and the simulated channel realizations for the 2×2 and 3×3 setups, respectively. The MIMO channel capacity for the IID MIMO channel is also plotted. It is concluded from Figure 14.2 that the capacity from the simulated MIMO channel realizations matches the measured MIMO channel capacity very well.

Modeling the wideband MIMO channel can be done by combining the Kronecker structure of the MIMO channel correlation matrix (14.10) with a SISO channel model, as long as the SISO channel model assumes the channel is zero mean complex Gaussian [36, 46]. Below, a simple COST 259 SISO channel model [46] is combined with (14.10) as an example. The channel impulse response matrix $\mathbf{H}(\tau)$ in this case can be modeled as [18]

$$\mathbf{H}(\tau) = \sum_{l=1}^{L} \sqrt{\bar{p}_l}\left(\mathbf{R}_{\mathrm{Rx}}^{l}\right)^{1/2}\mathbf{G}_l\left(\mathbf{R}_{\mathrm{Tx}}^{l}\right)^{T/2}\delta\left[\tau - (l-1)\Delta\tau\right], \tag{14.14}$$

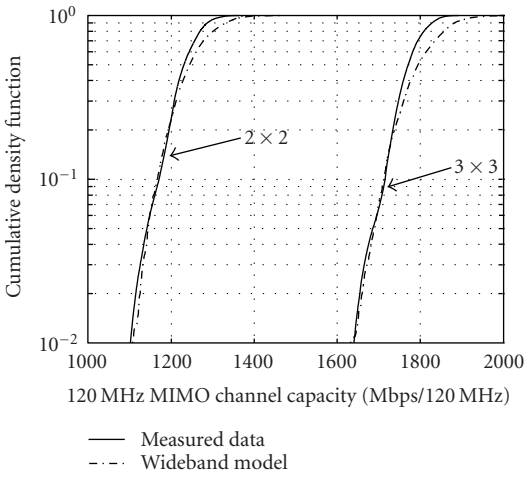

FIGURE 14.3. CDF of 120 MHz MIMO channel capacity. Power is equally allocated and the SNR at the receiver is 20 dB (Tx13-Rx3) [18]@2004 IEEE.

where $\mathbf{G}_l$ are random matrices with IID $\mathcal{CN}(0, 1)$ elements, $\bar{p}_l$ is the average power of each element and is modeled as

$$\bar{p}_l = Ae^{-(l-1)\Delta\tau/2\Gamma}, \tag{14.15}$$

where A is a normalization factor and Γ is the mean RMS delay spread which can be obtained from channel measurements.

Using (14.14), 1000 MIMO channel impulse response matrices were simulated with 120 MHz bandwidth. The wideband MIMO channel capacity was calculated and plotted in Figure 14.3, along with the MIMO channel capacity obtained from the measured MIMO channel realizations. It can be seen from Figure 14.3 that the wideband MIMO channel capacity can be well simulated by the proposed wideband MIMO channel model (14.14).

Note that the above two Kronecker-structure-based MIMO channel models have already been used in many published papers [22, 45, 47]. The model is not only useful in numerical performance evaluations, the simple structure also lends itself useful in theoretical analysis and design. For example, some closed-form analytical results on the MIMO channel capacity have been obtained in [48], exploiting this Kronecker structure of the MIMO channel covariance matrix. In [49], a spatial multiplexing design procedure is proposed based on partial CSI. By exploiting the Kronecker structure of the model above, a power and bit loading scheme is proposed balancing the bit error rates of the subchannels through efficient error calculations.

LOS scenarios. In contrast to the NLOS scenarios where no dominant component exists, the LOS scenarios usually have one dominant component (LOS component). It has been proposed in [50, 51, 52] to model the LOS MIMO channel as

$$\mathbf{H} = \sqrt{\frac{K}{1+K}}\mathbf{H}_{\text{LOS}} + \sqrt{\frac{1}{1+K}}\mathbf{H}_{\text{NLOS}}, \tag{14.16}$$

where $\mathbf{H}_{\text{LOS}}$ is a rank-one matrix which corresponds to the LOS component, $\mathbf{H}_{\text{NLOS}}$ is associated with the NLOS components and is modeled by (14.13). The K-factor is defined as $K(\text{dB}) = 10\log_{10}(P_{\text{LOS}}/P_{\text{NLOS}})$ [11], where P_{LOS} and P_{NLOS} are the power from the LOS component and the power from the NLOS components, respectively.

14.4.2. A generic MIMO channel model

As described previously, most of the physical MIMO channel models are proposed to match certain scenarios or phenomena. However, as it has been pointed out in [21, 39], they are not general enough to include all different propagation effects. In [21, 39], a generic MIMO channel model has been proposed for outdoor macrocells and microcells, which takes into account a wide variety of propagation effects.

Assuming there exist $L(t)$ multipaths between the transmitter and the receiver, the double-directional channel impulse response (DDCIR) $h(t, \tau, \theta_T, \theta_R)$ can be written as [21, 38]

$$h(t, \tau, \theta_T, \theta_R) = \sum_{l=1}^{L(t)} h_l(t, \tau_l, \theta_{T,l}, \theta_{R,l}), \tag{14.17}$$

where h_l is the contribution associated with the lth multipath component (MPC), τ is the time delay, θ_T and θ_R are the corresponding AOD and AOA at the transmitter and the receiver, respectively. In (14.17), both the number of multipaths $L(t)$ and the contribution of each individual MPC are functions of time t. Therefore, the DDCIR is time varying. This is mainly due to the movements of the scatterers, the transmitter, and the receiver. Note that when the antenna polarization is considered, the DDCIR $\mathbf{h}$ and the contribution of the individual MPC $\mathbf{h}_l$ become 2×2 matrices in order to describe the horizontal and vertical polarizations as well as the cross polarization [21].

The DDCIR describes the physical channel between the transmitter and the receiver and it does not depend on the system setups (e.g., the antenna patterns used at the transmitter and receiver). Assume that the antenna arrays at both the transmitter and receiver are small enough so that physical parameters of the MPCs do not change with the array sizes. Given the specific antenna patterns being used

and the positions of the transmit and receive arrays measured from a fixed reference point, the nonangle resolved deterministic channel impulse response between the ith transmit element and the jth receive element can be expressed as [21, 38]

$$\mathbf{H}_{ij}(\tau) = \sum_{l=1}^{L} g_R(\theta_R) \cdot h_l(\tau_l, \theta_{T,l}, \theta_{R,l}) \cdot g_T(\theta_T) \cdot e^{j\langle \vec{k}(\varphi_{R,l})\vec{x}_{R,j}\rangle} e^{j\langle \vec{k}(\varphi_{T,l})\vec{x}_{T,i}\rangle}, \quad (14.18)$$

where $g_T(\theta_T)$ and $g_R(\theta_R)$ are the antenna patterns at the transmitter and receiver, respectively. $\vec{k}$ is the wave vector, $\vec{x}_{T,i}$ and $\vec{x}_{R,j}$ are the position vectors for the ith transmit element and the jth receive element, respectively. Hence

$$\langle \vec{k}(\theta) \cdot \vec{x} \rangle = \frac{2\pi}{\lambda}(x \cos v \cos \varphi + y \cos v \sin \varphi + z \sin v), \quad (14.19)$$

where λ is the wavelength, φ is the azimuth, and v is the elevation.

The most important part of the above double-directional modeling approach is to find an accurate description of the properties of the MPCs $h_l(t, \tau_l, \theta_{T,l}, \theta_{R,l})$. In contrast to the COST 259 directional channel model [38] which only takes into account a limited number of propagation effects, a wide variety of propagation effects have been considered in [21, 39] to model $h_l(t, \tau_l, \theta_{T,l}, \theta_{R,l})$, namely, LOS propagation, single scattering, double scattering, scattering via far clusters, diffraction, waveguiding, large-scale variations, and moving scatterers. Below, these propagation effects will be briefly discussed.

A geometry-based approach has been used to simulate the propagation process between the BS and the MS, that is, randomly placing the scatterers according to certain statistical distributions. By using the geometry-based approach, it is straightforward to model the LOS propagation according to the geometry using the equations of free space propagation [11].

To model the single scattering effect, two groups of local scatterers are generated [21, 39] (i.e., the scatterers close to the BS and the scatterers close to the MS) according to some given PDFs. The scattering only happens through either the scatterers at the BS or the scatterers at the MS. The parameters of the MPCs, τ_l, $\theta_{T,l}$, and $\theta_{R,l}$, can be determined from the geometrical relationship. Moreover, two Ricean K-factors are introduced in order to characterize the power from the local scattering at the BS/MS comparing to the power from the LOS propagation. Unlike most conventional simulators, which tend to generate a large number of scatterers so that the Raleigh fading can be simulated, the number of scatterers in the generic MIMO channel model is decided by the physical scenario. Using too many scatterers may overestimate the MIMO channel capacity.

Similar to [23], double scattering is used in the model to simulate the pinhole phenomenon. Here, the scatterers generated in the single scattering are still valid. However in double scattering, the signal is scattered both by the scatterers at the

BS and by the scatterers at the MS. Furthermore, for each scatterer at the BS (or MS), an "illumination function" is defined, in order to determine which scatterers at the MS (or BS) are being illuminated [21].

In many outdoor scenarios, there are clusters located far away, corresponding to the mountains or high buildings. This can lead to an increase of the delay spread [21, 39]. Usually, there is a direct path from the BS to the far clusters and from the far cluster to the MS, similar to the single scattering process. It is also possible that the signal is double scattered by the far scatterers and the scatterers close to the MS. These propagation effects can be described similarly to the single scattering and double scattering as discussed before.

Waveguiding and roof-edge diffraction are two propagation processes which can lead to rank-deficient channel matrices. The waveguiding often happens when the waves are coupled into a street canyon and bounced between the walls. This causes the channel to lose rank and gives an increased delay dispersion [21]. The roof-edge diffraction, on the other hand, only leads to a rank-deficient channel matrix. When the location of the roof-edge is specified, the roof-edge diffraction can be modeled geometrically [21].

Modeling the waveguiding effect is a difficult task. In [21], it is suggested to model the waveguiding effect by mixing the geometry-based approach and a stochastic process. The scatterers are generated geometrically at the input and the output of the street canyon. The waves propagated from the transmitter to the input scatterers and from the output scatterers to the receiver are modeled based on simple geometry, similar to the single and double scattering. The waveguiding effect between the input scatterers and the output scatterers is then modeled stochastically as follows.

First, an IID complex Gaussian channel matrix is generated, followed by a singular value decomposition, that is, $\mathbf{H}_{\mathrm{IID}} = \mathbf{U}\boldsymbol{\Lambda}\mathbf{V}^H$. Then a rank-reducing diagonal matrix is introduced to describe the relative attenuation of different eigenmodes [21]:

$$\boldsymbol{\Lambda}_{rr} = \begin{bmatrix} \exp(-\lambda_1/\lambda_{rr}) & 0 & 0 & \cdots \\ 0 & \exp(-2\lambda_2/\lambda_{rr}) & 0 & \cdots \\ 0 & 0 & \exp(-3\lambda_3/\lambda_{rr}) & \cdots \\ \vdots & \vdots & \vdots & \ddots \end{bmatrix}, \tag{14.20}$$

where λ_{rr} is the attenuation parameter.

Finally, the waveguiding transfer function matrix between the input scatterers and the output scatterers can be expressed as [21]

$$\mathbf{H}_{wg} = \mathbf{U}\boldsymbol{\Lambda}_{rr}\mathbf{V}^H. \tag{14.21}$$

The above discussions all focus on modeling the small-scale fading. In reality, there are also large-scale variations due to the movement of the MS. For instance,

the parameters of the MPCs will change when the MS moves for some distance. It is suggested in [21] to use the same idea and parameters reported in [38] to simulate the large-scale variations. Another important fact that leads to time variations is the movement of the scatterers. To model this effect, the statistics of the movement and the size of the moving scatterers need to be known [21]. This, however, is still an open problem and needs to be investigated further.

The generic MIMO channel model described above gives a general framework of modeling macrocellular and microcellular MIMO wireless channels. The statistics of many parameters described above are crude and need to be further investigated from field measurements. For more details on parameterization of different propagation processes and a list of parameters with typical values, the readers are referred to [21].

Although the model described above is very general and can be made to fit a large range of measurement conditions with appropriate choices of parameters, this is also the main limitation of the model. Determining the actual distributions of the model parameters may be a formidable task and establishing model accuracy and reliability can be exceedingly difficult when a very large number of parameters are involved. Often, the estimation of parameter distributions is not a well-posed problem and the results may be unreliable. Although the statistics of a subset of the model may be established under controlled conditions, constructing models from subsets validated on different data sets may be questioned. Extrapolation and interpolation, as is often done in simulations, must be done with care from this model.

14.5. Industrial standardization work

MIMO channel modeling has been conducted within different industrial standardization bodies. Recently, MIMO channel models have been proposed by the IEEE 802.11n Working Group [53] and the 3GPP/3GPP2 Technical Specification Group [54], respectively. Below, we briefly describe these two MIMO channel models, more details can be found in [53, 54].

14.5.1. TGn channel models

The TGn channel models [53] developed by the High Throughput Task Group within the IEEE 802.11n Working Group have been designed for indoor MIMO wireless local area networks (WLANs). The models have 100 MHz bandwidth and can be used for both the 2 GHz and 5 GHz bands. Six different models (Model A–Model F) are proposed to cover different indoor scenarios, including flat fading, residential, small office, typical office, large office, and large space. The RMS delay spreads vary from 0 nanosecond (flat fading) to 150 nanoseconds (large space). Both LOS and NLOS scenarios are considered.

The TGn channel models are based on a combination of the Kronecker structure of the MIMO channel correlation matrix and the cluster channel modeling approach [36, 37]. First, the MIMO channel correlation matrix $\mathbf{R}_H^l$ is approximated

according to (14.10), where the correlation matrices $\mathbf{R}_{\mathrm{Tx}}^{l}$ and $\mathbf{R}_{\mathrm{Rx}}^{l}$ are obtained by the power angular spectrums (PASs) and the corresponding angular spreads (ASs) at the transmitter and the receiver, respectively [53, 55].

To find the PASs and the corresponding ASs, the cluster channel modeling approach has been used. It is based on the observation that the MPCs come in groups [36, 37]. In the TGn channel models, the number of clusters varies from 2 to 6 for different indoor scenarios, and the mean AOA and AOD for each cluster are assumed to be uniformly distributed over $[0, 2\pi)$.

In [37, 56, 57], the PAS of each cluster has been found to be matched by the Laplacian distribution, that is,

$$p(\theta) = \frac{1}{\sqrt{2}\sigma} \exp\left(- \left| \sqrt{2}\frac{\theta}{\sigma} \right| \right), \tag{14.22}$$

where σ is the AS of the PAS. The mean value of the cluster AS is selected in the range of 20°–40° for different indoor scenarios. For a specific scenario, the AS of each individual cluster is calculated using the correlation between the delay spread and the AS, see [53] for details. As mentioned earlier, finding the true distribution of the PAS of each cluster is difficult. In [25], examples are shown where the estimated distributions have infinite support even when in fact the true distribution has finite support. This holds true for a large class of parameter estimators used to draw conclusions about distributions. In general, it is easier to estimate the moments of the distributions and often this is sufficient for modeling/simulation purposes.

In order to obtain the correlation matrices $\mathbf{R}_{\mathrm{Tx}}^{l}$ and $\mathbf{R}_{\mathrm{Rx}}^{l}$ for each tap, the PAS and the AS of the lth tap should be known. It is assumed in [53] that the PAS of each individual tap within a cluster is also Laplacian distributed and its AS equals the AS of that cluster [53, 58].

The temporal variations of MIMO channels have been characterized by the Doppler spectrum. Three different Doppler components are considered in [53]. To describe the main temporal Doppler component, two Doppler power spectrums are introduced. For environments with fixed transmitters and receivers, the temporal variation is mostly caused by moving people and therefore a "bell"-shaped Doppler spectrum [53] has been used to fit the measurement data, while for mobile channels, the so-called "horn" spectrum has been suggested in [11, 59]. The second Doppler component is caused by vehicle movements. This mostly happens in large-space environments and therefore this Doppler component has only been used in Model F (large space). The last Doppler component is due to the fluorescent lights and has been used in Model D (typical office) and Model E (large office).

Other issues such as path loss modeling and antenna polarizations have also been treated in [53]. Tables of parameter settings for Model A–Model F are provided in [53, Appendix].

14.5.2. 3GPP/3GPP2 spatial channel models

The spatial channel models [54] proposed by 3GPP/3GPP2 include two different models for the link-level simulations and the system-level simulations, respectively. The link-level spatial channel model is developed for the purpose of calibration while the system-level spatial channel model is designed for algorithm comparison.

Four different cases have been included in the link-level spatial channel model, corresponding to different power delay profiles. For each case, a different number of paths (same as clusters) are predefined. Each path is independent of the others and is fully characterized by its spatial parameters, such as AS, PAS, AOA/AOD and so forth. The spatial parameters at the BS and the MS are discussed separately, see [54] for details. The channel model can then be obtained through correlation or ray-tracing-based techniques [54].

The system-level spatial channel model is modeled differently from the link-level spatial channel model. Three different environments are treated by the system-level spatial channel model; suburban macrocell, urban macrocell, and urban microcell. The model assumes that there exist N time-delayed paths received at the MS with different powers, and each path consists of M subpaths (same as MPCs). Both the paths and subpaths are characterized by their own spatial parameters. In [54], a parameter table has been given which lists all the important parameters, including powers, number of paths and subpaths, spatial parameters, and so forth. Note that the correlations between some of the parameters (i.e., the delay spread, AS, and shadow fading) are also incorporated in the model [54]. A detailed process on how to generate the user parameters can be found in [54]. After generating the user parameters, the MIMO channel coefficient for a specific path can be calculated as a sum of the contributions from its subpaths [54].

Other features, such as polarization, far scatterer clusters, LOS, and urban canyon are made optional in the system-level model. To handle the intercell interference, it is suggested in [54] to model the strong interferers as spatially correlated while weak interferers are modeled as spatially white.

14.6. Conclusions

In this chapter, we have focused on modeling MIMO radio propagation channels. After a brief overview of different modeling techniques and MIMO channel models, two typical MIMO channel models have been discussed in more detail. First, we have discussed the Kronecker-structure-based MIMO channel models, which decouple the MIMO channel correlation matrix as a Kronecker product of the correlation matrices at the transmitter and the receiver. Some examples were given where this simple model is well suited for analysis and design purposes. The second model we have discussed is a generic MIMO channel model based on geometry and physical parameters, which takes into account a wide variety of propagation effects. This MIMO model is well suited for simulation purposes where accuracy is

of primary importance. Finally, we have briefly described the recent developments in the IEEE 802.11n and 3GPP/3GPP2 standardization work.

Abbreviations

AOA	Angle of arrival
AOD	Angle of departure
AR	Autoregressive
ASs	Angular spreads
AWGN	Additive white Gaussian noise
BLAST	Bell Labs Layered Space-Time
BS	Base station
CSI	Channel state information
DDCIR	Double-directional channel impulse response
EM	Electromagnetic
GPs	Global parameters
IID	Independent and identically distributed
LOS	Line-of-sight
LPs	Local parameters
MIMO	Multiple-input multiple-output
MPC	Multipath component
MS	Mobile station
NLOS	Non-line-of-sight
PASs	Power angular spectrums
PDF	Probability density function
SISO	Single-input single-output
TOA	Time of arrival
ULA	Uniform linear array
WLANs	Wireless local area networks

Bibliography

[1] G. J. Foschini and M. J. Gans, "On limits of wireless communications in a fading environment when using multiple antennas," *Wireless Personal Communications*, vol. 6, no. 3, pp. 311–335, 1998.

[2] I. Emre Telatar, "Capacity of multi-antenna Gaussian channels," *European Trans. Telecommunications*, vol. 10, no. 6, pp. 585–595, 1999.

[3] G. J. Foschini, "Layered space-time architecture for wireless communication in a fading environment when using multiple antennas," *Bell Laboratories Technical Journal*, vol. 1, no. 2, pp. 41–59, 1996.

[4] G. G. Raleigh and J. M. Cioffi, "Spatio-temporal coding for wireless communication," *IEEE Trans. Commun.*, vol. 46, no. 3, pp. 357–366, 1998.

[5] S. M. Alamouti, "A simple transmit diversity technique for wireless communications," *IEEE J. Select. Areas Commun.*, vol. 16, no. 8, pp. 1451–1458, 1998.

[6] V. Tarokh, H. Jafarkhani, and A. R. Calderbank, "Space-time block codes from orthogonal designs," *IEEE Trans. Inform. Theory*, vol. 45, no. 5, pp. 1456–1467, 1999.

[7] N. Tarokh, V. Seshadri and A. R. Calderbank, "Space-time codes for high data rate wireless communication: performance criterion and code construction," *IEEE Trans. Inform. Theory*, vol. 44, no. 2, pp. 744–765, 1998.

[8] G. Jöngren, M. Skoglund, and B. Ottersten, "Combining beamforming and orthogonal space-time block coding," *IEEE Trans. Inform. Theory*, vol. 48, no. 3, pp. 611–627, 2002.

[9] G. Jöngren and M. Skoglund, "Improving orthogonal space-time block codes by utilizing quantized feedback information," in *Proceedings of IEEE International Symposium on Information Theory*, p. 220, Washington, DC, USA, June 2001.

[10] K. Pahlavan and A. H. Levesque, *Wireless Information Networks*, John Wiley & Sons, New York, NY, USA, 1995.

[11] T. S. Rappaport, *Wireless Communications, Principles and Practice*, Prentice Hall PTR, Upper Saddle River, NJ, USA, 1996.

[12] S. J. Howard and K. Pahlavan, "Autoregressive modeling of wide-band indoor radio propagation," *IEEE Trans. Commun.*, vol. 40, no. 9, pp. 1540–1552, 1992.

[13] R. Stridh, P. Karlsson, and B. Ottersten, "MIMO channel capacity on a measured indoor radio channel at 5.8 GHz," in *Proceedings of the Asilomar Conference on Signals, Systems and Computers*, vol. 1, pp. 733–737, Pacific Grove, Calif, USA, October 2000.

[14] C. C. Martin, J. H. Winters, and N. R. Sollenberger, "Multiple-input multiple-output (MIMO) radio channel measurements," in *Proceedings of IEEE Vehicular Technology Conference (VTC '00)*, vol. 2, pp. 774–779, Tokyo, Japan, May 2000.

[15] D. P. McNamara, M. A. Beach, P. N. Fletcher, and P. Karlsson, "Initial investigation of multiple-input multiple-output (MIMO) channels in indoor environments," in *Proceedings of IEEE Benelux Chapter Symposium on Communications and Vehicular Technology*, pp. 139–143, Leuven, Belgium, October 2000.

[16] A. F. Molisch, M. Steinbauer, M. Toeltsch, E. Bonek, and R. S. Thomä, "Capacity of MIMO systems based on measured wireless channels," *IEEE J. Select. Areas Commun.*, vol. 20, no. 3, pp. 561–569, 2002.

[17] J. P. Kermoal, L. Schumacher, K. I. Pedersen, P. E. Mogensen, and F. Frederiksen, "A stochastic MIMO radio channel model with experimental validation," *IEEE J. Select. Areas Commun.*, vol. 20, no. 6, pp. 1211–1226, 2002.

[18] K. Yu, M. Bengtsson, B. Ottersten, D. McNamara, P. Karlsson, and M. Beach, "Modeling of wide-band MIMO radio channels based on NLoS indoor measurements," *IEEE Trans. Veh. Technol.*, vol. 53, no. 3, pp. 655–665, 2004.

[19] S. M. Kay, *Fundamentals of Statistical Signal Processing. Volume I: Estimation Theory*, vol. 1, Prentice Hall PTR, Upper Saddle River, NJ, USA, 1993.

[20] J. W. Wallace and M. A. Jensen, "Modeling the indoor MIMO wireless channel," *IEEE Trans. Antennas Propagat.*, vol. 50, no. 5, pp. 591–599, 2002.

[21] A. F. Molisch, "A generic model for MIMO wireless propagation channels in macro- and microcells," *IEEE Trans. Signal Processing*, vol. 52, no. 1, pp. 61–71, 2004.

[22] D.-S. Shiu, G. J. Foschini, M. J. Gans, and J. M. Kahn, "Fading correlation and its effect on the capacity of multielement antenna systems," *IEEE Trans. Commun.*, vol. 48, no. 3, pp. 502–513, 2000.

[23] D. Gesbert, H. Bölcskei, D. A. Gore, and A. Paulraj, "Outdoor MIMO wireless channels: models and performance prediction," *IEEE Trans. Commun.*, vol. 50, no. 12, pp. 1926–1934, 2002.

[24] A. Abdi and M. Kaveh, "A space-time correlation model for multielement antenna systems in mobile fading channels," *IEEE J. Select. Areas Commun.*, vol. 20, no. 3, pp. 550–560, 2002.

[25] M. Bengtsson and B. Völcker, "On the estimation of azimuth distributions and azimuth spectra," in *Proceedings of IEEE Vehicular Technology Conference (VTC '01)*, vol. 3, pp. 1612–1615, Atlantic City, NJ, USA, October 2001.

[26] C.-N. Chuah, D. N. C. Tse, J. M. Kahn, and R. A. Valenzuela, "Capacity scaling in MIMO wireless systems under correlated fading," *IEEE Trans. Inform. Theory*, vol. 48, no. 3, pp. 637–650, 2002.

[27] K. Yu and B. Ottersten, "Models for MIMO propagation channels. A review," *Wiley Journal on Wireless Communications and Mobile Computing*, vol. 2, no. 7, pp. 553–666, 2002, special issue on Adaptive Antennas and MIMO Systems.

[28] D.-S. Shiu, *Wireless Communication Using Dual Antenna Arrays*, Kluwer Academic Publishers, Dordecht, The Netherlands, 2000.

[29] G. J. Byers and F. Takawira, "Spatially and temporally correlated MIMO channels: modeling and capacity analysis," *IEEE Trans. Veh. Technol.*, vol. 53, no. 3, pp. 634–643, 2004.

[30] D. Chizhik, G. J. Foschini, and R. A. Valenzuela, "Capacities of multi-element transmit and receive antennas: correlation and keyholes," *Electronic Letters*, vol. 36, no. 13, pp. 1099–1100, 2000.

[31] P. Almers, F. Tufvesson, and A. F. Molisch, "Measurement of keyhole effect in a wireless multiple-input multiple-output (MIMO) channel," *IEEE Commun. Lett.*, vol. 7, no. 8, pp. 373–375, 2003.

[32] M. Bengtsson, K. Yu, and B. Ottersten, "Single and dual multi-sensor channel characterisation—analysis and models: stochastic models," EU IST Program SATURN Project, IST-1999-10322, Deliverable 523, Part I, November 2001, version 2.0.

[33] C. Oestges, V. Erceg, and A. J. Paulraj, "A physical scattering model for MIMO macrocellular broadband wireless channels," *IEEE J. Select. Areas Commun.*, vol. 21, no. 5, pp. 721–729, 2003.

[34] Y. Z. Mohasseb and M. P. Fitz, "A 3-D spatio-temporal simulation model for wireless channels," *IEEE J. Select. Areas Commun.*, vol. 20, no. 6, pp. 1193–1203, 2002.

[35] T. Svantesson, "A physical MIMO radio channel model for multi-element multi-polarized antenna systems," in *Proceedings of IEEE Vehicular Technology Conference (VTC '01)*, vol. 2, pp. 1083–1087, Atlantic City, NJ, October 2001.

[36] A. Saleh and R. Valenzuela, "A statistical model for indoor multipath propagation," *IEEE J. Select. Areas Commun.*, vol. 5, no. 2, pp. 128–137, 1987.

[37] Q. H. Spencer, B. D. Jeffs, M. A. Jensen, and A. L. Swindlehurst, "Modeling the statistical time and angle of arrival characteristics of an indoor multipath channel," *IEEE J. Select. Areas Commun.*, vol. 18, no. 3, pp. 347–360, 2000.

[38] L. M. Correia, Ed., "Wireless flexible personalised communications," chapter 3, pp. 77–277, John Wiley & Sons, New York, NY, USA, 2001.

[39] A. F. Molisch, "A generic model for MIMO wireless propagation channels," in *Proceedings of IEEE International Conference on Communications (ICC '02)*, vol. 1, pp. 277–282, New York, NY, USA, May 2002.

[40] K. Yu, M. Bengtsson, B. Ottersten, D. McNamara, P. Karlsson, and M. Beach, "Second order statistics of NLOS indoor MIMO channels based on 5.2 GHz measurements," in *Proceedings of IEEE Global Telecommunications Conference (GLOBECOM '01)*, vol. 1, pp. 156–160, San Antonio, Tex, USA, November 2001.

[41] K. Yu, M. Bengtsson, D. Ottersten, B. McNamara, P. Karlsson, and M. Beach, "A wideband statistical model for NLOS indoor MIMO channels," in *Proceedings of IEEE Vehicular Technology Conference (VTC '02)*, vol. 1, pp. 370–374, Birmingham, Ala, USA, May 2002.

[42] P. Karlsson, D. McNamara, and M. Beach, "Indoor and campus single and dual multi-sensor channel characterisation: measurement data. Part 2: indoor dual multi-sensor characterisation data," EU IST Program SATURN Project, IST-1999-10322, Deliverable 522, Part 2, October 2000.

[43] C. Van Loan and N. Pitsianis, "Approximation with Kronecker products," in *Linear Algebra for Large Scale and Real Time Applications*, M. S. Moonen, G. H. Golub, and B. L. R. De Moor, Eds., Kluwer Publications, pp. 293–314, Kluwer Academic Publishers, Dordecht, The Netherlands, 1993.

[44] W. Weichselberger and E. Bonek, "On the decomposition of the MIMO channel correlation tensor," in *Proceedings of ITG Workshop on Smart Antennas*, Munich, Germany, March 2004.

[45] D. Chizhik, F. Rashid-Farrokhi, J. Ling, and A. Lozano, "Effect of antenna separation on the capacity of BLAST of correlated channels," *IEEE Commun. Lett.*, vol. 4, no. 11, pp. 337–339, 2000.

[46] J. Medbo, H. Andersson, P. Schramm, H. Asplund, and J. E. Berg, "Channel models for HIPERLAN/2 in different indoor scenarios," COST 259 TD(98)70, April 1998.

[47] H. Bölcskei, M. Borgmann, and A. J. Paulraj, "Performance of space-frequency coded broadband OFDM under real-world propagation conditions," in *Proceedings of European Conference on Signal Processing (EUSIPCO '02)*, pp. 413–416, Toulouse, France, September 2002.

[48] C. Martin and B. Ottersten, "Analytic approximations of eigenvalue moments and mean channel capacity for MIMO channels," in *Proc. IEEE International Conference on Acoustics, Speech, and Signal Processing (ICASSP '02)*, vol. 3, pp. 2389–2392, Orlando, Fla, USA, May 2002.

[49] S. Bergman, C. Martin, and B. Ottersten, "Bit and power loading for spatial multiplexing using partial channel state information," in *Proceedings of ITG Workshop on Smart Antennas*, Munich, Germany, March 2004.

[50] P. Soma, D. S. Baum, V. Erceg, R. Krishnamoorthy, and A. J. Paulraj, "Analysis and modeling of multiple-input multiple-output (MIMO) radio channel based on outdoor measurements conducted at 2.5 GHz for fixed BWA applications," in *Proceedings of IEEE International Conference on Communications (ICC '02)*, vol. 1, pp. 272–276, New York, NY, USA, May 2002.

[51] K. Yu, M. Bengtsson, B. Ottersten, and M. Beach, "Narrowband MIMO channel modeling for LOS indoor scenarios," in *Proc. 27th Triennial General Assembly of the International Union of Radio Science (URSI '02)*, Maastricht, The Netherlands, August 2002.

[52] A. Paulraj, R. Nabar, and D. Gore, *Introduction to Space-Time Wireless Communications*, Cambridge University Press, Cambridge, Mass, USA, 2003.

[53] V. Erceg, L. Schumacher, P. Kyritsi, et al., "TGn channel models," IEEE 802.11-03/940r4 (adopted), May 2004, http://www.802wirelessworld.com/.

[54] Technical Specification Group Radio Access Network, "Spatial channel model for multiple input multiple output (MIMO) simulations (Release 6)," Tech. Rep. 3GPP TR 25.996 V6.1.0, 3rd Generation Partnership Project, September 2003.

[55] J. Salz and J. H. Winters, "Effect of fading correlation on adaptive arrays in digital mobile radio," *IEEE Trans. Veh. Technol.*, vol. 43, no. 4, pp. 1049–1057, 1994.

[56] C.-C. Chong, C.-M. Tan, D. I. Laurenson, S. McLaughlin, M. A. Beach, and A. R. Nix, "A new statistical wideband spatio-temporal channel model for 5-GHz band WLAN systems," *IEEE J. Select. Areas Commun.*, vol. 21, no. 2, pp. 139–150, 2003.

[57] R. J.-M. Cramér, R. A. Scholtz, and M. Z. Win, "Evaluation of an ultra-wide-band propagation channel," *IEEE Trans. Antennas Propagat.*, vol. 50, no. 5, pp. 561–570, 2002.

[58] K. Yu, Q. Li, D. Cheung, and C. Prettie, "On the tap and cluster angular spreads of indoor WLAN channels," in *Proc. IEEE 59th Vehicular Technology Conference (VTC '04)*, vol. 1, pp. 218–222, Milano, Italy, May 2004.

[59] W. C. Jakes, Ed., *Microwave Mobile Communications*, John Wiley & Sons, New York, NY, USA, 1974.

Kai Yu: Department of Signals, Sensors and Systems, Royal Institute of Technology (KTH), Stockholm 100 44, Sweden

Email: kaiyu@s3.kth.se

Mats Bengtsson: Department of Signals, Sensors and Systems, Royal Institute of Technology (KTH), Stockholm 100 44, Sweden

Email: mats.bengtsson@s3.kth.se

Björn Ottersten: Department of Signals, Sensors and Systems, Royal Institute of Technology (KTH), Stockholm 100 44, Sweden

Email: bjorn.ottersten@s3.kth.se

15 Channel estimation

Geert Leus and Alle-Jan van der Veen

15.1. Introduction

As demonstrated in other chapters in this book, the deployment of multiple antennas at the transmit and receive sides (multiple-input multiple-output (MIMO)) can result in a significant capacity increase. This is due to two effects: (i) diversity, that is, robustness against fading of the channel between a transmit and a receive antenna, and (ii) space-time coding, that is, the parallel transmission of information via multiple transmit antennas. However, this capacity increase was based on an important assumption: all channels between the transmit antennas and the receive antennas are accurately known. In practice, these channels will have to be estimated, which is the focus of this chapter.

The wireless channel is highly complex. In general it is both frequency and time selective, and with multiple antennas, also the space selectivity plays a role. Physical models such as Jakes' model [1] usually simplify this to a multipath propagation model where each path is parametrized by an angle at the receiver array, perhaps an angle at the transmitter array, and further a propagation delay and a complex amplitude. This can be refined by making statistical assumptions on the distribution of these parameters. For channel *modeling*, one tries to use a general model that allows to describe a large class of observed channels. For channel *estimation*, however, there is a trade-off: a sophisticated model with more parameters may turn out to be less accurate when the parameters have to be estimated with a finite set of observations.

It is clear that channel estimation is an extensive topic. To limit ourselves, we will cover only a small subset of channel models and possible estimation techniques.

Channel model: FIR-MIMO. For broadband communications, the time dispersion or frequency selectivity due to multipath propagation is important. For the sake of conciseness, we will restrict ourselves to single-carrier MIMO systems in a frequency-selective fading channel. The channels are modeled by simple finite impulse response (FIR) filters with a common order L, assumed to be known.

Estimation techniques: training-based and semiblind. In practical systems, channels are invariably estimated using periodic bursts of known training symbols, therefore we focus mostly on these techniques. Conventional training-based methods only exploit the presence of the known training symbols. The results can be enhanced by also incorporating the convolutional properties of the surrounding unknown data symbols, which lead to the so-called enhanced training-based methods. Also discussed are semiblind methods that combine a training-based criterion with a purely blind criterion. Blind techniques do not exploit the knowledge of training symbols, and focus on deterministic or stochastic properties of the system. Note that all channel estimation methods considered in this chapter are *transparent to space-time coding*, that is, any structure introduced by these codes is not exploited.

Suggestions for further reading are found at the end of the chapter.

Notation. Matrices and column vectors are written in boldface uppercase and lowercase letters, respectively. For a matrix or column vector, superscript T is the transpose, H the complex conjugate transpose, and $\dagger$ the pseudoinverse (Moore-Penrose inverse). $\mathbf{I}_N$ is the $N \times N$ identity matrix. $\mathbf{0}_{M\times N}$ ($\mathbf{0}_N$) is the $M \times N$ ($N \times N$) matrix for which all entries are equal to zero. vec($\mathbf{A}$) is a stacking of the columns of a matrix $\mathbf{A}$ into a column vector. $\|\cdot\|$ represents the Frobenius norm. $\otimes$ is the Kronecker product. A notable property is (for matrices of compatible sizes) $\text{vec}(\mathbf{ABC}) = (\mathbf{C}^T \otimes \mathbf{A})\,\text{vec}(\mathbf{B})$. Finally, $\text{E}(\cdot)$ denotes the stochastic expectation operator.

15.2. Data model

We consider a convolutive MIMO system with A_t transmit antennas and A_r receive antennas. Suppose $\mathbf{x}(n)$ represents the $A_t \times 1$ symbol vector sequence transmitted at the A_t transmit antennas. Assuming symbol rate sampling at each receive antenna, the $A_r \times 1$ sample vector sequence received at the A_r receive antennas is then given by

$$\mathbf{y}(n) = \sum_{l=0}^{L} \mathbf{H}(l)\mathbf{x}(n-l) + \mathbf{e}(n), \tag{15.1}$$

where $\mathbf{e}(n)$ is the $A_r \times 1$ additive noise vector sequence on the A_r receive antennas, which we assume to be zero-mean white (spatially and temporally) Gaussian with variance σ_e^2, and $\mathbf{H}(l)$ is the $A_r \times A_t$ MIMO channel of order L (or length $L+1$). We will often make use of the vectorized form of $\mathbf{H}(l)$, which is obtained by stacking its columns: $\mathbf{h}(l) = \text{vec}[\mathbf{H}(l)]$.

In this chapter, we focus on estimating $\mathbf{H}(l)$ (or $\mathbf{h}(l)$) without assuming any structure on it. Hence, no calibration of the different transmit/receive antennas is required. We assume a burst of N symbol vectors is transmitted, in the form of K symbol blocks, where each symbol block consists of N_t training symbol vec-

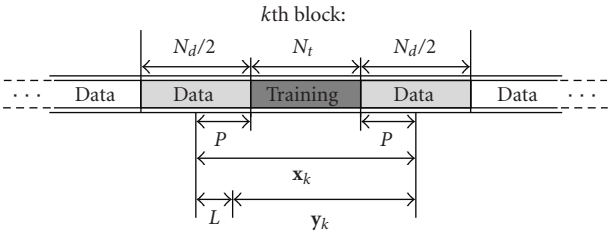

FIGURE 15.1. Partitioning of the transmitted symbol vectors into blocks, each consisting of N_t training and N_d data symbol vectors.

tors, surrounded at each side by $N_d/2$ unknown data symbol vectors, that is, $N = K(N_t + N_d)$ (see Figure 15.1). We will focus on training-based as well as semiblind channel estimation algorithms, where the latter rely on the combination of a training-based with a purely blind criterion.

To describe the different training-based methods that will be discussed in this chapter, consider the following subvector of the kth symbol block, as illustrated in Figure 15.1:

$$\mathbf{x}_k = \left[\mathbf{x}^T(n_k - P), \ldots, \mathbf{x}^T(n_k + N_t + P - 1)\right]^T, \tag{15.2}$$

where $n_k = k(N_t + N_d) + N_d/2$ indicates the start of the training symbol vectors in the kth symbol block, and $0 \leq P \leq N_d/2$. This vector contains all the N_t training symbol vectors transmitted during the kth symbol block, plus P unknown data symbol vectors at each side of it. Due to the convolutive channel, the first $L - 1$ received sample vectors corresponding to $\mathbf{x}_k$ are contaminated by preceding data symbol vectors. Therefore, the received samples that depend only on $\mathbf{x}_k$ are given by (see Figure 15.1)

$$\mathbf{y}_k = \left[\mathbf{y}^T(n_k - P + L), \ldots, \mathbf{y}^T(n_k + N_t + P - 1)\right]^T. \tag{15.3}$$

This vector can be expressed as

$$\mathbf{y}_k = \boldsymbol{\mathcal{H}}\mathbf{x}_k + \mathbf{e}_k, \tag{15.4}$$

where $\mathbf{e}_k$ is similarly defined as $\mathbf{y}_k$ and $\boldsymbol{\mathcal{H}}$ is the $A_r(N_t + 2P - L) \times A_t(N_t + 2P)$ block Toeplitz channel matrix defined in Figure 15.2:

Define the training part of $\mathbf{x}_k$ as

$$\mathbf{x}_k^{(t)} = \left[\mathbf{x}^T(n_k), \ldots, \mathbf{x}^T(n_k + N_t - 1)\right]^T, \tag{15.5}$$

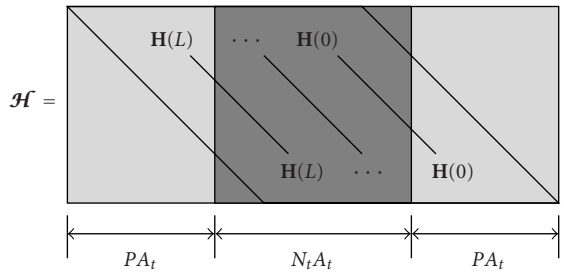

FIGURE 15.2. Definition of the block Toeplitz channel matrix.

and the unknown data part as

$$\mathbf{x}_k^{(d)} = \left[\mathbf{x}^T(n_k - P), \ldots, \mathbf{x}^T(n_k - 1), \mathbf{x}^T(n_k + N_t), \ldots, \mathbf{x}^T(n_k + N_t + P - 1)\right]^T. \tag{15.6}$$

Then we can split (15.4) into

$$\mathbf{y}_k = \boldsymbol{\mathcal{H}}^{(t)}\mathbf{x}_k^{(t)} + \boldsymbol{\mathcal{H}}^{(d)}\mathbf{x}_k^{(d)} + \mathbf{e}_k, \tag{15.7}$$

where $\boldsymbol{\mathcal{H}}^{(t)}$ is the $A_r(N_t + 2P - L) \times A_tN_t$ matrix obtained by collecting the N_t middle block columns of $\boldsymbol{\mathcal{H}}$ (the dark shaded area in Figure 15.2), and $\boldsymbol{\mathcal{H}}^{(d)}$ is the $A_r(N_t + 2P - L) \times 2A_tP$ matrix obtained by collecting the P left and P right block columns (the light shaded area in Figure 15.2).

The preceding equations have expressed $\mathbf{y}_k$ as a linear combination of the transmitted symbols $\mathbf{x}_k$. Alternatively, we can write the convolution operation (15.4) as a linear operation on the channel coefficient vector $\mathbf{h} = [\mathbf{h}^T(0), \ldots, \mathbf{h}^T(L)]^T$, which gives

$$\mathbf{y}_k = (\boldsymbol{\mathcal{X}}_k \otimes \mathbf{I}_{A_r})\mathbf{h} + \mathbf{e}_k, \tag{15.8}$$

where $\boldsymbol{\mathcal{X}}_k$ is the $(N_t + 2P - L) \times A_t(L + 1)$ block Toeplitz symbol matrix defined in Figure 15.3. Similarly as in (15.7), we can split (15.8) into a training and an unknown data part as

$$\mathbf{y}_k = (\boldsymbol{\mathcal{X}}_k^{(t)} \otimes \mathbf{I}_{A_r})\mathbf{h} + (\boldsymbol{\mathcal{X}}_k^{(d)} \otimes \mathbf{I}_{A_r})\mathbf{h} + \mathbf{e}_k, \tag{15.9}$$

where $\boldsymbol{\mathcal{X}}_k^{(t)}$ is obtained by setting the unknown data symbol vectors of $\mathbf{x}_k^{(d)}$ (the light shaded area in Figure 15.3) to zero in $\boldsymbol{\mathcal{X}}_k$, whereas $\boldsymbol{\mathcal{X}}_k^{(d)}$ is obtained by setting the training symbol vectors of $\mathbf{x}_k^{(t)}$ (the dark shaded area in Figure 15.3) to zero.

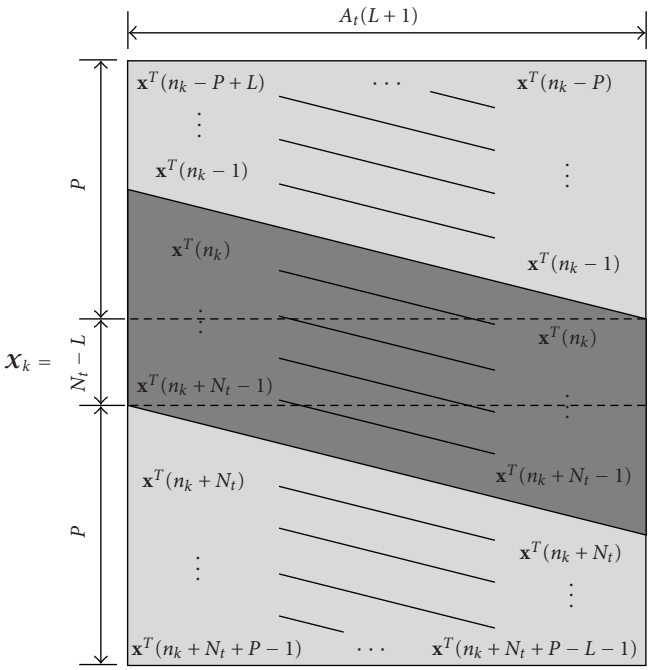

FIGURE 15.3. Definition of the block Toeplitz symbol matrix.

Although we will generally express the obtained results as a function of k, it will sometimes be convenient to stack all vectors $\mathbf{y}_k$ and all matrices $\boldsymbol{\mathcal{X}}_k^{(t)}$ and $\boldsymbol{\mathcal{X}}_k^{(d)}$ for $k = 0, \ldots, K-1$, leading to

$$\mathbf{y} = [\mathbf{y}_0^T, \ldots, \mathbf{y}_{K-1}^T]^T, \tag{15.10}$$

$$\boldsymbol{\mathcal{X}}^{(t)} = [\boldsymbol{\mathcal{X}}_0^{(t)T}, \ldots, \boldsymbol{\mathcal{X}}_{K-1}^{(t)T}]^T, \qquad \boldsymbol{\mathcal{X}}^{(d)} = [\boldsymbol{\mathcal{X}}_0^{(d)T}, \ldots, \boldsymbol{\mathcal{X}}_{K-1}^{(d)T}]^T. \tag{15.11}$$

We will now discuss training-based channel estimation using (15.7) and (15.9). We will make a distinction between conventional training-based channel estimation, which only takes into account received samples that solely depend on training symbols ($P = 0$), and enhanced training-based channel estimation, which next to these received samples also takes into account some surrounding received samples, which might depend on both training symbols and unknown data symbols or solely on unknown data symbols ($0 < P \leq N_d/2$). Although the latter techniques can be classified as semiblind methods, we will in a subsequent section focus on semiblind channel estimation methods that combine one of the previous training-based methods (conventional or enhanced) with a purely blind method.

15.3. Conventional training-based methods

15.3.1. Channel estimation

Conventional training solutions use only those received samples that solely depend on the training symbols. In other words, we consider $P = 0$, which allows us to simplify (15.9) as

$$\mathbf{y}_k = (\mathcal{X}_k^{(t)} \otimes \mathbf{I})\mathbf{h} + \mathbf{e}_k, \tag{15.12}$$

where $\mathbf{I} = \mathbf{I}_{A_r}$. Although many different channel estimation procedures can be applied to (15.12), we restrict ourselves to maximum likelihood (ML) channel estimation, which requires neither knowledge of the noise variance nor any statistical information about the channel [2].

The ML channel estimate related to (15.12) is obtained by solving the following optimization problem:

$$\begin{aligned}\mathbf{h}_{\mathrm{ML}} &= \arg\min_{\mathbf{h}} \sum_{k=0}^{K-1} ||\mathbf{y}_k - (\mathcal{X}_k^{(t)} \otimes \mathbf{I})\mathbf{h}||^2 \\ &= \arg\min_{\mathbf{h}} ||\mathbf{y} - (\mathcal{X}^{(t)} \otimes \mathbf{I})\mathbf{h}||,\end{aligned} \tag{15.13}$$

where the received sample vector $\mathbf{y}$ and training matrix $\mathcal{X}^{(t)}$ are defined in (15.10) and (15.11). This is a standard least-squares (LS) problem, whose solution is given in terms of a pseudo-inverse, $(\mathcal{X}^{(t)} \otimes \mathbf{I})^{\dagger}$, which is equal to $\mathcal{X}^{(t)\dagger} \otimes \mathbf{I}$. Assuming $\mathcal{X}^{(t)}$ has full-column rank, which requires $K \geq A_t(L+1)/(N_t - L)$, we obtain

$$\begin{aligned}\mathbf{h}_{\mathrm{ML}} &= (\mathcal{X}^{(t)\dagger} \otimes \mathbf{I})\mathbf{y} \\ &= \left[(\mathcal{X}^{(t)H}\mathcal{X}^{(t)})^{-1} \otimes \mathbf{I}\right](\mathcal{X}^{(t)H} \otimes \mathbf{I})\mathbf{y} \\ &= \left[\left(\sum_{k=0}^{K-1} \mathcal{X}_k^{(t)H}\mathcal{X}_k^{(t)}\right)^{-1} \otimes \mathbf{I}\right] \sum_{k=0}^{K-1} (\mathcal{X}_k^{(t)H} \otimes \mathbf{I})\mathbf{y}_k.\end{aligned} \tag{15.14}$$

If we insert the data model (15.12), it follows that

$$\mathbf{h}_{\mathrm{ML}} = \mathbf{h} + \left[\left(\sum_{k=0}^{K-1} \mathcal{X}_k^{(t)H}\mathcal{X}_k^{(t)}\right)^{-1} \otimes \mathbf{I}\right] \sum_{k=0}^{K-1} (\mathcal{X}_k^{(t)H} \otimes \mathbf{I})\mathbf{e}_k, \tag{15.15}$$

which shows that the ML estimate is unbiased. Furthermore, since the noise term

$\mathbf{e}_k$ has covariance $\mathrm{E}(\mathbf{e}_k\mathbf{e}_k^H) = \sigma_e^2\mathbf{I}$, the covariance of the channel estimation error is given by

$$\mathrm{E}\Big[(\mathbf{h}_{\mathrm{ML}}-\mathbf{h})(\mathbf{h}_{\mathrm{ML}}-\mathbf{h})^H\Big] = \sigma_e^2\left[\left(\sum_{k=0}^{K-1}\boldsymbol{\mathcal{X}}_k^{(t)H}\boldsymbol{\mathcal{X}}_k^{(t)}\right)^{-1}\otimes\mathbf{I}\right], \tag{15.16}$$

which is equal to the Cramér-Rao bound (CRB), and the mean square error (MSE) of the channel estimate can be expressed as

$$\begin{aligned} J_{\mathrm{ML}} &= \mathrm{E}\Big\{\big\|\mathbf{h}_{\mathrm{ML}}-\mathbf{h}\big\|^2\Big\} = \sigma_e^2 A_r \,\mathrm{tr}\left[\left(\sum_{k=0}^{K-1}\boldsymbol{\mathcal{X}}_k^{(t)H}\boldsymbol{\mathcal{X}}_k^{(t)}\right)^{-1}\right] \\ &= \sigma_e^2 A_r \,\mathrm{tr}\Big[\big(\boldsymbol{\mathcal{X}}^{(t)H}\boldsymbol{\mathcal{X}}^{(t)}\big)^{-1}\Big]. \end{aligned} \tag{15.17}$$

Note that this channel estimation problem can actually be decoupled into the different receive antennas, and is often presented as such. However, for the enhanced training-based methods discussed in the next section, the correlation between the different receive antennas will come into the picture, and the problem cannot be decoupled anymore. This does not mean that we cannot use the enhanced training-based methods on smaller subgroups of receive antennas, it simply means that the performance of such an approach will be different (see also Section 15.6).

15.3.2. Optimal training design

It is possible to design the training symbol vectors such that J_{ML} is minimized under a total training power constraint. In other words, we solve

$$\min_{\{\mathbf{x}_k^{(t)}\}} \mathrm{tr}\Big[\big(\boldsymbol{\mathcal{X}}^{(t)H}\boldsymbol{\mathcal{X}}^{(t)}\big)^{-1}\Big] \quad \text{s.t.} \sum_{k=0}^{K-1}\big\|\mathbf{x}_k^{(t)}\big\|^2 = E, \tag{15.18}$$

where E is a specified constant. To solve this problem, observe that

$$\mathrm{tr}\Big[\big(\boldsymbol{\mathcal{X}}^{(t)H}\boldsymbol{\mathcal{X}}^{(t)}\big)^{-1}\Big] \geq \sum_{i=1}^{A_t(L+1)}\frac{1}{\big\|\boldsymbol{\mathcal{X}}^{(t)}(:,i)\big\|^2}, \tag{15.19}$$

where equality is obtained if $\boldsymbol{\mathcal{X}}^{(t)H}\boldsymbol{\mathcal{X}}^{(t)}$ is diagonal (the notation $\mathbf{A}(:,i)$ represents the ith column of the matrix $\mathbf{A}$). From Figure 15.3 (with $P = 0$), it is clear that each block column of $\boldsymbol{\mathcal{X}}_k^{(t)}$ only contains $N_t - L$ training symbol vectors of the total amount of N_t training symbol vectors collected in $\mathbf{x}_k^{(t)}$. Hence, there is no immediate connection between $\sum_{k=0}^{K-1}\|\mathbf{x}_k^{(t)}\|^2$ and $\|\boldsymbol{\mathcal{X}}^{(t)}\|^2$, which complicates matters. We proceed in the following way. We first find the minimum of the right-hand side of (15.19) under the constraint, which is obtained when all terms are equal and as small as possible under this constraint, and we subsequently try to realize

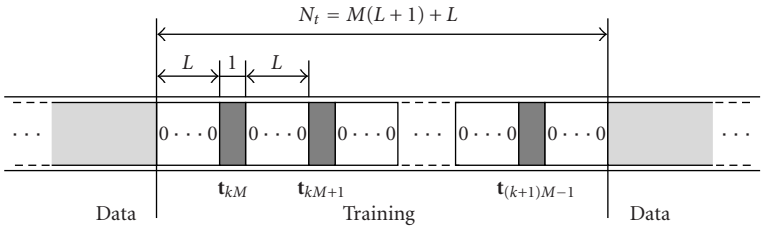

FIGURE 15.4. Structure of the solution for optimal training.

this minimum by a training design for which $\mathfrak{X}^{(t)H}\mathfrak{X}^{(t)}$ is diagonal, in order to obtain equality in (15.19).

We will consider the following two cases: the number of training symbols $N_t \geq 2L+1$, and $N_t = L+1$. For the remaining case where $L+1 < N_t < 2L+1$, the optimization problem is hard to solve in analytical form.

15.3.2.1. Case $N_t \geq 2L+1$.

In this case, the terms on the right-hand side of (15.19) are equal and as small as possible under the constraint $\sum_{k=0}^{K-1} \|\mathbf{x}_k^{(t)}\|^2 = E$, if

$$\begin{aligned} \mathbf{x}(n_k+l) = \mathbf{0}_{A_t\times 1}, \quad \mathbf{x}(n_k+N_t-1-l) = \mathbf{0}_{A_t\times 1}, \\ \text{for } l = 0,1,\ldots,L-1,\ k = 0,1,\ldots,K-1, \end{aligned} \tag{15.20}$$

$$\left|\left|\mathfrak{X}^{(t)}(:,i)\right|\right|^2 = \frac{E}{A_t}, \quad \text{for } i = 1,\ldots,A_t(L+1). \tag{15.21}$$

If we also choose $\mathfrak{X}^{(t)H}\mathfrak{X}^{(t)}$ diagonal, in order to obtain equality in (15.19), then the latter condition can be written as

$$\mathfrak{X}^{(t)H}\mathfrak{X}^{(t)} = \frac{E}{A_t}\mathbf{I}_{A_t(L+1)}, \tag{15.22}$$

which requires $K \geq A_t(L+1)/(N_t-L)$.

As an example, consider an integer $M \geq 1$ and set $N_t = M(L+1)+L$. An optimal solution is then given by using dispersed training symbol vectors separated by L zero vectors:

$$\mathbf{x}_k^{(t)} = \left[\mathbf{0}_{A_tL\times 1}^T, \mathbf{t}_{kM}^T, \mathbf{0}_{A_tL\times 1}^T, \mathbf{t}_{kM+1}^T, \ldots, \mathbf{0}_{A_tL\times 1}^T, \mathbf{t}_{(k+1)M-1}^T, \mathbf{0}_{A_tL\times 1}^T\right]^T, \tag{15.23}$$

where $\mathbf{T} = [\mathbf{t}_0,\ldots,\mathbf{t}_{KM-1}]$ is an $A_t \times KM$ matrix that satisfies $\mathbf{T}\mathbf{T}^H = E/A_t\,\mathbf{I}_{A_t}$, which requires $K \geq A_t/M$. The structure of the solution is shown in Figure 15.4.

Often, only $M = A_t$ (hence, $N_t = A_t(L+1)+L$) and a single message block ($K = 1$) is considered, since this option minimizes the total training overhead for a fixed total burst length N. For instance, the optimal training approach of [3],

which maximizes a lower bound on the ergodic capacity assuming linear minimum mean square error (LMMSE) channel estimation, falls within this special class. However, N_t and K cannot always be chosen freely. As a result, the other options might also be useful in practice, as well as the case that is considered next.

15.3.2.2. Case $N_t = L + 1$.

First of all, note from Figure 15.3 (with $P = 0$) that in this case $\mathbf{X}_k^{(t)} = \mathbf{x}_k^{(t)T}$, and consequently $\mathbf{X}^{(t)} = [\mathbf{x}_0^{(t)}, \ldots, \mathbf{x}_{K-1}^{(t)}]^T$. Therefore, the terms on the right-hand side of (15.19) are equal and as small as possible under the constraint $\sum_{k=0}^{K-1} \|\mathbf{x}_k^{(t)}\|^2 = E$, if

$$\left\|\mathbf{X}^{(t)}(:, i)\right\|^2 = \frac{E}{(A_t(L+1))}, \quad \text{for } i = 1, \ldots, A_t(L+1). \tag{15.24}$$

Again, if we also choose $\mathbf{X}^{(t)H}\mathbf{X}^{(t)}$ diagonal, this condition becomes

$$\mathbf{X}^{(t)H}\mathbf{X}^{(t)} = \frac{E}{(A_t(L+1))}\mathbf{I}_{A_t(L+1)}, \tag{15.25}$$

which requires $K \geq A_t(L+1)$. Since $\mathbf{X}^{(t)}$ has no specific block Toeplitz structure, condition (15.25) is easy to satisfy.

15.4. Enhanced training-based methods

In the previous section, we only considered those received samples that solely were depending on training symbols. However, an enhanced channel estimate can be obtained if we also take some surrounding received samples into account. Referring to Figure 15.1, we will consider $0 < P \leq N_d/2$, which, this time, does not allow us to simplify (15.9).

We will again apply ML channel estimation. However, since also unknown data symbols are involved, we can adopt different options now. We will here focus on deterministic ML (DML) and Gaussian ML (GML). In DML, we assume the data symbols are unknown deterministic parameters, whereas in GML we assume that they are unknown random variables with a Gaussian distribution. Both methods do not take the finite-alphabet property of the data symbols into account, because this often leads to more complex algorithms. For this extension, we refer the interested reader to [4], where the data symbols are viewed as discrete deterministic parameters, and to [5], where they are regarded as random variables with a discrete distribution (only flat-fading MIMO channels are considered in [4, 5]).

Since we restrict P to $0 < P \leq N_d/2$, two successive vectors $\mathbf{x}_k^{(d)}$ and $\mathbf{x}_{k+1}^{(d)}$ never overlap, which allows us to process them independently. See [6] for an overview of similar enhanced training-based ML methods for the single-input multiple-output (SIMO) case with $K = 1$.

15.4.1. Deterministic ML

Viewing the data symbols as unknown deterministic parameters, the ML channel estimate related to (15.9) is obtained by solving the following optimization problem:

$$\left(\mathbf{h}_{\mathrm{ML}}, \left\{\mathbf{x}_{k,\mathrm{ML}}^{(t)}\right\}\right) = \arg \min_{(\mathbf{h},\{\mathbf{x}_k^{(t)}\})} \sum_{k=0}^{K-1} \left\| \mathbf{y}_k - \left(\boldsymbol{\mathcal{X}}_k^{(t)} \otimes \mathbf{I}\right)\mathbf{h} - \left(\boldsymbol{\mathcal{X}}_k^{(d)} \otimes \mathbf{I}\right)\mathbf{h} \right\|^2 \tag{15.26}$$

$$= \arg \min_{(\mathbf{h},\{\mathbf{x}_k^{(t)}\})} \sum_{k=0}^{K-1} \left\| \mathbf{y}_k - \left(\boldsymbol{\mathcal{X}}_k^{(t)} \otimes \mathbf{I}\right)\mathbf{h} - \boldsymbol{\mathcal{H}}^{(d)}\mathbf{x}_k^{(d)} \right\|^2. \tag{15.27}$$

This can for instance be solved by alternating minimizations between $\mathbf{h}$ and $\{\mathbf{x}_k^{(d)}\}$ (initialized by $\mathbf{x}_k^{(d)} = \mathbf{0}_{2A_tP\times 1}$). In this context, note that the solution for $\mathbf{h}$ of (15.26) for a given estimate $\hat{\mathbf{x}}_k^{(d)}$ is, as in (15.14),

$$\begin{aligned}
\mathbf{h}_{\mathrm{ML}}\left(\left\{\hat{\mathbf{x}}_k^{(d)}\right\}\right) &= \arg\min_{\mathbf{h}} \sum_{k=0}^{K-1} \left\| \mathbf{y}_k - \left(\boldsymbol{\mathcal{X}}_k^{(t)} \otimes \mathbf{I}\right)\mathbf{h} - \left(\widehat{\boldsymbol{\mathcal{X}}}_k^{(d)} \otimes \mathbf{I}\right)\mathbf{h} \right\|^2 \\
&= \left\{ \left[\sum_{k=0}^{K-1} \left(\boldsymbol{\mathcal{X}}_k^{(t)} + \widehat{\boldsymbol{\mathcal{X}}}_k^{(d)}\right)^H \left(\boldsymbol{\mathcal{X}}_k^{(t)} + \widehat{\boldsymbol{\mathcal{X}}}_k^{(d)}\right) \right]^{-1} \otimes \mathbf{I} \right\} \\
&\quad \cdot \sum_{k=0}^{K-1} \left[\left(\boldsymbol{\mathcal{X}}_k^{(t)} + \widehat{\boldsymbol{\mathcal{X}}}_k^{(d)}\right)^H \otimes \mathbf{I} \right] \mathbf{y}_k,
\end{aligned} \tag{15.28}$$

whereas the solution for $\mathbf{x}_{k,\mathrm{ML}}^{(d)}$ of (15.27) for a given estimate $\hat{\mathbf{h}}$ is

$$\begin{aligned}
\mathbf{x}_{k,\mathrm{ML}}^{(d)}(\hat{\mathbf{h}}) &= \arg\min_{\mathbf{x}_k^{(d)}} \left\| \mathbf{y}_k - \left(\boldsymbol{\mathcal{X}}_k^{(t)} \otimes \mathbf{I}\right)\hat{\mathbf{h}} - \widehat{\boldsymbol{\mathcal{H}}}^{(d)}\mathbf{x}_k^{(d)} \right\|^2 \\
&= \widehat{\boldsymbol{\mathcal{H}}}^{(d)\dagger} \left[\mathbf{y}_k - \left(\boldsymbol{\mathcal{X}}_k^{(t)} \otimes \mathbf{I}\right)\hat{\mathbf{h}} \right].
\end{aligned} \tag{15.29}$$

Note that we assume here that $\boldsymbol{\mathcal{X}}^{(t)} + \widehat{\boldsymbol{\mathcal{X}}}^{(d)}$ always has full-column rank $A_t(L+1)$, which requires $K \geq A_t(L+1)/(N_t + 2P - L)$.

We can also plug (15.29) in (15.27) to obtain

$$\mathbf{h}_{\mathrm{ML}} = \arg\min_{\mathbf{h}} \sum_{k=0}^{K-1} \left\| \mathbf{y}_k - \left(\boldsymbol{\mathcal{X}}_k^{(t)} \otimes \mathbf{I}\right)\mathbf{h} \right\|^2_{\mathbf{P}_{\mathrm{col}}^{\perp}(\boldsymbol{\mathcal{H}}^{(d)})}, \tag{15.30}$$

where $\mathbf{P}_{\mathrm{col}}^{\perp}(\boldsymbol{\mathcal{H}}^{(d)}) = \mathbf{I}_{A_r(N_t+2P-L)} - \boldsymbol{\mathcal{H}}^{(d)}\boldsymbol{\mathcal{H}}^{(d)\dagger}$ is the projection matrix onto the orthogonal complement of the column space of $\boldsymbol{\mathcal{H}}^{(d)}$. This problem can be solved using gradient techniques which, unfortunately, are rather complex and probably not worth the additional effort. Note that the simplified quadratic DML techniques proposed for SIMO systems [6] cannot be applied for MIMO systems, because it is impossible to find a linear parametrization of the null space of $\boldsymbol{\mathcal{H}}^{(d)}$ as a function of $\mathbf{h}$.

The CRB for the DML channel estimate can be derived as in [7] and is given by

$$\mathrm{CRB}_{\mathrm{DML}} = \sigma_e^2 \left\{ \sum_{k=0}^{K-1} \left[\left(\mathbf{X}_k^{(t)} + \mathbf{X}_k^{(d)} \right)^H \otimes \mathbf{I} \right] \mathbf{P}_{\mathrm{col}}^{\perp}\left(\boldsymbol{\mathcal{H}}^{(d)} \right) \left[\left(\mathbf{X}_k^{(t)} + \mathbf{X}_k^{(d)} \right) \otimes \mathbf{I} \right] \right\}^{-1}. \tag{15.31}$$

Remark 15.1. If $N_t > L$, $A_r \leq A_t$, and $\boldsymbol{\mathcal{H}}^{(d)}$ has a nonempty left null space of dimension $A_r(N_t - L)$ (true with probability one if $N_t > L$ and $A_r \leq A_t$), then the matrix $\mathbf{P}_{\mathrm{col}}^{\perp}(\boldsymbol{\mathcal{H}}^{(d)}) = \mathbf{S}$, where $\mathbf{S}$ is the $A_r(N_t + 2P - L) \times A_r(N_t + 2P - L)$ selection matrix that selects the $A_r(N_t - L)$ middle rows and removes the $A_r P$ top and bottom rows. As a result, the iterative approach is not required, since we can solve (15.30) in closed form. Its solution is then given by

$$\mathbf{h}_{\mathrm{ML}} = \left[\sum_{k=0}^{K-1} \left(\mathbf{X}_k^{(t)H} \otimes \mathbf{I} \right) \mathbf{S} \left(\mathbf{X}_k^{(t)} \otimes \mathbf{I} \right) \right]^{-1} \sum_{k=0}^{K-1} \left(\mathbf{X}_k^{(t)H} \otimes \mathbf{I} \right) \mathbf{S} \mathbf{y}_k. \tag{15.32}$$

The CRB (15.31) can then be expressed as

$$\begin{aligned} \mathrm{CRB}_{\mathrm{DML}} &= \sigma_e^2 \left\{ \sum_{k=0}^{K-1} \left[\left(\mathbf{X}_k^{(t)} + \mathbf{X}_k^{(d)} \right)^H \otimes \mathbf{I} \right] \mathbf{S} \left[\left(\mathbf{X}_k^{(t)} + \mathbf{X}_k^{(d)} \right) \otimes \mathbf{I} \right] \right\}^{-1} \\ &= \sigma_e^2 \left[\sum_{k=0}^{K-1} \left(\mathbf{X}_k^{(t)H} \otimes \mathbf{I} \right) \mathbf{S} \left(\mathbf{X}_k^{(t)} \otimes \mathbf{I} \right) \right]^{-1}, \end{aligned} \tag{15.33}$$

where we have used that the $A_r(N_t - L)$ middle rows of $\mathbf{X}_k^{(d)}$ contain zero entries. It is clear that these results are exactly the same as the ones for the conventional training-based method (applying $\mathbf{S}$ is the same as taking $P = 0$).

Remark 15.2. Another special case arises when $N_t \leq L$, $A_r \leq A_t$, and the matrix $\boldsymbol{\mathcal{H}}^{(d)}$ has an empty left null space (true with probability one if $N_t \leq L$ and $A_r \leq A_t$). In that case, $\mathbf{P}_{\mathrm{col}}^{\perp}(\boldsymbol{\mathcal{H}}^{(d)}) = \mathbf{0}_{A_r(N_t+2P-L)}$, which actually means that the DML problem is underdetermined ((15.30) is underdetermined and the CRB (15.31) is infinity). However, the iterative approach can still be applied in order to find a reasonable channel estimate. Actually, the iterative approach will converge in one step to the solution that is obtained after the first step of the GML method (see Section 15.4.2). Hence, it can never outperform the GML method under these circumstances.

15.4.2. Gaussian ML

Recall (15.9), namely,

$$\mathbf{y}_k = \left(\mathbf{X}_k^{(t)} \otimes \mathbf{I} \right) \mathbf{h} + \left[\left(\mathbf{X}_k^{(d)} \otimes \mathbf{I} \right) \mathbf{h} + \mathbf{e}_k \right]. \tag{15.34}$$

Viewing the data symbols as unknown random variables with a Gaussian distribution, the term in brackets is a Gaussian noise term with covariance

$$\mathbf{Q} = \boldsymbol{\mathcal{H}}^{(d)} \mathbf{R}_{\mathbf{x}^{(d)}} \boldsymbol{\mathcal{H}}^{(d)H} + \sigma_e^2 \mathbf{I}_{A_r(N_t+2P-L)}, \tag{15.35}$$

where $\mathbf{R}_{\mathbf{x}^{(d)}} = \mathrm{E}\{\mathbf{x}_k^{(d)} \mathbf{x}_k^{(d)H}\}$ is the covariance of $\mathbf{x}_k^{(d)}$, which we assume to be known. Following standard techniques, the ML channel estimate related to (15.34) is then obtained by solving the optimization problem

$$(\mathbf{h}_{\mathrm{ML}}, \sigma^2_{e,\mathrm{ML}}) = \arg \min_{(\mathbf{h},\sigma_e^2)} K \ln |\mathbf{Q}| + \sum_{k=0}^{K-1} \left\| \mathbf{y}_k - \left(\boldsymbol{\mathcal{X}}_k^{(t)} \otimes \mathbf{I} \right) \mathbf{h} \right\|^2_{\mathbf{Q}^{-1}}. \tag{15.36}$$

This problem can be solved using gradient techniques. However, since these are rather complex, we will simplify (approximate) the problem by assuming that $\mathbf{Q}$ is an arbitrary matrix that is independent from $\mathbf{h}$ and σ_e^2. This approach has been proposed in [8] for the single-input single-output (SISO) case, and it has been shown there that the effect on the CRB is negligible. We then obtain

$$(\mathbf{h}_{\mathrm{ML}}, \mathbf{Q}_{\mathrm{ML}}) = \arg \min_{(\mathbf{h},\mathbf{Q})} K \ln |\mathbf{Q}| + \sum_{k=0}^{K-1} \left\| \mathbf{y}_k - \left(\boldsymbol{\mathcal{X}}_k^{(t)} \otimes \mathbf{I} \right) \mathbf{h} \right\|^2_{\mathbf{Q}^{-1}}, \tag{15.37}$$

which can be solved using alternating minimizations between $\mathbf{h}$ and $\mathbf{Q}$ (initialized by $\mathbf{Q} = \mathbf{I}_{A_r(N_t+2P-L)}$). Indeed, using similar derivations as in [8], we can show that for a given estimate $\hat{\mathbf{Q}}$, the optimal estimate for $\mathbf{h}$ is

$$\begin{aligned} \mathbf{h}_{\mathrm{ML}}(\hat{\mathbf{Q}}) &= \arg \min_{\mathbf{h}} K \ln |\hat{\mathbf{Q}}| + \sum_{k=0}^{K-1} \left\| \mathbf{y}_k - \left(\boldsymbol{\mathcal{X}}_k^{(t)} \otimes \mathbf{I} \right) \mathbf{h} \right\|^2_{\hat{\mathbf{Q}}^{-1}} \\ &= \left[\sum_{k=0}^{K-1} \left(\boldsymbol{\mathcal{X}}_k^{(t)H} \otimes \mathbf{I} \right) \hat{\mathbf{Q}}^{-1} \left(\boldsymbol{\mathcal{X}}_k^{(t)} \otimes \mathbf{I} \right) \right]^{-1} \sum_{k=0}^{K-1} \left(\boldsymbol{\mathcal{X}}_k^{(t)H} \otimes \mathbf{I} \right) \hat{\mathbf{Q}}^{-1} \mathbf{y}_k, \end{aligned} \tag{15.38}$$

whereas for a given estimate $\hat{\mathbf{h}}$, the optimal estimate for $\mathbf{Q}$ is

$$\begin{aligned} \mathbf{Q}_{\mathrm{ML}}(\hat{\mathbf{h}}) &= \arg \min_{\mathbf{Q}} K \ln |\mathbf{Q}| + \sum_{k=0}^{K-1} \left\| \mathbf{y}_k - (\boldsymbol{\mathcal{X}}_k^{(t)} \otimes \mathbf{I}) \hat{\mathbf{h}} \right\|^2_{\mathbf{Q}^{-1}} \\ &= K^{-1} \sum_{k=0}^{K-1} \left[\mathbf{y}_k - \left(\boldsymbol{\mathcal{X}}_k^{(t)} \otimes \mathbf{I} \right) \hat{\mathbf{h}} \right] \left[\mathbf{y}_k - \left(\boldsymbol{\mathcal{X}}_k^{(t)} \otimes \mathbf{I} \right) \hat{\mathbf{h}} \right]^H. \end{aligned} \tag{15.39}$$

Note that we assume here that $\boldsymbol{\mathcal{X}}^{(t)}$ has full-column rank $A_t(L+1)$, which requires $K \geq A_t(L+1)/(N_t + 2P - L)$, and that $\hat{\mathbf{Q}}$ is always invertible, which requires $K \geq A_r(N_t + 2P - L)$.

As already mentioned, the CRB does not change much by simplifying (approximating) the GML problem formulation. Hence, we will only show the CRB

of the simplified (approximated) GML channel estimate. This can be derived as in [8] and is given by

$$\mathrm{CRB}_{\mathrm{GML}} = \left[\sum_{k=0}^{K-1} \left(\boldsymbol{\mathcal{X}}_k^{(t)H} \otimes \mathbf{I}\right)\mathbf{Q}^{-1}\left(\boldsymbol{\mathcal{X}}_k^{(t)} \otimes \mathbf{I}\right)\right]^{-1}. \tag{15.40}$$

Remark 15.3. If we set the first and last L training symbol vectors to zero in each symbol block, as we did for the optimal training strategy of Section 15.3.2.1 (see (15.20)), then it is easy to show that

$$\mathbf{Q}^{-1}\left(\boldsymbol{\mathcal{X}}_k^{(t)} \otimes \mathbf{I}\right) = \sigma_e^{-2}\left(\boldsymbol{\mathcal{X}}_k^{(t)} \otimes \mathbf{I}\right). \tag{15.41}$$

As a result, the CRB (15.40) can be expressed as

$$\mathrm{CRB}_{\mathrm{GML}} = \sigma_e^2 \left[\left(\sum_{k=0}^{K-1} \boldsymbol{\mathcal{X}}_k^{(t)H}\boldsymbol{\mathcal{X}}_k^{(t)}\right)^{-1} \otimes \mathbf{I}\right]. \tag{15.42}$$

Because of (15.20), this CRB does not change with P, and is hence equivalent to the CRB for the conventional training-based method (which takes $P = 0$). Therefore, the GML method has no advantage over the conventional training-based method in this case.

Remark 15.4. A closed-form GML channel estimate can be obtained when $N_t = 1$ and $P = L$. First, observe that when $N_t = 1$ and $P = L$, $\boldsymbol{\mathcal{X}}_k^{(t)}$ can be written as

$$\boldsymbol{\mathcal{X}}_k^{(t)} = \mathbf{I}_{L+1} \otimes \mathbf{x}_k^{(t)T} = \mathbf{I}_{L+1} \otimes \mathbf{x}^T(n_k). \tag{15.43}$$

Due to this special structure, it can be shown that (15.38) becomes independent of $\hat{\mathbf{Q}}$ as long as it is invertible. As a result, the iterative approach converges in one step and the closed-form GML channel estimate is given by

$$\mathbf{h}_{\mathrm{ML}} = \left[\mathbf{I}_{L+1} \otimes \left(\sum_{k=0}^{K-1} \mathbf{x}^*(n_k)\mathbf{x}^T(n_k)\right)^{-1} \otimes \mathbf{I}\right]\sum_{k=0}^{K-1}\left(\mathbf{I}_{L+1} \otimes \mathbf{x}^*(n_k) \otimes \mathbf{I}\right)\mathbf{y}_k. \tag{15.44}$$

The CRB (15.40) becomes

$$\mathrm{CRB}_{\mathrm{GML}} = \left[\sum_{k=0}^{K-1} (\mathbf{I}_{L+1} \otimes \mathbf{x}^*(n_k) \otimes \mathbf{I})\mathbf{Q}^{-1}(\mathbf{I}_{L+1} \otimes \mathbf{x}^T(n_k) \otimes \mathbf{I})\right]^{-1}. \tag{15.45}$$

Note that in this case, we can again decouple the problem into the different receive antennas.

15.5. Semiblind channel estimation

15.5.1. A combined cost function

The enhanced training-based methods discussed in the previous section can be viewed as semiblind channel estimation methods, albeit in a limited form. We discuss in this section the combination of training-based methods (conventional or enhanced) with purely blind methods. We can arrive at such methods by combining the cost functions in Sections 15.3 or 15.4 with a blind criterion. We will limit ourselves to quadratic blind criteria which usually result from deterministic blind methods or stochastic blind methods based on second-order statistics (SOS). It would also be possible to exploit higher-order statistics (HOS) [9, 10] or constant modulus and finite-alphabet properties.

For the sake of simplicity, we restrict our attention to the conventional training-based criterion (15.13). Combining this criterion with a quadratic blind criterion, we obtain a semiblind problem that often can be formulated as

$$\mathbf{h}_o = \arg\min_{\mathbf{h}} \sum_{k=0}^{K-1} \left\| \mathbf{y}_k - \left(\mathcal{X}_k^{(t)} \otimes \mathbf{I}\right)\mathbf{h} \right\|^2 + \alpha \|\mathbf{V}\mathbf{H}\|^2, \tag{15.46}$$

where $\mathbf{H} = [\mathbf{H}^T(0), \ldots, \mathbf{H}^T(L)]^T$, and $\mathbf{V} = [\mathbf{V}(0), \ldots, \mathbf{V}(L)]$ is a matrix which depends on the received data and can be constructed in many different ways depending on the blind criterion that will be adopted, as discussed later on.

To rewrite this as a single condition on $\mathbf{h}$, let $\mathbf{W} = [\mathbf{W}(0), \ldots, \mathbf{W}(L)]$ be a matrix such that $\text{vec}(\mathbf{V}\mathbf{H}) = \mathbf{W}\mathbf{h}$. In particular, since

$$\text{vec}\left(\mathbf{V}(l)\mathbf{H}(l)\right) = \left(\mathbf{I}_{A_t} \otimes \mathbf{V}(l)\right) \text{vec}\left(\mathbf{H}(l)\right) = \mathbf{W}(l)\mathbf{h}(l), \tag{15.47}$$

$\mathbf{W}(l)$ is given by $\mathbf{W}(l) = \mathbf{I}_{A_t} \otimes \mathbf{V}(l)$. In terms of $\mathbf{W}$, the problem (15.46) can be rewritten as

$$\mathbf{h}_o = \arg\min_{\mathbf{h}} \sum_{k=0}^{K-1} \left\| \mathbf{y}_k - \left(\mathcal{X}_k^{(t)} \otimes \mathbf{I}\right)\mathbf{h} \right\|^2 + \alpha \|\mathbf{W}\mathbf{h}\|^2, \tag{15.48}$$

the solution of which is given by

$$\mathbf{h}_o = \left[\left(\sum_{k=0}^{K-1} \mathcal{X}_k^{(t)H} \mathcal{X}_k^{(t)} \right) \otimes \mathbf{I} + \alpha \mathbf{W}^H \mathbf{W} \right]^{-1} \sum_{k=0}^{K-1} \left(\mathcal{X}_k^{(t)H} \otimes \mathbf{I}\right)\mathbf{y}_k. \tag{15.49}$$

Note that the choice of a good weighting factor α will be crucial. We will come back to this in Section 15.5.4.

The matrix $\mathbf{V}$ in (15.46) can be obtained from many recently proposed blind MIMO channel estimation algorithms that determine the channel $\mathbf{H}$ up to an invertible (sometimes unitary) matrix. Usually, HOS are used to resolve this ambiguity. Here, the training-based part will take care of that (we assume that the channel

is identifiable using only the training part). Generally, only the received sample vectors that depend completely on unknown data symbol vectors are taken into account in the blind criterion. However, in the considered setup, this would mean that a lot of blind structural information is lost, because the training symbol vectors break up the total burst in many different pieces. In this work, we therefore construct the blind criterion based on all received sample vectors in order not to lose any blind information.

As examples on the construction of $\mathbf{V}$, we will present in Sections 15.5.2 and 15.5.3 two deterministic blind algorithms, capable of perfectly estimating $\mathbf{H}$ (up to an invertible matrix) using a finite number of samples in the absence of noise. The first is the subspace (SS) approach [11, 12, 13] whereas the second is the least-squares smoothing (LSS) approach [14, 15].

15.5.2. Subspace approach

The first example of a blind MIMO channel estimation algorithm is the so-called subspace approach, defined in [12, 13] (introduced in [11] for the SIMO case). Let $\mathcal{Y}$ be an extended data matrix constructed from the received sample vectors as

$$\mathcal{Y} = \begin{bmatrix} \mathbf{y}(L) & \mathbf{y}(L+1) & \cdots & \mathbf{y}(N-Q-1) \\ \vdots & \vdots & & \vdots \\ \mathbf{y}(L+Q) & \mathbf{y}(L+Q+1) & \cdots & \mathbf{y}(N-1) \end{bmatrix}. \tag{15.50}$$

$\mathcal{Y}$ is an $A_r(Q+1)\times(N-L-Q)$ block Hankel matrix, where Q is a design parameter that can be interpreted as the filter order of an equalizer acting on the sequence $\mathbf{y}(n)$, and is usually called the smoothing factor. This matrix can be written as

$$\mathcal{Y} = \mathcal{H}_Q \mathcal{X} + \mathcal{E}, \tag{15.51}$$

where the additive noise matrix $\mathcal{E}$ is similarly defined as $\mathcal{Y}$, $\mathcal{H}_Q$ is the $A_r(Q+1)\times A_t(L+Q+1)$ block Toeplitz channel matrix that is similarly defined as $\mathcal{H}$ in Figure 15.2 but with different dimensions, and $\mathcal{X}$ is the $A_t(L+Q+1)\times(N-L-Q)$ block Hankel data symbol matrix given by

$$\mathcal{X} = \begin{bmatrix} \mathbf{x}(0) & \cdots & \mathbf{x}(N-L-Q-1) \\ \vdots & & \vdots \\ \mathbf{x}(L+Q) & \cdots & \mathbf{x}(N-1) \end{bmatrix}. \tag{15.52}$$

We assume that there is no noise. If $\mathcal{H}_Q$ is tall and of full-column rank, and $\mathcal{X}$ is wide and of full-row rank, then $\mathcal{Y} = \mathcal{H}_Q\mathcal{X}$ is a low-rank factorization, and therefore $\mathcal{Y}$ has a nonempty left null space of dimension $d_{\mathrm{SS}} = A_r(Q+1) - A_t(L+Q+1)$. Denoting the $A_r(Q+1)\times d_{\mathrm{SS}}$ matrix $\mathbf{U}_{\mathrm{SS}}$ as the left singular vectors of $\mathcal{Y}$ corresponding to this null space, we have

$$\mathcal{H}_Q^H \mathbf{U}_{\mathrm{SS}} = \mathbf{0}_{A_t(L+Q+1)\times d_{\mathrm{SS}}}. \tag{15.53}$$

Each block row of (15.53) gives a linear relation on the block entries $\mathbf{H}(l)$ inside the structured matrix $\mathcal{H}_Q$. Subsequently, we use this structure to rewrite the equation:

$$\mathcal{H}_Q^H \mathbf{U}_{\mathrm{SS}} = \begin{bmatrix} \mathbf{H}^H(L) & & \\ \vdots & \ddots & \\ \mathbf{H}^H(0) & & \mathbf{H}^H(L) \\ & \ddots & \vdots \\ & & \mathbf{H}^H(0) \end{bmatrix} \begin{bmatrix} \mathbf{U}_{\mathrm{SS}}(0) \\ \vdots \\ \mathbf{U}_{\mathrm{SS}}(Q) \end{bmatrix} = \mathbf{0}_{A_t(L+Q+1)\times d_{\mathrm{SS}}}$$

$$\Updownarrow$$

$$\left[\mathbf{H}^H(0)\cdots\mathbf{H}^H(L)\right] \begin{bmatrix} \mathbf{U}_{\mathrm{SS}}(Q) & \cdots & \mathbf{U}_{\mathrm{SS}}(0) & & \\ & \ddots & & \ddots & \\ & & \mathbf{U}_{\mathrm{SS}}(Q) & \cdots & \mathbf{U}_{\mathrm{SS}}(0) \end{bmatrix} = \mathbf{H}^H \mathcal{U}_{\mathrm{SS}} = \mathbf{0}_{A_t\times d_{\mathrm{SS}}}. \tag{15.54}$$

As a result, we can choose $\mathbf{V} = \mathbf{V}_{\mathrm{SS}} = \mathcal{U}_{\mathrm{SS}}^H$ in (15.46). In the noiseless case, the solution is unique (up to an invertible matrix) if $\mathcal{H}_Q$ has full-column rank and $\mathcal{X}$ has full-row rank.

15.5.3. Least-squares smoothing approach

A second blind MIMO channel estimation technique is the so-called least-squares smoothing approach [15] (introduced in [14] for the SIMO case). Define the following block Hankel received sample matrices (viz., Figure 15.5):

$$\mathcal{Y}_p = \begin{bmatrix} \mathbf{y}(L) & \cdots & \mathbf{y}(N-2Q-L-3) \\ \vdots & & \vdots \\ \mathbf{y}(Q+L) & \cdots & \mathbf{y}(N-Q-L-3) \end{bmatrix} : A_r(Q+1)\times[N-2(Q+L+1)],$$

$$\mathcal{Y}_c = \begin{bmatrix} \mathbf{y}(Q+L+1) & \cdots & \mathbf{y}(N-Q-L-2) \\ \vdots & & \vdots \\ \mathbf{y}(Q+2L+1) & \cdots & \mathbf{y}(N-Q-2) \end{bmatrix} : A_r(L+1)\times[N-2(Q+L+1)],$$

$$\mathcal{Y}_f = \begin{bmatrix} \mathbf{y}(Q+2L+2) & \cdots & \mathbf{y}(N-Q-1) \\ \vdots & & \vdots \\ \mathbf{y}(2Q+2L+2) & \cdots & \mathbf{y}(N-1) \end{bmatrix} : A_r(Q+1)\times[N-2(Q+L+1)], \tag{15.55}$$

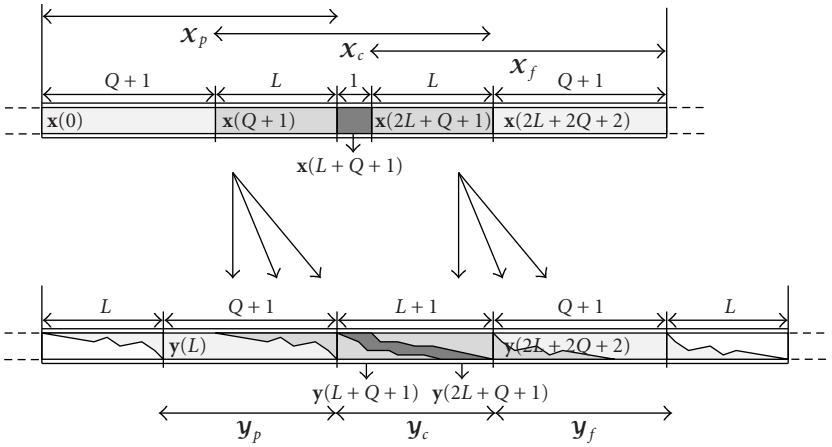

FIGURE 15.5. Least-squares smoothing data model.

corresponding to the "past," "current," and "future." L is the smoothing factor for $\mathcal{Y}_c$, and Q is the smoothing factor for $\mathcal{Y}_p$ and $\mathcal{Y}_f$. These matrices have the following models:

$$\begin{aligned}\mathcal{Y}_p &= \mathcal{H}_Q \mathcal{X}_p + \mathcal{E}_p,\\ \mathcal{Y}_c &= \mathcal{H}_L \mathcal{X}_c + \mathcal{E}_c,\\ \mathcal{Y}_f &= \mathcal{H}_Q \mathcal{X}_f + \mathcal{E}_f,\end{aligned} \tag{15.56}$$

where $\mathcal{H}_Q$ and $\mathcal{H}_L$ are $A_r(Q+1)\times A_t(Q+L+1)$ and $A_r(L+1)\times A_t(2L+1)$ block Toeplitz channel matrices, and $\mathcal{X}_p$, $\mathcal{X}_c$, and $\mathcal{X}_f$ are the past, current, and future block Hankel data symbol matrices given by

$$\mathcal{X}_p = \begin{bmatrix} \mathbf{x}(0) & \cdots & \mathbf{x}(N-2Q-2L-3) \\ \vdots & & \vdots \\ \mathbf{x}(Q+L) & \cdots & \mathbf{x}(N-Q-L-3) \end{bmatrix} : A_t(Q+L+1)\times[N-2(Q+L+1)],$$

$$\mathcal{X}_c = \begin{bmatrix} \mathbf{x}(Q+1) & \cdots & \mathbf{x}(N-Q-2L-2) \\ \vdots & & \vdots \\ \mathbf{x}(Q+2L+1) & \cdots & \mathbf{x}(N-Q-2) \end{bmatrix} : A_t(2L+1)\times[N-2(Q+L+1)],$$

$$\mathcal{X}_f = \begin{bmatrix} \mathbf{x}(Q+L+2) & \cdots & \mathbf{x}(N-Q-L-1) \\ \vdots & & \vdots \\ \mathbf{x}(2Q+2L+2) & \cdots & \mathbf{x}(N-1) \end{bmatrix} : A_t(Q+L+1)\times[N-2(Q+L+1)]. \tag{15.57}$$

Note that all the block rows of $\boldsymbol{\mathcal{X}}_c$, except for the block row

$$\mathbf{X} = \big[\mathbf{x}(Q+L+1), \ldots, \mathbf{x}(N-Q-L-2)\big], \tag{15.58}$$

are contained in $\boldsymbol{\mathcal{X}}_p$ and $\boldsymbol{\mathcal{X}}_f$. Hence, all different block rows can be collected in

$$\boldsymbol{\mathcal{X}}_{\text{tot}} = \big[\boldsymbol{\mathcal{X}}_p^T, \mathbf{X}^T, \boldsymbol{\mathcal{X}}_f^T\big]^T. \tag{15.59}$$

We assume that there is no noise. If $\boldsymbol{\mathcal{H}}_Q$ is tall and of full-column rank and $\boldsymbol{\mathcal{X}}_{\text{tot}}$ is wide and of full-row rank, then the orthogonal projection of $\boldsymbol{\mathcal{Y}}_c$ onto the orthogonal complement of the row space of $\boldsymbol{\mathcal{X}}_{p,f} = [\boldsymbol{\mathcal{X}}_p^T, \boldsymbol{\mathcal{X}}_f^T]^T$ is equal to the orthogonal projection of $\boldsymbol{\mathcal{Y}}_c$ onto the orthogonal complement of the row space of $\boldsymbol{\mathcal{Y}}_{p,f} = [\boldsymbol{\mathcal{Y}}_p^T, \boldsymbol{\mathcal{Y}}_f^T]^T$, and it is given by

$$\boldsymbol{\mathcal{Y}}_c \mathbf{P}_{\text{row}}^{\perp}(\boldsymbol{\mathcal{Y}}_{p,f}) = \boldsymbol{\mathcal{Y}}_c \mathbf{P}_{\text{row}}^{\perp}(\boldsymbol{\mathcal{X}}_{p,f}) = \mathbf{H}\mathbf{X}\mathbf{P}_{\text{row}}^{\perp}(\boldsymbol{\mathcal{X}}_{p,f}), \tag{15.60}$$

where $\mathbf{P}_{\text{row}}^{\perp}(\mathbf{A}) = \mathbf{I} - \mathbf{A}^{\dagger}\mathbf{A}$ is the projection matrix onto the orthogonal complement of the row space of $\mathbf{A}$. In addition, $\mathbf{H}$ has full-column rank and $\mathbf{X}\mathbf{P}_{\text{row}}^{\perp}(\boldsymbol{\mathcal{X}}_{p,f})$ has full-row rank, which means that the column span of $\boldsymbol{\mathcal{Y}}_c \mathbf{P}_{\text{row}}^{\perp}(\boldsymbol{\mathcal{Y}}_{p,f})$ coincides with the column span of $\mathbf{H}$. Let $\mathbf{U}_{\text{LSS}}$ be a matrix containing the left null space vectors of $\boldsymbol{\mathcal{Y}}_c \mathbf{P}_{\text{row}}^{\perp}(\boldsymbol{\mathcal{Y}}_{p,f})$. $\mathbf{U}_{\text{LSS}}$ has size $A_r(L+1) \times d_{\text{LSS}}$, where $d_{\text{LSS}} = A_r(L+1) - A_t$, and

$$\mathbf{H}^H \mathbf{U}_{\text{LSS}} = \mathbf{0}_{A_t \times d_{\text{LSS}}}. \tag{15.61}$$

In terms of the semiblind criterion, we can take $\mathbf{V} = \mathbf{V}_{\text{LSS}} = \mathbf{U}_{\text{LSS}}^H$ in (15.46). In the noiseless case, the blind solution is unique (up to an invertible matrix) if $\boldsymbol{\mathcal{H}}_Q$ has full-column rank and $\boldsymbol{\mathcal{X}}_{\text{tot}}$ has full-row rank.

15.5.4. Weighting factor

In (15.46), a weighting factor α scales the blind equation error relative to the training error. The choice of α is important: with an incorrect setting, the channel estimate can be worse than a training-only estimate! Ideally, one would want to choose α to minimize the channel MSE.

This is a well-known but essentially unsolved problem in semiblind channel estimation; an extensive discussion can be found in [6]. One heuristic way of handling the problem is trying to avoid it by adapting the blind cost function in such a way that the MSE becomes less sensitive to α, for example, by "denoising" [6]: a technique where the smallest eigenvalue of $\mathbf{W}^H\mathbf{W}$ is forced to zero by replacing $\mathbf{W}^H\mathbf{W}$ by $\mathbf{W}^H\mathbf{W} - \lambda_{\min}\mathbf{I}$, where $\lambda_{\min}$ is the minimal eigenvalue of $\mathbf{W}^H\mathbf{W}$. One could also try to find the optimal α in terms of the channel MSE, but this is usually very hard and represents a large computational cost.

15.5.5. Other blind channel estimation algorithms

The SS and LSS approaches basically require that all sources have the same channel order and that this channel order is known. Related to this latter requirement, it must be said that, in contrast to the SS approach, the LSS approach allows for a simple joint order-channel estimation technique (illustrated in [14] for the SIMO case).

To avoid the sensitive requirement on knowledge of the channel length as present in the SS and LSS techniques, some interesting stochastic blind techniques based on SOS have been developed, such as the outer-product decomposition (OPD) approach [15, 16, 17], and the multistep linear prediction (MSLP) approach [15, 18, 19], which is a generalization of the earlier (one-step) linear prediction (LP) approach [15, 20, 21, 22, 23]. Note that for the latter, a corresponding semiblind MIMO channel estimation procedure has been developed in [24]. The OPD and MLSP are closely related to each other and can be viewed as a stochastic version of the LSS approach. They do not require that all sources have the same channel order and that this channel order is known. However, they require the different sources to be zero-mean white (spatially and temporally), which is not always the case, for example, when space-time coding is used. Moreover, since the training-based part that we include in the cost function can remove any ambiguity problems due to the above identifiability requirements, we have observed that the deterministic techniques are to be preferred in a semiblind context if the total burst length N is short.

15.6. Simulation results

To finish the chapter, the proposed techniques are illustrated by means of simulation. We assume that the $A_t \times A_r$ MIMO channel $\mathbf{H}(l)$ of order L is Rayleigh fading, that is, has zero-mean Gaussian distributed channel taps. We further assume that these channel taps are i.i.d. with variance σ_h^2. Although the proposed methods are able to handle sources with correlations that are spatially or temporally colored, for example, due to space-time coding, we assume here a simple spatial multiplexing approach where the unknown data symbols are zero-mean i.i.d. (spatially and temporally) QPSK modulated with symbol energy 1. If possible, the training symbols are designed according to one of the optimal training strategies discussed in Section 15.3.2 in such a way that the average symbol energy is 1. If not possible, for example, when $N_t = 1$ as illustrated below, they are designed in a similar way as the unknown data symbols, with unit energy. The noise variance is σ_e^2, and the received signal-to-noise ratio (SNR) per transmit antenna is defined as

$$\mathrm{SNR} = \frac{(L+1)\sigma_h^2}{\sigma_e^2}. \tag{15.62}$$

To compare the different channel estimation methods, we will use the normalized

MSE (NMSE) as performance measure, which can be defined as

$$\text{NMSE} = \frac{1}{R}\sum_{r=0}^{R-1}\frac{\left\|\hat{\mathbf{h}}^{(r)} - \mathbf{h}^{(r)}\right\|^2}{(L+1)A_tA_r\sigma_h^2}, \tag{15.63}$$

where the superscript r indicates the simulation run, and R is the total number of runs. Note that in each run, we will consider a new channel, data, and noise realization. First, we will compare the different training-based methods. Next, we study the performance of the presented semiblind channel estimation procedures.

15.6.1. Training-based results

We consider a MIMO system with $A_t = 2$ transmit antennas and $A_r = 1, 2, 4$ receive antennas. The channel order we simulate is $L = 3$. For the enhanced training-based methods, we take $P = L = 3$ and we carry out three iterations (unless of course the method converges in one step). The total number of symbol blocks that will be taken into account is given by $K = 100$. To make a fair comparison between the different numbers, of receive antennas, we consider $R = 400, 200, 100$ simulation runs for $A_r = 1, 2, 4$ receive antennas, respectively. Note that decreasing A_r can be viewed either as reducing the number of receive antennas, or as treating the different receive antennas in smaller subgroups.

First, we take $N_t = 2L + 1 = 7$, such that we can implement the optimal training strategy of Section 15.3.2.1. From Remark 15.1, we know that the conventional ML method with $A_r = 1, 2, 4$ and the DML method with $A_r = 1, 2$ will produce the same result in this case. The DML method with $A_r = 4$ and the GML method with $A_r = 1, 2, 4$, on the other hand, will result in a different performance. However, since the GML method will not be able to outperform the conventional ML method in this case (see Remark 15.3), we will not consider it here. The simulation results and CRBs are shown in Figure 15.6. We observe that the simulation results match the CRBs well. We also notice that the DML method with $A_r = 4$ does a little bit better than the other methods.

Next, we take $N_t = L + 1 = 4$, such that we can implement the optimal training strategy of Section 15.3.2.2; the results are shown in Figure 15.6. From Remark 15.1, we can again deduce that the conventional ML method with $A_r = 1, 2, 4$ and the DML method with $A_r = 1, 2$ are the same. As before, the DML method with $A_r = 4$ and the GML method with $A_r = 1, 2, 4$ will be different, but this time there is no indication that the GML method cannot beat the conventional ML method. Hence, all methods will be considered. From Figure 15.6, we observe that the conventional ML method with $A_r = 1, 2, 4$ and the DML method with $A_r = 1, 2$ closely approach their CRB, which is by the way the worst among all CRBs. The DML method with $A_r = 4$ has the best CRB, but the simulated performance is saturated at high SNR. The saturation level can be lowered by increasing the number of iterations, but it goes slowly. The CRB of the GML method is somewhere in between and improves with A_r. As for the DML method with $A_r = 4$, its

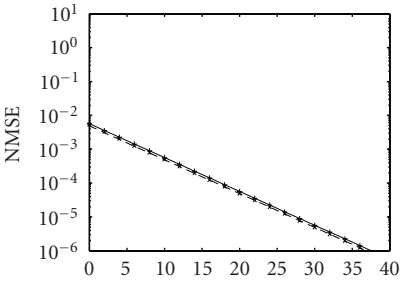

× sim. DML ($A_r = 4$)
+ sim. conv. ($A_r = 1, 2, 4$), sim. DML ($A_r = 1, 2$)
--- CRB DML ($A_r = 4$)
—— CRB conv. ($A_r = 1, 2, 4$), CRB DML ($A_r = 1, 2$)

(a)

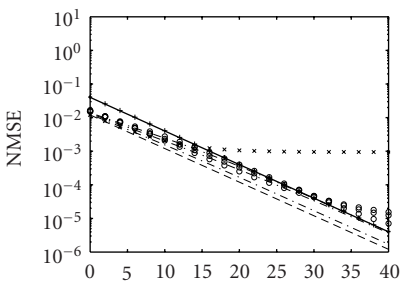

× sim. DML ($A_r = 4$)
○ sim. GML ($A_r = 1, 2, 4$)
+ sim. conv. ($A_r = 1, 2, 4$), sim. DML ($A_r = 1, 2$)
--- CRB DML ($A_r = 4$)
-·-· CRB GML ($A_r = 1, 2, 4$)
—— CRB conv. ($A_r = 1, 2, 4$), CRB DML ($A_r = 1, 2$)

(b)

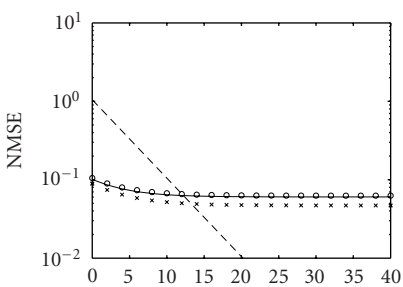

× sim. DML ($A_r = 4$)
--- CRB DML ($A_r = 4$)
○ sim. GML ($A_r = 1, 2, 4$)
—— CRB GML ($A_r = 1, 2, 4$)

(c)

FIGURE 15.6. Training-based algorithms: comparison of the different methods: (a) for $N_t = 2L+1 = 7$, (b) for $N_t = L + 1 = 4$, (c) for $N_t = 1$.

simulated performance moves away from the CRB, but not as much. In addition, only a few more iterations will shift the simulated performance close to its CRB.

We finally consider a situation where the conventional ML method cannot be used due to the fact that $N_t < L + 1$. This happens for instance for the pilot symbol assisted modulation (PSAM) scheme [25], where training symbols (pilots) are periodically inserted in the total burst. In the considered MIMO setup, the PSAM approach corresponds to taking $N_t = 1$. From Remark 15.2, we know that the DML method with $A_r = 1, 2$ corresponds to the first step of the GML method with $A_r = 1, 2$, and thus should not be considered. Remark 15.4, on the other hand, tells us that the GML method converges in one step and performs the same for $A_r = 1, 2, 4$. Only the DML method with $A_r = 4$ does better, as can be observed from Figure 15.6. Notice that whereas the GML method performs close to its CRB, the performance of the DML method with $A_r = 4$ is generally far from its CRB (in a positive sense at low SNR, but in a negative sense at high SNR). This gap reduces by increasing the number of iterations, but this goes very slowly.

15.6.2. Semiblind results

In this section, we illustrate the performance of the semiblind methods. We consider a MIMO system with $A_t = 2$ transmit antennas and $A_r = 4$ receive antennas. Note that $A_r > A_t$ is required for the semiblind criterion to be useful (this is in contrast with the enhanced training-based methods). The channel order is again assumed to be $L = 3$. We consider $K = 10$ symbols blocks, $N_t = 7$ training symbol vectors per block, and $N_d = 80$ unknown data symbol vectors per block (as a result, we have a total of $N = K(N_t + N_d) = 870$ symbol vectors in one burst). Since $N_t = 2L + 1 = 7$, we again use the optimal training strategy of Section 15.3.2.1. We consider $R = 100$ simulation runs and the received SNR per transmit antenna is set to 15 dB. Figure 15.7 compares the performance of the semiblind method using the subspace and the least-squares smoothing criterion with the conventional training-based method as a function of α. Clearly, at the optimal α (different for the two aproaches), the semiblind method outperforms the conventional training-based method. We also observe that the subspace approach does better than the least-squares smoothing approach. A similar behavior was observed for different settings.

15.7. Conclusions and additional pointers

This chapter has covered only a very small part of the available literature. As a general reference to wireless channel estimation algorithms, we suggest the edited book [26] and the overview article [27].

Optimal training symbol placement and design has recently become a popular topic, for example, in context of capacity maximization; some contributions are [28, 29, 30, 31, 32]. In particular relevant to the discussion in this chapter is [30], which gives optimal placement of training symbols in the semiblind context based

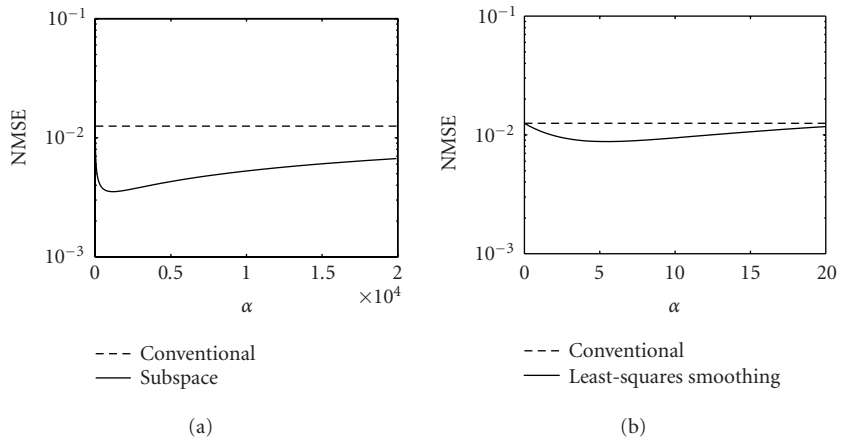

FIGURE 15.7. Semiblind algorithms: comparison of the different methods: (a) subspace method, (b) least-squares smoothing method.

on Cramér-Rao bound (CRB) considerations (i.e., minimizing the MSE of the channel estimate and unknown data symbols).

In this chapter, we did not cover multicarrier MIMO systems (e.g., based on orthogonal frequency division multiplexing (OFDM)). For these systems, the frequency-selective channel can be transformed into a set of parallel frequency-flat (or instantaneous) channels. Although each subband is a special case of a single-carrier MIMO system, more optimal methods can be adopted by exploiting the OFDM structure (the dependencies between subbands). For more details in this direction, we refer to [31, 32, 33, 34, 35] and references therein.

A new trend in the field of channel estimation considers *linear time-varying (LTV) channels*. Here, the channel is assumed to vary over a data block. There are two approaches: (i) channel tracking, where an initial estimate is updated as time progresses, and (ii) model-based block solutions, where the number of unknown channel coefficients is limited via a parametric model for the channel time variation, such as an exponential or polynomial basis expansion model. These parametric models are studied in, for example, [36, 37, 38, 39].

Another recent trend is to consider *superimposed training*. The schemes in this chapter were based on time-division multiplexing. Superimposed training is to add to the data stream $x^{(d)}(t)$ a known training signal $x^{(t)}(t)$, so that $x(t) = x^{(d)}(t)+x^{(t)}(t)$. Channel estimation is possible, for example, if the data symbols are i.i.d. and zero-mean, whereas the pilot has certain periodicities (cyclostationary properties) [40].

For the FIR-SIMO case, semiblind methods of the type we discussed have been presented in [6, 41]. Some of the earlier (FIR-SISO) semiblind papers are [42, 43, 44, 45]. In Section 15.5, we presented two deterministic techniques for blind channel estimation. In general, such techniques may exploit (i) the convolutive structure (Hankel/Toeplitz), via oversampling or multiple channels, (ii) instantaneous properties of the sources, such as their finite alphabet and constant

modulus, or (iii) stochastic properties such as statistical independence and cyclostationarity. This area has seen tremendous activity in the 1990s. Overviews can be found in [26, 46, 47, 48]. There are also several examples of algorithms which combine training with blind source properties, but the topic has not systematically been researched. As mentioned in Section 15.5.4, the problem of "α"-scaling of the training versus blind parts of the cost function remains essentially open, although several heuristics are known [6].

Acknowledgments

This work was supported by NWO-STW under the VICI programme (DTC.5893), and the Commission of the EC under contract no. 506790 (IST STREP "UBROAD").

Abbreviations

CRB	Cramér-Rao bound
DML	Deterministic ML
FIR	Finite impulse response
GML	Gaussian ML
HOS	Higher-order statistics
LMMSE	Linear minimum mean square error
LP	Linear prediction
LS	Least-squares
LSS	Least-squares smoothing
LTV	Linear time-varying
MIMO	Multi-input multi-output
ML	Maximum likelihood
MSE	Mean square error
MSLP	Multistep linear prediction
NMSE	Normalized MSE
OFDM	Orthogonal frequency division multiplexing
OPD	Outer-product decomposition
PSAM	Pilot symbol assisted modulation
QPSK	Quadrature phase-shift keying
SIMO	Single-input multiple-output
SISO	Single-input single-output
SNR	Signal-to-noise ratio
SOS	Second-order statistics
SS	Subspace

Bibliography

[1] W. Jakes, Ed., *Microwave Mobile Communications*, Wiley-IEEE Press, New York, NY, USA, 1994.

[2] O. Simeone and U. Spagnolini, "Lower bounds on the channel estimation error for fast-varying frequency-selective Rayleigh MIMO channels," in *Proc. IEEE International Conference on Acoustics, Speech, Signal Processing (ICASSP '03)*, vol. 5, pp. 69–72, Hongkong, China, April 2003.

[3] X. Ma, L. Yang, and G. B. Giannakis, "Optimal training for MIMO frequency-selective fading channels," in *Proc. 36th Asilomar Conference on Signals, Systems, and Computers*, vol. 2, pp. 1107–1111, Pacific Grove, Calif, USA, November 2002.

[4] S. Talwar, M. Viberg, and A. Paulraj, "Blind separation of synchronous co-channel digital signals using an antenna array. I. Algorithms," *IEEE Trans. Signal Processing*, vol. 44, no. 5, pp. 1184–1197, 1996.

[5] V. A. N. Barroso, J. M. F. Moura, and J. Xavier, "Blind array channel division multiple access (AChDMA) for mobile communications," *IEEE Trans. Signal Processing*, vol. 46, no. 3, pp. 737–752, 1998.

[6] E. de Carvalho and D. T. M. Slock, "Semi-blind methods for FIR multichannel estimation," in *Signal Processing Advances in Wireless and Mobile Communications: Trends in Channel Estimation and Equalization*, G. B. Giannakis, P. Stoica, Y. Hua, and L. Tong, Eds., vol. 1, chapter 7, pp. 211–254, Prentice Hall, Englewood Cliffs, NJ, USA, 2000.

[7] E. de Carvalho and D. T. M. Slock, "Cramér-Rao bounds for semi-blind, blind and training sequence based channel estimation," in *Proc. 1st IEEE Signal Processing Workshop on Signal Processing Advances in Wireless Communications (SPAWC '97)*, pp. 129–132, Paris, France, April 1997.

[8] O. Rousseaux, G. Leus, P. Stoica, and M. Moonen, "Gaussian maximum likelihood channel estimation with short training sequences," to appear in *IEEE Trans. Wireless Comm.*; see also *Proc. Globecom '03*.

[9] J. K. Tugnait, "Identification and deconvolution of multichannel linear non-Gaussian processes using higher order statistics and inverse filter criteria," *IEEE Trans. Signal Processing*, vol. 45, no. 3, pp. 658–672, 1997.

[10] J. K. Tugnait, "On blind separation of convolutive mixtures of independent linear signals in unknown additive noise," *IEEE Trans. Signal Processing*, vol. 46, no. 11, pp. 3117–3123, 1998.

[11] E. Moulines, P. Duhamel, J.-F. Cardoso, and S. Mayrargue, "Subspace methods for the blind identification of multichannel FIR filters," *IEEE Trans. Signal Processing*, vol. 43, no. 2, pp. 516–525, 1995.

[12] K. Abed-Meraim, P. Loubaton, and E. Moulines, "A subspace algorithm for certain blind identification problems," *IEEE Trans. Inform. Theory*, vol. 43, no. 2, pp. 499–511, 1997.

[13] P. Loubaton, E. Moulines, and P. Regalia, "Subspace method for blind identification and deconvolution," in *Signal Processing Advances in Wireless and Mobile Communications: Trends in Channel Estimation and Equalization*, G. B. Giannakis, Y. Hua, P. Stoica, and L. Tong, Eds., vol. 1, chapter 3, pp. 63–112, Prentice Hall, Englewood Cliffs, NJ, USA, 2000.

[14] L. Tong and Q. Zhao, "Joint order detection and blind channel estimation by least squares smoothing," *IEEE Trans. Signal Processing*, vol. 47, no. 9, pp. 2345–2355, 1999.

[15] Z. Ding, "Linear predictive algorithms for blind multichannel identification," in *Signal Processing Advances in Wireless and Mobile Communications: Trends in Channel Estimation and Equalization*, G. B. Giannakis, Y. Hua, P. Stoica, and L. Tong, Eds., vol. 1, chapter 6, pp. 179–210, Prentice Hall, Englewood Cliffs, NJ, USA, 2000.

[16] Z. Ding, "Matrix outer-product decomposition method for blind multiple channel identification," *IEEE Trans. Signal Processing*, vol. 45, no. 12, pp. 3053–3061, 1997.

[17] Z. Ding and L. Qiu, "Blind MIMO channel identification from second order statistics using rank deficient channel convolution matrix," *IEEE Trans. Signal Processing*, vol. 51, no. 2, pp. 535–544, 2003.

[18] D. Gesbert and P. Duhamel, "Robust blind channel identification and equalization based on multi-step predictors," in *Proc. IEEE International Conference on Acoustics, Speech, and Signal Processing (ICASSP '97)*, vol. 5, pp. 3621–3624, Munich, Germany, April 1997.

[19] J. K. Tugnait and B. Huang, "Multistep linear predictors-based blind identification and equalization of multiple-input multiple-output channels," *IEEE Trans. Signal Processing*, vol. 48, no. 1, pp. 26–38, 2000.

[20] D. T. M. Slock, "Blind fractionally-spaced equalization, perfect-reconstruction filter banks and multichannel linear prediction," in *Proc. IEEE International Conference on Acoustics, Speech, and Signal Processing (ICASSP '94)*, vol. 4, pp. 585–588, Adelaide, SA, Australia, April 1994.

[21] K. Abed-Meraim, E. Moulines, and P. Loubaton, "Prediction error method for second-order blind identification," *IEEE Trans. Signal Processing*, vol. 45, no. 3, pp. 694–705, 1997.

[22] D. T. M. Slock, "Blind joint equalization of multiple synchronous mobile users using oversampling and/or multiple antennas," in *Proc. 28th Asilomar Conference on Signals, Systems and Computers*, vol. 2, pp. 1154–1158, Pacific Grove, Calif, USA, October/November 1994.

[23] A. Gorokhov and P. Loubaton, "Blind identification of MIMO-FIR systems: a generalized linear prediction approach," *Signal Processing*, vol. 73, no. 1-2, pp. 105–124, 1999.

[24] A. Medles, D. T. M. Slock, and E. de Carvalho, "Linear prediction based semi-blind estimation of MIMO FIR channels," in *Proc. IEEE 3rd Workshop on Signal Processing Advances in Wireless Communications (SPAWC '01)*, pp. 58–61, Taiwan, China, March 2001.

[25] J. K. Cavers, "An analysis of pilot symbol assisted modulation for Rayleigh fading channels," *IEEE Trans. Veh. Technol.*, vol. 40, no. 4, pp. 686–693, 1991.

[26] G. B. Giannakis, Y. Hua, P. Stoica, and L. Tong, Eds., *Signal Processing Advances in Wireless and Mobile Communications: Trends in Channel Estimation and Equalization*, vol. 1, Prentice Hall, Englewood Cliffs, NJ, USA, 2000.

[27] J. K. Tugnait, L. Tong, and Z. Ding, "Single-user channel estimation and equalization," *IEEE Signal Processing Mag.*, vol. 17, no. 3, pp. 17–28, 2000.

[28] S. Adireddy and L. Tong, "Detection with embedded known symbols: optimal symbol placement and equalization," in *Proc. IEEE International Conference on Acoustics, Speech, Signal Processing (ICASSP '00)*, vol. 5, pp. 2541–2544, Istanbul, Turkey, Jun 2000.

[29] H. Vikalo, B. Hassibi, B. Hochwald, and T. Kailath, "Optimal training for frequency-selective fading channels," in *Proc. IEEE International Conference on Acoustics, Speech, Signal Processing (ICASSP '01)*, vol. 4, pp. 2105–2108, Salt Lake City, Utah, USA, May 2001.

[30] M. Dong and L. Tong, "Optimal design and placement of pilot symbols for channel estimation," *IEEE Trans. Signal Processing*, vol. 49, no. 12, pp. 3055–3069, 2002.

[31] B. Hassibi and B. Hochwald, "How much training is needed in multiple-antenna wireless links?," *IEEE Trans. Inform. Theory*, vol. 48, no. 4, pp. 951–963, 2003.

[32] S. Adireddy, L. Tong, and H. Viswanathan, "Optimal placement of training for frequency-selective block-fading channels," *IEEE Trans. Inform. Theory*, vol. 48, no. 8, pp. 2338–2353, 2002.

[33] T.-L. Tung and K. Yao, "Channel estimation and optimal power allocation for a multiple-antenna OFDM system," *EURASIP J. Appl. Signal Process.*, vol. 2002, no. 3, pp. 330–339, 2002.

[34] I. Barhumi, G. Leus, and M. Moonen, "Optimal training design for MIMO OFDM systems in mobile wireless channels," *IEEE Trans. Signal Processing*, vol. 51, no. 6, pp. 1615–1624, 2003.

[35] H. Bölcskei, R. W. Heath Jr., and A. J. Paulraj, "Blind channel identification and equalization in OFDM-based multiantenna systems," *IEEE Trans. Signal Processing*, vol. 50, no. 1, pp. 96–109, 2002.

[36] M. K. Tsatsanis and G. B. Giannakis, "Modeling and equalization of rapidly fading channels," *International Journal Adaptive Control Signal Process*, vol. 10, no. 2-3, pp. 159–176, 1996.

[37] G. B. Giannakis and C. Tepedelenlioğlu, "Basis expansion models and diversity techniques for blind equalization of time-varying channels," *Proc. IEEE*, vol. 86, no. 10, pp. 1969–1986, 1998.

[38] X. Ma, G. B. Giannakis, and S. Ohno, "Optimal training for block transmissions over doubly selective wireless fading channels," *IEEE Trans. Signal Processing*, vol. 51, no. 5, pp. 1351–1366, 2003.

[39] G. Leus, I. Barhumi, and M. Moonen, "MMSE time-varying FIR equalization of doubly-selective channels," in *Proc. IEEE International Conference on Acoustics, Speech, Signal Processing (ICASSP '03)*, vol. 4, pp. 485–488, Hongkong, China, April 2003.

[40] J. Tugnait and W. Luo, "On channel estimation using superimposed training and first-order statistics," *IEEE Comm. Letters*, vol. 7, no. 9, pp. 413–415, 2003.

[41] V. Buchoux, O. Cappé, E. Moulines, and A. Gorokhov, "On the performance of semi-blind subspace-based channel estimation," *IEEE Trans. Signal Processing*, vol. 48, no. 6, pp. 1750–1759, 2000.

[42] E. de Carvalho and D. T. M. Slock, "Cramér-Rao bounds for semi-blind, blind and training sequence based channel estimation," in *Proc. 1st IEEE Signal Processing Workshop on Signal Processing Advances in Wireless Communications*, pp. 129–132, Paris, France, April 1997.

[43] E. de Carvalho and D. T. M. Slock, "Maximum-likelihood blind FIR multi-channel estimation with Gaussian prior for the symbols," in *Proc. IEEE International Conference on Acoustics, Speech, Signal Processing (ICASSP '97)*, vol. 5, pp. 3593–3596, Munich, Germany, April 1997.

[44] D. Pal, "Fractionally spaced equalization of multipath channels: a semi-blind approach," in *Proc. IEEE International Conference on Acoustics, Speech, Signal Processing (ICASSP '93)*, vol. 3, pp. 9–12, Minneapolis, Minn, USA, April 1993.

[45] A. Gorokhov and P. Loubaton, "Semi-blind second order identification of convolutive channels," in *Proc. IEEE International Conference on Acoustics, Speech, Signal Processing (ICASSP '97)*, vol. 5, pp. 3905–3908, Munich, Germany, April 1997.

[46] L. Tong and S. Perreau, "Multichannel blind identification: from subspace to maximum likelihood methods," *Proc. IEEE*, vol. 86, no. 10, pp. 1951–1968, 1998.

[47] A.-J. van der Veen, "Algebraic methods for deterministic blind beamforming," *Proc. IEEE*, vol. 86, no. 10, pp. 1987–2008, 1998.

[48] K. Abed-Meraim, W. Qiu, and Y. Hua, "Blind system identification," *Proc. IEEE*, vol. 85, no. 8, pp. 1310–1322, 1997.

Geert Leus: Department of Electrical Engineering, Mathematics and Computer Science (EEMCS), Delft University of Technology, Mekelweg 4, 2628 CD Delft, The Netherlands

Email: leus@cas.et.tudelft.nl

Alle-Jan van der Veen: Department of Electrical Engineering, Mathematics and Computer Science (EEMCS), Delft University of Technology, Mekelweg 4, 2628 CD Delft, The Netherlands

Email: allejan@cas.et.tudelft.nl

16 Direction-of-arrival estimation

Mats Viberg

16.1. Signal models and problem formulation

The purpose of this chapter of the book is to review the area of direction-of-arrival (DOA) estimation, with special focus on wireless communication systems. Such information is useful for understanding the propagation environment, and gives empirical evidence for theoretical propagation models. Both detailed modeling including resolution of all propagation paths, and statistical models of scatter clusters can be of interest. Both these cases will be considered herein. The chapter is organized as follows: first the basic signal models are motivated and the estimation problems are introduced in Section 16.1. Then, in Section 16.2 a brief introduction to the standard DOA estimation problem is given. Section 16.3 considers estimation in case of spatially spread sources (i.e., unresolved scatterers). Finally, Section 16.4 applies the DOA estimation methods to parametric modeling of the wireless channel.

16.1.1. Spatial signal modeling

A traditional wireless communication system has one transmit and one receive antenna. To enable estimation of the direction to the transmitter, the received signal must be sampled at several spatial locations. The different elements of such an antenna array will all measure the same signal, but with different time delays depending on the DOA. In a realistic scenario, these time delays are much smaller than the reciprocal of the signal bandwidth, and can therefore be considered as phase shifts (see [1] for more details regarding this narrowband assumption). Let $s(t)$ be the complex baseband equivalent of the electromagnetic field at a reference position, due to a far-field transmitter in the direction θ. The vector-valued received signal at the positions of m antenna elements can then be expressed as

$$\mathbf{x}(t) = \begin{bmatrix} x_1(t) \\ x_2(t) \\ \vdots \\ x_m(t) \end{bmatrix} = \begin{bmatrix} e^{-j\omega_c \tau_1(\theta)} \\ e^{-j\omega_c \tau_2(\theta)} \\ \vdots \\ e^{-j\omega_c \tau_m(\theta)} \end{bmatrix} s(t) = \mathbf{a}(\theta) s(t), \tag{16.1}$$

where ω_c is the carrier frequency and $\tau_k(\theta)$ denotes the propagation delay from the reference to the kth element. The vector $\mathbf{a}(\theta)$ is termed the steering vector of the array. Assuming linear receivers with flat frequency responses over the signal bandwidth, the down-converted antenna outputs are proportional to $\mathbf{x}(t)$. Due to mutual coupling and other effects, the individual antenna elements may have θ-dependent gain and phase characteristics, that add to the phase-shifts due to geometry present in (16.1). As long as the receiver dynamics can be ignored, the antenna outputs can still be expressed as $\mathbf{x}(t) = \mathbf{a}(\theta)s(t)$, but the functional form of the steering vector would have to be adjusted accordingly. A structure of special interest arises if the antenna elements are nondirectional and uniformly spaced along a straight line. The steering vector for such a uniform linear array (ULA) has the form

$$\mathbf{a}_{\mathrm{ULA}}(\theta) = \left[1, e^{j\phi}, \ldots, e^{j(m-1)\phi}\right]^T, \tag{16.2}$$

where $\phi = kl\sin\theta$ is called the *electrical angle*, $k = \omega_c/c$ is the wave number, ω_c is the carrier frequency, c denotes the speed of propagation, and l is the element separation. The DOA θ is measured relative to the array normal. To uniquely determine θ, it is clear that $|\phi| \leq \pi$ must hold for all θ. In case the whole field of view is of interest, this leads to $l \leq \pi/k = \lambda/2$, where λ is the wavelength. A ULA with maximum element separation $l = \lambda/2$ is often termed a *standard* ULA, and is often used for comparison.

Due to linearity, the extension of (16.1) to the case of multiple signals is straightforward. Thus, assume there are d far-field emitters, transmitting the baseband signal waveforms $s_k(t)$, $k = 1, 2, \ldots, d$. The array output is then modeled by the familiar equation

$$\mathbf{x}(t) = \sum_{k=1}^{d} \mathbf{a}(\theta_k)s_k(t) + \mathbf{n}(t), \tag{16.3}$$

where we have also included an additive noise term $\mathbf{n}(t)$. In matrix form, the above reads

$$\mathbf{x}(t) = \mathbf{A}(\boldsymbol{\theta})\mathbf{s}(t) + \mathbf{n}(t), \tag{16.4}$$

where $\mathbf{A}(\boldsymbol{\theta}) = [\mathbf{a}(\theta_1), \ldots, \mathbf{a}(\theta_d)]$ is the steering matrix, $\boldsymbol{\theta} = [\theta_1, \ldots, \theta_d]^T$ contains the signal parameters, and $\mathbf{s}(t) = [s_1(t), \ldots, s_d(t)]^T$ is composed of the signal waveforms. In the "standard" DOA estimation literature, no information regarding $\mathbf{s}(t)$ is assumed to be available. The two prevalent models for the signal waveforms are that they are either regarded as deterministic parameters to be estimated, or they are drawn from a d-variate complex Gaussian distribution with zero mean and covariance matrix $\mathbf{P} = \mathrm{E}[\mathbf{s}(t)\mathbf{s}^*(t)]$. To enable reliable estimation of the DOA parameters, information about the spatial covariance matrix of the noise is necessary. For simplicity, it is assumed that a prewhitening has been performed, so that

$\mathrm{E}[\mathbf{n}(t)\mathbf{n}^*(t)] = \sigma^2\mathbf{I}$ holds. Assuming stochastic signals, the spatial covariance of the array output reads

$$\mathbf{R} = \mathrm{E}\left[\mathbf{x}(t)\mathbf{x}^*(t)\right] = \mathbf{A}(\boldsymbol{\theta})\mathbf{P}\mathbf{A}^*(\boldsymbol{\theta}) + \sigma^2\mathbf{I}. \tag{16.5}$$

The array output is assumed to be sampled at N discrete time instants, say $t_1, t_2, \ldots, t_N$. The standard DOA estimation problem is then to determine the DOA parameters θ_k, $k = 1, 2, \ldots, d$ based on the measurements $\mathbf{x}(t_n)$, $n = 1, 2, \ldots, N$. Included in this problem is to estimate the number of (significant) signal components, d. Most DOA estimation methods use the measurements only to form the sample covariance matrix

$$\hat{\mathbf{R}} = \frac{1}{N}\sum_{n=1}^{N}\mathbf{x}(t_n)\mathbf{x}^*(t_n). \tag{16.6}$$

Under fairly mild conditions on the signals and noise, it holds that $\hat{\mathbf{R}} \to \mathbf{R}$ with probability 1 as $N \to \infty$. Thus, provided the DOA estimation method gives correct estimates when $\mathbf{R}$ is used, we can expect good performance as long as N is "large enough."

The above model can be extended in various ways, for example, by taking both azimuth and elevation into account, considering near-field sources, or including effects of polarization. Of most importance in a mobile communication system, however, is the concept of multipath propagation.

16.1.2. Multipath propagation

In microwave communication, it is well known that a significant proportion of the signal energy is scattered via several propagation paths. Indeed, in many cases there is no line-of-sight (LOS) between the mobile and base station, implying that all of the energy is due to scattering. In the Jakes model [2], the scatterers are spread out evenly on a circle surrounding the mobile, but also other models have been proposed. For closely spaced scatterers, the propagation delays are similar, and the received signal components differ only in a possibly time-varying, complex scaling. The wideband case, where time delays need to be accounted for, is considered in Section 16.4. Adopting the spatial signal model (16.3), we have $s_k(t) = g_k(t)s(t)$, $k = 1, \ldots, d$, where $g_k(t)$ are termed the reflection (or scattering) coefficients. The array output is thus modeled as

$$\mathbf{x}(t) = \left(\sum_{k=1}^{d} g_k(t)\mathbf{a}\big(\theta_k(t)\big)\right)s(t) + \mathbf{n}(t) = \mathbf{v}(t)s(t) + \mathbf{n}(t). \tag{16.7}$$

The complex m-vector $\mathbf{v}(t)$ is usually referred to as the *spatial signature* of the transmitter. Since the scatterers are close, it is not practical to resolve all individual propagation paths. We therefore refer to this as a *spatially spread* source, as opposed to the standard case of point sources. In a time-varying scenario, the scatter

coefficients $g_k(t)$ are usually time-varying at a significantly higher rate than the DOAs $\theta_k(t)$ [3], and the latter may therefore be considered stationary over a short data collection interval. Both the scatterers and DOAs are modeled as random variables, with $\mathrm{E}[g_k(t)] = 0$, $\mathrm{E}[g_k(t)g_l^*(t)] = \sigma_g^2\delta_{k,l}$, $\mathrm{E}[g_k(t)g_l(t)] = 0$, $\mathrm{E}[\theta_k] = \theta_0$, and $\mathrm{E}[(\theta_k - \theta_0)^2] = \sigma_\theta^2$. The source is thus characterized by the mean (or nominal DOA) θ_0 and the standard deviation (or spreading factor) σ_θ. The scatter coefficients are usually normalized so that $\sigma_g^2 = 1/d$, by absorbing the power into $s(t)$. Under the stated assumptions, the spatial array covariance matrix takes the form

$$\mathbf{R}_s = \mathrm{E}\left[\mathbf{x}(t)\mathbf{x}^*(t)\right] = P\int_\theta \mathbf{a}(\theta)\mathbf{a}^*(\theta)p_\theta(\theta)d\theta + \sigma^2\mathbf{I}, \tag{16.8}$$

where $p_\theta(\theta)$ is the probability density function (PDF) of the DOAs. The number of incoming rays, d, is usually assumed large, implying that $\mathbf{x}(t)$ is well modeled as a zero-mean Gaussian random vector. Thus, ignoring the temporal correlation structure, $\mathbf{R}_s$ captures all information regarding the incoming energy. To get a reliable estimate of $\mathbf{R}_s$, one needs to see several realizations of the random propagation paths, all taken from the same underlying distribution. Thus, in this case the data $\mathbf{x}(t)$ should be observed slowly enough to enable each $g_k(t)$ and $\theta_k(t)$ to vary significantly between samples. In the literature, the scatter coefficients are often modeled as temporally white. Given data $\mathbf{x}(t_n)$, $n = 1,\ldots,N$, the usual sample covariance matrix

$$\hat{\mathbf{R}} = \frac{1}{N}\sum_{n=1}^{N}\mathbf{x}(t_n)\mathbf{x}^*(t_n) \tag{16.9}$$

is taken as the estimate of $\mathbf{R}_s$. The task is now to infer the characteristics of the scattering environment based on $\hat{\mathbf{R}}$. Usually, it is sufficient to determine θ_0 and σ_θ.

16.2. DOA estimation for point sources

This section presents methods for the case where the transmitters are resolvable, that is, they are modeled as point sources. This is the "standard" DOA estimation problem, which by now can be considered a mature research area. The following outlines some of the more influential methods. More details are available in, for example, [4, 5].

16.2.1. Beamforming techniques

The duality between uniform sampling in space (ULA) and time have lead researchers to apply methods from one domain to the other. The spatial Fourier transform of a single data snapshot $\mathbf{x}(t_n)$ is given by

$$\tilde{\mathbf{x}}(t_n,\phi) = \sum_{k=0}^{m-1} x_k(t_n)e^{-jk\phi}. \tag{16.10}$$

With $\mathbf{a}_{\mathrm{ULA}}(\theta)$ given by (16.2) we can express this as the inner product

$$\tilde{\mathbf{x}}(t_n, \theta) = \mathbf{a}^*_{\mathrm{ULA}}(\theta)\mathbf{x}(t_n). \tag{16.11}$$

The spatial periodogram of $\mathbf{x}(t_n)$ is then simply $|\tilde{\mathbf{x}}(t_n, \theta)|^2$. If no temporal correlation is assumed, it is natural to average the instantaneous spatial spectra to form the final estimate. When applying this to a general array, for which $\|\mathbf{a}(\theta)\|$ may depend on θ, it is useful to introduce a normalization of (16.11). The resulting spectral estimate, termed *conventional beamforming*, takes the form

$$P_{\mathrm{BF}}(\theta) = \frac{1}{N}\sum_{n=1}^{N} \frac{|\mathbf{a}^*(\theta)\mathbf{x}(t_n)|^2}{\mathbf{a}^*(\theta)\mathbf{a}(\theta)}. \tag{16.12}$$

Expanding the square $|\mathbf{a}^*(\theta)\mathbf{x}(t_n)|^2 = \mathbf{a}^*(\theta)\mathbf{x}(t_n)\mathbf{x}^*(t_n)\mathbf{a}(\theta)$ and inserting (16.6) leads to

$$P_{\mathrm{BF}}(\theta) = \frac{\mathbf{a}^*(\theta)\hat{\mathbf{R}}\mathbf{a}(\theta)}{\mathbf{a}^*(\theta)\mathbf{a}(\theta)}. \tag{16.13}$$

The locations $\hat{\theta}_k$ of the d highest peaks of $P_{\mathrm{BF}}(\theta)$ are taken as the beamforming DOA estimates. The averaging implies that $P_{\mathrm{BF}}(\theta)$ has a much reduced variance as compared to the classical periodogram for large N, but similar to the latter it has a limited resolution. In case of a ULA, the Rayleigh resolution expressed in electrical angle is $\Delta\phi = 2\pi/m$, which for large m translates to $\Delta\theta \approx 2\pi/(klm)$.

To improve the resolution of the conventional beamformer, Capon [6] advocated the use of adaptive beamforming. Although the original derivation is different, the following interpretation has become popular:

$$\min_{\mathbf{w}} \mathbf{w}^*\hat{\mathbf{R}}\mathbf{w} \quad \text{subject to } \mathbf{w}^*\mathbf{a}(\theta) = 1. \tag{16.14}$$

The energy $\mathbf{w}^*\hat{\mathbf{R}}\mathbf{w}$ of the beamformer output $\mathbf{w}^*\mathbf{x}(t_n)$ is to be minimized, while keeping a unit gain in the "look direction" θ. The optimizing beamforming weights are easily shown to be

$$\mathbf{w}_{\mathrm{CAP}} = \frac{\hat{\mathbf{R}}^{-1}\mathbf{a}(\theta)}{\mathbf{a}^*(\theta)\hat{\mathbf{R}}^{-1}\mathbf{a}(\theta)}, \tag{16.15}$$

which when inserted into $\mathbf{w}^*\hat{\mathbf{R}}\mathbf{w}$, leads to the Capon spectral estimate

$$P_{\mathrm{CAP}}(\theta) = \frac{1}{\mathbf{a}^*(\theta)\hat{\mathbf{R}}^{-1}\mathbf{a}(\theta)}. \tag{16.16}$$

In contrast to the conventional beamformer, the resolution of (16.16) improves with the SNR (signal-to-noise ratio) [7]. It is therefore preferable, at least in high-SNR scenarios. However, the resolution does not improve for increasing N. The Capon DOA estimates, which are the peak locations of $P_{\mathrm{CAP}}(\theta)$, therefore still fail to take full advantage of data model (16.4).

16.2.2. Subspace methods

In the late seventies, a new class of spectral-based estimators were introduced. These have their roots in principal component analysis, and are based on geometrical properties of the array covariance matrix. It is clear from (16.5) that any vector that is orthogonal to $\mathbf{A}(\boldsymbol{\theta})$ is an eigenvector of $\mathbf{R}$ with corresponding eigenvalue σ^2. The remaining eigenvectors are all in the range space of $\mathbf{A}(\boldsymbol{\theta})$ (provided $m > d$ and $\mathbf{P}$ is full rank), and are therefore termed *signal eigenvectors*. The eigendecomposition of $\mathbf{R}$ (16.5) is partitioned into a signal and a noise subspace as

$$\mathbf{R} = \sum_{k=1}^{m} \lambda_k \mathbf{e}_k \mathbf{e}_k^* = \mathbf{E}_s \boldsymbol{\Lambda}_s \mathbf{E}_s^* + \mathbf{E}_n \boldsymbol{\Lambda}_n \mathbf{E}_n^*, \tag{16.17}$$

where $\lambda_1 \geq \cdots \geq \lambda_d > \lambda_{d+1} = \cdots = \lambda_m = \sigma^2$, $\mathbf{E}_s = [\mathbf{e}_1, \ldots, \mathbf{e}_d]$, $\mathbf{E}_n = [\mathbf{e}_{d+1}, \ldots, \mathbf{e}_m]$, and $\boldsymbol{\Lambda}_n = \sigma^2 \mathbf{I}$. The signal eigenvectors in $\mathbf{E}_s$ span the range space of $\mathbf{A}(\boldsymbol{\theta})$, which is termed the *signal subspace*. For the noise eigenvectors we have instead $\mathbf{E}_n \perp \mathbf{A}(\boldsymbol{\theta})$. These relations constitute the fundament for subspace methods for DOA estimation. In passing, we note that the number of signals d can easily be determined from (estimates of) the eigenvalues, either as the number of "significant" eigenvalues or by determining the multiplicity of the minimum eigenvalue [8, 9]. The MUSIC (multiple signal classification) algorithm [10, 11] exploits the orthogonality relation $\mathbf{a}^*(\theta_k)\mathbf{E}_n = 0$, for $k = 1, \ldots, d$. Provided the array is free of ambiguities, there are no false solutions to this equation [12, 13]. The noise subspace matrix is estimated from the eigendecomposition of the sample covariance

$$\hat{\mathbf{R}} = \hat{\mathbf{E}}_s \hat{\boldsymbol{\Lambda}}_s \hat{\mathbf{E}}_s^* + \hat{\mathbf{E}}_n \hat{\boldsymbol{\Lambda}}_n \hat{\mathbf{E}}_n^*. \tag{16.18}$$

Using the estimated noise subspace, the so-called MUSIC pseudospectrum is then defined as

$$P_{\mathrm{MU}}(\theta) = \frac{\mathbf{a}^*(\theta)\mathbf{a}(\theta)}{\mathbf{a}^*(\theta)\hat{\mathbf{E}}_n \hat{\mathbf{E}}_n^* \mathbf{a}(\theta)}. \tag{16.19}$$

This is not a spectrum in the usual sense, since it is in fact dimensionless. Yet, for large enough N and/or SNR, $P_{\mathrm{MU}}(\theta)$ exhibits high peaks near the true DOAs $\theta_1, \ldots, \theta_d$. The MUSIC algorithm calculates the DOA estimates by computing $P_{\mathrm{MU}}(\theta)$ at a fine grid (using FFT with zero-padding in the case of a ULA), and then locating the d largest local maxima. If desired, the estimates can be refined by using a local search.

To illustrate the performance of the different spectral-based estimators, $N = 500$ snapshots of $\mathbf{x}(t_n)$ are generated according to the model (16.4). The array is a standard ULA of $m = 6$ sensors, and $d = 3$ emitters are located at $\boldsymbol{\theta} = [0^\circ, 5^\circ, 20^\circ]^T$. The waveforms are assumed uncorrelated and of equal power and the SNR is 10 dB. Both the signal waveforms and the noise are realizations of white Gaussian random processes. The conventional and Capon spatial spectra are

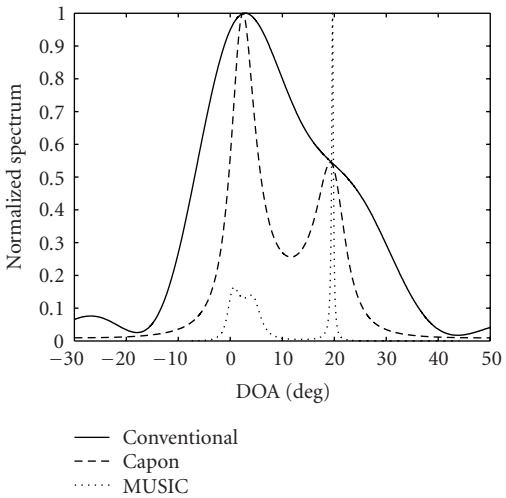

FIGURE 16.1. Spatial spectrum estimates using conventional beamforming, Capon's beamformer, and MUSIC. Standard ULA of $m = 6$ elements. True DOAs $\{0°, 5°, 20°\}$, SNR $= 10$ dB, $N = 500$.

displayed in Figure 16.1, along with the MUSIC pseudospectrum, all normalized to have maximum value one. The conventional beamformer shows just one peak around 3.4°, whereas the Capon spectrum exhibits two peaks at 2.4° and 19.2°. In contrast, the MUSIC pseudospectrum resolves all three signals with peaks at −0.5°, 5.9° and 19.5°. This is of course just one realization using random signals, but the general behavior in Figure 16.1 is representative.

Although the MUSIC algorithm can improve the resolution significantly over conventional spectral-based estimators, it requires a high SNR and/or N for this to happen. Several approaches have been proposed to increase resolution, including beamspace processing and the min-norm algorithm. For a useful comparison of these and other versions, see [14]. In case of a ULA, the threshold performance can be significantly enhanced by using a root-finding procedure instead of searching the pseudospectrum for peaks [15]. The idea is to express the spectrum as a polynomial in the complex variable $z = e^{j\phi}$. ULA steering vector (16.2) is written as

$$\mathbf{a}(z) = \left[1, z, \ldots, z^{m-1}\right]^T, \tag{16.20}$$

and the inverse of the MUSIC pseudospectrum (sometimes termed the "null spectrum") then becomes

$$P(z) = \mathbf{a}^T\left(z^{-1}\right)\hat{\mathbf{E}}_n\hat{\mathbf{E}}_n^*\mathbf{a}(z). \tag{16.21}$$

Regarding $P(z)$ (or rather $z^{m-1}P(z)$) as a polynomial in z, a standard numerical routine can be used to compute the $2m - 1$ roots. Out of these, the so-called root-MUSIC algorithm uses the d roots, say $\{z_k\}_{k=1}^d$, that are closest to the unit

circle. Since $z = e^{j\phi}$ where $\phi = kl\sin\theta$, the root-MUSIC DOA estimates are then computed as $\hat{\theta}_k = \arcsin[\text{angle}(z_k)/kl]$, $k = 1,\ldots,d$. It is known that the root-MUSIC DOA estimates have the same asymptotic properties as the standard spectral MUSIC. However, the threshold behavior is significantly improved, which according to [16] is explained by the fact that the errors in root locations have a large radial component. A further improvement is obtained by using forward-backward averaging [16].

The ESPRIT algorithm [17] is related to root-MUSIC, but requires computing only d roots. It is based on the assumption that the array is composed of two identical, spatially separated, subarrays that have the same orientation. For a ULA, there are several ways to construct subarrays. A popular choice is to let elements $1 : m-1$ constitute the first array and $2 : m$ the second. Let $\mathbf{A}_1$ denote the steering matrix for the first subarray, that is, rows 1 through $m-1$ of $\mathbf{A}(\boldsymbol{\theta})$. Similarly, $\mathbf{A}_2$ contains the $m-1$ last rows. Using (16.20), these matrices are related by

$$\mathbf{A}_2 = \mathbf{A}_1 \,\text{diag}\,[z_1,\ldots,z_d], \tag{16.22}$$

where $z_k = e^{j\phi_k}$ is the root corresponding to the kth source. This relation could be used to determine the roots if $\mathbf{A}(\boldsymbol{\theta})$ was known. In general, all that is available is an estimate of the spatial array covariance matrix $\mathbf{R}$. From the eigendecomposition (16.17), we collect the signal eigenvectors into $\mathbf{E}_s$, which is not identical to $\mathbf{A}$ but it spans the same range space. Therefore, $\mathbf{E}_s = \mathbf{AT}$ for some full-rank $d \times d$ matrix $\mathbf{T}$, and it follows that

$$\mathbf{E}_2 = \mathbf{E}_1\mathbf{T}\,\text{diag}\,[z_1,\ldots,z_d]\mathbf{T}^{-1}, \tag{16.23}$$

where $\mathbf{E}_s$ has been partitioned conformably with $\mathbf{A}$. Using the estimated $\hat{\mathbf{E}}_s$ in (16.23), the submatrices $\hat{\mathbf{E}}_1$ and $\hat{\mathbf{E}}_2$ will, in general, not span the same range space, and (16.23) has no exact solution. Instead, a least-squares or total-least-squares solution $\hat{\Psi}$ to the relation

$$\hat{\mathbf{E}}_2 \approx \hat{\mathbf{E}}_1\hat{\Psi} \tag{16.24}$$

is computed. The poles $\{z_k\}_{k=1}^{d}$ are then given as the eigenvalues of $\hat{\Psi}$, utilizing that Ψ and $\text{diag}[z_1,\ldots,z_d]$ are related by a similarity transformation and therefore share the same eigenvalues. Finally, the ESPRIT DOA estimates are computed as $\hat{\theta}_k = \arcsin[\text{angle}(z_k)/kl]$, $k = 1,\ldots,d$. The method is computationally very efficient, but exhibits slightly worse performance than root-MUSIC. Similar to the latter, ESPRIT benefits from forward-backward averaging. A clever implementation using only real-valued operations (and therefore reduced computational burden) was proposed in [18].

16.2.3. Nonlinear least-squares estimation

The subspace-based techniques mentioned above generally provide accurate DOA estimates at an affordable computational cost. However, the performance degrades when the signal waveforms are correlated ($\mathbf{P}$ nondiagonal), and fail to operate in the presence of coherent sources. Although forward-backward averaging and spatial smoothing techniques can mitigate the drawbacks somewhat (e.g., [19]), these techniques remain suboptimal. Given the model (16.4), a straightforward approach is to use a nonlinear least-squares (NLLS) [20] fit:

$$\{\hat{\boldsymbol{\theta}}, \hat{\mathbf{s}}(t_n)\} = \arg\min_{\boldsymbol{\theta}, \mathbf{s}(t_n)} \sum_{n=1}^{N} ||\mathbf{x}(t_n) - \mathbf{A}(\boldsymbol{\theta})\mathbf{s}(t_n)||^2. \tag{16.25}$$

This is a separable least-squares problem, and for fixed (but unknown) $\boldsymbol{\theta}$, the solution with respect to the linear parameter $\mathbf{s}(t_n)$ is

$$\hat{\mathbf{s}}(t_n) = (\mathbf{A}^*\mathbf{A})^{-1}\mathbf{A}^*\mathbf{x}(t_n). \tag{16.26}$$

Substituting (16.26) into (16.25) leads to the concentrated NLLS formulation

$$\hat{\boldsymbol{\theta}} = \arg\min_{\boldsymbol{\theta}} \operatorname{Tr}\{\boldsymbol{\Pi}_{\mathbf{A}}^{\perp}\hat{\mathbf{R}}\}, \tag{16.27}$$

where $\boldsymbol{\Pi}_{\mathbf{A}}^{\perp} = \mathbf{I} - \boldsymbol{\Pi}_{\mathbf{A}} = \mathbf{I} - \mathbf{A}(\mathbf{A}^*\mathbf{A})^{-1}\mathbf{A}^*$ is the orthogonal projection onto the nullspace of $\mathbf{A}^*$. The concentrated form (16.27) has a nice interpretation; $\operatorname{Tr}\{\boldsymbol{\Pi}_{\mathbf{A}}^{\perp}\hat{\mathbf{R}}\}$ is a measure of the remaining output power after removing all the energy stemming from the hypothetical DOA parameters $\boldsymbol{\theta}$. Clearly, this should reach its minimum when $\boldsymbol{\theta}$ is close to $\boldsymbol{\theta}_0$, because this removes all signal components from $\hat{\mathbf{R}}$. It is easy to see that the NLLS approach coincides with maximum likelihood (ML) if the signal waveforms $\mathbf{s}(t_n)$ are modeled as deterministic parameters and the noise is assumed to be Gaussian. In many applications, also $\mathbf{s}(t_n)$ can be regarded as Gaussian, which leads to a different ML estimator [21], often termed stochastic ML (SML). Regardless of the actual distribution of the signal waveforms, both the NLLS and the SML methods provide highly accurate DOA estimates [22]. However, they both require solution of a d-dimensional nonlinear optimization problem like (16.27), which is far from trivial. A practical approach at a reasonable cost is to employ a relaxed optimization procedure, where DOA parameters are adjusted one at a time. Such a method is usually able to rapidly yield preliminary estimates in the neighborhood of the true minimizers of the criterion function, but the local convergence rate is often unacceptably slow. Therefore, once sufficiently good initial estimates are available, it is preferable to switch to a Newton-type local optimization (see, e.g., [22]). In [23, 24], a modified NLLS criterion is derived, based on subspace decomposition (16.17). In its concentrated form, the *signal subspace fitting (SSF) criterion* takes the form

$$\hat{\boldsymbol{\theta}} = \arg\min_{\boldsymbol{\theta}} \operatorname{Tr}\{\boldsymbol{\Pi}_{\mathbf{A}}^{\perp}\hat{\mathbf{E}}_s\widehat{\mathbf{W}}\hat{\mathbf{E}}_s^*\}, \tag{16.28}$$

where $\widehat{\mathbf{W}}$ is a positive definite weighting matrix, which should reflect the reliability of the different eigenvectors appearing in $\hat{\mathbf{E}}_s$. The optimal choice of weighting, in terms of minimizing the variance of the DOA estimates, is the diagonal matrix

$$\widehat{\mathbf{W}} = \left(\hat{\Lambda}_s - \hat{\sigma}^2\mathbf{I}\right)^2 \hat{\Lambda}_s^{-1}, \tag{16.29}$$

where the noise variance estimate $\hat{\sigma}^2$ can be taken as the average of the $m - d$ smallest eigenvalues of $\hat{\mathbf{R}}$. The SSF formulation has certain advantages over the data-domain NLLS, in particular when $d \ll m$. It is then significantly cheaper to compute (16.28) than (16.27).

A few techniques have been proposed in the literature [25, 26, 27, 28] for implementing a relaxed optimization of NLLS-type criteria. We will describe the so-called RELAX procedure due to [26], which simultaneously updates θ_k and $s_k(t_n)$, $n = 1,\ldots,N$ while keeping the other parameters fixed. The method is closely related to the SAGE (space-alternating generalized expected maximization) algorithm of [25], although the motivation and interpretation is simpler for RELAX. We present the technique for the data-domain NLLS, noting that the SSF-RELAX algorithm is obtained by replacing the data matrix $\mathbf{X}$ with $\hat{\mathbf{E}}_s\widehat{\mathbf{W}}^{1/2}$. We express NLLS criterion (16.25) in matrix form as

$$V(\boldsymbol{\theta},\mathbf{S}) = \left|\left|\mathbf{X} - \mathbf{A}(\boldsymbol{\theta})\mathbf{S}\right|\right|^2 = \left|\left|\mathbf{X} - \sum_{k=1}^{d}\mathbf{a}(\theta_k)\mathbf{s}_k\right|\right|^2, \tag{16.30}$$

where $\|\cdot\|$ denotes the Frobenius matrix norm, $\mathbf{X} = [\mathbf{x}(t_1),\ldots,\mathbf{x}(t_N)]$, $\mathbf{S} = [\mathbf{s}(t_1),\ldots,\mathbf{s}(t_N)]$, and $\mathbf{s}_k$ is the kth row of $\mathbf{S}$. When searching for the parameters of the kth emitter, preliminary estimates of the other signal parameters are assumed available. Using these, the "cleaned" observation matrix

$$\mathbf{X}_l = \mathbf{X} - \sum_{k\neq l}\mathbf{a}(\hat{\theta}_k)\hat{\mathbf{s}}_k \tag{16.31}$$

is formed. The relaxed criterion

$$V_l(\theta_l,\mathbf{s}_l) = \left|\left|\mathbf{X}_l - \mathbf{a}(\theta_l)\mathbf{s}_l\right|\right|^2 \tag{16.32}$$

is again a separable NLLS criterion, which is minimized by

$$\hat{\theta}_l = \arg\max_{\theta}\frac{\left|\mathbf{a}^*(\theta)\mathbf{X}_l\right|^2}{\left|\left|\mathbf{a}(\theta)\right|\right|^2}, \tag{16.33}$$

$$\mathbf{s}_l = \frac{\mathbf{a}^*(\hat{\theta}_l)\mathbf{X}_l}{\left|\left|\mathbf{a}(\hat{\theta}_l)\right|\right|^2}. \tag{16.34}$$

Maximizing (16.33) requires a nonlinear optimization over one parameter only. This is easily accomplished by a course grid search (using FFT in the case of a

ULA), followed by a local Newton-type optimization. An iteration of the RELAX algorithm is now to sequentially update θ_l and $\mathbf{s}_l$ for $l = 1, \ldots, d$. At the first iteration, no initial estimates of θ_k and $\mathbf{s}_k$ are available for $k > l$, so these are usually ignored by letting $\mathbf{s}_k = 0$, $k > l$. The iterations continue until no significant change of the DOA parameters is observed, or until one chooses to switch to a Newton-type iterative search. In case the number of signals is unknown, a parametric enumeration technique (e.g., [29, 30]) is well suited to work with the iterative RELAX procedure.

16.3. Spread sources modeling

The DOA estimation problem for spread sources is quite different from the more commonly considered point source case. Since the individual rays are not resolvable, the task is to find a statistical characterization of the incoming energy. Parametric estimation methods are based on the availability of a parameterized PDF of θ. Popular choices are a Gaussian or a uniform PDF. For physics-based statistical models, consult, for example, [31, 32]. Nonparametric techniques make no such assumptions, but can on the other hand only deliver a limited description of the ray statistics, such as the nominal DOA θ_0 and the spread σ_θ.

16.3.1. Nonparametric beamforming techniques

Assume that the signal reaches the receiving antenna array via a single scatter cluster. Provided the distribution of scatterers (DOAs) has a symmetric PDF, a natural estimate of the nominal DOA θ_0 is the location of the peak of beamforming spectrum (16.13). However, for large spreading factors σ_θ, the variance of this estimate is unacceptably high [33]. The situation is even worse when using a high-resolution method [34]. A useful remedy is to use the center of gravity rather than the peak location of the spatial spectrum [35]. Provided the resolution of the latter is sufficient, it can be shown that $p_\theta(\theta)$ is approximately proportional to the spatial spectrum. For high SNR, the Capon spectrum has superior resolution, and may therefore be the preferred choice in this application. Using the definitions of the mean and variance of a distribution, the estimates are computed according to [35]

$$\begin{aligned} \widehat{\theta}_0 &= \frac{\int_{\theta\in\Omega} \theta P(\theta)\, d\theta}{\int_{\theta\in\Omega} P(\theta)\, d\theta}, \\ \widehat{\sigma}_\theta^2 &= \frac{\int_{\theta\in\Omega} (\theta - \widehat{\theta}_0)^2 P(\theta)\, d\theta}{\int_{\theta\in\Omega} P(\theta)\, d\theta}, \end{aligned} \tag{16.35}$$

where $P(\theta)$ is either $P_{\mathrm{BF}}(\theta)$ (16.13) or $P_{\mathrm{CAP}}(\theta)$ (16.16) and Ω refers to the support of the distribution, that is, the extent of the DOA cluster. The parameterization of $P(\theta)$ in terms of the physical DOA deserves some comments. For a linear array it is perhaps more natural to use the electrical angle ϕ, which is proportional to $\sin\theta$. However, for reasonably small DOA clusters the difference between the

parameterizations is negligible. The estimate $\hat{\theta}_0$ has in general very good performance, while $\hat{\sigma}_\theta$ is more sensitive to the choice of Ω and the resolution of $P(\theta)$. These parameters are particularly critical in the presence of several DOA clusters that are (nearly) overlapping.

16.3.2. Parametric estimation

A parametric estimator exploits the structure (16.8) of $\mathbf{R}_s$ in more detail. In general, this requires that a parameterized form of the DOA PDF is known, say $p_\theta(\theta;\boldsymbol{\phi})$. Here, $\boldsymbol{\phi}$ is a vector of unknown parameters, for example $\boldsymbol{\phi} = [\theta_0, \sigma_\theta]^T$ in the Gaussian case. Basically, these parameters are determined by matching the model (16.8) to the sample covariance $\hat{\mathbf{R}}$. An interesting "semiparametric" method was recently proposed in [36]. It is based on a generalization of the Capon formulation (16.14). Instead of requiring a unit gain in the look direction $\mathbf{a}(\theta)$, the authors of [36] proposed to keep a unit average signal power for a given set of parameters $\boldsymbol{\phi}$. The optimization problem is thus

$$\min_{\mathbf{w}} \mathbf{w}^* \hat{\mathbf{R}} \mathbf{w} \quad \text{subject to } \mathbf{w}^* \bar{\mathbf{R}}_s(\boldsymbol{\phi}) \mathbf{w} = 1, \tag{16.36}$$

where

$$\bar{\mathbf{R}}_s(\boldsymbol{\phi}) = \int_\theta \mathbf{a}(\theta)\mathbf{a}^*(\theta) p_\theta(\theta;\boldsymbol{\phi}) d\theta. \tag{16.37}$$

The resulting generalized Capon (GC) spectrum is obtained as

$$P_{\mathrm{GC}}(\boldsymbol{\phi}) = \frac{1}{\lambda_{\max}\{\hat{\mathbf{R}}^{-1}\bar{\mathbf{R}}_s(\boldsymbol{\phi})\}}, \tag{16.38}$$

where $\lambda_{\max}\{\cdot\}$ refers to the maximum eigenvalue of a matrix. The GC estimates are now taken as the locations of the highest peaks of $P_{\mathrm{GC}}(\boldsymbol{\phi})$. In this way, the parameters of several clusters can be determined using a search over only one set of parameters $\boldsymbol{\phi}$. The resolution in [36] is found to be superior to that of previously proposed computationally efficient estimators [37, 38, 39], although theoretical support for this claim is yet to be seen. The computational cost for the GC estimator is quite substantial, as it requires computing the maximum eigenvalue of an $m \times m$ matrix for each criterion function evaluation, besides solving the integral in (16.37). Approximate formulae for the latter is available in special cases [37, 40]. For a ULA and Gaussian-distributed DOAs, the approximate covariance matrix is given as

$$\bar{\mathbf{R}}_s(\theta_0, \sigma_\theta) \approx [\mathbf{a}(\theta_0)\mathbf{a}^*(\theta_0)] \odot \mathbf{B}, \tag{16.39}$$

where $\odot$ means elementwise multiplication, and the ijth element of the matrix $\mathbf{B}$ is given as

$$B_{ij} = e^{-2[\pi l(j-i)]^2 \sigma_\theta^2 \sin^2\theta_0}. \tag{16.40}$$

A general approach to parametric estimation is the principle of maximum likelihood (ML). If $\mathbf{x}(t)$ is modeled as zero-mean temporally white Gaussian, the ML estimate is found by solving

$$\{\hat{\boldsymbol{\phi}}, \hat{P}, \hat{\sigma}^2\} = \arg\min_{\boldsymbol{\phi}, P, \sigma^2} \log|\mathbf{R}_s| + \mathrm{Tr}\{\mathbf{R}_s^{-1}\hat{\mathbf{R}}\}. \tag{16.41}$$

Unfortunately, this is a multidimensional (4 in the Gaussian case) nonlinear optimization problem, even in the case of a single DOA cluster. In case of several clusters, the contributions from each will have to be added to $\mathbf{R}_s$, implying an even increased number of unknown parameters. The method is therefore often deemed impractical for the current application. A possible way to decrease the complexity is to use a covariance matching estimator (COMET), exploiting the fact that $\mathbf{R}_s$ is linear in the signal and noise powers as is clear from (16.8). The optimally weighted COMET estimator of [40] is formulated as the following optimization problem:

$$\{\hat{\boldsymbol{\phi}}, \hat{P}, \hat{\sigma}^2\} = \arg\min_{\boldsymbol{\phi}, P, \sigma^2} ||(\mathbf{R}_s - \hat{\mathbf{R}})\hat{\mathbf{R}}^{-1}||^2. \tag{16.42}$$

Since $\mathbf{R}_s$ is linear in P and σ^2, the above is in the form of a separable LS problem, and the minimum with respect to these parameters can easily be found for a fixed $\boldsymbol{\phi}$. The result is that only a search over $\boldsymbol{\phi}$ is necessary, similar to GC method (16.38). However, in the presence of several clusters, (16.42) requires a simultaneous search over all parameters. This is obviously more costly, but the benefit is an increased accuracy in large samples, since (16.42) can be shown to yield asymptotically the same performance as ML. For the special case of Gaussian-distributed DOA and a ULA, [41] presents a further simplification of (16.42). An approximate, but still asymptotically equivalent, technique is derived, where the search over $\boldsymbol{\phi} = [\theta_0, \sigma_\theta]^T$ is decoupled, so that only a 1D search is necessary. See [41] for details. A drawback of the covariance-matching-based methods is that they inherently assume a large sample size, and are thus less suited to scenarios where only a small number of observations are available.

16.4. Parametric channel modeling

Parametric channel modeling refers to the problem of finding a parsimonious representation of the wireless channel. The techniques described here use parameterizations in terms of physically meaningful quantities, but it is also possible to apply pure "black-box" methods. The data is assumed to be sensor outputs collected using a known transmitted waveform (probing signal). The task is to resolve all significant propagation paths and determine their DOAs, time delays, and strengths.

16.4.1. SIMO channels

The simplest case has a single transmitter and multiple receivers. This is referred to as a SIMO (single-input multiple-output) system. For narrowband signals, in

the sense that waveforms received via different propagation paths are all coherent, this is similar to the standard DOA estimation problem. However, since equipment for channel measurements is typically wideband, we consider the case where time delays are significant with respect to the inverse bandwidth. Referring to (16.7), the received signal is then modeled by

$$\mathbf{x}(t) = \sum_{k=1}^{d} g_k \mathbf{a}(\theta_k) s(t - \tau_k) + \mathbf{n}(t). \tag{16.43}$$

Here, $s(t)$ represents the transmitted continuous-time waveform, which for a digital communication system may be given in the form

$$s(t) = \sum_{l=-\infty}^{\infty} b_l p(t - lT), \tag{16.44}$$

where b_l are the (known) information symbols and $p(t)$ the pulse shaping waveform with support on $0 \le t < T$. The noise-free part of (16.43) can be thought of as the convolution of the transmitted signal $s(t)$ and the SIMO channel

$$\mathbf{h}(t) = \sum_{k=1}^{d} g_k \mathbf{a}(\theta_k) \delta(t - \tau_k), \tag{16.45}$$

where $\delta(\cdot)$ is the Dirac delta function. The high bandwidth and multiantenna receiver allows paths to be resolved in both space and time. We therefore assume that one wishes to obtain signal parameter estimates for the individual components in (16.43), in contrast to the modeling of spatially extended sources considered in Section 16.3. Given samples $\mathbf{x}(t_n)$, $n = 1, \ldots, N$ from (16.43), where the shape of $s(t)$ is assumed known, the task is to jointly determine θ_k, τ_k, and g_k. Often, the channel-sounder equipment does not give access to the raw data, but only nonparametric channel estimates. This case will be considered later. In essence, we are facing a 2D estimation problem. To reduce the computational complexity, such problems are often solved by treating one dimension at a time in some fashion. If the noise is Gaussian and spatially white, the optimal ML estimator employs the 2D NLLS criterion

$$\begin{aligned} V(\boldsymbol{\theta}, \boldsymbol{\tau}, \mathbf{g}) &= \sum_{k=1}^{N} \left\| \mathbf{x}(t_k) - \sum_{l=1}^{d} g_l \mathbf{a}(\theta_l) s(t_k - \tau_l) \right\|^2 \\ &= \left\| \mathbf{X} - \sum_{l=1}^{d} g_l \mathbf{a}(\theta_l) \mathbf{s}(\tau_l) \right\|_F^2, \end{aligned} \tag{16.46}$$

where $\mathbf{X} = [\mathbf{x}(t_1), \ldots, \mathbf{x}(t_N)]$ as before, and

$$\mathbf{s}(\tau_k) = [s(t_1 - \tau_k), \ldots, s(t_N - \tau_k)] \tag{16.47}$$

denotes the time-delayed signal vector. For fixed $\boldsymbol{\theta} = [\theta_1, \ldots, \theta_d]$ and $\boldsymbol{\tau} = [\tau_1, \ldots, \tau_d]$, it is easy to minimize (16.46) explicitly with respect to $\mathbf{g} = [g_1, \ldots, g_d]$. Substituting the so-obtained $\mathbf{g}(\boldsymbol{\theta}, \boldsymbol{\tau})$ back into (16.46) results in a nonlinear function of $2d$ parameters. To find the global minimum of this concentrated NLLS criterion is by no means a simple task. A natural approach is to apply the RELAX idea presented in Section 16.2.3, see also [42] for an application to time-delay estimation. This is an iterative procedure, where the joint estimation problem is in each iteration broken down into computationally simple beamforming-like (i.e., matched filter) operations. The technique has strong similarities with the SAGE algorithm, which was successfully applied in [43] to a scenario where also the Doppler-shifts due to the platform motion were taken into account. Similar to (16.31), (16.32), and (16.33), the RELAX algorithm for joint DOA and delay estimation consists of the following steps. First the data is "cleaned" from contributions from all signal paths except one:

$$\mathbf{X}_l = \mathbf{X} - \sum_{k \neq l} \hat{g}_k \mathbf{a}(\hat{\theta}_k)\mathbf{s}(\hat{\tau}_k), \tag{16.48}$$

where $\hat{(\cdot)}$ denotes the most recent estimates of the signal parameters corresponding to the other paths. The relaxed criterion is now

$$V_l(\theta_l, \tau_l, g_l) = ||\mathbf{X}_l - g_l \mathbf{a}(\theta_l)\mathbf{s}(\tau_l)||^2. \tag{16.49}$$

Minimizing explicitly with respect to g_l results after some simple algebra in the concentrated criterion

$$V_l(\theta_l, \tau_l) = \frac{|\,\mathbf{a}^*(\theta_l)\mathbf{X}_l\mathbf{s}^*(\tau_l)\,|^2}{||\mathbf{a}(\theta_l)||^2||\mathbf{s}(\tau_l)||^2}, \tag{16.50}$$

which is to be *maximized* with respect to θ_l and τ_l. The above allows a nice interpretation. The premultiplication by $\mathbf{a}^*(\theta_l)$ is a spatially matched filter, and the postmultiplication by $\mathbf{s}^*(\tau_l)$ acts as a temporally matched filter. The maximum of this normalized *space-time correlation* yields the estimates for the lth propagation path. Once updated estimates of θ_l and τ_l are found, the new g_l will be

$$\hat{g}_l = \frac{\mathbf{a}^*(\hat{\theta}_l)\mathbf{X}_l\mathbf{s}^*(\hat{\tau}_l)}{||\mathbf{a}(\hat{\theta}_l)||^2||\mathbf{s}(\hat{\tau}_l)||^2}. \tag{16.51}$$

One iteration of the RELAX algorithm is now to sequentially update the triple $\{\theta_l, \tau_l, g_l\}$ for $l = 1, \ldots, d$ as outlined above. At the first iteration one simply takes $g_k = 0$, $k > l$, unless some initial estimates of the parameters of these propagation paths are available.

The iterative procedure described above is simple in each step. But in high-resolution scenarios, several iterations may be necessary, implying a high total computational burden. Simpler subspace-based alternatives have been proposed

in, for example, [44]. The computationally most efficient techniques employ a Fourier transform of a nonparametric channel estimate along the delay dimension. Such a vector-valued impulse response estimate is obtained using a matched filter, which in matrix form is expressed as

$$\widehat{\mathbf{h}}(t) = \frac{\mathbf{X}\mathbf{s}^*(t)}{||\mathbf{s}(t)||^2}. \tag{16.52}$$

In fact, the available channel-sounder data is often given in the form of estimated impulse responses like the above. A natural approach is now to apply spatial beamforming to each available sample of the impulse response, say $\widehat{\mathbf{h}}(t_k)$, $k = 1,\ldots,M$, where $t_k = (k-1)T$ for uniform sampling. In case of a uniform linear array, each $\widehat{\mathbf{h}}(t_k)$ can be split into several subvectors, thus effectively creating several snapshots. Using this *spatial smoothing* technique, it is also possible to apply a high-resolution DOA estimation method, thus enabling closely spaced scatterers with (nearly) the same propagation delay to be resolved. Taking the discrete Fourier transform of $\widehat{\mathbf{h}}(t_k)$ and using (16.45), the nonparametric SIMO transfer function estimate is modeled by

$$\widehat{\mathbf{h}}(\omega_k) \approx \sum_{l=1}^{d} g_l \mathbf{a}(\theta_l) e^{-j\omega_k \tau_l}, \tag{16.53}$$

where $\omega_k = 2\pi(k-1)/M$, $k = 1,\ldots,M$ are the length-M DFT frequencies. The approximation above acknowledges the errors in (16.52), which are due to both noise and to finite temporal resolution. In effect, the Fourier transform has turned the delay estimation into one of frequency estimation, where τ_k plays the role of frequencies. If the array is a ULA, a computationally efficient technique for 2D frequency estimation (e.g., [45]) can now be employed to determine the signal parameters, as in [44].

16.4.2. MIMO channels

During the past several years there has been a growing interest in systems that employ multiple antennas both at the transmitter and the receiver, that is, MIMO systems. The main reason for this is a potential for dramatically increased capacity. From a propagation modeling point of view, MIMO transmission opens up an interesting new possibility. Besides finding the direction of the incoming rays, it is also possible to determine the directions-of-departure (DOD) of these rays [46], thus providing a more complete description of the wireless channel. Assuming a point source model, the received signal is now modeled as

$$\mathbf{x}(t) = \sum_{k=1}^{d} g_k \mathbf{a}_{rx}(\theta_k) \mathbf{a}_{tx}^T(\eta_k) \mathbf{s}(t-\tau_k) + \mathbf{n}(t). \tag{16.54}$$

Here, $\mathbf{a}_{tx}(\eta)$ denotes the $m_{tx} \times 1$ steering vector for the transmitter array, where η is the DOD, whereas $\mathbf{a}_{rx}(\theta)$ is the $m_{rx} \times 1$ steering vector for the receiving array with θ the DOA. Further, $\mathbf{s}(t) = [s_1(t), \ldots, s_{m_{tx}}(t)]^T$ contains the transmitted signal waveforms from each of the transmitting antennas (which are potentially different). As before, g_k is the complex gain of the kth path and τ_k is the time delay. Given $\mathbf{x}(t_n)$, $n = 1, \ldots, N$ from (16.54), where $\mathbf{s}(t)$ needs to be known to allow time-delay estimation, one desires to estimate all unknown parameters θ_k, η_k, τ_k, and g_k.

In matrix form, the NLLS criterion now takes the form

$$V(\boldsymbol{\theta}, \boldsymbol{\eta}, \boldsymbol{\tau}, \mathbf{g}) = \left\| \mathbf{X} - \sum_{l=1}^{d} g_l \mathbf{a}_{rx}(\theta_l) \mathbf{a}_{tx}^T(\eta_l) \mathbf{S}(\tau_l) \right\|^2, \tag{16.55}$$

where

$$\mathbf{S}(\tau_l) = [\mathbf{s}(t_1 - \tau_l), \ldots, \mathbf{s}(t_n - \tau_l)] \tag{16.56}$$

is the matrix of delayed transmit signals. The above is a 3D estimation problem. There is no conceptual difference to the 1D case, but the computational complexity associated with finding the signal parameters increases of course dramatically as new dimensions are opened up. The RELAX approach applied to (16.55) results in the following steps. First, a data cleaning is performed by

$$\mathbf{X}_l = \mathbf{X} - \sum_{k \neq l} g_k \mathbf{a}_{rx}(\theta_k) \mathbf{a}_{tx}^T(\eta_k) \mathbf{s}(t - \tau_k). \tag{16.57}$$

The concentrated criterion for the lth signal path is then

$$V_l(\theta_l, \eta_l, \tau_l) = \frac{|\, \mathbf{a}_{rx}^*(\theta_l) \mathbf{X}_l \mathbf{S}^*(\tau_l) \bar{\mathbf{a}}_{tx}(\eta_l) \,|^2}{||\mathbf{a}_{rx}(\theta_l)||^2 ||\mathbf{S}^*(\tau_l) \bar{\mathbf{a}}_{tx}(\eta_l)||^2}. \tag{16.58}$$

Again, we have the interpretation of space-time beamforming, but now in two spatial dimensions. The $\mathbf{a}_{rx}^*(\theta_l)$ does spatial beamforming along the rows of $\mathbf{X}_l$ (the receivers), whereas $\mathbf{S}^*(\tau_l)$ is a bank of temporal match filters, where each column (row of $\mathbf{S}(\tau_l)$) corresponds to one transmitter. The outputs of these filters are then weighted together by the transmit beamformer $\bar{\mathbf{a}}_{tx}(\eta_l)$, where $(\bar{\cdot})$ denotes complex conjugate. The description of the 3D RELAX algorithm is completed by the update of the amplitude parameter:

$$\hat{g}_l = \frac{\mathbf{a}_{rx}^*(\hat{\theta}_l) \mathbf{X}_l \mathbf{S}^*(\hat{\tau}_l) \bar{\mathbf{a}}_{tx}(\hat{\eta}_l)}{||\mathbf{a}_{rx}(\hat{\theta}_l)||^2 ||\mathbf{S}^*(\hat{\tau}_l) \bar{\mathbf{a}}_{tx}(\hat{\eta}_l)||^2}. \tag{16.59}$$

Running the above steps for $l = 1, \ldots, d$ and iterating until convergence, results ultimately in an approximate solution to the original NLLS problem (16.55).

The above assumes that the time-domain array data are available. Alternatively, the matrix-valued impulse response can be estimated by

$$\hat{\mathbf{H}}(t) = \mathbf{X}\mathbf{S}^*(t)\left(\mathbf{S}(t)\mathbf{S}^*(t)\right)^{-1}, \tag{16.60}$$

or it may be given directly from the measurement equipment. Here, the ijth element of $\hat{\mathbf{H}}(t)$ contains the estimated impulse response from transmitter i to receiver j. Similar to (16.53), the Fourier transform of $\hat{\mathbf{H}}(t)$ is modeled by

$$\hat{\mathbf{H}}(\omega_k) \approx \sum_{l=1}^{d} g_l \mathbf{a}_{rx}(\theta_l)\mathbf{a}_{tx}^T(\eta_l)e^{-j\omega_k\tau_l}, \quad k = 1,\ldots,M. \tag{16.61}$$

Either $\hat{\mathbf{H}}(t)$ or $\hat{\mathbf{H}}(\omega_k)$ can now be considered as measurement data, the task again being to determine the signal parameters g_l, θ_l, η_l, and τ_l for $l = 1,\ldots,d$. Several suboptimal techniques have been proposed to attack this problem. For example, in [47], the 2D ESPRIT method with spatial smoothing is applied to each sample $\hat{\mathbf{H}}(t_k)$ (the application in [47] is azimuth-elevation estimation, but the same approach can be applied to the DOD-DOA model). In [46], the delays are first determined using the 1D ESPRIT technique. A 2D RELAX-like approach is then applied to the so-obtained channel samples $\hat{\mathbf{H}}(\hat{\tau}_l)$. In [48], a 3D subspace method is proposed, assuming several observations of the matrix-valued transfer function $\hat{\mathbf{H}}(\omega_k)$ to be available. Finally, special methods for the case were only beamformed transmit and receive data are available are presented in [49, 50].

16.5. Summary

Direction-of-arrival (DOA) estimation is to a great extent a mature research area. We have in this chapter made an attempt to summarize the most influential methods to determine the signal parameters. For the standard DOA estimation problem, the nonlinear least-squares (NLLS) approach provides the most accurate estimates of the methods presented herein. An iterative method for computing the estimates was outlined, based on the RELAX idea presented in [26]. Subspace-based methods are computationally more attractive, especially the ESPRIT-type techniques, whenever applicable. These methods can give high resolution at moderate cost, provided the SNR and/or the number of available samples is sufficiently high. The conventional beamforming approach is applicable only when the array size is sufficiently large, whereas adaptive beamforming (Capon's method) can give increased resolution at high enough SNR.

Besides the standard DOA estimation problem, we have also considered the case where sources have a significant spatial extent, as compared to the array resolution. In this case, the incoming radiation is characterized in statistical terms, rather than as a point source only. Most commonly, the mean and the standard deviation of the DOA parameter are sought. In this case, beamforming-type methods are more likely to be useful than in the point-source case. However, the center of gravity of the beamforming spectrum should be used for estimation of the

mean DOA, rather than its peak location. Among high-resolution methods, a recent generalization of Capon's method due to [36] is found to be very promising. Finally, the case of parametric modeling of the communication channel, including propagation delay was also addressed. This leads to difficult multidimensional estimation problems, where easy solutions are likely to fail and optimal techniques are difficult to implement in practice. Iterative RELAX-type methods were presented for the various cases. Also subspace methods are available in the literature. These, and hybrids between subspace and NLLS have been found to give satisfactory results with real data, see, for example, [46, 47, 48].

Abbreviations

COMET	Covariance matching estimator
DFT	Discrete Fourier transform
DOA	Direction-of-arrival
DOD	Direction-of-departure
ESPRIT	Estimation of signal parameters via rotational invariance techniques
FFT	Fast Fourier transform
GC	Generalized Capon
LOS	Line-of-sight
LS	Least-squares
MIMO	Multiple-input multiple-output
ML	Maximum likelihood
MUSIC	Multiple signal classification
NLLS	Nonlinear least-squares
PDF	Probability density function
SAGE	Space-alternating generalized expected maximization
SIMO	Single-input multiple-output
SML	Stochastic maximum likelihood
SNR	Signal-to-noise ratio
SSF	Signal subspace fitting
ULA	Uniform linear array

Bibliography

[1] P. Stoica and R. Moses, *Introduction to Spectral Analysis*, Prentice Hall, Upper Saddle River, NJ, USA, 1997.

[2] W. Jakes, Ed., *Microwave Mobile Communications*, Wiley-Interscience, New York, NY, USA, 1974.

[3] A. Kavak, W. Yang, G. Xu, and W. J. Vogel, "Characteristics of vector propagation channels in dynamic mobile scenarios," *IEEE Trans. Antennas Propagat.*, vol. 49, no. 12, pp. 1695–1702, 2001.

[4] H. Krim and M. Viberg, "Two decades of array signal processing research: the parametric approach," *IEEE Signal Processing Mag.*, vol. 13, no. 4, pp. 67–94, 1996.

[5] H. L. Van Trees, *Optimum Array Processing*, John Wiley & Sons, Canada, 2002.

[6] J. Capon, "High resolution frequency wave number spectrum analysis," *Proc. IEEE*, vol. 57, pp. 1408–1418, 1969.

[7] G. V. Serebryakov, "Direction-of-arrival estimation of correlated sources by adaptive beamforming," *IEEE Trans. Signal Processing*, vol. 43, no. 11, pp. 2782–2787, 1995.

[8] M. Wax and T. Kailath, "Detection of signals by information theoretic criteria," *IEEE Trans. Acoustics, Speech, and Signal Processing*, vol. 33, no. 2, pp. 387–392, 1985.

[9] L. C. Zhao, P. R. Krishnaiah, and Z. D. Bai, "On detection of the number of signals in presence of white noise," *J. Multivariate Analysis*, vol. 20, no. 1, pp. 1–25, 1986.

[10] G. Bienvenu and L. Kopp, "Principe de la goniométrie passive adaptative," in *Proc. 7'eme Colloque sur le Traitement du Signal et ses Applications (GRETSI '79)*, pp. 106/1–106/10, Nice, France, 1979.

[11] R. O. Schmidt, "Multiple emitter location and signal parameter estimation," in *Proc. RADC Spectrum Estimation Workshop*, pp. 243–258, Rome, NY, USA, October 1979.

[12] R. O. Schmidt, *A signal subspace approach to multiple emitter location and spectral estimation*, Ph.D. thesis, Stanford University, Stanford, Calif, USA, November 1981.

[13] M. Wax and I. Ziskind, "On unique localization of multiple sources by passive sensor arrays," *IEEE Trans. Acoustics, Speech, and Signal Processing*, vol. 37, no. 7, pp. 996–1000, 1989.

[14] W. Xu and M. Kaveh, "Comparative study of the biases of MUSIC-like estimators," *Signal Processing*, vol. 50, no. 1-2, pp. 39–55, 1996.

[15] A. J. Barabell, "Improving the resolution performance of eigenstructure-based direction-finding algorithms," in *Proc. IEEE Int. Conf. Acoustics, Speech, Signal Processing (ICASSP '83)*, vol. 8, pp. 336–339, Cambridge, Mass, USA, April 1983.

[16] B. D. Rao and K. V. S. Hari, "Performance analysis of root-music," *IEEE Trans. Acoustics, Speech, and Signal Processing*, vol. 37, no. 12, pp. 1939–1949, 1989.

[17] R. Roy and T. Kailath, "ESPRIT—estimation of signal parameters via rotational invariance techniques," *IEEE Trans. Acoustics, Speech, and Signal Processing*, vol. 37, no. 7, pp. 984–995, 1989.

[18] M. Haardt and J. Nossek, "Unitary ESPRIT: how to obtain increased estimation accuracy with a reduced computational burden," *IEEE Trans. Signal Processing*, vol. 43, no. 5, pp. 1232–1242, 1995.

[19] B. Friedlander and A. Weiss, "Direction finding using spatial smoothing with interpolated arrays," *IEEE Trans. Aerosp. Electron. Syst.*, vol. 28, no. 2, pp. 574–587, 1992.

[20] J. F. Böhme, "Estimation of source parameters by maximum likelihood and nonlinear regression," in *Proc. IEEE Int. Conf. Acoustics, Speech, Signal Processing (ICASSP '84)*, vol. 9, pp. 271–274, San Diego, Calif, USA, March 1984.

[21] J. F. Böhme, "Separated estimation of wave parameters and spectral parameters by maximum likelihood," in *Proc. IEEE Int. Conf. Acoustics, Speech, Signal Processing (ICASSP '86)*, vol. 11, pp. 2818–2822, Tokyo, Japan, April 1986.

[22] B. Ottersten, M. Viberg, P. Stoica, and A. Nehorai, "Exact and large sample ML techniques for parameter estimation and detection in array processing," in *Radar Array Processing*, S. S. Haykin, J. Litva, and T. J. Shepherd, Eds., pp. 99–151, Springer, Berlin, Germany, 1993.

[23] P. Stoica and K. Sharman, "Maximum likelihood methods for direction-of-arrival estimation," *IEEE Trans. Acoustics, Speech, and Signal Processing*, vol. 38, no. July, pp. 1132–1143, 1990.

[24] M. Viberg and B. Ottersten, "Sensor array processing based on subspace fitting," *IEEE Trans. Signal Processing*, vol. 39, no. 5, pp. 1110–1121, 1991.

[25] J. A. Fessler and A. O. Hero, "Space-alternating generalized expectation-maximization algorithm," *IEEE Trans. Signal Processing*, vol. 42, no. 10, pp. 2664–2677, 1994.

[26] J. Li, D. Zheng, and P. Stoica, "Angle and waveform estimation via RELAXE," *IEEE Trans. Aerosp. Electron. Syst.*, vol. 33, no. 3, pp. 1077–1087, 1997.

[27] P. Pelin, "A fast minimization technique for subspace fitting with arbitrary array manifolds," *IEEE Trans. Signal Processing*, vol. 49, no. 12, pp. 2935–2939, 2001.

[28] I. Ziskind and M. Wax, "Maximum likelihood localization of multiple sources by alternating projection," *IEEE Trans. Acoustics, Speech, and Signal Processing*, vol. 36, no. October, pp. 1553–1560, 1988.

[29] M. Viberg, B. Ottersten, and T. Kailath, "Detection and estimation in sensor arrays using weighted subspace fitting," *IEEE Trans. Signal Processing*, vol. 39, no. 11, pp. 2436–2449, 1991.

[30] M. Wax, "Detection and localization of multiple sources via the stochastic signals model," *IEEE Trans. Signal Processing*, vol. 39, no. 11, pp. 2450–2456, 1991.

[31] J. B. Andersen and K. I. Pedersen, "Angle-of-arrival statistics for low resolution antennas," *IEEE Trans. Antennas Propagat.*, vol. 50, no. 3, pp. 391–395, 2002.

[32] R. B. Ertel, P. Cardieri, K. W. Sowerby, T. S. Rappaport, and J. H. Reed, "Overview of spatial channel models for antenna array communication systems," *IEEE Pers. Commun.*, vol. 5, no. 1, pp. 10–22, 1998.

[33] R. Raich, J. Goldberg, and H. Messer, "Bearing estimation for a distributed source via the conventional beamformer," in *Proc. 9th IEEE Signal Processing Statistical Signal and Array Processing*, pp. 5–8, Portland, Ore, USA, September 1998.

[34] D. Astély and B. Ottersten, "The effects of local scattering on direction of arrival estimation with MUSIC," *IEEE Trans. Signal Processing*, vol. 47, no. 12, pp. 3220–3234, 1999.

[35] M. Tapio, "On the use of beamforming for estimation of spatially distributed signals," in *Proc. IEEE Int. Conf. Acoustics, Speech, Signal Processing (ICASSP '03)*, vol. 3, pp. 3005–3008, Hong Kong, May 2003.

[36] A. Hassanien, S. Shahbazpanahi, and A. Gershman, "A generalized Capon estimator for multiple spread sources," *IEEE Trans. Signal Processing*, vol. 52, no. 1, pp. 280–283, 2004.

[37] M. Bengtsson and B. Ottersten, "Low-complexity estimators for distributed sources," *IEEE Trans. Signal Processing*, vol. 48, no. 8, pp. 2185–2194, 2000.

[38] Y. Meng, P. Stoica, and K. M. Wong, "Estimation of the direction of arrival of spatially dispersed sources," *IEE Proc. Radar, Sonar and Navigation*, vol. 143, no. 1, pp. 1–9, 1996.

[39] S. Valaee, B. Champagne, and P. Kabal, "Parametric localization of distributed sources," *IEEE Trans. Signal Processing*, vol. 43, no. 7, pp. 2144–2153, 1995.

[40] T. Trump and B. Ottersten, "Estimation of nominal direction of arrival and angular spread using and array of sensors," *Signal Processing*, vol. 50, no. 1-2, pp. 57–70, 1996.

[41] O. Besson and P. Stoica, "Decoupled estimation of DOA and angular spread for a spatially distributed source," *IEEE Trans. Signal Processing*, vol. 48, no. 7, pp. 1872–1882, 1983.

[42] R. Wu, J. Li, and Z.-S. Liu, "Super resolution time delay estimation via MODE-WRELAX," *IEEE Trans. Aerosp. Electron. Syst.*, vol. 35, no. 1, pp. 294–307, 1999.

[43] K. I. Pedersen, B. Fleury, and P. E. Mogensen, "High resolution of electromagnetic waves in time-varying radio channels," in *Proc. 8th IEEE International Symposium on Personal, Indoor and Mobile Radio Communications (PIMRC '97)*, vol. 2, pp. 650–654, Helsinki, Finland, September 1997.

[44] M. Vanderveen, A.-J. van der Veen, and A. Paulraj, "Estimation of multipath parameters in wireless communications," *IEEE Trans. Signal Processing*, vol. 46, no. 3, pp. 682–690, 1998.

[45] S. Rouquette and M. Najim, "Estimation of frequencies and damping factors by two-dimensional ESPRIT type methods," *IEEE Trans. Signal Processing*, vol. 49, no. 1, pp. 237–245, 2001.

[46] M. Steinbauer, A. F. Molisch, and E. Bonek, "The double-directional radio channel," *IEEE Antennas Propagat. Mag.*, vol. 43, no. 4, pp. 51–63, 2001.

[47] J. Fuhl, J.-P. Rossi, and E. Bonek, "High-resolution 3-D direction-of-arrival determination for urban mobile radio," *IEEE Trans. Antennas Propagat.*, vol. 45, no. 4, pp. 672–682, 1997.

[48] M. Pesavento, C. F. Mecklenbräuker, and J. F. Böhme, "Double-directional radio channel estimation using MD-RARE," in *Proc. 36th Asilomar Conference on Signals, Systems and Computers*, vol. 1, pp. 594–598, Pacific Grove, Calif, USA, November 2002.

[49] B. D. Jeffs, E. Pyper, and B. Hunter, "A wireless MIMO channel probing approach for arbitrary antenna arrays," in *Proc. IEEE Int. Conf. Acoustics, Speech, Signal Processing (ICASSP '01)*, vol. 4, pp. 2493–2496, Salt Lake City, Utah, USA, May 2001.

[50] T. Zwick, D. Hampicke, J. Maurer, et al., "Results of double-directional channel sounding measurements," in *Proc. IEEE Vehicular Technology Conference (VTC '00)*, vol. 3, pp. 2497–2501, Tokyo, Japan, May 2000.

Mats Viberg: Department of Signals and Systems, Chalmers University of Technology, 412 96 Göteborg, Sweden

Email: viberg@chalmers.se

III Transmitter

Contents

17 Introduction

Javier Rodríguez Fonollosa

The Transmitter part starts providing a unified perspective to the design of linear transceivers for MIMO systems in the case of availability of channel state information (CSI) at both sides of the link. Chapter 2, authored by Daniel P. Palomar, elaborates on the design of linear precoders at the transmit side under different optimisation criteria. On the other hand, the optimal linear receiver can be shown to be independent of the optimisation criterion used and follows the minimum mean-squared error design (also termed the Wiener filter) possibly incorporating the additional zero-forcing constraint.

Traditionally, MIMO transmitters were designed based on very simple cost functions as, for example, the mean-squared error, and more sophisticated quality of service (QoS) requirements demanded specific designs. These schemes were particularly difficult to obtain when nonconvex or matrix-valued variables were involved. Recently, Palomar showed how to solve these problems in an optimal way for the family of Schur-concave and Schur-convex cost functions. Although this is a quite general result, one can think of some interesting QoS requirements that fall out of these categories, such as the minimisation of the average BER when different constellations are used. Chapter 2 generalises the previous results to embrace any arbitrary cost function as quality criterion. When the function is convex, the originally complicated nonconvex problem with matrix-valued variables can be reformulated as a simple convex problem with scalar variables. This simplified problem can then be addressed under the framework of convex optimisation theory, accommodating and easily solving a great variety of design criteria.

Chapter 3 considers the situation in which the transmitter has access to some limited or imperfect channel state information. Conventional space-time codes do not need any channel knowledge at the transmit side, and this is a clear advantage given the difficulties of acquiring such knowledge, but it may also be a substantial drawback since CSI, when available at the transmit side, can be used to improve performance. This chapter, authored by Jöngren, Skoglund, and Ottersten, develops the concept of channel side information dependent codes.

The conventional way of exploiting the CSI at the transmit side is by the use of beamforming. However, the resulting rank-one type of transmission inherent

to beamforming (which can be interpreted as assigning only a single preferable direction) is too restrictive when there are imperfections in the channel knowledge. The emitted energy instead should be spread out over several directions, much like in conventional space-time coding. This naturally leads to the concept of channel side information dependent space-time codes, where the codeword matrices depend on the channel side information and the possibly imperfect channel knowledge is taken into account already at the design stage. The idea is to make use of the complementary strengths of both transmission methodologies. Conventional space-time codes are designed to operate without any channel knowledge and hence provide the system with a basic level of performance in the absence of reliable channel state information at the transmitter. Beamforming, on the other hand, is advantageous when the channel knowledge is reliable.

Chapter 4, authored by Michael Joham and Wolfgang Utschick, enters into the area of nonlinear transmit processing, and specifically considers Tomlinson Harashima precoding. This technique can be understood as a generalisation in the transmit side of decision feedback equalisation in the receiver. Whereas decision feedback equalisers apply a modulo operation and feed back already quantized symbols, Tomlinson Harashima precoders apply the modulo operation into already transmitted symbols before feeding them back into the transmitter. The analysis is restricted to nondispersive channels and noncooperative receivers meaning that the signals of the different receivers cannot be jointly transformed. In fact, receivers are restricted to apply scalar weightings. Algorithms for the optimum formulation and ordering of the zero-forcing and Wiener Tomlinson Harashima precoders are obtained together with suboptimal, but less complex, ordering schemes.

Chapter 5 considers the optimisation of the different transmission strategies in a multiuser environment. It is well known that MIMO channels can be used to increase spectral efficiency and performance of point-to-point links. Nevertheless, the extension of these benefits to the multiuser case requires the development of new transmission schemes. Specifically, the cellular uplink situation is considered in this chapter, formally known as the MIMO multiple access channel (MAC), in which the optimum transmission depends on the objective function, the power constraints, the channel statistics, or the channel realisation.

When considering optimisation of multiuser systems, objective functions can be defined based on either global or individual performance criteria. Examples of objective functions belonging to the first class are the maximisation of the sum capacity or the minimisation of the mean-squared error. The drawback of this type of optimisation problems is that they can be unfair for some users. If users experience poor channel conditions for long periods of time, they are not given the possibility to transmit. These problems are circumvented defining individual objective functions based on the fulfilment of rate, SINR, or MSE requirements with minimal power. This chapter, authored by Eduard A. Jorswieck, motivates and analyses important representative problems of both classes. The development from the single-antenna MAC to the MIMO MAC is shown and the differences and commonalities between the single-antenna and the multiple-antenna cases

are stressed. Furthermore, the chapter emphasises the connections between the different objective functions and their corresponding programming problems.

Chapter 6 concludes the Transmitter part and concentrates on the design of the appropriate multiplexing schemes in the presence of MIMO channel matrix ill-conditioning. Fading correlation or presence of a Rice component in the MIMO channel can cause this situation. Conventional multiplexing schemes based on the separation of the different streams using their spatial signatures (commonly referred to as spatial multiplexing, SM) rely on the linear independence between the channel responses corresponding to each transmit antenna. Consequently such schemes suffer considerably from effects of bringing ill-conditioning into the MIMO channel matrix. This chapter, authored by David Gesbert investigates the use of constellation multiplexing (CM) in an attempt to robustify SM schemes. Distinct M-QAM streams are superposed to form a higher-order QAM constellation, which has a rate equal to the sum of rates of all original streams. CM schemes do not rely on the full-rank property of the MIMO channel to function properly. This chapter investigates how to combine SM and CM schemes in the form of a linear diagonal precoder. This yields an adaptive rate-preserving MIMO multiplexing algorithm that can operate smoothly for any degree of correlation or Ricean factor. Conventional SM and CM schemes are shown to be particular cases of the presented family of schemes.

Javier Rodríguez Fonollosa: Technical University of Catalonia (UPC), Mdul D5, Campus Nord, Jordi Girona 1-3, E-08034 Barcelona, Spain

Email: javier.fonollosa@upc.edu

18 Unified design of linear transceivers for MIMO channels

Daniel Pérez Palomar

MIMO communication systems with CSI at both sides of the link can adapt to each channel realization to optimize the spectral efficiency and/or the reliability of the communication. A low-complexity approach with high potential is the use of linear MIMO transceivers (composed of a linear precoder at the transmitter and a linear equalizer at the receiver). The design of linear transceivers has been studied for many years (the first papers dating back to the 1970s) based on very simple cost functions as a measure of the system quality such as the trace of the MSE matrix. If more reasonable measures of quality are considered, the problem becomes much more complicated due to its nonconvexity and to the matrix-valued variables. Recent results showed how to solve the problem in an optimal way for the family of Schur-concave and Schur-convex cost functions. Although this is a quite general result, there are some interesting functions that fall outside of this category such as the minimization of the average BER when different constellations are used. In this chapter, these results are further generalized to include any cost function as a measure of the quality of the system. When the function is convex, the original complicated nonconvex problem with matrix-valued variables can always be reformulated a simple convex problem with scalar-valued variables. The simplified problem can then be addressed under the powerful framework of convex optimization theory, in which a great number of interesting design criteria can be easily accommodated and efficiently solved even though closed-form expressions may not exist.

18.1. Introduction

Multiple-input multiple-output (MIMO) channels are an abstract and general way to model many different communication systems of diverse physical nature; ranging from wireless multiantenna channels [1, 2, 3, 4] (see Figure 18.1) to wireline digital subscriber line (DSL) systems [5], and to single-antenna frequency-selective channels [6]. In particular, wireless multiantenna MIMO channels have been recently attracting a significant interest because they provide an important increase of spectral efficiency with respect to single-input single-output (SISO)

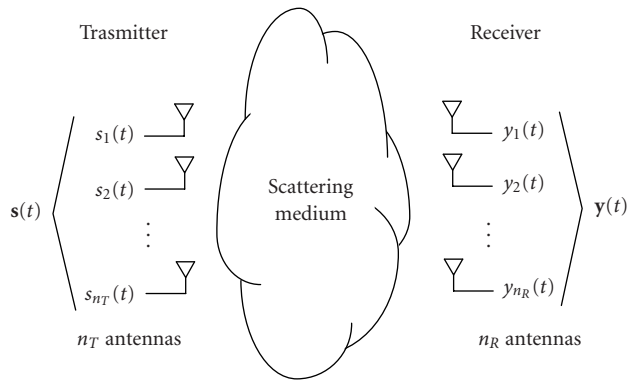

FIGURE 18.1. Example of a MIMO channel arising in wireless communications with multiple antennas at both the transmitter and the receiver.

channels [3, 4]. This abstract MIMO modeling allows for a unified treatment using a very elegant and convenient vector-matrix notation.

This chapter considers point-to-point MIMO communication systems with channel state information (CSI) at both sides of the link (cf. Section 18.2). For the case of no CSI at the transmitter, a great number of techniques have also been proposed in the literature which can globally referred to as *space-time coding* [1, 7, 8].

MIMO systems are not just mathematically more involved than SISO systems but also conceptually different and more complicated. Several substreams are typically established in MIMO channels (so-called multiplexing property [9]), whereas SISO channels can only support a single substream of information. It is this increase of dimensionality that makes the mathematical notation more involved, in the sense that the manipulation of scalar quantities becomes a vector-matrix manipulation. In addition, the existence of several substreams, each with its own quality, makes the definition of a global measure of the system quality very difficult; as a consequence, different design criteria have been pursued in the literature (cf. Section 18.2). In fact, such a problem is a multiobjective optimization problem characterized by not having just optimal solutions (as happens in single-objective optimization problems) but a set of Pareto-optimal solutions[1] [10]. Although to fully characterize such a problem, the Pareto-optimal set should be obtained, it is generally more convenient to use a single measure of the system quality to simplify the characterization.

Theoretically, the design of MIMO systems with CSI at both sides of the link has been known since 1948, when Shannon, in his ground-breaking paper [11], defined the concept of channel capacity—the maximum reliably achievable rate—and obtained the capacity-achieving signaling strategy. In particular, for a given realization of a MIMO channel, the optimal transmission is given by a Gaussian

[1] A Pareto-optimal solution is defined as any solution that cannot be improved with respect to any component without worsening the others [10].

signaling with a water-filling power profile over the channel eigenmodes [12, 3, 2]. From a more practical standpoint, however, the ideal Gaussian codes are substituted with practical constellations (such as QAM constellations) and coding schemes. To simplify the study of such a system, it is customary to divide it into an uncoded part, which transmits symbols drawn from some constellations, and a coded part that builds upon the uncoded system. Although the ultimate system performance depends on the combination of both parts (in fact, for some systems, such a division does not apply), it is convenient to consider the uncoded and coded parts independently to simplify the analysis and design. The focus of this chapter is on the uncoded part of the system and, specifically, on the employment of linear transceivers (composed of a linear precoder at the transmitter and a linear equalizer at the receiver) for complexity reasons.[2]

Hence, the problem faced when designing a MIMO system not only lies on the design itself but also on the choice of the appropriate measure of the system quality (which may depend on the application at hand and/or on the type of coding used on top of the uncoded system). The traditional results existing in the literature have dealt with the problem from a narrow perspective (due to the complexity of the problem); the basic approach has been to choose a measure of quality of the system sufficiently simple such that the problem can be analytically solved. Recent results have considered more elaborated and meaningful measures of quality. In the sequel, a unified framework for the systematic design of linear MIMO transceivers is developed.

This chapter is structured as follows. Section 18.2 gives an overview of the classical and recent results existing in the literature. After describing the signal model in Section 18.3, the general problem to be addressed is formulated in Section 18.4. Then, Section 18.5 gives the optimal receiver and Section 18.6 obtains the main result of this chapter: the unified framework for the optimization of the transmitter under different criteria. Section 18.7 addresses the issue of the diagonal/nondiagonal structure of the optimal transmission. Several illustrative examples are considered in detail in Section 18.8. The extension of the results to multiple MIMO channels is described in Section 18.9. Some numerical results are given in Section 18.10 to exemplify the application of the developed framework. Finally, Section 18.11 summarizes the main results of the chapter.

The following notation is used. Boldface uppercase letters denote matrices, boldface lowercase letters denote column vectors, and italics denote scalars. $\mathbb{R}^{m\times n}$ and $\mathbb{C}^{m\times n}$ represent the set of $m \times n$ matrices with real- and complex-valued entries, respectively. The superscripts $(\cdot)^T$, $(\cdot)^*$, and $(\cdot)^H$ denote transpose, complex conjugate, and Hermitian operations, respectively. $[\mathbf{X}]_{i,j}$ (also $[\mathbf{X}]_{ij}$) denotes the (ith, jth) element of matrix $\mathbf{X}$. $\mathrm{Tr}(\cdot)$ and $\det(\cdot)$ denote the trace and determinant of a matrix, respectively. A block-diagonal matrix with diagonal blocks given by the set $\{\mathbf{X}_k\}$ is denoted by $\mathrm{diag}(\{\mathbf{X}_k\})$. The operator $(x)^+ \triangleq \max(0, x)$ is the projection onto the nonnegative orthant.

[2]The choice of linear transceivers is also supported by their optimality from an information-theoretic viewpoint.

18.2. Historical overview of MIMO transceivers

The design of linear MIMO transceivers has been studied since the 1970s where cable systems were the main application [13, 14]. Initially, since the problem is very complicated, it was tackled by optimizing easily tractable cost function as a measure of the system quality such as the sum of the mean square error (MSE) of all channel substreams or, equivalently, the trace of the MSE matrix [13, 14, 15, 6]. Others examples include the minimization of the weighted trace of the MSE matrix [16], the minimization of the determinant of the MSE matrix [17], and the maximization of the signal-to-interference-plus-noise ratio (SINR) criterion with a zero-forcing (ZF) constraint [6]. Some criteria were considered under a peak power constraint in [18].

For these criteria, the original complicated design problem is greatly simplified because the channel turns out to be diagonalized by the optimal transmit-receive processing and the transmission is effectively performed on a diagonal or parallel fashion. The diagonal transmission allows a *scalarization* of the problem (meaning that all matrix equations are substituted with scalar ones) with the consequent simplification. In light of the optimality of the diagonal structure for transmission in all the aforementioned examples (including the capacity-achieving solution [12, 3, 19]), one may expect that the same holds for other criteria as well.

In [20], a general unifying framework was developed that embraces a wide range of different design criteria; in particular, the optimal design was obtained for the family of Schur-concave and Schur-convex cost functions which arise in majorization theory [21]. Interestingly, this framework gives a clear answer to the question of when the diagonal transmission is optimal.

However, rather than the MSE or the SINR, the ultimate performance of a system is given by the bit error rate (BER), which is more difficult to handle. In [22], the minimization of the BER (and also of the Chernoff upper bound) averaged over the channel substreams was treated in detail when a diagonal structure is imposed. Recently, the minimum BER design without the diagonal structure constraint has been independently obtained in [20, 23], resulting in an optimal nondiagonal structure. This result, however, only applies when the constellations used in all channel substreams are equal (in which case the cost function happens to be Schur-convex [20]). The general case of different constellations is much more involved (in such a case, the cost function is neither Schur-convex nor Schur-concave) and was solved in [24] via a primal decomposition approach.

There are two natural extensions of the existing results on point-to-point MIMO transceivers: to the case of imperfect CSI and to the multiuser scenario. With imperfect CSI (due, e.g., to estimation errors), robust transceivers are necessary to cope with the uncertainty. The existing results along this line are very few and further work is still needed; some results were obtained in [25, 26] with a worst-case robust approach and in [27, 28] with a stochastic robust approach (see also [29] for a combination of space-time coding with linear precoding). Regarding the extension to the multiuser scenario, the existing results are very scarce: in

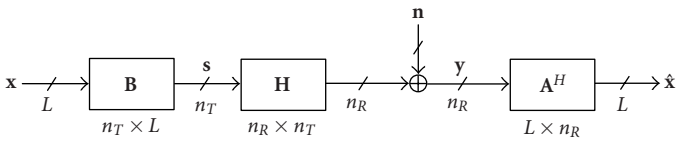

FIGURE 18.2. Scheme of a general MIMO communication system with a linear transceiver.

[30], a suboptimal joint design of the transmit-receive beamforming and power allocation in a wireless network was proposed; and, in [31], the optimal MIMO transceiver design in a multiple-access channel was obtained in terms of minimizing the sum of the MSEs of all the substreams and of all users (a similar approach was employed in [32] for a broadcast channel). Iterative single-user methods have also been applied to the multiuser case with excellent performance [33, 34].

In the sequel, the problem of linear MIMO transceiver design is formulated and solved in a very general way for an arbitrary cost function as a measure of the system quality. The design can then be approached from a unified perspective that provides great insight into the problem and simplifies it. The key step is in reformulating the originally nonconvex problem in convex form after some manipulations based on majorization theory [21]. The simplified problem can then be addressed under the powerful framework of convex optimization theory [35, 36], in which a great number of interesting design criteria can be easily accommodated and efficiently solved even though closed-form expressions may not exist.

18.3. System model

The signal model corresponding to a transmission through a general MIMO communication channel with n_T transmit and n_R receive dimensions is

$$\mathbf{y} = \mathbf{H}\mathbf{s} + \mathbf{n}, \tag{18.1}$$

where $\mathbf{s} \in \mathbb{C}^{n_T \times 1}$ is the transmitted vector, $\mathbf{H} \in \mathbb{C}^{n_R \times n_T}$ is the channel matrix, $\mathbf{y} \in \mathbb{C}^{n_R \times 1}$ is the received vector, and $\mathbf{n} \in \mathbb{C}^{n_R \times 1}$ is a zero-mean circularly symmetric complex Gaussian interference-plus-noise vector with arbitrary covariance matrix $\mathbf{R}_n$.

The transmitted vector can be written as (see Figure 18.2)

$$\mathbf{s} = \mathbf{B}\mathbf{x}, \tag{18.2}$$

where $\mathbf{B} \in \mathbb{C}^{n_T \times L}$ is the transmit matrix (precoder) and $\mathbf{x} \in \mathbb{C}^{L \times 1}$ is the data vector that contains the L symbols to be transmitted (zero mean,[3] normalized and uncorrelated, that is, $\mathbb{E}[\mathbf{x}\mathbf{x}^H] = \mathbf{I}$) drawn from a set of constellations. For the sake

[3] If a constellation does not have zero mean, the receiver can always remove the mean and then proceed as if the mean was zero, resulting in a loss of transmitted power. Indeed, the mean of the signal does not carry any information and can always be set to zero saving power at the transmitter.

of notation, it is assumed that $L \leq \min(n_R, n_T)$. The total average transmitted power (in units of energy per transmission) is

$$P_T = \mathbb{E}[\|\mathbf{s}\|^2] = \mathrm{Tr}\,(\mathbf{B}\mathbf{B}^H). \tag{18.3}$$

Similarly, the estimated data vector at the receiver is (see Figure 18.2)

$$\hat{\mathbf{x}} = \mathbf{A}^H\mathbf{y}, \tag{18.4}$$

where $\mathbf{A}^H \in \mathbb{C}^{L\times n_R}$ is the receive matrix (equalizer).

It is interesting to observe that the ith column of $\mathbf{B}$ and $\mathbf{A}$, $\mathbf{b}_i$ and $\mathbf{a}_i$, respectively, can be interpreted as the transmit and receive beamvectors, respectively, associated to the ith transmitted symbol x_i:

$$\hat{x}_i = \mathbf{a}_i^H(\mathbf{H}\mathbf{b}_i x_i + \mathbf{n}_i), \tag{18.5}$$

where $\mathbf{n}_i = \sum_{j\neq i}\mathbf{H}\mathbf{b}_j x_j + \mathbf{n}$ is the equivalent noise seen by the ith substream, with covariance matrix $\mathbf{R}_{n_i} = \sum_{j\neq i}\mathbf{H}\mathbf{b}_j\mathbf{b}_j^H\mathbf{H}^H + \mathbf{R}_n$.

It is worth noting that in some particular scenarios such as in multicarrier systems, although the previous signal model can be directly applied by properly defining the channel matrix $\mathbf{H}$ as a block-diagonal matrix containing the channel at each carrier, it may also be useful to model the system as a set of parallel and noninterfering MIMO channels (cf. Section 18.9).

18.3.1. Measures of quality

The quality of the ith established substream or link in (18.5) can be conveniently measured, among others, in terms of MSE, SINR, or BER, defined, respectively, as

$$\mathrm{MSE}_i \triangleq \mathbb{E}[\,|\hat{x}_i - x_i|^2\,] = |\,\mathbf{a}_i^H\mathbf{H}\mathbf{b}_i - 1\,|^2 + \mathbf{a}_i^H\mathbf{R}_{n_i}\mathbf{a}_i, \tag{18.6}$$

$$\mathrm{SINR}_i \triangleq \frac{\text{desired component}}{\text{undesired component}} = \frac{|\,\mathbf{a}_i^H\mathbf{H}\mathbf{b}_i\,|^2}{\mathbf{a}_i^H\mathbf{R}_{n_i}\mathbf{a}_i}, \tag{18.7}$$

$$\mathrm{BER}_i \triangleq \frac{\#\text{ bits in error}}{\#\text{ transmitted bits}} \approx \tilde{g}_i(\,\mathrm{SINR}_i\,), \tag{18.8}$$

where $\tilde{g}_i$ is a function that relates the BER to the SINR at the ith substream. For most types of modulations, the BER can indeed be analytically expressed as a function of the SINR when the interference-plus-noise term follows a Gaussian distribution [37, 38, 39]; otherwise, it is an approximation (see [24] for a more detailed discussion). For example, for square M-ary QAM constellations, the BER is [37, 39]

$$\mathrm{BER}(\mathrm{SINR}) \approx \frac{4}{\log_2 M}\left(1 - \frac{1}{\sqrt{M}}\right)\mathcal{Q}\left(\sqrt{\frac{3}{M-1}\,\mathrm{SINR}}\right), \tag{18.9}$$

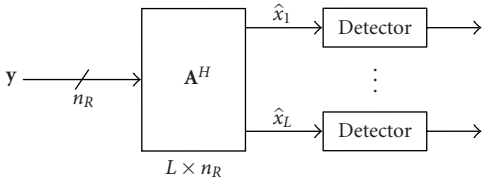

FIGURE 18.3. Independent detection of the substreams after the joint linear processing with matrix **A**.

where $\mathcal{Q}$ is the $\mathcal{Q}$-function defined as $\mathcal{Q}(x) \triangleq (1/\sqrt{2\pi}) \int_x^\infty e^{-\lambda^2/2} d\lambda$ [38].[4] It is sometimes convenient to use the Chernoff upper bound of the tail of the Gaussian distribution function $\mathcal{Q}(x) \leq (1/2)e^{-x^2/2}$ [38] to approximate the symbol error probability (which becomes a reasonable approximation for high values of the SINR).

It is worth pointing out that expressing the BER as in (18.8) implicitly assumes that the different links are independently detected after the joint linear processing with the receive matrix **A** (see Figure 18.3). This reduces the complexity drastically compared to a joint maximum-likelihood (ML) detection and is indeed the main advantage of using the receive matrix **A**.

Any properly designed system should attempt to somehow minimize the MSEs, maximize the SINRs, or minimize the BERs, as is mathematically formulated in the next section.

18.4. General problem formulation

The problem addressed in this chapter is the optimal design of a linear MIMO transceiver (matrices **A** and **B**) as a tradeoff between the power transmitted and the quality achieved. To be more specific, the problem can be formulated as the minimization of some cost function f_0 of the MSEs in (18.6), which measures the system quality (a smaller value of f_0 means a better quality), subject to a transmit power constraint [20, 40]:

$$\begin{aligned} &\min_{\mathbf{A},\mathbf{B}} \; f_0(\{\mathrm{MSE}_i\}) \\ &\text{s.t.} \;\; \mathrm{Tr}\left(\mathbf{B}\mathbf{B}^H\right) \leq P_0 \end{aligned} \tag{18.10}$$

or, conversely, as the minimization of the transmit power subject to a constraint on the quality of the system:

$$\begin{aligned} &\min_{\mathbf{A},\mathbf{B}} \; \mathrm{Tr}\left(\mathbf{B}\mathbf{B}^H\right) \\ &\text{s.t.} \quad f_0(\{\mathrm{MSE}_i\}) \leq \alpha_0, \end{aligned} \tag{18.11}$$

where P_0 and α_0 denote the maximum values for the power and for the cost function, respectively.

[4] The complementary error function is related to the $\mathcal{Q}$-function as $\mathrm{erfc}(x) = 2\,\mathcal{Q}(\sqrt{2}x)$ [38].

The cost function f_0 is an indicator of how well the system performs and should be properly selected for the problem at hand. In principle, any function can be used to measure the system quality as long as it is strictly increasing in each argument. Note that the increasingness of f_0 is a mild and completely reasonable assumption: if the quality of one of the substream improves while the rest remain unchanged, any reasonable function should properly reflect this difference.

The problem formulations in (18.10) and (18.11) are in terms of a cost function of the MSEs; however, similar design problems can be straightforwardly formulated with cost functions of the SINRs and of the BERs (when using cost functions of the BERs, it is implicitly assumed that the constellations have already been chosen such that (18.8) can be employed).

Alternatively, it is also possible to consider independent constraints on each of the links rather than a global measure of the quality [26, 40]:

$$\begin{aligned} &\min_{\mathbf{A},\mathbf{B}} \ \mathrm{Tr}\,(\mathbf{B}\mathbf{B}^H) \\ &\text{s.t.} \quad \mathrm{MSE}_i \leq \rho_i \quad 1 \leq i \leq L, \end{aligned} \tag{18.12}$$

where ρ_i denotes the maximum MSE value for the ith substream. Constraints in terms of SINR and BER can be similarly considered. Note that the solution to problem (18.12) allows a more detailed characterization of the fundamental multiobjective nature of the problem [10]; it allows, for example, to compute the exact region of achievable MSEs for a given power budget.

For the sake of space, this chapter focuses on the power-constrained problem in (18.10). The quality-constrained problem in (18.11), however, is so closely related that the results obtained also hold for this problem (in particular, Theorem 18.1 holds for problem (18.11)). Problem (18.12) is mathematically more involved and the interested reader is referred to [26, 40, 24].

If fact, since problems (18.10) and (18.11) characterize the same strictly monotonic tradeoff curve of power versus quality, each of them can be easily solved by iteratively solving the other one using, for example, the bisection method [35, Algorithm 4.1].

18.5. Receiver design

The receive matrix $\mathbf{A}$ can be easily optimized for a given fixed transmit matrix $\mathbf{B}$. In principle, the optimal receive matrix may depend on the specific choice of the cost function f_0. However, it turns out that the optimal solution is independent of f_0 as is now briefly described (for more details, the reader is referred to [20, 40]).

It will be notationally convenient to define the MSE matrix as

$$\mathbf{E} \triangleq \mathbb{E}\left[(\hat{\mathbf{x}} - \mathbf{x})(\hat{\mathbf{x}} - \mathbf{x})^H\right] = (\mathbf{A}^H\mathbf{H}\mathbf{B} - \mathbf{I})(\mathbf{B}^H\mathbf{H}^H\mathbf{A} - \mathbf{I}) + \mathbf{A}^H\mathbf{R}_n\mathbf{A} \tag{18.13}$$

from which the MSE of the ith link is obtained as the ith diagonal element of $\mathbf{E}$, that is, $\mathrm{MSE}_i = [\mathbf{E}]_{ii}$.

The minimization of the MSE of a substream with respect to the receive matrix $\mathbf{A}$ (for a fixed transmit matrix $\mathbf{B}$) does not incur any penalty on the other substreams (see, e.g., (18.5) where $\mathbf{a}_i$ only affects $\hat{x}_i$); in other words, there is no tradeoff among the MSEs and the problem decouples. Therefore, it is possible to minimize simultaneously all MSEs and this is precisely how the well-known linear minimum MSE (MMSE) receiver, also termed Wiener filter, is obtained [41] (see also [20, 26]). If the additional ZF constraint $\mathbf{A}^H\mathbf{H}\mathbf{B} = \mathbf{I}$ is imposed to avoid crosstalk among the substreams (which may happen with the MMSE receiver), then the well-known ZF receiver is obtained [40]. Interestingly, the MMSE and ZF receivers are also optimum in the sense that they maximize simultaneously all SINRs and, consequently, minimize simultaneously all BERs (cf. [20, 40]).

The MMSE and ZF receivers can be compactly written as

$$\mathbf{A} = \mathbf{R}_n^{-1}\mathbf{H}\mathbf{B}\left(\nu\mathbf{I} + \mathbf{B}^H\mathbf{H}^H\mathbf{R}_n^{-1}\mathbf{H}\mathbf{B}\right)^{-1}, \tag{18.14}$$

where ν is a parameter defined as

$$\nu \triangleq \begin{cases} 1 & \text{for the MMSE receiver,} \\ 0 & \text{for the ZF receiver.} \end{cases} \tag{18.15}$$

The MSE matrix reduces then to the following concentrated MSE matrix:

$$\mathbf{E} = \left(\nu\mathbf{I} + \mathbf{B}^H\mathbf{R}_H\mathbf{B}\right)^{-1}, \tag{18.16}$$

where $\mathbf{R}_H \triangleq \mathbf{H}^H\mathbf{R}_n^{-1}\mathbf{H}$ is the squared whitened channel matrix.

18.5.1. Relation among different measures of quality

It is convenient now to relate the different measures of quality, namely, MSE, SINR, and BER, to the concentrated MSE matrix in (18.16).

From the definition of MSE matrix, the individual MSEs are given by the diagonal elements:

$$\mathrm{MSE}_i = \left[\left(\nu\mathbf{I} + \mathbf{B}^H\mathbf{R}_H\mathbf{B}\right)^{-1}\right]_{ii}. \tag{18.17}$$

It turns out that the SINRs and the MSEs are trivially related when using the MMSE or ZF receivers as [20, 26, 40]

$$\mathrm{SINR}_i = \frac{1}{\mathrm{MSE}_i} - \nu. \tag{18.18}$$

Finally, the BERs can also be written as a function of the MSEs:

$$\mathrm{BER}_i = g_i(\,\mathrm{MSE}_i\,) \triangleq \tilde{g}_i(\,\mathrm{SINR}_i = \mathrm{MSE}_i^{-1} - \nu), \tag{18.19}$$

where $\tilde{g}_i$ was defined in (18.8).

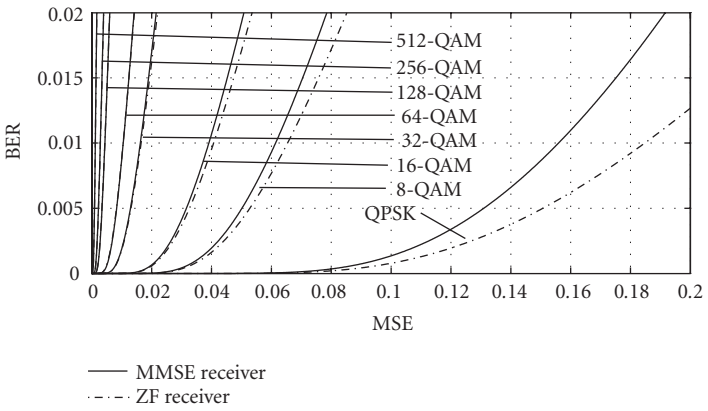

FIGURE 18.4. BER as a function of the MSE for different QAM constellations.

It is important to remark that the BER functions $\tilde{g}_i$ are convex decreasing in the SINR and the BER functions g_i are convex increasing in the MSE for sufficiently small values of the argument (see Figure 18.4) [20, 40] (this last property will be key when proving later in Section 18.8.2 that the average BER function is Schur-convex). As a rule of thumb, the BER as a function of the MSE is convex for a BER less than 2×10^{-2} (this is a mild assumption, since practical systems have in general a smaller uncoded BER[5]); interestingly, for BPSK and QPSK constellations, the BER function is always convex [20, 40].

Summarizing, the MMSE and ZF receivers have been obtained as the optimum solution in the sense of minimizing the MSEs, maximizing the SINRs, and minimizing the BERs. In addition, since the SINR and the BER can be expressed as a function of the MSE, (18.18) and (18.19), it suffices to focus on cost functions of the MSEs without loss of generality.

18.6. Transmitter design

Now that the MMSE and ZF receivers have been obtained as optimal solutions, the main problem addressed in this chapter can be finally formulated: the optimization of the transmit matrix $\mathbf{B}$ for an arbitrary cost function of the MSEs (recall that cost functions of the SINRs and BERs can always be reformulated as functions of the MSEs).

Theorem 18.1. *The following complicated nonconvex constrained optimization problem:*

$$\begin{aligned} &\min_{\mathbf{B}} \; f_0\left(\left\{\left[\left(\nu\mathbf{I}+\mathbf{B}^H\mathbf{R}_H\mathbf{B}\right)^{-1}\right]_{ii}\right\}\right) \\ &s.t. \quad \mathrm{Tr}\left(\mathbf{B}\mathbf{B}^H\right) \leq P_0, \end{aligned} \tag{18.20}$$

[5]Given an uncoded bit error probability of at most 10^{-2} and using a proper coding scheme, coded bit error probabilities with acceptable low values such as 10^{-6} can be obtained.

where $f_0 : \mathbb{R}^L \to \mathbb{R}$ is an arbitrary cost function (increasing in each argument and minimized when the arguments are sorted in decreasing order[6]), is equivalent to the simple problem

$$\begin{aligned} \min_{\mathbf{p},\boldsymbol{\rho}} \; & f_0(\rho_1, \ldots, \rho_L) \\ s.t. \; & \sum_{j=i}^{L} \frac{1}{\nu + p_j \lambda_{H,j}} \leq \sum_{j=i}^{L} \rho_j, \quad 1 \leq i \leq L, \\ & \rho_i \geq \rho_{i+1}, \\ & \sum_{j=1}^{L} p_j \leq P_0, \\ & p_i \geq 0, \end{aligned} \tag{18.21}$$

where the $\lambda_{H,i}$'s are L largest eigenvalues of $\mathbf{R}_H$ sorted in increasing order $\lambda_{H,i} \leq \lambda_{H,i+1}$ and $\rho_{L+1} \triangleq 0$. Furthermore, if f_0 is a convex function, problem (18.21) *is convex and the ordering constraint $\rho_i \geq \rho_{i+1}$ can be removed.*

More specifically, the optimal solution to problem (18.20) *is given by*

$$\mathbf{B} = \mathbf{U}_{H,1} \boldsymbol{\Sigma}_B \mathbf{Q}, \tag{18.22}$$

where $\mathbf{U}_{H,1} \in \mathbb{C}^{n_T \times L}$ is a (semi-)unitary matrix that has as columns the eigenvectors of $\mathbf{R}_H$ corresponding to the L largest eigenvalues in increasing order, $\boldsymbol{\Sigma}_B = \operatorname{diag}(\{\sqrt{p_i}\}) \in \mathbb{R}^{L \times L}$ is a diagonal matrix with the optimal power allocation $\{p_i\}$ obtained as the solution to problem (18.21)*, and $\mathbf{Q}$ is a unitary matrix such that $[(\nu \mathbf{I} + \mathbf{B}^H \mathbf{R}_H \mathbf{B})^{-1}]_{ii} = \rho_i$ for $1 \leq i \leq L$ (see* [42, Section IV-A] *for a practical algorithm to obtain $\mathbf{Q}$).*

In addition, the optimal solution can be further characterized for two particular cases of cost functions.

(i) *If f_0 is Schur-concave, then an optimal solution is*

$$\mathbf{B} = \mathbf{U}_{H,1} \boldsymbol{\Sigma}_B. \tag{18.23}$$

(ii) *If f_0 is Schur-convex, then an optimal solution is*

$$\mathbf{B} = \mathbf{U}_{H,1} \boldsymbol{\Sigma}_B \mathbf{Q}, \tag{18.24}$$

where $\mathbf{Q}$ is a unitary matrix such that $(\mathbf{I} + \mathbf{B}^H \mathbf{R}_H \mathbf{B})^{-1}$ has identical diagonal elements. This rotation matrix $\mathbf{Q}$ can be computed with the algorithm in [42, Section IV-A]*, as well as with any unitary matrix that satisfies $|[\mathbf{Q}]_{ik}| = |[\mathbf{Q}]_{il}|$, for all i, k, l such as the unitary discrete Fourier transform (DFT) matrix or the unitary*

[6] In practice, most cost functions are minimized when the arguments are in a specific ordering (if not, one can always use instead the function $\tilde{f}_0(\mathbf{x}) = \min_{\mathbf{P} \in \mathcal{P}} f_0(\mathbf{P}\mathbf{x})$, where $\mathcal{P}$ is the set of all permutation matrices) and, hence, the decreasing ordering can be taken without loss of generality.

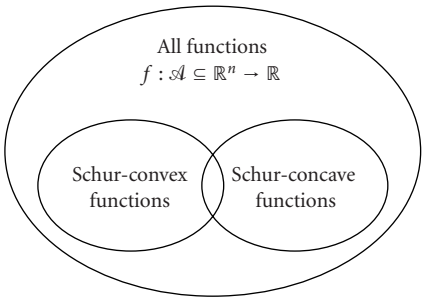

FIGURE 18.5. Illustration of the sets of Schur-convex and Schur-concave functions within the set of all functions $f : \mathcal{A} \subseteq \mathbb{R}^n \to \mathbb{R}$.

Hadamard matrix (when the dimensions are appropriate such as a power of two [38, page 66]*).*

Proof. The key simplification from (18.20) to (18.21) is based on an appropriate change of variable based on majorization theory [21]. A sketch of the proof is given in the appendix (see [20, 40] for details). □

Note that Theorem 18.1 is a generalization of previous results [20, 40] which only considered Schur-concave and Schur-convex functions.

Some comments on Theorem 18.1 are in order.

(i) The main result is in the simplification of the original complicated problem (18.20) with a matrix-valued variable to the simple problem (18.21) with a set of scalar variables that represent a power allocation over the channel eigenvalues. In other words, the problem has been *scalarized* in the sense that no matrix appears.

(ii) As stated in the theorem, when f_0 is a convex function, then the simplified problem (18.21) is convex. This has tremendous consequences, since the problem can always be optimally solved using the existing tools in convex optimization theory, either in closed-form (using the Karush-Kuhn-Tucker optimality conditions) or at least numerically (using very efficient algorithms recently developed such as interior-point methods) [35, 36]. Furthermore, additional constraints on the design can be easily incorporated without affecting the solvability of the problem as long as they are convex (cf. [20, 40]).

(iii) For Schur-concave/convex cost functions, the problem (18.21) is extremely simplified (cf. Sections 18.6.1 and 18.6.2) and in most cases closed-form solutions can be obtained (see Section 18.8 for a list of Schur-concave/convex cost functions and for a detailed treatment of two interesting cases such as the minimization of the average BER and the optimization of the worst substream).

(iv) The sets of Schur-concave and Schur-convex functions do no form a partition of the set of all functions as illustrated in Figure 18.5. This means that there may be cost functions that are neither Schur-concave nor Schur-convex (cf. Section 18.8.2). On the other hand, there are cost functions that are both Schur-concave and Schur-convex, such as $\mathrm{Tr}(\mathbf{E})$, and admit any rotation matrix $\mathbf{Q}$ [40].

(v) Surprisingly, for Schur-convex cost functions f_0, the optimal solution to the original problem (18.20) is independent of the specific choice of f_0 (cf. Section 18.6.2), as opposed to Schur-concave cost functions, whose solution depends on the particular choice of f_0.

(vi) As is explained in detail in Section 18.7, for Schur-concave functions, the optimal transmission is fully diagonal, whereas for Schur-convex functions, it is not due to the additional rotation matrix $\mathbf{Q}$ (see Figure 18.6)

(vii) For the simple case in which a single substream is established, that is, $L = 1$, the result in Theorem 18.1 simply means that the eigenmode with highest gain should be used.

18.6.1. Schur-concave cost functions

For Schur-concave cost functions, since the optimal rotation is $\mathbf{Q} = \mathbf{I}$ (from Theorem 18.1), the MSEs are given by

$$\mathrm{MSE}_i = \frac{1}{\nu + p_i \lambda_{H,i}}, \quad 1 \le i \le L \tag{18.25}$$

and the original optimization problem (18.20) can be finally written as

$$\begin{aligned} \min_{\mathbf{p}} \; & f_0\left(\left\{\frac{1}{\nu + p_i \lambda_{H,i}}\right\}_i\right) \\ \text{s.t.} \; & \sum_{j=1}^{L} p_j \le P_0, \\ & p_i \ge 0, \quad 1 \le i \le L. \end{aligned} \tag{18.26}$$

The solution to problem (18.26) clearly depends on the particular choice of f_0.

18.6.2. Schur-convex cost functions

For Schur-convex cost functions, since the diagonal elements of $\mathbf{E}$ are equal at the optimal solution (from Theorem 18.1), the MSEs are given by

$$\mathrm{MSE}_i = \frac{1}{L}\mathrm{Tr}(\mathbf{E}) = \frac{1}{L}\sum_{j=1}^{L} \frac{1}{\nu + p_j \lambda_{H,j}}, \qquad 1 \le i \le L \tag{18.27}$$

and the original optimization problem (18.20) can be finally written as

$$\begin{aligned} \min_{\mathbf{p}} \; & \frac{1}{L}\sum_{j=1}^{L} \frac{1}{\nu + p_j \lambda_{H,j}} \\ \text{s.t.} \; & \sum_{j=1}^{L} p_j \le P_0, \\ & p_i \ge 0, \quad 1 \le i \le L. \end{aligned} \tag{18.28}$$

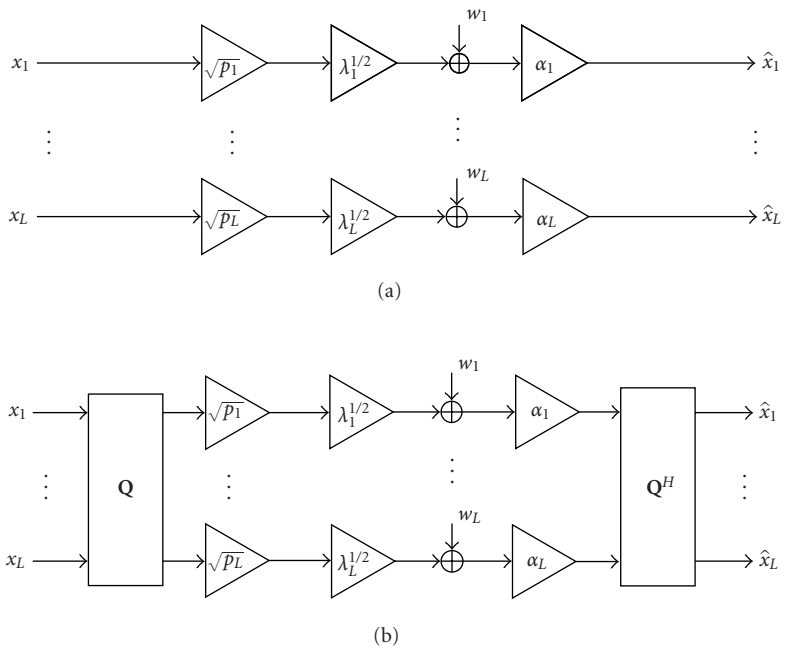

FIGURE 18.6. Scheme of diagonal and nondiagonal (due to the rotation) transmissions: (a) diagonal transmission and (b) nondiagonal (diagonal + rotation) transmission.

Surprisingly, this simplified problem for Schur-convex functions does not depend on the cost function f_0. The reason is that all the MSEs are equal and f_0 is increasing in each argument; consequently, minimizing the cost function is equivalent to minimizing the equal arguments given by (18.27). In addition, problem (18.28) is solved by the following water-filling solution:

$$p_i = \left(\mu\lambda_{H,i}^{-1/2} - \nu\lambda_{H,i}^{-1}\right)^+, \quad 1 \le i \le L, \tag{18.29}$$

where μ is the water-level chosen such that $\sum_i p_i = P_0$ (see [43] for practical implementation of water-filling expressions). Note that for the ZF receiver ($\nu = 0$), the water-filling solution (18.29) simplifies to $p_i = P_0\,\lambda_{H,i}^{-1/2} / \sum_j \lambda_{H,j}^{-1/2}$.

It is interesting to remark that problem (18.28) is equivalent to the minimization of the trace of the MSE matrix. Hence, among the infinite solutions that minimize $\mathrm{Tr}(\mathbf{E})$, only that which yields equal diagonal elements in $\mathbf{E}$ is the optimal solution for a Schur-convex objective function (which is obtained in fact with the water-filling solution in (18.29) and the rotation $\mathbf{Q}$ as described in Theorem 18.1).

18.7. Diagonal versus nondiagonal transmission

To better understand the underlying structure of the communication when using an MMSE/ZF receiver and a transmitter of the form $\mathbf{B} = \mathbf{U}_{H,1}\boldsymbol{\Sigma}_B\mathbf{Q}$, write the global

transmit-receive process $\hat{\mathbf{x}} = \mathbf{A}^H(\mathbf{HBx} + \mathbf{n})$ as

$$\hat{\mathbf{x}} = \mathbf{Q}^H\left(\nu\mathbf{I} + \boldsymbol{\Sigma}_B^H\mathbf{D}_{H,1}\boldsymbol{\Sigma}_B\right)^{-1}\boldsymbol{\Sigma}_B^H\mathbf{D}_{H,1}^{1/2}\left(\mathbf{D}_{H,1}^{1/2}\boldsymbol{\Sigma}_B\mathbf{Qx} + \mathbf{w}\right), \tag{18.30}$$

where $\mathbf{w}$ is an equivalent white noise and $\mathbf{D}_{H,1} = \mathbf{U}_{H,1}^H\mathbf{R}_H\mathbf{U}_{H,1}$ is the diagonalized squared whitened channel matrix. For the ZF receiver ($\nu = 0$), the previous expression simplifies to

$$\hat{\mathbf{x}} = \mathbf{x} + \mathbf{Q}^H\left(\boldsymbol{\Sigma}_B^H\mathbf{D}_{H,1}\boldsymbol{\Sigma}_B\right)^{-1/2}\mathbf{w} \tag{18.31}$$

which clearly satisfies the condition $\mathbf{A}^H\mathbf{HB} = \mathbf{I}$ (by definition) but has, in general, a correlated noise among the substreams. In other words, when using the ZF receiver, the global transmission is not really diagonal or parallel since the noise is colored.

Interestingly, having a fully diagonal or parallel transmission does not depend on whether the ZF or the MMSE receivers are used, but on the choice of the rotation $\mathbf{Q}$ (see Figure 18.6). Indeed, by setting $\mathbf{Q} = \mathbf{I}$, the global transmit-receive process is fully diagonalized:

$$\hat{\mathbf{x}} = \left(\nu\mathbf{I} + \boldsymbol{\Sigma}_B^H\mathbf{D}_{H,1}\boldsymbol{\Sigma}_B\right)^{-1}\boldsymbol{\Sigma}_B^H\mathbf{D}_{H,1}^{1/2}\left(\mathbf{D}_{H,1}^{1/2}\boldsymbol{\Sigma}_B\mathbf{x} + \mathbf{w}\right) \tag{18.32}$$

which can be rewritten as

$$\hat{x}_i = \alpha_i\left(\sqrt{p_i\lambda_{H,i}}x_i + w_i\right), \quad 1 \le i \le L, \tag{18.33}$$

where $\alpha_i = \sqrt{p_i\lambda_{H,i}}/(\nu + p_i\lambda_{H,i})$ (see Figure 18.6 with $\lambda_i \triangleq \lambda_{H,i}$). Note that when $\mathbf{Q} = \mathbf{I}$, the MMSE receiver also results in a diagonal transmission (which is never the case in the traditional approach where only the receiver is optimized).

18.8. Examples

The following list of Schur-concave and Schur-convex functions, along with the corresponding closed-form solutions, illustrates how powerful is the unifying framework developed in Theorem 18.1 (see [20, 40] for a detailed treatment of each case).

The following are examples of Schur-concave functions (when expressed as functions of the MSEs) for which the diagonal transmission is optimal:

(i) minimization of the sum of the MSEs or, equivalently, of $\mathrm{Tr}(\mathbf{E})$ [15, 6] with solution $p_i = (\mu\lambda_{H,i}^{-1/2} - \nu\lambda_{H,i}^{-1})^+$;

(ii) minimization of the weighted sum of the MSEs or, equivalently, of $\mathrm{Tr}(\mathbf{WE})$ [16], where $\mathbf{W} = \mathrm{diag}(\{w_i\})$ is a diagonal weighting matrix, with solution $p_i = (\mu w_i^{1/2}\lambda_{H,i}^{-1/2} - \nu\lambda_{H,i}^{-1})^+$;
(iii) minimization of the (exponentially weighted) product of the MSEs with solution $p_i = (\mu w_i - \nu\lambda_{H,i}^{-1})^+$;
(iv) minimization of $\det(\mathbf{E})$ [17] with solution $p_i = (\mu - \nu\lambda_{H,i}^{-1})^+$;
(v) maximization of the mutual information, for example, [12], with solution $p_i = (\mu - \lambda_{H,i}^{-1})^+$;
(vi) maximization of the (weighted) sum of the SINRs with solution given by allocating all the power on the channel eigenmode with highest weighted gain $w_i\lambda_{H,i}$;
(vii) maximization of the (exponentially weighted) product of the SINRs with solution $p_i = P_0\, w_i / \sum_j w_j$ (for the unweighted case, it results in a uniform power allocation).

The following are examples of Schur-convex functions for which the optimal transmission is nondiagonal with solution given by $p_i = (\mu\lambda_{H,i}^{-1/2} - \nu\lambda_{H,i}^{-1})^+$ plus the rotation $\mathbf{Q}$:

(i) minimization of the maximum of the MSEs;
(ii) maximization of the minimum of the SINRs;
(iii) maximization of the harmonic mean of the SINRs;[7]
(iv) minimization of the average BER (with equal constellations);
(v) minimization of the maximum of the BERs.

In the following, two relevant examples (with an excellent performance in practice) are considered to illustrate how easily linear MIMO transceivers can be designed with the aid of Theorem 18.1.

18.8.1. Optimization of the worst substream

The optimization of the worst substream can be formulated, for example, as the minimization of the maximum MSE:

$$\min_{\mathbf{A},\mathbf{B}} \max_i \{\,\mathrm{MSE}_i\,\} \tag{18.34}$$

which coincides with the minimization of the maximum BER if equal constellations are used. The optimal receive matrix is given by (18.14) and the problem reduces then to

$$\begin{aligned} &\min_{\mathbf{B}} \max_i \left\{ \left[\left(\nu\mathbf{I} + \mathbf{B}^H\mathbf{R}_H\mathbf{B}\right)^{-1} \right]_{ii} \right\} \\ &\text{s.t.} \quad \mathrm{Tr}\left(\mathbf{B}\mathbf{B}^H\right) \le P_0. \end{aligned} \tag{18.35}$$

[7] For the ZF receiver, the maximization of the harmonic mean of the SINRs is equivalent to the minimization of the unweighted sum of the MSEs, which can be classified as both Schur-concave and Schur-convex (since it is invariant to rotations).

Theorem 18.1 can now be invoked noting that $f_0(\mathbf{x}) = \max_i\{x_i\}$ is a Schur-convex function [20, 40] (if $\mathbf{y}$ majorizes $\mathbf{x}$, it must be that $x_{\max} \leq y_{\max}$ from the definition of majorization [21, 1.A.1] and, therefore, $f_0(\mathbf{x}) \leq f_0(\mathbf{y})$ which is precisely the definition of Schur-convexity [21, 3.A.1]). Hence, the final problem to be solved is (18.28) with solution given by (18.29) (recall that the rotation matrix $\mathbf{Q}$ is needed in this case as indicated in Theorem 18.1).

In light of Theorem 18.1 and the Schur-convexity of the cost function, it is now clear that the optimal transmission is nondiagonal (cf. Sections 18.6.2 and 18.7). However, one can still impose such a structure and solve the original problem in a suboptimal way. The transmit matrix would then be $\mathbf{B} = \mathbf{U}_{H,1}\mathbf{\Sigma}_B$ and the problem to be solved in convex form:

$$\begin{aligned} &\min_{\mathbf{p}} \; t \\ &\text{s.t.} \quad t \geq \frac{1}{\nu + p_i\lambda_{H,i}} \quad 1 \leq i \leq L \\ &\qquad \sum_{j=1}^{L} p_j \leq P_0 \\ &\qquad p_i \geq 0 \end{aligned} \tag{18.36}$$

with solution given by $p_i = P_0\,\lambda_{H,i}^{-1}/\sum_j \lambda_{H,j}^{-1}$.

18.8.2. Minimization of the average BER

The average (uncoded) BER is a good measure of the uncoded part of a system. Hence, its minimization may be regarded as an excellent (if not the best) criterion:

$$\min_{\mathbf{A},\mathbf{B}} \frac{1}{L}\sum_{i=1}^{L} g_i(\,\mathrm{MSE}_i\,), \tag{18.37}$$

where the functions g_i were defined in (18.19) and characterized as convex functions (see Figure 18.4). The optimal receive matrix is given by (18.14) and the problem reduces then to

$$\begin{aligned} &\min_{\mathbf{B}} \; \frac{1}{L}\sum_{i=1}^{L} g_i\Big(\big[\,(\nu\mathbf{I} + \mathbf{B}^H\mathbf{R}_H\mathbf{B})^{-1}\big]_{ii}\Big) \\ &\text{s.t.} \quad \mathrm{Tr}\,(\mathbf{B}\mathbf{B}^H) \leq P_0. \end{aligned} \tag{18.38}$$

Theorem 18.1 can now be invoked and the problem simplifies to the following

convex problem (provided that the constellations are chosen with increasing cardinality):

$$\begin{aligned}
&\min_{\mathbf{p},\boldsymbol{\rho}} \frac{1}{L}\sum_{i=1}^{L} g_i(\rho_i) \\
&\text{s.t.} \quad \sum_{j=i}^{L} \frac{1}{\nu + p_j \lambda_{H,j}} \leq \sum_{j=i}^{L} \rho_j, \quad 1 \leq i \leq L, \\
&\qquad \sum_{j=1}^{L} p_j \leq P_0, \\
&\qquad p_i \geq 0.
\end{aligned} \tag{18.39}$$

This particular problem was extensively treated in [24] via a primal decomposition approach which allowed the resolution of the problem with extremely simple algorithms (rather than using general purpose iterative algorithms such as interior-point methods).

In the particular case in which the constellations used in the L substreams are equal, the average BER cost function turns out to be Schur-convex since it is the sum of identical convex functions [21, 3.H.2]. Hence, the final problem to be solved is again (18.28) with solution given by (18.29) (recall that the rotation matrix $\mathbf{Q}$ is needed in this case as indicated in Theorem 18.1). As before, the minimization of the average BER can be suboptimally solved by imposing a diagonal structure.

18.9. Extension to parallel MIMO channels

As mentioned in Section 18.3, some particular scenarios, such as multicarrier systems, may be more conveniently modeled as a communication through a set of parallel MIMO channels

$$\mathbf{y}_k = \mathbf{H}_k \mathbf{s}_k + \mathbf{n}_k, \quad 1 \leq k \leq N, \tag{18.40}$$

where N is the number of parallel channels and k is the channel index.

It is important to remark that a multicarrier system can be modeled, not only as a set of parallel MIMO channels as in (18.40), but also as a single MIMO channel as in (18.1) with $\mathbf{H} = \operatorname{diag}(\{\mathbf{H}_k\})$. The difference lies on whether the transceiver operates independently at each MIMO channel as implied by (18.40) (block-diagonal matrices $\mathbf{B} = \operatorname{diag}(\{\mathbf{B}_k\})$ and $\mathbf{A} = \operatorname{diag}(\{\mathbf{A}_k\})$) or a global transceiver processes jointly all MIMO channels as a whole as implied by (18.1) (full matrices $\mathbf{B}$ and $\mathbf{A}$).

In the case of a set of N parallel MIMO channels with a single power constraint per channel, all the results obtained so far for a single MIMO channel clearly hold, since the optimization of a global cost function decouples into a set of N parallel optimization subproblems (under the mild assumption that the global

cost function f_0 depends on each MIMO channel through a subfunction f_k, that is, when it is of the form $f_0(\{f_k(\mathbf{x}_k)\}))$.

When the power constraint is global for the whole set of parallel MIMO channels, as is usually the case in multicarrier systems, the problem formulation in (18.10) becomes

$$\begin{aligned} \min_{\{\mathbf{A}_k,\mathbf{B}_k,P_k\}} \quad & f_0(\{\mathrm{MSE}_{k,i}\}) \\ \text{s.t.} \quad & \mathrm{Tr}\,(\mathbf{B}_k\mathbf{B}_k^H) \le P_k, \quad 1 \le k \le N, \\ & \sum_{k=1}^{N} P_k \le P_0. \end{aligned} \tag{18.41}$$

For this problem, the results previously obtained for a single MIMO channel still hold, but some comments are in order.

(i) The optimal receiver and MSE matrix for each of the MIMO channels have the same form as (18.14) and (18.16), respectively.

(ii) Theorem 18.1 still holds for each of the MIMO channels, with the additional complexity that the power P_k used in each of them is also an optimization variable, which has to comply with the global power constraint $\sum_{k=1}^{N} P_k \le P_0$. In particular, the resulting simplified problem is similar to (18.21) (which is convex provided that the cost function f_0 is) and the optimal transmitters have the same form as (18.22). When f_0 is Schur-concave/convex on a MIMO channel basis (i.e., when fixing the variables of all MIMO channels except the kth one, for all k), the simplifications (18.23) and (18.24) of the optimal transmitters are still valid.

(iii) The simplification of the problem for Schur-concave cost functions as described in Section 18.6.1 is still valid. For Schur-convex functions, however, the amazing simplification obtained in Section 18.6.2 is not valid anymore. That is, for multiple MIMO channels with a Schur-convex cost function f_0, the solution is not independent of the particular choice of f_0 as happened in the single MIMO case (see problem (18.28) and the solution (18.29)); to be more specific, the difference of the solutions is on how the total power is allocated among the MIMO channels.

(iv) The optimal solutions obtained for multiple MIMO channels [20, 40] are, in general, more complicated than the simple water-filling expressions for a single MIMO channel given in Section 18.8. In many cases, the solutions still present a water-filling structure, but with several water-levels coupled together [20, 40]. In any case, the numerical evaluation of such water-filling solutions can be implemented very efficiently in practice [43].

18.10. Numerical results

The aim of this section is not just to compare the different methods for designing MIMO transceivers, but to show that the design according to most criteria can now be actually solved using the unified framework.

In order to describe the simulation setup easily and since the observations and conclusions remain the same, a very simple model has been used to randomly

generate different realizations of the MIMO channel (for simulations with more realistic wireless multiantenna channel models including spatial and frequency correlation, the reader is referred to [20, 40]). In particular, the channel matrix $\mathbf{H}$ has been drawn from a Gaussian distribution with i.i.d. elements of zero mean and unit variance, and the noise has been modeled as white $\mathbf{R}_n = \sigma_n^2\mathbf{I}$, where σ_n^2 is the noise power. The SNR is defined as $\text{SNR} = P_T/\sigma_n^2$, which is essentially a measure of the transmitted power normalized with respect to the noise. The performance of the systems is measured in terms of BER averaged over the substreams; to be more precise, the outage BER[8] (over different realizations of $\mathbf{H}$) is considered since it is a more realistic measure than the average BER (which only makes sense when the system does not have delay constraints and the duration of the transmission is sufficiently long such that the fading statistics of the channel can be averaged out).

For illustration purposes, four different methods have been simulated: the classical minimization of the sum of the MSEs (SUM-MSE), the minimization of the product of the MSEs (PROD-MSE), the optimization of the worst substream (see Section 18.8.1) or minimization of the maximum of the MSEs (MAX-MSE), and the minimization of the average BER (see Section 18.8.2) or, equivalently, of the sum of the BERs (SUM-BER). Note that the methods SUM-MSE and PROD-MSE correspond to Schur-concave cost functions, whereas the methods MAX-MSE and SUM-BER correspond to Schur-convex ones.

In Figure 18.7, the BER (for a QPSK constellation) is plotted as a function of the SNR for a 4×4 MIMO channel with $L = 3$ for the cases of ZF and MMSE receivers. The first observation is that the performance of the ZF receiver is basically the same as that of the MMSE receiver thanks to the joint optimization of the transmitter and receiver (as opposed to the typically worse performance of the ZF receiver in the classical equalization setup where only the receiver is optimized). Another observation is that the performance of the methods MAX-MSE and SUM-BER is, as expected, exactly the same because they both correspond to Schur-convex cost functions (cf. Section 18.6.2).

In Figure 18.8, the same scenario is considered but with multiple parallel MIMO channels ($N = 16$) and only for the MMSE receiver. Two different approaches have been taken to deal with the multiple MIMO channels: a *joint processing* among all channels by modeling them as a whole as in (18.1) and a *parallel processing* of the channels by modeling them explicitly as parallel MIMO channels as in (18.40) (cf. Section 18.9). The joint processing clearly outperforms the parallel processing; the difference, however, may be as small as 0.5 dB or as large as 2 dB at a BER of 10^{-4}, for example, depending on the method. Hence, it is not clear whether the increase of complexity of the joint processing is worth (note, however, that the difference of performance increases with the loading factor of the system defined as $L/\min(n_T, n_R)$). With a parallel processing, the methods MAX-MSE and SUM-BER are not equivalent albeit being both Schur-convex, as opposed to a joint processing (cf. Section 18.9).

[8]The outage BER is the BER that is attained with some given probability (when it is not satisfied, an outage event is declared).

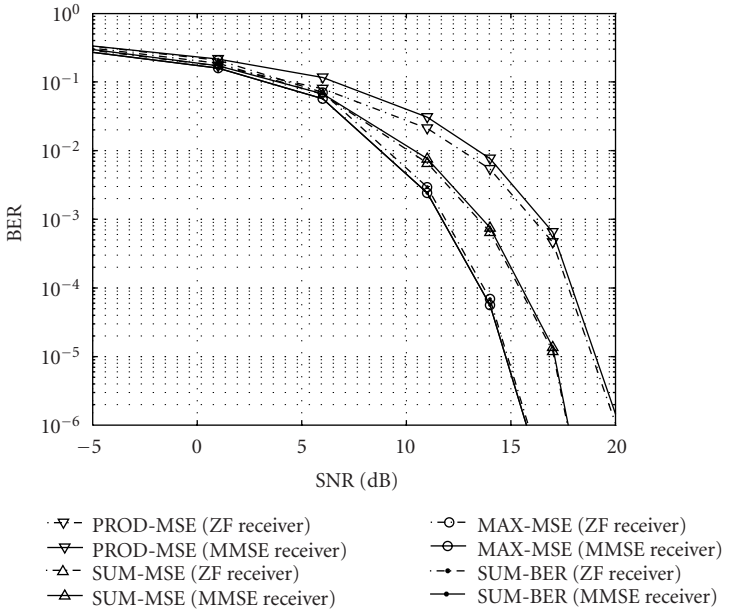

FIGURE 18.7. BER (at an outage probability of 5%) versus SNR when using QPSK in a 4×4 MIMO channel with $L = 3$ (with MMSE and ZF receivers) for the methods: PROD-MSE, SUM-MSE, MAX-MSE, and SUM-BER.

It is important to remark that Schur-convex methods are superior to Schur-concave ones (as observed from Figures 18.7 and 18.8). The reason is that Schur-concave methods transmit the symbols on a parallel fashion through the channel eigenmodes (diagonal structure), with the consequent lack of robustness to fading of some of the channel eigenmodes; whereas Schur-convex methods always transmit the symbols in a distributed way through the channels eigenmodes (nondiagonal structure), similar in essence to what CDMA systems do over the frequency domain. Among the Schur-convex methods, the SUM-BER is obviously the best (by definition) in terms of BER averaged over the substreams.

18.11. Summary

This chapter has dealt with the design of linear MIMO transceivers according to an arbitrary measure of the system quality. First, it has been observed that the results existing in the literature are isolated attempts under very specific design criteria such as the minimization of the trace of the MSE matrix. As a consequence, a unified framework has been proposed, which builds upon very recent results, to provide a systematic approach in the design of MIMO transceivers. Such a framework simplifies the original complicated problem to a simple convex problem which can then be tackled with the many existing tools in convex optimization theory (both numerical and analytical). In addition, for the family of Schur-concave/convex

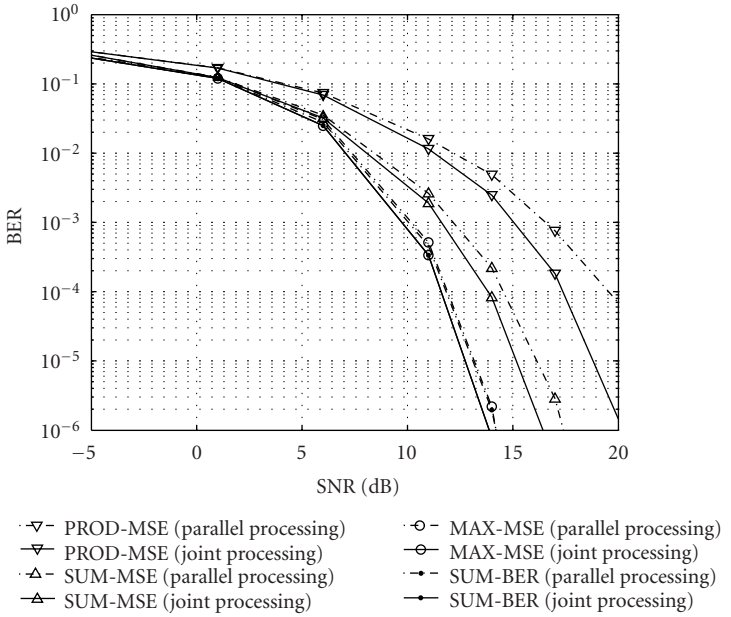

FIGURE 18.8. BER (at an outage probability of 5%) versus SNR (per MIMO channel) when using QPSK in 16 multiple 4×4 MIMO channels with $L = 3$ (with parallel and joint processing) for the methods: PROD-MSE, SUM-MSE, MAX-MSE, and SUM-BER.

functions, the problem simplifies further and practical solutions are obtained generally with a simple water-filling form.

Appendix

Sketch of the proof of Theorem 18.1

The proof hinges on majorization theory; the interested reader is referred to [21] for definitions and basic results on majorization theory (see also [40] for a brief overview) and to [20, 26, 40] for details overlooked in this sketch of the proof.

To start with, the problem (18.20) can be written as

$$\begin{aligned} &\min_{\mathbf{B},\boldsymbol{\rho}} \ f_0(\rho_1,\ldots,\rho_L) \\ &\text{s.t.} \ \ \left[\left(\nu\mathbf{I}+\mathbf{B}^H\mathbf{R}_H\mathbf{B}\right)^{-1}\right]_{ii} \le \rho_i, \quad 1 \le i \le L, \\ &\qquad \operatorname{Tr}\left(\mathbf{B}\mathbf{B}^H\right) \le P_0 \end{aligned} \tag{A.1}$$

which can always be done since f_0 is increasing in each argument. Also, since f_0 is minimized when $\rho_i \ge \rho_{i+1}$ and $\mathbf{B}$ can always include any desired permutation such that the diagonal elements of $(\nu\mathbf{I}+\mathbf{B}^H\mathbf{R}_H\mathbf{B})^{-1}$ are in decreasing order, the constraint $\rho_i \ge \rho_{i+1}$ can be explicitly included without affecting the problem.

The first main simplification comes by rewriting the problem as [26, Theorem 2]

$$\begin{aligned}
&\min_{\tilde{\mathbf{B}},\boldsymbol{\rho}} \ f_0(\rho_1,\ldots,\rho_L)\\
&\text{s.t.} \ \ \tilde{\mathbf{B}}^H\mathbf{R}_H\tilde{\mathbf{B}} \quad \text{diagonal (increasing diag. elements)},\\
&\qquad \mathbf{d}\big((v\mathbf{I}+\tilde{\mathbf{B}}^H\mathbf{R}_H\tilde{\mathbf{B}})^{-1}\big) \succ^w \boldsymbol{\rho},\\
&\qquad \rho_i \geq \rho_{i+1},\\
&\qquad \mathrm{Tr}\,(\tilde{\mathbf{B}}\tilde{\mathbf{B}}^H) \leq P_0,
\end{aligned} \tag{A.2}$$

where $\succ^w$ denotes the weakly majorization relation[9] [21] and $\mathbf{d}(\mathbf{X})$ denotes the diagonal elements of matrix $\mathbf{X}$ (similarly, $\boldsymbol{\lambda}(\mathbf{X})$ is used for the eigenvalues). The second constraint guarantees the existence of a unitary matrix $\mathbf{Q}$ such that $\mathbf{d}(\mathbf{Q}^H(v\mathbf{I}+\tilde{\mathbf{B}}^H\mathbf{R}_H\tilde{\mathbf{B}})^{-1}\mathbf{Q}) \leq \boldsymbol{\rho}$ [21, 9.B.2 and 5.A.9.a] or, in other words, such that $[(v\mathbf{I}+\mathbf{B}^H\mathbf{R}_H\mathbf{B})^{-1}]_{ii} \leq \rho_i$ with $\mathbf{B} = \tilde{\mathbf{B}}\mathbf{Q}$.

The second main simplification comes from the fact that $\tilde{\mathbf{B}}$ can be assumed without loss of optimality of the form $\tilde{\mathbf{B}} = \mathbf{U}_{H,1}\boldsymbol{\Sigma}_B$, as described in the theorem, since $\tilde{\mathbf{B}}^H\mathbf{R}_H\tilde{\mathbf{B}}$ is diagonal with diagonal elements in increasing order (cf. [20, Lemma 12], [26, Lemma 7], and [40, Lemma 5.11]).

Problem (18.21) follows then by plugging the expression of $\tilde{\mathbf{B}}$ into (A.2), denoting $p_i = |[\boldsymbol{\Sigma}_B]_{ii}|^2$ (which implies the need for the additional constraints $p_i \geq 0$), and by rewriting the weakly majorization constraint explicitly [21]. If f_0 is convex, the constraints $\rho_i \geq \rho_{i+1}$ are not necessary since an optimal solution cannot have $\rho_i < \rho_{i+1}$ (because the problem would have a lower objective value by using instead $\tilde{\rho}_i = \tilde{\rho}_{i+1} = (\rho_i + \rho_{i+1})/2$ [24]).

To obtain the additional simplification for Schur-concave/convex cost functions, rewrite the MSE constraints of (A.1) (since they are satisfied with equality at an optimal point) as

$$\boldsymbol{\rho} = \mathbf{d}\big(\mathbf{Q}^H(v\mathbf{I}+\tilde{\mathbf{B}}^H\mathbf{R}_H\tilde{\mathbf{B}})^{-1}\mathbf{Q}\big). \tag{A.3}$$

Now it suffices to use the definition of Schur-concavity/convexity to obtain the desired result. In particular, if f_0 is Schur-concave, it follows from the definition of Schur-concavity [21] (the diagonal elements and eigenvalues are assumed here in decreasing order) that

$$f_0(\mathbf{d}(\mathbf{X})) \geq f_0(\boldsymbol{\lambda}(\mathbf{X})) \tag{A.4}$$

which means that $f_0(\boldsymbol{\rho})$ is minimum when $\mathbf{Q} = \mathbf{I}$ in (A.3) (since $(v\mathbf{I}+\tilde{\mathbf{B}}^H\mathbf{R}_H\tilde{\mathbf{B}})^{-1}$ is already diagonal and with diagonal elements in decreasing order by definition).

[9] The weakly majorization relation $\mathbf{y} \succ^w \mathbf{x}$ is defined as $\sum_{j=i}^n y_j \leq \sum_{j=i}^n x_i$ for $1 \leq i \leq n$, where the elements of $\mathbf{y}$ and $\mathbf{x}$ are assumed in decreasing order [21].

If f_0 is Schur-convex, the opposite happens:

$$f_0(\mathbf{d}(\mathbf{X})) \geq f_0\left(\mathbf{1} \times \frac{\mathrm{Tr}(\mathbf{X})}{L}\right), \tag{A.5}$$

where $\mathbf{1}$ denotes the all-one vector. This means that $f_0(\boldsymbol{\rho})$ is minimum when $\mathbf{Q}$ is such that $\boldsymbol{\rho}$ has equal elements in (A.3), that is, when $\mathbf{Q}^H(\nu\mathbf{I}+\tilde{\mathbf{B}}^H\mathbf{R}_H\tilde{\mathbf{B}})^{-1}\mathbf{Q}$ has equal diagonal elements.

Acknowledgment

This work was supported in part by the Fulbright Program and Spanish Ministry of Education and Science; the Catalan Government (DURSI) 2001SGR-00268; and the Spanish Government (CICYT) TIC2003-05482.

Abbreviations

BER	Bit error rate
BPSK	Binary phase-shift keying
CSI	Channel state information
DSL	Digital subscriber line
QAM	Quadrature amplitude modulation
QPSK	Quaternary phase-shift keying
MIMO	Multiple-input multiple-output
ML	Maximum likelihood
MMSE	Minimum MSE
MSE	Mean square error
SINR	Signal-to-interference-plus-noise ratio
SISO	Single-input single-output
ZF	Zero forcing

Bibliography

[1] G. J. Foschini, "Layered space-time architecture for wireless communication in a fading environment when using multi-element antennas," *Bell Labs. Tech. J.*, vol. 1, no. 2, pp. 41–59, 1996.

[2] G. G. Raleigh and J. M. Cioffi, "Spatio-temporal coding for wireless communication," *IEEE Trans. Commun.*, vol. 46, no. 3, pp. 357–366, 1998.

[3] I. E. Telatar, "Capacity of multi-antenna Gaussian channels," *European Trans. Telecommunications*, vol. 10, no. 6, pp. 585–595, 1999.

[4] G. J. Foschini and M. J. Gans, "On limits of wireless communications in a fading environment when using multiple antennas," *Wireless Personal Communications*, vol. 6, no. 3, pp. 311–335, 1998.

[5] M. L. Honig, K. Steiglitz, and B. Gopinath, "Multichannel signal processing for data communications in the presence of crosstalk," *IEEE Trans. Commun.*, vol. 38, no. 4, pp. 551–558, 1990.

[6] A. Scaglione, G. B. Giannakis, and S. Barbarossa, "Redundant filterbank precoders and equalizers. I. Unification and optimal designs," *IEEE Trans. Signal Processing*, vol. 47, no. 7, pp. 1988–2006, 1999.

[7] S. M. Alamouti, "A simple transmit diversity technique for wireless communications," *IEEE J. Select. Areas Commun.*, vol. 16, no. 8, pp. 1451–1458, 1998.

[8] V. Tarokh, N. Seshadri, and A. R. Calderbank, "Space-time codes for high data rate wireless communication: performance criterion and code construction," *IEEE Trans. Inform. Theory*, vol. 44, no. 2, pp. 744–765, 1998.
[9] H. Bölcskei and A. J. Paulraj, "Multiple-input multiple-output (MIMO) wireless systems," in *The Communications Handbook*, J. Gibson, Ed., pp. 90.1–90.14, CRC Press, Boca Raton, Florida, USA, 2nd edition, 2002.
[10] K. Miettinen, *Nonlinear Multiobjective Optimization*, Kluwer Academic Publishers, Boston, Mass, USA, 1999.
[11] C. E. Shannon, "A mathematical theory of communication," *Bell System Tech. J.*, vol. 27, no. 4, pp. 379–423, 623–656, 1948.
[12] T. M. Cover and J. A. Thomas, *Elements of Information Theory*, Wiley, New York, NY, USA, 1991.
[13] K. H. Lee and D. P. Petersen, "Optimal linear coding for vector channels," *IEEE Trans. Commun.*, vol. 24, no. 12, pp. 1283–1290, 1976.
[14] J. Salz, "Digital transmission over cross-coupled line channels," *AT&T Technical Journal*, vol. 64, no. 6, pp. 1147–1159, 1985.
[15] J. Yang and S. Roy, "On joint transmitter and receiver optimization for multiple-input-multiple-output (MIMO) transmission systems," *IEEE Trans. Commun.*, vol. 42, no. 12, pp. 3221–3231, 1994.
[16] H. Sampath, P. Stoica, and A. Paulraj, "Generalized linear precoder and decoder design for MIMO channels using the weighted MMSE criterion," *IEEE Trans. Commun.*, vol. 49, no. 12, pp. 2198–2206, 2001.
[17] J. Yang and S. Roy, "Joint transmitter-receiver optimization for multi-input multi-output systems with decision feedback," *IEEE Trans. Inform. Theory*, vol. 40, no. 5, pp. 1334–1347, 1994.
[18] A. Scaglione, P. Stoica, S. Barbarossa, G. B. Giannakis, and H. Sampath, "Optimal designs for space-time linear precoders and decoders," *IEEE Trans. Signal Processing*, vol. 50, no. 5, pp. 1051–1064, 2002.
[19] A. Scaglione, S. Barbarossa, and G. B. Giannakis, "Filterbank transceivers optimizing information rate in block transmissions over dispersive channels," *IEEE Trans. Inform. Theory*, vol. 45, no. 3, pp. 1019–1032, 1999.
[20] D. P. Palomar, J. M. Cioffi, and M. A. Lagunas, "Joint Tx-Rx beamforming design for multicarrier MIMO channels: a unified framework for convex optimization," *IEEE Trans. Signal Processing*, vol. 51, no. 9, pp. 2381–2401, 2003.
[21] A. W. Marshall and I. Olkin, *Inequalities: Theory of Majorization and Its Applications*, Academic Press, New York, NY, USA, 1979.
[22] E. N. Onggosanusi, A. M. Sayeed, and B. D. V. Veen, "Efficient signaling schemes for wideband space-time wireless channels using channel state information," *IEEE Trans. Veh. Technol.*, vol. 52, no. 1, pp. 1–13, 2003.
[23] Y. Ding, T. N. Davidson, Z.-Q. Luo, and K. M. Wong, "Minimum BER block precoders for zero-forcing equalization," *IEEE Trans. Signal Processing*, vol. 51, no. 9, pp. 2410–2423, 2003.
[24] D. P. Palomar, M. Bengtsson, and B. Ottersten, "Minimum BER linear transceivers for MIMO channels via primal decomposition," *IEEE Trans. Signal Processing*, vol.53, no. 8, pp. 2866-2882, 2005.
[25] M. Bengtsson and B. Ottersten, "Optimal and suboptimal transmit beamforming," in *Handbook of Antennas in Wireless Communications*, L. C. Godara, Ed., CRC Press, Boca Raton, Fla, USA, 2001.
[26] D. P. Palomar, M. A. Lagunas, and J. M. Cioffi, "Optimum linear joint transmit-receive processing for MIMO channels with QoS constraints," *IEEE Trans. Signal Processing*, vol. 52, no. 5, pp. 1179–1197, 2004.
[27] J. Milanovic, T. N. Davidson, Z.-Q. Luo, and K. M. Wong, "Design of robust redundant precoding filter banks with zero-forcing equalizers for unknown frequency-selective channels," in *Proc. 2000 IEEE International Conference on Acoustics, Speech, and Signal Processing (ICASSP '00)*, vol. 5, pp. 2761–2764, Istanbul, Turkey, June 2000.
[28] F. Rey, M. Lamarca, and G. Vázquez, "Robust power allocation algorithms for MIMO OFDM systems with imperfect CSI," *IEEE Trans. Signal Processing*, vol. 53, no. 3, pp. 1070–1085, 2005.

[29] G. Jöngren, M. Skoglund, and B. Ottersten, "Combining beamforming and orthogonal space-time block coding," *IEEE Trans. Inform. Theory*, vol. 48, no. 3, pp. 611–627, 2002.
[30] J.-H. Chang, L. Tassiulas, and F. Rashid-Farrokhi, "Joint transmitter receiver diversity for efficient space division multiaccess," *IEEE Transactions on Wireless Communications*, vol. 1, no. 1, pp. 16–27, 2002.
[31] Z.-Q. Luo, T. N. Davidson, G. B. Giannakis, and K. M. Wong, "Transceiver optimization for block-based multiple access through ISI channels," *IEEE Trans. Signal Processing*, vol. 52, no. 4, pp. 1037–1052, 2004.
[32] R. H. Gohary, T. N. Davidson, and Z.-Q. Luo, "An efficient design method for vector broadcast systems with common information," in *Proc. IEEE Global Telecommunications Conference (GLOBECOM '03)*, vol. 4, pp. 2010–2014, San Francisco, Calif, USA, December 2003.
[33] M. Bengtsson, "A pragmatic approach to multi-user spatial multiplexing," in *Proc. 2nd IEEE Sensor Array and Multichannel Signal Processing Workshop (SAM-2002)*, pp. 130–134, Rosslyn, Va, USA, August 2002.
[34] E. Jorswieck and H. Boche, "Transmission strategies for the MIMO MAC with MMSE receiver: average MSE optimization and achievable individual MSE region," *IEEE Trans. Signal Processing*, vol. 51, no. 11, pp. 2872–2881, 2003.
[35] S. Boyd and L. Vandenberghe, *Convex Optimization*, Cambridge University Press, Cambridge, Mass, USA, 2004.
[36] D. P. Bertsekas, *Nonlinear Programming*, Athena Scientific, Belmont, Mass, USA, 2nd edition, 1999.
[37] S. Benedetto and E. Biglieri, *Principles of Digital Transmission with Wireless Applications*, Kluwer Academic Publishers, New York, NY, USA, 1999.
[38] S. Verdú, *Multiuser Detection*, Cambridge University Press, New York, NY, USA, 1998.
[39] K. Cho and D. Yoon, "On the general BER expression of one- and two-dimensional amplitude modulations," *IEEE Trans. Commun.*, vol. 50, no. 7, pp. 1074–1080, 2002.
[40] D. P. Palomar, *A unified framework for communications through MIMO channels*, Ph.D. dissertation, Technical University of Catalonia (UPC), Barcelona, Spain, 2003.
[41] S. M. Kay, *Fundamentals of Statistical Signal Processing: Estimation Theory*, vol. 1, Prentice Hall, Englewood Cliffs, NJ, USA, 1993.
[42] P. Viswanath and V. Anantharam, "Optimal sequences and sum capacity of synchronous CDMA systems," *IEEE Trans. Inform. Theory*, vol. 45, no. 6, pp. 1984–1991, 1999.
[43] D. P. Palomar and J. R. Fonollosa, "Practical algorithms for a family of waterfilling solutions," *IEEE Trans. Signal Processing*, vol. 53, no. 2, pp. 686–695, 2005.

Daniel Pérez Palomar: Department of Electrical Engineering, Princeton University, Princeton, NJ 08544, USA

Email: danielp@princeton.edu

19 Space-time block coding using channel side information

George Jöngren, Mikael Skoglund, and Björn Ottersten

19.1. Introduction

Multiple transmit and receive antennas can be used in wireless systems to achieve high data rate communication. An array of multiple antennas may be placed at the receiver, the transmitter, or at both sides of the communication link. Techniques for exploiting antenna arrays at the receive side represent the classical way of utilizing the spatial dimension for increasing the performance [1]. In contrast, methods for using antenna arrays for transmitting purposes have traditionally not received the same amount of interest. This since it has until recently been believed that accurate channel state information at the transmitter is needed for antenna array transmission techniques to be successful.

At first, the need for channel knowledge seems unavoidable as the transmission can otherwise not be adjusted so that the signals after passing through the channel are guaranteed to add constructively at the receiver, thereby increasing the signal-to-noise-ratio (SNR). Recent results show however that channel knowledge at the transmitter is not a prerequisite for gaining from an antenna array placed at the transmitter. Information theoretic investigations in fact demonstrate that multiple antennas at the transmitter may, through proper spatio-temporal processing, boost the performance tremendously compared with a single-antenna system, even in the complete absence of channel knowledge [2]. This is especially true if both the transmitter and the receiver are equipped with antenna arrays since the resulting multi-input multi-output (MIMO) channel offers more degrees of spatial freedom for the system to exploit.

The development of space-time codes [3, 4] provides new and important tools for realizing the high data rates promised by information theory. In space-time coding, the codewords are represented by matrices that by means of their two-dimensional structure allow coding in both the spatial as well as in the temporal domain. Properly designed such codes may as a result offer significant diversity and coding gains over traditional single-antenna transmission. Conventional

methods' need for channel knowledge is circumvented by striving for code designs that spread the emitted energy and information evenly in space.

A systematic approach to finding appropriate codes was pioneered in [3]. A major contribution in that paper was the development of a design criterion involving the rank and eigenvalues/determinant of a certain matrix. The design criterion was later generalized to multiple receive antennas and to other channel models in [4], where the now popular notion of space-time coding was coined. The latter work also included examples of trellis codes constructed based on the design criterion.

Ever since these two seminal papers, interest in space-time coding has literally exploded and many different types of codes have been designed. Code designs closely related to the development herein include the class of linear dispersive (LD) space-time block codes [5, 6]. The codeword matrices in such codes are formed as linear combinations of some information carrying scalar symbols, each weighted by a corresponding matrix that spreads the information both in time and space. By an appropriate choice of the weighting matrices, codes with appealing properties may be obtained. A particularly important type of LD codes is the well-known class of orthogonal space-time block (OSTB) codes where the weighting matrices are taken to satisfy certain conditions [7] that ensure optimal low-complexity decoding while providing full spatial diversity.

The fact that conventional space-time codes do not need any channel knowledge may, due to the difficulties of acquiring such knowledge, be a clear advantage but it may also be a substantial drawback. The latter is true since information about the channel, if available, can be used to improve the performance beyond what is possible to achieve with standard space-time codes that do not take channel knowledge into account. Information theoretic capacity results indeed show that the potential data rate increases substantially even if the channel knowledge is far from perfect [8]. Thus, the degree of channel knowledge at the transmitter determines whether space-time codes are suitable or not.

In some communication systems it is reasonable to assume that the transmitter has access to useful channel side information. This holds for many time-division-duplex (TDD) systems as well as for some frequency-division-duplex (FDD) systems. In the case of TDD the channel may be estimated in the receive mode and then often assumed to be the same for the transmit mode. Such a strategy typically does not work for FDD systems which instead need to be equipped with a dedicated feedback link that conveys channel estimates obtained at the receiver to the transmitter.

Unfortunately, the channel information is in practice far from perfect. Noise is not the only error source. In TDD systems, time-varying channel fading in conjunction with duplex delay may also impair the channel knowledge by making the channel information more or less outdated by the time it reaches the transmitter. Systems using FDD where channel information is obtained via a feedback link may similarly suffer from feedback delay [9]. The channel feedback is moreover often heavily quantized, further degrading the quality of the channel knowledge at

the transmitter. Bit errors introduced by the channel over which the feedback link operates may be another error source.

A common way of utilizing channel side information is to make use of beamforming techniques for maximizing the received energy, essentially steering the emitted energy in the direction of the receiver by means of rank-one signaling. Classical beamforming does not however take into account that the channel knowledge in practice is imperfect. Only in more recent works does this issue start to be addressed [10, 11, 12, 13].

A fundamental and serious problem with beamforming is that the resulting rank-one type of transmission is too restrictive when there are imperfections in the channel knowledge. The emitted energy instead needs to be spread out over several directions, much like in conventional space-time coding. This naturally leads to the concept of channel side information dependent space-time codes, where the codeword matrices are allowed to depend on the channel side information and the presence of possibly imperfect channel knowledge is taken into account already at the design stage. The concept is general in that it implicitly views any transmission scheme that utilizes channel knowledge as implementing some kind of code.

Channel side information dependent codes combine the best of space-time coding and beamforming. The idea is to make use of the complementary strengths of both transmission methodologies. Conventional space-time codes are designed to operate without any channel knowledge and hence provide the system with a basic level of performance in the absence of reliable channel state information at the transmitter. Beamforming, on the other hand, is advantageous when the channel knowledge is reliable.

These two transmission strategies may be seamlessly combined by considering a code/transmission structure where the output of a fixed OSTB encoder is adapted to the available channel information by means of a transmit weighting matrix. The structure is called weighted orthogonal space-time block coding (OSTBC) and can be shown to be capacity achieving in the case of two transmit antennas and one receive antenna [14]. Weighted OSTBC is in fact a simple example of separate space-time coding and transmit weighting. The latter is in certain situations an optimal structure in the sense that there exist space-time codes, that if weighted properly, achieve the channel capacity regardless of the number of transmit and receive antennas [8].

Other code structures also fit nicely into the above framework. Unstructured space-time block codes have codeword matrices where the elements are, except for a necessary constraint on the output power, freely chosen from the complex-field. This provides maximum performance but at the expense of high decoding complexity. Linear dispersive space-time block codes strike a balance between the highly structured case of weighted OSTBC and completely unstructured codes. Applying the linear dispersive structure to the present problem means that the transmission is adapted to the channel by letting the weighting matrices depend on the channel side information. A major benefit of the linear structure compared with the unstructured case is that for example sphere decoding [15] may be used to perform the decoding in a reasonably efficient manner.

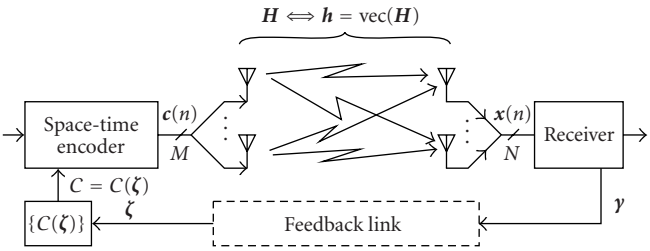

FIGURE 19.1. A model of the system under study.

Performance criteria for the design of channel side information dependent space-time codes have been developed in [16, 17]. These works effectively generalize the criterion used in conventional space-time coding to take possibly imperfect channel knowledge into account. In [16], a performance criterion applicable to codes of arbitrary structure was derived and thereafter used for designing the transmit weighting matrix in weighted OSTBC. The resulting transmission scheme has later also been investigated in [18]. A related performance measure tailored for quantized channel feedback was developed in [17] and utilized for designing unstructured codes. The same criterion may also be used to design weighted OSTBC and LD codes [14]. Ideas for exploiting related performance criteria to jointly design the code and feedback link are outlined in [19].

Space-time codes using channel information is a general concept and different types of codes can be designed for a wide range of scenarios. Space considerations however make it impractical to cover all possibilities herein. We will therefore focus on block codes used in systems equipped with a feedback link. Attention is further restricted to the performance criteria in [16, 17], which will be used to design efficient codes that exhibit robustness against impairments in the side information. Design procedures for unstructured codes, LD codes, and weighted OSTBC are explicitly presented and it will be shown how they all fit together under a common framework.

19.2. System model

Consider an MIMO wireless communication system in a flat block fading scenario in which the transmitter has access to channel side information. A complex baseband equivalent model of the symbol-sampled system is depicted in Figure 19.1. There are M transmit antennas, N receive antennas, and n denotes the integer-valued sample index.

At the transmitter, the information to be communicated is coded using a space-time encoder into a sequence of $M \times 1$ output vectors $\boldsymbol{c}(n)$. The result is M parallel and generally different channel symbol streams. Each symbol stream corresponds to the signal for a particular transmit antenna. The transmitter obtains information $\boldsymbol{\zeta}$ about the current channel state from the receiver, which conveys channel knowledge $\boldsymbol{\gamma}$ via a dedicated feedback link. The feedback link may

introduce distortion, resulting in channel side information $\boldsymbol{\zeta}$ that possibly differs from $\boldsymbol{y}$.

Based on the channel side information, the transmission is adapted to the channel characteristics. The space-time encoder has access to a set $\{\mathcal{C}(\boldsymbol{\zeta})\}$ of codes. Out of this set, the side information is utilized for determining the channel code $\mathcal{C}$ currently in use as $\mathcal{C} = \mathcal{C}(\boldsymbol{\zeta})$. After passing through the wireless transmission medium, the information carrying signals are picked up by the N antennas at the receiver producing the complex baseband equivalent $N \times 1$ received signal vector $\boldsymbol{x}(n)$.

The signal at each receive antenna is a superposition of the information carrying signals, disturbed by additive noise. The received signal vector can therefore be written as

$$\boldsymbol{x}(n) = \boldsymbol{H}^* \boldsymbol{c}(n) + \boldsymbol{e}(n), \tag{19.1}$$

where $(\cdot)^*$ denotes complex conjugate transpose and where $\boldsymbol{H}$, with complex-valued elements $\{H_{kl}\}$, is an $N \times M$ matrix that models the attenuations and phase shifts introduced by the transmission medium as well as front-end processing at the transmitter and receiver. Note that H_{kl}^* represents the scalar channel coefficient between the kth transmit and lth receive antenna. Furthermore, the noise term $\boldsymbol{e}(n)$ is assumed to be generated from a zero-mean, spatially and temporally white, complex Gaussian random process $\{\boldsymbol{e}(n)\}$. The variance of each element in $\boldsymbol{e}(n)$ is constant and denoted σ^2.

A block fading scenario is considered. Consequently, the channel $\boldsymbol{H}$ is assumed to be constant for a frame of L samples and may then fade from one frame to another. Let $\boldsymbol{h} \triangleq \mathrm{vec}(\boldsymbol{H})$ denote the $MN \times 1$ vector obtained by stacking the columns of $\boldsymbol{H}$ on top of each other using the vectorization operator $\mathrm{vec}(\cdot)$. The fading is such that the channel vector $\boldsymbol{h}$ obeys a complex Gaussian distribution with mean $\boldsymbol{m}_{\boldsymbol{h}} \triangleq \mathrm{E}[\boldsymbol{h}]$ and covariance $\boldsymbol{R}_{\boldsymbol{hh}} \triangleq \mathrm{E}[(\boldsymbol{h} - \boldsymbol{m}_{\boldsymbol{h}})(\boldsymbol{h} - \boldsymbol{m}_{\boldsymbol{h}})^*]$. This is a quite general fading model which includes scenarios such as spatially uncorrelated Rayleigh fading, which is popular in the space-time coding literature.

The channel coding is assumed to be performed independently for each frame and the codewords are of length L, meaning that a codeword covers an entire frame. Consequently, the particular frame number is irrelevant and we may without loss of generality consider a single frame spanning the time interval $n = 0, 1, \ldots, L-1$. Grouping the L consecutive vectors $\boldsymbol{x}(n)$ of this frame into an $N \times L$ matrix $\boldsymbol{X}$ gives

$$\boldsymbol{X} = \boldsymbol{H}^* \boldsymbol{C} + \boldsymbol{E}, \tag{19.2}$$

where $\boldsymbol{E}$ contains the noise vectors and

$$\boldsymbol{C} \triangleq \begin{bmatrix} \boldsymbol{c}(0) & \boldsymbol{c}(1) & \cdots & \boldsymbol{c}(L-1) \end{bmatrix} \tag{19.3}$$

corresponds to the codeword output by the space-time encoder. The transmitted codeword $\boldsymbol{C}$ belongs to the currently used code $\mathcal{C} = \mathcal{C}(\boldsymbol{\zeta}) \triangleq \{\boldsymbol{C}_k^{(\boldsymbol{\zeta})}\}_{k=1}^{K}$, where K

is the number of codewords and $\boldsymbol{C}_k^{(\boldsymbol{\zeta})}$ represents the kth codeword in $\mathcal{C}(\boldsymbol{\zeta})$. Note that each codeword is a function of the side information. Hence, the set $\{\mathcal{C}(\boldsymbol{\zeta})\}$ is possibly uncountable when $\boldsymbol{\zeta}$ is nondiscrete.

The data to be transmitted corresponds to a sequence of information bits. Since the length of the codewords is L, the coding results in a code rate of $\log_2(K)/L$ information bits per channel use. The choice of L and K allows an appropriate tradeoff between data rate and time redundancy.

Conditioned on the use of a certain code $\mathcal{C}(\boldsymbol{\zeta})$, it is assumed that the transmission is such that all the codewords are equally probable and that the average energy per channel use is P. In other words, the output power is limited by

$$\frac{\mathrm{E}\left[\|\boldsymbol{C}\|_{\mathrm{F}}^2 | \boldsymbol{\zeta}\right]}{L} = P, \tag{19.4}$$

where $\|\cdot\|_{\mathrm{F}}$ denotes the Frobenius norm and where the conditioning on $\boldsymbol{\zeta}$ prevents the transmitter from adjusting the output power based on the side information (no power control).

The receiver recovers the transmitted codewords by means of maximum likelihood (ML) decoding. Since the receiver is assumed to know both the channel and the side information perfectly, ML decoding amounts to detecting the codewords according to

$$\widehat{\boldsymbol{C}} = \arg \min_{\boldsymbol{C} \in \mathcal{C}(\boldsymbol{\zeta})} \|\boldsymbol{X} - \boldsymbol{H}^* \boldsymbol{C}\|_{\mathrm{F}}^2, \tag{19.5}$$

where $\widehat{\boldsymbol{C}}$ denotes the codeword chosen by the receiver.

19.2.1. The feedback link

In practice, the channel side information is often far from perfect. Estimation noise and quantization errors may, for example, degrade the quality of the channel information. Feedback delay in conjunction with time-varying channel fading may also lower the quality. This happens since the channel information might be outdated by the time it reaches the transmitter. The latter phenomenon is here modeled by thinking of $\boldsymbol{\gamma}$ as an old channel realization. Accordingly, $\boldsymbol{\gamma}$ is referred to as *initial channel information* and is assumed to be an $MN \times 1$ vector that is correlated, to an arbitrary degree, with $\boldsymbol{h}$. More precisely, $\boldsymbol{h}$ and $\boldsymbol{\gamma}$ are jointly complex Gaussian and related through the cross-covariance matrix $\boldsymbol{R}_{\boldsymbol{h}\boldsymbol{\gamma}} \triangleq \mathrm{E}[(\boldsymbol{h} - \boldsymbol{m}_{\boldsymbol{h}})(\boldsymbol{\gamma} - \boldsymbol{m}_{\boldsymbol{\gamma}})^*]$. The degree of correlation determines the quality of the initial channel information. Loosely speaking, the quality of the initial channel information improves as the correlation between $\boldsymbol{h}$ and $\boldsymbol{\gamma}$ grows larger, and conversely, deteriorates as the correlation becomes smaller.

It is important to strictly limit the data rate of the feedback link in order to make the whole system spectrally efficient. This contrasts sharply to the need of updating the side information at a high rate. To meet these conflicting goals, quantization may be used in the feedback link.

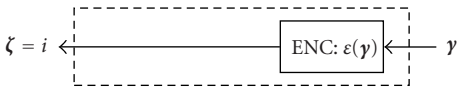

Figure 19.2. A generic model of a feedback link employing quantization.

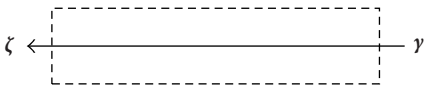

Figure 19.3. An idealized feedback link. Such a link arises in the limit of infinitely dense quantization.

A generic model of a feedback link employing quantization is depicted in Figure 19.2. The initial channel information $\boldsymbol{\gamma}$ is now quantized at the receiver into a b bit integer $i = \varepsilon(\boldsymbol{\gamma})$, which is transported over some kind of feedback channel to the transmitter. Since the feedback channel is here assumed to be ideal, i is conveyed undistorted to the transmitter where it constitutes the channel side information, that is, $\boldsymbol{\zeta} = i$.

The encoder function $\varepsilon(\boldsymbol{\gamma})$ is such that it partitions the set of all possible $\boldsymbol{\gamma}$ into 2^b different encoder regions $\{\mathcal{S}_i\}_{i=0}^{2^b-1}$ based on the mapping $\boldsymbol{\gamma} \in \mathcal{S}_i \Rightarrow \varepsilon(\boldsymbol{\gamma}) = i$. In addition to feedback delay, quantization errors now also degrade the quality of the side information. Only a few bits are typically used and the quantization is therefore coarse.

The encoder regions can be made smaller as the number of bits b increases. In the limit of infinitely dense quantization, the side information can, through a judicious choice of quantizer, be made to essentially equal the initial channel information $\boldsymbol{\gamma}$. Quantization errors are then no longer present. An illustration of such an *idealized* feedback link where $\boldsymbol{\zeta} = \boldsymbol{\gamma}$ is given in Figure 19.3.

The idealized feedback link is obviously a reasonable model if the system may afford spending many bits on the quantization. But the model is more general than it first may seem. This is because the model also makes sense whenever the errors in the side information lead to a statistical relation with the channel that is well approximated by the joint Gaussian distribution already used to describe the relation between $\boldsymbol{\gamma}$ and $\boldsymbol{h}$. Examples of such scenarios include TDD systems where side information is obtained by estimating the channel in the reverse link, resulting in errors primarily due to noise and duplex delay.

19.3. A performance measure

The codeword error probability $\Pr[\hat{\boldsymbol{C}} \neq \boldsymbol{C}]$ will here form the basis for developing a performance measure that can be used to design efficient channel information dependent codes. Working with closed-form expressions is obviously highly desirable for keeping the code design complexity within reasonable limits. Toward this end, the codeword error probability will be approximated through the use of various bounds.

We start, similarly to [17], by exploiting the well-known union bound technique and the upper bound $0.5\exp(-x^2/2)$ on the Gaussian tail function to upper bound the codeword error probability as

$$\Pr[\widehat{\boldsymbol{C}} \neq \boldsymbol{C}] \leq \frac{\mathrm{E}_{\boldsymbol{\zeta}}\left[\sum_{k<l} \mathrm{E}_{\boldsymbol{\gamma}}\left[e^{\ell(\boldsymbol{C}_k^{(\zeta)}, \boldsymbol{C}_l^{(\zeta)}; \boldsymbol{\gamma})} | \boldsymbol{\zeta}\right]\right]}{K \det\left(\boldsymbol{R}_{\boldsymbol{hh}|\boldsymbol{\gamma}}\right)} \triangleq P_{\mathrm{UB}}(\{\mathcal{C}(\boldsymbol{\zeta})\}), \tag{19.6}$$

where

$$\begin{aligned}\ell(\boldsymbol{C}_k^{(\zeta)}, \boldsymbol{C}_l^{(\zeta)}; \boldsymbol{\gamma}) \triangleq\ & \boldsymbol{m}_{\boldsymbol{h}|\boldsymbol{\gamma}}^* \boldsymbol{R}_{\boldsymbol{hh}|\boldsymbol{\gamma}}^{-1} \boldsymbol{\Psi}(\boldsymbol{C}_k^{(\zeta)} - \boldsymbol{C}_l^{(\zeta)})^{-1} \boldsymbol{R}_{\boldsymbol{hh}|\boldsymbol{\gamma}}^{-1} \boldsymbol{m}_{\boldsymbol{h}|\boldsymbol{\gamma}} \\ & - \boldsymbol{m}_{\boldsymbol{h}|\boldsymbol{\gamma}}^* \boldsymbol{R}_{\boldsymbol{hh}|\boldsymbol{\gamma}}^{-1} \boldsymbol{m}_{\boldsymbol{h}|\boldsymbol{\gamma}} - \log\det\left(\boldsymbol{\Psi}(\boldsymbol{C}_k^{(\zeta)} - \boldsymbol{C}_l^{(\zeta)})\right),\end{aligned} \tag{19.7}$$

with $\boldsymbol{m}_{\boldsymbol{h}|\boldsymbol{\gamma}} \triangleq \mathrm{E}[\boldsymbol{h}|\boldsymbol{\gamma}] = \boldsymbol{m}_{\boldsymbol{h}} + \boldsymbol{R}_{\boldsymbol{h\gamma}} \boldsymbol{R}_{\boldsymbol{\gamma\gamma}}^{-1}(\boldsymbol{\gamma} - \boldsymbol{m}_{\boldsymbol{\gamma}})$ and $\boldsymbol{R}_{\boldsymbol{hh}|\boldsymbol{\gamma}} \triangleq \mathrm{E}[(\boldsymbol{h} - \boldsymbol{m}_{\boldsymbol{h}|\boldsymbol{\gamma}})(\boldsymbol{h} - \boldsymbol{m}_{\boldsymbol{h}|\boldsymbol{\gamma}})^* | \boldsymbol{\gamma}] = \boldsymbol{R}_{\boldsymbol{hh}} - \boldsymbol{R}_{\boldsymbol{h\gamma}} \boldsymbol{R}_{\boldsymbol{\gamma\gamma}}^{-1} \boldsymbol{R}_{\boldsymbol{h\gamma}}^*$ denoting the conditional mean and covariance matrix, respectively, and

$$\boldsymbol{\Psi}(\boldsymbol{C}) \triangleq \boldsymbol{I}_N \otimes \boldsymbol{C}\boldsymbol{C}^* \eta + \boldsymbol{R}_{\boldsymbol{hh}|\boldsymbol{\gamma}}^{-1}, \quad \eta \triangleq \frac{1}{(4\sigma^2)}. \tag{19.8}$$

Here, $\boldsymbol{m}_{\boldsymbol{\gamma}}$ represents the mean vector, $\boldsymbol{R}_{\boldsymbol{\gamma\gamma}}$ is the covariance matrix of $\boldsymbol{\gamma}$, and $\otimes$ denotes the operator for the Kronecker product.

Unfortunately, the conditional expectation $\mathrm{E}_{\boldsymbol{\gamma}}[\cdot|\boldsymbol{\zeta}]$ depends on the code to be designed but cannot in general be evaluated in closed form. To still obtain an expression suitable for code design, an approximate version of $P_{\mathrm{UB}}(\{\mathcal{C}(\boldsymbol{\zeta})\})$ is therefore derived by utilizing that $\mathrm{E}[f(x)] \approx f(\mathrm{E}[x])$ if the variance of x is small. This relation is applied to (19.6) by taking $f(x) = e^x$. Since e^x is a convex function, Jensen's inequality implies that the approximation is actually a lower bound. Hence, $P_{\mathrm{UB}}(\{\mathcal{C}(\boldsymbol{\zeta})\})$ is lower bounded (or approximated) as

$$P_{\mathrm{UB}}(\{\mathcal{C}(\boldsymbol{\zeta})\}) \geq \frac{\mathrm{E}_{\boldsymbol{\zeta}}\left[\sum_{k<l} e^{\mathrm{E}_{\boldsymbol{\gamma}}[\ell(\boldsymbol{C}_k^{(\zeta)}, \boldsymbol{C}_l^{(\zeta)}; \boldsymbol{\gamma})|\boldsymbol{\zeta}]}\right]}{K \det\left(\boldsymbol{R}_{\boldsymbol{hh}|\boldsymbol{\gamma}}\right)} \triangleq P_{\mathrm{LBUB}}(\{\mathcal{C}(\boldsymbol{\zeta})\}). \tag{19.9}$$

Utilizing the relation $\mathrm{tr}(\boldsymbol{AB}) = \mathrm{tr}(\boldsymbol{BA})$, where $\mathrm{tr}(\cdot)$ denotes the trace operator, and exploiting the fact that $\boldsymbol{R}_{\boldsymbol{hh}|\boldsymbol{\gamma}}$ is constant with respect to $\boldsymbol{\gamma}$ shows that the exponent in (19.9) can, with a slight abuse of notation, be rewritten as

$$\begin{aligned}\mathrm{E}_{\boldsymbol{\gamma}}\left[\ell(\boldsymbol{C}_k^{(\zeta)}, \boldsymbol{C}_l^{(\zeta)}; \boldsymbol{\gamma}) | \boldsymbol{\zeta}\right] =\ & \mathrm{tr}\left(\boldsymbol{\Psi}^{-1} \boldsymbol{R}_{\boldsymbol{hh}|\boldsymbol{\gamma}}^{-1} \mathrm{E}_{\boldsymbol{\gamma}}\left[\boldsymbol{m}_{\boldsymbol{h}|\boldsymbol{\gamma}} \boldsymbol{m}_{\boldsymbol{h}|\boldsymbol{\gamma}}^* | \boldsymbol{\zeta}\right] \boldsymbol{R}_{\boldsymbol{hh}|\boldsymbol{\gamma}}^{-1}\right) \\ & - \mathrm{tr}\left(\boldsymbol{R}_{\boldsymbol{hh}|\boldsymbol{\gamma}}^{-1} \mathrm{E}_{\boldsymbol{\gamma}}\left[\boldsymbol{m}_{\boldsymbol{h}|\boldsymbol{\gamma}} \boldsymbol{m}_{\boldsymbol{h}|\boldsymbol{\gamma}}^* | \boldsymbol{\zeta}\right]\right) - \log\det(\boldsymbol{\Psi}).\end{aligned} \tag{19.10}$$

Inserting (19.10) into (19.9) gives the intended performance measure. All entities except the conditional expectation $\mathrm{E}_{\boldsymbol{\gamma}}[\boldsymbol{m}_{\boldsymbol{h}|\boldsymbol{\gamma}} \boldsymbol{m}_{\boldsymbol{h}|\boldsymbol{\gamma}}^* | \boldsymbol{\zeta}]$ can now be evaluated in closed form. The remaining conditional expectation does not pose a problem since it is independent of the codewords to be optimized. Hence, it can be evaluated once

using, for example, Monte-Carlo integration and stored for easy access during the code design process.

Note that the lower bound in (19.9) holds with equality if $\ell(\boldsymbol{C}_k^{(\zeta)}, \boldsymbol{C}_l^{(\zeta)}; \boldsymbol{\gamma})$ conditioned on $\boldsymbol{\zeta}$ is a constant. This is the case when the idealized feedback link is used since $\boldsymbol{\zeta} = \boldsymbol{\gamma}$ and hence $\mathrm{E}_{\boldsymbol{\gamma}}[\boldsymbol{m}_{\boldsymbol{h}|\boldsymbol{\gamma}}\boldsymbol{m}_{\boldsymbol{h}|\boldsymbol{\gamma}}^{*}|\boldsymbol{\zeta}] = \boldsymbol{m}_{\boldsymbol{h}|\boldsymbol{\gamma}}\boldsymbol{m}_{\boldsymbol{h}|\boldsymbol{\gamma}}^{*}$. From (19.6) and (19.9) it then follows that $P_{\mathrm{LBUB}}(\{\mathcal{C}(\boldsymbol{\zeta})\})$ is an upper bound on the codeword error probability.

In case of quantized feedback, it is realized that the lower bound $P_{\mathrm{LBUB}}(\{\mathcal{C}(i)\})$ approximates $P_{\mathrm{UB}}(\{\mathcal{C}(i)\})$ well when the variance of $\ell(\boldsymbol{C}_k^{(\zeta)}, \boldsymbol{C}_l^{(\zeta)}; \boldsymbol{\gamma})$ conditioned on $\boldsymbol{\zeta}$ is small. From (19.7) it follows that this occurs if the quantization is dense (so that $\boldsymbol{m}_{\boldsymbol{h}|\boldsymbol{\gamma}}$ is concentrated around $\mathrm{E}_{\boldsymbol{\gamma}}[\boldsymbol{m}_{\boldsymbol{h}|\boldsymbol{\gamma}}|\boldsymbol{\zeta}]$), σ^2 is low, and/or the correlation between $\boldsymbol{\gamma}$ and $\boldsymbol{h}$ is small.

It is interesting to note that the well-known determinant and rank criterion [4] used in the design of conventional space-time codes follows directly from the determinant part of (19.10). Hence, the design criterion developed in the present work can be seen as a generalization of the performance measures used in classic space-time code design.

19.4. Code design procedures

The approximative performance measure $P_{\mathrm{LBUB}}(\{\mathcal{C}(\boldsymbol{\zeta})\})$ developed in the previous section will now be used to design space-time block codes of different types. Such an approach automatically ensures that the available channel knowledge at the transmitter is taken into account, in contrast to conventional space-time code design.

Efficient codes are obtained by minimizing $P_{\mathrm{LBUB}}(\{\mathcal{C}(\boldsymbol{\zeta})\})$ with respect to the codewords in $\{\mathcal{C}(\boldsymbol{\zeta})\}$, while making sure that the power constraint is satisfied. This is accomplished by minimizing the quantity within the outer expectation in (19.9),

$$\sum_{k<l} e^{\mathrm{E}_{\boldsymbol{\gamma}}[\ell(\boldsymbol{C}_k^{(\zeta)}, \boldsymbol{C}_l^{(\zeta)}; \boldsymbol{\gamma})|\boldsymbol{\zeta}]}, \tag{19.11}$$

for each possible $\boldsymbol{\zeta}$ to produce the code $\mathcal{C}(\boldsymbol{\zeta})$. For convenience, parameter independent factors in (19.11) are now omitted leading to the *design criterion*

$$W(\boldsymbol{\mathcal{C}}) \triangleq \sum_{k<l} V(\boldsymbol{C}_k - \boldsymbol{C}_l), \tag{19.12}$$

where $\boldsymbol{\mathcal{C}} \triangleq [\boldsymbol{C}_1\ \boldsymbol{C}_2\ \cdots\ \boldsymbol{C}_K]$ is an $M \times KL$ matrix that contains K arbitrary codewords and

$$V(\boldsymbol{C}) \triangleq \frac{e^{\mathrm{tr}(\boldsymbol{\Psi}(\boldsymbol{C})^{-1}\boldsymbol{R}_{\boldsymbol{h}\boldsymbol{h}|\boldsymbol{\gamma}}^{-1}\boldsymbol{R}\boldsymbol{R}_{\boldsymbol{h}\boldsymbol{h}|\boldsymbol{\gamma}}^{-1})}}{\det(\boldsymbol{\Psi}(\boldsymbol{C}))} \tag{19.13}$$

is used to describe how each codeword pair influences the design criterion. The matrix $\boldsymbol{R}$ here depends on the type of feedback link that is considered. From the

discussion in the previous section it follows that $\boldsymbol{R} = \mathrm{E}[\boldsymbol{m}_{\boldsymbol{h}|\boldsymbol{\gamma}}\boldsymbol{m}_{\boldsymbol{h}|\boldsymbol{\gamma}}^{*}|\boldsymbol{\zeta}]$, which for idealized feedback further specializes into $\boldsymbol{R} = \boldsymbol{m}_{\boldsymbol{h}|\boldsymbol{\gamma}}\boldsymbol{m}_{\boldsymbol{h}|\boldsymbol{\gamma}}^{*}$.

The design criterion can now be utilized for minimizing $P_{\mathrm{LBUB}}(\{\mathcal{C}(\boldsymbol{\zeta})\})$ by designing each code $\mathcal{C}(\boldsymbol{\zeta})$ as

$$\boldsymbol{\mathcal{C}}(\boldsymbol{\zeta}) = \arg\min_{\boldsymbol{\mathcal{C}}\in\mathcal{C}_{\mathrm{s}}} W(\boldsymbol{\mathcal{C}}) \tag{19.14}$$

subject to the power constraint $\mathrm{E}[\|\boldsymbol{C}\|_{\mathrm{F}}^{2}|\boldsymbol{\zeta}] = PL$ introduced in (19.4). The code search is here restricted to a certain set $\mathcal{C}_{\mathrm{s}}$ that is used to describe the structure of the code. This means that $\mathcal{C}_{\mathrm{s}}$ varies from one code type to another. Consequently, (19.14) can be thought of as forming a framework for the design of arbitrary types of channel information dependent codes.

Another alternative design approach is to approximate the criterion function by only including terms in (19.12) that correspond to the worst codeword pairs, as measured by $V(\boldsymbol{C}_k - \boldsymbol{C}_l)$. This means that the code $\mathcal{C}(\boldsymbol{\zeta})$ is designed through

$$\boldsymbol{\mathcal{C}}(\boldsymbol{\zeta}) = \arg\min_{\boldsymbol{\mathcal{C}}\in\mathcal{C}_{\mathrm{s}}} \max_{k<l} V(\boldsymbol{C}_k - \boldsymbol{C}_l). \tag{19.15}$$

Which of the design procedures in (19.14) and (19.15) to use strongly depends on the type of code that is to be constructed. This will become more clear in a moment when the above generic formulation is specialized for some different code structures.

Introducing structure in the code makes it possible to trade performance for decoding/encoding complexity. A completely unstructured code provides maximum performance but must normally be decoded by means of a computationally expensive exhaustive search over all the codewords like indicated in (19.5). In contrast, decoding complexity can be decreased by limiting the choice of codewords so that they satisfy some structural constraints. Of course, this typically comes at the expense of poorer performance.

To investigate how structure affects the performance we will consider three different space-time block code structures—unstructured codes, LD codes, and weighted OSTBC. The codes here have been mentioned in order of increasingly restrictive structure and the particular details for each type are given below.

19.4.1. Unstructured codes

For unstructured space-time block codes, all the elements in all the codeword matrices can be chosen arbitrarily from the complex number field $\mathbb{C}$, subject only to the power constraint. This corresponds to $\mathcal{C}_{\mathrm{s}} = \mathbb{C}^{M\times KL}$. There is hence no structure and the design algorithm has therefore maximum freedom to choose the codewords. As already pointed out, unstructured codes have potentially the best performance but result in high decoding complexity since they require an exhaustive search as in (19.5).

For unstructured codes, the power constraint can be formulated explicitly in terms of the codewords as

$$\mathrm{E}\left[\|\boldsymbol{C}\|_{\mathrm{F}}^2|\boldsymbol{\zeta}\right] = \frac{1}{K}\sum_{k=1}^{K}\left\|\boldsymbol{C}_k^{(\boldsymbol{\zeta})}\right\|_{\mathrm{F}}^2 = \frac{1}{K}\|\boldsymbol{\mathcal{C}}\|_{\mathrm{F}}^2 = LP, \tag{19.16}$$

which relies on the assumption that the codewords are equally probable conditioned on $\boldsymbol{\zeta}$. The design problem in (19.14) can then be more precisely stated as

$$\boldsymbol{\mathcal{C}}(\boldsymbol{\zeta}) = \arg \min_{\substack{\boldsymbol{\mathcal{C}} \\ \|\boldsymbol{\mathcal{C}}\|_{\mathrm{F}}^2 = KLP}} W(\boldsymbol{\mathcal{C}}). \tag{19.17}$$

Numerical methods need to be employed in order to obtain a solution. One strategy successfully used in [17] is to use a simple gradient search technique where the limit on the output power is maintained by projecting in each iteration the $2KLM$ real-valued parameters in $\boldsymbol{\mathcal{C}}$ onto the surface of a $2KLM$-dimensional sphere with radius $\sqrt{KLP}$. The approach is facilitated by the fact that a closed-form expression for the gradient is easily derived. Unfortunately, the design complexity is so high that solving (19.17) in real time is probably infeasible in practice. For the case of quantized feedback, this is less of an issue since the codes can be designed offline and then stored in a lookup table for quick online access. Even with such an offline strategy, the design problem is for high-rate codes computationally challenging as the complexity quickly grows with the number of codewords K.

Numerical techniques are also required to solve the alternative min-max approach in (19.15). This is however made difficult by the fact that $\max_{k<l} V(\boldsymbol{C}_k - \boldsymbol{C}_l)$ is not differentiable at all points. We will therefore not use the min-max approach for designing unstructured codes.

19.4.2. Linear dispersive codes

When linear dispersive space-time block codes are used, the data to be transmitted corresponding to one codeword is first mapped into symbols s_m, $m = 1, 2, \ldots, L_{\mathrm{d}}$, each taken from some signal constellation alphabet $\mathcal{A}$. The transmitted codeword is thereafter formed as a linear combination of the information bearing symbols according to

$$\boldsymbol{C} = \sum_{m=1}^{L_{\mathrm{d}}} \boldsymbol{B}_m s_m, \tag{19.18}$$

where $\boldsymbol{B}_m \triangleq \boldsymbol{B}_m^{(\boldsymbol{\zeta})}$ represents a complex-valued $M \times L$ matrix used to weigh the mth symbol. Assume without loss of generality[1] that the signal constellation alphabet

[1] Complex-valued symbols may be handled within the present framework by dividing the symbols into their real and imaginary parts. The codewords can then be written in the same form as in (19.18) but with twice as many terms.

$\mathcal{A}$, and hence also the symbols s_m, are real-valued. Also assume that the symbols are independent and identically distributed (i.i.d.) with $\mathrm{E}[s_m] = 0$ and $\mathrm{E}[s_m^2] = 1$. The symbols depend only on the data to be transmitted while the weighting matrices may vary with the channel side information $\boldsymbol{\zeta}$.

By choosing the weights appropriately, the information may be spread both spatially and temporally to obtain diversity benefits and coding gain while taking the channel knowledge available at the transmitter into account. For the case of no channel side information, such linear dispersive structures have previously been described in, for example, [5, 6].

A major advantage of the above linear structure is that the decoding complexity may in some cases be drastically reduced compared with the complexity of an exhaustive search. Sphere decoding [15] may, for example, be used under certain conditions to substantially lower the complexity while maintaining ML performance.

For LD codes, the power constraint in (19.4) can be formulated in terms of the weighting matrices as

$$\begin{aligned}\mathrm{E}\left[\|\boldsymbol{C}\|_{\mathrm{F}}^2|\boldsymbol{\zeta}\right] &= \mathrm{E}\left[\,\mathrm{tr}\left(\boldsymbol{C}\boldsymbol{C}^*\right)|\boldsymbol{\zeta}\right] = \sum_{m=1}^{L_{\mathrm{d}}}\sum_{m'=1}^{L_{\mathrm{d}}}\mathrm{tr}\left(\boldsymbol{B}_m^{(\boldsymbol{\zeta})}\left(\boldsymbol{B}_{m'}^{(\boldsymbol{\zeta})}\right)^*\right)\mathrm{E}\left[s_m s_{m'}\right] \\ &= \sum_{m=1}^{L_{\mathrm{d}}}\mathrm{tr}\left(\boldsymbol{B}_m^{(\boldsymbol{\zeta})}\left(\boldsymbol{B}_m^{(\boldsymbol{\zeta})}\right)^*\right) = \sum_{m=1}^{L_{\mathrm{d}}}\left\|\boldsymbol{B}_m^{(\boldsymbol{\zeta})}\right\|_{\mathrm{F}}^2 = LP.\end{aligned} \tag{19.19}$$

The min-max design approach is again not convenient to use for the same reasons as previously mentioned. Consequently, the other design alternative in (19.14) is preferable. In case of LD codes, the design problem thus specializes into designing the weighting matrices according to

$$\left\{\boldsymbol{B}_m^{(\boldsymbol{\zeta})}\right\}_{m=1}^{L_{\mathrm{d}}} = \arg \min_{\substack{\left\{\boldsymbol{B}_m\right\}_{m=1}^{L_{\mathrm{d}}} \\ \sum_{m=1}^{L_{\mathrm{d}}}\|\boldsymbol{B}_m\|_{\mathrm{F}}^2 = LP}} W\left(\boldsymbol{\mathcal{C}}\left(\boldsymbol{B}_1,\ldots,\boldsymbol{B}_{L_{\mathrm{d}}}\right)\right), \tag{19.20}$$

where $\boldsymbol{\mathcal{C}}(\boldsymbol{B}_1,\ldots,\boldsymbol{B}_{L_{\mathrm{d}}}) \triangleq [\sum_{m=1}^{L_{\mathrm{d}}}\boldsymbol{B}_m s_m^{(1)} \;\cdots\; \sum_{m=1}^{L_{\mathrm{d}}}\boldsymbol{B}_m s_m^{(K)}]$ with $s_1^{(k)},\ldots,s_{L_{\mathrm{d}}}^{(k)}$ representing the symbol sequence corresponding to the kth codeword. This design problem must in general be solved using numerical methods. A gradient search technique similar to the one described in connection with the design of unstructured codes may be applied. Designing LD codes in this way is computationally demanding and can in practice only be carried out for situations with quantized feedback where offline design is possible.

19.4.3. Weighted OSTBC

The weighted OSTBC transmission structure is a simple yet effective way of exploiting channel side information in conjunction with space-time coding. The idea is to use the side information for improving a predetermined and fixed OSTB

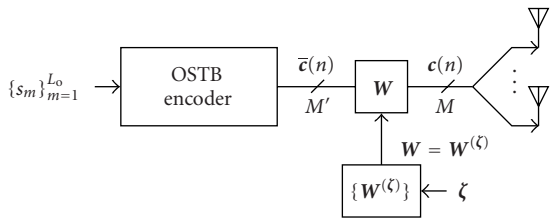

FIGURE 19.4. Transmitter structure in weighted OSTBC. Only the transmit weighting $\boldsymbol{W}$ is now affected by the channel side information.

code by means of a linear transformation that depends on the channel knowledge. This is in line with information theoretic results [8] concerning the optimality of separate space-time coding and transmit weighting. Indeed, the structure can be shown to be optimal in a capacity sense if there are two transmit antennas and one receive antenna [14].

The transmitted codeword in weighted OSTBC can be written in the form

$$\boldsymbol{C} = \boldsymbol{W}\bar{\boldsymbol{C}}, \tag{19.21}$$

where $\boldsymbol{W} \triangleq \boldsymbol{W}^{(\zeta)}$ is an $M \times M'$ transmit weighting matrix which depends on the side information $\boldsymbol{\zeta}$ and where $\bar{\boldsymbol{C}} \in \{\bar{\boldsymbol{C}}_k\}_{k=1}^{K}$ is an $M' \times L$ matrix representing the output of a fixed OSTB encoder. We will henceforth for simplicity assume that $L \geq M'$, meaning that $\bar{\boldsymbol{C}}$ has more columns than rows. The class of OSTB codes is a special case of the class of LD codes where the weighting matrices have been chosen in a certain way [7]. Consequently, the OSTB encoder takes the data to be transmitted corresponding to one codeword and first maps it into symbols $s_1, \ldots, s_{L_o}$, each taken from some real-valued signal constellation alphabet $\mathcal{A}$. The symbols are again assumed to be i.i.d. and normalized so that $\mathrm{E}[s_m^2] = 1$.

In contrast to the previous case of LD codes, the weighting matrices used by the OSTB encoder are fixed and hence independent of the side information. Thus, only the transmit weighting $\boldsymbol{W}$ is affected by the side information. This is illustrated in Figure 19.4, where $\bar{\boldsymbol{c}}(n)$ denotes the output of the OSTB encoder.

Like all conventional space-time codes, OSTB codes are intended for a scenario where there is no channel knowledge at the transmitter. Emitting energy isotropically in space is thus appropriate. When OSTB codes are used, this is ensured by an output matrix $\bar{\boldsymbol{C}}$ that always has orthogonal rows of equal norm. More precisely, the weighting matrices in the OSTB code are such that, for arbitrary real-valued constellation alphabets $\mathcal{A}$, the codewords satisfy

$$\bar{\boldsymbol{C}}_k \bar{\boldsymbol{C}}_k^* = \sum_{m=1}^{L_o} \left(s_m^{(k)}\right)^2 \boldsymbol{I}_{M'}, \quad k = 1, 2, \ldots, K, \tag{19.22}$$

where $s_1^{(k)}, \ldots, s_{L_o}^{(k)}$ represents the symbol sequence corresponding to the kth codeword $\bar{\boldsymbol{C}}_k$. The very notion of an OSTB code is in fact defined by the orthogonality property in (19.22), together with the linear dispersive structure of the code.

An important advantage of weighted OSTBC is that the underlying OSTB code results in very low decoding complexity. In fact, from the code's orthogonal property it follows that ML decoding as in (19.5) decouples into low-complexity individual symbol detection.

By appropriately choosing the weighting matrix $\boldsymbol{W}$, the properties of the transmitted signals can be modified so as to suit the current channel conditions. The orthogonal property in (19.22) again plays a fundamental role by considerably simplifying the design of the transmit weighting matrix. To see why, note that the terms in the design criterion (19.12) only depend on the codeword pairs through $(\boldsymbol{C}_k - \boldsymbol{C}_l)(\boldsymbol{C}_k - \boldsymbol{C}_l)^*$. Inserting $\boldsymbol{C}_k = \boldsymbol{W}\bar{\boldsymbol{C}}_k$ and $\boldsymbol{C}_l = \boldsymbol{W}\bar{\boldsymbol{C}}_l$ and thereafter exploiting (19.22) and the linearity of the code gives

$$(\boldsymbol{C}_k - \boldsymbol{C}_l)(\boldsymbol{C}_k - \boldsymbol{C}_l)^* = \boldsymbol{W}\boldsymbol{W}^*\mu_{kl}, \tag{19.23}$$

where $\mu_{kl} \triangleq \sum_{m=1}^{L_o} \left(s_m^{(k)} - s_m^{(l)}\right)^2$ is the only entity that depends on the codewords pair. This means that also $V(\boldsymbol{W}(\bar{\boldsymbol{C}}_k - \bar{\boldsymbol{C}}_l))$ depends on the codeword pair exclusively via the scaling factor μ_{kl}. Let $\ell(\boldsymbol{W}\boldsymbol{W}^*, \mu_{kl}) \triangleq \log(V(\boldsymbol{W}(\bar{\boldsymbol{C}}_k - \bar{\boldsymbol{C}}_l)))$ represent the logarithm of the resulting function. Since it can be easily verified that $\ell(\boldsymbol{W}\boldsymbol{W}^*, \mu_{kl})$ is a decreasing function with respect to μ_{kl}, finding the worst codeword pairs as in the min-max approach corresponds to finding the smallest μ_{kl}, that is,

$$\max_{k<l} V(\boldsymbol{W}(\bar{\boldsymbol{C}}_k - \bar{\boldsymbol{C}}_l)) = \ell(\boldsymbol{W}\boldsymbol{W}^*, \mu_{\min}). \tag{19.24}$$

The above relation radically simplifies the design problem because the design complexity no longer depends on the number of codewords and the weighting matrix can be designed as

$$\boldsymbol{W}^{(\zeta)} = \arg \min_{\substack{\boldsymbol{W} \\ \|\boldsymbol{W}\|_F^2 = LP/L_o}} \ell(\boldsymbol{W}\boldsymbol{W}^*, \mu_{\min}), \tag{19.25}$$

where the power constraint is expressed solely in terms of the $\boldsymbol{W}$ since

$$\begin{aligned} \mathrm{E}\left[\|\boldsymbol{C}\|_F^2 | \boldsymbol{\zeta}\right] &= \mathrm{E}\left[\|\boldsymbol{W}\bar{\boldsymbol{C}}\|_F^2 | \boldsymbol{\zeta}\right] \\ &= \mathrm{tr}\left((\boldsymbol{W}^{(\zeta)})^* \boldsymbol{W}^{(\zeta)} \mathrm{E}\left[\bar{\boldsymbol{C}}\bar{\boldsymbol{C}}^*\right]\right) \\ &= \mathrm{tr}\left((\boldsymbol{W}^{(\zeta)})^* \boldsymbol{W}^{(\zeta)} \sum_{m=1}^{L_o} \mathrm{E}\left[s_m^2\right]\right) \\ &= \mathrm{tr}\left((\boldsymbol{W}^{(\zeta)})^* \boldsymbol{W}^{(\zeta)}\right) L_o = L_o \left\|\boldsymbol{W}^{(\zeta)}\right\|_F^2 = LP. \end{aligned} \tag{19.26}$$

In contrast to the two previous code structures, the min-max approach is now clearly preferable over the other design strategy. This is not only because of its substantially lower design complexity. An additional benefit is that (19.25) can be shown to actually minimize an approximation of the symbol error probability instead of minimizing, as in (19.14), an approximation on the probability of codeword error (cf. [14]).

Solving the design problem in (19.25) typically requires the use of numerical optimization techniques. A simple reparametrization considerably simplifies this task by making the problem convex in cases when the weighting is square, that is, $M = M'$. Efficient techniques from convex optimization can then be used to solve the design problem.

As previously mentioned, quantized feedback means that the design can be carried out offline and the results stored in a lookup table. Complexity issues are hence not as critical as in the case of the idealized feedback link where the transmit weighting must be computed in real time. Unlike unstructured and LD codes, the convexity of the problem now makes even real time design feasible in practice. The computational requirements can sometimes be lowered even further. In the extreme case of two transmit antennas, one receive antenna and a certain spatially uncorrelated Rayleigh fading scenario, solving the design problem essentially reduces to solving a second-degree polynomial equation.

19.5. Properties of designed codes

Although finding analytical solutions to the code design problems described herein is usually not possible, the criterion function reveals important *properties* of the designed codes. Some of these properties will be briefly discussed in this section. Rigorous derivations will however be omitted in order not to obscure the intuition behind the results. Proofs justifying the discussion follows easily from an appropriate combination of the results in [14, 16, 17].

Consider first the criterion function as defined by (19.12) and (19.13). In (19.13), the exponent and the determinant can be seen to have different roles. Note that $\boldsymbol{R} = \mathrm{E}[\boldsymbol{m}_{\boldsymbol{h}|\boldsymbol{y}}\boldsymbol{m}_{\boldsymbol{h}|\boldsymbol{y}}^{*}|\boldsymbol{\zeta}]$ is a function of the actual realization of the side information and is therefore potentially time-varying while $\boldsymbol{R}_{\boldsymbol{hh}|\boldsymbol{y}}$ is fixed. Since $\boldsymbol{R}$ is not present in the determinant, it is realized that only the exponent deals with the time-varying part of the channel knowledge. When the quality of the initial channel information is high, it follows that the conditional covariance matrix $\boldsymbol{R}_{\boldsymbol{hh}|\boldsymbol{y}}$ is small (in some matrix norm) and hence $\det(\boldsymbol{I}_N \otimes \boldsymbol{C}\boldsymbol{C}^{*}\eta + \boldsymbol{R}_{\boldsymbol{hh}|\boldsymbol{y}}^{-1}) \approx \det(\boldsymbol{R}_{\boldsymbol{hh}|\boldsymbol{y}}^{-1})$. The exponent is then solely responsible for the code design. If in addition quantization effects can be neglected, the channel knowledge is essentially perfect at the transmitter and it can be shown that the design algorithms tend to distribute output power in space based on the singular values and left singular eigenvectors of the channel matrix $\boldsymbol{H}$. More precisely, directions corresponding to eigenvectors with strong singular values tend to be allocated more power than eigen-directions with weak eigenvalues. This is similar to the well-known water-filling type of transmission. Such a power distribution makes sense since there is no point in wasting

power in directions which contribute little or not at all to the received signal. It is also interesting to note that a similar nonuniform output power distribution arises when the SNR becomes low even if the channel knowledge is not perfect.

Unlike the exponent, the determinant only uses static channel knowledge in the form of the spatial correlations contained in $\boldsymbol{R}_{\boldsymbol{hh}|\boldsymbol{\gamma}}$. For sufficiently small $\boldsymbol{R}$, the exponent essentially vanishes and only the determinant affects the code design. This is, for example, the case when the quality of the initial channel information is low and the channel is zero-mean ($\boldsymbol{m}_{\boldsymbol{h}} = \boldsymbol{0}$). Assuming further that the channel covariance is given by $\boldsymbol{R}_{\boldsymbol{hh}} = \sigma_h^2 \boldsymbol{I}_{MN}$, corresponding to spatially uncorrelated Rayleigh fading, no transmission direction is more favorable than another. The transmitter is then completely without channel knowledge and it makes sense to distribute power isotropically in space. Experiments show that the design algorithms strive toward such transmission by attempting to make the rows in each codeword orthogonal to each other and of equal norm.

A scenario with high SNR turns out to lead to codewords with properties similar to those exhibited when there is no channel knowledge. Combined with the behavior for the low SNR case, it may be concluded that the usefulness of channel side information is very important at low SNR values but diminishes as the SNR increases. This is in line with the behavior of classic water-filling power distribution, which becomes more uniform with increasing SNR.

19.5.1. Weighted OSTBC with idealized feedback

To further illustrate how the presence of side information affects the transmission, it is instructive to study weighted OSTBC in conjunction with an idealized feedback link. Toward this end, assume for simplicity $N = 1$ receive antenna, a square weighting matrix ($M = M'$), and $\boldsymbol{m}_{\boldsymbol{h}} = \boldsymbol{0}$, $\boldsymbol{R}_{\boldsymbol{hh}} = \sigma_h^2 \boldsymbol{I}_{MN}$ so that the distribution describing the channel fading does not constitute any channel knowledge on its own. Further assume that $\boldsymbol{\gamma}$ and $\boldsymbol{h}$ are identically distributed and that each element γ_k in $\boldsymbol{\gamma}$ is correlated with the corresponding coefficient h_k in $\boldsymbol{h}$ and uncorrelated with all others. A scenario where $\boldsymbol{h}$ and $\boldsymbol{\gamma}$ are distributed in this manner will be referred to as a *simplified fading scenario*. It is reasonable in this scenario to let the absolute value of the normalized correlation coefficient, $\rho \triangleq |\,\mathrm{E}[h_k \gamma_k^*]/\sigma_h^2|$, define a measure for the quality of the initial channel information. Thus, $\rho = 0$ corresponds to no initial channel knowledge while $\rho \to 1$ represents a situation in which the initial channel information is perfect.

The development in [16] shows that the transmission scheme behaves as a seamless blend between OSTBC and beamforming. To be specific, consider the three cases listed below.

(1) *Perfect channel knowledge* ($\rho \to 1$)*:* the weighting matrix is now of rank-one and can be taken as $\boldsymbol{W} = \sqrt{LP/L_o}[\boldsymbol{\zeta}/\|\boldsymbol{\zeta}\|\ \boldsymbol{0}_{M\times(M-1)}]$. This is equivalent to classical beamforming. All power is therefore emitted in the direction of the side information $\boldsymbol{\zeta}$. Such a strategy is reasonable since $\boldsymbol{\zeta} = \boldsymbol{h}$, and the transmitter may therefore completely trust the side information.

(2) *Imperfect channel knowledge* ($0 < \rho < 1$): the designed weighting matrix is now of the form $\boldsymbol{W} = \sqrt{LP/L_o}[\alpha_1\boldsymbol{\zeta}/\|\boldsymbol{\zeta}\| \ \alpha_2\boldsymbol{\nu}_2 \ \cdots \ \alpha_M\boldsymbol{\nu}_M]$, where $\alpha_k > 0$ determines the amount of power along the kth direction and $\{\boldsymbol{\nu}_k\}$ is a set of orthonormal vectors that are all orthogonal to $\boldsymbol{\zeta}$. In other words, power is emitted in all directions but not uniformly. The direction given by the side information $\boldsymbol{\zeta}$ is still utilized but power is now also spent on directions orthogonal to $\boldsymbol{\zeta}$. Each of these orthogonal directions is allocated the same power while a higher power level is used along $\boldsymbol{\zeta}$. Exploiting also the orthogonal directions clearly makes sense since the information in $\boldsymbol{\zeta}$ about the true channel $\boldsymbol{h}$ is imperfect and thus cannot be completely trusted.

(3) *No channel knowledge* ($\rho = 0$): the weighting matrix is now unitary, for example, equal to the identity matrix. This corresponds to using the OSTB code without any transmit weighting. Power is hence distributed isotropically in space, just as conventional space-time coding strives for. Such a strategy clearly agrees well with intuition since the transmitter does not know anything about the true channel and should therefore not favor any direction over another.

19.6. Simulation results

To illustrate the performance of some constructed codes, simulations of the communication system in Section 19.2 have been conducted. A situation with spatially uncorrelated Rayleigh fading was considered in the form of the simplified fading scenario previously described in Section 19.5.1. In order to focus on a common situation in practice, $N = 1$ receive antenna was assumed throughout the simulations. How the quality of the side information impacts the performance was studied by using idealized as well as quantized feedback for various quality levels ρ of the initial channel information. Included in the study were the two extreme cases of no ($\rho = 0$ and/or $b = 0$) and perfect channel knowledge ($\rho \to 1$ with idealized feedback).

The no channel knowledge case corresponds to an open-loop system for which conventional space-time codes are appropriate. A system using unmodified OSTB codes taken from [7] was therefore utilized as a benchmark. A comparison with beamforming was also performed.

Beamforming is here taken to mean a scheme in which the transmitted signal can be written in the form $\boldsymbol{c}(n) = \boldsymbol{\nu}s(n)$, where $s(n)$ represents the nth information bearing data symbol and $\boldsymbol{\nu}$ is a transmit weighting vector. For *ideal* beamforming, the weighting vector is based on the true channel $\boldsymbol{h}$, while the imperfect channel information vector $\boldsymbol{\gamma}$ is used for *conventional* beamforming with idealized feedback.

The remaining assumptions in the simulations were as follows. For all the examined cases, information carrying bits were mapped into codewords/blocks of length L samples and conveyed over the spatially uncorrelated flat Rayleigh fading channel. An output power of $P = 1$ was used. The variance of the channel coefficients was set to $\sigma_h^2 = 1$. Systems using OSTBC or beamforming employed a binary phase-shift keying (BPSK) signal constellation. To make fair comparisons,

the effective data rates of all investigated schemes were fixed at 1 information bit per channel use. The SNR was measured for the conventional OSTBC system and defined as

$$\mathrm{SNR} \triangleq \frac{\mathrm{E}\left[\left\|\boldsymbol{H}^{*}\boldsymbol{C}\right\|_{\mathrm{F}}^{2}\right]}{\mathrm{E}\left[\left\|\boldsymbol{E}\right\|_{\mathrm{F}}^{2}\right]} = \frac{LNP\sigma_h^2}{LN\sigma^2} = \frac{P\sigma_h^2}{\sigma^2}, \tag{19.27}$$

where $\boldsymbol{C} = \sqrt{LP/(L_{\mathrm{o}}M)}\bar{\boldsymbol{C}}$ with $\bar{\boldsymbol{C}}$ denoting the codeword output from the OSTB encoder. The expression for the SNR is equal to the total received average signal energy, divided by the total average noise energy.

19.6.1. Weighted OSTBC versus conventional schemes

We start by investigating the performance of weighted OSTBC when the transmit weighting matrix is designed as in (19.25) and used together with idealized feedback. Only square transmit weighting will be considered, that is, $M = M'$. The bit error rate (BER) as a function of the SNR is depicted in Figure 19.5a. It is seen that the performance of the proposed weighted OSTBC transmission scheme with $\rho = 0.9$ is for all SNR values better than conventional OSTBC but, as expected, worse than ideal beamforming. Note that the two curves for conventional OSTBC and ideal beamforming also show the performance of weighted OSTBC in the case of $\rho = 0$ and $\rho \to 1$, respectively. Conventional beamforming is seen to give good performance at low SNR values, but as the SNR increases, the lack of correct channel knowledge leads to a serious performance degradation. In contrast, the curve for weighted OSTBC approaches the one for ideal beamforming as the SNR decreases, whereas for increasing SNR it approaches the performance of conventional OSTBC. Thus, the proposed scheme efficiently combines beamforming with OSTBC. This is also in good agreement with the observations in Section 19.5 regarding the allocation of power among the transmit directions.

The gains due to channel knowledge usually increase with the number of transmit antennas. To illustrate this effect, Figure 19.5b displays the performance when eight transmit antennas are used. As seen, channel knowledge now offers much larger gains than in the previous case.

19.6.2. Quantized feedback

A variant of a simple scheme called partial phase combining [12] will be used to study the effects of coarse quantization in the feedback link. Partial phase combining involves quantizing the differences in phase between the first coefficient γ_1 and the other coefficients $\{\gamma_k\}_{k=2}^{MN}$ in the initial channel information vector $\boldsymbol{\gamma}$. This is similar to the feedback scheme in the closed-loop mode of the WCDMA system [20].

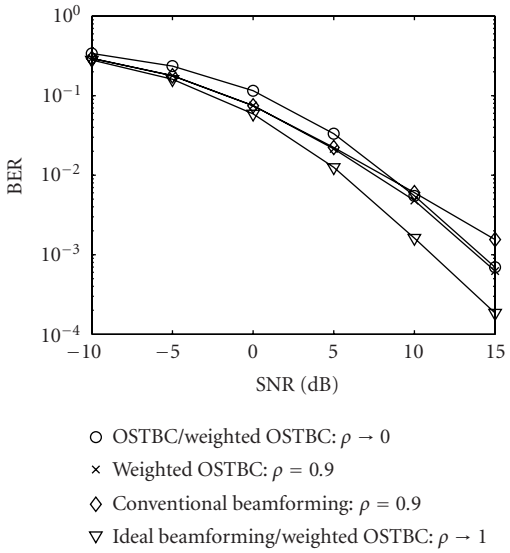

(a)

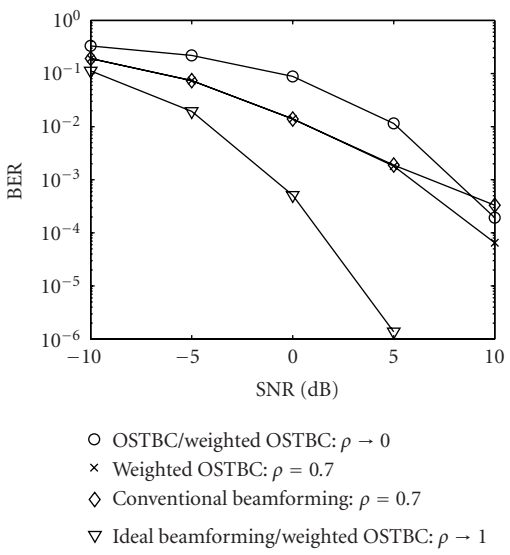

(b)

FIGURE 19.5. The performance of weighted OSTBC compared with conventional OSTBC and beamforming. (a) $M = 2$ transmit antennas. (b) $M = 8$ transmit antennas.

In the present work, a particularly simple form of partial phase combining is considered where each phase difference is uniformly quantized, independently

of all the others. Scalar quantization is thus employed, which reduces the computational complexity of the feedback encoder. The quantization scheme can be described in terms of the previously introduced framework as implementing the encoder function

$$\zeta = i = \varepsilon(\boldsymbol{\gamma}) = \arg \min_{k \in \{0,1,\ldots,2^b-1\}} \left\| \frac{\boldsymbol{\gamma}}{\gamma_1} - \hat{\boldsymbol{\gamma}}(k) \right\|^2, \tag{19.28}$$

where $\{\hat{\boldsymbol{\gamma}}(k)\}_{k=0}^{2^b-1}$ contains codebook vectors given by

$$\hat{\boldsymbol{\gamma}}(k) \triangleq \begin{bmatrix} 1 & e^{j\phi_{i_2(k)}} & \cdots & e^{j\phi_{i_{MN}(k)}} \end{bmatrix}^{\mathrm{T}}. \tag{19.29}$$

Here, $j \triangleq \sqrt{-1}$ and $\phi_{i_l(k)} \triangleq 2\pi i_l(k)/2^{\bar{b}}$ with $\bar{b} \triangleq b/(MN-1)$ representing the number of feedback bits per phase difference. The phase of γ_l/γ_1 is thus uniformly quantized into a $\bar{b}$ bit number $i_l(k) \in \{0, 1, \ldots, 2^{\bar{b}} - 1\}$ which may be defined implicitly through the relation $k = \sum_{l=2}^{MN} i_l(k) 2^{\bar{b}(l-2)}$.

Figure 19.6a depicts the performance for weighted OSTBC when $M = 2$ antennas are used at the transmitter and the channel information is coarsely quantized using $\bar{b} = b = 2$ bits per phase difference. Beamforming and OSTBC again serve as benchmarks. Conventional beamforming now uses $\hat{\boldsymbol{\gamma}}(i)$ as transmit weighting vector. For high SNR values, weighted OSTBC is seen to be robust against the impairments in the side information. Just as for conventional beamforming, an array gain is obtained when the SNR is low by successfully exploiting the side information. As expected, the gains due to channel knowledge increase as more transmit antennas are used. This is illustrated in Figure 19.6b which shows the performance when $M = 4$ transmit antennas are used and each phase difference is quantized using $\bar{b} = b/3 = 2$ bits.

Unstructured and LD codes have been designed using (19.17) and (19.20), respectively. To give an idea of how the choice of code structure influences the performance, the three code types are compared in Figure 19.7. Results for $M = 2$ transmit antennas are shown in Figure 19.7a while Figure 19.7b represents the $M = 4$ case. Performance is now measured in terms of codeword/block error rate (BLER) in order to avoid dealing with the problem of assigning bits to codewords. All codeword matrices are square, that is, $M = L$, and $\bar{b} = 2$ bits are used for quantizing each phase difference. It turns out that the differences in performance between the three code types are roughly preserved regardless of the degree of channel knowledge at the transmitter. Thus, the quality of the initial channel information is here arbitrarily set to $\rho = 0.9999$, meaning that essentially perfect channel knowledge is input to the feedback encoder.

As expected, the unstructured code is better than the two other code types. What may be more surprising is that the LD code and weighted OSTBC basically

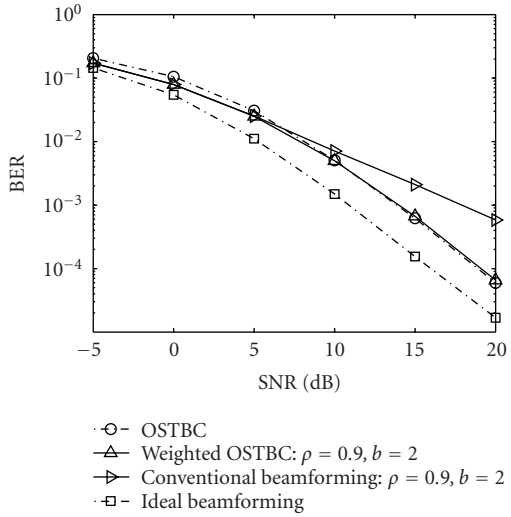

(a)

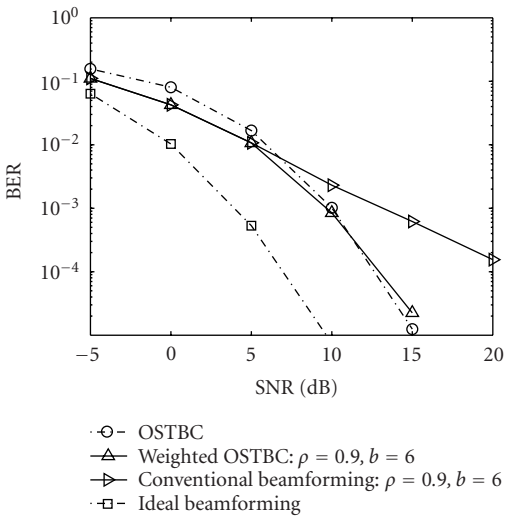

(b)

FIGURE 19.6. The performance of weighted OSTBC compared with conventional OSTBC and beamforming when side information is quantized using b bits. (a) $M = 2$ transmit antennas. (b) $M = 4$ transmit antennas.

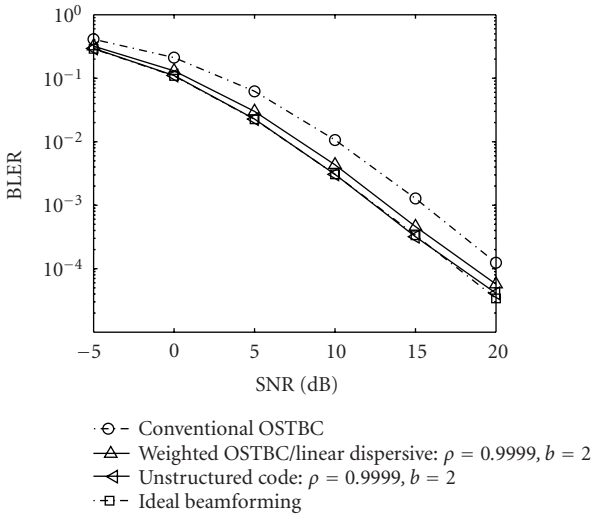

(a)

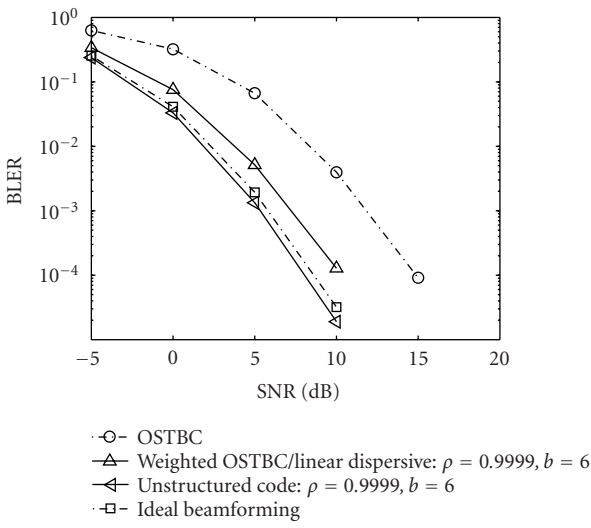

(b)

FIGURE 19.7. Illustrating how the choice of code structure affects the performance when the side information is quantized using b bits. (a) $M = 2$ transmit antennas. (b) $M = 4$ transmit antennas.

have the same performance, explaining why we let them share the same curve. Experimental investigations not presented here indicate that LD codes and weighted OSTBC exhibit similar performance in many different scenarios. Thus, it may seem like LD codes offer little, if any, performance advantage over weighted OSTBC. It is however important to keep in mind that the former code type exists for all possible combinations of antenna array sizes and data rates whereas weighted OSTBC is to a large degree limited by the fact that OSTB codes exist only for low symbol rates. A thin transmit weighting matrix, that is, $M' < M$, may to some extent offset this limitation. Nevertheless, it is reasonable to expect that LD codes have clear performance advantages over weighted OSTBC for systems requiring high data rates.

19.7. Summary and future research

The design of channel side information dependent space-time block codes was considered. A performance measure was developed that directly takes the imperfect nature of the channel knowledge into account. Based on the performance measure, design procedures for three different code structures were presented. The resulting codes showed robustness against quantization errors as well as feedback delay.

The field of channel side information dependent space-time is receiving growing interest but is yet in its infancy. Many open problems remain to be explored. How to apply the concept on type of codes other than block codes pose interesting problems. Designing schemes that maximize data rate instead of, as here, minimizing error probability is also an important topic for future research. Applications involving frequency-selective channels also deserve to be studied. Finally, it remains to be seen if the link level strategies investigated herein may be extended to handle multiuser situations in a tractable manner.

Abbreviations

BER	Bit error rate
BLER	Block error rate
BPSK	Binary phase-shift keying
ENC	Encoder
FDD	Frequency-division duplex
i.i.d.	Independent and identically distributed
LD	Linear dispersion
ML	Maximum likelihood
OSTB	Orthogonal space-time block
OSTBC	Orthogonal space-time block coding
SNR	Signal-to-noise ratio
TDD	Time-division duplex
WCDMA	Wideband code division multiple access

Bibliography

[1] A. J. Paulraj and C. B. Papadias, "Space-time processing for wireless communications," *IEEE Signal Processing Mag.*, vol. 14, no. 6, pp. 49–83, 1997.

[2] I. E. Telatar, "Capacity of multi-antenna gaussian channels," Bell Labs. Technical Memorandum BL0112170-950615-07TM, AT&T Bell Laboratories, Murray Hill, NJ, USA, 1995, *European Trans. Telecommunications*, vol. 10, pp. 585–595, 1999.

[3] J.-C. Guey, M. P. Fitz, M. R. Bell, and W. Y. Kuo, "Signal design for transmitter diversity wireless communication systems over rayleigh fading channels," *IEEE Trans. Commun.*, vol. 47, no. 4, pp. 527–537, 1999.

[4] V. Tarokh, N. Seshadri, and A. R. Calderbank, "Space-time codes for high data rate wireless communication: performance criterion and code construction," *IEEE Trans. Inform. Theory*, vol. 44, no. 2, pp. 744–765, 1998.

[5] B. Hassibi and B. M. Hochwald, "High-rate codes that are linear in space and time," *IEEE Trans. Inform. Theory*, vol. 48, no. 7, pp. 1804–1824, 2002.

[6] R. W. Heath Jr. and A. J. Paulraj, "Linear dispersion codes for MIMO systems based on frame theory," *IEEE Trans. Signal Processing*, vol. 50, no. 10, pp. 2429–2441, 2002.

[7] V. Tarokh, H. Jafarkhani, and A. R. Calderbank, "Space-time block codes from orthogonal designs," *IEEE Trans. Inform. Theory*, vol. 45, no. 5, pp. 1456–1467, 1999.

[8] M. Skoglund and G. Jöngren, "On the capacity of a multiple-antenna communication link with channel side information," *IEEE Journal of Selected Areas in Communications*, vol. 21, no. 3, pp. 395–405, 2003.

[9] E. N. Onggosanusi, A. Gatherer, A. G. Dabak, and S. Hosur, "Performance analysis of closed-loop transmit diversity in the presence of feedback delay," *IEEE Trans. Commun.*, vol. 49, no. 9, pp. 1618–1630, 2001.

[10] A. Wittneben, "Optimal predictive tx combining diversity in correlated fading for microcellular mobile radio applications," in *IEEE Global Telecommunications Conference. Conference record. Communication Theory Mini-Conference, GLOBECOM '95.*, pp. 48–54, ASCOM Tech. Ltd., Singapore, November 1995.

[11] A. Narula, M. J. Lopez, M. D. Trott, and G. W. Wornell, "Efficient use of side information in multiple-antenna data transmission over fading channels," *IEEE Journal on Selected Areas of Communications*, vol. 16, no. 8, pp. 1423–1436, 1998.

[12] R. W. Heath Jr. and A. J. Paulraj, "A simple scheme for transmit diversity using partial channel feedback," in *IEEE Asilomar Conference on Signals, Systems and Computers*, Pacific Grove, CALIF, USA, November 1998.

[13] E. Visotsky and U. Madhow, "Space-time transmit precoding with imperfect feedback," *IEEE Trans. Inform. Theory*, vol. 47, no. 6, pp. 2632–2639, 2001.

[14] G. Jöngren, *Utilizing channel state information in space-time coding: performance limits and transmission techniques*, Ph.d. dissertation, Royal Institute of Technology, Stockholm, Sweden, June 2003.

[15] H. Vikalo and B. Hassibi, "Maximum-likelihood sequence detection of multiple antenna systems over dispersive channels via sphere decoding," *EURASIP Journal on Applied Signal Processing*, vol. 2002, no. 5, pp. 525–531, 2002.

[16] G. Jöngren, M. Skoglund, and B. Ottersten, "Combining beamforming and orthogonal space-time block coding," *IEEE Trans. Inform. Theory*, vol. 48, no. 3, pp. 611–627, 2002.

[17] G. Jöngren, M. Skoglund, and B. Ottersten, "Design of channel-estimate-dependent space-time block codes," *IEEE Trans. Commun.*, vol. 52, no. 7, pp. 1191–1203, 2004.

[18] S. Zhou and G. B. Giannakis, "Optimal transmitter eigen-beamforming and space-time block coding based on channel mean feedback," *IEEE Transactions on Signal Processing*, vol. 50, no. 10, pp. 2599–2613, 2002.

[19] G. Jöngren, M. Skoglund, and B. Ottersten, "Utilizing partial channel information in the design of space-time block codes," in *Proceedings of the 5th International Symposium on Wireless Personal Multimedia Communications (WPMC '02)*, October 2002.

[20] 3rd Generation Partnership Project, "Physical layer procedures," Technical Specification Group Radio Access Network TS 25.214, 3GPP, France, March 2002.

George Jöngren: Department of Signals, Sensors and Systems, Royal Institute of Technology, SE-100 44 Stockholm, Sweden

Email: gjongren@s3.kth.se

Mikael Skoglund: Department of Signals, Sensors and Systems, Royal Institute of Technology, SE-100 44 Stockholm, Sweden

Email: skoglund@s3.kth.se

Björn Ottersten: Department of Signals, Sensors and Systems, Royal Institute of Technology, SE-100 44 Stockholm, Sweden

Email: otterste@s3.kth.se

20 Ordered spatial Tomlinson-Harashima precoding

Michael Joham and Wolfgang Utschick

20.1. Introduction

Similar to receive processing (e.g., [1]), linear transmit processing (see, e.g., [2]) can be outperformed by nonlinear transmit processing. Peel et al. [3, 4] recently proposed the *minimization* of the necessary *transmit energy* for every vector symbol of a flat fading MIMO system, when assuming that the receiver applies a *modulo operation*. The necessary search for the minimum length vector of a lattice has exponential complexity (see [5] for a near-optimum variant with $O(B^4)$, where B denotes the number of scalar data streams). Additionally, the transmit signal has to be weighted with a data-dependent scalar to meet the transmit energy constraint [3, 4], if the computation of the average transmit energy (a search of exponential complexity) has to be avoided. Consequently, we do not consider this approach. Another type of nonlinear transmit processing is the *minimization* of the *bit error probability* by choosing the appropriate transmit signal [6, 7]. As the resulting nonconvex optimization can only be solved analytically for special channel matrices [7], we will not investigate this approach due to its prohibitive complexity. In [8], Fischer et al. decomposed the real-valued representation of the channel matrix into the product of a real-valued matrix and an integer-valued matrix motivated by the promising result of Yao et al. [9] who included lattice reduction techniques in the receive filter design and achieved the same diversity order as the maximum likelihood detector. The precoder of [8] which nearly reaches the diversity order of the maximum likelihood detector only equalizes the real-valued matrix of the decomposition, since the modulo operation at the receiver removes the interference caused by the integer-valued matrix. However, the channel matrix decomposition was found by Monte-Carlo search in [8], because an algorithm to obtain the decomposition is an open problem.

An alternative type of nonlinear transmit processing is *Tomlinson-Harashima precoding* (THP) which is closely related to the *decision feedback equalizer* proposed by Austin [10] (see also [11, 12, 13, 14]). Whereas DFE feeds back already *quantized* symbols, the already *transmitted* symbols are fed back in a THP system

and *modulo operations* are applied in the transmitter and the receiver(s). The principle of THP was introduced by Tomlinson [15] and Harashima et al. [16] nearly at the same time. They applied THP to a SISO system without adaptive receive filter in order to suppress the ISI caused by the frequency selectivity of the channel, since the recursive filter necessary to equalize the channel can be unstable (see also [17]). Gibbard et al. [18] proposed an asymmetric transmission, where for the first link, the receiver performs DFE and in the second link, the transmitter applies THP. This approach leads to a simplification and a lower power consumption of the device(s) at one side of the link (e.g., the mobile terminal(s)). Spatial THP without ordering for flat fading MIMO channels was proposed by Ginis et al. in [19] and Fischer et al. in [20]. Whereas Ginis et al. included a feedforward filter at the transmitter and assumed a receive filter which is a diagonal matrix, Fischer et al. investigated a system with the feedforward filter at the receiver. THP was used for a DS-CDMA system by Fischer et al. in [21] and also by Liu et al. in [22]. THP with partial channel state information at the transmitter has only been investigated by Fischer et al. [23] and Simeone et al. [24], all other publications assumed full knowledge of the channel at the transmitter. Joham et al. presented the necessary optimizations for THP with FIR feedforward and feedback filters for frequency selective MIMO channels in [25, 26]. In [27], Fischer et al. designed THP for frequency selective MIMO channels with IIR feedforward filter by applying a spectral factorization of the channel transfer function.

We restrict ourselves to systems with nondispersive channels and noncooperative receivers (e.g., mobiles in the downlink), that is, the signals of the different receivers cannot be jointly transformed. Therefore, the feedforward filter has to be located at the transmitter and the receivers only apply scalar weightings. For simplicity, we make the additional assumption that all receivers use the same scalar weight. The examined THP approaches are based on full channel state information without estimation errors (for a robust design taking into account the estimation errors, see [28]). Note that the channel can only be fully equalized by the transmitter in a system with noncooperative receivers. Thus, receive processing is only a suboptimum approach for such systems.

Contrary to most other contributions on THP, we base the THP filter design on an optimization. Since the THP optimizations are an extension of the well-known optimizations for linear transmit filters, we first review the linear *transmit zero-forcing filter* (TxZF) and the linear *transmit Wiener filter* (TxWF) in Section 20.2. With the linear representation of THP introduced in Section 20.3, we are able to formulate the optimizations for *zero-forcing THP* (ZF-THP) and *Wiener THP* (WF-THP) including not only the THP filters but also the ordering in Section 20.4. Thus, we obtain the algorithms for the optimum orderings for the two THP types and since these algorithms are too complex, we also present suboptimum ordering algorithms closely related to the *vertical Bell Laboratories Layered Space Time* (V-BLAST) algorithm well known for spatial DFE [29]. The simulation results in Section 20.5 reveal that the Wiener THP clearly outperforms the state-of-the-art zero-forcing THP approaches.

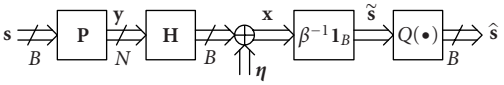

FIGURE 20.1. System with linear transmit filter.

Notation. Vectors and matrices are denoted by lower-case bold and capital bold letters, respectively. We use $\mathrm{E}[\bullet]$, "$*$," $(\bullet)^*$, $(\bullet)^{\mathrm{T}}$, and $(\bullet)^{\mathrm{H}}$ for expectation, convolution, complex conjugation, transposition, and conjugate transposition, respectively. The pseudoinverse is denoted by $(\bullet)^+$. All random variables are assumed to be zero mean and stationary. The variance of the scalar random variable y is denoted by $\sigma_y^2 = \mathrm{E}[|y|^2]$ and the covariance matrix of the vector random variable $\mathbf{x}$ by $\mathbf{R}_{\mathbf{x}} = \mathrm{E}[\mathbf{x}\mathbf{x}^{\mathrm{H}}]$. The $N \times M$ zero matrix is $\mathbf{0}_{N\times M}$, the M-dimensional zero vector is $\mathbf{0}_M$, and the $N \times N$ identity matrix is $\mathbf{1}_N$, whose nth column is $\mathbf{e}_n \in \{0,1\}^N$.

20.2. Linear transmit filters

In a system with linear transmit filter, the data signal $\mathbf{s} = [s_1, \ldots, s_B] \in \mathbb{C}^B$ comprising the symbols for the B noncooperative receivers is passed through the linear precoder $\mathbf{P} \in \mathbb{C}^{N\times B}$ to form the transmit signal of the N transmit antenna elements

$$\mathbf{y} = \mathbf{P}\mathbf{s} \in \mathbb{C}^N. \tag{20.1}$$

The transmit filter has to be designed to satisfy the transmit energy constraint, that is,

$$\mathrm{E}\left[\|\mathbf{P}\mathbf{s}\|_2^2\right] = \mathrm{tr}\left(\mathbf{P}\mathbf{R}_{\mathbf{s}}\mathbf{P}^{\mathrm{H}}\right) = E_{\mathrm{tr}}. \tag{20.2}$$

After propagation over the channel $\mathbf{H} \in \mathbb{C}^{B\times N}$ and perturbation by the noise $\eta \in \mathbb{C}^B$, the received signal $\mathbf{x} \in \mathbb{C}^B$ is weighted with the scalar β^{-1} to form the estimate (see Figure 20.1)

$$\widetilde{\mathbf{s}} = \beta^{-1}\mathbf{H}\mathbf{P}\mathbf{s} + \beta^{-1}\boldsymbol{\eta} \in \mathbb{C}^B. \tag{20.3}$$

Note that the scalar $\beta^{-1} \in \mathbb{R}_+$ at the receiver is necessary to correct the amplitude of the desired signal part in the estimate $\widetilde{\mathbf{s}}$, since the transmitter only has a limited transmit power E_{tr}. The estimate $\widetilde{\mathbf{s}}$ is the input of the nearest-neighbor quantizer $Q(\bullet)$, whose output is denoted by $\widehat{\mathbf{s}} \in \mathbb{C}^B$.

The TxZF minimizes the *mean square error* (MSE) under the transmit energy constraint (20.2) together with the constraint of full interference suppression and unbiasedness (see, e.g., [2]):

$$\{\mathbf{P}_{\mathrm{ZF}}, \beta_{\mathrm{ZF}}\} = \underset{\{\mathbf{P},\beta\}}{\mathrm{argmin}}\, \mathrm{E}\left[\|\mathbf{s} - \widetilde{\mathbf{s}}\|_2^2\right] \quad \text{s.t. } \mathrm{E}\left[\|\mathbf{P}\mathbf{s}\|_2^2\right] = E_{\mathrm{tr}},\ \widetilde{\mathbf{s}}|_{\boldsymbol{\eta}=\mathbf{0}} = \mathbf{s}. \tag{20.4}$$

The solution of the above optimization can be obtained with the method of Lagrangian multipliers (e.g., [30]) and reads as

$$\begin{aligned}\mathbf{P}_{\mathrm{ZF}} &= \beta_{\mathrm{ZF}}\mathbf{H}^{\mathrm{H}}\left(\mathbf{H}\mathbf{H}^{\mathrm{H}}\right)^{-1} \in \mathbb{C}^{N\times B},\\ \beta_{\mathrm{ZF}} &= \sqrt{\frac{E_{\mathrm{tr}}}{\mathrm{tr}\left(\left(\mathbf{H}\mathbf{H}^{\mathrm{H}}\right)^{-1}\mathbf{R}_{\mathbf{s}}\right)}} \in \mathbb{R}_{+}.\end{aligned} \tag{20.5}$$

Note that the MSE of the TxZF is simply the noise portion at the quantizer input due to the second constraint of (20.4), that is, $\mathrm{E}[\|\mathbf{s}-\widetilde{\mathbf{s}}\|_2^2] = \beta_{\mathrm{ZF}}^{-2}\,\mathrm{tr}(\mathbf{R}_{\boldsymbol{\eta}})$. Hence, we can expect that the performance of the TxZF is poor, when the channel matrix $\mathbf{H}$ is ill conditioned (see, e.g., [31]), since the weight β_{ZF} is small in this case.

To reduce this *noise enhancement* of the TxZF for ill-conditioned $\mathbf{H}$, we have to drop the second constraint in (20.4) and end up with the TxWF optimization [32, 33, 2]:

$$\left\{\mathbf{P}_{\mathrm{WF}},\beta_{\mathrm{WF}}\right\} = \underset{\{\mathbf{P},\beta\}}{\mathrm{argmin}}\,\mathrm{E}\left[\|\mathbf{s}-\widetilde{\mathbf{s}}\|_2^2\right] \quad \text{s.t. } \mathrm{E}\left[\|\mathbf{P}\mathbf{s}\|_2^2\right] = E_{\mathrm{tr}}. \tag{20.6}$$

As shown in [2], we get with Lagrangian multipliers:

$$\begin{aligned}\mathbf{P}_{\mathrm{WF}} &= \beta_{\mathrm{WF}}\left(\mathbf{H}^{\mathrm{H}}\mathbf{H}+\frac{\mathrm{tr}\left(\mathbf{R}_{\boldsymbol{\eta}}\right)}{E_{\mathrm{tr}}}\mathbf{1}_N\right)^{-1}\mathbf{H}^{\mathrm{H}} \in \mathbb{C}^{N\times B},\\ \beta_{\mathrm{WF}} &= \sqrt{\frac{E_{\mathrm{tr}}}{\mathrm{tr}\left(\left(\mathbf{H}^{\mathrm{H}}\mathbf{H}+\left(\mathrm{tr}\left(\mathbf{R}_{\boldsymbol{\eta}}\right)/E_{\mathrm{tr}}\right)\mathbf{1}_N\right)^{-1}\mathbf{H}^{\mathrm{H}}\mathbf{R}_{\mathbf{s}}\mathbf{H}\right)}} \in \mathbb{R}_{+}.\end{aligned} \tag{20.7}$$

Obviously, the TxWF leads to a smaller MSE than the TxZF, since the TxZF minimizes the MSE under an additional constraint. Moreover, the TxZF is independent of the properties of the noise, whereas the TxWF takes into account the mean noise power $\mathrm{tr}(\mathbf{R}_{\boldsymbol{\eta}})$, because it depends on the *signal-to-noise ratio* (SNR) $E_S/N_0 = E_{\mathrm{tr}}/\mathrm{tr}(\mathbf{R}_{\boldsymbol{\eta}})$, that is, the ratio of the average energy per transmitted scalar symbol over the average noise power per receive antenna. Thus, we can expect that the TxZF is outperformed by the TxWF.

20.3. System model for Tomlinson-Harashima precoding

Instead of directly applying the feedforward filter $\mathbf{P} \in \mathbb{C}^{N\times B}$ as in the case of linear transmit processing (see previous subsection), the data signal $\mathbf{s} = [s_1,\ldots,s_B]^{\mathrm{T}} \in \mathbb{M}^B$ is first transformed by the permutation matrix (see Figure 20.2):

$$\boldsymbol{\Pi}^{(\mathcal{O})} = \sum_{i=1}^{B}\mathbf{e}_i\mathbf{e}_{b_i}^{\mathrm{T}} \in \{0,1\}^{B\times B} \quad \text{with } \boldsymbol{\Pi}^{(\mathcal{O}),-1} = \boldsymbol{\Pi}^{(\mathcal{O}),\mathrm{T}}, \tag{20.8}$$

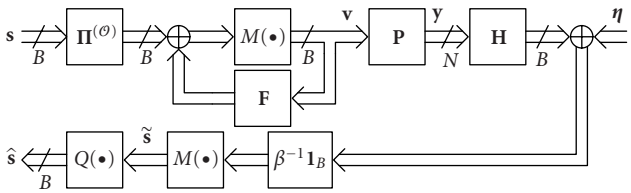

FIGURE 20.2. THP transmission over a nondispersive channel.

that is, the b_ith scalar symbol s_{b_i} is put at the ith position for $i = 1,\dots,B$. Thus, the b_1th data symbol s_{b_1} is precoded first and the b_Bth data symbol s_{b_B} last. For compactness, we collect the indices $b_1,\dots,b_B$ in the B-tupel

$$\mathcal{O} = (b_1,\dots,b_B) \quad \text{with } b_i \in \{1,\dots,B\} \setminus \{b_1,\dots,b_{i-1}\}. \tag{20.9}$$

We will also use the term *ordering* for the B-tupel $\mathcal{O}$. The transmitter can choose the ordering $\mathcal{O}$ freely, since the reordering by the permutation matrix $\mathbf{\Pi}^{(\mathcal{O})}$ cannot be recognized by the receiver. Hence, the ordering $\mathcal{O}$ represents additional degrees of freedom.

After the reordering by $\mathbf{\Pi}^{(\mathcal{O})}$, the signal is passed through the nonlinear feedback loop to get the signal $\mathbf{v} \in \mathbb{M}^B$. The modulo operator in Figure 20.2 is defined element-wise:

$$\begin{aligned} \mathrm{M}(\mathbf{x}) &= \left[\,\mathrm{M}\left(x_1\right),\dots,\mathrm{M}\left(x_B\right)\right]^{\mathrm{T}} \in \mathbb{M}^B \quad \text{with } \mathbf{x} \in \mathbb{C}^B, \\ \mathrm{M}\left(x_i\right) &= x_i - \left\lfloor \frac{\mathrm{Re}\left(x_i\right)}{\tau} + \frac{1}{2} \right\rfloor \tau - \mathrm{j} \left\lfloor \frac{\mathrm{Im}\left(x_i\right)}{\tau} + \frac{1}{2} \right\rfloor \tau, \end{aligned} \tag{20.10}$$

where $x_i \in \mathbb{C}$, $i = 1,\dots,B$, denotes the ith entry of $\mathbf{x}$ and $\lfloor \bullet \rfloor$ denotes the floor operator which gives the largest integer smaller than or equal to the argument. Note that the amplitude of the modulo operator is upper bounded, since $\mathrm{M}(x_i) \in \mathbb{M}$, where

$$\mathbb{M} = \left\{ z \in \mathbb{C} \mid -\frac{\tau}{2} \le \mathrm{Re}(z) < \frac{\tau}{2} \text{ and } -\frac{\tau}{2} \le \mathrm{Im}(z) < \frac{\tau}{2} \right\}. \tag{20.11}$$

The modulo constant $\tau \in \mathbb{R}_+$ is chosen depending on the modulation alphabet (all symbols of the modulation alphabet have to be elements of $\mathbb{M}$, see, for example, [34]). For example, we set $\tau = 2\sqrt{2}$ for QPSK modulation (see Figure 20.3) whose symbols are elements of the set $\{\exp(\mathrm{j}\boldsymbol{\mu}\pi/4) \mid \boldsymbol{\mu} \in \{-3,-1,+1,+3\}\}$.

We assume that the scalar entries $v_1,\dots,v_B \in \mathbb{M}$ of the modulo operator output $\mathbf{v} \in \mathbb{M}^B$ are uncorrelated due to the modulo operation $\mathrm{M}(\bullet)$, that is, $\mathbf{R}_{\mathbf{v}} = \mathrm{diag}(\sigma_{v_1}^2,\dots,\sigma_{v_B}^2) \in \mathbb{R}_+^{B\times B}$. Additionally, we make the popular assumption that the ith output v_i, $i = 2,\dots,B$, of the modulo operator $\mathrm{M}(\bullet)$ at the transmitter

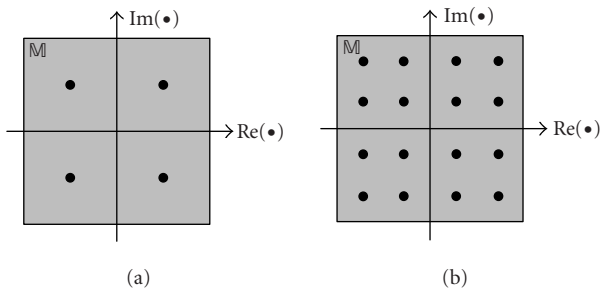

FIGURE 20.3. Modulo operator M(•): set $\mathbb{M}$ of output values, (a) QPSK: $\tau = 2\sqrt{2}$, (b) 16QAM: $\tau = 8/\sqrt{10}$.

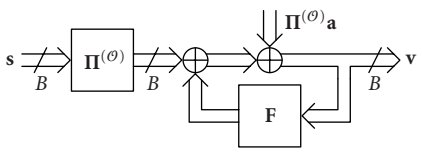

FIGURE 20.4. Linear representation of the modulo operator at the transmitter.

is uniformly distributed over $\mathbb{M}$, which results in the variance

$$\sigma_{\nu_i}^2 = \sigma_{\nu}^2 = \mathrm{E}\Big[\,|\,\nu_i\,|^2\Big] = \frac{\tau^2}{6}, \quad i = 2,\ldots,B. \tag{20.12}$$

Since the first modulo operator output ν_1 is simply s_{b_1} as we will see in the following, its variance is $\sigma_{\nu_1}^2 = \sigma_s^2$, where $\sigma_s^2 = \mathrm{E}[|s_{b_1}|^2]$.

Since M(•) is defined element-wise and we assume an ordering such that the first entry of the permuted data vector $\mathbf{\Pi}^{(\mathcal{O})}\mathbf{s}$ is precoded first and the last entry last, the feedback filter $\mathbf{F} \in \mathbb{C}^{B\times B}$ has to be *lower triangular with zero main diagonal* to ensure the realizability of the feedback loop.[1] This property of $\mathbf{F}$ is often called *spatial causality*, as only data symbols which have already been precoded are fed back.

Due to the definition of M(•) in (20.10), we can follow that the output of the modulo operator M(•) is simply the sum of the input and a term which ensures that all scalar entries of the output are elements of $\mathbb{M}$. When taking this observation into account, we end up with the linear representation of the feedback loop at the transmitter depicted in Figure 20.4. Note that the auxiliary signal $\mathbf{\Pi}^{(\mathcal{O})}\mathbf{a} \in \mathbb{C}^B$,

[1]The scalar signal ν_1 is constructed without feedback (the first row of $\mathbf{F}$ is zero) and is equal to s_{b_1}, whereas the scalar signal ν_B depends on s_{b_B} and $\nu_1,\ldots,\nu_{B-1}$ but not on itself (the last element of the last row of $\mathbf{F}$ is zero). We could also assume alternative orderings, for example, the reverse ordering, that is, s_{b_B} is precoded first and s_{b_1} last. The resulting $\mathbf{F}$ would be upper triangular with zero main diagonal instead.

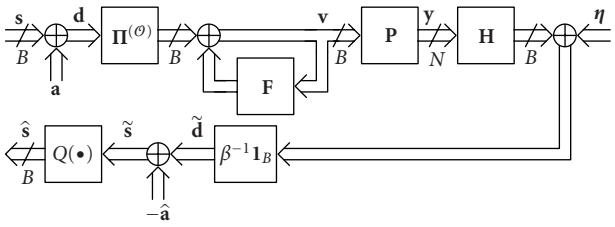

FIGURE 20.5. Linear representation of THP transmission.

whose scalar entries have real and imaginary parts which are integer multiples of the modulo constant τ, can be moved from the inside to the front of the feedback loop.[2] When replacing the modulo operators in Figure 20.2 by the summation with the appropriate auxiliary signals and moving the auxiliary signal $\boldsymbol{\Pi}^{(\mathcal{O})}\mathbf{a}$ at the transmitter to the front of the feedback loop, we obtain the linear representation in Figure 20.5. As the auxiliary signals $\mathbf{a}$ and $-\tilde{\mathbf{a}}$ which are added at the transmitter and the receiver, respectively, are included automatically by the modulo operators, we use $\mathbf{d}$ as the desired signal and $\tilde{\mathbf{d}}$ as the estimate in the following optimizations. We see in Figure 20.5 that the system whose input and output is $\mathbf{d}$ and $\widetilde{\mathbf{d}}$, respectively, is linear. Consequently, we can apply the optimizations for the linear transmit filters reviewed in the previous subsection also for the design of the THP filters, but we have to take into account the special structure of the feedback filter $\mathbf{F}$ and the statistical properties of the modulo operator output $\mathbf{v}$. We can conclude that the advantage of THP compared to the linear transmit filters is due to the advantageous statistical properties of the signal $\mathbf{v}$, whose amplitude is upper bounded, since $\mathbf{v} \in \mathbb{M}^B$.

The desired signal $\mathbf{d}$ as a function of the modulo operator output $\mathbf{v} \in \mathbb{M}^B$ can be expressed as (see Figure 20.5)

$$\mathbf{d} = \boldsymbol{\Pi}^{(\mathcal{O}),\mathrm{T}}(\mathbf{1}_B - \mathbf{F})\mathbf{v} \in \mathbb{C}^B. \tag{20.13}$$

The output $\mathbf{v}$ of the modulo operator is passed through the feedforward filter $\mathbf{P} \in \mathbb{C}^{N_a \times B}$, propagates over the channel $\mathbf{H} \in \mathbb{C}^{B \times N_a}$, is perturbed by the noise $\boldsymbol{\eta} \in \mathbb{C}^B$, and is weighted with β^{-1} at the receiver to form the estimate

$$\tilde{\mathbf{d}} = \beta^{-1}\mathbf{HPv} + \beta^{-1}\boldsymbol{\eta} \in \mathbb{C}^B. \tag{20.14}$$

Note that the scalar weight β^{-1} at the receiver is always necessary in a THP system, since the choice of the modulo constant τ is based on the assumption that the

[2] From Figure 20.4, we see that $\mathbf{v} = \boldsymbol{\Pi}^{(\mathcal{O})}\mathbf{s} + \boldsymbol{\Pi}^{(\mathcal{O})}\mathbf{a} + \mathbf{Fv}$ or equivalently, we obtain for the output signal of the modulo operator at the transmitter $\mathbf{v} = (\mathbf{1}_B - \mathbf{F})^{-1}\boldsymbol{\Pi}^{(\mathcal{O})}(\mathbf{s} + \mathbf{a})$. Consequently, $\mathbf{a}$ can be directly added to $\mathbf{s}$ in front of the feedback loop.

amplitude at the modulo operator input is correct. The transmit signal is simply $\mathbf{y} = \mathbf{P}\mathbf{v} \in \mathbb{C}^{N_a}$ and hence, the expression for the transmit energy reads as

$$\mathrm{E}\left[||\mathbf{y}||_2^2\right] = \mathrm{tr}\,(\mathbf{P}\mathbf{R}_{\mathbf{v}}\mathbf{P}^{\mathrm{H}}). \tag{20.15}$$

20.4. Spatial Tomlinson-Harashima precoding

20.4.1. Zero-forcing spatial Tomlinson-Harashima precoding

The zero-forcing variant of *spatial THP* (S-THP) for nondispersive channels can be found by applying an optimization which is based on the optimization for linear zero-forcing transmit processing (cf. (20.4)). First, we have to replace the desired signal $\mathbf{s}$ by $\mathbf{d}$ and the estimate $\hat{\mathbf{s}}$ by $\tilde{\mathbf{d}}$. Second, we have to include the ordering $\mathcal{O}$ and a constraint that the feedback filter $\mathbf{F} \in \mathbb{C}^{B\times B}$ is spatially causal:

$$\begin{aligned}\left\{\mathbf{P}_{\mathrm{ZF}}^{\mathrm{THP}}, \mathbf{F}_{\mathrm{ZF}}^{\mathrm{THP}}, \beta_{\mathrm{ZF}}^{\mathrm{THP}}, \mathcal{O}_{\mathrm{ZF}}^{\mathrm{THP}}\right\} &= \underset{\{\mathbf{P},\mathbf{F},\beta,\mathcal{O}\}}{\operatorname{argmin}} \mathrm{E}\left[||\mathbf{d}-\tilde{\mathbf{d}}||_2^2\right] \\ \text{s.t. : } \tilde{\mathbf{d}}|_{\boldsymbol{\eta}=\mathbf{0}_B} &= \mathbf{d}, \quad \mathrm{E}\left[||\mathbf{y}||_2^2\right] = E_{\mathrm{tr}}, \\ \mathbf{F} &: \text{lower triangular, zero main diagonal.}\end{aligned} \tag{20.16}$$

When plugging (20.13), (20.14), and (20.15) into the above optimization, we get

$$\begin{aligned}\left\{\mathbf{P}_{\mathrm{ZF}}^{\mathrm{THP}}, \mathbf{F}_{\mathrm{ZF}}^{\mathrm{THP}}, \beta_{\mathrm{ZF}}^{\mathrm{THP}}, \mathcal{O}_{\mathrm{ZF}}^{\mathrm{THP}}\right\} &= \underset{\{\mathbf{P},\mathbf{F},\beta,\mathcal{O}\}}{\operatorname{argmin}} \beta^{-2}\,\mathrm{tr}\,(\mathbf{R}_{\boldsymbol{\eta}}) \\ \text{s.t. } \beta^{-1}\mathbf{H}\mathbf{P} &= \boldsymbol{\Pi}^{(\mathcal{O}),\mathrm{T}}(\mathbf{1}_B - \mathbf{F}), \quad \mathrm{tr}\,(\mathbf{P}\mathbf{R}_{\mathbf{v}}\mathbf{P}^{\mathrm{H}}) = E_{\mathrm{tr}}, \\ \mathbf{S}_i\mathbf{F}\mathbf{e}_i &= \mathbf{0}_i,\ i = 1,\ldots,B,\end{aligned} \tag{20.17}$$

where we split up the constraint on the spatial causality of $\mathbf{F}$ into B constraints for the columns of $\mathbf{F}$. Here, $\mathbf{e}_i \in \{0,1\}^B$ and we introduced the selection matrix

$$\mathbf{S}_i = \mathbf{S}_{(0,i,B-i)} = \left[\mathbf{1}_i, \mathbf{0}_{i\times B-i}\right] \in \{0,1\}^{i\times B} \tag{20.18}$$

which cuts out the first i elements of a B-dimensional vector.

Obviously, the optimization in (20.17) is not convex due to the first constraint. However, we obtain necessary conditions for the optimum *zero-forcing S-THP* (ZF-S-THP) filters, when setting the derivatives of the Lagrangian function

$$\begin{aligned}&L(\mathbf{P},\mathbf{F},\beta,\mathcal{O},\boldsymbol{\Lambda},\rho,\boldsymbol{\mu}_1,\boldsymbol{\mu}_2,\ldots,\boldsymbol{\mu}_B) \\ &\quad= \beta^{-2}\,\mathrm{tr}\,(\mathbf{R}_{\boldsymbol{\eta}}) - \rho(\,\mathrm{tr}\,(\mathbf{P}\mathbf{R}_{\mathbf{v}}\mathbf{P}^{\mathrm{H}}) - E_{\mathrm{tr}}) \\ &\qquad- 2\,\mathrm{Re}\,(\,\mathrm{tr}\,(\boldsymbol{\Lambda}(\beta^{-1}\mathbf{H}\mathbf{P} - \boldsymbol{\Pi}^{(\mathcal{O}),\mathrm{T}}(\mathbf{1}_B - \mathbf{F})))) - \sum_{i=1}^{B} 2\,\mathrm{Re}\,(\boldsymbol{\mu}_i^{\mathrm{T}}\mathbf{S}_i\mathbf{F}\mathbf{e}_i),\end{aligned} \tag{20.19}$$

with the Lagrangian multipliers $\boldsymbol{\Lambda} \in \mathbb{C}^{B\times B}$, $\rho \in \mathbb{R}$, and $\boldsymbol{\mu}_i \in \mathbb{C}^i$, $i = 1,\ldots,B$, to zero:

$$\begin{aligned}
\frac{\partial L(\mathbf{P},\mathbf{F},\beta,\boldsymbol{\Lambda},\rho,\boldsymbol{\mu}_1,\boldsymbol{\mu}_2,\ldots,\boldsymbol{\mu}_B)}{\partial \mathbf{P}} &= -\beta^{-1}\mathbf{H}^{\mathrm{T}}\boldsymbol{\Lambda}^{\mathrm{T}} - \rho\mathbf{P}^{*}\mathbf{R}_{\mathbf{v}}^{\mathrm{T}} = \mathbf{0}_{N_{\mathrm{a}}\times B},\\
\frac{\partial L(\mathbf{P},\mathbf{F},\beta,\boldsymbol{\Lambda},\rho,\boldsymbol{\mu}_1,\boldsymbol{\mu}_2,\ldots,\boldsymbol{\mu}_B)}{\partial \mathbf{F}} &= -\boldsymbol{\Pi}^{(\mathcal{O})}\boldsymbol{\Lambda}^{\mathrm{T}} - \sum_{i=1}^{B}\mathbf{S}_i^{\mathrm{T}}\boldsymbol{\mu}_i\mathbf{e}_i^{\mathrm{T}} = \mathbf{0}_{B\times B},\\
\frac{\partial L(\mathbf{P},\mathbf{F},\beta,\boldsymbol{\Lambda},\rho,\boldsymbol{\mu}_1,\boldsymbol{\mu}_2,\ldots,\boldsymbol{\mu}_B)}{\partial \beta} &= -2\beta^{-3}\,\mathrm{tr}\,(\mathbf{R}_{\boldsymbol{\eta}}) + \beta^{-2}\,\mathrm{Re}\,(\,\mathrm{tr}(\boldsymbol{\Lambda}\mathbf{H}\mathbf{P})).
\end{aligned} \tag{20.20}$$

From the derivative with respect to the feedback filter $\mathbf{F}$, it follows that

$$\boldsymbol{\Lambda}^{\mathrm{H}} = -\boldsymbol{\Pi}^{(\mathcal{O}),\mathrm{T}}\sum_{i=1}^{B}\mathbf{S}_i^{\mathrm{T}}\boldsymbol{\mu}_i^{*}\mathbf{e}_i^{\mathrm{T}}. \tag{20.21}$$

Plugging this result into the derivative of the Lagrangian function with respect to the feedforward filter $\mathbf{P}$ yields

$$\rho\sigma_{v_i}^2\mathbf{P}\mathbf{e}_i = \beta^{-1}\mathbf{H}^{\mathrm{H}}\boldsymbol{\Pi}^{(\mathcal{O}),\mathrm{T}}\mathbf{S}_i^{\mathrm{T}}\boldsymbol{\mu}_i^{*}, \tag{20.22}$$

where we multiplied by $\mathbf{e}_i \in \{0,1\}^B$ and used the assumption that the output $\mathbf{v}$ of the modulo operation at the transmitter is uncorrelated. Due to the first constraint of (20.17), the ith column of the feedback filter can be written as

$$\mathbf{F}\mathbf{e}_i = \mathbf{e}_i - \rho^{-1}\sigma_{v_i}^{-2}\beta^{-2}\boldsymbol{\Pi}^{(\mathcal{O})}\mathbf{H}\mathbf{H}^{\mathrm{H}}\boldsymbol{\Pi}^{(\mathcal{O}),\mathrm{T}}\mathbf{S}_i^{\mathrm{T}}\boldsymbol{\mu}_i^{*}. \tag{20.23}$$

Consequently, by employing the last constraint of (20.17), we obtain for the Lagrangian multiplier

$$\boldsymbol{\mu}_i^{*} = \rho\sigma_{v_i}^2\beta^2\left(\mathbf{S}_i\boldsymbol{\Pi}^{(\mathcal{O})}\mathbf{H}\mathbf{H}^{\mathrm{H}}\boldsymbol{\Pi}^{(\mathcal{O}),\mathrm{T}}\mathbf{S}_i^{\mathrm{T}}\right)^{-1}\mathbf{S}_i\mathbf{e}_i, \tag{20.24}$$

which leads to following expression for the ith column of the feedforward filter $\mathbf{P}$:

$$\mathbf{P}\mathbf{e}_i = \beta\mathbf{H}^{\mathrm{H}}\boldsymbol{\Pi}^{(\mathcal{O}),\mathrm{T}}\mathbf{S}_i^{\mathrm{T}}\left(\mathbf{S}_i\boldsymbol{\Pi}^{(\mathcal{O})}\mathbf{H}\mathbf{H}^{\mathrm{H}}\boldsymbol{\Pi}^{(\mathcal{O}),\mathrm{T}}\mathbf{S}_i^{\mathrm{T}}\right)^{-1}\mathbf{S}_i\mathbf{e}_i. \tag{20.25}$$

Note that the columns of $\mathbf{P}$ are orthogonal, that is,

$$\mathbf{e}_j^{\mathrm{T}}\mathbf{P}^{\mathrm{H}}\mathbf{P}\mathbf{e}_i = 0, \tag{20.26}$$

for $j \neq i$, since the selection matrix $\mathbf{S}_i = [\mathbf{1}_i, \mathbf{0}_{i\times B-i}] \in \{0,1\}^{i\times B}$ has the following properties:

$$\mathbf{S}_j = \mathbf{S}_j\mathbf{S}_i^{\mathrm{T}}\mathbf{S}_i, \quad \mathbf{S}_j\mathbf{e}_i = \mathbf{0}_j, \quad \text{for } j < i. \tag{20.27}$$

Since the modulo output $\mathbf{v}$ is uncorrelated, we can rewrite the transmit energy constraint:

$$\operatorname{tr}\left(\mathbf{P}\mathbf{R}_{\mathbf{v}}\mathbf{P}^{\mathrm{H}}\right) = \beta^2 \sum_{i=1}^{B} \sigma_{v_i}^2 \mathbf{e}_i^{\mathrm{T}} \mathbf{S}_i^{\mathrm{T}} \left(\mathbf{S}_i \boldsymbol{\Pi}^{(\mathcal{O})} \mathbf{H}\mathbf{H}^{\mathrm{H}} \boldsymbol{\Pi}^{(\mathcal{O}),\mathrm{T}} \mathbf{S}_i^{\mathrm{T}}\right)^{-1} \mathbf{S}_i \mathbf{e}_i = E_{\mathrm{tr}}, \tag{20.28}$$

which leads to the ZF-S-THP solution depending on the ordering $\mathcal{O}$:

$$\begin{aligned}
\mathbf{P}_{\mathrm{ZF}}^{\mathrm{THP}} &= \beta_{\mathrm{ZF}}^{\mathrm{THP}} \sum_{i=1}^{B} \mathbf{H}^{\mathrm{H}} \boldsymbol{\Pi}^{(\mathcal{O}),\mathrm{T}} \mathbf{S}_i^{\mathrm{T}} \left(\mathbf{S}_i \boldsymbol{\Pi}^{(\mathcal{O})} \mathbf{H}\mathbf{H}^{\mathrm{H}} \boldsymbol{\Pi}^{(\mathcal{O}),\mathrm{T}} \mathbf{S}_i^{\mathrm{T}}\right)^{-1} \mathbf{S}_i \mathbf{e}_i \mathbf{e}_i^{\mathrm{T}}, \\
\mathbf{F}_{\mathrm{ZF}}^{\mathrm{THP}} &= \mathbf{1}_B - \beta_{\mathrm{ZF}}^{\mathrm{THP},-1} \boldsymbol{\Pi}^{(\mathcal{O})} \mathbf{H} \mathbf{P}_{\mathrm{ZF}}^{\mathrm{THP}} \in \mathbb{C}^{B \times B}, \\
\beta_{\mathrm{ZF}}^{\mathrm{THP}} &= \sqrt{\frac{E_{\mathrm{tr}}}{\sum_{i=1}^{B} \sigma_{v_i}^2 \mathbf{e}_i^{\mathrm{T}} \mathbf{S}_i^{\mathrm{T}} \left(\mathbf{S}_i \boldsymbol{\Pi}^{(\mathcal{O})} \mathbf{H}\mathbf{H}^{\mathrm{H}} \boldsymbol{\Pi}^{(\mathcal{O}),\mathrm{T}} \mathbf{S}_i^{\mathrm{T}}\right)^{-1} \mathbf{S}_i \mathbf{e}_i}} \in \mathbb{R}_+.
\end{aligned} \tag{20.29}$$

We observe that the ith column of the ZF-S-THP feedforward filter $\mathbf{P}_{\mathrm{ZF}}^{\mathrm{THP}}$ only depends on the first i rows of the sorted channel matrix $\boldsymbol{\Pi}^{(\mathcal{O})}\mathbf{H}$. Thus, the first column of $\mathbf{P}_{\mathrm{ZF}}^{\mathrm{THP}}$ is simply the weighted *transmit matched filter* (TxMF, see, e.g., [2]) for the first scalar data stream s_{b_1} and the last column is the weighted b_Bth column of the linear TxZF $\mathbf{P}_{\mathrm{ZF}}$. We can conclude that the first scalar data stream s_{b_1} is transmitted without taking into account the interference which is introduced in the other scalar estimates, since this interference is removed by the feedback filter $\mathbf{F}_{\mathrm{ZF}}^{\mathrm{THP}}$ and the modulo operations. The second column of the feedforward filter $\mathbf{P}_{\mathrm{ZF}}^{\mathrm{THP}}$ is orthogonal to the b_1th row of the channel $\mathbf{H}$, that is, the second precoded signal v_2 is not interfering with the estimate $\widetilde{s}_{b_1}$ of the first scalar data stream, but as the second column of $\mathbf{P}_{\mathrm{ZF}}^{\mathrm{THP}}$ only depends on the first two rows of the sorted channel matrix $\boldsymbol{\Pi}^{(\mathcal{O})}\mathbf{H}$, the signal v_2 contributes interference to the other estimates, namely, the estimates for $s_{b_3}, \ldots, s_{b_B}$. This interference has to be removed by the feedback filter $\mathbf{F}_{\mathrm{ZF}}^{\mathrm{THP}}$ and the modulo operations. The signals $v_1, \ldots, v_{B-1}$ cause interference in the estimate for the last data stream s_{b_B}. Thus, the feedback filter $\mathbf{F}_{\mathrm{ZF}}^{\mathrm{THP}}$ has to suppress this interference and the resulting output of the modulo operation v_B does not interfere with the estimates of the other data streams, since the last column of $\mathbf{P}_{\mathrm{ZF}}^{\mathrm{THP}}$ is orthogonal to the first $B-1$ rows of the sorted channel matrix $\boldsymbol{\Pi}^{(\mathcal{O})}\mathbf{H}$.

Note that we can employ the *Cholesky factorization* (e.g., [31, 35]) of the channel Gram with *symmetric permutation*,[3]

$$\boldsymbol{\Pi}^{(\mathcal{O})} \mathbf{H}\mathbf{H}^{\mathrm{H}} \boldsymbol{\Pi}^{(\mathcal{O}),\mathrm{T}} = \mathbf{L}\mathbf{L}^{\mathrm{H}}, \tag{20.30}$$

[3] Alternatively, we can use the QR factorization (e.g., [31, 35]) of the Hermitian $\mathbf{H}^{\mathrm{H}} \boldsymbol{\Pi}^{(\mathcal{O}),\mathrm{T}} = \mathbf{Q}\mathbf{R}$ of the sorted channel matrix. Then, $\mathbf{L} = \mathbf{R}^{\mathrm{H}}$.

with the lower triangular matrix $\mathbf{L} \in \mathbb{C}^{B\times B}$, to find following alternative expressions for the ZF-S-THP filters:

$$\begin{aligned}\mathbf{P}_{\mathrm{ZF}}^{\mathrm{THP}} &= \beta_{\mathrm{ZF}}^{\mathrm{THP}}\mathbf{H}^{\mathrm{H}}\boldsymbol{\Pi}^{(\mathcal{O}),\mathrm{T}}\mathbf{L}^{\mathrm{H},-1}\,\mathrm{diag}\,(l_{1,1}^{-1},\ldots,l_{B,B}^{-1}),\\ \mathbf{F}_{\mathrm{ZF}}^{\mathrm{THP}} &= \mathbf{1}_B - \mathbf{L}\,\mathrm{diag}\,(l_{1,1}^{-1},\ldots,l_{B,B}^{-1}),\end{aligned} \tag{20.31}$$

and

$$\beta_{\mathrm{ZF}}^{\mathrm{THP}} = \sqrt{\frac{E_{\mathrm{tr}}}{\mathrm{tr}\,(\,\mathrm{diag}\,(l_{1,1}^{-2},\ldots,l_{B,B}^{-2})\mathbf{R}_{\mathbf{v}})}}, \tag{20.32}$$

where $l_{i,i} \in \mathbb{R}_+$ denotes the ith diagonal element of $\mathbf{L}$. Remember that we have obtained this result by solving the optimization in (20.17) and afterwards rewriting the solution with the Cholesky decomposition of the symmetrically permuted channel Gram or the QR factorization of the Hermitian of the sorted channel matrix. Contrarily, *no optimization* was performed and the expressions for the S-THP filters were found intuitively by using the *unsorted* QR factorization in [19, 21], where the weighting at the receiver was assumed to be the diagonal matrix $\mathrm{diag}(l_{1,1}^{-1},\ldots,l_{B,B}^{-1})$ instead of $\beta^{-1}\mathbf{1}_B$, although this choice for the diagonal weighting is suboptimum (see [25]).

When using the projector

$$\boldsymbol{\Pi}_i^{(\mathcal{O})} = \boldsymbol{\Pi}^{(\mathcal{O}),\mathrm{T}}\mathbf{S}_i^{\mathrm{T}}\mathbf{S}_i\boldsymbol{\Pi}^{(\mathcal{O})} = \mathbf{1}_B - \sum_{j=i+1}^{B}\mathbf{e}_{b_j}\mathbf{e}_{b_j}^{\mathrm{T}} \in \{0,1\}^{B\times B}, \tag{20.33}$$

we can rewrite the ZF-S-THP solution in (20.29):

$$\begin{aligned}\mathbf{P}_{\mathrm{ZF}}^{\mathrm{THP}} &= \beta_{\mathrm{ZF}}^{\mathrm{THP}}\sum_{i=1}^{B}\mathbf{H}^{\mathrm{H}}\boldsymbol{\Pi}_i^{(\mathcal{O})}\left(\boldsymbol{\Pi}_i^{(\mathcal{O})}\mathbf{H}\mathbf{H}^{\mathrm{H}}\boldsymbol{\Pi}_i^{(\mathcal{O})}\right)^{+}\mathbf{e}_{b_i}\mathbf{e}_i^{\mathrm{T}} \in \mathbb{C}^{N_{\mathrm{a}}\times B},\\ \mathbf{F}_{\mathrm{ZF}}^{\mathrm{THP}} &= \mathbf{1}_B - \beta_{\mathrm{ZF}}^{\mathrm{THP},-1}\boldsymbol{\Pi}^{(\mathcal{O})}\mathbf{H}\mathbf{P}_{\mathrm{ZF}}^{\mathrm{THP}},\\ \beta_{\mathrm{ZF}}^{\mathrm{THP}} &= \sqrt{\frac{E_{\mathrm{tr}}}{\sum_{i=1}^{B}\sigma_{v_i}^2\mathbf{e}_{b_i}^{\mathrm{T}}\left(\boldsymbol{\Pi}_i^{(\mathcal{O})}\mathbf{H}\mathbf{H}^{\mathrm{H}}\boldsymbol{\Pi}_i^{(\mathcal{O})}\right)^{+}\mathbf{e}_{b_i}}} \in \mathbb{R}_+.\end{aligned} \tag{20.34}$$

The result for the scalar weight $\beta_{\mathrm{ZF}}^{\mathrm{THP}}$ depending on the ordering $\mathcal{O}$ enables us to further minimize the MSE by the appropriate ordering:

$$\mathcal{O}'_{\mathrm{ZF}} = \underset{\mathcal{O}}{\mathrm{argmin}}\,\frac{\mathrm{tr}\,(\mathbf{R}_{\boldsymbol{\eta}})}{E_{\mathrm{tr}}}\sum_{i=1}^{B}\sigma_{v_i}^2\mathbf{e}_{b_i}^{\mathrm{T}}\left(\boldsymbol{\Pi}_i^{(\mathcal{O})}\mathbf{H}\mathbf{H}^{\mathrm{H}}\boldsymbol{\Pi}_i^{(\mathcal{O})}\right)^{+}\mathbf{e}_{b_i}. \tag{20.35}$$

Thus, the optimal ordering $\mathcal{O}'_{\mathrm{ZF}}$ can only be found by computing the MSEs for all $B!$ possible orderings and choosing the ordering with the minimum MSE. Since the above optimization is very complex, we suggest to use the following suboptimum

approach. Instead of minimizing the sum of MSEs for the B scalar data streams, the ordering is found by successively minimizing each MSE summand under the assumption that the ordering of the *succeeding* MSE summands is fixed:

$$\mathcal{O}_{\mathrm{ZF}} = (b_{\mathrm{ZF},1}, \ldots, b_{\mathrm{ZF},B}) \tag{20.36}$$

with

$$b_{\mathrm{ZF},i} = \underset{b \in \{1,\ldots,B\} \setminus \{b_{\mathrm{ZF},i+1},\ldots,b_{\mathrm{ZF},B}\}}{\operatorname{argmin}} \mathbf{e}_b^{\mathrm{T}} \left(\boldsymbol{\Pi}_i^{(\mathcal{O}_{\mathrm{ZF}})} \mathbf{H}\mathbf{H}^{\mathrm{H}} \boldsymbol{\Pi}_i^{(\mathcal{O}_{\mathrm{ZF}})} \right)^{+} \mathbf{e}_b, \tag{20.37}$$

where $i = B, \ldots, 1$. Note that $\boldsymbol{\Pi}_i^{(\mathcal{O}_{\mathrm{ZF}})}$ only depends on the already computed $b_{\mathrm{ZF},i+1}$, $\ldots, b_{\mathrm{ZF},B}$ and hence, the pseudoinverse of $\boldsymbol{\Pi}_i^{(\mathcal{O}_{\mathrm{ZF}})} \mathbf{H}\mathbf{H}^{\mathrm{H}} \boldsymbol{\Pi}_i^{(\mathcal{O}_{\mathrm{ZF}})}$ is independent of b. Therefore, the complexity is $\mathrm{O}(B^4)$, whereas the optimum ordering of (20.35) has $\mathrm{O}(B!B^3)$. The above suboptimum procedure for ZF-S-THP is similar to the ordering optimization known as V-BLAST for spatial DFE, but the sorting is computed starting with the index for the data stream precoded *last*, whereas V-BLAST starts with the index of the data stream detected *first*.

20.4.2. Wiener spatial Tomlinson-Harashima precoding

The *Wiener S-THP* (WF-S-THP) filters for nondispersive channels results from the minimization of the mean square error together with the transmit energy constraint and the restriction of a spatially causal feedback filter:

$$\begin{aligned} &\left\{ \mathbf{P}_{\mathrm{WF}}^{\mathrm{THP}}, \mathbf{F}_{\mathrm{WF}}^{\mathrm{THP}}, \beta_{\mathrm{WF}}^{\mathrm{THP}}, \mathcal{O}_{\mathrm{WF}}^{\mathrm{THP}} \right\} = \underset{\{\mathbf{P},\mathbf{F},\beta,\mathcal{O}\}}{\operatorname{argmin}} \mathrm{E}\left[||\mathbf{d} - \tilde{\mathbf{d}}||_2^2 \right] \\ &\text{s.t. } \mathrm{E}\left[||\mathbf{y}||_2^2 \right] = E_{\mathrm{tr}}, \quad \mathbf{F} : \text{lower triangular, zero main diagonal.} \end{aligned} \tag{20.38}$$

With (20.13), (20.14), and (20.15), the above optimization can be written as

$$\begin{aligned} &\left\{ \mathbf{P}_{\mathrm{WF}}^{\mathrm{THP}}, \mathbf{F}_{\mathrm{WF}}^{\mathrm{THP}}, \beta_{\mathrm{WF}}^{\mathrm{THP}}, \mathcal{O}_{\mathrm{WF}}^{\mathrm{THP}} \right\} = \underset{\{\mathbf{P},\mathbf{F},\beta,\mathcal{O}\}}{\operatorname{argmin}} \sigma_{\boldsymbol{\varepsilon}}^2(\mathbf{P}, \mathbf{F}, \beta, \mathcal{O}) \\ &\text{s.t. } \mathrm{tr}\left(\mathbf{P}\mathbf{R}_{\mathbf{v}}\mathbf{P}^{\mathrm{H}}\right) = E_{\mathrm{tr}}, \qquad \mathbf{S}_i \mathbf{F} \mathbf{e}_i = \mathbf{0}_i, \ i = 1, \ldots, B, \end{aligned} \tag{20.39}$$

where the MSE $\sigma_{\boldsymbol{\varepsilon}}^2(\mathbf{P}, \mathbf{F}, \beta, \mathcal{O}) = \mathrm{E}[\|\mathbf{d} - \tilde{\mathbf{d}}\|_2^2]$ is defined as

$$\begin{aligned} &\sigma_{\boldsymbol{\varepsilon}}^2(\mathbf{P}, \mathbf{F}, \beta, \mathcal{O}) \\ &\quad = -2\beta^{-1} \mathrm{tr}\left(\mathrm{Re}\left(\boldsymbol{\Pi}^{(\mathcal{O}),\mathrm{T}} (\mathbf{1}_B - \mathbf{F}) \mathbf{R}_{\mathbf{v}} \mathbf{P}^{\mathrm{H}} \mathbf{H}^{\mathrm{H}} \right) \right) \\ &\qquad + \mathrm{tr}\left((\mathbf{1}_B - \mathbf{F}) \mathbf{R}_{\mathbf{v}} (\mathbf{1}_B - \mathbf{F}^{\mathrm{H}}) \right) + \beta^{-2} \mathrm{tr}\left(\mathbf{H}\mathbf{P}\mathbf{R}_{\mathbf{v}}\mathbf{P}^{\mathrm{H}}\mathbf{H}^{\mathrm{H}} + \mathbf{R}_{\boldsymbol{\eta}} \right). \end{aligned} \tag{20.40}$$

The selection matrix $\mathbf{S}_i = [\mathbf{1}_i, \mathbf{0}_{i \times B - i}] \in \{0,1\}^{i \times B}$ cuts out the first i elements of a B-dimensional column vector and $\mathbf{e}_i \in \{0,1\}^B$. Employing the Lagrangian

multipliers $\rho \in \mathbb{R}$ and $\boldsymbol{\mu}_i \in \mathbb{C}^i$ with $i = 1, \ldots, B$, we form the Lagrangian function

$$\begin{aligned} &L(\mathbf{P}, \mathbf{F}, \beta, \mathcal{O}, \rho, \boldsymbol{\mu}_1, \boldsymbol{\mu}_2, \ldots, \boldsymbol{\mu}_B) \\ &\quad = \sigma_{\boldsymbol{\varepsilon}}^2(\mathbf{P}, \mathbf{F}, \beta, \mathcal{O}) - \rho\big(\operatorname{tr}\left(\mathbf{P}\mathbf{R}_{\mathbf{v}}\mathbf{P}^{\mathrm{H}}\right) - E_{\mathrm{tr}}\big) - \sum_{i=1}^{B} 2\operatorname{Re}\left(\boldsymbol{\mu}_i^{\mathrm{T}}\mathbf{S}_i\mathbf{F}\mathbf{e}_i\right), \end{aligned} \tag{20.41}$$

whose derivatives with respect to the feedforward filter $\mathbf{P}$, the feedback filter $\mathbf{F}$, and the scalar weight β must vanish:

$$\begin{aligned} \frac{\partial L(\cdots)}{\partial \mathbf{P}} &= \beta^{-2}\mathbf{H}^{\mathrm{T}}\mathbf{H}^{*}\mathbf{P}^{*}\mathbf{R}_{\mathbf{v}}^{\mathrm{T}} - \beta^{-1}\mathbf{H}^{\mathrm{T}}\boldsymbol{\Pi}^{(\mathcal{O}),\mathrm{T}}(\mathbf{1}_B - \mathbf{F}^{*})\mathbf{R}_{\mathbf{v}}^{\mathrm{T}} \\ &\quad - \rho\mathbf{P}^{*}\mathbf{R}_{\mathbf{v}}^{\mathrm{T}} = \mathbf{0}_{N\times B}, \\ \frac{\partial L(\cdots)}{\partial \mathbf{F}} &= -(\mathbf{1}_B - \mathbf{F}^{*})\mathbf{R}_{\mathbf{v}}^{\mathrm{T}} + \beta^{-1}\boldsymbol{\Pi}^{(\mathcal{O})}\mathbf{H}^{*}\mathbf{P}^{*}\mathbf{R}_{\mathbf{v}}^{\mathrm{T}} - \sum_{i=1}^{B}\mathbf{S}_i^{\mathrm{T}}\boldsymbol{\mu}_i\mathbf{e}_i^{\mathrm{T}} = \mathbf{0}_{B\times B}, \\ \frac{\partial L(\cdots)}{\partial \beta} &= 2\beta^{-2}\operatorname{tr}\left(\operatorname{Re}\left(\boldsymbol{\Pi}^{(\mathcal{O}),\mathrm{T}}(\mathbf{1}_B - \mathbf{F})\mathbf{R}_{\mathbf{v}}\mathbf{P}^{\mathrm{H}}\mathbf{H}^{\mathrm{H}}\right)\right) \\ &\quad - 2\beta^{-3}\operatorname{tr}\left(\mathbf{H}\mathbf{P}\mathbf{R}_{\mathbf{v}}\mathbf{P}^{\mathrm{H}}\mathbf{H}^{\mathrm{H}} + \mathbf{R}_{\boldsymbol{\eta}}\right) = 0. \end{aligned} \tag{20.42}$$

When taking the complex conjugate of the derivative with respect to $\mathbf{P}$, multiplying with $\mathbf{P}^{\mathrm{H}}$ from the right, and applying the trace operator, we find following equality:

$$\begin{aligned} &-\beta^{-1}\operatorname{tr}\left(\mathbf{H}^{\mathrm{H}}\boldsymbol{\Pi}^{(\mathcal{O}),\mathrm{T}}(\mathbf{1}_B - \mathbf{F})\mathbf{R}_{\mathbf{v}}\mathbf{P}^{\mathrm{H}}\right) \\ &\qquad + \beta^{-2}\operatorname{tr}\left(\mathbf{H}^{\mathrm{H}}\mathbf{H}\mathbf{P}\mathbf{R}_{\mathbf{v}}\mathbf{P}^{\mathrm{H}}\right) - \rho\operatorname{tr}\left(\mathbf{P}\mathbf{R}_{\mathbf{v}}\mathbf{P}^{\mathrm{H}}\right) = 0. \end{aligned} \tag{20.43}$$

We can conclude that $\operatorname{tr}(\mathbf{H}^{\mathrm{H}}\boldsymbol{\Pi}^{(\mathcal{O}),\mathrm{T}}(\mathbf{1}_B - \mathbf{F})\mathbf{R}_{\mathbf{v}}\mathbf{P}^{\mathrm{H}}) \in \mathbb{R}$, since all other terms are real valued. Therefore, we can plug the above result into the derivative of the Lagrangian function with respect to the scalar weight β to obtain

$$\rho = -\beta^{-2}\frac{\operatorname{tr}\left(\mathbf{R}_{\boldsymbol{\eta}}\right)}{E_{\mathrm{tr}}}, \tag{20.44}$$

where we used the transmit energy constraint, that is, $\operatorname{tr}(\mathbf{P}\mathbf{R}_{\mathbf{v}}\mathbf{P}^{\mathrm{H}}) = E_{\mathrm{tr}}$. In the following, we use the abbreviation

$$\xi_{\mathrm{WF}} = \frac{\operatorname{tr}\left(\mathbf{R}_{\boldsymbol{\eta}}\right)}{E_{\mathrm{tr}}}. \tag{20.45}$$

Due to the derivative with respect to $\mathbf{P}$ and the above expression for the Lagrangian

multiplier ρ, the feedforward filter can be written as

$$\mathbf{P} = \beta \mathbf{H}^{\mathrm{H}} \left(\mathbf{H}\mathbf{H}^{\mathrm{H}} + \xi_{\mathrm{WF}} \mathbf{1}_B \right)^{-1} \mathbf{\Pi}^{(\mathcal{O}),\mathrm{T}} \left(\mathbf{1}_B - \mathbf{F} \right), \tag{20.46}$$

where we also applied the matrix inversion lemma. Plugging this result into the derivative of the Lagrangian function with respect to the feedback filter $\mathbf{F}$ yields

$$\mathbf{F} = \mathbf{1}_B + \xi_{\mathrm{WF}}^{-1} \left(\mathbf{\Pi}^{(\mathcal{O})} \mathbf{H}\mathbf{H}^{\mathrm{H}} \mathbf{\Pi}^{(\mathcal{O}),\mathrm{T}} + \xi_{\mathrm{WF}} \mathbf{1}_B \right) \sum_{i=1}^{B} \sigma_{v_i}^{-2} \mathbf{S}_i^{\mathrm{T}} \boldsymbol{\mu}_i^* \mathbf{e}_i^{\mathrm{T}}, \tag{20.47}$$

which can be used to find the Lagrangian multipliers $\boldsymbol{\mu}_i$, $i = 1, \ldots, B$, with the second constraint of (20.39):

$$\boldsymbol{\mu}_i^* = -\xi_{\mathrm{WF}} \sigma_{v_i}^2 \left(\mathbf{S}_i \mathbf{\Pi}^{(\mathcal{O})} \mathbf{H}\mathbf{H}^{\mathrm{H}} \mathbf{\Pi}^{(\mathcal{O}),\mathrm{T}} \mathbf{S}_i^{\mathrm{T}} + \xi_{\mathrm{WF}} \mathbf{S}_i \mathbf{S}_i^{\mathrm{T}} \right)^{-1} \mathbf{S}_i \mathbf{e}_i, \tag{20.48}$$

with $i = 1, \ldots, B$. For the last two expressions, we employed the assumption that the modulo operator outputs at the transmitter are uncorrelated, that is, $\mathbf{R}_{\mathbf{v}} = \mathrm{diag}(\sigma_{v_1}^2, \ldots, \sigma_{v_B}^2)$. When we replace the identity matrix $\mathbf{1}_B$ in the expression for the feedback filter $\mathbf{F}$ by

$$\begin{aligned} \mathbf{1}_B &= \sum_{i=1}^{B} \mathbf{e}_i \mathbf{e}_i^{\mathrm{T}} = \sum_{i=1}^{B} \mathbf{S}_i^{\mathrm{T}} \mathbf{S}_i \mathbf{e}_i \mathbf{e}_i^{\mathrm{T}} \\ &= \sum_{i=1}^{B} -\xi_{\mathrm{WF}}^{-1} \sigma_{v_i}^{-2} \mathbf{S}_i^{\mathrm{T}} \mathbf{S}_i \left(\mathbf{\Pi}^{(\mathcal{O})} \mathbf{H}\mathbf{H}^{\mathrm{H}} \mathbf{\Pi}^{(\mathcal{O}),\mathrm{T}} + \xi_{\mathrm{WF}} \mathbf{1}_B \right) \mathbf{S}_i^{\mathrm{T}} \boldsymbol{\mu}_i^* \mathbf{e}_i^{\mathrm{T}}, \end{aligned} \tag{20.49}$$

we obtain for the feedback filter

$$\mathbf{F} = \sum_{i=1}^{B} \xi_{\mathrm{WF}}^{-1} \sigma_{v_i}^{-2} \left(\mathbf{1}_B - \mathbf{S}_i^{\mathrm{T}} \mathbf{S}_i \right) \mathbf{\Pi}^{(\mathcal{O})} \mathbf{H}\mathbf{H}^{\mathrm{H}} \mathbf{\Pi}^{(\mathcal{O}),\mathrm{T}} \mathbf{S}_i^{\mathrm{T}} \boldsymbol{\mu}_i^* \mathbf{e}_i^{\mathrm{T}}, \tag{20.50}$$

because $\mathbf{S}_i^{\mathrm{T}} \mathbf{S}_i \mathbf{S}_i^{\mathrm{T}} - \mathbf{S}_i^{\mathrm{T}} = \mathbf{0}_{B \times i}$. With the alternative expression for the Lagrangian multipliers

$$\boldsymbol{\mu}_i^* = -\xi_{\mathrm{WF}} \sigma_{v_i}^2 \mathbf{S}_i \mathbf{\Pi}^{(\mathcal{O})} \left(\mathbf{\Pi}_i^{(\mathcal{O})} \mathbf{H}\mathbf{H}^{\mathrm{H}} \mathbf{\Pi}_i^{(\mathcal{O})} + \xi_{\mathrm{WF}} \mathbf{1}_B \right)^{-1} \mathbf{e}_{b_i}, \quad i = 1, \ldots, B, \tag{20.51}$$

where we again introduced the projector

$$\mathbf{\Pi}_i^{(\mathcal{O})} = \mathbf{\Pi}^{(\mathcal{O}),\mathrm{T}} \mathbf{S}_i^{\mathrm{T}} \mathbf{S}_i \mathbf{\Pi}^{(\mathcal{O})} = \mathbf{1}_B - \sum_{j=i+1}^{B} \mathbf{e}_{b_j} \mathbf{e}_{b_j}^{\mathrm{T}} \in \{0, 1\}^{B \times B}, \tag{20.52}$$

we finally get the WF-S-THP solution for flat fading channels depending on the ordering $\mathcal{O}$:

$$\mathbf{P}_{\mathrm{WF}}^{\mathrm{THP}} = \beta_{\mathrm{WF}}^{\mathrm{THP}} \sum_{i=1}^{B} \mathbf{H}^{\mathrm{H}} \boldsymbol{\Pi}_i^{(\mathcal{O})} \mathbf{A}_{\mathrm{WF},i}^{-1} \mathbf{e}_{b_i} \mathbf{e}_i^{\mathrm{T}} \in \mathbb{C}^{N \times B}, \tag{20.53}$$

$$\mathbf{F}_{\mathrm{WF}}^{\mathrm{THP}} = \sum_{i=1}^{B} \left(\mathbf{S}_i^{\mathrm{T}} \mathbf{S}_i - \mathbf{1}_B\right) \boldsymbol{\Pi}^{(\mathcal{O})} \mathbf{H}\mathbf{H}^{\mathrm{H}} \boldsymbol{\Pi}_i^{(\mathcal{O})} \mathbf{A}_{\mathrm{WF},i}^{-1} \mathbf{e}_{b_i} \mathbf{e}_i^{\mathrm{T}}, \tag{20.54}$$

and

$$\beta_{\mathrm{WF}}^{\mathrm{THP}} = \sqrt{\frac{E_{\mathrm{tr}}}{\sum_{i=1}^{B} \sigma_{v_i}^2 \mathbf{e}_{b_i}^{\mathrm{T}} \mathbf{A}_{\mathrm{WF},i}^{-2} \boldsymbol{\Pi}_i^{(\mathcal{O})} \mathbf{H}\mathbf{H}^{\mathrm{H}} \boldsymbol{\Pi}_i^{(\mathcal{O})} \mathbf{e}_{b_i}}} \in \mathbb{R}_+, \tag{20.55}$$

where $\mathbf{A}_{\mathrm{WF},i} = \boldsymbol{\Pi}_i^{(\mathcal{O})} \mathbf{H}\mathbf{H}^{\mathrm{H}} \boldsymbol{\Pi}_i^{(\mathcal{O})} + \xi_{\mathrm{WF}} \mathbf{1}_B$. The expression for the scalar $\beta_{\mathrm{WF}}^{\mathrm{THP}}$ was found with the transmit energy constraint. Interestingly, we get the same scalar weight $\xi_{\mathrm{WF}} = \mathrm{tr}(\mathbf{R}_{\boldsymbol{\eta}})/E_{\mathrm{tr}}$ for the identity matrix inside the inverse as for the linear TxWF (cf. (20.7)). Note that we can alternatively write for the feedback filter:

$$\mathbf{F}_{\mathrm{WF}}^{\mathrm{THP}} = \beta_{\mathrm{WF}}^{\mathrm{THP},-1} \sum_{i=1}^{B} \left(\mathbf{S}_i^{\mathrm{T}} \mathbf{S}_i - \mathbf{1}_B\right) \boldsymbol{\Pi}^{(\mathcal{O})} \mathbf{H}\mathbf{P}_{\mathrm{WF}}^{\mathrm{THP}} \mathbf{e}_i \mathbf{e}_i^{\mathrm{T}}, \tag{20.56}$$

that is, the ith column of the feedback filter is constructed by using the ith column of the filter chain $\beta_{\mathrm{WF}}^{\mathrm{THP},-1} \mathbf{H}\mathbf{P}_{\mathrm{WF}}^{\mathrm{THP}}$ and setting the first i elements to zero. The MSE for the WF-S-THP approach in terms of the feedback filter $\mathbf{F}_{\mathrm{WF}}^{\mathrm{THP}}$ can be expressed as

$$\sigma_{\boldsymbol{\varepsilon}}^2 \left(\mathbf{P}_{\mathrm{WF}}^{\mathrm{THP}}, \mathbf{F}_{\mathrm{WF}}^{\mathrm{THP}}, \beta_{\mathrm{WF}}^{\mathrm{THP}}, \mathcal{O}\right) = \xi_{\mathrm{WF}} \,\mathrm{tr}\left(\left(\mathbf{1}_B - \mathbf{F}_{\mathrm{WF}}^{\mathrm{THP}}\right) \mathbf{R}_{\mathbf{v}} \left(\mathbf{1}_B - \mathbf{F}_{\mathrm{WF}}^{\mathrm{THP,H}}\right) \mathbf{A}_{\mathrm{WF},i}^{-1}\right). \tag{20.57}$$

The MSE is further minimized by the choice of the ordering $\mathcal{O}$. With (20.54), we find the WF-S-THP ordering optimization:

$$\mathcal{O}'_{\mathrm{WF}} = \underset{\mathcal{O}}{\mathrm{argmin}}\, \xi_{\mathrm{WF}} \sum_{i=1}^{B} \sigma_{v_i}^2 \mathbf{e}_{b_i}^{\mathrm{T}} \left(\boldsymbol{\Pi}_i^{(\mathcal{O})} \mathbf{H}\mathbf{H}^{\mathrm{H}} \boldsymbol{\Pi}_i^{(\mathcal{O})} + \xi_{\mathrm{WF}} \mathbf{1}_B\right)^{-1} \mathbf{e}_{b_i}. \tag{20.58}$$

To avoid the high complexity $\mathrm{O}(B!B^3)$ of this optimization, we suggest to employ the following suboptimum approach instead:

$$\mathcal{O}_{\mathrm{WF}}^{\mathrm{THP}} = \left(b_{\mathrm{WF},1}^{\mathrm{THP}}, \ldots, b_{\mathrm{WF},B}^{\mathrm{THP}}\right) \tag{20.59}$$

with

$$b_{\mathrm{WF},i}^{\mathrm{THP}} = \underset{b \in \mathbb{O}_i}{\mathrm{argmin}}\, \mathbf{e}_b^{\mathrm{T}} \left(\boldsymbol{\Pi}_i^{(\mathcal{O}_{\mathrm{WF}}^{\mathrm{THP}})} \mathbf{H}\mathbf{H}^{\mathrm{H}} \boldsymbol{\Pi}_i^{(\mathcal{O}_{\mathrm{WF}}^{\mathrm{THP}})} + \xi_{\mathrm{WF}} \mathbf{1}_B\right)^{-1} \mathbf{e}_b, \tag{20.60}$$

$\mathbb{O} \leftarrow \{1, \ldots, B\}$
$\mathbf{G} \leftarrow \mathbf{H}$
for $i = B, \ldots, 1$:
4: $\quad \mathbf{P} \leftarrow (\mathbf{G}\mathbf{G}^{\mathrm{H}} + \xi_{\mathrm{WF}}\mathbf{1}_B)^{-1}$
5: $\quad b_i \leftarrow \underset{b \in \mathbb{O}}{\operatorname{argmin}}\, \mathbf{e}_b^{\mathrm{T}}\mathbf{P}\mathbf{e}_b$
6: $\quad \mathbf{p}_i \leftarrow \mathbf{G}^{\mathrm{H}}\mathbf{P}\mathbf{e}_{b_i}$
$\quad \mathbb{O} \leftarrow \mathbb{O} \setminus \{b_i\}$
$\quad \mathbf{G} \leftarrow (\mathbf{1}_B - \mathbf{e}_{b_i}\mathbf{e}_{b_i}^{\mathrm{T}})\mathbf{G}$
for $i = 1, \ldots, B$:
10: $\quad \mathbf{f}_i \leftarrow (\mathbf{S}_i^{\mathrm{T}}\mathbf{S}_i - \mathbf{1}_B)\mathbf{\Pi}^{(\mathcal{O})}\mathbf{H}\mathbf{p}_i$
11: $\chi \leftarrow \sigma_{\mathbf{s}}^2 \|\mathbf{p}_1\|_2^2 + \sigma_{\mathbf{v}}^2 \sum_{i=2}^{B} \|\mathbf{p}_i\|_2^2$
$\beta \leftarrow \sqrt{E_{\mathrm{tr}}/\chi}$
$\mathbf{P} \leftarrow \beta[\mathbf{p}_1, \ldots, \mathbf{p}_B]$

Algorithm 20.1. Filter and ordering computation for spatial WF-THP over nondispersive channels.

for $i = 1, \ldots, B$:
2: $\quad \nu_i \leftarrow \mathrm{M}\left(s_{b_i} + \sum_{j=1}^{i-1} \mathbf{e}_i^{\mathrm{T}}\mathbf{f}_j\nu_j\right)$
$\mathbf{v} = [\nu_1, \ldots, \nu_K]^{\mathrm{T}}$
$\mathbf{y} = \mathbf{P}\mathbf{v}$

Algorithm 20.2. Ordered spatial THP over nondispersive channels.

where $\mathbb{O}_i = \{1, \ldots, B\} \setminus \{b_{\mathrm{WF},i+1}^{\mathrm{THP}}, \ldots, b_{\mathrm{WF},B}^{\mathrm{THP}}\}$ and $i = B, \ldots, 1$. Thus, each summand of (20.58) is minimized for fixed *succeeding* indices $b_{\mathrm{WF},i+1}^{\mathrm{THP}}, \ldots, b_{\mathrm{WF},B}^{\mathrm{THP}}$ starting from the index of the data stream precoded last and ending with the index of the data stream precoded first. Note that $\mathbf{\Pi}_i^{(\mathcal{O}_{\mathrm{WF}}^{\mathrm{THP}})}$ only depends on the succeeding indices $b_{\mathrm{WF},i+1}^{\mathrm{THP}}, \ldots, b_{\mathrm{WF},B}^{\mathrm{THP}}$. Thus, the inverse of $\mathbf{\Pi}_i^{(\mathcal{O}_{\mathrm{WF}}^{\mathrm{THP}})}\mathbf{H}\mathbf{H}^{\mathrm{H}}\mathbf{\Pi}_i^{(\mathcal{O}_{\mathrm{WF}}^{\mathrm{THP}})} + \xi_{\mathrm{WF}}\mathbf{1}_B$ only has to be computed once for each step and the complexity of the above optimization is $\mathrm{O}(B^4)$.

In Algorithm 20.1, we present the resulting algorithm to compute the WF-S-THP filters as pseudocode. S-THP for nondispersive channels is illustrated by Algorithm 20.2. Note that we included the assumption in line 11 that all modulo outputs have variance $\sigma_{\mathbf{v}}^2 = \tau^2/6$ except the first modulo output ν_1 which is equal to s_{b_1} (see line 2 of Algorithm 20.2).

The ZF-S-THP variant can be found with a similar algorithm as the one in Algorithm 20.1, we only have to replace the lines 4–6 and 10 by the respective lines in Algorithm 20.3. Note that this step is equivalent to the limit $\xi_{\mathrm{WF}} \to 0$. However, the replacement is necessary, since we would end up with an inversion of a rank deficient matrix (see line 4 in Algorithm 20.1).

4: $\mathbf{P} \leftarrow \mathbf{G}^{+}$
5: $b_i \leftarrow \operatorname{argmin}_{b \in \mathbb{O}} \|\mathbf{P}\mathbf{e}_b\|_2^2$
6: $\mathbf{p}_i \leftarrow \mathbf{P}\mathbf{e}_{b_i}$
10: $\mathbf{f}_i \leftarrow \mathbf{e}_i - \mathbf{\Pi}^{(\mathcal{O})}\mathbf{H}\mathbf{p}_i$

Algorithm 20.3. Filter and ordering computation for spatial ZF-THP over nondispersive channels.

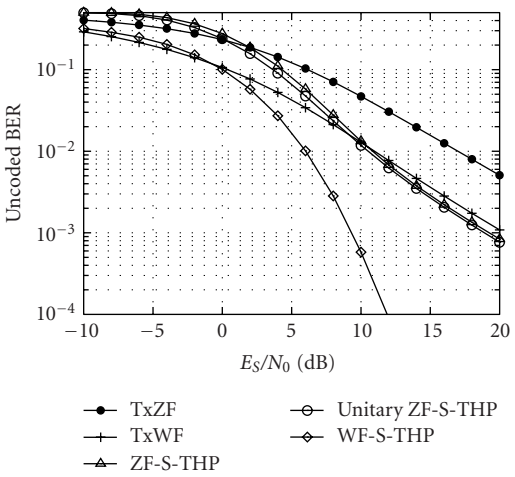

Figure 20.6. QPSK transmission over nondispersive MIMO channel with four transmitting and four receiving antenna elements: BER versus SNR for linear and nonlinear transmit processing.

20.5. Simulation results

We apply the spatial THP approaches discussed in this section to a nondispersive *multiple-input multiple-output* (MIMO) system, where we assume that the entries of the channel matrix are i.i.d. complex Gaussian distributed. The uncoded BER results are the mean of 240 000 channel realizations, where 100 vector symbols are transmitted per realization. The linear transmit filters TxZF and TxWF discussed in Section 20.2 are used for comparison to highlight the capabilities of THP. Additionally, we include the uncoded BER results for *unitary ZF-S-THP* [21] which is a variant of ZF-S-THP with unitary feedforward filter and a weighting with a diagonal matrix at the receiver instead of the scalar weighting employed in this section.

In Figure 20.6, we present the results for a system with four antenna elements deployed at the transmitter and four antenna elements at the receiver. Four QPSK symbols are transmitted per channel use. We observe that the S-THP approaches clearly outperform the respective linear filters, where WF-S-THP needs about 4 dB less SNR than ZF-S-THP for a BER of 10%. The unitary ZF-S-THP is slightly

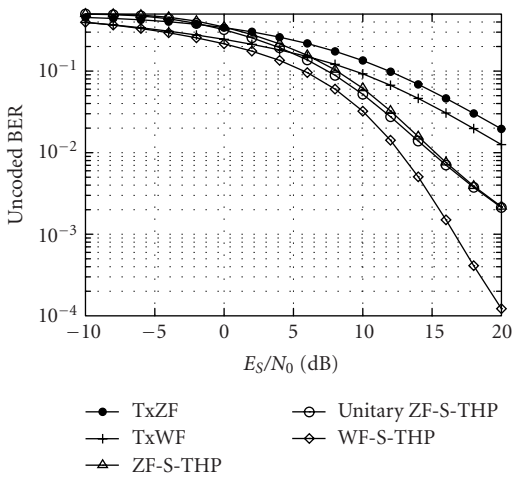

FIGURE 20.7. 16QAM transmission over nondispersive MIMO channel with four transmitting and four receiving antenna elements: BER versus SNR for linear and nonlinear transmit processing.

better than ZF-S-THP with scalar weighting, since the diagonal weighting of unitary ZF-S-THP offers more degrees of freedom. Note that the BERs of the two zero-forcing THP variants have the same slope as the two linear filters for high SNR. This behavior can be explained by the fact that the last column of the feedforward filter $\mathbf{P}_{\mathrm{ZF}}^{\mathrm{THP}}$ is the weighted b_Bth column of the TxZF $\mathbf{P}_{\mathrm{ZF}}$. Thus, the diversity order of the THP data stream precoded last is the same as the diversity order of the TxZF data streams (in our case, diversity order 1, slop is one magnitude of BER per 10 dB SNR). As the smallest diversity order is dominant, the ZF-THP approaches have the same diversity order as the linear transmit filters for high SNR.

The results for 16QAM transmission in Figure 20.7 are similar to the QPSK results in Figure 20.6. WF-S-THP is superior compared to all other depicted approaches and outperforms the linear TxWF even for low SNR. This result illustrates the dependence of THP on the modulation alphabet, since the modulo operation at the receiver introduces additional allowed constellation points. As the number of constellation points for 16QAM is larger than for QPSK, the impact of the modulo operation at the receiver is less pronounced for 16QAM.

When reducing the number of antenna elements at the receiver to three and transmitting three QPSK symbols per channel use, we end up with the results in Figure 20.8. Due to the increased number of freedoms compared to the case with four data streams of Figure 20.6, the linear transmit filters lead to better results than the THP approaches for low and medium SNRs, for example, the TxWF has a lower uncoded BER than WF-S-THP for an SNR below 1 dB. We can also observe that unitary ZF-S-THP is outperformed by ZF-S-THP with scalar weighting at the receiver. Consequently, the intuitively chosen diagonal weighting of unitary ZF-S-THP is suboptimum.

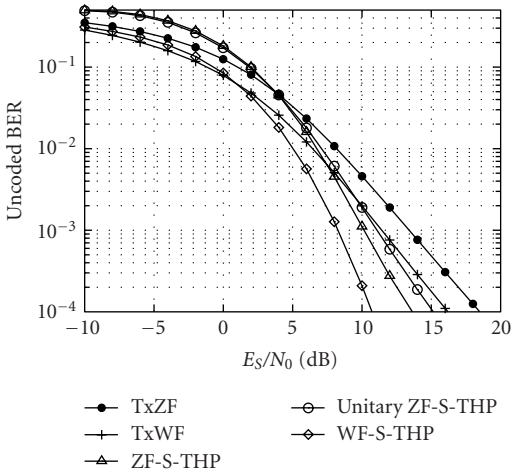

FIGURE 20.8. QPSK transmission over nondispersive MIMO channel with four transmitting and three receiving antenna elements: BER versus SNR for linear and nonlinear transmit processing.

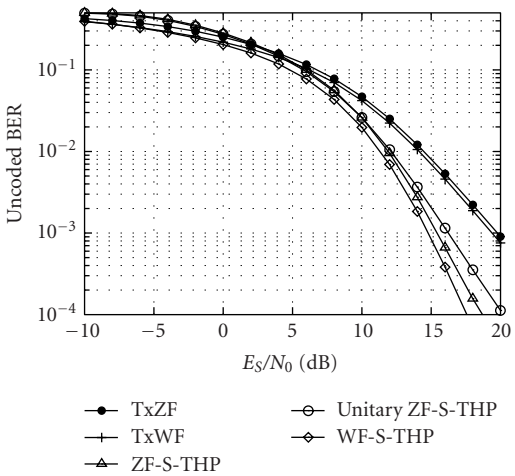

FIGURE 20.9. 16QAM transmission over nondispersive MIMO channel with four transmitting and three receiving antenna elements: BER versus SNR for linear and nonlinear transmit processing.

In Figure 20.9, three 16QAM symbols are transmitted per channel use. As the modulo operation at the receiver is less harmful for 16QAM, WF-S-THP exhibits the best uncoded BER results in the whole depicted SNR region contrary to Figure 20.8. Note how close the BER curves of the zero-forcing and Wiener precoder types lie in Figure 20.9 due to the available degrees of freedom, because the number of receive antenna elements is smaller than the number of transmit antenna elements.

Abbreviations

BER	Bit error rate
DFE	Decision feedback equalizer
DS-CDMA	Direct-sequence code-division multiple access
FIR	Finite impulse response
IIR	Infinite impulse response
MIMO	Multiple-input multiple-output
MSE	Mean square error
QAM	Quadrature amplitude modulation
QPSK	Quaternary phase-shift keying
SISO	Single-input single-output
SNR	Signal-to-noise ratio
S-THP	Spatial Tomlinson-Harashima precoding
THP	Tomlinson-Harashima precoding
TxMF	Transmit matched filter
TxWF	Transmit Wiener filter
TxZF	Transmit zero-forcing filter
V-BLAST	Vertical Bell Laboratories Space Time
WF-S-THP	Wiener spatial Tomlinson-Harashima precoding
WF-THP	Wiener Tomlinson-Harashima precoding
ZF-S-THP	Zero-forcing spatial Tomlinson-Harashima precoding
ZF-THP	Zero-forcing Tomlinson-Harashima precoding

Bibliography

[1] S. Verdú, *Multiuser Detection*, Cambridge University Press, New York, NY, USA, 1998.

[2] M. Joham, W. Utschick, and J. A. Nossek, "Linear transmit processing in MIMO communications systems," to appear in *IEEE Trans. Signal Processing*.

[3] C. B. Peel, B. M. Hochwald, and A. L. Swindlehurst, "A vector-perturbation technique for near-capacity multiantenna multiuser communication—Part I: channel inversion and regularization," *IEEE Trans. Commun.*, vol. 53, no. 1, pp. 195–202, 2005.

[4] C. Peel, B. Hochwald, and L. Swindlehurst, "A vector-perturbation technique for near-capacity multi-antenna multi-user communication—Part II: perturbation," to appear in *IEEE Trans. Commun.*

[5] C. Windpassinger, R. F. H. Fischer, and J. B. Huber, "Lattice-reduction-aided broadcast precoding," in *Proc. 5th International ITG Conference on Source and Channel Coding (SCC '04)*, pp. 403–408, Erlangen, Germany, January 2004.

[6] R. Irmer, R. Habendorf, W. Rave, and G. Fettweis, "Nonlinear multiuser transmission using multiple antennas for TDD-CDMA," in *Proc. IEEE 6th International Symposium on Wireless Personal Multimedia Communications (WPMC '03)*, vol. 3, pp. 251–255, Yokosuka, Japan, October 2003.

[7] T. Weber and M. Meurer, "Optimum joint transmission: potentials and dualities," in *Proc. IEEE 6th International Symposium on Wireless Personal Multimedia Communications (WPMC '03)*, vol. 1, pp. 79–83, Yokosuka, Japan, October 2003.

[8] R. F. H. Fischer and C. Windpassinger, "Improved MIMO precoding for decentralized receivers resembling concepts from lattice reduction," in *Proc. IEEE Global Telecommunications Conference (GLOBECOM '03)*, vol. 4, pp. 1852–1856, San Francisco, Calif, USA, December 2003.

[9] H. Yao and G. W. Wornell, "Lattice-reduction-aided detectors for MIMO communication systems," in *Proc. IEEE Global Telecommunications Conference (IEEE GLOBECOM '02)*, vol. 1, pp. 424–428, Taipei, Taiwan, November 2002.

[10] M. E. Austin, "Decision-feedback equalization for digital communication over dispersive channels," Tech. Rep. 437, MIT/Lincoln Laboratory, Lexington, Mass, USA, August 1967.
[11] N. Al-Dhahir and A. H. Sayed, "The finite-length multi-input multi-output MMSE-DFE," *IEEE Trans. Signal Processing*, vol. 48, no. 10, pp. 2921–2936, 2000.
[12] C. A. Belfiore and J. H. Park, "Decision feedback equalization," *Proc. IEEE*, vol. 67, no. 8, pp. 1143–1156, 1979.
[13] A. Duel-Hallen, "Equalizers for multiple input/multiple output channels and PAM systems with cyclostationary input sequences," *IEEE J. Select. Areas Commun.*, vol. 10, no. 3, pp. 630–639, 1992.
[14] P. Monsen, "Feedback equalization for fading dispersive channels," *IEEE Trans. Inform. Theory*, vol. 17, no. 1, pp. 56–64, 1971.
[15] M. Tomlinson, "New automatic equaliser employing modulo arithmetic," *Electronics Letters*, vol. 7, no. 5/6, pp. 138–139, 1971.
[16] H. Harashima and H. Miyakawa, "Matched-transmission technique for channels with intersymbol interference," *IEEE Trans. Commun.*, vol. 20, no. 4, pp. 774–780, 1972.
[17] G. D. Forney and M. V. Eyuboğlu, "Combined equalization and coding using precoding," *IEEE Commun. Mag.*, vol. 29, no. 12, pp. 25–34, 1991.
[18] M. R. Gibbard and A. B. Sesay, "Asymmetric signal processing for indoor wireless LAN's," *IEEE Trans. Veh. Technol.*, vol. 48, no. 6, pp. 2053–2064, 1999.
[19] G. Ginis and J. M. Cioffi, "A multi-user precoding scheme achieving crosstalk cancellation with application to DSL systems," in *Proc. Asilomar Conference on Signals, Systems, and Computers*, vol. 2, pp. 1627–1631, Pacific Grove, Calif, USA, October 2000.
[20] R. F. H. Fischer, C. Windpassinger, A. Lampe, and J. B. Huber, "Space-time transmission using Tomlinson-Harashima precoding," in *Proc. 4th International ITG Conference on Source and Channel Coding (SCC '02)*, pp. 139–147, Erlangen, Germany, January 2002.
[21] R. Fischer, C. Windpassinger, A. Lampe, and J. Huber, "MIMO precoding for decentralized receivers," in *Proc. IEEE International Symposium on Information Theory (ISIT '02)*, p. 496, Lausanne, Switzerland, June–July 2002.
[22] J. Liu and A. Duel-Hallen, "Tomlinson-Harashima transmitter precoding for synchronous multiuser communications," in *Proc. CISS '03*, Baltimore, Md, USA, March 2003.
[23] R. F. H. Fischer, C. Windpassinger, A. Lampe, and J. B. Huber, "Tomlinson-Harashima precoding in space-time transmission for low-rate backward channel," in *Proc. International Zurich Seminar on Broadband Communications (IZS '02)*, pp. 7-1–7-6, Zurich, Switzerland, February 2002.
[24] O. Simeone, Y. Bar-Ness, and U. Spagnolini, "Linear and nonlinear preequalization/equalization for MIMO systems with long-term channel state information at the transmitter," *IEEE Transactions on Wireless Communications*, vol. 3, no. 2, pp. 373–378, 2004.
[25] M. Joham, J. Brehmer, and W. Utschick, "MMSE approaches to multiuser spatio-temporal Tomlinson-Harashima precoding," in *Proc. 5th International ITG Conference on Source and Channel Coding (SCC '04)*, pp. 387–394, Erlangen, Germany, January 2004.
[26] M. Joham, J. Brehmer, A. Voulgarelis, and W. Utschick, "Multiuser spatio-temporal Tomlinson-Harashima precoding for frequency selective vector channels," in *Proc. ITG Workshop on Smart Antennas*, pp. 208–215, Munich, Germany, March 2004.
[27] R. F. H. Fischer, C. Stierstorfer, and J. B. Huber, "Precoding for point-to-multipoint transmission over MIMO ISI channels," in *Proc. International Zurich Seminar on Broadband Communications (IZS '04)*, pp. 208–211, Zurich, Switzerland, February 2004.
[28] R. Hunger, F. Dietrich, M. Joham, and W. Utschick, "Robust transmit zero-forcing filters," in *Proc. ITG Workshop on Smart Antennas*, pp. 130–137, Munich, Germany, March 2004.
[29] P. W. Wolniansky, G. J. Foschini, G. D. Golden, and R. A. Valenzuela, "V-BLAST: an architecture for realizing very high data rates over the rich-scattering wireless channel," in *Proc. International Symposium on Signals, Systems, and Electronics (ISSSE '98)*, pp. 295–300, Pisa, Italy, September 1998.
[30] R. Fletcher, *Practical Methods of Optimization*, John Wiley & Sons, New York, NY, USA, 1987.
[31] G. Golub and C. V. Loan, *Matrix Computations*, Johns Hopkins University Press, Baltimore, Md, USA, 1996.

[32] R. L. Choi and R. D. Murch, "Transmit MMSE pre-RAKE pre-processing with simplified receivers for the downlink of MISO TDD-CDMA systems," in *Proc. IEEE Global Telecommunications Conference (GLOBECOM '02)*, vol. 1, pp. 429–433, Taipei, Taiwan, November 2002.

[33] M. Joham, K. Kusume, M. H. Gzara, W. Utschick, and J. A. Nossek, "Transmit Wiener filter for the downlink of TDD DS-CDMA systems," in *Proc. IEEE 7th International Symposiumon Spread Spectrum Techniques and Applications (ISSSTA '02)*, vol. 1, pp. 9–13, Prague, Czech Republic, September 2002.

[34] R. F. H. Fischer, *Precoding and Signal Shaping for Digital Transmission*, John Wiley & Sons, New York, NY, USA, 2002.

[35] L. N. Trefethen and D. Bau, *Numerical Linear Algebra*, Society for Industrial and Applied Mathematics (SIAM), Philadelphia, Pa, USA, 1997.

Michael Joham: Institute for Circuit Theory and Signal Processing, Munich University of Technology, 80 290 München, Germany

Email: joham@tum.de

Wolfgang Utschick: Institute for Circuit Theory and Signal Processing, Munich University of Technology, 80 290 München, Germany

Email: wolfgang.utschick@tum.de

21 Transmission strategies for the MIMO MAC

Eduard A. Jorswieck

21.1. Introduction

In wireless point-to-point links, one applies multiple antennas to increase the spectral efficiency and the performance of wireless systems [1, 2]. On the other hand, in multiuser scenarios, multiple antennas at the base or even at the mobiles require the development of new transmission strategies in order to achieve the benefits of using the spatial domain. In multiple-input multiple-output (MIMO) multiple access channels (MAC), the optimum transmission strategy depends on the objective function, the power constraints, the channel statistics or the channel realization, the type of channel state information (CSI), and the SNR range.

The analysis of multiuser MIMO systems is very important since usually more than one user are involved in cellular as well as ad hoc systems. Up to now, only little has been found out about MIMO multiuser systems. The achievable rates and the transmission strategy depend at least on the following.

(i) *Structure of the wireless MIMO system.* In the common cellular approach, many mobiles share one base station which controls the scheduling and transmission strategies, for example, power control in a centralized manner. In cellular systems the inter- and intracell interference can be controlled by spectrum and time allocation. In MIMO systems an additional dimension, namely the space, is available for allocation purposes.

(ii) *Transmit strategies.* Obviously, the transmit strategies of the participating mobiles influence the achievable rate and the properties of the complete system. In turn, the transmit strategies depend on the type of CSI at the transmitter, that is, the more CSI is known about the own channel as well as about the other users and the interference, the more adaptive and smart transmission strategies can be applied. If no CSI is available at the transmitter, it is the best to use multiuser space-time (-spreading) codes.

(iii) *Receiver strategies.* Different decoding and detection strategies can be used at the receiver. The range leads from single-user detection algorithms which treat

the other users as a noise up to linear and even nonlinear multiuser detection algorithms. Of course, the receiver architecture depends on the type of CSI, too.

(iv) *System parameters.* In general, an important factor is the scenario in which the wireless system works. In home or office scenarios, the system parameter heavily differs from parameters in public access, hot spots, or high velocity scenarios. User parameters, resource parameters, and especially channel parameters have to be taken into account. The achievable performance and throughput depend on those system parameters.

The optimization problems which arise in multiuser MIMO wireless systems are divided into two classes. In the first one, the objective function measures a global performance criteria of the system. In order to increase the throughput of the MIMO MAC, the sum capacity can be maximized [3, 4, 5, 6] or the normalized mean-square error can be minimized [7]. The solution of this class optimization problems leads to transmission strategies which can be unfair for some users. If users experience poor channel conditions for long periods of time, they are not allowed to transmit. Therefore, the other class of optimisation problems deals with the fulfilment of rate [8], SINR [9], or MSE [10] requirements with minimal power. We study performance criteria for one user subject to fulfilment constraints. In order to solve this class of problems, it is necessary to understand the geometry of the achievable rate, SINR, or MSE region. In both classes of optimization problems, the constraints can be either individual power constraints of each user or a sum power constraint. The second class of programming problems are nonconvex nonlinear programming problems which are notoriously complicate to analyze. The large number of degrees of freedom in the temporal as well as the spatial domain increases the number of parameters which can be controlled. In order to simplify the analysis, it is of advantage to divide the programming problem into parts which can be solved in an iterative fashion.

In this chapter, we motivate and analyze important representative problems of both classes. The development from the single-antenna MAC to the MIMO MAC is shown and the differences and common ground between the single-antenna and the multiple-antenna cases are stressed. Furthermore, we focus on the connections between the different objective functions and their corresponding programming problems. We show which results of recent literature can be reused and which results must not be reused. Finally, we illustrate the optimum transmission strategies by examples.

21.2. Preliminaries

21.2.1. System model

Consider the multiple access channel in Figure 21.1. The communication channel between each user and the base station is modelled by a quasistatic block flat fading MIMO channel.

We have K mobiles with n_T antennas. We can easily extend the results to the case in which every mobile has a different number of transmit antennas. The base

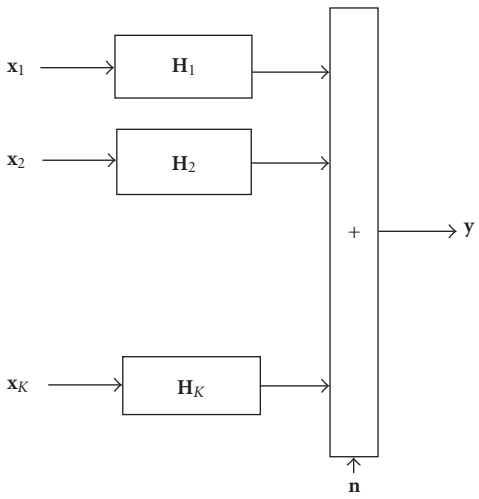

Figure 21.1. MIMO MAC system.

station owns n_R receive antennas. In the discrete time model, the received vector $\mathbf{y}$ at one time slot at the base station can be described by

$$\mathbf{y} = \sum_{k=1}^{K} \mathbf{H}_k \mathbf{x}_k + \mathbf{n} \tag{21.1}$$

with the receiver noise $\mathbf{n} \in \mathbb{C}^{n_R \times 1}$ which is additive white Gaussian noise (AWGN), flat fading channel matrices $\mathbf{H}_k \in \mathbb{C}^{n_R \times n_T}$, and transmit signals $\mathbf{x}_k \in \mathbb{C}^{n_T \times 1}$. We assume uncorrelated noise with covariance $\sigma_n^2 \mathbf{I}_{n_R}$. The inverse noise power is denoted by $\rho = 1/\sigma_n^2$.

Equation (21.1) can be rewritten in compact form as

$$\mathbf{y} = \hat{\mathbf{H}}\hat{\mathbf{x}} + \mathbf{n} \tag{21.2}$$

with $\hat{\mathbf{H}} = [\mathbf{H}_1, \mathbf{H}_2, \ldots, \mathbf{H}_K]$ and $\hat{\mathbf{x}} = [\mathbf{x}_1^T, \ldots, \mathbf{x}_K^T]^T$. We collect the transmit covariance matrices in

$$\hat{\mathbf{Q}} = \begin{pmatrix} \mathbf{Q}_1 & 0 & 0 & \cdots & 0 \\ 0 & \mathbf{Q}_2 & 0 & \cdots & 0 \\ & & \ddots & & \\ 0 & 0 & & & 0 \\ 0 & 0 & 0 & 0 & \mathbf{Q}_K \end{pmatrix}. \tag{21.3}$$

21.2.2. Performance metrics

Under the assumption that the receiver knows the channel realization $\mathbf{H}_k$, the mutual information for user k is given by

$$I(\mathbf{y};\mathbf{x}_k|\mathbf{H}_k) = \log\det\left(\mathbf{I}+\rho\sum_{l=1}^{K}\mathbf{H}_l\mathbf{Q}_l\mathbf{H}_l^H\right) - \log\det\left(\mathbf{I}+\rho\sum_{l=1,l\neq k}^{K}\mathbf{H}_l\mathbf{Q}_l\mathbf{H}_l^H\right) \tag{21.4}$$

with SNR ρ and transmit covariance matrices $\mathbf{Q}_k$. The transmit signals of the users are assumed to be zero-mean independent complex Gaussian distributed with covariance matrix $\mathbf{Q}_k$. This probability density function (pdf) maximizes the individual mutual information of each user. Obviously, the individual mutual information of user k depends on the multiuser interference and noise, that is, it is a function of all transmission matrices $\mathbf{H}_k$ between the users and the base, the SNR ρ and the transmit strategies $\mathbf{Q}_k$ of all users,

$$R_k(\mathcal{Q},\mathcal{H},\rho) = \log\det\left(\frac{\mathbf{I}+\rho\sum_{l=1}^{K}\mathbf{H}_l\mathbf{Q}_l\mathbf{H}_l^H}{\mathbf{I}+\rho\sum_{l=1,l\neq k}^{K}\mathbf{H}_l\mathbf{Q}_l\mathbf{H}_l^H}\right) \tag{21.5}$$

with the set of covariance matrices $\mathcal{Q}$ and the set of channel realizations $\mathcal{H}$

$$\mathcal{Q} = \{\mathbf{Q}_1,\mathbf{Q}_2,\ldots,\mathbf{Q}_K\}, \qquad \mathcal{H} = \{\mathbf{H}_1,\mathbf{H}_2,\ldots,\mathbf{H}_K\}. \tag{21.6}$$

The achievable rate of user k is denoted by R_k. It is possible that the receiver first detects the signals of a set of users and subtracts them from the received signal before detecting the user k. As long as the users transmit at a rate smaller than or equal to their achievable rate, their signals are detected with arbitrary small probability of error and are therefore correctly subtracted. We assume that the signals of users 1 to $k-1$ are correctly subtracted. In this case, the individual mutual information of user k is given by

$$R_k^{\mathrm{SIC}}(\mathcal{Q},\mathcal{H},\rho) = \log\det\left(\frac{\mathbf{I}+\rho\sum_{l=1}^{K}\mathbf{H}_l\mathbf{Q}_l\mathbf{H}_l^H}{\mathbf{I}+\rho\sum_{l=k+1}^{K}\mathbf{H}_l\mathbf{Q}_l\mathbf{H}_l^H}\right). \tag{21.7}$$

The receiver starts with user one, detects its data, and subtracts it from the received signal. The received signal for user one is interfered by all other users. Then the second user is detected and subtracted. The second user gets interference from all but the first user. This procedure continues until the last user is detected without any interference. This approach is called successive interference cancellation (SIC). Usually, one assumes that the data of all users are detected without any errors because the users transmit with rate below their capacity.

If we assume that the receiver detects the user signals in a linear fashion, the optimal choice is the linear multiuser MMSE receiver. If we apply the linear MMSE receiver, the performance metric is the *normalized MSE* [11]. The linear MMSE receiver weights the received signal vector $\mathbf{y}$ by the Wiener filter

$$\hat{x}_k = \mathbf{Q}_k \mathbf{H}_k^H \left(\sum_{l=1}^{K} \mathbf{H}_l \mathbf{Q}_l \mathbf{H}_l^H + \sigma_n^2 \mathbf{I} \right)^{-1} \mathbf{y}. \tag{21.8}$$

The covariance matrix of the estimation error $\mathbf{K}_\epsilon$ is given by

$$\mathbf{K}_\epsilon = \mathbb{E}_{\mathbf{H}} \left[(\hat{\mathbf{x}} - \mathbf{x}) (\hat{\mathbf{x}} - \mathbf{x})^H \right]. \tag{21.9}$$

The *normalized MSE* is defined as the trace of the normalized covariance matrix of the estimation error in (21.9). The corresponding performance metric is the individual normalised MSE of user k which is given by

$$\begin{aligned} \mathrm{MSE}_k &= \mathrm{tr}\left(\mathbf{Q}^{-1/2} \mathbf{K}_\epsilon \mathbf{Q}^{-1/2}\right) \\ &= n_T - \mathrm{tr}\left(\rho \mathbf{H}_k \mathbf{Q}_k \mathbf{H}_k^H \left(\rho \sum_{l=1}^{K} \mathbf{H}_l \mathbf{Q}_l \mathbf{H}_l^H + \mathbf{I} \right)^{-1} \right). \end{aligned} \tag{21.10}$$

In contrast to the capacity, it is not possible to perform SIC without error propagation, since the argument of error free reception is missing. Therefore, each user k experiences interference from all other users. The achievable MSE region is given by all MSE tuples $(m_1, \ldots, m_K)$ for which $(m_1 \geq \mathrm{MSE}_1, \ldots, m_K \geq \mathrm{MSE}_K)$ holds.

Using the individual rate or the individual MSE, each user can require its quality-of-service (QoS) by giving a minimum rate r_k or a maximum MSE m_k which has to be achieved. The problem of the fulfilment of service requirements consists of computing a transmit strategy which fulfills for all $1 \leq k \leq K$ that $R_k \geq r_k$ or $\mathrm{MSE}_k \leq m_k$ by minimizing the individual $p_k \leq P_k$ or sum transmit power $\sum_{k=1}^{K} p_k \leq P$. The transmit power p_k of user k corresponds to the trace of its transmit covariance matrix $p_k = \mathrm{trace}(\mathbf{Q}_k)$.

Another performance metric is the sum of the individual performance metrics. The sum capacity is simply defined as the sum of the individual capacities $\sum_{k=1}^{K} R_k^{\mathrm{SIC}}(\mathcal{Q}, \mathcal{H}, \rho)$, that is, with SIC, we obtain

$$C(\mathcal{Q}, \mathcal{H}, \rho) = \log\det\left(\mathbf{I} + \rho \sum_{k=1}^{K} \mathbf{H}_k \mathbf{Q}_k \mathbf{H}_k^H \right). \tag{21.11}$$

The normalized sum MSE is defined in the same manner, that is, $\mathrm{MSE} = \sum_{k=1}^{K} \mathrm{MSE}_k$ and it is given by

$$\mathrm{MSE}(\mathcal{Q}, \mathcal{H}, \rho) = K n_T - n_R + \mathrm{tr}\left(\left[\rho \sum_{k=1}^{n_T} \mathbf{H}_k \mathbf{Q}_k \mathbf{H}_k^H + \mathbf{I} \right]^{-1} \right). \tag{21.12}$$

The sum capacity and the sum MSE describe the performance of the complete MAC. The system throughput can be measured by the sum capacity in (21.11) or by the sum MSE (21.12).

21.2.3. Assumptions and constraints

We assume that the transmitter as well as the receiver know the channel perfectly. This ideal leads to an upper bound on the achievable performance. The channel between each mobile and the base station is frequency flat. The coherence time of the channel is large enough

(i) to encode over a sufficiently large number of blocks for achieving approximately the capacity conditioned on one channel realization if the capacity is considered as the performance metric, or

(ii) to transmit one symbol which could be even a space-time symbol if the MSE is considered as the performance metric.

SIC without error propagation at the base station is assumed for capacity optimization. For MSE minimization, no SIC is performed.

The transmit power of the mobiles can be constrained in various ways depending on the scenario considered. The most constrained scenario corresponds to a power constraint on each single antenna of each mobile. This constraint is relevant from a transmit antenna amplifier point of view.

Less restricted constraints are individual power constraints of the users, that is,

$$p_k = \operatorname{tr}(\mathbf{Q}_k) \leq p_k^{\max}. \tag{21.13}$$

Individual power constraints are important in regard to public health conditions.

A less restricted constraint is a sum power constraint for all mobiles in one cell, that is,

$$\sum_{k=1}^{K} p_k = \sum_{k=1}^{K} \operatorname{tr}(\mathbf{Q}_k) \leq P. \tag{21.14}$$

The sum power constraint is important if the power can be distributed across the users in one cell, but the cell sum power is limited in order to keep the intercell interference under control. In addition to this, the sum power constraint can be motivated by the downlink transmission in which the base station has a power constraint.

Usually, two different temporal power allocation constraints are applied on top of the sum, individual, and antenna constraint, namely, the short-term and long-term power constraint. The short-term power constraint operates on the power allocated to the transmitted signal vector over one constant channel realization, that is, the individual short-term power constraint is the one given above in (21.13). If it is allowed to distribute the power amount over ergodic many channel fading blocks, the transmit policy is a function of the channel realization $\mathbf{H}_k$.

The long-term individual power constraint for user k is given by

$$\mathbb{E}_{\mathbf{H}_k}\left[\operatorname{tr}\mathbf{Q}_k(\mathbf{H}_k)\right] \leq P_k \tag{21.15}$$

and the corresponding long-term sum power constraint is given by

$$\sum_{k=1}^{K} \mathbb{E}_{\mathbf{H}_k}\left[\operatorname{tr}\mathbf{Q}_k(\mathbf{H}_k)\right] \leq P. \tag{21.16}$$

The optimum transmit policy under short-term and long-term power constraints differs in the additional degree of freedom for the long-term power constraint which leads to some kind of temporal water-filling with perfect CSI at transmitter and receiver. Since we are interested in the impact of the spatial dimension (and not in the temporal), we assume only short-term power constraints in this section.

21.3. Sum performance optimization

The first problem is as follows. *Assume that the channel realizations* $\mathbf{H}_k$ *are known and fixed. Solve the sum capacity optimization under the sum power constraint, that is,*

$$\begin{aligned} &\max \log\det\left(\mathbf{I}+\rho\sum_{k=1}^{K}\mathbf{H}_k\mathbf{Q}_k\mathbf{H}_k^H\right) \\ &\textit{subject to} \\ &\sum_{k=1}^{K}\operatorname{tr}\mathbf{Q}_k \leq P, \quad \mathbf{Q}_k \succeq 0,\ 1\leq k\leq K. \end{aligned} \tag{21.17}$$

The second problem is given as follows. *Assume that the channel realizations* $\mathbf{H}_k$ *are known and fixed. Solve the normalized sum* MSE[1] *minimization under the sum power constraint, that is,*

$$\begin{aligned} &\min \operatorname{tr}\left(\left[\mathbf{I}+\rho\sum_{k=1}^{K}\mathbf{H}_k\mathbf{Q}_k\mathbf{H}_k^H\right]^{-1}\right) \\ &\textit{subject to} \\ &\sum_{k=1}^{K}\operatorname{tr}\mathbf{Q}_k \leq P, \quad \mathbf{Q}_k \succeq 0,\ 1\leq k\leq K. \end{aligned} \tag{21.18}$$

The optimal transmit strategies in sum capacity maximization as well as sum MSE minimization have a very interesting intrinsic structure. This leads to one algorithmic structure which solves both programming problems. We start with

[1]For convenience, we omitted the constant terms $Kn_T - n_R$ in the normalized sum MSE.

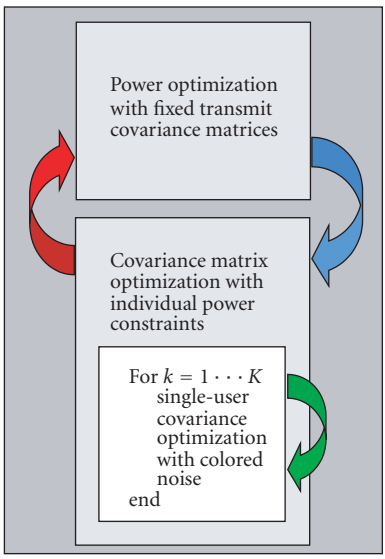

FIGURE 21.2. Sum performance optimization algorithm.

a top-down approach and present the signal processing structure which achieves the sum capacity or minimizes the normalized sum MSE, at first. The original problem of transmit strategy optimization is decomposed into two subproblems, namely the power allocation and the covariance matrix optimization under individual power constraints. This scheme is illustrated in Figure 21.2.

The transmit strategies of the K users are divided into two parts, namely, the power allocation and the transmit covariance matrix optimization for fixed power allocation. The outer loop is between power allocation $p_1, \ldots, p_K$ and covariance matrix $\mathbf{Q}_1, \ldots, \mathbf{Q}_K$ optimization under individual power constraints. The covariance matrix optimization can be decomposed into an inner loop in which single-user covariance matrix optimization with respect to the effective channel is performed. In the case in which the sum performance is measured by the sum capacity, the inner single-user waterfilling algorithm can be derived in closed form [4]. Then, the covariance matrix optimisation corresponds to iterative waterfilling. In the following, the two parts of the iterative algorithm are described in more detail.

21.3.1. Power optimization with fixed transmit covariance matrices

The programming problem for fixed transmit covariance matrices $\mathbf{Q}_1, \ldots, \mathbf{Q}_K$ reduces to a convex vector-valued optimization problem [12], that is, for the sum capacity optimization. *The channel realizations* $\mathbf{H}_k$ *of all users* k *are assumed to be known. Keep the transmit covariance matrices fixed* $\mathbf{Q}'_1, \mathbf{Q}'_2, \ldots, \mathbf{Q}'_K$. *Distribute a*

fixed amount of transmit power P across the mobiles, that is, solve

$$\begin{aligned} &\max \log\det\left(\mathbf{I}+\rho\sum_{k=1}^{K} p_k \mathbf{H}_k \mathbf{Q}_k' \mathbf{H}_k^H\right) \\ &\textit{subject to} \\ &\sum_{k=1}^{K} p_k \le P, \quad p_k > 0,\ 1 \le k \le K \end{aligned} \tag{21.19}$$

or for sum MSE minimization, *solve*

$$\begin{aligned} &\min \operatorname{tr}\left(\left[\mathbf{I}+\rho\sum_{k=1}^{K} p_k \mathbf{H}_k \mathbf{Q}_k' \mathbf{H}_k^H\right]^{-1}\right) \\ &\textit{subject to} \\ &\sum_{k=1}^{K} p_k \le P, \quad p_k > 0,\ 1 \le k \le K. \end{aligned} \tag{21.20}$$

Since, the programming problems in (21.19) and (21.20) are convex problems, they can be effectively solved by convex optimization techniques like interior point methods [12]. Especially for the sum capacity optimization, a tool called MAXDET [13] can be used. By analyzing the necessary and sufficient Karush-Kuhn-Tucker (KKT) optimality conditions, the optimal power allocation $p_1, \ldots, p_K$ can be characterized in the following way: for small SNR values, that is, for small P, only one user is supported, that is, $p_k = P$ and $p_{l\neq k} = 0$. If we increase the available transmit power (and the SNR), more and more users obtain partial transmit power. The first user which is supported has the maximum channel matrix eigenvalue, that is, $\lambda_{\max}(\mathbf{H}_k\mathbf{H}_k^H) \ge \lambda_{\max}(\mathbf{H}_{l\neq k}\mathbf{H}_{l\neq k})$. This has been shown in [7] for the sum MSE minimization and in [14] for the optimal transmit covariance matrices.

21.3.2. Transmit covariance matrix optimization under individual power constraints

We have the following two problems. For sum capacity optimization: *in order to maximize the sum capacity for fixed and known channel realizations* $\mathbf{H}_k$*, and for fixed power allocation* $p_1, \ldots, p_K$*, find the optimal transmit covariance matrices* $\mathbf{Q}_1^*, \ldots, \mathbf{Q}_K^*$*, that is, solve*

$$\begin{aligned} &\max \log\det\left(\mathbf{I}+\rho\sum_{k=1}^{K} \mathbf{H}_k \mathbf{Q}_k \mathbf{H}_k^H\right) \\ &\textit{subject to} \\ &\operatorname{tr}\mathbf{Q}_k \le p_k, \quad \mathbf{Q}_k \succeq 0,\ 1 \le k \le K \end{aligned} \tag{21.21}$$

or for sum MSE minimization:

$$\begin{aligned} &\max \operatorname{tr}\left(\left[\mathbf{I}+\rho\sum_{k=1}^{K}\mathbf{H}_k\mathbf{Q}_k\mathbf{H}_k^H\right]^{-1}\right) \\ &\textit{subject to} \\ &\operatorname{tr}\mathbf{Q}_k \le p_k, \quad \mathbf{Q}_k \succeq 0,\ 1 \le k \le K. \end{aligned} \tag{21.22}$$

The optimization problems in (21.21) and (21.22) are convex with respect to the transmit covariance matrices $\mathbf{Q}_1,\ldots,\mathbf{Q}_K$. However, since the objective function is matrix valued, the optimization is not as easy as in the power allocation case. Therefore, the optimization is further split into a series of single-user optimization problems which are to be solved one after the other. In each single-user optimization step, the other users and their received signals $\mathbf{H}_l\mathbf{Q}_l\mathbf{H}_l^H$ are treated as additional colored noise. This reduces the complexity of the algorithm from simultaneously optimizing K transmit covariance matrices to K succeeding single transmit covariance matrix optimizations. Especially for a large number of users K in the cell, the complexity is reduced. Hence, we arrive at the following two single-user optimization problems with colored noise. We treat the two cases sum capacity optimization and sum MSE minimization separately. For the kth user, we write the noise plus interference as

$$\mathbf{Z}_k = \mathbf{I}+\rho\sum_{\substack{l=1\\ l\neq k}}^{K}\mathbf{H}_l\mathbf{Q}_l\mathbf{H}_l^H. \tag{21.23}$$

21.3.2.1. Sum capacity

In the case in which the performance metric is the sum capacity, the single-user problem which is iteratively solved is the waterfilling with respect to the effective channel $\mathbf{Z}_k^{-1/2}\mathbf{H}_k$. For each user $k \in [1\cdots K]$, we solve the optimization problem

$$\begin{aligned} &\max \log\det\left(\mathbf{I}+\rho\overbrace{\mathbf{Z}_k^{-1/2}\mathbf{H}_k}^{\widetilde{\mathbf{H}}_k}\mathbf{Q}_k\mathbf{H}_k^H\mathbf{Z}_k^{-1/2}\right) \\ &\text{subject to} \\ &\operatorname{tr}(\mathbf{Q}_k) \le p_k, \quad \mathbf{Q}_k \succeq 0. \end{aligned} \tag{21.24}$$

The next result shows that the single-user covariance optimizations for all users $1 \le k \le K$ in (21.24) mutually solve the optimization problem (21.21). This result corresponds to [4, Theorem 3].

If all covariance matrices $\mathbf{Q}_k^*$ mutually solve the optimization problem in (21.24) *for $\mathbf{Z}_k$ in* (21.23)*, then they solve optimization problem in* (21.21) *for the sum capacity, too.*

The result follows from the fact that the optimization problem in (21.24) has the same optimality conditions as the original problem in (21.21).

In order to prove convergence of the iterative single-user water filling, note that the objective in (21.24) differs from the objective in (21.21) only by a constant which is independent of $\mathbf{Q}_k$. Therefore, in each single-user water filling step the sum capacity is increased. The channel matrix $\widetilde{\mathbf{H}}_k = \mathbf{Z}_k^{-1/2}\mathbf{H}_k$ in (21.24) is the effective channel which is weighted by the inverse noise plus interference. The iterative single-user performance algorithm in (21.24) solves the original optimization problem in (21.21).

21.3.2.2. Sum MSE

In the case in which the performance metric is the sum MSE, the single-user problem which is iteratively solved is the original sum MSE problem for fixed transmit strategies of the other users. For each user $k \in [1 \cdots K]$, we solve the optimization problem

$$\begin{aligned} &\min \operatorname{tr}\left(\left[\mathbf{I} + \mathbf{Z}_k + \rho \mathbf{H}_k \mathbf{Q}_k \mathbf{H}_k^H\right]^{-1}\right) \\ \text{subject to} \quad & \\ &\operatorname{tr}(\mathbf{Q}_k) \leq p_k, \quad \mathbf{Q}_k \succeq 0. \end{aligned} \tag{21.25}$$

The next result shows that the single-user covariance optimizations for all users $1 \leq k \leq K$ in (21.25) solve the optimization problem (21.22).

If all covariance matrices $\mathbf{Q}_k^*$ mutually solve the optimization problem in (21.25) *for*

$$\mathbf{Z}_k = \sigma_n^2 \mathbf{I} + \sum_{l=1, l\neq k}^{K} \mathbf{H}_l \mathbf{Q}_l \mathbf{H}_l^H, \tag{21.26}$$

then they solve optimization problem in (21.22)*, too.*

Note that the single-user optimization problem in (21.24) has an interesting interpretation: assume the single-user MSE optimization with colored noise $\mathbf{Z}_k = \mathbf{U}_Z \mathbf{\Lambda}_Z \mathbf{U}_Z^H$. We can write

$$\begin{aligned} \operatorname{tr}\left(\left[\mathbf{Z}_k + \rho \mathbf{H}_k \mathbf{Q}_k \mathbf{H}_k^H\right]^{-1}\right) &= \operatorname{tr}\left(\mathbf{\Lambda}_Z \left[\mathbf{I} + \rho \widetilde{\mathbf{H}}_k \mathbf{Q}_k \widetilde{\mathbf{H}}_k^H\right]^{-1}\right) \\ &= \sum_{l=1}^{n_R} \lambda_Z^{-1}(l) \left(\left[\mathbf{I} + \rho \widetilde{\mathbf{H}}_k \mathbf{Q}_k \widetilde{\mathbf{H}}_k^H\right]^{-1}\right)_{l,l}. \end{aligned} \tag{21.27}$$

The channel matrix $\widetilde{\mathbf{H}}_k = \mathbf{Z}_k^{-1/2}\mathbf{H}_k$ in (21.27) is the weighted effective channel. The iterative single-user MSE algorithm solves the original optimization problem in (21.22). However, in contrast to the iterative water filling algorithm, we cannot derive a simple algorithm which solves the single-user MSE problem because of the dependence on the noise eigenvalues in (21.27).

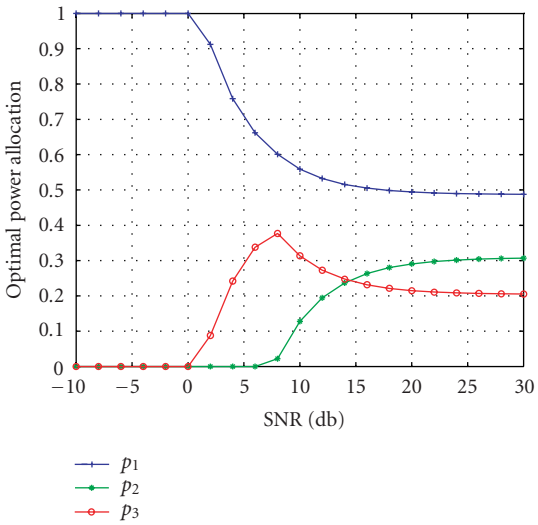

FIGURE 21.3. Example MIMO MAC, power allocation over SNR for sum capacity maximization, for MIMO $K = 3, n_t = 2, n_r = 2$.

21.3.3. Illustration of iterative algorithm

In Figure 21.3, the optimal power allocation for the three users of a MIMO system with three users with two transmit antenna each and a base with two receive antennas, is shown.

In Figure 21.3, it can be observed that SNR values up to 0 dB, only one user is active (user one). Then for SNR values up to 7 dB two users are active. For SNR values above 7 dB all three users are active. In contrast to the SIMO scenario, for SNR values approaching infinity, equal power allocation is not optimal. It is worth mentioning that the second user who is active for SNR values greater than zero, gets less transmit power than the third active user for SNR values above 15 dB. The roles of the users change in MIMO MAC due to the additional degree of freedom in choosing the transmit covariance matrices. Furthermore, the optimal power allocation does not converge to equal power allocation for SNR approaching infinity.

21.4. Performance region analysis

In contrast to the sum performance of multiuser MIMO systems, very little is known up to now about the complete performance region and how to achieve required points in the interior of the region. The difference between the sum performance and the complete region will be illustrated by an example for the capacity region and the sum capacity. We focus in this section on the mutual information as the performance metric. However, the results can be applied to other performance metrics as the individual MSEs or SINRs as well.

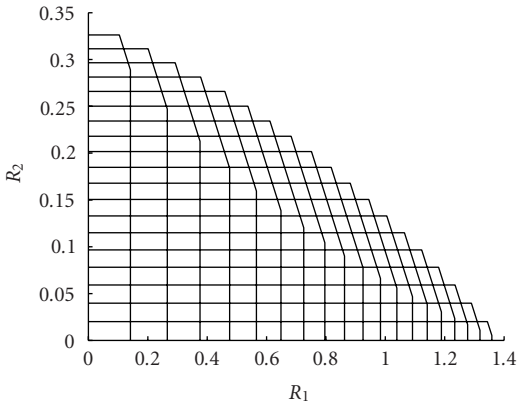

FIGURE 21.4. Example of a MAC capacity region.

In Figure 21.4, an example capacity region of a MAC is shown. It can be observed that the "atom" element which constitutes the whole region is one pentagon. For each power allocation p_1, p_2 and fixed pair of transmit covariance matrices $\mathbf{Q}_1$, $\mathbf{Q}_2$, the rate tupels inside one pentagon can be achieved. Since the base station performs SIC, there are two permutation orders in which the users signals can be decoded. The edge points in the interior of the capacity region correspond exactly with the two different decoding orders. For fixed transmit covariance matrices of user one $\mathcal{Q}_1$ and of user two $\mathcal{Q}_2$, respectively, the two rate tupels with the sum rate $R_s = \log\det(\mathbf{I} + \rho\mathbf{H}_1\mathcal{Q}_1\mathbf{H}_1^H + \rho\mathbf{H}_2\mathcal{Q}_2\mathbf{H}_2^H)$ are given by

$$\begin{aligned}(R_1^1, R_2^1) &= (\log\det(\mathbf{I} + \rho\mathbf{H}_1\mathcal{Q}_1\mathbf{H}_1^H), R_s - R_1^1),\\ (R_1^2, R_2^2) &= (R_s - R_2^2, \log\det(\mathbf{I} + \rho\mathbf{H}_1\mathcal{Q}_1\mathbf{H}_1^H)).\end{aligned} \tag{21.28}$$

In (R_1^1, R_2^1), the second user is decoded first without errors and subtracted since he is communicating with rate less than or equal to his capacity. For K users the resulting region is no longer a two-dimensional pentagon but a polymatroid. Polymatroids were introduced by Edmonds in [15]. This important structure of the achievable region has been used in [16, 17] for analyzing the ergodic and delay-limited capacity region for SISO multiuser channels under long-term power constraints.

In order to illustrate the recent results on the capacity region of multiple-antenna multiple-user channels and their achievability, we will assume in the following that the K users have rate requirements[2] $\gamma_1, \ldots, \gamma_K$ which has to be fulfilled.

[2]In general, the users have some QoS requirements depending on their service. The QoS requirement can be expressed in terms of rate requirements, SINR requirements, MSE requirements, or even in bit error rate (BER) requirements. We will focus on rate requirements.

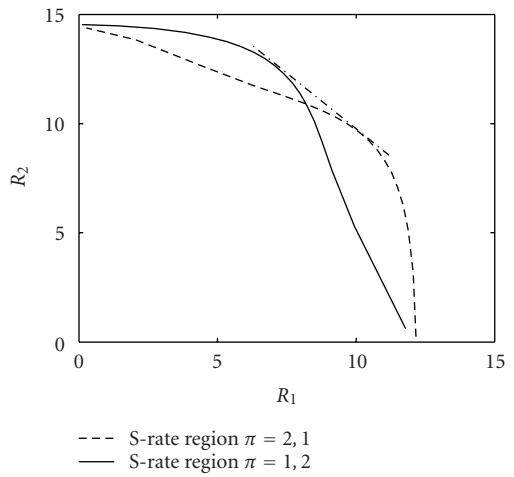

FIGURE 21.5. Example of a MIMO MAC capacity region.

The rate requirements should be fulfilled with minimum total transmit power, that is,

$$\min P \text{ subject to} \quad R_k \geq \gamma_k \quad \forall 1 \leq k \leq K. \tag{21.29}$$

It is well known for the SISO MAC that the region created by all achievable polymatroids is itself convex. In multiple antenna systems this in general is not the case. We show a typical MIMO MAC capacity region in Figure 21.5.

In Figure 21.5, it can be observed that the union of the achievable rate regions with decoding orders $\pi = \{1, 2\}$ and $\pi = \{2, 1\}$ is not convex. The line on which the sum capacity is achieved is missing (point-dashed line). Using the standard time sharing argument, the convex hull of the both so-called spatial (S) rate regions is the complete capacity region [18]. It turns out that all points on these S-rate regions can be achieved by convex optimization. However the points under the sum capacity area are only achievable by a linear combination of $K!$ corners of the sum capacity area. An efficient algorithm which computes the set of optimal transmit covariance matrices that achieve given performance requirements with minimal sum transmit power is still missing.

21.4.1. SISO MAC

First, we consider the SISO MAC channel with perfect CSI at the receiver and at the transmitter. The scalar channels of the users are given by $h_1, \ldots, h_K$. The following approach solves the programming problem in (21.29).

(1) First, order the users according to their channel realizations in descending order, with permutation π, that is, $h_{\pi_1} \leq h_{\pi_2} \leq \cdots \leq h_{\pi_K}$.

(2) Start with the first user and allocate power p_{π_1}, such that his rate requirement γ_{π_1} is fulfilled with identity

$$p_{\pi_1} = \frac{2^{\gamma_{\pi_1}} - 1}{\rho h_{\pi_1}}. \tag{21.30}$$

(3) Treat the interference which is created by undetected users as noise and go on for the next user in a similar manner.

In the SISO MAC the performance metrics of user k rate R_k, SINR_k, MSE_k are closely related by

$$R_k = \log\left(1 + \mathrm{SINR}_k\right) = \log\left(\frac{1}{\mathrm{MSE}_k}\right). \tag{21.31}$$

The described procedure solves the general problem of QoS requirement fulfillment. This result is included in [16, 17] for the multiple access channel and in [19, 20] for the broadcast channel with long-term power constraint and the optimization with respect to ergodic and delay-limited and outage capacity. If a long-term power constraint is applied, the power is distributed across the users as well as across time.

21.4.2. SIMO MAC

In the SIMO case, we concentrate on the performance metric SINR which is closely related to the rate and MSE (compare to (21.31)). Therefore, the time sharing argument cannot be applied, since we have stringent delay constraint. The results from this section can be found in [21, 22]. The SINR for the SIMO MAC with beamforming vectors $\mathbf{u}_1, \ldots, \mathbf{u}_K$ and power allocation $p_1, \ldots, p_K$ is given by

$$\mathrm{SINR}_k = \frac{p_k \mathbf{u}_k^H \mathbf{h}_k \mathbf{h}_k^H \mathbf{u}_k}{\mathbf{u}_k^H \mathbf{Z}_k \mathbf{u}_k} \tag{21.32}$$

with $\mathbf{Z}_k = \sum_{l=1}^{k-1} p_l \mathbf{h}_l \mathbf{h}_l^H + \sigma_n^2 \mathbf{I}$ as interference plus noise for the kth user. It is assumed that the base station performs SIC beginning with user K, then $K-1$ and so on. For fixed transmit powers $p_1, \ldots, p_K$ the optimal beamformers are scaled MMSE receivers, that is,

$$\mathbf{u}_k^* = \frac{\mathbf{Z}_k^{-1} \mathbf{h}_k}{\|\mathbf{Z}_k^{-1} \mathbf{h}_k\|^2}. \tag{21.33}$$

It remains to find the optimal power allocation that achieves the targets $\gamma_1, \ldots, \gamma_K$. The cascaded interference structure facilitates efficient computation of the optimal

power allocation. Start with $k = 1$ and solve

$$\mathbf{p}_k^* \mathbf{h}_k^H \mathbf{Z}_k^{-1} \mathbf{h}_k = \gamma_k \tag{21.34}$$

for all $k = 1, 2, \ldots, K$. The optimal decoding order is not known in general. It depends on the channel realizations as well as on the correlation between them. The interested reader is referred to [22, Section III].

21.4.3. MIMO MAC

In the MIMO case the problem in (21.29) has to be solved for rates $R_k^{\mathrm{SIC}}(\mathcal{Q}, \mathcal{H}, \rho)$ defined in (21.7). The approach in [18, Section IV B] provides the complete achievable S-rate region for the MIMO MAC. By solving the following optimization problem:

$$\max_{\mathcal{Q}} \sum_{k=1}^{K} q_k R_k^{\mathrm{SIC}}(\mathcal{Q}, \mathcal{H}, \rho) \tag{21.35}$$

under the constraint that the sum transmit power is constraint and all transmit covariance matrices are positive definite for a decoding order which corresponds to $q_1 \geq q_2 \geq \cdots \geq K$. The optimization problem in (21.35) is convex and can be efficiently solved by convex optimization methods [12].

In [7] it has been shown that the two-user region of unachievable individual MSEs is convex. It follows that the two-user region over $1 - \mathrm{MSE}_1$ and $1 - \mathrm{MSE}_2$ is convex, too. Because no SIC can be applied for MSE optimization, the optimization in (21.35) can be performed in order to achieve all points on the boundary of the achievable MSE region. The question remains, whether the K user region of unachievable individual MSEs is convex, or not. In general, it is a philosophical question what kind of performance measure to use and how to scale it properly.

Multiuser MIMO performance analysis and fulfillment of QoS requirement is a very active research area with many interesting puzzles and problems.

21.5. Open problems and further research topics

This section provided an overview of recent results in the area of information theoretic and performance analysis of multiple-user multiple-antenna systems. Recently, one of the big open problems in information theory was solved, namely, the capacity region of the nondegraded MIMO broadcast channel [23, 24, 25]. Nevertheless, there are many open problems in this area and we list a few of them.

(i) How to find all points on the boundary of the capacity region? This has been discussed in Section 21.4.

(ii) What happens if the perfect CSI assumption is relaxed? The case in which the mobiles have partial CSI, for example, covariance knowledge is discussed in [26, 27].

(iii) Duality theory: the capacity region of the MIMO MAC and the MIMO BC are equal under perfect CSI at transmitters and receivers [28]. Therefore, the results for the MIMO MAC can be transferred to the MIMO BC. What happens without the perfect CSI assumption?

(iv) Incorporating cross layer design issues, the queues, their arrival rates, and length at the mobiles, have to be taken into account. One established performance metric is the stability of the overall wireless communication system. Recently, many results were presented regarding this interesting topic [29, 18, 30].

Abbreviations

MIMO	Multiple-input multiple-output
MAC	Multiple access channels
CSI	Channel state information
SNR	Signal-to-noise ratio
SINR	Signal-to-interference and noise ratio
MSE	Mean Squared error
AWGN	Additive white gaussian noise
pdf	Probability density function
SIC	Successive interference cancellation
MMSE	Minimum mean square error
QoS	Quality-of-Service
BER	Bit error rate
SISO	Single-input single-output
SIMO	Single-input multiple-output
BC	Broadcast channel

Bibliography

[1] G. J. Foschini and M. J. Gans, "On limits of wireless communications in a fading environment when using multiple antennas," *Wireless Personal Communications*, vol. 6, no. 3, pp. 311–335, 1998.

[2] E. Telatar, "Capacity of multi-antenna Gaussian channels," *European Trans. Telecommunications*, vol. 10, no. 6, pp. 585–595, 1999.

[3] W. Yu, W. Rhee, S. Boyd, and J. M. Cioffi, "Iterative water-filling for vector multiple access channels," in *Proc. IEEE International Symposium on Information Theory (ISIT 2001)*, p. 322, Washington, DC, USA, June 2001.

[4] W. Yu, W. Rhee, S. Boyd, and J. M. Cioffi, "Iterative water-filling for Gaussian vector multiple access channels," *IEEE Trans. Inform. Theory*, vol. 50, no. 1, pp. 145–151, 2004.

[5] H. Boche and E. A. Jorswieck, "Sum capacity optimization of the MIMO Gaussian MAC," in *Proc. 5th Intern. Symp. on Wireless Personal Multimedia Communications (WPMC 2002)*, vol. 1, pp. 130–134, Honolulu, Hawaii, USA, October 2002, invited paper.

[6] W. Yu, W. Rhee, and J. M. Cioffi, "Optimal power control in multiple access fading channels with multiple antennas," in *Proc. IEEE International Conference on Communications (ICC '2001)*, vol. 2, pp. 575–579, Helsinki, Finland, June 2001.

[7] E. A. Jorswieck and H. Boche, "Transmission strategies for the MIMO MAC with MMSE receiver: average MSE optimization and achievable individual MSE region," *IEEE Trans. Signal Processing*, vol. 51, no. 11, pp. 2872–2881, 2003.

[8] E. A. Jorswieck and H. Boche, "Rate balancing for the multi-antenna Gaussian broadcast channel," in *Proc. 7th IEEE Intern. Symp. on Spread Spectrum Techniques and Applications (ISSSTA 2002)*, vol. 2, pp. 545–549, Prague, Czech Republic, September 2002.

[9] H. Boche and M. Schubert, "Solution of the SINR downlink beamforming problem," in *Proc. 36th Conf. on Information Sciences and Systems (CISS 2002)*, Princeton, NJ, USA, March 2002.

[10] E. A. Jorswieck and H. Boche, "On the optimal transmission strategy for the MIMO MAC with MMSE receiver," in *Proc. IEEE International Conference on Acoustics, Speech and Signal Processing (ICASSP '2003)*, vol. 5, pp. 109–112, Hong Kong, China, April 2003.

[11] D. N. C. Tse and S. V. Hanly, "Linear multiuser receivers: effective interference, effective bandwidth and user capacity," *IEEE Trans. Inform. Theory*, vol. 45, no. 2, pp. 641–657, 1999.

[12] S. Boyd and L. Vandenberghe, "Convex optimization," Course reader for EE364 (Stanford) and EE236 (UCLA), 2003.

[13] S. P. Wu, L. Vandenberghe, and S. Boyd, "MAXDET: software for determinant maximization problems, user's guide," Alpha Version, Stanford University, May 1996.

[14] H. Boche and E. A. Jorswieck, "Multiple antenna multiple user channels: optimisation in low SNR," in *Proc. IEEE Wireless Communications and Networking Conference (WCNC 2004)*, vol. 1, pp. 513–518, Atlanta, Ga, USA, March 2004.

[15] J. Edmonds, "Submodular functions, matroids, and certain polyhedra," in *Combinatorial Structures and Their Applications*, pp. 69–87, Gordon and Breach, New York, USA, 1970.

[16] D. N. C. Tse and S. V. Hanly, "Multiaccess fading channels. I. Polymatroid structure, optimal resource allocation and throughput capacities," *IEEE Trans. Inform. Theory*, vol. 44, no. 7, pp. 2796–2815, 1998.

[17] S. V. Hanly and D. N. C. Tse, "Multiaccess fading channels. II. Delay-limited capacities," *IEEE Trans. Inform. Theory*, vol. 44, no. 7, pp. 2816–2831, 1998.

[18] H. Boche and M. Wiczanowski, "Queueing theoretic optimal scheduling for multiple input multiple output multiple access channel," in *Proc. IEEE International Symposium on Signal Processing and Information Technology (ISSPIT 2003)*, pp. 576–579, Darmstadt, Germany, December 2003, invited paper.

[19] L. Li and A. J. Goldsmith, "Capacity and optimal resource allocation for fading broadcast channels. I. Ergodic capacity," *IEEE Trans. Inform. Theory*, vol. 47, no. 3, pp. 1083–1102, 2001.

[20] L. Li and A. J. Goldsmith, "Capacity and optimal resource allocation for fading broadcast channels. II. Outage capacity," *IEEE Trans. Inform. Theory*, vol. 47, no. 3, pp. 1103–1127, 2001.

[21] M. Schubert, *Power-aware spatial multiplexing with unilateral antenna cooperation*, Ph.D. thesis, Technical University of Berlin, Berlin, Germany, 2002.

[22] M. Schubert and H. Boche, "Iterative multiuser uplink and downlink beamforming under SINR constraints," to appear in *IEEE Trans. Signal Processing*.

[23] S. Vishwanath, G. Kramer, S. Shamai, S. Jafar, and A. Goldsmith, "Capacity bounds for Gaussian vector broadcast channels," in *Multiantenna Channels: Capacity, Coding and Signal Processing (Piscataway, NJ, 2002)*, vol. 62 of *DIMACS Ser. Discrete Math. Theoret. Comput. Sci.*, pp. 107–122, American Mathematical Society, Providence, RI, USA, 2003.

[24] P. Viswanath and D. N. C. Tse, "Sum capacity of the vector Gaussian broadcast channel and uplink-downlink duality," *IEEE Trans. Inform. Theory*, vol. 49, no. 8, pp. 1912–1921, 2003.

[25] H. Weingarten, Y. Steinberg, and S. Shamai (Shitz), "The capacity region of the Gaussian MIMO broadcast channel," in *Proc. Conference on Information Sciences and Systems (CISS 2004)*, pp. 7–12, Princeton, NJ, USA, March 2004.

[26] S. A. Jafar and A. Goldsmith, "Vector MAC capacity region with covariance feedback," in *Proceedings of International Symposium on Information Theory (ISIT)*, Washington, DC, USA, 2001.

[27] H. Boche and E. Jorswieck, "Uplink sum rate maximization with different types of channel state information at the transmitters," in *Proc. IEEE International Symposium on Signal Processing and Information Technology (ISSPIT 2003)*, pp. 423–426, Darmstadt, Germany, December 2003, invited paper.

[28] S. Vishwanath, N. Jindal, and A. Goldsmith, "Duality, achievable rates, and sum-rate capacity of Gaussian MIMO broadcast channels," *IEEE Trans. Inform. Theory*, vol. 49, no. 10, pp. 2658–2668, 2003.

[29] E. M. Yeh, "An inter-layer view of multiaccess communications," in *Proc. IEEE International Symposium on Information Theory (ISIT 2002)*, p. 112, Lausanne, Switzerland, June 2002.
[30] M. J. Neely, E. Modiano, and C. E. Rohrs, "Power allocation and routing in multibeam satellites with time-varying channels," *IEEE/ACM Trans. Networking*, vol. 11, no. 1, pp. 138–152, 2003.

Eduard A. Jorswieck: Heinrich-Hertz-Institut, Fraunhofer Institute for Telecommunications, Einsteinufer 37, 10587 Berlin, Germany
Email: eduard.jorswieck@hhi.fhg.de

22 Transmitting over ill-conditioned MIMO channels: from spatial to constellation multiplexing

David Gesbert and Jabran Akhtar

This chapter addresses the problem of multiplexing multiple data streams in a multiple-input multiple-output (MIMO) system in the presence of channel matrix ill-conditioning brought by fading correlation and/or a Rice component. Conventional multiplexing schemes based on the separation of the stream's spatial signatures (commonly referred to as spatial multiplexing—SM, V-BLAST architecture) rely on the *linear* independence between the channel responses corresponding to each transmit antenna. Consequently, such schemes suffer considerably from effects bringing ill conditioning in the MIMO channel matrix, such as fading correlation and Rice components. In an attempt to robustify SM schemes for deployment in a wide range or propagation terrains, we investigate the use of so-called *constellation* multiplexing (CM) whereby distinct M-QAM streams are superposed to form a higher-order QAM constellation with rate equivalent to the sum of rates of all original streams. CM schemes do not rely on MIMO channel full rankness to function properly. We thus seek an approach that allows bridging SM and CM schemes. We show that this can be realized in the form of a linear diagonal precoder. This in turn yields an adaptive rate-preserving MIMO multiplexing algorithm that can operate smoothly at any degree of correlation or Ricean factor. Conventional SM and CM schemes are shown to be particular cases of the presented family of schemes.

22.1. Introduction

Multiple-input multiple-output (MIMO) systems, are capable of providing a large increase in capacity compared to traditional single antenna systems [1, 2] (see also [3] for an overview of the area). This increase in capacity is however dependent upon the fact that the channels from a certain transmitter to the array of receivers, seen as vectors, are linearly separable. In other words, the conditioning of the equivalent MIMO channel matrix should be as good as possible. The capacity of MIMO systems can be shown to degrade if there are, for example, severe correlations present at the transmitter and/or receiver side [4, 5]. Similarly, [6] demonstrated that line of sight (LOS) components, while having a positive effect

on the outage behavior of the channel, are also capable of reducing the ergodic (i.e., average) capacity of MIMO systems. That is because the matrix representing the LOS component of wireless MIMO channels is typically extremely ill conditioned [5], at least if the base station antennas are located on a single array, and thus does not lend itself to matrix inversion. In fact with either strong transmit correlations or a high Ricean factor, the capacity behavior of the MIMO channel will ultimately become similar to that of a SIMO/MISO, with a possible additional array gain depending on the partial channel knowledge at the transmitter. If the LOS channel is very dominating, then the capacity falls back to that of an AWGN SISO system with additional array gain at the receiver.

Although the negative impact of correlation and the Rice component on average capacity behavior of MIMO systems is significant, the effect it has on the BER behavior of actual spatial multiplexing schemes [1, 7] is much more dramatic. That is, because conventional SM schemes (such as in linear MIMO detectors) rely explicitly or implicitly (such as in maximum likelihood MIMO detectors) on linear separability of the input spatial signatures to detect the data, unless a form of joint encoding is applied across the streams to differentiate them. In fact, any ill-conditioned components present in the channel effectively increase the linear dependence of the input streams and makes stream separation and decoding a difficult task. For example, current schemes like SM (V-BLAST) literally break down in the presence of correlation levels close to one or high Ricean factors. As a result, algorithms such as V-BLAST simply fail to adapt themselves and extract the nonzero capacity that is present in highly correlated or strongly Ricean channels.

Designing appropriate transmission techniques that can adjust to various kinds of channel and terrain scenarios is therefore an important and practical issue for the successful deployment of MIMO systems. To tackle this problem, the correlation and LOS component structure can be assumed to remain static over a "long-enough" period of time so that the corresponding channel parameters, unlike the fast fading coefficients, can be sent to the transmitter at regular intervals using a low rate feedback logical channel. This is consistent with upcoming third generation wireless standards and beyond.

To robustify the transmission of independent streams we build on the concept of constellation multiplexing (CM) whereby distinct streams (e.g., M-QAM) are superposed to form a higher-order constellation (say N-QAM $N > M$) with rate equivalent to the sum of rates of all original streams. For instance, a 16-QAM signal is the superposition of two 4-QAM signals. By construction CM schemes do not rely on MIMO channel full rankness to function properly. In contrast to SM schemes, the substreams in CM schemes are differentiated through *power scaling* rather than through spatial signatures. Indeed, two 4-QAM signals with appropriate scaling, forming a single 16-QAM, require only one transmit and receive antenna to be sent and detected. Hence, such schemes are clearly robust with respect to fading correlation and the Ricean factor. In this paper, we build upon the following two simple observations.

(i) CM schemes can be cast as spatial multiplexing schemes over a low-rank MIMO channel cascaded with a linear diagonal precoder.

(ii) In the case of constellations with regular lattice, the precoder is such that the probability of error for each stream is identical.

This suggests that simple linear precoding can be used for spatial multiplexing schemes as an attempt to circumvent effect of channel ill conditioning. This also suggests an optimization metric based on equating probabilities of error among the substreams. Precoding for correlated/Ricean MIMO channels has been considered among others in the case of (low-rate) space-time (ST) block coding schemes (including but not limited to [8]). In the case of spatial mutiplexing schemes (which can be seen as high-rate ST codes) however, the effect of propagation-related ill conditioning is much more dramatic because the transmitter design cannot guarantee channel orthogonality.

Although precoding for such correlated scenarios have previously been considered [9, 10, 11], the focus has mainly been on transmit correlation and quite often on capacity issues rather than on designing robust practical algorithms. To minimize the BER in the presence of transmit correlation and LOS channel, a transmit precoding scheme based on per-antenna phase shifting was proposed in [12] to improve the system performance. The main downside of this approach is that a numerical search is required to find the optimal phases.

Here, instead, the focus is on low-complexity, closed-form solutions for SM precoders that tackle both transmit correlation and Ricean channels. The precoder is found as the solution to a linear equation parametrized as a function of the transmit correlation coefficient and the line-of-sight MIMO channel matrix.

The precoder is derived under the BER balancing criterion (BBC) which aims at giving the same error performance over all spatially multiplexed streams, a criterion that is proved to determine our precoder fully. Clearly, the BBC criterion can be further weighted in order to accommodate unequal quality of service (QoS) targets.[1] The precoder is obtained under the hypothesis of a hybrid linear receiver (mixing concepts of maximum ratio and minimum mean square error receivers), but the resulting precoding coefficients are applicable over a wider range of receivers as shown in our simulations. In fact, the precoder can be interpretated as a linear data transform, bridging between SM and CM schemes. Under the case of zero correlation, Rayleigh channels, it matches the conventional SM approach. To the other extreme, it simply falls back to a CM scheme in the case of rank deficiency of the channel matrix. In that case, the scheme behaves equivalent to sending a single higher-order modulation whose independent components are mapped to the different antennas. In between these cases, the proposed algorithm will operate smoothly at all levels of correlation and Ricean factors.

The paper is organized as follows. First we present the mathematical models for signals and channels under the MIMO spatial multiplexing framework (Section 22.2). Then we introduce constellation multiplexing and its interpretation as a precoded form of spatial multiplexing for single transmit antenna systems (Section 22.3). In Section 22.4 we derive the precoder for the general case of MIMO with correlation and Rice component, first for two transmitters and then

[1] This issue is not addressed here however.

for any number of transmitters. We give numerical results in Section 22.6. Conclusions are given in Section 22.7.

Notations. The following notations are adopted throughout this paper. Vectors and matrices are denoted using bold-face lower-case letters and capitals, respectively. The symbol $(\cdot)^{\dagger}$ is used to refer to the Moore-Penrose pseudoinverse, while $\mathbf{H}_{:,i}$ points to the i'th column of the matrix $\mathbf{H}$ in a Matlab fashion. Similarly, $\mathbf{H}_{i,:}$ denotes the i'th row. $E\{\}$ is the expectation operator. The symbol $*$ refers to complex transpose of a vector/matrix.

22.2. Signal and channel models

22.2.1. Signal model

We consider the multiplexed transmission of N simultaneous data symbols s_1, $s_2, \ldots, s_N$ over a memoryless channel. The symbols are *treated as* independent, but an outer-code may be applied across the streams prior to multiplexing.

The symbols are selected from a normalized constellation such that $E\{|s_i|^2\}=1$. The minimum distance between two symbols for the given modulation is denoted by $d_{\min}$, while $d_{\max}$ $(\geq d_{\min})$ is the minimum distance between two constellation points with highest amplitude. In the 4-QAM case, $d_{\min} = d_{\max}$ as all symbols are transmitted with equal power. For 16-QAM, we have $d_{\min} = 3d_{\max}$, and so forth.

22.2.2. Channel model

We consider a Ricean MIMO flat fading channel consisting of N transmit antennas and M $(\geq N)$ receive antennas. For the sake of tractability, we will deal with correlation present at the transmitter only. A generalization of the precoding problem to deal in an elegant way with the receive correlation remains an open problem, although another version of this problem for precoding of space-time block codes was addressed in several papers, including, for example, [8, 13].

With transmit correlation and LOS component the channel matrix can be described by

$$\mathbf{H} = \sqrt{\frac{1}{K+1}}\mathbf{H}_0\mathbf{R}_t^{1/2} + \sqrt{\frac{K}{K+1}}\mathbf{H}_{\text{los}}. \tag{22.1}$$

The $M \times N$ channel matrix $\mathbf{H}_0$ consists of complex Gaussian zero mean unit-variance independent and identically distributed (i.i.d) elements, while $\mathbf{R}_t$ is the $N \times N$ transmit correlation matrix. $\mathbf{H}_{\text{los}}$, also of dimensions $M \times N$, is the LOS channel matrix, possibly being ill conditioned, and K defines the Ricean factor. The choice of $K = 0$ leads to a standard Rayleigh fading channel.

The baseband equivalent of the N-dimensional signal vector observed at the receiver can be expressed as

$$\mathbf{y} = \mathbf{H}\mathbf{s} + \mathbf{n}, \tag{22.2}$$

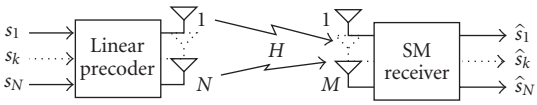

FIGURE 22.1. Spatial multiplexing with precoding.

where $\mathbf{n}$ is the M-dimensional noise vector whose entries are i.i.d complex Gaussian with zero mean and a variance of σ_n^2.

22.2.3. Linear precoding

We consider a memory less linear precoding of the N symbols according to the illustration in Figure 22.1. Although the most general precoder would take the form of an N by N matrix, we limit ourselves to a *diagonal* precoding of the symbols for the sake of closed-form derivability of the precoding coefficients. Furthermore, we argue (and confirm later) that robustness with respect to ill conditioning is brought about by the diagonal elements of the precoder first and foremost, as is also hinted at in Section 22.3.

The diagonally precoded transmitted vector, denoted by $\mathbf{s}$, is given by

$$\mathbf{s} = \left[\sqrt{P}_1 s_1 \sqrt{P}_2 e^{j\phi_2} s_2 \cdots \sqrt{P}_N e^{j\phi_N} s_N\right]^T. \tag{22.3}$$

$P_1, \ldots, P_N$ represent power levels allocated, respectively, to input symbols $s_1, \ldots, s_N$, and are selected to satisfy $\sum_{i=1}^{N} P_i = 1$. $\phi_2, \ldots, \phi_N$ correspond to phase shifts on each transmit antenna. Notice that the first symbol does not undergo a phase change and can be regarded as a reference point for all other phase components. We therefore define $\phi_1 = 0$. Standard SM (e.g., V-BLAST) assigns equal weights $P_i = 1/N$ and $\phi_i = 0$ for $1 \le i \le N$.

22.3. Constellation multiplexing

The concept of constellation multiplexing lies in the remark that higher (say QAM) constellations can be designed from the superposition of lower-order constellations. For instance, a single 16-QAM constellation achieving a rate of 4 bits per symbol can be realized by superposing two 4-QAM constellations, each achieving a rate of 2 bits per symbol, with scaling of 1/4 between the two 4-QAM signals, as shown in Figure 22.2 [14]. In the same manner, two superposed 16-QAM signals can be used from a 256-QAM signal if the second one is scaled in power by a factor 1/16. Or, again, three superposed 4-QAM signals will form a single 64-QAM signals if a power scaling of, respectively, 1/4 and 1/16 is used for the second and third 4-QAM signals. In general, the superposition of N 2^m-QAM constellations, achieving each m bits per symbol for a total rate of mN bits per symbol, can be represented by a single 2^{mN}-QAM constellation with the same total rate. To obtain

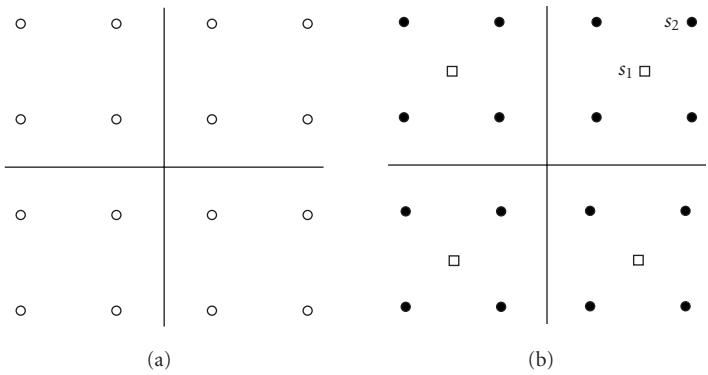

FIGURE 22.2. (a) Resulting equivalent 16-QAM constellation. (b) Illustration of two superimposed 4-QAM signals s_1 and s_2. The latter is scaled down in power by 1/4.

a regular grid for the 2^{mN}-QAM constellation, it suffices to apply a geometric scaling with factor r_m for every additional 2^m-QAM constellation. The factor r_m is a function of the ratio $d_{\max}/d_{\min}$ corresponding to the constellation used.

In other words, let s belong to a regular 2^{mN}-QAM constellation. Then there exist $r_m \in [0,1]$ and $s_1, s_2, \ldots, s_N$ symbols, each belonging to a 2^m-QAM constellation, such that s can be written in the form of

$$s = \sum_{k=1}^{N} r_m^k s_k, \tag{22.4}$$

where r_m is such that $\sum_{k=1}^{N} r_m^{2k} = 1$ so as to preserve the unit power of the signal.

22.3.1. Precoding for rank-one channels

Clearly, the signal shown in (22.4) can be reinterpretated as the signal being transmitted in a MIMO channel with rank-one with a simple precoder. Taking (22.2) with a rank-one MIMO channel in the generic form of $\mathbf{H} = [\mathbf{h}, \mathbf{h}, \ldots, \mathbf{h}]$, where $\mathbf{h}$ is an $M \times 1$ complex vector, and using (22.3) we find

$$\mathbf{y} = \mathbf{H}\mathbf{s} + \mathbf{n} = \mathbf{h} \sum_{k=1}^{N} \sqrt{P_k} e^{j\phi_k} s_k + \mathbf{n} = \mathbf{h}s + \mathbf{n}, \tag{22.5}$$

where the precoding coefficients are selected as

$$\begin{aligned} P_k &= r_m^{2k}, \quad k = 1 \cdots N, \\ \phi_k &= 0, \quad k = 1 \cdots N. \end{aligned} \tag{22.6}$$

Therefore, transmitting over a rank-one MIMO channel with an appropriate diagonal precoder is equivalent to transmitting over a higher-order constellation signal over a SIMO channel. This suggests that linear precoding can be used to deal effectively with rank deficient MIMO channels. In what follows, we explore this idea further and obtain closed-form precoding coefficients to handle all in-between scenarios with intermediate correlation and Ricean factors. We assume that the transmitter, in order to derive the precoder, has only knowledge of the slow-varying parameters of the channel (TDD system or FDD system with a low-rate feedback) such as the correlation structure, the line-of-sight MIMO component, and the Ricean factor.

For the sake of exposition, in the next section we start by describing the optimization procedure for the 2×2 case. The derivation is later extended to the case of arbitrary number of transmitter and receiver antennas.

22.4. Precoder optimization for 2×2 MIMO system

22.4.1. Receiver structure

As an aid toward finding a simple closed-form expression for the precoding weights, our calculation assumes a particular receiver combining structure based on maximum ratio combining (MRC). The principle behind the decoding structure is to successively estimate the substreams symbols in an iterative fashion, similar to V-BLAST [1], where the zero-forcing procedure is replaced with an MRC.

Although no optimality of this decoding method is claimed here, we draw the reader's attention on the fact that this approach allows us to derive the precoder expression in a compact fashion. It also yields results which make good intuitive sense and can easily be interpretated. Note that the use of MRC is consistent with bringing robustness against an ill conditioned channel, since a matrix inversion-based detector will generate a large noise enhancement in that case. Nevertheless, we show through simulations that the precoder behaves well when matched at the receiver with other more practical decoding methods such as maximum likelihood (ML) decoding. Simulation results are also presented with under MMSE decoding.

22.4.2. Detected signals

Writing out in full, the Ricean, transmit correlated, channel matrix in (22.1) in the 2×2 situation:

$$\mathbf{H} = \sqrt{\frac{1}{K+1}}\mathbf{H}_0 \begin{bmatrix} \alpha & \beta e^{j\psi} \\ \beta e^{-j\psi} & \alpha \end{bmatrix} + \sqrt{\frac{K}{K+1}} \begin{bmatrix} h_{1,1} & h_{1,2} \\ h_{2,1} & h_{2,2} \end{bmatrix}, \tag{22.7}$$

where by construction $\alpha^2 + \beta^2 = 1$, and $\rho = 2\alpha\beta$ is the modulus of the antenna correlation coefficient, and channel coefficients $h_{i,j}$ describe the components of the LOS matrix.

Without loss of generality in the decoding procedure we assume $P_1 \geq P_2$ and as the first part of the decoding, the receiver implements an MRC with the first row of $\mathbf{H}^*$. We find the following from (22.2), (22.3), and (22.7):

$$z_1 = (\mathbf{H}^*)_{1,:}\mathbf{y} = \tau_1\sqrt{P}_1 s_1 + \tau_2\sqrt{P}_2 e^{j\phi_2} s_2 + (\mathbf{H}^*)_{1,:}\mathbf{n}, \tag{22.8}$$

τ_1 denotes the total gain (normalized by $\sqrt{P_1}$) for s_1 as a result of the MRC, while τ_2 represents the effects of the interference. Further normalizing z_1 in (22.8), or alternatively from

$$\frac{1}{\tau_1} z_1 = \sqrt{P}_1 s_1 + \frac{\tau_2}{\tau_1}\sqrt{P}_2 e^{j\phi_2} s_2 + \frac{1}{\tau_1}(\mathbf{H}^*)_{1,:}\mathbf{n}, \tag{22.9}$$

where

$$\tau_1 = (\mathbf{H}^*)_{1,:}\mathbf{H}_{:,1}, \qquad \tau_2 = (\mathbf{H}^*)_{1,:}\mathbf{H}_{:,2}, \tag{22.10}$$

is the channel-related interference factor.

Equations (22.8) and (22.9) show that symbol s_2 will be superimposed upon s_1 as a function of the channel matrix, whose long-term behavior depends on the transmit correlation, the K factor, and the LOS channel matrix. Notice that this superimposition effectively reduces the minimum distance for detection of symbol s_1.

At this point we make the assumption that the interference's magnitude is small enough not to "move" the symbol s_1 out of its decision boundary, that is,

$$\left|\frac{\tau_2}{\tau_1}\right| \sqrt{P}_2 d_{\max} \leq \frac{1}{2}\sqrt{P_1} d_{\min}, \tag{22.11}$$

a symbol decision can be made on z_1 to obtain an estimate for s_1. For the sake of deriving the precoder, we assume that the correct decision is made on s_1, hence the symbol is subtracted from $\mathbf{y}$:

$$\hat{\mathbf{y}} = \mathbf{y} - \mathbf{H}_{:,1}\sqrt{P}_1 s_1. \tag{22.12}$$

The robustness of the precoder with respect to the assumption made in (22.11) is demonstrated implicitly in the simulations. An estimate for the second symbol can now be obtained through a second MRC,

$$z_2 = (\mathbf{H}^*)_{2,:}\hat{\mathbf{y}} = \tau_3\sqrt{P}_2 e^{j\phi_2} s_2 + (\mathbf{H}^*)_{2,:}\mathbf{n}, \tag{22.13}$$

where $\tau_3 = (\mathbf{H}^*)_{2,:}\mathbf{H}_{:,2}$.

22.4.3. Average channel behavior

We wish to design the precoder exclusively based upon knowledge of long-term parameters $h_{i,j}$, K, α, β, ψ, with no dependence on short-term varying parameter $\mathbf{H}_0$.

The performance of detection of s_1 depends on the instantaneous minimum distance in $\hat{z}_1$, however for the optimization of the weights P_1, P_2, and phases to be independent of $\mathbf{H}_0$, we base ourselves upon an "average" channel behavior. To this end, we introduce the following quantity modified from (22.8) by averaging over the instantaneous channel realizations:

$$\hat{z}_1 = E\{\tau_1\}\sqrt{P}_1 s_1 + E\{\tau_2\}\sqrt{P}_2 e^{j\phi_2} s_2. \tag{22.14}$$

A rather straightforward calculation can then be used to show that (see Section 22.5)

$$\begin{aligned} E\{\tau_1\} &= \frac{1}{K+1}\left(2 + K\left(h_{1,1}^* h_{1,1} + h_{2,1}^* h_{2,1}\right)\right), \\ E\{\tau_2\} &= \frac{1}{K+1}\left(2\rho e^{j\psi} + K\left(h_{1,1}^* h_{1,2} + h_{2,1}^* h_{2,2}\right)\right). \end{aligned} \tag{22.15}$$

Clearly, with $\rho = 0$ and $K = 0$ we find $E\{\tau_1\} = 2$ and $E\{\tau_2\} = 0$. This shows the MRC returning an average array gain factor of 2 (3 dB).

22.4.4. Evaluation of minimum distances under average channel behavior

Next we evaluate the minimum distances, which dictate the error performance of the symbols, under average channel behavior, by considering the absolute average value of each individual gain factor in $E\{\tau_1\}$ and $E\{\tau_2\}$. For s_1, the minimum distance is found from (22.14) for, for example, $s_2 = -s_1$,

$$\delta_1 = E\{\tau_1\}\sqrt{P}_1 d_{\min} - \overline{E\{\tau_2\}}\sqrt{P}_2 d_{\max}, \tag{22.16}$$

where

$$\overline{E\{\tau_2\}} = \frac{1}{K+1}\left(2\rho + K\left|h_{1,1}^* h_{1,2} + h_{2,1}^* h_{2,2}\right|\right), \tag{22.17}$$

$\overline{E\{\tau_2\}}$ represents the average absolute gain coming from the correlation and the LOS channel components.

Similarly, the gain for s_2 under average channel behavior in (22.13) can be described by

$$\hat{z}_2 = E\{\tau_3\}\sqrt{P}_2 e^{j\phi_2} s_2, \tag{22.18}$$

where one can show that (see Section 22.5)

$$E\{\tau_3\} = \frac{1}{K+1}\left(2 + K\left(h_{1,2}^* h_{1,2} + h_{2,2}^* h_{2,2}\right)\right). \tag{22.19}$$

This leads to the following minimum distance for s_2:

$$\delta_2 = E\{\tau_3\}\sqrt{P}_2 d_{\min}. \tag{22.20}$$

22.4.5. Precoding coefficients with the BER balancing criterion (BBC)

22.4.5.1. Phase optimization

If the average gain coming from $E\{\tau_2\}$ is nonzero, then by selecting the phase ϕ_2 accordingly, the distance from the decision boundary can be maximized for s_1. For an arbitrary QAM modulation, this is done by selecting ϕ_2 at the emitter such that

$$\phi_2 = -\angle E\{\tau_2\}, \tag{22.21}$$

which aligns up the symbols in a coherent fashion.

22.4.5.2. Power optimization

The noise entries of $\mathbf{H}_{1,:}^{*}\mathbf{n}$ and $\mathbf{H}_{2,:}^{*}\mathbf{n}$ all follow the same distribution, similarly all components in $\mathbf{H}^{*}$ also have an identical statistical structure. Thus, the noise factors have identical variance when averaged over $\mathbf{H}_0$. We can therefore equate the average probability of error for s_1 and s_2 simply by equating the minimum distances found in (22.16) and (22.20),

$$E\{\tau_1\}\sqrt{P}_1 d_{\min} - \overline{E\{\tau_2\}}\sqrt{P}_2 d_{\max} = E\{\tau_3\}\sqrt{P}_2 d_{\min}, \tag{22.22}$$

under constraint

$$P_1 + P_2 = 1. \tag{22.23}$$

For clarity we rewrite (22.22) as

$$\mu_1\sqrt{P}_1 - \mu_2\sqrt{P}_2 = \mu_3\sqrt{P}_2, \tag{22.24}$$

where we have defined $\mu_1 = E\{\tau_1\}d_{\min}$, $\mu_2 = \overline{E\{\tau_2\}}d_{\max}$, and $\mu_3 = E\{\tau_3\}d_{\min}$. The weights for this 2×2 system can easily be computed as functions of μ to be

$$P_1 = \frac{(\mu_2 + \mu_3)^2}{\mu_1^2 + (\mu_2 + \mu_3)^2}, \qquad P_2 = \frac{\mu_1^2}{\mu_1^2 + (\mu_2 + \mu_3)^2}, \tag{22.25}$$

or written out in full:

$$P_1 = \frac{\left[d_{\max}(2\rho + K|\alpha|) + d_{\min}\left(2 + K\left(|h_{1,2}|^2 + |h_{2,2}|^2\right)\right)\right]^2}{d_{\min}^2\left(2+K\left(|h_{1,1}|^2+|h_{2,1}|^2\right)\right)^2+\left[d_{\max}(2\rho+K|\alpha|)+d_{\min}\left(2+K\left(|h_{1,1}|^2+|h_{2,1}|^2\right)\right)\right]^2},$$

$$P_2 = \frac{d_{\min}^2\left(2+K\left(|h_{1,1}|^2+|h_{2,1}|^2\right)\right)^2}{d_{\min}^2\left(2+K\left(|h_{1,1}|^2+|h_{2,1}|^2\right)\right)^2+\left[d_{\max}(2\rho+K|\alpha|)+d_{\min}\left(2+K\left(|h_{1,1}|^2+|h_{2,1}|^2\right)\right)\right]^2}, \tag{22.26}$$

where $\alpha = h_{1,1}^* h_{1,2} + h_{2,1}^* h_{2,2}$.

22.4.6. Interpretations

Observe that $\alpha = h_{1,1}^* h_{1,2} + h_{2,1}^* h_{2,2}$ in the expression for $\overline{E\{\tau_2\}}$ directly measures the ill conditioning of $\mathbf{H}_{\text{los}}$. For instance, in the (unrealistic) case that the LOS component is orthogonal, then $\alpha = 0$. This is intuitively appealing because one expects the precoder to depend on whether the LOS component is easily invertible or not.

Special cases.

(i) **No LOS:** with a small K, the expressions give more attention to the effects of transmit correlation. For instance, $K = 0$ gives $\phi_2 = -\psi$, while $\mu_1 = 2$, $\mu_2 = 2\rho$, and $\mu_3 = 2$, which results in the following solution:

$$P_1 = \frac{\left(1 + (d_{\max}/d_{\min})\rho\right)^2}{1 + \left(1 + (d_{\max}/d_{\min})\rho\right)^2},$$
$$P_2 = \frac{1}{1 + \left(1 + (d_{\max}/d_{\min})\rho\right)^2}. \tag{22.27}$$

Notice that $d_{\max}/d_{\min} = 1$ for 4-QAM and $d_{\max}/d_{\min} = 3$ for 16-QAM, for example. In the 4-QAM case, the precoder is thus

$$P_1 = \frac{(1+\rho)^2}{1 + (1+\rho)^2},$$
$$P_2 = \frac{1}{1 + (1+\rho)^2}. \tag{22.28}$$

(a) **Uncorrelated:** with no correlation $\rho = 0$ which yields equal power transmission, justifying the standard V-BLAST design corresponding to spatial multiplexing.

(b) **Fully correlated:** with full correlation $\rho = 1$ we find $P_1 = 0.8$ and $P_2 = 0.2$. Interestingly, this corresponds to the power allocation for a regular 2D constellation. For instance, a unit power 16-QAM constellation can be seen as the superposition of two 4-QAM constellations with respective powers 0.8 and 0.2 (see Figure 22.2). Hence, the spatial multiplexing is here replaced by constellation multiplexing.

(ii) **Strong LOS:** with $K \to \infty$ and a strongly ill conditioned $\mathbf{H}_{\text{los}}$, we find $\mu_1 \approx \mu_2 \approx \mu_3$, giving $P_1 = 0.8$ and $P_2 = 0.2$ (4-QAM). If the LOS component is better conditioned, the scheme performs a mix of spatial and constellation multiplexing.

22.5. Optimization for an arbitrary MIMO system

For a general MIMO setup, the MRC precoder may easily be extended as follows. We first assume that the power weights satisfy

$$P_1 \geq P_2 \geq \cdots \geq P_N. \tag{22.29}$$

Thus, in an iterative detection procedure, s_1 becomes the first symbol to be decoded, followed by s_2, and so forth, in a chronological order.

To derive the appropriate values of $P_1, \ldots, P_N$ and phases, the average gain and interference factors need to be calculated. The average gain coming from cross interference of the LOS channel and the remaining channel $\mathbf{H}_0\mathbf{R}_t^{1/2}$ is clearly zero, that is, $E\{(\mathbf{H}_0\mathbf{R}_t^{1/2})^*\mathbf{H}_{\text{los}}\} = E\{\mathbf{H}_{\text{los}}^*(\mathbf{H}_0\mathbf{R}_t^{1/2})\} = \mathbf{0}$.

We therefore obtain

$$\begin{aligned} E\{\mathbf{H}^*\mathbf{H}\} &= \frac{1}{K+1}E\left\{\left(\mathbf{H}_0\mathbf{R}_t^{1/2}\right)^*\left(\mathbf{H}_0\mathbf{R}_t^{1/2}\right)\right\} + \frac{K}{K+1}\mathbf{H}_{\text{los}}^*\mathbf{H}_{\text{los}} \\ &= \frac{M}{K+1}\mathbf{R}_t + \frac{K}{K+1}\mathbf{H}_{\text{los}}^*\mathbf{H}_{\text{los}}. \end{aligned} \tag{22.30}$$

Element k,l $(1 \leq k,l \leq N)$ can then be written out explicitly as

$$E\{\mathbf{H}^*\mathbf{H}\}_{k,l} = \frac{1}{K+1}\left(M\rho_{k,l} + K\sum_{i=1}^{M} h_{i,l}^* h_{i,k}\right). \tag{22.31}$$

Taking into account the absolute gain coming from both factors, we define

$$\gamma_{k,l} = \frac{1}{K+1}\left(M\rho_{k,l} + K\left|\sum_{i=1}^{M} h_{i,l}^* h_{i,k}\right|\right). \tag{22.32}$$

As previously, channel coefficients $h_{i,j}$ represent elements of the LOS matrix, while $\rho_{k,l}$ describes the nonnegative coefficients of the correlation matrix $\mathbf{R}_t$, where $\rho_{k,k} = 1$.

Assuming an iterative MRC receiver, the average minimum distance for s_1 becomes

$$\delta_1 = \gamma_{1,1}\sqrt{P}_1 d_{\min} - \gamma_{1,2}\sqrt{P}_2 d_{\max} - \cdots - \gamma_{1,N}\sqrt{P}_N d_{\max}. \tag{22.33}$$

After a symbol estimation/subtraction, the minimum distance for s_2 can be found:

$$\delta_2 = \gamma_{2,2}\sqrt{P}_2 d_{\min} - \gamma_{2,3}\sqrt{P}_3 d_{\max} - \cdots - \gamma_{2,N}\sqrt{P}_N d_{\max}. \tag{22.34}$$

By repeating this N times, we obtain expressions for N minimum distances,

$$\delta_N = \gamma_{N,N}\sqrt{P}_N d_{\min}. \tag{22.35}$$

22.5.1. Phase optimization

To cancel out the phase shifts introduced for s_1, the most significant symbol, we set

$$\phi_i = -\angle E\{\mathbf{H}^*\mathbf{H}\}_{1,i} = -\angle\left(M\rho_{1,i} + K\sum_{k=1}^{M} h_{k,i}^* h_{k,1}\right), \tag{22.36}$$

for $i = 2,\ldots,N$.

If the transmitter and receivers are positioned far from each other, and the arrays are placed broadside to each other, which is a practical situation in many applications, then the channel model can be approximated as [6]

$$\mathbf{H} = \sqrt{\frac{1}{K+1}}\mathbf{H}_0\mathbf{R}_t^{1/2} + \sqrt{\frac{K}{K+1}}e^{j\theta}\mathbf{1}. \tag{22.37}$$

If, in addition, a constant phase shift, or an exponential correlation model, is applied for the transmit correlation matrix, then the solution provided by (22.36) will hold for all symbols [15] as long as K is small. For larger values of K, $\mathbf{H}_{\text{los}}$ will dominate and the single phase shift it introduces can be canceled out for all symbols by selecting $\phi_i = -\theta$, $i = 2,\ldots,N$.

Nevertheless, for this particular MRC receiver, the exact phase rotation is also dependent upon $\mathbf{H}_0$, which the transmitter is unaware of, and the selection of (22.36) will in practice therefore only have minor effect. In contrast, the decoder of [16] eliminates $\mathbf{H}_0$ before further processing and the phase change thus plays a more important role. The essential information destined to differentiate the signals is though determined by the choice of power weights.

22.5.2. Weight optimization

To guarantee all symbols an equal error rate, it is sufficient that values for $\sqrt{P}_1$, $\sqrt{P}_2, \ldots, \sqrt{P}_N$ be selected so that on average the minimum symbol distance observed for each symbol is identical,

$$\delta_1 = \delta_N, \qquad \delta_2 = \delta_N, \ldots, \delta_{N-1} = \delta_N. \tag{22.38}$$

Based on (22.38), the following linear system can then be set up as part of the problem to find the appropriate power levels:

$$\mathbf{\Delta p} = \mathbf{0}, \tag{22.39}$$

where

$$\mathbf{\Delta} = \begin{bmatrix} \gamma_{1,1}\check{d} & -\gamma_{1,2}\hat{d} & -\gamma_{1,3}\hat{d} & \cdots & -\gamma_{N,N}\check{d} - \gamma_{1,N}\hat{d} \\ 0 & \gamma_{2,2}\check{d} & -\gamma_{2,3}\hat{d} & \cdots & -\gamma_{N,N}\check{d} - \gamma_{2,N}\hat{d} \\ & & \cdots & & \\ 0 & 0 & 0 & \gamma_{N-1,N-1}\check{d} & -\gamma_{N,N}\check{d} - \gamma_{N-1,N}\hat{d} \end{bmatrix}, \tag{22.40}$$

$$\mathbf{p} = \left[\sqrt{P}_1 \sqrt{P}_2 \cdots \sqrt{P}_N\right]^T \tag{22.41}$$

and $\mathbf{0}$ is a vector with N zero elements. To obtain a compact notation we have used $\check{d} = d_{\min}$ and $\hat{d} = d_{\max}$.

The upper triangular system (22.40) only contains $N - 1$ equations for N unknowns, however, any solution must also satisfy $\sum_{i=1}^{N} P_i = 1$. Therefore, $\mathbf{p}$ can be found as the only unit-norm all-positive vector in the null space of $\mathbf{\Delta}$. For a proof we refer to the appendix. Therefore, the BBC criterion determines the precoder in a unique way (up to trivial ambiguities like a rotation, etc.).

Extreme LOS cases. (i) Ideal Rayleigh case: if $K = 0$ and $\rho = 0$, we find $\gamma_{k,l} = 0$, $(1 \le k,\ l \le N,\ k \ne l)$ and from (22.40) one can easily see that this gives $P_i = 1/N$, that is, equal power distribution across all streams.

(ii) On the other hand, with a strong K factor and high level of ill conditionality (e.g., (22.37)), we can assume all $\gamma_{k,l}$ to be of roughly equal value. For instance, in the 4-QAM case (i.e., with $d_{\min} = d_{\max}$), this gives rise to the following (scale corrected) matrix:

$$\mathbf{\Delta} = \begin{bmatrix} 1 & -1 & -1 & \cdots & -2 \\ 0 & 1 & -1 & \cdots & -2 \\ & & \cdots & & \\ 0 & 0 & & 1 & -2 \end{bmatrix}. \tag{22.42}$$

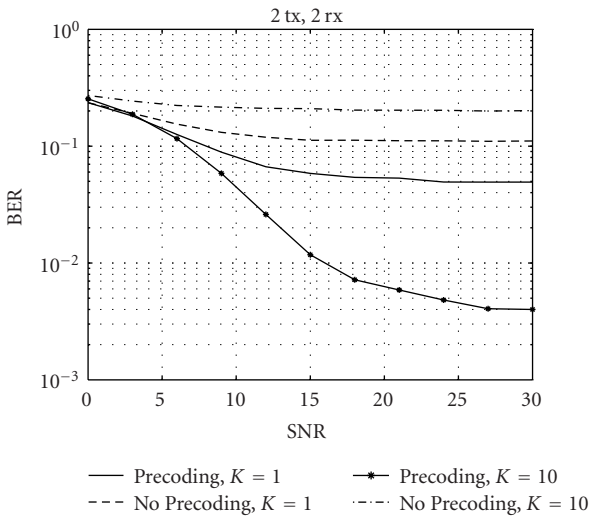

FIGURE 22.3. $K = 1$, $K = 10$, MRC with/without precoding.

This linear system can easily be solved through back substitution and under the energy constrain one arrives to

$$P_i = \frac{3 \cdot 4^N}{4^i(4^N - 1)}, \quad i = 1, \ldots, N. \tag{22.43}$$

The energy for this setup decreases by one quarter from symbol s_i to s_{i+1}. The final form of the received signal $\hat{z}_1$ will conclusively simply correspond to a standard 4^N-QAM modulation.

22.6. Simulations

This section demonstrates the effectiveness of the precoder through Monte Carlo simulations. We use the following receiver structures and compare the results with and without precoding

(i) MRC SIC (successive interference cancelling) decoder, used to derive the precoding weights.
(ii) MMSE SIC decoder. The receiver is similar to the one above, but rather implements an MMSE matrix inversion to estimate the symbols in each iteration.
(iii) ML, an exhaustive maximum likelihood search is carried out.

Illustrating the first simulation, Figure 22.3 shows the simulation results for the MRC decoder assuming $K = 1$, $K = 10$ under the channel model of (22.37) and no transmit correlation. The use of MRC introduces residual symbol interference showing up as a flooring effect, however, the precoder nevertheless manages to bring in a noticeable improvement.

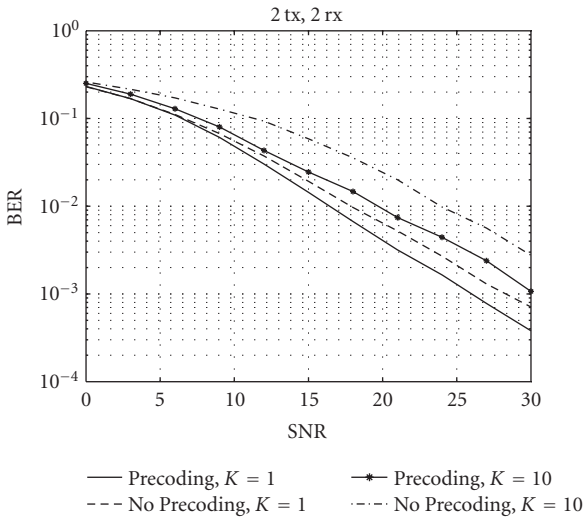

FIGURE 22.4. $K = 1$ and $K = 10$, MMSE SIC with/without precoding.

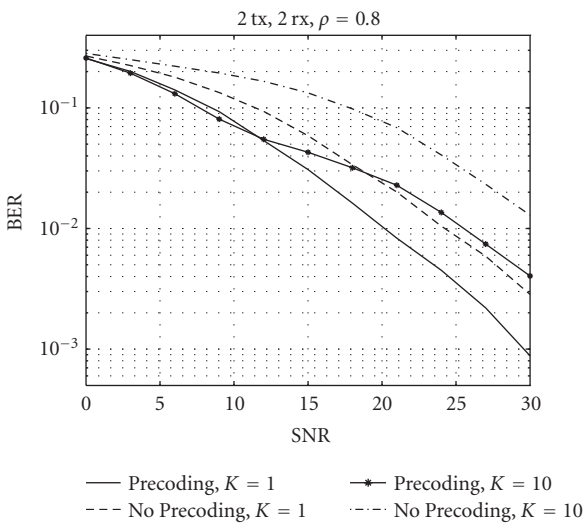

FIGURE 22.5. $K = 1$ and $K = 10$, $\rho = 0.8$, MMSE SIC with/without precoding.

Illustrating the second simulation plot, Figure 22.4 displays the use of MMSE SIC receiver structure with/without precoding under the same channel conditions as previously. In Figure 22.5, the same simulations have been extended with transmit correlation being set at $\rho = 0.8$. Even at low K-factors, having a precoder clearly becomes beneficial.

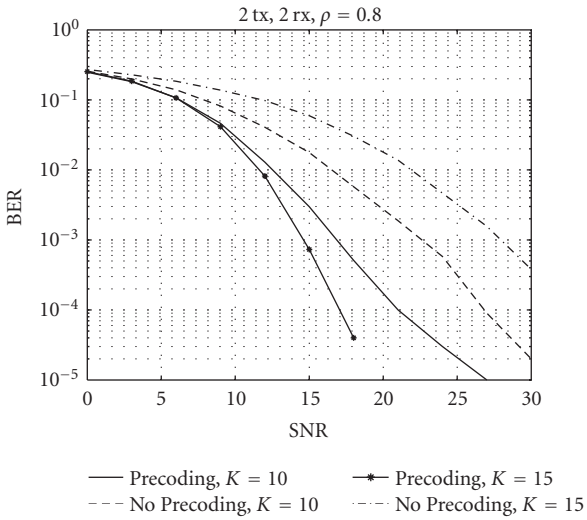

FIGURE 22.6. $K = 10$ and $K = 15$, ML with/without precoding.

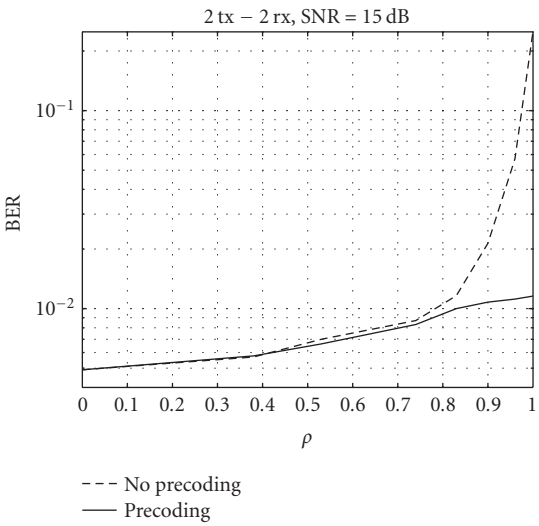

FIGURE 22.7. 2×2 case. Improvement due to the proposed precoder with the ML receiver as function of correlation.

Figure 22.6 uses ML as the decoder, the K-factors being 10 and 15 and with no transmit correlation assumption. A high K-factor with precoding makes the slope of the curve steeper as the fading is virtually nonexisting.

Finally, in Figure 22.7 we demonstrate the use of ML decoding at SNR of 15 dB, $K = 0$, for a 2×2 setup with transmitter correlation ranging from $\rho = 0$ to $\rho = 1$. The difference between ML with or without precoding is relatively small at

low correlation levels but becomes very substantial with higher degrees of transmit correlation.

22.7. Conclusions

In this chapter, we proposed a simple closed-form power weighting approach making use of the average channel knowledge to adapt the transmitted constellation. The derivation assumes an MRC-based decoder however the weights may be applied on a wider range of receiver structures. This offers a way to preserve a constant data rate for any correlation level and for well- or ill-behaved LOS components.

Appendix

Due to the specific structure of (22.40) there exists a solution to (22.39), where all entries of $\mathbf{p}$ are nonnegative. Observe that the left $N-1 \times N-1$ submatrix of $\boldsymbol{\Delta}$ is upper triangular and contains unit entries on the diagonal, while all other elements are nonpositive. The last column of $\boldsymbol{\Delta}$ however consists of all strictly negative entries.

From the format of (22.40), it is clear that $\sqrt{P}_N \neq 0$ otherwise all elements in $\mathbf{p}$ would become zero. Without loss of generality, we can therefore set $\sqrt{P}_N = 1$. Moving the last column to the right-hand side gives a strictly positive vector and the upper unit triangular system can be solved by back substitution to find $\sqrt{P_{N-1}}, \ldots, \sqrt{P_1}$. A suitable scaling can then assure proper normalization and the result follows.

Acknowledgments

The authors acknowledge the support in part of Telenor AS, Norway. Part of this paper appeared in the proceedings of the IEEE Globecom 2004.

Abbreviations

AWGN	Additive white Gaussian noise
BER	Bit error rate
BBC	BER balancing criterion
CM	Constellation multiplexing
LOS	Line of sight
MIMO	Multiple-input multiple-output
MISO	Multiple-input single-output
M-QAM	M-quadrature amplitude modulation
QoS	Quality of service
SIMO	Single-input multiple-output
SM	Spatial multiplexing
V-BLAST	Vertical Bell-Labs Layered Space-Time

Bibliography

[1] G. J. Foschini, "Layered space-time architecture for wireless communication in a fading environment when using multiple antennas," *Bell Labs. Technical Journal*, vol. 1, no. 2, pp. 41–59, 1996.

[2] G. J. Foschini and M. J. Gans, "On limits of wireless communications in a fading environment when using multiple antennas," *Wireless Personal Communications*, vol. 6, no. 3, pp. 311–335, 1998.

[3] D. Gesbert, M. Shafi, D. Shiu, P. J. Smith, and A. Naguib, "From theory to practice: an overview of MIMO space-time coded wireless systems," *IEEE J. Select. Areas Commun.*, vol. 21, no. 3, pp. 281–302, 2003.

[4] D. Shiu, G. J. Foschini, M. J. Gans, and J. M. Kahn, "Fading correlation and its effect on the capacity of multielement antenna systems," *IEEE Trans. Commun.*, vol. 48, no. 3, pp. 502–513, 2000.

[5] D. Gesbert, H. Bölcskei, D. A. Gore, and A. J. Paulraj, "Outdoor MIMO wireless channels: models and performance prediction," *IEEE Trans. Commun.*, vol. 50, no. 12, pp. 1926–1934, 2002.

[6] M. A. Khalighi, J. M. Brossier, G. Jourdain, and K. Raoof, "On capacity of Ricean MIMO channels," in *Proc. 2001 IEEE 12th Int. Symposium Personal, Indoor Mobile Radio Communications*, vol. 1, pp. A150–A154, San Diego, Calif, USA, September-October 2001.

[7] D. Gesbert, "Robust linear MIMO receivers: a minimum error-rate approach," *IEEE Trans. Signal Processing*, vol. 51, no. 11, pp. 2863–2871, 2003.

[8] G. Jongren, M. Skoglund, and B. Ottersten, "Combining beamforming and orthogonal space-time block coding," *IEEE Trans. Inform. Theory*, vol. 48, no. 3, pp. 611–627, 2002.

[9] S. A. Jafar, S. Vishwanath, and A. J. Goldsmith, "Channel capacity and beamforming for multiple transmit and receive antennas with covariance feedback," in *Proc. IEEE International Conference on Communications (ICC '01)*, vol. 7, pp. 2266–2270, Helsinki, Finland, 2001.

[10] M. Ivrlač and J. Nossek, "On the impact of correlated fading for MIMO-systems," in *Proc. IEEE International Symposium on Circuits and Systems*, vol. 3, pp. 655–658, Scottsdale, Ariz, USA, May 2002.

[11] R. U. Nabar, H. Bölcskei, and A. Paulraj, "Transmit optimization for spatial multiplexing in the presence of spatial fading correlation," in *Proc. IEEE Global Telecommunications Conference (GLOBECOM '01)*, vol. 1, pp. 131–135, San Antonio, Tex, USA, November 2001.

[12] R. U. Nabar, H. Bölcskei, and A. Paulraj, "Cut-off rate based transmit optimization for spatial multiplexing on general MIMO channels," in *Proc. IEEE International Conference on Acoustics, Speech, and Signal Processing*, vol. 5, pp. V61–V64, Hong Kong, China, April 2003.

[13] A. Hjørungnes, D. Gesbert, and J. Akhtar, "Precoding of space time block coded signals for joint transmit-receive correlate MIMO channels," to appear in *IEEE Trans. on Wireless Communications*.

[14] B. Sklar, *Digital Communications*, Prentice Hall, Upper Saddle River, NJ, USA, 2000.

[15] J. Akhtar and D. Gesbert, "Spatial multiplexing over correlated MIMO channels with a closed form precoder," to appear in *IEEE Trans. Wireless Communications*.

[16] J. Akhtar and D. Gesbert, "A closed-form precoder for spatial multiplexing over correlated MIMO channels," in *Proc. IEEE Global Telecommunications Conference (GLOBECOM '03)*, pp. 1847–1851, San Francisco, Calif, USA, December 2003.

David Gesbert: Department of Mobile Communications, Eurecom Institute, 2229 Routes des Cretes, BP 193 06904, Sophia Antipolis, France

Email: gesbert@eurecom.fr

Jabran Akhtar: Department of Informatics, University of Oslo, 0316 Oslo, Norway

Email: jabrana@ifi.uio.no

IV Network Theory

Contents

23 Introduction

Holger Boche

The objective of classical mobile communication research was in the past to optimize the point-to-point communication. Due to the economical success of mobile systems we are now facing totally new challenges: from link optimization we have to proceed to network optimization and then further to channel-adjusted optimization, keeping in focus the channel quality and, of course, the QoS demands of the user, and finally crossing over from centrally organized to self-organizing systems. Of course, for all applications in multiantenna systems, which are presented in this book, self-organizing systems will play a subordinated role, but it is also clear that self-organization is a welcome enhancement for systems with infrastructure, for example, multihop to range extension. The first steps to optimize and build these kinds of systems are already made and are incorporated in high-speed uplink package access/high-speed downlink package access (HSUPA/HSDPA) standardization for 3GPP. For future systems a high granularity of resources as, for example, time, frequency, space, power is required, and the allocation of these resources under real-time conditions presents a tremendous challenge regarding the complexity. In this part, new results for multiantenna systems in consideration of network aspects are presented. One important step for resource allocation is to understand the QoS tradeoff in multiuser systems and the influence of different QoS performance measures on feasible QoS regions. With the knowledge of these factors we have the perfect tool for cross-layer optimization, taking into account channel quality.

In wireless communications it is important to understand and to control the channel. For the case of multiantenna systems this is investigated in connection with the capacity by Andreas Molisch and Fredrik Tufvesson in Chapter 2 of this part. It is well known that the capacity depends on the numbers of antennas and on the correlation of the antennas. To evaluate the gain of performance due to high-speed uplink package access/high-speed downlink package access (HSUPA/HSDPA) under network aspects, the mobility behavior of the users and the fading pattern for the users play a crucial part, since they have a great impact on the optimal scheduling strategy.

Sergio Barbarossa, Gesualdo Scutari, and Loreto Pescosolido analyze distributed space-time coding in Chapter 3. In this connection, a further shift of paradigm in wireless communication is taking place, because here a cooperation between the users is not only accepted but even favored. This makes distributed space-time coding an active research area with a number of very interesting open problems. In Chapter 4 of this part authored by Slawomir Stanczak and Holger Boche, the geometry of feasible QoS regions is characterized. In particular it is investigated if the feasible QoS region is a convex set, which is highly beneficial for resource allocation optimization. In this chapter, a simple scheme for resource allocation is established, which gives the operator the possibility to control the working point of its system and to conduct a weighting of the requested services. Fairness conditions of resource allocation are also analyzed.

The problem of feasible QoS regions in the downlink and uplink of multi antenna systems with a given SINR is surveyed in Chapter 5, authored by Holger Boche and Martin Schubert. The duality between uplink and downlink, which allows to find the downlink optimum by solving an equivalent uplink problem instead is stated and an optimization strategy for the problem of jointly optimizing beamformers and transmit power can be deviced. Based on network stability as one interesting criterion for optimization, in Chapter 6, authored by Holger Boche and Marcin Wiczanowski, a scheduler is developed, which achieves the maximal stability region for HSUPA. To reach maximal stability a simple weighted sum of rates has to be optimized which validates the results from Chapter 4. As a result it is shown that the problem can be reduced to a convex problem, when the optimal successive interference cancelation (SIC) order is classified. In the appendix of Chapter 6, authored by Thomas Haustein, the results of the preceding chapters are implemented and experimental results are presented.

Holger Boche: Heinrich Hertz Chair for Mobile Communications, Faculty of EECS, Technical University of Berlin, Einsteinufer 25, D-10587 Berlin, Germany; Fraunhofer German-Sino Lab for Mobile Communications, Einsteinufer 37, D-10587 Berlin, Germany; Fraunhofer-Institute for Telecommunications, Heinrich-Hertz-Institut, Einsteinufer 37, D-10587 Berlin, Germany

Email: boche@hhi.fhg.de

24 MIMO channel capacity and measurements

Andreas F. Molisch and Fredrik Tufvesson

Multiple-input multiple-output (MIMO) systems, which use multiple antennas at both transmitter (TX) and receiver (RX), are an extremely promising way to enhance data rates of wireless communications systems without requiring additional spectrum.[1] Within a short time, this concept has emerged as one of the major research topics in telecommunications, with literally thousands of papers being devoted to the different aspects. These systems are also poised to be standardized for high-data-rate modes of both cellular (3GPP) and local area network (IEEE 802.11) communications standards.

The design of good MIMO systems is a difficult task and involves aspects from many different areas of communications engineering. However, the performance is ultimately limited by the wireless channel and the (information-theoretic) capacity that this channel allows. This chapter will concentrate on this capacity—both on its theoretical derivation, and on the measurement in real environments. Further details can be found in the textbook [1] and the review papers [2, 3], and references therein.

24.1. Beamforming, diversity, and spatial multiplexing

The multiple antennas in MIMO systems can be used to achieve different goals.

(i) *Diversity*. This generalizes the concepts of diversity at the transmitter and receiver.

(ii) *Beamforming*. The array pattern at the transmitter and the receiver can be formed in such a way that the average SNR is increased. Again, this is a straightforward generalization of the principles of smart antennas, see Chapter 9.

(iii) *Spatial multiplexing*. Antenna arrays at the transmitter and the receiver allow the transmission (and reception) of multiple data streams. An intuitive picture

[1] Alternatively, multiple-antenna systems have been named MEA (multielement arrays) and MIMO (multiple-input multiple-output) systems. In the following, we will use the latter name, as it is more popular.

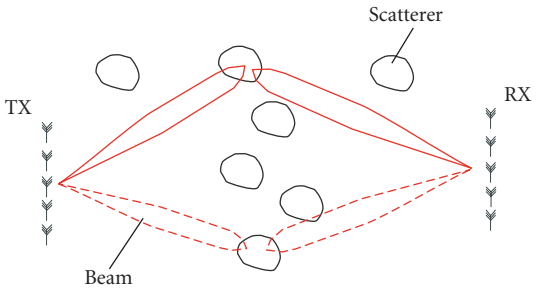

FIGURE 24.1. Principle of spatial multiplexing.

of this fact can be gathered from Figure 24.1.[2] If we have N_t transmit antennas, the TX can form N_t independent beams towards scatterers and transmit different data streams on each of them. Similarly, the receiver can form N_r beams that point at those scatterers. Thus, each beam can receive one data stream without interference from the other beams.[3] It is clear that in order to transmit N_s streams, we need at least N_s beams to be able to point at the different streams. Finally, we also see that a sufficient number of scatterers is required. Thus, the existence of many scatterers, and its associated multipath propagation, which is normally considered to be a major drawback, becomes a benefit in the context of MIMO systems.

The principle of spatial multiplexing can also be explained as a generalization of conventional smart antennas. Consider the uplink of a cellular system with a smart-antenna base station (with N_r receive antennas), and multiple mobile stations that have a single antenna each. Then we have seen in Chapter 2 that in each time slot in a TDMA system (for each spreading code in a CDMA system), the base station can serve N_r mobile stations—for each user, it can employ $N_r - 1$ antenna elements to suppress the signals from all *other* users [4]. Now imagine that the different "users" are really just antenna elements of a single transmitter. Obviously, in that case this transmitter can handle data at a much higher data rate than a "normal" (single-antenna) transmitter. This picture also establishes a useful link between the research areas of MIMO and multiuser detection. If the different transmit antenna elements are viewed as different users, then a receiver for the different data streams is essentially a multiuser receiver. The many multiuser detection schemes that have been established in the literature [5] can thus be immediately applied to MIMO receivers.

The three goals of MIMO cannot be achieved simultaneously to their full extent. In channels with dense scattering (which allows full diversity), the beamforming gain is upper limited by $(\sqrt{N_t}+\sqrt{N_r})^2$. More importantly, there is a fundamental trade-off between spatial multiplexing and diversity [6]: define the diversity order as $d = -\lim_{\mathrm{SNR}\to\infty} \log[P_e(\mathrm{SNR})]/\log(\mathrm{SNR})$ where P_e is the error probability, and

[2]This picture gives us thus some basic insights; however, we have to keep in mind that some of the assumptions are overly simplified. More exact descriptions will be developed in the following sections.

[3]Note that this is different from conventional beamforming, where we form only one beam (at TX and RX each), and do so with the purpose of increasing the SNR.

the spatial multiplexing gain as $r = \lim_{\mathrm{SNR}\to\infty} R(\mathrm{SNR})/\log(\mathrm{SNR})$, where R is the rate. The optimum trade-off curve is piecewise linear, connecting the points:

$$d(r) = (N_\mathrm{t} - r)(N_\mathrm{r} - r), \quad r = 0, \ldots, \min(N_\mathrm{t}, N_\mathrm{r}). \tag{24.1}$$

This implies that maximum diversity order $N_\mathrm{t}N_\mathrm{r}$ and maximum rate $\min(N_\mathrm{t}, N_\mathrm{r})$ cannot be achieved simultaneously.

Different environments, signal-to-noise ratios, and channel state information might require different trade-offs between the three goals in order to maximize capacity.

24.2. System model and general considerations

Before going into further details, we first establish the notation and the generic system that will be considered in the following. Figure 24.2 exhibits a block diagram. At the transmitter, the data stream enters an encoder, whose outputs are forwarded to the N_t transmit antennas. The signals are subsequently up converted to passband, amplified by a power amplifier, and filtered. For our model, we omit these stages, as well as their equivalents at the receiver, which allows us to treat the whole problem in equivalent baseband. From the antennas, the signal is sent through the mobile radio channel, which is assumed to be quasi-static and frequency flat if not stated otherwise. By quasi-static we mean that the coherence time of the channel is so long that "a large number" of bits can be transmitted within this time.

We denote the $N_\mathrm{r} \times N_\mathrm{t}$ matrix of the channel as

$$\mathbf{H} = \begin{pmatrix} h_{11} & h_{12} & \cdots & h_{1N_\mathrm{t}} \\ h_{21} & h_{22} & \cdots & h_{2N_\mathrm{t}} \\ \cdot & \cdot & \cdots & \cdot \\ h_{N_\mathrm{r}1} & h_{N_\mathrm{r}2} & & h_{N_\mathrm{r}N_\mathrm{t}} \end{pmatrix} \tag{24.2}$$

whose entries h_{ij} are the channel gains (transfer functions) from the jth transmit to the ith receive antenna.

If the channel is Rayleigh fading, the h_{ij} are i.i.d. zero mean, circularly symmetric complex Gaussian random variables with unit variance, that is, the real and imaginary parts each has variance 1/2 [7]. This is the case we will consider henceforth, unless stated otherwise. Consequently, the power carried by each transmission channel h_{ij} is chi-squared distributed with 2 degrees of freedom. This is the simplest possible channel model; it assumes "heavy multipath." It becomes clear from both the mathematical formulation and the intuitive picture in the previous section that the existence of many multipath components (MPCs), which is usually considered a drawback, becomes a major advantage in MIMO systems. The channel also adds white Gaussian noise, which is assumed to be independent among the N_r receiver antenna elements. More involved channel models are discussed in Section 24.11.

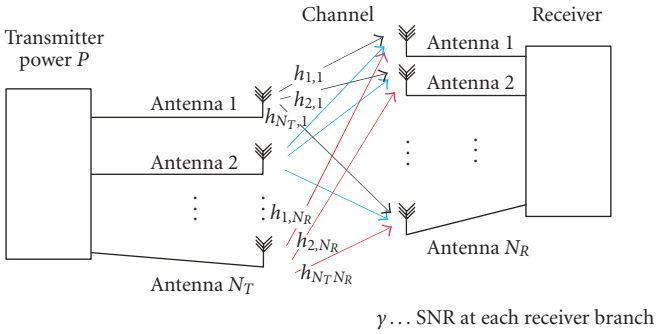

FIGURE 24.2. Block diagram of a MIMO system.

The received signal vector

$$\mathbf{y} = \mathbf{H}\mathbf{s} + \mathbf{n} = \mathbf{x} + \mathbf{n} \tag{24.3}$$

is received by N_r antenna elements, where $\mathbf{s}$ is the transmit signal vector, and $\mathbf{n}$ is the noise vector.

The capacity equations, as well as many space-time structures, can be best understood when considering the singular value decomposition of the channel $\mathbf{H} = \mathbf{U}\boldsymbol{\Sigma}\mathbf{W}^{\dagger}$, where $\boldsymbol{\Sigma}$ is a diagonal matrix containing the singular values, and $\mathbf{U}$ and $\mathbf{W}^{\dagger}$ are unitary matrices composed of the left and right singular vectors, respectively. Then, multiplication of the transmit data vector with a matrix $\mathbf{W}$ at the TX and $\mathbf{U}^{\dagger}$ at the receiver diagonalizes the channel, resulting in R independent channels with SNR σ_k^2, where σ_k is the kth singular value of $\mathbf{H}$, and R is the rank of $\mathbf{H}$ (number of nonzero singular values).

The capacity of the channel $\mathbf{H}$ is thus given by the sum of the capacities of the subchannels (modes of the channel):

$$C = \sum_{k=1}^{R} \log_2 \left[1 + \frac{P_k}{\sigma_n^2} \sigma_k^2 \right], \tag{24.4}$$

where σ_n^2 is the noise variance, and P_k is the power allocated to the kth mode; we assume that $\Sigma P_k = P$ is independent of the number of antennas. This capacity expression can be shown to be equivalent to

$$C = \log_2 \left[\det \left(\mathbf{I}_{N_r} + \frac{\overline{\Gamma}}{N_t} \mathbf{H}\mathbf{R}_{xx}\mathbf{H}^{\dagger} \right) \right], \tag{24.5}$$

where $\mathbf{I}_{N_r}$ is the $N_r \times N_r$ identity matrix, $\overline{\Gamma}$ is the mean signal-to-noise ratio (SNR) per receiver branch, and $\mathbf{R}_{xx}$ is the correlation matrix of the transmit data (for data at the different antenna elements that are uncorrelated, it is a diagonal matrix

with entries that describe the power distribution among the antennas). The distribution of the power among the different eigenmodes (or antennas) depends on the amount of channel state information (CSI) at the transmitter; this will be discussed in more detail below. The equations above confirm our intuitive picture that the capacity increases linearly with $\min(N_t, N_r)$, as the number of nonzero singular values R is upper limited by $\min(N_t, N_r)$.

The capacity given in (24.4) and (24.5) is for a deterministic, time-invariant channel matrix **H**. In case the channel changes, we can compute two different types of capacity.

(i) *The ergodic (Shannon) capacity*. This is the expected value of the capacity, taken over all realizations of the channel. This quantity assumes an infinitely long code that extends over all the different channel realizations.

(ii) *The outage capacity*. This is the minimum capacity that is achieved at a certain fraction of the time, for example, 90% or 95%. We assume that the data are encoded with a near Shannon limit achieving code that extends over a period that is much shorter than the channel coherence time. It has been shown that LDPC codes with a block length of 10 000 bits are less than 1 dB away from the Shannon limit [8]. For a data rate of 10 Mbps, such a block can be transmitted within 1 milliseconds. This is much shorter than 10 milliseconds, which is a typical coherence time of wireless channels. Thus, each channel realization can be associated with a (Shannon) capacity value. The capacity thus becomes a random variable (rv), with an associated cumulative distribution function (cdf). It is then of great interest to investigate this distribution function or equivalently the capacity that can be guaranteed for x% of all channel realizations.

24.3. Capacity without CSI at the TX, full CSI at the RX

In this section, we analyze the capacity that can be obtained when the receiver knows the channel perfectly, but no CSI is available at the TX. In that case, it is optimum to assign equal transmit power to all the TX antennas, $P_k = P/N_t$. The capacity thus takes on the now-famous form

$$C = \log_2 \left[\det \left(\mathbf{I}_{N_r} + \frac{\overline{\Gamma}}{N_t} \mathbf{H}\mathbf{H}^\dagger \right) \right]. \tag{24.6}$$

It is quite noteworthy that the capacity of a MIMO system increases linearly with $\min(N_t, N_r)$, irrespective of whether the channel is known at the transmitter or not.

Figure 24.3 shows the exact capacity distribution for various systems [7], as obtained from Monte Carlo simulations. We see that using multiple antennas at only one link end leads to a rather small increase of the average capacity, but drastically increases the outage capacity if low outage is required. The use of multiple antennas on both link ends, on the other hand, increases both the ergodic and the outage capacity.

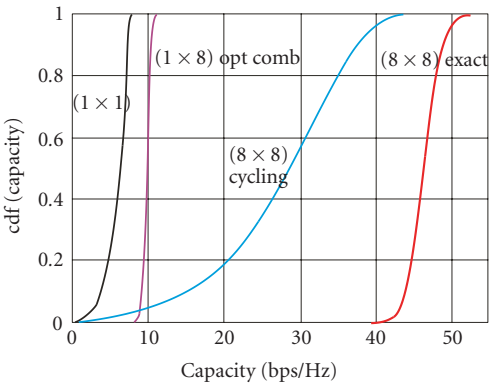

FIGURE 24.3. Cumulative distribution function of the capacity for a 1×1, 1×8, 8×8 cycling, and the 8×8 optimum scheme. $\gamma = 21$ dB.

The exact expression for the *ergodic capacity* was derived by Telatar [9] as

$$E\{C\} = \int_0^\infty \log_2\left[1 + \frac{\overline{\Gamma}}{N_t}\right] \sum_{k=0}^{m-1} \frac{k!}{(k+n-m)!} \left[L_k^{n-m}(\lambda)\right]^2 \lambda^{n-m} \exp(-\lambda) d\lambda, \quad (24.7)$$

where $m = \min(N_t, N_r)$ and $n = \max(N_t, N_r)$ and $L_k^{n-m}(\lambda)$ are associated Laguerre polynomials [10]. For the case of a large number of antenna elements, the ergodic capacity can be computed easily using random matrix theory [11, 12].

Exact analytical expressions for the cdfs of the capacity are rather complicated, but are described in [13]. Two approximations are in widespread use.

(i) The capacity can be well approximated by a Gaussian distribution [14], so that only the mean (i.e., the ergodic capacity given above) and the variance need to be computed.

(ii) From physical considerations, the following upper and lower bounds for the capacity distribution have been derived in [7] for the case $N_t \geq N_r$:

$$\sum_{k=N_t-N_r+1}^{N_t} \log_2\left[1 + \frac{\overline{\Gamma}}{N_t}\chi_{2k}^2\right] < C < \sum_{k=1}^{N_t} \log_2\left[1 + \frac{\overline{\Gamma}}{N_t}\chi_{2N_t}^2\right], \quad (24.8)$$

where χ_{2k}^2 is a chi-square distributed random variable with $2k$ degrees of freedom.

The above equations are valid for frequency-flat channels. If the channel varies over frequency, the capacity per unit frequency is

$$C = \frac{1}{B}\int_B \log_2\left[\det\left(\mathbf{I}_{N_r} + \frac{\overline{\Gamma}}{N_t}\mathbf{H}(f)\mathbf{H}(f)^\dagger\right)\right] df, \quad (24.9)$$

where B is the bandwidth of the considered system. This equation implies that frequency selectivity offers additional diversity that increases the slope of the capacity cdf.

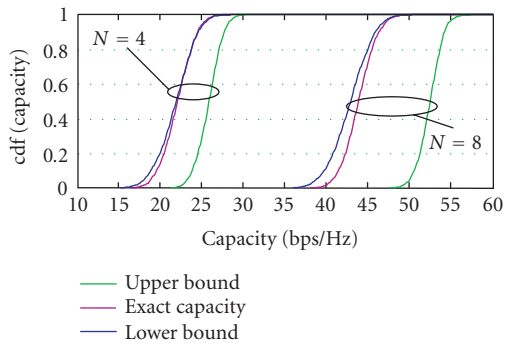

FIGURE 24.4. Exact capacity, upper bound, and lower bound of a MIMO system in an i.i.d. channel at 20 dB SNR, with $N_r = N_t = N$ equal to 4 and 8.

24.4. Capacity with full CSI at the TX and RX

If the TX has full channel state information, then it can distribute the transmission energy in a way that makes maximum use of the available resources. The problem of assigning the right amount of energy to available parallel channels has already been solved—in a different context—by Shannon, and is known as water filling [15]. The power allocation, P_k of the kth eigenmode is

$$P_k = \max\left(0, \varepsilon - \frac{\sigma_n^2}{\sigma_k^2}\right), \tag{24.10}$$

where the threshold ε is determined by the constraint of the total transmitted power P as

$$P = \sum_{k=1}^{R} P_k. \tag{24.11}$$

The capacity gain by water filling (compared to the equal-power distribution) is rather small when the number of transmit and receive antennas is identical. This is especially true in the limit of large SNRs. When N_t is larger than N_r, the benefits of water filling become more pronounced, see Figure 24.5. Essentially, water filling makes sure that energy is not wasted on eigenmodes that do not carry any significant energy. This can be viewed as another trade-off between spatial multiplexing and beamforming gain: water filling reduces the number of channel eigenmodes that are used for communications, in order to improve the SNR on the actually employed eigenmodes.

With water filling, the power is allocated preferably to modes that have a good SNR ("give to the rich" principle). This is optimum from the point of view of the theoretical capacity; however, it requires that the transmitter can use a Gaussian alphabet. This implies that the constellation size, and thus the peak-to-average ratio, has to be unlimited. For the case of a finite-modulation alphabet, it might be

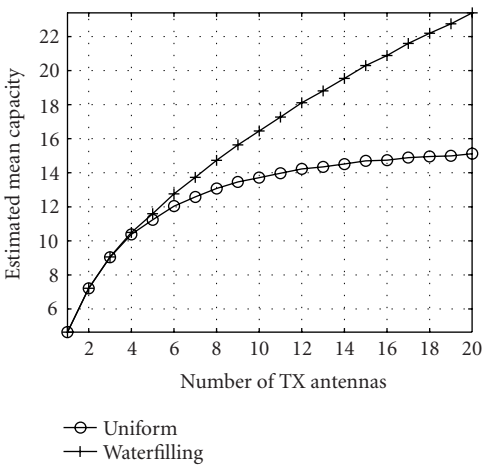

FIGURE 24.5. Capacity with and without CSI at the TX with $N_r = 8$ antennas and SNR $= 5$ dB.

preferable to use a different power allocation strategy. The capacity per stream is limited by $\log_2(N_a)$, where N_a is the size of the symbol alphabet. It is thus wasteful to assign more energy to one stream than can be actually exploited by the alphabet. In that case, a "giving to the poor" principle is preferable [16].

24.5. Capacity with average CSI at the TX and full CSI at the RX

For many systems, instantaneous CSI at the transmitter is not feasible. For frequency-division duplex (FDD) systems, in which the forward and the reverse links operate at different frequencies, instantaneous CSI at the TX requires a fast feedback, which decreases the spectral efficiency of the system. For time-division duplex (TDD) systems, in which the forward and reverse links operate at the same frequency, reusing the CSI requires that the delays between the forward and reverse links be much shorter than the coherence time of the channel, which is impractical for many situations as well. These problems can be circumvented by the use of covariance knowledge (*average* CSI) $\mathbf{R_{HH}} = E\{\mathbf{H}\mathbf{H}^{\dagger}\}$ at the transmitter. For the case of i.i.d. fading channels, this is equivalent to the no-CSI case, as $\mathbf{R_{HH}}$ is an identity matrix. For the case of channel correlation, it turns out that the eigenspace of the transmit signal should match the eigenspace of $\mathbf{R_{HH}}$ [17].

24.6. Capacity with erroneous CSI

All of the above considerations assumed that the available CSI is correct. However, in practice, it is impossible to obtain perfect CSI; rather, it is afflicted by systematic as well as random errors.

(i) *Outdated CSI*. This case is especially critical for CSI at the TX. It can occur when the CSI is based on feedback from the receiver and is not instantaneous. In

time-domain duplexing systems, the TX can obtain CSI during the timeslots when it acts as a receiver. In that case, the changes of the channels during the time the transceiver changes from RX to TX mode render the CSI partially outdated. It must be noted that while the deviation between true and used CSI is often modeled as Gaussian distributed, this need not be a physically viable model for all channels.

(ii) *Noisy CSI*. Gaussian (observation) noise can affect the CSI at both the TX and the RX. In addition, the CSI at the TX can suffer also from quantization noise when it is based on feedback. Two different approaches have been devised to analyze this problem. Mutual information bounds for vector channels with imperfect CSIR can be established [18]. Several other papers assumed a "mismatched receiver", where the TX and RX process the signal based on the *observed* channel $\mathbf{H}_{\text{obs}}$, while in reality, the signals pass through a channel $\mathbf{H}_{\text{true}}$

$$\mathbf{H}_{\text{true}} = \mathbf{H}_{\text{obs}} + \mathbf{\Delta}. \tag{24.12}$$

Some papers have taken this into account by an ad hoc modification of the noise variance (replacing σ_n^2 by $\sigma_n^2 + \sigma_e^2$, where σ_e^2 is the variance of the entries of $\mathbf{\Delta}$), however, recent investigations [19] show that this is not justified in all cases.

A general framework for the effect of possibly erroneous CSI on the capacity is given in [20]. They also show that an optimum transmitter can be split into an encoder, followed by a linear weighting according to the channel state information (beamforming).

24.7. Capacity with partial or no CSI at TX and RX

It is remarkable that communication with high spectral efficiency is also possible when neither the TX nor the RX has CSI. The possibility for a signaling scheme that allows such communication was first pointed out in [21]. The modulation method can be understood as a generalization of differential modulation [22]. For high SNR, the capacity no longer increases linearly with $m = \min(N_t, N_r)$, but rather increases as $\tilde{m}(1 - \tilde{m}/T)$, where $\tilde{m} = \min(N_t, N_r, \lfloor T/2 \rfloor)$, and T is the coherence time of the channel in units of symbol duration [23].

24.8. Correlation and other channel nonidealities

24.8.1. Channel correlation

As seen in previous sections, the capacity is determined by the distribution of the singular values and the SNR. For a given SNR, the maximum capacity is achieved when the channel transfer matrix has full rank and the singular values of $\mathbf{H}$ are equally strong. A prerequisite for approximating this situation is to have low correlation between the signals at the different antenna elements and a radio channel where no single multipath component dominates the channel impulse response. If there is strong correlation between the fading at the different antenna elements, then the spread of the eigenvalues is much larger. This leads to a reduction in capacity at high SNRs.

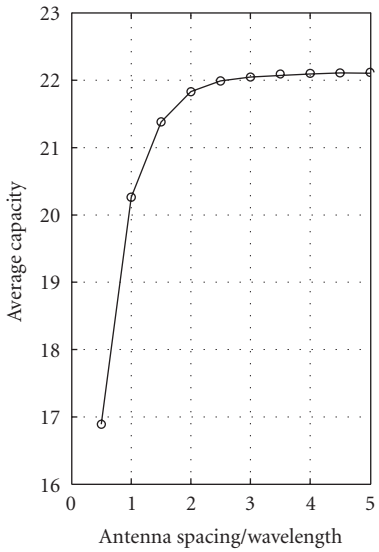

FIGURE 24.6. Average capacity of a 4×4 MIMO system with 10 degree rms angular spread as seen from the BS as a function of the antenna spacing at the BS.

Fading correlation is influenced by the angular spectrum of the channel, as well as the arrangement and spacing of the antenna elements. For antennas that are spaced half a wavelength apart, a uniform angular power spectrum leads approximately to a decorrelation of the incident signals. For a smaller angular spread, the correlation increases; Figure 24.6 shows the capacity of a 4×4 MIMO system with uniform linear arrays at TX and RX as a function of the angular spread at one link end. Note that this figure is based on the idealized assumption that there is no mutual coupling between the antenna elements; recent investigations have shown that mutual coupling influences the capacity by introducing pattern diversity as well as changing the average power received in the different antenna elements [24].

Analytical computation of the capacity is much more complicated in the case of correlated channels. For the case that correlation occurs only at one link end, the exact capacity distribution is computed in [25]. For the more general case of correlation at the transmitter and receiver, mostly asymptotic results (for large antenna arrays) exist [12, 26, 27]; the ergodic capacity for channels with correlation at both link ends can be found in [28].

24.8.2. LOS versus NLOS

Often one distinguishes between line-of-sight (LOS) and non line-of-sight (NLOS) channels. When there is a LOS component, it is generally the strongest MPC, dominating the channel impulse response and thereby the behavior of the channel transfer matrix. As all antenna elements have the same dominant component, the channel transfer function does not change significantly from one antenna element

to another, which results in a large spread of the singular values. This results in a decrease of the capacity (compared to an i.i.d. channel with the same SNR); one should however note that the SNR is often better in the LOS case compared to the NLOS case. For a power-limited scenario with realistic channels, the LOS case often gives the highest capacity, despite the imbalance between the singular values.

A strong LOS component leads to a larger spread of the eigenvalues if the LOS component is a *plane* wave. Even a single *spherical* wave leads to a transfer function matrix that can have full rank if the antenna elements are spaced appropriately [29]. For indoor scenarios, where the curvature of the waves is noticeable at typical TX-RX distances, this can have an important impact on the capacity [30].

24.8.3. Keyhole channels

There are some special cases where the capacity is low though the signals at the antenna elements are uncorrelated or have only low correlations. These cases are often referred to as *keyholes* or *pinholes*. An example of a keyhole scenario is a rich scattering environment at both the transmitter and receiver sides, and between there is only one narrow path of propagation and this path allows only one degree of freedom. A keyhole channel can be generated as a dyad [31]:

$$\mathbf{H} = \begin{pmatrix} b_1 \\ b_2 \\ \vdots \\ b_{N_r} \end{pmatrix} (a_1, a_2, \ldots, a_{N_t}), \tag{24.13}$$

where a_i and b_i are complex Gaussian variables.

In [32], the authors pointed out a scenario where the distance between the two scattering environments were large, thereby causing the keyhole effect. In [31] a keyhole scenario was described where the two environments were connected with a tunnel or hallway. It should, however, be noted that keyhole channels occur very seldom in practice. A keyhole was measured in a controlled environment in [33], but not in real environments.

24.8.4. Limited number of scatterers

As we have stated in the introduction, we need a sufficient amount of scatterers to "carry" the data streams. While the number of scatterers is always large, the number of *significant* scatterers may not. This is of crucial importance in practice. Scatterers that are too weak to provide appreciable SNR (and thus capacity) are not useful in carrying data streams. A theoretical treatment of this fact is discussed in [12], where random matrix theory is used to compute the impact of a limited number of scatterers. Reference [34] provides experimental investigations into the impact of the number of scatterers (see also Figure 24.7).

A related question is the number of antenna elements that can gainfully be used within a given volume. Even in rich scattering, the capacity per unit volume

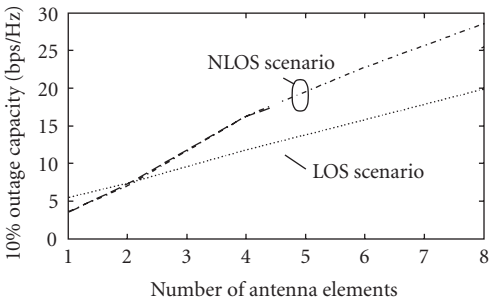

FIGURE 24.7. 10% outage capacity as a function of the number of antenna elements at transmitter and receiver in measured LOS and NLOS scenarios (see [34]).

that contains the antenna elements is limited [35]. Thus, increasing the number of antenna elements beyond a certain point does not increase the channel capacity; this can be viewed as a spatial sampling theorem.

24.9. Capacity in interference

The considerations above have dealt with the capacity of a single MIMO link without interference. In a cellular context, the existence of multiple users influences the capacity and decreases the data rate that is possible for a single user. The first investigation of this topic was in [36], which assumed MMSE suppression of multiple-access interference in a cellular TDMA system. Under these assumptions, it was shown that the *cellular* capacity of a MIMO system is hardly larger than that of a system with multiple antennas at the base station only. The reason for this somewhat astonishing result is that in a cellular system with multiple antennas at the BS only, those antennas can be used to suppress neighboring-cell interference and thus decrease the reuse distance. For a cellular MIMO system with $N_r = N_t$, the degrees of freedom created by the multiple BS antennas are all used for the separation of the multiple data streams from a single user, and none for the suppression of interfering users. Depending on the SINR, it is sometimes the best to put all available power into a single antenna [37].

However, MIMO can be combined with other techniques for multiple-access interference. The combination of interference-cancellation techniques with MIMO systems decreases the impact of this interference [38]. On a more general note, multiuser interference can be eliminated by base station cooperation [39]. For the uplink, cooperating base stations can be viewed as a giant MIMO system with $N_r N_{BS}$ antenna elements, where N_{BS} is the number of cooperating base stations. The capacity for such a system can be approximated by inserting the generalized channel matrix into (24.5).[4] For the downlink, the effect of interfering base stations can be minimized by appropriate preprocessing if the BSs cooperate and

[4]This capacity cannot be completely achieved, as the MSs cannot cooperate in the encoding of the information. A lower limit is thus given by the capacity of an HBLAST system. However, also such a system has a capacity that linearly increases with the number of antennas.

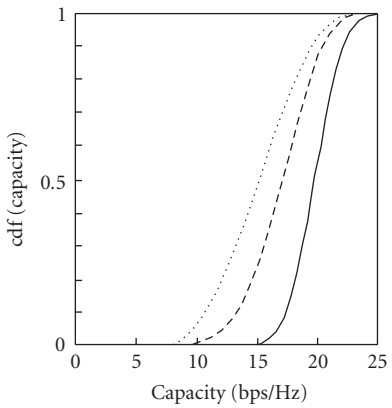

FIGURE 24.8. Capacity of a 4×4 MIMO system at 18 dB SNR, with diagonal BLAST (solid), horizontal BLAST (dashed), and single outer code (dotted).

each BS has the CSI for all MSs. It has been shown that appropriate nonlinear precoding, known as "writing on dirty paper" coding [40], can completely eliminate the effect of interference; linear preprocessing can only approximate these gains. Further information-theoretic results are reviewed in [41].

24.10. Capacity for specific transceiver architectures

The information-theoretic capacity does not make specific assumptions about the structure of the transceivers and the signaling schemes. Practically viable schemes that approximate the capacity are layered space-time schemes, also known as BLAST. It has been shown that diagonal BLAST with rate feedback achieves capacity, while horizontal BLAST[5] (which separately encodes the data streams for the different antenna elements) leads to a capacity loss (Figure 24.8). MMSE-BLAST receivers (based on MMSE interference-cancellation schemes) lead to a further reduction in capacity, but are very popular because of their low complexity and analytical tractability.

Another group of transceiver structures that has received great attention is space-time coded systems. Space-time block-coded systems, including the Alamouti code, are being used in several standardized multiantenna systems. For more details, see Chapter 19.

24.11. Channel models for MIMO

Investigations of the MIMO capacity make use of simplified channel models that have—more or less—a basis in real wireless propagation channels. For understanding MIMO capacity, it is thus important to understand the different channel models and the restrictions they have in practice. Due to space restrictions, we

[5]In many papers, this scheme is referred to as VBLAST.

mention only the most important properties. More information can be found, for example, in [42, 43].

24.11.1. Analytical channel models

A stochastic analytical (also known as nonphysical) model characterizes the correlation functions of the entries in the channel matrix. A complete description of *second-order* statistics is provided by the correlation matrix. It describes the correlation between any two pairs of antenna elements:

$$\mathbf{R}_{\text{full}} = \mathrm{E}\{\,\mathrm{vec}(\mathbf{H}) \cdot \mathrm{vec}(\mathbf{H})^{\mathrm{H}}\}, \tag{24.14}$$

where the vec(•) operator stacks the columns of **H** into a single large column vector. Again, we stress that second-order statistics are a sufficient description only for zero-mean (complex) Gaussian fading. Note that the correlation matrix in the above equation can depend on delay (frequency), as the angular spectrum (which determines **R**) can vary with delay.

The Kronecker model. The Kronecker model [44] approximates the correlation matrix **R** as a Kronecker product of the (marginal) correlation matrices at the transmitter, $\mathbf{R}_{\text{TX}}$, and the receiver, $\mathbf{R}_{\text{RX}}$. A realization of the channel matrix can then be obtained as

$$\mathbf{H}_{\text{kron}} = \frac{1}{\sqrt{\mathrm{tr}\,(\mathbf{R}_{\text{RX}})}}\mathbf{R}_{\text{RX}}^{1/2}\mathbf{G}\left(\mathbf{R}_{\text{TX}}^{1/2}\right)^{\mathrm{T}}, \tag{24.15}$$

where **G** is a matrix with i.i.d. complex Gaussian entries, and $\mathbf{R}^{1/2}$ is defined by $\mathbf{R}^{1/2}\mathbf{R}^{1/2} = \mathbf{R}$.

This implies that the correlation at the receiver is assumed to be independent of the transmit direction (and vice versa). While this simplifies the description, it also leads to less generality, results in an underestimation of the channel capacity, especially for indoor environments and for large antenna arrays [45]. A generalization of the Kronecker model was recently suggested by Weichselberger et al. in [46]. Their model preserves the dependencies between directions of arrival and directions of departure, by modeling the spatial eigenbasis of the receiver (and transmitter) correlation matrix, denoted by $\mathbf{U}_{\text{RX}}$ and $\mathbf{U}_{\text{TX}}$, and a power-coupling matrix $\mathbf{\Omega}$ between these two. Each pair of receive and transmit eigenmodes spans a SISO channel that is uncorrelated from all other pairs; its average energy forms one element of the power-coupling matrix.

Beam space models. The beam space of "virtual channel" representation [47] represents the rays in the "beam" domain. The virtual channel is represented as

$$\mathbf{H} = \sum_{m}\sum_{k} H_V(k,m)\vec{a}_R(\tilde{\Psi}_k)\vec{a}_T^{H}(\tilde{\Omega}_m) = \tilde{\mathbf{A}}_R\mathbf{H}_V\tilde{\mathbf{A}}_T^{H}, \tag{24.16}$$

where $\vec{a}_R(\tilde{\Psi}_k)$ and $\vec{a}_T(\tilde{\Omega}_m)$ are the steering vectors with the virtual angles defined as $\tilde{\psi}_k = k/N_R$ and $\tilde{\Omega}_m = m/N_T$, with $-N_R \leqslant k \leqslant N_R$ and $-N_T \leqslant m \leqslant N_T$.

Different fading statistics. The models described above implicitly assume Rayleigh fading at the antenna elements. However, in a "keyhole channel" the fading statistics follow a "double-Rayleigh" distribution. This distribution can be emulated by replacing **G** in (24.15) by a rank-deficient matrix [48]

$$\mathbf{G} = \mathbf{G}_{\mathrm{RX}} \mathbf{R}_{\mathrm{IO}}^{1/2} \mathbf{G}_{\mathrm{TX}}. \tag{24.17}$$

24.11.2. Physical channel models

Physical channel models describe the statistics of the multipath components (MPCs) that transmit information from the TX to the RX. The MPCs are modeled as plane waves and thus characterized by their (complex) amplitude, delay τ, direction of departure (DOD) Ω, direction of arrival (DOA) Ψ, and polarization (to simplify notation, we henceforth neglect the polarization). The contribution of the lth MPC can be written as

$$h_l(\vec{r}_R, \vec{r}_T, \tau, \Psi, \Omega) = a_l e^{j\varphi_l} \delta(\tau - \tau_l) \delta(\Psi - \Psi_l) \delta(\Omega - \Omega_l), \tag{24.18}$$

where the complex amplitude $a_l e^{j\varphi_l}$, the DOA, and the DOD vary slowly with the position of transmitter $\vec{r}_R$ and receiver $\vec{r}_R$, while the phase φ of the complex amplitude varies quickly. The total double-directional impulse response [49] is the sum of contributions from the different MPCs:

$$h(\vec{r}_R, \vec{r}_T, \tau, \Psi, \Omega) = \sum_{l=1}^{L(\vec{r})} h_l(\vec{r}_R, \vec{r}_T, \tau, \Psi, \Omega), \tag{24.19}$$

where $L(\vec{r})$ is the number of MPCs. From the double-directional impulse response, the channel matrix can be easily obtained by adding the contributions from all the MPCs at the different antenna element locations; the components have to be phase shifted (to account for the runtime to the different antenna elements), and weighted with the antenna element patterns in the directions of their DOAs and DODs. Thus, a physical model describes only the actual propagation channel and can easily include different kinds of antenna arrangements and patterns.

Generalized tapped-delay line approach. A stochastic double-directional model characterizes the autocorrelation functions (ACFs) of the double-directional impulse response. A generalized WSSUS description describes the fading of MPCs with (i) different delays and/or (ii) different Doppler shifts and/or (iii) different DOAs and/or (iv) different DODs as independent. Note that this model implies the

stationarity of all channel statistics and thus does not cover large-scale movements of TX or RX that could change delays, DODs, DOAs, or absolute amplitudes. The generalized WSSUS model allows an easy discretization, resulting in a generalized tapped-delay line model, where each tap is now characterized by DOAs and DODs as well as delays [50]. Such a model is especially suitable for hardware and software simulators.

Geometry-based stochastic channel models. A geometry-based stochastic channel model (GSCM) is a compromise between a deterministic and a stochastic approach. The location of interacting objects (IOs, often also called scatterers) is prescribed at random, following a given probability density function. The simulation procedure then performs a ray tracing that is limited to some simple interaction processes (e.g., only single or double scattering processes). This "ray tracing" inherently produces all required information about DOAs and DODs as well as other parameters of the MPCs. A general GSCM-based model structure is given in [51].

Measurement-based stochastic models. A further step towards deterministic modeling is obtained by the "random-phase model" of [34]. The DOAs, DODs, and delays of the MPCs are extracted from measurement data by, for example, high-resolution parameter estimation methods. Subsequently, random phases are ascribed to the MPCs, resulting in different realizations of the MIMO channel without the necessity to actually measure at many closely spaced locations. A modification of that method uses phase shifts for the MPCs that are derived from synthetic displacements of the antenna arrays.

24.11.3. Standardized channel models

In the past years, a number of standardized channel models have emerged that reflect at least some properties of MIMO channels: the COST 259 model, the 3GPP model, and the IEEE 802.11n model. These models, all of which are physical models, are distinguished by the different radio environments for which they are intended, as well as by the simplifications that they make.

The COST 259 directional channel model (DCM) [52] was originally established for the simulation of systems with multiple-antenna elements at either the base station or the mobile station, describing the marginal angular power spectra. However, it can be used for MIMO simulations as well, by implicitly assuming that the joint DOA/DOD spectrum is the product of the marginal power spectra. The model is specified for macrocells, microcells, and picocells and describes the joint effects of small-scale as well as large-scale effects.

The 3GPP model [53] is designed for the simulation of third-generation systems in suburban and urban macrocells, and urban microcells. It has 6 taps in the delay domain, and for each of those delays, 20 taps in the angular domain at each of the link ends. Delay spread, angular spread, and shadowing are modeled as correlated random variables. The basic version of the model assumes only a single cluster of taps, with a Laplacian angular spectrum and an exponential

power delay profile (PDP). Far scatterer clusters (for urban macrocells), line of sight (for microcells), modified angular spectra corresponding to waveguiding in street canyons (for urban cells), and polarization have been defined as options.

The IEEE 802.11n model [54] is intended for the use of indoor wireless LANs. Six different models, corresponding to different environments, are specified. The model contains multiple clusters, each of which has a different mean DOA and DOD, which are chosen at random. The angular spectra for each cluster are Laplacian, and the PDP is exponential.

Another, very detailed, model is currently under development by the COST 273 standardization organization, and will be finished by mid 2005.

24.12. Measurements of capacity

24.12.1. Measurement of the transfer function matrix

Ultimately, we are interested in the capacity that occurs in "real" operating environments. Thus, it is important to *measure* the channel transfer matrix **H**; these results can be either used directly or as a basis for establishing channel models. In the following, we discuss principles of MIMO channel measurement devices ("channel sounders") as well as measurement and evaluation techniques.

The starting point is a channel sounder for nondirectional wideband channels, based on different available principles (network analyzer, correlator, sliding correlator). This is now combined with antenna arrays at both the transmitter and the receiver. We first consider the receiver, see Figure 24.9. In a "physical array" arrangement, we have one "normal" channel sounder connected to each antenna element, so that the impulse responses at the different elements $h_{j,1}$ can be measured simultaneously. In a "multiplexed array" arrangement, there are several antenna elements connected to a single sounder via a fast RF switch. We thus first measure the impulse response at the first antenna element $h_{1,1}$, then connect the switch to the second element, measure $h_{2,1}$, and so on. Finally, in a "virtual array" arrangement, there is only a single antenna element, which is moved mechanically from one position to the next, measuring the $h_{j,1}$. A basic assumption for the evaluation is that the environment does not change during the measurement procedure. "Virtual arrays" (which require a few seconds or even minutes for one measurement run) can thus only be used in static environments—this precludes scenarios where cars or moving persons are significant scatterers. On the other hand, they avoid all problems with mutual coupling between antenna elements. In nonstatic environments, multiplexed arrays are usually the best compromise between measurement speed and hardware effort.

At the transmitter, we need to send signals from the different antennas that are orthogonal in either time (i.e., sending only from one antenna at any given time), frequency (transmission of offset carriers from the different antennas), or code (e.g., transmission of different Walsh-Hadamard sequences from the different antennas), see Figure 24.10. In any case, each receiver antenna has to sort out which contribution stems from which transmit antenna element.

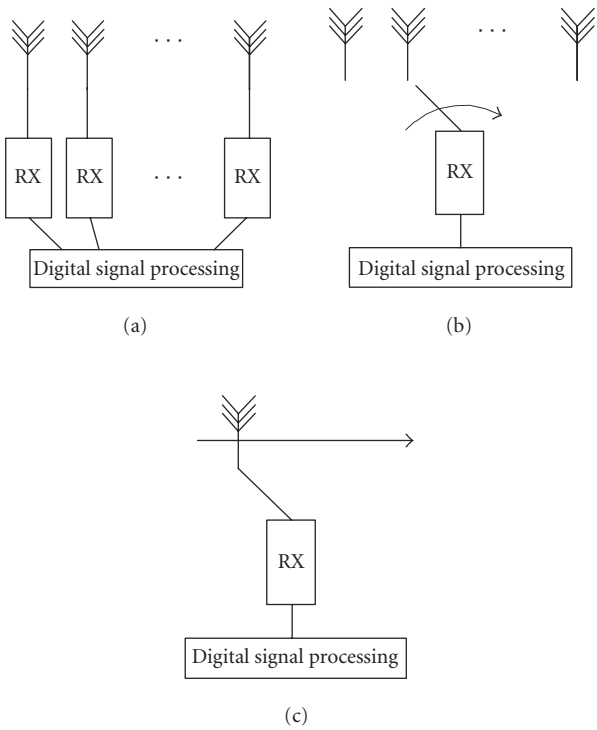

FIGURE 24.9. (a) Real, (b) multiplexed, and (c) virtual receive array.

24.12.2. Measurement of the double-directional impulse response

One possible way of obtaining directional impulse responses is to combine a non-directional channel sounder with directional (e.g., horn) antennas. A step motor is used to point the antenna into different directions, and for each direction, the impulse response is recorded. The drawbacks of this method are the long measurement time and the fact that the resolution is limited by the beam width of the directional antenna.

Alternatively, the directional information can be obtained by first measuring the transfer function matrix (as described above) by extracting discrete multipath components.[6] The simplest approach is a spatial Fourier analysis; however, the resolution is usually very poor. High-resolution parametric approaches include MUSIC, ESPRIT, SAGE [55], and the minimum variance method; these algorithms have an estimation accuracy on the order of one degree. We stress, however, that they might sometimes lead to numerical problems, and some of them are limited in the number L of MPCs h_l that can be estimated. We also note that the joint

[6]Plus a possible "diffuse" background.

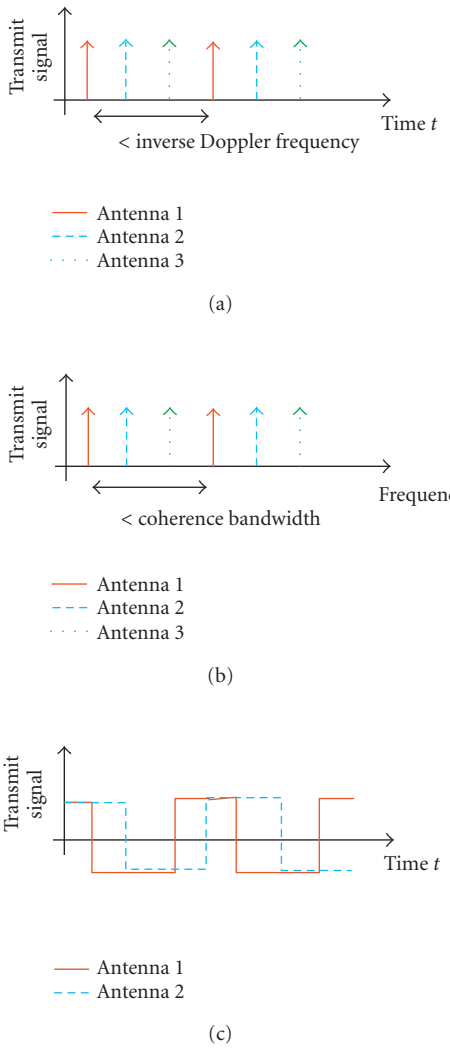

FIGURE 24.10. Sounding signals that are orthogonal in (a) time, (b) frequency, or (c) code.

determination of DOAs and DODs shows significant differences from the determination of the marginal angular spectra. Finally, we note that double-directional impulse responses or transfer function matrices can also be obtained from deterministic channel models (solution of Maxwell's equations, ray tracing).

24.12.3. Impact of noise

As for all kinds of measurements, it is of vital importance to be able to distinguish between the quantity of interest and contributions from the measurement system.

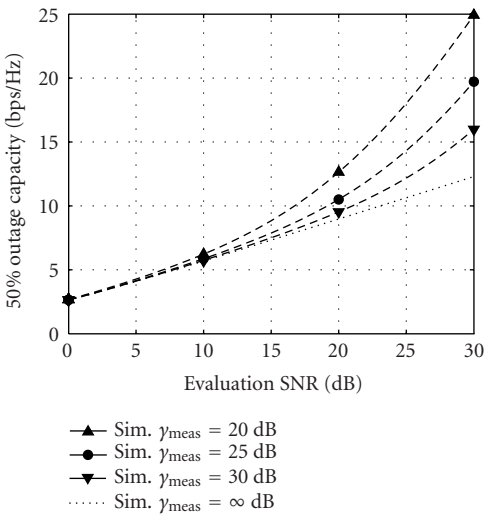

FIGURE 24.11. Measured capacity (50% outage capacity) for different levels of measurement noise. Ideally the measured capacity should follow the dotted line.

If we assume that the contribution from the measurement system itself can be modeled as additive white Gaussian noise, the measured capacity, directly calculated from the transfer function matrix, overestimates the true capacity because of the additional (noise) terms in the channel transfer function. This is especially true when the capacity is evaluated for high SNR values. As a rule of thumb, the capacity calculated from measurements should not be evaluated for a higher SNR than the measurement system can provide, which is in line with [56]. When measuring low-rank channels a measurement SNR of 10 dB better than the SNR used for the capacity evaluation is recommended [57]. In Figure 24.11 we show the measured capacity (50% outage capacity) of a keyhole scenario for different measurement SNRs when the capacity is evaluated for different SNR levels. Ideally the measured capacity should follow the dotted line, but with noise contributions from the measurement system the capacity seems to be larger than it actually is.

24.12.4. Measurement of capacity in different environments

Many measurements of the MIMO capacity have been performed in different environments. For indoor environments, it was found in [58] that the capacity is similar to an i.i.d. channel for a 2×2 array but shows a relatively smaller value for larger arrays. In corridors and tunnels, the orientation of the antenna array has a considerable influence [59, 60]. In outdoor metropolitan environments, the measured mean capacity was measured to be approximately 20% smaller than for the i.i.d. case; the cdf shows a flatter slope especially for larger numbers of antennas [61]. The capacity of fixed-wireless MIMO links was investigated in [62].

Acknowledgments

Part of this work was financed by an INGVAR grant from the Swedish Strategic Research Initiative. The authors thank Dr. Neelesh Mehta for critical reading of the manuscript.

Abbreviations

3GPP	Third-Generation Partnership Project
AFC	Autocorrelation function
BLAST	Bell Laboratories Layered Space Time
BS	Base station
CDMA	Code-division multiple access
CSI	Channel state information
CSIT	Channel state information at the transmitter
CSIR	Channel state information at the receiver
DCM	Directional channel model
DOA	Direction of arrival
DOD	Direction of departure
FDD	Frequency-division duplex
GSCM	Geometry-based stochastic channel model
IO	Interacting objects
LAN	Local area network
LOS	Line of sight
MIMO	Multiple-input multiple-output
MMSE	Minimum mean square error
MPC	Multipath component
MS	Mobile station
NLOS	Non line of sight
PDP	Power delay profile
RF	Radio frequency
RX	Receiver
SISO	Single-input single-output
SNR	Signal-to-noise ratio
TDD	Time-division duplex
TX	Transmitter
WSSUS	Wide-sense stationary uncorrelated scatterers

Bibliography

[1] A. Paulraj, D. Gore, and R. Nabar, *Multiple Antenna Systems*, Cambridge University Press, Cambridge, UK, 2003.

[2] D. Gesbert, M. Shafi, D. shan Shiu, P. J. Smith, and A. Naguib, "From theory to practice: an overview of MIMO space-time coded wireless systems," *IEEE J. Select. Areas Commun.*, vol. 21, no. 3, pp. 281–302, 2003.

[3] S. N. Diggavi, N. Al-Dhahir, A. Stamoulis, and A. R. Calderbank, "Great expectations: the value of spatial diversity in wireless networks," *Proc. IEEE*, vol. 92, no. 2, pp. 219–270, 2004.

[4] J. H. Winters, "Optimum combining in digital mobile radio with cochannel interference," *IEEE J. Select. Areas Commun.*, vol. 2, no. 4, pp. 528–539, 1984.

[5] S. Verdu, *Multiuser Detection*, Cambridge University Press, Cambridge, UK, 1998.

[6] L. Zheng and D. N. C. Tse, "Diversity and multiplexing: a fundamental tradeoff in multiple-antenna channels," *IEEE Trans. Inform. Theory*, vol. 49, no. 5, pp. 1073–1096, 2003.
[7] G. J. Foschini and M. J. Gans, "On limits of wireless communications in a fading environment when using multiple antennas," *Wireless Personal Communications*, vol. 6, no. 3, pp. 311–335, 1998.
[8] T. J. Richardson, M. A. Shokrollahi, and R. L. Urbanke, "Design of capacity-approaching irregular low-density parity-check codes," *IEEE Trans. Inform. Theory*, vol. 47, no. 2, pp. 619–637, 2001.
[9] I. E. Telatar, "Capacity of multi-antenna Gaussian channels," *European Trans. Telecommunications*, vol. 10, no. 6, pp. 585–595, 1999.
[10] M. Abramowitz and I. A. Stegun, *Handbook of Mathematical Functions*, Dover Publications, New York, NY, USA, 1965.
[11] C.-N. Chuah, D. N. C. Tse, J. M. Kahn, and R. A. Valenzuela, "Capacity scaling in MIMO wireless systems under correlated fading," *IEEE Trans. Inform. Theory*, vol. 48, no. 3, pp. 637–650, 2002.
[12] R. R. Müller, "A random matrix model of communication via antenna arrays," *IEEE Trans. Inform. Theory*, vol. 48, no. 9, pp. 2495–2506, 2002.
[13] Z. Wang and G. B. Giannakis, "Outage mutual information of space-time MIMO channels," *IEEE Trans. Inform. Theory*, vol. 50, no. 4, pp. 657–662, 2004.
[14] P. Smith and M. Shafi, "An approximate capacity distribution for MIMO systems," *IEEE Trans. Commun.*, vol. 52, no. 6, pp. 887–890, 2004.
[15] G. G. Raleigh and J. M. Cioffi, "Spatio-temporal coding for wireless communication," *IEEE Trans. Commun.*, vol. 46, no. 3, pp. 357–366, 1998.
[16] B. N. Getu, J. B. Andersen, and J. R. Farserotu, "MIMO systems: optimizing the use of eigenmodes," in *Proc. 14th IEEE International Symposium on Personal, Indoor and Mobile Radio Communications (PIMRC '03)*, vol. 2, pp. 1129–1133, Beijing, China, September 2003.
[17] S. A. Jafar and A. Goldsmith, "Transmitter optimization and optimality of beamforming for multiple antenna systems," *IEEE Transactions on Wireless Communications*, vol. 3, no. 4, pp. 1165–1175, 2004.
[18] M. Medard, "The effect upon channel capacity in wireless communications of perfect and imperfect knowledge of the channel," *IEEE Trans. Inform. Theory*, vol. 46, no. 3, pp. 933–946, 2000.
[19] N. B. Mehta, F. F. Digham, A. F. Molisch, and J. Zhang, "Rate of MIMO systems with CSI at transmitter and receiver from pilot-aided estimation," in *Proc. IEEE Vehicular Technology Conference (VTC '04)*, Los Angeles, Calif, USA, Fall 2004.
[20] M. Skoglund and G. Jongren, "On the capacity of a multiple-antenna communication link with channel side information," *IEEE J. Select. Areas Commun.*, vol. 21, no. 3, pp. 395–405, 2003.
[21] T. L. Marzetta and B. M. Hochwald, "Capacity of a mobile multiple-antenna communication link in Rayleigh flat fading," *IEEE Trans. Inform. Theory*, vol. 45, no. 1, pp. 139–157, 1999.
[22] B. M. Hochwald and W. Sweldens, "Differential unitary space-time modulation," *IEEE Trans. Commun.*, vol. 48, no. 12, pp. 2041–2052, 2000.
[23] L. Zheng and D. N. C. Tse, "Information theoretic limits for non-coherent multi-antenna communications," in *Proc. IEEE Wireless Communications and Networking Conference (WCNC '00)*, vol. 1, pp. 18–22, Chicago, Ill, USA, September 2000.
[24] J. W. Wallace and M. A. Jensen, "Mutual coupling in MIMO wireless systems: a rigorous network theory analysis," *IEEE Transactions on Wireless Communications*, vol. 3, no. 4, pp. 1317–1325, 2004.
[25] M. Chiani, M. Z. Win, and A. Zanella, "The distribution of eigenvalues of a Wishart matrix with correlation and application to MIMO capacity," in *IEEE Global Telecommunications Conference (GLOBECOM '03)*, vol. 4, pp. 1802–1805, San Francisco, Calif, USA, December 2003.
[26] C.-N. Chuah, D. N. C. Tse, J. M. Kahn, and R. A. Valenzuela, "Capacity scaling in MIMO wireless systems under correlated fading," *IEEE Trans. Inform. Theory*, vol. 48, no. 3, pp. 637–650, 2002.
[27] H. Shin and J. H. Lee, "Capacity of multiple-antenna fading channels: spatial fading correlation, double scattering, and keyhole," *IEEE Trans. Inform. Theory*, vol. 49, no. 10, pp. 2636–2647, 2003.
[28] M. Kiessling and J. Speidel, "Exact ergodic capacity of MIMO channels in correlated Rayleigh fading environments," in *Proc. International Zurich Seminar on Communications (IZS '04)*, pp. 128–131, Zurich, Switzerland, February 2004.

[29] P. F. Driessen and G. J. Foschini, "On the capacity formula for multiple input-multiple output wireless channels: a geometric interpretation," *IEEE Trans. Commun.*, vol. 47, no. 2, pp. 173–176, 1999.

[30] J.-S. Jiang and M. A. Ingram, "Comparison of beam selection and antenna selection techniques in indoor MIMO systems at 5.8 GHz," in *IEEE Radio and Wireless Conference (RAWCON '03)*, pp. 179–182, Boston, Mass, USA, August 2003.

[31] D. Chizhik, G. J. Foschini, M. J. Gans, and R. A. Valenzuela, "Keyholes, correlations, and capacities of multielement transmit and receive antennas," *IEEE Transactions on Wireless Communications*, vol. 1, no. 2, pp. 361–368, 2002.

[32] D. Gesbert, H. Bölcskei, D. Gore, and A. Paulraj, "MIMO wireless channels: capacity and performance prediction," in *IEEE Global Telecommunications Conference (GLOBECOM '00)*, vol. 2, pp. 1083–1088, San Francisco, Calif, USA, November 2000.

[33] P. Almers, F. Tufvesson, and A. F. Molisch, "Measurement of keyhole effect in a wireless multiple-input multiple-output (MIMO) channel," *IEEE Commun. Lett.*, vol. 7, no. 8, pp. 373–375, 2003.

[34] A. F. Molisch, M. Steinbauer, M. Toeltsch, E. Bonek, and R. S. Thoma, "Capacity of MIMO systems based on measured wireless channels," *IEEE J. Select. Areas Commun.*, vol. 20, no. 3, pp. 561–569, 2002.

[35] L. W. Hanlen and M. Fu, "Capacity of MIMO channels: a volumetric approach," in *Proc. IEEE International Conference on Communications (ICC '03)*, vol. 5, pp. 3001–3005, Anchorage, Alaska, USA, May 2003.

[36] F. R. Farrokhi, G. J. Foschini, A. Lozano, and R. A. Valenzuela, "Link-optimal space-time processing with multiple transmit and receive antennas," *IEEE Commun. Lett.*, vol. 5, no. 3, pp. 85–87, 2001.

[37] R. S. Blum, "MIMO capacity with antenna selection and interference," in *Proc. IEEE International Conference on Acoustics, Speech, and Signal Processing (ICASSP '03)*, vol. 4, pp. 824–827, Hong Kong, China, April 2003.

[38] H. Dai, A. F. Molisch, and H. V. Poor, "Downlink capacity of interference-limited MIMO systems with joint detection," *IEEE Transactions on Wireless Communications*, vol. 3, no. 2, pp. 442–453, 2004.

[39] A. Molisch, H. Dai, M. Z. Win, and J. Winters, "Reducing interference in multiple-input multiple-output systems," Tech. Rep., AT&T, 2001.

[40] M. Costa, "Writing on dirty paper (corresp.)," *IEEE Trans. Inform. Theory*, vol. 29, no. 3, pp. 439–441, 1983.

[41] A. Goldsmith, S. A. Jafar, N. Jindal, and S. Vishwanath, "Capacity limits of MIMO channels," *IEEE J. Select. Areas Commun.*, vol. 21, no. 5, pp. 684–702, 2003.

[42] K. Yu and B. Ottersten, "Models for MIMO propagation channels, a review," *Journal of Wireless Communications and Mobile Computing*, vol. 2, no. 7, pp. 653–666, 2002.

[43] A. F. Molisch and F. Tufvesson, "Multipath propagation models for broadband wireless systems," in *Digital Signal Processing for Wireless Communications Handbook*, M. Ibnkahla, Ed., pp. 2.1–2.43, CRC Press, Boca Raton, Fla, USA, December 2004.

[44] J. P. Kermoal, L. Schumacher, K. I. Pedersen, P. E. Mogensen, and F. Frederiksen, "A stochastic MIMO radio channel model with experimental validation," *IEEE J. Select. Areas Commun.*, vol. 20, no. 6, pp. 1211–1226, 2002.

[45] H. Özcelik, M. Herdin, W. Weichselberger, J. Wallace, and E. Bonek, "Deficiencies of "Kronecker" MIMO radio channel model," *IEE Electronics Letters*, vol. 39, no. 16, pp. 1209–1210, 2003.

[46] W. Weichselberger, H. Özcelik, M. Herdin, and E. Bonek, "A novel stochastic MIMO channel model and its physical interpretation," in *Proc. 6th International Symposium on Wireless Personal Multimedia Communications (WPMC '03)*, Yokosuka, Kanagawa, Japan, October 2003.

[47] A. M. Sayeed, "Deconstructing multiantenna fading channels," *IEEE Trans. Signal Processing*, vol. 50, no. 10, pp. 2563–2579, 2002.

[48] D. Gesbert, H. Bolcskei, D. A. Gore, and A. J. Paulraj, "Outdoor MIMO wireless channels: models and performance prediction," *IEEE Trans. Commun.*, vol. 50, no. 12, pp. 1926–1934, 2002.

[49] M. Steinbauer, A. F. Molisch, and E. Bonek, "The double-directional mobile radio channel," *IEEE Antennas Prop. Mag.*, vol. 43, no. 4, pp. 51–63, 2001.

[50] H. Xu, D. Chizhik, H. Huang, and R. Valenzuela, "A wave-based wideband MIMO channel modeling technique," in *Proc. 13th IEEE International Symposium on Personal, Indoor and Mobile Radio Communications (PIMRC '02)*, vol. 4, pp. 1626–1630, Lisbon, Portugal, September 2002.

[51] A. F. Molisch, "A generic model for MIMO wireless propagation channels in macro- and microcells," *IEEE Trans. Signal Processing*, vol. 52, no. 1, pp. 61–71, 2004.

[52] M. Steinbauer and A. F. Molisch, *Directional Channel Modelling*, John Wiley & Sons, New York, NY, USA, 2001.

[53] 3GPP/3GPP2 Spatial Channel Model Ad hoc Group, "Spatial channel model for MIMO systems," Tech. Rep. 3GPP and 3GPP2; TR 25.966, download at http://www.3gpp.org, 2003.

[54] V. Erceg, L. Schumacher, P. Kyritsi, D. S. Baum, A. F. Molisch, and A. Y. Gorokhov, "Indoor MIMO WLAN channel models," in *Standardization Drafts of IEEE 802 Meeting Dallas*, March 2003, doc. no. 03/161r1.

[55] B. H. Fleury, M. Tschudin, R. Heddergott, D. Dahlhaus, and I. K. Pedersen, "Channel parameter estimation in mobile radio environments using the SAGE algorithm," *IEEE J. Select. Areas Commun.*, vol. 17, no. 3, pp. 434–450, 1999.

[56] P. Kyritsi, R. A. Valenzuela, and D. C. Cox, "Channel and capacity estimation errors," *IEEE Commun. Lett.*, vol. 6, no. 12, pp. 517–519, 2002.

[57] P. Almers, F. Tufvesson, and A. F. Molisch, "Keyhole effects in MIMO wireless channels - measurements and theory," in *IEEE Global Telecommunications Conference (GLOBECOM '03)*, vol. 4, pp. 1781–1785, San Francisco, Calif, USA, December 2003.

[58] J. W. Wallace, M. A. Jensen, A. L. Swindlehurst, and B. D. Jeffs, "Experimental characterization of the MIMO wireless channel: data acquisition and analysis," *IEEE Transactions on Wireless Communications*, vol. 2, no. 2, pp. 335–343, 2003.

[59] M. Lienard, P. Degauque, J. Baudet, and D. Degardin, "Investigation on MIMO channels in subway tunnels," *IEEE J. Select. Areas Commun.*, vol. 21, no. 3, pp. 332–339, 2003.

[60] P. Almers, F. Tufvesson, P. Karlsson, and A. F. Molisch, "The effect of horizontal array orientation on MIMO channel capacity," in *Proc. 57th IEEE Semiannual Vehicular Technology Conference (VTC '03)*, vol. 1, pp. 34–38, Jeju, Korea, Spring 2003.

[61] D. Chizhik, J. Ling, P. W. Wolniansky, R. A. Valenzuela, N. Costa, and K. Huber, "Multiple-input multiple-output measurements and modeling in Manhattan," *IEEE J. Select. Areas Commun.*, vol. 21, no. 3, pp. 321–331, 2003.

[62] P. Soma, D. S. Baum, V. Erceg, R. Krishnamoorthy, and A. J. Paulraj, "Analysis and modeling of multiple-input multiple-output (MIMO) radio channel based on outdoor measurements conducted at 2.5 GHz for fixed BWA applications," in *Proc. IEEE International Conference on Communications (ICC '02)*, vol. 1, pp. 272–276, New York, NY, USA, May 2002.

Andreas F. Molisch: Mitsubishi Electric Research Laboratories, 201 Broadway, Cambridge, MA 02139, USA; Department of Electroscience, Lund University, 22100 Lund, Sweden

Email: andreas.molisch@ieee.org

Fredrik Tufvesson: Department of Electroscience, Lund Institute of Technology, Lund University, Box 118, 221 00 Lund, Sweden

Email: fredrik.tufvesson@es.lth.se

25 Distributed space-time coding techniques for multihop networks

Sergio Barbarossa, Gesualdo Scutari, and Loreto Pescosolido

25.1. Introduction

The primary goal in the design of a telecommunication network is to devise strategies that make possible the flow of information through the network with a desired quality of service, typically expressed in terms of delay and/or bit error rate. Looking at the problem from a historical perspective, the first networks were wired and this has somehow driven the initial research towards a certain direction. In the wired context, in fact, the links are always point-to-point and the information is conveyed through paths composed of the links between the nodes where the information packets are actually routed. Conversely, wireless channels are fundamentally different from wired channels, for two main reasons: (i) they are much more random and unpredictable than wired channels; (ii) they are intrinsically broadcast channels. The goal of this chapter is to show that if these differences are explicitly taken into account in the design of a wireless network, there is the possibility to convert them into a potential benefit, rather than considering them only as an annoying feature.

The most interesting aspect in the design of wireless networks is that most of the previous shortcomings can be actually converted into potential sources of performance improvement, provided that the design strategy is appropriate. The goal of this chapter is to show some possible methods to exploit the broadcasting nature of the radio links together with the channel randomness to devise schemes capable of a considerable gain.

The channel random fading is a characteristic of wireless channels and it can induce considerable performance losses. Since fading is a multiplicative phenomenon, it cannot be counteracted by simply increasing the transmission power, but it needs specific countermeasures. The other major shortcoming of radio links is their broadcasting nature. The information emitted by a given radio node travels in fact through all directions, so that part of the energy is inevitably wasted as it goes towards directions where there are no intended users. To limit such a waste, one should use directive antennas, but this would be highly impractical, especially

on portable handsets, as it would require the use of large arrays (with respect to the transmit wavelength).

The most effective strategy to combat fading is diversity. Diversity relies on the existence of more than one path between transmitter and receiver through which the information bits may be conveyed. If the paths are random, but (almost) independent of each other, one can find optimal strategies to combine the multiple replicas of the received signal in order to minimize the bit error rate (BER). The most known form of diversity is spatial receive diversity, obtainable when the receiver has multiple receive antennas. However, receive diversity is difficult to achieve on portable handsets whose limited size prevents the possibility of having independently fading channels. To overcome this limitation, the last years have witnessed a huge amount of research on methods capable of achieving a spatial diversity, even in the case where the receiver has only one antenna but the transmitter has multiple antennas. In such a case, it is necessary to transmit the data using a particular form of coding that spreads the information bits across the two-dimensional (2D) space-time domain, using the so-called *space-time coding* [1, 2]. If properly designed, space-time coding guarantees full diversity gain, even in cases where the transmitter does not have any information about the channels.

However, if both transmitters and receivers have only one antenna, it looks like there should be no way to achieve any spatial diversity. Indeed, this is not true if more radio nodes (relays) contribute to the transmission from one source to the intended destination. In fact, the broadcasting of the information makes possible the presence of the same information over potentially more than one radio node. If the radio nodes that have received the same message correctly cooperate to retransmit the information to the final destination, the overall system may benefit from spatial diversity even when each radio node has only one antenna. This chapter focuses on this idea and on the ways to achieve diversity through cooperation.

Multihop radio networking is indeed a field whose study started a long time ago (see, e.g., [3] and the references therein). Some basic theorems on the capacity of relaying networks were established in, for example, [4, 5, 6, 7]. Conventional relaying can indeed be seen as a particular form of *distributed space-time coding*, where the same information is transmitted by different points (relays), at different times. From this perspective, relaying can thus be interpreted as a repetition code in the space-time domain. As is well known, repetition coding is not the best coding strategy, and thus one should achieve a considerable gain by using more sophisticated space-time coding techniques. This form of space-time coding that coordinates the transmission of source and relays is called *distributed* space-time coding. Quite recently, the interest in relaying networks, especially in the form of cooperation among nodes, has increased considerably. One result that sparked great interest was that cooperation among users can increase the capacity in an uplink multiuser channel [8]. A thorough analysis of the diversity gain achievable with cooperation was given in [9, 10, 11], where different distributed cooperation protocols were compared. Cooperation was proved to be very useful to combat shadowing effects, as shown in [12], and it can occur in different forms, as suggested in many recent works, like, for example, [10, 13, 14, 15, 16, 17, 18, 19, 20,

21, 22]. Among all these possibilities, there is the basic idea of using the relays as if they were the antennas of a multiantenna transmitter. With this perspective, cooperation induces a *virtual* array between transmitter and receiver. This opens the field to a huge amount of possibilities provided by all coding methods devised for multi-input multi-output (MIMO) transceivers. In this more general framework, the relaying problem becomes the problem of mapping the algorithms valid for real MIMO systems into cooperation strategies of a virtual MIMO system.

The chapter is organized as follows. In Section 25.2, we show how a single-user system can achieve a considerable gain thanks to the cooperation with relay nodes scattered randomly in a given territory. In Section 25.3, we introduce the so-called distributed space-time coding (DSTC) strategy, where source and relays transmit in a coordinate manner according to a space-time code distributed among the cooperating nodes. In Section 25.4, we consider in detail a specific single-user system where source and relay adopt a block-distributed Alamouti strategy for transmission over frequency-selective channels. We show the performance achieved over simulated as well as real data. Although DSTC follows the main ideas of conventional space-time coding (STC) techniques, there are aspects that clearly differentiate DSTC from STC. The main differences are related to the fact that in DSTC the cooperating antennas are not colocated. This implies that the signals received by the destination from source and relays might arrive out of synchronization, and without the right power balance between them. We analyze these aspects in Section 25.4.3, where we consider possible ways to distribute the power between source and relays optimally, in order to minimize the average BER, and in Section 25.4.6, where we consider the synchronization problem.

The performance of a cooperative network improves as the density of the relay nodes increases. However, taking into account both technical as well as economic factors, this implies that a cooperative strategy is appealing only if the cost of the relay nodes is extremely small. One possibility is to use as relays, in cellular networks, portable phones that are in standby, whose owners have previously agreed on their availability to act as relays, maybe against appropriate incentives. The other possibility consists in deploying extremely simple relays, such as, for example, nonregenerative, or amplify-and-forward (A&F) relays that amplify and forward the received messages. Such relays need only the radio-frequency section (antenna and amplifier) and are then much more economical than any other transceiver. To assess the performance of such relays, in Section 25.5 we compare the performance of regenerative, that is, decode-and-forward (D&F) relays and nonregenerative relays. Finally, in Section 25.6 we compare alternative DSTC strategies for a multiuser system.

25.2. Cooperation gain

We consider a region with a certain number n of radio nodes scattered randomly. Among these nodes, there is one source node S and the corresponding destination node D. All other nodes are potential relays R. The radio nodes are uniformly distributed over a circle of radius r, with density $\rho = n/(\pi r^2)$. In the limit of n

and r large, but constant density ρ, the spatial distribution of the points can be well described by a 2D homogeneous Poisson process [23]. The probability that k nodes fall within any given circle of radius r_0 is then

$$p_R(k) = \frac{(\rho\pi r_0^2)^k}{k!} e^{-\rho\pi r_0^2}. \tag{25.1}$$

We say that a node may act as a relay for the source node only if its BER does not exceed a given maximum BER, $P_{e\max}$, with a given outage probability. Using QAM constellations of order M, the BER is

$$P_e = cQ\left(\sqrt{g\frac{\mathcal{E}_b}{\sigma_n^2}|h|^2}\right) \leq ce^{-g\mathcal{E}_b|h|^2/\sigma_n^2}, \tag{25.2}$$

where $\mathcal{E}_b$ is the energy per bit, σ_n^2 is the noise variance, h is the channel flat fading coefficient, and c and g are two coefficients that depend on the order M of the QAM constellation as follows [24]:

$$c = 4\frac{\sqrt{M}-1}{\sqrt{M}\cdot\log_2 M}, \qquad g = \frac{3}{M-1}\log_2 M. \tag{25.3}$$

We assume here the Rayleigh channel model, so that h is a complex Gaussian random variable with zero mean and variance σ_h^2. We assume that $\sigma_h^2 = 1/d^\alpha$, where the exponent α depends on the propagation environment. Typically, α is between 2 and 5. In (25.2) we have also introduced an upper bound useful for deriving closed-form expressions. The out-of-service probability is defined as

$$P_{\text{os}} = \mathcal{P}\{P_e > P_{e\max}\} \leq \mathcal{P}\{ce^{-g\mathcal{E}_b|h|^2/\sigma_n^2} > P_{e\max}\}. \tag{25.4}$$

Since the channel is Rayleigh, $|h|^2$ is an exponential random variable. Hence P_{os} can be upper bounded as

$$P_{\text{os}} \leq 1 - e^{-\sigma_n^2\log(c/P_{e\max})/(g\mathcal{E}_b\sigma_h^2)}. \tag{25.5}$$

Within this set-up, a link is reliable and it is established only if the out-of-service event occurs with a probability smaller than a given value P_{os}. Setting $\sigma_h^2 = 1/r^\alpha$ in (25.5) and inverting (25.5), we find that the source covers a circle of radius

$$r_0 = \left[-\frac{g\mathcal{E}_b\log(1-P_{\text{os}})}{\sigma_n^2\log(c/P_{e\max})}\right]^{1/\alpha}. \tag{25.6}$$

This coverage radius depends on the energy $\mathcal{E}_b$, as well as on the transmission rate (throughout the two coefficients c and g). Clearly, increasing $\mathcal{E}_b$ increases the coverage, but more energy is wasted only to send information towards the relays instead of the final intended destination. There is in general an optimal energy

distribution between the two phases where the source sends data to the relay and when source and relays transmit together towards the destination. We denote by $\mathcal{E}_T$ the total energy per bit for all cooperating nodes. Introducing the real coefficient β, with $0 \leq \beta \leq 1$, we indicate with $\beta\mathcal{E}_T$ the portion of the total energy dedicated to send information from the set of cooperating nodes to the destination, and with $(1-\beta)\mathcal{E}_T$ the energy spent by the source to send data to the relays.

If k is the number of relays that receive the data from the source with the prescribed reliability, the k relays plus the source can then transmit together towards the destination as if they were the transmit antennas of a single-user.[1] Denoting with h_i the channel coefficients from source and relays towards the destination, using a full diversity space-time coding scheme, such as, for example, orthogonal coding, the error probability at the receiver is[2]

$$P_e(k+1;\mathbf{h}) = cQ\left(\sqrt{g\frac{\beta\mathcal{E}_T}{\sigma_n^2(k+1)}\sum_{i=1}^{k+1}|h_i|^2}\right). \tag{25.7}$$

Assuming that the channels are statistically independent, the expected value of $P_e(k+1) := E_{\mathbf{h}}\{P_e(k+1;\mathbf{h})\}$ is [25]

$$P_e(k+1) = \frac{4\sqrt{M}-1}{\sqrt{M}\log_2(M)}\left(\frac{1-\mu}{2}\right)^{(k+1)n_R}\cdot\sum_{m=0}^{k}\binom{k+m}{m}\left(\frac{1+\mu}{2}\right)^m, \tag{25.8}$$

where

$$\mu := \sqrt{\frac{3\beta\mathcal{E}_T\log_2(M)\sigma_h^2}{3\beta\mathcal{E}_T\log_2(M)\sigma_h^2+2(M-1)(k+1)\sigma_n^2}}. \tag{25.9}$$

The final average error probability at the destination, in case of cooperation, is then

$$\overline{P}_e = \sum_{k=0}^{\infty} p_{r_0}(k)P_e(k+1), \tag{25.10}$$

where $p_{r_0}(k)$ is given by (25.1), with r_0 given by (25.6) setting $\mathcal{E}_b = (1-\beta)\mathcal{E}_T$, whereas $P_e(k+1)$ is given by (25.8).

An example of average BER is reported in Figure 25.1 for a network of nodes with different node densities. We can clearly see the advantage of using cooperation with respect to the noncooperative case and how the gain increases as the

[1] Since a node is chosen as a relay only if its BER is below a given threshold, with a given outage probability, we assume here that the errors at the relay nodes are negligible.

[2] In case of coordinated transmission from $k+1$ nodes, we normalize the transmit power of each node by $k+1$, so that the overall radiated power is independent of k.

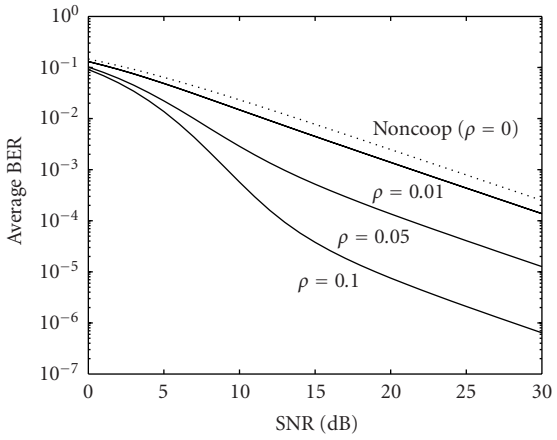

FIGURE 25.1. Average BER at the final destination in a cooperating network for different values of node density.

node density increases. At high SNR, the dominant term in (25.10) is the term with $k = 0$, as it corresponds to the slowest decay rate of the average BER. The term $P_e(1)$ goes like $1/\text{SNR}$, at high SNR. Hence, in a random network there is no real diversity gain. Nevertheless, since $P_e(1)$ is multiplied by $p_R(0)$, there still is a coding gain equal to $1/p_R(0)$, that is,

$$G_c = e^{\pi\rho r_0^2}. \tag{25.11}$$

Hence, cooperation introduces diversity in the sense of the existence of multiple paths for the transmitted data, but unlike conventional systems, this results in a coding gain, not in a diversity gain. The coding gain is always greater than one and it grows exponentially with the increase of the relay nodes density. To obtain a higher G_c, for a given ρ, it is necessary to increase the coverage radius r_0. This requires that more energy is used in the first phase, when S sends data to the relays. If there is a constraint on the total energy $\mathcal{E}_T$, it is interesting to see the optimal power distribution between the two transmission phases acting on β.

As an example, in Figure 25.2 we show the average BER, for a given SNR at the destination, as a function of β. We can see that, depending on the final SNR, there is an optimal β.

25.3. Distributed space-time coding

The choice of the right space-time coding technique depends on several factors. As with conventional space-time coding, the choice depends on the desired trade-off between rate, diversity, and receiver complexity. The number n_R of real receive antennas plays a fundamental role. If $n_R = 1$, the cooperation induces a virtual multi-input single-output (MISO) communication, introducing diversity into the

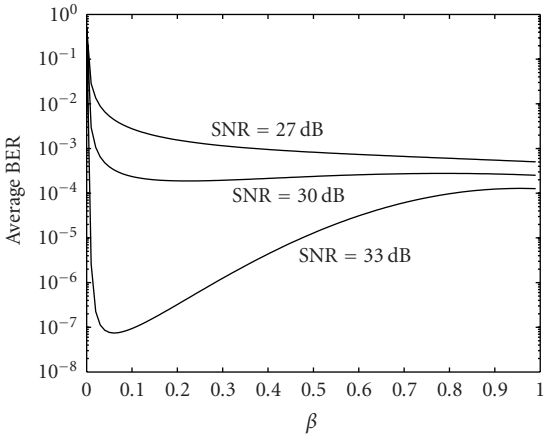

FIGURE 25.2. Average BER as a function of β for different SNR values.

system, but not a rate gain. Conversely, if $n_R > 1$, we can think of schemes capable of both diversity and rate gains, exploiting the resulting virtual MIMO structure. Basically, one could choose among the following classes of STC techniques: (i) orthogonal STC (OSTC) [2], as a strategy that maximizes the diversity gain and minimizes the receiver complexity; (ii) full-rate/full diversity[3] codes (FRFD) [26, 27], as codes that yield maximum diversity gain and transmission rate, but with high receiver complexity; (iii) V-BLAST codes [29], as a technique that maximizes the rate, sacrificing the diversity gain, but with limited receiver complexity. Alternatively, one could use the trace-orthogonal design [30] as a flexible way to trade complexity, bit rate, and BER. It is worth noticing that the optimal trade-off among these alternative strategies, in the distributed case does not coincide, necessarily, with the trade-off achievable with conventional space-time coding.

The first evident difference between conventional STC and DSTC is the presence of the time-slot necessary for the exchange of data between source and relays. This induces an inevitable rate loss. To reduce this loss, it is necessary to allow for the reuse of the same time-slot by more than one set of source-relay pairs. In Figure 25.3, we show, as an example, three sources (circles) and some potential relays (dots). If the relays are associated to the nearest sources[4] and the sources are sufficiently far apart, we can assign the same time-slot for the exchange of information between each source and its own relays. Clearly, this does not prevent the interference between different source-relay pairs. In general, the relay discovery phase should follow a strategy that gives rise to many spatially separated microcells, as in Figure 25.3, where each source acts as a local base station broadcasting

[3]The term full rate here is used in the same sense as [26, 27] and it means that a transmitter with n_T antennas transmits n_T^2 symbols in n_T time-slots. This does not imply anything about the final BER and then it has to be distinguished by the information rate concept used in [28].

[4]We will comment later on the meaning of distance between source and relay, as it has to take into account also the channel fading.

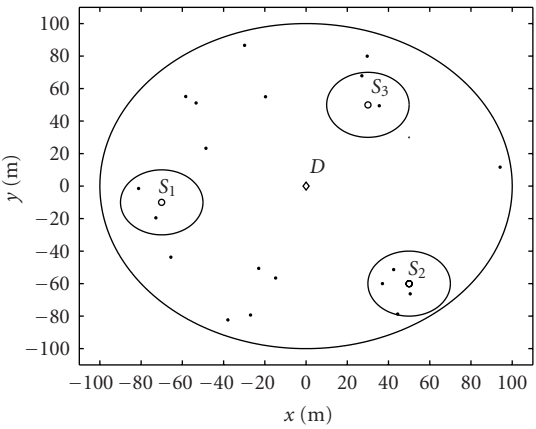

FIGURE 25.3. Geometry of cooperative network with three source nodes (circles), potential relays (dots), and one destination (D).

to its relays, who may get interference from other microcells (sources). The need to limit the coverage of each source, in its relay discovery phase, is also useful because (i) less power is wasted in the source-relay link; (ii) there are less synchronization problems in the final link towards the destination; (iii) there is less interference between different source-relay sets.

We compute now the rate loss for different cooperation structures assuming that there are N simultaneous source-relays pairs sharing the same time-slot. We denote with T_{S2R} and T_{SR2D} the duration of the S2R and SR2D time-slots. T_s is the symbol duration in all slots. For a given bit rate, the durations depend on the constellation order used in the different slots. We denote with Q and M the constellation orders used in the S2R and in the SR2D slots, respectively. We consider a frame containing both S2R and the N SR2D links which then has a duration $T_F = T_{\mathrm{S2R}} + NT_{\mathrm{SR2D}}$. The rate reduction factor, with respect to the noncooperative case, in a TDMA context, is then

$$\eta = \frac{NT_{\mathrm{SR2D}}}{T_{\mathrm{S2R}} + NT_{\mathrm{SR2D}}}. \tag{25.12}$$

Clearly, the rate loss can be reduced by decreasing T_{S2R}, that is, by increasing Q, or by increasing N. In the first case, the relay needs a higher signal-to-noise-plus-interference ratio (SNIR). In the second case, SNIR decreases at the relay as there is more interference. In both cases, it is less likely to discover a relay with sufficient SNIR. Hence, the right choice has to result from a trade-off between rate and performance. We discuss now in detail the alternative DSTC strategies corresponding to OSTC, FRFD, and V-BLAST codes. In all cases, we denote with $s(n)$ the sequence of symbols sent by S during the SR2D slot, whereas $\hat{s}(n)$ indicates the estimate of $s(n)$ performed at the relay. For simplicity, we refer to a context where each source cooperates with only one relay.

25.3.1. Distributed orthogonal STC

Distributed orthogonal STC (D-OSTC) guarantees maximum receiver simplicity and full diversity, and it can be implemented also when the final destination has a single antenna. D-OSTC was proposed in [11, 14, 17], where the relays are essentially error-free, and in [21], where the decoding errors at the relay are explicitly taken into account. D-OSTC transmits 2 symbols over two successive time periods, so that $T_{\mathrm{SR2D}} = 2T_s$ and $T_{\mathrm{S2R}} = 2\log_2(M)T_s/\log_2(Q)$. The sequence transmitted by the source-relay pair is

$$\begin{bmatrix} s(n) & -s^*(n+1) \\ \hat{s}(n+1) & \hat{s}^*(n) \end{bmatrix}. \tag{25.13}$$

The first row of this matrix contains the symbols transmitted by the source, whereas the second row refers to the symbols transmitted by the relay (different columns refer to successive time instants). The overall bit rate, incorporating also the rate loss, is

$$R = \frac{2N\log_2 M}{2N + 2\log_2 M/\log_2 Q}\ \text{b/s/Hz}. \tag{25.14}$$

25.3.2. Distributed full-rate/full diversity

If the final destination has two antennas, there is a virtual 2×2 MIMO, with the possibility of increasing the rate. This can be achieved, for example, using distributed full-rate/full diversity (D-FRFD) or distributed (D-BLAST). With D-FRFD, the pair S/R transmits 4 symbols over two consecutive time periods. The transmitted matrix is (see [26] or [27])

$$\begin{bmatrix} s(n) + \varphi s(n+1) & \theta(s(n+2) + \varphi s(n+3)) \\ \theta(\hat{s}(n+2) - \varphi\hat{s}(n+3)) & \hat{s}(n) - \varphi\hat{s}(n+1) \end{bmatrix}, \tag{25.15}$$

where $\varphi = e^{j/2}$, $\theta = e^{j/4}$ are two rotation parameters (see, e.g., [26] or [27], for the choice of φ and θ). The bit rate is

$$R = \frac{4N\log_2 M}{2N + 4\log_2 M/\log_2 Q}\ \text{b/s/Hz}. \tag{25.16}$$

25.3.3. Distributed BLAST

We consider here the version of BLAST where two independent streams of data are transmitted from the two antennas. In its distributed version, D-BLAST requires that the relay receives only half of the bits to be transmitted. This implies an advantage with respect to D-FRFD, as it allows us to reduce the duration of the S2R time-slot. The price paid with respect to D-FRFD is that D-BLAST is not full

diversity. The transmitted matrix in the D-BLAST case is

$$\begin{bmatrix} s(n) & s(n+2) \\ \hat{s}(n+1) & \hat{s}(n+3) \end{bmatrix}, \tag{25.17}$$

and the bit rate is

$$R = \frac{4N \log_2 M}{2N + 2 \log_2 M / \log_2 Q} \text{ b/s/Hz}. \tag{25.18}$$

Comparing the transmission rates of all the distributed schemes, for a given choice of the constellation orders Q and M, we see that D-BLAST has the highest transmission rate.

25.3.4. Relay discovery phase

This section describes a possible resource discovery phase. A source looking for potential relays starts sending a sounding signal to verify whether there are available neighbors. The sounding signal is a pseudo noise code identifying the source. A potential relay may receive the sounding signals from more than one source. The radio nodes available to act as relays compute the SNIR for each source.[5] This step requires the node to be able to separate the signals coming from different sources. This is made possible by the use of orthogonal codes. The potential relays retransmit an acknowledgment signal back only to those sources whose SNIR exceeds a certain threshold. The source then receives the acknowledgments and the relative SNIR from all potential relays and it decides which relays to use. This phase insures that the relay, once chosen, is sufficiently reliable. Given the variability of the wireless channel, this operation has to be repeated at least once every channel coherence time. To avoid excessive complications, a node may act as a relay for no more than one source. The basic philosophy we follow to discover relays is that source and relays should be as close as possible. This is justified by the following concurring reasons: (i) less power is wasted in the S2R slot; (ii) there are less synchronization problems in the final SR2D slot; (iii) there is less interference between different source-relay sets. In summary, this relay discovery phase creates many spatially separated microcells where each source acts as a local base station broadcasting to its relays, who may get interference from other microcells (sources).

25.4. Regenerative relaying with block-distributed orthogonal space-time coding

In this section, we analyze in detail an example of distributed space-time coding, using D-OSTC and regenerative relay [21]. We assume that the source has found

[5]The SNIR may be evaluated for each channel realization or in average sense, considering the channel statistics such as mean and covariance. The first option provides better performance, but it requires more frequent channel estimation updates than the second option.

its own relay[6] and that the interference due to the other active source-relay links is negligible. We consider, thus, a two-hop relay channel, composed of a source (S), a relay (R) and a destination (D).

Differently from common STC, with DSTC, (i) regenerative relays might make decision errors, so that the symbols transmitted from R could be affected by errors; (ii) the links between S and D and between R and D do not have the same statistical properties, in general; (iii) even if S and R are synchronous, their packets might arrive at D at different times, as S and R are not colocated. In the following, we will address all these problems specifically.

We illustrate the proposed transmission protocol by referring to a TDD scheme, but the same considerations could apply to an FDD mode. In a TDD system, each frame is subdivided in consecutive time-slots: in the first slot S transmits and R receives; in the second slot, S and R transmit simultaneously. We describe the distributed space-time protocol within the following setup: (a1) all channels are FIR of (maximum) order L_h and time-invariant over at least a pair of consecutive blocks; (a2) the channel coefficients are i.i.d. complex Gaussian random variables with zero mean and variance $1/d^2$, where d is the link length; (a3) the information symbols are i.i.d. BPSK symbols that may assume the values A or $-A$ with equal probability;[7] (a4) the received data are degraded by additive white Gaussian noise (AWGN); (a5) the channels are perfectly known at the receive side and are unknown at the transmit side; (a6) the transmission scheme for all terminals is blockwise, where each block is composed of M symbols, incorporating a cyclic prefix of length L equal to the sum of the relative delay with which packets from S and R arrive at D plus the maximum channel order L_h.

We will use the following notation. We denote with h_{sd}, h_{sr}, and h_{rd}, the impulse responses between S and D, S and R, and R and D, respectively. Each block of symbols $\mathbf{s}(i)$ has size M and it is linearly encoded so as to generate the N-size vector $\mathbf{x}_s(n) := \mathbf{F}\mathbf{s}(n)$, where $\mathbf{F}$ is the $N \times M$ precoding matrix. A CP of length $L \geq L_h$ is inserted at the beginning of each block to facilitate elimination of interblock interference, synchronization, and channel equalization at the receiver. $\mathbf{A}^\dagger$ denotes the pseudo-inverse of $\mathbf{A}$; $\Re\{x\}$ indicates the real part of x; when applied to a vector, $\Re\{\mathbf{x}\}$ is the vector whose entries are the real part of the entries of $\mathbf{x}$.

D-OSTC, for frequency-selective channels, works as follows. During the first time-slot, S sends consecutively, the two N-size information symbols blocks $\mathbf{s}(i)$ and $\mathbf{s}(i+1)$. The blocks are linearly encoded using the precoding matrix $\mathbf{F}$, so that the corresponding transmitted blocks are $\mathbf{x}_s(n) := \mathbf{F}_s\mathbf{s}(n)$, with $n = i, i+1$. Under (a6), after removing the guard interval at the receiver, the N-size vectors $\mathbf{y}_r(n)$ received from R are

$$\mathbf{y}_r(n) = \mathbf{H}_{sr}\mathbf{F}_s\mathbf{s}(n) + \mathbf{w}_r(n), \quad n = i, i+1, \tag{25.19}$$

[6]Thanks to the assumption that the relay nodes are not error-free, the probability of finding a relay in the discovery phase increases with respect to the schemes that use a relay, only if it is error-free.

[7]Assumption (a3) is made only for simplifying our derivations, but there is no restriction to use higher-order constellations.

where $\mathbf{w}_r(n)$ is the additive noise at the relay. Thanks to the insertion of the CP, the channel matrix $\mathbf{H}_{sr}$ is $N \times N$ circulant Toeplitz and it is diagonalized as $\mathbf{H}_{sr} = \mathbf{W}\mathbf{\Lambda}_{sr}\mathbf{W}^H$, where $\mathbf{W}$ is the $N \times N$ IFFT matrix with $\{W\}_{kl} = \mathrm{e}^{j2\pi kl/N}/\sqrt{N}$, whereas $\mathbf{\Lambda}_{sr}$ is the $N \times N$ diagonal matrix, whose entries are $\Lambda_{sr}(k,k) = \sum_{l=0}^{L_h-1} h_{sr}(l)\mathrm{e}^{-j2\pi lk/N}$.

The relay node decodes the received vectors and provides the estimated vectors $\hat{\mathbf{s}}(i)$ and $\hat{\mathbf{s}}(i+1)$.

During the successive time-slot, S and R transmit *simultaneously*, using a block Alamouti's strategy [31]. More specifically, in the first half of the second time-slot, S transmits $\mathbf{x}_s(i+2) = \alpha_1\mathbf{F}\mathbf{s}(i)$ and R transmits $\mathbf{x}_r(i+2) = \alpha_2\mathbf{F}\hat{\mathbf{s}}(i+1)$. In the second half, S transmits $\mathbf{x}_s(i+3) = \alpha_1\mathbf{G}\mathbf{s}^*(i+1)$ while R transmits $\mathbf{x}_r(i+3) = -\alpha_2\mathbf{G}\hat{\mathbf{s}}^*(i)$. To guarantee maximum spatial diversity, the two matrices $\mathbf{G}$ and $\mathbf{F}$ are related to each other by $\mathbf{G} = \mathbf{J}\mathbf{F}^*$, as in [31], where $\mathbf{J}$ is a time reversal (plus a one-chip cyclic shift) matrix. If N is even, $\mathbf{J}$ has all null entries except the elements of position $(1,1)$ and $(k, N-k+2)$, with $k = 2,\ldots,N$, which are equal to one. If N is odd, $\mathbf{J}$ is the antidiagonal matrix. The two real coefficients α_1 and α_2 are related to each other by $\alpha_1^2 + \alpha_2^2 = 1$. They are introduced in order to have a degree of freedom in the power distribution between S and R, under a constraint on the total transmit power. In Section 25.4.3, we will show how to choose α_1 (and then α_2) in order to minimize the final average BER.

After discarding the CP and using (a1), the blocks received by D in the two consecutive time-slots $i+2$, and $i+3$ are given by

$$\begin{aligned}\mathbf{y}_d(i+2) &= \alpha_1\mathbf{H}_{sd}\mathbf{F}\mathbf{s}(i) + \alpha_2\mathbf{H}_{rd}\mathbf{F}\hat{\mathbf{s}}(i+1) + \mathbf{w}_d(i+2),\\ \mathbf{y}_d(i+3) &= \alpha_1\mathbf{H}_{sd}\mathbf{G}\mathbf{s}^*(i+1) - \alpha_2\mathbf{H}_{rd}\mathbf{G}\hat{\mathbf{s}}^*(i) + \mathbf{w}_d(i+3),\end{aligned} \tag{25.20}$$

where $\mathbf{H}_{sd}$ and $\mathbf{H}_{rd}$ refer to the channels between S and D and between R and D, respectively. Exploiting, again, the diagonalizations $\mathbf{H}_{sd} = \mathbf{W}\mathbf{\Lambda}_{sd}\mathbf{W}^H$ and $\mathbf{H}_{rd} = \mathbf{W}\mathbf{\Lambda}_{rd}\mathbf{W}^H$, if we premultiply in (25.20) $\mathbf{y}_d(i+2)$ by $\mathbf{W}^H$ and $\mathbf{y}_d^*(i+3)$ by $\mathbf{W}^T$, we get

$$\begin{aligned}\mathbf{W}^H\mathbf{y}_d(i+2) &= \alpha_1\mathbf{\Lambda}_{sd}\tilde{\mathbf{F}}\mathbf{s}(i) + \alpha_2\mathbf{\Lambda}_{rd}\tilde{\mathbf{F}}\hat{\mathbf{s}}(i+1) + \mathbf{W}^H\mathbf{w}_d(i+2),\\ \mathbf{W}^T\mathbf{y}_d^*(i+3) &= \alpha_1\mathbf{\Lambda}_{sd}^*\tilde{\mathbf{G}}^*\mathbf{s}(i+1) - \alpha_2\mathbf{\Lambda}_{rd}^*\tilde{\mathbf{G}}^*\hat{\mathbf{s}}(i) + \mathbf{W}^T\mathbf{w}_d^*(i+3),\end{aligned} \tag{25.21}$$

where $\tilde{\mathbf{F}} := \mathbf{W}^H\mathbf{F}$ and $\tilde{\mathbf{G}} := \mathbf{W}^H\mathbf{G}$. For the sake of simplicity, we assume that OFDM is performed at both S and R nodes, so that $N = M$, $\mathbf{F} = \mathbf{W}$ and thus $\tilde{\mathbf{F}} = \mathbf{I}_N$ and $\mathbf{G} = \mathbf{W}$. We also introduce the orthogonal matrix

$$\mathbf{\Lambda} := \begin{pmatrix} \alpha_1\mathbf{\Lambda}_{sd} & \alpha_2\mathbf{\Lambda}_{rd} \\ -\alpha_2\mathbf{\Lambda}_{rd}^* & \alpha_1\mathbf{\Lambda}_{sd}^* \end{pmatrix} \tag{25.22}$$

such that $\mathbf{\Lambda}^H\mathbf{\Lambda} := \mathbf{I}_2 \otimes \bar{\mathbf{\Lambda}}^2$, where $\bar{\mathbf{\Lambda}}^2 := \alpha_1^2|\mathbf{\Lambda}_{sd}|^2 + \alpha_2^2|\mathbf{\Lambda}_{rd}|^2$ and $\otimes$ denotes the Kronecker product. We introduce also the unitary matrix[8] $\mathbf{Q} := \mathbf{\Lambda}(\mathbf{I}_2 \otimes \bar{\mathbf{\Lambda}}^{-1})$, satisfying

[8] We suppose that the channels do not share common zeros on the grid $z_q = \mathrm{e}^{j2\pi q/N}$, with q denoting an integer, so that $\bar{\mathbf{\Lambda}}$ is invertible.

the relationships $\mathbf{Q}^H\mathbf{Q} = \mathbf{I}_{2N}$ and $\mathbf{Q}^H\mathbf{\Lambda} = \mathbf{I}_2 \otimes \bar{\mathbf{\Lambda}}$. Exploiting the above equalities and multiplying the vector $\mathbf{u} := [(\mathbf{W}^H\mathbf{y}_d(i+2))^T, (\mathbf{W}^T\mathbf{y}_d^*(i+3))^T]^T$ by the matrix $\mathbf{Q}^H$, without compromising the decision optimality (because of the unitarity of $\mathbf{Q}$), we get

$$\begin{bmatrix} \mathbf{r}(i) \\ \mathbf{r}(i+1) \end{bmatrix} := \mathbf{Q}^H\mathbf{u} = \begin{bmatrix} |\tilde{\Lambda}_{sd}|^2 & -\tilde{\Lambda}_{sd}^*\tilde{\Lambda}_{rd} \\ \tilde{\Lambda}_{sd}\tilde{\Lambda}_{rd}^* & |\tilde{\Lambda}_{sd}|^2 \end{bmatrix} \mathbf{s} + \begin{bmatrix} |\tilde{\Lambda}_{rd}|^2 & \tilde{\Lambda}_{sd}^*\tilde{\Lambda}_{rd} \\ -\tilde{\Lambda}_{sd}\tilde{\Lambda}_{rd}^* & |\tilde{\Lambda}_{rd}|^2 \end{bmatrix} \hat{\mathbf{s}} + \bar{\mathbf{w}}, \tag{25.23}$$

where $\mathbf{s} := [\mathbf{s}(i)^T, \mathbf{s}(i+1)^T]^T$, $\hat{\mathbf{s}} := [\hat{\mathbf{s}}(i)^T, \hat{\mathbf{s}}(i+1)^T]^T$, $\tilde{\mathbf{\Lambda}}_{sd} := \alpha_1\mathbf{\Lambda}_{sd}\bar{\mathbf{\Lambda}}^{-1/2}$, $\tilde{\mathbf{\Lambda}}_{rd} := \alpha_2\mathbf{\Lambda}_{rd}\bar{\mathbf{\Lambda}}^{-1/2}$, $\bar{\mathbf{w}} := [\bar{\mathbf{w}}^T(i), \bar{\mathbf{w}}^T(i+1)]^T = \mathbf{Q}^H[\mathbf{w}^T(i+2), \mathbf{w}^H(i+3)]^T$. As expected, the previous equations reduce to the classical block Alamouti equations, see for example, [31], if the two transmit antennas use the same power, that is, $\alpha_1 = \alpha_2$, and there are no decision errors at the relay node, that is, $\hat{\mathbf{s}}(n) \equiv \mathbf{s}(n)$, $n = i, i+1$.

Since $\mathbf{Q}^H$ is unitary, if $\mathbf{w}$ is white, $\bar{\mathbf{w}}$ is also white, with covariance matrix $\mathbf{C}_w = \sigma_n^2\mathbf{I}_{2N}$. Furthermore, since all matrices $\mathbf{\Lambda}$ appearing in (25.23) are diagonal, the system (25.23) of $2N$ equations can be decoupled into N independent systems of two equations in two unknowns, each equation referring to a single subcarrier. More specifically, introducing the vectors $\mathbf{r}_k := [r_k(i), r_k(i+1)]^T$, $\mathbf{s}_k := [s_k(i), s_k(i+1)]^T$, $\hat{\mathbf{s}}_k := [\hat{s}_k(i), \hat{s}_k(i+1)]^T$, and $\bar{\mathbf{w}}_k := [\bar{w}_k(i), \bar{w}_k(i+1)]^T$, referring to the kth subcarrier, with $k = 0, \ldots, N-1$ (for simplicity of notation, we drop the block index and we set $\tilde{\Lambda}_{sd} = \tilde{\Lambda}_{sd}(k,k)$ and $\tilde{\Lambda}_{rd} = \tilde{\Lambda}_{rd}(k,k)$), (25.23) is equivalent to the following system of equations:

$$\mathbf{r}_k = \begin{pmatrix} |\tilde{\Lambda}_{sd}|^2 & -\tilde{\Lambda}_{sd}^*\tilde{\Lambda}_{rd} \\ \tilde{\Lambda}_{sd}\tilde{\Lambda}_{rd}^* & |\tilde{\Lambda}_{sd}|^2 \end{pmatrix} \mathbf{s}_k + \begin{pmatrix} |\tilde{\Lambda}_{rd}|^2 & \tilde{\Lambda}_{sd}^*\tilde{\Lambda}_{rd} \\ -\tilde{\Lambda}_{sd}\tilde{\Lambda}_{rd}^* & |\tilde{\Lambda}_{rd}|^2 \end{pmatrix} \hat{\mathbf{s}}_k + \bar{\mathbf{w}}_k. \tag{25.24}$$

Since the noise vector $\bar{\mathbf{w}}_k$ is also white with covariance matrix $\mathbf{C}_w = \sigma_n^2\mathbf{I}_{2N}$, and there is no intersymbol interference (ISI) between vectors $\mathbf{s}_k$ and $\mathbf{r}_k$ corresponding to different subcarriers, $\mathbf{r}_k$ represents a sufficient statistic for the decision on the transmitted symbols vector $\mathbf{s}_k$.

25.4.1. ML detector

We derive now the structure of the maximum likelihood (ML) detector at the final destination. Besides the previous assumptions, we assume also that D has perfect knowledge of the vector of error probabilities $p_{e_1}(k)$ and $p_{e_2}(k)$, $k = 0, \ldots, N-1$, occurring at the relay. This requires an exchange of information between R and D. This information has to be updated with a rate depending on the channel coherence time. Later on, we will show an alternative (suboptimum) detection scheme that does not require such a knowledge.

We denote with $\mathcal{S}$ the set of all possible transmitted vectors $\mathbf{s}_k$ and with $p_{e1}(k)$ and $p_{e2}(k)$ the conditional (to a given channel realization) error probabilities, at the relay node, on $s_k(1)$ and $s_k(2)$, respectively. After detection, at the node R, we

have $\hat{s}_k(l) = s_k(l)$, with probability $(1 - p_{el}(k))$, or $\hat{s}_k(l) = -s_k(l)$, with probability $p_{el}(k)$, $l = 1, 2$. Since the symbols are independent, the probability density function of the received vector $\mathbf{z}$, conditioned to having transmitted $\mathbf{s}_k$, is [32]

$$\begin{aligned} f_{\mathbf{z}|\mathbf{s}_k}(\mathbf{z}|\mathbf{s}_k) = \frac{1}{\pi^2\sigma_n^2}\Bigg[& (1 - p_{e1}(k))(1 - p_{e2}(k)) \exp\left\{ - \frac{|\mathbf{z} - \mathbf{A}_k(1,1)\mathbf{s}_k|^2}{\sigma_n^2} \right\} \\ & + p_{e1}(k)p_{e2}(k) \exp\left\{ - \frac{|\mathbf{z} - \mathbf{A}_k(-1,-1)\mathbf{s}_k|^2}{\sigma_n^2} \right\} \\ & + (1 - p_{e1}(k))p_{e2}(k) \exp\left\{ - \frac{|\mathbf{z} - \mathbf{A}_k(1,-1)\mathbf{s}_k|^2}{\sigma_n^2} \right\} \\ & + p_{e1}(k)(1 - p_{e2}(k)) \exp\left\{ - \frac{|\mathbf{z} - \mathbf{A}_k(-1,1)\mathbf{s}_k|^2}{\sigma_n^2} \right\} \Bigg], \end{aligned} \tag{25.25}$$

where $\mathbf{A}_k(\theta_1, \theta_2)$ is defined as follows:

$$\mathbf{A}_k(\theta_1, \theta_2) = \begin{bmatrix} |\tilde{\Lambda}_{sd}|^2 + |\tilde{\Lambda}_{rd}|^2\theta_1, & \tilde{\Lambda}_{sd}^*\tilde{\Lambda}_{rd}\theta_2 - \tilde{\Lambda}_{sd}^*\tilde{\Lambda}_{rd} \\ \tilde{\Lambda}_{sd}\tilde{\Lambda}_{rd}^* - \tilde{\Lambda}_{sd}\tilde{\Lambda}_{rd}^*\theta_1, & |\tilde{\Lambda}_{sd}|^2 + |\tilde{\Lambda}_{rd}|^2\theta_2 \end{bmatrix}. \tag{25.26}$$

Based on (25.25), the ML detector is

$$\hat{\mathbf{s}}_k = \arg\max_{\mathbf{s}_k \in \mathcal{S}} \{ f_{\mathbf{r}_k|\mathbf{s}_k}(\mathbf{r}_k|\mathbf{s}_k) \}. \tag{25.27}$$

Note that, thanks to the orthogonal space-time block coding strategy, the optimal detector preserves the receiver's simplicity, because under (a1)–(a6), the ML solution performs an exhaustive search only among four possible transmitted vectors $\mathbf{s}_k$'s.

25.4.2. Suboptimum detector

The ML detector described above requires the knowledge, at the destination node, of the set of error probabilities $p_{e1}(k)$ and $p_{e2}(k)$, with $k = 0, \ldots, N - 1$. If this knowledge is not available, a suboptimum scalar detector can be implemented instead of the ML detector. More specifically, the decision on the transmitted symbol $s_k(n)$ can be simply obtained as

$$\hat{\mathbf{s}}(n) = \text{sign}\{\Re[\mathbf{r}(n)]\}, \quad n = i, i + 1, \tag{25.28}$$

where $\mathbf{r}(n)$ is given by (25.23). Note that for high SNR at the relay (i.e., when R

makes no decision errors), the symbol-by-symbol decision in D becomes optimal and thus, the decoding rule (25.28) provides the same performance as the optimal receiver (25.27). When the decision errors at the relay side cannot be neglected, the suboptimal receiver introduces a floor in the bit-error-rate (BER) curve, because the symbol-by-symbol decision (25.28) treats the wrong received symbols as interference. The choice between the decoding rules (25.27) and (25.28) should then result as a trade-off between performance and computational complexity, taking into account the need for the ML detector to make available at the destination node the error probabilities of the relay node. We will show a comparison between ML and suboptimum strategies in Section 25.4.4.

25.4.3. Power allocation between source and relays

While in conventional STC the transmit antennas typically use the same power over all the transmit antennas, with DSTC it is useful to distribute the available power between source and relay as a function of their relative position with respect to the final destination, since they are not colocated. In this section, we show how to distribute a given total power optimally between source and relay. We provide first a closed-form analysis in the ideal case where there are no decision errors at the relay, and then we will show some performance results concerning the real case where the errors are taken into account.

25.4.3.1. Error-free S2R link

Under the assumption that there are no errors at the relay side, using the same derivations introduced in Section 25.4, the optimal detector is a symbol-by-symbol detector and the signal-to-noise ratio on the kth symbol in the nth block is

$$\mathrm{SNR}_k(n) = \frac{A^2}{\sigma_n^2}\left(\alpha\left|\Lambda_{sd}(k,k)\right|^2 + (1-\alpha)\left|\Lambda_{rd}(k,k)\right|^2\right), \tag{25.29}$$

for $k = 1,\ldots,N$ and $n = i, i+1$. The error probability for binary antipodal constellation conditioned to a given channel realization is given by

$$P_{e|h}(k) = \frac{1}{2}\,\mathrm{erfc}\left(\sqrt{0.5\,\mathrm{SNR}_k}\right), \tag{25.30}$$

where SNR_k is given by (25.29). For each subcarrier k, the signal-to-noise ratio SNR_k is given by the sum of two statistically independent random variables, each one distributed according to a χ^2 pdf with two degrees of freedom. Thus, using (25.29) and (25.30), the BER P_b averaged over the channel realizations is given by [25]

$$P_b = \frac{1}{2}\frac{\gamma_2}{\gamma_2-\gamma_1}\left(1-\sqrt{\frac{\gamma_1}{1+\gamma_1}}\right) + \frac{1}{2}\frac{\gamma_1}{\gamma_1-\gamma_2}\left(1-\sqrt{\frac{\gamma_2}{1+\gamma_2}}\right), \tag{25.31}$$

where

$$\gamma_1 := \frac{A^2}{\sigma_n^2}\frac{\alpha\tilde{\sigma}_h^2}{d_{sd}^{\alpha}}, \qquad \gamma_2 := \frac{A^2}{\sigma_n^2}\frac{(1-\alpha)\tilde{\sigma}_h^2}{d_{rd}^{\alpha}}, \qquad \tilde{\sigma}_h^2 = \sigma_h^2(L_h+1). \tag{25.32}$$

From (25.31), we infer that if the errors in the relay's detection are negligible, D-OSTC scheme achieves, as expected, the maximum available diversity gain, equal to two. The optimum value of α can be found by minimizing (25.31). Since the average BER (25.31) is a convex function with respect to α [32], the optimal value of the minimization admits a unique solution.

It is straightforward to show that if D is equipped with n_R antennas, the achieved diversity gain is $2n_R$.

25.4.3.2. S2R link with errors

When the errors at the relay side are explicitly taken into account, it is not easy to derive the performance of the optimal detector (25.27) in closed form. In this case, it is interesting to check the performance of the suboptimal detector (25.28), to quantify the loss with respect to the more complex but optimal detector (25.27). In [32] a closed-form expression for the BER of the suboptimum scheme, in the presence of relay decision errors, was derived. For a given total transmitted power from S and R, we can optimize the power allocation between S and R, depending on the relative distances between S, R, and D, in order to minimize the final average BER. We address this issue in the following example.

Example 25.1 (optimal power allocation). We show the behavior of the final average BER as a function of the power allocation between S and R, depending on the relative distances between S, R, and D. As an example, in Figure 25.4 we report the average BER versus α, as defined in Section 25.4.3.2, for different values of the distance d_{rd} (and thus of SNR_R) between R and D (all distances are normalized with respect to the distance d_{sd} between S and D). In Figure 25.4a, we consider the ideal case where there are no errors at the relay node. The SNR_D at the final destination is fixed equal to 10 dB. We can observe that when $d_{sd} = d_{rd} = 1$, the value of α that minimizes the average BER is $\alpha = 0.5$, that is, the two transmitters use the same power. However, as R gets closer to D, the optimal α tends to increase, that is, the system allocates more power to S, with respect to R. The reverse happens when d_{rd} is greater than 1. Thus, as expected, the system tends to somehow put S and R in the same conditions with respect to D, in order to get the maximum diversity gain.

The real case, where there are decision errors at the relay node, is reported as an example in Figure 25.4b, where the average BER is again plotted as a function of α, but for different values of the SNR_R at the relay node. Interestingly, we can observe that as SNR_R decreases, the system tends to allocate less power to the relay node (the optimal value of α is greater than 0.5) as the relay node becomes less and less reliable.

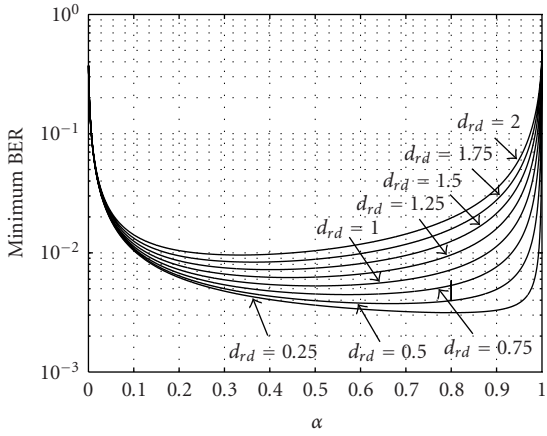

(a)

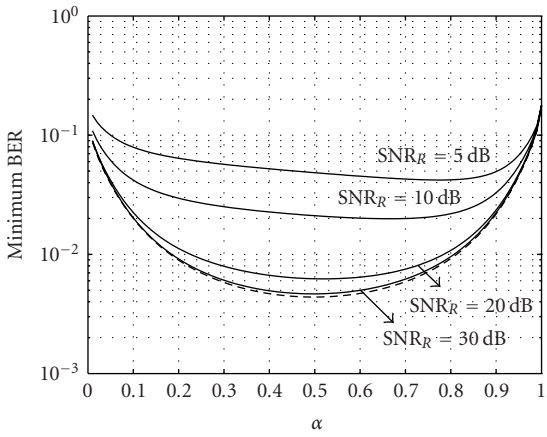

(b)

FIGURE 25.4. Average BER versus α: (a) no errors at R; (b) including errors at R.

25.4.4. Performance

In this section, we compare alternative cooperative strategies. We assume a block length $N = 32$ and channel order $L = 6$. To make a fair comparison of the alternative transmission schemes, we enforce all systems to transmit with the same overall power. More specifically, if $\mathcal{P}$ is the total power radiated by the noncooperative scheme, we denote by $\mathcal{P}_I$ the power radiated by S during the first time-slot and by $\alpha\mathcal{P}_{II}$ and $(1-\alpha)\mathcal{P}_{II}$ the power spent respectively by S and R in the second time-slot. Since the overall radiated power is always $\mathcal{P}$, it must be $\mathcal{P} = \mathcal{P}_I + \mathcal{P}_{II}$.

The coefficient α is chosen in order to minimize the final average bit-error probability (25.31) (see also Example 25.1).[9] The power $\mathcal{P}_I$ is chosen in order to achieve a required average SNR_R at the relay, defined as $\text{SNR}_R := \mathcal{P}_I/\sigma_n^2 d_{sr}^2$. All distances in the network are normalized with respect to the distance d_{sd} between S and D.

Example 25.2 (ML versus suboptimum detector). In Figure 25.5, we compare the average BER obtained using alternative cooperative and noncooperative schemes. The BER is averaged over 2000 independent channel realizations. All curves are plotted versus the SNR in D, defined as $\text{SNR}_D := \mathcal{P}/\sigma_n^2 d_{sd}^2$. This is also the SNR of the single-hop (noncooperative) case. The variance of the noise at both R and D is unitary. In this example, we set $d_{sr} = 0.1$ and $d_{rd} = 0.9$. The results shown in Figure 25.5 are achieved via transmitting with a power $\mathcal{P}_I$, yielding an average SNR_R at the relay equal to 15 dB for all values of SNR_D reported in the abscissas. Since the noise power and SNR_R are both fixed, increasing SNR_D means that $\mathcal{P}_{II}$ increases. In Figure 25.5 we report, for the sake of comparison, the average BER obtained with the following schemes: (i) the single-hop method (dotted line); (ii) the ideal ML detector for O-DSTC scheme with no errors at the relay (dashed and dotted line); (iii) the real ML detector incorporating the decision errors at the relay (dashed line); (iv) the suboptimum scalar decoder for O-DSTC scheme, showing both the theoretical average BER (solid line) and the corresponding simulation results (circles), obtained using a zero-forcing detector at the relay node. In Figure 25.5b we report the performance of the optimal versus suboptimal detector, on real wideband channel measurements, kindly provided by Professors A. Nix and M. Beach, University of Bristol. The data are collected in an urban environment (the city of Bristol) in the band between 1920 and 1930 MHz. We can observe a very good agreement between our theoretical derivations for the suboptimum detector and the corresponding simulation results. The floor on the BER of the suboptimum receiver is due to the decision errors at the relay node. It is also interesting to notice, from Figure 25.5, that the suboptimum O-DSTC scheme exhibits performance very close to the optimal O-DSTC ML detector at low SNR_D, that is, before the BER floor when the relay is relatively close to the source. This indicates that the suboptimum detector is indeed a very good choice under such a scenario, because it is certainly less complicated to implement than the ML detector. Most important, differently from ML, the suboptimum scheme does not require any exchange of information between R and D about the BER in R. The price paid for this simplicity is that the R node must have a sufficiently high SNR to guarantee that the BER of interest be above the floor. In Figure 25.5a we have also reported the average BER (solid line with stars) obtained using a transmission strategy for O-DSTC scheme, where instead of OFDM, in the S/R slot we used a linear precoding method that insures minimum BER at the relay under the assumption of adopting an (suboptimal) MMSE linear decoder (solid line with stars). In such a case, we observe that with minimum additional complexity at the

[9] We use theoretical derivations, valid in the absence of errors at the relay, to simplify the strategy. One could improve upon this choice by using the BER resulting in the presence of errors at the relay.

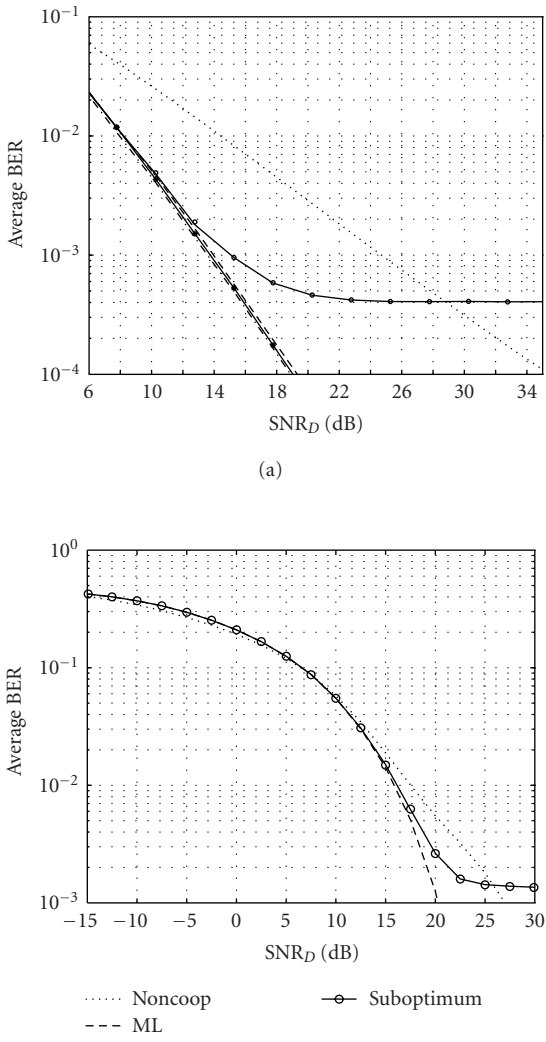

FIGURE 25.5. Comparison between average BER versus SNR_D (dB) achieved with different decision schemes: single *S*-*D* link (dotted line); ideal ML (dashed-dotted line); real ML detector (dashed line); suboptimum receiver: theoretical results (solid line) and simulation (circles); $SNR_R = 15$ dB; (a) Rayleigh channels; (b) real channel measurements.

relay, the performance of the suboptimal O-DSTC scheme becomes closer to the ML decoder because of the lower BER at the relay.

Finally, looking at the slopes of the average BER curves of the ML O-DSTC detector shown in Figure 25.5, it is worth noticing that in the absence of errors at the relay, the cooperative scheme achieves full spatial diversity gain, provided

that the relay can be used, as we have assumed in this section. In practice, there are two reasons for the lack of full diversity gain. The first one is that in a network where the relays are randomly spatially distributed, the probability of finding no relay is not zero (see Section 25.2). The second one is that given a set of terminals available as relays, because of the presence of decoding errors at the relay side, all cooperative schemes exhibit an asymptotic average BER behavior proportional to $1/\mathrm{SNR}_D$. Nevertheless, there is a considerable coding gain which justifies the use of cooperation. Indeed, a more attentive look at the results shows that the average BER starts approaching the slope with maximum diversity, as far as the errors at the relay are negligible with respect to the errors at the destination. Then, when the errors at the relay become dominant, the final BER curve follows the $1/\mathrm{SNR}$ behavior.

25.4.5. Choice of the constellation order in the source-relay slot

The other major critical aspect of cooperative schemes is their rate loss due to the insertion of the *S*/*R* time-slot. As an example, if all the links would use a BPSK constellation, the rate loss factor would be 1/2. To reduce this loss factor, we can use higher-order constellations in the *S*/*R* link, with respect to the constellations used in the other links, so that the duration of the *S*/*R* slot can be made smaller than the duration of the other slots. In this section, we assume BPSK transmissions over all links except the *S*/*R* link, where the constellation order is allowed to increase. More specifically, using a constellation $\mathcal{A}$ of cardinality $M = 2^{n_b}$ in the *S*/*R* link, the rate loss factor is $n_b/(n_b + 1)$. On the other hand, cooperation reduces the final BER and then it induces a capacity increase. To quantify the overall balance in terms of rate, we compared the maximum rate achievable by O-DSTC system with the maximum rate achievable with a noncooperative scheme. We define as achievable rate the maximum number of bits per symbol (bps) that can be decoded with an arbitrarily low error probability, provided that sufficient error correction coding is incorporated in the system, and conditioned to the assumptions (a1)–(a6).[10] We have shown in Section 25.4 that the combination of O-DSTC and OFDM makes the overall time-dispersive channel equivalent to a set of parallel nondispersive subchannels. The final *S*2*D* link over each subchannel, in the presence as well as in the absence of the relay link, can always be made equivalent to a binary symmetric channel (BSC) with crossover probability depending on the specific cooperative (or noncooperative) scheme adopted. Thus, the maximum rate $R(k|\mathbf{h})$ that can be reliably transmitted over the kth subcarrier for a given channel realization $\mathbf{h}$, incorporating the rate loss due to the insertion of the *S*2*R* slot, is

$$R(k|\mathbf{h}) = \frac{1}{1 + 1/n_b} C_{\mathrm{BSC}}\left(P_{e|h}(k)\right) \quad \text{bps}, \tag{25.33}$$

[10] It is important to remark that the rate defined above is smaller than the capacity of the system, because the proposed scheme is designed to maximize the spatial diversity gain and not to maximize information rate.

where $P_{e|h}(k)$ denotes the binary error probability on the kth subcarrier, conditioned to the channel realizations, $C_{\mathrm{BSC}}(p) := 1 + p\log_2(p) + (1-p)\log_2(1-p) := 1 - H(p)$ is the capacity of a binary symmetric channel[11] with crossover probability p. From (25.33) we infer that, because of the S2R link, cooperative transmission induces a systematic rate loss of $n_b/(n_b+1)$ with respect to the case of no cooperation. But, at the same time, cooperation yields a smaller error probability $P_{e|h}(k)$ and thus a higher $C_{\mathrm{BSC}}(P_{e|h}(k))$. Then, we may expect a trade-off in the choice of n_b. This trade-off can be better understood through the following example.

Example 25.3 (rate and diversity gain). We report in Figures 25.6a and 25.6b the achievable rate versus the SNR_D in D for an SNR_R in R equal to 15 and 3 dB, respectively, for different choices of the constellation used in the S2R link, achieved with or without cooperation. To preserve the receiver simplicity, zero-forcing equalization and symbol-by-symbol detection are performed at the relay. We can see that at high SNR_D, the noncooperative case approaches the maximum value, equal to 1 bps, whereas the cooperative cases tend to an asymptote less than 1 depending on the constellation used in S2R slot. We observe from Figure 25.6a that for $\mathrm{SNR}_R = 15$ dB, increasing the constellation order from BPSK to 16-QAM in the S2R link improves the achievable rate; however passing from 16-QAM to 64-QAM does not induce any further gain because of the higher BER at the relay. For lower values of SNR_R, that is $\mathrm{SNR}_R = 3$ dB for example, there is no appreciable rate gain in increasing the constellation order because of the excessive BER at the relay. Nevertheless, it is interesting to notice that at low/medium SNR_D at the final destination (within a range depending on SNR_R), the cooperative case can outperform the noncooperative case also in terms of achievable rate, because the BER decrease can more than compensate the rate insertion loss due to the S2R slot.

25.4.6. Synchronization

Besides errors at the relay node, one more distinguishing feature of DSTC is that the cooperating transmit antennas are not colocated. This means that the packets arriving at the final destination from source and relays might be asynchronous. Interestingly, if the difference in arrival times τ_d is incorporated in the CP used from both S and R, D is still able to get N samples from each received block without interblock interference (IBI). In such a case, the different arrival time does not cause any trouble to the final receiver. In fact, we take as a reference time the instant when the ith block coming from R arrives at D. If the block coming from S arrives with a delay of L_d samples, the only difference with respect to the case of perfect synchronization is that the transfer function $\tilde{\Lambda}_{sd}(k)$ in (25.24) will be substituted by $\tilde{\Lambda}_{sd}(k)e^{-j2\pi L_d k/N}$. From (25.24), it is clear that such a substitution does not affect the useful term, as it only affects the interfering term. However, in the hypothesis of Rayleigh fading channel, $\tilde{\Lambda}_{sd}(k)$ is statistically indistinguishable from

[11] We can use this formula because the S-D is always BPSK, regardless of the constellation used in the S2R link.

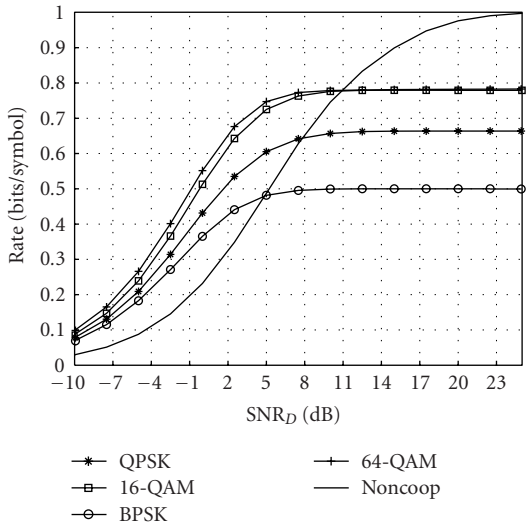

(a)

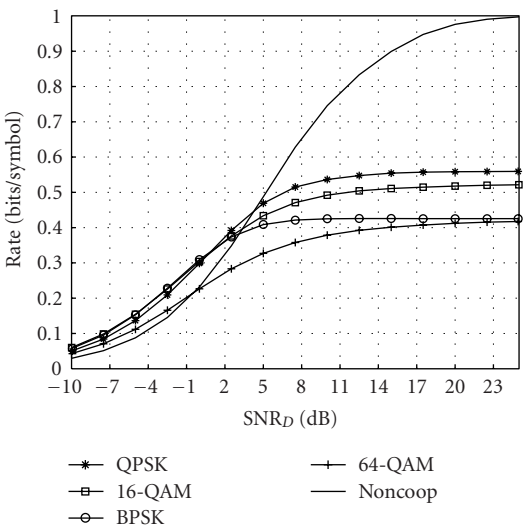

(b)

FIGURE 25.6. Achievable rate (bps) versus SNR (dB)—noncooperative case (solid line), cooperative case using BPSK (circle marker), QPSK (star marker), 16-QAM (square marker), 64-QAM ("+") in the S2R link—(a) $\text{SNR}_R = 15$ dB; (b) $\text{SNR}_R = 3$ dB.

$\tilde{\Lambda}_{sd}(k)e^{-j2\pi L_d k/N}$. Hence, the combination of Alamouti (more generally, orthogonal STC) and OFDM is robust with respect to lack of synchronization between the time of arrival of packets from S and from R (as long as (a6) holds true). The price

paid for this robustness is the increase of the CP length L, which in turn, reflects into a rate loss. However, this loss can be made small by choosing a blocklength N much greater than L or by selecting only relays that are relatively close to the source, so as to make the relative delay small.

25.5. Regenerative versus nonregenerative relays

In nonregenerative schemes, the relay node simply amplifies and retransmits the received signal without performing any A/D conversion on the signal. Thus, A&F can be useful to simplify the implementation of the relay because the relay of an A&F system only needs to have an antenna and an RF amplifier.

Since no detection can be performed at the relay side in the A&F scheme, the relay can only retransmit the received signal. Thus, in order to implement the distributed version of Alamouti scheme, in the first time-slot S has to transmit consecutively, the blocks $-A_s\mathbf{Fs}(i+1)$ and $A_s\mathbf{Gs}^*(i)$.[12] In the second time-slot S transmits consecutively, $A_s\mathbf{Fs}(i)$ and then $A_s\mathbf{Gs}^*(i+1)$ and R sends $A_r(-\mathbf{H}_{sr}\mathbf{Fs}(i+1)+\mathbf{v}_R(i))$ first and then $A_r(\mathbf{H}_{sr}\mathbf{Gs}^*(i)+\mathbf{v}_R(i+1))$. The amplitude coefficients A_s and A_r are used to impose the power available at the S and R nodes, respectively. In the A&F case, differently from the D&F case, the coefficient A_r depends also on the S2R channel as well as on the noise at the R node. Clearly, A_r changes depending on which strategy is implemented in R.

Thanks to the combination of Alamouti's coding and OFDM, the overall systems is equivalent to a series of N parallel channels. Proceeding as in Section 25.4 to obtain (25.24), the received symbol $\mathbf{r}_k$ pertaining to the kth subcarrier in the ith and $(i+1)$th time-slots is given by[13]

$$\mathbf{r}_k = \begin{bmatrix} g_k & 0 \\ 0 & g_k \end{bmatrix} \mathbf{s}_k + \boldsymbol{\nu}_k, \tag{25.34}$$

where $\mathbf{s}_k = [s_k(i), s_k(i+1)]^T$, $g_k := A_s^2|\Lambda_{sd}(k)|^2 + A_r^2|\Lambda_{rd}(k)|^2|\Lambda_{sr}(k)|^2$, and $\boldsymbol{\nu}_k$ is a Gaussian vector with zero mean and diagonal covariance matrix $\mathbf{C}_{\boldsymbol{\nu}} = \sigma_v^2\mathbf{I}$ with $\sigma_v^2 = (A_r^2|\Lambda_{rd}(k)|^2\sigma_r^2 + \sigma_d^2)(A_s^2|\Lambda_{sd}(k)|^2 + A_r^2|\Lambda_{rd}(k)|^2|\Lambda_{sr}(k)|^2)$.

Example 25.4 (comparison between A&F and D&F). In Figure 25.7, we compare the average BER versus the SNR_D at the destination node obtained using the following strategies: (a) decode-and-forward using ML detector (dashed line) or suboptimal detector: theoretical value (solid line) and simulation results (circles); (b) amplify-and-forward (dashed-dotted line); (c) single-hop (noncooperative) case

[12] Differently from A&F scheme, in the D&F system there is no constraint on the sequence of information blocks transmitted from the source node.

[13] We drop the block index i for simplicity of notation, because the same relationships hold true for all blocks.

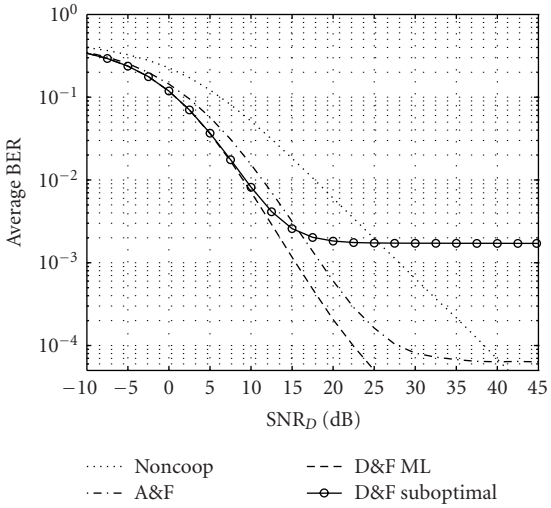

FIGURE 25.7. Average BER versus SNR_D (dB) achieved with different strategies: (a) decode-and-forward using ML detector (dashed line) or suboptimal detector: theoretical value (solid line) and simulation results (circles); (b) amplify-and-forward (dashed-dotted line); (c) single-hop (noncooperative) case (dotted line); $SNR_R = 20$ dB.

(dotted line). The block length is $N = 16$; the channels are simulated as FIR filters of order $L_h = 6$, whose taps are i.i.d. complex Gaussian random variables with zero mean and variance $1/d^2$. The SNR_R at the relay is equal to 20 dB. Comparing the D&F and A&F schemes, we observe that the D&F method performs better than the A&F at low and intermediate SNR_D values, but for high values of SNR_D, the A&F performs better. This shows that A&F is indeed a valuable choice.

25.6. Comparison among alternative STC techniques in a multiuser context

In this section, we compare alternative DSTC strategies. We consider a cell of radius 300 m with $N_{\text{tot}} = 200$ total radio terminals located randomly. We consider only the uplink channel and we assume that the base station (destination) has two real antennas. Within the set of all radio terminals, $N = 10$ is the number of sources, whereas the remaining nodes are potential relays. All channels are slowly-varying, Rayleigh flat fading. The alternative strategies are compared enforcing the same overall radiated energy and the same bit rate in the SR2D phase. In case of cooperation, the energy includes the energy used to send data from the source to the relays and the sum of the energy used by source and relay to transmit their data to the destination. For each channel realization and radio nodes distribution, we associate a relay to a source according to the protocol described in Section 25.3.4. We have used a 16-QAM constellation for the conventional SISO system that acts as a benchmark term, while for the DSTC schemes the following choices have been made, in order to enforce the same bit rate in the SR2D phase.

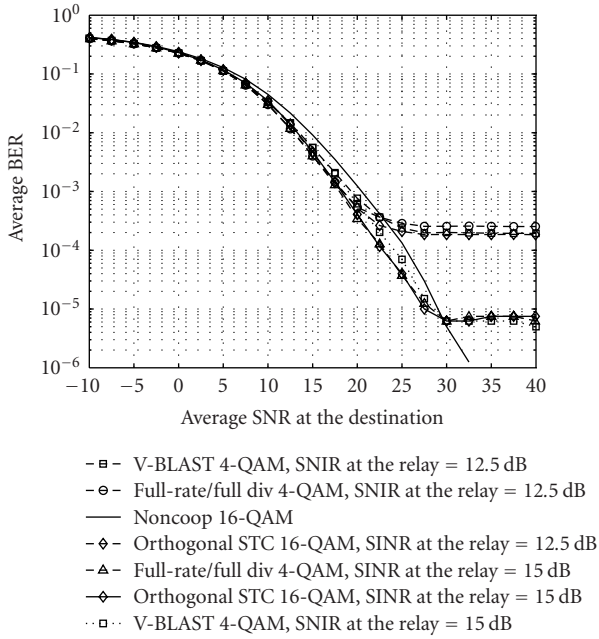

FIGURE 25.8. BER comparison of different DSTC schemes. Averages are presented over 5 realizations of the terminals' deployment, 10(×5) realizations of the active sources locations, 20(×10 × 5) channel realizations (for each source). Block length $N_b = 10$; number of terminals = 200; number of active sources = 10; $\alpha = 0.1$.

(a) D-OSTC. As the symbol rate of the OSTC scheme is the same as an SISO system, the constellation used is the same, both if the source finds a relay and if it transmits alone. We have chosen 16-QAM so that each source transmits 8 bits every 22 symbol intervals. Two symbol intervals are reserved for the common S2R phase ($T_{S2R} = 2$), hence also in this phase 16-QAM is adopted.

(b) D-BLAST. A 4-QAM constellation is used in case of cooperation and a 16-QAM constellation is used in case of no cooperation.

The cooperative case can use a lower-order constellation because a 2×2 D-BLAST provides a higher transmission rate.

(c) D-FDFR. A 4-QAM constellation is used in case of cooperation and a 16-QAM constellation is used in case of no cooperation.

Also in this case, as with D-BLAST, the cooperative case can use a lower-order constellation with respect to the noncooperative case.

The simulation results are reported in Figure 25.8. Throughout the simulations, the power used in the S2R slot is one tenth of the power used in the noncooperative case. As explained in Section 25.2, this portion could be optimized. A node is chosen as a relay if its SNIR, conditioned to the channel, exceeds a threshold of 12.5 or 15 dB. Requiring an SNIR of 12.5 dB, a relay has been found with probability $p_R(1) = 0.72$, whereas for SNIR = 15 dB, we obtained $p_R(1) = 0.65$.

Clearly, increasing the target SNIR decreases the probability of finding a relay, but at the same time, there are less decision errors at the relay. The overall performance is then a combination of these two aspects. The average BER reported in Figure 25.8 takes into account both situations where the relay has been found or not. We can check from Figure 25.8 that indeed, by increasing the SNIR from 12.5 to 15, even though $p_{r_0}(1)$ decreases, the floor on the BER decreases by more than a decade. Of course, this result is also a consequence of the relay density. Finally, in the case of an SNIR of 15 dB, we can observe a gain of approximately 3 dB at BER $= 1.e-4$.

25.7. Conclusion

In conclusion, distributed space-time coding can be an important tool to reduce the overall radiated power in wireless networks. We have considered here only the case with two hops, but further improvements are expected in the multihop case. The price paid for these advantages is the additional signaling required to coordinate the transmission of source and relay nodes, an important issue which is currently under investigation.

Acknowledgment

This work has been supported by the project IST-2001-32549 (ROMANTIK) funded by the European Community.

Abbreviations

A&F	Amplify-and-forward
AWGN	Additive white Gaussian noise
BER	Bit error rate
bps	Bits per symbol
BPSK	Binary phase-shift keying
CP	Cyclic prefix
D	Destination
D-BLAST	Distributed BLAST
DCTS	Distributed space-time coding
D&F	Decode-and-forward
D-FRFD	Distributed full-rate/full diversity
D-OSTC	Distributed orthogonal STC
FIR	Finite impulse response
FRFD	Full-rate/full diversity
IBI	Interblock interference
IFFT	Inverse fast Fourier transform
i.i.d.	Independent indentically distributed
ISI	Intersymbol interference
MIMO	Multi-input multi-output
MISO	Multi-input single-output
ML	Maximum likelihood

OFDM	Orthogonal frequency division multiplexing
OSTC	Orthogonal STC
QAM	Quadrature amplitude modulation
pdf	Probability density function
R	Relay
S	Source
SISO	Single-input single-output
SR2D	Soure-relay to destination
S2R	Source to relay
V-BLAST	Vertical-BLAST
ZF	Zero forcing

Bibliography

[1] A. Paulraj, R. Nabar, and D. Gore, *Introduction to Space-Time Wireless Communications*, Cambridge University Press, Cambridge, UK, 2003.

[2] E. G. Larsson and P. Stoica, *Space-Time Block Coding for Wireless Communications*, Cambridge University Press, Cambridge, UK, 2003.

[3] F. Tobagi, "Modeling and performance analysis of multihop packet radio networks," *Proc. IEEE*, vol. 75, no. 1, pp. 135–155, 1987.

[4] T. Cover and A. El Gamal, "Capacity theorems for the relay channel," *IEEE Trans. Inform. Theory*, vol. 25, no. 5, pp. 572–584, 1979.

[5] P. Gupta and P. R. Kumar, "Critical power for asymptotic connectivity in wireless networks," in *Stochastic Analysis, Control, Optimization and Applications*, pp. 547–566, Birkhäuser Boston, Boston, Mass, USA, 1999.

[6] P. Gupta and P. R. Kumar, "The capacity of wireless networks," *IEEE Trans. Inform. Theory*, vol. 46, no. 2, pp. 388–404, 2000.

[7] A. Host-Madsen, "On the capacity of wireless relaying," in *Proc. IEEE 56th Vehicular Technology Conference (VTC 2002-Fall)*, vol. 3, pp. 1333–1337, Vancouver, BC, Canada, September 2002.

[8] A. Sendonaris, E. Erkip, and B. Aazhang, "Increasing uplink capacity via user cooperation diversity," in *Proc. IEEE International Symposium on Information Theory (ISIT '98)*, p. 156, Cambridge, Mass, USA, August 1998.

[9] J. N. Laneman and G. W. Wornell, "Energy-efficient antenna sharing and relaying for wireless networks," in *Proc. IEEE Wireless Communications and Networking Conference (WCNC '00)*, vol. 1, pp. 7–12, Chicago, Ill, USA, September 2000.

[10] J. N. Laneman and G. W. Wornell, "Distributed space-time coded protocols for exploiting cooperative diversity in wireless networks," in *Proc. IEEE Global Telecommunications Conference (GLOBECOM '02)*, vol. 1, pp. 77–81, Taipei, Taiwan, November 2002.

[11] J. N. Laneman and G. W. Wornell, "Distributed space-time-coded protocols for exploiting cooperative diversity in wireless networks," *IEEE Trans. Inform. Theory*, vol. 49, no. 10, pp. 2415–2425, 2003.

[12] V. Emamian and M. Kaveh, "Combating shadowing effects for systems with transmitter diversity by using collaboration among mobile users," in *Proc. International Symposium on Communications (ISCOM '01)*, vol. 9.4, pp. 105.1–105.4, Taiwan, November 2001.

[13] T. E. Hunter and A. Nosratinia, "Cooperation diversity through coding," in *Proc. IEEE International Symposium on Information Theory (ISIT '02)*, p. 220, Lausanne, Switzerland, June–July 2002.

[14] M. Dohler, E. Lefranc, and H. Aghvami, "Space-time block codes for virtual antenna arrays," in *Proc. 13th IEEE International Symposium on Personal, Indoor and Mobile Radio Communications (PIMRC '02)*, vol. 1, pp. 414–417, Lisbon, Portugal, September 2002.

[15] A. Stefanov and E. Erkip, "Cooperative coding for wireless networks," in *Proc. 4th International Workshop on Mobile and Wireless Communications Network*, pp. 273–277, Stockholm, Sweden, September 2002.

[16] I. Hammerstroem, M. Kuhn, B. Rankov, and A. Wittneben, "Space-time processing for cooperative relay networks," in *Proc. IEEE 58th Vehicular Technology Conference (VTC 2003-Fall)*, vol. 1, pp. 404–408, Orlando, Fla, USA, October 2003.

[17] P. A. Anghel, G. Leus, and M. Kaveh, "Multi-user space-time coding in cooperative networks," in *Proc. IEEE International Conference on Acoustics, Speech, and Signal Processing (ICASSP '03)*, vol. 4, pp. IV-73–IV-76, Hong Kong, April 2003.

[18] S. Barbarossa and G. Scutari, "Cooperative diversity through virtual arrays in multihop networks," in *Proc. IEEE International Conference on Acoustics, Speech, and Signal Processing (ICASSP '03)*, vol. 4, pp. IV-209–IV-212, Hong Kong, April 2003.

[19] G. Scutari, S. Barbarossa, and D. Ludovici, "Cooperation diversity in multihop wireless networks using opportunistic driven multiple access," in *Proc. IEEE Workshop on Signal Processing Advances in Wireless Communications (SPAWC '03)*, pp. 170–174, Rome, Italy, June 2003.

[20] S. Barbarossa and G. Scutari, "Distributed space-time coding strategies for wideband multihop networks: Regenerative vs. non-regenerative relays," in *Proc. IEEE International Conference on Acoustics, Speech, and Signal Processing (ICASSP '04)*, vol. 4, pp. IV-501–IV-504, Montreal, Canada, May 2004.

[21] S. Barbarossa and G. Scutari, "Distributed space-time coding for multihop networks," in *Proc. IEEE International Conference on Communications (ICC '04)*, vol. 2, pp. 916–920, Paris, France, June 2004.

[22] S. Barbarossa, L. Pescosolido, D. Ludovici, L. Barbetta, and G. Scutari, "Cooperative wireless networks based on distributed space-time coding," in *Proc. International Workshop on Wireless Ad-Hoc Networks (IWWAN '04)*, Oulu, Finland, May–June 2004.

[23] N. A. C. Cressie, *Statistics for Spatial Data*, John Wiley & Sons, New York, NY, USA, 1993.

[24] M. K. Simon and M.-S. Alouini, *Digital Communications over Fading Channels: A Unified Approach to Performance Analysis*, John Wiley & Sons, New York, NY, USA, 2000.

[25] J. Proakis, *Digital Communications*, McGraw-Hill, New York, NY, USA, 4th edition, 2000.

[26] H. El Gamal and M. O. Damen, "Universal space-time coding," *IEEE Trans. Inform. Theory*, vol. 49, no. 5, pp. 1097–1119, 2003.

[27] X. Ma and G. B. Giannakis, "Full-diversity full-rate complex-field space-time coding," *IEEE Trans. Signal Processing*, vol. 51, no. 11, pp. 2917–2930, 2003.

[28] L. Zheng and D. N. C. Tse, "Diversity and multiplexing: A fundamental tradeoff in multiple-antenna channels," *IEEE Trans. Inform. Theory*, vol. 49, no. 5, pp. 1073–1096, 2003.

[29] G. J. Foschini, "Layered space-time architecture for wireless communication in a fading environment when using multiple antennas," *Bell Labs. Technical Journal*, vol. 1, no. 2, pp. 41–59, 1996.

[30] S. Barbarossa and A. Fasano, "Trace-orthogonal space-time coding design for multiuser systems," in *Proc. 30th IEEE Int. Conf. on Acoustics, Speech, and Signal Processing (ICASSP '05)*, vol. III, pp. III-1093–III-1096, Philadelphia, Pa, USA, March 2005.

[31] S. Barbarossa and F. Cerquetti, "Simple space-time coded SS-CDMA systems capable of perfect MUI/ISI elimination," *IEEE Commun. Lett.*, vol. 5, no. 12, pp. 471–473, 2001.

[32] G. Scutari and S. Barbarossa, "Distributed space-time coding for regenerative relay networks," to appear in *IEEE Trans. Wireless Communications*.

[33] K. Cho and D. Yoon, "On the general BER expression of one- and two-dimensional amplitude modulations," *IEEE Trans. Commun.*, vol. 50, no. 7, pp. 1074–1080, 2002.

[34] A. Stefanov and E. Erkip, "On the performance analysis of cooperative space-time coded systems," in *Proc. IEEE Wireless Communications and Networking Conference (WCNC '03)*, vol. 2, pp. 729–734, New Orleans, La, USA, March 2003.

[35] P. A. Anghel, G. Leus, and M. Kaveh, "Relay assisted uplink communication over frequency-selective channels," in *Proc. IEEE Workshop on Signal Processing Advances in Wireless Communications (SPAWC '03)*, pp. 125–129, Rome, Italy, June 2003.

[36] T. E. Hunter and A. Nosratinia, "Performance analysis of coded cooperation diversity," in *Proc. IEEE International Conference on Communications (ICC '03)*, vol. 4, pp. 2688–2692, Anchorage, Alaska, USA, May 2003.

[37] B. Bollobás, *Modern Graph Theory*, vol. 184 of *Graduate Texts in Mathematics*, Springer, NY, USA, New York, 1998.

[38] M. Penrose, *Random Geometric Graphs*, vol. 5 of *Oxford Studies in Probability*, Oxford University Press, Oxford, UK, 2003.

[39] C. Bettstetter, "On the minimum node degree and connectivity of a wireless multihop network," in *Proc. 3rd ACM International Symposium on Mobile Ad Hoc Networking and Computing (MobiHoc '02)*, pp. 80–91, Lausanne, Switzerland, June 2002.

[40] M. Penrose, "On k-connectivity for a geometric random graph," *Random Structures & Algorithms*, vol. 15, no. 2, pp. 145–164, 1999.

[41] Y.-C. Cheng and T. G. Robertazzi, "Critical connectivity phenomena in multihop radio models," *IEEE Trans. Commun.*, vol. 37, no. 7, pp. 770–777, 1989.

[42] S. Barbarossa, *Multiantenna Wireless Communication Systems*, Artech House Publishers, Norwood, Mass, USA, March 2005.

Sergio Barbarossa: INFOCOM Department, University of Rome "La Sapienza," Via Eudossiana 18, 00184 Rome, Italy

Email: sergio@infocom.uniroma1.it

Gesualdo Scutari: INFOCOM Department, University of Rome "La Sapienza," Via Eudossiana 18, 00184 Rome, Italy

Email: aldo.scutari@infocom.uniroma1.it

Loreto Pescosolido: INFOCOM Department, University of Rome "La Sapienza," Via Eudossiana 18, 00184 Rome, Italy

Email: loreto@infocom.uniroma1.it

26 Towards a better understanding of the QoS tradeoff in multiuser multiple-antenna systems

Slawomir Stanczak and Holger Boche

26.1. Introduction

Future generations of wireless networks will have to support a wide range of services having fundamentally different quality of service (QoS) requirements and traffic characteristics. Moreover, the number of transmission links with high QoS requirements is expected to surpass that of the traditional voice connections. As a consequence, the problem of providing acceptable QoS to users will become one of the central problems in wireless network design. This problem will be intensified by the physical limitation of the mobile radio propagation channel as well as limitation of the bandwidth and the power.

Multiuser beamforming techniques have been seen as a remedy for this problem [1]. Power control and link scheduling are two other important mechanisms to provide QoS to the users [2, 3, 4, 5]. For instance, scheduling strategies that exploit the relative delay tolerance of data applications can be used to achieve performance gains. Furthermore, channel-aware scheduling algorithms such as the proportional fair algorithm for CDMA 1xEV-DO exploit channel fluctuations to improve the throughput performance.

A key ingredient in the design of power control and link scheduling strategies is the convexity of the feasible QoS region, which is defined as a set of all QoS requirements that can be supported by a network with all users transmitting concurrently (see [6, 7] and references therein). The convexity property opens the door to a widely developed theory for characterizing optimal power control strategies (see Figure 26.1). Moreover, the geometry of the feasible QoS region strongly influences optimal scheduling strategies. This is particularly true for the feasible rate region. It is easy to see that if the feasible rate region is a convex set, the effect on scheduling is to prefer simultaneous transmission of users (Figure 26.1). In contrast, when the feasible rate region is not a convex set, a scheduling policy involving a time-sharing protocol over subsets of simultaneously transmitting users may improve the network performance [3, 8]. Note that in order to satisfy strict

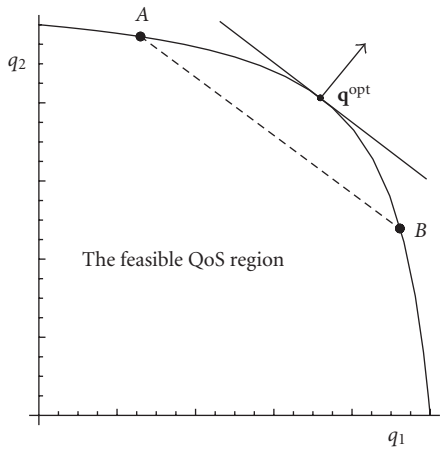

FIGURE 26.1. The convexity of the feasible QoS region opens the door to a widely developed theory for identifying the optimal power control strategies.

QoS requirements, such protocols may require unacceptably high peak transmission powers.

In this chapter, we present sufficient conditions for the convexity of the feasible QoS region in systems with and without power constraints. It is shown that this set is convex if the signal to interference-plus-noise (SINR) at the output of a linear receiver is a strictly monotone log-convex function of a QoS parameter value. Recall that any positive function f is log-convex if $\log f$ is convex. Thus, any positive log-convex function is always a convex one but not vice versa [9]. Two important examples of log-convex functions are $x \to e^x$, $x \in \mathbb{R}$, and $x \to 1/x$, $x > 0$ (see Section 26.4.4 for applications). The log-convexity requirement is sometimes too restrictive. Some important functions are convex but not log-convex. For instance, the inverse function of $x \to \log(1+x)$, $x \geq 0$, is $x \to e^x - 1$, $x \geq 0$, which is convex but not log-convex. This immediately raises the following question. Is the log-convexity property necessary for the feasible QoS region to be a convex set? In this chapter, we study this problem under the assumption that there are no power constraints. In this case, the geometry of the feasible QoS region is determined by the spectral radius of a certain nonnegative irreducible matrix whose entries depend on QoS requirements. Consequently, if the spectral radius is a jointly convex function of the QoS requirements, the feasible QoS region is a convex set. Now it turns out that the log-convexity property mentioned above is necessary if the spectral radius is required to be convex for any interference scenario. In contrast, when confined to special interference scenarios, the log-convexity requirement can be weakened to a less restrictive requirement.

26.2. System model

We consider a single-cell multiple-antenna system with a linear receiver structure. It is assumed that the base station alone uses a multielement antenna (with

M antenna elements) to receive and transmit signals from and to the mobile. No antenna arrays are considered for the mobile.

26.2.1. Base-to-mobile link

We first focus on the downlink scenario from the base station to K mobile users being arbitrarily distributed in the cell. The data stream for each user, say user k, is spread over the antenna array by the kth column of the matrix $\mathbf{U} = (\mathbf{u}_1, \ldots, \mathbf{u}_K) \in \mathbb{C}^{M\times K}$. The columns of $\mathbf{U}$ are referred to as beamforming vectors. Without loss of generality, we assume that $\|\mathbf{u}_k\|_2 = 1$ for each $1 \le k \le K$. Let[1]

$$\mathbf{p} := (p_1, \ldots, p_K) \ge 0 \tag{26.1}$$

denote power allocation, let the system noise for user k (excluding interference from other users) be $\tilde{\sigma}_k^2 > 0$, and finally let $\mathbf{h}_1, \ldots, \mathbf{h}_K$ be the corresponding channel signatures. In the downlink channel, there is a total power constraint in the sense that the total transmission power of all users must be smaller than or equal to a predefined value $P > 0$. Formally, we have $\mathbf{p} \in \mathcal{P}$ where

$$\mathcal{P} := \left\{ \mathbf{x} \ge 0 : \|\mathbf{x}\|_1 = \sum_k x_k \le P \right\} \tag{26.2}$$

is the set of all power allocations satisfying the total power constraint.

Now assuming a perfect instantaneous power control, SINR measured at the antenna output of the kth receiver is given by (see also the foregoing chapter)

$$\mathrm{SINR}_k(\mathbf{U}, \mathbf{p}) = \frac{p_k \mathbf{u}_k^H \mathbf{R}_k \mathbf{u}_k}{\sum_{\substack{l=1 \\ l\neq k}}^{K} p_l \mathbf{u}_l^H \mathbf{R}_k \mathbf{u}_l + \tilde{\sigma}_k^2}, \quad 1 \le k \le K, \tag{26.3}$$

where $\mathbf{R}_k$, $1 \le k \le K$ is used to denote the spatial covariance matrix. If the channel is slowly varying in the sense that the channel signatures remain constant within the observation window, then $\mathbf{R}_k = \mathbf{h}_k \mathbf{h}_k^H$, $1 \le k \le K$, is a one-rank matrix. Otherwise, if the channels are independent and rapidly time varying, $\mathbf{R}_k = E[\mathbf{h}_k \mathbf{h}_k^H]$ has a full rank.

26.2.2. Mobile-to-base link

In the uplink scenario, the antenna array acts as a linear receiver. We use the same notation for the beamforming vectors, power allocation, and channel signatures as before. In contrast to the downlink scenario, however, there are individual power

[1] If $\mathbf{x}$ is a vector in $\mathbb{R}^K$, the notations $\mathbf{x} > 0$ and $\mathbf{x} \ge 0$ indicate that all coordinates of $\mathbf{x}$ are positive or nonnegative, respectively. Similarly, if $\mathbf{X}$ is a real matrix, the notations $\mathbf{X} > 0$ and $\mathbf{X} \ge 0$ indicate that all entries of $\mathbf{X}$ are positive or nonnegative, respectively. $\mathbb{R}_+$ denotes the set of nonnegative reals.

constraints on each user denoted by $P_1, \ldots, P_K > 0$. Hence, in this case, we require that $\mathbf{p} \in \mathcal{P}_i$ where

$$\mathcal{P}_i := \{\mathbf{x} \geq 0 : x_k \leq P_k, 1 \leq k \leq K\}. \tag{26.4}$$

Moreover, we have

$$\mathrm{SINR}_k(\mathbf{U}, \mathbf{p}) = \frac{p_k \mathbf{u}_k^H \mathbf{R}_k \mathbf{u}_k}{\sum_{\substack{l=1 \\ l \neq k}}^{K} p_l \mathbf{u}_k^H \mathbf{R}_l \mathbf{u}_k + \tilde{\sigma}_k^2}, \quad 1 \leq k \leq K. \tag{26.5}$$

Thus, unlike the downlink SINR, the uplink SINR depends on all channel signatures.

26.2.3. Power control for fixed beamformers

The best system performance can be achieved only by jointly optimizing power and beamforming vectors. The optimum is usually found by means of iterative algorithms that alternately optimize a given function of $\mathrm{SINR}_k(\mathbf{U}, \mathbf{p})$, $k = 1, \ldots, K$, with respect to $\mathbf{p} \in \mathcal{P}$ (or $\mathbf{p} \in \mathcal{P}_i$) and $\mathbf{U}$ with $\|\mathbf{u}_k\|_2 = 1$, $1 \leq k \leq K$ (see the preceding chapter and [2]). In this chapter, however, we consider a classical approach of power control for fixed beamformers. Due to its simplicity, this approach may be interesting for some practical systems. For instance, one reasonable choice is $\mathbf{u}_k = \mathbf{h}_k$, $1 \leq k \leq K$, in which case beamforming vectors are matched to channel signatures.

If beamforming vectors are fixed, then there is, except for the power constraints, no substantial difference between the downlink and uplink scenarios. Thus, it is reasonable to rewrite SINR so as to include both scenarios. To this end, define $V_{k,l} \geq 0$ and $\sigma_k^2 \geq 0$ as

$$V_{k,l} = \begin{cases} \mathbf{u}_l^H \mathbf{R}_k \mathbf{u}_l & \text{downlink}, \\ \mathbf{u}_k^H \mathbf{R}_l \mathbf{u}_k & \text{uplink}, \end{cases} \qquad \sigma_k^2 = \frac{\tilde{\sigma}_k^2}{V_{k,k}}, \tag{26.6}$$

respectively. Moreover, let $\nu_{k,l} \geq 0$ be the interference factor defined to be

$$\nu_{k,l} = \begin{cases} \dfrac{V_{k,l}}{V_{k,k}}, & l \neq k, \\ 0, & l = k. \end{cases} \tag{26.7}$$

Using these definitions, we can write (26.3) and (26.5) as

$$\mathrm{SINR}_k(\mathbf{p}) := \mathrm{SINR}_k(\mathbf{U}, \mathbf{p}) = \frac{p_k}{\sum_{l=1}^{K} p_l \nu_{k,l} + \sigma_k^2}, \quad 1 \leq k \leq K, \tag{26.8}$$

where the interference factor $\nu_{k,l}$ depends on the transmission scenario under consideration and the beamforming matrix $\mathbf{U}$ with $\|\mathbf{u}_k\|_2 = 1$, $1 \leq k \leq K$, is arbitrary but fixed.

Note that since $v_{k,l} = 0$ if $k = l$, there is no self-interference in (26.8). However, we point out that most of the results hold if $v_{k,k} = c_k > 0$ for some positive constant c_k proportional to the self-interference level at the receiver output. In fact, in Section 26.6, we implicitly assume that $v_{k,k} > 0$ for each $1 \le k \le K$.

26.2.4. Quality of service and SINR

We assume that there is a one-to-one relationship between SINR given by (26.8) and a certain QoS parameter of interest. To be more specific, let $Q_k \in \mathbb{G}$, $k = 1, \ldots, K$, be given QoS parameter values where $\mathbb{G}$ denotes any interval on the real line. Then, by assumption, there exists a bijective function $\varphi : \mathbb{R}_+ \to \mathbb{G}$ (called QoS function) so that

$$Q_k = \varphi(\mathrm{SINR}_k), \quad 1 \le k \le K. \tag{26.9}$$

For instance, if the linear receiver is followed by single-user decoders, one for each user, the information theoretic rate is a logarithmic function of SINR so that in this case $\varphi(x) = \log(1 + x)$, $x > 0$. Common examples of QoS parameters are the data rate and service delay, but other QoS parameters such as the effective spreading gain have been also considered in the literature [10]. Note that in general, the function φ depends on the desired bit error rate.

Due to the bijectivity of φ, we know that there is a certain quality of service for the users if

$$\begin{aligned} &\varphi(\mathrm{SINR}_k) \le q_k \quad \text{if } \varphi \text{ is strictly decreasing,} \\ &q_k \le \varphi(\mathrm{SINR}_k) \quad \text{if } \varphi \text{ is strictly increasing} \end{aligned} \tag{26.10}$$

for each $1 \le k \le K$, where $q_1, \ldots, q_K \in \mathbb{G}$ are given real numbers referred to as QoS requirements. We can rewrite (26.10) to obtain

$$0 < \gamma(q_k) \le \mathrm{SINR}_k(\mathbf{p}), \quad 1 \le k \le K, \tag{26.11}$$

or, equivalently,

$$1 \le \min_{1 \le k \le K} \frac{\mathrm{SINR}_k(\mathbf{p})}{\gamma(q_k)}, \tag{26.12}$$

where $\gamma : \mathbb{G} \to \mathbb{R}_+$ is referred to as the inverse QoS function, that is, we have

$$\gamma(\varphi(x)) \equiv x, \quad x > 0. \tag{26.13}$$

The positive real numbers $\gamma(q_1), \ldots, \gamma(q_K)$, referred to as SINR requirements, can be interpreted as the minimum SINR levels necessary to satisfy the QoS requirements. In order to simplify the notation, sometimes we write $\gamma_k := \gamma(q_k)$, $1 \le k \le K$.

One of the central problems in communications network design is the problem of admissibility [5]. Here, the question is whether or not there exists a power allocation $\mathbf{p} \geq 0$ for which (26.12) holds. If such a power allocation exists, we say that $\mathbf{q} := (q_1, \ldots, q_K) \in \mathbb{G}^K$ is feasible. The set of all feasible QoS vectors $\mathbf{q}$ is called the feasible QoS region. Note that the feasible QoS region is parameterized by the inverse QoS function γ. Moreover, it is important to emphasize that these definitions assume a concurrent transmission of all users (no time-sharing protocol).

26.3. The optimal power allocation and the feasible QoS region

If there are no power constraints, a necessary and sufficient condition for the vector $\mathbf{q} \in \mathbb{G}^K$ to be feasible immediately follows from (26.12) by taking the supremum of the right-hand side with respect to $\mathbf{p} \geq 0$. To be precise, the QoS vector $\mathbf{q}$ is feasible if and only if

$$1 < \sup_{\mathbf{p}\geq 0} \min_{1\leq k\leq K} \frac{\mathrm{SINR}_k(\mathbf{p})}{\gamma(q_k)}. \tag{26.14}$$

We point out that unlike some other strategies, (26.14) ensures that all users meet their individual QoS requirements provided that they are feasible. The price for this is that the cost function is not continuously differentiable so that smooth optimization methods such as the gradient method cannot be used to solve this problem. However, we can rewrite (26.14) in terms of the spectral radius of a certain nonnegative matrix. To this end, let $\mathbf{V} = (v_{k,l}) \in \mathbb{R}_+^{K\times K}$ be the interference matrix and $\boldsymbol{\Gamma}(\mathbf{q}) := \mathrm{diag}(\gamma(q_1), \ldots, \gamma(q_K))$. Now if $\mathbf{V}$ is irreducible,[2] we know from the Perron-Frobenius theory that $\mathbf{q} \in \mathbb{G}^K$ is feasible if and only if [5, 11]

$$\rho(\mathbf{q}) < 1, \tag{26.15}$$

where $\rho(\mathbf{q})$ is the spectral radius (the Perron root) of $\boldsymbol{\Gamma}(\mathbf{q})\mathbf{V}$. Consequently, if there are no power constraints, the feasible QoS region $\mathbb{F}_\gamma \subset \mathbb{G}^K$ is

$$\mathbb{F}_\gamma = \{\mathbf{q} \in \mathbb{G}^K : \rho(\mathbf{q}) < 1\}. \tag{26.16}$$

In Section 26.7, we investigate the complement of $\mathbb{F}_\gamma$ in $\mathbb{G}^K$, which is called the infeasible QoS region and is denoted by $\mathbb{F}_\gamma^c = \mathbb{G}^K \setminus \mathbb{F}_\gamma$.

Recall that a matrix $\mathbf{A} \in \mathbb{R}_+^{K\times K}$ is said to be reducible if there exists a permutation matrix $\mathbf{P}$ such that $\mathbf{P}^T\mathbf{A}\mathbf{P} = \left(\begin{smallmatrix} \mathbf{X} & \mathbf{Y} \\ 0 & \mathbf{Z} \end{smallmatrix}\right)$ where $\mathbf{X}$ and $\mathbf{Z}$ are both square matrices. Otherwise, $\mathbf{A}$ is said to be irreducible. In a special case, when all nondiagonal elements of $\mathbf{V}$ are positive, $\boldsymbol{\Gamma}(\mathbf{q})\mathbf{V}$ is irreducible. A comprehensive reference on the Perron-Frobenius theory and its application is [11].

When users operate under some power constraints, inequality (26.14) or, equivalently, (26.15) is not sufficient anymore. This is because we additionally

[2] There is no loss in generality in assuming that $\mathbf{V}$ is irreducible since otherwise the problem decomposes into small problems of the same type [10].

need to satisfy the power constraints. First we consider the downlink scenario. In this case, the right-hand side of (26.12) attains its maximum on $\mathcal{P}$ defined by (26.2). Consequently, with a total power constraint assumed, $\mathbf{q} \in \mathbb{G}^K$ is feasible if and only if

$$1 \leq \max_{\mathbf{p}\in\mathcal{P}} \min_{1\leq k\leq K} \frac{\mathrm{SINR}_k(\mathbf{p})}{\gamma(q_k)}. \tag{26.17}$$

This max-min problem can be reformulated in terms of the minimum total power $P_{\mathrm{m}} : \mathbb{F}_\gamma \to \mathbb{R}_+$ defined to be [12]

$$P_{\mathrm{m}}(\mathbf{q}) := \min_{\substack{\mathbf{p}\in\mathbb{R}_+^K \\ \gamma(q_k)\leq \mathrm{SINR}_k(\mathbf{p}),\, 1\leq k\leq K}} \|\mathbf{p}\|_1 < +\infty. \tag{26.18}$$

Now it is easy to see that (26.17) is satisfied if and only if the minimum total power $P_{\mathrm{m}}(\mathbf{q}) < +\infty$ exists and satisfies the total power constraint:

$$P_{\mathrm{m}}(\mathbf{q}) \leq P. \tag{26.19}$$

Thus, the feasible QoS region under a total power constraint $\mathbb{F}_\gamma(P)$ is given by

$$\mathbb{F}_\gamma(P) = \{\mathbf{q} \in \mathbb{G}^K : P_{\mathrm{m}}(\mathbf{q}) \leq P\}. \tag{26.20}$$

Note that $P_{\mathrm{m}}(\mathbf{q})$ is the minimum total power for which all users satisfy their QoS requirements. Any power allocation $\mathbf{p}^* := \mathbf{p}^*(\mathbf{q}) \geq 0$ with

$$\|\mathbf{p}^*\|_1 = P_{\mathrm{m}}(\mathbf{q}) < +\infty \tag{26.21}$$

is called optimal. It may be easily verified [13] that if $\|\mathbf{p}^*\|_1 = P_{\mathrm{m}}(\mathbf{q})$, then

$$\gamma(q_k) = \mathrm{SINR}_k(\mathbf{p}^*), \quad 1 \leq k \leq K. \tag{26.22}$$

Using (26.8), we can rewrite this to obtain

$$p_k^* - \gamma_k \sum_{l=1}^{K} p_l^* v_{k,l} = \sigma_k^2 \gamma_k, \quad 1 \leq k \leq K. \tag{26.23}$$

In the matrix form, this becomes

$$(\mathbf{I} - \boldsymbol{\Gamma}(\mathbf{q})\mathbf{V})\mathbf{p}^* = \boldsymbol{\Gamma}(\mathbf{q})\mathbf{C}\mathbf{1}, \tag{26.24}$$

where $\mathbf{1}$ denotes the vector of K ones and $\mathbf{C} := \mathrm{diag}(\sigma_1^2, \ldots, \sigma_K^2)$. Consequently, the vector $\mathbf{p}^* = \mathbf{p}^*(\mathbf{q})$ must be a positive solution to (26.24). By the Perron-Frobenius theorems [11, Theorem 1.5 and Theorem 2.1], there exists a positive solution to

(26.24) if and only if (26.15) holds. Furthermore, the solution is unique and given by

$$\mathbf{p}^*(\mathbf{q}) = \left(\mathbf{I} - \boldsymbol{\Gamma}(\mathbf{q})\mathbf{V}\right)^{-1}\boldsymbol{\Gamma}(\mathbf{q})\mathbf{C}\mathbf{1}. \tag{26.25}$$

Consequently, if $\rho(\mathbf{q}) < 1$ is true, then the minimum total power $P_{\mathrm{m}}(\mathbf{q}) < +\infty$ exists and

$$P_{\mathrm{m}}(\mathbf{q}) = \mathbf{1}^T\left(\mathbf{I} - \boldsymbol{\Gamma}(\mathbf{q})\mathbf{V}\right)^{-1}\boldsymbol{\Gamma}(\mathbf{q})\mathbf{C}\mathbf{1}. \tag{26.26}$$

Now we consider the uplink channel. Clearly, under individual power constraints, $\mathbf{q} \in \mathbb{G}^K$ is feasible if and only if

$$1 \le \max_{\mathbf{p}\in\mathcal{P}_i} \min_{1\le k\le K} \frac{\mathrm{SINR}_k(\mathbf{p})}{\gamma(q_k)}, \tag{26.27}$$

where $\mathcal{P}_i$ is given by (26.4). The following lemma provides everything we need for identifying the feasible QoS region [6].

Lemma 26.1. *Inequality* (26.27) *is satisfied if and only if* (26.25) *exists and* $p_k^*(\mathbf{q}) \le P_k$ *for each* $1 \le k \le K$.

Thus, by Lemma 26.1, it is sufficient to find the optimal power allocation (if exists), and then verify whether or not the power allocation satisfies individual power constraints. As an immediate consequence of this, the feasible QoS region under individual power constraints is

$$\mathbb{F}_\gamma\left(P^{(i)}\right) = \left\{\mathbf{q} \in \mathbb{G}^K : p_k^*(\mathbf{q}) \le P_k\right\}. \tag{26.28}$$

26.4. Convexity of the feasible QoS region: sufficient conditions

In this section, we provide sufficient conditions for the convexity of the feasible QoS region.

26.4.1. Systems with no power constraints

First we show that the spectral radius is jointly log-convex if γ defined by (26.13) is log-convex. Note that the log-convexity is stronger than the ordinary convexity and both imply the convexity of the feasible QoS region. Indeed, since the logarithmic function is concave, it is easy to see that any positive log-convex function is a convex one but not vice versa [9]. More precisely, if $f : \mathbb{R} \to \mathbb{R}_+$ is log-convex, then, for all $\hat{x}, \check{x} \in \mathbb{R}$ and $\alpha \in [0,1]$,

$$\begin{aligned} f\left((1-\alpha)\hat{x} + \alpha\check{x}\right) &\le f(\hat{x})^{1-\alpha} f(\check{x})^{\alpha} \\ &\le (1-\alpha) f(\hat{x}) + \alpha f(\check{x}) \\ &\le \max\left\{f(\hat{x}), f(\check{x})\right\}. \end{aligned} \tag{26.29}$$

In what follows, let $\hat{\mathbf{q}} = (\hat{q}_1, \ldots, \hat{q}_K) \in \mathbb{G}^K$ and $\check{\mathbf{q}} = (\check{q}_1, \ldots, \check{q}_K) \in \mathbb{G}^K$ be two arbitrary vectors of QoS requirements. Moreover, given $\hat{\mathbf{q}}, \check{\mathbf{q}} \in \mathbb{G}^K$, define $\mathbf{q}(\alpha) \in \mathbb{G}^K$ with $\alpha \in [0,1]$ as

$$\mathbf{q}(\alpha) = (1-\alpha)\hat{\mathbf{q}} + \alpha\check{\mathbf{q}}. \tag{26.30}$$

The key ingredient in the proof of the main result is the following lemma [14].

Lemma 26.2. *Let $\mathbf{X} \in \mathbb{R}_+^{K\times K}$ be irreducible. Then,*

$$\log \rho(\mathbf{X}) = \sup_{\mathbf{A}\in\mathcal{S}} \left(\sum_{k,l=1}^{K} u_k a_{k,l} \log \frac{x_{k,l}}{a_{k,l}} \right), \tag{26.31}$$

where $\mathcal{S} := \mathcal{S}(\mathbf{X})$ is a set of all stochastic matrices so that $a_{k,l} = 0$ whenever $x_{k,l} = 0$ for each $\mathbf{A} \in \mathcal{S}$ and $\mathbf{u} = (u_1, \ldots, u_K)$ is the left Perron eigenvector of $\mathbf{A}$ with $\sum_{k=1}^{K} u_k = 1$. The supremum in (26.31) is attained if and only if $a_{k,l} = x_{k,l} w_l / (w_k \rho(\mathbf{X}))$, where $\mathbf{w} = (w_1, \ldots, w_K)$ is a positive right eigenvector of $\mathbf{X}$, that is, $\mathbf{X}\mathbf{w} = \mathbf{w}\rho(\mathbf{X})$.

By Lemma 26.2, if $\mathbf{X} = \boldsymbol{\Gamma}(\mathbf{q})\mathbf{V}$ and γ is log-convex, then each sum term, say term (k,l), on the right-hand side of (26.31) is a convex function of q_k. Thus, since the sum of convex functions is convex and $\sup(f+g) \le \sup f + \sup g$ for any positive functions f and g, the left-hand side of (26.31) is a convex function of $\mathbf{q} = (q_1, \ldots, q_K)$. This gives rise to the following theorem.

Theorem 26.3. *Suppose that $\mathbf{V}$ is irreducible. If $\gamma : \mathbb{G} \to \mathbb{R}_+$ defined by (26.13) is log-convex, then the spectral radius $\rho : \mathbb{G}^K \to \mathbb{R}_+$ is jointly log-convex. In other words, if*

$$\gamma\big((1-\alpha)\hat{x} + \alpha\check{x}\big) \le \gamma(\hat{x})^{1-\alpha}\gamma(\check{x})^{\alpha} \tag{26.32}$$

for all $\hat{x}, \check{x} \in \mathbb{G}$ and $\alpha \in [0,1]$, then

$$\rho\big(\mathbf{q}(\alpha)\big) \le \rho(\hat{\mathbf{q}})^{1-\alpha}\rho(\check{\mathbf{q}})^{\alpha} \tag{26.33}$$

holds for all $\hat{\mathbf{q}}, \check{\mathbf{q}} \in \mathbb{G}^K$ and $\alpha \in [0,1]$.

Thus, by Theorem 26.3 and (26.29), we can conclude that if $\hat{\mathbf{q}}$ and $\check{\mathbf{q}}$ are feasible and γ is log-convex, then $\rho(\mathbf{q}(\alpha)) \le \max\{\rho(\hat{\mathbf{q}}), \rho(\check{\mathbf{q}})\} < 1, \alpha \in [0,1]$, is feasible as well. We summarize this observation in a corollary.

Corollary 26.4. *If $\mathbf{V}$ is irreducible and $\gamma : \mathbb{G} \to \mathbb{R}_+$ is log-convex, then $\mathbb{F}_\gamma$ is a convex set.*

26.4.2. Systems with a total power constraint

Corollary 26.4 does not carry over to systems with power constraints. This is because (26.15) is necessary but not sufficient for the QoS vector $\mathbf{q}$ to be feasible. For this reason, in [12], we proved the following result.

Theorem 26.5. *If $\gamma : \mathbb{G} \to \mathbb{R}_+$ is log-convex, then $P_{\mathrm{m}} : \mathbb{F}_\gamma \to \mathbb{R}_+$ is jointly log-convex so that*

$$P_{\mathrm{m}}\big(\mathbf{q}(\alpha)\big) \leq P_{\mathrm{m}}(\hat{\mathbf{q}})^{1-\alpha} P_{\mathrm{m}}(\check{\mathbf{q}})^{\alpha} \tag{26.34}$$

for all $\hat{\mathbf{q}}, \check{\mathbf{q}} \in \mathbb{F}_\gamma$ and $\alpha \in [0,1]$.

As in Theorem 26.3, Theorem 26.5 requires that γ is log-convex. It is worth pointing out that in contrast to systems without power constraints, there is no need for $\mathbf{V}$ to be irreducible. An immediate consequence of Theorem 26.5 is the following corollary.

Corollary 26.6. *If $\gamma : \mathbb{G} \to \mathbb{R}_+$ is log-convex, then $\mathbb{F}_\gamma(P)$ is a convex set.*

26.4.3. Systems with individual power constraints

A trivial but important observation is that if $p_k^*(\mathbf{q})$ was jointly log-convex for each $1 \leq k \leq K$, then $\mathbb{F}_\gamma(P^{(i)})$ would be a convex set since the intersection of convex sets is convex. To see that $p_k^*(\mathbf{q})$ is jointly log-convex if γ is log-convex, note that

$$p_k^*(\mathbf{q}) = \mathbf{e}_k^T \big(\mathbf{I} - \boldsymbol{\Gamma}(\mathbf{q})\mathbf{V}\big)^{-1} \boldsymbol{\Gamma}(\mathbf{q})\mathbf{C}\mathbf{1}, \quad 1 \leq k \leq K, \tag{26.35}$$

where $\mathbf{e}_k = (0, \ldots, 0, 1, 0, \ldots, 0)$ is a unit vector with a 1 in the kth position and zeros elsewhere. Comparing this with (26.26) reveals that instead of the vector of K ones, we have the unit vector $\mathbf{e}_k$. Consequently, proceeding essentially as in the proof of Theorem 26.5 proves the following theorem.

Theorem 26.7. *If $\gamma : \mathbb{G} \to \mathbb{R}_+$ is log-convex, then $\mathbb{F}_\gamma(P^{(i)})$ is a convex set.*

In fact, if $p_k^*(\mathbf{q})$ is jointly log-convex, so is $\sum_k w_k p_k^*(\mathbf{q})$ for any positive coefficients $w_1, \ldots, w_K$ since the sum of positive log-convex functions is log-convex. Finally, we point out that the same reasoning as above shows that if the function γ is log-convex, the feasible QoS region under both individual power constraints and a total power constraint is a convex set. Figure 26.2 depicts the feasible QoS region for two users and $\varphi(x) = \gamma(x) = 1/x$, $x > 0$.

26.4.4. Applications

All the results above hold provided that the function $\gamma : \mathbb{G} \to \mathbb{R}_+$ is log-convex. Thus, there are at least two interesting applications of these results.

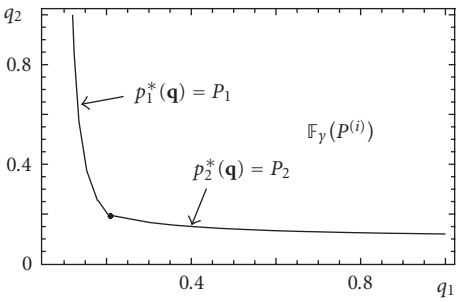

FIGURE 26.2. An example of the feasible QoS region $\mathbb{F}_\gamma(P^{(i)})$ under individual power constraints.

(1) $\varphi(x) = \log(x)$, $x > 0$, in which case $\gamma(x) = \exp(x)$, $x \in \mathbb{G} = \mathbb{R}$. Obviously, the exponential function is log-convex on $\mathbb{R}$ since $(\log\exp(x))'' = x'' = 0$ for all $x \in \mathbb{R}$.[3] Thus, by Theorems 26.3 and 26.5, the spectral radius $\rho(\mathbf{q})$ and the minimum total power $P_{\mathrm{m}}(\mathbf{q})$ are both log-convex functions when SINR requirements are expressed in logarithmic scale (for instance in decibels). Furthermore, by Corollaries 26.4 and 26.6, the corresponding feasible log-SINR regions are convex sets. This case is of practical interest since if $\mathrm{SINR}_k(\mathbf{p}) \gg 1$, then

$$\log\left(1 + \mathrm{SINR}_k(\mathbf{p})\right) \approx \log\left(\mathrm{SINR}_k(\mathbf{p})\right). \tag{26.36}$$

Consequently, in systems in which the rate-power curve for each user, say user k, is given by $\alpha\log(1+\beta\mathrm{SINR}_k(\mathbf{p}))$ for some arbitrary positive constants α and β, the set of feasible rates at large values of SINR is a convex set. The logarithmic rate-power curve can be approximated by a piecewise constant rate-power curve determined by different QAM modulation schemes designed for a given bit error probability [15].

(2) $\varphi(x) = 1/x$, $x > 0$, so that $\gamma(x) = 1/x$, $x > 0$. Since $(\log(1/x))'' = 1/x^2 > 0$ for all $x > 0$, the function $\gamma(x) = 1/x$, $x > 0$, is log-convex on $\mathbb{G} = \mathbb{R}_+$. Thus, if $\gamma(x) = 1/x$, $x > 0$, the spectral radius and the minimum total power are log-convex. Furthermore, the feasible inverse-SINR regions are convex sets. Now consider a system with random packet arrivals and transmission rate for user k given by $W\log_2(1 + \mathrm{SINR}_k(\mathbf{p}))$ bits per second where W denotes a total bandwidth. If $\lambda_k < W\log_2(1+\mathrm{SINR}_k(\mathbf{p}))$ is the packet arrival rate (expressed in bits/s) of user k, then the average customer delay is often well approximated by [16]

$$\frac{1}{W\log_2\left(1 + \mathrm{SINR}_k(\mathbf{p})\right) - \lambda_k} \approx \frac{1}{W\mathrm{SINR}_k(\mathbf{p}) - \lambda_k}, \quad \mathrm{SINR}_k(\mathbf{p}) \ll 1. \tag{26.37}$$

Note that if $\mathrm{SINR}_k(\mathbf{p}) \ll 1$, $\log_2(1+\mathrm{SINR}_k(\mathbf{p})) \approx \mathrm{SINR}_k(\mathbf{p})$ is a reasonable approximation for the rate-power curve [3]. Consequently, at low values of SINR, the set

[3] $(f(x))''$ denotes the second derivative of $f(x)$ with respect to x.

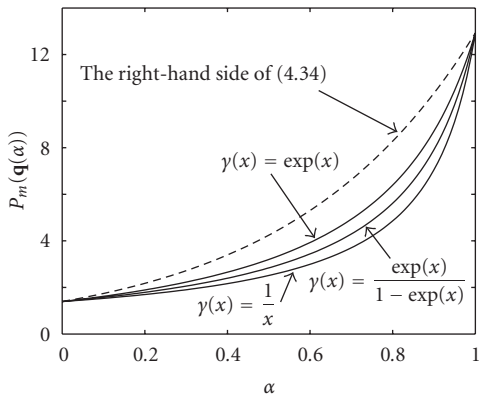

FIGURE 26.3. The minimum total power $P_{\mathrm{m}}(\mathbf{q}(\alpha))$ as a function of $\alpha \in [0, 1]$ for some given $\hat{\mathbf{q}}$ and $\check{\mathbf{q}}$. We have $v_{k,l} > 0$, $1 \le k, l \le K$, $k \ne l$.

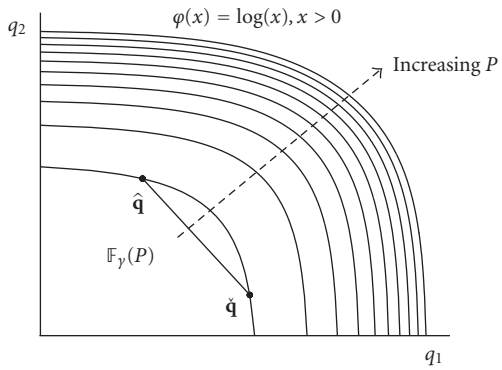

FIGURE 26.4. The feasible log-SINR region for a 2-user system with different total power constraints P.

of feasible delays can be assumed to be convex. Finally, we point out that the effective spreading gains of the users considered in [10] are also inversely proportional to SINR.

Figure 26.3 depicts $P_{\mathrm{m}}(\mathbf{q}(\alpha))$ as a function of $\alpha \in [0, 1]$ for three examples of the function γ corresponding to the following QoS functions: $\varphi(x) = \log(x)$, $x > 0$, $\varphi(x) = 1/x$, $x > 0$, and $\varphi(x) = \log(x/(1 + x))$, $x > 0$, where the latter one is the effective bandwidth expressed in logarithmic scale [17]. Figure 26.4 shows the feasible log-SINR regions ($\varphi(x) = \log(x)$, $x > 0$) for different total power constraints.

26.4.5. Necessity of the log-convexity

The above results provide sufficient conditions for the feasible QoS region to be a convex set. In fact, they provide more than that. From Theorem 26.3, we know that if $\gamma : \mathbb{G} \to \mathbb{R}_+$ is log-convex, then the spectral radius $\rho(\mathbf{q})$ is a jointly log-convex

function of the QoS requirements. However, for the feasible QoS region to be a convex set, it is not necessary that the spectral radius is log-convex. This gives rise to the following problem.

Problem 26.8. Let $K > 1$ be arbitrary. Suppose that the Perron root $\rho(\mathbf{q})$ is jointly convex on $\mathbb{G}^K$ for any irreducible matrix $\mathbf{V} \geq 0$. Is the inverse QoS function $\gamma : \mathbb{G} \to \mathbb{R}_+$ log-convex?

The theorem below shows that if γ is at least twice differentiable, the answer is that this function is indeed log-convex.

Theorem 26.9. *Let $K > 1$ be arbitrary and let $\gamma : \mathbb{G} \to \mathbb{R}_+$ be twice differentiable. Suppose that $\rho(\mathbf{q})$ is convex on $\mathbb{G}^K$ for any irreducible interference matrix $\mathbf{V}$. Then, γ is log-convex on $\mathbb{G}$.*

Note that if $\gamma : \mathbb{G} : \mathbb{R}_+$ is twice differentiable, a necessary and sufficient condition for γ to be log-convex is [9]

$$\gamma'(x)^2 \leq \gamma(x)\gamma''(x), \quad x \in \mathbb{G}. \tag{26.38}$$

It should be emphasized that, by Theorem 26.9, the function γ needs to be log-convex if the spectral radius is required to be convex for any interference matrix $\mathbf{V} \geq 0$. This is not true if $\mathbf{V}$ is fixed, in which case the requirement on γ may be less restrictive. For instance, if the linear receiver is followed by single-user decoders, one for each user, then the information theoretic rate is proportional to $\log(1 + \mathrm{SINR})$ nats per channel use. In this case, the QoS function and its inverse are $\rho(x) = \log(1 + x)$, $x > 0$, and $\gamma(x) = e^x - 1$, respectively. Unlike the exponential function, the map $x \to e^x - 1$ is not log-convex since $(\log(e^x - 1))'' = -1/4(\mathrm{csch}(x/2))^2 < 0$, $x > 0$, where $\mathrm{csch}(x)$ denotes the hyperbolic cosecant of x. However, despite the fact that $\gamma(x) = e^x - 1$ is not log-convex, it may be easily verified that the feasible QoS region becomes convex for sufficiently small entries of the interference matrix $\mathbf{V}$.

26.5. Symmetric interference matrices

When confined to certain classes of interference matrices, the inverse QoS function γ does not need to be log-convex in order to obtain a convex feasible QoS region. Symmetric matrices constitute an important class of such matrices.

The following theorem provides a necessary and sufficient condition for the spectral radius to be a convex function of the QoS requirements.

Theorem 26.10. *Let $F_\gamma : \mathbb{G}^2 \to \mathbb{R}_+$ be defined as*

$$F_\gamma(x, y) := \sqrt{\gamma(x)\gamma(y)}. \tag{26.39}$$

Then, the spectral radius $\rho(\mathbf{q})$ is convex on $\mathbb{G}^K$ for any irreducible symmetric matrix $\mathbf{V}$ if and only if $F_\gamma : \mathbb{G}^2 \to \mathbb{R}_+$ is jointly convex on $\mathbb{G}^2$.

The necessary condition is easily derived by considering the 2-user case with $\mathbf{V} = \left(\begin{smallmatrix} 0 & \varrho \\ \varrho & 0 \end{smallmatrix}\right)$ and $\rho(\mathbf{q}) = \sqrt{\gamma(q_1)\gamma(q_2)}\varrho$. Thus, F_γ defined above must be a jointly convex function on $\mathbb{G}^2$ for the spectral radius to be jointly convex. To see the converse, note that for any symmetric matrix $\mathbf{V}$,

$$\rho(\mathbf{q}(\alpha)) = \rho(\mathbf{W}(\alpha)), \quad \alpha \in [0,1], \tag{26.40}$$

where $\mathbf{W}(\alpha) := \mathbf{\Gamma}^{1/2}(\mathbf{q}(\alpha))\mathbf{V}\mathbf{\Gamma}^{1/2}(\mathbf{q}(\alpha))$. The entries of $\mathbf{W}(\alpha)$ are

$$w_{k,l}(\alpha) = \sqrt{\gamma(q_k(\alpha))}v_{k,l}\sqrt{\gamma(q_l(\alpha))} = F_\gamma(q_k, q_l)v_{k,l}. \tag{26.41}$$

Hence, by the joint convexity of F_γ,

$$w_{k,l}(\alpha) \le (1-\alpha)F(\hat{q}_k, \hat{q}_l)v_{k,l} + \alpha F(\check{q}_k, \check{q}_l)v_{k,l}, \quad \alpha \in [0,1], \tag{26.42}$$

and the converse immediately follows from the monotony of the spectral radius. Also, it is easy to see that the spectral radius is strictly convex if and only if F_γ defined above is strictly convex.

26.6. Positive semidefinite interference matrices

Positive semidefinite matrices form another important class of interference matrices. Observe that if $\operatorname{trace}(\mathbf{V}) = 0$, then the interference matrix $\mathbf{V}$ is always indefinite. Roughly speaking, the interference matrix becomes positive semidefinite when the diagonal entries of the matrix are dominant, which is the case in systems with relatively strong self-interference.

Now assume that $\mathbf{V} \ge 0$ is positive semidefinite. Then, there exist a unitary matrix $\mathbf{U}$ and a diagonal matrix $\mathbf{\Lambda} \ge 0$ so that $\mathbf{V} = \mathbf{U}\mathbf{\Lambda}\mathbf{U}^H$. Furthermore, we have

$$\rho(\mathbf{q}) = \lambda_{\max}(\mathbf{\Gamma}(\mathbf{q})^{1/2}\mathbf{V}\mathbf{\Gamma}(\mathbf{q})^{1/2}), \tag{26.43}$$

where $\lambda_{\max}(\mathbf{\Gamma}(\mathbf{q})^{1/2}\mathbf{V}\mathbf{\Gamma}(\mathbf{q})^{1/2})$ is the largest eigenvalue of $\mathbf{\Gamma}(\mathbf{q})^{1/2}\mathbf{V}\mathbf{\Gamma}(\mathbf{q})^{1/2}$. Using elementary algebra, these basic observations lead to the following theorem.

Theorem 26.11. *Suppose that $\mathbf{V} \ge 0$ is positive semidefinite and $\gamma : \mathbb{G} \to \mathbb{R}_+$ is any convex function. Then, $\rho(\mathbf{q})$ is jointly convex on $\mathbb{G}^K$.*

As an immediate consequence of the theorem, we know that $\mathbb{F}_\gamma$ is a convex set if $\mathbf{V}$ is positive semidefinite and $\gamma : \mathbb{G} \to \mathbb{R}_+$ is a convex function. In particular, we can conclude that $\mathbb{F}_\gamma$ is convex when $\gamma(x) = x$, $x > 0$. This case is of particular interest and is considered in Section 26.7.

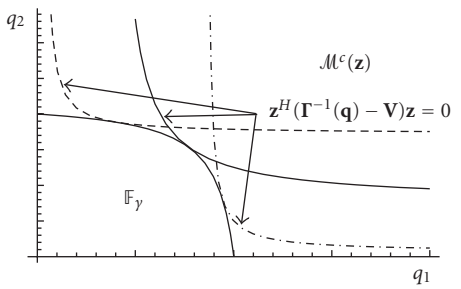

FIGURE 26.5. The feasible SINR region for a positive semidefinite interference matrix.

Note that due to (26.43), the feasibility region is given by

$$\mathbb{F}_\gamma = \{\mathbf{q} : \lambda_{\max}(\mathbf{\Gamma}^{1/2}(\mathbf{q})\mathbf{V}\mathbf{\Gamma}^{1/2}(\mathbf{q})) < 1\}. \tag{26.44}$$

Thus, since $\lambda_{\max}(\mathbf{\Gamma}^{1/2}(\mathbf{q})\mathbf{V}\mathbf{\Gamma}^{1/2}(\mathbf{q})) < 1$ if and only if $\lambda_{\min}(\mathbf{\Gamma}^{-1}(\mathbf{q}) - \mathbf{V}) > 0$ or, equivalently, if and only if

$$0 < \mathbf{z}^H(\mathbf{\Gamma}^{-1}(\mathbf{q}) - \mathbf{V})\mathbf{z} \tag{26.45}$$

for all $\mathbf{z} \in \mathbb{R}^K$, we can write

$$\mathbb{F}_\gamma = \bigcap_{\mathbf{z}\in\mathbb{R}^K} \mathcal{M}(\mathbf{z}) = \left(\bigcup_{\mathbf{z}\in\mathbb{R}^K} \mathcal{M}^c(\mathbf{z}) \right)^c, \tag{26.46}$$

where $\mathcal{M}^c(\mathbf{z})$ is used to denote the complement of $\mathcal{M}(\mathbf{z})$ in $\mathbb{G}^K$ and

$$\mathcal{M}(\mathbf{z}) := \{\mathbf{q} : \mathbf{z}^H(\mathbf{\Gamma}^{-1}(\mathbf{q}) - \mathbf{V})\mathbf{z} > 0\}. \tag{26.47}$$

Thus, given an arbitrary positive semidefinite matrix, the feasible QoS region, which by Theorem 26.11 is a convex set for any convex function γ, can be represented as the intersection of the sets $\mathcal{M}(\mathbf{z})$ with respect to all vectors $\mathbf{z} \in \mathbb{R}^K$. This is illustrated in Figure 26.5 for $\gamma(x) = x$, $x > 0$. It is important to notice that although $\mathcal{M}(\mathbf{z})$ are not convex in general, the intersection of these sets yields a convex set for any convex function γ. Finally, note that $\mathcal{M}^c(\mathbf{z})$ is a convex set if $\gamma(x) = x$, $x > 0$ (see Figure 26.5). This immediately follows from (26.45) whose right-hand side is

$$\mathbf{z}^H\mathbf{\Gamma}^{-1}(\mathbf{q})\mathbf{z} - \mathbf{z}^H\mathbf{V}\mathbf{z} = \sum_k \frac{|z_k|^2}{\gamma(q_k)} - \mathbf{z}^H\mathbf{V}\mathbf{z}. \tag{26.48}$$

Clearly, this function is convex if $\gamma(x) = x$, $x > 0$, so that $\mathcal{M}^c(\mathbf{z})$ as the sublevel set of this function with respect to the zero value must be a convex set for any fixed $\mathbf{z}$. The linear case $\gamma(x) = x, x > 0$, is of great practical interest, and hence is separately considered in the next section.

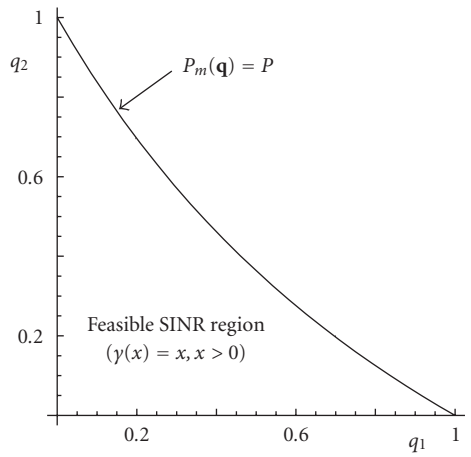

FIGURE 26.6. The feasible SINR region with SNR = 1 and $\varrho = 1/2$.

26.7. The feasible and infeasible SINR regions

Unfortunately, since $\gamma(x) = x$, $x > 0$, is not log-convex, the results of Section 26.4 do not apply to this linear case. Note that if $\gamma(x) = x$, $x > 0$, SINR is itself the QoS parameter of interest and $\mathbb{F}_\gamma$, $\mathbb{F}_\gamma(P)$, and $\mathbb{F}_\gamma(P^{(i)})$ are sets of all feasible SINR requirements referred to as feasible SINR regions. Throughout this section, we drop the subscript γ and write $\mathbb{F}$, $\mathbb{F}(P)$, and $\mathbb{F}(P^{(i)})$ while referring to the feasible SINR regions. The complements of these sets in $\mathbb{G}^K$ are called the infeasible SINR regions and are designated by the superscript "c." For instance, $\mathbb{F}^c = \mathbb{G}^K \setminus \mathbb{F}$.

Since $\gamma(x) = x$, $x > 0$, is convex, Theorem 26.11 implies that the feasible SINR region is convex when $\mathbf{V}$ is positive semidefinite. Otherwise, there is little known about the feasible SINR region. In what follows, we assume that $\operatorname{trace}(\mathbf{V}) = 0$ so that $\mathbf{V}$ cannot be positive semidefinite. We conjecture that the infeasible SINR regions $\mathbb{F}^c$ and $\mathbb{F}^c(P)$ are convex sets when $\operatorname{trace}(\mathbf{V}) = 0$ [12]. The consequences of this conjecture (if true) are far-reaching. Indeed, if this conjecture were true, the optimal scheduling for the downlink scenario in the low SINR regime would involve a simple time-sharing protocol between different users transmitting at the maximal power (see also Figure 26.6). In contrast, in the uplink scenario (individual power constraints), neither the feasible nor infeasible SINR region is convex (see Figure 26.7). Thus, in this case, a more sophisticated time-sharing protocol between groups of several users may help improve the system performance.

26.7.1. An upper bound

As $\log \rho(\mathbf{q})$ depends logarithmically on the SINR requirements and $\gamma(x) = x$, $x > 0$, is a log-concave function, one might be inclined to prove the conjecture mentioned above by showing that the spectral radius is log-concave. However, because of the supremum operator in (26.31), this approach must fail. This

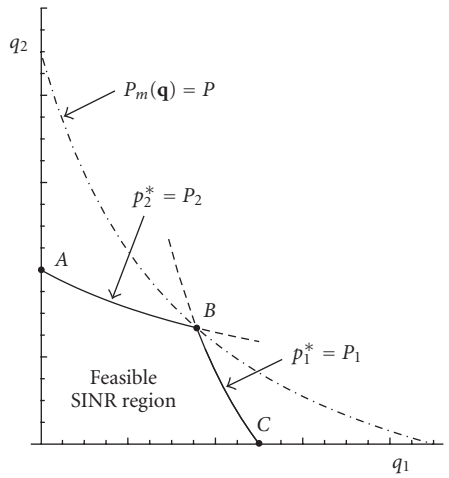

FIGURE 26.7. The feasible SINR region under individual power constraints.

is because exchanging the supremum and sum operator always yields an upper bound instead of a lower bound that would be necessary for proving the log-concavity property.

The problem is left open. In [6], we derived the following upper bound, which supports the conjecture for systems without power constraints.

Theorem 26.12. *Let* $\mathbf{V} \geq 0$ *be irreducible. If* $q_1, \ldots, q_K$ *are feasible, then*

$$\prod_{l=1}^{K} \left(\gamma(q_l)\right)^{x_l y_l} < \frac{1}{\rho(\mathbf{V})}, \tag{26.49}$$

where $\mathbf{y}$ *and* $\mathbf{x}$ *with* $\mathbf{x}^T\mathbf{y} = 1$ *are positive left and right eigenvectors of* $\mathbf{V}$*, respectively.*

The bound leads to a superset of the feasible QoS region, and in particular to the feasible SINR region if $\gamma(x) = x$, $x > 0$. It is easy to see that the complement of this superset is a convex set. Obviously, this result does not solve the original problem but the bound provides a convenient necessary condition for the feasibility of QoS requirements. Furthermore, (26.49) gives a useful insight into the optimal QoS tradeoff.

The bound in (26.49) still requires the computation of both the spectral radius and the corresponding eigenvectors. When all nondiagonal elements of $\mathbf{V}$ are positive, this computation can be avoided completely at the expense of tightness of the bound. To see this, observe that if all nondiagonal elements of $\mathbf{V}$ are positive, then the matrix $\mathbf{A}$ in (26.31) can be chosen to be $a_{k,l} = 1/(K-1)$ if $k \neq l$ and zero otherwise. Thus, since the corresponding Perron eigenvector is $\mathbf{u} = (1/K, \ldots, 1/K)$,

we obtain

$$\log\rho(\mathbf{q}) \geq \frac{1}{K(K-1)}\sum_{\substack{k,l\\k\neq l}}\log v_{k,l} + \log(K-1) + \frac{1}{K}\sum_{l=1}^{K}\log\gamma(q_l). \tag{26.50}$$

Now due to (26.15), we conclude that if $q_1,\ldots,q_K$ are feasible, then

$$\prod_{l=1}^{K}\left(\gamma(q_l)\right)^{1/K} < \frac{1}{(K-1)\prod_{\substack{k,l=1\\k\neq l}}^{K}\left(v_{k,l}\right)^{1/K(K-1)}}. \tag{26.51}$$

Note that neither the spectral radius of $\mathbf{V}$ nor the corresponding eigenvectors appear in (26.51).

26.7.2. The 2-user case

To illustrate some of the results, we consider a simple 2-user system. In this case, the minimum total power can be explicitly computed to give

$$P_{\mathrm{m}}(\mathbf{q}) = \sigma^2\frac{\gamma(q_1)+\gamma(q_2)+2\varrho\gamma(q_1)\gamma(q_2)}{1-\varrho^2\gamma(q_1)\gamma(q_2)}, \tag{26.52}$$

where, without loss of generality, we assumed that $\varrho = v_{1,2} = v_{2,1}$ and $\mathbf{C} = (\sigma^2,\sigma^2)$. The characteristic polynomial for the matrix $\mathbf{\Gamma}(\mathbf{q})\mathbf{V}$ is $p(\lambda) = \lambda^2 - \varrho^2\gamma(q_1)\gamma(q_2)$. Hence, $P_{\mathrm{m}} < +\infty$ exists if and only if

$$\rho(\mathbf{q}) = \varrho\sqrt{\gamma(q_1)\gamma(q_1)} < 1. \tag{26.53}$$

Thus, since $\rho(\mathbf{q})$ is concave on $\mathbb{G}^2$ if $\gamma(x) = x$, $x > 0$, the infeasible SINR region in the 2-user case is a convex set. This is also true if there is a total power constraint. To see this, let $\gamma(x) = x$, $x > 0$, and $q_k = \gamma(q_k)$. We need to show that $P_{\mathrm{m}}(\mathbf{q}) = P$ or, equivalently,

$$q_2(q_1) = \frac{\mathrm{SNR} - q_1}{1 + 2\varrho q_1 + \varrho^2 q_1\,\mathrm{SNR}} \tag{26.54}$$

is convex, where $\mathrm{SNR} = P/\sigma^2$. It may be easily verified that

$$q_2'(q_1) = \frac{-(1+\varrho\,\mathrm{SNR})^2}{\left(1+\varrho(2+\varrho\,\mathrm{SNR})q_1\right)^2}. \tag{26.55}$$

Since the numerator is independent of q_1 and the denominator is increasing in $q_1 > 0$, we must have $q_2''(q_1) \geq 0$ for every $q_1 > 0$. From this, it follows that q_2 is a convex function of q_1, and hence $\mathbb{F}^c(P)$ must be a convex set. Furthermore, if

$\varrho > 0$, then $q_2''(q_1) > 0$ for every $q_1 > 0$ in which case $q_2(q_1)$ is strictly convex. Assuming SNR $= 1$ and $\varrho = 1/2$, Figure 26.6 shows the resulting feasible SINR region.

If there are individual power constraints on each user and $\gamma(x) = x$, $x > 0$, we know from Section 26.4.3 that $(q_1, q_2) \in \mathbb{F}(P^{(i)})$ if and only if

$$p_1^* = \sigma^2 \frac{q_1 + \varrho q_1 q_2}{1 - \varrho^2 q_1 q_2} \leq P_1, \qquad p_2^* = \sigma^2 \frac{q_2 + \varrho q_1 q_2}{1 - \varrho^2 q_1 q_2} \leq P_2, \tag{26.56}$$

where $\mathbf{p}^* = (p_1^*, p_2^*)$ is given by (26.25). Proceeding essentially as before shows that $p_1^* = P_1$ and $p_2^* = P_2$ are both convex if they are written as functions of q_1. Obviously, $\mathbb{F}(P^{(i)}) = \mathbb{F}_1(P^{(i)}) \cap \mathbb{F}_2(P^{(i)})$ is not convex since $\mathbb{F}_1(P^{(i)}) = \{(q_1, q_2) : p_1^* \leq P_1\}$ and $\mathbb{F}_2(P^{(i)}) = \{(q_1, q_2) : p_2^* \leq P_2\}$ are not convex sets but their complements $\mathbb{F}_1^c(P^{(i)})$ and $\mathbb{F}_2^c(P^{(i)})$. Also, the infeasible SINR region

$$\mathbb{F}^c(P^{(i)}) = \left(\mathbb{F}_1(P^{(i)}) \cap \mathbb{F}_2(P^{(i)})\right)^c = \mathbb{F}_1^c(P^{(i)}) \cup \mathbb{F}_2^c(P^{(i)}) \tag{26.57}$$

does not need to be convex since the union of convex sets ($\mathbb{F}_1^c(P^{(i)})$ and $\mathbb{F}_2^c(P^{(i)})$) is not convex in general. This situation is illustrated in Figure 26.7.

26.7.3. The conjecture and its consequences

The preceding results support the conjecture about the convexity of $\mathbb{F}^c$ and $\mathbb{F}(P)^c$. Although the problem is open, it is interesting to consider the consequences of this conjecture.

Note that in order to prove the conjecture for systems without power constraints, it is sufficient to show that

$$\rho(\mathbf{q}(\alpha)) = \rho\left((1-\alpha)\boldsymbol{\Gamma}(\hat{\mathbf{q}})\mathbf{V} + \alpha\boldsymbol{\Gamma}(\check{\mathbf{q}})\mathbf{V}\right) \geq 1 \tag{26.58}$$

for all $\alpha \in [0, 1]$ and arbitrary QoS vectors $\hat{\mathbf{q}}, \check{\mathbf{q}} \in \mathbb{G}^K$ with

$$\rho(\hat{\mathbf{q}}) = \rho(\check{\mathbf{q}}) = 1. \tag{26.59}$$

In other words, if $\hat{\mathbf{q}}$ and $\check{\mathbf{q}}$ lie on the boundary of $\mathbb{F}$, then the line connecting them should be outside of the feasible SINR region. The following theorem provides a necessary and sufficient condition for (26.58) with (26.59) to be satisfied.

Theorem 26.13. *Inequality* (26.58) *with* (26.59) *holds if and only if the spectral radius* $\rho(\mathbf{q})$ *is concave on* $\mathbb{G}^K$.

It is worth pointing out that if

$$\rho(\mathbf{q}(\alpha)) \geq \min\{\rho(\hat{\mathbf{q}}), \rho(\check{\mathbf{q}})\}, \quad \alpha \in [0,1] \tag{26.60}$$

holds for all $\hat{\mathbf{q}}, \check{\mathbf{q}} \in \mathbb{G}^K$, so does (26.58) with (26.59). Thus, by Theorem 26.13, this inequality is equivalent to concavity of the spectral radius.

In fact, Theorem 26.13 applies to any function $\gamma : \mathbb{G} \to \mathbb{R}_+$ for which (26.58) with (26.59) holds. Thus, considering the special case of $\gamma(x) = x$, $x > 0$, the theorem implies that the infeasible SINR region is convex if and only if the spectral radius is concave on $\mathbb{G}^K$. The problem whether or not the spectral radius is concave strongly depends on the diagonal elements of $\mathbf{\Gamma}(\mathbf{q})\mathbf{V}$. To see this, let $\gamma(x) = x$, $x > 0$, and consider

$$\mathbf{\Gamma}(\mathbf{q})\mathbf{V} = \begin{pmatrix} q_1 & 0 \\ 0 & q_2 \end{pmatrix} \begin{pmatrix} \alpha & \beta \\ \beta & \alpha \end{pmatrix} = \begin{pmatrix} \alpha q_1 & \beta q_1 \\ \beta q_2 & \alpha q_2 \end{pmatrix}, \tag{26.61}$$

where $\alpha \geq 0$ and $\beta > 0$ are some real constants. It may be easily verified that

$$\rho(\mathbf{q}) = \frac{\alpha(q_1 + q_2) + \left(\alpha^2 (q_1 - q_2)^2 + 4\beta^2 q_1 q_2\right)^{1/2}}{2}. \tag{26.62}$$

Thus $\rho(\mathbf{q})$ may be either jointly convex or jointly concave or neither of them depending on the constants α and β. However, when $\alpha = 0$ or, equivalently, trace$(\mathbf{V})$= 0, we obtain $\rho(\mathbf{q}) = \beta\sqrt{q_1 q_2}$, which is jointly concave. Thus, in order to prove the conjecture, it is necessary to exploit the fact that trace$(\mathbf{V}) = 0$.

26.8. Further remarks and future work

We presented necessary and sufficient conditions for the convexity of the feasible QoS region in multiuser systems with a linear antenna array at the base station. The beamforming vectors were assumed to be fixed so that power control was the only mechanism to provide desired QoS performance to the users. This immediately raises the following question: do the convexity results hold for systems in which beamforming vectors are adjusted to changing channel signatures? Here we are particularly interested in the case when beamforming vectors are optimized to maximize the right-hand side of (26.12). Note that the convexity results do not carry over to this case because of the fact that the union of convex sets is not convex in general. In contrast, the intersection of convex sets is always convex. Consequently, the infeasible SINR region under the optimal beamforming strategy would be a convex set if the conjecture discussed in Section 26.7 was true.

The convexity property of the feasible QoS region plays a fundamental role in the design of power control strategies which aims at optimizing a certain global QoS function. In some sense, such functions correspond to a QoS measure of the entire cell and can be interpreted as the utility of a network operator who is interested in the maximization of his revenue. Although there are many possibilities for choosing such a global QoS function, the most common approach is to find a power allocation $\mathbf{p}^*$ given by [8, 15, 18]:

$$\mathbf{p}^* = \begin{cases} \arg\max\limits_{\mathbf{p}\geq 0} \sum\limits_{k=1}^{K} w_k \cdot \varphi(\mathrm{SINR}_k(\mathbf{p})), & \varphi \text{ strictly increasing}, \\ \arg\min\limits_{\mathbf{p}\geq 0} \sum\limits_{k=1}^{K} w_k \cdot \varphi(\mathrm{SINR}_k(\mathbf{p})), & \varphi \text{ strictly decreasing}, \end{cases} \tag{26.63}$$

where φ is the QoS function defined by (26.10) and $w_1, \ldots, w_K > 0$ are given positive weights to prioritize the users. The weights represent the significance of the users and are usually adjusted to some system variables to achieve higher global utility or better system fairness. Indeed, if the weights were constant, the approach in (26.63) could be quite unfair in the sense that only users having the highest impact on the QoS functional are assigned power resources and all other users are kept idle. This stands in clear contrast to a "social" system where all users are treated fairly according to some price factors. In an ideal social system with no prioritization, all users are provided with the same QoS. The tradeoff between fairness and efficiency is investigated in [19, 20].

The optimization problem in (26.63) is not convex in general. However, if the inverse QoS function $\gamma, \gamma(\varphi(x)) \equiv x, x > 0$, is log-convex, there is a unique optimum and the KKT (Karush-Kuhn-Tucker) conditions are both necessary and sufficient for this optimum [9, 18]. In [21], we propose iterative algorithms that have been shown to converge to the global optimum provided that γ is a log-convex function. These algorithms require a central network controller with a global knowledge of all system parameters and variables. So, in light of distributed wireless networks, it would be important to find a distributed version of these algorithms.

Finally, it would be interesting to extend this work to other (nonlinear) receivers. Note that the results presented here do not apply to the linear minimum mean square error (MMSE) receiver. This is because the MMSE receiver depends on power allocation. References [2, 22] considered a multiple-input multiple-output uplink channel with successive decoding at the receiver and random arrivals. The authors proved the capacity and stability region as well as presented the optimal scheduling policy in the sense of achieving the largest stability region.

Acknowledgment

This work was supported by the German Ministry for Education and Research (BMBF).

Abbreviations

CDMA 1xEV-DO	Code division multiple access 1x Evolution-data only
KKT	Karush-Kuhn-Tucker
MMSE	Minimum mean square error
QAM	Quadrature amplitude modulation
QoS	Quality of service
SINR	Signal to interference-plus-noise ratio
SNR	Signal-to-noise ratio

Bibliography

[1] S. Verdu, *Multiuser Detection*, Cambridge University Press, Cambridge, UK, 1st edition, 1998.
[2] H. Boche and M. Wiczanowski, "Stability region of arrival rates and optimal scheduling for MIMO-MAC—A cross-layer approach," in *Proc. IEEE International Zurich Seminar on Communications (IZS 2004)*, pp. 18–21, Zurich, Switzerland, February 2004.
[3] R. L. Cruz and A. V. Santhanam, "Optimal routing, link scheduling and power control in multihop wireless networks," in *Proc. 22nd IEEE Conference Computer Communications (INFOCOM)*, pp. 702–711, San Francisco, Calif, USA, March/April 2003.
[4] T. ElBatt and A. Ephremides, "Joint scheduling and power control for wireless ad hoc networks," *IEEE Transactions on Wireless Communications*, vol. 3, no. 1, pp. 74–85, 2004.
[5] S. Hanly and D. Tse, "Power control and capacity of spread spectrum wireless networks," *Automatica*, vol. 35, no. 12, pp. 1987–2012, 1999.
[6] H. Boche and S. Stanczak, "Convexity of some feasible QoS regions and asymptotic behavior of the minimum total power in CDMA systems," to appear in *IEEE Trans. Commun.*, 2004.
[7] H. Boche and S. Stanczak, "Optimal QoS tradeoff and power control in CDMA systems," in *Proc. 23rd IEEE Conference on Computer Communications (INFOCOM '04)*, Hong Kong, March 2004.
[8] K. Kumaran and L. Qian, "Uplink scheduling in cdma packet-data systems," in *Proc. 22nd IEEE Conference Computer Communications (INFOCOM '03)*, vol. 1, pp. 292–300, San Francisco, Calif, USA, March/April 2003.
[9] S. Boyd and L. Vandenberghe, *Convex Optimization*, Cambridge University Press, Cambridge, UK, 2004.
[10] D. Catrein, L. Imhof, and R. Mathar, "Power control, capacity, and duality of up- and downlink in cellular CDMA systems," Tech. Rep., RWTH Aachen, Aachen University, Germany, 2003.
[11] E. Seneta, *Non-Negative Matrices and Markov Chains*, Springer, New York, NY, USA, 1981.
[12] H. Boche and S. Stanczak, "Log-convexity of the minimal feasible total power in CDMA channels," in *Proc. 14th IEEE International Symposium on Personal, Indoor and Mobile Radio Communications (PIMRC)*, Beijing, China, September 2003.
[13] H. Boche and S. Stanczak, "Iterative algorithm for finding resource allocation in symbol-asynchronous CDMA channels with different SIR requirements," in *Proc. 36th Asilomar Conference on Signals, Systems, and Computers*, Monterey, Calif, USA, November 2002.
[14] H. Boche and S. Stanczak, "Representation for the Perron root and its applications," preprint, 2004.
[15] M. J. Neely, E. Modiano, and C. E. Rohrs, "Dynamic power allocation and routing for time varying wireless networks," in *Proc. 22nd IEEE Conference Computer Communications (INFOCOM)*, pp. 745–755, San Francisco, Calif, USA, March/April 2003.
[16] D. P. Bertsekas and R. G. Gallager, *Data Networks*, Prentice Hall, Englewood Cliffs, NJ, USA, 1992.
[17] D. Tse and S. Hanly, "Linear multiuser receivers: effective interference, effective bandwidth and user capacity," *IEEE Trans. Inform. Theory*, vol. 45, no. 2, pp. 641–657, 1999.
[18] H. Boche, M. Wiczanowski, and S. Stanczak, "Characterization of optimal resource allocation in cellular networks," in *Proc. 5th IEEE Workshop on Signal Processing Advances in Wireless Communications (SPAWC 2004)*, Lisbon, Portugal, July 2004.

[19] H. Boche, M. Wiczanowski, and S. Stanczak, "Tradeoff between utility optimization and providing max-min fairness in cellular networks: The saddle point problem," preprint, 2004.
[20] S. Stanczak and H. Boche, "Information theoretic approach to the Perron root of nonnegative irreducible matrices," in *Proc. Information Theory Workshop (ITW '04)*, San Antonio, Tex, USA, October 2004.
[21] M. Wiczanowski, H. Boche, and S. Stanczak, "Characterization of optimal resource allocation in cellular networks: Optimization theoretic view and algorithmic solutions," preprint, 2004.
[22] H. Boche and M. Wiczanowski, "Optimal scheduling for high speed uplink packet access—A cross-layer approach," in *Proc. IEEE Vehicular Technology Conference (VTC Spring)*, vol. 5, pp. 2575–2579, Milan, Italy, May 2004.
[23] M. Schubert and H. Holger, "Solution of the multi-user downlink beamforming problem with individual SINR constraints," *IEEE Trans. Veh. Technol.*, vol. 53, no. 1, pp. 18–28, 2004.

Slawomir Stanczak: Fraunhofer German-Sino Lab for Mobile Communications, Einsteinufer 37, D-10587 Berlin, Germany

Email: stanczak@hhi.fhg.de

Holger Boche: Heinrich Hertz Chair for Mobile Communications, Faculty of EECS, Technical University of Berlin, Einsteinufer 25, D-10587 Berlin, Germany; Fraunhofer German-Sino Lab for Mobile Communications, Einsteinufer 37, D-10587 Berlin, Germany; Fraunhofer-Institute for Telecommunications, Heinrich-Hertz-Institut, Einsteinufer 37, D-10587 Berlin, Germany

Email: boche@hhi.fhg.de

27 Duality theory for uplink and downlink multiuser beamforming

Holger Boche and Martin Schubert

27.1. Introduction and problem statement

Beamforming has historically evolved from radar and sonar applications, where it can be used to detect and locate objects by steering the angular response of a $\lambda/2$ antenna array in any desired direction. Undesired interference can be suppressed by null steering. The processing of the array elements can be seen as sampling and filtering in the space domain [1, 2, 3, 4, 5].

This traditional view of beamforming has meanwhile been partly replaced by a broader approach, which sees beamforming within a more general framework, where one is interested in optimizing the transmission of digital information over multiple antennas, provided that channel information is available. This view is supported by information theoretical insights, which show that beamforming can be a capacity-achieving strategy [6, 7].

The theory of beamforming is relatively well understood from a user-centric point of view. That means that one user is the "desired one," and all other users act as interferers. From a network point of view, however, this assumption is not valid. Consider a cellular wireless system with an antenna array deployed at the base station and K decentralized users. Also assume that all users share the same carrier and time slot. Thus, each user is a potential interferer to all other users. This results in a competitive situation where each user tries to counteract interference by increasing its transmit power and by properly adjusting its beam pattern. Each user simultaneously acts as "desired user" and as an interferer for the rest of users. Hence, all beamformers and transmit powers should be jointly optimized.

In the following we will discuss joint optimization strategies in a single-frequency multiuser beamforming scenario, which may be limited by cochannel interference. We start by revisiting the uplink scenario, which has already been widely studied in the past decades (see, e.g., [1, 2, 3, 4, 5] and the references therein). Then, we turn our attention to the downlink, which is more difficult to handle due to its point-to-multipoint structure (as described later). Downlink beamforming recently gained more attention because of its potential of boosting

the capacity without the need of costly signal processing at the mobile station [8, 9, 10, 11, 12, 13, 14].

One main result of this chapter will be to show that multiuser beamforming for uplink and downlink are closely linked and are actually dual problems of each other. Here, the term duality is not used in a mathematical sense, but rather to emphasize that both problems can be solved by a unified approach. By solving the dual uplink problem, a solution for the downlink is obtained, and vice versa. Although the problem under consideration is highly nonlinear in nature, its special mathematical structure allows for the design of very efficient algorithms [15, 16].

From a network operator's perspective, it is desirable to support individual target QoS with optimal spectral efficiency. The QoS of a given link mainly depends on the signal-to-interference-plus-noise ratio (SINR). It can be modeled as $f(\text{SINR})$, where the function f takes into account various system aspects, like modulation, coding, pulse shaping, and so forth. For successful communication (both uplink and downlink), it is necessary to fulfill individual target SINRs $\gamma_1, \ldots, \gamma_K$, where each SINR depends on the choice of all beamformers and transmission powers (as specified later).

Thus, a straightforward strategy for joint optimization is to maximize $\min_i \text{SINR}_i/\gamma_i$. We refer to this problem as (P1), that is,

(P1) $\max(\min_{1\le i\le K} \text{SINR}_i/\gamma_i)$ under a total power constraint.

Certain targets $\gamma_1, \ldots, \gamma_K$ are feasible if and only if the optimum of (P1) is greater than or equal to one. The optimization problem (P1) therefore provides a single performance measure that reflects the quality of the corporate multiuser channel. Such a measure is required, for example, by the medium access control to decide whether spatial multiplexing is meaningful or not. In other words, (P1) measures the "spatial separability" of a given set of users.

If a set of SINR requirements is feasible, then another interesting problem formulation is as follows:

(P2) minimize the total transmission power while fulfilling $\text{SINR}_i \ge \gamma_i$ for all $i \in \{1, 2, \ldots, K\}$.

This strategy not only improves the power efficiency of the system, but also minimizes the interference to neighboring cells. Both (P1) and (P2) play an important role for a thorough understanding of multiuser beamforming and will be discussed in the following.

Note, that (P1) and (P2) have already been studied in the context of single-antenna power control (see, e.g., [17]). Despite the obvious similarities, the multiantenna case considered here has a more complicated analytical structure, which is due to the interaction between powers and beamformers. Single-antenna power control can be seen as a special case of the more general problem addressed here.

We start by showing how to jointly optimize beamformers when there is a linear mapping between the information signals and the array antennas. We refer to this case as "classical beamforming." Then, it is shown how the system performance can be further improved by nonlinear interference cancellation and precoding. Such a strategy is spectrally efficient and decouples the users to a degree

that the system is no longer interference-limited. This has an interesting relation to problems in information theory.

Finally, we investigate the interaction of beamforming with the resource allocation. That is, how the power resource should be allocated according to different utility functions. The tradeoff between throughput maximization and fairness will be discussed.

27.2. Classical beamforming

Partial results on joint beamforming and power control already appeared in [8, 10, 11, 12, 13, 14, 18, 19], mainly in a downlink context. An overview is also given in [9]. The different strategies can be classified as follows.

(i) Problem (P1) was studied and solved in [20] for fixed beamformers, which reduces the problem to pure power control.

(ii) Problem (P1) was also studied in [11, 12, 18, 19] without power constraints (neglecting noise and assuming interference-limitedness). An iterative strategy based on eigenvalue optimization was proposed in [12]. This work has been extended by [18], where global convergence was proved. An alternative strategy based on ℓ_1-norm optimization was proposed in [11]. Both strategies are compared within a unified theoretical framework in [19], where it was shown that the ℓ_1-norm approach is in general suboptimal.

(iii) Problem (P2) was studied in [10, 13, 14]. In [10] a heuristic strategy was proposed. In [13, 14] an iterative solution based on "virtual uplink powers" was derived. This result already indicates that there is an interesting duality between uplink and downlink multiuser channels (this will be specified and further exploited later in this chapter). The disadvantage of this iterative strategy is that the aspect of feasibility is neglected. Algorithms designed under the assumption that a solution exists may yield unpredictable results in case that the SINR constraints are infeasible. A more integral strategy, that accounts for the aspect of feasibility, will be discussed in Section 27.2.7.

(iv) A conceptually different approach to (P2) appeared in [8, 9], where it was proposed to embed the beamforming problem in a semidefinite optimization program. Thus, recently developed semidefinite programming techniques can be applied, and are able to handle infeasible scenarios. However, the optimization is performed over matrices with more degrees of freedom than the original beamforming vectors. Hence, the solution comes at the cost of relatively high computational complexity. This approach will not be discussed here.

27.2.1. Downlink transmit beamforming

Consider K independent signals $s_1, s_2, \ldots, s_K$ with zero mean and power allocation $\mathbf{p} = [p_1, \ldots, p_K]^T$. The signals are jointly transmitted from an M-element antenna array to K decentralized receivers, as depicted in Figure 27.1. Since the transmitter is assumed to have channel knowledge, it can adapt its transmit strategy to the spatial structure of the propagation channel. The spatial signatures (complex,

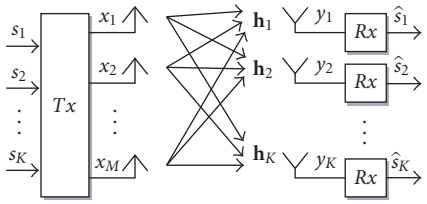

FIGURE 27.1. Downlink broadcast channel with cooperative transmit antennas and noncooperative receivers.

vector-valued path attenuations) of all K users are denoted by $\mathbf{h}_1, \mathbf{h}_2, \ldots, \mathbf{h}_K$. Each receiver performs single-user detection, thus most of the processing complexity resides at the transmitter. Note that the model under consideration can be seen as a multiple-input multiple-output (MIMO) channel with partial antenna cooperation.

Channel knowledge at the transmit side can be obtained either by estimating the channels at the receiver and feeding back the information via a separate channel, or by transferring the estimated uplink channel to the downlink. Both strategies have limitations, which are discussed, for example, in [9].

For fast fading channels, the assumption of perfect channel knowledge is somewhat unrealistic. Thus, the channel signatures are often considered as stochastic quantities, and beamforming is performed based on the spatial covariance matrices

$$\mathbf{R}_i = \mathrm{E}\left[\mathbf{h}_i(t)\mathbf{h}_i^*(t)\right], \quad 1 \le i \le K, \tag{27.1}$$

where the operator $\mathrm{E}\{\cdot\}$ denotes the ensemble average over the time-fluctuating fading channel.

Note, that the representation (27.1) can be used in the following to incorporate both cases: stochastic and deterministic channel knowledge. Coherent spatial processing is possible if $\mathrm{rank}\{\mathbf{R}_i\} = 1$. This corresponds to the deterministic case and is fulfilled, for example, when the channel does not change within the observation window. If the channel is rapidly time-variant and the total number of transmission paths per user exceeds the number of antenna elements, then $\mathbf{R}_i$ has full rank. This assumption will be required later when we study beamforming in the absence of noise.

One simple way to perform preprocessing at the transmitter is to map the data streams on the M transmit antennas by using a matrix $\mathbf{U} \in \mathbb{C}^{M\times K}$. The ith data stream is spread over the antenna array by the ith column of

$$\mathbf{U} = \left[\mathbf{u}_1, \ldots, \mathbf{u}_K\right] \in \mathbb{C}^M, \tag{27.2}$$

which is constrained as follows:

$$\left\|\mathbf{u}_i\right\|_2 = 1, \quad 1 \le i \le K. \tag{27.3}$$

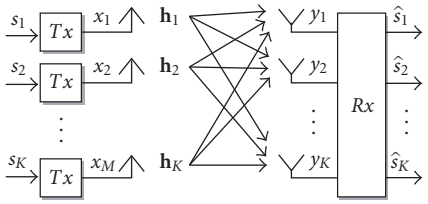

FIGURE 27.2. Uplink multiple access channel with noncooperative transmitters and cooperative receive antennas.

The resulting SINR measured at the antenna output of the ith receiver is

$$\mathrm{SINR}_i^{\mathrm{DL}}(\mathbf{U},\mathbf{p}) = \frac{p_i \mathbf{u}_i^* \mathbf{R}_i \mathbf{u}_i}{\sum_{\substack{k=1 \\ k\neq i}}^{K} p_k \mathbf{u}_k^* \mathbf{R}_i \mathbf{u}_k + \sigma_i^2}, \quad 1 \le i \le K, \tag{27.4}$$

where σ_i^2 is the variance of the additive white Gaussian noise. The superscript "DL" stands for downlink.

It can be observed from (27.4) that the users are coupled by interference, which not only depends on the transmit powers, but also on the choice of *all* beamformers $\mathbf{u}_1, \ldots, \mathbf{u}_K$, which therefore cannot be optimized independently, not even for a fixed power allocation. This makes the downlink channel more difficult to handle than its uplink counterpart, which will be introduced next.

27.2.2. Uplink receive beamforming

Consider the uplink scenario depicted in Figure 27.2. The antenna array acts as a receiver for the K independent data streams transmitted from the decentralized mobile units. The transmit power allocation is $\mathbf{q} = [q_1, \ldots, q_K]^T$. The same beamforming matrix $\mathbf{U} = [\mathbf{u}_1, \ldots, \mathbf{u}_K]$ that has been used for downlink transmission is now used for reception. We also assume reciprocity of the propagation channel, that is, downlink and uplink are both characterized by $\mathbf{R}_1, \ldots, \mathbf{R}_K$. Then, the uplink SINR is given by

$$\mathrm{SINR}_i^{\mathrm{UL}}(\mathbf{u}_i,\mathbf{q}) = \frac{q_i \mathbf{u}_i^* \mathbf{R}_i \mathbf{u}_i}{\mathbf{u}_i^* \left(\sum_{\substack{k=1 \\ k\neq i}}^{K} q_k \mathbf{R}_k + \sigma_i^2 \mathbf{I} \right) \mathbf{u}_i}, \quad 1 \le i \le K. \tag{27.5}$$

As for the downlink channel, the uplink SINR (27.5) are coupled by the transmit powers $\mathbf{q}$. The crucial difference is that the interference coupling no longer depends on the beamformers but on the channel signatures $\mathbf{h}_1, \ldots, \mathbf{h}_K$. That is, for a fixed power allocation $\mathbf{q}$, the beamformers can be found by independently maximizing the expressions (27.5). The optimal beamformer of the ith user is given as

the principal generalized eigenvector of the matrix pair $(\mathbf{R}_i, \mathbf{Z}_i)$, where

$$\mathbf{Z}_i = \sum_{\substack{k=1 \\ k \neq i}}^{K} q_k \mathbf{R}_k + \sigma_i^2 \mathbf{I} \tag{27.6}$$

is the interference-plus-noise spatial covariance matrix (see, e.g., [3]).

Due to this special structure, the uplink is easier to handle than the downlink. However, the users are still coupled by the power allocation and a joint approach is required for optimization. Thus, the coupling between the users will be studied in more detail in the following section.

27.2.3. SINR feasibility

An important question is which SINR levels can be simultaneously achieved? This problem was already studied by Zander in [21, 22] in the context of power control, and in [23] in the general context of QoS tradeoff regions (see also Chapter 26).

To answer this question, assume that the link gains between all possible transmitter/receiver pairs are collected in a $K \times K$ matrix

$$\big[\boldsymbol{\Psi}(\mathbf{U})\big]_{ik} \begin{cases} \mathbf{u}_k^* \mathbf{R}_i \mathbf{u}_k, & k \neq i, \\ 0, & k = i. \end{cases} \tag{27.7}$$

Assume that some (fixed) beamforming matrix $\hat{\mathbf{U}}$ is given, and let $\hat{\boldsymbol{\Psi}} := \boldsymbol{\Psi}(\hat{\mathbf{U}})$ for short. The vector $\hat{\boldsymbol{\Psi}}\mathbf{p}$ contains the interference levels experienced by all K downlink users and $\hat{\boldsymbol{\Psi}}^T\mathbf{q}$ the interference of the uplink users. By properly choosing the transmit powers, all SINRs can be jointly controlled. The relationship between power allocations $\mathbf{p}$, $\mathbf{q}$, and SINR values $\gamma_1, \ldots, \gamma_K$ is described by (27.4) and (27.5). Using matrix notation, these sets of equations can be rewritten as

$$\hat{\boldsymbol{\Psi}}\mathbf{p} + \boldsymbol{\sigma} = \mathbf{D}^{-1}\mathbf{p} \quad \text{(downlink)}, \tag{27.8}$$

$$\hat{\boldsymbol{\Psi}}^T\mathbf{q} + \boldsymbol{\sigma} = \mathbf{D}^{-1}\mathbf{q} \quad \text{(uplink)}, \tag{27.9}$$

where $\boldsymbol{\sigma} = [\sigma_1^2, \ldots, \sigma_K^2]^T$ and

$$\mathbf{D} = \operatorname{diag}\left\{ \frac{\gamma_1}{\mathbf{u}_1^* \mathbf{R}_1 \mathbf{u}_1}, \ldots, \frac{\gamma_K}{\mathbf{u}_K^* \mathbf{R}_K \mathbf{u}_K} \right\}. \tag{27.10}$$

The vector on the left-hand side of (27.8) and (27.9) contains the interference-plus-noise powers. While the downlink users are coupled by $\hat{\boldsymbol{\Psi}}$, the uplink users are coupled by $\hat{\boldsymbol{\Psi}}^T$, thus both channels are a transpose of each other.

A set of SINRs $\gamma_1, \ldots, \gamma_K$ is feasible whenever there exists a positive power allocation such that (27.8) (resp., (27.9)) is fulfilled. The following result can be shown [24, 22].

Proposition 27.1. *Targets $\gamma_1, \ldots, \gamma_K$ are jointly feasible in uplink and downlink if and only if the spectral radius ρ of the weighted coupling matrix satisfies*

$$\rho(\mathbf{D}\hat{\boldsymbol{\Psi}}) < 1. \tag{27.11}$$

Note, that $\rho(\mathbf{D}\hat{\boldsymbol{\Psi}}) = \rho(\mathbf{D}\hat{\boldsymbol{\Psi}}^T)$. Thus, target SINRs $\gamma_1, \ldots, \gamma_K$ are feasible in the uplink if and only if the same targets are feasible in the downlink. The following power allocations achieve the targets with minimal total power:

$$\hat{\mathbf{p}} = \left(\mathbf{D}^{-1} - \hat{\boldsymbol{\Psi}}\right)^{-1}\boldsymbol{\sigma} \quad \text{(downlink)}, \tag{27.12}$$

$$\hat{\mathbf{q}} = \left(\mathbf{D}^{-1} - \hat{\boldsymbol{\Psi}}^T\right)^{-1}\boldsymbol{\sigma} \quad \text{(uplink)}. \tag{27.13}$$

The vectors $\hat{\mathbf{p}}$ and $\hat{\mathbf{q}}$ are guaranteed to be strictly positive as long as (27.11) is fulfilled. Otherwise, at least one component of the power vector will be negative or zero.

27.2.4. Sum-power-constrained SINR region

So far we have established a duality between uplink and downlink beamforming in terms of feasible SINR. Possible constraints on the powers have been neglected.

In [15, 16, 25, 26] it was independently shown that a similar result holds when the total power is limited by $P_{\max}$. Suppose that $\rho(\mathbf{D}\hat{\boldsymbol{\Psi}}) < 1$ is fulfilled, that is, the targets can be achieved in downlink and uplink by power allocations (27.12) and (27.13), respectively. Let $\boldsymbol{\sigma} = \sigma^2\mathbf{1}_K$ be a noise power vector with equal components, and $\mathbf{1}_K$ denotes the all-one vector. Then, the total required uplink power $\|\hat{\mathbf{q}}\|_1$ is the same as the downlink power $\|\hat{\mathbf{p}}\|_1$. This result follows immediately from the following relation:

$$\begin{aligned} ||\hat{\mathbf{q}}||_1 &= \mathbf{1}_K^T\hat{\mathbf{q}} = \sigma^2\mathbf{1}_K^T\left(\left(\mathbf{D}^{-1} - \hat{\boldsymbol{\Psi}}\right)^{-1}\right)^T\mathbf{1}_K \\ &= \sigma^2\mathbf{1}_K^T\left(\mathbf{D}^{-1} - \hat{\boldsymbol{\Psi}}\right)^{-1}\mathbf{1}_K = \mathbf{1}_K^T\hat{\mathbf{p}} = ||\hat{\mathbf{p}}||_1. \end{aligned} \tag{27.14}$$

Hence the following proposition.

Proposition 27.2. *Both uplink and downlink have the same SINR feasible region under a sum-power constraint, that is, target SINRs are feasible in the downlink if and only if the same targets are feasible in the uplink.*

Note, that this duality holds under the assumption of reciprocal propagation channels and equal noise powers. An analysis of the unequal case can be found in [24].

With Proposition 27.2 it is possible to focus on the uplink. All the results can be transferred to the downlink. The feasibility issue is closely linked with the

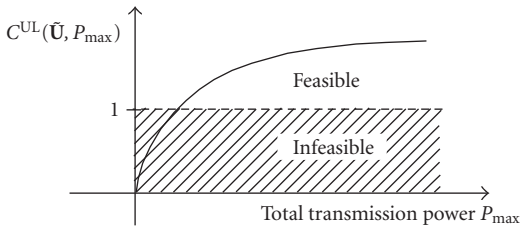

FIGURE 27.3. Balanced SINR margin $C^{\mathrm{UL}}(\tilde{\mathbf{U}}, P_{\max})$ versus total transmission power $P_{\max}$.

problem of finding a power allocation $\mathbf{q}$ with total power $\|\mathbf{q}\|_1 \leq P_{\max}$ that fulfills $1 \leq \min_i \mathrm{SINR}_i^{\mathrm{UL}}/\gamma_i$. This leads to the following problem formulation:

$$C^{\mathrm{UL}}(\hat{\mathbf{U}}, P_{\max}) = \max_{\mathbf{q}} \min_{1\leq i\leq K} \frac{\mathrm{SINR}_i^{\mathrm{UL}}(\hat{\mathbf{u}}_i, \mathbf{q})}{\gamma_i} \quad \text{subject to } \|\mathbf{q}\|_1 \leq P_{\max},\ \mathbf{q} \in \mathbb{R}_+^K. \tag{27.15}$$

Some important observations can be made.

(1) Target SINRs $\gamma_1, \ldots, \gamma_K$ are feasible if and only if $C^{\mathrm{UL}}(\hat{\mathbf{U}}, P_{\max}) > 1$. Then $\mathrm{SINR}_i^{\mathrm{UL}}/\gamma_i > 1$ for all $i \in \{1, 2, \ldots, K\}$.

(2) The function $C^{\mathrm{UL}}(\hat{\mathbf{U}}, P_{\max})$ is strictly monotonically increasing in $P_{\max}$, as illustrated in Figure 27.3. Thus, there is a one-to-one relationship between each balanced SINR margin and the total transmission power.

(3) The optimum of (27.15) is balanced and the inequality constraint is fulfilled with equality. Any optimizer $\tilde{\mathbf{q}}$ fulfills the following equations:

$$C^{\mathrm{UL}}(\hat{\mathbf{U}}, P_{\max}) = \frac{\mathrm{SINR}_i^{\mathrm{UL}}(\hat{\mathbf{u}}_i, \tilde{\mathbf{q}})}{\gamma_i}, \quad 1 \leq i \leq K, \qquad P_{\max} = \|\tilde{\mathbf{q}}\|_1. \tag{27.16}$$

For a given total power $P_{\max}$, there is a unique optimizer $\tilde{\mathbf{q}}$ which is characterized by (27.16), which can be rewritten in matrix notation as an eigensystem

$$\boldsymbol{\Lambda}(\tilde{\mathbf{U}}, P_{\max}) \begin{bmatrix} \tilde{\mathbf{q}} \\ 1 \end{bmatrix} = \frac{1}{C^{\mathrm{UL}}(\tilde{\mathbf{U}}, P_{\max})} \begin{bmatrix} \tilde{\mathbf{q}} \\ 1 \end{bmatrix}, \tag{27.17}$$

where $\boldsymbol{\Lambda}$ is the extended uplink coupling matrix

$$\boldsymbol{\Lambda}(\mathbf{U}, P_{\max}) = \begin{bmatrix} \mathbf{D}\boldsymbol{\Psi}^T(\mathbf{U}) & \mathbf{D}\boldsymbol{\sigma} \\ \dfrac{1}{P_{\max}} \mathbf{1}_K^T \mathbf{D}\boldsymbol{\Psi}^T(\mathbf{U}) & \dfrac{1}{P_{\max}} \mathbf{1}_K^T \mathbf{D}\boldsymbol{\sigma} \end{bmatrix}. \tag{27.18}$$

Thus, the balanced level $C^{\mathrm{UL}}(\tilde{\mathbf{U}}, P_{\max})$ is a reciprocal eigenvalue of the nonnegative extended coupling matrix $\boldsymbol{\Lambda}$.

However, not all eigenvalues represent physically meaningful balanced levels. In particular, $\mathbf{q} \in \mathbb{R}_+^K$ and $C^{\mathrm{UL}}(\tilde{\mathbf{U}}, P_{\max}) \in \mathbb{R}_+$ must be fulfilled. It is known (see, e.g., [27]) that for any nonnegative square matrix $\mathbf{B} \geq 0$ with spectral radius $\rho(\mathbf{B})$, there exists a vector $\mathbf{q}^{(B)} \geq 0$ and $\lambda^{(B)} = \rho(\mathbf{B})$ such that $\mathbf{B}\mathbf{q}^{(B)} = \lambda^{(B)}\mathbf{q}$. Thus, the nonnegative eigenvector associated with the maximal eigenvalue (equal to the spectral radius) is associated with a valid solution. If the matrix $\boldsymbol{\Lambda}$ is irreducible, then it follows from the Perron/Frobenius theorem [27] that this solution is the only valid solution. All eigenvectors associated with other eigenvalues have at least one negative component.

Note, that for the special problem under consideration, it is even not necessary to invoke the assumption of irreducibility. Due to the special structure of the extended coupling matrix $\boldsymbol{\Lambda}$, it can be shown that only the maximum eigenvalue is associated with a valid solution [20]. This follows from the monotonicity of $C^{\mathrm{UL}}(\tilde{\mathbf{U}}, P_{\max})$, which can be used to rule out the existence of two different balanced levels with the same total power.

Hence, the solution of the SINR balancing problem (27.15) is given by

$$C^{\mathrm{UL}}(\hat{\mathbf{U}}, P_{\max}) = \frac{1}{\rho(\boldsymbol{\Lambda}(\hat{\mathbf{U}}, P_{\max}))}. \tag{27.19}$$

The power allocation which balances the relative SINRs at the level (27.19) is obtained as the first K components of the principal eigenvector of $\boldsymbol{\Lambda}(\hat{\mathbf{U}}, P_{\max})$, scaled such that its last component equals one. The optimally balanced uplink SINR margin is associated with the spectral radius $\rho(\boldsymbol{\Lambda}(\hat{\mathbf{U}}, P_{\max}))$. Clearly, $\rho(\boldsymbol{\Lambda}(\hat{\mathbf{U}}, P_{\max})) \leq 1$ must be fulfilled, otherwise the targets $\gamma_1, \ldots, \gamma_K$ are not feasible.

The same argumentation can be used for the downlink, where the users are coupled by an extended coupling matrix

$$\boldsymbol{\Upsilon}(\mathbf{U}, P_{\max}) = \begin{bmatrix} \mathbf{D}\boldsymbol{\Psi}(\mathbf{U}) & \mathbf{D}\boldsymbol{\sigma} \\ \dfrac{1}{P_{\max}}\mathbf{1}_K^T\mathbf{D}\boldsymbol{\Psi}(\mathbf{U}) & \dfrac{1}{P_{\max}}\mathbf{1}_K^T\mathbf{D}\boldsymbol{\sigma} \end{bmatrix}. \tag{27.20}$$

In analogy to the uplink, it can be shown that $\gamma_1, \ldots, \gamma_K$ are feasible if and only if $\rho(\boldsymbol{\Upsilon}(\hat{\mathbf{U}}, P_{\max})) \leq 1$. The optimal power allocation which balances the relative SINRs is given as the first K components of the principal eigenvector of $\boldsymbol{\Upsilon}(\hat{\mathbf{U}}, P_{\max})$.

From Proposition 27.2 (duality), we know that uplink and downlink have the same SINR achievable regions, thus $\rho(\boldsymbol{\Lambda}(\hat{\mathbf{U}}, P_{\max})) = \rho(\boldsymbol{\Upsilon}(\hat{\mathbf{U}}, P_{\max}))$. Hence the following proposition, which provides a measure for the feasibility of target SINRs under a sum-power constraint.

Proposition 27.3. *Targets $\gamma_1, \ldots, \gamma_K$ are jointly feasible in uplink and downlink under a sum-power constraint $P_{\max}$ if and only if the spectral radius ρ of the extended coupling matrix satisfies*

$$\rho(\boldsymbol{\Lambda}(\hat{\mathbf{U}}, P_{\max})) \leq 1. \tag{27.21}$$

27.2.5. Max-min SIR downlink beamforming

In the previous sections we have studied the feasible SINR values under the assumption of fixed beamformers. The choice of the beamformers, however, depends on the power allocation. On the other hand, power allocation depends on beamforming, thus a joint optimization approach is required.

We start by studying the effect of interference balancing in the absence of noise, which brings out clearly the analytical structure of the underlying problem. This is the first step towards finding the more general solution of power-constrained SINR balancing, which will be studied in Section 27.2.6.

For given channel covariance matrices $\mathbf{R}_1, \ldots, \mathbf{R}_K$, one is interested in the beamforming matrix $\mathbf{U}$ and power allocation $\mathbf{p}$, which jointly balance the values $\mathrm{SIR}_i^{\mathrm{DL}}/\gamma_i$, $1 \le i \le K$, as high as possible. Each SIR is a function of $\mathbf{p}$ and $\mathbf{U}$, that is,

$$\mathrm{SIR}_i^{\mathrm{DL}}(\mathbf{p}, \mathbf{U}) = \frac{p_i \mathbf{u}_i^* \mathbf{R}_i \mathbf{u}_i}{\sum_{\substack{k=1 \\ k \neq i}}^{K} p_k \mathbf{u}_k^* \mathbf{R}_i \mathbf{u}_k}, \quad 1 \le i \le K. \tag{27.22}$$

This problem can be expressed mathematically as

$$B_{\mathrm{Inf}}^{\mathrm{DL}} = \max_{\mathbf{U},\mathbf{p}} \left(\min_{1 \le i \le K} \frac{\mathrm{SIR}_i^{\mathrm{DL}}(\mathbf{U}, \mathbf{p})}{\gamma_i} \right) \quad \text{subject to } \|\mathbf{u}_i\|_2 = 1,\ 1 \le i \le K, \quad \|\mathbf{p}\|_1 = 1. \tag{27.23}$$

In the absence of noise, we have to assume that $\boldsymbol{\Psi}$ is irreducible [27]. Roughly speaking, this means that all users are coupled by interference. Then the optimum $B_{\mathrm{Inf}}^{\mathrm{DL}}$ exists.

One example for which this is always fulfilled is the case where positive semidefinite covariance matrices $\mathbf{R}_i$ have full rank K, that is, $\mathbf{u}_i^* \mathbf{R}_k \mathbf{u}_k \neq 0$. Then, the optimum is characterized by balanced relative SIR levels. The max-min operations are interchangeable and one can equivalently balance the reciprocal quantities $\gamma_i / \mathrm{SIR}_i^{\mathrm{DL}}$. Hence, problem (27.23) is solved by minimizing the ℓ_∞-norm of the vector

$$\boldsymbol{\xi}(\mathbf{U}, \mathbf{p}) = \left[\frac{\gamma_1}{\mathrm{SIR}_1^{\mathrm{DL}}(\mathbf{U}, \mathbf{p})}, \ldots, \frac{\gamma_K}{\mathrm{SIR}_K^{\mathrm{DL}}(\mathbf{U}, \mathbf{p})} \right]^T. \tag{27.24}$$

By optimizing over both $\mathbf{U}$ and $\mathbf{p}$, the optimally balanced level $B_{\mathrm{Inf}}^{\mathrm{DL}}$ is found:

$$\frac{1}{B_{\mathrm{Inf}}^{\mathrm{DL}}} = \min_{\mathbf{U},\mathbf{p}} \|\boldsymbol{\xi}(\mathbf{U}, \mathbf{p})\|_\infty. \tag{27.25}$$

Assuming that all users are coupled by interference, the optimum of (27.25) will be balanced, that is, all components of $\boldsymbol{\xi}$ are the same. Using similar arguments as in Section 27.2.4, it can be shown, that the balanced optimum can be expressed by an eigensystem and $B_{\mathrm{Inf}}^{\mathrm{DL}}$ is given by the inverse eigenvalue of the coupling matrix

$\mathbf{D\Psi}(\mathbf{U}^{\text{opt}})$, where $\mathbf{U}^{\text{opt}}$ is an optimizer of (27.23). Thereby, it can be shown [11, 12] that problem (27.25) is equivalent to an eigenvalue optimization problem

$$B_{\text{Inf}}^{\text{DL}} = \frac{1}{\min_{\mathbf{U}} \rho\big(\mathbf{D\Psi}(\mathbf{U})\big)} \quad \text{subject to } \big|\big|\mathbf{u}_i\big|\big|_2 = 1,\ 1 \le i \le K. \tag{27.26}$$

Note, that this problem no longer depends on $\mathbf{p}$. Once an optimizer $\mathbf{U}^{\text{opt}}$ is found, the associated $\mathbf{p}^{\text{opt}}$ is given as the dominant right-hand eigenvector of the matrix $\mathbf{D\Psi}(\mathbf{U}^{\text{opt}})$.

The coupling matrix $\mathbf{\Psi}$ is generally nonsymmetric, thus (27.26) is a nonconvex optimization problem. Nevertheless, very efficient algorithms have been devised which solve the problem iteratively [12, 18, 19]. They are based on the duality that has been established in Section 27.2.3. That is, the optimizer $\mathbf{U}^{\text{opt}}$ is equivalently found by minimizing the spectral radius $\rho(\mathbf{D\Psi}^T(\mathbf{U}))$, which is associated with the dual uplink channel.

In the following we exploit that the maximal eigenvalue of any nonnegative irreducible matrix $\mathbf{B}$ can be expressed as [28]

$$\rho(\mathbf{B}) = \max_{\mathbf{x}>0} \min_{\mathbf{y}>0} \frac{\mathbf{x}^T\mathbf{B}\mathbf{y}}{\mathbf{x}^T\mathbf{y}} = \min_{\mathbf{x}>0} \max_{\mathbf{y}>0} \frac{\mathbf{x}^T\mathbf{B}\mathbf{y}}{\mathbf{x}^T\mathbf{y}}. \tag{27.27}$$

This characterization will turn out very useful for the development of algorithmic solutions for eigenvalue optimization problems of the form (27.26). In particular, the eigenvalue minimization problem (27.26) can be rewritten as

$$\frac{1}{B_{\text{Inf}}^{\text{UL}}} = \min_{\mathbf{U}:\|\mathbf{u}_i\|_2=1} \min_{\mathbf{q}>0} \hat{f}(\mathbf{U},\mathbf{q}) \quad \text{with } \hat{f}(\mathbf{U},\mathbf{q}) = \max_{\mathbf{x}>0} \frac{\mathbf{x}^T\mathbf{D\Psi}^T(\mathbf{U})\mathbf{q}}{\mathbf{x}^T\mathbf{q}}. \tag{27.28}$$

Here, $\mathbf{x}$ is an auxiliary variable which has no physical meaning. The vector $\mathbf{q}$ can be interpreted as the uplink power vector. Even though problem (27.28) depends on more variables than the original eigenvalue optimization problem (27.22), it will turn out to prove useful for developing an algorithmic solution. We start with the following observations.

(1) For a fixed beamforming matrix $\hat{\mathbf{U}}$ the objective function $\hat{f}(\hat{\mathbf{U}},\mathbf{q})$ is minimized by the dominant eigenvector of $\mathbf{D\Psi}^T(\hat{\mathbf{U}})$.

(2) For a fixed power allocation $\tilde{\mathbf{q}}$ the objective function $\hat{f}(\mathbf{U},\tilde{\mathbf{q}})$ is minimized by $\tilde{\mathbf{U}} = [\tilde{\mathbf{u}}_1,\ldots,\tilde{\mathbf{u}}_K]$, where $\tilde{\mathbf{u}}_i$ is the dominant eigenvector which solves the generalized eigenproblem

$$\mathbf{R}_i\mathbf{u}_i = \lambda_{\max} \cdot \mathbf{Q}_i(\tilde{\mathbf{q}})\mathbf{u}_i \quad \text{with } \mathbf{Q}_i(\mathbf{q}) = \sum_{\substack{k=1 \\ k\neq i}}^{K} [\mathbf{q}]_k \mathbf{R}_k. \tag{27.29}$$

These properties together with the characterization (27.27) can be used to prove the following necessary and sufficient condition for optimality [18].

(1) $n := 0$
(2) $\mathbf{q}^{(0)} := [1, \ldots, 1]^T$
(3) $\rho(0) := 0$
(4) *repeat*
(5) $\quad n := n + 1$
(6) $\quad \mathbf{u}_i^{(n)} := \arg\max_{\mathbf{u}_i} \dfrac{\mathbf{u}_i^* \mathbf{R}_i \mathbf{u}_i}{\mathbf{u}_i^* \mathbf{Q}_i(\mathbf{q}^{(n-1)})\mathbf{u}_i}$, subject to $\|\mathbf{u}_i\|_2 = 1$, $1 \le i \le K$
(7) $\quad (\rho(n), \mathbf{q}^{(n)})$ is solution of $\mathbf{D}\boldsymbol{\Psi}^T(\mathbf{U}^{(n)}) \cdot \mathbf{q}^{(n)} = \rho(n) \cdot \mathbf{q}^{(n)}$
(8) *until* $|\rho(n) - \rho(n-1)| \le \epsilon$

Algorithm 27.1. Solution of the eigenvalue minimization problem (27.26).

Proposition 27.4. *A beamforming matrix* $\bar{\mathbf{U}}$ *solves the eigenvalue minimization problem* (27.26) *if and only if for all* $\mathbf{x} > 0$

$$\frac{\mathbf{x}^T \mathbf{D}\boldsymbol{\Psi}^T(\bar{\mathbf{U}})\bar{\mathbf{q}}}{\mathbf{x}^T \bar{\mathbf{q}}} = \min_{\mathbf{U}} \frac{\mathbf{x}^T \mathbf{D}\boldsymbol{\Psi}^T(\mathbf{U})\bar{\mathbf{q}}}{\mathbf{x}^T \bar{\mathbf{q}}}, \tag{27.30}$$

where $\bar{\mathbf{q}}$ *fulfills*

$$\mathbf{D}\boldsymbol{\Psi}^T(\bar{\mathbf{U}}) \cdot \bar{\mathbf{q}} = \rho(\mathbf{D}\boldsymbol{\Psi}^T(\bar{\mathbf{U}})) \cdot \bar{\mathbf{q}}. \tag{27.31}$$

This motivates an alternating optimization scheme that keeps one of the variables $\mathbf{U}$ and $\mathbf{q}$ fixed while minimizing with respect to the other. The iteration is stopped as soon as the conditions (27.30) and (27.31) are jointly fulfilled, that is, if the optimization does not yield any further improvement. The algorithm is summarized in Algorithm 27.1.

It should be noted that the method of alternating variables in general is known to approach the optimum very slowly and may even get stuck. The above algorithm, however, exploits the analytical structure of the given problem and therefore rapidly converges towards the global optimum of the eigenvalue minimization problem. Monotonicity and convergence are proved in [18]. Typically, only a few iterations are required to approach the global optimum with very good accuracy.

The beamformers obtained by the algorithm solve the joint beamforming problem (27.23), as well as the corresponding problem formulation for the uplink. The optimal downlink power vector solving (27.23) is the principal eigenvector of the coupling matrix $\mathbf{D}\boldsymbol{\Psi}(\mathbf{U}^{\text{opt}})$. The optimal uplink power vector is the principal eigenvector of the coupling matrix $\mathbf{D}\boldsymbol{\Psi}^T(\mathbf{U}^{\text{opt}})$.

27.2.6. Joint beamforming under a sum-power constraint

Next, the results are extended to the case where each receiver has a certain noise level and a sum-power constraint is imposed. The goal is to achieve SINR thresholds $\gamma_1, \ldots, \gamma_K$ by jointly optimizing over all beamforming vectors and transmission powers. In the downlink, the target SINRs are feasible if and only if

$C_{\text{opt}}^{\text{DL}}(P_{\max}) > 1$, where

$$\begin{aligned} C_{\text{opt}}^{\text{DL}}(P_{\max}) = \max_{\mathbf{U},\mathbf{p}} \min_{1\le i\le K} & \frac{\text{SINR}_i^{\text{DL}}(\mathbf{U},\mathbf{p})}{\gamma_i} \\ \text{subject to } & \|\mathbf{p}\|_1 \le P_{\max}, \\ & \left\|\mathbf{u}_i\right\|_2 = 1,\ 1 \le i \le K. \end{aligned} \tag{27.32}$$

The achievable margin $C_{\text{opt}}^{\text{DL}}(P_{\max})$ provides a single performance measure for the quality of the composite multiuser channel. Each beamforming solution obtained by (27.32) is optimal in the sense that no other beamforming algorithm can achieve a balanced level larger than $C_{\text{opt}}^{\text{DL}}(P_{\max})$ under the same power constraint. Since $C_{\text{opt}}^{\text{DL}}(P_{\max})$ is monotonically increasing in $P_{\max}$, the SINR levels $\text{SINR}_i^{\text{DL}} = C_{\text{opt}}^{\text{DL}}(P_{\max})\gamma_i$ are achieved with minimal transmission power.

The same optimization problem can be formulated for the uplink:

$$\begin{aligned} C_{\text{opt}}^{\text{UL}}(P_{\max}) = \max_{\mathbf{U},\mathbf{q}} \min_{1\le i\le K} & \frac{\text{SINR}_i^{\text{UL}}(\mathbf{u}_i,\mathbf{q})}{\gamma_i} \\ \text{subject to } & \|\mathbf{q}\|_1 \le P_{\max}, \\ & \|\mathbf{u}_i\|_2 = 1,\ 1 \le i \le K. \end{aligned} \tag{27.33}$$

From the duality discussed in Section 27.2.4, we know that problems (27.32) and (27.33) have the same optimum $C_{\text{opt}}^{\text{DL}}(P_{\max}) = C_{\text{opt}}^{\text{UL}}(P_{\max})$. Moreover, the optimum is achieved by the same beamforming matrix $\mathbf{U}^{\text{opt}}$. Thus, it is sufficient to focus on the uplink problem (27.33), which has a more convenient structure, as will be shown in the following. Once, the optimizer $\mathbf{U}^{\text{opt}}$ has been found, the optimal power allocations for downlink and uplink are given by (27.12) and (27.13), respectively.

Problem (27.33) can be solved in a similar way as the SIR balancing problem studied in Section 27.2.5. First, it can be shown [15] that the problem is equivalent to an eigenvalue optimization problem

$$C_{\text{opt}}^{\text{UL}}(P_{\max}) = \frac{1}{\min_{\mathbf{U}} \rho(\boldsymbol{\Lambda}(\mathbf{U},P_{\max}))}, \tag{27.34}$$

where the extended coupling matrix $\boldsymbol{\Lambda}$ has been defined in (27.18). Like the SIR balancing problem in the absence of noise, the joint SINR balancing problem can be transformed into an equivalent problem, which no longer depends on the transmit powers.

To solve this nonconvex problem, we again make use of the characterization (27.27). By introducing a function

$$\hat{\lambda}(\mathbf{U},\mathbf{y}) = \max_{\mathbf{x}>0} \frac{\mathbf{x}^T\boldsymbol{\Lambda}(\mathbf{U},P_{\max})\mathbf{y}}{\mathbf{x}^T\mathbf{y}}, \tag{27.35}$$

problem (27.34) can be rewritten as

$$C_{\text{opt}}^{\text{DL}}(P_{\max}) = \frac{1}{\min_{\mathbf{U}} \min_{\mathbf{q}_{\text{ext}}>0} \widehat{\lambda}(\mathbf{U}, \mathbf{q}_{\text{ext}})}. \tag{27.36}$$

Here, $\mathbf{q}_{\text{ext}} = \left[\begin{smallmatrix}\mathbf{q}\\ 1\end{smallmatrix}\right]$ is the extended uplink power vector, as introduced in (27.17), whereas the $(K+1)$-dimensional vector $\mathbf{x} > 0$ has no physical meaning. The global optimum is found by minimizing the cost function $\widehat{\lambda}(\mathbf{U}, \mathbf{q}_{\text{ext}})$ over all $\mathbf{U}$ and $\mathbf{q}_{\text{ext}} > 0$.

At first sight, the problem (27.36) seems to be more complicated than the original problem (27.34), since it depends on more variables. However, the representation (27.36) allows for an efficient algorithmic solution.

A key observation is that the cost function $\widehat{\lambda}(\mathbf{U}, \mathbf{q}_{\text{ext}})$ does not depend on the last row of the extended coupling matrix $\mathbf{\Lambda}$, that is,

$$\begin{aligned}\max_{\mathbf{x}>0} \frac{\mathbf{x}^T \mathbf{\Lambda}(\mathbf{U}, P_{\max})\mathbf{q}_{\text{ext}}}{\mathbf{x}^T \mathbf{q}_{\text{ext}}} &= \max_{\mathbf{x}:[\mathbf{x}]_{K+1}=0} \frac{\mathbf{x}^T \mathbf{\Lambda}(\mathbf{U}, P_{\max})\mathbf{q}_{\text{ext}}}{\mathbf{x}^T \mathbf{q}_{\text{ext}}} \\ &= \max_{1\le i\le K} \frac{\gamma_i}{\text{SINR}_i^{\text{UL}}(\mathbf{u}_i, \mathbf{q})} \quad \text{where } \mathbf{q} = [\mathbf{q}_{\text{ext}}]_{1:K}.\end{aligned} \tag{27.37}$$

The same relation holds when replacing max by min. A beneficial consequence is that minimizing the cost function $\widehat{\lambda}(\mathbf{U}, \mathbf{q}_{\text{ext}})$ with respect to $\mathbf{U}$ (keeping $\mathbf{q}_{\text{ext}} = \left[\begin{smallmatrix}\mathbf{q}\\ 1\end{smallmatrix}\right]$ fixed) leads to a set of K decoupled problems

$$\widehat{\mathbf{u}}_i = \arg\max_{\mathbf{u}_i} \text{SINR}_i^{\text{UL}}(\mathbf{u}_i, \mathbf{q}) = \arg\max_{\mathbf{u}_i} \frac{\mathbf{u}_i^* \mathbf{R}_i \mathbf{u}_i}{\mathbf{u}_i^* \mathbf{Z}_i(\mathbf{q}) \mathbf{u}_i}, \quad 1 \le i \le K. \tag{27.38}$$

The interference-plus-noise covariance matrices

$$\mathbf{Z}_i(\mathbf{q}) = \sum_{\substack{k=1\\k\neq i}}^{K} [\mathbf{q}]_k \mathbf{R}_k + \sigma^2 \mathbf{I}, \quad 1 \le i \le K \tag{27.39}$$

are nonsingular and symmetric, thus (27.38) can be solved efficiently by eigendecomposition. These observations are summarized as follows.

(1) For fixed $\widehat{\mathbf{q}}_{\text{ext}}$, the cost function $\widehat{\lambda}(\mathbf{U}, \widehat{\mathbf{q}}_{\text{ext}})$ is minimized by $\widehat{\mathbf{U}}=[\widehat{\mathbf{u}}_1, \ldots, \widehat{\mathbf{u}}_K]$, where $\widehat{\mathbf{u}}_k$ is the dominant generalized eigenvector of the matrix pair $(\mathbf{R}_k, \mathbf{Z}_k(\widehat{\mathbf{q}}_{\text{ext}}))$, $1 \le k \le K$.

(2) For fixed $\tilde{\mathbf{U}}$, the cost function $\widehat{\lambda}(\tilde{\mathbf{U}}, \mathbf{q}_{\text{ext}})$ is minimized by the vector $\tilde{\mathbf{q}}_{\text{ext}}$, which fulfills

$$\mathbf{\Lambda}(\tilde{\mathbf{U}}, P_{\max}) \cdot \tilde{\mathbf{q}}_{\text{ext}} = \rho(\mathbf{\Lambda}(\tilde{\mathbf{U}}, P_{\max})) \cdot \tilde{\mathbf{q}}_{\text{ext}} \quad \text{with } [\tilde{\mathbf{q}}_{\text{ext}}]_{K+1} = 1. \tag{27.40}$$

(1) $n := 0$
(2) $\mathbf{q}_{\text{ext}}^{(0)} := [0, \ldots, 0, 1]^T$
(3) *repeat*
(4) $n := n + 1$
(5) for given $\mathbf{q}_{\text{ext}}^{(n-1)}$ compute $\mathbf{U}^{(n)} = [\mathbf{u}_1^{(n)}, \ldots, \mathbf{u}_K^{(n)}]$ as the solution of

$$\mathbf{u}_i^{(n)} = \arg\max_{\mathbf{u}_i} \frac{\mathbf{u}_i^* \mathbf{R}_i \mathbf{u}_i}{\mathbf{u}_i^* \mathbf{Z}_i\left(\mathbf{q}_{\text{ext}}^{(n-1)}\right)\mathbf{u}_i}, \quad 1 \le i \le K$$

(6) for given $\mathbf{U}^{(n)}$ compute $\mathbf{q}_{\text{ext}}^{(n)}$ as the solution of

$$\mathbf{\Lambda}(\mathbf{U}^{(n)}, P_{\max})\mathbf{q}_{\text{ext}}^{(n)} = \rho(n)\mathbf{q}_{\text{ext}}^{(n)} \quad \text{with } \left[\mathbf{q}_{\text{ext}}^{(n)}\right]_{K+1} = 1$$

(7) *until* $\rho(n-1) - \rho(n) < \epsilon$

Algorithm 27.2. Algorithmic solution of the eigenvalue minimization problem (27.34).

We can again use the characterization (27.27) to prove the following optimality condition [15].

Proposition 27.5. *A matrix* $\hat{\mathbf{U}} = [\hat{\mathbf{u}}_1, \ldots, \hat{\mathbf{u}}_K]$ *solves the eigenvalue minimization problem* (27.34)*, as well as the joint beamforming problems* (27.32) *and* (27.33)*, if and only if there exists a* $\hat{\mathbf{q}}_{\text{ext}}$ *such that*

$$\hat{\lambda}(\hat{\mathbf{U}}, \hat{\mathbf{q}}_{\text{ext}}) = \min_{\mathbf{U}} \hat{\lambda}(\mathbf{U}, \hat{\mathbf{q}}_{\text{ext}}), \qquad \mathbf{\Lambda}(\hat{\mathbf{U}}, P_{\max})\hat{\mathbf{q}}_{\text{ext}} = \rho(\mathbf{\Lambda}(\hat{\mathbf{U}}, P_{\max}))\hat{\mathbf{q}}_{\text{ext}}. \quad (27.41)$$

This motivates the alternating algorithm summarized in Algorithm 27.2. The quantities associated with the nth iteration step are denoted by the superscript $(\cdot)^{(n)}$. Monotony and global convergence of the algorithm can be proved by exploiting the max-min characterization (27.27) of the spectral radius [15].

The optimization problems (27.32) and (27.33) are both solved by a beamforming matrix $\mathbf{U}^{\text{opt}} = \mathbf{U}^{(n\to\infty)}$. The associated power allocations, however, may be different. The power allocation which balances the relative uplink SINRs at the level (27.33) is obtained as the first K components of the principal eigenvector of $\mathbf{\Lambda}(\mathbf{U}^{\text{opt}}, P_{\max})$, scaled such that its last component equals one. The optimal downlink powers are associated with the coupling matrix $\mathbf{\Upsilon}(\mathbf{U}^{\text{opt}}, P_{\max})$.

27.2.7. Power minimization under SINR constraints

In the previous section it has been shown that the max-min SINR balancing problem is equivalent to an eigenvalue optimization problem, where the optimization is over the beamformers. There always exists a set of beamformers, which maximizes the jointly achievable SINR margin.

In this section, we focus on the total transmit power. To this end, suppose that there exists a beamforming matrix $\tilde{\mathbf{U}}$ such that $\rho(\mathbf{\Lambda}(\tilde{\mathbf{U}}, P_{\max})) < 1$. That is, target

(1) *initialize:* $n := 0$, $\mathbf{q}^{(0)} := [0, \ldots, 0]^T$, $C^{(0)} := 0$
(2) *repeat*
(3) $\quad n := n + 1$
(4) $\quad \mathbf{U}^{(n)} = [\mathbf{u}_1^{(n)}, \ldots, \mathbf{u}_K^{(n)}] := \arg\max_{\mathbf{u}_i} \dfrac{\mathbf{u}_i^* \mathbf{R}_i \mathbf{u}_i}{\mathbf{u}_i^* \mathbf{Z}_i(\mathbf{q}^{(n-1)})\mathbf{u}_i}$, $1 \le i \le K$
(5) $\quad$ *if* $C^{(n)} < 1$ *then*
(6) $\quad\quad P_{\text{sum}}^{(n)} := P_{\max}$
(7) $\quad\quad$ solve $\boldsymbol{\Lambda}(\mathbf{U}^{(n)}, P_{\text{sum}}^{(n)})[\,\mathbf{q}_1^{(n)}\,] = \rho(n)[\,\mathbf{q}_1^{(n)}\,]$
(8) $\quad\quad C^{(n)} := 1/\rho(n)$
(9) $\quad$ *else*
(10) $\quad\quad \mathbf{q}^{(n)} := (\mathbf{I} - \mathbf{D}\boldsymbol{\Psi}^T(\mathbf{U}^{(n)}))^{-1}\mathbf{D}\boldsymbol{\sigma}$
(11) $\quad\quad P_{\text{sum}}^{(n)} := \|\mathbf{q}^{(n)}\|_1$
(12) $\quad\quad C^{(n)} := 1$
(13) $\quad$ *end if*
(14) *until* $\max_{1\le i\le K} \text{SINR}_i^{\text{UL}}(\mathbf{u}_i^{(n)}, \mathbf{q}^{(n-1)}) - \min_{1\le i\le K} \text{SINR}_i^{\text{UL}}(\mathbf{u}_i^{(n)}, \mathbf{q}^{(n-1)}) < \epsilon$

Algorithm 27.3. Algorithmic solution of the power minimization problem (27.42).

SINRs $\gamma_1, \ldots, \gamma_K$ are not only feasible, but there are even excess degrees of freedom which can be used for minimizing the total power.

We start with the problem formulation for the uplink channel, which can be written as

$$\min_{\mathbf{U},\mathbf{q}} \sum_{i=1}^{K} q_i \quad \text{subject to } \text{SINR}_i^{\text{UL}} \ge \gamma_i,\ 1 \le i \le K, \qquad \|\mathbf{u}_i\|_2 = 1,\ 1 \le i \le K. \tag{27.42}$$

Note, that this problem formulation is only meaningful if the SINR constraints are feasible. Since all users are coupled, the optimum is characterized by balanced quantities $\text{SINR}_i^{\text{UL}}/\gamma_i = 1$ [14]. Thus, problem (27.42) can be seen as a special case of the more general max-min balancing problem (27.32). Since (27.42) is only feasible if the target SINRs can be achieved, a two-stage strategy must be pursued:

(1) check whether the constraints $\text{SINR}_i^{\text{UL}} \ge \gamma_i$ can be fulfilled (by solving (27.33)). If the targets are infeasible (i.e., $C_{\text{opt}}^{\text{UL}}(P_{\max}) \le 1$), then relax the targets $\gamma_1, \ldots, \gamma_K$ until the problem becomes feasible,
(2) for given targets, minimize the total power by solving (27.42).

Both steps are contained in Algorithm 27.3, which was proposed in [15]. It starts the same way as Algorithm 27.2. As soon as it turns out that the problem is feasible, the global power minimum (27.42) can be found by changing the power control policy. Instead of computing the power allocation which maximizes the balanced ratio $\text{SINR}_i^{\text{UL}}/\gamma_i$ for given $P_{\max}$, we are now interested in finding the allocation that minimizes the total transmission power while satisfying $\text{SINR}_i^{\text{UL}}/\gamma_i = 1$. The power allocation with minimal total power is known to be (27.13). These steps are

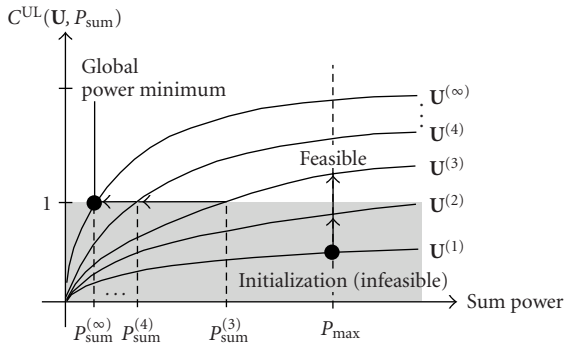

FIGURE 27.4. Schematic illustration of the iterative power minimizer (Algorithm 27.3).

repeated until convergence. The algorithm is summarized in Algorithm 27.3 and illustrated in Figure 27.4. The proof of convergence can be found in [15].

Proposition 27.6. *If the target SINRs $\gamma_1, \ldots, \gamma_K$ are feasible, then Algorithm 27.3 yields a monotonically decreasing sequence $\|\mathbf{p}^{(n)}\|_1$. The sequence converges to the optimum of the optimization problem* (27.42).

The beamforming matrix obtained by the algorithm not only solves the uplink problem (27.42), but also the corresponding downlink problem. Having found the optimal beamformers, the associated downlink and uplink power allocations with minimum total power are given by (27.12) and (27.13), respectively.

27.2.8. Semi-algebraic approach

The eigenvalue optimization approach (27.34) shows that joint beamforming optimization does not necessarily need explicit optimization over the transmit powers. The optimization only depends on the beamformers (although the problem structure is still determined by the power coupling). Now we show that the problem can also be seen from a different perspective, where the optimization is carried out with respect to transmit powers only [29].

Suppose that targets $\gamma_1, \ldots, \gamma_K$ are feasible and $\hat{\mathbf{u}}_i, \hat{\mathbf{q}}$ are optimizers of (27.42), then the constraints are active, that is, $\mathrm{SINR}_i(\hat{\mathbf{u}}_i, \hat{\mathbf{q}}) = \gamma_i$, $i \in \{1, 2, \ldots, K\}$. This can be rewritten as

$$\hat{\mathbf{u}}_i^* \mathbf{B}_i(\hat{\mathbf{q}}) \hat{\mathbf{u}}_i = 0, \tag{27.43}$$

where

$$\mathbf{B}_i(\mathbf{q}) := \sigma^2 \mathbf{I} + \sum_{\substack{k=1 \\ k \neq i}}^{K} q_k \mathbf{R}_k - \frac{1}{\gamma_i} q_i \mathbf{R}_i. \tag{27.44}$$

It follows from the optimality of $\hat{\mathbf{u}}_i$ that for any $\mathbf{z} \in \mathbb{C}^M$ the optimizers $\hat{\mathbf{u}}_i$ and $\hat{\mathbf{q}}$ jointly fulfill

$$0 = \hat{\mathbf{u}}_i^* \mathbf{B}_i(\hat{\mathbf{q}}) \hat{\mathbf{u}}_i \leq \mathbf{z}^* \mathbf{B}_i(\hat{\mathbf{q}}) \mathbf{z} \quad \forall i \in \{1, \ldots, K\}. \tag{27.45}$$

Thus, $\mathbf{B}_i(\hat{\mathbf{q}}) \succeq 0$ (positive semidefinite). It can be concluded that (27.43) can only be fulfilled if $\mathbf{B}_i(\hat{\mathbf{q}})$ is singular, that is, $\det |\mathbf{B}_i(\hat{\mathbf{q}})| = 0$. Thus, $\hat{\mathbf{u}}_i$ is an element of the nullspace of $\mathbf{B}_i(\hat{\mathbf{q}})$.

It can be shown [29] that the optimal power allocation $\hat{\mathbf{q}}$ is contained in the intersection of polynomial roots

$$\mathcal{B} = \bigcap_{i=1}^{K} \{\mathbf{q} : \phi_i(\mathbf{q}) = 0\} \bigcap \mathbb{R}_+^K, \tag{27.46}$$

where

$$\phi_i(\mathbf{q}) := \det \left| \mathbf{B}_i(\mathbf{q}) \right| \quad \forall i \in \{1, 2, \ldots, K\}. \tag{27.47}$$

Assuming that the target SINRs are feasible, a solution $\hat{\mathbf{q}} \in \mathcal{B}$ solving the joint beamforming problem (27.42) is given by

$$\hat{\mathbf{q}} = \arg \min_{\mathbf{q} \in \mathcal{B}} \|\mathbf{q}\|_1. \tag{27.48}$$

That is, $\hat{\mathbf{q}}$ together with $\hat{\mathbf{u}}_i$ arbitrarily chosen from the nullspace of $\mathbf{B}_i(\hat{\mathbf{q}})$, $1 \leq i \leq K$, jointly achieve the targets $\gamma_1, \ldots, \gamma_K$ with minimal total power $P = \|\hat{\mathbf{q}}\|_1$.

It is known from semi-algebraic geometry that if the polynomials $\phi_i(\mathbf{q})$ are different, then $\mathcal{B}$ is always finite. Thus, the optimization in (27.48) is over a finite set. For the special problem at hand, it can even be shown that the subset of optimal solutions $\{\mathbf{q} : \mathbf{q} \in \mathcal{B}, \|\mathbf{q}\|_1 = P\}$ cannot contain more than a single element.

Proposition 27.7. *The multiuser beamforming problem* (27.42) *has a unique optimizer* $\hat{\mathbf{q}}$. *Having found* $\hat{\mathbf{q}}$, *an optimal beamformer* $\hat{\mathbf{u}}_i$ *of the ith user can be arbitrarily chosen from the nullspace of* $\mathbf{B}_i(\hat{\mathbf{q}})$.

27.2.9. Discussion

The results show that SINR-based multiuser beamforming has an interesting analytical structure, which allows to solve the joint optimization problems (P1) and (P2), which we have introduced at the beginning of this chapter.

The same problems can be formulated for other performance measures, for example, the information theoretical capacities

$$\mathcal{R}_k = \log_2 \left(1 + \mathrm{SINR}_k(\mathbf{U}, \mathbf{p})\right), \quad 1 \leq k \leq K, \tag{27.49}$$

under the assumption that Gaussian-distributed codebooks are used for signaling. Since there is a one-to-one correspondence between SINR and capacity, the proposed beamforming strategy can be used to distribute the system resources according to individual target capacities $\hat{R}_1, \ldots, \hat{R}_K$. Provided that these rates are feasible, the strategy with optimal power efficiency is

$$\min_{\mathbf{U},\mathbf{p}} \sum_{k=1}^{K} \mathbf{p}_k \text{ subject to } \quad \mathcal{R}_i \geq \hat{R}_i \ \forall i \in \{1, \ldots, K\}. \tag{27.50}$$

The rate constraints directly translate into SINR constraints, thus the algorithm in Section 27.3 can be used to find the optimum. Moreover, it can be concluded that the duality theory derived in Section 27.2.4 immediately carries over to a duality of rate regions. That is, a rate point is achievable in the uplink if and only if the same point is achievable in the downlink.

This duality has been shown to be very useful for the development of algorithms. The uplink problem is easier to handle than the corresponding downlink problem, which is because the users are coupled by the channels, rather than by the beamformers. Instead of optimizing the downlink directly, one can find the optimum by solving the equivalent dual problem.

For MIMO links, it would be desirable to find a similar duality. Important steps have been made in [26, 30, 31], under the assumption that the information content of the signals can be exploited in an optimal way, that is, by canceling known interference (as will be discussed in the following section). For the "classical" approach considered in this section, the K data streams and the M array antennas are related by a linear mapping. Under this assumption, the capacity of the kth link of the Gaussian multiuser MIMO is

$$\mathcal{C}_k = \log_2 \det \left| \mathbf{I} + \mathbf{H}_k \mathbf{Q}_k \mathbf{H}_k^* \mathbf{Z}_k^{-1} \right|, \tag{27.51}$$

where $\mathbf{H}_k$ is the $n_r \times n_t$ channel matrix (n_r receive antennas, n_t transmit antennas) and $\mathbf{Q}_k$ is the transmit covariance matrix with power $\mathrm{Tr}\{\mathbf{Q}_k\}$. The users are coupled by interference, which is included in the noise covariance matrix

$$\mathbf{Z}_k = \sigma^2 \mathbf{I} + \sum_{l \neq k}^{K} \mathbf{H}_l \mathbf{Q}_l \mathbf{H}_l^*. \tag{27.52}$$

Thus, the kth user receives interference from all other users $l \neq k$. In order to fulfill individual target capacities $\hat{R}_1, \ldots, \hat{R}_K$ with optimal power efficiency, one has to solve a joint optimization problem

$$\min_{\mathbf{Q}_i \geq 0, 1 \leq i \leq K} \sum_{k=1}^{K} \mathrm{Tr}\{\mathbf{Q}_k\} \quad \text{subject to } \mathcal{C}_i \geq \hat{R}_i \ \forall i \in \{1, \ldots, K\}. \tag{27.53}$$

This multiuser MIMO problem has a complicated structure and is still open. One

way to gain intuition about multiuser MIMO is to analyze the capacity $\mathcal{C}(\mathbf{Q}, \mathbf{Z})$ as a function of the desired signal $\mathbf{Q}$ and the noise $\mathbf{Z}$ [32].

The beamforming problem discussed in Section 27.3 can be seen as a special case, where the channels can be expressed as vectors. For the more general MIMO case, it is still not clear whether a similar duality between uplink and downlink holds. Duality has been shown under the assumption of Gaussian channels with interference cancellation (resp., precompensation) [30, 31, 33]. However, the general case is still open.

27.3. Precoding and successive interference cancellation

Next, we will discuss the joint beamforming problem in an information theoretical context. The uplink is often modeled as a multiple access channel (MAC) and the downlink as a broadcast channel (BC).

The MAC capacity region has been established in [34] based on earlier results [35, 36]. The problem formulation goes back to Shannon itself. See also [37, 38] for an overview. In [39] it was shown for a vector channel (e.g., beamforming) that the vertices of the region can be achieved by a combination of linear filtering and successive interference cancellation (SIC).

The broadcast channel was introduced by Cover in [40]. The general (nondegraded) capacity region has been a longstanding problem, which was not solved until [33] based on earlier results [30, 31, 41]. It turns out that both BC and MAC are duals of each other and their regions coincide (see Figure 27.5). The points within this region can be achieved by "dirty paper" precoding, nicknamed after Costa's result [42]. This information theoretical result says (for a scalar single-antenna channel) that if interference is known noncausally at the transmitter, then this knowledge can be taken into account by a precoding strategy, which achieves the same capacity as if the interference would not exist. Moreover, such an ideal precoding comes at no extra cost in terms of transmit power. The result has been extended to vector channels and practical strategies have been proposed [30, 43, 44, 45, 46, 47].

27.3.1. Uplink beamforming with SIC

Uplink successive interference cancellation can be applied in combination with linear receivers (beamformers). In [39] it was shown that the vertices of the capacity region can be achieved by using a combination of successive interference cancellation (SIC) and normalized linear MMSE receivers

$$\mathbf{u}_i^{\mathrm{MMSE}} = \frac{\mathbf{Z}_i^{-1}\mathbf{h}_i}{\left|\left|\mathbf{Z}_i^{-1}\mathbf{h}_i\right|\right|_2} \quad \forall i \in \{1, 2, \ldots, K\}, \tag{27.54}$$

where $\mathbf{Z}_1, \ldots, \mathbf{Z}_K$ are the interference-plus-noise spatial covariance matrices, which depend on the order in which SIC is performed. The users can be renumbered

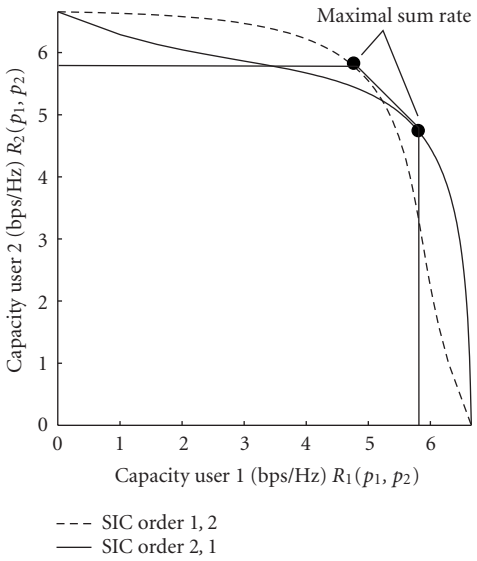

FIGURE 27.5. Uplink (MAC) capacity region under a sum-power constraint $P_{\max}$. The region is the convex hull of the unions of pentagons defined by individual power constraints $p_1 + p_2 \leq P_{\max}$ (see, e.g., [37]).

arbitrarily, thus $K!$ different combinations exist. Assuming an order $K, \ldots, 1$, we have

$$\mathbf{Z}_i(q_1, \ldots, q_{i-1}) = \sigma^2 \mathbf{I} + \sum_{k=1}^{i-1} q_k \mathbf{h}_k \mathbf{h}_k^*. \tag{27.55}$$

The following signal is obtained at the ith cancellation step:

$$y_i(t) = s_i(t)\mathbf{u}_i^* \mathbf{h}_i + \sum_{k=1}^{i-1} s_k(t)\left(\mathbf{u}_i^{\mathrm{MMSE}}\right)^* \mathbf{h}_k + n_i(t), \quad 1 \leq i \leq K. \tag{27.56}$$

This leads to "coded" SINRs

$$\mathrm{SINR}_i^{\mathrm{UL,SD}}\left(\mathbf{u}_i^{\mathrm{MMSE}}, q_1, \ldots, q_i\right) = \frac{q_i \left| \left(\mathbf{u}_i^{\mathrm{MMSE}}\right)^* \mathbf{h}_i \right|^2}{\left(\mathbf{u}_i^{\mathrm{MMSE}}\right)^* \mathbf{Z}_i(q_1, \ldots, q_{i-1}) \mathbf{u}_i^{\mathrm{MMSE}}} = q_i \mathbf{h}_i^* \mathbf{Z}_i^{-1} \mathbf{h}_i. \tag{27.57}$$

Similar to classical beamforming studied in Section 27.2, we are interested in the power allocation and beamformers that solve the power minimization problem

$$\min_{\mathbf{q},\mathbf{U}} \sum_{i=1}^{K} q_i \quad \text{subject to } \mathrm{SINR}_i^{\mathrm{UL,SD}}\left(\mathbf{u}_i, q_1, \ldots, q_i\right) \geq \gamma_i,\ 1 \leq i \leq K. \tag{27.58}$$

Note, that unlike the linear beamforming problem studied before, problem (27.58)

(1) $\mathbf{Z}_1^{-1} := \mathbf{I}/\sigma^2$
(2) *for* $i = 1$–K *do*
(3) $\quad q_i^{\text{opt}} := \dfrac{\gamma_i}{\mathbf{h}_i^* \mathbf{Z}_i^{-1} \mathbf{h}_i}$
(4) $\quad \mathbf{u}_i^{\text{opt}} := \mathbf{Z}_i^{-1}\mathbf{h}_i / \|\mathbf{Z}_i^{-1}\mathbf{h}_i\|_2$
(5) $\quad \mathbf{Z}_{i+1}^{-1} := \mathbf{Z}_i^{-1} - \dfrac{q_i^{\text{opt}} \mathbf{Z}_i^{-1}\mathbf{h}_i\mathbf{h}_i^*\mathbf{Z}_i^{-1}}{1+\gamma_i}$
(6) *end for*

Algorithm 27.4. Solution of the uplink problem (27.58): joint beamforming and power allocation under the assumption of SIC (order $K, \ldots, 1$).

is *always* feasible in the absence of power constraints. This is due to the triangular channel structure imposed by the successive decoding. The interference-plus-noise covariance matrix has a recursive structure

$$\mathbf{Z}_{i-1}(\mathbf{q}) = \mathbf{Z}_i(\mathbf{q}) + q_i \mathbf{h}_i \mathbf{h}_i^*, \quad 1 \le i \le K, \tag{27.59}$$

where $\mathbf{Z}_K = \sigma^2 \mathbf{I}$ (the last decoded user transmits over an effective AWGN channel). Thus, we can use the rank-one update formula for matrix inversion to compute the matrix inverses. For any nonsingular matrix $\mathbf{A}$ and vectors $\mathbf{c}$, $\mathbf{d}$, we have (see, e.g., [27])

$$\left(\mathbf{A} + \mathbf{c}\mathbf{d}^*\right)^{-1} = \mathbf{A}^{-1} - \frac{\mathbf{A}^{-1}\mathbf{c}\mathbf{d}^*\mathbf{A}^{-1}}{1 + \mathbf{c}^*\mathbf{A}^{-1}\mathbf{d}}. \tag{27.60}$$

Using the shorthand notation $\mathbf{Z}_i := \mathbf{Z}_i(\mathbf{q})$ and (27.60), we have

$$\mathbf{Z}_{i-1}^{-1} = \mathbf{Z}_i^{-1} - \frac{q_i \mathbf{Z}_i^{-1}\mathbf{h}_i\mathbf{h}_i^*\mathbf{Z}_i^{-1}}{1+\gamma_i}, \qquad \mathbf{Z}_K^{-1} = \frac{\mathbf{I}}{\sigma^2}. \tag{27.61}$$

This leads to Algorithm 27.4, which provides a recursive solution for the uplink problem (27.58). The proof is given in [16]. Note, that the total transmit power required to achieve certain targets generally depends on the coding order. Additional performance gains can be achieved by optimizing over the coding order as well.

27.3.2. Closed form solution for the two-user case

The results show that the highly nonlinear optimization problem (27.58) can in principle be solved in closed form, by recursive back-substitution. For $K = 2$ and a decoding order 2, 1, this leads to the following *jointly optimal* transmit powers:

$$q_1^{\text{opt}} = \frac{\gamma_1 \sigma^2}{\|\mathbf{h}_1\|^2}, \qquad q_2^{\text{opt}} = \frac{\gamma_2 \sigma^2}{\|\mathbf{h}_2\|^2}\left(1 - \frac{\gamma_1}{1+\gamma_1}\rho_{12}^2\right)^{-1}, \tag{27.62}$$

where ρ_{ik} denotes the normalized inner product between the channels $\mathbf{h}_i$ and $\mathbf{h}_k$, that is,

$$\rho_{ik} = \frac{\mathbf{h}_i^* \mathbf{h}_k}{||\mathbf{h}_i||\,||\mathbf{h}_k||}. \tag{27.63}$$

Hence, for fully correlated channels or equal targets it is always optimal to decode first the user with the largest channel norm. If both channels have the same norm, then both coding orders yield the same total power. For uncorrelated or partly correlated channels $|\rho_{12}| < 1$, the optimal decoding order also depends on the choice of the target SINRs.

With $q_1 + q_2 \leq P_{\max}$, the SINR achievable region with successive decoding (order 2, 1) is characterized by the following inequality:

$$\gamma_2 \leq ||\mathbf{h}_2||^2 \left(1 - \frac{\gamma_1}{1+\gamma_1}\rho_{12}^2\right)\left(\frac{P_{\max}}{\sigma^2} - \frac{\gamma_1}{||\mathbf{h}_1||^2}\right). \tag{27.64}$$

It can be observed that for uncorrelated channels $\rho_{12} = 0$, there is a linear tradeoff between the achievable SINR values γ_2 and γ_1.

27.3.3. Downlink beamforming with precoding

In [41] it was proposed to use "dirty paper precoding" to precompensate interference in a multiuser broadcast channel (downlink). The basic idea is as follows: if the users are subsequently encoded with order $1,\ldots,K$, and perfect channel knowledge is available, then the interference caused by the users $i+1,\ldots,K$ to the user i is known prior to transmission. The interference can therefore be rendered harmless by an appropriate encoding and has no effect at the decoder output. This imposes a triangular structure on the interference structure and leads to a partial decoupling of the users. In particular, the Kth user sees no interference after demodulation.

The duality theory discussed in Section 27.2.4 extends to the nonlinear case (SIC/precoding) in a straightforward way. In analogy to classical downlink beamforming (Section 27.2), the optimal beamformers and powers required for precoding can be found as well by solving a dual uplink problem instead. Target SINRs $\gamma_1,\ldots,\gamma_K$ are achieved in the downlink with optimal power efficiency by Algorithm 27.5. It starts by computing the optimal transmit beamformers $\mathbf{u}_1^{\text{opt}},\ldots,\mathbf{u}_K^{\text{opt}}$ by solving the dual uplink problem with SIC. The SIC decoding order has to be chosen as the reverse encoding order. Having found the optimal beamformers, the associated downlink power allocation $\mathbf{p}^{\text{opt}}$ can be computed.

27.4. Network resource allocation

In order to provide end-to-end QoS for individual users, a system-wide point of view is required. A common approach to handle various system parameters

(1) compute $\mathbf{u}_1^{\text{opt}}, \ldots, \mathbf{u}_K^{\text{opt}}$ with Algorithm 27.4 (order $K, \ldots, 1$)
(2) *for* $i = K$ to 1 *do*
(3) $\quad p_i^{\text{opt}} := \dfrac{\gamma_i}{|\mathbf{u}_i^* \mathbf{h}_i|^2} \left(\sum_{k=i+1}^{K} p_k^{\text{opt}} |\mathbf{u}_k^* \mathbf{h}_i|^2 + \sigma^2 \right)$
(4) *end for*

Algorithm 27.5. Joint downlink beamforming and power allocation under the assumption of interference precompensation (dirty paper precoding) with encoding order $1, \ldots, K$.

is to model the QoS of all users as SINR-dependent functions $f_k(\text{SINR}_k), k \in \{1, \ldots, K\}$. QoS control for mixed services with individual priorities and rate requirements can be realized by optimizing a weighted sum

$$F(\mathbf{p}, \mathbf{U}) = \sum_{k=1}^{K} w_k f_k\big(\text{SINR}_k(\mathbf{p}, \mathbf{U})\big). \tag{27.65}$$

The factors w_i account for the individual user requirements and possibly incorporate system aspects like scheduling, resource allocation, priorities, and so forth. Some possible strategies will be discussed in the remainder of this chapter.

27.4.1. Throughput maximization

A special realization of $f(\text{SINR})$ is the Shannon capacity $\log_2(1 + \text{SINR})$, which was already used in Section 27.3, where the tradeoff region between the users was characterized. Now, we consider a special point on the boundary of this region, namely the maximal sum rate

$$\mathcal{C}_{\text{sum}} = \max_{\mathbf{U}, \|\mathbf{q}\|_1 \le P_{\max}} \sum_{k=1}^{K} \log_2 \left(1 + \text{SINR}_k(\mathbf{p}, \mathbf{U})\right), \tag{27.66}$$

which is obtained by maximization over all beamformers $\mathbf{U}$ and power allocations $\mathbf{p}$ with total power $\|\mathbf{p}\|_1 \le P_{\max}$. All users are weighted equally, that is, $w_k = 1$, for all $k \in \{1, 2, \ldots, K\}$.

27.4.1.1. Uplink sum capacity

Assuming MMSE beamformers (27.54) and SIC with order $K, \ldots, 1$, we have

$$\begin{aligned} \log_2 \left(1 + \text{SINR}_i\right) &= \log_2 \left(1 + q_i \mathbf{h}_i^* \mathbf{Z}_i^{-1} \mathbf{h}_i\right) \\ &= \log_2 \left| \mathbf{I} + q_i \mathbf{Z}_i^{-1/2} \mathbf{h}_i \mathbf{h}_i^* \mathbf{Z}_i^{-1/2} \right| \\ &= \log_2 \left| q_i \mathbf{h}_i \mathbf{h}_i^* + \mathbf{Z}_i \right| - \log_2 \left| \mathbf{Z}_i \right|, \end{aligned} \tag{27.67}$$

where the interference-plus-noise spatial covariance $\mathbf{Z}_i$ has the special recursive

structure $\mathbf{Z}_{i+1} = \mathbf{Z}_i + q_i \mathbf{h}_i \mathbf{h}_i^*$, with $\mathbf{Z}_1 = \sigma^2 \mathbf{I}$, thus

$$\begin{aligned} \sum_{k=1}^{K} \log_2 \left(1 + \mathrm{SINR}_k\right) &= \sum_{k=1}^{K} \log_2 \left|\mathbf{Z}_{k+1}\right| - \sum_{k=1}^{K} \log_2 \left|\mathbf{Z}_k\right| \\ &= \log_2 \left| \sigma^2 \mathbf{I} + \sum_{k=1}^{K} q_k \mathbf{h}_k \mathbf{h}_k^* \right| - \log_2 \left|\sigma^2 \mathbf{I}\right|. \end{aligned} \tag{27.68}$$

Hence, the sum capacity is

$$\mathcal{C}_{\mathrm{sum}} = \max_{\|\mathbf{q}\|_1 \leq P_{\max}} \log_2 \left| \mathbf{I} + \frac{1}{\sigma^2} \sum_{k=1}^{K} q_k \mathbf{h}_k \mathbf{h}_k^* \right|. \tag{27.69}$$

The objective in (27.69) is concave on the set of transmit powers. The optimal power allocation $\mathbf{q}^{\mathrm{opt}}$, with $\|\mathbf{q}^{\mathrm{opt}}\|_1 = P_{\max}$, can be computed efficiently by recently developed interior point methods, like the one in [48].

Finally, it should be noted that the sum capacity does not depend on the coding order, as can be observed from (27.69).

27.4.1.2. Downlink sum capacity

It follows from the uplink/downlink duality in Section 27.2.4 that the sum capacity (27.69) is also the sum capacity of the broadcast channel (see also [26, 31, 49] for a discussion of more general MIMO channels).

In particular, the SINR levels which are associated with the uplink sum capacity (27.69) must equal the SINRs associated with the BC sum capacity. Thus, the joint beamforming approach proposed in Section 27.2.6 can be used to determine the optimal BC power allocation and transmit beamformers. In particular, it is known that the MAC beamformers also achieve the BC sum capacity, however with a different power allocation. For known SINR targets, the optimal downlink power allocation has been derived in Section 27.3.3. As for the MAC, the BC sum capacity does not depend on the encoding order.

27.4.1.3. Sum capacity with classical beamforming

Consider the uplink channel (due to duality, all results can be transferred to the downlink). Without interference cancellation, the covariance of interference-plus-noise is

$$\mathbf{Z}_k(\mathbf{q}) = \sigma^2 \mathbf{I} + \sum_{\substack{k=1 \\ k \neq i}}^{K} q_k \mathbf{h}_k \mathbf{h}_k^*. \tag{27.70}$$

Thus, the sum rate is given by

$$C_{\text{lin}}(\mathbf{q}) = K \log_2 \left| \sigma^2 \mathbf{I} + \sum_{k=1}^{K} q_k \mathbf{h}_k \mathbf{h}_k^* \right| - \sum_{k=1}^{K} \log_2 \left| \mathbf{Z}_k(\mathbf{q}) \right|. \tag{27.71}$$

The function $C_{\text{lin}}(\mathbf{q})$ is the sum of a convex and a concave term. The result need not be convex nor concave, as can be observed from the two-user example depicted in Figure 27.6. Nevertheless, there are some properties which can be used for numerical optimization.

(i) The sum rate function is continuous and infinitively often differentiable.

(ii) The optimum always lies on the boundary of the domain defined by the sum-power constraint.

Thus, iterative algorithms might lead to acceptable results. Starting the iteration process from the interior of the domain, it is always assured that the algorithm converges towards an optimum on the boundary, where the sum-power constraint is fulfilled with equality. Thus, instead of searching the entire domain, only the boundary has to be searched.

27.4.2. Max-min fairness

Throughput maximization does not account for the individual capacity requirements. This may lead to a situation where all the available power resource is focused on a single user. Often, a more fair approach is required.

The max-min technique proposed in Section 27.2.6 and the constrained power minimization strategy in Section 27.3.1 both offer optimal fairness based on the SINR criterion (also denoted as max-min fairness). However, forcing all SINRs to achieve a given target threshold may be a waste of resource, for example, when the path attenuation of some link is so high that meaningful communication is not possible. Thus, a tradeoff between throughput maximization and max-min fairness is required. An optimal strategy should be flexible enough to not only incorporate the channel condition, but also other system parameters, for example, the lengths of the data queues.

As a first step, we show how optimal max-min fairness can be achieved within the framework of the sum-optimization strategy (27.65). In particular, we consider the case where the QoS depends inversely on the SIR. Suppose that all beamformers are constrained to fulfill $\mathbf{u}_i^* \mathbf{R}_i \mathbf{u}_i = 1$, then we are interested in minimizing the cost function

$$F(\mathbf{U}, \mathbf{p}) = \frac{1}{K} \sum_{k=1}^{K} w_k \frac{\gamma_k}{\text{SIR}_k^{\text{DL}}(\mathbf{U}, \mathbf{p})} = \frac{1}{K} \sum_{i=1}^{K} p_i \mathbf{u}_i^* \left(\sum_{\substack{k=1 \\ k \neq i}}^{K} \frac{w_k \gamma_k \mathbf{R}_k}{p_k} \right) \mathbf{u}_i. \tag{27.72}$$

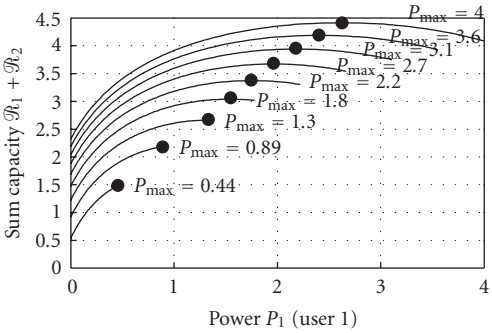

(a)

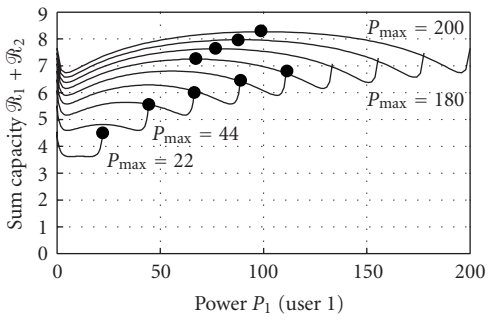

(b)

FIGURE 27.6. Sum capacity with (a) SIC/precoding: $\|h_1\|_2 = 2$, $\|h_2\| = 1$, and (b) classical beamforming: $\|h_1\|_2 = 1$, $\|h_2\|_2 = 0.99$. $K = 2$, $M = 2$, $\sigma^2 = 1$, and $P_1 + P_2 = P_{\max}$.

The optimization problem can be written as

$$\min_{\mathbf{U},\mathbf{p}} F(\mathbf{U},\mathbf{p}) \quad \text{subject to } \mathbf{u}_i\mathbf{R}_i\mathbf{u}_i = 1,\ 1 \le i \le K, \qquad \|\mathbf{p}\|_1 = 1. \tag{27.73}$$

A similar problem was introduced in [11], where equal weighting $w_i = 1$ was assumed (we add the fixed factors γ_i to enable comparison with the max-min problem discussed in Section 27.1) in order to achieve max-min fairness. It was shown in [19] that equal weighting generally does not lead to the optimum of the max-min balancing problem (27.23), except for the two-user case.

Necessary and sufficient conditions for the equivalence of problem (27.73) and the max-min problem (27.23) are given in [19]. In particular, it can be shown [50] that the problem is convex on $\mathbf{U}$ and log-convex on $\mathbf{p}$. This motivates an alternating optimization scheme that keeps one of the variables $\mathbf{U}$ and $\mathbf{q}$ fixed while minimizing with respect to the other. In each optimization step, the weighting

(1) $n := 0$
(2) $\mathbf{q}^{(0)} := [1,\ldots,1]^T$, $w^{(0)} := [1,\ldots,1]$
(3) $\rho(0) := 0$
(4) *repeat*
(5) $n := n + 1$
(6) for given $\mathbf{q}^{(n)}$ compute

$$\mathbf{U}^{(n)} := \arg\min_{\mathbf{U}} F(\mathbf{U}, \mathbf{p}^{(n-1)}, w^{(n-1)}), \quad \text{s.t. } \mathbf{u}_i^* \mathbf{R}_i \mathbf{u}_i = 1, 1 \le i \le K$$

(7) compute $\mathbf{q}^{(n)}$ and $\mathbf{p}^{(n)}$ as the left and right-hand principal eigenvectors of $\mathbf{\Gamma\Psi}(\mathbf{U}^{(n)})$, respectively. The spectral radius is $\rho(n)$
(8) $w_i = \hat{p}_i \cdot \hat{q}_i$, $i \in \{1,\ldots,K\}$, $w_i^{(n)} = p_i^{(n)} \cdot q_i^{(n)}$, $i \in \{1,\ldots,k\}$
(9) *until* $\rho(n-1) - \rho(n) \le \epsilon$

Algorithm 27.6. Problem (27.73): max-min fairness by minimizing the sum of weighted inverse downlink SIR..

factors w_i (which are constrained to fulfill $\sum_i w_i = 1$) must be adjusted as follows [50]:

$$w_i = \hat{p}_i \cdot \hat{q}_i, \quad i \in \{1,\ldots,K\}, \tag{27.74}$$

where $\hat{\mathbf{p}} = [\hat{p}_1,\ldots,\hat{p}_K]^T$ is the right-hand eigenvector of the coupling matrix $\mathbf{\Gamma\Psi}$ and $\hat{\mathbf{q}}$ is the left-hand eigenvector.

Problem (27.73) is solved by the algorithm summarized in Algorithm 27.6. We define $\mathbf{\Gamma} = \operatorname{diag}\{\gamma_1,\ldots,\gamma_K\}$. The beamformers computed by the algorithm solve the max-min SIR problem (27.23) (after rescaling such that $\|\mathbf{u}_i\|_2 = 1$). Monotonicity and convergence are shown in [51].

27.5. Implementation aspects and conclusions

The problem of jointly optimizing beamformers and transmit powers has an interesting analytical structure. Although it is highly nonlinear, very efficient optimization strategies can be devised. This is due to the duality between uplink and downlink, which allows to find the downlink optimum by solving an equivalent uplink problem instead.

The proposed beamforming strategies rely on channel knowledge, which can only be obtained by sacrificing a part of the available bandwidth for channel estimation. For downlink beamforming, the situation is even more difficult, since the information has to be available prior to transmission. Promising strategies to obtain channel knowledge are available (e.g., [9]). Nevertheless, robustness to channel mismatch remains an important aspect.

The classical beamforming approach discussed in Section 27.2 only relies on covariance channel information, which is obtained by averaging over the time-fluctuating fading channel. It exploits the slow-varying geometry of the propagation paths and is therefore inherently robust. This strategy could be assisted

by directional information. A study on calibration strategies for directional array transmission can be found in [52, 53, 54]. An example of a successful implementation of multiuser beamforming can be found in [55], where spatial multiplexing is combined with bit loading and adaptive modulation.

Future work will have to focus on the interaction of the proposed techniques with higher layer functionalities, for example, transmit scheduling, link control, and resource management. To this end, the SINR alone may not be sufficient as a performance criterion. Other performance measures were investigated, for example, in [56], where the balancing of effective bandwidths was considered. More general measures have been recently studied, for example, in [57, 58, 59].

After this chapter has been completed, it has been shown [60, 61] that the resource allocation problem discussed in Section 27.4 can be treated within a more generic framework, where interference is described by parameter-dependent coupling matrices. Thereby, it is possible to analyze the interaction between power control and receiver (resp., precoder) design in a more general way. These results could be useful for the development of future cross-layer strategies, which still require simple, yet comprehensive analytical models for optimization.

Acknowledgment

This work was supported in part by the *Bundesministerium für Bildung und Forschung (BMBF)* under Grant 01BU150.

Abbreviations

QoS	Quality of service
MAC	Multiple access channel
BC	Broadcast channel
SINR	Signal-to-interference-plus-noise ratio
SIR	Signal-to-interference ratio
SNR	Signal-to-noise ratio
MIMO	Multiple-input multiple-output
SIC	Successive interference cancellation
MMSE	Minimum mean square error
AWGN	Additive white Gaussian noise

Bibliography

[1] L. C. Godara, "Applications of antenna arrays to mobile communications. I. Performance improvement, feasibility, and system considerations," *Proc. IEEE*, vol. 85, no. 7, pp. 1029–1060, 1997.

[2] L. C. Godara, "Application of antenna arrays to mobile communications. II. Beam-forming and direction-of-arrival considerations," *Proc. IEEE*, vol. 85, no. 8, pp. 1193–1245, 1997.

[3] R. A. Monzingo and T. W. Miller, *Introduction to Adaptive Arrays*, John Wiley & Sons, New York, NY, USA, 1980.

[4] S. U. Pillai, *Array Signal Processing*, Springer, New York, NY, USA, 1989.

[5] B. D. Van Veen and K. M. Buckley, "Beamforming: a versatile approach to spatial filtering," *IEEE ASSP Mag.*, vol. 5, no. 2, pp. 4–24, 1988.

[6] H. Boche and E. A. Jorswieck, "On the optimality-range of beamforming for MIMO systems with covariance feedback," *IEICE Trans. Fund. Electron., Commun., and Comput. Sci*, vol. E85-A, no. 11, pp. 2521–2528, 2002.

[7] S. A. Jafar and A. J. Goldsmith, "On optimality of beamforming for multiple antenna systems with imperfect feedback," in *Proc. IEEE Intern. Symp. on Information Theory (ISIT '01)*, p. 321, Washington DC, USA, June 2001.

[8] M. Bengtsson and B. Ottersten, "Optimal downlink beamforming using semidefinite optimization," in *Proc. 37th Annual Allerton Conference on Communication, Control, and Computing*, pp. 987–996, Monticello, Ill, USA, September 1999.

[9] M. Bengtsson and B. Ottersten, "Optimal and suboptimal transmit beamforming," in *Handbook of Antennas in Wireless Communications*, CRC press, Boca Raton, Fla, USA, August 2001.

[10] C. Farsakh and J. A. Nossek, "Spatial covariance based downlink beamforming in an SDMA mobile radio system," *IEEE Trans. Commun.*, vol. 46, no. 11, pp. 1497–1506, 1998.

[11] D. Gerlach and A. Paulraj, "Base station transmitting antenna arrays for multipath environments," *Signal Processing*, vol. 54, no. 1, pp. 59–73, 1996.

[12] G. Montalbano and D. T. M. Slock, "Matched filter bound optimization for multiuser downlink transmit beamforming," in *Proc. IEEE International Conference on Universal Personal Communications (ICUPC '98)*, Florence, Italy, October 1998.

[13] F. Rashid-Farrokhi, K. J. R. Liu, and L. Tassiulas, "Transmit beamforming and power control for cellular wireless systems," *IEEE J. Select. Areas Commun.*, vol. 16, no. 8, pp. 1437–1450, 1998.

[14] E. Visotsky and U. Madhow, "Optimal beamforming using transmit antenna arrays," in *Proc. IEEE Semiannual Vehicular Techn. Conf. (VTC '99)*, vol. 1, pp. 851–856, Houston, Tex, USA, Spring 1999.

[15] M. Schubert and H. Boche, "Solution of the multi-user downlink beamforming problem with individual SINR constraints," *IEEE Trans. Veh. Technol.*, vol. 53, no. 1, pp. 18–28, 2004.

[16] M. Schubert and H. Boche, "Iterative multiuser uplink and downlink beamforming under SINR constraints," *IEEE Trans. Signal Processing*, vol. 53, no. 7, pp. 2324–2334, 2005.

[17] J. Zander and S.-L. Kim, *Radio Resource Management for Wireless Networks*, Artech House, Boston, Mass, USA, 2001.

[18] H. Boche and M. Schubert, "Optimal multi-user interference balancing using transmit beamforming," *Wireless Personal Communications*, vol. 26, no. 4, pp. 305–324, 2003.

[19] M. Schubert and H. Boche, "Comparison of infinity-norm and 1-norm optimization criteria for SIR-balanced beamforming," *Signal Processing (Elsevier Science)*, vol. 84, no. 2, pp. 367–378, 2004.

[20] W. Yang and G. Xu, "Optimal downlink power assignment for smart antenna systems," in *Proc. IEEE Int. Conf. Acoustics, Speech, Signal Processing*, vol. 6, pp. 3337–3340, Seattle, Wash, USA, May 1998.

[21] J. Zander, "Performance of optimum transmitter power control in cellular radio systems," *IEEE Trans. Veh. Technol.*, vol. 41, no. 1, pp. 57–62, 1992.

[22] J. Zander and M. Frodigh, "Comment on performance of optimum transmitter power control in cellular radio systems," *IEEE Trans. Veh. Technol.*, vol. 43, no. 3, pp. 636, 1994.

[23] H. Boche and S. Stanczak, "Optimal QoS tradeoff and power control in CDMA systems," in *Proc. 23rd Conference of the IEEE Communications Society (INFOCOM '04)*, pp. 1078–1088, Hong Kong, China, March 2004.

[24] H. Boche and M. Schubert, "A general duality theory for uplink and downlink beamforming," in *Proc. 56th IEEE Semiannual Vehicular Techn. Conf. (VTC '02)*, vol. 1, pp. 87–91, Vancouver, Canada, Fall 2002.

[25] D. Tse and P. Viswanath, "Downlink-uplink duality and effective bandwidths," in *Proc. IEEE Intern. Symp. on Information Theory (ISIT '02)*, p. 52, Lausanne, Switzerland, June–July 2002.

[26] P. Viswanath and D. Tse, "Sum capacity of the multiple antenna Gaussian broadcast channel and uplink-downlink duality," *IEEE Trans. Inform. Theory*, vol. 49, no. 8, pp. 1912–1921, 2003.

[27] C. D. Meyer, *Matrix Analysis and Applied Linear Algebra*, Society for Industrial and Applied Mathematics (SIAM), Philadelphia, Pa, USA, 2000.

[28] E. Seneta, *Nonnegative Matrices and Markov Chains*, Springer, New York, NY, USA, 1981.

[29] H. Boche and M. Schubert, "A semialgebraic approach to multiuser beamforming and power control," in *Proc. IEEE Intern. Symp. on Information Theory (ISIT '04)*, Chicago, Ill, USA, June–July 2004.
[30] G. Caire and S. Shamai (Shitz), "On the achievable throughput of a multi-antenna Gaussian broadcast channel," *IEEE Trans. Inform. Theory*, vol. 49, no. 7, pp. 1691–1706, 2003.
[31] S. Vishwanath, N. Jindal, and A. Goldsmith, "Duality, achievable rates, and sum-rate capacity of Gaussian MIMO broadcast channels," *IEEE Trans. Inform. Theory*, vol. 49, no. 10, pp. 2658–2668, 2003.
[32] E. A. Jorswieck and H. Boche, "Performance analysis of capacity of MIMO systems under multiuser interference based on worst-case noise behavior," *EURASIP Journal on Wireless Communications and Networking*, vol. 2004, no. 2, pp. 273–285, 2004.
[33] H. Weingarten, Y. Steinberg, and S. Shamai (Shitz), "The capacity region of the Gaussian MIMO broadcast channel," in *Proc. 38th Annual Conf. on Information Sciences and Systems (CISS '04)*, pp. 7–12, Princeton, NJ, USA, March 2004.
[34] R. G. Gallager, "Energy limited channels: Coding, multiaccess and spread spectrum," in *Proc. 22nd Annual Conf. on Information Sciences and Systems (CISS '88)*, p. 372, Princeton, NJ, USA, March 1988.
[35] T. M. Cover, "Some advances in broadcast channels," in *Advances in Communications Systems Theory and Applications*, pp. 229–260, Academic Press, New York, USA, 1975.
[36] A. D. Wyner, "Recent results in Shannon theory," *IEEE Trans. Inform. Theory*, vol. 20, no. 1, pp. 2–10, 1974.
[37] T. M. Cover and J. A. Thomas, *Elements of Information Theory*, John Wiley & Sons, New York, NY, USA, 1991.
[38] A. El. Gamal and T. M. Cover, "Multiple user information theory," *Proc. IEEE*, vol. 68, no. 12, pp. 1466–1483, 1980.
[39] M. K. Varanasi and T. Guess, "Optimum decision feedback multiuser equalization with successive decoding achieves the total capacity of the Gaussian multiple-access channel," in *Proc. Asilomar Conf. on Signals, Systems and Computers*, pp. 1405–1409, Monterey, Calif, USA, November 1997.
[40] T. M. Cover, "Broadcast channels," *IEEE Trans. Inform. Theory*, vol. 18, no. 1, pp. 2–14, 1972.
[41] G. Caire and S. Shamai (Shitz), "On achievable rates in a multi-antenna broadcast downlink," in *Proc. 38th Annual Allerton Conference on Communication, Control and Computing*, pp. 1188–1193, Monticello, Ill, USA, October 2000.
[42] M. Costa, "Writing on dirty paper," *IEEE Trans. Inform. Theory*, vol. 29, no. 3, pp. 439–441, 1983.
[43] G. Caire and S. Shamai (Shitz), "On the multiple-antenna broadcast channel," in *Proc. Asilomar Conf. on Signals, Systems and Computers*, vol. 2, pp. 1188–1193, Pacific Grove, Calif, USA, November 2001.
[44] U. Erez, S. Shamai (Shitz), and R. Zamir, "Capacity and lattice-strategies for cancelling known interference," in *Proc. Intern. Symposium on Information Theory and Its Application (ISITA '00)*, pp. 681–684, Honolulu, Hawaii, USA, November 2000.
[45] R. F. H. Fischer, Ch. Windpassinger, A. Lampe, and J. B. Huber, "MIMO precoding for decentralized receivers," in *Proc. IEEE Intern. Symp. on Information Theory (ISIT '02)*, p. 496, Lausanne, Switzerland, June–July 2002.
[46] R. F. H. Fischer, *Precoding and Signal Shaping for Digital Transmission*, John Wiley & Sons, New York, NY, USA, 2002.
[47] W. Yu and J. Cioffi, "Trellis precoding for the broadcast channel," in *Proc. IEEE Global Telecommunications Conference (GLOBECOM '01)*, vol. 2, pp. 1344–1348, San Antonio, Tex, USA, November 2001.
[48] L. Vandenberghe, S. Boyd, and S.-P. Wu, "Determinant maximization with linear matrix inequality constraints," *SIAM J. Matrix Anal. Appl.*, vol. 19, no. 2, pp. 499–533, 1998.
[49] W. Yu and J. M. Cioffi, "Sum capacity of Gaussian vector broadcast channels," *IEEE Trans. Inform. Theory*, vol. 50, no. 9, pp. 1875–1892, 2004.
[50] H. Boche, M. Wiczanowski, and S. Stanczak, "Characterization of optimal resource allocation in cellular networks—optimization theoretic view and applications," in *Proc. 23rd Conference of the IEEE Communications Society (INFOCOM '04)*, Hong Kong, China, March 2004.

[51] H. Boche and M. Schubert, "Resource allocation for multi-antenna multi-user systems," in *Proc. IEEE Int. Conf. on Comm. (ICC '05)*, Seoul, South Korea, May 2005.
[52] A. Kortke, "A new calibration algorithm for smart antenna arrays," in *Proc. 57th IEEE Semiannual Vehicular Techn. Conf. (VTC '03)*, vol. 2, pp. 1030–1034, Jeju, Korea, Spring 2003.
[53] K. H. Pensel and J. A. Nossek, "Uplink and downlink calibration of smart antennas," in *Proc. International Conference on Telecommunications (ICT '98)*, Porto Carras, Greece, June 1998.
[54] J. Pierre and M. Kaveh, "Experimental performance of calibration and direction-finding algorithms," in *Proc. IEEE Int. Conf. Acoustics, Speech, Signal Processing*, pp. 1365–1368, Toronto, Canada, May 1991.
[55] T. Haustein, A. Forck, H. Gäbler, C. v. Helmolt, V. Jungnickel, and U. Krüger, "Implementation of adaptive channel inversion in a real-time MIMO transmission system," in *Proc. IEEE 15th International Symposium on Personal, Indoor and Mobile Radio Communications (PIMRC '04)*, Barcelona, Spain, September 2004.
[56] H. Boche and M. Schubert, "Effective bandwidth maximization for uplink/downlink multi-antenna systems," in *Proc. IEEE Int. Conf. on Comm. (ICC '03)*, vol. 5, pp. 3215–3219, Anchorage, Alaska, USA, May 2003.
[57] H. Boche and E. A. Jorswieck, "Optimization of matrix monotone functions: Saddle-point, worst case noise analysis, and applications," in *Proc. IEEE Intern. Symp. on Information Theory (ISIT '04)*, p. 62, Chicago, Ill, USA, June–July 2004.
[58] H. Boche and E. A. Jorswieck, "Universal approach to performance optimization of multiuser MIMO systems," in *Proc. IEEE Workshop on Signal Processing Advances in Wireless Communications (SPAWC '04)*, Lisbon, Portugal, July 2004.
[59] E. A. Jorswieck and H. Boche, "On the impact of correlation on the capacity in MIMO systems without CSI at the transmitter," in *Proc. 37th Annual Conference on Information Sciences and Systems (CISS '03)*, Baltimore, Md, USA, March 2003.
[60] H. Boche and M. Schubert, "A unifying approach to multiuser receiver design under QoS constraints," in *Proc. IEEE Semiannual Vehicular Techn. Conf. (VTC '05)*, Stockholm, Sweden, Spring 2005.
[61] H. Boche, M. Schubert, S. Stanczak, and M. Wiczanowski, "An axiomatic approach to resource allocation and interference balancing," in *Proc. IEEE Int. Conf. Acoustics, Speech, Signal Processing*, Philadelphia, Pa, USA, March 2005.
[62] H. Boche and M. Schubert, "Solution of the SINR downlink beamforming problem," in *Proc. 36th Annual Conf. on Information Sciences and Systems (CISS '02)*, Princeton, NJ, USA, March 2002.

Holger Boche: Heinrich Hertz Chair for Mobile Communications, Faculty of EECS, Technical University of Berlin, 10587 Berlin, Germany; Fraunhofer Institute for Telecommunications, Heinrich-Hertz-Institut (HHI), 10587 Berlin, Germany; Fraunhofer German-Sino Lab for Mobile Communications (MCI), 10587 Berlin, Germany

Email: boche@hhi.fhg.de

Martin Schubert: Fraunhofer German-Sino Lab for Mobile Communications (MCI), 10587 Berlin, Germany

Email: schubert@hhi.fhg.de

28 Scheduling in multiple-antenna multiple-access channel

Holger Boche, Marcin Wiczanowski, and Thomas Haustein

28.1. Introduction to problem statement

Recent evolution of services in cellular wireless networks exhibits a growing importance of pure data traffic, currently in form image transmission and low-rate data download. In future cellular wireless networks *beyond 3G* data connections are expected to become the most significant part of the overall traffic. Such evolution enforces fundamental changes in the philosophy of resource allocation in wireless networks. Classical networks are dominated by voice connections. The aim of classical resource allocation is the satisfaction of SINR (*signal-to-interference-and-noise ratio*) thresholds, which allow for sufficiently perspicuous speech perception [1]. Once the threshold is exceeded, any differences in the SINR values do not lead to perceivable differences in the quality of speech understanding. This is not the case for nonvoice connections in the framework of the so-called *new services*, like, for example, multimedia download, real-time streaming, data upload, and so forth. Under *nonelasticity* of the traffic, that is, in the case when some minimum service quality must be satisfied permanently, equal SINR thresholds are replaced by link-specific thresholds of *quality of service* (QoS). These could be, for example, maximal tolerable delay or minimum tolerable throughput. In the nonvoice case, SINR variations do have influence on human-perceived service quality, which is mirrored, for example, in the fluency of the multimedia stream. A counterpart to nonelastic traffic is *elastic* traffic [2], which has no minimum service requirements and accepts temporary transmission periods with deficient QoS. Optimal resource allocation aims in such case at the optimization of a global cell QoS measure, regarded also as cell, respectively, operator, utility [2]. The example of such elastic connection is high-rate data download. An important class of QoS measures arises from the cross-layer view of the physical and data link layer [3]. This is due to the strong association of issues like queuing delay, buffer occupancy, buffer overflow prevention with human-perceived service quality. In this context, there arises the notion of *scheduling*, which comes originally from computer science, precisely from the investigations of job-sharing schemes. In the context of

wireless networks scheduling is meanwhile understood as the resource allocation and medium access/transmission policy, which is based on some multiuser data link layer objectives like minimum sum of delays, equalization of buffer occupancies, and so forth.[1]

We investigate the cellular uplink, representing a multiple-access channel (MAC) in terms of information theory. The considerations in the remainder concentrate on the scheduling aiming at system *stability*. Stability can be regarded as a global, binary (whether the system is stable or not) QoS measure of the network cell. In these terms stability belongs formally to the framework of scheduling of elastic traffic, but its importance is spanning the traffic-type classes. The central element of the cross-layer uplink model represents queues of bits, which await their transmission at user nodes. Informally said, the system of queues is stable if there is no queue, such that its length blows up to infinity with time. If any queue in the cellular uplink suffers instability, the corresponding buffer overflows and the node is forced to drop the transmission. This machinery makes stability an attractive objective from the system and network operator point of view. The queues are fed by arrival processes of bits or bit-bursts incoming from higher layers. The depletion of the queue system is determined by the physical layer scheduling policy and the quality of channels. Hence, the dynamic behaviour of the queue system, including the stability behaviour, depends on the issues of both physical and data link layer. With any depletion policy is associated a *stability region* of bit arrival rates. In broad terms, it is the set of arrival rate tuples for which the queue system remains stable. From the system point of view it is therefore desired to optimize the queue server, that is, the scheduling policy, in terms of the size of the achievable stability region. Stability-optimal scheduling policy achieves the largest possible stability region and hence allows the operator to carry the densest possible traffic without the need of dropping service of any links.

The presented theoretical framework is developed for multiple-input multiple-output MAC (MIMO-MAC). This is motivated by the high interest in the multiantenna transmission technique, which is a promising candidate for standardization in future networks and includes the SISO transmission as a special case. We first introduce the notation and fundamental definitions arising from the cross-layer view. Then we present formal notions of stability and stability region and introduce the framework of *Lyapunov drift* of Markov chains essential for our results. With these basics we characterize the stability-optimal scheduling policy and analyse the stochastic behaviour of the queue system under its use. Next, we step into the physical layer and study the stability-optimal policy in terms of physical rates and achievable rate regions. Finally, we consider the optimization-theoretic side of stability-optimal scheduling and propose an iterative way of computing the optimal policy.

[1] In numerous works, scheduling is understood as a general medium access/transmission policy, not restricted to data link layer objectives.

28.2. Notation and preliminaries

We consider the uplink with K user nodes $k = 1, 2, \ldots, K$ transmitting to the base station. We time-discretize the considerations in that we observe and influence the system only at discrete-time instances nT, $n \in \mathbb{N}$. When there is no risk of ambiguity, we sometimes omit the dependence on n in the notation. The lack of differentiation between processes and process realizations in our notation does not lead to ambiguities. Symbol $E[x]$ denotes the mean with regards to all values influencing process x.

28.2.1. Data link layer

The traffic of the multiple-access data link layer and higher layers is organized in bursts. The processed data bursts destined for transmission arrive at the data link layer of every user node at arrival times, which are assumed here to be independent of each other. This feature characterizes the *Poisson* arrival process. Knowing or estimating the mean packet lengths $E[l_k]$ and packet arrival rates λ_k, $k = 1, 2, \ldots, K$, we can easily derive bit arrival rates $\rho_k = E[l_k]\lambda_k$, grouped into $\boldsymbol{\rho} = (\rho_1, \rho_2, \ldots, \rho_K)$ [4]. The vector $\mathbf{a}(n) = (a_1(n), a_2(n), \ldots, a_K(n))$ contains the numbers of bits arrived at every queue in the time interval $[(n-1)T; nT]$. Clearly, due to fading channels and interference limitation of the MAC, the data packets in general cannot be transmitted immediately and are queued in queues of lengths $q_k(n)$, grouped into $\mathbf{q}(n) = (q_1(n), q_2(n), \ldots, q_K(n))$. We assume the vector valued process of queue system evolution $\mathbf{q}(n)$ to be stationary and ergodic. The base station is always assumed to have knowledge of the current queue system state $\mathbf{q}(n)$.

28.2.2. Physical layer

Each user node is equipped with n_t transmit antennas and the base station has n_r receiver antennas. However, all results are easily generalizable to the case with different antenna numbers $n_t(k)$, $k = 1, 2, \ldots, K$. Instantaneous and average link rates are grouped into the vectors $\mathbf{R}(n) = (R_1(n), R_2(n), \ldots, R_K(n))$ and $\mathbf{R}^{(E)} = (R_1^{(E)}, R_2^{(E)}, \ldots, R_K^{(E)})$, respectively. The fading process is assumed to be an ergodic process with instantaneous values $\mathcal{H}(n) = \{\mathbf{H}_1(n), \mathbf{H}_2(n), \ldots, \mathbf{H}_K(n)\}$ as K-element sets of $n_r \times n_t$ matrices, such that for any pair (m, n), $m \neq n$, $\mathcal{H}(m)$ and $\mathcal{H}(n)$ are independent (memoryless process). It is assumed that the realizations $\mathcal{H}(n)$ remain nearly constant within time slots $[(n-1)T; nT]$, for any $n \in \mathbb{N}$, which corresponds to the usual block-fading assumption. We assume an additive, spatially uncorrelated white Gaussian noise with covariance matrix $\mathbf{I}\sigma^2$. The $n_t \times n_t$ transmit covariance matrix of node k in time slot $[(n-1)T; nT]$ is $\mathbf{Q}_k(n) = E[\mathbf{x}_k(n)\mathbf{x}_k^H(n)]$, with $\mathbf{x}_k(n)$ as the column vector-valued transmit process. Transmit covariance matrices are grouped in the set $\mathcal{Q}(n) = \{\mathbf{Q}_1(n), \mathbf{Q}_2(n), \ldots, \mathbf{Q}_K(n)\}$ (clearly, $\mathcal{Q}(n)$ with variable $n \in \mathbb{N}$ is a matrix-set-valued process). Transmit covariance matrices can be either calculated at each user node when the channels are known at the transmitters, or be computed at the base station and fed back

through a reliable feedback channel. Hence, we assume perfect channel knowledge at both sides of every link or reliable delayless feedback channels. The power allocation to user nodes during $[(n-1)T; nT]$ is $\mathbf{p}(n) = (p_1(n), p_2(n), \ldots, p_K(n))$. We consider the case of individual transmit power constraints $\hat{\mathbf{p}} = (\hat{p}_1, \hat{p}_2, \ldots, \hat{p}_K)$ and of a global sum-power constraint P. The base station is assumed to perform successive decoding with negligible error propagation. We use the permutation symbol π_k, with $k \in \{1, 2, \ldots, K!\}$, to denote one of $K!$ possible successive interference cancellation (SIC) orders. In such notation link signal $\pi_k(K)$ is decoded first, link signal $\pi_k(K-1)$ is decoded second, ..., and link signal $\pi_k(1)$ is decoded last. Alternatively we write $\pi_k = \pi_k(1) \leftarrow \pi_k(2) \leftarrow \cdots \leftarrow \pi_k(K)$.

28.2.3. Scheduling policies

We regard the scheduling policy as a mapping, which assigns a set of transmit covariance matrices and an SIC order to the set of current channel states, current queue system state, and the time instant itself. Define first a general mapping

$$\{\mathcal{H}(n), \mathbf{q}(n), n\} \longrightarrow \phi(\{\mathcal{H}(n), \mathbf{q}(n), n\}) := \{\mathcal{Q}(n), \pi_k(n)\}. \tag{28.1}$$

We also use the splitted notation for the the mapping according to

$$\begin{aligned} \{\mathcal{H}(n), \mathbf{q}(n), n\} &\longrightarrow \phi_{\mathcal{Q}}(\{\mathcal{H}(n), \mathbf{q}(n), n\}) := \mathcal{Q}(n), \\ \{\mathcal{H}(n), \mathbf{q}(n), n\} &\longrightarrow \phi_{\pi}(\{\mathcal{H}(n), \mathbf{q}(n), n\}) := \pi_k(n) \end{aligned} \tag{28.2}$$

in order to access separately the assigned transmit covariance matrices and the SIC order. The policies of the form (28.1) are realizable in constrained MIMO-MAC only if they pertain to the set

$$\mathcal{M}_{\hat{\mathbf{p}}} = \{\phi : \forall(\mathcal{H}, \mathbf{q}, n, k)\, \text{trace}\,(\phi_{\mathcal{Q},k}(\mathcal{H}, \mathbf{q}, n)) = \mathbf{Q}_k(n) \leq \hat{p}_k\} \tag{28.3}$$

in case of individual power constraints and to the set

$$\mathcal{M}_P = \left\{\phi : \forall(\mathcal{H}, \mathbf{q}, n) \sum_{k=1}^{K} (\phi_{\mathcal{Q},k}(\mathcal{H}, \mathbf{q}, n)) = \sum_{k=1}^{K} \mathbf{Q}_k(n) \leq P\right\} \tag{28.4}$$

in case of sum-power constraint. The dependence on all arguments in (28.1) is not necessary. In particular, in Section 28.5, the special subclass of policies

$$\{\mathcal{H}(n), \mathbf{q}(n)\} \longrightarrow \phi(\{\mathcal{H}(n), \mathbf{q}(n)\}) := \{\mathcal{Q}(n), \pi_k(n)\} \tag{28.5}$$

called *spatial* is of interest. The scheduling policies are assumed to remain constant within time slots $[(n-1)T; nT]$ for any $n \in \mathbb{N}$. The scheme of a routine computing the scheduling policy in the described sense is depicted in Figure 28.1.

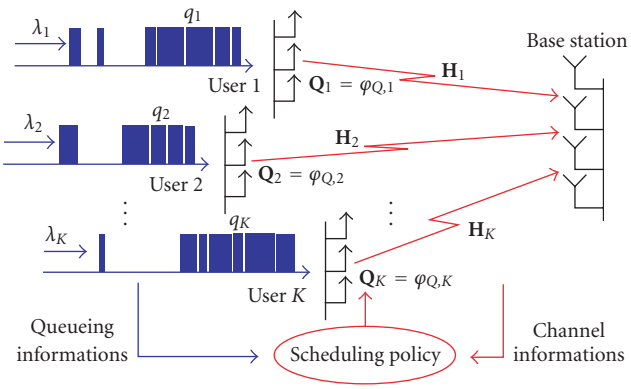

FIGURE 28.1. The routine of computation of a scheduling policy in the MIMO-MAC.

28.2.4. Markov property

The queue lengths evolve according to

$$q_k(n+1) = \left[q_k(n) - R_k(\phi, \mathcal{H}(n))\,T\right]_+ + a_k(n), \tag{28.6}$$

for $n \in \mathbb{N}$ and $k = 1, 2, \ldots, K$, where $[\cdot]_+$ suppresses the term inside, whenever it is negative. In opposition to classical queueing-theoretic literature, we utilize a more precise model of the system and allow for noninteger depletion in every time slot. This implies that $\mathbf{q} \in \mathbb{R}_+^K$ and hence that the domain of $\mathbf{q}$ is uncountable. Utilizing the statements regarding the PASTA (*Poisson arrivals see time averages*) property of Markov chains on countable spaces in [4] and the general theory of Markov chains in [5] the following can be shown.

(i) Due to memorylessness of $\mathcal{H}(n)$ and definition (28.1) the process $\mathbf{q}(n)$ is a DTMC (*discrete-time Markov chain*) on $\mathbb{R}_+^K$.

(ii) The DTMC $\mathbf{q}(n)$ is ψ-irreducible, with ψ as the *maximal irreducibility measure*.

The last property corresponds to simple irreducibility of Markov chains on countable spaces, since it implies that there is a nonzero probability of achieving a state in any set $A \subset \mathbb{R}_+^K$, with $\psi(A) > 0$ (in most cases we can take ψ simply as the K-fold product measure of Lebesque measures on $\mathbb{R}_+$).

28.3. Stability analysis

With the above statements we are prepared for the brief introduction of the framework of stability analysis. Due to the Markov property of the queue system behaviour in the MIMO-MAC our concern is in Markovian systems. In this field we find the drift techniques basing on *Lyapunov* functions to be the key tool in our considerations.

28.3.1. Different stability notions

There are three notions of stability, which are of interest.

Definition 28.1 (observation based stability). The system of K queues is called stable, if for all $k = 1, 2, \ldots, K$, it holds that

$$\lim_{M\to\infty} g_k(M) = 0, \tag{28.7}$$

with

$$\begin{aligned} g_k(M) &= \operatorname{limsup}_{t\to\infty} \frac{1}{t} \int_0^t \mathbf{1}_{\{q_k(\tau)\geq M\}} \tau d\tau, \\ \mathbf{1}_{\{q_k(\tau)\geq M\}} &= \begin{cases} 1 & q_k(\tau) \geq M, \\ 0 & \text{elsewhere.} \end{cases} \end{aligned} \tag{28.8}$$

Definition 28.2 (weak stability). The queue system is called weakly stable, if for every $\epsilon > 0$, there exist $B > 0$ and $n_0 = n_0(\epsilon)$, such that for all $n \geq n_0$,

$$\Pr\left[||\mathbf{q}(n)|| > B\right] < \epsilon, \tag{28.9}$$

where $\|\cdot\|$ denotes any vector norm.

Definition 28.3 (strong stability). The queue system is called strongly stable, if

$$\operatorname{limsup}_{n\to\infty} E[||\mathbf{q}(n)||] < \infty. \tag{28.10}$$

In broad terms, observation-based stability notion requires the queue system to assume infinite lengths of any queue extremely rarely. With Markov inequality, it can be further shown that strong stability implies the weak one but not inversely. Interestingly, none of the above stability definitions requires the existence of a steady-state distribution of the DTMC describing the system evolution. The existence of the steady state of the DTMC is implied by its *positive recurrence*, which means that any accessible state can be achieved in finite number of steps when starting from an arbitrary state. Positive recurrence of a DTMC is also a sufficient condition for its weak stability [5]. Under steady-state existence, limit expressions arise in Definitions 28.1 and 28.3. With ergodicity of the queue evolution process there also arises a connection to observation-based notion of stability. Since under ergodicity the time portion spend in any state corresponds to the stationary probability of this state, the observation-based stability becomes the weak one.

28.3.2. Stability region

We can associate different stability regions with different policies of serving the queue system. We use the term stability region to describe the largest achievable stability region for the given queue system.

Definition 28.4. The stability region $\mathcal{D}$ of the system of K queues is the set of all arrival rate vectors $\boldsymbol{\rho}$, such that there exists a possibility to achieve stability in the observation-based sense for all arrival rate vectors lying in the interior of $\mathcal{D}$.

Loynes' theorem [6] additionally says that for vectors pertaining to the boundary of the stability region, stability is possible, but not guaranteed. Moreover, in such case also the so-called *substability* can occur [6].

28.3.3. Drift and Lyapunov functions

Stability of the queue system can be determined using a specific lower-bounded real-valued function $L(\mathbf{q}(n))$, called *Lyapunov* function. The theory of stability determination by means of drift conditions and Lyapunov functions is well developed [5, 7]. Here we only outline statements of interest and refer to the literature for details.

Theorem 28.5. *Given the system of K queues evolving according to a ψ-irreducible DTMC, if there exist $B < \infty$, $\alpha > 0$, and a lower-bounded real-valued function $L : \mathbb{R}^K \to \mathbb{R}$, such that*

$$\begin{aligned} \forall \mathbf{q}(n) : ||\mathbf{q}(n)|| \leq B, \quad E[L(\mathbf{q}(n+1))\,|\mathbf{q}(n)] < \infty, \\ \forall \mathbf{q}(n) : ||\mathbf{q}(n)|| > B, \quad E[L(\mathbf{q}(n+1)) - L(\mathbf{q}(n))\,|\,\mathbf{q}(n)] \leq -\alpha, \end{aligned} \tag{28.11}$$

then the DTMC is positive recurrent and for all $\epsilon > 0$, there exists $B > 0$, such that

$$\lim_{n\to\infty} \Pr\left[||\mathbf{q}(n)|| > B\right] = \Pr_{\text{stat}}\left[\|\mathbf{q}\| > B\right] < \epsilon. \tag{28.12}$$

In other words, the queue system does not blow up to infinity and approaches a steady state in the sense of stationary distribution, if for the corresponding DTMC, there exists a Lyapunov function with finite conditional one-step mean. Further it must hold that the DTMC has the tendency to decrease the conditional one-step mean of the Lyapunov function, whenever the state is outside some compact set of states. From the last subsection it is also clear that Theorem 28.5 implies weak stability of the queue system.

Theorem 28.6. *Given the system of K queues evolving according to a ψ-irreducible DTMC, if there exist a lower-bounded real-valued function $L : \mathbb{R}^K \to \mathbb{R}$ and positive scalars α and $C < \infty$, such that*

$$\forall \mathbf{q}(n), \quad E[L(\mathbf{q}(n+1)) - L(\mathbf{q}(n))\,|\mathbf{q}(n)] \leq C - \alpha||\mathbf{q}(n)||, \tag{28.13}$$

then the DTMC is positive recurrent and additionally

$$\lim_{n\to\infty} E[||\mathbf{q}(n)||] = E_{\text{stat}}[\|\mathbf{q}\|] < \infty. \tag{28.14}$$

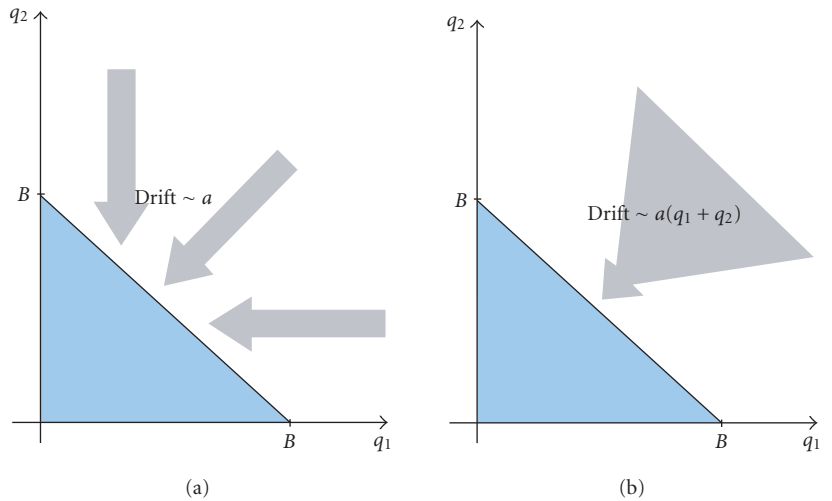

FIGURE 28.2. Schematic illustration of the drift of the DTMC describing the queue system evolution in the weak (left) and strong (right) stability case assuming $\|\mathbf{q}(n)\| := \|\mathbf{q}(n)\|_1$ and two queues.

The theorem implies strong stability and provides a concrete illustration of strong stability property and its difference to weak stability. If the tendency of the DTMC to decrease the conditional mean of the Lyapunov function increases proportionally to the norm of the system state, then there exists a stationary distribution with finite mean and the stability is strong. In the general case, when the drift is proportional to any nonnegative function of the system state $f(\mathbf{q}(n))$, the system property implied by Theorem 28.6 is called *f-ergodicity* (not to be confused with the ergodicity in the usual sense!). Figure 28.2 illustrates schematically the drift theorems in the two-queue case. For more details regarding drift conditions, like, for example, the type of convergence to the stationary distribution, we refer to [5, 7].

28.4. Optimal scheduling policy—the data link layer view

With the general insights from the last section we now step into the particular analysis of stability in the MIMO-MAC. We propose a stability-optimal scheduling policy and show its influence on the stochastic system behaviour.

28.4.1. Stability-optimal scheduling

We desire to analyse the Lyapunov drift in the queue system in the MIMO-MAC using simple quadratic Lyapunov function of the form

$$L(\mathbf{q}) = ||\mathbf{q}(n)||_2^2 = \sum_{k=1}^{K} q_k^2(n), \tag{28.15}$$

as is done, for example, in [8, 9]. With this function we are able to characterize a scheduling policy achieving the largest stability region. This is expressed by the following theorem proven in [10] (see also [8]). In the theorem, $\mathcal{M}$ is a universal notation for $\mathcal{M}_{\hat{\mathbf{P}}}$ and $\mathcal{M}_P$, depending on constraint type.

Theorem 28.7. *The largest stability region in the MIMO-MAC with K links is achieved by the scheduling policy $\hat{\phi}$ satisfying*

$$\hat{\phi} = \arg\max_{\phi \in \mathcal{M}} \sum_{k=1}^{K} q_k(n) R_k\big(\phi, \mathcal{H}(n)\big), \tag{28.16}$$

for all $n \in \mathbb{N}$.

For readers familiar with system control and dynamic system theory, the result is not surprising. The principle of weighted sum, as in (28.16), occurs in the context of stability-optimal policies in many fields, like, for example, switch theory in wired networks [11, 12] and automation network control [9]. An obvious conclusion from (28.16) is that the knowledge of arrival rate vector cannot be utilized to improve the stability behaviour of the MIMO-MAC, since the functional in (28.16) is independent of it. This is a specific feature of stability-optimal scheduling. If any other cross-layer policy is utilized, like, for example, the one aiming at minimizing the maximal queue length or the sum of all queue lengths, then knowledge of ρ is required. We observe that the objective $\sum_{k=1}^{K} q_k(n) R_k(\phi, \mathcal{H}(n))$ is maximized if the majorization order of assigned rates complies with the majorization order of corresponding queue lengths. The length of the queue can be regarded as a temporary measure of threat by instability. According to Theorem 28.7, the most threatened queues are assigned highest depletion rates, which reduces their instability potential, relatively to other queues, until the next scheduling time instant. This machinery shows the plausibility behind Theorem 28.7.

28.4.2. Stochastic behaviour

Since the proof of Theorem 28.7 is based on the Lyapunov drift condition for weak stability in Theorem 28.5, it can be concluded that the DTMC $\mathbf{q}(n)$ approaches a stationary state and weak stability of $\mathbf{q}(n)$ is guaranteed. The next corollary shows even more.

Corollary 28.8. *Under the use of policy $\hat{\phi}$ in the MIMO-MAC, for any vector of bit arrival rates from the interior of the stability region achieved by $\hat{\phi}$, it holds that*

$$\lim_{n \to \infty} E[||\mathbf{q}(n)||] < \infty. \tag{28.17}$$

Hence, the policy $\hat{\phi}$ guarantees strong stability for stabilizable arrival rate vectors. Regarding the norm in (28.17) as the maximum norm, it follows that the

average occupancy of every buffer in the steady state is finite. We can go even a step further and provide a bound for the first moment of the system in the steady state.

Corollary 28.9. *Under the use of policy $\hat{\phi}$ in the MIMO-MAC, for any vector of bit arrival rates from the interior of the stability region achieved by $\hat{\phi}$, the first moment of the queue system satisfies*

$$\lim_{n\to\infty} E[||\mathbf{q}(n)||] \leq \frac{TC}{2\alpha}, \tag{28.18}$$

with $C < \infty$ and α expressing the distance $\mathbf{d} := \alpha\mathbf{1}$ between $\boldsymbol{\rho}$ and the boundary of the stability region.

We conclude that with decreasing distance of the arrival rate vector to the boundary of the stability region the bound on average system occupancy (28.18) increases and becomes trivial at the boundary (possible instability). By means of Markov inequality we can extract from (28.18) steady-state buffer occupancy asymptotics. For any threshold value γ, we yield

$$\begin{aligned}\lim_{n\to\infty} \Pr\left[||\mathbf{q}(n)|| \geq \gamma\right] &= \lim_{n\to\infty} \Pr\left[\frac{||\mathbf{q}(n)||}{\gamma} \geq 1\right] \\ &\leq \lim_{n\to\infty} \frac{1}{\gamma} E[||\mathbf{q}(n)||] \leq \frac{TC}{2\alpha\gamma}.\end{aligned} \tag{28.19}$$

To completely characterize the behaviour under policy $\hat{\phi}$ it is necessary to have insights holding for nT, with $n \in \mathbb{N}$, and not only for the stochastically stationary state under $n \to \infty$. Some insights are provided by the following theorem.

Theorem 28.10. *Under the use of policy $\hat{\phi}$ in the MIMO-MAC, for any vector of bit arrival rates from the interior of the stability region achieved by $\hat{\phi}$, it holds that*

(i) $E[\sup_n \|\mathbf{q}(n)\|] < \infty$, *which further implies*

(ii) $\Pr[\|\mathbf{q}(n)\|_m^m < \infty] = 1$, *for* $m = 1, 2$.

Especially property (i) illustrates that the system is very well behaved under the use of $\hat{\phi}$.

In [10], we outline further features of the stochastic behaviour and characterize the type of convergence to the stationary state. Further we assume there a modified, event-dependent pattern of control instances $\{t_n\}_{n\in\mathbb{N}}$ instead of nT. This is an analytical model accounting for boundness of the number of arrivals in time slots, which is the case under real-world conditions. In such realistic case the geometric moment $E[\exp(\epsilon\|\mathbf{q}(n)\|)]$ ($\epsilon > 0$ is some system-dependent constant) can be shown to be bounded. This very restrictive feature further implies an

asymptote on buffer occupancies of the form

$$\limsup_{\gamma\to\infty} \frac{\log\left(\Pr\left[||\mathbf{q}(t_n)|| > \gamma\right]\right)}{\gamma} \leq -\epsilon. \tag{28.20}$$

28.4.3. Stability region

The remaining question is the question of possibility of further characterization of the stability region of the MIMO-MAC, which is achieved by policy $\widehat{\phi}$. The next statement, proven in [10], provides such characterization.

Theorem 28.11. *The stability region of the MIMO-MAC is equal to the ergodic capacity region of the MIMO-MAC (i.e., the set of all achievable* $\mathbf{R}^{(E)}$*).*

The above theorem provides a junction between pure queuing-theoretic phenomena of the data link layer and the physical layer issues like capacity and capacity region. Such interlayer dependence could be expected since the service process of the queue system is determined by physical layer issues. The plausibility behind the result is clear. The arrival rate tuples which componentwise do not exceed the achievable service rate tuples lead to a stable MIMO-MAC. The system disposes in such case of sufficient depletion resources to prevent exploding queue lengths. On the other side, if any arrival rate is greater than the achievable depletion rate, the queue length will blow up to infinity with $n \to \infty$ regardless of utilized scheduling policy.

28.5. Optimal scheduling policy—the physical layer view

We now move one layer downwards in the communication stack and study the stability-optimal scheduling policy in the framework of physical layer transmit strategies. The section gives insights in the geometry behind stability-optimal scheduling and explains the stability-optimal choice of the link decoding order.

28.5.1. Geometry behind optimization

Consider the optimization problem leading to the stability-optimal policy

$$\max_{\phi\in\mathcal{M}} \mathbf{q}(n)^T \mathbf{R}(\phi, \mathcal{H}(n)), \tag{28.21}$$

for $n \in \mathbb{N}$. It is obvious that in terms of rates the above problem can be rewritten as

$$\max_{\mathbf{R}(n)\in\mathcal{C}(\mathcal{H}(n))} \mathbf{q}(n)^T \mathbf{R}(n), \tag{28.22}$$

with $\mathcal{C}(\mathcal{H}(n))$ as the instantaneous capacity region of the MIMO-MAC, which is

$$\begin{aligned}&\mathcal{C}(\mathcal{H}(n))\\&\quad=\mathbf{cl}\left\{\bigcup_{\phi(\mathcal{H}(n)):\phi\in\mathcal{M}}\left\{\mathbf{R}\geq 0:\sum_{k\in A}R_k\right.\right.\\&\qquad\left.\left.\leq\log\det\left(\mathbf{I}+\frac{1}{\sigma^2}\sum_{k\in A}\mathbf{H}_k(n)\phi_{\mathcal{Q},k}(\mathcal{H}(n))\mathbf{H}_k^H(n)\right),\ A\subseteq\{1,\ldots,K\}\right\}\right\},\end{aligned}\tag{28.23}$$

where **cl** denotes the closure operation (depending on constraint type $\mathcal{M}=\mathcal{M}_{\hat{\mathbf{p}}}$ or $\mathcal{M}=\mathcal{M}_P$). From basics of information theory we know that the capacity region of MAC is convex [13]. Further, the objective in (28.22) corresponds to a hyperplane with normal vector $\mathbf{q}(n)$. Hence, the optimization (28.22) corresponds to finding a point (rate vector), at which the hyperplane $\mathbf{q}(n)^T\mathbf{R}(n)=\text{const}$ supports the instantaneous capacity region [14]—the so-called *Pareto optimal* or *Pareto efficient* point.

28.5.2. Stability optimality of the SIC order and spatial scheduling policy

The rate vectors included in the capacity region can be achieved by different transmit-receive strategies, like successive decoding, linear joint decoding, and time sharing (combination over time) of both of them, and so forth. From information theory we know again [13] that all vectors at the boundary of the capacity region can be achieved by SIC and time sharing (the approach of the so-called *rate splitting* is also known [15]). In this context, we define special subregions $\mathcal{S}_{\pi_k}(\mathcal{H}(n))$ of the entire capacity region $\mathcal{C}(\mathcal{H}(n))$, with $k=1,2,\ldots,K!$, which are the regions of all rate vectors achievable by transmit strategies utilizing the SIC order π_k. They can be described as

$$\begin{aligned}&\mathcal{S}_{\pi_k}(\mathcal{H}(n))\\&=\mathbf{cl}\left\{\bigcup_{\substack{\phi(\mathcal{H}(n)):\\ \phi\in\mathcal{M},\phi_\pi(\mathcal{H}(n))=\pi_k}}\ \bigcup_{\substack{0\leq\boldsymbol{\beta}\leq\mathbf{1}\\ \beta_{\pi_k(K)}=1}}\left\{\mathbf{R}\geq 0:R_{\pi_k(i)}\right.\right.\\&\left.\left.\leq\log\frac{\det\left(\mathbf{I}\sigma^2+\sum_{j=1}^{i}\beta_{\pi_k(j)}\mathbf{H}_{\pi_k(j)}(n)\phi_{\mathcal{Q},\pi_k(j)}(\mathcal{H}(n))\mathbf{H}_{\pi_k(j)}^H(n)\right)}{\det\left(\mathbf{I}\sigma^2+\sum_{j=1}^{i-1}\beta_{\pi_k(j)}\mathbf{H}_{\pi_k(j)}(n)\phi_{\mathcal{Q},\pi_k(j)}(\mathcal{H}(n))\mathbf{H}_{\pi_k(j)}^H(n)\right)},\ i\in\{1,\ldots,K\}\right\}\right\},\end{aligned}\tag{28.24}$$

with $k=1,2,\ldots,K!$. We refer to regions $\mathcal{S}_{\pi_k}(\mathcal{H}(n))$ as the *S-rate regions*, since they are associated with transmit-receive strategies utilizing pure spatial channelization of link signals within one SIC order. Analogically, we refer to scheduling policies utilizing pure spatial channelization in all time slots $[(n-1)T;nT]$ as spatial policies. Spatial policies are mappings of the form (28.5), where in comparison

to (28.1) the time argument accounting for possible time sharing disappears. Consequently, under a spatial policy the transmit strategy is determined solely by the queue system state and the channel states and does not depend directly on time.

For the instantaneous capacity region, it holds obviously that

$$\mathcal{C}(\mathcal{H}) = \mathbf{conv}\left(\bigcup_{k=1,2,\ldots,K!} \mathcal{S}_{\pi_k}(\mathcal{H})\right), \tag{28.25}$$

with the convex-hull operator **conv** accounting for arbitrary time-sharing combinations. An immediately arising conclusion is that stability-optimal rate tuples resulting from (28.22) can be achievable by different SIC orders at different time instants $n \in \mathbb{N}$, depending on the current state $\mathbf{q}(n)$. In this context we desire a more detailed characterization of the optimal scheduling policy $\hat{\phi}$ in terms of the $\mathbf{q}(n)$-dependent choice of SIC order. Such characterization is done in the following theorem, which is based on the results from [16].

Theorem 28.12. *The largest stability region in the MIMO-MAC with K links is achieved by the spatial scheduling policy $\hat{\phi}^S$ satisfying*

$$\hat{\phi}^S_{\mathcal{Q}} = \arg\max_{\phi_{\mathcal{Q}}:\phi\in\mathcal{M}} \sum_{k=1}^{K} q_k(n) R_k(\phi_{\mathcal{Q}}, \mathcal{H}(n)), \tag{28.26}$$

$$q_{\pi(1)}(n) \geq q_{\pi(2)}(n) \geq \cdots \geq q_{\pi(K)}(n) \geq 0, \tag{28.27}$$

with $\pi = \phi^S_\pi$ for all $n \in \mathbb{N}$.

An obvious conclusion is that since there exists a spatial stability-optimal scheduling policy, there is no need to resort to time sharing among different SIC orders. This is a significant advantage in terms of implementation efficiency and cost. Another interesting insight following from the theorem is that at any time $n \in \mathbb{N}$ the stability-optimal SIC order is determined solely by the current queue system state and is independent of the channel fading states. Chain inequality (28.27) is illustrative and says that under stability-optimal policy link signals have to be decoded in the order complying with the increasing order of current queue lengths. Assuming the choice of SIC order satisfying (28.27), the set of transmit covariance matrices $\phi^S_{\mathcal{Q}} = \mathcal{Q}$ then has to satisfy (28.26). Depending on the dynamics of queue system evolution, it is possibly not necessary to change the SIC order at every control time instant nT. On the other side, the frequency of changes of transmit covariance matrices depends highly on the fading process. In Figure 28.3 a scheme of the routine conducting spatial stability-optimal scheduling is presented. Using the introduced notion of S-rate regions, Theorem 28.12 is easily interpretable in terms of optimization over rates. Precisely, the theorem says that the stability-optimal rate tuple solves

$$\max_{\mathbf{R}\in\mathcal{S}_\pi(\mathcal{H}(n))} \mathbf{q}^T(n)\mathbf{R}(n) \tag{28.28}$$

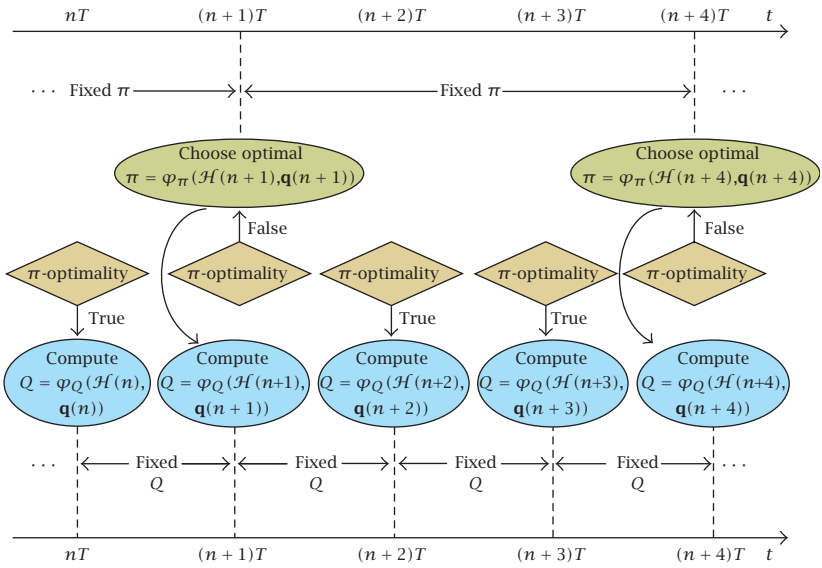

FIGURE 28.3. A schematic graph of the routine computing spatial stability-optimal scheduling policy in the MIMO-MAC.

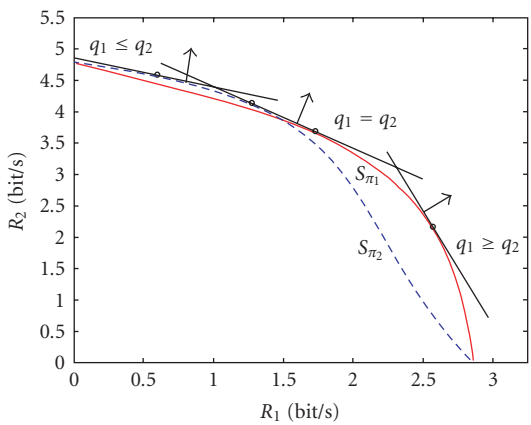

FIGURE 28.4. Exemplary instantaneous capacity region of a 2×2 sum-power constrained MIMO-MAC with two links (channel matrices generated randomly from the elementwise uniform distribution with average SINR = 6 dB, SIC orders $\pi_1 = 1 \leftarrow 2$, $\pi_2 = 2 \leftarrow 1$). Three exemplary optimization objectives are modelled by lines with normal vectors corresponding to queue system states.

for $n \in \mathbb{N}$ with π characterized by (28.27). This is a precise restatement of (28.22) for spatial scheduling policies. The geometric view of (28.22) and (28.28) is provided in Figure 28.4, where an exemplary instantaneous capacity region and S-rate regions of a two-link MIMO-MAC are plotted. The optimization objectives are associated with queue system states satisfying (28.27) for two different SIC orders and both SIC orders together (i.e., $q_1 = q_2$). Given any such $\mathbf{q}(n)$, the

stability-optimal rate tuple represents the point of support at the boundary of the capacity region, which pertains to S-rate region $\mathcal{S}_{\pi_k}(\mathcal{H}(n))$ if $\phi_\pi^S = \pi_k$ satisfies (28.27). For the symmetric queue system state, both SIC orders are stability-optimal and the associated hyperline supports both S-rate regions. Figure 28.4 makes plausible (which is shown with more formality in [16]) that the boundary part of any S-rate region $\mathcal{S}_{\pi_k}(\mathcal{H}(n))$, which is supportable by hyperplanes satisfying (28.27) with $\pi = \pi_k$, is convex, whereas the complementary boundary parts are in general nonconvex. Moreover, the independence of channel states in (28.27) shows that the geometric "positions" of convex boundary parts of all S-rate regions do not depend on fading states.

28.5.3. Overall optimality of the SIC order

Chain inequality (28.27) characterizes the stability-optimal SIC order for a current queue system state $\mathbf{q}(n)$. We ask if there is a possibility that a certain SIC order $\widehat{\pi}$ is optimal regardless of the queue system state. It can be concluded from Figure 28.4 and Theorem 28.12 that in such case the entire boundary of the capacity region must pertain to the S-rate region $\mathcal{S}_{\widehat{\pi}}(\mathcal{H}(n))$ and for the normal vectors $\mathbf{q}$ of all supporting hyperplanes condition (28.27) must hold with $\pi = \widehat{\pi}$. Consequently, it must hold that $\mathcal{C}(\mathcal{H}(n)) = \mathcal{S}_{\widehat{\pi}}(\mathcal{H}(n))$, that is, $\widehat{\pi}$ is a unique superior SIC order also in terms of capacity. The answer to the question turns out to be constraint-type dependent.

Theorem 28.13. *In the MIMO-MAC with individual power constraints no SIC order can be instantaneously stability-optimal for all queue system states. In the sum-power constrained MIMO-MAC the SIC order $\widehat{\pi}$ is instantaneously stability-optimal for all queue system states if and only if there exist a queue system state $\mathbf{q}$ and a constant C satisfying*

$$\begin{aligned}
&\lambda_{\mathrm{MAX}}\left(q_{\widehat{\pi}(K)}\mathbf{H}_{\widehat{\pi}(K)}^H\left(\mathbf{I}\sigma^2 + \mathbf{H}_{\widehat{\pi}(K)}\mathbf{Q}_{\widehat{\pi}(K)}\mathbf{H}_{\widehat{\pi}(K)}^H\right)^{-1}\mathbf{H}_{\widehat{\pi}(K)}\right) = C,\\
&\lambda_{\mathrm{MAX}}\left(q_{\widehat{\pi}(K)}\mathbf{H}_{\widehat{\pi}(k)}^H\left(\mathbf{I}\sigma^2 + \mathbf{H}_{\widehat{\pi}(K)}\mathbf{Q}_{\widehat{\pi}(K)}\mathbf{H}_{\widehat{\pi}(K)}^H\right)^{-1}\mathbf{H}_{\widehat{\pi}(i)}\right.\\
&\qquad\left. + \frac{1}{\sigma^2}(q_{\widehat{\pi}(k)} - q_{\widehat{\pi}(K)})\mathbf{H}_{\widehat{\pi}(k)}^H\mathbf{H}_{\widehat{\pi}(k)}\right) \le C \quad \forall 1 \le k < K.
\end{aligned} \tag{28.29}$$

The theorem is proven in [17]. The illustration to overall optimality of SIC order is provided in Figure 28.5. It can be seen there that the SIC order $\widehat{\pi} = \pi_1 = 1 \leftarrow 2$ is optimal for all queue system states, since the corresponding S-rate region $\mathcal{S}_{\pi_1}(\mathcal{H}(n))$ equals the capacity region. The other S-rate region is a proper subset of the overall optimal one. Moreover, the convex-hull part of the capacity region vanishes and the capacity region can be shown to be strictly convex.

28.6. Optimal scheduling policy—the optimization-theoretic view

From the last section we already know the machinery behind the stability-optimal policy in terms of physical rates and decoding orders. Now, we approach the

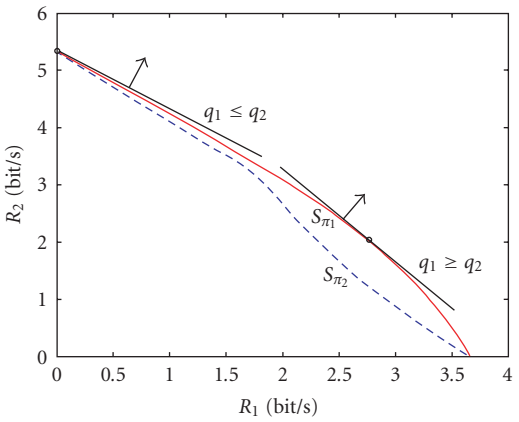

FIGURE 28.5. Exemplary instantaneous capacity region of a 2×2 sum-power constrained MIMO-MAC with two links (channel matrices generated randomly from the elementwise uniform distribution with average SINR = 6 dB, SIC orders $\pi_1 = 1 \leftarrow 2$, $\pi_2 = 2 \leftarrow 1$) under overall optimality of SIC order $\pi_1 = 1 \leftarrow 2$.

problem of determining instantaneous stability-optimal transmit strategy in more detail in terms of optimization theory.

28.6.1. Stability-optimal transmit covariance matrices

Having the characterization of stability-optimal SIC order at hand, the interest is in the manner of specification of stability-optimal transmit covariance matrix set $\phi_{\mathcal{Q}}^{S} = \mathcal{Q}$, that is, in the more precise reformulation of (28.26). For this aim, the optimization problem stated over the capacity region (28.22) must be transferred into the domain of trace-constrained positive-semidefinite matrix sets $\mathcal{Q}$. Since every S-rate region is in general a nonconvex set and represents the optimization domain in (28.28), it can be expected that the optimization problem leading to optimal transmit covariance matrices is also nonconvex. Interestingly, the next theorem shows the counterpart.

Theorem 28.14. *Given any queue system state* $\mathbf{q}(n)$*, any set of fading states* $\mathcal{H}(n)$ *and the stability-optimal SIC order* π *satisfying* (28.27)*, the optimization problem leading to stability-optimal transmit covariance matrix set has the form*

$$\max_{\substack{\mathcal{Q}=\phi_{\mathcal{Q}}^{S}:\mathbf{Q}_k\geq 0\\ \phi^{S}\in\mathcal{M}}} \sum_{k=1}^{K} \left(q_{\pi(k)} - q_{\pi(k+1)}\right) \log\det\left(\mathbf{I}\sigma^2 + \sum_{j=1}^{i} \mathbf{H}_{\pi(j)}(n)\mathbf{Q}_{\pi(j)}\mathbf{H}_{\pi(j)}^{H}(n)\right) \quad (28.30)$$

and is convex ($\mathcal{M} = \mathcal{M}_{\hat{\mathbf{P}}}$ *or* $\mathcal{M} = \mathcal{M}_P$ *depending on constraint type).*

The theorem results from simple regrouping of capacity terms of successively decoded links in the functional $\mathbf{q}^T\mathbf{R}$. Convexity of the problem specifying stability-optimal transmit covariance matrices is of extreme importance in terms of design

and implementation of iterative optimization routines in real-world systems. Contrary to general nonconvex optimization problems the solution to the convex optimization problem can be found iteratively regardless of the starting point of the search. The optimizer set of the convex problem is a connected set, in particular, a unique optimizer. Iterative convex optimization methods are well developed and allow also for the analysis of convergence rate to the optimum. The Karush-Kuhn-Tucker (KKT) conditions of convex problems are necessary and sufficient for the optimum, and can be utilized in the design of iterative optimization methods (e.g., dual and primal-dual interior-point methods, see [14]). All these features of convex optimization let us regard convex optimization problems as efficiently solvable. On the other side, a great class of nonconvex problems is not efficiently solvable in real-world applications because of existence of several disconnected local optimizer sets and hence the dependence on the starting search point in the corresponding optimization routines. In Section 28.6.5, we present our iterative approach to computing the instantaneous stability-optimal set of transmit covariance matrices.

The KKT conditions for the problem (28.30) can be written in case of MIMO-MAC with individual power constraints, for all $1 \leq k \leq K$, as [17]

$$\begin{gathered}
-\mathbf{Q}_{\pi(k)} \preceq 0, \\
\operatorname{trace}\left(\mathbf{Q}_{\pi(k)}\right) - p_{\pi(k)} \leq 0, \\
\mathbf{Z}_{\pi(k)} \succeq 0, \\
\lambda_{\pi(k)} \geq 0, \\
\operatorname{trace}\left(\mathbf{Q}_{\pi(k)}\mathbf{Z}_{\pi(k)}\right) = 0, \\
\lambda_{\pi(k)}\left(\operatorname{tr}\left(\mathbf{Q}_{\pi(k)}\right) - p_{\pi(k)}\right) = 0, \\
\sum_{j=k}^{K}\left(q_{\pi(j)} - q_{\pi(j+1)}\right)\mathbf{H}_{\pi(k)}^{H} \times \left(\mathbf{I}\sigma^2 + \sum_{i=1}^{j}\mathbf{H}_{\pi(i)}\mathbf{Q}_{\pi(i)}\mathbf{H}_{\pi(i)}^{H}\right)^{-1}\mathbf{H}_{\pi(k)} = \lambda_{\pi(k)}\mathbf{I} - \mathbf{Z}_{\pi(k)}
\end{gathered} \tag{28.31}$$

and in case of sum-power constrained MIMO-MAC, for all $1 \leq k \leq K$, as

$$\begin{gathered}
-\mathbf{Q}_{\pi(k)} \preceq 0, \\
\sum_{k=1}^{K}\operatorname{trace}\left(\mathbf{Q}_{\pi(k)}\right) - P \leq 0, \\
\mathbf{Z}_{\pi(k)} \succeq 0, \\
\lambda \geq 0, \\
\operatorname{tr}\left(\mathbf{Q}_{\pi(k)}\mathbf{Z}_{\pi(k)}\right) = 0, \\
\lambda\left(\sum_{k=1}^{K}\operatorname{trace}\left(\mathbf{Q}_{\pi(k)}\right) - P\right) = 0, \\
\sum_{j=k}^{K}\left(q_{\pi(j)} - q_{\pi(j+1)}\right)\mathbf{H}_{\pi(k)}^{H} \times \left(\mathbf{I}\sigma^2 + \sum_{i=1}^{j}\mathbf{H}_{\pi(i)}\mathbf{Q}_{\pi(i)}\mathbf{H}_{\pi(i)}^{H}\right)^{-1}\mathbf{H}_{\pi(k)} = \lambda\mathbf{I} - \mathbf{Z}_{\pi(k)}.
\end{gathered} \tag{28.32}$$

The scalar λ, vector $\boldsymbol{\lambda} = (\lambda_1, \lambda_2, \ldots, \lambda_K)$, and matrix sets $\mathcal{Z} = \{\mathbf{Z}_k\}_{k=1}^{K}$ are dual variables resulting from the Lagrangean statement for the problem (28.30). The sets of KKT conditions are the origin of our optimization-theoretic insights to be presented.

28.6.2. Stability-optimal transmission for $N < K$ busy queues

It is plausible that in the real-world cellular uplink some nodes happen to have empty queues during single time slots $[(n-1)T; nT]$ or possibly even over longer time periods. We call such nodes (and queues) idle, in difference to other active or busy nodes (and queues). It is of importance for the network provider to dispose of insights in the features of instantaneous stability-optimal transmission strategy under only $N < K$ busy queues. Precisely, the question of interest can be the allocation of powers among all links as in the case of overall optimality of the SIC order, this issue turns out to be constraint-type dependent.

Theorem 28.15. *In the MIMO-MAC with individual power constraints subject to stability-optimal scheduling policy all links corresponding to idle queues can be allocated transmit powers* $0 \leq p_k \leq \widehat{p}_k$, *whereas in the sum-power constrained MIMO-MAC subject to stability-optimal scheduling the links corresponding to idle queues must also be kept idle.*

The theorem is proven in [17]. We conclude that the intuitively plausible equivalence idle queue $\equiv$ idle link holds only in the case of sum-power constrained MIMO-MAC and does not hold under individual power constraints. This feature can be explained by the fact that in case of sum-power constraints the links are coupled both by interference and by the joint resource budge. Hence, busy nodes needing the power resource to deplete the queues have to partition it optimally and entirely among them and there remains no residual resource to be partitioned among idle queues. In opposition to this, under individual power constraints, every node transmit power is constrained and hence node power budgets are decoupled. Due to this busy nodes cannot use more power than the sum of their power constraints, so that there remains power to be allocated to idle nodes. Idle nodes are allowed to use this power, when their transmission does not disturb the optimality of transmission of busy links characterized by (28.27) and (28.30). This is the case when their links are decoded before all links corresponding to busy nodes, since then the busy nodes do not "see" the interference caused by the links of idle nodes. On the other side, links of idle nodes suffer the entire interference from busy nodes.

28.6.3. Stability optimality of $N < K$ link regime

The problem of $N < K$ link regimes is someway complementary to the problem of optimal transmission under $N < K$ busy queues. We now assume that all queues

in the MIMO-MAC are busy and study stability optimality of the transmission strategy allowing only $N < K$ links be allocated nonzero transmit powers. Assuming a subset of active links A, with $\mathrm{Card}(A) = N$, we call such transmission scheme N link regime and denote it by $\mathcal{U}(A)$. Conditions for instantaneous optimality of any $N < K$ link regime can lead to reduction of computational complexity of the stability-optimal policy. This is because the evaluation of such conditions preceding the optimization process can lead to the identification of active link subset and reduce the dimension of the optimization process by $K - N$. Again, our results from [17] stated in the following theorem indicate constraint-type dependence of the optimality of N link regimes.

Theorem 28.16. *Assume that there are no idle queues in the MIMO-MAC. Then,*

(i) *under individual power constraints and stability-optimal scheduling policy, all links have to be allocated maximal powers* $\widehat{p}_k$, $k = 1, 2, \ldots, K$,

(ii) *under sum-power constraints and stability-optimal scheduling policy, the* N *link regime of a link subset* $A \subset \{1, 2, \ldots, K\}$ *is stability-optimal for some queue system state* $\mathbf{q}$ *if and only if*

$$\lambda_{\mathrm{MAX}}\left(\sum_{j=k}^{K}\left(q_{\pi(j)} - q_{\pi(j+1)}\right)\mathbf{H}_{\pi(k)}^{H} \times \left(\mathbf{I}\sigma^2 + \sum_{i=1,\pi(i)\in A}^{j}\mathbf{H}_{\pi(i)}\mathbf{Q}_{\pi(i)}\mathbf{H}_{\pi(i)}^{H}\right)^{-1}\mathbf{H}_{\pi(k)}\right) = C \quad \forall \pi(k) \in A,$$

$$\lambda_{\mathrm{MAX}}\left(\sum_{j=k}^{K}\left(q_{\pi(j)} - q_{\pi(j+1)}\right)\mathbf{H}_{\pi(k)}^{H} \times \left(\mathbf{I}\sigma^2 + \sum_{i=1,\pi(i)\in A}^{j}\mathbf{H}_{\pi(i)}\mathbf{Q}_{\pi(i)}\mathbf{H}_{\pi(i)}^{H}\right)^{-1}\mathbf{H}_{\pi(k)}\right) \leq C \quad \forall \pi(k) \notin A, \tag{28.33}$$

where π *denotes the stability-optimal SIC order satisfying* (28.27), $\mathbf{Q}_{\pi(k)}$ *denote stability-optimal transmit covariance matrices, and* C *denotes some constant.*

The above optimality condition becomes especially useful under optimality of any single-link regime, since then the K single-link optimal transmit covariance matrices are needed for the evaluation and they are easily computable according to the *water-filling* principle [18]. Although in the case of sum-power constraints there is no possibility to reduce the problem dimension due to nonexistence of any N link regime optimality, we have a nice feature that whenever the queue is busy, its link must be allocated nonzero transmit power.

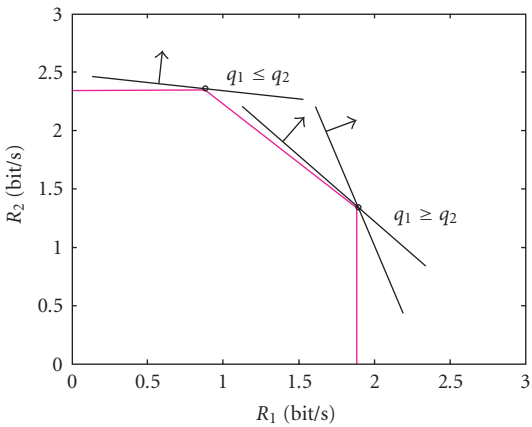

FIGURE 28.6. Exemplary instantaneous capacity region of a SISO-MAC with individual power constraints and two links (channel coefficients generated randomly from the uniform distribution with average SINR = 6 dB). The vertex rate tuples are the only rate tuples, which can be stability-optimal.

28.6.4. Vertex property

The fact that the capacity region of the MIMO-MAC is a nonpolyhedral set can be regarded in terms of optimization as a slight disadvantage compared to the SISO case. In case of stability-optimal scheduling, this is because with high probability for a certain queue system state, there exists a unique optimal value of the scheduling policy $\{\phi_Q, \phi_\pi\}$ and hence a unique stability-optimal rate tuple. Hence, with high probability (however, depending on queue system evolution and the fading process) the stability-optimal scheduling policy forces the network operator to change the transmit strategy from slot to slot. This is not the case in the SISO-MAC with individual power constraints, where only $K!$ rate tuples and their time combinations are stability-optimal for certain ranges of the queue system state and the optimization problem corresponding to (28.30) becomes combinatorial. In the geometrical view $K!$ rate tuples which can be stability-optimal correspond to vertices of the capacity region, which has a special polyhedral structure called *polymatroid* [19]. In Figure 28.6 this geometry behind stability-optimal scheduling in the SISO-MAC with individual power constraints is presented in the two-link case. We conclude that the vertex rate tuple remains stability-optimal in the SISO-MAC whenever the queue system state evolves within the range of system states associated with stability optimality of this tuple (in particular, in the two-link case from Figure 28.6 whenever $q_1(n) \geq q_2(n)$ or $q_1(n) \leq q_2(n)$ hold over some time period). This feature gives potential to reduce the operational effort of stability-optimal scheduling in real-world systems, compared with the multiple antenna case. The worth studying question is therefore the question of occurrence of vertices in the capacity region of the MIMO-MAC. In order to address this issue we first introduce the following special transmission scheme. Given any SIC order π, assume that all nodes utilize single-link capacity optimal transmit

strategy. Precisely, assume that the transmit covariance matrix of the $\pi(k)$th link with $k = 1, 2, \ldots, K$ in $[(n-1)T; nT]$ for $n \in \mathbb{N}$ is

$$\mathbf{Q}_{\pi(k)}^{(\pi)} = \underset{\mathbf{Q}_{\pi(k)} = \phi^S_{\mathcal{Q},k} : \phi^S \in \mathcal{M}}{\arg\max} \log\det \frac{\mathbf{I}\sigma^2 + \sum_{j=1}^{k} \mathbf{H}_{\pi(j)}(n)\mathbf{Q}_{\pi(j)}\mathbf{H}_{\pi(j)}(n)^H}{\mathbf{I}\sigma^2 + \sum_{j=1}^{k-1} \mathbf{H}_{\pi(j)}(n)\mathbf{Q}_{\pi(j)}\mathbf{H}_{\pi(j)}(n)^H}, \tag{28.34}$$

with $\mathcal{M} = \mathcal{M}_{\hat{\mathbf{p}}}$ or $\mathcal{M} = \mathcal{M}_P$ depending on constraint type. This means that every link disposes of transmit covariance matrix optimally (in terms of achievable rate) adapted to the "seen" interference from link signals decoded later in the SIC order. The computational principle of such matrix set $\mathcal{Q}^{(\pi)}$ corresponds to K-fold water-filling and is well known and efficiently implementable. Due to the specific geometrical position of the rate tuple achieved by $\phi^S := \{\mathcal{Q}^{(\pi)}, \pi\}$ on the boundary of the capacity region, we denote it as *marginal* rate tuple (for details, see [20]). With the above, we can now restate the key results from [20] as follows.

Theorem 28.17. *Assume any queue system state* $\mathbf{q}(n)$ *and the corresponding stability-optimal SIC order* π *satisfying* (28.27).

(i) *Transmit strategy* $\phi^S := \{\mathcal{Q}^{(\pi)}, \pi\}$ *is stability-optimal for* $\mathbf{q}(n)$ *in the MIMO-MAC with individual power constraints if and only if, for* $k = 1, 2, \ldots, K$,

$$\begin{aligned} \operatorname{eigvec}\left(\mathbf{Q}_{\pi(k)}^{(\pi)}\right) &= \operatorname{eigvec}\left(\mathbf{H}_{\pi(k)}^H(n)\left(\mathbf{I}\sigma^2 + \sum_{j=1}^{K} \mathbf{H}_{\pi(j)}(n)\mathbf{Q}_{\pi(j)}^{(\pi)}\mathbf{H}_{\pi(j)}^H(n)\right)^{-1}\mathbf{H}_{\pi(k)}(n)\right), \\ q_{\pi(K)}\operatorname{eigval}&\left(\mathbf{H}_{\pi(k)}^H(n)\left(\mathbf{I}\sigma^2 + \sum_{j=1}^{K} \mathbf{H}_{\pi(j)}(n)\mathbf{Q}_{\pi(j)}^{(\pi)}\mathbf{H}_{\pi(j)}^H(n)\right)^{-1}\mathbf{H}_{\pi(k)}(n)\right) \\ &= \lambda_{\pi(k)} - \lambda_{\pi(k)}|_{q_{\pi(K)=0}}, \end{aligned} \tag{28.35}$$

hold for all eigenvectors associated with nonzero eigenvalues, with $\lambda_{\pi(k)}$ *as dual variables associated with* $\pi(k)$*th power constraint.*

(ii) *If transmit strategy* $\phi^S := \{\mathcal{Q}^{(\pi)}, \pi\}$ *is optimal for some queue system state* $\mathbf{q}(n)$*, then it is optimal for all queue system states satisfying* (28.27).

Property (ii) corresponds to the vertex property of $\mathbf{R}(\phi^S, \mathcal{H}(n))$ in the geometrical sense. The conclusion is that when vertices on the boundary of the capacity region of the MIMO-MAC with individual power constraints occur, then they correspond to marginal rate tuples achieved by (28.34). Hence, when the conditions in (i) are satisfied during some number of slots with sufficient accuracy, the network operator and user nodes can benefit from the ease of transmit strategy computation consisting in K-fold water-filling. Moreover, due to vertex property under condition (28.35) optimality of K-fold water-filling holds as long as queue system evolution does not violate (28.27). This is satisfied with high probability if for $k = 1, 2, \ldots, K$, $q_k(n) \gg a_k(n)$ in some time interval $n_1 \leq n \leq n_2$, that is, during a low traffic period with busy queues. In Figure 28.7 an exemplary capacity

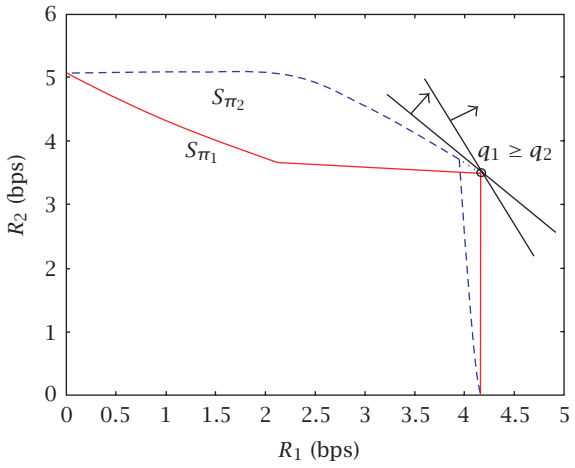

FIGURE 28.7. Exemplary instantaneous capacity region of a MIMO-MAC with individual power constraints and two links (channel matrices generated randomly from the elementwise uniform distribution with average SINR = 6 dB, SIC orders $\pi_1 = 1 \leftarrow 2$, $\pi_2 = 2 \leftarrow 1$) with one vertex corresponding to SIC order $\pi_1 = 1 \leftarrow 2$.

region of a two-link MIMO-MAC with individual power constraints and the vertex $\mathbf{R}(\{\mathcal{Q}^{(\pi)}, \pi\}, \mathcal{H}(n))$, with $\pi = 1 \leftarrow 2$, is depicted. For completeness it has to be stated that in case of the MIMO-MAC with sum-power constraint vertices cannot occur on the boundary of the capacity region. This holds also for sum-power constrained SISO-MAC. For further details regarding the occurrence of vertices and their behaviour subject to power variations, we refer to [20].

28.6.5. Iterative computation of the stability-optimal policy

We show now that the multilink scheduling problem (28.30) can be splitted into K coupled single-link optimization problems. We present an iterative algorithm (Algorithm 28.1) for such splitted optimization. The presented splitting of the optimization bases on the approaches taken in [18, 21] regarding the maximization of the sum rate. Splitted optimization can be utilized in the design of optimization routines in the real-world system in order to partially distribute the computational load among all nodes in the cell. The single-link optimization problem for the kth link arises, by fixing the transmit covariance matrices $\mathbf{Q}_j$ for all $j = 1, 2, \ldots, K$, $j \neq k$, in the stability scheduling problem (28.30). Hence, the stability objectives for such problems are

$$\begin{aligned} f_{\mathbf{q},\pi(k)}\left(\mathbf{Q}_{\pi(k)}\right) = &\sum_{j=k}^{K} \left(q_{\pi(j)} - q_{\pi(j+1)}\right) \log\det\left(\mathbf{N}_{\pi(i)}^{(j)} + \mathbf{H}_{\pi(k)}\mathbf{Q}_{\pi(k)}\mathbf{H}_{\pi(k)}^{H}\right) \\ &- \sum_{j=1}^{k-1} \left(q_{\pi(j)} - q_{\pi(j+1)}\right) \log\det\left(\mathbf{N}_{\pi(k)}^{(j)}\right), \end{aligned} \tag{28.36}$$

Initialization phase

(1) Set inner counter $l := 1$.

(2) Set outer counter $m := 1$.

(3) Set $\pi = \pi(\mathbf{q}(n))$ satisfying $q_{\pi(1)}(n) \geq q_{\pi(2)}(n) \geq \cdots \geq q_{\pi(K)}(n) \geq 0$.

(4) For $k = 1$ to K,

(a) set $\mathbf{Q}_k^{(l)} := \mathbf{Q}_k^{(0)}$,

(b) for $j = k$ to K, compute $\mathbf{N}_{\pi(k)}^{(j),(l)}$,

(c) if (sum-power constraint = true), then set $p_k^{(m)} := p_k^{(0)}$, else $p_k^{(m)} := p_k$.

(5) Repeat (*outer loop*)

(a) repeat (*inner loop*)

(i) for $k = 1$ to K

(i1) maximize $f_{\mathbf{q}(n),\pi(k)}(\mathbf{Q}_{\pi(k)}) = \sum_{j=k}^{K}(q_{\pi(j)}(n) - q_{\pi(j+1)}(n))\times \log\det(\mathbf{N}_{\pi(k)}^{(j),(l)} + \mathbf{H}_{\pi(k)}(n)\mathbf{Q}_{\pi(k)}\mathbf{H}_{\pi(k)}^{H}(n))$ subject to $\text{trace}(\mathbf{Q}_{\pi(k)}) \leq p_{\pi(k)}^{(m)}$ for all $k = 1, 2, \ldots, K$,

(i2) set $\mathbf{Q}_{\pi(k)}^{(l)} = \arg\max_{\mathbf{Q}_{\pi(k)}} f_{\mathbf{q}(n),\pi(k)}(\mathbf{Q}_{\pi(k)})$,

(i3) for $j = k$ to K, update $\mathbf{N}_{\pi(k)}^{(j),(l)}$,

(ii) set inner counter $l := l + 1$,

(iii) for $k = 1$ to K, for $j = k$ to K, set $\mathbf{N}_{\pi(k)}^{(j),(l+1)} := \mathbf{N}_{\pi(k)}^{(j),(l)}$ until (desired accuracy 1 = true)

(b) if (sum-power constraint = true), then

(i) maximize $f_{\pi}(\mathbf{p}) = \sum_{k=1}^{K}(q_{\pi(k)}(n) - q_{\pi(k+1)}(n))\times \log\det(\mathbf{I}\sigma^2 + \sum_{j=1}^{k} p_{\pi(j)}\mathbf{H}_{\pi(j)}(n)\mathbf{Q}_{\pi(j)}^{(l-1)}/ \text{trace}(\mathbf{Q}_{\pi(j)}^{(l-1)})\mathbf{H}_{\pi(j)}^{H}(n))$, subject to $\sum_{k=1}^{K} p_k = P$,

(ii) set outer counter $m := m + 1$,

(iii) set $\mathbf{p}^{(m)} = \arg\max_{\mathbf{p}} f_{\pi}(\mathbf{p})$,

until (desired accuracy 2 = true).

Algorithm 28.1

with $k = 1, 2, \ldots, K$, where the terms $\mathbf{N}_{\pi(k)}^{(j)}$ are defined as

$$\mathbf{N}_{\pi(k)}^{(j)} = \mathbf{I}\sigma^2 + \sum_{l=1, l\neq k}^{j} \mathbf{H}_{\pi(l)}\mathbf{Q}_{\pi(l)}\mathbf{H}_{\pi(l)}^{H}, \tag{28.37}$$

for all $j = 1, 2, \ldots, K$. The terms $\mathbf{N}_{\pi(k)}^{(j)}$ consist of noise and interference caused by links $j \neq k$ at the base station, so that the second sum in (28.36) becomes negligible in the optimization. It is evident that the transmit covariance matrices

$\hat{\mathbf{Q}}_k$ (positive semidefinite and satisfying given power constraints) solving single-link scheduling problems with objective (28.36) for $k = 1, 2, \ldots, K$ build a matrix set $\hat{\mathcal{Q}}$, which solves the multilink scheduling problem (28.30). From [17] we know that the KKT conditions for the kth single-link optimization problem in case of individual power constraints are

$$\begin{gathered}
-\mathbf{Q}_{\pi(k)} \preceq 0, \\
\operatorname{trace}(\mathbf{Q}_{\pi(k)}) - p_{\pi(k)} \leq 0, \\
\mathbf{Z}_{\pi(k)} \succeq 0, \\
\lambda_{\pi(k)} \geq 0, \\
\operatorname{trace}(\mathbf{Q}_{\pi(k)}\mathbf{Z}_{\pi(k)}) = 0, \\
\lambda_{\pi(k)}(\operatorname{trace}(\mathbf{Q}_{\pi(k)}) - p_{\pi(k)}) = 0, \\
\sum_{j=k}^{K} (q_{\pi(j)} - q_{\pi(j+1)}) \mathbf{H}_{\pi(k)}^{H} \left(\mathbf{N}_{\pi(k)}^{(j)} + \mathbf{H}_{\pi(k)}\mathbf{Q}_{\pi(k)}\mathbf{H}_{\pi(k)}^{H}\right)^{-1} \mathbf{H}_{\pi(k)} = \lambda_{\pi(k)}\mathbf{I} - \mathbf{Z}_{\pi(k)}
\end{gathered} \tag{28.38}$$

and in case of sum-power constraint are

$$\begin{gathered}
-\mathbf{Q}_{\pi(k)} \preceq 0, \\
\operatorname{trace}(\mathbf{Q}_{\pi(k)}) - P_{\pi(k)} \leq 0, \\
\mathbf{Z}_{\pi(k)} \succeq 0, \\
\lambda_{\pi(k)} \geq 0, \\
\operatorname{trace}(\mathbf{Q}_{\pi(k)}\mathbf{Z}_{\pi(k)}) = 0, \\
\lambda_{\pi(k)}(\operatorname{trace}(\mathbf{Q}_{\pi(k)}) - P_{\pi(k)}) = 0, \\
\sum_{j=k}^{K} (q_{\pi(j)} - q_{\pi(j+1)}) \mathbf{H}_{\pi(k)}^{H} \left(\mathbf{N}_{\pi(k)}^{(j)} + \mathbf{H}_{\pi(k)}\mathbf{Q}_{\pi(k)}\mathbf{H}_{\pi(k)}^{H}\right)^{-1} \mathbf{H}_{\pi(k)} = \lambda_{\pi(k)}\mathbf{I} - \mathbf{Z}_{\pi(k)},
\end{gathered} \tag{28.39}$$

with

$$P_{\pi(k)} = P - \sum_{l=1, l\neq k}^{K} \operatorname{tr}(\mathbf{Q}_{\pi(l)}). \tag{28.40}$$

Although we splitted the optimization into K problems, the problems remain coupled. On the one side, the optimal transmit covariance matrix for every link is dependent on the transmit covariance matrices of links decoded later in the SIC order, since they influence the problem in form of interference. On the other side, due to retained multilink character of the stability objective, every link signal adapts spatially to the link signals decoded earlier in the SIC order. As already mentioned in Section 28.6.2 (28.40) indicates further that under sum-power constraints the single-link problems are coupled additionally due to common power

budget. Hence, it is evident that the dual variables $\lambda_{\pi(k)}$, for $k = 1, 2, \ldots, K$, become equal at the optimum, which corresponds to a unique dual scalar variable of the multilink problem.

Constructing the iterative algorithm we make use of the fact that the MIMO capacity functional is concave over $\mathbf{p}$, when the spatial signal correlations (in form of ratios between all pairs of elements of transmit covariance matrices) remain fixed. With this insight we can conduct splitted optimization in sum-power constrained MIMO-MAC in two steps. The first step corresponds to the sequence of maximizations of K single-link objectives (28.36), subject to some constraint vector $\mathbf{p}$ satisfying $\sum_{k=1}^{K} p_k \leq P$. The second step is the multilink optimization over $\mathbf{p}$ itself, subject to the same sum-constraint (in the algorithm we therefore denote the constraint vector as if it were a variable). Clearly, under individual power constraints, the second optimization step is superfluous.

The input values of our algorithm are the queue system state $\mathbf{q}(n)$, set of fading states $\mathcal{H}(n)$, noise variance σ^2, power constraint vector $\hat{\mathbf{p}}$ or power budget P, and two levels of accuracy. The start values are $\mathbf{p}^{(0)}$, with $\sum_{k=1}^{K} p_k^{(0)} \leq P$ and $\mathcal{Q}^{(0)}$. The algorithm can be described as follows.

The inner loop of the algorithm corresponds to the series of single-link optimization steps. The ordering of single-link optimization steps in the inner loop was chosen above to comply with π, but it can be chosen arbitrarily.

Theorem 28.18. *The presented iterative optimization algorithm converges to the solution of the multilink problem* (28.30)*, that is, for* $k = 1, 2, \ldots, K$*,*

$$\lim_{l \to \infty} \mathbf{Q}_k^{(l)} = \hat{\mathbf{Q}}_k, \tag{28.41}$$

with l *the number of inner iteration.*

Fortunately using the analysis method from [18] we are able to make a statement about the speed of convergence of the algorithm.

Theorem 28.19. *Assume the ordering of single-link optimization steps in the inner loop of the algorithm complying with* π *and a power constraint vector* $\hat{\mathbf{p}}$*. Then, the distance to the value of the multilink objective after the first inner cycle, when starting with* $\mathbf{Q}_k^{(0)} = 0$ *for* $k = 1, 2, \ldots, K$*, is not larger than* $\sum_{k=2}^{K} q_k n_r$*.*

Both theorems are proven in [17].

28.7. Conclusions

In the cross-layer view of the physical and data link layer of a cellular uplink stability is a fundamental requirement for efficient system operation. The size of the

stability region expresses systems capability of carrying dense data traffic without occurring buffer overflows and resulting service dropouts. Therefore, on the one side, the scheduling policy achieving the largest stability region is desirable from the social point of view at the system. On the other side, it provides the network operator with the highest achievable utility from serving the user links. In contrast to common SISO uplink the stability-optimal scheduling policy in multiple-antenna uplink is of more intricated nature. Its construction combines physical and data link layer issues and utilizes interdependences among the spatial signal structure and the order of link signal decoding. The machinery behind such policy is easily understood from the analysis of the geometry of the capacity region and spatially achievable rate regions. Furthermore, some useful features of the policy behaviour, like, for example, conditions for link idling, can be extracted from the optimality conditions. A great advantage is convexity of the underlying optimization problem, which facilitates the design and implementation of efficient iterative optimization routines. The queue system under the stability-optimal policy is well behaved and allows for several bounds and asymptotics.

Appendix

A. Real-time multiple-user multiple-antenna scheduling

A.1. Multiple-user transmission experiments with multiple antennas and channel-aware scheduling and bit loading

Since the work of [22, 23], a lot of research effort has been directed into radio transmission schemes with multiple antennas. Meanwhile many results found entry into the actual standardization in 3GPP for the high-speed uplink and downlink packet access.

A further extension of the single-user multiantenna results towards multiuser multiple-access scenarios was found to be a challenging task. Basic papers towards the solution of the multiuser scheduling problem [24] considering, for example, stability [25] or detection order [26], were published recently. Independently, [27] discussed a similar but simplified scenario for the optimization problem.

Despite the fact that the optimum solution [20, 28] appears to be rather complex, it is possible to implement suboptimum variations on state-of-the-art hardware today. In multiuser transmission experiments with multiple antennas at the base station, we could show that tremendous gains towards sum throughput and queue length can be achieved when the X-laxer optimized solutions are applied onto a real-time system.

The experiments were conducted on a multiantenna transmission test bed which is reconfigurable and capable of real-time data transmission at several hundred Mbps. The aim was to show that already with today's hardware real-time algorithms can be implemented which can evaluate instantaneous channel state information to improve the reliability of the transmission over the fading radio channel and increase the achievable data throughput by spatial multiplexing. Being able to exploit the advantages of channel-aware bit loading [29, 30] with only

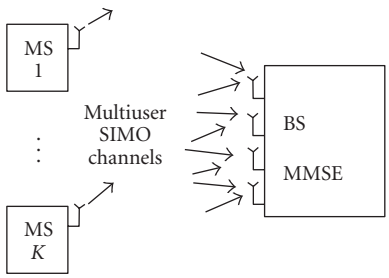

FIGURE A.1. Multiuser multiple-antenna MAC system.

little feedback from the Rx to the Tx, we could enhance the system performance towards reliability and throughput dramatically [31]. A further step was the implementation of multiuser (MU) scheduling policies which are or great interest for mobile network providers to increase the spectral efficiency by spatial multiplexing.

Since the search for an optimum scheduling solution can easily exceed the time constraints for real-time channel adaptivity, we proposed a suboptimum fair scheduling algorithm [32] which considers the channel between all users and the base station and all individual queue states of the users. An implementation [33] of the proposed fair scheduler in an indoor scenario with 4 users and 3 BS antennas showed that the sum throughput could be tripled at high SNR compared to the best-user-only strategy which is still very common, despite the fact that single-user support with multiple antennas at the BS is only optimum at very low SNR. Therefore MU detection in spatial domain is a prerequisite to exploit the high potential of the multipath channel. A sum throughput optimum approach achieved a slightly higher average throughput but the queuing states grew unbalanced since they were not considered.

A.2. Measured capacity of the MIMO channel

The prediction of an immense channel capacity which can be exploited in multipath propagation environment [22, 23] by means of smart multiantenna signal processing led to an intense research into the MIMO area. In a first experiment [34], Wolniansky et al. could prove that the successful exploitation of the multipath environment can be realized with spatial multiplexing. Narrowband channel measurements campaigns conducted in indoor environments [35, 36] or dense urban environments like Manhattan [37, 38] showed a similar richness in the multipath channel which should allow spatial separation of up to 16 independent data streams transmitted at the same time at the same frequency at high signal-to-noise ratio (SNR).

Our own independent broad band measurements (BW = 120 MHz@5.2 GHz) focused on the channel capacity in quasi static scenarios between two or more

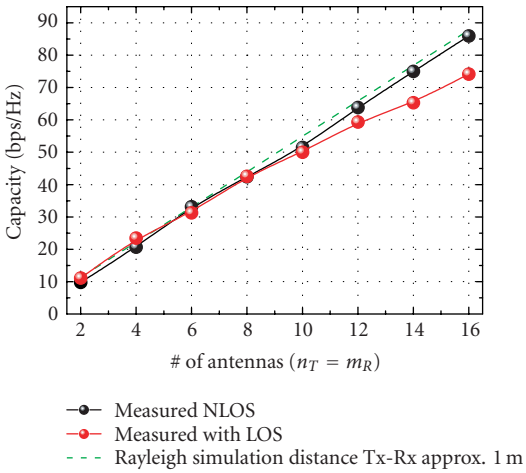

FIGURE A.2. Linear increase of the ergodic capacity versus the number of antennas ($n_T = m_R$), theory and measurements (broadband measurements).

multiantenna terminals. The dependence on antenna configurations and environment was studied in detail in [39, 40, 41, 42] and the main results are summarized in the following.

(i) In indoor environments, the capacity increases linearly with the number of antennas $\min(n_T, m_R)$ (see Figure A.2).

(ii) The statistical distribution of the eigenvalues is very similar to that of a synthetic Rayleigh or Ricean channel with low Ricean factor ($k \leq 10$ dB) obtainable from Monte Carlo simulations (see Figure A.3).

(iii) Even in a worst case scenario with little multipath to exploit the channel has at least two strong eigenvalues due to the polarization multiplex if suitable antennas are used for transmission.

(iv) Moving objects in the surrounding of the terminals induce much less channel variation than a movement of one of the terminals itself.

Narrowband measurements/flat fading. For the experiments the receiver was driven by a little electric motor thus enabling varying speed and reproducible channel statistics with high accuracy. The trek was 5 meters long and the min/max distance between Tx and Rx was 1 m and 3 m, respectively. The start and the end were marked on the floor and the antennas looked into fixed directions in all experiments. During all measurements only one person was operating the system avoiding unnecessary movements about 2 m away from the Rx antennas. By this means all measurements could be reproduced very accurately.

Channel statistics. For the statistical channel measurements, about $2 \cdot 10^3$ channel realizations were monitored and file logged. The 10×8 real-valued channel matrices (4 Tx and 5 Rx antennas) were normalized to unit channel gain and decomposed by singular value decomposition (SVD).

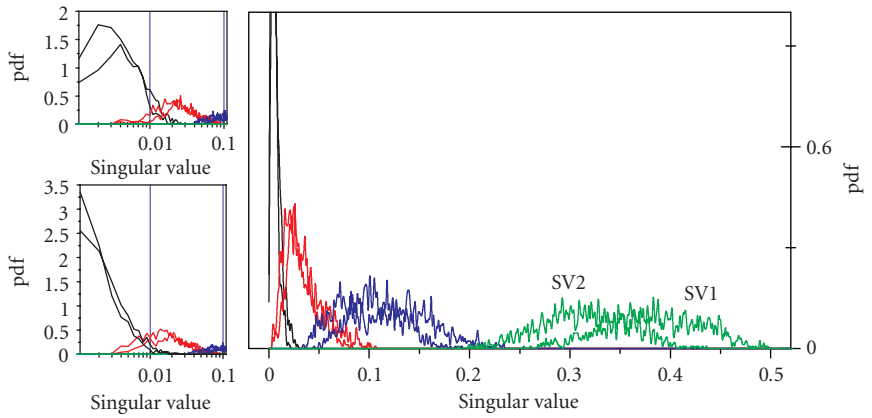

FIGURE A.3. Channel statistics along 5 m trek across the lab. The distribution of the singular values is shown for a 4×5 MIMO configuration at the right. The shift of the smallest SVs can be seen in logarithmic scale on the left.

Figure A.3 shows the belonging singular value (SV) distribution. The distribution (right) clearly reflects the I/Q—imbalance caused by the analog up- and downconversion [43]. The 8 SVs of the real-valued channel matrix $\mathbf{H}$ should be pairwise degenerated, for example, SV 1 and SV 2. Due to the I/Q imbalance this degeneracy is split up and we find 8 SVs instead of 2×4. This effect can be modelled as an additive noisy channel estimation error $\Delta\mathbf{H}$ on the real-valued channel matrix $\mathbf{H}$. Furthermore we see the increase of the smallest SVs when we add one more antenna (the left part of the figure). This shift in the SV distribution was discussed in detail in [44, 45]. It explains the improvement of the BER performance generally described by a rising diversity order for high SNR.

We can conclude from these results that a sufficient channel statistics was found in the chosen environment which is in accordance to the extensive channel measurements conducted at 5.2 GHz (bandwidth 120 MHz) [40]. Now, further experiments to study the diversity gain [31] and the effect of channel adaptive rate control [31, 46] could be conducted.

A.3. Multiuser SIMO MAC—scheduling and bit loading

We assume an MMSE receiver and SIC at the BS. Then the optimization problem for the power allocation under a sum power constraint is a concave functional which was shown in detail in [47]:

$$f^{\mathrm{SIC}} = \sum_{k=1}^{K} R_k^{\mathrm{SIC}} = \log_2 \left| \mathbf{I} + \sum_{k=1}^{K} p_k \mathbf{h}_k \mathbf{h}_k^H \right|, \tag{A.1}$$

where R_k is the rate of user k, p_k is its allocated transmit power, and $\mathbf{h}_k$ is the

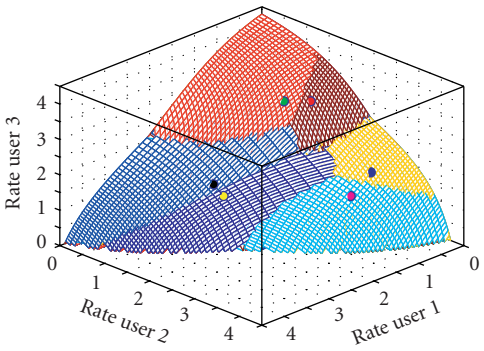

$H = [1\,1\,1, 0.3\,0.3\,0, 0.4\,0\,0.4]$, sum Tx power = 16

FIGURE A.4. Sum rate region for 3 users and different detection order with SIC-MMSE. Colored dots show the maximum sum rate for each detection order. The belonging power allocation of all 6 maxima is identical.

receive vector from user k to all BS antennas. The optimum power allocation can be found by convex optimization techniques, like the *maxdet* algorithm [48].

In [30], we showed that the maximum sum rate and the optimum power allocation per user is independent of the detection order of the users (see simulation results in Figure A.4). This is of great importance towards rate control for the individual users. Without loosing sum capacity the individual user rates can be controlled at least partially by simply changing their detection order. In [32], it was shown by simulation that this law still holds in principle even when we perform bit loading with discrete symbol alphabets, for example, M-QAM.

For the assumption of individual power constraints which can be motivated by a limited amplifier range at the transmitter, the sum rate functional becomes monotonically rising in $\mathbf{p}$, therefore all users will transmit with maximum power each.

We exploit this behavior in our proposed fair scheduler which is very easy to implement. The scheduling strategy is as follows.

(i) Choose one or some (k) users with the longest queue states.

(ii) Choose then the remaining $m_R - k$ users such that the sum rate is maximized.

(iii) Choose the detection order according to the queue length as proposed in [26].

A detailed numerical performance comparison with algorithms like round robin, best-user-only, maximum sum rate, and so forth towards sum rate and queue length can be found in [32, 33]. The same algorithms were then implemented and their performance was measured in an experiment [33] (see Figure A.6a).

Experiments on multiuser SIMO scheduling. The scheduling policies discussed before are implemented in the real-time demonstration test bed at HHI. The experimental setup of the test bed (Figure A.5) which is based on a hybrid setup of FPGAs and a DSP at the BS was published in detail in [31, 43].

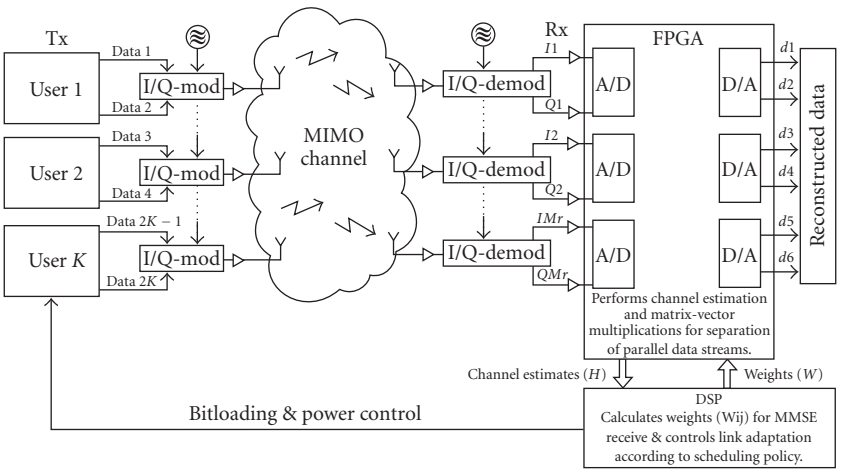

FIGURE A.5. Setup of the test bed for the multiuser multiple-antenna MAC scenario.

For the first time to our knowledge, we show measurement results on achievable data throughput, delay, and buffer size with real-time channel adaptive bitloading and scheduling. The performance of several scheduling policies is evaluated with regard to sum throughput and delay (queuing state) under certain QoS (BER and average rate) requirements of the individual users. We show the pros and cons of each scheduler depending on the available SNR at the BS. The real-time data transmission was performed with up to 5 MSymbols/s and up to 64-QAM modulation. The transmission scenario consists of 4 users which are distributed in the lab, assuming the same average individual rate request during the measurement. The BS is equipped with only 3 antennas, meaning that spatial multiplexing can be performed with up to 3 users maximum. The BS is moved over 5 meters (speed approx. 5 cm/s) across the room on a railway-like construction to ensure the same channel realizations for all experiments.

Figure A.6a shows the achievable average sum rate along the 5m trek across the room. The 3 of 4 cyclic scheduler (black) is outperformed by the fair scheduler (red) and the maximum capacity approach (blue) in the high SNR region. With decreasing SNR the fair scheduler degrades below the cyclic scheduler since the sum rate is here dominated by the user which has the worst average channel. The best-user-only scheme shows the lowest cutoff rate while the other schemes tends to reach three times as much at high SNR.

The possible average throughput per user is displayed Figure A.6b. The filled symbols represent the averaged rate of the best user and the open symbols the average rate of the worst user. Here, over the whole SNR range, the newly proposed fair scheduler achieves the highest QoS (average rate)—highest minimum average rate. This rate, at least, can be assured (open circles) to all users. This clearly shows that already with today's hardware simple but efficient fair scheduling algorithms can be implemented.

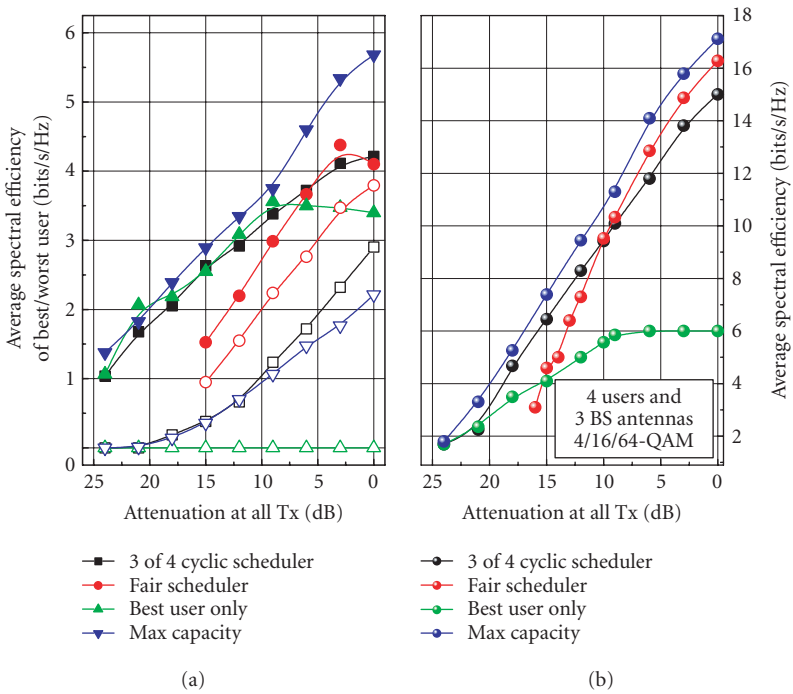

FIGURE A.6. (a) Achieved average spectral efficiency with different scheduling schemes. BS: 3 antennas and 4 users with one antenna each. (b) Average spectral efficiency per user with different scheduling schemes. Filled symbols: user with best rate, open symbols: user with lowest rate. Note that the minimum rate can be assured to all users as a QoS.

Figure A.7 depicts the comparison of the sum throughput achieved in the experiment (circles) with the expected throughput on the measured channel along the 5 m trek in the lab (solid lines) and a simulated Rayleigh channel (dotted lines). The slope of 3 bps/Hz per 3 dB SNR increase is not found in the experiment which is due to the fact that before full-spatial multiplexing can be exploited, the sum rate is cutoff due to the limited level of the QAM modulation. Therefore the figure coincide very well with what can be expected from the theory.

A.4. Conclusion

This work shows that channel-aware bit loading and scheduling are key factors to exploit the high capacity of the multipath channel efficiently. We showed that multiple-antenna techniques are applicable already on today's hardware by implementing channel-aware bit loading and scheduling on a real-time experimental test bed. We achieved an average spectral efficiency of 17 bps/Hz with 3 BS antennas and 4 users which means 75 Mbps average payload data rate in the uplink with an assured uncoded average BER $\leq 10^{-3}$.

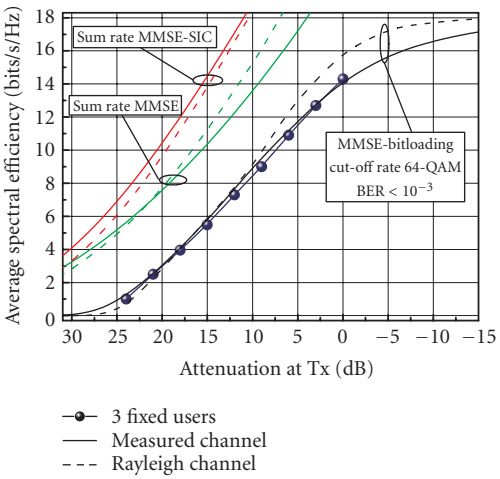

FIGURE A.7. Comparison of theoretical and experimental results. Simulated and measured sum throughput with bit loading. Simulation on Rayleigh channels (–), simulation on the measured channels (· · ·), measured throughput in the experiment (•).

Acknowledgments

The author wants to thank Professor Holger Boche for his support and for many helpful discussions on multiuser SIMO MAC sum capacity and sum performance. Further thanks go to my colleagues Andreas Forck, Holger Gäbler, Udo Krüger, Gheorghe Istoc, and Armin Brylka who contributed important parts for the experimental test bed. Additional thanks go to Chan Zhou with whom the experiments were planned, conducted, analyzed, and discussed. The research is partially supported by the German Ministry for Education and Research (Bundesministerium für Bildung und Forschung (BMBF)).

Abbreviations

SINR	Signal-to-interference-and-noise ratio
QoS	Quality of service
MAC	Multiple-access channel
MIMO-MAC	Multiple-input multiple-output MAC
SIC	Successive interference cancellation
PASTA	Poisson arrivals see time averages
DTMC	Discrete-time Markov chain
KKT	Karush-Kuhn-Tucker
SISO	Single-input multiple-output
SISO-MAC	Single-input multiple-output MAC
3GGP	3rd-Generation Partnership Project
MU	Multiuser
BS	Base station
SNR	Signal-to-noise ratio

BW	Bandwidth
SVD	Singular value decomposition
SV	Singular value
BER	Bit error rate
MMSE	Minimum mean square error
M-QAM	M-quadrature amplitude modulation
SIMO	Single-input multiple-output
FPGA	Field-programmable gate array
DSP	Digital signal processor

Bibliography

[1] D. J. Goodman and N. B. Mandayam, "Power control for wireless data," *IEEE Personal Communications Magazine*, vol. 7, no. 2, pp. 48–54, 2000.

[2] F. P. Kelly, "Charging and rate control for elastic traffic," *European Trans. Telecommunications*, vol. 8, no. 1, pp. 33–37, 1997, corrected version.

[3] S. Shakkottai, T. S. Rappaport, and P. C. Karlsson, "Cross-layer design for wireless networks," *IEEE Commun. Mag.*, vol. 41, pp. 74–80, 2003.

[4] L. Kleinrock, *Queueing Systems Volume I: Theory*, John Wiley & Sons, New York, NY, USA, 1975.

[5] S. P. Meyn and R. L. Tweedie, *Markov Chains and Stochastic Stability*, Springer, New York, NY, USA, 1996.

[6] R. Loynes, "The stability region of a queue with non-independent inter-arrival and service times," *Proc. Cambridge Philos. Soc.*, vol. 58, pp. 497–520, 1962.

[7] S. Assmusen, *Applied Probability and Queues*, Springer, New York, NY, USA, 2000.

[8] M. J. Neely, E. Modiano, and C. E. Rohrs, "Power allocation and routing in multibeam satellites with time-varying channels," *IEEE/ACM Trans. Networking*, vol. 11, no. 1, pp. 138–152, 2003.

[9] P. R. Kumar and S. P. Meyn, "Duality and linear programs for stability and performance analysis of queuing networks and scheduling policies," *IEEE Trans. Automat. Contr.*, vol. 41, pp. 4–17, 1996.

[10] H. Boche and M. Wiczanowski, "Optimal scheduling for high speed uplink packet access—a cross-layer approach," Tech. Rep., Heinrich Hertz Chair for Mobile Communications, Technical University of Berlin.

[11] N. McKeown, V. Anantharam, and J. Walrand, "Achieving 100% throughput in an input-queued switch," in *Fifteenth Annual Joint Conference of the IEEE Computer Societies (INFOCOM '96)*, vol. 1, pp. 296–302, March 1996.

[12] E. Leonardi, M. Mellia, F. Neri, and M. A. Marsan, "Bounds on average delays and queue size averages and variances in input-queued cell-based switches," in *Proceedings of IEEE Twentieth Annual Joint Conference of Computer and Communications Societies (INFOCOM '01)*, vol. 2, pp. 1095–1103, April 2001.

[13] T. M. Cover and J. A. Thomas, *Elements of Information Theory*, John Wiley & Sons, New York, NY, USA, 1991.

[14] S. Boyd and L. Vandenberghe, *Convex Optimization*, Cambridge University Press, 2004.

[15] B. Rimoldi and R. Urbanke, "A rate-splitting approach to the Gaussian multiple-access channel," *IEEE Trans. Inform. Theory*, vol. 42, no. 2, pp. 364–375, 1996.

[16] H. Boche and M. Wiczanowski, "Stability-optimal transmission policy for the multiple antenna multiple access channel in the geometric view," Tech. Rep., Heinrich Hertz Chair for Mobile Communications, Technical University of Berlin, Berlin, Germany, to appear in *EURASIP Journal*.

[17] H. Boche and M. Wiczanowski, "Optimization-theoretic analysis of stability-optimal transmission policy for multiple antenna multiple access channel," Tech. Rep., Heinrich Hertz Chair for Mobile Communications, Technical University of Berlin, Berlin, Germany, 2004.

[18] W. Yu, W. Rhee, S. Boyd, and J. M. Ciofli, "Iterative water-filling for Gaussian vector multiple access channels," in *IEEE International Symposium on Information Theory (ISIT)*, June 2001.

[19] D. D. Yao and L. Zhang, "Stochastic scheduling via polymatroid optimization," in *Mathematics of Stochastic Manufacturing Systems (LAM)*, vol. 33, pp. 333–364, Springer, 1997.
[20] H. Boche and M. Wiczanowski, "Optimal transmit covariance matrices for MIMO high speed uplink packet access," in *IEEE Wireless Communications and Networking Conference (WCNC '04)*, vol. 2, pp. 771–776, March 2004.
[21] H. Boche and E. A. Jorswieck, "Sum capacity optimization of the MIMO Gaussian MAC," in *The 5th International Symposium on Wireless Personal Multimedia Communications (WPMC '02)*, vol. 1, pp. 130–134, Berlin, Germany, October 2002.
[22] I. E. Telatar, "Capacity of multi-antenna Gaussian channels," Tech. Rep., AT&T Bell Lab. Internal Tech. Memo., 1995.
[23] G. J. Foschini, "Layered space-time architecture for wireless communication in a fading environment when using multiple antennas," *Bell Labs. Technical Journal*, vol. 1, no. 2, pp. 41–59, 1996.
[24] H. Boche, E. A. Jorswieck, and T. Haustein, "Channel aware scheduling for multiple antenna multiple access channels," in *Conference Record of the Thirty-Seventh Asilomar Conference on Signals, Systems and Computers*, vol. 1, pp. 992–996, Berlin, Germany, November 2003.
[25] H. Boche and M. Wiczanowski, "Stability region of arrival rates and optimal scheduling for MIMO-MAC—a cross-layer approach," in *IEEE International Zurich Seminar on Communications*, pp. 18–21, Berlin, Germany, 2004.
[26] H. Boche and M. Wiczanowski, "Queueing theoretic optimal scheduling for multiple input multiple output multiple access channel," in *Proceedings of the 3rd IEEE International Symposium on Signal Processing and Information Technology (ISSPIT '03)*, pp. 576–579, December 2003.
[27] E. M. Yeh and A. Cohen, *Throughput and Delay Optimal Resource Allocation in Multiple Fading Channels*, DIMACS Network Information Theory Workshop, March 2003.
[28] H. Boche and M. Wiczanowski, "Optimal scheduling for high speed uplink packet access—a cross-layer approach," in *IEEE 59th Vehicular Technology Conference (VTC '04)*, vol. 5, pp. 2575–2579, Hsinchu, Taiwan, May 2004.
[29] T. Haustein and H. Boche, "Optimal power allocation for MSE and bit-loading in MIMO systems and the impact of correlation," in *IEEE International Conference on Acoustics, Speech, and Signal Processing (ICASSP '03)*, vol. 4, pp. 405–408, Berlin, Germany, April 2003.
[30] T. Haustein, H. Boche, and G. Lehmann, "Bitloading for the SIMO multiple access channel," in *14th IEEE Proceedings on Personal, Indoor and Mobile Radio Communications (PIMRC '03)*, vol. 2, pp. 1678–1682, Berlin, Germany, September 2003.
[31] T. Haustein, A. Forck, H. Gäbler, C. von Helmolt, V. Jungnickel, and U. Krueger, "Real-time MIMO transmission experiments with adaptive bitloading," in *IEEE Conference on Wireless and Optical Communication*, Banff, Canada, USA, July 2004.
[32] C. Zhou, "Scheduling strategien für Mehrnutzerdetektion mit multi-antennen-system an der basisstation," M.S. thesis, Technical University of Berlin, Germany, 2003.
[33] T. Haustein, A. Forck, H. Gäbler, C. von Helmolt, V. Jungnickel, and U. Krueger, "Implementation of channel aware scheduling and bit-loading for the multiuser SIMO MAC in a real-time demonstration test-bed at high data rate," in *IEEE Vehicular Technology Conference (VTC '04)*, September 2004.
[34] P. W. Wolniansky, G. J. Foschini, G. D. Golden, and R. A. Valenzuela, "V-BLAST: an architecture for realizing very high data rates over the rich-scattering wireless channel," in *International Symposium on Signals, Systems, and Electronics (ISSSE '98)*, pp. 295–300, Pisa, Italy, September–October 1998, Invited Paper.
[35] P. Kyritsi, P. Wolniansky, and R. A. Valenzuela, "Indoor BLAST measurements: capacity of multielement antenna systems," in *Multiaccess, Mobility and Teletraffic for Wireless Communications*, vol. 5, pp. 49–60, Kluwer, Norwell, MA, USA, 2000.
[36] P. Kyritsi, R. A. Valenzuela, and D. C. Cox, "Effect of the channel estimation on the accuracy of the capacity estimation," in *IEEE 53rd Vehicular Technology Conference (VTC '01)*, vol. 1, pp. 293–297, 2001.
[37] J. Ling, D. Chizhik, P. Wolniansky, R. Valenzuela, N. Costa, and K. Huber, "Multiple transmit multiple receive (MTMR) capacity survey in manhattan," *IEE Electronics Letters*, vol. 37, no. 16, pp. 1041–1042, 2001.

[38] D. Chizhik, J. Ling, P. Wolniansky, R. Valenzuela, N. Costa, and K. Huber, "Multiple input multiple output measurements and modelling in manhattan," in *IEEE Selected Areas in Communications*, vol. 21, pp. 321–331, 2003.

[39] V. Pohl, V. Jungnickel, T. Haustein, and C. von Helmolt, "Antenna spacing in MIMO indoor channels," in *IEEE 55th Vehicular Technology Conference (VTC '02)*, vol. 2, pp. 749–753, Berlin, Germany, 2002.

[40] V. Jungnickel, V. Pohl, H. Nguyen, U. Kruger, T. Haustein, and C. von Helmolt, "High capacity antennas for MIMO radio systems," in *The 5th International Symposium on Wireless Personal Multimedia Communications (WPMC '02)*, vol. 2, pp. 407–411, Berlin, Germany, October 2002.

[41] V. Jungnickel, V. Pohl, and C. von Helmolt, "Capacity of MIMO systems with closely spaced antennas," *IEEE Communications Letters*, vol. 7, no. 8, pp. 361–363, 2003.

[42] V. Jungnickel, V. Pohl, and C. von Helmolt, "Experiments on the element spacing in multi-antenna systems," in *The 57th IEEE Semiannual Vehicular Technology Conference (VTC '03)*, vol. 2, pp. 1124–1126, Berlin, Germany, April 2003.

[43] V. Jungnickel, T. Haustein, A. Forck, U. Krueger, V. Pohl, and C. von Helmolt, "Over-the-air demonstration of spatial multiplexing at high data rates using real-time base-band processing," in *Advances in Radio Science*, vol. 2, pp. 135–140, 2003.

[44] T. Haustein, E. Jorswieck, V. Jungnickel, U. Krueger, V. Pohl, and C. von Helmolt, "Bit error rates for a MIMO system in Rayleigh and Ricean channels," in *IEEE 54th Vehicular Technology Conference (VTC '01)*, vol. 4, pp. 1984–1987, Atlantic City, NJ, USA, July–November 2001.

[45] E. Jorswieck, G. Wunder, V. Jungnickel, and T. Haustein, "Inverse eigenvalue statistics for Rayleigh and Ricean MIMO channels," in *IEE Seminar on MIMO: Communications Systems from Concept to Implementations*, pp. 3/1–3/6, Berlin, Germany, December 2001.

[46] T. Haustein, A. Forck, H. Gäbler, C. von Helmolt, V. Jungnickel, and U. Krueger, "Implementation of adaptive channel inversion in a real-time MIMO system," in *IEEE 15th International Symposium on Personal, Indoor and Mobile Radio Communications (PIMRC '04)*, vol. 4, pp. 2524–2528, Berlin, Germany, September 2004.

[47] H. Boche and M. Schubert, "Solution of the SINR downlink beamforming problem," in *IEEE Proc. 36th Conf. on Information Sciences and Systems (CISS '02)*, Princeton, USA, March 2002.

[48] L. Vandenberghe, S. Boyd, and S.-P. Wu, "Determinant maximization with linear matrix inequality constraints," *SIAM Journal on Matrix Analysis and Applications*, vol. 19, no. 2, pp. 499–533, 1998.

Holger Boche: Heinrich Hertz Chair for Mobile Communications, Faculty of EECS, Technical University of Berlin, Einsteinufer 25, 10587 Berlin, Germany; Fraunhofer German-Sino Lab for Mobile Communications (MCI), Einsteinufer 37, 10587 Berlin, Germany; Fraunhofer Institut for Broadband Communications, Heinrich Hertz Institute, Einsteinufer 37, 10587 Berlin, Germany

Email: boche@hhi.de

Marcin Wiczanowski: Heinrich Hertz Chair for Mobile Communications, Faculty of EECS, Technical University of Berlin, Einsteinufer 25, 10587 Berlin, Germany

Email: marcin.wiczanowski@mk.tu-berlin.de

Thomas Haustein: Fraunhofer Institut for Broadband Communications, Heinrich Hertz Institute, Einsteinufer 37, 10587 Berlin, Germany

Email: haustein@hhi.de

V Technology

Contents

29 Technology

André Bourdoux

This part deals with the real physical elements of a multiantenna transceiver and their nonidealities. Indeed, these systems operate in real life with physical components or supercomponents such as antennas, front ends, modems, and so forth. Many of the benefits of multiantenna techniques (rate enhancements, more robust links, etc.) are dependent on the characteristics of these physical components. The scope of this part is very broad and encompasses antenna (array) design, parallel transceivers, transceiver nonidealities, emerging air interfaces, and prototyping issues.

The second chapter in this part addresses the antenna: how is the spatial propagation channel sampled and modified by the antenna array? This is of prime importance to the system designer since the antenna elements characteristics (e.g., gain, radiation pattern) as well as their spatial location can significantly modify the channel matrix and the mutual coupling between antennas. An accurate way of modeling antenna arrays for wireless communications is described. The exploitation of spatial, pattern, and polarization diversity for MIMO systems is discussed. The power budget analysis of multiantenna systems is reviewed, taking into account mutual coupling. After that, a broadband antenna concept, called multimode diversity, is presented. The chapter closes with a major challenge for antenna engineers: the integration of arrays in small hand-held devices.

Multiantenna transceivers are usually thought of as a parallel implementation in which N antennas each feed or are fed by their own transceiver. The third chapter of this part takes a new look at the implied parallelization and analyzes how "conventional" multiplexing techniques such as frequency, time, or code division multiplex can be exploited to share a single transceiver between several antennas. These three techniques are compared with the classical full parallel approach and the relative merits of each technique are highlighted. Ideal transceiver(s) are assumed in this chapter.

In the next chapter, the issue of nonidealities in multiantenna front ends is addressed. Nonidealities such as IQ imbalance, ADC or DAC resolution, phase noise, and amplifier nonlinearities can degrade the performance of multiantenna transmission. The modeling aspect of such nonidealities is described and their

impact on several MIMO schemes will be assessed. Spatial multiplexing and diversity, transmit or receive processing, and multicarrier transmission are covered in this analysis and in the simulation results.

The trend in modern wireless communication systems is to go for more complex waveforms that are better suited to cope with the intersymbol interference and the multiuser access. Chapter 5 addresses the combination of multicarrier modulation and code-division multiple access (MC-CDMA). This combination can be done in several ways and each can be used to achieve a certain benefit. Performance metrics such as multiuser separation, receiver complexity, peak-to-average power ratio, robustness to channel time variation can be cleverly traded off in this context. The chapter also covers how MC-CDMA can benefit from MIMO techniques.

The last chapter deals with prototyping. After some motivation and a brief classification of prototypes in general, an overview of some of the recently presented MIMO prototypes is given. Subsequently, digital hardware issues that need to be considered for a successful implementation are considered for SISO and later in particular for MIMO systems. The end of the chapter concentrates on rapid prototyping design methodology and tools.

André Bourdoux: Wireless Research, Interuniversity MicroElectronics Center (IMEC), Kapeldreef 75, 3001 Leuven, Belgium

Email: bourdoux@imec.be

30 Antenna design for multiantenna systems

Christian Waldschmidt, Werner Sörgel, and Werner Wiesbeck

30.1. Introduction

Antennas are the connecting elements between the propagation channel and the radio frequency circuits. The characteristics of antennas and antenna arrays determine the options for exploiting multipath propagation channels. Only by choosing appropriate arrays, smart antenna and MIMO systems can work well. Smart antenna and MIMO systems both require multiple antennas, in other words antenna arrays. The theoretical description as well as the practical setup of antenna arrays is more complex than the consideration of single antennas, in particular if the antennas are closely spaced. Mutual coupling between the single antennas leads to an interaction of all antenna elements in an array. Considering the antennas in an array as independent radiators is a simplification that is only valid for large spacings between the antennas. Most practical applications require rather small antenna spacings, thus considering the interaction between antennas is essential.

This chapter deals with new developments in antenna engineering for MIMO systems. First, an accurate way of modeling antenna arrays for communications is given. The exploitation of spatial, pattern, and polarization diversity for MIMO systems is discussed. One key point of the consideration of antennas in MIMO systems is the power budget, since mutual coupling strongly influences the efficiency of arrays. Therefore, it is shown how to assess antenna arrays in terms of power for the application in MIMO systems. After that a broadband antenna concept, called multimode diversity, is presented. The chapter closes with a new challenge for antenna engineers: the integration of arrays in small handheld devices.

30.2. Characterization of antennas

Antennas radiate electromagnetic fields. To describe the radiation properties of an antenna, fundamental measures are defined in the following section.

30.2.1. Gain

Antennas focus the radiated energy into certain directions. This property is described by the directivity and the gain. For the definition it is necessary to consider a reference antenna, usually an isotropic radiator. The gain G of an antenna is the ratio of the power P_i fed into the isotropic lossless radiator to the power P_s fed into the antenna, if both powers are chosen to excite the same power density for a certain distance r from the antennas. Note that the antenna gain is not an amplification. It is just the ratio of the transmitted power density in a certain direction to the power density of an isotropic and lossless radiator.

30.2.2. Pattern

The radiating properties as a function of the angles θ and ψ are given by the radiation pattern $C(\theta, \psi)$

$$C(\theta,\psi) = \left.\frac{|\vec{E}(\theta,\psi)|}{|\vec{E}(\theta,\psi)|_{\max}}\right|_{r\to\infty} = \left.\frac{|\vec{H}(\theta,\psi)|}{|\vec{H}(\theta,\psi)|_{\max}}\right|_{r\to\infty}, \tag{30.1}$$

where $\vec{E}$ and $\vec{H}$ are the field vectors of the electric and magnetic fields in the far field. The pattern is a directional measure between 0 and 1. For a complete description of the far field the phase information as a function of the angles θ and ψ has to be added. The complex radiation pattern includes both phase and amplitude information:

$$\vec{C}(\theta,\psi) = \left.\frac{\vec{E}(\theta,\psi)e^{jkr}}{|\vec{E}(\theta,\psi)|_{\max}}\right|_{r\to\infty} = C_\theta(\theta,\psi)\vec{e_\theta} + C_\psi(\theta,\psi)\vec{e_\psi}, \tag{30.2}$$

where k is the wave number. With the complex radiation pattern the radiation properties of an antenna are completely given.

30.3. Antennas in a MIMO system: network theory analysis

30.3.1. Introduction

The capacity or spectral efficiency, respectively, of MIMO systems depends on the signal-to-noise ratio (SNR), the correlation properties among the channel transfer functions of different pairs of transmit and receive antennas, and the number of transmit and receive antennas.

In almost all studies about MIMO, the SNR is assumed to be independent of the spatial correlation properties of the channel matrix H, which contains the channel transfer functions or, in the flat fading case, the channel coefficients. Many handheld devices like laptops or palmtops require small antenna spacings. Especially when investigating small antenna spacings the assumption of the independence of H and SNR is critical, as mutual coupling influences both. The efficiency

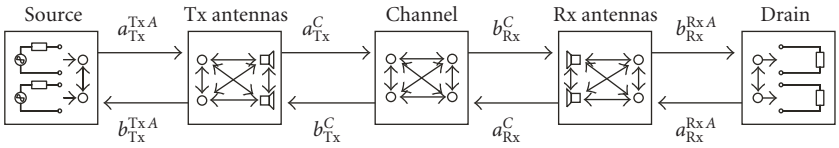

FIGURE 30.1. System model of the complete radio frequency transmission chain. All elements are described by scattering matrices.

of single antennas in an array depends on mutual coupling and influences the power gain of the transmission channel. Thus the SNR is also influenced, if a constant transmit power is assumed, which has to be taken into account for a fair comparison of different arrays. In recent studies about mutual coupling this effect has been neglected and a constant mean SNR was assumed, see [1, 2]. The same holds for mismatching of the antenna arrays. Mismatching and mutual coupling may lead to signals that oscillate between the antennas and the loads connected to them, thus influence both SNR and H.

For compact antenna arrays it is necessary to analyze the SNR and the properties of H together to allow for a fair comparison of different antenna arrays. Therefore an extended channel, including signal source (transmitter), signal drain (receiver), antennas, and the physical channel is taken into account. This network model of the channel allows to analyze the whole radio frequency transmission chain, including mutual coupling and mismatching effects.

30.3.2. Components of the network model

The complete radio frequency transmission chain consists of five elements: signal source (transmitter), transmit antennas, physical channel, receive antennas, and signal drain (receiver), given in Figure 30.1. The number of transmit antennas is M, the number of receive antennas N. For the analysis of the transmission chain by network theory the single components are modeled as networks which are described by scattering matrices [3]. First, some general remarks on scattering matrices are given. A scattering matrix as used here is defined by the following equation:

$$\begin{pmatrix} b_1^{(X\times 1)} \\ b_2^{(Y\times 1)} \end{pmatrix} = \begin{pmatrix} S_{11}^{(X\times X)} & S_{12}^{(X\times Y)} \\ S_{21}^{(Y\times X)} & S_{22}^{(Y\times Y)} \end{pmatrix} \begin{pmatrix} a_1^{(X\times 1)} \\ a_2^{(Y\times 1)} \end{pmatrix}, \tag{30.3}$$

where a_1 and b_1 are the inward and outward propagating wave vectors with the unit $\sqrt{W}$ of port group 1 with X ports and a_2 and b_2 of port group 2 with Y ports. The submatrices S_{ii} represent the reflection of the wave vector a_i to b_i and S_{ij} $(i \neq j)$ the transmission from a_j to b_i.

Signal source. The signal source is the beginning of the transmission chain and determines the power distribution among the transmit antennas. It has M ports,

according to the number of transmit antennas. The output impedances of the signal source are characterized by the reflection matrix r^S_{Tx}, where the upper index S denotes source. The outward propagating wave vector is

$$b^S_{\mathrm{Tx}} = b^S_{0,S} + r^S_{\mathrm{Tx}} a^S_{\mathrm{Tx}}. \tag{30.4}$$

$b^S_{0,S}$ is the wave vector fed into the network, which determines the power distribution among the source ports. a^S_{Tx} is the wave vector reflected by the transmit antennas. The impedance matching of signal source and transmit antennas influences the mutual coupling effects.

Transmit antennas. The antennas suffer from different effects when placed close together. They couple and interact, and cannot be considered as independent elements. The main effects, which have to be taken into account, are the following.

(i) The shape of the radiation pattern of the single antennas changes due to the other adjacent antennas. If, for example, omnidirectional antennas are used a pattern diversity effect occurs.

(ii) The active gain of the single antennas has to be considered. The *active gain* is defined as the gain of a single antenna surrounded by the other terminated antennas. As the other antennas influence the pattern, the gain in terms of directivity changes, accordingly we call it the active gain. Additionally, the energy radiated from an antenna may be directly absorbed by another closely spaced antenna, see [4], thus the active gain is reduced. With this definition the active gain is a property of each individual antenna in an array and depends on the array topology and termination of the antennas. It is not a function of the incident field.

(iii) The signals received or transmitted by an antenna directly couple to the other antennas, shifted in amplitude and phase.

All these effects are included in the general scattering parameter description of the transmit antennas based on [5]

$$\begin{pmatrix} b^{\mathrm{Tx}\,A}_{\mathrm{Tx}} \\ b^{\mathrm{Tx}\,A}_{F} \end{pmatrix} = \begin{pmatrix} S^{\mathrm{Tx}\,A}_{\mathrm{Tx}\,\mathrm{Tx}} & S^{\mathrm{Tx}\,A}_{\mathrm{Tx}\,F} \\ S^{\mathrm{Tx}\,A}_{F\,\mathrm{Tx}} & S^{\mathrm{Tx}\,A}_{FF} \end{pmatrix} \begin{pmatrix} a^{\mathrm{Tx}\,A}_{\mathrm{Tx}} \\ a^{\mathrm{Tx}\,A}_{F} \end{pmatrix}, \tag{30.5}$$

where the upper index Tx A denotes transmit antennas. Each antenna in the array is basically seen as a two-port network. One port describes the excitation side of the antenna whereas the other port describes the far field properties. The submatrix $S^{\mathrm{Tx}\,A}_{\mathrm{Tx}\,\mathrm{Tx}}$ describes the excitation ports of the antennas. It contains the scattering parameters corresponding to the self-coupling (diagonal elements) and mutual coupling (off-diagonal elements) impedances of the array [4]. The self-impedance of an antenna is the input impedance if the antenna is remote, in other words isolated, from its surrounding. With other antennas in the near surrounding of an antenna the influence of these antennas on the input impedance is considered. The mutual coupling impedances describe the coupling between the antennas. The submatrices $S^{\mathrm{Tx}\,A}_{F\,\mathrm{Tx}}$ and $S^{\mathrm{Tx}\,A}_{\mathrm{Tx}\,F}$ describe the transmission of the signals from the excitation side of the antenna network to the far field and vice versa, thus contain

information on the pattern and active gain of the antennas. They are reciprocal. The submatrix $S_{FF}^{\mathrm{Tx}\,A}$ contains the structural antenna scattering of the array with the excitation ports of the antennas terminated in matched loads. The elements of the structural antenna scattering matrix and the transmission matrices are directional, that is, they are a function of the geometry and change for different angles of arrival and departure for different paths.

Physical channel. The physical channel is modeled by

$$\begin{pmatrix} b_{\mathrm{Tx}}^{C} \\ b_{\mathrm{Rx}}^{C} \end{pmatrix} = \begin{pmatrix} S_{\mathrm{Tx}}^{C} & S_{\mathrm{Tx\,Rx}}^{C} \\ S_{\mathrm{Rx\,Tx}}^{C} & S_{\mathrm{Rx}}^{C} \end{pmatrix} \begin{pmatrix} a_{\mathrm{Tx}}^{C} \\ a_{\mathrm{Rx}}^{C} \end{pmatrix}, \tag{30.6}$$

where the upper index C denotes channel. This scattering matrix expresses the relationship between the far field ports of the transmit and receive antenna arrays thus the coupling disappears by definition. Note, that the coupling between single antennas is included in the scattering matrices for the antennas. Additionally it is assumed that there is no reflection from the far field. In other words nothing of the once radiated transmit power is received by the transmit antennas, thus the submatrices S_{Tx}^{C} and S_{Rx}^{C} equal the zero matrix. $S_{\mathrm{Tx\,Rx}}^{C}$ and $S_{\mathrm{Rx\,Tx}}^{C}$ are reciprocal and directional.

Receive antennas. The receive antennas are described analogously to the transmit antennas. For the sake of completeness the scattering matrix with the upper index $\mathrm{Rx}\,A$ (receive antennas) is given:

$$\begin{pmatrix} b_{F}^{\mathrm{Rx}\,A} \\ b_{\mathrm{Rx}}^{\mathrm{Rx}\,A} \end{pmatrix} = \begin{pmatrix} S_{FF}^{\mathrm{Rx}\,A} & S_{F\,\mathrm{Rx}}^{\mathrm{Rx}\,A} \\ S_{\mathrm{Rx}\,F}^{\mathrm{Rx}\,A} & S_{\mathrm{Rx\,Rx}}^{\mathrm{Rx}\,A} \end{pmatrix} \begin{pmatrix} a_{F}^{\mathrm{Rx}\,A} \\ a_{\mathrm{Rx}}^{\mathrm{Rx}\,A} \end{pmatrix}. \tag{30.7}$$

Signal drain. The signal drain is similar to the signal source. It is described by the reflection matrix r_{Rx}^{D} with the dimension $N \times N$, where the upper index D denotes drain. It describes the reflections from the signal drain in case the receive antennas are not perfectly matched.

30.3.3. Assembled network model

The five units given in the previous section are connected together in two steps. The outward propagating wave vectors of a component of the network model are the inward propagating wave vectors of the adjacent components. First, the inner three components, that is, transmit antennas, physical channel, and the receive antennas are merged. The unilateral channel is introduced, which simplifies the problem. Second, the signal source and signal drain are connected to the network. After that the power gain of the transmission chain is available and the channel matrix H of the extended channel with signal source and drain is given, which allows for capacity calculation.

Merging of inner components. The transmit antenna scattering matrix is connected to the scattering matrix of the physical channel by a cascaded connection. Considering that S^C_{Tx} and S^C_{Rx} equal the zero matrix, one yields

$$\begin{aligned} S^{\mathrm{Tx}\,A+C}_{\mathrm{Tx}\,\mathrm{Tx}} &= S^{\mathrm{Tx}\,A}_{\mathrm{Tx}\,\mathrm{Tx}}, \\ S^{\mathrm{Tx}\,A+C}_{\mathrm{Tx}\,\mathrm{Rx}} &= S^{\mathrm{Tx}\,A}_{\mathrm{Tx}\,F} S^{C}_{\mathrm{Tx}\,\mathrm{Rx}}, \\ S^{\mathrm{Tx}\,A+C}_{\mathrm{Rx}\,\mathrm{Tx}} &= S^{C}_{\mathrm{Rx}\,\mathrm{Tx}} S^{\mathrm{Tx}\,A}_{F\,\mathrm{Tx}}, \\ S^{\mathrm{Tx}\,A+C}_{\mathrm{Rx}\,\mathrm{Rx}} &= S^{C}_{\mathrm{Rx}\,\mathrm{Tx}} S^{\mathrm{Tx}\,A}_{FF} S^{C}_{\mathrm{Tx}\,\mathrm{Rx}}. \end{aligned} \tag{30.8}$$

These matrices are then connected to the scattering matrices of the receive antennas, which yields

$$\begin{aligned} S^{H}_{\mathrm{Tx}\,\mathrm{Tx}} = {} & S^{\mathrm{Tx}\,A}_{\mathrm{Tx}\,\mathrm{Tx}} + S^{\mathrm{Tx}\,A}_{\mathrm{Tx}\,F} S^{C}_{\mathrm{Tx}\,\mathrm{Rx}} \left(I - S^{\mathrm{Rx}\,A}_{FF} S^{C}_{\mathrm{Rx}\,\mathrm{Tx}} S^{\mathrm{Tx}\,A}_{FF} S^{C}_{\mathrm{Tx}\,\mathrm{Rx}}\right)^{-1} \\ & \cdot S^{\mathrm{Rx}\,A}_{FF} S^{C}_{\mathrm{Rx}\,\mathrm{Tx}} S^{\mathrm{Tx}\,A}_{F\,\mathrm{Tx}}, \end{aligned} \tag{30.9}$$

$$S^{H}_{\mathrm{Tx}\,\mathrm{Rx}} = S^{\mathrm{Tx}\,A}_{\mathrm{Tx}\,F} S^{C}_{\mathrm{Tx}\,\mathrm{Rx}} \left(I - S^{\mathrm{Rx}\,A}_{FF} S^{C}_{\mathrm{Rx}\,\mathrm{Tx}} S^{\mathrm{Tx}\,A}_{FF} S^{C}_{\mathrm{Tx}\,\mathrm{Rx}}\right)^{-1} S^{\mathrm{Rx}\,A}_{F\,\mathrm{Rx}}, \tag{30.10}$$

$$S^{H}_{\mathrm{Rx}\,\mathrm{Tx}} = S^{\mathrm{Rx}\,A}_{\mathrm{Rx}\,F} \left(I - S^{C}_{\mathrm{Rx}\,\mathrm{Tx}} S^{\mathrm{Tx}\,A}_{FF} S^{C}_{\mathrm{Tx}\,\mathrm{Rx}} S^{\mathrm{Rx}\,A}_{FF}\right)^{-1} S^{C}_{\mathrm{Rx}\,\mathrm{Tx}} S^{\mathrm{Tx}\,A}_{F\,\mathrm{Tx}}, \tag{30.11}$$

$$\begin{aligned} S^{H}_{\mathrm{Rx}\,\mathrm{Rx}} = {} & S^{\mathrm{Rx}\,A}_{\mathrm{Rx}\,\mathrm{Rx}} + S^{\mathrm{Rx}\,A}_{\mathrm{Rx}\,F} \left(I - S^{C}_{\mathrm{Rx}\,\mathrm{Tx}} S^{\mathrm{Tx}\,A}_{FF} S^{C}_{\mathrm{Tx}\,\mathrm{Rx}} S^{\mathrm{Rx}\,A}_{FF}\right)^{-1} \\ & \cdot S^{C}_{\mathrm{Rx}\,\mathrm{Tx}} S^{\mathrm{Tx}\,A}_{FF} S^{C}_{\mathrm{Tx}\,\mathrm{Rx}} S^{\mathrm{Rx}\,A}_{F\,\mathrm{Rx}}. \end{aligned} \tag{30.12}$$

Equations (30.9)–(30.12) describe the extended channel without signal source and drain:

$$S^{H} = \begin{pmatrix} S^{H}_{\mathrm{Tx}\,\mathrm{Tx}} & S^{H}_{\mathrm{Tx}\,\mathrm{Rx}} \\ S^{H}_{\mathrm{Rx}\,\mathrm{Tx}} & S^{H}_{\mathrm{Rx}\,\mathrm{Rx}} \end{pmatrix}. \tag{30.13}$$

The back transmission of signals through the physical channel is subject to the channel attenuation, thus the power reradiated by the receiver and received by the transmitter is twice as strong attenuated as the signals at the receiver. Therefore it is justified to neglect the back transmission, see also [6], and to set $S^C_{\mathrm{Tx}\,\mathrm{Rx}} = 0$, which simplifies (30.9)–(30.12). We call this a unilateral channel. The result is

$$S^{H} = \begin{pmatrix} S^{\mathrm{Tx}\,A}_{\mathrm{Tx}\,\mathrm{Tx}} & 0 \\ S^{\mathrm{Rx}\,A}_{\mathrm{Rx}\,F} S^{C}_{\mathrm{Rx}\,\mathrm{Tx}} S^{\mathrm{Tx}\,A}_{F\,\mathrm{Tx}} & S^{\mathrm{Rx}\,A}_{\mathrm{Rx}\,\mathrm{Rx}} \end{pmatrix}. \tag{30.14}$$

The term $S^{\mathrm{Rx}\,A}_{\mathrm{Rx}\,F} S^{C}_{\mathrm{Rx}\,\mathrm{Tx}} S^{\mathrm{Tx}\,A}_{F\,\mathrm{Tx}}$ in (30.14) describes the transmission of the signals from the input ports of the transmit antennas to the output ports of the receive antennas. Using the Heaviside transformation, it can be expressed as the ratio of

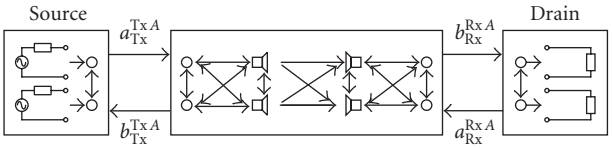

FIGURE 30.2. The transmit antennas, physical channel, and receive antennas are merged into one network. Source and drain terminate the network.

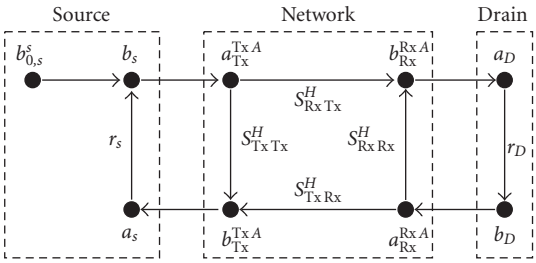

FIGURE 30.3. Signal flow graph for the network above.

the voltages U at the mth transmit and nth receive antenna.

$$S_{\mathrm{Rx\,Tx},nm}^{H} = \sqrt{\frac{Z_{0,m}}{Z_{0,n}}}\,\frac{U_n}{U_m}\bigg|_{a_k=0} \qquad \forall k \neq m, \tag{30.15}$$

where Z_0 is the characteristic impedance of the scattering parameters.

Termination with source and drain. Since the mutual coupling effects strongly depend on the termination of the transmit and receive antennas, the signal source and drain are added to the inner components of the network. There can be signals oscillating between the antennas and the loads (source/drain) connected to them. Figures 30.2 and 30.3 show the merged inner components network terminated with source and drain. With the wave vectors $a_{\mathrm{Tx}}^{\mathrm{Tx}\,A}$, $a_{\mathrm{Rx}}^{\mathrm{Rx}\,A}$, $b_{\mathrm{Tx}}^{\mathrm{Tx}\,A}$, and $b_{\mathrm{Rx}}^{\mathrm{Rx}\,A}$ at the input and output ports of the terminated network it is possible to calculate the power gain of the extended channel and the extended channel matrix H.

$$\begin{aligned}
a_{\mathrm{Tx}}^{\mathrm{Tx}\,A} &= \left(I - r_{\mathrm{Tx}}^{S} S_{\mathrm{Tx\,Tx}}^{H}\right)^{-1} b_{0,S}^{S},\\
a_{\mathrm{Rx}}^{\mathrm{Rx}\,A} &= \left(I - r_{\mathrm{Rx}}^{D} S_{\mathrm{Rx\,Rx}}^{H}\right)^{-1} r_{\mathrm{Rx}}^{D} S_{\mathrm{Rx\,Tx}}^{H} \left(I - r_{\mathrm{Tx}}^{S} S_{\mathrm{Tx\,Tx}}^{H}\right)^{-1} b_{0,S}^{S},\\
b_{\mathrm{Tx}}^{\mathrm{Tx}\,A} &= \left(I - S_{\mathrm{Tx\,Tx}}^{H} r_{\mathrm{Tx}}^{S}\right)^{-1} S_{\mathrm{Tx\,Tx}}^{H} b_{0,S}^{S},\\
b_{\mathrm{Rx}}^{\mathrm{Rx}\,A} &= \left(I - S_{\mathrm{Rx\,Rx}}^{H} r_{\mathrm{Rx}}^{D}\right)^{-1} \left(S_{\mathrm{Rx\,Tx}}^{H} + S_{\mathrm{Rx\,Tx}}^{H} r_{\mathrm{Tx}}^{S} \cdot \left(I - S_{\mathrm{Tx\,Tx}}^{H} r_{\mathrm{Tx}}^{S}\right)^{-1} S_{\mathrm{Tx\,Tx}}^{H}\right) b_{0,S}^{S}.
\end{aligned} \tag{30.16}$$

The extended channel matrix H, which allows for the capacity calculations in the next section, expresses the ratio of the voltages at the receive antennas U_{Rx} to

the voltages at the transmit antennas U_{Tx}.

$$U_{\mathrm{Rx}} = HU_{\mathrm{Tx}}. \tag{30.17}$$

Using the Heaviside transformation leads to

$$Z_{0,\mathrm{Rx}}^{1/2}\left(a_{\mathrm{Rx}}^{\mathrm{Rx}\,A} + b_{\mathrm{Rx}}^{\mathrm{Rx}\,A}\right) = HZ_{0,\mathrm{Tx}}^{1/2}\left(a_{\mathrm{Tx}}^{\mathrm{Tx}\,A} + b_{\mathrm{Tx}}^{\mathrm{Tx}\,A}\right). \tag{30.18}$$

To solve this equation for H the voltages U_{Rx} can be expressed as a function of the voltages U_{Tx}. By using (30.16) the result is

$$\begin{aligned} H = {} & \left(Z_{0,\mathrm{Rx}}\right)^{1/2}\left(I + r_{\mathrm{Rx}}^{D}\right)\left(I - S_{\mathrm{Rx\,Rx}}^{H} r_{\mathrm{Rx}}^{D}\right)^{-1} \\ & \cdot S_{\mathrm{Rx\,Tx}}^{H}\left(I + S_{\mathrm{Tx\,Tx}}^{H}\right)^{-1}\left(Z_{0,\mathrm{Tx}}\right)^{-1/2}. \end{aligned} \tag{30.19}$$

The power gain G_H of the extended channel is the ratio of the real power delivered to the signal drain to the real power fed into the transmit antennas. It allows to draw conclusions on the efficiency of the whole transmission chain.

$$G_H = \frac{b_{\mathrm{Rx}}^{\mathrm{Rx}\,A\dagger} b_{\mathrm{Rx}}^{\mathrm{Rx}\,A} - a_{\mathrm{Rx}}^{\mathrm{Rx}\,A\dagger} a_{\mathrm{Rx}}^{\mathrm{Rx}\,A}}{a_{\mathrm{Tx}}^{\mathrm{Tx}\,A\dagger} a_{\mathrm{Tx}}^{\mathrm{Tx}\,A} - b_{\mathrm{Tx}}^{\mathrm{Tx}\,A\dagger} b_{\mathrm{Tx}}^{\mathrm{Tx}\,A}}. \tag{30.20}$$

Using this definition the power gain depends on the power distribution among the elements of the excitation vector $b_{0,S}^{S}$. Since in MIMO system simulations or measurements a large number of different channel realizations are considered the power gain of the extended channel G_H is a random variable.

In order to assess the performance of an array in terms of power we define the *effective array gain*. The effective array gain G_{eff} of an array is the ratio of the mean received (or transmitted) power of the array to the mean power received by an isotropic antenna, used in the same physical channel with the same transmit antenna. This definition is similar to the mean effective gain definition for single antennas given in [7]. The effective array gain is a function of the antenna array, but also of the physical channel (in particular the conformance of pattern and spatial channel characteristics), the load impedances (source/drain), that are connected to the array, and of $b_{0,S}^{S}$, that is, the power distribution among the antennas. Since the physical channel influences the effective array gain, it is a random variable, thus we use the 10% outage probability as a statistical value.

30.3.4. Comparison of different compact antenna arrays

In this chapter, different antenna array configurations are discussed. First the relationship of the network model to path-based channel models is shown. The influence of the correlation among the elements of the channel matrix on the capacity of different types of MIMO systems is discussed. After that MIMO systems with antenna arrays consisting of parallel dipoles are analyzed. Finally the potential of polarization diversity for compact MIMO arrays is shown.

Antennas and channel model. A frequently used transmission channel representation is path models (here the physical channel, Section 30.3.2). Each path p is described by the polarimetric transfer matrix

$$\Gamma_p = \begin{pmatrix} \Gamma_{\vartheta\vartheta,p} & \Gamma_{\vartheta\psi,p} \\ \Gamma_{\psi\vartheta,p} & \Gamma_{\psi\psi,p} \end{pmatrix}, \tag{30.21}$$

where the single matrix elements contain the amplitude and phase information of the path between a transmit and a receive antenna. With the transfer matrix of each path the voltage at the receive antennas for a given voltage at the transmit antennas can be calculated, according to [8]. Using (30.15), one yields for the scattering parameter between transmit antenna m and receive antenna n:

$$\begin{aligned} S^H_{\mathrm{Rx\,Tx},nm} = {} & \sqrt{\frac{Z_{0,m}}{Z_{0,n}}} \sqrt{\frac{\Re\{Z_{A,n}\}}{\Re\{Z_{A,m}\}}} \sqrt{\left(\frac{\lambda_0}{4\pi}\right)^2 G_n G_m} \\ & \cdot \sum_{p=1}^{P} \begin{pmatrix} C_{\vartheta,n}(\vartheta_p,\psi_p) \\ C_{\psi,n}(\vartheta_p,\psi_p) \end{pmatrix}^T \Gamma_p \begin{pmatrix} C_{\vartheta,m}(\vartheta_p,\psi_p) \\ C_{\psi,m}(\vartheta_p,\psi_p) \end{pmatrix}. \end{aligned} \tag{30.22}$$

G denotes the active gain and C is the complex, polarimetric pattern of the coupled antennas. P is the number of relevant paths. $\Re\{Z_A\}$ is the real part of the self-impedance of the antennas. The channel model used here is a polarimetric, three-dimensional, and double-directional indoor model [9] with the extension given in [10]. For all capacity calculations (following section) the same 1000 channel realizations are used each with the same mean attenuation.

For all following simulations the array configuration under test is always used at both the transmitter and the receiver. Since in realistic systems a perfect conjugate complex matching is impossible due to the coupling effects, self-impedance matching is assumed. In other words the source and drain are perfectly matched to the self-impedances of the antennas, but the mutual coupling impedances are not matched.

The transmit power of the MIMO systems is determined, so that the 10% outage capacity of a single-input single-output (SISO) system with one transmit and one receive dipole on each side of the link is 3.5 bps/Hz.

Parallel half-wavelength dipoles. The determining parameter for a compact antenna array is its total size. Therefore the three antenna array configurations (a)–(c) given in Figure 30.4 are compared with regard to the total array width D. The results are given in Figure 30.5 for MIMO systems with uniform and optimal (water filling) transmit power distribution among the transmit antennas. If the area covered by the dipoles is smaller than $0.2\lambda^2$, systems with two dipoles reach higher capacities than systems with three or four dipoles.

Figure 30.6 shows the cumulative distribution function of the power gain of the extended channel for different antenna spacings between the two dipoles, which are used as transmit and receive arrays. The transmit power is uniformly

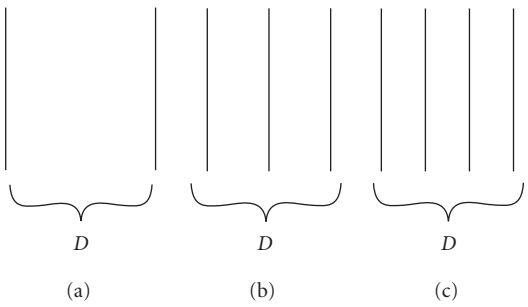

FIGURE 30.4. Antenna configurations of parallel dipoles.

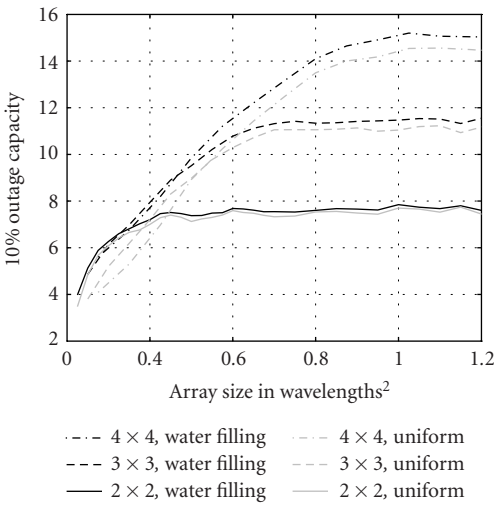

FIGURE 30.5. Capacity of the MIMO systems given in Figure 30.4 with uniform and optimal (water filling) transmit power distribution among the transmit antennas.

distributed among the transmit antennas. With decreasing antenna spacings the active gain of the antennas decreases, which reduces the power gain of the extended channel. For extremely small spacings the mean power gain of the 2×2 MIMO system can be worse than the one of a SISO system. But for low outage probabilities MIMO always outperforms SISO.

Polarization and pattern diversity. The main disadvantage of MIMO systems with arrays consisting of parallel dipoles is the sensitivity to polarization mismatching, when applied in handheld devices due to random orientations of the device. If the transmit and receive arrays are orthogonal only the cross polarization is received, thus the SNR is very low. To overcome this effect, polarization diversity may be exploited. Figure 30.7 shows antenna array configurations (d)–(h) with different

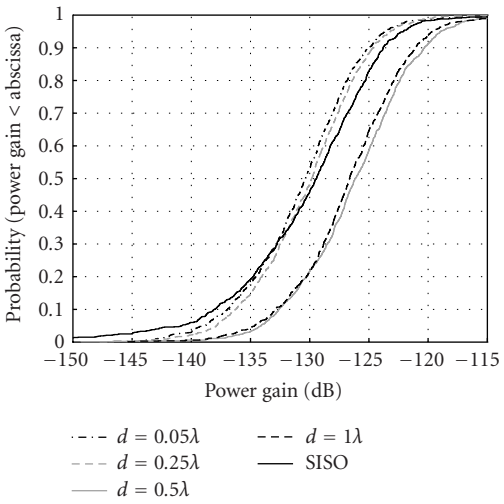

FIGURE 30.6. Power gain distributions of the extended channel for different antenna spacings of array (a). The mean attenuation of the physical channel is 132 dB, which is given by the channel model.

TABLE 30.1. 10% outage capacity in bit/s/Hz and 10% outage effective array gain for different antenna array configurations. Systems (a)–(d) have an array size of $0.25\lambda^2$.

Array	(a)	(b)	(c)	(d)	(e)	(f)	(g)	(h)
Capacity	7.4	8.3	7.7	12	8.4	6	9.5	6.7
G_{eff} (dBi)	3.8	4.3	2.6	4.8	4.1	3.8	5.1	3.6

numbers of dipoles based on either polarization and pattern diversity or combinations of polarization and spatial diversity. The area the antennas cover is indicated in gray. The comparison of the capacities is given in Figure 30.8. For antenna configuration (d) the spacing of the antennas is increased as a parameter. The other antenna configurations have a fixed size, but the transmit and receive antennas are rotated against one another to demonstrate the robustness against polarization mismatching. The systems based on the combination of polarization and spatial diversity perform best in the tradeoff between space and capacity. Mutual coupling can extremely influence the system performance, which leads to the bad performance of system (f). The comparison of configuration (f) with (h) shows again that two antennas can perform better than three on a limited amount of space.

Table 30.1 gives the effective array gain of different arrays for a uniform transmit power distribution in $b^S_{0,S}$. It is evident that the 10% outage capacity depends on both the correlation properties of H and the effective array gain, which determines the SNR. For example system (b) has a larger effective array gain than system (e), but the 10% outage capacity is lower, which is explicable by the correlation properties.

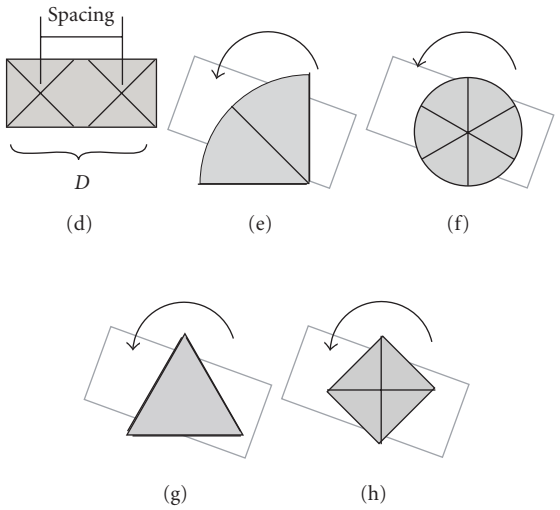

FIGURE 30.7. Different dipole antenna array configurations. The array size is indicated in gray. Systems (e)–(h) are rotated to show the robustness against polarization mismatching, see Figure 30.8.

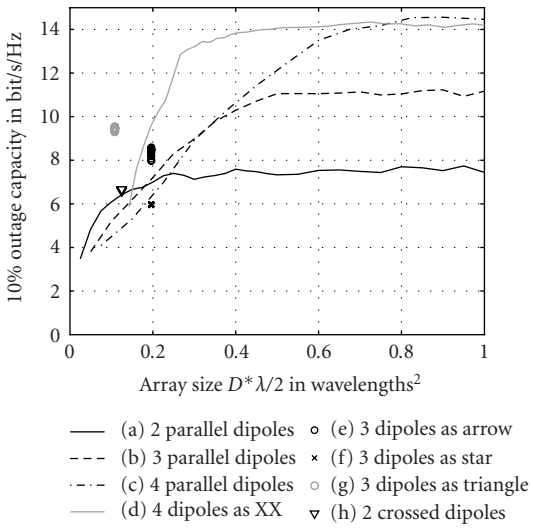

FIGURE 30.8. Capacity of the MIMO systems given in Figure 30.7 with uniform transmit power distribution among the transmit antennas. For the systems exploiting polarization diversity (e)–(h) the transmit array is rotated between 0° and 180° against the receive array. For the parallel dipoles (a)–(c) and array configuration (d) the total array size is changed.

30.3.5. Summary

The RF system model presented here allows for a comparison of small arrays for MIMO. It connects detailed and accurate antenna simulations with sophisticated channel models, without restrictive simplifications. All aspects of mutual coupling are completely taken into account. The properties of the channel matrix and the SNR have to be considered together to compare the performance of different compact arrays, since mutual coupling influences both. It is shown that placing too many antennas on a small area deteriorates the MIMO system performance. For arrays that are robust against polarization mismatching, polarization and spatial diversity have to be combined. The power gain of the extended transmission channel and the effective array gain are used to compare the efficiency of complete arrays within the physical channel.

30.4. Multimode antennas: a compact wideband antenna concept for MIMO and diversity

30.4.1. Introduction

This section presents new broadband antenna solutions, that are small enough to fit into laptops or organizers, but that still yield uncorrelated signals for MIMO or diversity applications. The compactness of the broadband MIMO antenna system is not achieved by using different antennas, but by one antenna with different, independently fed, modes. This results in multimode diversity, a combination of pattern and polarization diversity to obtain uncorrelated channel impulse responses for the MIMO or diversity system. Multimode diversity for MIMO has already been suggested in [11], but this chapter presents a completely new antenna concept, based on spiral antennas.

This section is organized as follows. In Section 30.4.2, four-arm spiral and sinuous antennas and the different excitations for the modes are presented. In Section 30.4.3, the correlation properties of signals received by different modes of the antenna are given as a function of the incident field and its spatial distribution. In Section 30.4.4, MIMO capacity calculations and measurements with spiral antennas are given.

30.4.2. Spiral antennas

The self-complementary, Archimedian, four-arm spiral antenna is well described in the literature, see, for example, [12, 13, 14], thus only the properties crucial for multimode diversity are given here. The spiral antenna, see Figure 30.9, can basically radiate three different modes depending on the excitation. For this application mode 1 and mode 2 are used. Mode 1 is characterized by a phase shift of 90° between adjacent sources at the single arms of the spiral, see Figure 30.9. Mode 2 has a phase shift of 180°. Due to the self-complementarity the antennas are frequency independent or, in other words, extremely broadband. Since the

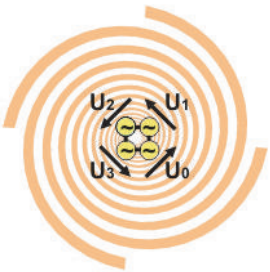

FIGURE 30.9. Geometry of a spiral antenna with voltage sources between the single arms of the spiral.

geometrical structure of the spiral antenna is finite, there exists a lower frequency bound. This bound is

$$f_{\text{min,mode 1}} = \frac{c_0}{2\pi r\sqrt{\varepsilon_{r,\text{eff}}}}, \qquad f_{\text{min,mode 2}} = \frac{c_0}{\pi r\sqrt{\varepsilon_{r,\text{eff}}}}, \tag{30.23}$$

where c_0 is the speed of light, r the outer radius of the spiral, and $\epsilon_{r,\text{eff}}$ the effective substrate permittivity. Above this lower frequency bound, all antenna properties are almost stable and do only slightly change with frequency. The patterns in elevation $C(\theta)$ of modes 1 and 2 are given in Figures 30.10 and 30.11. The azimuth patterns $C(\psi)$ are omnidirectional. The phase of the complex radiation pattern, which among other parameters determines the correlation among the receive signals, is shown in Figure 30.12. The phase of mode 1 changes 360° and the one of mode 2 changes 720° for each circulation around the antenna. The modes can be excited in two ways: first by feeding the spiral arms at the inner ends, that is, at the center of the spiral and second at the outer ends of the arms. Those modes are orthogonally polarized left-hand circular (lhc) and right-hand circular (rhc). The third mode of the spiral antenna (270° phase shift between adjacent arms at the excitation) has a pattern similar to mode 2, but the unwrapped phase of the pattern changes 1080° per circulation around the antenna.

30.4.3. Multimode diversity

MIMO transmission channels are characterized by the channel matrix H, which contains the channel impulse responses or the channel coefficients in the flat fading case between different sets of transmit and receive antenna ports. The diversity gain or MIMO capacity strongly depends on the correlation coefficients among those channel coefficients of H, see [15]. The correlation is influenced by the statistical properties of the wave propagation and the antenna properties, in this case the properties of the single modes. In the following the correlation coefficient among two receive signals as a function of the incident field is calculated. This is equivalent to the correlation among the channel coefficients of H for one transmit and two receive antennas in a MIMO system.

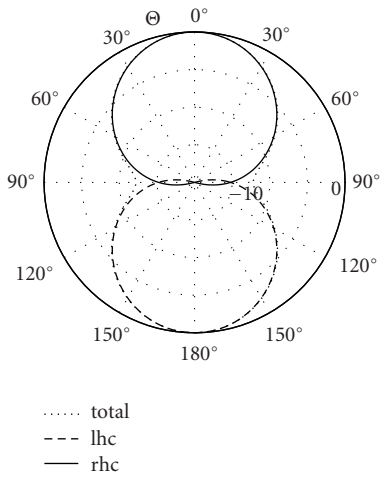

FIGURE 30.10. Pattern of mode 1 of the spiral antenna with a radius of 10 cm at 2 GHz separated into left- (lhc) and right-hand circular (rhc) polarization. If the spiral is fed at the outer end of the arms, the polarization is orthogonal to the one obtained by exciting at the center of the spiral.

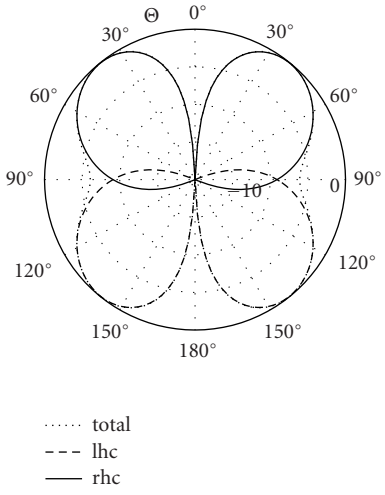

FIGURE 30.11. Pattern of mode 2 of the spiral antenna with a radius of 10 cm at 2 GHz. The pattern hardly changes versus frequency for frequencies above 1.2 GHz.

The spatial wave propagation properties are describable by the power azimuth and elevation profile $p_{\theta,\psi}(\psi)$ and $p_{\theta,\psi}(\theta)$ for both polarizations θ and ψ. Measurements have shown that the power azimuth spectrum $p_{\theta,\psi}(\psi)$ is best modeled by a Laplacian function [16] for both polarizations. For the power elevation profile $p_{\theta,\psi}(\theta)$ a Gaussian function is assumed. The total power angle spectrum is given by the product of the Laplacian function for the azimuth and a Gaussian function

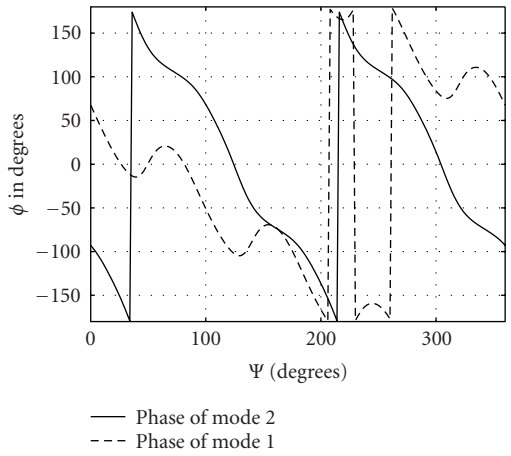

FIGURE 30.12. Phase of the patterns of mode 1 and mode 2, shown in Figures 30.10 and 30.11. The phase of mode 1 changes 360° per circulation around the antenna, mode 2 changes 720°.

for the elevation, normalized so that $\int p_{\theta,\psi}(\theta)p_{\theta,\psi}(\psi)d\Omega = 1$. With [7] it can easily be shown that the complex correlation coefficient among two signals received by different antennas, in this case different modes, is given by

$$\rho_{12} = \frac{R_{12}}{\sqrt{\sigma_1^2\sigma_2^2}} \tag{30.24}$$

with the covariance R_{12}

$$\begin{aligned} R_{12} = K \int_{-\pi}^{\pi}\int_{0}^{\pi} [\,&\mathrm{XPR}\cdot C_{\theta 1}(\theta,\psi)\cdot C^*_{\theta 2}(\theta,\psi)\cdot p_\theta(\theta,\psi) \\ &+ C_{\psi 1}(\theta,\psi)\cdot C^*_{\psi 2}(\theta,\psi)\cdot p_\psi(\theta,\psi)]\sin(\theta)d\theta\, d\psi, \end{aligned} \tag{30.25}$$

where K is constant and the variance σ_i^2

$$\begin{aligned} \sigma_i^2 = K \int_{-\pi}^{\pi}\int_{0}^{\pi} [\,&\mathrm{XPR}\cdot |\,C_{\theta i}(\theta,\psi)\,|^2\cdot p_\theta(\theta,\psi) \\ &+ |\,C_{\psi i}(\theta,\psi)\,|^2\cdot p_\psi(\theta,\psi)]\sin(\theta)d\theta\, d\psi. \end{aligned} \tag{30.26}$$

XPR is the ratio of the power in θ polarization to the power in ψ polarization at the receiver. Note that ρ_{12} is a function of the polarimetric radiation pattern, thus disappears for orthogonally polarized antennas or left- and right-hand circular polarized modes.

Basically it is possible to use spiral or sinuous antennas with any different modes and polarizations for multimode diversity. In the following a spiral antenna is used to calculate the correlation coefficients among receive signals. The orientation of the antenna plane is vertical. A spiral antenna with mode 1 and mode 2,

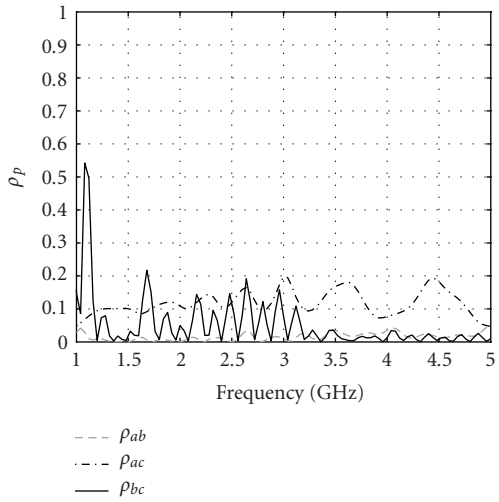

FIGURE 30.13. Correlation $|\rho_{12}|^2$ among mode 1 (a) and mode 2 (c), excited at the center of the spiral, and mode 1 (b), excited at the outer edge of the spiral to generate orthogonal polarizations. The incident field has an elevation spread of 5° and azimuth spread of 60°. The lower frequency bound of mode 2 is 1.2 GHz, thus the spiral does not work correctly for lower frequencies.

excited at the center of the antenna, and a third mode (mode 1) with orthogonal polarization excited at the outer edge of the antenna is used. Figures 30.13 and 30.14 show the power correlation coefficient $|\rho_{12}|^2$ between different modes for a large azimuth angular spread of 60° and a small spread of 20° of the incident waves. The third mode is orthogonally polarized to the other modes, thus the correlation is almost zero. The other modes are more strongly correlated as the patterns of modes 1 and 2 partly overlap. On the other hand, the different phases of the patterns of mode 1 and 2 (see Figure 30.12) decorrelate the received signals, since the single plane waves from different directions superpose differently for each mode.

The correlation coefficients are low enough to obtain a diversity gain or capable MIMO system over a large bandwidth.

30.4.4. Capacity of MIMO systems based on multimode diversity

In order to show the potential of multimode antennas in MIMO systems, simulations of the capacity of a MIMO system with one multimode spiral antenna on each side of the link were performed. Additionally a comparison with dipole antennas, arranged in parallel, is drawn. Figure 30.15 shows the capacity distribution for a fixed SNR of 10 dB for 1000 channel realizations at 2 GHz. The 10% outage capacity is approximately 7.3 bps/Hz.

For comparison two dipole arrays, consisting of three dipoles each, were used, one at each side of the link. The dipoles were arranged in parallel with spacings of $\lambda/4$ and vertical polarization. The array covers approximately the same space as

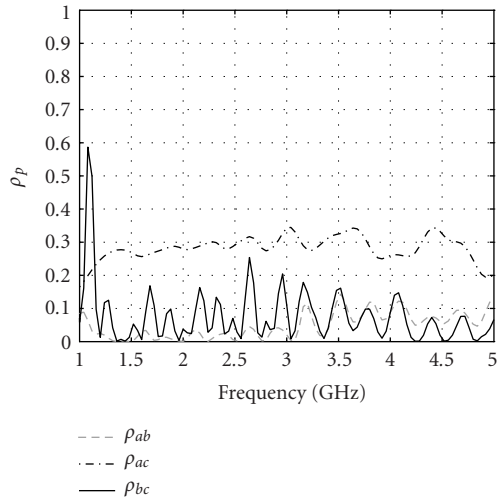

FIGURE 30.14. Correlation among the same modes as in Figure 30.13, but the incident field has an elevation spread of 5° and an azimuth spread of 20°. Due to slight changes in the pattern for different frequencies the correlation coefficient changes. But it is over the whole frequency range low enough to obtain a diversity gain.

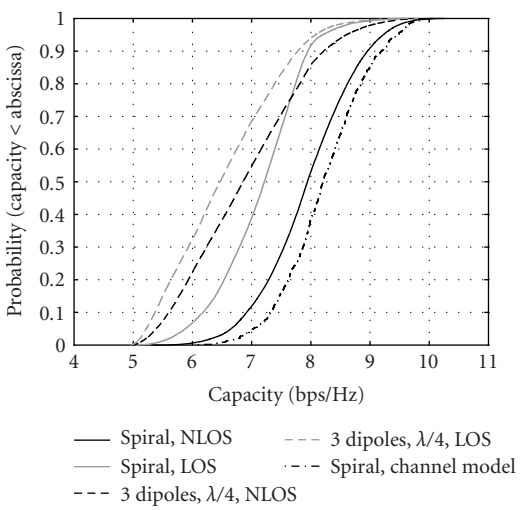

FIGURE 30.15. Cumulative distribution functions of the capacity for different antenna scenarios at 2 GHz for a constant mean SNR of 10 dB. The three dipoles have spacings of $\lambda/4$.

the spiral antenna with dimensions, so that the resonance frequency of the dipoles equals the lower frequency bound of the spiral. Figure 30.15 shows that the dipoles perform worse than the spiral, since neither polarization nor pattern diversity is exploited. The spatial diversity is very limited due to the small antenna spacings.

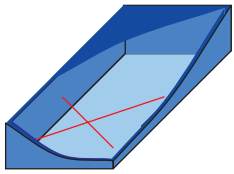

FIGURE 30.16. Cellular phone model with two crossed dipole antennas.

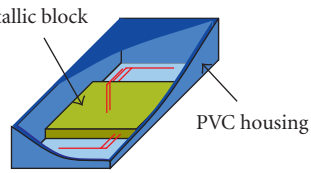

FIGURE 30.17. Cellular phone model with three inverted-F antennas. The size of the housing is $43 \times 105 \times 27\,\text{mm}^3$.

30.5. The new challenge: multiple antennas in handhelds

For the application of MIMO it is essential to integrate antenna arrays in small handheld devices for mobile communications. Since uncorrelated signals at the antennas and high efficiencies of the arrays are required for mobile devices, it is difficult to design capable arrays. The integration of several antennas into handheld devices is possible by a detailed analysis and simulation of the arrays. In the following an example showing the feasibility is given.

30.5.1. Simulation setup

For the handheld devices half-wavelength dipole antennas and inverted-F antennas were used. The aim of the antenna setup was to combine different diversity techniques, such as pattern, spatial, and polarization diversity, to obtain uncorrelated signals at the antennas, see [17]. Additionally polarization diversity makes the antenna system robust against polarization mismatching. The simulation model of the handheld device consists of a metallic block, representing the battery and the display, and a PVC housing with a wall thickness of 2 mm. The size of the housing is $43 \times 105 \times 27\,\text{mm}^3$. Three different antenna configurations in the handheld device were modeled: (a) two crossed dipoles, see Figure 30.16, (b) 3 inverted-F antennas at a large (length = 5 cm), and (c) at a small (length = 3 cm) metallic block, see Figure 30.17. Usually inverted-F antennas require a large ground plane, which is not given in the small handheld device. Thus the metallic block, representing the ground plane, acts as a part of the antenna and influences the system performance. Due to that reason, the size of the metallic block changes the pattern of the inverted-F antennas compared to an idealized antenna and the mutual coupling impedances among the antennas. For the system simulations, self-impedance matching between the antennas and the loads (signal source and

Table 30.2

Antenna configuration	Power correlation at mobile	10% outage capacity in bps/Hz	G_H/G_{SISO} at 50% in dB
2 dipoles, λ spacing	≤ 0.1	12.9	8
3 dipoles, λ spacing	≤ 0.1	14.5	11
2 crossed dipoles	≤ 0.1	11.5	6.9
3 inv.-F, large block	≤ 0.35	13	9.6
3 inv.-F, small block	≤ 0.2	13.5	9.6
SISO	—	3.5	0

drain) was assumed. Perfect (in terms of power) conjugate complex matching is very unrealistic for handheld devices, since the mutual coupling impedances can hardly be matched. They change during usage of the device.

In the following scenario, a link between a small handheld device and a base station in a microcell scenario is considered.[1] The focus here is on the antennas in the handheld device and the base station, thus no interference or multiple users are assumed.

30.5.2. Simulation results

Table 30.2 shows the results. In the second column the maximum power correlation coefficient among all the signals at the handheld device is given. The third column shows the 10% outage capacity in bps/Hz for a given constant transmit power. The transmit power was chosen to result in a 10% outage capacity for the SISO system of 3.5 bps/Hz. In the last column the ratio of the mean transmission gain of the MIMO system to the mean transmission gain of a SISO system with one half-wavelength dipole at the transmitter and at the receiver is given. For comparison large antenna arrays with two and three dipoles with one-wavelength antenna spacing were used instead of the small integrated arrays. The MIMO systems with one-wavelength antenna spacings and no influence of any housing, and so forth perform best, as shown in the first and second rows of Table 30.2. They can be considered as a reference for the other antenna configurations in the handheld device for a comparison of MIMO systems with equal number of antennas. It is

[1]The base station is equipped with three antennas with spacings of 1 meter. The pattern of the commercially available base station antenna "Kathrein Antenne 735 147 (GSM 1800)" was modeled, see [18], for the simulations. The channel data were obtained from ray-tracing simulations of a microcell scenario. The campus of the University of Karlsruhe and the surrounding buildings were used for the simulations. The base station with three Kathrein antennas radiating into the same 120° sector, is placed on one of the highest buildings in the scenario, 3 meters above the roof. At 2000 randomly distributed locations on the campus the channel data are collected. The power azimuth spectrum at the base station is relatively narrow, since there are no scatterers around the antennas. At the mobile the angular spread is wide, as the mobile is surrounded by scatterers.

evident, that all small antenna arrays in the handheld device perform well in terms of correlation and power and thus lead to capable MIMO systems. Surprisingly the handheld device with the large metallic block does not outperform the one with the small block, though the antenna spacings are larger. This is due to the fact that the pattern diversity between the antennas is stronger for the small metallic block. That clearly shows that the whole configuration of the handheld device has to be taken into account.

Further details on the integration of arrays into handhelds and the influence of the user can be found in [19, 20, 21].

30.6. Conclusion and future trends

In this chapter, new antenna concepts for MIMO have been shown. The key observation is that antennas may not be seen independent of the propagation channel or the front ends of the communication devices. For the antenna engineer it becomes essential to understand the whole RF transmission chain to optimize antennas for MIMO systems. On the other hand, system engineers may not neglect the antennas with their specific properties. Using a suitable antenna setup, that, for example, exploits different types of diversity, can improve the MIMO system performance distinctly.

In the near future, many wireless handheld devices will have several antennas to allow for diversity and MIMO. Today's development tools for antennas will have to be extended for the analysis of antenna arrays and their specific properties in diversity and MIMO systems. Classical characteristics of antennas as the pattern and gain are not sufficient for multiantenna systems, new characteristics as the correlation, effective gain, and the capacity will have to be used.

While the theoretical influence of compact antenna arrays on the MIMO system performance is meanwhile well understood, there have been hardly any publication on practical implementations. Future work will fill that gap. Another key topic for antenna engineers will be base station antennas for MIMO and diversity. In the past, this topic has been disregarded because large antenna spacings have been considered to be unproblematic. But due to extremely small angular spread at base stations new concepts like distributed antenna elements of an array need to be discussed.

Abbreviations

MIMO	Multiple-input multiple-output
SISO	Single-input single-output
SNR	Signal-to-noise ratio
lhc	Left-hand circular (polarization)
rhc	Right-hand circular (polarization)
XPR	Cross-polarization scattering ratio

Bibliography

[1] C. Waldschmidt, J. V. Hagen, and W. Wiesbeck, "Influence and modelling of mutual coupling in MIMO and diversity systems," in *Proc. IEEE Antennas and Propagation Society International Symposium*, vol. 3, pp. 190–193, San Antonio, Tex, USA, June 2002.

[2] T. Svantesson, "On capacity and correlation of multi-antenna systems employing multiple polarisations," in *Proc. IEEE Antennas and Propagation Society International Symposium*, vol. 3, pp. 202–205, San Antonio, Tex, USA, June 2002.

[3] D. M. Pozar, *Microwave Engineering*, John Wiley & Sons, New York, NY, USA, 2nd edition, 1998.

[4] J. D. Kraus, *Antennas*, McGraw-Hill Electrical and Electronic Engineering Series. McGraw-Hill, New York, NY, USA, 2nd edition, 1988.

[5] W. Wiesbeck and E. Heidrich, "Wide-band multiport antenna characteristics by polarimetric RCS measurements," *IEEE Transactions on Antennas and Propagation*, vol. 46, no. 3, pp. 341–350, 1998.

[6] J. W. Wallace and M. A. Jensen, "The capacity of MIMO wireless systems with mutual coupling," in *Proc. IEEE Vehicular Technology Conference (VTC '02)*, vol. 2, pp. 696–700, Birmingham, Ala, May 2002.

[7] K. Fujimoto and J. R. James, *Mobile Antenna Systems Handbook*, Artech House, Boston, Mass, USA, 1994.

[8] N. Geng and W. Wiesbeck, *Planungsmethoden für die Mobilkommunikation*, Springer, Berlin, Germany, 1998.

[9] T. Zwick, C. Fischer, and W. Wiesbeck, "A stochastic multipath channel model including path directions for indoor environments," *IEEE Journal on Selected Areas in Communications*, vol. 20, no. 6, pp. 1178–1192, 2002.

[10] C. Waldschmidt, T. Fügen, and W. Wiesbeck, "Spiral and dipole antennas for indoor MIMO-systems," *IEEE Antennas and Wireless Propagation Letters*, vol. 1, pp. 176–178, 2002.

[11] T. Svantesson, "An antenna solution for MIMO channels: the multimode antenna," in *Proc. 34th Asilomar Conference on Signals, Systems, and Computers*, vol. 2, pp. 1617–1621, Pacific Grove, Calif, USA, October 2000.

[12] E. Gschwendtner and W. Wiesbeck, "Multi-service dual-mode spiral antenna for conformal integration into vehicle roofs," in *Proc. IEEE Int. Symposium on Antennas and Propagation*, vol. 3, pp. 1532–1535, Salt Lake City, Utah, USA, July 2000.

[13] R. G. Corzine and J. A. Mosko, *Four-Arm Spiral Antennas*, Artech House, Boston, Mass, USA, 1990.

[14] T. T. Chu and H. G. Oltman, "The sinuous antenna," *Microwave Systems, News and Communication Technology*, vol. 18, pp. 40–48, June 1988.

[15] C. Chuah, D. N. C. Tse, J. M. Kahn, and R. A. Valenzuela, "Capacity scaling in MIMO wireless systems under correlated fading," *IEEE Transactions on Information Theory*, vol. 48, no. 3, pp. 637–650, 2002.

[16] K. I. Pedersen, P. M. Mogensen, and B. H. Fleury, "Spatial channel characteristics in outdoor environments and their impact on BS antenna system performance," in *Proc. IEEE Vehicular Technology Conference (VTC '98)*, pp. 719–724, Ottawa, Canada, May 1998.

[17] C. Waldschmidt, S. Schulteis, and W. Wiesbeck, "Pattern and polarization diversity in MIMO systems," in *IEEE International Symposium on Advances in Wireless Communications (ISWC '02)*, pp. 11–12, Victoria, BC, Canada, September 2002.

[18] M. Baldauf, A. Herschlein, and W. Wiesbeck, "Schutzabstände in der mobilkommunikation," *Frequenz*, vol. 55, no. 11–12, pp. 310–316, 2001.

[19] C. Waldschmidt, C. Kuhnert, S. Schulteis, and W. Wiesbeck, "MIMO handheld performance in the presence of a person," in *URSI International Symposium on Electromagnetic Theory*, Pisa, Italy, May 2004.

[20] C. Waldschmidt and W. Wiesbeck, "Quality measures and examples of arrays for MIMO in handheld devices," in *Proc. IEEE Antennas and Propagation Society International Symposium*, Monterey, Calif, USA, June 2004.

[21] C. Waldschmidt, C. Kuhnert, S. Schulteis, and W. Wiesbeck, "On the integration of MIMO systems into handheld devices," in *Proc. ITG Workshop on Smart Antennas*, Munich, Germany, March 2004.

Christian Waldschmidt: Institut für Höchstfrequenztechnik und Elektronik, Universität Karlsruhe, 76128 Karlsruhe, Germany

Email: waldschmidt@ihe.uka.de

Werner Sörgel: Institut für Höchstfrequenztechnik und Elektronik, Universität Karlsruhe, 76128 Karlsruhe, Germany

Email: werner.soergel@ihe.uka.de

Werner Wiesbeck: Institut für Höchstfrequenztechnik und Elektronik, Universität Karlsruhe, 76128 Karlsruhe, Germany

Email: werner.wiesbeck@ihe.uka.de

31 Radio architectures for multiple-antenna systems

D. Evans

31.1. Introduction

Multiple-input multiple-output antenna systems invariably suffer a complexity and cost penalty. The signals from each antenna must have a means of being independently connected to the associated processing so that the spatial and temporal integrity of the antenna signals are preserved. This requirement appears to necessitate a complete transmitter or receiver for each antenna element in the multiple-antenna array. However, this does not mean that a physically complete transmitter or receiver is necessarily required for each antenna. A question should be asked as to whether it is possible by some means to reduce the inherent replication or parallelism of the transceiver system without sacrificing overall performance.

There are several other systems that exploit multiple transmit and receive elements and these range from phased-arrays radar to ultrasound imaging. Along with MIMO systems, they all share the need to convert and connect signals from the sensor elements to the associated processing. In most instances, the number of elements in these systems is much larger than is typical for MIMO systems indicating greater need to avoid replication in the transceiver systems. However, there is no obvious evidence that this has been given a due consideration. A likely reason for this is that some of these systems are invariably wideband systems and they have many channels ($\gg 10$). It is probably very difficult to combine the channels, and hence the reason that there is no evidence of any techniques to reduce replication in either their transmitter or receiver systems.

There are two ways of approaching the replication problem. The first is to consider whether there is replication that could be removed from multiple transceiver architectures by sharing certain common functions. An example of this is where a common local oscillator is shared by the multiple radios. The second approach is to investigate whether there are radical ways of reusing or sharing the functional elements of the radio architecture between the several antennas by exploiting an additional dimension. Here we could consider whether a radio can be multiplexed between several antennas noting that the multiplexing can be done either in time

or in frequency, or by using codes, analogous to the commonly used multiple access schemes in communications.

Of the various MIMO test beds and demonstrators, the European IST METRA project seems to have given the most consideration to the issues discussed here. Not only has the METRA project studied the impact of using multiple antennas in terms of baseband processing, implementation details, and the cost and complexity overhead; the project also considered the architecture for receiver systems [1]. They describe three potential approaches to radio receiver design but unfortunately give little of their detailed implementation or their likely performance. The successor I-METRA project does not seem to have continued to investigate this aspect of the former project's work. The IST FLOWS project has subsequently taken up this work and considered it in detail and has now proposed a fourth approach which overcomes some of the limitations of the others [2]. Overall, it appears that as yet, little consideration has been given to the topic of multiple-antenna radio systems and for most demonstrators a traditional full-parallel radio architecture is used [3].

The following sections consider the various approaches that may be used, how they can be implemented, and what limitations they may pose to the performance of the radio system. The techniques are mainly implemented in the radio front end whose primary role is to convert the RF signals at the antennas to and from baseband, and this is performed mostly in the analogue domain.

31.2. Architectures for MIMO RF front ends

The scope of the RF front-end architectures that are considered here extends from the antenna to the analogue-to-digital interface at either the DAC or the ADC. The elements of the front end are taken as generic functional blocks and, except in some limited instances, no consideration is given to the detailed performance of these blocks. The description of the four architectures focuses on the receiver though some issues that may affect the performance of the transmitter are noted when a particular technique is used.

31.3. Multiple-radio architectures

This approach assumes that each antenna will use a complete radio system at least as far down as the ADC. Each receiver consists of a complete chain of functional elements comprised of an RF filter, LNA, mixer, LO, IF and IF filter, I and Q mixers, channel filters, and finally a pair of ADC. The receiver may be a zero-IF configuration in which case the first IF will be missing, this arrangement is shown in Figure 31.1 for two receivers.

From the elements within the receiver chain, the entity that can most obviously be shared between multiple receivers is the LO. This is a worthwhile saving since the LO is a high-performance element and may itself consist of several elements such as a synthesiser and frequency reference. An increase in power will be required so that the LO can drive several mixers but this is not a significant penalty.

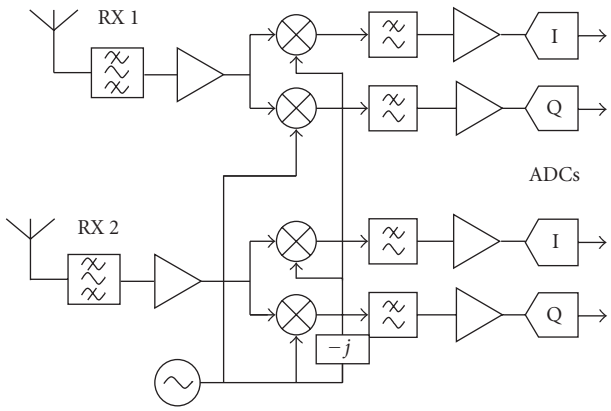

Figure 31.1. Multiple-radio architectures for two antennas.

There are several other common or sharable elements that are not obvious from the figure. These are the housekeeping and conditioning functions such as power distribution and circuit biases, and these can easily be distributed between several transmitters and receivers. This benefit would mostly be gained where multiple receivers are integrated into a single chip. Consequently, a doubling of the functions in an integrated circuit does not necessarily imply a doubling of the silicon area of the die. Another advantage that comes from integration is the sharing of the associated bonding pads since these usually require a significant area. These advantages would be even greater when four receivers are integrated into a single chip. Most of these benefits so far result in a saving of silicon-chip area by exploiting the sharing functions. A further advantage may be gained in low-transmission-power MIMO radio systems, where the housekeeping functions may consume a significantly higher proportion of the overall power.

The performance issues that may need to be considered with the full-parallel approach are the balance between the multiple receivers or transmitters, and RF components in particular can be prone to this. However, the integration of several parallel systems onto a single silicon chip may help to minimise the device and circuit performance variations. Furthermore such imbalances will most likely be taken into account by the MIMO radio channel estimation processes. Intercircuit coupling is more significant in an integrated circuit than in separate circuits but this is still much lower than the coupling within the MIMO antenna array where the typical levels of intercoupling are not thought to have a significant impact on system performance. The specification and performance of the RF stages including the ADCs is therefore expected to be the same as that of a single-input single-output system.

31.4. Multiplexing in time

In the time-multiplexed approach, the outputs from the antenna array are multiplexed together by using an RF switch. The combined signals are then passed into

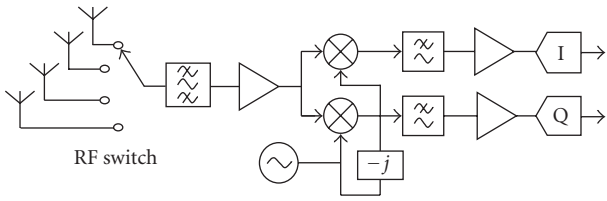

FIGURE 31.2. Single receiver multiplexed in time between four antennas.

a single radio receiver for the purposes of down conversion to baseband [1]. The radio contains all of the necessary functions such as the front-end filter and LNA, RF mixer, LO, IF, and channel filter; this arrangement is shown in Figure 31.2. The individual signals can then be recovered by demultiplexing at baseband, though this is not shown in the figure. Since the received signals at each antenna must be preserved in each sample interval for the chosen transmission scheme, the multiplexing together of all of the signals from the antennas must take place within the sample interval. The switch therefore has to operate at a speed of N times the sampling rate, where N is the number of antennas.

The demultiplexing may be implemented either before or after the ADC. Clearly only one pair of ADCs is required if the demultiplexing is done in the digital domain but the rate that the ADC is running at must be proportionately higher. The choice is therefore between having N ADCs running at S samples/s with a resolution of X bits versus one ADC running at $N \times S$ samples/s and potentially also having X bits. Providing that the resolution is the same in both cases, the power consumption is the same. The demand on the dynamic range would initially appear to be the same in both cases. However, it is interesting to note that this might need to be larger than the situation where separate receivers (plus associated ADCs) are used for each antenna. Here each receiver can set its own AGC level according to the instantaneous received signal strength at each antenna so as to be able to position the signal within the dynamic range window of the ADC. When several received signals are combined, the dynamic range is likely to be larger since it now has to cover the range from faded to strong signals. This will necessitate supporting a higher dynamic range, and hence an ADC having a larger resolution may be required.

The main weakness of this approach, as far as the receiver performance is concerned, is that the signal at each antenna is only sampled for a fraction of the nominal sample or symbol period, that is, $1/N$ times sample time. Therefore only a fraction of the received power that is available at each antenna is actually being used. If the system is using two antennas ($N = 2$), then an inherent 3 dB loss is experienced and proportionately more when further antennas are used. It is possible that the loss of performance may be more than offset by the gain when using a MIMO system so there could be a substantial cost saving in the radio component count at the expense of some loss of performance. There are however a few more issues that need to be considered.

Firstly, can a radio switch perform sufficiently well given that the associated losses are near to the antenna? This loss will result in a degradation of the receiver noise figure. This situation will be compounded by the need for switching rates that are typically well in the MHz region for wireless LANs and by the need for N-way switching. It is possible to overcome the loss by placing the switch after a set of low-noise amplifiers that are directly connected to the antennas but this then defeats the objective of trying to reduce the replication in the system.

Secondly, since the sample interval of the data in the RF chain has increased by N, then the bandwidth of the IF must increased proportionately. For the same reason, the sampling rate of the ADC must be increased. Care will need to be taken to ensure that the aliasing into and out of the adjacent channels does not affect performance.

Thirdly, the effects of this approach have only been considered when applied to the receiver, and similar issues apply equally to the transmitter. Each transmitter would only be transmitting for $1/N$ of the time and hence its efficiency is reduced. The switching rate is potentially so rapid that it is probably not possible to turn off or power down each transmitter when it is not being used. In addition and as a consequence of the switching at the output of transmitters, there will be a $\sin x/x$ type of spectrum from each transmitter and the necessary spectrum control and filtering will be difficult to achieve.

Finally, there may be some interesting array effects that could be associated with this approach. Since only one antenna is "sampled" at any one instant, the question arises as to whether the array is still behaving like an array as far as the MIMO processing is concerned. It is possible that the switching process can be exploited by providing certain impedance terminations on the "off" antennas to deliberately affect the directional properties of the array.

It should be noted that something slightly similar to the time-multiplexed approach was previously suggested by Hammerschmidt et al. [4]. In their proposal, the antenna switching was only a means of preselecting one of the set of antennas during a training interval. The switch then remained locked for the rest of the transmission burst so that the maximum received power was obtained.

31.5. Multiplexing in frequency

Several signals can be multiplexed together by applying a different frequency offset to each of them. This offset would typically correspond to a radio channel spacing (FCH) or a multiple thereof and this would allow several signals to be combined and then passed through a common receiver [5]. This arrangement for up to three antennas is shown in Figure 31.3.

Following down conversion to baseband, the three combined frequency offset signals are then separated into individual signals. There are several weaknesses to this approach. Firstly, there is a need for additional RF local oscillators, probably synthesisers, to create the necessary frequency offsets. Secondly, the RF amplifiers and associated RF filters are probably required between each antenna and mixer to overcome the high loss in each mixer. This is not shown in the figure. Thirdly,

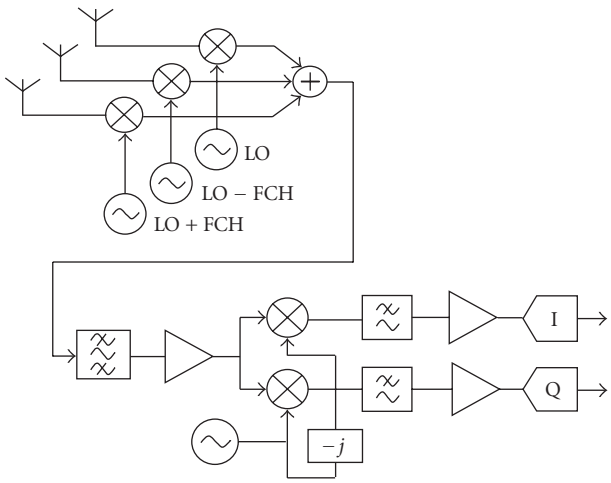

FIGURE 31.3. Single receiver where the signals from three antennas are multiplexed together by the use of differing frequency offsets.

there is a requirement to position the signals from the antennas into what is effectively the adjacent RF channels even though this is being performed within an IF frequency band. This last point may give rise to problems if the adjacent channels are already occupied though [5] indicates that the use of clear channels that are two or more adjacent channels away could also be used if the immediate ones are known to be occupied. It is likely that only the IF stage can most usefully be shared in this scheme and given these potential problems, this approach appears not to have been pursued in any great detail.

31.6. Multiplexing using orthogonal codes

The third method of combining several individual signals into a single channel is to use a code-division technique. An example of this method is the use of Walsh functions (orthogonal codes) to differentiate users and services in CDMA mobile telephony [6]. This technique can also be applied as a solution to the problem that is being addressed here. The received signal at each antenna is given a unique identity by the application of an orthogonal code and the signals are then combined into one signal prior to passing them through a single RF receiver chain [2]. This approach is shown in Figure 31.4.

The combined signals can then be separated by making use of the orthogonal property of the coding such that

$$\begin{aligned} \mathrm{RX}\,1 &= \sum \mathrm{Wal}(0,\theta) \times [\,\mathrm{RX}\,1 \times \mathrm{Wal}(0,\theta) + \mathrm{RX}\,2 \times \mathrm{Wal}(1,\theta)\,], \\ \mathrm{RX}\,2 &= \sum \mathrm{Wal}(1,\theta) \times [\,\mathrm{RX}\,1 \times \mathrm{Wal}(0,\theta) + \mathrm{RX}\,2 \times \mathrm{Wal}(1,\theta)\,], \end{aligned} \tag{31.1}$$

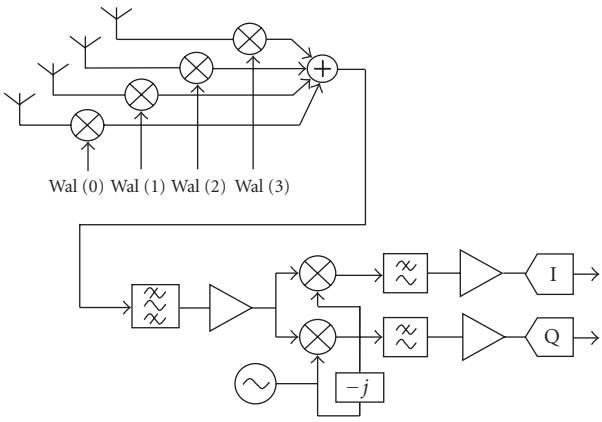

FIGURE 31.4. Single receiver using orthogonal codes to combine the signals from four antennas.

where RX 1 and RX 2 are the signals from the two antennas, the summation is over the nominal sample time, and $\mathrm{Wal}(0,\theta)$ and $\mathrm{Wal}(1,\theta)$ are the zeroth and the first Walsh functions, respectively. If additional antennas are used, then higher-order Walsh functions can be used accordingly as indicated in Figure 31.4.

Since the application of the digital coding signals is in the analogue domain, it is appropriate for mixer elements to apply a constant amplitude biphase modulation to the RF signals. Signal recovery is assumed to be after the ADCs and at baseband though the original received signals could be recovered in either the analogue or digital domains.

Several of the issues that apply to the previous case of multiplexing or switching in time also apply here such as the choice of ADCs, the increase in the receiver bandwidth, and the losses within the biphase modulators, plus the need for subsample time switching speeds. Significantly though, the orthogonally coded approach does not suffer the $1/N$ sensitivity degradation that the time-multiplexed approach is subjected to since all of the received energy is retained over the full-symbol period. The orthogonal multiplexed receiver is therefore a potentially promising approach.

Clearly, the key components in this scheme are the biphase modulators. These will be required to have a relatively low loss, perhaps 1 dB or lower at the desired RF frequency. Likewise, the phase accuracy and the amplitude balance between the 0 and 180 degrees states will need to be within acceptable limits so as not to degrade the MIMO performance. In addition and depending on the number of antennas, they will have to switch several times during a nominal symbol period and for a wideband system, such as a wireless LAN having for example a bandwidth of 20 MHz, the switching times will need to be about a nanosecond or less. The implication here is that these are potentially high-performance components though within the capabilities of a technology such as GaAs.

Table 31.1. Comparative merits of the four proposed MIMO radio architectures.

Feature	Full-parallel	Time	Frequency	Code
System redundancy	High	Low	Medium	Low
Complexity	2	1	4	3
Inherent system loss	None	$1/N$	None	Not significant
Implementation loss	None	In switch	In mixers	In bi-f mods
IF bandwidth increase	No	Yes, N	Yes, N	Yes, N
Increased dynamic range at ADC	No	Potentially	Potentially	Potentially
Imbalance between antennas	Yes	No	No	No
Applicable to TX as well as RX	Yes	No	No	No

31.7. Comparison

Table 31.1 lists the key features of the four approaches for a receiver having N antennas. The system redundancy that is considered here is the level of radio function replication and clearly represents an indication of the cost overhead. However it should be noted that high level of redundancy does imply a robust system, this may be of interest in some instances [1]. The complexity is ranked on a subjective scale, a value of 4 is deemed to be the most complex and 1 is the least.

The performance and complexity of all these four approaches varies considerably though it would appear that only the full-parallel and the code-multiplexed schemes offer potentially usable solutions where the issues of performance and cost savings are important.

31.8. Conclusion

Four radio front-end schemes for multiple-antenna systems were described. The traditional approach is to use a full-parallel scheme with a shared local oscillator. Further investigation shows that additional circuit functions may be shared and that the assumed complexity and associated cost seem to be less severe than initially expected. Three alternative approaches are possible that enable sharing the single radio between several antennas by means of either time or frequency or code multiplexing. Of these three, only the code-multiplexing scheme offers an acceptable performance and worthwhile savings in component replication.

The full-parallel approach has the least risk and offers an RF system performance very similar to that of a single transmitter and receiver system. The code multiplexing scheme needs further investigation before the potential advantages can be exploited.

Acknowledgment

The author wishes to acknowledge the support given to this work by Philips Research Laboratories, Redhill, the assistance of his colleagues in the IST FLOWS

Project, and the partial funding from the European Union's 5th Framework Programme.

Abbreviations

ADC	Analogue-to-digital convertor
AGC	Automatic gain control
CDMA	Code-division multiple access
DAC	Digital-to-analogue convertor
I	In-phase
IF	Intermediate frequency
IST	Information society technologies
GaAs	Gallium arsenide
LAN	Local area network
MIMO	Multiple-input multiple-output
LNA	Low-noise amplifier
LO	Local oscillator
Q	Quadrature phase
RF	Radio frequency
RX	Receiver
TX	Transmitter
Wal	Walsh

Bibliography

[1] J. Ylitalo, A. Pollard, M. Heikkila, and J. R. Fonollosa, "Cost versus Benefit Trade-offs of Multi-Element Transmission/Reception," IST-1999-11729 METRA, Deliverable no. D5.1, 28th August 2001.

[2] D. Evans, D. Raynes, A. Spencer, and P. Mendizabal, "Development and Simulation of a Single Standard MIMO Transceiver," IST-2001-32125 FLOWS Deliverable no. D9 version 2, 30th June 2003.

[3] T. Horseman, J. Webber, M. Beach, and A. Nix, "SIMO and MIMO Hardware Description," IST-1999-10322 SATURN, Deliverable no. D532, 2nd August 2001.

[4] J. S. Hammerschmidt, C. Drewes, and A. A. Hutter, "Adaptive space-time equalization for mobile receivers," in *Proc. IEEE International Conference on Acoustics, Speech, and Signal Processing (ICASSP '00)*, vol. 5, pp. 3013–3016, Istanbul, Turkey, 2000.

[5] D. Evans and R. Fifield, "Frequency offset diversity receiver," UK patent application No. 0129077.4, 5th December 2001. Applicant: Koninklijke Philips Electronics NV.

[6] H. Holma and A. Toskala, Eds., *WCDMA for UMTS: Radio Access for Third Generation Mobile Communications*, John Wiley & Sons, Chichester, England, 2002.

D. Evans: Philips Research Laboratories, Redhill, Surrey RH1 5HA, England, UK

Email: dave.evans@philips.com

32 Transceiver nonidealities in multiantenna systems

André Bourdoux and Jian Liu

32.1. Introduction

The great benefits of MIMO transmission described and analyzed in the previous chapters do not come, unfortunately, for free. If only one drawback of MIMO transmission had to be mentioned, the higher complexity—both digital and analog—would certainly rank first. This complexity impacts both the hardware cost and the power consumption. Especially the analog part of the MIMO transceiver needs a careful design approach to avoid performance loss or a prohibitive implementation. Chapter 3 of this part covers in detail the architectural alternatives of MIMO transceivers that can potentially lead to saving in hardware real estate. The assumption throughout the architectural analysis was that the analog building blocks such as mixers, amplifiers, A/D and D/A converters, and so forth were ideal. This chapter will address the issue of nonidealities.

The correct analysis and specification of the transmitter and receiver modems is important for the following reasons:

(i) to assess the performance degradation (e.g., BER or PER degradation) of a given nonideality or combination of nonidealities;

(ii) to be able to provide specifications to the analog designers. It indeed turns out that overspecifying a front end can result in dramatic increase in silicon area, cost and power consumption in a practical commercial application. This is even more crucial for multiantenna systems because of the larger number of transceivers;

(iii) because of standardization and regulatory issues, the transmitted signal must comply with a transmit frequency mask and the received signal can be impaired by interference from adjacent bands due to finite out-of-band rejection and/or intermodulation.

In this chapter, the coverage of nonidealities in MIMO transmission will follow the following approach.

(i) We will describe a generic transceiver architecture and describe a low-pass equivalent model for the MIMO transceiver and the nonidealities.

(ii) Our analysis will be made for the combination of MIMO techniques with OFDM because this is a practical design challenge and MIMO-OFDM transmission is, at the time of this writing, seen as a strong candidate for upcoming standards (e.g., IEEE 802.11n).
(iii) We will consider several types of MIMO transmission, including spatial division multiplex (SDM), space-time block coding (STBC), and maximum ratio combining (MRC); SDM and MRC will be applied at either the transmitter or receiver side; joint transmit-receive processing (with SVD prefilters and postfilters) will also be addressed.
(iv) The following nonidealities will be analyzed:
  (a) IQ mismatch, assuming a frequency flat behavior of the transceiver;
  (b) clipping and quantization;
  (c) saturation (AM-AM);
  (d) phase noise, effect (common contribution, noncommon, tracking).

Note that we will not consider the effect of nonperfect synchronization or nonideal channel estimation since these effects are addressed in Part 1, Chapter 6 and Part 2, Chapter 5, respectively. More specifically, in the following, we will assume that the carrier and clock frequency and timing offsets have been perfectly compensated and that, whenever or wherever channel knowledge is needed, it has been perfectly estimated.

32.2. Analog transceivers and nonidealities

32.2.1. Ideal transceiver

Figure 32.1 shows 2 generic transceiver architectures. In the analog SSB architecture (Figure 32.1a), the complex digital signal is converted to analog at baseband or higher rate, lowpass filtered and SSB modulation is achieved by mixing with a local oscillator (LO) with 0° and 90° components. If needed (super-heterodyne architecture), additional upconversion is added to bring the signal to RF where it is filtered, amplified and a filter removes unwanted harmonics generated by the power amplifier. The digital SSB transmitter (Figure 32.1b) generates the SSB modulation by digitally upsampling and lowpass filtering the I and Q components of the complex baseband signal. The resulting complex upsampled signal is digitally mixed with a complex exponential. The real part of this mixing is the SSB modulated carrier which is then converted to analog and upconverted.

Two dual generic receiver architectures are shown in Figure 32.2. In the analog quadrature architecture (Figure 32.2a), the received signal is filtered (to remove out-of-band interference), amplified by an LNA, which is usually the dominant noise contribution of the receiver, and filtered again to remove undesired signals at the input of the mixer. After optional down conversion, the signal is fed to two mixers with LOs in quadrature, yielding the in-phase and quadrature components that are further lowpass filtered and digitized. The digital quadrature receiver (Figure 32.2b) achieves quadrature in the digital domain after IF or bandpass sampling, mixing with a complex exponential having the components

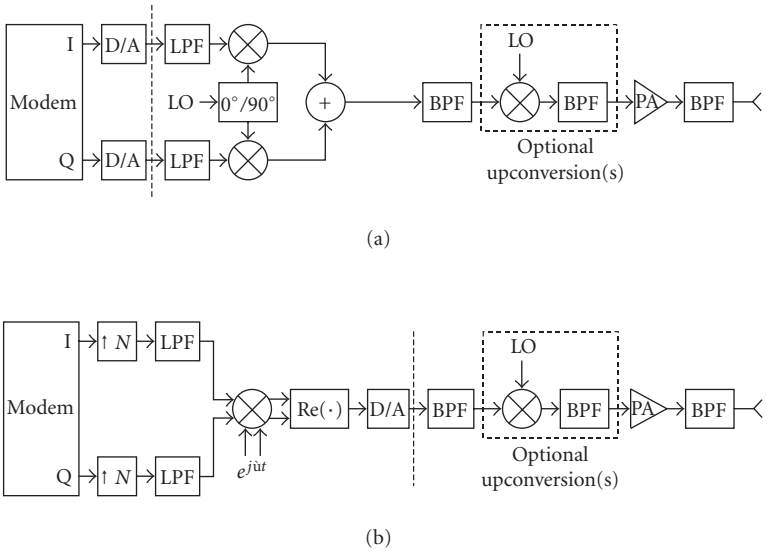

FIGURE 32.1. Generic transmitter (a) analog SSB, (b) digital SSB architecture.

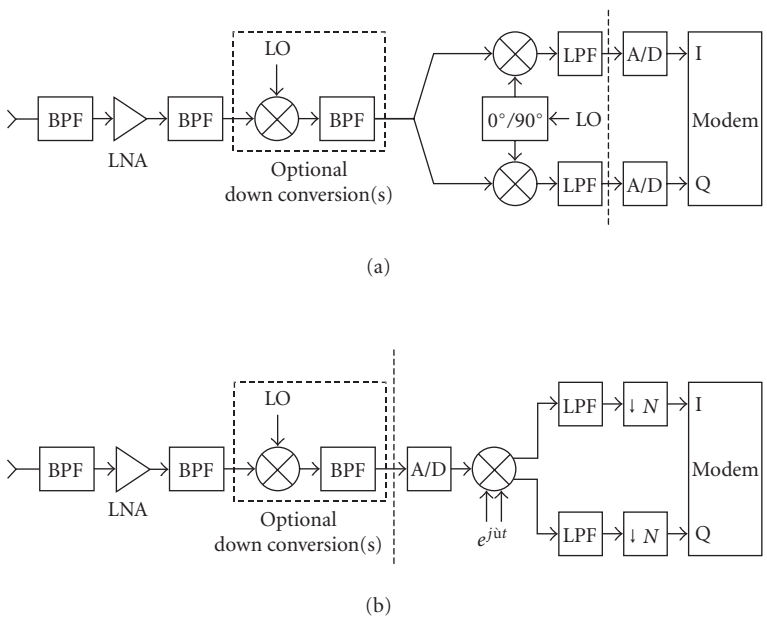

FIGURE 32.2. Generic (a) analog, (b) digital quadrature receiver architecture.

0° and 90° out-of-phase, lowpass filtering and decimating to baseband rate. Note that without optional up- or down-conversion architecture, the analog SSB transmitter architecture and analog quadrature receiver architecture correspond to the so-called zero-IF or direct conversion architecture [1].

32.2.2. Nonidealities in analog transceivers

Clipping and quantization. The number of bits (NOB) of the ADC and DAC must be kept as low as possible for obvious reasons of cost and power consumption. On the other hand, a large number of bits is desirable to reduce the effect of quantization noise, reduce the risk of clipping, and accommodate signal level variations. Following the derivations in [2, 3], the total SNR after quantization and clipping on an L^2-QAM modulated signal is

$$\mathrm{SNR}_{\mathrm{TOT}} = \left[(\mathrm{SNR}_{\mathrm{Quant}})^{-1} + (\mathrm{SNR}_{\mathrm{Clip}})^{-1} \right]^{-1}, \tag{32.1}$$

where

$$\mathrm{SNR}_{\mathrm{Quant}} = \frac{12 \cdot 2^{2b}}{(2\mu)^2}. \tag{32.2}$$

$$\mathrm{SNR}_{\mathrm{Clip}} = \left\{ (1+\mu^2)\,\mathrm{erfc}\left(\frac{\mu}{\sqrt{2}}\right) - \sqrt{\frac{2}{\pi}} \cdot \mu e^{\mu^2/2} \right\}^{-1} \tag{32.3}$$

and m is the normalized clipping level, that is, the ratio of the clipping level to the rms amplitude of the time-domain signal. Figure 32.3 shows the evolution of the total SNR for various values of NOB. All curves exhibit an optimal value for μ between 3 and 5. The presence of an optimum is logical since, at constant NOB, increasing the value of μ first improves the total SNR. But, when μ is so large that clipping does not occur, further increasing μ does not improve $\mathrm{SNR}_{\mathrm{Clip}}$ and only degrades $\mathrm{SNR}_{\mathrm{Quant}}$.

IQ imbalance. The SSB modulation and quadrature conversion described in the ideal architectures are usually not perfect: the amplitude of the two components can differ slightly and their phase difference can be different from 90°. IQ imbalance typically arises with the analog SSB generation at the transmitter or with the analog quadrature generation at the receiver or both. The degradation due to IQ imbalance is best interpreted in the frequency domain. It can be shown that, for a positive frequency component, IQ imbalance will slightly modify the amplitude and phase of that component and introduce a spurious signal at the image (i.e., opposite) frequency. For an amplitude mismatch ϵ and a phase orthogonality mismatch $\Delta\varphi$ (Figure 32.4), an ideal complex baseband signal $r(t)$ is transformed

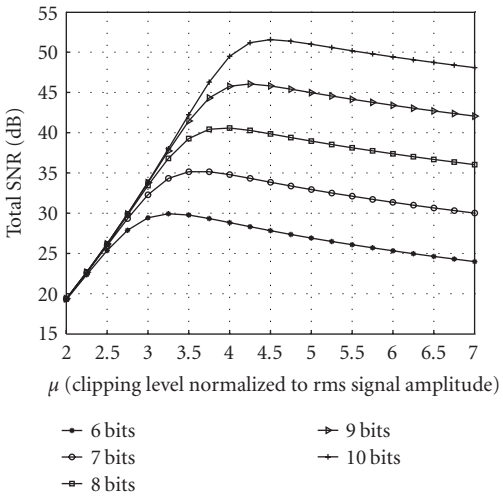

FIGURE 32.3. Total SNR resulting from combined clipping and quantization, showing the optimum value of μ for OFDM modulation.

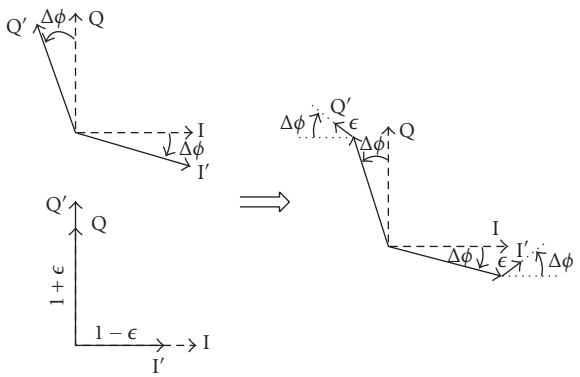

FIGURE 32.4. The effect of ϵ% amplitude mismatch and $\Delta\varphi$ radian phase mismatch on hypothetical I and Q constellation points. I, Q are transformed into I′ and Q′.

into a distorted complex signal $r_{\mathrm{IQ}}(t)$ as follows [1, 4]:

$$\begin{aligned} r_{\mathrm{IQ}}(t) &= (1+\epsilon)\cos\Delta\phi\,\Re\{r(t)\} - (1+\epsilon)\sin\Delta\phi\,\Im\{r(t)\} \\ &\quad + \jmath\big[(1-\epsilon)\cos\Delta\phi\,\Im\{r(t)\} - (1-\epsilon)\sin\Delta\phi\,\Re\{r(t)\}\big] \\ &= (\cos\Delta\varphi + \jmath\varepsilon\sin\Delta\varphi)\cdot r(t) + (\varepsilon\cos\Delta\varphi - \jmath\sin\Delta\varphi)\cdot r^*(t) \\ &= \alpha\cdot r(t) + \beta\cdot r^*(t), \end{aligned} \tag{32.4}$$

where $\Re\{\}$ denotes the real part and $\Im\{\}$ the imaginary part. The SNR resulting

from IQ imbalance is given by

$$\mathrm{SNR}_{\mathrm{IQ}} = \frac{\cos^2\Delta\phi + \varepsilon^2\sin^2\Delta\varphi}{\varepsilon^2\cos^2\Delta\phi + \sin^2\Delta\varphi} = \frac{1+\varepsilon^2\tan^2\Delta\phi}{\varepsilon^2+\tan^2\Delta\phi}. \tag{32.5}$$

Phase noise. Phase noise originates from nonideal clock oscillators and frequency synthesis circuits. In the frequency domain, phase noise is most often characterized by the SSB phase noise, which is the power spectral density (PSD) of the phase $\varphi_n(t)$ of the oscillator signal $\Re(e^{J\omega t+J\varphi_n(t)})$. An ideal oscillator has a Dirac-like PSD at DC, corresponding to no phase fluctuation at all. In practice, the PSD exhibits an approximately decreasing behavior as the offset from the carrier frequency increases. Nonmonotonic behavior is attributable to, for example, phase locked loop (PLL) filters in the frequency synthesis circuit. The effect of phase noise on OFDM signals has been extensively reported and analyzed in the literature. A good treatment is provided in [5]. Phase noise can be thought of as consisting of a large number of complex exponentials, each at an offset Δf from the carrier and with an amplitude weighted by the value of the PSD at that offset. Each of these complex exponentials create 2 sorts of effects:

(i) a rotation of the constellations, identical on all subcarriers, called own noise contribution in [5] and that we will refer to as common phase error (CPE);

(ii) leakage on all subcarriers, appearing as noise on all subcarriers, called foreign noise contribution in [5] and which is commonly known as intercarrier interference (ICI). Because of the large number of subcarriers, this contribution is approximately Gaussian.

The CPE and ICI contributions can be captured by a single equation:

$$\eta[n] = e^{J\pi(\Delta f/B_s - n)((P-1)/P)}\frac{\sin\pi(\Delta f/B_s - n)}{\sin(\pi/P)(\Delta f/B_s - n)} \tag{32.6}$$

with Δf the frequency offset of the phase noise component, B_s the subcarrier spacing, P the number of subcarriers, and n the frequency index. With $n = 0$, the value of the CPE is returned while $n \neq 0$ will return the value of the ICI. The total impact of phase noise is obtained by integrating the leakage for all frequency components weighted by their PSD and the FFT filter bank characteristic.

Nonlinear power amplification. Nonlinear behaviors can occur in any amplifier but it is more likely to occur in the last amplifier of the transmitter (power amplifier or PA) where the signal power is the highest. For power consumption reasons, this amplifier must have a saturated output power that is as low as possible, compatible with the system level constraints such as TX power and link budget. The gain characteristic of an amplifier is almost exactly linear at low input level and, for increasing input power, deviates from the linear behavior as the input power approaches the 1 dB compression point (IP1: the point at which the gain

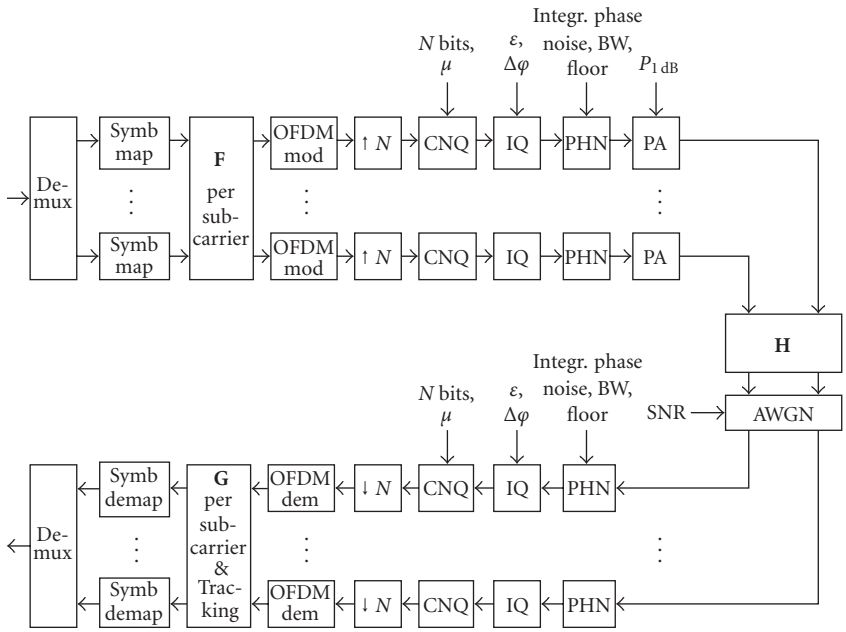

FIGURE 32.5. The global simulation model allows simulating the nonidealities together with many MIMO transmission schemes.

is reduced by 1 dB because the amplifier is driven into saturation) and eventually reaches complete saturation. The input third-order intercept point (IIP3) is also often used to quantify the nonlinear behavior of amplifiers. It is the input power at which the power of the two-tone third-order intermodulation product would become equal to the power of the first-order term. There is no analytical link between the real IIP3 and the 1 dB compression point but "rules of thumb" are often used to relate one to the other. Because of the high peak-to-average power ratio of the OFDM waveform, several dB of back-off are necessary, that is, the rms input power level must be kept several dB below the 1 dB compression point so that the high peaks present in the OFDM waveform can be reliably amplified. This back-off actually dramatically reduces the power efficiency of the power amplifier and must be kept to a minimum.

32.2.3. Modeling nonidealities

Global simulation model. The nonidealities analyzed in this section do not easily lend themselves to analytical derivations. Especially, the prediction of the BER degradation in presence of these effects is not easily performed analytically. We have therefore developed a simulation model to assess the performance degradations. Figure 32.5 illustrates the functional block diagram of the MIMO-OFDM simulation environment, including the nonidealities. The nonidealities can be added at the transmitter, the receiver, or both. However, in our coverage of MIMO

transmission, we will only apply the nonidealities where the MIMO processing actually takes place, which is at the receiver for RX processing, at the transmitter for TX processing, or at both sides for TX-RX processing. Indeed, a nonideality applied where the antenna branches are independent will not directly introduce MSI and have the same effect as in SISO-OFDM transmission, which has been extensively covered in the literature, for example, in [3].

Note that the order in which the nonidealities are applied is important. It has to correspond to the order in which they physically occur in the hardware.

MIMO transmission model and MIMO modes. We consider a generic linear MIMO transmission scheme where K symbols are transmitted from M TX antennas and received by N RX antennas.

It can be described by the following equation:

$$\hat{\mathbf{x}} = \mathbf{Gr} = \mathbf{G} \cdot (\mathbf{Hs} + \mathbf{n}) = \mathbf{G} \cdot (\mathbf{HFx} + \mathbf{n}), \tag{32.7}$$

where $\mathbf{x}$ is the Kx1 transmitted symbol vector, $\mathbf{s}$ is the Mx1 transmitted signal vector, $\mathbf{r}$ is the received signal vector, $\hat{\mathbf{x}}$ is the estimated received symbol vector, $\mathbf{F}$ is the MxK TX spatial filter, and $\mathbf{G}$ is the KxN RX spatial filter. OFDM with P subcarriers is used and the MIMO processing in (32.7) is applied per subcarrier. Processing per subcarrier according to (32.7) is valid if the following conditions are fulfilled.

(i) Correct timing and carrier frequency synchronization occurs (no ICI and no ISI).

(ii) The channel delay spread is shorter than the OFDM cyclic prefix.

Note that the nonidealities that are considered here basically violate the first assumptions: they generate a mixture of ICI and MSI that cause performance degradation when the linear model in (32.7) is used. Table 32.1 shows the various MIMO transmission schemes that are analyzed in this section, together with the prefilter and postfilter used and the number of TX and RX antennas.[1] An important point is that in the case of TX processing, no channel state information (CSI) is *theoretically* needed at the receiver because no spatial processing needs to be applied. In practice, per-stream channel estimation and equalization is still needed in order to scale and rotate the received constellations because of transceiver effects such as AGC, residual frequency offsets, phase noise, and so forth.

Clipping and quantization. The amount of clipping depends on where the rms level of the signal is put in the dynamic range of the A/D or D/A converter. Once this is done, quantization and clipping are easily performed. The parameters for

[1] Almost all the transmission schemes indicated in Table 32.1 can be described by the linear model of (32.7). STBC requires a small modification to take into account the simultaneous transmission of 2 symbols in 2 symbol periods. Note that STBC (which is a transmit diversity technique) has been included in both the RX and TX processing schemes because it does require processing, though very simple, at both sides.

TABLE 32.1. MIMO set-ups simulated in the analysis of transceiver nonidealities. ($\mathbf{H} = \mathbf{U}\boldsymbol{\Sigma}\mathbf{V}^H$, $\mathbf{u}_1$ and $\mathbf{v}_1$ are the principal left and right singular vectors, $\tilde{\mathbf{H}}$ is the virtual matrix corresponding to the STBC precoding).

Type	Transmission scheme	Spatial filter		Number of antennas
		$\mathbf{F}$	$\mathbf{G}$	$M \times N$
RX	SDM-ZF	$\mathbf{I}_{M,M}$	$\mathbf{H}^{-1}$ or $\mathbf{H}^{\dagger}$	$2 \times 2, 2 \times 3$
	SDM-MMSE	$\mathbf{I}_{M,M}$	$\mathbf{H}^H(\mathbf{H}\mathbf{H}^H + \sigma_n^2\mathbf{I})^{-1}$	$2 \times 2, 2 \times 3$
	MRC	$\mathbf{I}_{M,M}$	$\mathbf{H}^H$	1×2
	STBC	Alamouti	$\tilde{\mathbf{H}}^H$	$2 \times 1, 2 \times 2$
TX	SDM-ZF	$\mathbf{F}_u = \mathbf{H}^{-1}$ or $\mathbf{H}^{\dagger}$ $\mathbf{F} = \mathbf{F}_u / \lVert\mathbf{F}_u\rVert_{FRO}$	$\mathbf{I}_{N,N}$	$2 \times 2, 3 \times 2$
	SDM-MMSE	$\mathbf{F}_u = \mathbf{H}^H(\mathbf{H}\mathbf{H}^H + \sigma_n^2\mathbf{I})^{-1}$ $\mathbf{F} = \mathbf{F}_u / \lVert\mathbf{F}_u\rVert_{FRO}$	$\mathbf{I}_{N,N}$	$2 \times 2, 3 \times 2$
	MRC	$\mathbf{H}^H / \lVert\mathbf{H}\rVert_{FRO}$	$\mathbf{I}_{N,N}$	1×2
	STBC	Alamouti	$\tilde{\mathbf{H}}^H$	$2 \times 1, 2 \times 2$
TX-RX	SDM-MMSE	$\mathbf{V}\boldsymbol{\Sigma}_{\text{MMSE}}$	$(\boldsymbol{\Sigma}\boldsymbol{\Sigma}_{\text{MMSE}})^{-1}\mathbf{U}^H$	$2 \times 2, 2 \times 3, 3 \times 2$
	MRC	$\mathbf{v}_1$	$\frac{1}{\sigma_1}\mathbf{u}_1^H$	$2 \times 2, 2 \times 3, 3 \times 2$

clipping and quantization are

(i) the number of bits;

(ii) the clipping level expressed as a multiple of the signal average power.

IQ imbalance. IQ imbalance can be directly modeled by means of (32.4). The parameters for IQ imbalance are

(i) the amplitude imbalance;

(ii) the phase imbalance.

Phase noise generation. Phase noise can be generated by generating values of the phase $\varphi(t)$ at the desired sample rate with the desired PSD. The phase noise PSD is usually defined by a piecewise linear model. There are two basic approaches: generation in the time domain or in the frequency domain. In the time domain approach (Figure 32.6a), the PSD is first used to define the impulse response of a filter whose frequency-domain transfer function is equal to the square root of the PSD. Then, the samples of the phase of the phase noise are obtained by filtering (convolving) a gaussian noise source with this filter impulse response.

In the frequency domain approach (Figure 32.6b), a complex gaussian noise sequence is first generated. It is then element-wise multiplied with the square root of the desired PSD and converted to the time domain by means of an inverse Fourier transform. Note that the frequency-domain sequence must be complex conjugate symmetric about DC so that its corresponding time-domain signal is purely real.

For MIMO transmission, it is assumed that the same LO is used across all antenna branches. If this is not the case, the impact of the phase noise can be shown to be higher and a more sophisticated tracking loop is needed (one tracking

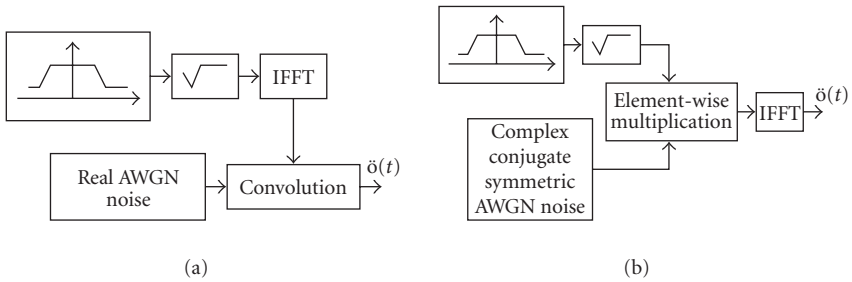

FIGURE 32.6. The phase noise can be generated in the (a) time domain or (b) frequency domain and then transformed to the time domain.

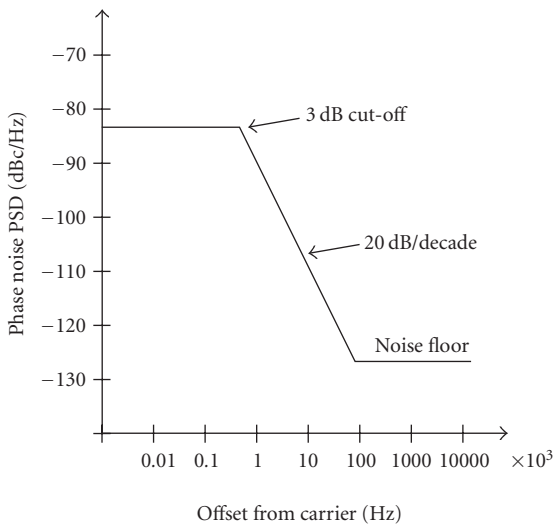

FIGURE 32.7. Piecewise linear phase noise PSD definition used in the phase noise model.

loop per stream). The PSD of the phase noise can be defined by a few parameters to model real behaviors. We characterize the phase noise by a set of 3 parameters (Figure 32.7) [3]:

(i) the integrated PSD, expressed in dBc, which is the two-sided integral of the phase noise PSD;
(ii) the 3 dB bandwidth;
(iii) the noise floor.

Note that these 3 parameters will fix the value of the phase noise PSD at low-frequency offsets.

The CPE due to either TX or RX phase noise can largely be tracked by the receiver in a common frequency offset/phase noise tracking loop. The tracking loop for MIMO-OFDM relies on the presence of pilot signals on certain subcarriers.

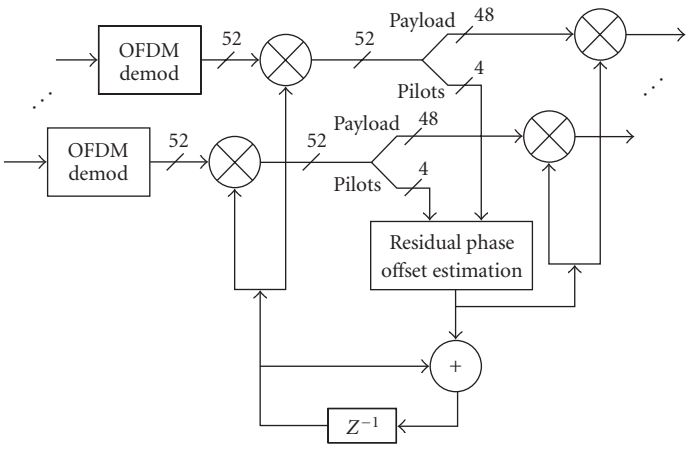

FIGURE 32.8. A single-phase noise tracking loop can be used in the receiver if both the transmitter and the receiver use a single LO distributed over all antenna branches.

Tracking is performed in the frequency domain, that is, after OFDM demodulation. For a given (multiantenna) symbol, the frequency offset of the previous symbol is first applied. Then, the residual frequency offset of the symbol is measured on the pilot subcarriers. This residual frequency offset correction is applied to the current payload symbol and accumulated/filtered with the correction of the previous OFDM symbol. This is illustrated in Figure 32.8. In synchronization terminology, this structure can be classified as data-aided hybrid feedback/feedforward synchronization.

Since both the transmitter and the receiver use a common LO for all antenna branches, a single-phase noise/carrier frequency offset tracking loop can be used.

Nonlinear amplification. When a signal $x(t)$ is fed to the input of a power amplifier modeled by a third-order AM-AM nonlinearity, the output signal $y(t)$ takes the form [3]

$$y(t) = x(t) \cdot G \cdot \left(1 - \alpha \cdot \left|x(t)\right|^2\right), \tag{32.8}$$

where G is the amplifier gain and α is the third-order coefficient given by

$$\alpha = \frac{4}{3 \cdot \mathrm{IIP3}^2} = \frac{4 \cdot \left(1 - 10^{-1/20}\right)}{3 \cdot \mathrm{IP}_{1\,\mathrm{dB}}^2}. \tag{32.9}$$

In (32.9), IIP3 is the input third-order intercept point and $\mathrm{IP}_{1\,\mathrm{dB}}$ is the input 1 dB compression point. In this cubic model, IIP3 and $\mathrm{IP}_{1\,\mathrm{dB}}$ are linked as follows: $\mathrm{IIP3} - \mathrm{IP}_{1\,\mathrm{dB}} = 9.6\,\mathrm{dB}$.

Table 32.2. Simulation parameters.

Number of subcarriers	64
Number of data subcarriers	48
Number of pilots subcarriers	4
Sample rate	20 Msps
Upsampling	Upsampling by 4
Synchronization offsets	None
Channel estimation	Ideal
Channel	Hiperlan2 type A profile, Rayleigh fading on each tap
Mode	Uncoded QAM64
Number of channel realizations	1000 or more
Number of bits per channel realization	13824

32.2.4. Impact of nonidealities

32.2.4.1. Simulation parameters

The simulation parameters are derived from the IEEE 802.11a or Hiperlan2 standards and extended for MIMO transmission. They are summarized in Table 32.2.

32.2.4.2. Simulation results

We first introduce how the performance degradations are estimated for an individual MIMO mode and then show results for all modes together in a more compact form. The uncoded BER performance for MIMO-RX-SDM-ZF with 2 TX and 3 RX antennas is shown in Figure 32.9 for IQ imbalance at the receiver side. We take the uncoded performance at a BER of 10^{-3} as a reference.

From these curves, the performance degradation of MIMO-RX-SDM-ZF at a BER of 10^{-3} can be derived. It is, for example, 2.2 dB for an IQ imbalance of 1.5% for MIMO-SDM-ZF with 2 TX and 3 RX antennas. The same procedure will be used throughout this section to assess the performance degradation of other transmission schemes in the presence of other impairments. In order to emphasize on the MIMO aspect, nonidealities will be introduced where the spatial processing takes place: at the receiver side for MIMO-RX processing, at the transmitter side for MIMO-TX processing, and at both sides for MIMO-TX-RX processing.

RX processing schemes. The performance degradation for the RX processing schemes is illustrated in Figures 32.10, 32.11, and 32.12 for clipping and quantization, IQ imbalance, and phase noise, respectively, all at the receiver side. Some interesting conclusions can be drawn from these figures.

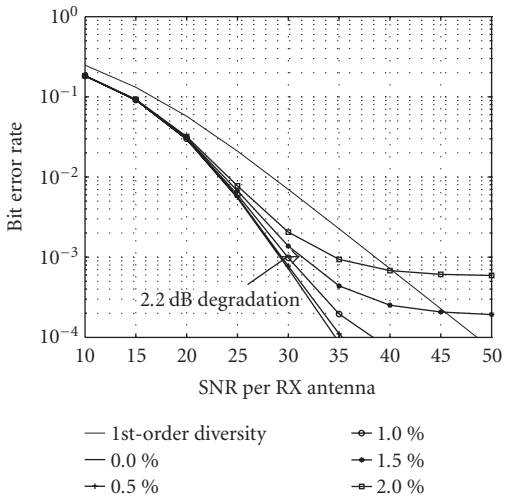

FIGURE 32.9. Example of performance degradation: BER performance of RX-SDM zero forcing, 2×3, with IQ offsets.

(i) The RX-SDM schemes at full load ($N = K$) are the most sensitive to all 3 types of degradation. ZF and MMSE are equally sensitive.

(ii) The RX-SDM schemes become less sensitive when receive diversity is present (diversity order: $N - M + 1 = 3 - 2 + 1 = 2$). This can be explained by the fact that the SNR required to achieve the same BER of $10 - 3$ is lower in the 2×3 case. Hence, for the same BER, more MSI noise can be added before it becomes comparable with the AWGN noise and degrade the performance.

(iii) The 2×2 STBC scheme is less sensitive than the 2×1 STBC for the same reason.

(iv) The RX-MRC scheme (diversity order: $N - M + 1 = 2 - 1 + 1 = 2$) is slightly less sensitive than the 2×3 RX-SDM scheme (diversity order: $N - M + 1 = 3 - 2 + 1 = 2$). This is due to the fact that, for MRC, no MSI interference exists.

(v) For the SDM schemes at full load, 10 bits are necessary and it is better to have the AGC fixing the average incoming power to 5σ. When spatial diversity is present, a smaller number of bits is acceptable (7 or 8) and it is better to set the average level to 4σ. This last point is very important when different MIMO modes are implemented on the same platform, since it allows to make trade-offs and possibly to tune the receiver hardware for different optimization criteria.

(vi) The phase noise has a smaller impact on the schemes with diversity. These schemes indeed allow to combine the tracking over the various RX antennas, yielding a diversity gain. This gain is not apparent on the 2×2 RX-SDM schemes where the (irreducible) MSI is dominant.

(vii) Globally, the SISO sensitivity to nonidealities is somewhat between that of the RX-SDM schemes at full load and that of the other schemes with diversity order 2 or more.

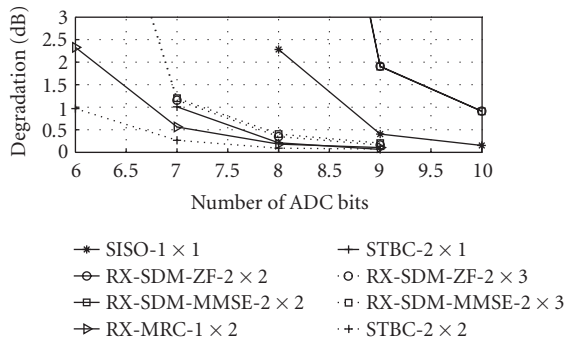

(a)

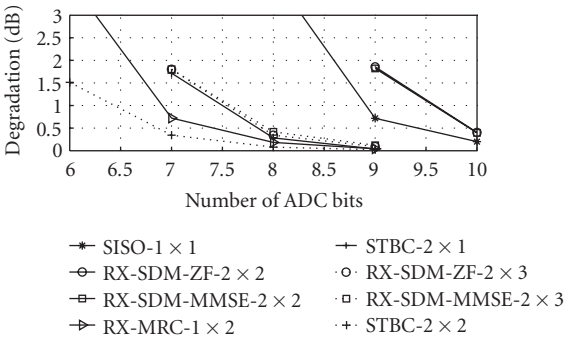

(b)

FIGURE 32.10. SNR degradation of MIMO-RX schemes at BER $= 10^{-3}$ in the presence of clipping and quantization: (a) 4σ, (b) 5σ.

TX processing schemes. The performance degradation for the TX processing schemes is illustrated in Figures 32.13, 32.14, 32.15, and 32.16 for clipping and quantization, IQ imbalance, phase noise, and amplifier nonideality, respectively, all at the transmitter side. Most observations made for the MIMO-RX schemes are also applicable for the MIMO-TX schemes (fully loaded SDM is highly sensitive, less sensitivity is observed when spatial diversity is present, and comments on the required number of bits). The following are additional observations.

(i) With IQ imbalance, all MIMO-TX modes are more sensitive than SISO. In fact it is the SISO behavior that is very insensitive to IQ imbalance at the TX side [4].

(ii) The phase noise influence is smaller for the MIMO-TX schemes.

(iii) The power amplifier nonlinearity analysis shows a major performance degradation for the TX-SDM schemes at full system load ($M = K$). At reduced load ($M > K$), the TX-SDM scheme is much less degraded and so are all other schemes that enjoy diversity order 2 or more.

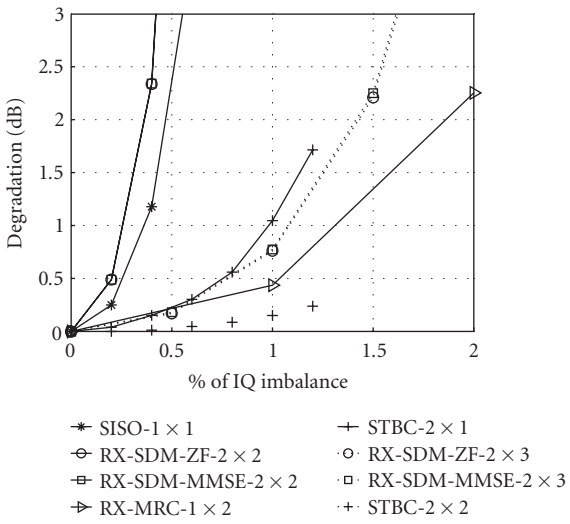

FIGURE 32.11. SNR degradation of MIMO-RX schemes at BER $= 10^{-3}$ in the presence of IQ imbalance.

(iv) The TX-SDM schemes at full load are also more sensitive than the SISO case, requiring about 6 dB more input back-off.

Globally, this nonideality analysis of the MIMO TX and RX schemes shows that moving the MIMO processing from the receiver to the transmitter also moves the MIMO specific transceiver requirements (IQ imbalance, DAC/ADC, and phase noise) from the receiver to the transmitter. It places an additional requirement on the linearity of the power amplifier for the fully loaded SDM cases.

TX-RX processing schemes. The performance degradation for the TX-RX processing schemes is illustrated in Figures 32.17, 32.18, 32.19, 32.20, 32.21, 32.22, 32.23, 32.24, and 32.25 for clipping and quantization, IQ imbalance, phase noise, and amplifier nonideality, respectively. Transmitter and receiver nonidealities were applied separately so that their effect can be analyzed independently. The observations for the impact of nonidealities on the TX-RX schemes are as follows.

(i) Both the clipping and quantization and the IQ imbalance cause a higher degradation at the RX side. This effect has already been observed in the case of SISO-OFDM [4]. The reason is that the receiver equalizer can be seen as suffering from noise enhancement, which is aggravated by the nonidealities. A 7-bit resolution is needed at the TX side while 9 bits are needed at the RX side.

(ii) The phase noise has a similar impact at the transmitter side and the receiver side.

(iii) The impact of nonlinear amplification calls several comments.
   (a) Globally, all TX-RX schemes perform well in the presence of amplifier nonlinearity.

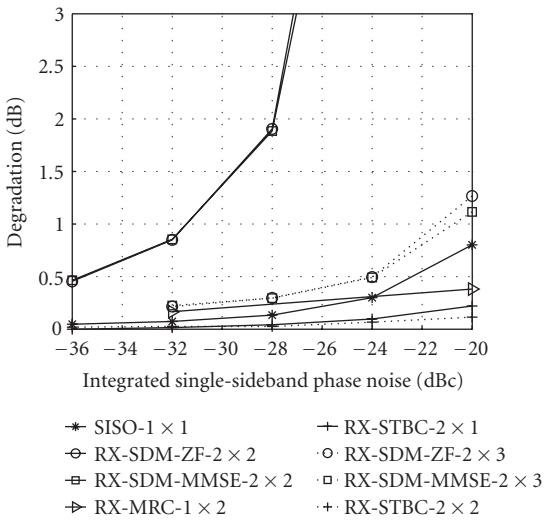

FIGURE 32.12. SNR degradation of MIMO-RX schemes at BER = 10^{-3} in the presence of phase noise.

(b) The 2×3 TX-RX-MRC case has a higher degradation than the 2×2 case. This is due to the fact that the limiting factor for the 2×3 case is the nonlinearity itself. Observation of the BER curved showed that the 2×2 and 2×3 cases have the same error floor, hence the difference between the ideal case and the nonideal case is higher for the 2×3 case.

Comparison between RX, TX, and TX-RX processing schemes

Clipping and quantization. The TX and RX processing exhibit similar sensitivity to this nonideality. The TX-RX processing is much less sensitive at both the TX and RX sides.

IQ imbalance. The TX and RX processing exhibit similar sensitivity to this nonideality, with the exception of STBC and SISO that are much less sensitive to IQ imbalance at the TX side. Both TX-SDM and RX-SDM have tough requirement at full load (about 0.2%). As far as the TX-RX processing is concerned, TX nonidealities cause significantly less interference. Nevertheless, since the IQ imbalance requirement is on the order of 0.4 to 2% according to the TX-RX scheme, it is likely that IQ imbalance mitigation will also be required for TX-RX schemes, at least for direct conversion (zero IF) architecture that have nonideal quadrature generation.

Phase noise. Since a value of -32 dBc integrated phase noise is moderately easy to achieve, the worst case is for receiver phase noise for the fully loaded RX-SDM case. Even in that case, a degradation of 0.8 dB could be tolerable. All other schemes show less than 0.5 dB degradation even at -28 dBc.

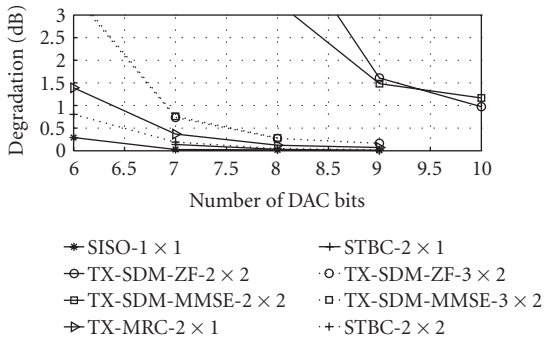

(a)

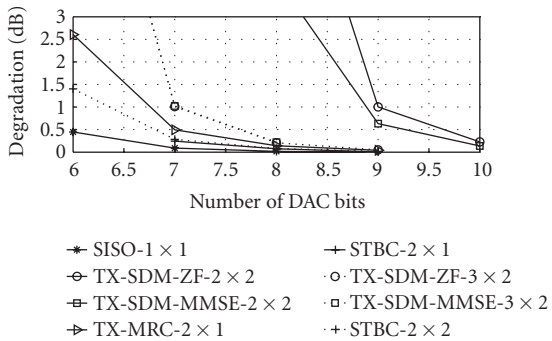

(b)

FIGURE 32.13. SNR degradation of MIMO-TX schemes at BER $= 10^{-3}$ in the presence of clipping and quantization: (a) 4σ, (b) 5σ.

Power amplifier nonideality. The TX-RX scheme exhibits much less sensitivity to PA nonlinearity than the TX schemes. The reason for this lies in the structure of the prefilter: the TX-RX scheme uses the right singular vectors of the channel matrix which are by definition vectors of unitary matrices and do not need to be normalized; the TX schemes use (pseudo-)inverse of the channel matrix or channel covariance matrix and must be normalized by their Frobenius norm to keep the total TX power constant. Because of this, the TX schemes are comparatively more sensitive to additive MUI than the TX-RX schemes.

32.2.5. Mitigation of nonidealities

The nonidealities analyzed in the previous section can to some extent be mitigated at implementation, architecture, or system level. We will briefly review the possible solutions against the nonidealities analyzed in this section.

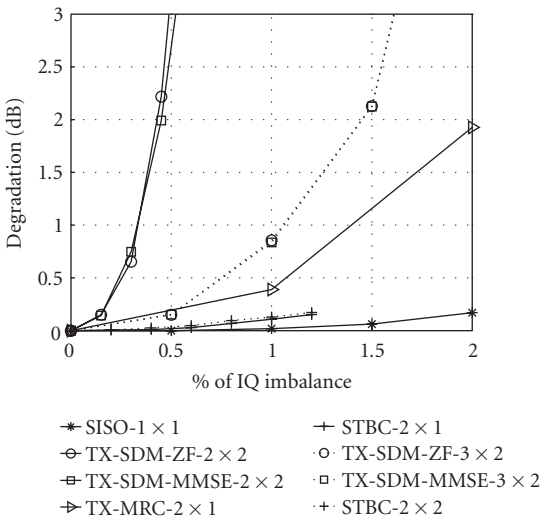

FIGURE 32.14. SNR degradation of MIMO-TX schemes at BER $= 10^{-3}$ in the presence of IQ imbalance.

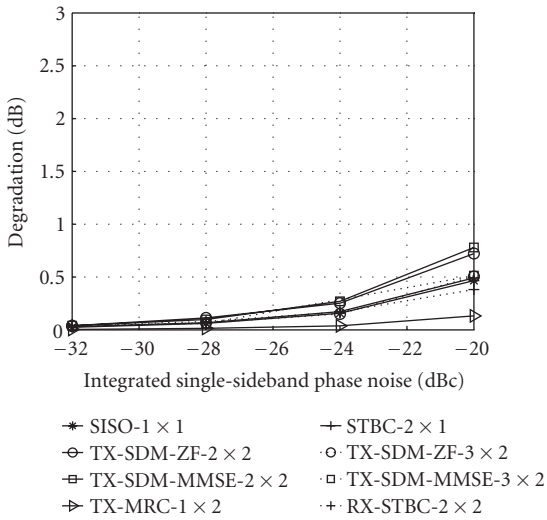

FIGURE 32.15. SNR degradation of MIMO-TX schemes at BER $= 10^{-3}$ in the presence of phase noise.

Clipping and quantization. (i) This is mostly an implementation issue. As shown in Section 32.2.2 and in the simulation results, for a given resolution, the clipping level can be optimized in order to minimize the degradation.

(ii) At the system level, providing spatial diversity and/or resorting to TX-RX processing will reduce the adverse impact of low-resolution converters.

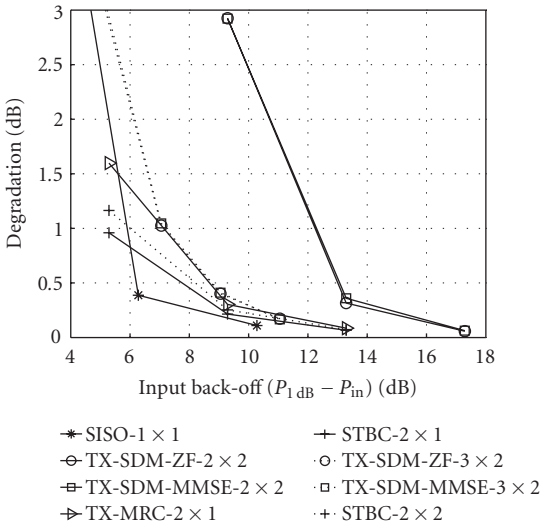

FIGURE 32.16. SNR degradation of MIMO-TX schemes at BER $= 10^{-3}$ in the presence of TX power amplifier nonlinearity.

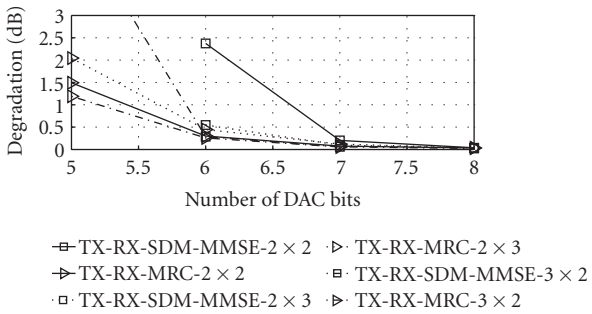

(a)

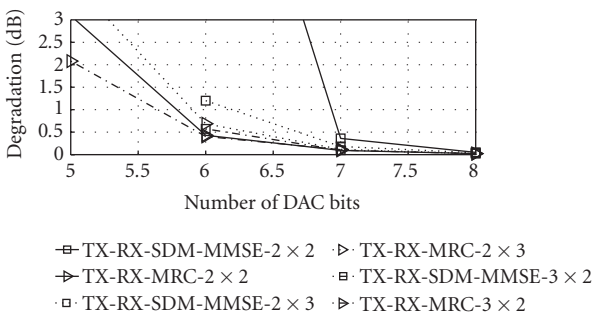

(b)

FIGURE 32.17. SNR degradation of MIMO-TX-RX schemes at BER $= 10^{-3}$ in the presence of clipping and quantization at the TX side: (a) 4σ, (b) 5σ.

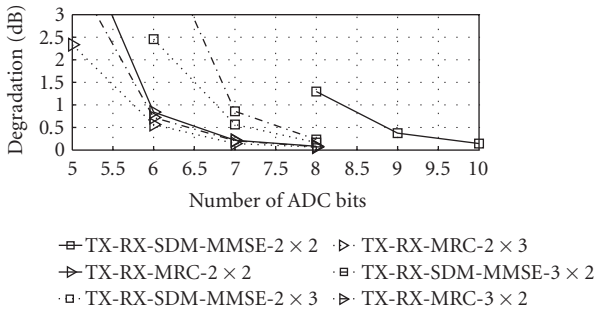

(a)

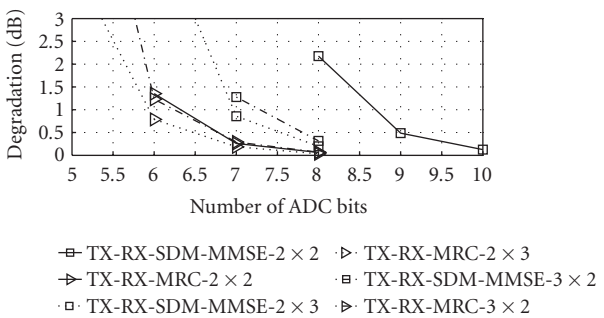

(b)

FIGURE 32.18. SNR degradation of MIMO-TX-RX schemes at BER $= 10^{-3}$ in the presence of clipping and quantization at the RX side: (a) 4σ, (b) 5σ.

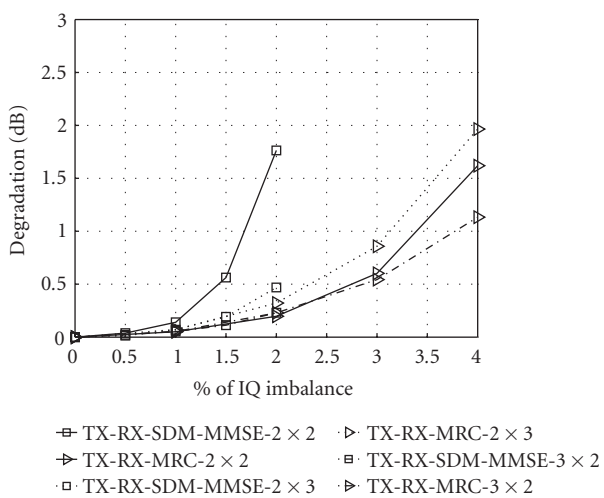

FIGURE 32.19. SNR degradation of MIMO-TX-RX schemes at BER $= 10^{-3}$ in the presence of IQ imbalance at the TX side.

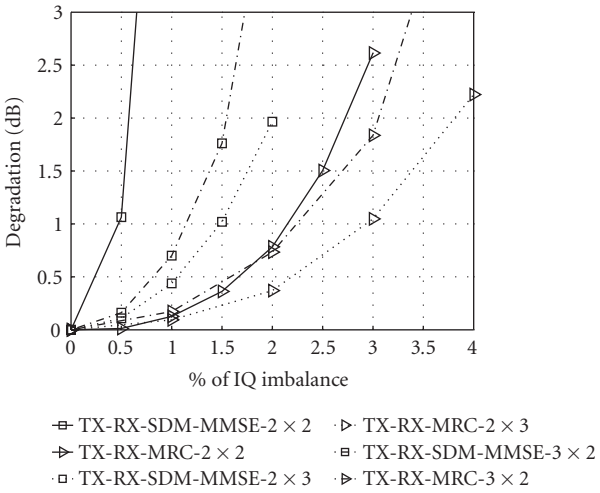

FIGURE 32.20. SNR degradation of MIMO-TX-RX schemes at BER = 10^{-3} in the presence of IQ imbalance at the RX side.

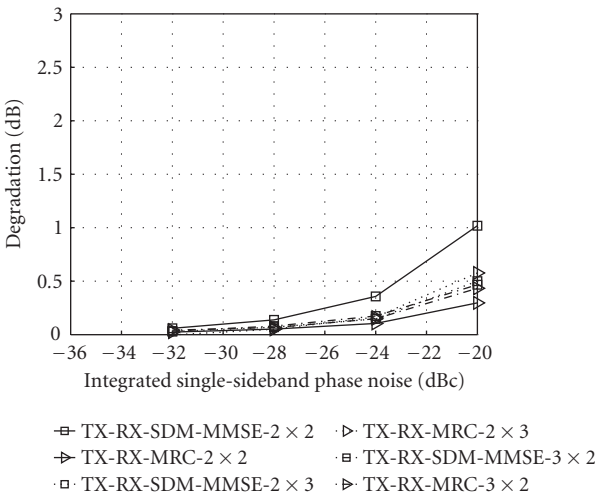

FIGURE 32.21. SNR degradation of MIMO-TX-RX schemes at BER = 10^{-3} in the presence of phase noise at the TX side.

IQ imbalance. (i) At the architecture level, selecting super-heterodyne architectures with digital SSB and quadrature generation introduced in Section 32.2.1 can completely eliminate IQ imbalance provided that the receiver down sampling filters have sufficient rejection in the stopband.

(ii) Since zero-IF architectures are highly desirable, it is also possible to extend the SISO-OFDM IQ imbalance compensation techniques proposed in [4] to MIMO schemes. This method consists in estimating the values of α and β

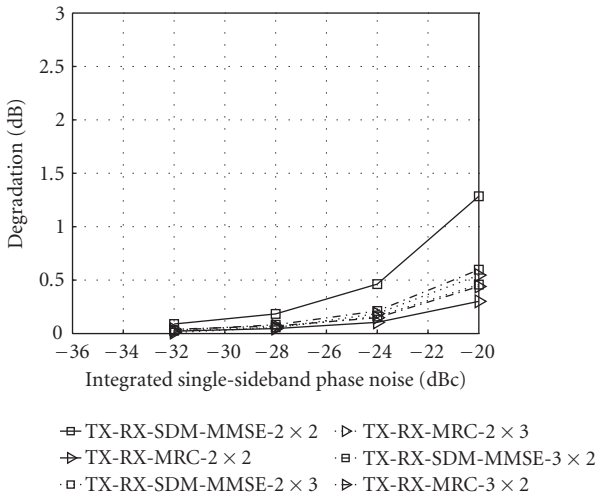

FIGURE 32.22. SNR degradation of MIMO-TX-RX schemes BER $= 10^{-3}$ in the presence of phase noise at the RX side.

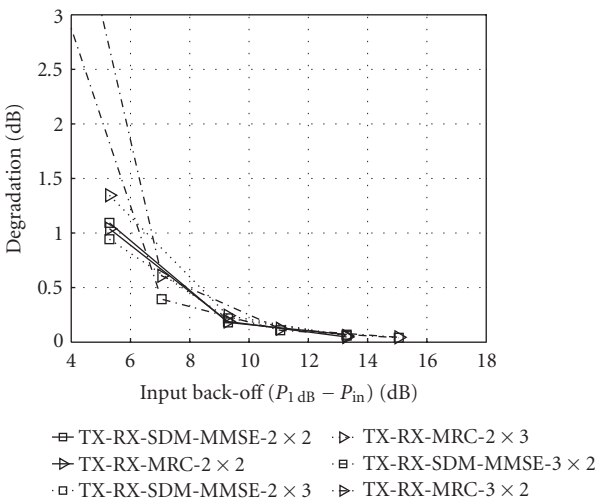

FIGURE 32.23. SNR degradation of MIMO-TX-RX schemes at BER $= 10^{-3}$ in the presence of TX amplifier nonlinearity.

introduced in (32.4) and then compensating digitally to recover the in-phase and quadrature components free of IQ (image frequency) interference, as follows:

$$\hat{r} = \frac{\hat{\alpha}^* r_{\mathrm{IQ}} - \hat{\beta} r_{\mathrm{IQ}}^*}{|\hat{\alpha}|^2 - |\hat{\beta}|^2}. \tag{32.10}$$

The method can be directly extended to multiantenna reception by implementing the estimation and compensation in each receive antenna branch. However, when the number of transmit antennas is greater than 1, the training symbols from each TX antenna must be transmitted one after the other to allow the measurement of the IQ imbalance interference in the receiver without additional interference from other transmit antennas. The receiver IQ imbalance compensation method in [6, 7] also applies in the presence of phase noise and carrier frequency offset. As far as the transmitter is concerned, the automatic calibration introduced in [8] can easily be extended to multiantenna transmitters.

Phase noise. (i) For a given integrated phase noise level, it is possible to distribute the PSD so as to have more phase noise power close or far from the carrier. For OFDM systems, it is desirable to have more close-in phase noise and less far phase noise since this will result in more CPE (that can be tracked) and less (irreducible) ICI. This amounts to a trade-off between the voltage-controlled oscillator (VCO) noise floor and the cut-off frequency of the PLL used in the frequency synthesizer. The phase/frequency tracking loop of the receiver can be optimized for this trade-off (cut-off frequency of the tracking loop).

(ii) In a MIMO context, the phase noise can be made identical in all branches of the transmitter by using common LOs and sampling clocks in all antenna branches. The same applies to the receiver. In this way, a single global phase noise has to be estimated and tracked.

(iii) Pilot signals are of prime importance to help tracking the phase noise over the total duration of an OFDM burst. They are usually implemented as known BPSK symbols on a subset of evenly spaced subcarriers. The use of identical pilot symbols—combined with common LOs—allows to implement the tracking before the spatial processing, thereby significantly simplifying the architecture when several STP algorithms are supported.

Power amplifier nonlinearity. (i) At the system level and as shown in the simulation results, the impact of nonlinearities can significantly be reduced by the use of TX-RX schemes or spatial diversity order greater than 1.

(ii) At the implementation level, conventional SISO methods (pre-distortion, linearization, ...) can be applied at the TX side.

32.2.6. Conclusions

To conclude, transceiver nonidealities can have a dramatic impact on overall system performances. We have shown by means of a case study of MIMO-OFDM transmission that the impact can vary at a large degree according to the transmission scheme, the spatial diversity order, and whether TX or RX nonideality is introduced. Such a system level approach is of paramount importance when designing a system since it allows to make system level trade-offs, thereby optimizing complexity and power consumption, which is especially important for mobile or portable MIMO terminals.

32.3. Transceiver reciprocity for MIMO with TX processing

This section analyzes specific transceiver requirements related to the reciprocity for MIMO-TX and MIMO-TX-RX schemes.

32.3.1. System model with the reciprocity assumption

We consider a wireless communication setup with a multiantenna access point (AP) and a single-antenna or multiantenna terminal (UT). The AP intends to apply a downlink OFDM-MIMO scheme with TX processing, thus requiring CSI knowledge at the AP. This CSI knowledge will be acquired through an uplink burst with the assumption of channel reciprocity. The uplink model is as follows on every subcarrier p:

$$\mathbf{y}^{UL}[p] = \mathbf{H}^{UL}[p] \cdot \mathbf{x}^{UL}[p] + \mathbf{n}[p], \tag{32.11}$$

where $\mathbf{x}^{UL}[p]$ is the vector of the N frequency-domain symbols transmitted by the terminals, $\mathbf{y}^{UL}[p]$ is the vector of the M signals received by the AP antenna branches, and $\mathbf{H}^{UL}$ is the composite uplink channel. In the sequel, we drop the explicit dependency on $[p]$ for clarity. Including the terminal transmitters and the AP receiver, $\mathbf{H}^{UL}$ can be expressed as

$$\mathbf{H}^{UL} = \mathbf{D}_{\mathrm{RX},AP} \cdot \mathbf{H} \cdot \mathbf{D}_{\mathrm{TX},UT}, \tag{32.12}$$

where $\mathbf{D}_{\mathrm{RX},AP}$ and $\mathbf{D}_{\mathrm{TX},UT}$ are complex diagonal matrices containing, respectively, the AP receivers and UT transmitters frequency responses (throughout the analysis, we use the letter $\mathbf{D}$ to emphasize that the matrices are diagonal). The matrix $\mathbf{H}$ contains the propagation channel itself, which is reciprocal. In order to recover the transmitted symbols, the AP uses a channel estimation algorithm that provides the estimate $\hat{\mathbf{H}}^{\mathbf{UL}}$ affected by $\mathbf{D}_{\mathrm{RX},AP}$ and $\mathbf{D}_{\mathrm{TX},UT}$. To simplify the analysis, we will assume that there are no channel estimation errors so that $\hat{\mathbf{H}}^{\mathbf{UL}} = \mathbf{H}^{\mathbf{UL}}$. In the downlink, the stream separation is achieved by applying a per-carrier prefilter that pre-equalizes the channel. This prefiltering is contained in the matrix $\mathbf{F}^{DL}$ of the linear model

$$\mathbf{y}^{DL} = \mathbf{H}^{DL} \cdot \mathbf{F}^{DL} \cdot \mathbf{x}^{DL} + \mathbf{n}. \tag{32.13}$$

$\mathbf{H}^{DL}$ also captures the AP and UT transceiver transfer function:

$$\mathbf{H}^{DL} = \mathbf{D}_{\mathrm{RX},UT} \cdot \mathbf{H}^{T} \cdot \mathbf{D}_{\mathrm{TX},AP}, \tag{32.14}$$

where $\mathbf{D}_{\mathrm{TX},AP}$ and $\mathbf{D}_{\mathrm{RX},UT}$ are complex diagonal matrices containing, respectively, the AP transmitters and mobile terminal receivers frequency responses and $\mathbf{H}^{T}$ is the transpose of $\mathbf{H}$, the uplink propagation channel. We can use $\mathbf{H}^{T}$ for the downlink if two conditions are fulfilled: the duplex scheme is TDD and the downlink

transmission occurs without significant delay after the uplink channel estimation, compared to the coherence time of the channel. In what follows, we assume that the channel is static.

For the zero-forcing strategy, the prefiltering matrix is the inverse (or pseudoinverse if $N \leq M$) of the transpose of the uplink channel matrix so that, ideally, the product of the prefiltering matrix and the downlink channel matrix is equal to the identity matrix [9]:

$$\mathbf{F}^{DL} = \left(\mathbf{H}^{-T}\right) = \left(\mathbf{D}_{\mathrm{RX},AP} \cdot \mathbf{H} \cdot \mathbf{D}_{\mathrm{TX},UT}\right)^{-T}. \tag{32.15}$$

By replacing $\mathbf{H}^{DL}$ and $\mathbf{F}^{DL}$ from (32.14) and (32.15) in the downlink linear system model (32.13), the received downlink signal per subcarrier becomes

$$\mathbf{y}^{DL} = \underbrace{\mathbf{D}_{\mathrm{RX},UT} \cdot \mathbf{H}^{T} \cdot \mathbf{D}_{\mathrm{TX},AP}}_{\mathbf{H}^{DL}} \cdot \underbrace{\mathbf{D}_{\mathrm{RX},AP}^{-1} \cdot \mathbf{H}^{-T} \cdot \mathbf{D}_{\mathrm{TX},UT}^{-1}}_{(\mathbf{H}^{UL})^{-T}} \cdot \mathbf{x}^{DL} + \mathbf{n}. \tag{32.16}$$

32.3.2. Multistream interference due to nonreciprocity

The linear model in (32.16) lends itself to several useful interpretations and highlights the origin of the MUI.

(i) The effect of channel prefiltering is altered by the two diagonal matrices appearing between $\mathbf{H}^{T}$ and $\mathbf{H}^{-T}$ in (32.16). Interestingly, this is solely due to transceiver effects at the AP. What causes MUI is the AP nonreciprocity: $\mathbf{D}_{\mathrm{TX},AP} \cdot \mathbf{D}_{\mathrm{RX},AP}^{-1}$ is not equal to the identity matrix multiplied by a scalar, although this product is diagonal. However, the identity matrix, multiplied by an arbitrary complex scalar could be inserted between $\mathbf{H}^{T}$ and $\mathbf{H}^{-T}$ in (32.16) without causing MUI.

(ii) The UT front end effects ($\mathbf{D}_{\mathrm{RX},UT}$ and $\mathbf{D}_{\mathrm{TX},UT}$) do not contribute to MUI. The net effect of the UT front-end frequency responses is to scale and rotate the received signals on each antenna branch. This can be equalized at the UT by a conventional time-only equalizer in each receive antenna branch (as opposed to a space-time equalizer). This equalizer is also needed to compensate the unknown phase difference between the AP and UT at TX time.

(iii) The propagation matrix $\mathbf{H}$ in this model also includes the parts of the AP or terminals that are common to uplink and downlink, hence reciprocal. This is the case for the antennas and for any common component inserted between the antenna and the TX/RX switch (or circulator).

(iv) For the product $\mathbf{D}_{\mathrm{TX},AP} \cdot \mathbf{D}_{\mathrm{RX},AP}^{-1}$ to have all diagonal elements equal, common LOs are mandatory. This condition is desirable at the transmitter side for MIMO-RX since it simplifies the carrier frequency offset/phase noise tracking loop (see Section 32.2.3); for MIMO-TX, it is mandatory.

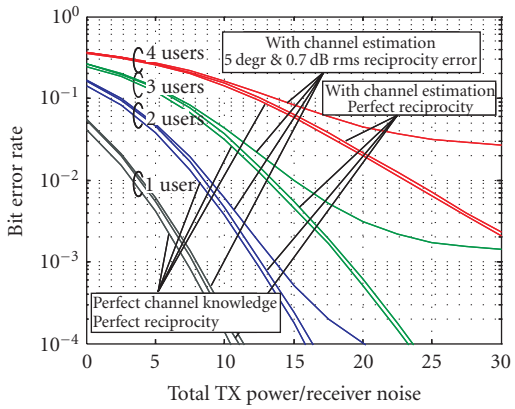

Figure 32.24. Effect of nonreciprocal access point on BER performance of zero-forcing MIMO-TX transmission.

32.3.3. Effects of transceiver nonreciprocity

To illustrate the dramatic impact of the AP transceiver nonreciprocity, we show here simulation results of a MIMO-OFDM system with a zero-forcing prefilter used at the transmitter side. The simulations were run for Hiperlan2 parameters [10] with the Hiperlan2 type A channel [11] (non-LOS, 50- nanosecond delay spread) between any pair of antenna. The AP had 4 antennas and the UT number of antennas (hence the number of transmitted streams) was varied from 1 to 4. Other important parameters were QPSK modulation on all subcarriers, OFDM with 16 samples cyclic prefix length. The entries of the channel matrix were zero mean iid gaussian random variables with variance 1 and were generated independently for each realization. No channel coding was applied. Since channel knowledge is critical in this discussion, we have included uplink channel estimation in the simulations (uplink and downlink SNR were assumed identical). The channel estimation itself is based on a classical least-squares method with a constraint on the length of the channel [12]. The following simulations have been carried out:

(i) simulation 1: perfect reciprocity, perfect channel knowledge,
(ii) simulation 2: perfect reciprocity, downlink channel obtained from uplink channel estimation,
(iii) simulation 3: a random 5 degree rms phase error and 0.7 dB rms amplitude error is introduced in the downlink transmitters; these errors are introduced on each subcarrier before transmission (a different error on each subcarrier). Note that this level of matching is very hard to achieve for complete TX and RX chains unless special design and manufacturing techniques are used.

The simulation results (Figure 32.24) show that

(i) even small phase/amplitude differences between the transmitter and receiver sections of the AP significantly degrade the quality of the MIMO-TX transmission;

(ii) the highest performance degradation occurs at high system load, confirming that the degradation is due to MSI. Obviously, for higher-order constellations, the sensitivity to transceiver nonreciprocity would be even higher.

32.3.4. Transceiver calibration

In a practical system, there are basically two ways to avoid the MSI introduced by the AP front-end nonreciprocity:

(i) perform some form of manufacturing-time matching that ensures that the transmitter is matched to the receiver. This is not very realistic since it imposes a very tight overall matching of the magnitude and phase response of the transmitter and receiver (with an accuracy of a fraction of 1 dB and of 1 degree for the most demanding schemes such as fully loaded SDM with QAM64),

(ii) online calibration loop that measures the transmitter and receiver frequency responses so that the mismatches can be pre-compensated digitally at the transmitter. We opt for the calibration option and develop further this idea.

The calibration aims at estimating the product $\mathbf{D}_{\mathrm{RX},AP} \cdot \mathbf{D}_{\mathrm{TX},AP}^{-1}$ so that it can be applied at transmit time to remove the effect of $\mathbf{D}_{\mathrm{TX},AP} \cdot \mathbf{D}_{\mathrm{RX},AP}^{-1}$ appearing in (32.16). An unknown common complex multiplicative error of the form $\alpha \cdot \mathbf{I}_{nxn}$ is allowed. Mathematically, without compensation the transmitted signal is $\mathbf{F} \cdot \mathbf{x}$ and with calibration it becomes $\alpha \mathbf{D}_{\mathrm{RX},AP} \cdot \mathbf{D}_{\mathrm{TX},AP}^{-1} \cdot \mathbf{F} \cdot \mathbf{x}$.

Before calibration, the carrier frequency and all transceiver parameters that have an effect on the amplitude or phase response of the transmitter and/or receiver are set. This includes attenuator, power level, pre-selection filters, carrier frequency, gain of variable gain amplifiers, and so forth. Note that this may require several calibrations for a given carrier frequency. Once the parameters are set, the frequency responses are assumed static and the calibration can be carried out for this set of parameters. Note that all described calibration operations are complex. We now introduce two calibration methods: method (A) uses a noise source as a reference and method (B) uses an auxiliary transceiver.

(A) Calibration with a noise source. The block diagram of the AP transceiver with the calibration hardware is illustrated in Figure 32.25. In this block diagram, the complex frequency response of each transmitter is represented by a single transfer function $d_{\mathrm{TX},m}$, which is, for the transmitter of antenna branch m, the concatenation (product) of the frequency response of the baseband section with the lowpass equivalent [13] of the IF/RF section frequency response. These terms are the diagonal elements of the $\mathbf{D}_{\mathrm{TX},AP}$ matrix. A similar definition holds for $d_{\mathrm{RX},m}$.

Step 1 (transmit-receive calibration (measurement of $\mathbf{D}_{\mathrm{TX}} \cdot \mathbf{D}_{\mathrm{RX}}$)). The transmit-receive switch is connected so as to realize a loop-back connection. A known signal is generated in the baseband section of the transmitter and is routed all the

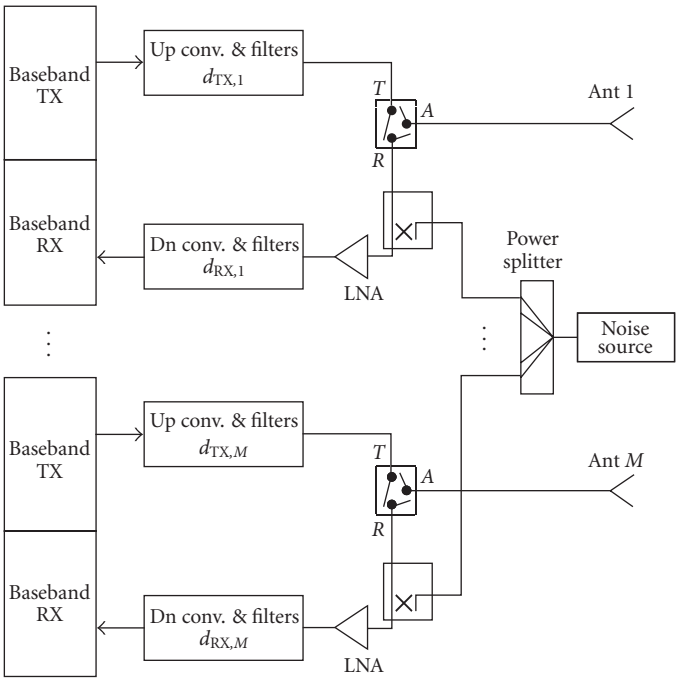

FIGURE 32.25. Multiantenna AP with calibration loops, noise source method (shown for 2 antennas).

way from baseband to RF and back from RF to baseband in the receiver. The RF calibration noise source is turned off. In each antenna branch, this yields, after averaging an estimate of the product of the transmitter frequency response by the receiver frequency response, the product $\mathbf{D}_1 = \mathbf{D}_{TX} \cdot \mathbf{D}_{RX}$. Note that this is not equal to the desired estimate.

Step 2 (RX-only calibration (measurement of $\mathbf{D}_{RX}$)). The transmit-receive switch is connected so as to isolate the receiver from both the transmitter and the antenna. The calibration noise source is turned on. Its excess noise ratio (ENR) must be sufficient to exceed the thermal noise generated by the LNAs by, for example, 20 dB or more. The signal is sampled and measured at baseband in the receiver of all antenna branches simultaneously, which is essential for perfect phase calibration. As shown in [14], using one of the (unknown) receiver branches as a reference, this yields, after some manipulations and averaging, $\mathbf{D}_2 = (1/d_{RX,1}) \cdot \mathbf{D}_{RX}$ which is a diagonal matrix containing the frequency responses of the receiver branches with a complex error coefficient $1/d_{RX,1}$, common to all antenna branches. The multiplication of $\mathbf{D}_2^2$ by the inverse of $\mathbf{D}_1$ yields the desired calibration values, namely,

$$\mathbf{D}_2^2 \cdot \mathbf{D}_1^{-1} = \frac{1}{d_{RX,1}^2} \cdot \mathbf{D}_{RX} \cdot \mathbf{D}_{TX}^{-1}. \tag{32.17}$$

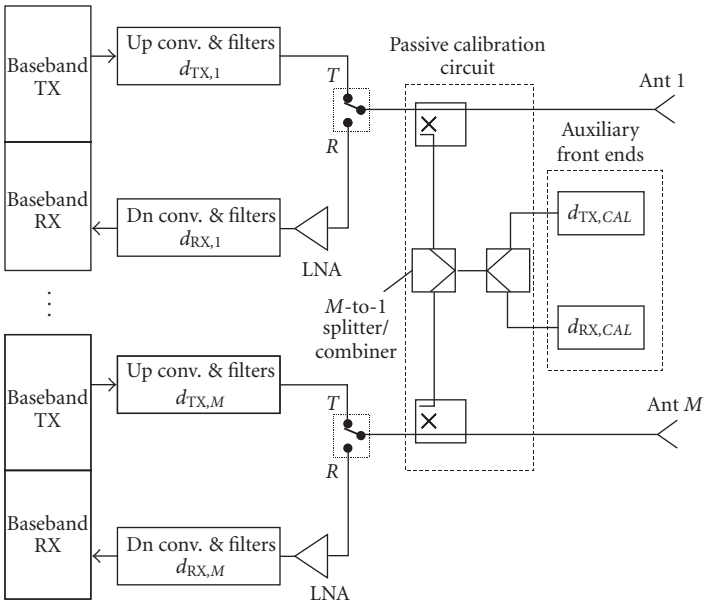

FIGURE 32.26. Multiantenna AP with calibration loops, auxiliary front-end method (shown for 2 antennas).

(B) Calibration with an auxiliary front end. The second calibration method is based on an auxiliary front end. The setup for this calibration method is illustrated in Figure 32.26. The auxiliary front end used for the calibration is a conventional front end. Remarkably, its frequency responses need not to be known.

Step 1 (measurement of $\mathbf{D}_{\mathrm{TX}}$). A known signal is generated by the AP transmitter and received by the calibration receiver. This yields the following measurement: $\mathbf{D}_T = \mathbf{D}_{\mathrm{TX}} \cdot \mathbf{D}_C \cdot d_{\mathrm{RX},CAL}$ where $\mathbf{D}_C$ contains the transfer function of the passive calibration circuit linking the calibration front end to the AP front ends that need to be calibrated.

Step 2 (measurement of $\mathbf{D}_{\mathrm{RX}}$). A known signal is generated by the calibration transmitter and received by the AP receiver front end. This yields the following measurement: $\mathbf{D}_R = d_{\mathrm{TX},CAL} \cdot \mathbf{D}_C \cdot \mathbf{D}_{\mathrm{RX}}$.

The multiplication of $\mathbf{D}_R$ by the inverse of $\mathbf{D}_T$ yields the desired calibration values (the product of diagonal matrices is commutative) $\mathbf{D}_R \cdot \mathbf{D}_T^{-1} = \mathbf{D}_{\mathrm{RX}} \cdot \mathbf{D}_{\mathrm{TX}}^{-1} \cdot d_{\mathrm{TX},CAL} \cdot d_{\mathrm{RX},CAL}^{-1}$. The unknown last term in this calibration value is allowed since it is common for all antenna branches.

Comparison of the two calibration methods. The two methods are in fact very similar: they exploit at best the peculiar problem at hand, namely, the estimation of the AP frequency responses with the degree of freedom allowed (the common error coefficient). In the first method, the unknown noise values and the first antenna

branch make up the unknown coefficient while in the second method it is the auxiliary front end and the coupling values that make up the unknown coefficient.

(i) Method (A) has a clear advantage in implementation cost since the only extra hardware is the noise source (a lousy RF amplifier will do!) and the coupling circuitry. However, the splitter and the coupler transfer function do not cancel out as in method (B), thereby placing some (moderate) requirement on these components.

(ii) Method (B) is more costly. However, it has the advantage of being able do define arbitrarily the baseband signal used to measure the AP receiver: it is then possible to generate special training sequences to achieve certain purposes such as partial spectral filling, longer cyclic prefix, and so forth. This method also allows a fine control of the signal level during the measurement.

Avoiding pitfalls in the calibration. Several precautions need to be taken so that the use of the calibration data is correct.

(i) When doing the uplink channel estimation, each receive antenna branch at the AP will use a particular AGC setting, according to the power received by that antenna. The calibration value corresponding to that AGC setting must then be used.

(ii) During both UL channel estimation and downlink transmission, all AP antennas must be synchronized. More specifically, timing synchronization offsets are allowed as long as they are identical to those present during the calibration.

(iii) The calibration must be executed repeatedly. The frequency of the measurement depends on the stability over time and temperature of the analog circuitry.

These calibration methods are very general and can be used in all MIMO-TX schemes were TX-CSI is acquired in the reverse link with the assumption of channel reciprocity.

32.3.5. Conclusions

If reverse link channel knowledge is used to compute the MIMO-TX or MIMO-TX-RX prefiltering matrix, near-perfect channel reciprocity is required. We have shown that the transceiver nonreciprocity at the transmit side is the source of MUI. The nonreciprocity at the receive side does not create MUI and can be compensated by a conventional equalizer. We have introduced two inexpensive calibration methods in order to yield after calibration, in each antenna branch, identical transmitter and receiver frequency response, up to a common coefficient.

Abbreviations

A/D	Analog-to-digital (converter)
AGC	Automatic gain control
BER	Bit error rate
CPE	Common phase error
CSI	Channel state information

D/A	Digital-to-analog (converter)
FFT	Fast Fourier transform
ICI	Intercarrier interference
IIP3	Input third-order intercept point
IP1	1 dB compression point
LO	Local oscillator
MIMO	Multiple-input multiple-output
MRC	Maximum ratio combining
NOB	Number of bits
OFDM	Orthogonal frequency division multiplex
PA	Power amplifier
PER	Packet error rate
PLL	Phase locked loop
PSD	Power spectral density
SDM	Spatial division multiplex
SSB	Single sideband
STBC	Space-time block coding
STP	Space-time processing
SVD	Singular value decomposition
VCO	Voltage control oscillator

Bibliography

[1] B. Razavi, *RF Microelectronics*, Prentice Hall, Upper Saddle River, NJ, USA, 1998.

[2] D. J. G. Mestdagh, P. M. P. Spruyt, and B. Biran, "Effect of amplitude clipping in DMT-ADSL transceivers," *Electronic Letters*, vol. 29, no. 15, pp. 1354–1355, 1993.

[3] M. Engels, Ed., *Wireless OFDM Systems: How to Make Them Work?*, Kluwer Academic Publishers, Norwell, Mass, USA, 2002.

[4] J. Tubbax, B. Côme, L. Van der Perre, L. Deneire, S. Donnay, and M. Engels, "Compensation of IQ imbalance in OFDM systems," in *Proc. IEEE International Conference on Communications (ICC '03)*, vol. 5, pp. 3403–3407, Anchorage, Alaska, USA, May 2003.

[5] C. Muschallik, "Influence of RF oscillators on an OFDM signal," *IEEE Trans. on Consumer Electronics*, vol. 41, no. 3, pp. 592–603, 1995.

[6] B. Tubbax, J. Côme, L. Van der Perre, et al., "Joint compensation of IQ imbalance and frequency offset in OFDM systems," in *Proc. IEEE Global Communications Conference (GLOBECOM '03)*, vol. 4, pp. 2365–2369, San Fransisco, Calif, USA, December 2003.

[7] J. Tubbax, B. Côme, L. Van der Perre, et al., "Compensation of IQ imbalance and phase noise in OFDM systems," *IEEE Transactions on Wireless Communications*, vol. 4, no. 3, pp. 872–877, 2005.

[8] J. Craninckx and S. Donnay, "Automatic calibration of a direct upconversion transmitter," in *Proc. Radio and Wireless Conference (RAWCON '03)*, pp. 249–252, Boston, Mass, USA, August 2003.

[9] S. Thoen, L. Van der Perre, B. Gyselinckx, M. Engels, and H. De Man, "Adaptive loading in the downlink of OFDM/SDMA-based wireless local networks," in *Proc. IEEE Vehicular Technology Conference (VTC '00)*, pp. 235–239, Tokyo, Japan, May 2000.

[10] *Broadband Radio Access Networks (BRAN); HIPERLAN Type 2; Physical (PHY) layer*, ETSI specification TS 101 475 v1.2.1A, April, 2000.

[11] J. Medbo and P. Schramm, *Channel models for HIPERLAN/2*, ETSI/BRAN Document No. 3ERI085B, 1998.

[12] P. Vandenameele, *Space division multiple access for wireless local area networks*, Ph.D. dissertation, October 2000.

[13] J. Proakis, *Digital Communications*, McGraw-Hill, New York, NY, USA, 4th edition, 2001.
[14] A. Bourdoux, B. Côme, and N. Khaled, "Non-reciprocal transceivers in OFDM/SDMA systems: impact and mitigation," in *Proc. Radio and Wireless Conference (RAWCON '03)*, pp. 183–186, Boston, Mass, USA, August 2003.

André Bourdoux: Interuniversity MicroElectronic Center, Wireless Research Group, 3001 Leuven, Belgium
Email: andre.bourdoux@imec.be

Jian Liu: Interuniversity MicroElectronic Center, Wireless Research Group, 3001 Leuven, Belgium
Email: jian.liu@imec.be

33 Multiple antennas for 4G wireless systems

François Horlin, Frederik Petré,
Eduardo Lopez-Estraviz,
and Frederik Naessens

> It is not the strongest species that will survive, nor the most intelligent, but the one most responsive to change.
>
> Charles Darwin

33.1. New air interfaces

New air interfaces for 4G broadband cellular networks are being developed under the auspices of the World Wireless Research Forum (WWRF) [1] and the IEEE 802.20 study group for Mobile Broadband Wireless Access (MBWA) [2].

Cellular systems of the third generation (3G) are based on the recently emerged direct-sequence code-division multiple-access (DS-CDMA) technique [3]. Intrinsically, DS-CDMA has interesting networking abilities. First, the communicating users do not need to be time synchronized in the uplink. Second, soft handover is supported between two cells making use of different codes at the base stations. However, the system suffers from intersymbol interference (ISI) and multiuser interference (MUI) caused by multipath propagation, leading to a high loss of performance.

The use of the orthogonal frequency-division multiplexing (OFDM) modulation is widely envisaged for wireless local area networks (WLANs) [4]. At the cost of the addition of a cyclic prefix, the time-dispersive channel is seen in the frequency domain as a set of parallel independent flat subchannels and can be equalized at a low-complexity. Using channel state information (CSI) at the transmitter, the constellation on each subchannel can be further adapted to the quality, which is known as bit loading for adaptive OFDM. An alternative approach to OFDM, that benefits from the same low-complexity equalization property, is single-carrier block transmission (SCBT), also known as single-carrier (SC) modulation with cyclic prefix [5, 6]. As a counterpart of adaptive OFDM, it has been proposed to use a decision-feedback equalizer at the receive side of an SCBT system. It has been shown in [7, 8] that the two approaches perform equally well. Since the SCBT technique benefits from a lower peak-to-average power ratio (PAPR), [9] encourages

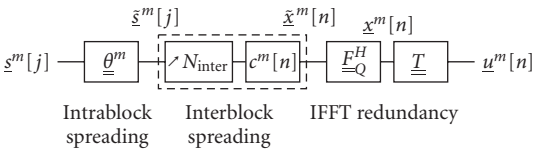

FIGURE 33.1. GMCBS-CDMA transmitter model.

the use of SCBT in the uplink and OFDM in the downlink in order to reduce the constraints on the analog front end and the processing complexity at the terminal.

There are potential benefits in combining OFDM (or SCBT) and DS-CDMA. Basically the frequency-selective channel is first equalized in the frequency domain using the OFDM modulation technique. DS-CDMA is applied on top of the equalized channel, keeping the interesting orthogonality properties of the codes. The DS-CDMA signals are either spread across the OFDM carriers, leading to multicarrier CDMA (MC-CDMA) [10, 11, 12, 13], or along the carriers, leading to multicarrier block-spread CDMA (MCBS-CDMA) [14, 15, 16, 17, 18, 19]. The SCBT counterparts named here single-carrier CDMA (SC-CDMA) and single-carrier block-spread CDMA (SCBS-CDMA) have also been proposed in [20, 21] and [19, 22, 23], respectively.

33.2. Generic transmission scheme

We propose a transmission chain composed of generic blocks and able to instantiate all the communication modes combining OFDM/SCBT and TDMA/CDMA as special cases. In contrast with the transceiver proposed in [24, 25, 26] that relies on a sharing of the set of carriers to retain the orthogonality between the users, our transmission scheme relies on orthogonal CDMA, and thus inherits the nice advantages of CDMA related to universal frequency reuse in a cellular network, like increased capacity and simplified network planning. Furthermore, the focus is especially put on the communication modes emerging in the standards.

The generalized (G) MCBS-CDMA transmission scheme for the mth user ($m = 1, \ldots, M$) is depicted in Figure 33.1. Since we focus on a single-user transmission, the transmission scheme applies to both the uplink and downlink. In the uplink, the different user signals are multiplexed at the receiver, after propagation through their respective multipath channels. In the downlink, the different user signals are multiplexed at the transmitter, before the inverse fast Fourier transform (IFFT) operation.

The GMCBS-CDMA transmission scheme comprises four basic operations: intrablock spreading, interblock spreading, IFFT, and adding transmit redundancy. The information symbols $s^m[j]$ are first serial-to-parallel converted into blocks of B symbols, leading to the block sequence

$$\underline{s}^m[j] := \left[s^m[jB] \quad \cdots \quad s^m[(j+1)B-1] \right]^T. \tag{33.1}$$

The blocks $\underline{s}^m[j]$ are linearly precoded with a $Q \times B$ ($Q \geq B$) matrix, $\underline{\underline{\theta}}^m$, which possibly introduces some redundancy and spreads the symbols in $\underline{s}^m[j]$ with length-Q codes:

$$\underline{\tilde{s}}^m[j] := \underline{\underline{\theta}}^m \cdot \underline{s}^m[j]. \tag{33.2}$$

We refer to this first operation as *intrablock spreading*, since the information symbols $s^m[j]$ are spread *within* a single precoded block, $\underline{\tilde{s}}^m[j]$. The precoded block sequence $\underline{\tilde{s}}^m[j]$ is then block spread with the length-N_{inter} code sequence $c^m[n]$ leading to N_{inter} successive chip blocks:

$$\underline{\tilde{x}}^m[n] := \underline{\tilde{s}}^m[j]c^m[n - jN_{\text{inter}}], \tag{33.3}$$

where $j = \lfloor n/N_{\text{inter}} \rfloor$. We refer to this second operation as *interblock spreading*, since the information symbols $s^m[j]$ are spread *along* N_{inter} different chip blocks. The third operation involves the transformation of the frequency domain chip block sequence $\underline{\tilde{x}}^m[n]$ into the time-domain chip block sequence:

$$\underline{x}^m[n] := \underline{\underline{F}}_Q^H \cdot \underline{\tilde{x}}^m[n], \tag{33.4}$$

where $\underline{\underline{F}}_Q^H$ is the $Q \times Q$ IFFT matrix. Finally, the $K \times Q$ ($K \geq Q$) transmit matrix $\underline{\underline{T}}$ possibly adds some transmit redundancy to the time-domain chip blocks:

$$\underline{u}^m[n] := \underline{\underline{T}} \cdot \underline{x}^m[n]. \tag{33.5}$$

With $K = Q + L$, $\underline{\underline{T}} = \underline{\underline{T}}_{\text{cp}} := [\underline{\underline{I}}_{\text{cp}}^T, \underline{\underline{I}}_Q^T]^T$, where $\underline{\underline{I}}_Q$ is the identity matrix of size Q and $\underline{\underline{I}}_{\text{cp}}$ consists of the last L rows of $\underline{\underline{I}}_Q$, $\underline{\underline{T}}$ adds redundancy in the form of a length-L cyclic prefix (CP). The chip block sequence $\underline{u}^m[n]$ is parallel-to-serial converted into the scalar sequence $[u^m[nK] \quad \cdots \quad u^m[(n+1)K - 1]]^T := \underline{u}^m[n]$ and transmitted over the air at a rate $1/T_c$.

In the following, we will detail how our generic transmission scheme instantiates different communication modes and, thus, supports different emerging communication standards. We distinguish between the multicarrier modes, on the one hand, and the single-carrier modes, on the other hand.

33.2.1. Instantiation of the multicarrier modes

The multicarrier (MC) modes always comprise the IFFT operation and add transmit redundancy in the form of a cyclic prefix ($\underline{\underline{T}} = \underline{\underline{T}}_{\text{cp}}$). The MC modes comprise MC-CDMA and MCBS-CDMA as particular instantiations of GMCBS-CDMA.

33.2.1.1. MC-CDMA

As we have indicated in the introduction, MC-CDMA first performs classical DS-CDMA symbol spreading, followed by OFDM modulation, such that the information symbols are spread across the different subcarriers [10, 11, 12]. With $Q = BN_{\text{intra}}$ and N_{intra} the intrablock spreading code length, the $Q \times B$ intrablock spreading matrix $\underline{\underline{\theta}}^m = \underline{\underline{\beta}}^m$ spreads the chips across the subcarriers, where the mth user's $Q \times B$ spreading matrix $\underline{\underline{\beta}}^m$ is defined as

$$\underline{\underline{\beta}}^m := \underline{\underline{I}}_B \otimes \underline{a}^m, \tag{33.6}$$

with $\underline{a}^m := [a^m[0] \quad \cdots \quad a^m[N_{\text{intra}} - 1]]^T$ the mth user's $N_{\text{intra}} \times 1$ code vector and $\otimes$ the Kronecker product. The interblock spreading operation is discarded by setting $N_{\text{inter}} = 1$. Since it does not preserve the orthogonality among users in a frequency-selective channel, MC-CDMA requires advanced multiuser detection for uplink reception in the base station, and frequency domain chip equalization for downlink reception in the mobile station. MC-CDMA has been proposed as a candidate air interface for future broadband cellular systems [13].

33.2.1.2. MCBS-CDMA

The MCBS-CDMA transmission scheme is the only MC mode that comprises the interblock spreading operation $N_{\text{inter}} = N$. As detailed in [18, 19], by relying on block spreading, MCBS-CDMA retains the orthogonality among users in both the uplink and downlink, even after propagation through a frequency-selective channel. Hence, it converts a difficult multiuser detection problem into an equivalent set of simpler and independent single-user equalization problems. In case no CSI is available at the transmitter, it performs linear precoding to robustify the transmitted signal against frequency-selective fading. In case CSI is available at the transmitter, it allows to optimize the transmit spectrum of each user separately through adaptive power and bit loading. Note that classical MC-DS-CDMA can be seen as a special case of MCBS-CDMA, since it does not include linear precoding, but, instead, relies on bandwidth consuming forward error correction (FEC) coding to enable frequency diversity [14, 15, 17].

33.2.2. Instantiation of the single-carrier modes

The single-carrier (SC) modes employ a fast Fourier transform (FFT) as part of the intrablock spreading operation to annihilate the IFFT operation. For implementation purposes, however, the IFFT is simply removed (and not compensated by an FFT), in order to minimize the implementation complexity. The SC modes rely on cyclic prefixing ($\underline{\underline{T}} = \underline{\underline{T}}_{\text{cp}}$) to make the channel appear circulant. The SC modes comprise SC-CDMA and SCBS-CDMA as particular instantiations of GMCBS-CDMA.

33.2.2.1. SC-CDMA

The SC-CDMA transmission scheme, which combines SCBT with DS-CDMA, can be interpreted as the SC counterpart of MC-CDMA [20, 21]. This mode is captured through our general transmission scheme, by setting $Q = BN_{\text{intra}}$. The intrablock spreading matrix $\underline{\underline{\theta}}^m = \underline{\underline{F}}_Q \cdot \underline{\underline{\beta}}^m$ with $\underline{\underline{\beta}}^m$ defined in (33.6), performs symbol spreading on the B information symbols, followed by an FFT operation to compensate for the subsequent IFFT operation. The interblock spreading operation is left out by setting $N_{\text{inter}} = 1$.

33.2.2.2. SCBS-CDMA

The SCBS-CDMA transceiver can be considered as the SC counterpart of MCBS-CDMA. It is the only SC mode that entails the interblock spreading operation $N_{\text{inter}} = N$. The intrablock spreading matrix $\underline{\underline{\theta}}^m = \underline{\underline{F}}_Q$ only performs an FFT operation to compensate for the subsequent IFFT operation. Like MCBS-CDMA, SCBS-CDMA retains the orthogonality among users in both the uplink and downlink, even after propagation through a frequency-selective channel, and, hence, converts a difficult multiuser detection problem into an equivalent set of simpler and independent single-user equalization problems.

33.3. Multiple antennas

To meet the data rate and quality-of-service (QoS) requirements of future broadband cellular systems, their spectral efficiency and link reliability should be considerably improved, which cannot be realized by using traditional single-antenna communication techniques. To achieve these goals, multiple-input multiple-output (MIMO) systems, which deploy multiple antennas at both ends of the wireless link, exploit the extra spatial dimension, besides the time, frequency, and code dimensions, which allows to significantly increase the spectral efficiency and to significantly improve the link reliability relative to single-antenna systems [27, 28, 29]. On the one hand, MIMO systems promise huge capacity gains by creating a number of spatial pipes, through which independent information streams can be simultaneously transmitted at the same frequency [30, 31]. This is called the spatial multiplexing gain. On the other hand, they also enable huge performance gains by creating an independently fading channel between each transmit/receive antenna pair, which allows to receive many independently fading replicas of the same signal [32, 33, 34]. This is called the spatial diversity gain.

However, until very recently, the main focus of MIMO research was on single-user communications over narrowband channels, thereby neglecting the multiple access aspects and the frequency-selective fading channel effects, respectively. In this section, we demonstrate the rewarding synergy between existing and evolving MIMO communication techniques and our generalized MCBS-CDMA transmission technique, which allows to increase the spectral efficiency and to improve the link reliability of multiple users in a broadband cellular network.

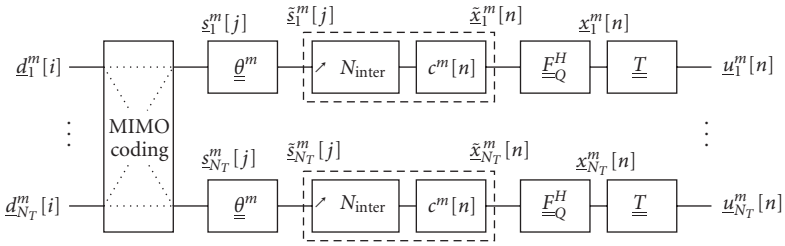

FIGURE 33.2. MIMO GMCBS-CDMA transmitter model.

The generic transmission model is extended in Figure 33.2 to include the two types of MIMO techniques. We assume N_T antennas at the transmit side and N_R antennas at the receive side. The information symbols $d_{n_T}^m[i]$, which are assumed independent and of variance equal to σ_d^2, are first serial-to-parallel converted into blocks of B symbols, leading to the block sequence

$$\underline{d}_{n_T}^m[i] := \left[d_{n_T}^m[iB] \quad \cdots \quad d_{n_T}^m[(i+1)B-1] \right]^T \tag{33.7}$$

for $n_T = 1, \ldots, N_T$. A MIMO coding operation is performed across the different transmit antenna streams, that results into the N_T antenna sequences, $\underline{s}_{n_T}^m[j]$, input to the generic transmission scheme.

33.3.1. Space-division multiplexing

On the one hand, MIMO systems create $N_{\min}$ parallel spatial pipes, which allows to realize an $N_{\min}$-fold capacity increase in rich scattering environments, where $N_{\min} = \min\{N_T, N_R\}$ is called the spatial multiplexing gain [27, 28, 29]. Specifically, space-division multiplexing (SDM) techniques exploit this spatial multiplexing gain, by simultaneously transmitting $N_{\min}$ independent information streams at the same frequency [30] (see also [31]). In [35], SDM is combined with SC-CDMA to increase the data rate of multiple users in a broadband cellular network.

In this section, we combine our generalized MCBS-CDMA transmission scheme with SDM, which allows to instantiate all combinations of SDM with OFDM/SCBT and TDMA/CDMA as special cases. The SDM technique is implemented by sending independent streams on each transmit antenna n_T, as expressed in

$$\underline{s}_{n_T}^m[j] = \underline{d}_{n_T}^m[i], \tag{33.8}$$

where $j = i$.

33.3.2. Space-time block coding

On the other hand, MIMO systems also create $N_T N_R$ independently fading channels between the transmitter and the receiver, which allows to realize an $N_T N_R$-fold

diversity increase, where $N_T N_R$ is called the multiantenna diversity gain. Specifically, space-time coding (STC) techniques exploit diversity and coding gains, by encoding the transmitted signals not only over the temporal domain but also over the spatial domain [32, 33, 34].

Space-time block coding (STBC) techniques, introduced in [33] for $N_T = 2$ transmit antennas, and later generalized in [34] for any number of transmit antennas, are particularly appealing because they facilitate ML detection with simple linear processing. However, these STBC techniques have originally been designed for frequency-flat fading channels exploiting only multiantenna diversity of order $N_T N_R$. Therefore, time-reversal (TR) STBC techniques, originally proposed in [36] for single-carrier serial transmission, have been combined with SCBT in [37, 38] for signaling over frequency-selective fading channels. While [37] only exploits multiantenna diversity, [38] exploits multiantenna as well as multipath diversity, and achieves maximum diversity gains of order $N_T N_R(L + 1)$ over frequency-selective fading channels, where L is the order of the underlying multipath channels.

In [39, 40], the TR-STBC technique of [37] is combined with SC-CDMA to improve the performance of multiple users in a broadband cellular network. Although this technique enables low-complexity chip equalization in the frequency domain, it does not preserve the orthogonality among users and, hence, still suffers from multiuser interference. The space-time coded multiuser transceiver of [19, 41], which combines the TR-STBC technique of [38] with SCBS-CDMA, preserves the orthogonality among users as well as transmit streams, regardless of the underlying multipath channels. This allows for deterministic ML user separation through low-complexity code-matched filtering as well as deterministic ML transmit stream separation through linear processing. Moreover, applying ML Viterbi equalization for every transmit stream separately guarantees symbol recovery. Therefore, maximum diversity gains of $N_T N_R \cdot (L+1)$ can be achieved for every user in the system, irrespective of the system load. Another alternative to remove MUI deterministically in a space-time coded multiuser setup [42, 43] combines generalized multicarrier (GMC) CDMA, originally developed in [24], with the STBC techniques of [34] but implemented on a per-carrier basis.

In this section, we combine our generalized MCBS-CDMA transmission scheme with STBC, which encompasses the previously discussed space-time coded multiuser transceivers as special cases. For conciseness, we limit ourselves to the case of $N_T = 2$ transmit antennas. The STBC coding is implemented by coding the two antenna streams across two time instants, as expressed in

$$\begin{bmatrix} \underline{s}_1^m[j] \\ \underline{s}_2^m[j] \end{bmatrix} = \begin{bmatrix} \underline{d}_1^m[i] \\ \underline{d}_2^m[i] \end{bmatrix},$$
$$\begin{bmatrix} \underline{s}_1^m[j+1] \\ \underline{s}_2^m[j+1] \end{bmatrix} = \underline{\underline{\chi}} \cdot \begin{bmatrix} \underline{d}_1^m[i]^* \\ \underline{d}_2^m[i]^* \end{bmatrix}, \tag{33.9}$$

where $i = \lfloor j/2 \rfloor$ and

$$\underset{=}{\chi} := \underset{=N_T}{\chi} \otimes \underset{=B}{\chi} \quad \text{with } \underset{=N_T}{\chi} := \begin{bmatrix} 0 & -1 \\ 1 & 0 \end{bmatrix}. \tag{33.10}$$

In the case of the MC modes, the STBC coding is applied in the frequency domain on a per-carrier basis, so that

$$\underset{=B}{\chi} := \underset{=B}{I}. \tag{33.11}$$

In the case of the SC modes, the STBC coding is applied in the time domain by further permuting the vector elements, so that

$$\underset{=B}{\chi} := \underset{=B}{F}^T \cdot \underset{=B}{F} \tag{33.12}$$

is a $B \times B$ permutation matrix implementing a time reversal.

It is easily checked that the transmitted block at time instant $j + 1$ from one antenna is the time-reversed conjugate of the transmitted symbol at time instant j from the other antenna (with possible permutation and sign change). As we will show later, this property allows for deterministic transmit stream separation at the receiver, regardless of the underlying frequency-selective channels.

33.4. Receiver design

33.4.1. Cyclo-stationarization of the channels

Adopting a discrete-time baseband equivalent model, the chip-sampled received signal at antenna n_R ($n_R = 1, \ldots, N_R$), $v_{n_R}[n]$, is the superposition of a channel-distorted version of the MN_T transmitted user signals, which can be written as

$$v_{n_R}[n] = \sum_{m=1}^{M} \sum_{n_T=1}^{N_T} \sum_{l=0}^{L^m} h^m_{n_R,n_T}[l] u^m_{n_T}[n-l] + w_{n_R}[n], \tag{33.13}$$

where $h^m_{n_R,n_T}[l]$ is the chip-sampled finite impulse response (FIR) channel of order L^m that models the frequency-selective multipath propagation between the mth user's antenna n_T and the base station antenna n_R, including the effect of transmit/receive filters and the remaining asynchronism of the quasi-synchronous users, and $w_{n_R}[n]$ is additive white Gaussian noise (AWGN) at the base station antenna n_R with variance σ_w^2. Furthermore, the maximum channel order L, that is, $L = \max_m\{L^m\}$, can be well approximated by $L \approx \lfloor (\tau_{\max,a} + \tau_{\max,s})/T_c \rfloor + 1$, where $\tau_{\max,a}$ is the maximum asynchronism between the nearest and the farthest users of the cell, and $\tau_{\max,s}$ is the maximum excess delay within the given propagation environment.

The received sequence $v_{n_R}[n]$ is serial-to-parallel converted into the block sequence $\underline{v}_{n_R}[n] := [v_{n_R}[nK] \quad \cdots \quad v_{n_R}[(n+1)K-1]]^T$, assuming perfect time and

frequency synchronization. From the scalar input/output relationship in (33.13), we can derive the corresponding block input/output relationship

$$\underline{v}_{n_R}[n] = \sum_{m=1}^{M} \sum_{n_T=1}^{N_T} \left(\underline{\underline{H}}^{m}_{n_R,n_T}[0] \cdot \underline{u}^{m}_{n_T}[n] + \underline{\underline{H}}^{m}_{n_R,n_T}[1] \cdot \underline{u}^{m}_{n_T}[n-1] \right) + \underline{w}_{n_R}[n], \tag{33.14}$$

where $\underline{w}_{n_R}[n] := [w_{n_R}[nK] \quad \cdots \quad w_{n_R}[(n+1)K-1]]^T$ is the corresponding noise block sequence, $\underline{\underline{H}}^{m}_{n_R,n_T}[0]$ is a $K \times K$ lower triangular Toeplitz matrix with entries $[\underline{\underline{H}}^{m}_{n_R,n_T}[0]]_{p,q} = h^{m}_{n_R,n_T}[p-q]$, and $\underline{\underline{H}}^{m}_{n_R,n_T}[1]$ is a $K \times K$ upper triangular Toeplitz matrix with entries $[\underline{\underline{H}}^{m}_{n_R,n_T}[1]]_{p,q} = h^{m}_{n_R,n_T}[K+p-q]$ (see, e.g., [24] for a detailed derivation of the single-user case). The delay-dispersive nature of multipath propagation gives rise to so-called interblock interference (IBI) between successive blocks, which is modeled by the second term in (33.14).

The $Q \times K$ receive matrix $\underline{\underline{R}}$ removes the redundancy from the chip blocks, that is, $\underline{y}_{n_R}[n] := \underline{\underline{R}} \cdot \underline{v}_{n_R}[n]$. With $\underline{\underline{R}} = \underline{\underline{R}}_{\text{cp}} = [\underline{\underline{0}}_{Q\times L}, \underline{\underline{I}}_{Q}]$ in which $\underline{\underline{0}}_{Q\times L}$ is a matrix of zeros of size $Q \times L$, $\underline{\underline{R}}$ again discards the length-L cyclic prefix. The purpose of the transmit/receive pair is twofold. First, it allows for simple block-by-block processing by removing the IBI, that is, $\underline{\underline{R}} \cdot \underline{\underline{H}}^{m}_{n_R,n_T}[1] \cdot \underline{\underline{T}} = \underline{\underline{0}}$, provided the CP length is at least the maximum channel order L. Second, it enables low-complexity frequency domain processing by making the linear channel convolution appear circulant to the received block. This results in a simplified block input/output relationship in the time domain:

$$\underline{y}_{n_R}[n] = \sum_{m=1}^{M} \sum_{n_T=1}^{N_T} \dot{\underline{\underline{H}}}^{m}_{n_R,n_T} \cdot \underline{x}^{m}_{n_T}[n] + \underline{z}_{n_R}[n], \tag{33.15}$$

where $\dot{\underline{\underline{H}}}^{m}_{n_R,n_T} = \underline{\underline{R}} \cdot \underline{\underline{H}}^{m}_{n_R,n_T}[0] \cdot \underline{\underline{T}}$ is a circulant channel matrix, and $\underline{z}_{n_R}[n] = \underline{\underline{R}} \cdot \underline{w}_{n_R}[n]$ is the corresponding noise block sequence. Note that circulant matrices can be diagonalized by FFT operations, that is, $\dot{\underline{\underline{H}}}^{m}_{n_R,n_T} = \underline{\underline{F}}^{H}_{Q} \cdot \underline{\underline{\Lambda}}^{m}_{n_R,n_T} \cdot \underline{\underline{F}}_{Q}$, where $\underline{\underline{\Lambda}}^{m}_{n_R,n_T}$ is a diagonal matrix composed of the frequency domain channel response between the mth user's antenna n_T and the base station antenna n_R.

33.4.2. Matrical model

The generalized input/output matrix model that relates the MIMO coded symbol vector defined as

$$\bar{\underline{s}}[j] := \left[\bar{\underline{s}}^{1}[j]^T \quad \cdots \quad \bar{\underline{s}}^{M}[j]^T \right]^T \tag{33.16}$$

with

$$\underline{\overline{s}}^{m}[j] := \left[\underline{s}_1^m[j]^T \quad \cdots \quad \underline{s}_{N_T}^m[j]^T\right]^T, \tag{33.17}$$

for $m = 1, \ldots, M$, to the received and noise vectors defined as

$$\begin{aligned} \underline{\overline{y}}[j] &:= \left[\underline{\overline{y}}_1[j]^T \quad \cdots \quad \underline{\overline{y}}_{N_R}[j]^T\right]^T, \\ \underline{\overline{z}}[j] &:= \left[\underline{\overline{z}}_1[j]^T \quad \cdots \quad \underline{\overline{z}}_{N_R}[j]^T\right]^T \end{aligned} \tag{33.18}$$

with

$$\begin{aligned} \underline{\overline{y}}_{n_R}[j] &:= \left[\left(\underline{y}_{n_R}[jN_{\text{inter}}]\right)^T \quad \cdots \quad \left(\underline{y}_{n_R}[(j+1)N_{\text{inter}}-1]\right)^T\right]^T, \\ \underline{\overline{z}}_{n_R}[j] &:= \left[\left(\underline{z}_{n_R}[jN_{\text{inter}}]\right)^T \quad \cdots \quad \left(\underline{z}_{n_R}[(j+1)N_{\text{inter}}-1]\right)^T\right]^T, \end{aligned} \tag{33.19}$$

for $n_R = 1, \ldots, N_R$, is given by

$$\underline{\overline{y}}[j] = \underline{\underline{C}} \cdot \underline{\underline{F}}^H \cdot \underline{\underline{\Lambda}} \cdot \underline{\underline{\theta}} \cdot \underline{\overline{s}}[j] + \underline{\overline{z}}[j], \tag{33.20}$$

where the channel matrix is

$$\underline{\underline{\Lambda}} := \begin{bmatrix} \underline{\underline{\Lambda}}_1^1 & \cdots & \underline{\underline{0}}_Q \\ \vdots & \ddots & \vdots \\ \underline{\underline{0}}_Q & \cdots & \underline{\underline{\Lambda}}_1^M \\ \vdots & \vdots & \vdots \\ \underline{\underline{\Lambda}}_{N_R}^1 & \cdots & \underline{\underline{0}}_Q \\ \vdots & \ddots & \vdots \\ \underline{\underline{0}}_Q & \cdots & \underline{\underline{\Lambda}}_{N_R}^M \end{bmatrix} \tag{33.21}$$

with

$$\underline{\underline{\Lambda}}_{n_R}^m := \left[\underline{\underline{\Lambda}}_{n_R,1}^m \quad \cdots \quad \underline{\underline{\Lambda}}_{n_R,N_T}^m\right], \tag{33.22}$$

for $m = 1, \ldots, M$ and $n_R = 1, \ldots, N_R$, and

$$\begin{aligned}
\underline{\underline{\theta}} &= \begin{bmatrix} \underline{\underline{I}}_{N_T} \otimes \underline{\underline{\theta}}^1 & \cdots & \underline{\underline{0}}_{N_T Q \times N_T B} \\ \vdots & \ddots & \vdots \\ \underline{\underline{0}}_{N_T Q \times N_T B} & \cdots & \underline{\underline{I}}_{N_T} \otimes \underline{\underline{\theta}}^M \end{bmatrix}, \\
\underline{\underline{F}} &= \underline{\underline{I}}_{N_R M} \otimes \underline{\underline{F}}_Q, \\
\underline{\underline{C}} &= \underline{\underline{I}}_{N_R} \otimes \begin{bmatrix} \underline{\underline{C}}^1 & \cdots & \underline{\underline{C}}^M \end{bmatrix}
\end{aligned} \tag{33.23}$$

in which

$$\underline{\underline{C}}^m := \underline{c}^m \otimes \underline{\underline{I}}_Q \tag{33.24}$$

with $\underline{c}^m := [c^m[0], \ldots, c^m[N_{\text{inter}} - 1]]^T$.

33.4.2.1. Space-division multiplexing

Taking (33.8) into account, the model (33.20) is extended to the SDM input/output matrix model

$$\overline{\underline{y}}_{\text{sdm}}[i] = \underline{\underline{C}}_{\text{sdm}} \cdot \left(\underline{\underline{F}}_{\text{sdm}}\right)^H \cdot \underline{\underline{\Lambda}}_{\text{sdm}} \cdot \underline{\underline{\theta}}_{\text{sdm}} \cdot \underline{\underline{\chi}}_{\text{sdm}} \cdot \overline{\underline{d}}[i] + \overline{\underline{z}}_{\text{sdm}}[i], \tag{33.25}$$

where the vector of transmitted symbols is defined as

$$\overline{\underline{d}}[i] := \left[\overline{\underline{d}}^1[i]^T \quad \cdots \quad \overline{\underline{d}}^M[i]^T\right]^T \tag{33.26}$$

with

$$\overline{\underline{d}}^m[i] := \left[\underline{d}_1^m[i]^T \quad \cdots \quad \underline{d}_{N_T}^m[i]^T\right]^T, \tag{33.27}$$

for $m = 1, \ldots, M$, and the received and noise vectors are defined as

$$\begin{aligned}
\overline{\underline{y}}_{\text{sdm}}[i] &:= \underline{y}[j], \\
\overline{\underline{z}}_{\text{sdm}}[i] &:= \underline{z}[j], \\
\underline{\underline{\chi}}_{\text{sdm}} &:= I_{MN_T B}, \\
\underline{\underline{\theta}}_{\text{sdm}} &:= \underline{\underline{\theta}}, \\
\underline{\underline{\Lambda}}_{\text{sdm}} &:= \underline{\underline{\Lambda}}, \\
\underline{\underline{F}}_{\text{sdm}} &:= \underline{\underline{F}}, \\
\underline{\underline{C}}_{\text{sdm}} &:= \underline{\underline{C}}.
\end{aligned} \tag{33.28}$$

33.4.2.2. Space-time block coding

Taking (33.9) into account, the model (33.20) is extended to the STBC input/output matrix model

$$\underline{\overline{y}}_{\text{stbc}}[i] = \underset{=\text{stbc}}{C} \cdot \left(\underset{=\text{stbc}}{F}\right)^{H} \cdot \underset{=\text{stbc}}{\Lambda} \cdot \underset{=\text{stbc}}{\theta} \cdot \underset{=\text{stbc}}{\chi} \cdot \underline{\overline{d}}[i] + \underline{\overline{z}}_{\text{stbc}}[i], \tag{33.29}$$

where the vector of transmitted symbols is given in (33.27) assuming $N_T = 2$, the received and noise vectors are defined as

$$\begin{aligned}
\underline{\overline{y}}_{\text{stbc}}[i] &:= \begin{bmatrix} \overline{y}[j] \\ \overline{y}[j+1]^* \end{bmatrix}, \\
\underline{\overline{z}}_{\text{stbc}}[i] &:= \begin{bmatrix} \overline{z}[j] \\ \overline{z}[j+1]^* \end{bmatrix}, \\
\underset{=\text{stbc}}{\chi} &:= \begin{bmatrix} \underset{=MN_TB}{I} \\ \underset{=M}{I} \otimes \underset{=}{\chi} \end{bmatrix}, \\
\underset{=\text{stbc}}{\theta} &:= \begin{bmatrix} \underset{=}{\theta} & \underset{=MN_TQ\times MN_TB}{0} \\ \underset{=MN_TQ\times MN_TB}{0} & \underset{=}{\theta}^* \end{bmatrix}, \\
\underset{=\text{stbc}}{\Lambda} &:= \begin{bmatrix} \underset{=}{\Lambda} & \underset{=N_RMQ\times MN_TQ}{0} \\ \underset{=N_RMQ\times MN_TQ}{0} & \underset{=}{\Lambda}^* \end{bmatrix}, \\
\underset{=\text{stbc}}{F} &:= \begin{bmatrix} \underset{=}{F} & \underset{=N_RMQ\times N_RMQ}{0} \\ \underset{=N_RMQ\times N_RMQ}{0} & \underset{=}{F}^* \end{bmatrix}, \\
\underset{=\text{stbc}}{C} &:= \begin{bmatrix} \underset{=}{C} & \underset{=N_RN_{\text{inter}}Q\times N_RMQ}{0} \\ \underset{=N_RN_{\text{inter}}Q\times N_RMQ}{0} & \underset{=}{C}^* \end{bmatrix}.
\end{aligned} \tag{33.30}$$

33.4.3. Multiuser joint detector

In order to detect the transmitted symbol block of the pth user $\underline{\overline{d}}^{p}[i]$, based on the received sequence of blocks within the received vector, $\underline{\overline{y}}_{\text{mode}}[i]$ ("mode" stands for "SDM" or "STBC"), a first solution consists of using a single-user receiver, that inverts successively the channel and all the operations performed at the transmitter. The single-user receiver relies implicitly on the fact that CDMA spreading has been applied on top of a channel equalized in the frequency domain. After CDMA despreading, each user stream is handled independently. However the single-user receiver can fail in the uplink where multiple channels have to be inverted at the same time.

The optimal solution is to jointly detect the transmitted symbol blocks of the different users within the transmitted vector, $\underline{\overline{d}}[i]$, based on the received sequence of blocks within the received vector, $\underline{\overline{y}}_{\text{mode}}[i]$. The optimum linear joint detector according to the minimum mean square error (MMSE) criterion is computed in [44]. At the output of the MMSE multiuser detector, the estimate of the transmitted vector is

$$\underline{\hat{\overline{d}}}[i] = \left(\frac{\sigma_w^2}{\sigma_d^2} \underline{\underline{I}}_{MN_TB} + \underline{\underline{G}}_{\text{mode}}^H \cdot \underline{\underline{G}}_{\text{mode}} \right)^{-1} \cdot \underline{\underline{G}}_{\text{mode}}^H \cdot \underline{\overline{y}}_{\text{mode}}[i], \tag{33.31}$$

where

$$\underline{\underline{G}}_{\text{mode}} := \underline{\underline{C}}_{\text{mode}} \cdot \left(\underline{\underline{F}}_{\text{mode}} \right)^H \cdot \underline{\underline{\Lambda}}_{\text{mode}} \cdot \underline{\underline{\theta}}_{\text{mode}} \cdot \underline{\underline{\chi}}_{\text{mode}}. \tag{33.32}$$

The MMSE linear joint detector consists of two main operations [44, 45].

(i) First, a filter matched to the composite impulse responses multiplies the received vector in order to minimize the impact of the white noise. The matched filter consists of the CDMA interblock despreading, the FFT operator to move to the frequency domain, the maximum ratio combining (MRC) of the different received antenna channels, the CDMA intrablock despreading, the IFFT to go back to the time domain in case of the SC-modes, and the STBC de-coding.

(ii) Second, the output of the matched filter is still multiplied by the inverse of the composite impulse response autocorrelation matrix of size MN_TB that mitigates the remaining intersymbol, interuser, and interantenna interference.

When no linear precoding is considered in the system, it can be easily checked that the linear MMSE estimate in (33.31) exactly reduces to the single-user receiver estimate for the MC and SCBS-CDMA systems.

In the case of MC and SC-CDMA, however, the linear MMSE receiver is different from the single-user receiver and suffers from a higher computational complexity. Fortunately, both the initialization complexity, which is required to compute the MMSE receiver, and the data processing complexity can be significantly reduced for MC and SC-CDMA, by exploiting the initial cyclo-stationarity property of the channels. Based on a few permutations and on the properties of the block circulant matrices given in [20], it can be shown that the initial inversion of the square autocorrelation matrix of size MN_TB can be replaced by the inversion of B square autocorrelation matrices of size MN_T.

33.5. Results

In this section, a performance comparison between the different communication modes is made, which can serve as an input for an optimal mode selection strategy. We consider a static cellular system, which operates in an outdoor urban microcell propagation environment. According to the 3GPP TR25.996 spatial channel model, this propagation environment is characterized by a specular multipath

with a mean excess delay of 251 nanoseconds, a mean angle spread at the base station of 19 degrees and a mean angle spread at the mobile terminals of 68 degrees. The system operates at a carrier frequency of 2 GHz, with a system bandwidth of 5 MHz. We assume an antenna spacing of 2 wavelengths at the mobile terminals and of 10 wavelengths at the base station. Monte-Carlo simulations have been performed to average the bit error rate (BER) over 500 stochastic channel realizations and to compute the corresponding goodput defined as the actual throughput offered to the user assuming a retransmission of the erroneous packets. The information bandwidth is spread by a spreading factor (SF) equal to 8. The user signals are spread by periodic Walsh-Hadamard codes for spreading, which are overlayed with an aperiodic Gold code for scrambling. QPSK, 16-QAM, or 64-QAM modulation is used with $Q = 128$ subchannels and a cyclic prefix length of $L = 32$. We assume a packet size of 512 symbols (4 blocks of 128 symbols in case of MC/SCBS-CDMA or 32 blocks of 16 symbols in case of MC/SC-CDMA). Convolutional channel coding in conjunction with frequency domain interleaving is employed according to the IEEE 802.11a/g standard. The code rate is 1/2, 2/3, or 3/4. At the receiver, soft-decision Viterbi decoding is used.

We distinguish between the uplink and the downlink. In the uplink, transmit power control is applied, such that the received symbol energy is constant for all users. The power transmitted by each terminal depends on the actual channel experienced by it. The BER (or the goodput) is determined as a function of the received bit energy or, equivalently, as a function of the transmit power averaged over the different channel realizations. In the downlink, no transmit power control is applied. For a constant transmit power at the base station, the received symbol energy at each terminal depends on the channel under consideration. The BER (or the goodput) is determined as a function of the transmit power or, equivalently, as a function of the received bit energy averaged over the channel realizations. For a given received symbol energy, the required transmit powers for the different communication modes appear to be very similar.

Rather than comparing all possible modes for the two link directions, we only consider the relevant modes for each direction. For the uplink, SC demonstrates two pronounced advantages compared to OFDM [9]. First, SC exhibits a smaller PAPR than OFDM modulation, which allows to reduce the power amplifier backoff and, thus, leads to increased power efficiency. Second, SC allows to move the IFFT at the transmitter to the receiver, which results in reduced terminal complexity. No computational effort is needed at the transmitter. For the downlink, OFDM is the preferred modulation scheme, since it only incurs a single FFT operation at the receiver side (as opposed to two FFT operations for SC), which leads to reduced terminal complexity.

Figure 33.3 illustrates the gain obtained by the use of different multiple-antenna techniques in the downlink of an MCBS-CDMA-based system. Three different system configurations have been considered ($1 \times 1, 1 \times 2, 2 \times 2$). A full user load is assumed (number of users is equal to the SF). A 16-QAM constellation is used and the coding rate is equal to 1/2. A gain of maximum 4 dB is achieved by combining the signals received through 2 antennas at the mobile terminal (MRC

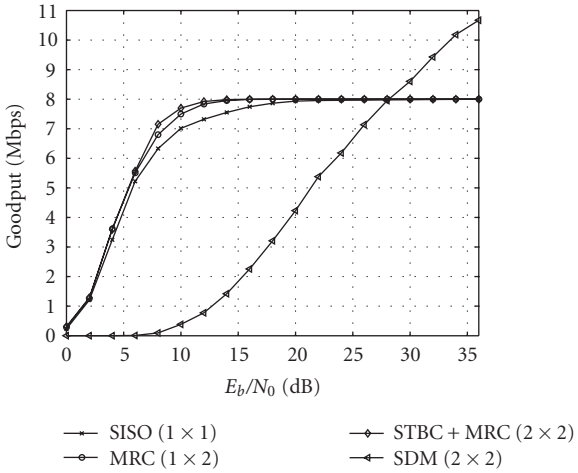

FIGURE 33.3. Multiple-antenna gain in the downlink of an MCBS-CDMA-based communication system.

technique), while a supplementary gain of maximum 1 dB can be achieved by further performing STBC coding across two antennas at the base station (STBC and MRC techniques together). On the other hand, SDM suffers from a high 15 dB loss in the goodput regions that can also be reached by a single-antenna system. One can only achieve an increase of capacity by the use of multiple-antennas at very high signal-to-noise-ratio (SNR) values. Due to the limited angle spread that characterizes the outdoor channels, the gain obtained by the use of multiple antennas is on the overall quite low. In the next simulation results, one directive antenna will be assumed at the base station to increase the cell capacity and two antennas will be assumed at the mobile terminal to improve the link reliability. The MRC combining technique is performed in the downlink, while the STBC coding scheme is applied in the uplink.

Figure 33.4 illustrates the total goodput of the MCBS-CDMA communication mode in the downlink for different combinations of the constellation sizes and code rates. A full user load has been assumed. Looking to those combinations that give the same asymptotic goodput (16-QAM and CR 3/4 compared to 64-QAM and CR 1/2), it is always preferable to combine a high constellation size with a low code rate. The same conclusion holds in order to get the optimal trade-off for each SNR value. The envelope is obtained by progressively employing QPSK, 16-QAM, 64-QAM constellations, and a code rate equal to 1/2, and then by increasing the code rate progressively to the values 2/3, 3/4 while keeping the constellation size fixed to 64-QAM.

Figure 33.5 compares the user goodput of MC-CDMA versus MCBS-CDMA in the downlink for a varying load (number of users is equal to 1, 5, and 8). Again a 16-QAM constellation and a coding rate equal to 1/2 are selected. The MMSE multiuser receiver for MCBS-CDMA reduces to an equivalent but simpler

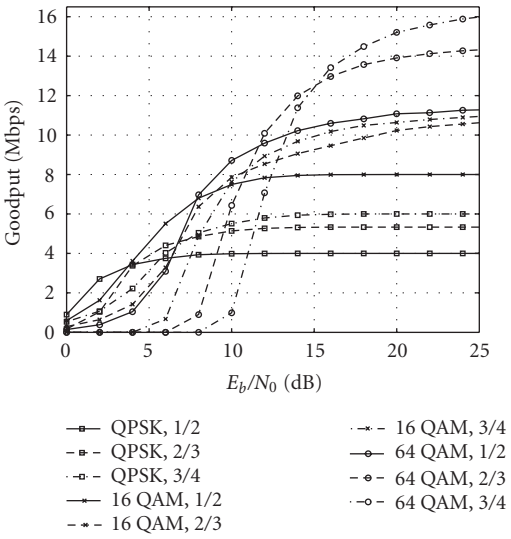

FIGURE 33.4. Trade-off channel coding rate and constellation for the downlink of an MCBS-CDMA-based communication system performing MRC combining.

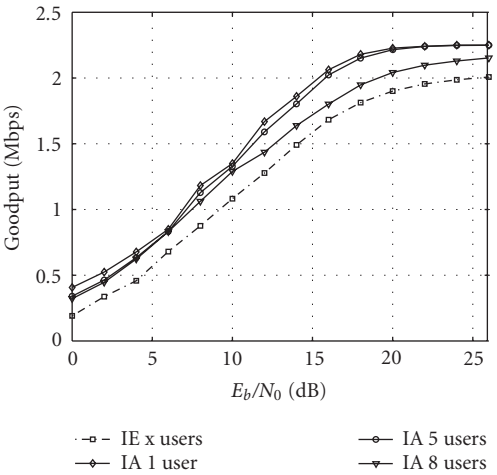

FIGURE 33.5. Comparison of MCBS-CDMA and MC-CDMA in the downlink of a communication system performing MRC combining (IA stands for intrablock spreading and IE stands for interblock spreading).

single-user receiver, which performs channel-independent block despreading followed by MMSE single-user equalization. The performance of MC-CDMA increases for a decreasing number of users, since it is limited by MUI. On the other hand, MCBS-CDMA is an MUI-free transceiver, such that its performance remains unaffected by the user load. Nevertheless, MCBS-CDMA always performs

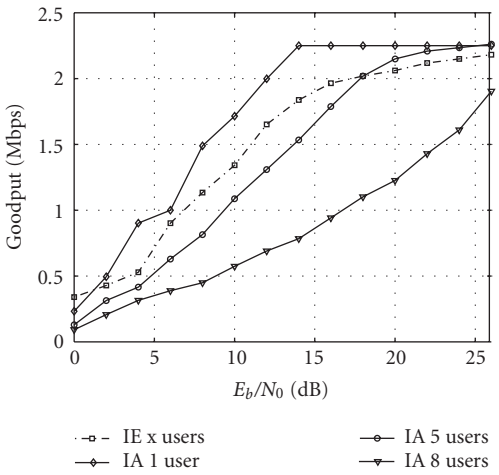

FIGURE 33.6. Comparison SCBS-CDMA and SC-CDMA in the uplink of a communication system performing STBC coding (IA stands for intrablock spreading and IE stands for interblock spreading).

worse than MC-CDMA, because the latter benefits from the diversity offered by spreading.

Figure 33.6 compares the user goodput of SC-CDMA versus SCBS-CDMA in the uplink for a varying load (number of users is equal to 1, 5, and 8). As for MC-CDMA, MMSE multiuser reception is needed for SC-CDMA, since a single-user receiver cannot get rid of the MUI, and features a BER curve flattening already at low SNRs. For the SCBS-CDMA mode, the MMSE multiuser receiver also reduces to a set of independent and low-complexity MMSE single-user receivers, which perform channel-independent block despreading followed by MMSE single-user equalization. The performance of SC-CDMA increases for a decreasing number of users, since it is limited by MUI. This effect is more pronounced than for the downlink MC-CDMA since the signals propagate through different channels, which is more difficult to compensate for. On the other hand, since SCBS-CDMA is an MUI-free transceiver that preserves the orthogonality among users (even after propagation through frequency-selective channels), its performance is independent of the user load.

33.6. Summary

Because of the limited frequency bandwidth on one hand and the potential limited power of terminal stations on the other hand, spectral and power efficiency of future systems should be as high as possible. New air interfaces need to be developed to meet the new system requirements. Combinations of the multicarrier (MC) and spread-spectrum (SS) modulations, named multicarrier-spread-spectrum techniques, could be interesting candidates. They might benefit from the main advantages of both MC and SS schemes such as high spectral efficiency, multiple-access capabilities, narrowband interference rejection, simple one-tap equalization, and

so forth. The huge potential of multiple antenna technologies is now widely recognized. One could rely on the diversity offered by the wireless channels to improve significantly the link reliability. Another possibility is to create artificially independent channel pipes between the transmit and receive antenna arrays so that the link capacity is highly increased.

Different flavors exist to mix the MC and SS modulations, that complement each other and allow to make an optimal trade-off between the spectral and power efficiency according to the user requirements, channel propagation characteristics (time and frequency selectivity), and terminal resources. In this chapter, we proposed a generic transmission scheme that allows to instantiate all the combinations of orthogonal frequency-division multiplexing (OFDM) and cyclic-prefixed single-carrier (SC) modulations with direct-sequence code-division multiple access (DS-CDMA). The space-division multiplexing (SDM) and spacetime block coding (STBC) multiple-antenna techniques are next integrated in the generic transmission scheme. For each resulting mode, the optimal linear minimum mean square error (MMSE), multiuser receiver is derived. An optimal strategy for the selection of the communication mode is proposed. It is shown that an adaptive transceiver is interesting to support different communication modes and to optimally track the changing communication conditions.

Acknowledgments

Before closing this chapter, we would like to acknowledge all our colleagues who have contributed to this work. We thank especially Liesbet Van der Perre for having enthusiastically launched and sustained this activity.

Abbreviations

AWGN	Additive white Gaussian noise
BER	Bit error rate
CIR	Channel impulse response
CSI	Channel state information
CDMA	Code-division multiple access
DS-CDMA	Direct-sequence code-division multiple access
FEC	Forward error coding
FIR	Finite impulse response
FFT	Fast Fourier transform
GMCBS-CDMA	Generalized multicarrier block-spread code-division multiple access
IBI	Interblock interference
IFFT	Inverse fast Fourier transform
MC	Multicarrier
MC-CDMA	Multicarrier CDMA
MCBS-CDMA	Multicarrier block-spread CDMA
MBWA	Mobile broadband wireless access
MIMO	Multiple-input multiple-output
MMSE	Minimum mean square error

MRC	Maximum ratio combining
MUI	Multiple-user interference
OFDM	Orthogonal frequency-division multiplexing
PAPR	Peak-to-average power ratio
QoS	Quality-of-service
SC	Single carrier
SC-CDMA	Single-carrier CDMA
SCBS-CDMA	Single-carrier block-spread CDMA
SCBT	Single-carrier block transmission
SDM	Space-division multiplexing
SF	Spreading factor
SNR	Signal-to-noise ratio
STBC	Space-time block coding
STC	Space-time coding
TR-STBC	Time-reversal space-time block coding
WLAN	Wireless local area network
WWRF	World Wireless Research Forum

Bibliography

[1] "Wireless World Research Forum homepage," http://www.wireless-world-research.org.

[2] "IEEE 802.20 Homepage," http://www.ieee802.org/20.

[3] T. Ojanperä and R. Prasad, *Wideband CDMA for Third Generation Mobile Communications*, Artech House Publishers, Boston, Mass, USA, 1998.

[4] R. van Nee, G. Awater, M. Morikura, H. Takanashi, M. Webster, and K. W. Halford, "New high-rate wireless LAN standards," *IEEE Commun. Mag.*, vol. 37, no. 12, pp. 82–88, 1999.

[5] H. Sari, G. Karam, and I. Jeanclaude, "Transmission techniques for digital terrestrial TV broadcasting," *IEEE Commun. Mag.*, vol. 33, no. 2, pp. 100–109, 1995.

[6] A. Czylwik, "Comparison between adaptive OFDM and single carrier modulation with frequency domain equalization," in *Proc. 47th IEEE Vehicular Technology Conference (VTC '97)*, vol. 2, pp. 865–869, Phoenix, Ariz, USA, May 1997.

[7] N. Benvenuto and S. Tomasin, "On the comparison between OFDM and single carrier modulation with a DFE using a frequency-domain feedforward filter," *IEEE Trans. Commun.*, vol. 50, no. 6, pp. 947–955, 2002.

[8] J. Louveaux, L. Vandendorpe, and T. Sartenaer, "Cyclic prefixed single carrier and multicarrier transmission: bit rate comparison," *IEEE Commun. Lett.*, vol. 7, no. 4, pp. 180–182, 2003.

[9] D. Falconer, S. L. Ariyavisitakul, A. Benyamin-Seeyar, and Eidson B., "Frequency domain equalization for single-carrier broadband wireless systems," *IEEE Commun. Mag.*, vol. 40, no. 4, pp. 58–66, 2002.

[10] N. Yee, J.-P. Linnartz, and G. Fettweis, "Multicarrier CDMA in indoor wireless radio networks," in *Proc. IEEE International Symposium on Personal, Indoor and Mobile Radio Communications (PIMRC '93)*, vol. 1, pp. 109–113, Yokohama, Japan, September 1993.

[11] K. Fazel, "Performance of CDMA/OFDM for mobile communication system," in *Proc. 2nd IEEE International Conference on Universal Personal Communications (ICUPC '93)*, vol. 2, pp. 975–979, Ottawa, Ont, Canada, October 1993.

[12] K. Fazel, S. Kaiser, and M. Schnell, "A flexible and high performance cellular mobile communications system based on orthogonal multi-carrier SSMA," *Kluwer Journal of Wireless Personal Communications*, vol. 2, no. 1/2, pp. 121–144, 1995.

[13] S. Kaiser, "OFDM code-division multiplexing in fading channels," *IEEE Trans. Commun.*, vol. 50, no. 8, pp. 1266–1273, 2002.

[14] V. M. DaSilva and E. S. Sousa, "Multicarrier orthogonal CDMA signals for quasi-synchronous communication systems," *IEEE J. Select. Areas Commun.*, vol. 12, no. 5, pp. 842–852, 1994.

[15] Q. Chen, E. S. Sousa, and S. Pasupathy, "Performance of a coded multi-carrier DS-CDMA system in multipath fading channels," *Kluwer Journal of Wireless Personal Communications*, vol. 2, no. 1–2, pp. 167–183, 1995.

[16] S. Kondo and B. Milstein, "Performance of multicarrier DS CDMA systems," *IEEE Trans. Commun.*, vol. 44, no. 2, pp. 238–246, 1996.

[17] L.-L. Yang and L. Hanzo, "Multicarrier DS-CDMA: a multiple access scheme for ubiquitous broadband wireless communications," *IEEE Commun. Mag.*, vol. 41, no. 10, pp. 116–124, 2003.

[18] F. Petré, G. Leus, M. Moonen, and H. De Man, "Multi-carrier block-spread CDMA for broadband cellular downlink," *EURASIP Journal on Applied Signal Processing*, vol. 2004, no. 10, pp. 1568–1584, 2004.

[19] F. Petré, *Block-spread CDMA for broadband cellular networks*, Ph.D. thesis, Katholieke Universiteit Leuven, Leuven, Belgium, December 2003.

[20] M. Vollmer, M. Haardt, and J. Gotze, "Comparative study of joint-detection techniques for TD-CDMA based mobile radio systems," *IEEE J. Select. Areas Commun.*, vol. 19, no. 8, pp. 1461–1475, 2001.

[21] K. L. Baum, T. A. Thomas, F. W. Vook, and V. Nangia, "Cyclic-prefix CDMA: an improved transmission method for broadband DS-CDMA cellular systems," in *Proc. IEEE Wireless Communications and Networking Conference (WCNC '02)*, vol. 1, pp. 183–188, Orlando, Fla, USA, March 2002.

[22] S. Zhou, G. B. Giannakis, and C. Le Martret, "Chip-interleaved block-spread code division multiple access," *IEEE Trans. Commun.*, vol. 50, no. 2, pp. 235–248, 2002.

[23] F. Petré, G. Leus, L. Deneire, and M. Moonen, "Downlink frequency-domain chip equalization for single-carrier block transmission DS-CDMA with known symbol padding," in *Proc. IEEE Global Telecommunications Conference (GLOBECOM '02)*, vol. 1, pp. 453– 457, Taipei, Taiwan, November 2002.

[24] Z. Wang and G. B. Giannakis, "Wireless multicarrier communications," *IEEE Signal Processing Magazine*, vol. 17, no. 3, pp. 29–48, 2000.

[25] G. B. Giannakis, P. A. Anghel, and Z. Wang, "Wideband generalized multicarrier CDMA over frequency-selective wireless channels," in *Proc. IEEE International Conference on Acoustics, Speech, and Signal Processing (ICASSP '00)*, vol. 5, pp. 2501–2504, Istanbul, Turkey, June 2000.

[26] G. B. Giannakis, Z. Wang, A. Scaglione, and S. Barbarossa, "AMOUR-generalized multicarrier transceivers for blind CDMA regardless of multipath," *IEEE Trans. Commun.*, vol. 48, no. 12, pp. 2064–2076, 2000.

[27] G. J. Foschini and M. J. Gans, "On limits of wireless communications in a fading environment when using multiple antennas," *Kluwer Journal of Wireless Personal Communications*, vol. 6, no. 3, pp. 311–335, 1998.

[28] G. G. Raleigh and J. M. Cioffi, "Spatio-temporal coding for wireless communication," *IEEE Trans. Commun.*, vol. 46, no. 3, pp. 357–366, 1998.

[29] D. Gesbert, H. Bolcskei, D. A. Gore, and A. J. Paulraj, "Outdoor MIMO wireless channels: models and performance prediction," *IEEE Trans. Commun.*, vol. 50, no. 12, pp. 1926–1934, 2002.

[30] A. Paulraj and T. Kailath, "Increasing capacity in wireless broadcast systems using distributed transmission/directional reception (DTDR)," U.S. Patent 5345599, Stanford University, Stanford, Calif, USA, September 1994.

[31] G. J. Foschini, "Layered space-time architecture for wireless communication in a fading environment when using multiple antennas," *Bell Labs. Tech. J.*, vol. 1, no. 2, pp. 41–59, 1996.

[32] V. Tarokh, N. Seshadri, and A. R. Calderbank, "Space-time codes for high data rate wireless communication: performance criterion and code construction," *IEEE Trans. Inform. Theory*, vol. 44, no. 2, pp. 744–765, 1998.

[33] S. M. Alamouti, "A simple transmit diversity technique for wireless communications," *IEEE J. Select. Areas Commun.*, vol. 16, no. 8, pp. 1451–1458, 1998.

[34] V. Tarokh, H. Jafarkhani, and A. R. Calderbank, "Space-time block codes from orthogonal designs," *IEEE Trans. Inform. Theory*, vol. 45, no. 5, pp. 1456–1467, 1999.

[35] F. W. Vook, T. A. Thomas, and K. L. Baum, "Transmit array processing for cyclic-prefix CDMA," in *Proc. 56th IEEE Vehicular Technology Conference (VTC '02)*, vol. 1, pp. 270–274, Vancouver, BC, Canada, September 2002.

[36] E. Lindskog and A. Paulraj, "A transmit diversity scheme for channels with intersymbol interference," in *Proc. IEEE International Conference on Communications (ICC '00)*, vol. 1, pp. 307–311, New Orleans, La, USA, June 2000.

[37] N. Al-Dhahir, "Single-carrier frequency-domain equalization for space-time block-coded transmissions over frequency-selective fading channels," *IEEE Commun. Lett.*, vol. 5, no. 7, pp. 304–306, 2001.

[38] S. Zhou and G. B. Giannakis, "Single-carrier space-time block-coded transmissions over frequency-selective fading channels," *IEEE Trans. Inform. Theory*, vol. 49, no. 1, pp. 164–179, 2003.

[39] S. Barbarossa and F. Cerquetti, "Simple space-time coded SS-CDMA systems capable of perfect MUI/ISI elimination," *IEEE Commun. Lett.*, vol. 5, no. 12, pp. 471–473, 2001.

[40] F. W. Vook, T. A. Thomas, and K. L. Baum, "Cyclic-prefix CDMA with antenna diversity," in *Proc. 55th IEEE Vehicular Technology Conference (VTC '02)*, vol. 2, pp. 1002–1006, Birmingham, Alabama, May 2002.

[41] F. Petré, G. Leus, L. Deneire, M. Engels, M. Moonen, and H. De Man, "Space-time block coding for single-carrier block transmission DS-CDMA downlink," *IEEE J. Select. Areas Commun.*, vol. 21, no. 3, pp. 350–361, 2003.

[42] Z. Liu and G. B. Giannakis, "Space-time block-coded multiple access through frequency-selective fading channels," *IEEE Trans. Commun.*, vol. 49, no. 6, pp. 1033–1044, 2001.

[43] A. Stamoulis, L. Zhiqiang, and G. B. Giannakis, "Space-time block-coded OFDMA with linear precoding for multirate services," *IEEE Trans. Signal Processing*, vol. 50, no. 1, pp. 119–129, 2002.

[44] A. Klein, G. K. Kaleh, and P. W. Baier, "Zero forcing and minimum mean-square-error equalization for multiuser detection in code-division multiple-access channels," *IEEE Trans. Veh. Technol.*, vol. 45, no. 2, pp. 276–287, 1996.

[45] L. Vandendorpe, "Performance analysis of IIR and FIR linear and decision-feedback MIMO equalizers for transmultiplexers," in *Proc. IEEE International Conference on Communications (ICC '97)*, vol. 2, pp. 657–661, Montreal, Que, Canada, June 1997.

François Horlin: Interuniversity MicroElectronic Center (IMEC), Wireless Research, Kapeldreef, 75 B-3001 Leuven, Belgium

Email: horlinf@imec.be

Frederik Petré: Interuniversity MicroElectronic Center (IMEC), Wireless Research, Kapeldreef, 75 B-3001 Leuven, Belgium

Email: petre@imec.be

Eduardo Lopez-Estraviz: Interuniversity MicroElectronic Center (IMEC), Wireless Research, Kapeldreef, 75 B-3001 Leuven, Belgium

Email: lopezest@imec.be

Frederik Naessens: Interuniversity MicroElectronic Center (IMEC), Wireless Research, Kapeldreef, 75 B-3001 Leuven, Belgium

Email: naessen@imec.be

34 Demonstrators and testbeds

Andreas Burg and Markus Rupp

34.1. Introduction

Since the establishment of the first point-to-point radio communication by Guglielmo Marconi in 1895, the complexity of communication systems has grown dramatically in the continuing search for higher system capacity, higher data rates, and bandwidth efficiency. Research in information theory and digital signal processing has been the foundation for the development of systems that are able to handle millions of users all over the globe.

However, the enormous proliferation of systems such as GSM or IS-95 has only become possible through the additional significant advances in integrated circuits technology. The ability to integrate complex algorithms and systems in a small, low-power device at a reasonable price has been the key factor for the success of mobile communication.

While modern ASIC technology allows for the integration of systems, the cost factor is largely dependent on the development effort and time to market. As systems become larger and more complex, the majority of the development effort is spent on its verification and performance analysis [1, 2]. With the necessity to introduce standards as the basis for enormous future development efforts, important decisions need to be made very early in the design cycle of a new system. At this point the actual implementation of a product is often not an immediate issue or might even not yet be feasible at reasonable cost. Erroneous decisions at this point can have significant impact on the success of a future system. An example of this is the introduction of HIPERLAN/1, where after many years of successful standardization, only one product came on the market, see http://www.proxim.com. At the time of standardization, it was believed that an equalizer would solve all observed transmission problems. Although equalizer algorithms are well explored in literature and showed very promising behavior in simulations, once the equalizer was to be implemented, the realization became very difficult. Particular solutions had to be investigated [3, 4, 5] in order to meet the stringent requirements, which finally turned out to be far too expensive to become a successful product.

A *quick-and-dirty* implementation of a proposed system or at least of its critical components (sometimes referred to as "rapid" prototyping) is often a means to detect potential problems early and thus de-risk a future product development.

34.1.1. Overview of the chapter

After some motivation and a brief classification of prototypes in general, this chapter first gives an overview of some of the recently presented MIMO prototypes. Subsequently hardware issues that need to be considered for a successful implementation are considered for SISO and later in particular for MIMO systems. The last section concentrates on rapid prototyping design methodology and tools.

34.1.2. Implementation types

Three types of systems can be identified, which from the management perspective serve a different purpose and from an engineering perspective are based on very different design and implementation requirements. It therefore makes sense to distinguish between the three experimental platforms based on the following definitions which are derived from their use in the literature [6] and from the dictionary.

(1) A *prototype* is the initial realization of a research idea or a standard, either as a reference, a proof of concept, or as a vehicle for future developments and improvements. As opposed to a simulation, it is not an imitative representation of the device. Instead it has significant similarities. In industry, a migration into a product is often intended.

(2) A *demonstrator* mainly serves as a sales vehicle and to show technology to customers. In general it will implement a new idea, concept, or standard that has already been established and has been finalized to some degree. Requirements on scalability are therefore less important than its functionality and often the required design time.

(3) A *testbed* on the other hand is generally used for research. It is a vehicle for further developments or for verification of algorithms or ideas under real-world or real time conditions. This results in the requirement for scalability, modularity, and extendibility.

A second criterion that allows a categorization of an implemented system is the real-time aspect. Most systems that have been implemented operate based on one of the following two paradigms.

(1) *Offline processing* schemes have the least stringent real-time requirements and are in general the easiest to implement. They have therefore been frequently used in a number of testbeds [7]. These schemes are often also called record and playback. They are based on offline preparation of a radio frame that is then sent in real time through the channel. A simple device records the received signal and all further processing is done offline without any timing constraints. The most stringent limitation of such a system is its inability to support feedback loops between

transmitter and receiver. Also, no (or only little) information will be gained about the actual implementation complexity of an algorithm.

(2) *Real-time* processing on the other hand generates the transmitted signal on the fly. The receiver processing takes place at essentially the same rate at which data is transmitted. This allows for a continuous operation of the system, which is its main characteristic and difference with respect to the offline-processing approach. However, at the same time it should be noted that real-time operation does not necessarily require the system to operate at its final target frequency or bandwidth. This is, for example, of interest if an appropriate scaling of all transmitter- receiver-, and channel-parameters is possible (e.g., when operating through a channel emulator).

34.1.3. Justification of a prototyping effort

It has been widely recognized that prototype implementations and field trials are an essential part of the verification of new system concepts, standards, and products. Consequently, extensive prototyping efforts have been carried out for today's single-input single-output (SISO) systems, such as GSM/GPRS, WLAN, HIPERLAN, and UMTS/HSDPA.

While the effort for a MIMO prototype is significantly higher than for a SISO system, its justification is also much more obvious and is founded on five critical issues.

(1) The availability of multiple antennas at the transmitter and at the receiver allows for a variety of new algorithms. Each of them has particular advantages and disadvantages and the optimum choice depends strongly on the actual channel conditions and the overall system context. Due to poor knowledge of the behavior of the MIMO channel, simulations often do not reflect them accurately and real-time/real-world experiments as well as field trials are necessary.

(2) In addition to the more realistic channel conditions and operating environment, a prototype also has the advantage over simulations of providing a significantly more exhaustive data set. The full or near real-time operation allows to test a system with a dramatically higher number of scenarios that can never be fully covered in slow computer simulations, especially in the high-SNR (low-BER) regime.

(3) It is also noticed that computer simulations often make numerous assumptions and rely on mathematical models which may turn out to be overly optimistic. Examples are the assumption of perfect channel- or even SNR knowledge at the receiver.

(4) From an implementation point of view, prototyping efforts have the advantage of pointing out complexity issues early in the design cycle of a new product or even already during standardization. Critical implementation issues are discussed from the beginning and delays due to unrealistic specifications (as in the rollout of UMTS) are avoided.

(5) Demonstrators are also important from a marketing perspective, as they show the ability of the company or product division to realize the latest technology.

34.1.4. Prototyping and SDR

Numerous synergies are recognized between rapid prototyping of communication systems and what is generally referred to as software-defined radio (SDR), see http://www.sdrforum.org/index.html. Both efforts aim at the implementation of a radio system on a generic reusable platform. A significant portion of the available literature in both fields is therefore of interest. A difference between the two subjects can be seen in the level at which the development is conducted and in the constraints under which the efforts are made.

For rapid prototyping (RP), design time of a new system is most critical and often more important than its cost, form-factor, or power consumption. A major focus is therefore on the efficiency of the tools that are being used in the development process. The hardware is built on standard components, flexible *at design time*.

In an SDR project, an efficient and flexible hardware platform capable of being reprogrammed or even reorganized (reconfigured) instantly *after design time* is the key to success. While of course suitable tools need to be available that allow to use the platforms capabilities, they are less crucial than the hardware itself and the supporting real-time operating system (RTOS). Consequently, most SDR projects are concerned with the development of flexible processing devices in order to meet the stringent constraints of mobile communication. Once such HW devices are available, they are interesting candidates for the hardware of a testbed. On the other hand, tools from RP-efforts may eventually be considered as valuable support tools for an actual SDR platform, which itself might have been developed and tested initially in an RP-environment.

From this short discussion it can be concluded that RP and SDR efforts complement each other quite well and will profit from each other.

34.2. Existing systems

In 1998 Bell-Labs reported the first narrowband MIMO prototype using the V-BLAST architecture. The prototype was built to obtain initial measurements to verify the predicted gains [8] of MIMO transmission. The system supported 8 transmit and 12 receive antennas; signal processing was performed offline on a frame-by-frame basis on a Pentek platform using TI-C40-DSPs [9].

Between 2000 and 2002, the first prototypes appeared applying MIMO concepts to broadband systems. In particular Lucent had shown the application of MIMO as an extension to the CDMA-based UMTS-FDD downlink. As opposed to the original V-BLAST prototype the new design used a combination of DSPs and FPGAs and was able to operate in real time [10]. IOSpan Wireless was the first company to develop and demonstrate MIMO-OFDM system prototypes as a basis for products that were then tested in field trials. Some of the results from this work are summarized in [11].

Table 34.1. List of selected MIMO prototypes.

	Tx/Rx	Mode	Platform	F_c/BW	Year	Ref.
Lucent	8/12	Offline	Pentek C-40 DSP	1.9 GHz 30 KHz/QAM	1998	[8]
Virginia Tech.	2/2	Real time	TI-EVM Boards	2.05 GHz 750 KHz	2001	[14]
IOSpan	3/2	Real time	ASIC FPGA/DSP	2.5 GHz 2 MHz	2001/02	[11]
Lucent/ETH	4/4	Real time	Custom FPGA/DSP	2 GHz 5 MHz/CDMA	2002	[10]
Lucent	4/4	Real time	ASIC FPGA/DSP	2 GHz/5 MHz 5 MHz/CDMA	2003	[13]
Brigham	16/16	Offline	PC	2.4 GHz	2003	[15]
Rice Univ.	2/2	Real time	Nallatech FPGA	2.5 GHz 20 MHz	2003	[16]
HHI	4/5	Real time	DSP/FPGA	5.2 GHz/12.5 MHz	2003	[17]
TU-Eindhoven	3/3	Offline	PC	5 GHz/20 MHz 20 MHz/OFDM	2003	[18]
ETH	4/4	Real time	Hunt Eng. FPGA	2 GHz 20 MHz/OFDM	2004	[19]
TU Wien	4/4	Offline	Sundance DSP/FPGA	2.45 GHz 6 MHz	2004	[20]
IMEC	2/2	Real time	FPGA ASIC	5.2 GHz 20 MHz	2004	[12]

Since then a number of universities have developed their own testbeds and experimental platforms to perform MIMO measurements and real-time experiments. Many of these systems (in particular those considering wideband systems) are based on offline processing of sampled data and use commercially available prototyping platforms. These again are often intended to perform channel measurements and to verify the performance of algorithms without considering implementation issues. Consequently, the usage of feedback is generally not possible.

However, some implementations are also capable and specifically designed for real-time operation, either to demonstrate adaptive modulation and other algorithms involving feedback or to also consider implementation complexity. An example for the former is the demonstrators reported by the Heinrich Hertz Institute (HHI) or for the latter the MIMO-OFDM demonstrator, developed at the Swiss Federal Institute of Technology (ETH). Another testbed [12], developed at IMEC, implements real-time operation of a 2×2 OFDM system with up- and downlink to demonstrate and evaluate MIMO processing at the transmitter.

Prototyping has also been used in conjunction with ASIC design [13] to demonstrate and test their functionality. Thereby the ASIC contains a critical part of the entire system and is supported by other ASICs, FPGAs, DSPs, and microprocessors.

An overview of some existing MIMO platforms is given in Table 34.1. Note that the distinction between *real-time* and *offline* processing in the table only refers

to how the platform has been used in recent publications, while some of the described offline hardware platforms also do support real-time signal processing. Also note that work in this field is also conducted at numerous other universities, research institutes, and companies. An extensive list of prototypes and products, which use smart antennas on only one side of the link to extend the capacity of existing systems is given in [21].

34.3. Hardware platform

34.3.1. Processing architectures and partitioning

Today, three main processing options are available for a prototyping hardware setup in wireless communications: FPGAs, high-performance DSPs, and microprocessors. Each of them is most suitable for a particular kind of operation and typically takes a particular role in a wireless communication system.

FPGAs are most suitable for high-rate regular datapath-dominated operations (e.g., despreading) that can be carried out in fixed-point arithmetic with relatively short word lengths. They also allow the efficient implementation of simple but real-time critical control functions that can often be realized efficiently in finite state machines with a limited number of states. FPGAs are found in almost all modern prototype designs. The amount of functionality that is realized by them generally grows rapidly as the real-time aspect becomes increasingly important. In a prototype design for a future ASIC implementation, FPGAs have the advantage that the code can often be mapped directly onto an ASIC process with only minor modification, which greatly eases the verification and reduces the coding time. While different FPGA vendors exist, the market is clearly dominated by the Xilinx-Virtex(II) series and the Altera Apex and Stratix series (see http://www.xilinx.com and http://www.altera.com), due to their very high capacity. Devices with integrated processors are also available. Both vendors focus on wireless communications for which the devices are well suited in prototyping. From the examples reported in the literature it appears that Xilinx devices are used more frequently in research prototypes.

DSPs are also mostly suited for regular arithmetic operations but impose less constraints on the regularity of an algorithm and thus also support control-dominated functions. Some DSPs are also able to efficiently carry out floating-point operations, which makes them a particularly appealing choice for numerically critical algorithms. From the rapid prototyping point of view, they are easier to program as compared to FPGAs. Their ability to directly use code from high-level simulations (typically ANSI C or even C++) makes them attractive wherever they provide sufficient performance.

Microprocessors (usually in a host PC) are most frequently used in offline processing prototypes, where no real-time constraints apply for the actual processing of the data. In this configuration, only little knowledge is gained about the actual complexity of an algorithm, but this is often also not of interest. The large variety of available tools greatly simplifies in general the implementation. In a real-time

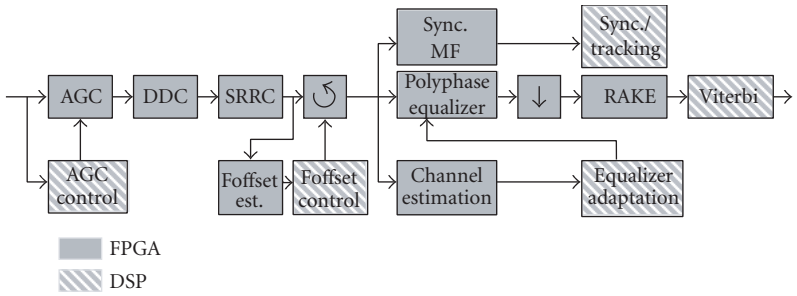

Figure 34.1. Partitioning example of a UMTS-FDD receiver.

prototype, microprocessors usually handle the higher layers of the protocol stack and interfaces to the outside world.

34.3.2. Partitioning

The previously discussed properties of the processing components dictate the partitioning of the system to a large extent. As an example, a block diagram of the physical layer of a UMTS-FDD downlink is given in Figure 34.1. It can be seen that almost all of the straightforward sample- and chip-rate processing is done in the FPGAs, covering a significant part of the overall complexity [22]. The DSP handles low-rate control functions and those parts of the design that are under development and require constant modifications. Important criteria for the partitioning are also the real-time and bandwidth constraints of the communication between the functional blocks.

34.3.3. A basic setup

Building a dedicated and highly optimized hardware platform from scratch for a particular system appears initially often to be a cost effective and powerful solution. However, the effort for the development of the hardware itself and especially of suitable middleware (device drivers and interfaces) and the debugging of the system is enormous and reliable schedules are hard to make. This is particularly true for systems that combine different processing architectures such as DSPs, microprocessors, and FPGAs. Such risky development may jeopardize the entire project. As a consequence, commercially available or existing proprietary processing or even dedicated prototyping platforms are mostly used. These are available from a variety of vendors offering configurations from data acquisition modules with virtually no processing capability over dedicated FPGA or DSP modules to flexible systems that can be equipped with different processing elements, according to the individual requirements. Widely used are products from Sundance, Pentek, Nallatech, Spectrum Signal Processing, Hunt Engineering, and many others. Some companies offer complete design environments, consisting of hardware and

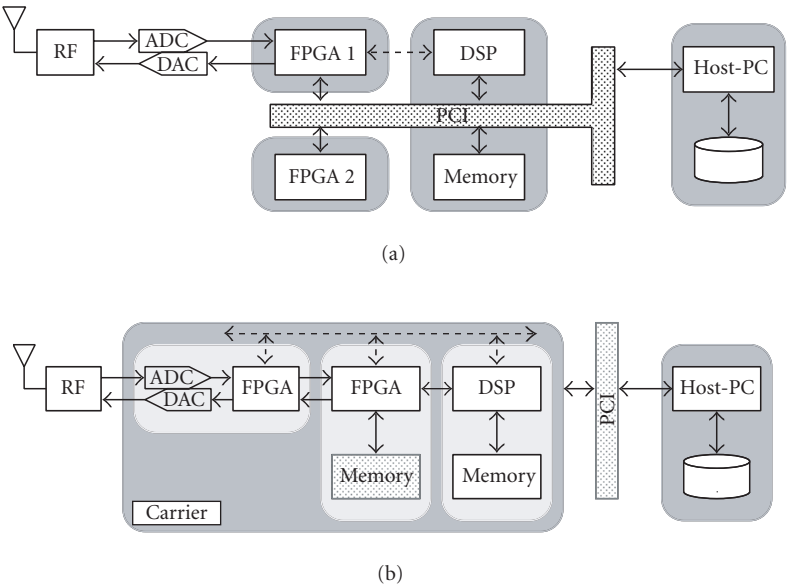

FIGURE 34.2. Typical architectures of commercial prototyping platforms: (a) common bus structure and (b) point-to-point interconnect of a carrier/module-based system.

software either for system development (such as Lyrtech) or for so-called presilicon prototyping of ASICs (such as Aptix). However at the same time, custom-designed platforms are often still of interest in the industry for customer demonstrations and field trials.

Whether a proprietary system is to be designed or a commercially available prototyping platform is to be used, a few basic points should be considered carefully.

System topology and connectivity. For the topology of a system two basic approaches are generally considered (see Figure 34.2). The first integrates all components of the system as independent modules, connected through a standard bus or point-to-point links [23, 24]. Especially the bus-based architecture allows to combine products from various vendors and provides a maximum flexibility. It also allows seamless access from a DSP or microprocessor to the remaining hardware which appears as part of its address space. This greatly facilitates the implementation of interfaces and improves the operability of the hardware for debugging or performance analysis. The common bus architecture typically resembles an architecture as it would most likely be used in a future system-on-chip (SoC) integration. However it also quickly becomes a performance bottleneck that ultimately limits the extension of such systems.

The second alternative is a modular (*carrier-based*) system which is often realized on the basis of a carrier board extendable by different (DSP, FPGA) modules. This type represents the majority of the commercially available prototyping

platforms. Such systems often use a more restrictive proprietary module interconnect scheme (such as the Hunt Engineering HEART system, the Sundance SHB-bus, or the Pentek VIM interconnect) on the basis of point-to-point links or ring structures supported by FIFO-interfaces. While this often provides a significantly increased bandwidth between the components, it reduces the flexibility and limits the use of boards from other vendors. Moreover, it often requires tedious protocols to allow a mapping of hardware components into a DSP or host processors address space. Consequently, the observability of the hardware states is reduced and significant interface changes are required when a successfully tested prototype is to be integrated as an SoC. A combination of a bus architecture with high-speed point-to-point connections based on a standard bus is therefore most desirable.

Integration of custom components. The ability to integrate custom boards or components into a system is a great advantage. On one hand it allows to supplement an existing system with custom ASICs implementing functions exceeding the capabilities of the prototyping system. On the other hand it allows the verification and debugging of custom boards or circuits in the system for which it was originally developed.

Standalone operation. While for a pure R&D platform a standalone operation is not of utmost importance, its marketing value in a technology demonstrator setup should not be underestimated. Depending on the field of application it is therefore important to consider the ability of a system to function and startup autonomously, for example, from a configuration in a flash memory or (E)EPROM.

Real-time capability. As a system needs to be partitioned into multiple DSP devices, real-time capability becomes an important aspect. The resulting requirements are essentially low-latency links between the components or boards with predictable deterministic delays. For systems which are partially based on DSPs and/or processors, interrupt capabilities are also of significant importance. A typical example is guaranteeing real-time constraints in time critical control functions such as in the IEEE 802.11 medium access control layer.

Memory. In particular when real-time processing is not required or a system can tolerate some latency, block processing has proven to be significantly more efficient than stream processing. However, on the other hand this gain often comes along with large memory requirements that may exceed the already significant amounts of storage on today's FPGAs. It is therefore advantageous to ensure that sufficient additional memory is or can be made available on a system.

Clocks and synchronization. In particular in a carrier-based system with multiple modules, clock distribution and synchronization becomes an important issue. If a common reference clock cannot be distributed between modules, resynchronization measures have to be taken to effectively design a system that works as an ensemble of locally synchronous, but globally asynchronous components. This can often be tedious and error-prone and adds additional hardware and latency, especially in systems that use a stream based processing (e.g., CDMA).

Baseband versus digital IF. In a SISO system, convincing arguments can be made for both digital baseband and digital-IF architectures. A digital-IF architecture, however, is known to avoid a number of problems such as carrier leakage and IQ-imbalance and is therefore often preferred. An appealing choice seems to be an approach, where the low-IF mixer of a superheterodyne receiver is substituted by bandpass sampling using an appropriate IF. Similarly at the transmitter, an image of the digital IF would be used directly as the low IF. The disadvantage of such a topology is its sensitivity to jitter, which requires high-quality clock sources for the converters. The resulting requirements often exceed the specifications of the DLLs that are usually contained in FPGAs. A thorough frequency planning is also required that leaves almost no room for scaling of the bandwidth of the signal if the system cannot immediately operate at its final speed.

34.3.4. Additional requirements for MIMO systems

The previous section discussed some basic requirements for the hardware of a generic prototyping platform. However, the systems considered so far were not particularly assuming multiple transmit and receive antennas; their constraints would equally apply to single-antenna systems. For the realization of a multiple-antenna system, some additional points need to be considered.

Baseband versus digital IF. In addition to the general arguments that were already presented for the SISO case, the reduced number of converters needed for a digital-IF realization becomes another strong argument in a MIMO scenario. The reduced cost, size, and number of connections needed usually compensate clearly for the higher sampling rate requirements which, for reasonable system bandwidth, still lie in the range of numerous available devices.

Clocks and synchronization. As the number of antennas grows, it becomes often necessary to distribute DA/AD conversion to multiple boards. As many MIMO systems rely on the in principle reasonable assumption of fully synchronized antennas, a timing or frequency offset can often not be tolerated. These constraints apply equally to the transmit and receive chains, but generally not between them. Having all transmit chains on one board and all receive chains on the other should therefore be strongly preferred over a solution where A/D and D/A converters are combined and the antennas are distributed over different boards.

Bandwidth and storage. A further important point is the significant increase in internal communication bandwidth in MIMO systems. While data rates between data acquisition and processing modules grow only linearly with the number of transmit/receive antennas, most existing platforms have been designed with SISO systems in mind. In a MIMO configuration, many of them quickly approach their performance limits even with moderate number of antennas (such as in a 4×4 system). In offline processing systems more high-speed storage needs to be provided close to the converters. However for some parts of a MIMO system, in particular for the channel state information (CSI), storage requirements grow quadratic

Table 34.2. Rate and storage requirements for future MIMO systems.

	$N_T \times N_R$	Baseband data rate	Raw bitrate	Samples for 1 frame	Words for 1 set of CSI
HSDPA	1×1	15.36 Msps	4.8 Mbps	150 K	64
	4×4	61.44 Msps	19.2 Mbps	600 K	1024
802.11a	1×1	20.00 Msps	54 Mbps	107 K	64
	4×4	80.00 Msps	216 Mbps	427 K	1024

with the number of antennas. Two examples are given in Table 34.2. They consider a MIMO extension of HSDPA and 802.11a with four antennas on both sides of the link. The former assumes an oversampling factor of four while the latter applies no oversampling. For the channel, 64 taps are considered in both cases. In an offline processing setup, for example, the on-chip memory of a large FPGA would be sufficient to record an entire SISO frame, while the corresponding MIMO configuration would require additional external memory. Similarly with some effort, the PCI bandwidth would allow a direct transfer of the baseband samples to the PC for a SISO system, while in the MIMO setting the PCI bandwidth would not be sufficient.

Module connectivity. A typical partitioning, especially in an open MIMO system, often allows for multiple data acquisition modules each of which supports only one or two channels. Many of these modules (as they are available) combine ADCs (DACs) with some limited processing capability through an FPGA. This is desirable to allow, for example, digital up-/down-conversion (DUC/DDC), automatic gain control (AGC), or subsampling algorithms to be placed as close to the converters as possible to avoid unnecessary data traffic to the main processing units. However, in MIMO designs some of these functions need to be coordinated among the different modules. It is therefore important that in addition to the high-speed data links they also provide a means for communicating with each other and to exchange control information. Direct coordination is typically only required within the receive and transmit chains, but not between them. Combining all transmit chains on one board and all receive chains on another should therefore again be preferred over a mix of both, distributed over two or more boards.

Processing requirements. Often MIMO systems are derived directly from similar SISO systems. Therefore, the actual MIMO processing is typically separated from the remaining part of the transmitter/receiver. The complexity of the latter generally scales linearly or quadratically (for channel estimation and equalization related parts) with the number of antennas. However, the complexity of the MIMO decoding itself (typically matrix inversions or ML-detection) can quickly become the dominant part. A quantification of the processing requirements, however, is certainly difficult to make as it strongly depends on the implemented system and algorithms. Therefore, it is even more important in MIMO systems to ensure an open system architecture that can be extended with new processing devices, which

can be connected to each other with sufficient bandwidth. It is also noted that FPGA technology evolves quickly and it should always be ensured that an upgrade to new devices remains possible without fundamental architecture changes.

34.3.5. System evolution: from SISO to MIMO

As mentioned before, most MIMO systems are based on an underlying SISO modulation scheme which by itself (e.g., in wideband systems) can be quite challenging to implement. It therefore appears most useful to develop a MIMO prototype on the basis of a suitable successfully tested SISO link implementation. Good example are CDMA or OFDM-based systems, where a significant amount of the processing is merely a replication of a corresponding SISO link from an algorithmic point of view [25]. This is generally exploited in DSP-based prototypes. However, for FPGA-based system components, simple replication is often not possible due to area constraints and/or because it is simply not economic. In this case interleaving of the multiple data streams is an interesting option. While this leads to a higher clock rate and still requires more storage elements in a design, it avoids replication of complex functional units (e.g., multipliers) and thereby leads to more efficient designs. Some FPGAs even provide dedicated hardware inside their configurable logic blocks (CLBs) for interleaved processing of multiple streams (e.g., Xilinx Virtex FPGAs). In this context it should be noted that interleaving is even recommended by FPGA vendors as a means to improve the utilization of their devices and to increase throughput through the resulting pipelining. This is founded on the observation that sampling rates even in wideband systems are often far below the capabilities of today's FPGA technology. An example is the straightforward realization of transversal SRRC filters in a four times oversampled UMTS system, which will run at a clock of less than 16 MHz, while 64 MHz are easily achievable on most commercially available FPGAs. It is noted that interleaved processing of multiple independent streams allows even pipelining of recursive algorithms, without causing stalls due to data dependency problems (e.g., multiple FFTs/IFFTs).

34.3.6. Channel emulation

While in most cases the eventual goal is the demonstration of a system under real-world and real-time conditions, this might sometimes not be feasible or is not even required. In particular when a system is designed for high mobility and large cell sizes, practical experiments are major cost factors that are often overlooked or underestimated at the beginning of a project. Only a few of them will be briefly mentioned here to undermine the argument for the necessity of channel emulation.

(i) Operating licenses for a particular spectrum need to be obtained, as power restrictions in the ISM bands do not allow for experiments with larger cells.

(ii) Power amplifiers with their undesired nonlinear behavior and other expensive RF equipment are needed.

(iii) Prototyping systems are usually not suitable for mobility and mechanical problems are most likely to occur.

Moreover, real-world scenarios are inherently uncontrollable and unpredictable and therefore particularly unsuitable for the initial analysis of a new algorithm. Instead, artificial but repeatable conditions are necessary to obtain an intuitive understanding for a prototype's behavior and to be able to compare it to other alternatives and simulations. From a functional verification point of view, debugging also calls for the ability to reproduce a problem and its history as accurately as possible to be able to analyze its origins. Therefore in addition to the control over channel conditions, it might be desirable to have full control over the noise in the system. This is only possible if all analog components are eliminated. Consequently, channel emulation is an essential development method that cannot be avoided and fully digital-IF or baseband interfaces are definitely a helpful feature. SISO systems have been available for quite some time. However, emulators with a sufficient number of channels for the emulation of a MIMO system have only emerged recently (see http://www.elektrobit.com and www.spirentcom.com) and are still extremely expensive. The main reason is the high complexity. To put this into perspective, the number of sample-spaced taps that can be emulated in a state-of-the-art FPGA (Xilinx XC2V6000-6) is illustrated in the following, assuming a bandwidth of 20 MHz. In a 1×1 system, the 144 integrated real-valued multipliers suffice to support 144 taps, whereby each multiplier is timeshared to perform a complex multiplication. In a 2×2 system only 36 taps can be emulated. In a 4×4 system the limit comes down to only 9 taps.

34.4. Design flow and tools

While many different HW platforms for prototyping exist, only little attention has been paid in the past to design methods and utilities. On the one hand expensive electronic design automation (EDA) tools for chip design were used, on the other hand particular DSP chips and FPGAs always come with development tools, some even being excellent. As long as cost and complexity of a design is not an issue, such tools can offer excellent design environments. However, in wireless MIMO prototypes, the designer has to realize very high complexities of the involved algorithms and thus a design methodology supporting a team effort as well as different hardware targets becomes more and more important. This section will discuss requirements of such a design methodology and give an overview of existing flows and available tools.

34.4.1. Requirements

Rapid prototyping of wireless MIMO systems faces similar problems as today's chip design in wireless: *high complexity algorithms* are to be implemented in a *short time* by a *design team*. While high complexity can easily be solved by parallel systems, in particular in prototyping where size and power consumption is not so

much of interest, short implementation time, changing specifications, and team effort, clearly require some organization.

In a classical chip design cycle [26], several design teams are working more or less interconnected one after the other using different design environments and languages, always those that suit their needs best. Since such languages and environments are incompatible, manual work is required to translate intermediate design results from one team to the next. Naturally, such a procedure is inconsistent, unnecessarily slow, and error-prone.

In [26] five concepts to improve design efficiency in a rapid prototyping design flow have been specified:

(1) *one* design environment,
(2) *one* automatic documentation by specification,
(3) *one* forward-backward compatible code revision tool,
(4) *one* code to be worked on by refinement steps,
(5) *one* team, to improve communication.

This paradigm is called the *five-ones approach*.

(1) It is shown that the design effort appears as a feed-forward system, handing the design over from one part of the design team to the next and a feedback loop concerning communication about the common design goals, and progress achieved. Such feedback slows down the design process. Since communication is required, the feedback loops cannot be broken. Also the required skill sets are not present in all parts of the teams. However, the response time can be changed dramatically, once all design teams share **one-design environment**. This observation on its own is not new and many tools in the EDA community exist (Simulink, COSSAP/CoCentric System Studio, and SPW to name the most widespread). However, since they have been developed to support specifically chip design (and to some extent algorithmic design) the architectural level and its exploration, as well as testing and system integration on specific hardware platforms (so-called platform-based design) are not supported. Also, due to specific language constraints, many researchers refuse to use such systems, since they believe their productivity is dramatically reduced by them. On top of that, high license costs prevent many companies from using them throughout the entire design chain.

(2) A second aspect is the missing documentation of the research part of the design team. While such people focus on meaningful results of their simulations, the following design teams are mostly interested in functional specifications. Graphical systems like COSSAP/CoCentric System Studio, SPW, and Simulink offer the possibility to define functional blocks with clearly defined input and output ports and corresponding data rates. Using such a graphical system **induces a documentation** while specifying the functional blocks. Specification allows detection of flaws at an early stage and, much more importantly, it can be used to supply additional information into functional descriptions of algorithms. The graphical description has further advantages: it avoids global variables. Global variables can lead to the undesired effect that information from the transmitter and/or channel is known at the receiver and some (undesired) cheating can be the result. It is, for example, quite common in the literature to present MMSE receivers having

perfect knowledge of the signal-to-noise ratio (SNR), while this value in reality needs to be estimated. The problem of estimating such a value is typically underestimated. In addition to the graphical specification, COSSAP, for example, allows writing so-called *Generic-C*, an ANSI C program enriched by essentially a header specifying the names, types, and rates of the input and output variables, a feature well preserved in the so-called PRIM models of the new version CoCentric System Studio.

(3) A third aspect of the slowdown in the product flow is the required permanent recoding. Although the research part of the design team defines a code for simulation, the system design team is not able to reuse the code, mainly due to its poor documentation and coding style used. Based on the anticipated hardware platform, other languages (assembler, VHDL) have to be used at a certain level of refinement, requiring time-consuming hand recoding. Such foregoing is error prone and requires a solution based on automatic recoding tools. See, for example, [27] where it is claimed that errors found late in the design process cost up to 100 times more than those found early. While graphical tools do not provide an immediate solution to the tedious recoding process, they can support it by allowing multiple, but different descriptions for each block. This alleviates the transformation and allows doing it piece by piece. Simulink, COSSAP/CoCentric System Studio (see http://www.synopsys.com), and SPW (see http://www.cadence.com) allow for such code versions, but only on a block level, that is, if a modification impacts several blocks at the same time, the system does not work out the required consistency.

Revision control tools (such as CVS, see http://www.gnu.org/software/cvs/, or ClearCase, see http://www.rational.com/products/clearcase/index.jsp) can help here. At certain times in the design flow, the entire design becomes frozen and can be reinstantiated at a later time allowing to track a bug that shows up at a certain (refinement) stage in the design flow, but was not noticed before. Further aspects of revision level tools are personal responsibility: the blocks can be assigned to specific people in the team and cannot be altered by others. Using such blocks, it is guaranteed that everybody in the team is working in the same, rather than in a personal environment. In order to guarantee backward compatibility, it is important to stick with one code and the same language for as long as possible.

(4) Furthermore, graphical systems allow an easy method of **code refinement** by cosimulation. The code can be refined from one revision level to the next and by instantiating the two versions at the same time, their output can be compared while they are fed by the same input. An important step in code refinement is the switch from float to fix-point code. The recent *SystemC* initiative [28], and also see http://www.systemc.org supports this step by extending ANSI C with fix-point data types. A|RT-Library from Adelante Technologies (now owned by ARM) offered such C++ Library extension for many years. The underlying idea is that by providing more and more details in the code at a very high level, the automatic tools modify the code iteratively into the required (meta-) descriptions until the final product is defined in every (technical) detail. These final descriptions express the code in a desired form, that is, assembler code to program a DSP chip, VHDL,

or VERILOG code to program an FPGA or synthesize the required masks for an ASIC. However, since the automatic tools map the code from a high level to each of the lower levels, the refinement of the code is only performed on the high level description, that is, the C-code. By iteratively rewriting the original C-code used in simulation to suit the needs of a specific hardware platform, the code remains backward compatible at any state and thus allows all teams to share the code and investigate problems. Specifically, there is no need to switch design environments or test benches when transferring from one team to another. While commercial tools rarely support hardware-in-the-loop, this becomes an important feature to check proper functionality and should be a requirement for future prototyping platforms. In [26], a so-called real-sync method is reported which allows to map DSP algorithms automatically from Simulink to TI C6X DSPs and run them there while the rest of the environment still runs under Simulink.

(5) One last aspect when analyzing the slow development process is the team size. Poor communication is a drawback of rather large teams. Fortunately, the required amount of people in a prototype team is much smaller and it is possible to keep all team members as **one team** supporting full information to everybody. This is clearly a particularity in rapid prototyping that cannot easily be realized in a large product design team.

34.4.2. Existing tools

DSP providers, in particular TI (see http://www.ti.com) offer a rich design environment that can be customized to specific DSP evaluation boards, including also real-time operating systems. Due to the excellent C-compiler and optimizer, signal processing procedures can be specified in a high-level language and mapped automatically onto a DSP. Many prototyping platform providers take advantage of this environment and customize their platforms accordingly. Mathworks (see http://www.mathworks.com) offers Simulink, a graphical interface with a rich library of toolboxes and fixed-point design tools, easing the design of communication algorithms. The recent introduction of cosimulation links between Matlab/Simulink and Mentor Graphics' popular ModelSim VHDL simulator helps to close the gap between algorithm and VHDL simulations. Most interesting is also the real-time workshop supporting automatic mapping of Simulink designs into C code for TIs C6x and other processors. However, so far the efficiency of the coding is quite limited. Harsh conditions on real time as they are common in wireless designs are not supported. FPGA providers like Xilinx and Altera enriched Simulink with their own libraries, called Xilinx System Generator and Altera's DSP Builder, respectively. They allow to simulate predefined DSP functions under Simulink and map the designs directly onto the corresponding FPGA chips. These tools lead to quite efficient FPGA designs, provided the DSP functions are available in the libraries. Especially, data-flow-oriented designs can be performed quickly, utilizing such tools.

34.5. Summary

The number of recently published papers on MIMO prototypes and testbeds by companies and universities is a clear indication that the effort is justified from a research as well as from a business point of view. It is therefore expected that the number of reported MIMO prototypes will significantly increase in the next years.

While on the hardware side the basic requirements for a successful realization are quite similar to SISO systems, more attention needs to be paid to proper synchronization of the system components, the increased communication bandwidth between them, and the higher processing and storage requirements. The variety of complex algorithms makes an open extendable system even more important than in the SISO case.

From the design methodology and implementation side, the more complex designs call for a well-organized design and prototyping methodology. Clearly defined interfaces between the design stages are most important. A common design environment using one language for high-level simulations and implementation based on successive refinements of the code is highly desirable.

Acknowledgments

Andreas Burg would like to thank his colleagues in the IIS and CTL at ETH whose work and experiences contributed significantly to the content of this chapter.

This work was funded by the Christian Doppler Pilot Laboratory for Design Methodology of Signal Processing Algorithms

Abbreviations

ADCs	Analog-to-digital converters
AGC	Automatic gain control
ASIC	Application-specific integrated circuit
CLBs	Configurable logic blocks
CSI	Channel state information
DACs	Digital-to-analog converters
DDC	Digital down-conversion
DLLs	Delay-locked loops
DSPs	Digital signal processors
DUC	Digital up-conversion
EDA	Electronic design automation
FPGAs	Field programmable gate arrays
GPRS	General packet radio service
GSM	Global system for mobile communication
HSDPA	High-speed downlink packet access
IF	Intermediate frequency
MIMO	Multiple-input multiple-output
PLLs	Phase-locked loops
RP	Rapid prototyping

RTOS	Real-time operating system
SDR	Software-defined radio
SISO	Single-input single-output
SoC	System-on-chip
UMTS	Universal mobile telecommunication system
WLAN	Wireless local area network

Bibliography

[1] B. Bailey, "The waking of the sleeping giant-verification," http://www.mentor.com/consulting/techpapers/mentorpaper_8226.pdf, April 2002.

[2] A. Hoffmann, T. Kogel, and H. Meyr, "A framework for fast hardware-software co-simulation," in *Proc. IEEE Conference and Exhibition Design, Automation and Test in Europe (DATE '01)*, pp. 760–765, Munich, Germany, March 2001.

[3] Y. Sun, A. R. Nix, D. R. Bull, et al., "Design of a novel delayed LMS decision feedback equaliser for HIPERLAN/1 FPGA implementation," in *Proc. 49th IEEE Vehicular Technology Conference (VTC '99)*, vol. 1, pp. 300–304, Houston, Tex, USA, May 1999.

[4] J. S. Wang, P. L. Lin, W. H. Sheen, D. Sheng, and Y. M. Huang, "A compact adaptive equalizer IC for HIPERLAN system," in *Proc. IEEE International Symposium on Circuits and Systems (ISCAS '00)*, vol. 2, pp. 265–268, Geneva, Switzerland, May 2000.

[5] Y. Baltaci, I. Kaya, and A. Nix, "Implementation of a HIPERLAN/1 compatible CMF-DFE equaliser," in *Proc. 51st IEEE Vehicular Technology Conference (VTC '00)*, vol. 3, pp. 1884–1888, Tokyo, Japan, May 2000.

[6] F. Kordon and J. Henkel, "An overview of rapid system prototyping today," *Kluwer Journal on Design Automation for Embedded Systems*, vol. 8, no. 4, pp. 275–282, 2003.

[7] T. Kaiser, A. Wilzeck, M. Berentsen, and M. Rupp, "Prototyping for MIMO systems: an overview," in *Proc. 12th European Signal Processing Conference (EUSIPCO '04)*, Vienna, Austria, September 2004.

[8] P. W. Wolniansky, G. J. Foschini, G. D. Golden, and R. A. Valenzuela, "V-BLAST: an architecture for realizing very high data rates over the rich-scattering wireless channel," in *Proc. International Symposium on Signals, Systems, and Electronics (ISSSE '98)*, pp. 295–300, Pisa, Italy, October 1998.

[9] D. Samardzija, C. Papadias, and R. Valenzuela, "Experimental evaluation of unsupervised channel deconvolution for wireless multiple-transmitter/multiple-receiver systems," *Electronics Letters*, vol. 38, no. 20, pp. 1214–1216, 2002.

[10] A. Adjoudani, E. Beck, A. Burg, et al., "Prototype experience for MIMO BLAST over third-generation wireless system," *IEEE J. Select. Areas Commun.*, vol. 21, no. 3, pp. 440–451, 2003.

[11] D. Gesbert, L. Haumonte, H. Bolcskei, R. Krishnamoorthy, and A. J. Paulraj, "Technologies and performance for non-line-of-sight broadband wireless access networks," *IEEE Commun. Mag.*, vol. 40, no. 4, pp. 86–95, 2002.

[12] M. Wouters, A. Bourdoux, S. Derore, S. Janssens, and V. Derudder, "An approach for real time prototyping of MIMO-OFDM systems," in *Proc. 12th European Signal Processing Conference (EUSIPCO '04)*, Vienna, Austria, September 2004.

[13] D. Garrett, G. Woodward, L. Davis, G. Knagge, and C. Nicol, "A 28.8 Mb/s 4×4 MIMO 3G high-speed downlink packet access receiver with normalized least mean square equalization," in *Proc. IEEE International Solid-State Circuits Conference (ISSCC '04)*, vol. 1, pp. 420–536, San Francisco, Calif, USA, February 2004.

[14] R. Gozali, R. Mostafa, R. C. Palat, et al., "Virginia tech space-time advanced radio (VT-STAR)," in *Proc. IEEE Radio and Wireless Conference (RAWCON '01)*, pp. 227–231, Waltham, Mass, USA, August 2001.

[15] J. W. Wallace, M. A. Jensen, A. L. Swindlehurst, and B. D. Jeffs, "Experimental characterization of the MIMO wireless channel: data acquisition and analysis," *IEEE Transactions on Wireless Communications*, vol. 2, no. 2, pp. 335–343, 2003.

[16] P. Murphy, F. Lou, A. Sabharwal, and P. Frantz, "An FPGA based rapid prototyping platform for MIMO systems," in *Proc. 37th IEEE Asilomar Conference on Signals, Systems, and Computers*, pp. 900–904, Pacific Grove, Calif, USA, November 2003.

[17] http://www.hhi.fraunhofer.de/english/mimo_at_globecom2003.pdf.

[18] A. van Zelst and T. C. W. Schenk, "Implementation of a MIMO OFDM-based wireless LAN system," *IEEE Trans. Signal Processing*, vol. 52, no. 2, pp. 483–494, 2004.

[19] H. Bölcskei, S. Häne, D. Perels, et al., "Implementation aspects of a real-time multi-terminal MIMO-OFDM testbed," in *IEEE Radio and Wireless Conference (RAWCON '04)*, Boston, Mass, USA, August 2004, http://www.nari.ee.ethz.ch/commth/pubs/p/RAWCON2004.

[20] E. Aschbacher, S. Caban, C. Mehlfuehrer, G. Mayer, and M. Rupp, "Design of a Flexible and Scalable 4×4 MIMO Testbed," in *Proc. 11th Digital Signal Processing Workshop 3rd Signal Processing Education Workshop*, pp. 178–181, Taos Ski Valley, NM, USA, August 2004.

[21] A. O. Boukalov and S. Haggman, "System aspects of smart-antenna technology in cellular wireless communications-an overview," *IEEE Transactions on Microwave Theory and Techniques*, vol. 48, no. 6, pp. 919–929, 2000.

[22] A. A. Kountouris, C. Moy, L. Rambaud, and P. Le Corre, "A reconfigurable radio case study: a software based multi-standard transceiver for UMTS, GSM, EDGE and Bluetooth," in *Proc. 54th IEEE Vehicular Technology Conference (VTC '01)*, vol. 2, pp. 1196–1200, Atlantic City, NJ, USA, October 2001.

[23] P. Murphy, J. P. Frantz, E. Welsh, R. Hardy, T. Mohsenin, and J. Cavallaro, "VALID: custom ASIC verification and FPGA education platform," in *Proc. IEEE International Conference on Microelectronic Systems Education (MSE '03)*, pp. 64–65, Anaheim, Calif, USA, June 2003.

[24] M. Vasilko, L. Machacek, M. Matej, P. Stepien, and S. Holloway, "A rapid prototyping methodology and platform for seamless communication systems," in *Proc. 12th IEEE International Workshop on Rapid System Prototyping*, pp. 70–76, Monterey, Calif, USA, June 2001.

[25] A. Burg, E. Beck, M. Rupp, D. Perels, N. Felber, and W. Fichtner, "FPGA implementation of a MIMO receiver front-end for UMTS," in *Proc. International Zurich Seminar on Broadband Communication (IZS '02)*, pp. 8.1–8.6, Zurich, Switzerland, February 2002.

[26] M. Rupp, A. Burg, and E. Beck, "Rapid prototyping for wireless designs: the five-ones approach," *Signal Processing*, vol. 83, no. 7, pp. 1427–1444, 2003.

[27] R. S. Janka, *Specification and Design Methodology for Real-Time Embedded Systems*, Kluwer Academic Publishers, Norwell, Mass, USA, 2002.

[28] W. Mueller, J. Ruf, D. Hoffmann, J. Gerlach, T. Kropf, and W. Rosenstiehl, "The simulation semantics of SystemC," in *Proc. Design, Automation and Test in Europe (DATE '01)*, pp. 64–70, Munich, Germany, March 2001.

Andreas Burg: Integrated Systems Laboratory, Swiss Federal Institute of Technology Zurich, Gloriastrasse 35, 8092 Zurich, Switzerland

Email: apburg@iis.ee.ethz.ch

Markus Rupp: Institute of Communications and Radio-Frequency Engineering, Vienna University of Technology, Gusshausstrasse 25/389, 1040 Wien, Austria

Email: mrupp@nt.tuwien.ac.at

VI Applications and Systems

Contents

35 Introduction

Thomas Kaiser

Nowadays, first prestandard MIMO products for wireless local area networks (WLANs) are already commercially available. While the corresponding *indoor* MIMO-WLAN standard is likely to be released in 2006, the *outdoor* world looks quite different. Here, progress in standardization is slow, mainly because spectral efficiency today is rather low (e.g., UMTS up to 0.4) and therefore MIMO represents merely an extension to other sophisticated data-rate accelerating techniques (e.g., high-speed downlink packet access (HSDPA)). Hence, "MIMO-HSDPA" is likely to get ready for the market, although not immediately. It will take a few more years, probably until 2010. However, the smart antenna world is partially opposite to "MIMO" for cellular systems. More than 250 000 smart antenna base stations, fully compliant to the Asian PHS standard designed for low mobility, have been sold, but nothing comparable can be observed for systems with high mobility, for example, CDMA 2000 or WCDMA, yet.

This part, therefore, takes on board two aspects. On one hand, future applications of multiantenna techniques in cellular communication systems are discussed, on the other hand two examples for multiantenna testbeds, facilitating and validating the all-embracing design of MIMO-WLAN- and MIMO-UMTS-based systems are explained in detail.

Chapter 2 addresses smart antenna solutions for UMTS as the forerunner of full cellular MIMO systems. Smart antennas (SAs) are considered here only at the base station, because the user terminal suffers from size and power limitations, severely complicating successful multiantenna deployment. Moreover, because the downlink data rate is on average greater than the uplink data rate, and uplink beamforming is rather well understood, this contribution is focused on downlink beamforming only. Note that UMTS offers a low-rate feedback channel, so that the corresponding algorithms for weight estimation can take into account the channel characteristics and are therefore *adaptive* in nature. While numerous contributions on link-level downlink beamforming have been published in the last few years, not much literature is devoted to system-level aspects, for example, system capacity, system coverage, and electromagnetic emission. Hence, the present contribution further fills this gap by focusing on the network level, while not losing track of

the link-level by adequately considering it within the signal-to-interference calculation.

As an extension of the second chapter, Chapter 3 is devoted to UMTS link-level simulations with SAs. The constraints imposed by standardization complicate the successful exploitation of multiantenna benefits. The aim of this chapter is to point out several low-complexity algorithmical approaches aiming for integrated circuit solutions. A review of conventional UMTS-SISO terminals, with special emphasis on well-proven RAKE receiver structures, is followed by an extension to the SIMO link where the base station acts as a space-time RAKE receiver. Furthermore, MIMO aspects including radio frequency (RF) and baseband (BB) decoding techniques are considered, and future realisations of MIMO prototypes are discussed to allow a wider perspective.

As an extension of the third chapter, Chapter 4 continues the discussion of MIMO algorithms for the HSDPA frequency division duplex (FDD) mode of UMTS. After summarizing HSDPA features relevant for applying multiantenna techniques, various MIMO-HSDPA transceiver architectures, for example, space-time transmit diversity, vertical BLAST, and linear dispersion codes on the transmitter side and RAKE, reduced maximum-likelihood, and turbo space-time decoder-typed receivers are discussed and evaluated by simulations with respect to fading and mobility.

Chapter 5 introduces a modular real-time MIMO platform from several perspectives, with the goal of enabling the reader to set up a complete MIMO testbed on his own. It covers the basic testbed concept, an offline, hybrid, and online processing mode as well as selected network topologies. Moreover, hardware and software for BB and RF processing are highlighted, for example, module interfacing, digital signal processor (DSP) programming, and field programmable gate array (FPGA) synthesis, plus project and revision control software. In addition to hints on system debugging some real-time requirements are pointed out. A major algorithmical challenge for any MIMO testbed working in online mode consists in reliable and accurate synchronisation issues, for example, coarse and fine timing acquisition, carrier frequency synchronisation, and tracking. At the end, a simplified MIMO testbed, based on acoustical transmission is presented, facilitating access to complex MIMO theory and practice to students in a somewhat playful manner.

In Chapter 6 another more sophisticated testbed is presented, targeting real-time prototyping of broadband MIMO-WLAN systems. Special emphasis is given to analog front-end impairments, for example, phase noise and amplifier nonlinearity and to possibilities of their cancellation. Starting with a single-antenna prototype and progressing step-by-step to a multiantenna scenario allows reuse of ideas from SISO impairment compensation also for the multiantenna case. Calibration architectures and higher-layer issues are addressed as well. An outlook on further developments winds up this contribution.

Thomas Kaiser: Smart Antenna Research Team, University of Duisburg Essen, 47057 Duisburg, Germany

Email: thomas.kaiser@uni-duisburg.de

36 Smart antenna solutions for UMTS

Andreas Czylwik, Armin Dekorsy, and Batu Chalise

Standards of third-generation mobile communication systems such as UMTS (universal mobile telecommunications system) are designed to support various smart antenna techniques. Smart antennas exploit the inherent spatial diversity of the mobile radio channel, provide an antenna gain, and also enable spatial interference suppression leading to reduced intra- as well as intercell interference. While it is feasible to adopt antenna arrays at base stations, however, their implementation in a handset is difficult with today's hardware due to its limitations in size, cost, and energy storage capability.

In such a setting, transmit beamforming at base stations provides a powerful method for increasing downlink capacity [1, 2, 3, 4]. Here, we focus on downlink beamforming concepts being in line with third generation partnership project (3GPP) standardization [5]. In particular, the beamforming concepts illuminated are fixed beamforming (FxB) and adaptive (user-specific) beamforming (ABF). While the latter one will be the main scope of this section, FxB is of minor interest. Since UMTS-FDD uplink channels are designed to be low-rate feedback channels, all downlink beamforming concepts described exploit uplink information being measured by the base station for spatially filtering the downlink signals. We further restrict to circuit-switched data transmission in UMTS-FDD mode [6]. In what follows, 3GPP terminology is used throughout this section, thus, the user equipment (UE) represents the user or mobile station and Node-B the base station, respectively.

The main scope of this section is to give an insight on system-level performance for UMTS-FDD downlink beamforming concepts if beamforming is subject to UMTS constraints. In general, system-level investigations supplement link-level simulations and deliver assessments in terms of system capacity, system coverage, as well as radiated electromagnetic power. System-level investigations carried out by static simulation approaches are described in [7, 8, 9]. Dynamic simulations of beamforming concepts for different antenna array topologies can, for example, be found in [10, 11, 12, 13, 14]. Apart from delivering system performance assessments, the dynamic simulation approach used in this section is discussed in detail. The simulation approach takes into account relevant UMTS-FDD concepts

and side information such as UMTS-FDD fast power control, UMTS-FDD physical channel structure, models for wave propagation, typical UMTS traffic models, and user mobility.

For adaptive beamforming, maximization of the SINR (signal-to-interference-and-noise power ratio) is investigated. We work out its performance especially under UMTS constraints such as strong interference from pilot and control channels. To obtain suitable assessments, we focus on three essential aspects. First, proper SINR modelling is considered including spatially formed inter- and intracell interference as well as pilot interference prevailing UMTS networks. Although we focus on the network level, fast channel fluctuations are taken into account by including them analytically into the signal-to-interference calculation. Furthermore, receiver techniques like maximum ratio combining of multipath components play an important role in the system performance. Finally, the interaction between UMTS specific radio resource management algorithms (power and load control) and beamforming concepts is discussed.

36.1. Signal model

In this section, either a uniform linear array (ULA) or a uniform circular array (UCA) is considered for the base station (Node-B), where the number of array elements for both array topologies is M. Mobile stations (user equipments—UEs) use one single antenna for transmission and reception only. For notational clarity, it is assumed that the multipath components of the frequency-selective mobile radio channel can be lumped into spatially or temporally resolvable (macro-)paths. The number of resolvable paths is determined by the angular resolution of the antenna array and the angular power distribution of the propagation scenario as well as by the relation of the delay spread to the symbol duration of the signal of interest. It is assumed that the number of resolvable paths is the same for uplink and downlink. Here, the number of resolvable paths between the kth mobile station and the jth base station is denoted by $L_{k,j}$. The total number of users in the entire network is K and the number of base stations is J. Throughout this section, uplink parameters and variables will be denoted by "$\hat{\ }$" and correspondingly downlink parameters and variables by "$\check{\ }$."

In the following, we focus on uplink transmission at first. The mobile station k is assigned to the base station $j(k)$. At the receiver, the base stations see a sum of resolvable distorted versions of the transmitted signals $\hat{s}_k(t)$ of users $k = 0, \ldots, K-1$. The complex baseband representation of the antenna array output signal vector of base station j is given by

$$\hat{\mathbf{r}}_j(t) = \sum_{k=0}^{K-1} \sqrt{\hat{P}_k} \sum_{l=0}^{L_{k,j}-1} \hat{\mathbf{h}}_{l,k,j} \hat{s}_k\left(t - \hat{\tau}_{l,k,j}\right) + \hat{\mathbf{n}}_j(t), \tag{36.1}$$

where $\hat{P}_k$ is the transmitted power from the kth user and $\hat{\mathbf{h}}_{l,k,j}$ represents the channel vector of length M of path l between user k and base station j. It is assumed that the channel is quasi-time-invariant within the period of interest. The kth user

uplink signal $\hat{s}_k(t)$ includes the complete baseband signal processing as channel encoding, data modulation, and spreading for UMTS WCDMA transmission, and $\hat{\tau}_{l,k,j}$ is the time delay of the lth path between user k and base station j. Finally, $\hat{\mathbf{n}}_j(t)$ is a spatially and temporally white Gaussian random process with covariance matrix

$$\hat{\mathbf{R}}_N = \mathrm{E}\left\{\hat{\mathbf{n}}_j \hat{\mathbf{n}}_j^H\right\} = \hat{\sigma}_N^2 \mathbf{I} \quad \text{for } j = 0, \ldots, J-1, \tag{36.2}$$

where $\mathrm{E}\{\cdot\}$ denotes the expectation.

The angular spread of the individual incoming resolvable paths determines the amount of spatial fading seen at an antenna array [2] and the size of the array employed will affect the coherence of the array output signals as well as which detection algorithms are applicable. For the remainder of this section, we assume closely spaced antenna elements yielding highly spatially correlated signals at the array elements. For this case, we can express the channel vector as

$$\hat{\mathbf{h}}_{l,k,j} = \hat{\alpha}_{l,k,j} \hat{\mathbf{a}}(\hat{\theta}_{l,k,j}), \tag{36.3}$$

where $\hat{\alpha}_{l,k,j}$ is the channel coefficient which is composed of path loss, log-normal shadow fading, as well as fast Rayleigh fading. The vector $\hat{\mathbf{a}}(\hat{\theta}_{l,k,j})$ denotes the array response or steering vector to a planar wave impinging from an azimuth direction $\hat{\theta}_{l,k,j}$. In our model, we assume that the angles of arrival $\hat{\theta}_{l,k,j}$ with $l = 0, \ldots, L_{k,j} - 1$ are Laplacian distributed variables with mean $\theta_{k,j}$, which equals the line-of-sight direction between user k and base station j [7, 8].

With the assumption of planar waves and uniformly located array elements, the frequency-dependent array response of a ULA is given by [7, 15, 16]

$$\mathbf{a}_{\mathrm{L}}(\theta) = \left[1, \mathrm{e}^{-\mathrm{j}2\pi(d/\lambda)\sin(\theta)}, \ldots, \mathrm{e}^{-\mathrm{j}2\pi(M-1)(d/\lambda)\sin(\theta)}\right]^T. \tag{36.4}$$

The interelement spacing of the antenna array is d, and λ represents the wavelength of the impinging wave. For the UCA, we have [15]

$$\mathbf{a}_{\mathrm{C}}(\theta) = \left[1, \mathrm{e}^{-\mathrm{j}2\pi(R/\lambda)\cos(\theta - 2\pi/M)}, \ldots, \mathrm{e}^{-\mathrm{j}2\pi(R/\lambda)\cos(\theta - 2\pi(M-1)/M)}\right]^T, \tag{36.5}$$

where R represents the radius of the array.

In order to form a beam for user k and detect its signal at base station $j(k)$, the received vector signal $\hat{\mathbf{r}}_{j(k)}(t)$ is weighted by the weight vector $\hat{\mathbf{w}}_k$:

$$\hat{y}_k(t) = \hat{\mathbf{w}}_k^H \hat{\mathbf{r}}_{j(k)}(t). \tag{36.6}$$

These weights depend on the optimization criterion, for example, maximizing the received signal power (equivalent to SNR), maximizing the SINR, and minimizing the mean squared error between the received signal and some reference signal to be known at the base station [2].

Equation (36.6) which also holds for fixed beamforming, can be rewritten with (36.1), (36.3), and either (36.4) or (36.5) as

$$\begin{aligned}\hat{y}_k(t) = \sqrt{\hat{P}_k} \sum_{l=0}^{L_{k,j(k)}-1} \hat{\alpha}_{l,k,j(k)} \hat{\mathbf{w}}_k^H \hat{\mathbf{a}}\big(\hat{\theta}_{l,k,j(k)}\big) \hat{s}_k\big(t - \hat{\tau}_{l,k,j(k)}\big) \\ + \sum_{\substack{\kappa=0 \\ \kappa \neq k}}^{K-1} \sqrt{\hat{P}_\kappa} \sum_{l=0}^{L_{\kappa,j(k)}-1} \hat{\alpha}_{l,\kappa,j(k)} \hat{\mathbf{w}}_k^H \hat{\mathbf{a}}\big(\hat{\theta}_{l,\kappa,j(k)}\big) \hat{s}_\kappa\big(t - \hat{\tau}_{l,\kappa,j(k)}\big) + \hat{\mathbf{w}}_k^H \hat{\mathbf{n}}_{j(k)}(t).\end{aligned} \tag{36.7}$$

The first term describes the desired signal, the second term represents the inter- as well as intracell interference, and the last expression describes additive Gaussian noise. Assuming that the data signals $\hat{s}_k(t - \hat{\tau}_{l,k,j(k)})$ and the additive noise $\hat{\mathbf{n}}_{j(k)}(t)$ are zero-mean and statistically independent random processes, the total received uplink signal power of the user of interest at the base station can be expressed in the form

$$\begin{aligned}\hat{P}_{\mathrm{R},k} &= \mathrm{E}\Big\{ \big| \hat{y}_k(t) \big|^2 \Big\} \\ &= \hat{P}_k \sum_{l=0}^{L_{k,j(k)}-1} \big| \hat{\alpha}_{l,k,j(k)} \big|^2 \cdot \big| \hat{\mathbf{w}}_k^H \hat{\mathbf{a}}\big(\hat{\theta}_{l,k,j(k)}\big) \big|^2 \\ &\quad + \sum_{\substack{\kappa=0 \\ \kappa \neq k}}^{K-1} \hat{P}_\kappa \sum_{l=0}^{L_{\kappa,j(k)}-1} \big| \hat{\alpha}_{l,\kappa,j(k)} \big|^2 \cdot \big| \hat{\mathbf{w}}_k^H \hat{\mathbf{a}}\big(\hat{\theta}_{l,\kappa,j(k)}\big) \big|^2 + \mathrm{E}\Big\{ \big| \hat{\mathbf{w}}_k^H \hat{\mathbf{n}}_{j(k)}(t) \big|^2 \Big\} \\ &= \hat{\mathbf{w}}_k^H \hat{\mathbf{R}}_{\mathrm{S},k} \hat{\mathbf{w}}_k + \hat{\mathbf{w}}_k^H \hat{\mathbf{R}}_{\mathrm{I},k} \hat{\mathbf{w}}_k + \hat{\mathbf{w}}_k^H \hat{\mathbf{R}}_N \hat{\mathbf{w}}_k,\end{aligned} \tag{36.8}$$

where the expectation operation is carried out with respect to the fast varying data signal and the additive noise. Note that the expectation is not carried out with respect to the fast fading processes, since we assume that the channel remains unchanged during a block of data. Here, it has been assumed that also time-delayed versions of the same data signal are uncorrelated. The kth user signal is normalized by $\mathrm{E}\{|s_k|^2\} = 1$ for $k = 0, \ldots, K-1$. The essential elements in antenna array beamforming design are the spatial covariance matrices $\hat{\mathbf{R}}_{\mathrm{S},k}$ for the desired signal as well as the spatial covariance matrices $\hat{\mathbf{R}}_{\mathrm{I},k}$ for the interference of user k. Both matrices are instantaneous covariance matrices which are fluctuating according to fast fading. According to (36.8), these matrices are given by

$$\begin{aligned}\hat{\mathbf{R}}_{\mathrm{S},k} &= \hat{P}_k \sum_{l=0}^{L_{k,j(k)}-1} \big| \hat{\alpha}_{l,k,j(k)} \big|^2 \cdot \hat{\mathbf{a}}\big(\hat{\theta}_{l,k,j(k)}\big) \hat{\mathbf{a}}\big(\hat{\theta}_{l,k,j(k)}\big)^H, \\ \hat{\mathbf{R}}_{\mathrm{I},k} &= \sum_{\substack{\kappa=0 \\ \kappa \neq k}}^{K-1} \hat{P}_\kappa \sum_{l=0}^{L_{\kappa,j(k)}-1} \big| \hat{\alpha}_{l,\kappa,j(k)} \big|^2 \cdot \hat{\mathbf{a}}\big(\hat{\theta}_{l,\kappa,j(k)}\big) \hat{\mathbf{a}}\big(\hat{\theta}_{l,\kappa,j(k)}\big)^H.\end{aligned} \tag{36.9}$$

These covariance matrices include all the spatial information necessary for beamforming. They can be measured in the uplink by correlating all antenna array output signals:

$$\mathrm{E}\left\{\hat{\mathbf{r}}_{j(k)}\hat{\mathbf{r}}_{j(k)}^{H}\right\} = \hat{\mathbf{R}}_{\mathrm{S},k} + \hat{\mathbf{R}}_{\mathrm{I},k} + \hat{\mathbf{R}}_{N}. \tag{36.10}$$

The only remaining task is to distinguish between the contribution of the desired signal and the contribution of interference plus noise. This can be accomplished by evaluating user-specific training sequences. In case of UMTS, the signals prior to despreading and after RAKE combining may be evaluated [17].

Next, downlink transmission is considered. A mobile terminal receives the desired signal from the base station to which it is connected. But it also receives interference from all other base stations. The received signal is given by

$$\check{y}_k(t) = \sqrt{\check{P}_k}\sum_{l=0}^{L_{k,j(k)}-1}\check{\alpha}_{l,k,j(k)}\check{\mathbf{w}}_k^{H}\check{\mathbf{a}}\left(\check{\theta}_{l,k,j(k)}\right)\check{s}_k\left(t-\check{\tau}_{l,k,j(k)}\right) + \check{i}_k(t) + \check{n}_k(t). \tag{36.11}$$

The first term in (36.11) is the desired signal and the second term $\check{i}_k(t)$ is interference which is composed of intracell as well as intercell interference. Here, $\check{P}_k$ denotes the total transmitted downlink power at base station $j(k)$. The last term $\check{n}_k(t)$ is additive white Gaussian noise which is created from thermal and amplifier noise. Assuming that the data signals for different mobile stations are statistically independent and that also time-delayed versions of the same data signal are uncorrelated, the power of the received signal at mobile station k yields

$$\begin{aligned}\check{P}_{\mathrm{R},k} &= \mathrm{E}\left\{\left|\check{y}_k(t)\right|^2\right\}\\ &= \check{P}_k\sum_{l=0}^{L_{k,j(k)}-1}\left|\check{\alpha}_{l,k,j(k)}\right|^2\cdot\left|\check{\mathbf{w}}_k^{H}\check{\mathbf{a}}\left(\check{\theta}_{l,k,j(k)}\right)\right|^2 + \mathrm{E}\left\{\left|\check{i}_k\right|^2\right\} + \mathrm{E}\left\{\left|\check{n}_k\right|^2\right\}\\ &= \check{\mathbf{w}}_k^{H}\check{\mathbf{R}}_{\mathrm{S},k}\check{\mathbf{w}}_k + \mathrm{E}\left\{\left|\check{i}_k\right|^2\right\} + \mathrm{E}\left\{\left|\check{n}_k\right|^2\right\}.\end{aligned} \tag{36.12}$$

Here, $\check{\mathbf{R}}_{\mathrm{S},k}$ denotes the downlink covariance matrix for the desired signal component:

$$\check{\mathbf{R}}_{\mathrm{S},k} = \check{P}_k\sum_{l=0}^{L_{k,j(k)}-1}\left|\check{\alpha}_{l,k,j(k)}\right|^2\cdot\check{\mathbf{a}}\left(\check{\theta}_{l,k,j(k)}\right)\check{\mathbf{a}}\left(\check{\theta}_{l,k,j(k)}\right)^{H}. \tag{36.13}$$

For UMTS WCDMA as an FDD system, fast fading processes in uplink and downlink are almost uncorrelated. Therefore, the instantaneous uplink covariance matrix cannot be used directly for downlink beamforming. But on the other hand, measurements have shown that the following spatial transmission characteristics for uplink and downlink are almost the same if—as in case of WCDMA—the frequency spacing between uplink and downlink bands is not too large (see [18],

[19, Section 3.2.2], and [20]):

$$\hat{\theta}_{l,k,j} \cong \check{\theta}_{l,k,j}, \tag{36.14}$$

$$\hat{\tau}_{l,k,j} \cong \check{\tau}_{l,k,j}, \tag{36.15}$$

$$\mathrm{E}\left\{ \left| \hat{\alpha}_{l,k,j} \right|^2 \right\} \cong \mathrm{E}\left\{ \left| \check{\alpha}_{l,k,j} \right|^2 \right\}. \tag{36.16}$$

In (36.16), the expectation is taken over the fast fading processes. The equation implies that fading processes from shadowing are almost the same for uplink and downlink. Because of this reason, a part of the spatial information which is available from the uplink covariance matrices can be utilized also for the downlink.

Since the instantaneous full spatial information is not available for the downlink, downlink beamforming has to be based on averages (with respect to fast fading) of the covariance matrices.

36.2. UMTS downlink beamforming solutions

In this section, we briefly illuminate applicable UMTS downlink beamforming solutions, with a focus on the UMTS frequency-division duplex (FDD) mode. We further restrict the description to UMTS-dedicated physical channels (DPCH), that is, the dedicated physical data channel (DPDCH) and the dedicated physical control channel (DPCCH). We review the opportunities and constraints for application of beamforming techniques for these channels. Throughout the section, we will adopt UMTS terminology, so a base station is referred to as Node-B and a mobile terminal as user equipment (UE). Further descriptions on UMTS-FDD beamforming solutions can be found in [5, 21, 22].

UMTS-FDD offers to support different beamforming concepts depending on the designed UMTS network structure which is mainly determined by the primary common pilot channel (P-CPICH) assignment. In this context, a logical UMTS cell[1] refers to the area covered by the P-CPICH. First, beamforming solutions synthesizing beams within one logical cell are fixed and adaptive beamforming where the latter one is also denoted as user-specific beamforming [5]. Fixed beamforming refers to the case where a finite set of beams is synthesized at Node-B and the beams are formed to cover the area of a logical cell. The second and more computational intensive concept is user-specific beamforming by adaptively synthesizing beams in order to meet an optimum criterion as to minimize the SINR.

Apart from applying beamforming in a logical cell, high-order sectorization via beamforming represents a further approach for UMTS-FDD. Here, the antenna array at Node-B is exploited to create individual cells where the coverage area of each beam represents a logical cell. This implies that each beam is transmitted under a unique primary scrambling code, and, in addition, each beam will have its own P-CPICH as well as further broadcasted UMTS downlink channels like BCH (broadcast channel), PCH (paging channel), and so forth.

[1] In this section, the terms cell and sector are used in the same manner.

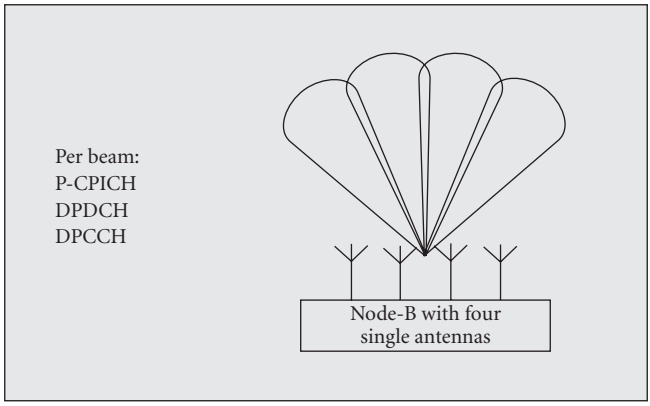

FIGURE 36.1. High-order sectorization with four synthesized beams each representing a logical cell with its own P-CPICH.

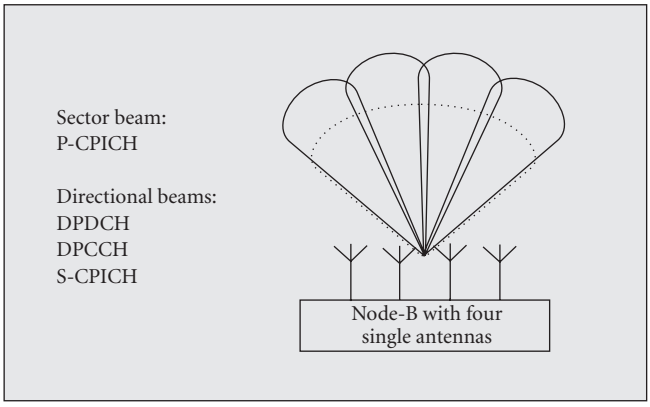

FIGURE 36.2. Fixed beamforming with four beams per logical cell (no sidelobes of beams and antenna patterns are shown).

Figure 36.1 shows the high-order sectorization principle with four beams representing one logical cell each. Note that neither the attenuation of the beams due to the single antenna array beam pattern nor sidelobes are depicted. Further information about high-order sectorization via beamforming can be found in [3, 5, 21]. In the following, we restrict to beamforming solutions in a logical cell-like fixed as well as adaptive beamforming.

36.2.1. Fixed beamforming

With fixed beamforming, the antenna array installed at Node-B is used to create a number of fixed beams covering the area of a cell, so multiple UEs may receive signals transmitted under the same beam. Figure 36.2 shows the separation of one logical cell (120° sector) in a grid of four beams.

Assignment of users to beams is based on the received uplink power per user at Node-B. In particular, Node-B measures the average uplink SINR on the uplink dedicated physical control channel (DPCCH) received from each UE. A UE is assigned to cell portions of the logical cell due to UMTS-FDD soft/softer handover algorithms. In the third-generation partnership project (3GPP) terminology, a cell portion is defined as the part of a cell that is covered by a specific radiated antenna pattern. Hence, the terms cell portion and beam may be used interchangeably. This pseudo-direction-of-arrival (DoA) measurement is reported to the radio network controller (RNC) where it is further used for managing available radio resources [5]. Even though fixed beamforming is referred to as fixed, radio resource management algorithms can be used to slowly vary the beam arrangement over time to adjust to long-term load variations in the logical cell as in case of time-variant hot-spot scenarios.

In addition to the broadcasted P-CPICH, with fixed beamforming, each beam is associated with a unique secondary common pilot channel (S-CPICH). This associated S-CPICH allows for proper channel estimation as well as beam identification since UEs may be informed to use it for phase reference via higher-layer protocols. But, on the other hand, S-CPICH implementation suffers from higher interference levels limiting the system performance. A further potential loss of using a grid of fixed beams evolves from the finite set of steering directions resulting in received power fluctuations at the UE if it moves [21]. This drawback is also often denoted as steering error.

The signals toward different UEs assigned to the same logical cell are typically transmitted under the same primary scrambling code while separation is performed by orthogonal channelization codes selected from a channelization code tree [23]. The number of channelization codes is rather limited severely cutting down expected performance gains of capacity enhancing techniques like beamforming. With fixed beamforming, however, some of the beams of a logical cell may be transmitted under a secondary scrambling code with its own associated channelization code tree. Especially, the same channelization code trees with different secondary scrambling codes could be assigned to spatially nonoverlapping beams. The secondary scrambling codes are any of 15 different secondary scrambling codes associated with the primary scrambling code.

Comparisons of several beamforming solutions also including a detailed description of fixed beamforming can be found in [24, 25, 26]. An overall conclusion reveals that for interference-limited UMTS-FDD networks where the traffic is exclusively carried on dedicated channels, fixed beamforming shows quite similar results in terms of system capacity as well as power reduction at Node-B compared to the more sophisticated solution of user-specific beamforming. Furthermore, evolving UMTS networks (Release 5 and beyond) will support packet data transmission on channels commonly shared by several users in a time-division mode like the high-speed downlink shared channel (HS-DSCH) in high-speed downlink packet access (HSDPA). There, the support of user-specific beamforming is not mandatory and the preferred beamforming mode might be fixed beamforming to ensure compatibility with traffic carried on dedicated channels (DCHs) [21].

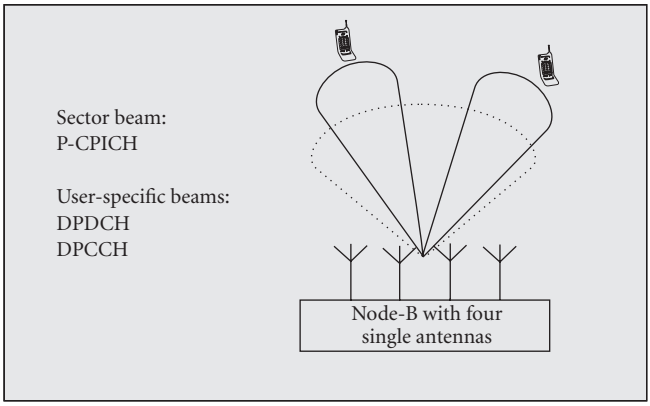

FIGURE 36.3. User-specific beamforming with two UEs in a logical cell with its own P-CPICH (no sidelobes of beams and antenna patterns are shown).

36.2.2. Adaptive downlink beamforming

36.2.2.1. Application to UMTS

The most sophisticated beamforming solution is to assign each UE an individual beam which is to be adapted to the interference situation and location of the user considered. With user-specific beamforming, also denoted as adaptive beamforming [15, 22], the dedicated physical data and control channel in UMTS are both spatially formed by an individual spatial filter while the P-CPICH is transmitted over the entire sector providing coverage for the entire sector area, see Figure 36.3.

This prevents the UE from using the P-CPICH as phase reference for channel estimation, since the transfer function of the P-CPICH is likely to be different from the one of the transmitted dedicated signal. In order to properly estimate the downlink channel, a UE subject to user-specific beamforming is to be informed via higher-layer protocols to use the pilot bits of the dedicated physical control channel (DPCCH) for phase reference. Note that this channel estimation lacks of quality compared to P-CPICH-based estimation as in case of fixed beamforming [5] and results in higher signal-to-interference ratio requirements. The UMTS specification allows for using a secondary common pilot channel (S-CPICH) per UE, but this method is very unattractive due to the high interference caused. The UMTS specification is also open for a hybrid beamforming concept. For this case, each UE is user-specific beamformed and, in addition, S-CPICHs are transmitted via fixed beams enabling S-CPICH reception for phase reference at the UE.

The signals toward different UEs from the same sector are typically transmitted under the same primary scrambling code. Separation is performed by orthogonal channelization codes in a CDMA manner where the codes are selected from a channelization code tree [3, 27]. The number of available channelization codes is rather limited corresponding to the minimum data rate carried on the DCHs [27]. With fixed beamforming, different (secondary) scrambling codes each with

its own associated channelization code tree can be assigned to different beams avoiding code limitation in a sector. In case of user-specific beamforming, all UEs have to share one channelization code tree under one primary scrambling code likely resulting in code limitation. Utilizing the above-mentioned joint combination of fixed and user-specific beamforming avoids code limitation.

To fully exploit spatial filtering capabilities, complete downlink spatial information is required at the base station to reduce intercell as well as intracell interference. Complete spatial information comprises the knowledge of the covariance matrices which include the knowledge of instantaneous magnitudes of the channel coefficients $|\alpha_{l,k,j(k)}|$, the angles of arrival $\theta_{l,k,j(k)}$, and transmitted powers P_k. The beamforming strategies, which will be discussed later in this section, are directly based on covariance matrices.

Usually, spatial information is only available for uplink transmission by evaluating user-specific training sequences at base stations. For the downlink, a backward transmission of channel state information from the mobile stations to the base stations would be necessary. Since mobile communication systems as UMTS are commonly designed with low data rate signalling feedback channels in order to obtain high bandwidth efficiency [3], neither the instantaneous channel coefficients nor steering vectors are known at the base station. Although the fast fading processes for uplink and downlink are uncorrelated, the averaged magnitudes of channel coefficients can be assumed to be insensitive to small changes in frequency. Thus, the averaged channel coefficients (averaged with respect to fast fading) and angles of arrival can be estimated from the time-averaged uplink covariance matrices. For power control procedures which are controlled by base stations, all transmitted power levels are also known at the base stations.

The following methods can be used to estimate the downlink covariance matrices.

(i) After estimation of angles of arrival and power transfer factors with high-resolution estimation methods [28] from the time-averaged uplink covariance matrices, the downlink covariance matrices are calculated using (36.13).

(ii) Alternatively, the covariance matrices are transformed directly from uplink to downlink carrier frequency by linear transformations as proposed in the literature [17, 29, 30].

Estimation errors cause some degradation compared with the ideal case where the covariance matrices are exactly known. A downlink beamforming method that provides robustness against such estimation errors can be found in [30]. For simplicity and in order to estimate the ultimate performance, in this section, we assume perfectly known time-averaged downlink covariance matrices.

The optimum beamforming method optimizes all transmit powers as well as all beam patterns jointly for all UEs [31, 32]. This optimum centralized beamforming method is by far too complex for an implementation in a practical system. Therefore, we discuss in the following only noncentralized suboptimum beamforming methods. A first suboptimum beamforming method maximizes the virtual signal-to-interference-and-noise ratio. This ratio is defined as the ratio of the received signal power at the desired mobile to the total interference (and noise)

power caused at any other mobile. Clearly, this ratio cannot be measured anywhere—therefore, it is called *virtual* SINR. The second suboptimum method maximizes the received power at the UE. It can be derived from the optimum centralized beamforming method by separating beamforming and power control as well as assuming that the interference causes spatially white noise.

36.2.2.2. Maximum (virtual) SIR beamforming

The optimum centralized beamforming method maximizes the SINRs at all mobiles k jointly. The instantaneous received signal power at UE k is given by

$$\check{P}_{\mathrm{S},k} = \check{\mathbf{w}}_k^H \check{\mathbf{R}}_{\mathrm{S},k} \check{\mathbf{w}}_k, \tag{36.17}$$

where $\check{\mathbf{R}}_{\mathrm{S},k}$ denotes the instantaneous downlink covariance matrix of the desired signal (36.13). As mentioned before, the instantaneous downlink covariance matrix is not known at Node-B. Instead, we are using the time-averaged version which can be calculated with the above-described methods. Therefore, a suboptimum beamforming algorithm can be based on the time-averaged downlink covariance matrix $\widetilde{\mathbf{R}}_{\mathrm{S},k}$ which corresponds to the expectation of the instantaneous covariance matrix $\check{\mathbf{R}}_{\mathrm{S},k}$ (see (36.13)):

$$\widetilde{\mathbf{R}}_{\mathrm{S},k} = \mathrm{E}\{\check{\mathbf{R}}_{\mathrm{S},k}\} = \check{P}_k \sum_{l=0}^{L_{k,j(k)}-1} \mathrm{E}\left\{ \left| \check{\alpha}_{l,\kappa,j(k)} \right|^2 \right\} \cdot \check{\mathbf{a}}(\check{\theta}_{l,\kappa,j(k)}) \check{\mathbf{a}}(\check{\theta}_{l,\kappa,j(k)})^H. \tag{36.18}$$

Be aware that the steering vectors have to be determined at downlink frequency. Since we are averaging with respect to Rayleigh fading, the actual beamforming strategy for the downlink is to maximize the average downlink power,

$$\widetilde{P}_{\mathrm{S},k} = \check{\mathbf{w}}_k^H \widetilde{\mathbf{R}}_{\mathrm{S},k} \check{\mathbf{w}}_k, \tag{36.19}$$

while keeping the average intracell and intercell interference power $\widetilde{P}_{\mathrm{I},k}$ received at UE k constant, which is derived from (36.11):

$$\widetilde{P}_{\mathrm{I},k} = \sum_{\substack{\kappa=0 \\ \kappa\neq k}}^{K-1} \check{P}_\kappa \sum_{l=0}^{L_{k,j(\kappa)}-1} \mathrm{E}\left\{ \left| \check{\alpha}_{l,k,j(\kappa)} \right|^2 \right\} \cdot \left| \check{\mathbf{w}}_\kappa^H \check{\mathbf{a}}(\check{\theta}_{l,k,j(\kappa)}) \right|^2 = \sum_{\substack{\kappa=0 \\ \kappa\neq k}}^{K-1} \check{\mathbf{w}}_\kappa^H \widetilde{\mathbf{R}}_{\mathrm{I},k,\kappa} \check{\mathbf{w}}_\kappa. \tag{36.20}$$

Here, $\widetilde{\mathbf{R}}_{\mathrm{I},k,\kappa}$ denotes the downlink covariance matrix of interference received at mobile k from the downlink signal of mobile κ which is transmitted from Node-B $j(\kappa)$. It is averaged with respect to the data signals and Rayleigh fading processes:

$$\widetilde{\mathbf{R}}_{\mathrm{I},k,\kappa} = \check{P}_\kappa \sum_{l=0}^{L_{k,j(\kappa)}-1} \mathrm{E}\left\{ \left| \check{\alpha}_{l,k,j(\kappa)} \right|^2 \right\} \cdot \check{\mathbf{a}}(\check{\theta}_{l,k,j(\kappa)}) \check{\mathbf{a}}(\check{\theta}_{l,k,j(\kappa)})^H. \tag{36.21}$$

With these definitions, the downlink SINR of user k results in

$$\mathrm{SINR}_k = \frac{\breve{\mathbf{w}}_k^H \widetilde{\mathbf{R}}_{\mathrm{S},k} \breve{\mathbf{w}}_k}{\sum_{\substack{\kappa=0 \\ \kappa \neq k}}^{K-1} \breve{\mathbf{w}}_\kappa^H \widetilde{\mathbf{R}}_{\mathrm{I},k,\kappa} \breve{\mathbf{w}}_\kappa + \breve{\sigma}_N^2}, \tag{36.22}$$

where σ_N^2 represents the additive noise power, respectively. For simplicity of a suboptimum approach, the intracell and intercell interference in the denominator of (36.22) are replaced by the sum of interference powers received at all other mobile stations caused by the signal transmitted to mobile station k. This results in

$$\mathrm{SINR}_{k,\mathrm{virt}} = \frac{\breve{\mathbf{w}}_k^H \widetilde{\mathbf{R}}_{\mathrm{S},k} \breve{\mathbf{w}}_k}{\sum_{\substack{\kappa=0 \\ \kappa \neq k}}^{K-1} \breve{\mathbf{w}}_k^H \widetilde{\mathbf{R}}_{\mathrm{I},\kappa,k} \breve{\mathbf{w}}_k + \breve{\sigma}_N^2}. \tag{36.23}$$

Note that the SINR of (36.23) cannot be measured at any terminal since the denominator contains the sum of interference powers measured at different mobile stations. Therefore, we call it virtual SINR.

The optimization problem to maximize the virtual SINR can mathematically be expressed as follows: maximize the received power of the desired signal corresponding to (36.19) while keeping the virtual interference-plus-noise power constant:

$$\widetilde{P}_{\mathrm{I},k,\mathrm{virt}} = \breve{\mathbf{w}}_k^H \widetilde{\mathbf{R}}_{\mathrm{I},k,\mathrm{virt}} \breve{\mathbf{w}}_k + \breve{\sigma}_N^2 = \mathrm{const.} \tag{36.24}$$

with

$$\mathbf{R}_{\mathrm{I},k,\mathrm{virt}} = \sum_{\substack{\kappa=0 \\ \kappa \neq k}}^{K-1} \breve{\mathbf{w}}_k^H \widetilde{\mathbf{R}}_{\mathrm{I},\kappa,k} \breve{\mathbf{w}}_k. \tag{36.25}$$

Using the method of Lagrange multipliers, this optimization problem leads to a generalized eigenvalue problem. The optimum weight vector $\breve{\mathbf{w}}_k^{\mathrm{opt}}$ equals the eigenvector of the matrix pair associated with the largest eigenvalue [2, 7, 17]. That is,

$$\widetilde{\mathbf{R}}_{\mathrm{S},k} \breve{\mathbf{w}}_k^{\mathrm{opt}} = \lambda_{\max} \widetilde{\mathbf{R}}_{\mathrm{I},k} \breve{\mathbf{w}}_k^{\mathrm{opt}}, \tag{36.26}$$

where $\lambda_{\max}$ denotes the largest eigenvalue. This beamforming method will be called max-SIR method since only the signal and the interference covariance matrices have an influence on the optimum weights.

36.2.2.3. Maximum SNR beamforming

Another suboptimum beamforming method may be adopted which assumes that the denominator of (36.22) is constant and does not depend on the weight vector

$\check{\mathbf{w}}_k$. This corresponds to the assumption that the interference can be interpreted as spatially white noise. The only remaining boundary condition for the beamforming problem is that the transmit power is limited:

$$||\check{\mathbf{w}}_k||^2 = \check{\mathbf{w}}_k \mathbf{I} \check{\mathbf{w}}_k^{\mathrm{H}} = 1. \tag{36.27}$$

So the optimization problem can be stated as follows: maximize the received downlink power (36.19) while keeping the transmit power constant (36.27). Using again the method of Lagrange multipliers, this leads to the generalized eigenvalue problem:

$$\widetilde{\mathbf{R}}_{\mathrm{S},k} \check{\mathbf{w}}_k^{\mathrm{opt}} = \lambda_{\max} \mathbf{I} \check{\mathbf{w}}_k^{\mathrm{opt}}. \tag{36.28}$$

In the following, this beamforming method which only maximizes the received downlink power and which does not try to minimize interference will be called max-SNR method.

36.2.2.4. Maximum SINR beamforming

Finally, a heuristic beamforming approach is considered in this section. Instead of using one of the boundary conditions (36.24) or (36.27), a linear combination of these boundary conditions may be used. This corresponds to a diagonal loading of the max-SIR eigenvalue problem:

$$\widetilde{\mathbf{R}}_{\mathrm{S},k} \check{\mathbf{w}}_k^{\mathrm{opt}} = \lambda_{\max} (c_1 \widetilde{\mathbf{R}}_{\mathrm{I},k} + c_2 \mathbf{I}) \check{\mathbf{w}}_k^{\mathrm{opt}}. \tag{36.29}$$

In the following, this beamforming method which forms a compromise between max-SIR and max-SNR beamforming will be called max-SINR method.

36.3. Downlink SINR

The total gain of the antenna array is given by [15]

$$\check{G}_k^{\mathrm{tot}}(\theta) = \left| \check{\mathbf{w}}_k^{\mathrm{opt}} \check{\mathbf{a}}(\theta) \right|^2 \cdot G^{\mathrm{ele}}(\theta), \tag{36.30}$$

where the first term is due to the applied beamforming method and dependent on the topology used, $\check{\mathbf{a}}(\theta)$ is given by (36.4) or (36.5), respectively. The second term $G^{\mathrm{ele}}(\theta)$ takes into account the antenna-element-specific antenna pattern. Typical patterns of base station sector antennas show a smooth behavior within the main beam. Such a characteristic can be modelled quite well with a squared cosine characteristic:

$$G^{\mathrm{ele}}(\theta) = \begin{cases} \cos^2\left(\dfrac{\pi}{2} \cdot \dfrac{\theta}{\theta_{3\mathrm{dB}}}\right) & \text{for } |\theta| \le \theta_0, \\ 10^{-a_{\mathrm{R}}/10} & \text{for } |\theta| \ge \theta_0 \end{cases} \tag{36.31}$$

with $\theta_0 = \theta_{3\text{dB}} \cdot 2/\pi \cdot \arccos 10^{-a_R/20}$. In (36.31), the angle $\theta_{3\text{dB}}$ is the 3 dB two-sided angular aperture of an antenna element (often termed half-power beam width) and a_R denotes the backward attenuation. By taking very large values for $\theta_{3\text{dB}}$, an omnidirectional antenna characteristic can be modelled.

As introduced before, each resolvable path at the base station receiver is composed of micropaths (often modelled by many small scatterers) with slightly different angles of arrival at the antenna arrays. Thus, the power is spread around the average angle of arrival $\check{\theta}_{l,k,j(k)}$ of each resolvable path and a (path-specific) azimuthal power spectrum has to be incorporated in the calculation of the signal and interference power for downlink transmission. To carry out the calculation, we again fall back on the long-term reciprocity of the uplink and the downlink channel, see (36.14), (36.15), and (36.16). For the remainder of this section, we assume identical Laplacian-shaped azimuthal power spectra $p_{l,k,j}(\theta) = p(\theta)$ for all paths in the system [7, 33]. With this assumption, the resulting gain factor seen by the lth departing path of user k at base station $j(k)$ can be evaluated by convolving the total antenna gain diagram (36.30) with the azimuthal power spectrum:

$$G_k^{\text{path}}(\check{\theta}_{l,k,j}) = \int_{-\pi}^{\pi} \check{G}_k^{\text{tot}}(\theta) p(\theta - \check{\theta}_{l,k,j})\, d\theta. \tag{36.32}$$

Within this section, G_k^{path} is also referred to as a path diagram [34].

In the following, we will give an expression for the SIR at a mobile station based on beamformed antenna diagrams at all base stations in the network. We consider CDMA systems with RAKE reception and assume the systems to be interference limited. Thus, the influence of thermal and amplifier noise can be neglected. With these assumptions and with reference on (36.12), the (instantaneous) post-despreading SIR per path of the user of interest (indexed with k) is given by

$$\gamma_{l,k} = \frac{G_S \check{P}_{l,k}}{\check{P}_{l,k}^{\text{cross}} + \check{P}_k^{\text{intra}} + \check{P}_k^{\text{inter}}}, \quad l = 0, \ldots, L_{k,j(k)} - 1 \tag{36.33}$$

with path power

$$\check{P}_{l,k} = \check{P}_k \left| \check{\alpha}_{l,k,j(k)} \right|^2 \check{G}_k^{\text{path}}(\check{\theta}_{l,k,j(k)}) \tag{36.34}$$

and path-crosstalk interference [35]

$$\check{P}_{l,k}^{\text{cross}} = \sum_{\substack{l'=0 \\ l' \neq l}}^{L_{k,j(k)}-1} \check{P}_k \left| \check{\alpha}_{l',k,j(k)} \right|^2 \check{G}_k^{\text{path}}(\check{\theta}_{l',k,j(k)}). \tag{36.35}$$

Here, $\check{P}_k$ with $k = 0, \ldots, K-1$ denotes the transmitted power to be adjusted by power control [32, 36, 37]. In the remainder of this subsection, we neglect the effect of power control and therefore assume $\check{P}_k = \check{P}$ for $k = 0, \ldots, K-1$. Since

we focus on CDMA systems, G_S denotes the processing gain (despreading gain) [3, 35]. The variable $\breve{\alpha}_{l,k,j(k)}$ is given by (36.16) and includes signal fading. In implementable CDMA receivers, the number of paths to be evaluated is determined by the applied number of RAKE fingers [35]. Since we are interested in upper-bound assessments for beamforming concepts, we neglect this restriction and assume all paths to be exploited by the RAKE receiver. Note that this leads to the highest degree of achievable path diversity in the time domain [35]. The intracell interference power yields

$$\breve{P}_k^{\text{intra}} = \sum_{\kappa \in \mathcal{A}_k} \sum_{l=0}^{L_{k,j(k)}-1} \breve{P}_\kappa \left| \breve{\alpha}_{l,k,j(k)} \right|^2 \breve{G}_\kappa^{\text{path}}(\breve{\theta}_{l,k,j(k)}). \tag{36.36}$$

The set $\mathcal{A}_k$ contains intracell users of user k. Note that the intracell signals pass through the same mobile channel as the signals of the user of interest, but they are weighted with their corresponding user-specific path diagram $\breve{G}_\kappa^{\text{path}}$. Finally, the intercell interference power can be expressed as

$$\breve{P}_k^{\text{inter}} = \sum_{\kappa \in \mathcal{B}_k} \sum_{l=0}^{L_{k,j(\kappa)}-1} \breve{P}_\kappa \left| \breve{\alpha}_{l,k,j(\kappa)} \right|^2 \breve{G}_\kappa^{\text{path}}(\breve{\theta}_{l,k,j(\kappa)}), \tag{36.37}$$

where $\mathcal{B}_k$, $k = 0, \ldots, K-1$, describes the set of users causing intercell interference seen by the kth user. The interference signals differ from the signals of interest by the mobile channels as well as path diagrams. Note that a large number of interfering signals arrive at each mobile. Thus, it is valid to approximate the path-crosstalk interference by including the path of interest, that is, $\breve{P}_{l,k}^{\text{cross}} \approx \sum_l \breve{P}_k |\breve{\alpha}_{l,k,j(k)}|^2 \breve{G}_k^{\text{path}}(\breve{\theta}_{l,k,j(k)})$. This leads to identical interference powers (identical denominators in (36.33)) for all paths and simplifies the following analysis.

Not only in link-level simulations but also in system-level simulations, short-term propagation aspects as fast fading have to be taken into account. First, it has to be mentioned that combining of the resolvable paths is done by maximum ratio combining (MRC). Secondly, rather than explicitly modelling fast fading, we mathematically incorporate it in the evaluation of the SIR distribution when MRC is applied for different path power transfer factors [33, 35].

In many analyses [7, 8, 33] related to performance improvement obtained from antenna arrays, the cumulative distribution function (CDF) of the SIR is taken as a key parameter. It is assumed that all channel coefficients $\breve{\alpha}_{l,k,j}$ are complex Gaussian random variables which correspond to Rayleigh fading magnitudes. We furthermore presume that the channel coefficients $\breve{\alpha}_{l,k,j}$ are statistically independent. The path gain factor $\breve{G}_k^{\text{path}}(\breve{\theta}_{l,k,j(k)})$ in (36.34) depends on the optimum beam pattern (solution of (36.26)) which changes only very slowly with time since it is based on time-averaged covariance matrices. Because of the large number of terms in the denominator of (36.33), we can neglect the fluctuations of the denominator. Therefore, the only variables which fluctuate because of the Rayleigh

fading are the channel coefficients $\breve{\alpha}_{l,k,j}$. The Gaussian distribution of channel coefficients results in an exponentially distributed signal power per path (numerator of (36.33)). Since the interference power and all other terms of (36.33) (except the coefficients $\breve{\alpha}_{l,k,j}$) are assumed to be fixed or very slowly fluctuating, the signal-to-interference power ratios $\gamma_{l,k}$ per path are distributed according to an exponential distribution [35]. That is,

$$f_{\gamma_{l,k}}(\gamma_{l,k}) = \frac{1}{\overline{\gamma_{l,k}}} \mathrm{e}^{-\gamma_{l,k}/\overline{\gamma_{l,k}}}, \tag{36.38}$$

where $\overline{\gamma_{l,k}}$ denotes the average SIR of a single path (ensemble average with respect to fast fading). Assuming that the interference in each path is independent, the SIR after MRC results in

$$\gamma_k = \sum_{l=0}^{L_{k,j(k)}-1} \gamma_{l,k}. \tag{36.39}$$

Furthermore, it is assumed that the small scale fading of the individual desired paths is statistically independent. Since γ_k is the sum of the random variables $\gamma_{l,k}$, the resulting probability density function (PDF) is obtained from convolving the individual PDFs:

$$f_{\gamma_k}(\gamma_k) = f_{\gamma_{1,k}} * f_{\gamma_{2,k}} * f_{\gamma_{3,k}} * \cdots * f_{\gamma_{L_{k,n(k)}-1,k}}. \tag{36.40}$$

Utilizing the characteristic functions of the PDFs, the resulting PDF of γ_k can be found to be [33, 35]

$$f_{\gamma_k}(\gamma_k) = \sum_{l=0}^{L_{k,j(k)}-1} \frac{c_{l,k}}{\overline{\gamma_{l,k}}} \mathrm{e}^{-\gamma_k/\overline{\gamma_{l,k}}} \tag{36.41}$$

with the coefficients

$$c_{l,k} = \prod_{\substack{l'=0 \\ l' \neq l}}^{L_{k,j(k)}-1} \frac{\overline{\gamma_{l,k}}}{\overline{\gamma_{l,k}} - \overline{\gamma_{l',k}}}. \tag{36.42}$$

In order to compare the different beamforming concepts, the CDF has to be averaged over all mobiles and possibly over several simulations where different locations for the mobiles and different radio channels are determined. Most information can be extracted from the averaged distribution function of the SIR:

$$F_{\gamma_k} = \int_0^{\gamma_k} \mathrm{E}\{f_{\gamma_k}(u)\}\,\mathrm{d}u, \tag{36.43}$$

where the expectation is taken over all mobile stations and snapshots.

36.4. Power and load control

36.4.1. Power control

The enhancement of UMTS networks by advanced technologies like downlink beamforming requires investigation of the interaction of these more sophisticated techniques with given UMTS-FDD radio resource management algorithms like power control or load control. To cope with quality-of-service (QoS) constraints, we introduce $\gamma_{k,\min}$ denoting the required SINR per user to underrun a certain block error rate (BLER) in order to maintain a particular service quality. Power control is applied to ensure the QoS constraints per user at the mobile stations. But, power control in conjunction with the use of optimum downlink beamforming [1, 22, 36] leads to a coupled optimization problem, where the optimization has to be performed jointly with respect to powers and beamforming weights. Because all the beamformers of users assigned to the logical cell of interest are involved in the joint power control beamforming solution, there is a clear indication that the optimum joint solution must be calculated centrally for the logical cell. Also, the mobile radio channel between every combination of node-B and UE has to be known. These are two main objections to implement optimum joint beamforming and power control in real system-like UMTS-FDD. Therefore, we restrict, in this section, to suboptimum downlink beamforming solutions where we leverage the long-term spatial characteristics of the uplink (see also Section 36.2.2). Thus, from the downlink power control perspective, the beamforming weights per user are computed in advance.

With this assumption of precomputed, and thus, fixed beamforming weights in the downlink, the objective of power control is to find all transmitted powers $\check{P}_k > 0$ with $k = 0,\ldots,K-1$ such that the total transmitted power is minimized while the required QoS is guaranteed for each user. The instantaneous signal-to-interference-plus-noise ratio at mobile station k is given by

$$\mathrm{SINR}_k = \frac{\check{P}_k \psi_{k,k}}{\sum_{\kappa \neq k} \check{P}_\kappa \psi_{k,\kappa} + \sigma_N^2}. \tag{36.44}$$

The element $\psi_{k,\kappa}$ is the total power transfer factor between Node-B $j(\kappa)$ transmitting to UE κ and the kth user receiving interference. The elements $\psi_{k,\kappa}$ can be collected in a $K \times K$ matrix $\boldsymbol{\Psi}$. The matrix $\boldsymbol{\Psi}$ includes system characteristics like the user-specific signatures and beamforming weights, receiver structures (RAKE, etc.), as well as mobile radio channel profiles. For the following, a power vector $\check{\mathbf{p}}$ is defined which contains all transmit powers: $\check{\mathbf{p}} = [\check{P}_0,\ldots,\check{P}_{K-1}]^T$. Utilizing (36.44) as well as the SINR constraint $\gamma_{k,\min}$, the power control problem can mathematically be expressed in the form

$$\min_{\check{\mathbf{p}}} \sum_{k=0}^{K-1} \check{P}_k \quad \text{s.t. } \mathrm{SINR}_k \geq \gamma_{k,\min},\ 0 < \check{P}_k \leq P_L^{\max} \tag{36.45}$$

for $k = 0, \ldots, K-1$. Each transmit power $\check{P}_k$ is restricted to be positive as well as lower than the maximum allowable link power $P_L^{\max}$. Zander introduced in [38] a centralized optimal solution with the necessity of controlling the entire power vector $\check{\mathbf{p}}$. Therein it is shown that for this optimum solution, the constraints in (36.45) are active (i.e., they are satisfied with equality) leading to

$$\check{P}_k^{\text{opt}} = \min\{\check{P}_k^*, P_L^{\max}\} \tag{36.46}$$

with

$$\check{\mathbf{p}}^* = (\mathbf{I} - \boldsymbol{\Gamma}\boldsymbol{\Psi})^{-1}\boldsymbol{\Gamma}\mathbf{n}. \tag{36.47}$$

Here, the matrix $\boldsymbol{\Gamma} = \text{diag}[\gamma_{0,\min}, \ldots, \gamma_{K-1,\min}]$ is of diagonal structure including the user-specific SINR requirements $\gamma_{k,\min}$ and vector $\mathbf{n}$ summarizes the noise components including all pilot channels like P-CPICH or S-CPICH in case of fixed beamforming (see Section 36.2.1), intercell interference, as well as thermal noise. Finally, $\mathbf{I}$ is a $K \times K$ identity matrix.

An iterative approach to find the optimal power settings was introduced by Foschini and Miljanic in [39]. This algorithm controls each power adjustment separately without requiring knowledge of power settings of all other users. Hence, it can be implemented in a decentralized or distributed fashion, that is, per mobile station, and it is used as the basic approach in UMTS-FDD fast power control [27]. The power update procedure can be expressed mathematically in the form

$$\check{P}_{S,k}(t) = \frac{\gamma_{k,\min}}{\text{SINR}_k}\check{P}_{S,k}(t-1), \tag{36.48}$$

where t denotes the iteration index and SINR_k the instantaneous SINR measured after the RAKE receiver. It is mathematically proven in [36, 39, 40] that (36.48) converges to the optimum solution (36.46) if a feasible solution of the power control problem (36.45) exists.

36.4.2. Load control

Beside link-specific power restrictions in (36.46), it is of utmost importance in UMTS-FDD to keep the air interface load under predefined thresholds, especially in order to guarantee the needed QoS requirements of already established calls. Load control for UMTS-FDD dedicated channels composes admission and congestion control. While the first one controls the setup of new calls, the latter one is responsible for already established calls. In UMTS, the cell-specific load can be monitored by measuring the total radiated or transmitted power of a logical cell utilizing the power rise in downlink and noise rise in uplink [3, 41]. The power rise PR is defined as a cell's total transmit power P^{tot} over the power P_{pilot} dedicated to the P-CPICH:

$$\text{PR} = \frac{P^{\text{tot}}}{P_{\text{pilot}}}, \tag{36.49}$$

where the total power P^{tot} composes the sum of all user powers $\check{P}_k$ and the P-CPICH power. Note that P-CPICH consumes 10% of the maximum transmitted cell power. If secondary common pilot channels (S-CPICHs) are transmitted to mobile stations as in case of fixed beamforming [42], these channels also contribute to P^{tot}.

For the uplink, the noise rise is defined as

$$\text{NR} := \frac{I_0}{I\text{th}}. \tag{36.50}$$

In the third-generation partnership project (3GPP) terminology, I_0 denotes the total received wideband power at the antenna connector including user signal, interference, as well as noise, and Ith is the thermal noise power in the 3.84 MHz frequency band. A new call will be set up if both the NR as well as PR remain below a maximum allowable threshold. This decision is due to admission control and requires an a priori estimation of expected load after the new UE is set up [43]. Moreover, congestion control drops an active subscriber if the NR or PR exceeds a given congestion threshold. Typical values for both NR and PR are 6 dB in case of admission control and 10 dB in case of congestion control [41].

For cells with beamforming capabilities, inclusion of spatial filtering into the admission and congestion thresholds is advantageous [5]. An attractive power-based admission control scheme was introduced in [43] where the load in different beams is monitored via beam-specific power measurements yielding beam-dependent noise or power rise measurements, respectively. More information on the impact of beamforming strategies on radio resource management algorithms, especially a detailed description of handover strategies being not covered in this section, can be found in [5, 21].

36.5. Cellular simulation model and methodology

In this section, a dynamic system-level simulator for analyzing the system-level performance of a UMTS-FDD cellular system which uses smart antennas at the base stations is presented. The key parameter to express performance is the average number of mobile stations that can be supported in the downlink with the fulfillment of some quality-of-service (QoS) requirement. A mobile station is dropped if its SINR measured after RAKE reception with maximum ratio combining falls below the service-dependent required SINR threshold. The dynamic system-level simulator incorporates a mobility model for describing the movement of the mobile stations and a traffic model for arranging the incoming and outgoing calls from mobile stations. The mobility and traffic models are based upon a random walk model [44] and Poisson processes [45], respectively. Soft handover, power control, downlink SINR calculation, and so forth. are implemented as proposed in [46]. The traffic or dedicated channels (DPDCH) are transmitted directionally using beamforming method while pilot channels (CPICH) are transmitted omnidirectionally. Beamforming along with power control for DPDCH channels is carried out after preassigning each mobile station to a set of base stations from

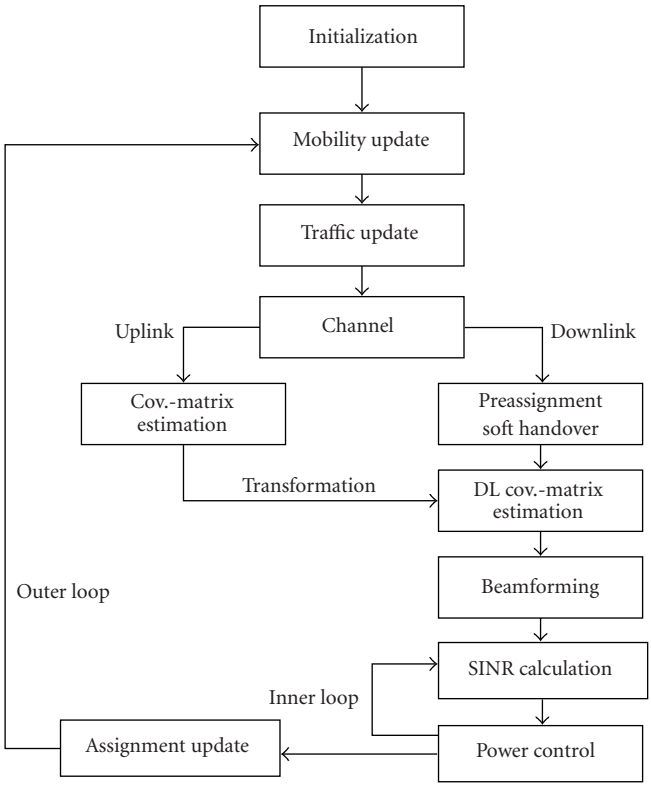

Figure 36.4. Block diagram of simulation flow.

which the mobile station receives the strongest pilot channel. No power control is used for CPICH channel.

36.5.1. Simulation flow

Figure 36.4 shows the simulation flow. The simulation is based upon snapshots. In each snapshot, mobile stations move, traffic situation changes, and hence the channels between the mobile stations and base stations are either newly calculated or updated. The uplink spatial covariance matrix is calculated for all the possible combinations of channels between the base stations and active [45] mobile stations. Mobile stations are assigned to base stations based upon the received primary common pilot channel (P-CPICH) power. Using the long-term uplink channel covariance matrix downlink beamforming can be performed for the DPDCH channel. The uplink spatial channel covariance matrix can also be transformed into downlink frequency for downlink beamforming. The SINR values for the DPDCH and CPICH channels are calculated at each mobile station. An iterative fast closed-loop power control method with a frequency of $f_{pc} = 1.5$ kHz is used to

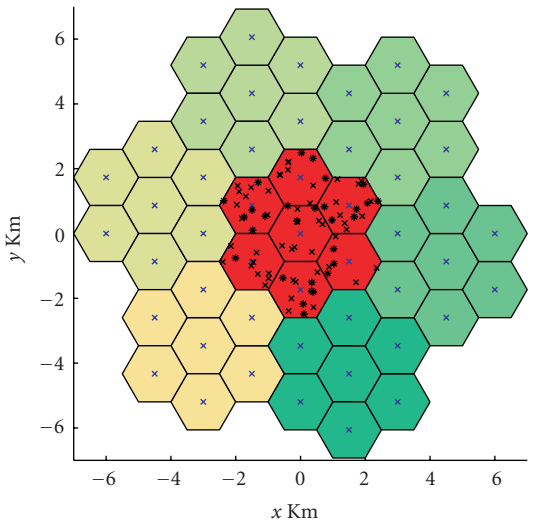

FIGURE 36.5. Locations of base and mobile stations.

adjust the powers of DPDCH channels from all the base stations so that the mobile stations achieve the SINR target value for the DPDCH. The mobile stations that cannot be provided with the target SINR for DPDCH at the end of power control loop are considered to be in outage. The assignment of mobile stations to base stations is updated after dropping the mobile stations that are out of the coverage range or could not be provided with required quality of service. The outer loop starts the next iteration with a new snapshot. The inner loop or power control loop is assumed to be converged within the time difference T between two consecutive snapshots. The time duration of the outer loop T represents the sampling time used for simulation. More detailed description of the different modules of simulator can be found in [45].

36.5.2. Cell configuration

A cellular configuration consisting of a main area and six surrounding areas is created as shown in Figure 36.5.

In order to enhance the computational speed of the simulator, a wrap-around technique is used. This means that the areas other than the main area represent the periodic continuation of the main area in all possible directions, assuming there identical behaviour of all base and mobile stations. Each area consists of a central hexagonal cell surrounded by six other hexagonal cells. Each cell has a single base station at its centre. Before the first snapshot is calculated, mobile stations are distributed uniformly in the main area. Although the SINR evaluation is done only for mobile stations in the main area, because of the wrap-around technique, the effect of equivalent mobile and base stations of all other areas has to be considered. A base station of the main area and its equivalent base stations in all other

areas have the same downlink beam patterns and the same transmission powers. We consider a system with uniform circular arrays (UCAs) at the base stations thus not considering sectorization.

36.5.3. Propagation model

A realistic model of the wave propagation plays an important role in the significance of the simulation results. One common approach, especially in context with downlink beamforming, is to use deterministic propagation scenarios [17, 47] or to apply propagation models which do not take into account the probabilistic nature of all parameters (e.g., the number of paths) [48, 49]. In this section, a completely probabilistic propagation model between each base station and each mobile station is used which has the following properties.

The number of resolvable propagation paths is random and exhibits a binomial distribution [50]. Shadowing is modelled by a log-normal fading of the total received power [19, Section 3.1.1.2]. The random distribution of the total (log-normal fading) power to individual propagation paths (often denoted as macropaths or paths from scattering clusters) is modelled by applying an additional log-normal fading to the delayed paths with respect to the direct path (line-of-sight). Furthermore, a basic path attenuation and an extra attenuation that is proportional to the excess delay are taken into account. The basic attenuation is determined by the COST-Hata model [51] and a break point limits the attenuation to a certain minimum value for small distances. The excess delay of reflected paths is exponentially distributed leading to an exponential power delay profile [19, Section 3.1.1.3.3]. As mentioned before, the directions of arrival which are denoted by $\hat{\theta}_{l,k,j(k)}$ obey a Laplacian distribution with respect to the direct path (standard deviation = several tens of degrees) [19, Section 3.2.2.1]. Moreover, according to (36.32), the azimuthal power spectrum of each individual path is also incorporated in the simulations. As mentioned before, the azimuthal power spectra follow also a Laplacian shape (standard deviation in the order of one degree or less) and are identical for the different paths. In order to reduce the computational complexity, fast fading processes are included analytically as described in Section 36.3.

As the mobile stations move slowly, the channel parameters, for example, log-normal fading, do not change rapidly. The time correlation of log-normal fading is not known in general. However, measured data [52] reveal that it can be modeled as a simple exponentially decreasing correlation function. This can be realized by filtering white Gaussian noise by a simple first-order infinite impulse response (IIR) filter with a pole at

$$a = \varepsilon^{v(kT)T/D} \Longrightarrow H(z) = \frac{z}{z-a}, \tag{36.51}$$

where ε is the spatial correlation between two points separated by a distance D, T denotes the sampling period, and $v(kT)$ is the velocity of the mobile station.

36.5.4. Simulation methodology and parameters

One main objective of this section is to find the average number of mobile stations that can be supported in the downlink provided that the SINR of DPDCH and CPICH channels for each mobile station is above the service-dependent required SINR threshold. The average number of mobile stations supported in the downlink depends on a large number of parameters like the number of antenna elements, beamforming methods, mobility, traffic scenarios, and so forth. The performance indicating factor, that is, the number of supported mobile stations is computed in a dynamic way using beamforming with power control and without power control for different numbers of antenna elements. During all simulations, the parameters that characterise traffic model (call arrival rate and average call duration), mobility model (standard deviation of the mobile station speeds and average velocity of mobile stations), and channel model (average number of paths, mean number of paths, etc.) are fixed. All mobile stations are provided with the same service, that is, the transmission of data at 384 kbps in the downlink. For this specific service, the spreading factor $G_S = 8$ is used. The CPICH channel is spread with a higher spreading gain of 256. If the SINR requirement for a mobile station is not fulfilled, that particular mobile station is not dropped immediately. A time window is implemented so that within its period the channel situation may improve and this mobile station may stay connected.

Note that the simulations are based on snapshots, and hence no admission control or congestion control methods are applied. In each snapshot, the number of mobile stations that can be supported with the required SINR threshold can be determined. The following list gives a short overview of the main simulation steps.

(1) We calculate the downlink spatial covariances under the assumption of perfectly known downlink radio channels as well as with the transformation of the uplink spatial covariance matrices from uplink to downlink frequency.

(2) In a second step, the path diagrams are evaluated taking into account the beamformed diagram, the element-specific diagrams, as well as the azimuthal power distribution of each resolvable path.

(3) With this, the user-specific SINRs after RAKE reception for both DPDCH and CPICH channels are calculated.

(4) Finally, the average number of mobile stations that fulfill the SINR requirement for DPDCH and CPICH channels is determined.

The main simulation parameters are summarized in Tables 36.1 and 36.2. It has to be mentioned that for the dynamic system-level investigations, we simulate seven different areas, each with seven base stations (see Figure 36.5).

For illustration purposes, Figures 36.6 and 36.7 show examples of path diagrams for an identical propagation scenario with a UCA having 4 and 8 array elements, respectively. It can be observed in Figures 36.6 and 36.7 that the beamforming algorithm tries to suppress the undesired paths. Obviously, the four- or eight-element antenna array cannot produce nulls in the direction of all interferers because of the fact that the number of interferers is greater than the number of antenna elements. However, the eight-element antenna array has greater degrees of

Table 36.1. Simulation parameters.

Number of base stations	49
Cell radius	1 km
Average number of paths	3
Max. number of paths	6
Standard deviation of slow fading	10 dB
Standard deviation of path fading	6 dB
Standard deviation of DoAs	20°
Standard deviation of mobile station speeds	5 m/s
Call arrival rate	$5\,s^{-1}$
Mean call duration	1.5 min
Sampling period	0.2 s
Max. TX base station power	43 dBm
Max. DPDCH power	30 dBm
CPICH power	30 dBm
Thermal noise power	−99 dBm
Handover margin	3 dB
Orthogonality factor	0.4
SINR threshold for DPDCH	4.5 dB
Upper bound for the DPDCH SINR (for power control)	6.5 dB
Power control step size	1 dB
Spreading factor for CPICH	256
Spreading factor for DPDCH	8
Data rate per user	384 kbps
User activity	100%

Table 36.2. Antenna arrays.

Uplink carrier frequency	1950 MHz
Downlink carrier frequency	2140 MHz
Number of elements (UCA)	1, 2, 4, 8
Element spacing	$\lambda/2 = 0.075$ m
Antenna height of base stations	30 m
Antenna height of mobile stations	1.7 m

freedom and is able to suppress interferers more efficiently than the four-element antenna array. The bars in the diagrams correspond to the gain factors of the individual paths—for the displayed example, only one desired path exists.

36.6. Simulation results

The simulation results are the average of ten simulation runs. Each simulation run is carried out for a time interval of $2000T$ with the parameters listed in Tables 36.1 and 36.2.

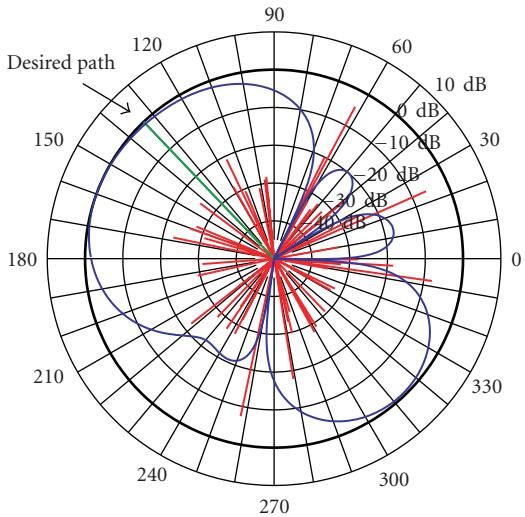

FIGURE 36.6. Example for an optimized path diagram for a UCA with 4 antenna elements.

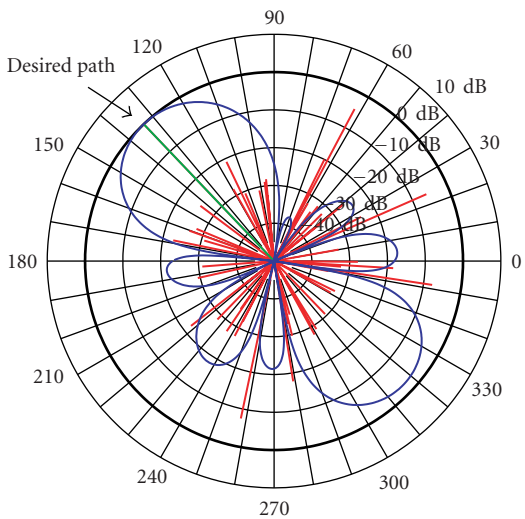

FIGURE 36.7. Example for an optimized path diagram for a UCA with 8 antenna elements.

The number of mobile stations that can be supported in the downlink with a data rate of 384 kbps for different numbers of antenna elements ($M = 1, 2, 4, 8$) with a beamforming algorithm that uses no diagonal loading of the interference covariance matrix is shown in Figure 36.8. These mobile stations are also referred to as active users [45]. After a transient, the number of mobile stations that can be supported in the downlink remains more or less constant. This indicates that even if new mobile stations are generating calls in each snapshot, the number of

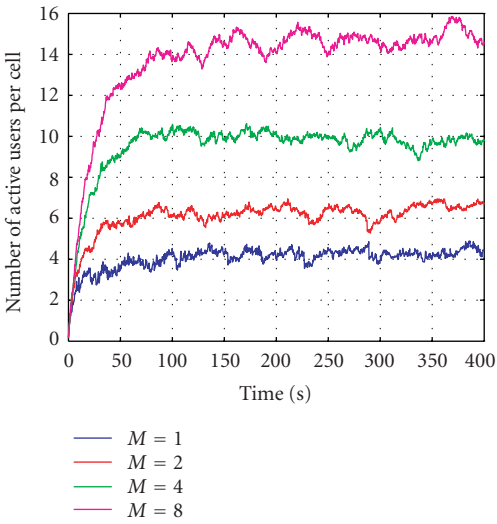

FIGURE 36.8. Number of active users versus time with different antenna elements (max-SIR).

mobile stations that can be served is limited. Thus, the downlink capacity of the system reaches saturation. The fluctuations in the curves are because of the limited number of simulation runs that are averaged. It can be easily seen that as the number of array elements increases, the downlink capacity also increases. The results of Figure 36.8 correspond to the max-SIR beamforming method. Although the omnidirectionally transmitted P-CPICH channel causes severe interference to the directionally transmitted DPDCH channel, the improvement in capacity due to higher number of antenna elements is significant.

A comparison of the beamforming methods max-SIR, max-SNR, and max-SINR is presented in Figure 36.9 for a UCA with 4 antenna elements. The simulation result shows that diagonal loading increases the capacity compared with virtual max-SIR beamforming. The highest capacity is achieved using the max-SNR beamforming method which even does not try to suppress individual interferers. The reason for this effect might be the strong influence of the omnidirectionally transmitted CPICH channel which results in almost spatially white noise.

The number of active users versus time that can be supported in the downlink with a data rate of 384 kbps with and without transformation techniques [53] is shown in Figure 36.10 for $M = 2, 4, 8$ antenna elements. Note that for illustrative convenience, only 10 out of 2000 samples have been shown with the marks connected by straight lines. We compare the capacity improvement with the following methods:

(a) taking directly the uplink covariance matrix for downlink beamforming without any frequency transformation;

(b) a linear transformation based upon the minimum mean square error (MMSE) method [29];

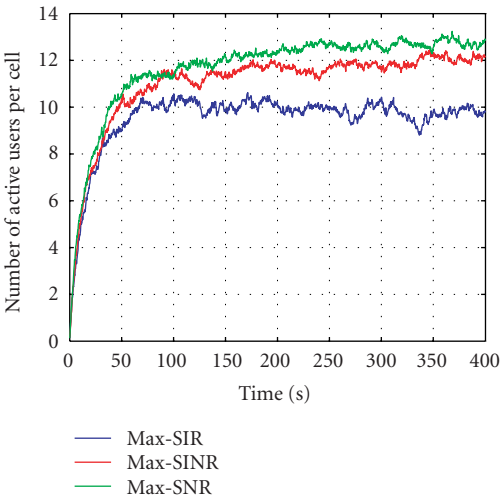

FIGURE 36.9. Number of active users versus time with different beamforming methods.

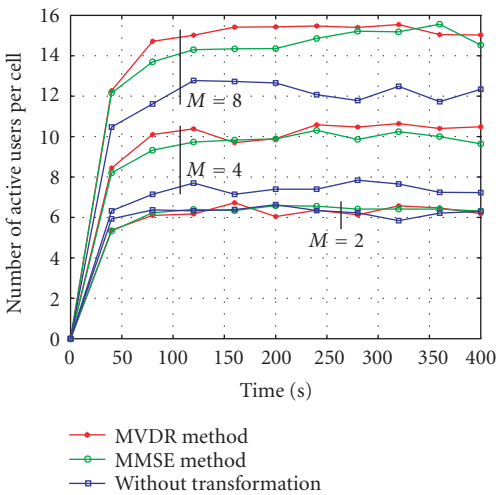

FIGURE 36.10. Number of active users versus time for different number of antenna arrays.

(c) a transformation based upon the minimum variance distortionless response (MVDR) method [54].

It can be observed that in all cases, the downlink capacity increases with the number of antenna elements. The MMSE and MVDR transformation methods perform equally well for $M = 2, 4, 8$ antenna elements. However, if no transformation is carried out, the downlink capacity decreases significantly. For example, with $M = 4$ array elements, MMSE and MVDR methods support about 32% and 36% more users than without transformation, respectively. This is due to the fact that

as the number of antenna elements increases, the effect of different uplink and downlink steering vectors becomes more significant.

Bibliography

[1] H. Boche and M. Schubert, "Theoretical and experimental comparisons of optimization criteria for downlink beamforming," *European Trans. Telecommunications*, vol. 12, no. 5, pp. 417–426, 2001, Special Issue on Smart Antennas.

[2] R. M. Buehrer, A. G. Kogiantis, S.-C. Liu, J. Tsai, and D. Uptegrove, "Intelligent antennas for wireless communications-uplink," *Bell Labs. Technical Journal*, vol. 4, no. 3, pp. 73–103, 1999.

[3] H. Holma and A. Toskala, *WCDMA for UMTS*, John Wiley & Sons, Chichester, UK, 1st edition, 2000.

[4] A. Yener, R. D. Yates, and S. Ulukus, "Interference management for CDMA systems through power control, multiuser detection, and beamforming," *IEEE Trans. Commun.*, vol. 49, no. 7, pp. 1227–1239, 2001.

[5] Technical Specification Group Radio Access Network 3GPP, "Beamforming Enhancements (Release 6)," Tech. Rep. 25.887, European Telecommunications Standards Institute, Sophia Antipolis, France, 2002.

[6] Technical Specification Group Radio Access Network 3GPP, "Physical channels and mapping of transport channels on physical channels (Release 99)," Tech. Rep. 25.211, European Telecommunications Standards Institute, Sophia Antipolis, France, 1999.

[7] A. Czywik and A. Dekorsy, "System level simulations for downlink beamforming with different array topologies," in *Proc. IEEE Global Telecommunications Conference (GLOBECOM '01)*, vol. 5, pp. 3222–3226, San Antonio, Tex, USA, November 2001.

[8] A. Czylwik and A. Dekorsy, "Optimization of downlink beamforming for systems with frequency division duplex," in *Proc. IEEE International Zurich Seminar on Broadband Communications (IZS '02)*, pp. 111–116, Zurich, Switzerland, February 2002.

[9] T. Baumgartner, T. Neubauer, and E. Bonek, "Performance of downlink beam switching for UMTS FDD in the presence of angular spread," in *Proc. IEEE International Conference on Communications (ICC '02)*, vol. 2, pp. 851–855, New York, NY, USA, April 2002.

[10] J. W. Liang and A. J. Paulraj, "On optimizing base station antenna array topology for coverage extension in cellular radio networks," in *Proc. 45th IEEE Vehicular Technology Conference (VTC '95)*, vol. 2, pp. 866–870, Chicago, Ill, USA, July 1995.

[11] J. Fuhl, D. J. Cichon, and E. Bonek, "Optimum antenna topologies and adaptation strategies for SDMA," in *Proc. IEEE Global Telecommunications Conference (GLOBECOM '96)*, vol. 1, pp. 575–580, London, UK, November 1996.

[12] R. Martinez, D. Trosa, L. de Haro, and M. Calvo, "Smart antennas performance evaluation and capacity increase for WCDMA UMTS," in *Proc. 53rd IEEE VTS Vehicular Technology Conference (VTC '01)*, vol. 1, pp. 147–151, Rhodes, Greece, May 2001.

[13] A. Osseiran, M. Ericson, J. Barta, B. Goransson, and B. Hagerman, "Downlink capacity comparison between different smart antenna concepts in a mixed service W-CDMA system," in *Proc. 54th IEEE VTS Vehicular Technology Conference (VTC '01)*, vol. 3, pp. 1528–1532, Atlantic City, NJ, USA, October 2001.

[14] M. Pettersen, L. E. Braten, and A. G. Spilling, "An evaluation of adaptive antennas for UMTS FDD by system simulations," in *Proc. 58th IEEE Vehicular Technology Conference (VTC '03)*, vol. 1, pp. 227–231, Orlando, Fla, USA, October 2003.

[15] J. Litva and T. K.-Y. Lo, *Digital Beamforming in Wireless Communications*, Artech House, Boston, Mass, USA, 1st edition, 1996.

[16] M. Schacht, A. Dekorsy, and P. Jung, "Downlink beamforming concepts in UTRA FDD," in *Kleinheubacher Tagung*, Kleinheubach, Germany, September 2002.

[17] W. Utschick and J. A. Nossek, "Downlink beamforming for FDD mobile radio systems based on spatial covariances," in *Proc. European Wireless (EW '99); Proc. ITG-Fachtagung Mobile Kommunikation (ITG-Fachbericht 157)*, pp. 65–67, Munich, Germany, October 1999.

[18] K. I. Pedersen, P. E. Mogensen, and F. Frederiksen, "Joint-directional properties of uplink and downlink channel in mobile communications," *Electronics Letters*, vol. 35, no. 16, pp. 1311–1312, 1999.

[19] L. M. Correia, *Wireless Flexible Personalised Communications: COST 259: European Co-Operation in Mobile Radio Research*, John Wiley & Sons, Chichester, UK, 2001.

[20] K. Hugl, K. Kalliola, and J. Laurila, "Spatial reciprocity of uplink and downlink radio channels in FDD systems," in *COST 273 MCM Technical Document TD(02)066*, Espoo, Finland, May 2002.

[21] K. I. Pedersen, P. E. Mogensen, and J. Ramiro-Moreno, "Application and performance of downlink beamforming techniques in UMTS," *IEEE Commun. Mag.*, vol. 41, no. 10, pp. 134–143, 2003.

[22] L. C. Godara, Ed., *Handbook of Antennas in Wireless Communications*, CRC Press, Boca Raton, Fla, USA, 2002.

[23] Technical Specification Group Radio Access Network 3GPP, "Beamforming Enhancements (Release 6)," Tech. Rep. 25.101, European Telecommunications Standards Institute, Sophia Antipolis, France, 2002.

[24] A. Dekorsy, M. Schacht, and P. Jung, "On capacity and emission improvements by smart antennas in mixed traffic UMTS networks," in *Proc. 3rd IEEE International Symposium on Signal Processing and Information Technology (ISSPIT '03)*, pp. 572–575, Darmstadt, Germany, December 2003.

[25] A. Osseiran, M. Ericson, J. Barta, B. Goransson, and B. Hagerman, "Downlink capacity comparison between different smart antenna concepts in a mixed service W-CDMA system," in *Proc. 54th IEEE VTS Vehicular Technology Conference (VTC '01)*, vol. 3, pp. 1528–1532, Atlantic City, NJ, USA, October 2001.

[26] E. Jugl, M. Schacht, A. Dekorsy, and J. Muckenheim, "Downlink beamforming and data rate adaptation applied for packet data transmission over the UMTS dedicated channel," in *Proc. ITG/IEEE Workshop on Smart Antennas (WSA '04)*, pp. 160–166, Munich, Germany, March 2004.

[27] Technical Specification Group Radio Access Network 3 GPP, "Physical Layer Procedures (Release 99)," Tech. Rep. 25.214, European Telecommunications Standards Institute, Sophia Antipolis, France, 1999.

[28] M. Haardt, *Efficient one-, two-, and multidimensional high-resolution array signal processing*, Ph.D. thesis, Lehrstuhl für Netzwerktheorie und Schaltungstechnik, Technische Universität München Shaker Verlag, Munich, Germany, 1997.

[29] T. Aste, P. Forster, L. Fety, and S. Mayrargue, "Downlink beamforming avoiding DoA estimation for cellular mobile communications," in *Proc. IEEE International Conference on Acoustics, Speech, and Signal Processing (ICASSP '98)*, vol. 6, pp. 3313–3316, Seattle, Wash, USA, May 1998.

[30] B. Chalise, L. Häring, and A. Czylwik, "Robust uplink to downlink spatial covariance matrix transformation for downlink beamforming," in *Proc. IEEE International Conference on Communications (ICC '04)*, vol. 5, pp. 3010–3014, Paris, France, June 2004.

[31] F. Rashid-Farrokhi, L. Tassiulas, and K. J. R. Liu, "Joint optimal power control and beamforming in wireless networks using antenna arrays," *IEEE Trans. Commun.*, vol. 46, no. 10, pp. 1313–1324, 1998.

[32] E. Visotsky and U. Madhow, "Optimum beamforming using transmit antenna arrays," in *Proc. 49th IEEE Vehicular Technology Conference (VTC '99)*, vol. 1, pp. 851–856, Houston, Tex, USA, July 1999.

[33] A. Czylwik, "Downlink beamforming for mobile radio systems with frequency division duplex," in *Proc. 11th IEEE International Symposium on Personal, Indoor and Mobile Radio Communications (PIMRC '00)*, vol. 1, pp. 72–76, London, UK, September 2000.

[34] A. Czylwik, "Comparison and optimization of antenna concepts for downlink beamforming," in *Proc. 10th IEEE International Conference on Telecommunications (ICT '03)*, vol. 1, pp. 192–197, Papeete, Tahiti, French Polynesia, March 2003.

[35] J. G. Proakis, *Digital Communications*, McGraw-Hill, New York, NY, USA, 3rd edition, 1995.

[36] F. Rashid-Farrokhi, K. J. R. Liu, and L. Tassiulas, "Transmit beamforming and power control for cellular wireless systems," *IEEE J. Select. Areas Commun.*, vol. 16, no. 8, pp. 1437–1450, 1998.

[37] M. Schubert and H. Boche, "A unifying theory for uplink and downlink multiuser beamforming," in *Proc. IEEE International Zurich Seminar (IZS '02)*, pp. 271–276, Zurich, Switzerland, February 2002.

[38] J. Zander, "Performance of optimum transmitter power control in cellular radio systems," *IEEE Trans. Veh. Technol.*, vol. 41, no. 1, pp. 57–62, 1992.
[39] G. J. Foschini and Z. Miljanic, "A simple distributed autonomous power control algorithm and its convergence," *IEEE Trans. Veh. Technol.*, vol. 42, no. 4, pp. 641–646, 1993.
[40] S. A. Grandhi and J. Zander, "Constrained power control in cellular radio systems," in *Proc. 44th IEEE Vehicular Technology Conference (VTC '94)*, vol. 2, pp. 824–828, Stockholm, Sweden, June 1994.
[41] J. Muckenheim and U. Bernhard, "A framework for load control in 3rd generation CDMA networks," in *Proc. IEEE Global Telecommunications Conference (GLOBECOM '01)*, vol. 6, pp. 3738–3742, San Antonio, Tex, USA, November 2001.
[42] M. Schacht, A. Dekorsy, and P. Jung, "System capacity from UMTS smart antenna concepts," in *Proc. 58th IEEE Vehicular Technology Conference (VTC '03)*, vol. 5, pp. 3126–3130, Orlando, Fla, USA, October 2003.
[43] K. I. Pedersen and P. E. Mogensen, "Directional power-based admission control for WCDMA systems using beamforming antenna array systems," *IEEE Trans. Veh. Technol.*, vol. 51, no. 6, pp. 1294–1303, 2002.
[44] S. A. Ghorashi, E. Homayounvala, F. Said, and A. H. Aghvami, "Dynamic simulator for studying WCDMA based hierarchical cell structures," in *Proc. 12th IEEE International Symposium on Personal, Indoor and Mobile Radio Communications (PIMRC '01)*, vol. 1, pp. 32–37, San Diego, Calif, USA, September 2001.
[45] L. Häring, B. Chalise, and A. Czylwik, "Dynamic system level simulations of downlink beamforming for UMTS FDD," in *Proc. IEEE Global Telecommunications Conference (GLOBECOM '03)*, vol. 1, pp. 492–496, San Francisco, Calif, USA, December 2003.
[46] Technical Specification Group 3GPP, "RF Scenarios," Tech. Rep. 25.942, European Telecommunications Standards Institute, Sophia Antipolis, France, 2000.
[47] C. Farsakh and J. A. Nossek, "Spatial covariance based downlink beamforming in an SDMA mobile radio system," *IEEE Trans. Commun.*, vol. 46, no. 11, pp. 1497–1506, 1998.
[48] G. G. Raleigh, S. N. Diggavi, V. K. Jones, and A. Paulraj, "A blind adaptive transmit antenna algorithm for wireless communication," in *Proc. IEEE International Conference on Communications (ICC '95)*, vol. 3, pp. 1494–1499, Seattle, Wash, USA, June 1995.
[49] H. Asakura and T. Matsumoto, "Cooperative signal reception and down-link beam forming in cellular mobile communications," *IEEE Trans. Veh. Technol.*, vol. 48, no. 2, pp. 333–341, 1999.
[50] U. Martin, "Private communication," unpublished work at Deutsche Telekom AG, 1999.
[51] J. S. Lee and L. E. Miller, *CDMA Systems Engineering Handbook*, Artech House, London, UK, 1st edition, 1998.
[52] M. Gudmundson, "Correlation model for shadow fading in mobile radio systems," *Electronics Letters*, vol. 27, no. 23, pp. 2145–2146, 1991.
[53] B. Chalise, L. Häring, and A. Czylwik, "System level performance of UMTS-FDD with covariance transformation based DL beamforming," in *Proc. IEEE Global Telecommunications Conference (GLOBECOM '03)*, vol. 1, pp. 133–137, San Francisco, Calif, USA, December 2003.
[54] K. Hugl, J. Laurila, and E. Bonek, "Downlink beamforming for frequency division duplex systems," in *Proc. IEEE Global Telecommunications Conference (GLOBECOM '99)*, vol. 4, pp. 2097–2101, Rio de Janeireo, Brazil, December 1999.

Andreas Czylwik: Department of Communication Systems, University Duisburg-Essen, Bismarckstr. 81, 47057 Duisburg, Germany

Email: czylwik@sent5.uni-duisburg.de

Armin Dekorsy: Bell Labs Europe, Lucent Technologies, Thurn-und-Taxis street 10, 90411 Nuremberg, Germany

Email: dekorsy@lucent.com

Batu Chalise: Department of Communication Systems, University Duisburg-Essen, Bismarckstr. 81, 47057 Duisburg, Germany

Email: chalise@sent5.uni-duisburg.de

37 UMTS link-level demonstrations with smart antennas

Klemens Freudenthaler, Mario Huemer, Linus Maurer, Steffen Paul, and Markus Rupp

With the exploration of multiple antennas at transmitter and possibly also at receiver end, the original concept of UMTS (universal mobile telecommunications system), specified within 3GPP (3rd-generation partnership project), needs to be reconsidered. While the so-called MIMO (multiple-input multiple-output) techniques promise huge improvements in spectral efficiency, in general, once constraints by standards are specified, it can become quite cumbersome to achieve such improvements. The success of MIMO techniques in UMTS depends on the availability of technically feasible and affordable solutions. The terminal side needs special attention due to its limitations in computational and battery power. In general, MIMO algorithms are rather complex, making their implementation as FPGA or ASIC difficult. Therefore, low-complexity solutions for MIMO systems attract more and more attention.

In this chapter, steps towards integrated circuit solutions for MIMO systems are reported. The discussion starts with a review of a state-of-the-art UMTS SISO (single-input single-output) mobile terminal in Section 37.1. RF (radio frequency) as well as baseband signal processing challenges and requirements are addressed. Furthermore, principle RFIC (radio frequency integrated circuit) and baseband chip architectures, with particular regard to the RAKE receiver, are discussed. In Section 37.2 the SISO RAKE concept is extended to the SIMO (single-input multiple-output) case, which is especially of interest for the uplink. Space-time (ST) RAKE receivers for UMTS base stations (node B) are presented. General MIMO system considerations covering RF aspects as well as baseband MIMO decoding techniques, including their implementation constraints, are highlighted in Section 37.3. In addition, insight in the complexity of MIMO decoding algorithms is provided. First realizations of UMTS MIMO prototypes and even ASICs are reported on in Section 37.4.

37.1. SISO UMTS receiver review

In this section, we review the principle architecture of a UMTS standard Release 4 [1] compliant mobile terminal. For a more detailed structure of a node B UMTS

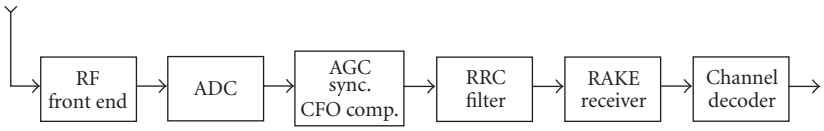

FIGURE 37.1. Receiver structure for mobile terminal.

receiver, we refer to [2]. The receiver structure for a UMTS mobile terminal is shown in Figure 37.1. After passing the RF front end and the ADC (analog-to-digital converter), the digital signal processing starts with a synchronization phase including AGC (automatic gain control) and CFO (carrier frequency offset) compensation. Subsequently, the signal is processed by an RRC (root raised cosine) filter, which results in an overall RC (raised cosine) pulse shape of the received symbols, since the transmit pulse shaping filter has also an RRC response. The actual data detection is performed by a RAKE receiver followed by the channel decoder. This chapter focuses on the RF front end on the one hand, and on the crucial data detection algorithms and architectures, for example, the RAKE receiver, on the other hand.

Compared to GSM (global system for mobile communications) compliant solutions, the development of UMTS RF chipsets results in some new challenges. Obviously, the higher channel bandwidth of UMTS influences the RFIC design. Beyond that, there are some other critical points that clearly distinguish UMTS from GSM in terms of RF requirements. Both, transmitter and receiver have to fulfill much tighter dynamic range demands. Moreover, the higher ACS (adjacent channel-selectivity) requirements aggravate the receiver design. The transmitter architecture is mainly influenced by the large peak-to-average power ratio (PAR) and the tighter requirements on the output power control. Current solutions use linear power amplifiers to limit RF emissions in neighbouring channels. As a consequence, the power amplifiers have to be operated with adequate backoffs, which results in low PAE (power added efficiency) values. The general tendency in RF transceiver design for wireless communications systems leads towards direct conversion architectures, which do not require costly IF filters, for example, surface acoustic wave (SAW) devices, that are not amenable to monolithic integration (see Section 37.1.2).

By comparison, UMTS is by far the most challenging wireless cellular standard in terms of baseband computational complexity. In [3] it is shown that a GSM, a GPRS, and an EDGE modem requires approximately 100, 350, and 1200 MIPS, respectively. This grows to around 5000 MIPS for a UMTS modem, but a more precise figure depends on the mobility class and the data rate. It is not possible to map the entire set of operations onto a standard, single DSP chip with today's technology. As a consequence, the most complex parts have to be implemented in hardware. These dedicated hardware accelerators are typically supported by a DSP, which handles the less costly tasks. The approximate computational complexity in MIPS for the different functional modules of a UMTS mobile terminal (Release 4)

Table 37.1. MIPS complexity of receiver blocks for 384 kbps class modem.

Digital filtering (RRC, channelization)	2000 MIPS
Searcher (slot and frame synch., code identification)	2500 MIPS
RAKE receiver	850 MIPS
Maximum ratio combining (MRC)	24 MIPS
Channel estimation	12 MIPS
AGC, AFC	10 MIPS
Deinterleaving, rate matching	14 MIPS
Turbo decoding	65 MIPS
Total	5500 MIPS

Table 37.2. RF performance characteristics and related TCs.

Reference sensitivity TC	Noise figure
Adjacent channel selectivity TC	Selectivity
Intermodulation TC	3rd-order intercept point
Maximum input TC	1-dB compression point, tolerable inchannel distortions
Blocking TC	Reciprocal mixing

is shown in Table 37.1. It has to be noted that different mobility classes and data rates result in different complexity.

Interestingly, the bulk of the computational complexity is concentrated in two blocks.

(i) *Digital filtering.* The functions for signal shaping up to the RRC filter are of high computational complexity due to the high sample rate, which is at least twice the chip rate (i.e., 7.68 MHz sample rate).

(ii) *Searcher.* The aim of the cell search module is to detect the slot/frame sequence of the base station among all received signals in order to establish a communication link. In a low SNR environment, the detection probability can be enhanced by retrying this procedure. This increases the processing load until the correct sequence is detected. Hence, this detection is of random nature and its final MIPS count is difficult to estimate.

37.1.1. Basic 3GPP requirements

RF requirements. The requirements for a UMTS-FDD (frequency division duplex) mode compliant RF transceiver can be derived from the testcases (TCs) given in [4]. Almost all receiver related TCs in this document define the required receiver performance indirectly, that is, by stating that under given signal conditions at the terminal antenna connector, a predefined BER (bit error rate) or BLER (block error rate) of a certain value must not be exceeded. The most important receiver TCs together with their related RF performance measures are summarized in Table 37.2.

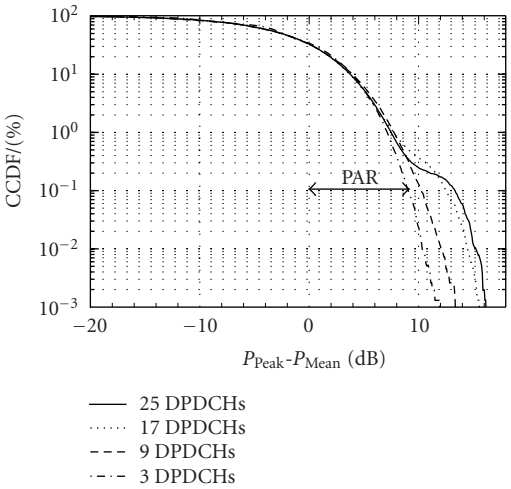

FIGURE 37.2. CCDF for several numbers of DPDCHs including CPICH (common pilot channel), CCPCH (common control physical channel), PICH (paging indicator channel), SCH (synchronization channel).

Most of the RFIC performance figures mentioned in Table 37.2 have to be derived via detailed system simulations, taking into account the RF-receiver architecture and the subsequent digital baseband receiver structure. Requirements that can be estimated by means of simple calculations are rare. One notable exception is the calculation of the receiver noise figure (NF) based on the reference sensitivity-level TC [5]. The impact of limited receiver linearity has been evaluated in [6]. The influence of channel-selection filtering is investigated in [7, 8]. A link between the RF performance measures for sinusoidal signals and for W-CDMA (wideband code division multiple access) signals can be found in [9].

Most of the RF performance figures are defined for sinusoidal signals excitation only. These measures cannot readily be applied for W-CDMA signals due to different signal statistics and bandwidths. Especially important in this context is the PAR, which can be derived from the complementary cumulative probability density function (CCDF). The peak power P_{Peak} for the calculation of the PAR is defined as

$$\text{CCDF}\left(P_{\text{Peak}}\right) = 0.1\%. \tag{37.1}$$

Thus, the instantaneous signal power is lower than the peak signal power P_{Peak} with a 99.9% probability. Figure 37.2 shows the CCDF of a downlink UMTS signal for several numbers of dedicated physical data channels (DPDCHs). Remarkably, the peak power increases substantially for higher numbers of DPDCHs.

Baseband requirements. The main parameters for the physical layer of the UMTS mobile communications system are defined in the standards document [4]. These parameters impose constraints on hardware design aspects such as the processing

speed and the temporary storage of information among others. UMTS is a CDMA system with chip rate $f_c = 3.84$ Mcps leading to a sample rate of at least 7.68 Msps for baseband signal processing. The data frames consist of 15 slots, each one with 2560 chips. The base station transmits a CPICH with a fixed spreading factor (SF) of 256 and identical spreading code to support parameter estimation at the terminal side. The SF for data ranges from 4 to 256.

A low BER can only be achieved, if as much as possible transmit power is received. In a multipath environment, several receive paths with significantly different time delays have to be combined. The UMTS standard [4] defines TCs with channel delays up to 20 microseconds. The RAKE receiver for a UMTS system combines several receive paths into a single output signal. The direction, the intensity, and the arrival time of the received signals change as the user moves. Therefore, the path search window has to be sufficiently large around the peak level. In practice, the observation window spans from -10 microseconds to $+20$ microseconds, which corresponds to the chip positions -40 to $+80$. Furthermore, in *soft handover mode*, the terminal combines the received signal of up to six base stations. In this case, the observation window is extended to ± 38.5 microseconds (equivalent to ± 148 chips).

The dynamic channel properties naturally depend on the mobile's speed. Assuming a mobile moving with 250 kmph results in a path delay change of approximately half a chip duration within 56 frames or 560 milliseconds. This exhibits that the delay estimation rate may be substantially lower than the frame rate.

37.1.2. RF front end

The first step in receiver design is the choice of the receiver architecture. Besides achieving the required RF performance, several criteria like the number of external components, cost, power dissipation, and complexity determine the selected receiver structure. However, as IC technologies evolve, the relative importance of each of these criteria changes, allowing to return to approaches that once seemed impractical as plausible solutions. UMTS compliant RF receivers are quite different from their 2nd-generation TDMA/FDMA (TDMA: time division multiple access, FDMA: frequency division multiple access)-based counterparts, due to the separation of the user signal in the code domain rather than in the time and/or frequency domain. In this section, we will only focus on the two dominant receiver architectures used for cellular terminals, which are the homodyne and the heterodyne receiver structures.

Heterodyne receiver architecture. Figure 37.3 shows the heterodyne receiver structure. This architecture first translates the signal band down to some intermediate frequency (IF), which is usually much lower than the initially received frequency band. Channel-select filtering is usually done at this IF, which requires some bandpass filter with a center frequency equal to the IF. The choice of the IF is a principle consideration in heterodyne receiver design (see Figure 37.4).

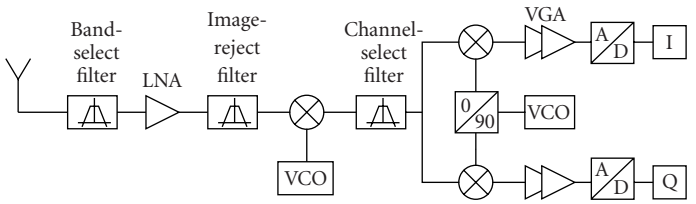

FIGURE 37.3. Heterodyne receiver structure.

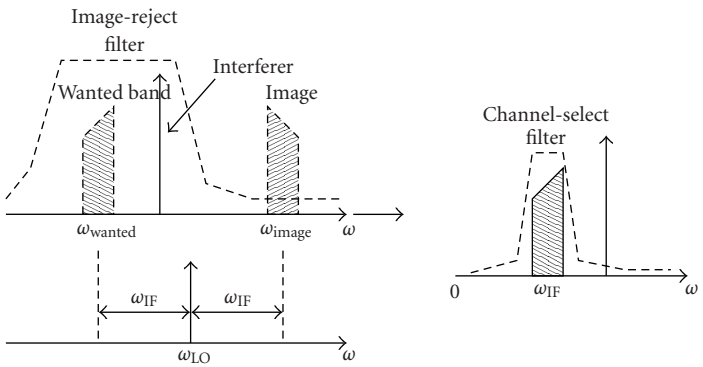

FIGURE 37.4. Image rejection and channel selection for the heterodyne receiver structure.

As the first mixer downconverts frequency bands symmetrically located above and below the local oscillator (LO) to the same center frequency, an image-reject filter in front of the mixer is needed. As depicted in the left part of Figure 37.4, the filter is designed to have a relatively small loss in the desired band and a large attenuation in the image band, two requirements that can be simultaneously met if $2 \cdot \omega_{\text{IF}}$ is sufficiently large. Thus, a large IF relaxes the requirements for the image reject filter, which is placed in front of the mixer (see Figure 37.3). On the other hand it complicates the design of the channel-selection filter (right part of Figure 37.4), because of the higher IF. In today's cellular systems, the channel-selection filtering is normally achieved with external SAW filters, because implementations amenable to monolithic integration like active-RC or $Gm - C$-filters would be too power consuming for the required performance.

An interesting situation arises if an interferer with frequency

$$\frac{\omega_{\text{wanted}} + \omega_{\text{LO}}}{2} \tag{37.2}$$

is present. If this interferer experiences second-order distortion and the LO contains a significant second harmonic, then a component at

$$\left| (\omega_{\text{wanted}} + \omega_{\text{LO}}) - 2\omega_{\text{LO}} \right| = \omega_{\text{IF}} \tag{37.3}$$

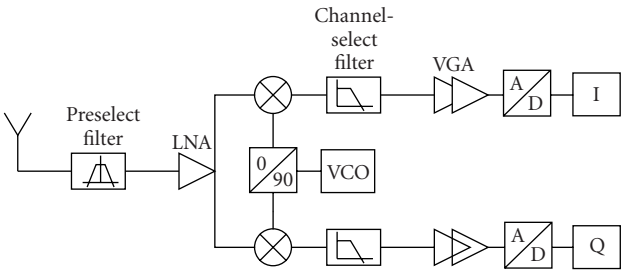

FIGURE 37.5. Homodyne receiver structure.

arises, which can be extremely troublesome, because this interference source directly occurs in the receive band. Thus, it cannot be removed by filtering in subsequent receiver stages. This phenomenon is called half-IF problem.

Due to the fixed receive bandwidth of the heterodyne receiver structure caused by the external IF-filter, the multimode and multiband capabilities can only be implemented by using separate IF sections for each mode. Clearly, this would result in high costs and a complex receiver structure. One example of an RFIC for UMTS based on this architecture can be found in [10].

Homodyne receiver architecture. The homodyne receiver structure (also called zero-IF or direct-conversion architecture) depicted in Figure 37.5 avoids the disadvantages of the heterodyne concept by reducing the IF to zero. This saves the first mixer, the LO, and the IF channel-selection filter. Moreover, also the image problem vanishes if a quadrature converter is used. Thus, the simplicity of this structure offers two important advantages over its heterodyne counterpart. First, the problem of image is circumvented because ω_{IF} is 0. As a result no image filter is required. This may also simplify the LNA (low noise amplifier) design because there is no need for the LNA to drive a 50Ω load, which is often necessary when dealing with image-rejection filters [11]. Second, the IF SAW filter and IF amplifiers can be replaced by lowpass filters and baseband amplifiers that are amenable to monolithic integration.

The zero-IF or homodyne receiver topology entails a number of issues that do not exist or are not as serious in a heterodyne receiver. Since in a homodyne topology the downconverted band extends to zero frequency, offset voltages can corrupt the signal and, more importantly, saturate the following stages. There are three main possibilities of how DC offsets are generated. First, the isolation between the LO port and the inputs of the mixer and the LNA is not infinite. Therefore, a finite amount of feedthrough from the LO port to the mixer or the LNA input always exists. This "LO leakage" arises from capacitive and substrate coupling and, if the LO signal is provided externally, bond wire couplings. This leakage signal is now mixed with the LO signal, thus producing a DC component at the mixer output. This phenomenon is called "self-mixing." A similar effect occurs if a large interferer leaks from the LNA or mixer input to the LO port and is multiplied by itself.

A time-variant DC offset is generated if the LO leaks to the antenna and is radiated and subsequently reflected from moving objects back to the receiver.

Large amplitude modulated signals that are converted to the baseband section via second-order distortion of the IQ mixers may also lead to time-variant DC offsets. The spectral shape of this signal contains a significant component at DC accounting for approximately 50% of the energy. The rest of the spurious signal extends to twice the signal bandwidth before being downconverted by the second-order nonlinearity of the mixers. The reason for the large signal content at DC is due to the fact that every spectral component of the incident interferer is coherently downconverted with itself to DC. In order to prevent this kind of DC offset, a large second-order intercept point (IP2) of the IQ mixer is necessary.

3GPP compliant receivers approximately need 80 dB gain. Most of this gain is contributed by the baseband amplifiers. That means that even small DC offsets (in the range of several mV) at the mixer outputs may lead to DC levels sufficient to saturate the ADCs.

In TDMA systems, idle time intervals can be used to carry out offset cancellation. This would be a practical solution for the 3GPP-TDD (time division duplex) mode. It cannot be used for offset cancellation in the FDD mode because of the continuous signal reception. Here, the natural solution for DC offset cancellation is highpass filtering. Since the signal band extends from DC to approximately 2 MHz, a high-pass filter with a cutoff frequency of several kHz results in an acceptable degradation of the system performance [12]. This approach is only possible because of the wideband nature of the signal. An interesting solution to overcome the switching transients due to highpass filtering is presented in [13]. A system level DC offset compensation approach can be found in [14].

IQ mismatches are another critical issue for the zero-IF receiver topology. Fortunately, pilot-symbol-assisted channel estimation is performed in W-CDMA systems. Irrespective of the pilot symbols used (either the time-multiplexed pilot symbols or the common pilot signal), this estimation additionally leads to a correction of the IQ phase and amplitude mismatch.

Most of the published work on receiver design is based on the direct conversion topology [15, 16, 17, 18, 19]. This comes at no surprise due to the importance of the highest possible integration, which is clearly advantageous for the zero-IF receiver structure. All these receivers are designed using standard BiCMOS processes. An interesting option is the use of SiGe bipolar technology for the receiver front end [20, 21]. Recent advances in UMTS compliant RFIC receiver design are often focused on the use of RF-CMOS as the semiconductor technology of choice [22, 23].

37.1.3. Baseband receiver architectures—the RAKE receiver

The RAKE receiver as shown in Figure 37.6 combines signal energy arriving from different paths requiring a correlator assigned to each (relevant) propagation path. In the RAKE literature, these correlators are called RAKE fingers. They are parameterized by the positions of the propagation paths in time, such that the code

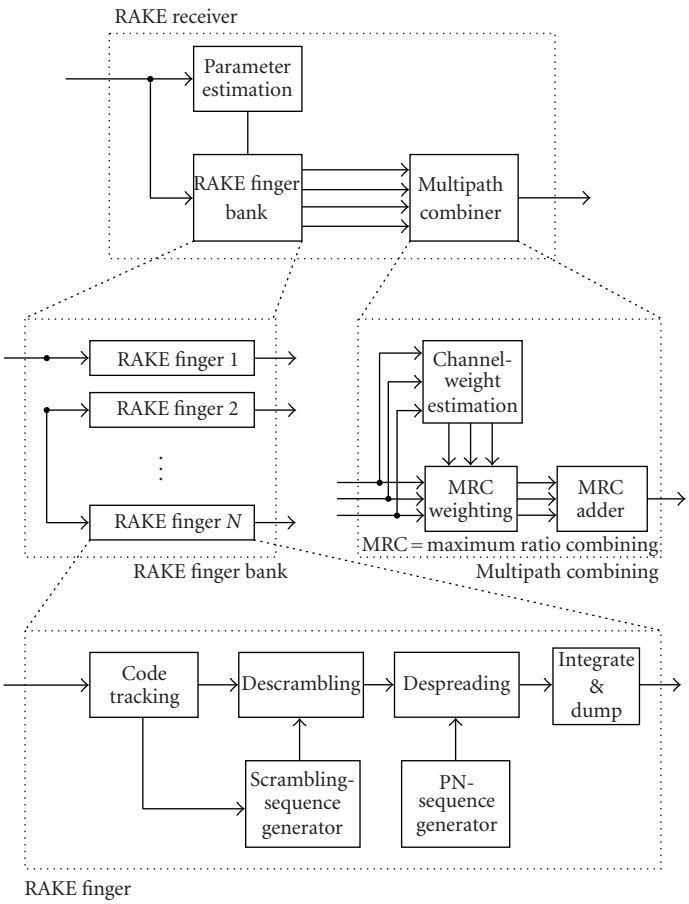

Figure 37.6. Principle structure of a RAKE receiver.

generator for descrambling/despreading runs synchronously to the slot start. The finger outputs are combined to one signal in a maximum ratio combiner.

Typically, the RAKE fingers process samples at twice the chip rate. However, the actual path delay is, in general, not a multiple of half a chip duration. Hence, the analog signal is not sampled at the optimum time. Therefore, a code-tracking unit is used at each finger to reconstruct the input signal for optimum sampling (see Figure 37.7). Each RAKE finger contains a timing error correction (code-tracking unit), a descrambler to distinguish different base stations, a despreader, and an integrate-and-dump operation. The descrambling and despreading codes are generated in respective code generators. The code numbers are available prior to the start of the data demodulation.

The multipath combiner comprises a channel estimation block to estimate the channel weights for each individual path, and an MRC weighting and MRC

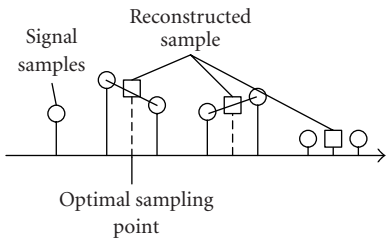

FIGURE 37.7. Reconstruction of the optimal sampling point.

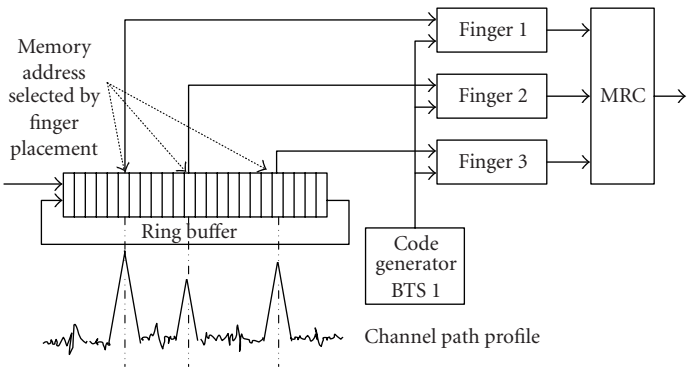

FIGURE 37.8. Input buffer for delay compensation at chip level.

adder block, which combine the received signals according to the maximum ratio criterion.

The RAKE receiver processes the sampled and quantized output signal of the RRC filter. To achieve adequate system performance, a path resolution of $\pm(1/16)T_c$ (with chip duration $T_c = 1/f_c$) is required. This accuracy may either be achieved by using a high oversampling rate (OSR), or by using a low OSR (e.g., the minimum OSR of two) in combination with interpolation methods. The latter case implicates a lower ADC clock rate. The interpolator reconstructs the signal from the received samples, for example, by linear or quadratic interpolation (see Figure 37.7). The code-tracking unit selects the sample closest to the optimal sampling point.

Due to multipath propagation, the signals of different paths arrive with a time difference. In order to combine them coherently, the arrival delays have to be compensated. This can either be performed at chip level, that is, at the input of the RAKE fingers (see Figure 37.8) or at symbol level, that is, at the output of the RAKE fingers (see Figure 37.9). The preferred method depends on the number of fingers, the OSR, as well as the spreading factor.

In the first case, an input buffer is required and the RAKE fingers point at different locations in this buffer. Since data is stored consecutively, there is a unique

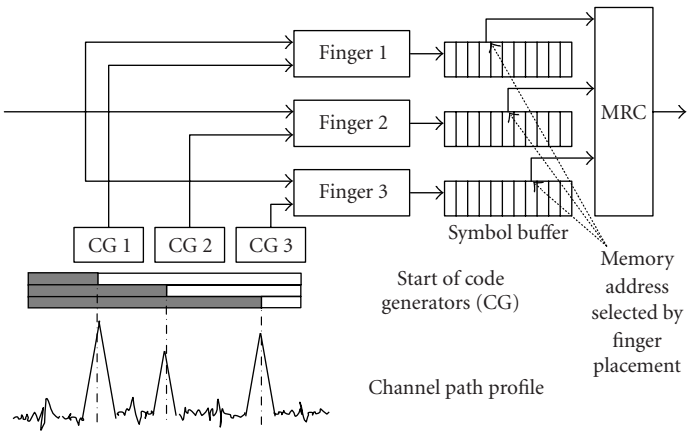

FIGURE 37.9. Output buffer for delay compensation at symbol level.

relation between path delay and memory address. The buffer size is determined by the OSR and the maximum path difference to be covered (see Section 37.1.1). All the RAKE fingers run synchronously, their corresponding code generators start at the same point in time, which simplifies a synchronous design.

In the second case, the path delay is compensated at the output of the RAKE fingers, where the symbols have to be buffered. The multipath combiner selects symbols from these buffers according to their path delays. In this approach, the fingers run asynchronously, therefore the code generators have to be adjusted according to the path delays.

The buffer size for data and control overhead is different for both approaches. The choice depends on the number of fingers and the spreading factor. For comparison, the buffer size is calculated for both cases. The signal is assumed to be complex-valued (IQ = 2), the OSR is set to two, and soft handover mode is assumed. SHO chips are stored and maximum channel delay spread (corresponding to DS chips) has also been taken into account. Considering the requirements discussed in Section 37.1.1, the size of the input buffer (IB, see Figure 37.8) follows to be

$$\begin{aligned} \mathrm{IB} &= \mathrm{IQ} \cdot \mathrm{OSR} \cdot (2 \cdot \mathrm{SHO} + \mathrm{DS}) \\ &= 2 \cdot 2 \cdot (2 \cdot 148 + 120)\ \text{samples} \\ &= 1664\ \text{samples}. \end{aligned} \tag{37.4}$$

This amounts to a memory size of around 13 kb for an 8-bit data input.

The second option is to process the input data without prior delay compensation. In this case, a separate code generator is used for each path synchronized to the corresponding path delay. The symbol rate at the output of the fingers is f_c/ SF

with SF ranging from 4 to 256. The size of the output buffer (OB) is given by

$$\begin{aligned} \mathrm{OB} &= \mathrm{IQ} \cdot F \cdot \frac{2 \cdot \mathrm{SHO} + \mathrm{DS}}{\mathrm{SF}} \\ &= 2 \cdot 10 \cdot \frac{2 \cdot 148 + 120}{4} \text{ samples} \\ &= 2080 \text{ samples.} \end{aligned} \tag{37.5}$$

In this estimation, $F = 10$ was assumed. For the chosen parameter set, a 16 kb data memory would be required. The first solution is preferable for a large number of RAKE fingers and a small OSR. An additional problem that arises with the architecture shown in Figure 37.9 occurs when a terminal is moving towards the base station. In this case, the path delay decreases, and the phase of the code generator has to be adjusted accordingly. A solution to this problem applying a one-bit delay line at the output of the code generator is proposed in [24].

37.2. Extensions of SISO RAKE receiver

The RAKE receiver for SISO UMTS discussed in Section 37.1.3 is very effective in optimum combining of multipath components, and thus represents a receiver structure utilizing time diversity (multipath diversity). The use of multiple antennas at the receiver additionally enables to exploit the spatial dimension, that is, it allows for spatial diversity. This section focuses on ST RAKE receivers which are especially interesting for the UMTS uplink because of the obvious facility to apply multiple antennas at the base stations. This system approach illustrates a SIMO extension of the scheme addressed in Section 37.1.2.

In this section, we will present two different approaches of how to exploit the spatial dimension, namely, the MRC-ST RAKE receiver in Section 37.2.1 and the beamforming-ST RAKE receiver in Section 37.2.2.

37.2.1. MRC-space-time RAKE receiver

This straight forward approach combines the outputs of individual temporal RAKE receivers (one for each antenna) in an MRC sense. This scheme [25] (see Figure 37.10), called MRC-ST RAKE, accomplishes diversity by means of temporal and subsequently spatial combining. Note that the order of temporal and spatial combining can also be exchanged without performance degradation.

As it is shown in Figure 37.10, the entire SISO RAKE receiver chain (Figure 37.6) has to be implemented for each antenna. If n_R is the number of receive antennas, the computational complexity of the MRC-ST RAKE is approximately n_R-fold that of a SISO RAKE (see Table 37.1):

$$C_{\text{MRC-ST-RAKE}} \approx n_R \cdot C_{\text{SISO-RAKE}}. \tag{37.6}$$

Due to the close spacing of the receiver antennas, the delays of the dominant temporal taps (RAKE fingers) of the individual channel profiles are strongly correlated.

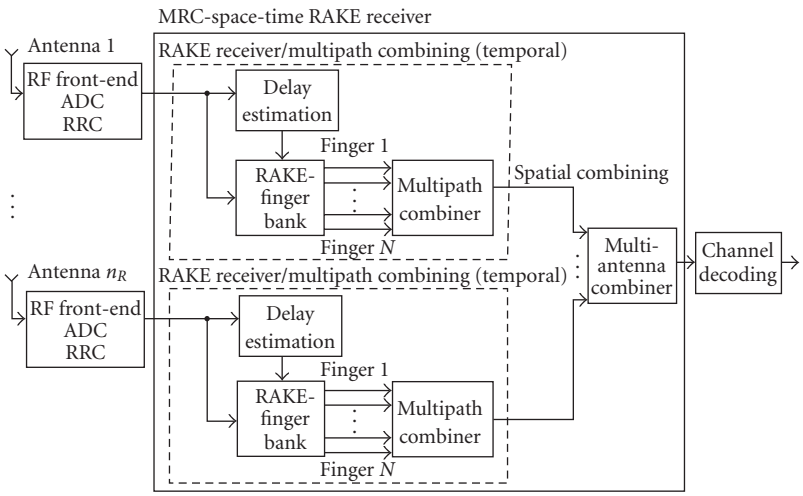

Figure 37.10. MRC-space-time RAKE receiver.

Complexity can therefore essentially be reduced by centralizing the delay estimation block, which does not need to be implemented for each branch individually. Since the delay estimation is the most complex part in the RAKE receiver (see Table 37.1), this may reduce the overall complexity of the MRC-ST RAKE significantly.

37.2.2. Beamforming-space-time RAKE receiver

The use of multiple antennas enables to exploit the spatial diversity of the channel and, in addition, to reduce the effects of multiuser interference (MUI) by the use of beamforming. Figure 37.11 shows the block diagram of a beamforming-ST RAKE receiver. Here, spatial beamforming is implemented for each path (i.e., for each RAKE finger), followed by a temporal RAKE combiner. Each spatial beamforming operation (one beamforming for each temporal path) is implemented by applying a spatial weight vector to the n_R antenna signals. The position of each RAKE finger in turn is determined by the delay estimation block.

Applying the spatial weight vectors can be regarded as a beamforming procedure, one for each temporal RAKE finger, which rejects interfering signals of other users. This rejection is achieved by pointing one or more narrow beams at the incoming desired signals. Any one of several beamforming criteria such as minimum mean square error (MMSE) or minimum variance distortionless response (MVDR) may be used to calculate the spatial weight vector. Both MMSE and MVDR require the antenna array covariance matrix and its inverse [2]. A less complex alternative to these beamforming criteria called approximate MVDR is described in [26].

Note that the multipath combiner block in Figure 37.11 not only consists of the MRC weighting and adder parts, but also comprises an estimation block for

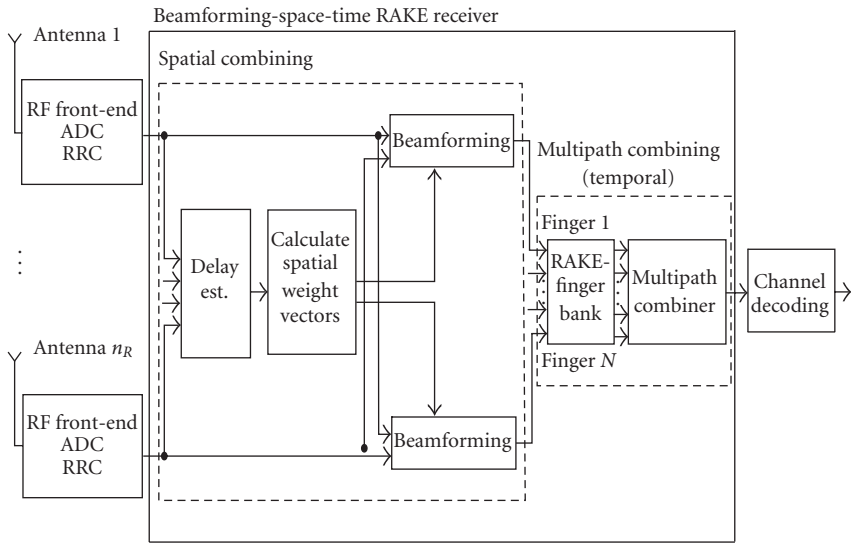

Figure 37.11. Beamforming-space-time RAKE receiver.

determining the weights of the temporal RAKE fingers (see Figure 37.6). These temporal weight vectors should be updated every time slot to track the fast fading, while the spatial weight vectors can be averaged over several slots since the spatial characteristics change much slower than the fast fading.

In rural environments (i.e., high spatial correlations), the beamforming-ST RAKE typically outperforms the MRC-ST RAKE, because it directs its beams towards the strongest incoming signal (dominant eigenvector). On the other hand, in the so-called pico-environments (low spatial correlation), the MRC-ST RAKE typically outperforms the beamforming-ST RAKE, since in that case the beamforming-ST RAKE is hardly able to exploit spatial diversity (only the strongest eigenvector which represents only a small part of the corresponding path is exploited) [25, 27].

In [25] the idea of ST RAKE receivers is furthermore extended to closed loop diversity schemes, on the W-CDMA downlink. In such schemes parts of the complexity and multiple antenna processing are shifted to the base station where the transmit signals are predistorted. Note that the predistortion requires channel state information, therefore a feedback channel is needed. For further improvements on ST RAKE receiver concepts (eigen-RAKE, joint-ST RAKE) and performance comparison demonstrations, we refer to [25, 27].

37.3. MIMO system architectures

Most of the published work in the MIMO field focuses on the algorithmic parts and on their respective implementations in the digital domain. There is only little work available that specifically takes MIMO compliant RF front ends into account.

In Section 37.3.1, the principle conceivable MIMO RF receiver architectures are discussed. In Section 37.3.2, MIMO baseband algorithms are considered and their complexity is evaluated.

37.3.1. RF front end

Basic work on MIMO RF receiver architectures is reported in [28, 29]. One of the obvious challenges in MIMO optimized RF front-end design is the separation of the antennas. Obviously, small-sized mobile terminals fit poorly for multiantenna implementations. To properly implement multiple antennas into a small terminal, a minimum distance of half the wavelength λ could be taken as a rule of thumb to sufficiently decouple the antennas. Further decoupling can be realized by using cross-polarized antennas. At 2 GHz carrier frequency, $\lambda/2$ corresponds to 7.5 cm. Therefore, the size limitations of cellular terminals set a natural limit on the respective number of implemented antennas.

The straight forward approach of a MIMO capable RF front-end implementation is the use of one dedicated receiver per antenna to preserve the spatial and temporal integrity of the antennas signals. This structure is called a full-parallel MIMO RF receiver. In principle, it is also possible to separate the received signals from different antennas in the analog front end in the time, frequency, or code domain. All of the mentioned techniques have their distinct advantages and shortcomings. At least the separation in frequency and time does not seem to be an option for a highly integrated RFIC due to inherent technical problems.

Frequency-domain-multiplexed MIMO RF receiver. In this approach, the received signals from different antennas would typically be mixed onto different frequency bands. Obviously, each receive path requires separate LOs and mixers, but the analog IF or baseband section and the subsequent ADCs could be shared. The resulting frequency bands should be as close as possible, that is, one channel spacing of the standard under consideration. There are however some severe disadvantages inherent to this concept. All the problems common to the design of heterodyne receivers would aggrevate for such frequency-domain-multiplexed MIMO receiver. Trying to implement this receiver structure on a single RFIC could prove to be impractical due to frequency planning issues taking into account the number of different frequency sources needed. Furthermore, filtering requirements would be hard to realize.

Time-domain-multiplexed MIMO RF receiver. In the time-multiplexed approach, the outputs from the different antennas are multiplexed together using an RF switch. The combined signals are subsequently downconverted to baseband by a single radio receiver. Since the sample interval of the received signals at each antenna has to be preserved, the RF switch must operate at $N \cdot S$ (N-number of antennas, S-nominal sampling frequency). One disadvantage of this approach is the fact that only a fraction of the received power that is available at each antenna is actually being used for further processing. From an implementation point of view, this concept seems even more challenging than the frequency-domain-multiplexed RF

receiver described above. Finding suitable RF switches and realizing the demultiplexing operation correctly are just two issues that make this architecture only a theoretical option.

Code-domain-multiplexed MIMO RF receiver. This method uses a code-division approach for the signal separation similar to techniques employed in CDMA systems. A unique identity is assigned to each received antenna signal by application of an orthogonal code (i.e., a Walsh code). Due to the orthogonality of the used codes the combined signals can be separated in the digital domain after they passed through a single RF chain with subsequent ADCs. Biphase modulators can be used to apply the code domain multiplexing in the analog domain.

Full parallel MIMO RF receiver. This approach necessitates one full receiver front end (see Figures 37.3 or 37.5) per antenna. However, it should be noted that important blocks can be shared among the different receivers. The sharable blocks include the frequency generation (VCO, PLL), the IQ divider, the biasing circuitry, and the clock generation functionality. Furthermore, the digital calibration circuits, for example, for the analog channel-selection filters, can be commonly used by all the receiver chains. Consequently, the integration of, for example, two parallel receivers onto one RFIC would not simply result in a doubling of the required die area compared to the single receiver implementation. Thus, the area and power saving potential of an optimized RFIC implementation of a full-parallel MIMO RF receiver might be significant.

From all the mentioned architectures only the full-parallel MIMO RF receiver offers the full benefits of a MIMO system. Due to the severe technical challenges of the frequency- and time-domain multiplexing approaches, only the code-domain multiplexing RF receiver is left as a second potential solution.

37.3.2. Baseband receiver architectures

General MIMO decoder considerations. The actual decoding stage takes place after AGC, RRC filtering, synchronization, and frequency offset compensation have been performed. The decoder comprises from the RAKE receiver correlators for channel estimation (CE), the correlator bank (CB) of selected fingers, the MIMO decoder (M-Dec), and the finger position search and management (FPM) unit as shown in Figure 37.12. The channel estimator is supported by a pilot code generator (PCG), while the correlator bank is supported by separate code generators depending on the user codes. In MIMO transmissions, the linear RAKE combiner is typically replaced by a specific decoder unit that performs ML (maximum likelihood) decoding or matrix inversion techniques, like ZF (zero forcing), MMSE, or V-BLAST (vertical Bell Laboratories Layered Space-Time) [30]. Finally, the control unit (Cntr) converts the timing synchronization into appropriate signals for each block. The channel decoding is done by a turbo decoder (turbo).

The complexity of all these units depends strongly on the channel requirements. For a channel impulse response of 10 microsecond duration, roughly 40 channel taps are required when running a T-spaced receiver. For higher sampling

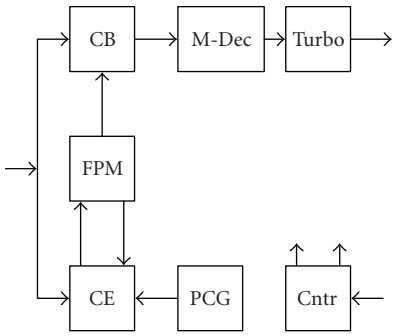

Figure 37.12. Decoder and RAKE structure.

rates, the number increases accordingly. Note that for a MIMO system with n_T transmit and n_R receive antennas, a total number of $n_T n_R$ subchannels need to be estimated. The channel example (10 microsecond impulse response duration) above with four transmit and four receive antennas and an oversampling rate of four, easily ends up in 2560 channel taps to estimate. While this estimation requires 2560 correlator operations, it does not require 2560 correlators working independently. The relative long time duration of 260 nanoseconds between two chips allows to reuse the correlators, that is, to fold the required HW. Also, the several pilot sequences for the antennas do not need to be independent sequences. In [31] a real-time system with four transmit antennas was reported using the secondary pilot channel (SPICH) to transmit four pilot sequences stemming from the same branch of the OVSF (orthogonal variable spreading factor) code tree. This allowed to substantially decrease complexity. In the 3GPP standard document TR 25.869 [32], a four-antenna transmit and receive system is proposed for UMTS Release 6. There, the four transmit antennas are supported by one CPICH signal only, but this signal is split into two patterns (AA) and (−AA) and further split into four different antenna signals by using two different OVSF codes. A low-complex solution for the receiver can also be found in this 3GPP document.

In particular, there will be more than one OVSF code assigned to each user in HSDPA (high-speed downlink packet access) mode (see also proposed 3GPP standard document TR 25.848 [33]). Many complexity reductions are possible [34, 35, 36] since the codes can be grouped into stems from the same branch of the code tree. Higher modulation schemes (16-QAM and 64-QAM) have also been proposed for increased data rates, but at the price of increased complexity for the decoding algorithm.

Further advantages that can be elaborated on are the dynamic channel properties. Due to the Doppler speed, a finger appearing on a certain position will not change its position abruptly. Since radio waves propagate with the speed of light, they travel about 75 m in 260 nanoseconds. Assume a slow mobile moving with 3.6 kmph, or, equivalently, 1 mps. At this speed, it takes 75 seconds or 7500 frames until the finger position moves to the next chip. For a fast mobile moving with

180 kmph, this duration decreases to 1.5 seconds or 150 frames, still a very long time that can be used either for averaging and thus improving estimation quality or can be traded against complexity by assigning only fractions of this period per channel tap estimation. Thus, it is possible to substantially reduce the estimation rate of the channels and at the same time to reduce the HW complexity.

Due to noisy estimation and fast Doppler, the finger energy may vary substantially over time while its position remains constant for a much longer period. In this case, it may be a better strategy to keep the location of the finger fixed even if its observed energy drops below a certain level. While for a short period other locations may appear as better choices, they can easily be mistaken and are of random nature. An intelligent FPM unit is thus required to decide whether a finger position remains unchanged even if the corresponding observed finger energy drops or a new finger location is selected. Measuring the finger energy at a certain finger position requires the computation of a norm of the correlator output signals. This can be performed by a complex-valued multiplication, computing the squared l_2-norm:

$$\|r\|_2^2 = \Re^2\{r\} + \Im^2\{r\}. \tag{37.7}$$

Thus, two multiplications per finger are required. If this is to be reduced in complexity, a good approximation of the nonsquared l_2-norm is given by

$$\|r\|_2 \approx \frac{3}{8}\max\left(|\Re\{r\}|, |\Im\{r\}|\right) + \frac{5}{8}\left(|\Re\{r\}| + |\Im\{r\}|\right), \tag{37.8}$$

which gave excellent results in [31, 34].

Furthermore, the optimal number of fingers is a challenging question. In some wireless channels, many strong reflections appear, while in others such reflections may be so close to each other that their received superposition cannot be resolved as independent paths.

The number of detection fingers allocated to a specific code has to be kept low, since it determines the complexity of the receiver. Thus, an intelligent finger management unit allocates the fingers separately for each code based on the channel estimation and the available resources.

While the classical RAKE receiver linearly combines the signals on the various finger outputs, better methods for MIMO transmissions are available (see Section 37.2 for SIMO extensions and Section 37.3.2 for MIMO extensions of the SISO UMTS system).

Complexity considerations for MIMO decoding algorithms. Decoding algorithm for MIMO transmissions can be divided into two groups: (i) matrix inversion methods and (ii) ML decoding. Since ML decoding is considered the most complex algorithm, it is typically not considered in transmission techniques and only the lower complexity version utilizing suboptimal ML sequence estimation techniques are used instead. However, for QPSK and transmission systems of order 4×4, it has

been shown [34] that an ML implementation can be much cheaper than a BLAST technique, achieving much higher decoding quality. In ML decoding, the complexity of the algorithm is typically of the order (n_R number of receive antennas, n_T number of transmit antennas)

$$C_{\mathrm{ML}} = \mathcal{O}\left(n_R (n_T K)^P\right), \tag{37.9}$$

for K transmitted antenna symbols with P being the alphabet size. For flat Rayleigh fading channels, the symbols sent in different time periods arrive independently in time, reducing the ML complexity to

$$C_{\mathrm{ML}} = \mathcal{O}\left(n_R n_T^P\right), \tag{37.10}$$

for each transmitted antenna symbol. In particular, for higher-order constellations, this seems to be a very high complexity. However, in [37, 38, 39], techniques for low-complexity implementations especially for 16-QAM and 64-QAM have been proposed reducing the complexity considerably. Also smart, suboptimal techniques like sphere decoding [40], geometrical approaches [41], and other techniques [42] have been proposed.

Suboptimal ML sequence estimation techniques, originally invented by Viterbi [43], are usually favoured since their complexity is given by

$$C_{\mathrm{ML}} = \mathcal{O}\left(n_R (n_T n_C)^P\right), \tag{37.11}$$

with n_C denoting the channel length. Since such techniques also work in non-flat channels and, in particular, when the encoding part forces a certain memory, this technique can be found in 3GPP in form of turbo coding [44] (see also Figure 37.12). While many turbo coding implementations for UMTS in ASICs [45, 46] and standard DSPs [47] have been reported, there is only little information available on implementations for MIMO systems.

Matrix inversion methods are ZF, MMSE, and V-BLAST techniques, the simplest one being ZF, forcing the symbols $\mathbf{s}$ to be correct no matter what happens to the noise symbol $\mathbf{v}$. Let $\mathbf{r} = \mathbf{H}s + \mathbf{v}$ be the received symbol, with $\mathbf{H}$ denoting the channel matrix. Then, $\hat{\mathbf{s}} = (\mathbf{H}^H\mathbf{H})^{-1}\mathbf{H}^H\mathbf{r}$ is the ZF estimate. Such operation will force the noise to be filtered: $\hat{\mathbf{s}} = \mathbf{s} + \tilde{\mathbf{v}}$ with $\tilde{\mathbf{v}} = (\mathbf{H}^H\mathbf{H})^{-1}\mathbf{H}^H\mathbf{v}$. The complexity is next to the required channel estimation defined by the inverse operation of a matrix, thus, in general,

$$C_{\mathrm{ZF}} = \mathcal{O}\left(n_T^3\right), \tag{37.12}$$

and does only need to be performed once the channel changes. The decoding part is then simply a matrix multiplication of $\mathbf{r}$ by the term $(\mathbf{H}^H\mathbf{H})^{-1}\mathbf{H}^H$, thus of order $n_T n_R$ for each transmitted symbol. A hard decision is usually required afterwards to decide which symbol from the symbol alphabet has been received. While the order $n_T n_R$ per symbol seems to be much smaller than in the case of ML, the matrix

inversion operation requires high-precision techniques. Standard 16-bit DSPs have problems performing such operations with sufficient precision. Alternatives are either expensive floating-point processors or dedicated logic with QR algorithms [48, 49] or similar techniques using *energy preserving* CORDIC operations [50].

While ZF usually gives the poorest performance, only slightly better than linear combination techniques, MMSE promises better quality with approximately the same complexity. Different to ZF, the noise impact is taken into consideration when forming the matrix inverse: $\hat{\mathbf{s}} = (\mathbf{H}^H\mathbf{H} + \sigma_v^2 I)^{-1}\mathbf{H}^H\mathbf{r}$ is the MMSE estimate. While the computation of the matrix inverse is not more complex, the additive noise term improves the condition number and thus the requirement on floating point precision. However, such matrix inverse still requires, in general, more than 16-bit precision and thus nonstandard HW. Also the additive noise part of the channel needs to be estimated now, a task not simple in a time-variant channel environment. In case the noise estimation is more than 3 dB off, the quality improvement compared to ZF is typically lost again [51].

A better method utilizing matrix inversion is given by the so-called V-BLAST algorithm. It exists in ZF and MMSE form. Rather than performing the matrix inverse for all symbols, it is only performed for the symbol with the strongest energy, estimated on the matrix inverse. After the first symbol has been detected, the channel matrix is reduced in rank and the entire procedure is repeated until the last symbol is detected. The V-BLAST complexity is thus of n_T times the ZF complexity. Performance quality is substantially improved compared to ZF and MMSE. However, like in the ZF and MMSE case, a standard, low-cost 16-bit DSP has problems in computing accurate matrix inverses.

37.4. Implementation examples

In this section, we only focus on MIMO baseband prototype and chip solutions, since little work is available on MIMO complient RFICs. MIMO systems are currently in the process of 3GPP standardization. It turns out that MIMO will only be established for the HSDPA extension of UMTS [52]. Naturally no low-cost mass products are available yet. However, two trends can be observed. At universities and research centers, demonstrations are performed with off-the-shelf equipment (see, e.g., [53, 54, 55], a more complete listing will be provided in the chapter *Demonstrators and Testbeds* in this book). A second trend in MIMO realization, mainly driven by the semiconductor industry, concerns first steps towards integrated solutions.

Demonstrator and prototype developments are often evolutionary starting with rather simple and easy manageable approaches, which are enhanced step by step, finally resulting in real-time systems. The air interface is usually realized by standard RF and mixed signal components (see Figure 37.13) covering the WLAN and/or the UMTS band. Typically, a PC generates data, which is transmitted over real or artificial channels. After down conversion, the received signals are stored and processed, again in a PC, online or offline. The transmission is typically performed in burst mode. Such a configuration is ideally suited for algorithm

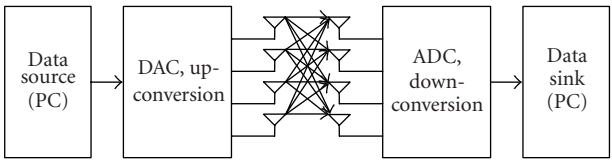

Figure 37.13. MIMO demonstrator system.

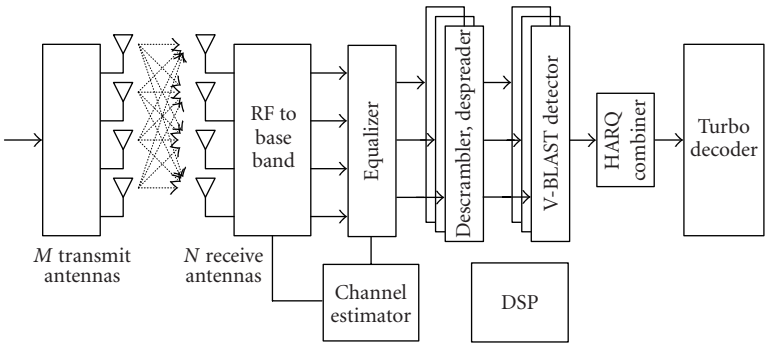

Figure 37.14. HSDPA MIMO receiver as reported in [2].

development under real physical channel conditions. A modular and flexible design allows to enhance the system towards real-time processing by replacing PC software by DSP and FPGA modules step by step. A complete four-antenna receiver design following this approach was presented in [31, 34] for the UMTS downlink. In [31] the authors report on the prototype experience of a UMTS MIMO system with four transmit (TX) and receive (RX) antennas considering ZF-V-BLAST and ML algorithms. The different MIMO detectors including appropriate channel estimation procedures are evaluated by comparing their performance and complexity.

A number of experimental and commercial smart antenna systems are published in [56]. The purpose of these systems was the demonstration of the performance increase through the use of smart antennas.

Several chip solutions have already been presented by Lucent Technologies and Agere Systems. A baseband chip for the base station was presented in [2]. The detection is performed using the V-BLAST algorithm, a 0.16 μm CMOS technology is used for chip implementation. Figure 37.14 shows a simplified block diagram of the receiver.

In this implementation, the channel estimation and matrix inversion are performed by a DSP. An ML detector for a flat-fading channel is introduced in [57]. The block diagram of this receiver is shown in Figure 37.15.

The detection is performed either for four RX antennas in combination with QPSK, or for two RX antennas and 8PSK/16QAM. A maximum number of 10

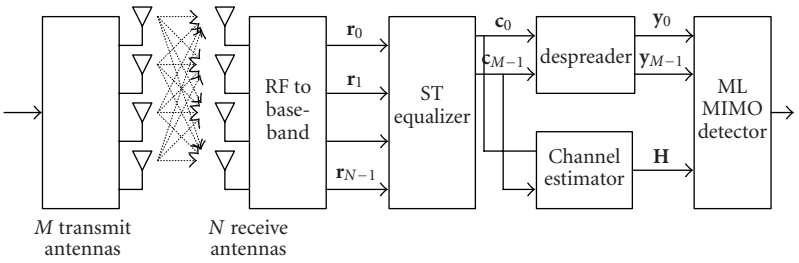

FIGURE 37.15. HSDPA MIMO receiver as reported in [57].

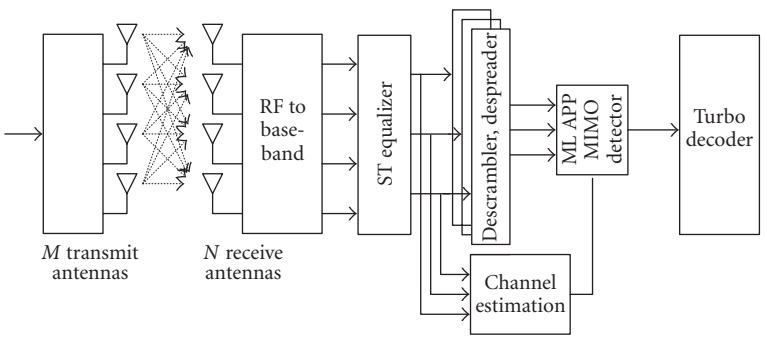

FIGURE 37.16. HSDPA MIMO receiver for frequency-selective fading channel as reported in [60].

spreading codes of length 16 allows a data rate of 19.2 Mbps. The detector outputs are derived by approximating the log-likelihood ratios of the a posteriori probability (APP). Hence, this algorithm is called ML-APP detector.

Different MIMO 3GPP-HSDPA detectors have been reported in [57, 58, 59, 60] by the same group of authors. As an example, Figure 37.16 shows the block diagram of a 28.8 Mbps 4×4 MIMO 3GPP-HSDPA receiver [60]. This approach is capable of handling frequency-selective channels by applying an ST equalizer at chip level. A normalized least mean square (LMS) algorithm is used for the estimation of the equalizer coefficients. A peak data rate of 28.8 Mbps can be achieved by using 15 spreading codes and a 4×4 system.

Implementation examples of square root MIMO detection algorithms are reported in [48, 61, 62].

All these chip implementations and prototypes depict important steps towards cost efficient integrated MIMO HSDPA solutions. They play a crucial role in the standardization process, which is currently in progress. Note that final MIMO HSDPA solutions have to be downwards compatible to current 3GPP standard releases.

37.5. Summary

The development of MIMO techniques for UMTS is a major field of ongoing research at university and industry level. MIMO algorithms typically exhibit

extremely high complexity. Therefore, the exploration of low-complexity solutions is highly desirable with respect to today's semiconductor technology implementations. A number of prototype systems and chip solutions have already been reported. Most of these solutions act on simplified assumptions, for example, flat-fading channels. Nevertheless, these first prototypes are extremely helpful in identifying problems inherent to MIMO signal processing. Thus, they are driving the standardization process of UMTS MIMO systems.

There is only little work available that specifically deals with MIMO compliant RF front ends. The straight forward approach of a MIMO RF front-end implementation is the use of a dedicated receiver per antenna. This approach shows significant area and power saving potential, and therefore tends to be the most favored technology.

Acknowledgment

This work has been funded by the Christian Doppler Pilot Laboratory for Design Methodology of Signal Processing Algorithms.

Abbreviations

3GGP	3rd-Generation Partnership Project
MIMO	Multiple-input multiple-output
SISO	Single-input single-output
RFIC	Radio frequency integrated circuit
ST	Space-time
ADC	Analog-to-digital converter
AGC	Automatic gain control
RRC	Root raised cosine
GSM	Global system for mobile communication
ACS	Adjacent channel selectivity
PAR	Peak-to-average ratio
PAE	Power added efficiency
SAW	Surface acoustic wave
MIPS	Million instructions per second
UMTS-FDD	UMTS-frequency division duplex
BER	Bit error rate
BLER	Block error rate
W-CDMA	Wideband code division multiple access
CCDF	Complementary cumulative probability density function
DPDCH	Dedicated physical data channel
CPICH	Common pilot channel
CCPCH	Common control physical channel
PICH	Paging indicator channel
SCH	Synchronization channel
SF	Spreading factor
TDMA	Time division multiple access
FDMA	Frequency division multiple access

LO	Local oscillator
LNA	Low noise amplifier
IP2	Intercept point
OSR	Oversampling rate
MRC	Maximum ratio combining
MUI	Multiuser interference
MMSE	Minimum mean square error
MVDR	Minimum variance distortionless response
FPM	Finger position search and management
PCG	Pilot code generator
ML	Maximum likelihood
ZF	Zero forcing
V-BLAST	Vertical Bell Laboratories Layered Space-Time
SPICH	Secondary pilot channel
HSDPA	High-speed downlink packet access
APP	A posteriori probability

Bibliography

[1] 3GPP, *Technical Specification Group Radio Access Networks*, RAN WG1, http://www.3gpp.org.

[2] C. Nicol and M. Cooke, "Integrated circuits for 3GPP mobile wireless systems," in *Proc. IEEE Custom Integrated Circuits Conference (CICC '02)*, pp. 381–388, Orlando, Fla, USA, May 2002.

[3] J. Hausner, "Integrated circuits for next generation wireless systems," in *Proc. IEEE European Solid-State Circuits Conference (ESSCIRC '01)*, pp. 26–29, Villach, Austria, September 2001.

[4] 3GPP, "User Equipment (UE) radio transmission and reception (FDD)," Technical Specification TS 25.101, V5.9.0, December 2003.

[5] L. Maurer, C. Lanschützer, A. Springer, and R. Weigel, "System-defined design and performance of RFICs for W-CDMA mobile radio terminals," *Elektrotechnik und Informationstechnik*, pp. 487–492, October 2001.

[6] L. Maurer, W. Schelmbauer, H. Pretl, et al., "Influence of receiver front end nonlinearities on W-CDMA signals," in *Proc. Asia-Pacific Microwave Conference (APMC 00)*, pp. 249–252, Sydney, Australia, December 2000.

[7] L. Maurer, W. Schelmbauer, H. Pretl, Z. Boos, R. Weigel, and A. Springer, "Impact of IF-SAW filtering on the performance of a W-CDMA receiver," in *Proc. IEEE Ultrasonics Symposium*, vol. 1, pp. 375–378, San Juan, Puerto Rico, October 2000.

[8] L. Maurer, W. Schelmbauer, H. Pretl, A. Springer, and R. Weigel, "Impact of channel select filtering on W-CDMA signal properties," in *Proc. SBMO/IEEE MTT-S International Microwave and Optoelectronics Conference (IMOC '01)*, vol. 1, pp. 39–42, Belem, Brasil, August 2001.

[9] H. Pretl, L. Maurer, W. Schelmbauer, R. Weigel, B. Adler, and J. Fenk, "Linearity considerations of W-CDMA front-ends for UMTS," in *Proc. IEEE MTT-S International Microwave Symposium Digest*, vol. 1, pp. 433–436, Boston, Mass, USA, June 2000.

[10] W. Thomann, J. Fenk, R. Hagelauer, and R. Weigel, "Fully integrated W-CDMA IF receiver and IF transmitter including IF synthesizer and on-chip VCO for UMTS mobiles," *IEEE J. Solid-State Circuits*, vol. 36, no. 9, pp. 1407–1419, 2001.

[11] A. Springer, L. Maurer, and R. Weigel, "Rf system concepts for highly integrated rfics for w-cdma mobile radio terminals," *IEEE Trans. Microwave Theory Tech.*, vol. 50, no. 1, pp. 254–267, 2002.

[12] J. H. Mikkelsen, T. E. Kolding, T. Larsen, T. Klingenbrunn, K. I. Pedersen, and P. E. Mogensen, "Feasibility study of DC offset filtering for UTRA-FDD/WCDMA direct-conversion receiver," in *Proc. 17th IEEE NORCHIP Conference*, pp. 34–39, Oslo, Norway, November 1999.

[13] W. Schelmbauer, H. Pretl, L. Maurer, et al., "An analog baseband chain for a UMTS zero-IF receiver in a 75 GHz SiGe BiCMOS technology," in *Proc. IEEE MTT-S International Microwave Symposium Digest*, vol. 1, pp. 13–16, Seattle, Wash, USA, June 2002.

[14] H. Tsurumi, M. Soeya, H. Yoshida, T. Yamaji, H. Tanimoto, and Y. Suzuki, "System-level compensation approach to overcome signal saturation, dc offset, and 2nd-order nonlinear distortion in linear direct conversion receiver," *IEICE Trans. Electron.*, vol. E82-C, no. 5, pp. 708–716, 1999.

[15] M. Goldfarb, W. Palmer, T. Murphy, et al., "Analog baseband IC for use in direct conversion W-CDMA receivers," in *Proc. IEEE Radio Frequency Integrated Circuits Symposium (RFIC '00)*, pp. 79–82, Boston, Mass, USA, June 2000.

[16] K. Itoh, T. Katsura, H. Nagano, et al., "2 GHz band even harmonic type direct conversion receiver with ABB-IC for W-CDMA mobile terminal," in *Proc. IEEE MTT-S International Microwave Symposium Digest*, vol. 3, pp. 1957–1960, Boston, Mass, USA, June 2000.

[17] A. Pärssinen, J. Jussila, J. Ryynänen, L. Sumanen, and K. Halonen, "A wide-band direct conversion receiver for wcdma applications," in *Proc. IEEE International Solid-State Circuits Conference (ISSCC '99)*, pp. 220–221, San Francisco, Calif, USA, February 1999.

[18] A. Pärssinen, J. Jussila, J. Ryynänen, L. Sumanen, and K. A. I. Halonen, "A 2-GHz wide-band direct conversion receiver for WCDMA applications," *IEEE J. Solid-State Circuits*, vol. 34, no. 12, pp. 1893–1903, 1999.

[19] B. Sam, "Direct conversion receiver for wide-band CDMA," in *Proc. Spring Wireless Symposium/Portable by Design*, San Jose, Calif, USA, February 2000.

[20] H. Pretl, W. Schelmbauer, B. Adler, L. Maurer, J. Fenk, and R. Weigel, "A SiGe-bipolar down-conversion mixer for a UMTS zero-IF receiver," in *Proc. Bipolar/BiCMOS Circuits and Technology Meeting*, pp. 40–43, Minneapolis, Minn, USA, September 2000.

[21] H. Pretl, W. Schelmbauer, L. Maurer, et al., "A W-CDMA zero-IF front-end for UMTS in a 75 GHz SiGe BiCMOS technology," in *Proc. IEEE Radio Frequency Integrated Circuits Symposium (RFIC '01)*, pp. 9–12, Phoenix, Ariz, USA, May 2001.

[22] K.-Y. Lee, S.-W. Lee, Y. Koo, et al., "Full-CMOS 2-GHz WCDMA direct conversion transmitter and receiver," *IEEE J. Solid-State Circuits*, vol. 38, no. 1, pp. 43–53, 2003.

[23] J. Rogin, I. Kouchev, G. Brenna, D. Tschopp, and Q. Huang, "A 1.5-V 45-mW direct-conversion WCDMA receiver IC in 0.13-μm CMOS," *IEEE J. Solid-State Circuits*, vol. 38, no. 12, pp. 2239–2248, 2003.

[24] L. Harju, M. Kuulusa, and J. Nurmi, "Flexible implementation of a WCDMA RAKE receiver," in *Proc. IEEE Workshop on Signal Processing Systems (SIPS '02)*, pp. 177–182, San Diego, Calif, USA, October 2002.

[25] C. Brunner, W. Utschick, and J. A. Nossek, "Exploiting the short-term and long-term channel properties in space and time: eigenbeamforming concepts for the BS in WCDMA," *European Trans. Telecommunications*, vol. 12, no. 5, pp. 365–378, 2001.

[26] W. Wenjie, J. Bofeng, and Y. Qinye, "A new scheme of 2-D RAKE receiver based on space-time searching and tracking algorithm," in *Proc. 5th IEEE International Signal Processing Proceedings (WCCC-ICSP '00)*, vol. 3, pp. 1750–1753, Beijing, China, August 2000.

[27] C. Brunner, M. Haardt, and J. A. Nossek, "On space-time RAKE receiver structures for WCDMA," in *Proc. 33rd IEEE Asilomar Conference on Signals, Systems, and Computers*, vol. 2, pp. 1546–1551, Pacific Grove, Calif, USA, October 1999.

[28] D. H. Evans, D. L. Raynes, A. G. Spencer, and P. Mendizabal, "Development and simulation of a single standard MIMO transceiver," IST-2001-32125 FLOWS, Deliverable Number: D9 version 2, June 2003.

[29] J. Ylitalo, A. Pollard, M. Heikkila, and J. R. Fonollosa, "Cost versus benefit trade-offs of multi-element transmit and receive," Tech. Rep. D5.1, European IST-1999-11729 Project METRA, Germany, August 2001.

[30] M. Rupp, M. Guillaud, and S. Das, "On MIMO decoding algorithms for UMTS," in *Proc. 35th Asilomar Conference on Signals, Systems and Computers*, vol. 2, pp. 975–979, Pacific Grove, Calif, USA, November 2001.

[31] A. Adjoudani, E. Beck, A. Burg, et al., "Prototype experience for MIMO BLAST over third-generation wireless system," *IEEE J. Select. Areas Commun.*, vol. 21, no. 3, pp. 440–451, 2003, Special Issue JSAC on MIMO Systems.

[32] 3GPP, "Tx diversity solutions for multiple antennas," Tech. Rep. TR 25.869, V1.2.0, August 2003.

[33] 3GPP, "Physical layer aspects of UTRA high speed downlink packet access," Tech. Rep. TR 25.848, V4.0.0, March 2001.

[34] A. Burg, E. Beck, M. Rupp, D. Perels, N. Felber, and W. Fichtner, "FPGA implementation of a MIMO receiver front-end for the UMTS downlink," in *Proc. IEEE International Zurich Seminar on Broadband Communications, Access, Transmission, Networking,* pp. 8-1–8-6, Zurich, Switzerland, February 2002.

[35] M. Guillaud, A. Burg, M. Rupp, E. Beck, and S. Das, "Rapid prototyping design of a 4×4 BLAST-over-UMTS system," in *Proc. 35th IEEE Asilomar Conference on Signals, Systems and Computers*, vol. 2, pp. 1256–1260, Pacific Grove, Calif, USA, November 2001.

[36] W. Ha, J. Bae, and J. Park, "A code grouping interference cancellation receiver in OVSF DS-CDMA downlink," in *Proc. 8th IEEE International Conference on Communication Systems (ICCS '02)*, vol. 2, pp. 697–700, Singapore, November 2002.

[37] H. Lou, M. Rupp, R. L. Urbanke, et al., "Efficient implementation of parallel decision feedback decoders for broadband applications," in *Proc. 6th IEEE International Conference on Electronics, Circuits and Systems (ICECS '99)*, vol. 3, pp. 1475–1478, Pafos, Cyprus, September 1999.

[38] M. Rupp and J. Balakrishnan, "Efficient chip design for pulse shaping," in *Proc. IEEE Workshop on Signal Processing Advances in Wireless Communications (SPAWC '99)*, pp. 304–307, Annapolis, Md, USA, May 1999.

[39] M. Rupp and H. Lou, "On efficient multiplier-free implementation of channel estimation and equalization," in *Proc. IEEE Global Telecommunications Conference, (GLOBECOM '00)*, vol. 1, pp. 6–10, San Francisco, Calif, USA, December 2000.

[40] U. Fincke and M. Pohst, "Improved methods for calculating vectors of short length in a lattice, including a complexity analysis," *Math. of Comput.*, vol. 44, no. 170, pp. 463–471, 1985.

[41] H. Artés, D. Seethaler, and F. Hlawatsch, "Efficient detection algorithms for MIMO channels: a geometrical approach to approximate ML detection," *IEEE Trans. Signal Processing*, vol. 51, no. 11, pp. 2808–2820, 2003, Special Issue on Signal Processing for Multiple-Input Multiple-Output (MIMO) Wireless Communications Systems.

[42] M. Rupp, G. Gritsch, and H. Weinrichter, "Approximate ML decoding with very low complexity," in *Proc. IEEE International Conference on Acoustics, Speech, and Signal Processing (ICASSP '04)*, pp. 809–812, Montreal, Canada, May 2004.

[43] A. Viterbi, "Error bounds for convolutional codes and an asymptotically optimum decoding algorithm," *IEEE Trans. Inform. Theory*, vol. 13, no. 2, pp. 260–269, 1967.

[44] C. Berrou, A. Glavieux, and P. Thitmajshima, "Near Shannon limit error-correcting coding and decoding: turbo-codes," in *Proc. IEEE International Conference on Communications (ICC '93)*, vol. 2, pp. 1064–1070, Geneva, Switzerland, May 1993.

[45] G. Kreiselmaier, T. Vogt, N. Wehn, and F. Berens, "Combined turbo and convolutional decoder architecture for UMTS wireless applications," in *Proc. 15th IEEE Symposium on Integrated Circuits and Systems Design (SBCCI '02)*, pp. 337–342, Porto Alegre, RS, BRAZIL, September 2002.

[46] M. J. Thul, F. Gilbert, T. Vogt, G. Kreiselmaier, and N. Wehn, "A scalable system architecture for high-throughput turbo-decoders," in *Proc. IEEE Workshop on Signal Processing Systems, (SIPS '02)*, pp. 152–158, San Diego, Calif, USA, October 2002.

[47] J. P. Woodard, "Implementation of high rate turbo decoders for third generation mobile communications," in *Proc. IEE Colloquium on Turbo Codes in Digital Broadcasting—Could It Double Capacity?*, pp. 12/1–12/6, London, UK, November 1999.

[48] B. Hassibi, "A fast square-root implementation for BLAST," in *Proc. 34th IEEE Asilomar Conference on Signals, Systems and Computers*, vol. 2, pp. 1255–1259, Pacific Grove, Calif, USA, November 2000.

[49] S. Haykin, *Adaptive Filter Theory*, Prentice Hall, New Jersey, NJ, USA, 2002.

[50] B. Parhami, *Computer Arithmetic*, Oxford University Press, Oxford, UK, 2000.

[51] M. Rupp, "On the influence of uncertainties in MIMO decoding algorithms," in *Proc. 36th Asilomar Conference on Signals, Systems and Computers*, vol. 1, pp. 570–574, Pacific Grove, Calif, USA, November 2002.

[52] 3GPP, "Multiple-input multiple-output in UTRA," Tech. Rep. TR 25.876, V1.3.0, February 2004.

[53] E. Aschbacher, S. Caban, C. Mehlführer, G. Maier, and M. Rupp, "Design of a flexible and scalable 4×4 MIMO testbed," in *Proc. 11th Digital Signal Processing Workshop*, Taos Ski Valley, NM, USA, August 2004.

[54] V. Jungnickel, "Towards real-time processing in MIMO communication systems," in *European Microwave Week*, Munich, Germany, October 2003.

[55] J. Rinas, A. Scherb, T. Haase, and K. D. Kammeyer, "A hardware demonstrator for MIMO- communication systems: application to blind source separation," in *European Summer School on ICA—from Theory to Applications*, Berlin, Germany, June 16–17, 2003.

[56] A. O. Boukalov and S. Haggman, "System aspects of smart-antenna technology in cellular wireless communications-an overview," *IEEE Trans. Microwave Theory Tech.*, vol. 48, no. 6, pp. 919–929, 2000.

[57] D. Garrett, L. Davis, and G. Woodward, "19.2 Mbit/s 4×4 BLAST/MIMO detector with soft ML outputs," *Electronics Letters*, vol. 39, no. 2, pp. 233–235, 2003.

[58] M. Bickerstaff, L. Davis, C. Thomas, D. Garrett, and C. Nicol, "A 24 Mb/s radix-4 logMAP turbo decoder for 3GPP-HSDPA mobile wireless," in *Proc. IEEE International Solid-State Circuits Conference (ISSCC '03)*, vol. 1, pp. 150–484, San Francisco, Calif, USA, February 2003.

[59] L. Davis, D. Garrett, G. Woodward, M. Bickerstaff, and F. Mullany, "System architecture and ASICs for a MIMO 3GPP-HSDPA receiver," in *Proc. 57th IEEE Semiannual Vehicular Technology Conference (VTC '30)*, vol. 2, pp. 818–822, Jeju, Seoul, Korea, April 2003.

[60] D. Garrett, G. Woodward, L. Davis, G. Knagge, and C. Nicol, "A 28.8 Mb/s 4×4 MIMO 3G high-speed downlink packet access receiver with normalized least mean square equalization," in *Proc. IEEE International Solid-State Circuits Conference (ISSCC '04)*, vol. 1, pp. 420–536, San Francisco, Calif, USA, February 2004.

[61] Z. Guo and P. Nilsson, "A VLSI implementation of MIMO detection for future wireless communications," in *Proc. 14th IEEE International Symposium on Personal, Indoor and Mobile Radio Communications (PIMRC '03)*, vol. 2, pp. 697–700, Beijing, China, September 2003.

[62] Z. Guo and P. Nilsson, "A low-complexity VLSI architecture for square root MIMO detection," in *Proc. IASTED International Conference Circuits, Signals, and Systems (CSS '03)*, Cancun, Mexico, May 2003.

[63] R. Peterson, R. Ziemer, and D. Borth, *Introduction to Spread Spectrum Communications*, Prentice Hall, Upper Saddle River, NJ, USA, 1995.

Klemens Freudenthaler: Hardware/Software Systems Engineering, University of Applied Sciences of Upper Austria, 4232 Hagenberg, Austria

Email: klemens.freudenthaler@fh-hagenberg.at

Mario Huemer: Hardware/Software Systems Engineering, University of Applied Sciences of Upper Austria, 4232 Hagenberg, Austria

Email: mario.huemer@fh-hagenberg.at

Linus Maurer: DICE GmbH & Co KG, 4040 Linz, Austria

Email: linus.maurer@infineon.com

Steffen Paul: Infineon Technologies AG, 81669 Munich, Germany

Email: steffen.paul@infineon.com

Markus Rupp: Institut für Nachrichtentechnik und Hochfrequenztechnik, Technische Universität Wien (TU Wien), 1040 Wien, Austria

Email: markus.rupp@tuwien.ac.at

38 MIMO systems for the HSDPA FDD mode UMTS service

Alba Pagès-Zamora and Markku J. Heikkilä

38.1. Introduction

The high speed downlink packet access (HSDPA) concept was first standardized by the Third Generation Partnership Project (3GPP) in UMTS Release 5 specifications [1]. It considers several enhancements for a downlink shared channel to provide UTRA with a downlink packet access service with data rates up to 10 Mbps. These enhancements are (a) adaptive modulation and coding (AMC), (b) Hybrid Automatic Repeat on reQuest (H-ARQ), (c) fast cell selection, (d) MIMO antenna processing, and (e) stand alone DSCH. The first two technologies were under study in Release 5, the MIMO antenna processing technology was initially scheduled for Release 6, and the fast cell selection and stand alone DSCH technologies were postponed for future evolutions.

This chapter focuses on the incorporation of MIMO techniques in the HSDPA service of the UMTS FDD mode. First, those features of the HSDPA service that are more relevant for the MIMO systems are summarized. Then, several MIMO transmitter and receiver schemes fully compliant with the HSDPA specifications are proposed for evaluating the MIMO systems in the HSDPA service. Some simulation results are also included in order to show their performance under several fading conditions and mobile speeds. The chapter ends with the conclusions.

38.2. HSDPA features and physical layer HS-DSCH structure

The HSDPA service is based on a high-speed downlink shared channel (HS-DSCH) shared by several users in the time and code domains. The spreading factor for the HSDPA physical channels is 16. One code is for the CPICH channel, up to 15 codes are for the HSDPA users, and the rest are for dedicated channels usually for speech services. Figure 38.1 illustrates an example of the time-code multiplex division of 3 HSDPA users. In this example, 10 codes are assigned to the HSDPA service and 5 would remain for other services. In the FDD mode, the HS-DSCH frame structure is organized in time transmission intervals (TTIs) of

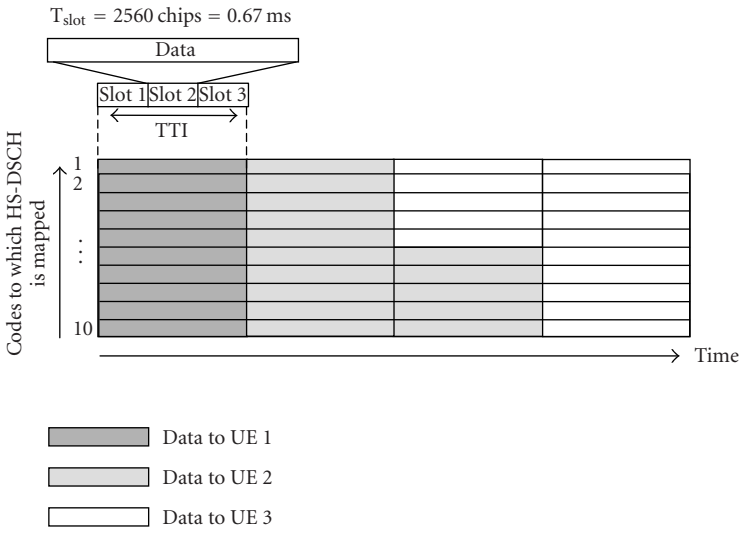

FIGURE 38.1. HSDPA mapping to physical channels with fixed spreading code and shared by means of time multiplex.

2 milliseconds, which consist of 3 slots with a length of 0.67 milliseconds and with 2560 chips in each slot.

As mentioned before, the AMC and H-ARQ technologies were studied for the HSDPA service in UMTS/UTRA Release 5. The AMC technique allows updating the modulation and channel coding configuration at each TTI according to the channel propagation conditions. The purpose is to increase the overall system throughput assigning higher rates to those users under the most favorable channel conditions and lower rates to the users experiencing poor channel conditions. The H-ARQ technique allows the retransmission of those packets erroneously detected by the HSDPA user. Both technologies rely on the HS-DSCH associated uplink channel that carries information about the channel state and the ACK/NACK of the received packet. The details of the codification of this feedback information can be found in [2]. According to this information sent by the HSDPA user and the network state information, the Node B schedules the HSDPA transmission.

The transport channel coding structure for the HS-DSCH channel is shown in Figure 38.2. A CRC of 24 bits is attached to the information bits before the TTI is segmented into code blocks. The CRC polynomial and the code block segmentation details are specified in [3]. Then, a turbo encoder with coding rate 1/3 [2] with the internal interleaver given in [3] encodes each code block. Other code rates based on that turbo encoder can be obtained using puncturing or repetition. After channel encoding, the TTI is mapped to several physical channels each one with a different spreading code. The bit rearrangement stage and the spreading/scrambling and modulation procedures can all be found in [2]. The modulations specified for the HSDPA service are QPSK and 16-QAM.

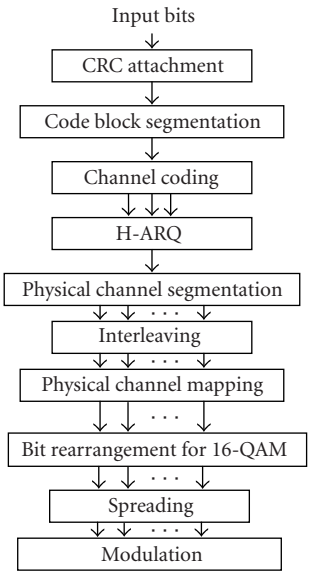

Figure 38.2. Transport channel coding structure for HS-DSCH.

38.3. HSDPA MIMO transmitter techniques

The main interest of MIMO techniques is twofold. On the one hand, the diversity MIMO techniques improve the transmission reliability since the multiple antennas are useful to increase the diversity gain [4]. On the other hand, the layered MIMO techniques increase the data rate by means of spatially multiplexing several data streams. Since the HSDPA service aims at providing a high-speed data service, the main motivation of MIMO techniques for HSDPA is to achieve, or even exceed, the 10 Mbps upper limit data rate of the single-input single-output channel under sufficient reliability conditions. However, it is widely accepted that the multiplexing gain cannot be increased without a penalization in the diversity gain [5]. Therefore, both diversity and layered MIMO schemes should be evaluated when specifically developed for the HSDPA service. The MIMO transmitter schemes selected to be tested for the HSDPA service are four classical MIMO space and/or time coding schemes:

(1) space-time transmit diversity (STTD),
(2) double-STTD (D-STTD),
(3) vertical-BLAST (V-BLAST),
(4) linear dispersion codes (LDC).

The STTD technique [6] is an orthogonal space-time block code for a MIMO configuration with $M = 2$ antennas at the transmitter and $N = 1$ antennas at the receiver (although more receive antennas can be used). The D-STTD technique is based on the STTD technique for $M = 4$. It doubles the data rate but it loses the orthogonal properties of the STTD code. The third proposed scheme is V-BLAST,

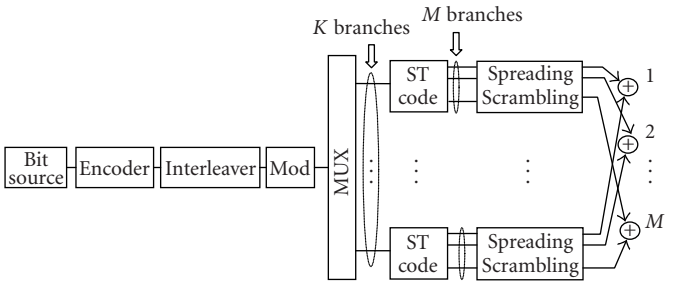

FIGURE 38.3. Transmitter block diagram.

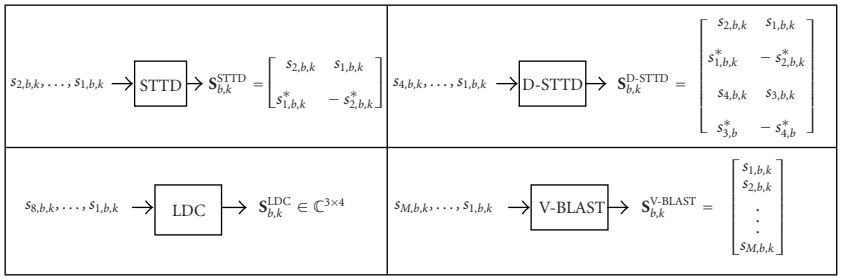

FIGURE 38.4. Specification of the ST coding block of Figure 38.3 for the four proposed MIMO transmission schemes.

which multiplexes the data symbols in as many streams as transmit antennas. The theoretical capacity of this layered MIMO scheme was studied in [7] assuming the receiver detects the different data streams by means of a successive interference canceller algorithm. Finally, a specific LDC for $M = 3$ and $N = 2$ is proposed [8]. The main features of the LDC codes are their near-optimal capacity properties and the linear relation that simplifies the receiver design.

The transmitter scheme for each HSDPA user is shown in Figure 38.3. The data bits are first grouped into code blocks and then channel encoded. After the interleaving, the signal is modulated and then the symbols are multiplexed in K branches, with K the number of spreading codes assigned to that HSDPA user. The symbols corresponding to each branch are grouped in B blocks of Q symbols. Each block is either space-time encoded (STTD, D-STTD, or LDC) or multiplexed into several parallel streams (V-BLAST). It is important to remark that although V-BLAST is not usually denoted as a space-time coding technique, the "ST code" name will be used for all the schemes in this section. Finally, the spreading and scrambling procedures are applied before the signal is transmitted.

The ST coding block of Figure 38.3 encodes the Q symbols of the bth block of code k, denoted by $\{s_{(q,b,k)}\ \forall q = 1, \ldots, Q\}$, in a matrix $\mathbf{S}_{b,k} \in \mathbb{C}^{M\times T}$, with T being the number of channel uses before spreading. Figure 38.4 specifies the $\mathbf{S}_b$ matrix for each MIMO transmission scheme (for the LDC code see details in [8]). Table 38.1 includes the $\{Q, T, M, N\}$ values.

Table 38.1. Selected $\{Q, T, M, N\}$ values for each transmitter scheme.

	STTD	D-STTD	V-BLAST	LDC
Q	2	4	2	8
T	2	2	1	4
M	2	4	2	3
N	{1,2}	{1,2}	2	2

Now we want to show that the signal at the receiver depends linearly on the real and imaginary parts of the symbols. For that purpose, first note that matrix $\mathbf{S}_{b,k}$ could be expressed as follows:

$$\mathbf{S}_{b,k} = \sum_{q=1}^{Q} \left(\mathbf{A}_q \operatorname{Re}\left\{s_{(q,b,k)}\right\} + j\mathbf{B}_q \operatorname{Im}\left\{s_{(q,b,k)}\right\}\right), \tag{38.1}$$

with $\{s_{(q,b,k)}\ \forall q = 1, \ldots, Q\}$ the Q symbols of block b and code k, and with an appropriate definition of matrices $\{\mathbf{A}_q, \mathbf{B}_q\} \in \mathbb{R}^{M\times T}$ specific for each transmitter scheme [8]. After the spreading and scrambling procedure, the chip-level signal transmitted through the M antennas corresponding to block b can be gathered in matrix $\mathbf{X}_b \in \mathbb{C}^{M\times TF}$, with F the spreading factor. Assuming K active spreading codes,

$$\mathbf{X}_b = \sum_{k=1}^{K} \left(\mathbf{S}_{b,k} \otimes \mathbf{c}_k^T\right) \odot \mathbf{C}_b^{\text{scr}}, \tag{38.2}$$

where $\otimes$ denotes the Kronecker product, $\odot$ the element-by-element matrix product, $\mathbf{c}_k \in \mathbb{C}^{F\times 1}$ is the vector with the Walsh sequence of the kth spreading code, and $\mathbf{C}_b^{\text{scr}} \in \mathbb{C}^{M\times TF}$ is a matrix defined as follows:

$$\mathbf{C}_b^{\text{scr}} = 1 \cdot \left(\mathbf{c}_b^{\text{scr}}\right)^T, \tag{38.3}$$

and it applies the long complex scrambling code of vector $\mathbf{c}_b^{\text{scr}} \in \mathbb{C}^{TF\times 1}$. For convenience, matrix $\mathbf{X}_b$ is stacked in columns to build vector $\mathbf{x}_b \in \mathbb{C}^{MTF\times 1}$ as follows:

$$\mathbf{x}_b = \operatorname{vec}\left(\mathbf{X}_b\right) = \mathbf{D}_b \cdot \mathbf{s}_b, \tag{38.4}$$

with $\mathbf{D}_b \in \mathbb{C}^{MTF\times 2QK}$ and $\mathbf{s}_b \in \mathbb{R}^{2QK\times 1}$ defined, respectively, as

$$\begin{aligned}
\mathbf{D}_b = [\ & \operatorname{vec}\left(\left(\mathbf{A}_1 \otimes \mathbf{c}_1^T\right) \odot \mathbf{C}_b^{\text{scr}}\right) \cdots \operatorname{vec}\left(\left(\mathbf{A}_Q \otimes \mathbf{c}_1^T\right) \odot \mathbf{C}_b^{\text{scr}}\right) \\
& \cdots j \operatorname{vec}\left(\left(\mathbf{B}_1 \otimes \mathbf{c}_1^T\right) \odot \mathbf{C}_b^{\text{scr}}\right) \cdots j \operatorname{vec}\left(\left(\mathbf{B}_Q \otimes \mathbf{c}_1^T\right) \odot \mathbf{C}_b^{\text{scr}}\right) \\
& \cdots \operatorname{vec}\left(\left(\mathbf{A}_1 \otimes \mathbf{c}_2^T\right) \odot \mathbf{C}_b^{\text{scr}}\right) \cdots j \operatorname{vec}\left(\left(\mathbf{B}_Q \otimes \mathbf{c}_K^T\right) \odot \mathbf{C}_b^{\text{scr}}\right)], \\
\mathbf{s}_b = [\ & \operatorname{Re}\left\{s_{(1,b,1)}\right\} \cdots \operatorname{Re}\left\{s_{(Q,b,1)}\right\} \operatorname{Im}\left\{s_{(1,b,1)}\right\} \\
& \cdots \operatorname{Im}\left\{s_{(Q,b,1)}\right\} \operatorname{Re}\left\{s_{(1,b,2)}\right\} \cdots \operatorname{Im}\left\{s_{(Q,b,K)}\right\}]^T.
\end{aligned} \tag{38.5}$$

For each block b, the transmitter sends vector $\mathbf{x}_b$ through the MIMO channel and vector $\mathbf{y}_b \in \mathbb{C}^{NTF\times 1}$ is received. We now define vector $\mathbf{x} \in \mathbb{C}^{BMTF\times 1}$ and vector $\mathbf{y} \in \mathbb{C}^{BNTF\times 1}$ as follows:

$$\mathbf{x} = \left[\mathbf{x}_1^T \mathbf{x}_2^T \cdots \mathbf{x}_B^T\right]^T, \qquad \mathbf{y} = \left[\mathbf{y}_1^T \mathbf{y}_2^T \cdots \mathbf{y}_B^T\right]^T. \tag{38.6}$$

Assuming a frequency-selective MIMO channel with L resolvable paths with a channel impulse response defined by the matrix set $\{\mathbf{H}_{(l)} \in \mathbb{C}^{N\times M};\ \forall l = 1,\ldots,L\}$,[1] the received chip-level signal is equal to

$$\mathbf{y} = \mathbf{H}\mathbf{x} + \mathbf{w}, \tag{38.7}$$

with $\mathbf{H} \in \mathbb{C}^{BNTF\times BMTF}$ being the block convolutional matrix built with $\{\mathbf{H}_{(l)}\ \forall l = 1,\ldots,L\}$ and $\mathbf{w}$ the additive noise. This additive noise models the intracell interference due to non-HSDPA channels, the intercell interference, and the thermal noise. Equations (38.7), (38.6), and (38.4) show the linear relation between the received signal and the in-phase and in-quadrature components of the symbols. Therefore, relatively simple schemes can be proposed in the receiver design.

38.4. HSDPA MIMO receiver techniques

There are several sources of interference in HSDPA systems which combined with a multiantenna transmission technique and a high-order modulation form a difficult environment for a mobile handset. A main source of interference is multipath propagation in the radio channel. Although the used Walsh spreading codes are orthogonal, the received spreading waveform is a convolution of the channel and the original spreading code. The distorted spreading codes are not orthogonal causing signal leak between code channels. Also the fact that a neighbouring cell can use the same carrier frequency makes it difficult to apply higher-order modulation near the cell edge. The service range of high-speed connections may thus be very limited. The third type of interference is the interference between the transmit antennas of a MIMO downlink. Layered MIMO transmission techniques, such as BLAST, completely rely on the receiver's ability to separate the parallel data streams, while diversity MIMO transmission applies an orthogonal or near-orthogonal block code to provide the receiver with diversity while trying to avoid interantenna interference.

The emphasis in this section is on practical HSDPA MIMO receivers that are implementable with reasonable complexity and also on more advanced receivers. In both cases the special requirements set by the current HSDPA air-interface are taken into account.

[1] If $L = 1$, then the channel is frequency nonselective.

38.4.1. RAKE

A RAKE receiver collects the signal energy given knowledge of the channel impulse response and spreading codes. The RAKE receiver can be implemented using a bank of code correlators the outputs of which are maximal-ratio combined using estimated channel coefficients.

We define the vector $\mathbf{c}_{k,b,t} \in \mathbb{C}^{F\times 1}$ which gathers the spreading and scrambling codes corresponding to code channel k and tth channel use of ST code block b, with $t = 1,\ldots,T$. For each channel use t of block b, the output of the correlator for code k decoupled to receive antenna n and synchronized to multipath l can be written as

$$z_{n,l,k}(bT+t) = \mathbf{c}_{k,b,t}^{\mathrm{H}} \cdot \mathbf{y}_{n,l}(bT+t), \tag{38.8}$$

where $\mathbf{y}_{n,l}(bT+t) \in \mathbb{C}^{F\times 1}$ is obtained by taking chip-spaced samples from (38.7) corresponding to symbol interval $bT+t$ and multipath delay τ_l. The correlator output carries information about the desired symbol through the applied space-time code spanning over T symbol intervals. For instance, the correlator outputs for STTD-encoded signal of the kth code can be expressed as ($T = 2$)

$$\begin{aligned} z_{n,l,k}(bT) &= h_{1,n,l}s_{2,b,k} + h_{2,n,l}s_{1,b,k}^{*} + \eta_{n,l,k}(bT), \\ z_{n,l,k}(bT+1) &= h_{1,n,l}s_{1,b,k} - h_{2,n,l}s_{2,b,k}^{*} + \eta_{n,l,k}(bT+1). \end{aligned} \tag{38.9}$$

$h_{m,n,l}$ is the channel coefficient from antenna m to antenna n through multipath l (time indices neglected) and $\eta_{n,l,k}$ is noise. Correlator outputs for all N antennas and L multipaths can be stacked into a single vector, $\mathbf{z}_k(bT+t) \in \mathbb{C}^{NL\times 1}$ for $t = 1,2$. Correspondingly arranged channel coefficient vector $\mathbf{h}_m$ holds the channel coefficients corresponding to transmit antenna m. STTD decoder generates estimates for the data symbols as

$$\begin{aligned} \hat{s}_{1,b,k} &= \mathbf{h}_1^{\mathrm{H}}\mathbf{z}_k(bT+1) + \left(\mathbf{h}_2^{\mathrm{H}}\mathbf{z}_k(bT)\right)^{*}, \\ \hat{s}_{2,b,k} &= \mathbf{h}_1^{\mathrm{H}}\mathbf{z}_k(bT) - \left(\mathbf{h}_2^{\mathrm{H}}\mathbf{z}_k(bT+1)\right)^{*}. \end{aligned} \tag{38.10}$$

The RAKE receiver does not try to suppress the various sources of interference and relies on the interference suppression due to the despreading operation. In case of diversity MIMO transmission, the orthogonality of the underlying space-time block code (such as the STTD code) suppresses most of the interantenna interference, but the interference caused by a multipath channel may prohibit the use of higher-order modulation. Moreover, the interantenna interference due to layered MIMO transmission causes inadequate performance of the receiver even in flat channels.

38.4.2. Linear space-time equalisers

Linear channel equalisation can be used for restoration of the orthogonality of the spreading waveforms. When equipped with multiple receive antennas, it is

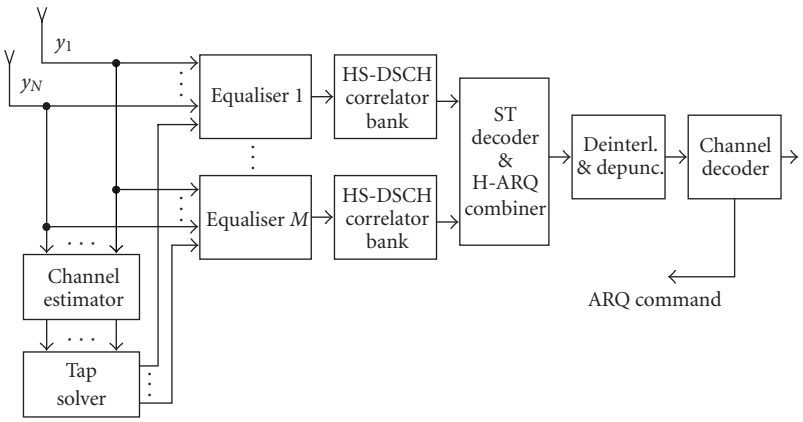

FIGURE 38.5. Linear multiantenna space-time equaliser for MIMO HSDPA channels.

also possible to suppress interantenna interference effectively through linear space-time processing.

A key point in utilization of linear equalisation is to notice that, despite the fact that multiuser chip vector $\mathbf{x}$ in (38.7) is formed as a sum of multiple spreading codes each modulated by its own data symbol, it is enough to estimate the transmitted multiuser chip vector to remove the interference from other code channels. That is, information about the active spreading codes is not necessary if the transmitted chip stream is considered to be a random sequence. This assumption is also statistically valid due to the applied scrambling and simplifies the equaliser solution significantly.

Figure 38.5 illustrates the structure of linear multiantenna equaliser for M-by-N MIMO channels. Each BS transmit antenna requires its own space-time equaliser. An option is to apply the linear minimum mean-square error (LMMSE) criterion in the tap solver blocks decoupled to the equalisers. Given knowledge of the channel, LMMSE tap solver finds a solution for system of equations

$$\mathbf{C}_{\mathbf{y}}\mathbf{u}_m = \sigma_x^2 \mathbf{H}\delta_D, \tag{38.11}$$

where $\mathbf{u}_m \in \mathbb{C}^{BTFM}$ is the unknown equaliser for transmit antenna m, σ_x^2 is the chip variance, and vector $\delta_D \in \mathbb{C}^{BTFM}$ is a unit vector with unity in the Dth position. Note that $\delta_D^T\mathbf{x}$ is the multiuser chip to be estimated by the equaliser and $\mathbf{H}\delta_D$ gives the corresponding channel coefficient vector. In practice, equaliser vector $\mathbf{u}_m$ and the matrices in (38.11) are truncated to correspond to a signal vector the length of which is a function of the channel delay spread. Typically, a vector length of three times the channel delay spread multiplied by the number of receive antennas results in near-optimal performance.

The signal covariance matrix in (38.11) is defined as

$$\mathbf{C}_{\mathbf{y}} = E\{\mathbf{y}\mathbf{y}^{\mathrm{H}}\} = \sigma_x^2 \mathbf{H}\mathbf{H}^{\mathrm{H}} + \mathbf{C}_{\mathbf{w}} \tag{38.12}$$

assuming that the spreading codes are random. If deterministic spreading codes were assumed, then (38.12) would be a function of the spreading codes. Since scrambling changes the effective codes symbol-by-symbol, each chip interval would require a different equaliser filter leading to intolerable complexity. It should be noted that, in principle, also the covariance of the intercell interference and thermal noise, $\mathbf{C}_{\mathbf{w}}$, should be known.

There are several algorithms for solving (38.11) such as direct matrix inversion (DMI), Cholesky decomposition, and conjugate-gradient method. Also adaptive techniques are possible. The eigenvalue spread (spectral condition number) of the underlying covariance matrix plays an important role in the stability or convergence rate of the system solver. With multiple antennas and especially with oversampling, a form of preconditioning might be useful.

Equaliser outputs are obtained as

$$\hat{x}_m(i) = \mathbf{u}_m^{\mathrm{H}}(i) \cdot \mathbf{y}, \quad m = 1, 2, \ldots, M, \tag{38.13}$$

which is an LMMSE estimate of multiuser chip $x_m(i)$ for $i = 1, \ldots, BTF$. In general, the approach is referred to as chip-equalisation. For HSDPA reception, it is sufficient to decouple a single code correlator (per each HS-DSCH) to the equaliser output to generate a symbol estimate, as shown in Figure 38.5.

If space-time coding was applied in the transmitter, the corresponding decoder uses the correlator outputs to recover the original symbols similarly to Section 38.4.1. A difference is that a single path channel can be assumed due to equalisation.

The equaliser suppresses the multiple access interference due to multipath, interantenna interference, and intercell interference at the same time. A property of a chip-equaliser is also that it suppresses interference from code channels whose activity, power level, and spreading code is unknown to the receiver. Unfortunately, the more there are transmit antennas and multipaths, the more there are signals to be suppressed. This is why the degrees of freedom supplied by a limited number of receive antennas are quickly depleted causing high residual interference in many practical HSDPA MIMO environments.

38.4.3. Maximum-likelihood detection and interference cancellation techniques

To improve the performance of linear space-time equalisation-based receivers, nonlinear techniques can be considered. Many of the receiver algorithms proposed for MIMO detection are modifications of the techniques proposed for multiuser detection. Multiuser detectors often approximate ML criterion which, assuming white Gaussian noise, finds an estimate for the unknown symbol vector $\mathbf{s}$ as

$$\hat{\mathbf{s}} = \arg\min_{\mathbf{s}} \left(|\mathbf{z} - \mathbf{R}\mathbf{s}|^2 \right) \tag{38.14}$$

in which $\mathbf{z}$ is the input data collected, for example, using spreading code correlator bank similar to (38.8). Matrix $\mathbf{R}$ holds the information on how the symbols

interfere with each other; a nondiagonal matrix indicates intersymbol interference in the signal. Assuming, for example, ten HSDPA code channels and two MIMO data layers using QPSK and code reuse results in more than 10^{12} combinations which need to be tested for an ML solution even if the interference between successive symbols is neglected. Going through all possible combinations is clearly impossible and an approximation must be used.

A way to reduce the complexity is to concentrate on the most significant off-diagonal elements of **R**. In case of layered MIMO HSDPA transmission, the dominating interference is due to the parallel data symbols that are received with the same propagation delay and spreading code. The residual interference due to multipath may however limit the performance of this approach.

Nonlinear interference cancellation (IC) techniques may be useful in approximating the ML solution especially with layered MIMO HSDPA transmission which suffers from strong interlayer interference. IC methods in general involve three basic steps: (a) generation of tentative symbol decisions, (b) regeneration of interference, and (c) interference cancellation. The processing can be repeated for the detection of remaining symbols or for improving already detected symbol decisions iteratively.

Parallel IC (PIC) generates tentative symbol estimates and subtracts the regenerated interference between the symbols. Since the off-diagonal elements of **R** are the source of the interference, PIC estimates symbols iteratively as

$$\hat{\mathbf{s}}_j = \text{decision}\{\mathbf{z} - (\mathbf{R} - \text{diag}(\mathbf{R}))\hat{\mathbf{s}}_{j-1}\}, \tag{38.15}$$

where j is an iteration index. Depending on the quality of the initial estimates, the iterations may improve the symbol estimates. However, an aspect of HSDPA MIMO systems is that there are only few (2 to 4) transmit antennas in the system, which function as time varying interference sources to each other. Parallel IC schemes tend to suffer from error propagation, if the levels of the interfering signal streams vary significantly with respect to each other. Because of the time varying nature of the layers and because there are only few of them, successive IC methods may be more robust for MIMO communication.

A successive interference canceller structure suitable for layered HSDPA MIMO reception with two layers (data streams) is illustrated in Figure 38.6. The receiver applies ordered successive interference cancellation (OSIC) where the strongest layer is first detected using a ST equaliser. The signal is regenerated and cancelled from the input signal. This involves respreading of the data and filtering with the channel response. After this, the next strongest layer is detected. It should be noted that IC is performed to the original signal samples since chip-level equalisation has been assumed. Figure 38.6 shows that interference cancellation may also be based on channel-decoded data. This requires that each layer is separately encoded in the transmitter and reencoded prior its cancellation. This so-called postdecoding IC is not a preferred option compared to predecoding IC due to its higher complexity and delay requirements.

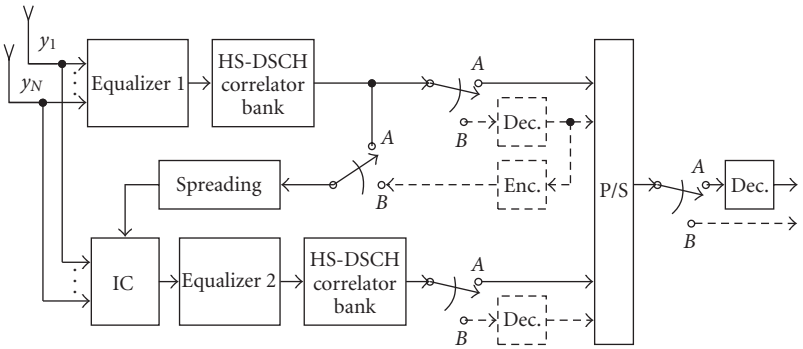

FIGURE 38.6. OSIC MIMO detector for dual-layer transmission with predecoding (A) or postdecoding (B) interference cancellation.

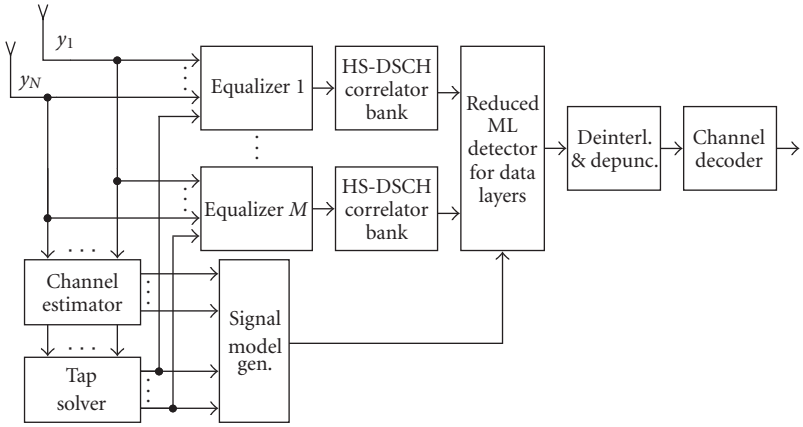

FIGURE 38.7. Receiver structure applying linear ST equalisation prior to symbol-wise ML detector.

38.4.4. Composite linear and nonlinear techniques

Interference cancellation techniques rely on an accurate signal model used for interference regeneration and cancellation. A property of WCDMA downlink is that it may simultaneously support several speech users and MIMO HSDPA users while the receiver may have information only about the code channels intended for the terminal in question. IC techniques may thus be ineffective in a practical system since only a part of the signal can be modeled accurately.

A solution to the problem is combining linear and nonlinear methods: a linear equaliser is able to suppress interference from all code channels without knowledge of their activity while nonlinear techniques are more efficient in suppressing interantenna interference. Such a receiver is illustrated in Figure 38.7.

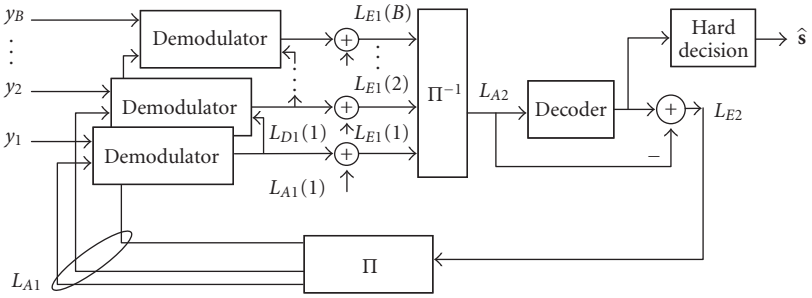

FIGURE 38.8. Iterative scheme of the turbo space-time decoder.

38.4.5. Turbo space-time decoding receivers

As mentioned in Section 38.4.3, the optimal ML receiver would be too complex. It would involve a Viterbi algorithm of the effective supertrellis associated with the concatenated encoders and the frequency-selective channel. Therefore, a suboptimal approach first presented in [9] based on the "turbo algorithm" is proposed. As shown in Figure 38.8, the interleaver allows decoupling the demodulation stage and the decoding stage. They exchange soft information iteratively until a hard decision $\hat{\mathbf{s}}$ is made on the transmitted symbols.

The soft information is expressed using log-likelihood ratios (LLRs). The input to each stage is the a priori LLRs denoted by $L_A(d)$. The a posteriori LLRs denoted by $L_D(d)$ can then be calculated. The difference between these LLRs is usually referred to as extrinsic LLR and is denoted by $L_E(d)$. The extrinsic LLRs of each stage are used as the a priori LLRs for the next stage. This procedure is repeated in an iterative fashion.

The decoder uses the well-known BCJR algorithm [10] which calculates the a posteriori LLR of each bit as a function of the a priori LLR of all the other bits and correlations between them induced by the encoder's trellis. Similarly, the demodulation algorithm calculates the extrinsic LLR of each bit as a function of the a priori LLR of all the other bits and the received samples. This algorithm was first proposed in [9] and is based on the soft-input soft-output linear multiuser detector of [11].

As shown in Figure 38.8, the inputs of each demodulator are the a priori LLRs and vector $\mathbf{y}_b$, that is, the received chip-level signal of the bth space-time block. According to (38.7) and (38.4), $\mathbf{y}_b$ is equal to

$$\mathbf{y}_b = \hat{\mathbf{H}}\mathbf{x}_b + \mathbf{H}_{\mathrm{IBI}}\mathbf{x}_{b-1} + \mathbf{w}_b = \hat{\mathbf{H}}\mathbf{D}_b\mathbf{s}_b + \mathbf{H}_{\mathrm{IBI}}\mathbf{x}_{b-1} + \mathbf{w}_b, \tag{38.16}$$

with $\hat{\mathbf{H}} \in \mathbb{C}^{NTF \times MTF}$ the block convolutional matrix built with $\{\mathbf{H}_{(l)}\ \forall l = 1, \ldots, L\}$, the term $\mathbf{H}_{\mathrm{IBI}}\mathbf{x}_{b-1}$ that accounts for the interblock interference (IBI), and the noise $\mathbf{w}_b$. As shown in Figure 38.9, the demodulator consists of a decision-feedback equaliser (DFE), a maximum-likelihood estimator, and additional functions that

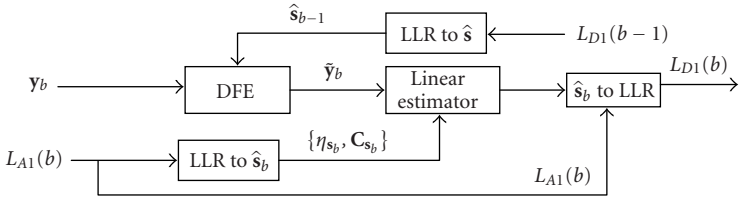

FIGURE 38.9. Turbo demodulator scheme.

transform symbols to LLR and vice versa. Firstly, the DFE assumes perfect channel knowledge and eliminates the IBI from $\mathbf{y}_b$. Therefore, the output of the DFE denoted by $\tilde{\mathbf{y}}_b$ is equal to

$$\tilde{\mathbf{y}}_b = \hat{\mathbf{H}}\mathbf{D}_b\mathbf{s}_b + \mathbf{w}_b = \mathbf{G}_b \cdot \mathbf{s}_b + \mathbf{w}_b, \tag{38.17}$$

with matrix $\mathbf{G}_b \in \mathbb{C}^{NTF \times MTF}$ defined as $\hat{\mathbf{H}} \cdot \mathbf{D}_b$. For convenience, we now isolate the contribution of the ith component of $\mathbf{s}_b$ in $\tilde{\mathbf{y}}_b$ to obtain

$$\tilde{\mathbf{y}}_b = \mathbf{G}_b\delta_i\mathbf{s}_b + \mathbf{G}_b(\mathbf{I} - \delta_i\delta_i^T)\mathbf{s}_b + \mathbf{w}, \tag{38.18}$$

with δ_i the ith unity vector. Then, the linear estimator is derived from (38.18) as the maximum-likelihood estimate of the ith component of $\mathbf{s}_b$ assuming it to be a deterministic parameter while taking all the other components as Gaussian random variables. As detailed in [9], the resulting estimator of $\mathbf{s}_b$ vector becomes

$$\hat{\mathbf{s}}_b = \boldsymbol{\eta}_{\mathbf{s}_b} + \tilde{\mathbf{C}}_{\mathbf{s}_b}\mathbf{G}_b^T\mathbf{C}_{\mathbf{y}}^{-1}(\mathbf{y}_b - \mathbf{G}_b\boldsymbol{\eta}_{\mathbf{s}_b}), \tag{38.19}$$

with $\boldsymbol{\eta}_{\mathbf{s}_b} = E[\mathbf{s}_b]$ and $\mathbf{C}_{\mathbf{s}_b} = E[\mathbf{s}_b\mathbf{s}_b^T]$ being the second-order statistics of $\mathbf{s}_b$ obtained by transforming the a priori LLRs L_{A1} of the symbols delivered by the decoder in the previous iteration (see Figure 38.9). $\tilde{\mathbf{C}}_{\mathbf{s}_b}$ is a diagonal matrix with elements $1/\lambda_l$, where λ_l are the diagonal elements of the matrix $\mathbf{G}_b\mathbf{C}_{\mathbf{y}}\mathbf{G}_b^T$ with

$$\mathbf{C}_{\mathbf{y}} = \mathbf{G}_b\mathbf{C}_{\mathbf{s}_b}\mathbf{G}_b^T + \sigma_\omega^2\mathbf{I}, \tag{38.20}$$

and σ_ω^2 the equivalent noise variance. This scheme assumes perfect channel knowledge, although an extension of this receiver incorporating channel estimation was proposed in [12].

38.5. Numerical results

This section evaluates the MIMO systems in the FDD mode UMTS HSDPA service. For this purpose, several simulation results will be presented for different combinations of the transmitter and receiver schemes presented previously and detailed in Table 38.2.

Table 38.2. Selected combinations of transmitter and receiver schemes.

	1 TX (1×2)	STTD ($2 \times N$)	D-STTD (4×2)	V-BLAST (2×2)	LDC (3×2)
RAKE	—	X	—	—	—
Linear ST equaliser	X	—	—	—	—
OSIC	—	—	—	X	—
Reduced ML	—	—	X	X	—
Turbo ST decoder	—	X	—	X	X

Table 38.3. Simulation channel models.

Channel model	Relative path powers (dB)	UE velocity (km/h)
Ped. A	0; −12.7	3
Veh. A	0; −1.9; −7.3; −10.4; −10.9	50

The results are based on link-level simulations without adaptive modulation and coding (MC) schemes or scheduling. However, H-ARQ technique is used for some of the results. The HSDPA service may use QPSK or 16-QAM modulation and three different channel coding rates, $R = \{1/3, 1/2, 3/4\}$. The selected modulation and coding scheme together with the number of spreading codes assigned to the HSDPA sets the maximum bit rate provided by the service. Two different channel scenarios compliant with 3GPP specifications are considered: (a) pedestrian A (PEDA) channel with two chip-spaced multipath components and 3 km/h mobile velocity and (b) vehicular A (VEHA) channel with five chip-spaced multipath components and 50 km/h mobile velocity. Table 38.3 illustrates the temporal properties of the channel models.

38.5.1. Comparison of MIMO transmission and low-complexity reception techniques

In this section, the performance of MIMO techniques is demonstrated using different transmission schemes with a receiver algorithm that has been considered practical for the specific MIMO HSDPA system. The shown simulation results point out the problems faced in MIMO channels but are not intended for making any final conclusions about the relative performance of different MIMO HSDPA schemes. Two receive antennas have been assumed to limit the complexity of the terminal receiver. This basically limits the number of MIMO data layers to two.

Figure 38.10 shows data throughput with uncorrelated antennas in PEDA channel as a function of geometry factor G, which is defined as a ratio of the average received base station power and intercell interference power. The factor is large when the terminal is close to the serving base station and gets smaller near the cell edge. Modulation and coding scheme with channel coding rate R was fixed during the simulations and the HSDPA user had five code channels in use. The

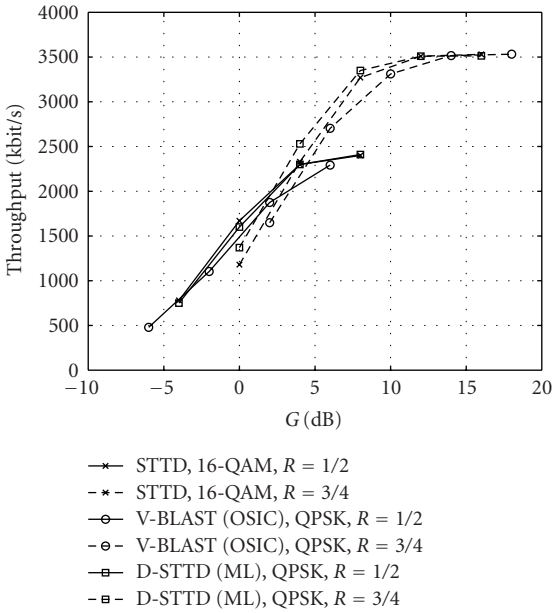

FIGURE 38.10. HSDPA throughput in uncorrelated MIMO PEDA channel, 80% HSDPA power allocation, 5 HSDPA code channels, and dual-antenna receiver.

simulations applied H-ARQ technique for packet retransmissions using so-called Chase-combining at the receiver. Channel estimation was based on orthogonal common pilot symbol streams transmitted from the base station antennas. The base station transmit power is divided into three parts. Ten percent is allocated for the CPICH channel, HSDPA code channels use 80% of the total power, and the remaining 10% is for speech services. Note that the transmit power is evenly divided between the transmit antennas.

Figure 38.10 shows how the throughput increases with G until the maximum data rate of the specific MC scheme is reached. Surprisingly no significant differences between the MIMO schemes can be seen. The receiver for 4×2 D-STTD scheme applies a symbol-level maximum-likelihood (ML) detector that neglects interference due to multipath but optimally takes into account the interference between parallel STTD code blocks that use the same spreading code. The dual-layer 2×2 V-BLAST scheme uses OSIC receiver since signals from two transmit antennas can be separated with a dual-antenna receiver. Note that post-decoding IC was not used in OSIC receiver. The simple STTD diversity transmission achieves the same nominal peak data rate by using 16-QAM instead of QPSK used by the layered MIMO schemes. The results show that STTD performance is comparable to layered MIMO schemes although simple RAKE receiver has been used.

The results are totally different in VEHA channel which has five resolvable multipaths. Figure 38.11 shows that V-BLAST using OSIC receiver is able to suppress the multipath interference to some extent and the interlayer interference

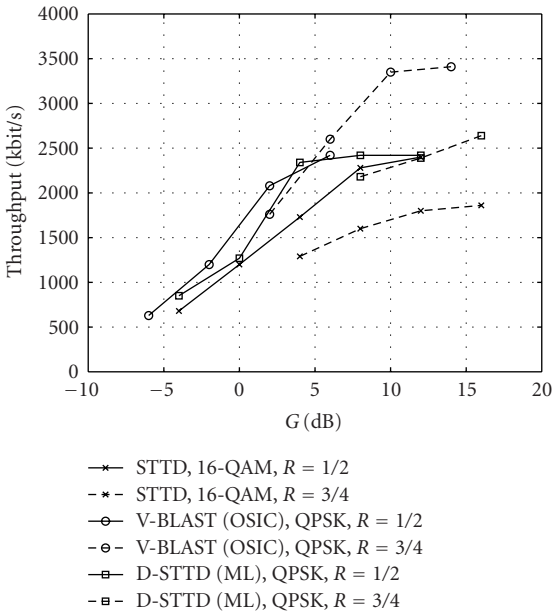

FIGURE 38.11. HSDPA throughput in uncorrelated MIMO VEHA channel, 80% HSDPA power allocation, 5 HSDPA code channels, and dual-antenna receiver.

while D-STTD with the simplified ML receiver suffers from the multipath propagation when a weak channel code is used. The RAKE receiver used with STTD transmission also neglects the multipath interference and, thus, has similar problems as D-STTD.

Assumption of uncorrelated transmit and receive antennas favours diversity schemes and especially layered MIMO schemes. In addition, the number of active HSDPA code channels may be unrealistically low compared to the used HSDPA power allocation of 80% used in Figures 38.10 and 38.11. In Figure 38.12, the HSDPA transmit power is divided between ten code channels while the antennas are spatially correlated. Two parallel layers transmitted from correlated antennas cannot be separated reliably by using the OSIC receiver with two strongly correlated antennas. The figure also shows V-BLAST results with an ML receiver similar to the used D-STTD receiver. Its performance is much better than that of OSIC indicating that the linear processing used in OSIC receiver is inefficient with correlating antennas. In addition, linear suppression of the interfering layer causes loss of diversity order even with uncorrelated antennas.

D-STTD benefits from the diversity of the STTD code and outperforms V-BLAST while pure STTD transmission achieves slightly better performance. The figure also shows a SIMO (single-input multiple-output) performance curve with single-antenna transmitter and dual-antenna ST equaliser, which was discussed in Section 38.4.2. Especially in high G region, the method is superior to other methods.

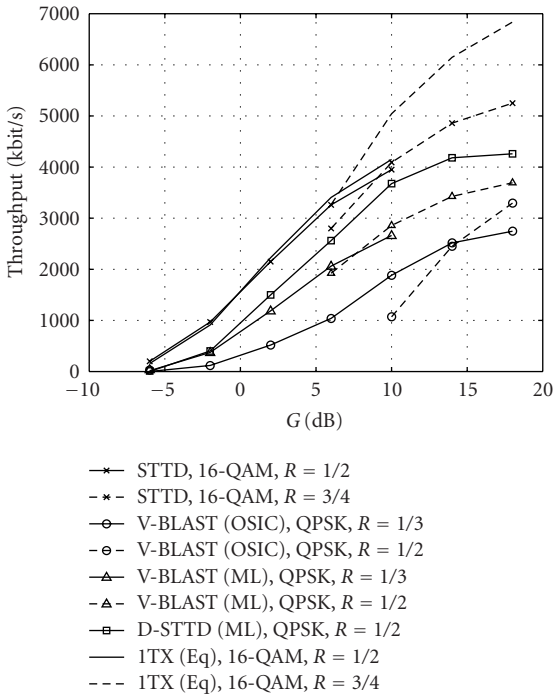

FIGURE 38.12. HSDPA throughput in correlated MIMO PEDA channel, 80% HSDPA power allocation, 10 HSDPA code channels, and dual-antenna receiver.

Taking into account the problems caused by significant multipath propagation as was shown in Figure 38.11 and the problems caused by antenna correlation, even more complex receivers may be required to make layered MIMO techniques work reliably in a practical HSDPA environment. With a small number of receive antennas, conventional single-antenna transmission with a channel equaliser at the receiver may offer the best performance-complexity trade-off. STTD offers transmit diversity but makes channel equalisation difficult due to introduction of the second transmit antenna.

38.5.2. Simulation results with the turbo space-time decoder

The simulation results for the STTD scheme with $M = 2$ and $N = 1$ at the transmitter and the turbo space-time decoder at the receiver are first presented. In this subsection, the antennas are assumed to be spatially correlated and no packet retransmissions are considered. Figure 38.13 shows the throughput in kbit/s versus E_b/N_0 in a PEDA channel at 3 km/h for one HSDPA user with different MC schemes. Figure 38.14 shows the same kind of results but in the VEHA channel at 50 km/h. In these simulations, both the intercell and intracell interferences are modelled as zero-mean white Gaussian noise (see [13] for details).

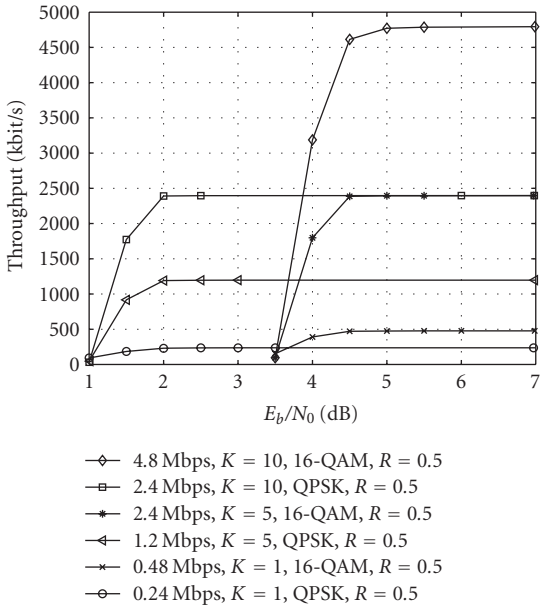

FIGURE 38.13. Throughput for STTD 2×1 and PEDA channel at 3 km/h for one single HSDPA user with $K = \{1, 5, 10\}$ spreading codes for QPSK and 16-QAM modulations and coding rate 1/2.

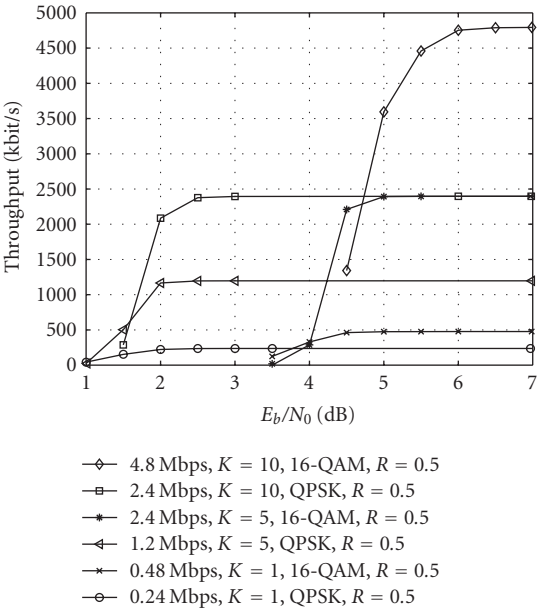

FIGURE 38.14. Throughput for STTD 2×1 and VEHA channel at 50 km/h for one single HSDPA user with $K = \{1, 5, 10\}$ spreading codes for QPSK and 16-QAM modulations and coding rate 1/2.

As expected, the MC schemes with QPSK modulation require a lower E_b/N_0 to attain the maximum rate than the ones with 16-QAM. Moreover, if we compare the two MC schemes with the same maximum bit rate of 2.4 Mbps, it can be seen that the one with QPSK needs 2.5 dB less power to achieve the maximum rate. Another remark is that the receiver performs almost independently of the number of spreading codes of the HSDPA user in the PEDA channel, that is, all the MC schemes with the same modulation attain the maximum rate almost with the same E_b/N_0. In the VEHA channel, this property also holds for the MC schemes with QPSK but fails for the MC schemes with 16-QAM, which is due to their higher sensitivity to multipath interference.

A significant parameter to evaluate the results is the maximum E_b/N_0 that the MIMO system can attain for a given HSDPA power percentage, denoted hereafter by $(E_b/N_0)_{\max}$. This value is equal to the E_b/N_0 only when the intracell interference is present, and is not affected by the used channel profile. Assuming that 80% of the available power is assigned to the HSDPA user, $(E_b/N_0)_{\max}$ for the MC schemes used in Figures 38.13 and 38.14 is usually much greater than the minimum E_b/N_0 required to attain the maximum throughput. For instance, $(E_b/N_0)_{\max}$ for the MC scheme of 2.4 Mbps with QPSK modulation is 8 dB, which is higher than the 2 dB needed to achieve the maximum rate. The most critical case is the MC scheme with the 4.8 Mbps maximum rate, because the $(E_b/N_0)_{\max}$ is equal to 5 dB, which is lower than the minimum E_b/N_0 required to attain the maximum rate, especially in the VEHA channel. Therefore, the effective data rate attained by this MC scheme will be lower than the theoretical 4.8 Mbps. In practice, this means that this MC would be rarely scheduled.

Figures 38.15 and 38.16 show the throughput curves for the LDC scheme with $M = 3$ and $N = 2$ at the transmitter and the turbo space-time decoder at the receiver in a PEDA channel at 3 km/h and in a VEHA channel at 50 km/h, respectively. The achieved performance is rather disappointing in the PEDA channel even with a QPSK modulation. For instance, the same MC scheme in the PEDA channel needs 5 or 6 dB more than in the VEHA channel to attain the maximum rate. Since the PEDA channel at 3 km/h is a slowly fading channel, the LDC MIMO system designed to achieve a relatively high multiplexing gain performs poorly. The MIMO systems with high multiplexing gains perform reliably only in fast fading channels. In such a channel, the receiver deals with several realizations of the channel impulse response within one code block and therefore, the error probability is not only limited by the probability of the channel outage but by other aspects such as the noise and the spatio-temporal channel encoder. This phenomenon is even more critical in case of V-BLAST with $M = 4$ and $N = 4$. Detailed results for 4×4 V-BLAST system with the presented turbo space-time decoder can be found in [13].

38.5.3. Conclusions

Application of MIMO techniques in the HSDPA environment has been shown to be difficult. The main cause for the problems is the multipath channel often

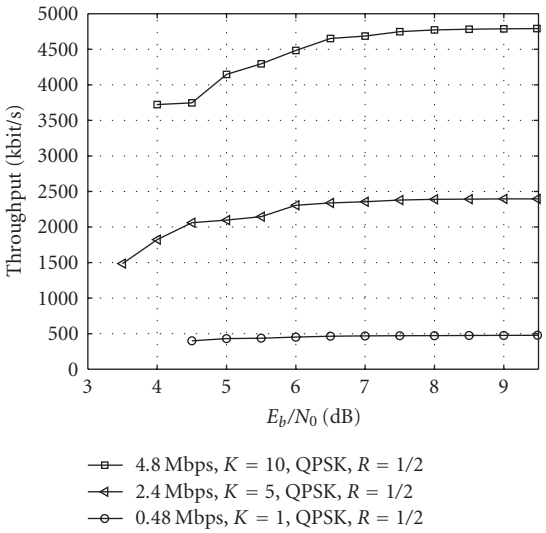

FIGURE 38.15. Throughput for LDC 3×2 and PEDA channel at 3 km/h for one single HSDPA user with 1, 5, or 10 codes for QPSK and 16-QAM modulations and coding rate 1/2.

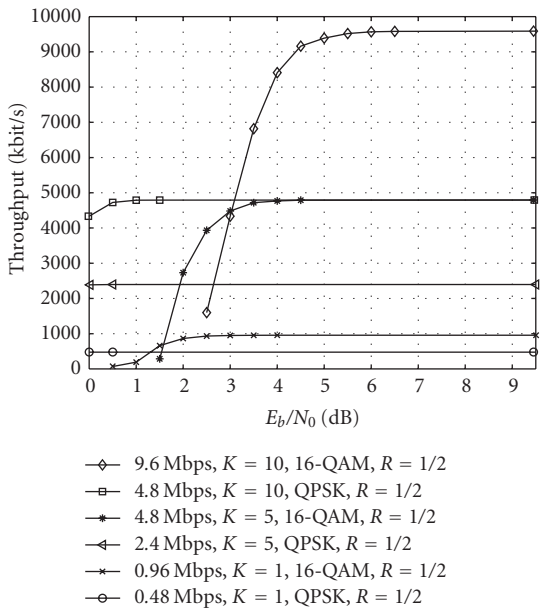

FIGURE 38.16. Throughput for LDC 3×2 and VEHA channel at 50 km/h for one single HSDPA user with 1, 5, or 10 codes for QPSK and 16-QAM modulations and coding rate 1/2.

encountered in CDMA-based systems. The complex structure of the multipath propagated signal makes linear separation of the parallel data streams a challenging task. On the other hand, nonlinear maximum-likelihood techniques suffer from very high complexity unless the signal model is artificially simplified. This, however, causes residual interference that may compromise the performance.

An option is to decouple linear and simplified nonlinear processing to overcome the weaknesses of the two techniques as was described in Section 38.4.4. An even more complex approach is to further apply iterative processing by using the presented turbo space-time decoding approach studied in Section 38.4.5. The simplest transmission schemes, such as single antenna or STTD transmission, seem to offer the best trade-off between performance and receiver complexity as long as only a few receive antennas can be considered practical in a mobile receiver.

Acknowledgment

The simulations presented in this chapter were obtained within the I-METRA 5FP IST Project [14].

Abbreviations

ACK	Acknowledgment
AMC	Adaptive modulation and coding
BS	Base station
CDMA	Code division multiple access
CPICH	Common pilot channel
CRC	Cyclic redundancy check
DFE	Decision-feedback equaliser
DSCH	Downlink shared channel
D-STTD	Double-STTD
FDD	Frequency division duplex
H-ARQ	Hybrid automatic repeat on request
HS-DSCH	High-speed DSCH
HSDPA	High-speed downlink packet access
IBI	Interblock interference
IC	Interference cancellation
LDC	Linear dispersion codes
LLR	Log-likelihood ratio
LMMSE	Linear minimum mean-square error
MC	Modulation and coding
MIMO	Multiple-input multiple-output
ML	Maximum likelihood
OSIC	Ordered successive interference cancellation
PEDA	Pedestrian A
PIC	Parallel IC

QPSK	Quadrature (quaternary) phase-shift keying
SIMO	Single-input multiple-output
ST	Space-time
STTD	Space-time transmit diversity
TTI	Time transmission interval
UE	User equipment
UMTS	Universal mobile telecommunications system
UTRAN	Universal terrestrial radio access network
UTRA	UMTS terrestrial radio access
V-BLAST	Vertical-BLAST
VEHA	Vehicular A
WCDMA	Wideband code division multiple access
3GPP	Third Generation Partnership Project
16-QAM	16-quadrature amplitude modulation

Bibliography

[1] 3GPP REL5_FEATURES_V_2003_09_09.DOC., "Overview of 3GPP releases. Summary of all Release 5 features," http://www.3gpp.org.

[2] 3GPP TR 25.858 v.5.0.0., "High speed downlink packet access: physical layer (Release 5)," http://www.3gpp.org.

[3] 3GPP TS 25.212 v.5.0.0., "Multiplexing and channel coding (FDD) (Release 4)," http://www.3gpp.org.

[4] V. Tarokh, H. Jafarkhani, and A. R. Calderbank, "Space-time block codes from orthogonal designs," *IEEE Trans. Inform. Theory*, vol. 45, no. 5, pp. 1456–1467, 1999.

[5] L. Zheng and D. N. C. Tse, "Diversity and multiplexing: a fundamental tradeoff in multiple-antenna channels," *IEEE Trans. Inform. Theory*, vol. 49, no. 5, pp. 1073–1096, 2003.

[6] S. M. Alamouti, "A simple transmit diversity technique for wireless communications," *IEEE J. Select. Areas Commun.*, vol. 16, no. 8, pp. 1451–1458, 1998.

[7] G. J. Foschini, G. D. Golden, R. A. Valenzuela, and P. W. Wolniansky, "Simplified processing for high spectral efficiency wireless communication employing multi-element arrays," *IEEE J. Select. Areas Commun.*, vol. 17, no. 11, pp. 1841–1852, 1999.

[8] B. Hassibi and B. M. Hochwald, "High-rate codes that are linear in space and time," *IEEE Trans. Inform. Theory*, vol. 48, no. 7, pp. 1804–1824, 2002.

[9] A. Wiesel, X. Mestre, A. Pagès-Zamora, and J. R. Fonollosa, "Turbo equalization and demodulation of multicode space time codes," in *Proc. IEEE International Conference on Communications (ICC '03)*, vol. 4, pp. 2296–2300, Anchorage, Alaska, USA, May 2003.

[10] S. Benedetto, D. Divsalar, G. Montorsi, and F. Pollara, "A soft-input soft-output maximum a posteriori module to decode parallel and serial concatenated codes," TDA Progress Report 42-127, November 1996.

[11] X. Wang and H. V. Poor, "Iterative (turbo) soft interference cancellation and decoding for coded CDMA," *IEEE Trans. Commun.*, vol. 47, no. 7, pp. 1046–1061, 1999.

[12] L. García, A. Pagès-Zamora, and J. R. Fonollosa, "Iterative channel estimation for turbo receivers in DS-CDMA," in *Proc. IEEE International Conference on Acoustics, Speech, and Signal Processing (ICASSP '04)*, vol. 4, pp. 989–992, Montreal, Quebec, Canada, May 2004.

[13] IST-2000-30148 I-METRA, "DELIVERABLE 4 performance evaluation," http://www.ist-imetra.org.

[14] IST-2000-30148 I-METRA, http://www.ist-imetra.org.

[15] K. Hooli, M. Juntti, M. J. Heikkilä, P. Komulainen, M. Latva-Aho, and J. Lilleberg, "Chip-level channel equalization in WCDMA downlink," *EURASIP J. Appl. Signal Process.*, vol. 2002, no. 8, pp. 757–770, 2002.

Alba Pagès Zamora: Signal Processing and Communications Group, Technical University of Catalonia (UPC), 08034 Barcelona, Spain

Email: alba@gps.tsc.upc.es

Markku J. Heikkilä: Technology Platforms, Nokia Corporation, 90570 Oulu, Finland

Email: markku.j.heikkila@nokia.com

39 A MIMO platform for research and education

T. Kaiser, A. Wilzeck, M. Berentsen, A. Camargo, X. Peng, L. Häring, S. Bieder, D. Omoke, A. Kani, O. Lazar, R. Tempel, and F. Ancona

39.1. Introduction

While the first breakthroughs in multiple-input multiple-output (MIMO) research were mostly of theoretical nature, the past few years reflected a significant progress in application-oriented MIMO systems. Meanwhile, MIMO techniques are under intense discussion in the standardization bodies for wireless local area networks (WLAN), wireless metropolitan area networks (WMAN), and cellular communication systems of third generation (3G). Above all, "MIMO" will probably become mandatory in fourth-generation systems (4G) with high spectral efficiency. Moreover, the first prestandard MIMO products for WLANs are already commercially available on the mass market.

Despite these auspicious indications, numerous open questions on how to efficiently implement MIMO systems still remain. For example, optimized topology of compact antenna arrays, cost-effective large-scale integration of multiple radio-frequency (RF) branches, multichannel analog-to-digital (AD) conversions, algorithm complexity versus performance tradeoffs, appropriate protocol designs, and last but not least low-power consumption and chip die will be persistent research and development topics for the next years.

Nowadays, development of communication systems is achieved either with specialized software packages (digital part) only, or by successively improving prototype chips through multiple test runs (analog part). While the digital part (baseband (BB) processing) is primarily faced with a limited chip die and low power constraints, the reduction of the algorithm complexity without significant performance loss is most often in the foreground. The analog part (RF processing) confronts its limitations by physical effects so that designated circuit design expertise is mandatory. Hence, with some exceptions, the conventional interface between the analog world and the digital world is usually well defined in such a way that the all-embracing development can be separated into two major parts. The clear advantage of such a separation is the split of complexity into two seemingly independent tasks facilitating the overall design. Quite the contrary, "MIMO" requires

a closer alliance between the analog and the digital world, because of the additional interactions among them, for example, adequate consideration of antenna coupling in the baseband. This may largely prevent the complexity splitting and reveals the need for a MIMO platform covering simultaneously all components of a communication link. In other words, a close team play among the RF and the BB worlds seems to be required for successful MIMO development. Thus, a corresponding MIMO development platform has to possess a large degree of flexibility and modularity to take into account as many real-world limitations as possible. Needless to say that the computational performance should be close to the state of the art. Last but not least, a MIMO platform hosted by an academic institution should be obviously of educational value in order to inspire scientific novices, foster teamwork, and improve communication skills.

Hence, our aim was the development of a flexible and modular MIMO platform satisfying the following major needs:

(i) multistandard capability;
(ii) RF controllability by dedicated BB links;
(iii) state of the art in high-speed data transmission;
(iv) algorithm testing and development in real-world environments (i.e., offline mode);
(v) algorithm testing and development under real-world constraints (i.e., online mode);
(vi) educational value.

Since "MIMO" is without doubt a multidisciplinary field of research, a close collaboration among different experts is essential in order to rapidly progress towards the targeted goals. The German RF-design group of the Californian company ATMEL cares about the analog MIMO front ends, the English enterprise SUNDANCE developed the baseband hardware in a modular manner and, Duisburg's Smart Antenna Research Team (SmART) assembles the hardware, carries out the measurements, and primarily focuses on MIMO algorithm development and testing.

The unifying platform is called SmarT Antenna Real-time System (STARS) and is shown in Figure 39.1.

STARS is split into independent devices, so that not only classical multiuser scenarios can be investigated but also cooperation among users becomes feasible.

The aim of this section is to explain STARS in such a deep detail that the reader is equipped with a thorough knowledge to place him into the position of setting up a MIMO testbed by his own. Hence, we do not focus on performance of algorithms (this is done at several other places within this book), but describe a testbed from various other perspectives, that is,

(i) the STARS basic concept, processing modes, technical data, network topologies;
(ii) the hardware for baseband (BB) and radio-frequency (RF) processing, internal and external interfaces, periphery;
(iii) the software for digital signal processor (DSP) and field programmable gate arrays (FPGAs) development, project, and revision control;

FIGURE 39.1. Presentation of STARS at EUSIPCO 2004 in Vienna, Austria.

(iv) the system debugging;
(v) the evaluation of real-time requirements;
(vi) the *synchronisation* as a major algorithmical challenge for an online MIMO testbed, including coarse and fine timing acquisition, carrier frequency synchronisation, tracking, and its implementation;
(vii) the STARS "little brother" testbed with educational value;
(viii) some exemplary results.

A conclusion and an outlook finish this contribution.

39.2. Overview

STARS offers a rich variety of state-of-the-art modules for processing, analog-to-digital conversion, digital-to-analog conversion, and logging of signals, assisted by a comprehensive set of software tools like a multi-DSP real-time operating system (RTOS), DSP development tools, software development kits (SDKs), and FPGA development tools. A microcontroller-based transparent interface to control and setup different analog RF front ends (IEEE 802.11b,g,a; UMTS) facilitates the targeted flexibility. Four independent units each equipped with multiple antennas enable to investigate multiuser scenarios, point-to-point links, ad hoc networks, as well as infrastructured networks (networks with access point/base station). Therefore, several system configurations can be envisioned.

The integration of powerful FPGAs and DSPs beside large memory modules makes STARS feasible for testing MIMO algorithms not only with recorded real data but also for real-time systems meeting real-world needs. This is of particular relevance if a feedback link from the receiver to the transmitter and/or cooperation among multiple users or systems are under consideration. Furthermore, the facility to log data on high sampling rates (105 MHz) with suitable resolution (14 bits) permits, beside system debugging, to some extent even channel sounding. The complete system, including host PCs, can be remotely controlled over local area

network (LAN) using TCP/IP, which also supports its use in an isolated measurement chamber.

39.2.1. STARS concept

Before the underlying concept of STARS is illustrated, the properties and limitations of today's processing devices, like DSPs and FPGAs, are briefly revisited.

DSPs provide a specialized core with multiple-functional units, which is optimized for digital signal processing operations like filtering and transformations. These operations can be accomplished either in a floating-point number format or a fixed-point number format. In order to fully exploit the provided hardware, scheduling of the resources is mandatory. Indeed, the DSP obtains most of its power from advanced software pipelining, hardwired instructions, and specialized instruction set. Another relevant feature is the memory architecture. To ensure that the DSP core can fetch instruction and data in parallel, the Harvard architecture is typically chosen. This architectural concept has been modified and improved over the past decades, for example, by introducing a cache hierarchy and allowing dual data accesses. Beside highly optimized code in assembly language written by hand, the C/C++ language facilitates DSP programming.

The technological barriers of DSPs lie in the inefficient bit-level operation and in unavoidable sharing of the DSP core, which limit the parallelism of operation. In addition, the restricted data transfer rate to the external memory interface is a typical bottleneck in high-speed signal processing.

Programmable logic devices (PLDs) like FPGA are today a feasible alternative or an extension to DSPs. One advantage of FPGAs concerning MIMO is the ability to provide special hardware structures in parallel, and to handle high data rates without affecting the other implemented algorithms. They provide true bit-level operations and have almost no restrictions concerning the word width. Nevertheless, an FPGA loses flexibility in programming in contrast to a DSP. There is a wide variety of techniques to design and simulate hardware systems, ranging from gate-level schematics up to functional-level C-like description languages (for instance, SystemC or VHDL). Unfortunately, all such techniques require distinct development experience of such systems. Automatic tools can help to evaluate an approach and may alleviate the experience burden.

In conclusion, FPGAs are the processing devices of choice for regular and seldom varying algorithms, especially if they have to operate at high data rates. DSPs in contrast are more appropriate if the algorithm is less regular and often varying over time, but require only limited computational demands. To take advantage of both technologies, STARS is based on a mixed FPGA/DSP concept.

Basic concept. The basic concept of STARS is shown in Figure 39.2. The block diagram is organized in stages, representing the processing stages of a transceiver. The processing stages are connected by either analog cables or digital buses. These buses must be able to handle the required data rate, which depends on the resolution and conversion rate of analog-to-digital converters (ADCs), digital-to-analog converters (DACs), and on the number of antennas.

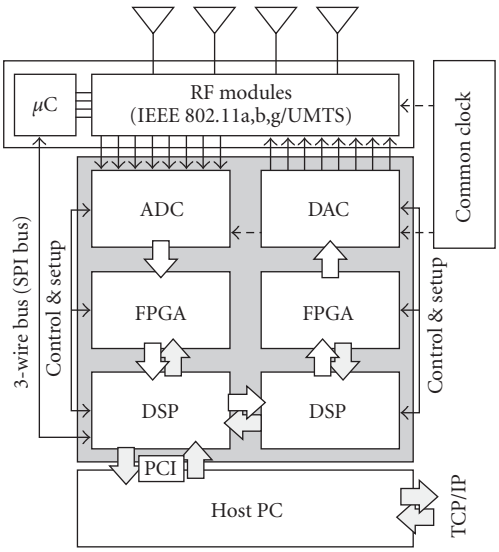

Figure 39.2. Basic concept for a 4×4 transceiver.

The first stage consists of the RF modules mixing the signals of each antenna from RF to BB (in-phase signal (I) and quadrature (Q) signal). A common clock is adopted in order to provide each mixer with synchronized oscillator signals so as to avoid individual frequency offsets. The RF modules are controlled by a microcontroller providing a transparent interface between the BB processing controller (implemented on DSP) and the RF components. This generic approach eases an exchange of RF modules, for example, to investigate different wireless standards. Following the receiver path, the next stage consists of the ADCs triggered by a common sampling clock derived from the common clock signal. The succeeding FPGA stage allows high-speed parallel data processing for regular and seldom-varying processing tasks. Therefore, the FPGA stage covers the complete digital MIMO front end, that is, hosting per antenna the filtering operations, the synchronization of time and frequency, the basic signal demodulation, and all other regular processing operations. The FPGA operates on the incoming high-data-rate digital signal and reduces the data-rate stepwise, so that the subsequent DSP stage is not overstrained. In the DSP stage, all less regular MIMO processing takes place, that is, algorithms which are under study. The DSPs are also used to control and setup all components of STARS.

The transmitter path is opposite to the receiver path, but it might be reasonable to share the DSP-based processing power among the transmitter and the receiver to some extent. The upload of firmware to the FPGA stages and the configuration of ADCs or DACs are done by an internal communication link. The microcontroller for the RF modules is controlled over a 3-wire bus (SPI) provided by the DSP stage.

The components contained in the gray box represent the real-time system for baseband processing, which is mounted in a host PC offering also the power

supply. The host PC is used to initialize the system, to upload applications to the real-time components, and to provide hard-disk space for data and applications. Using the PCI bus, data transfer between the real-time components and the host PC is possible. The host PC further allows remote control of the whole system over LAN using TCP/IP.

39.2.2. Processing modes

Based on the presented concept, we introduce two main modes which are developed in parallel in a step-by-step manner.

The first mode is the so-called *offline mode*, where preprocessed digital data are transmitted from memory and received data are stored into memory. The requirement here is that the memories must be accessible in real time by the ADC or DAC, respectively. The FPGA stage can be skipped and is replaced by fast memory modules. The DSP stage only acts as controller; it provides access to the host for uploading/downloading data and while being responsible for the setup of the ADC, DAC, and RF modules. This mode is especially reasonable for algorithm testing on logged real data and also for system debugging purposes. However, it does not allow deeper insight into the system behavior, for example, how the receiver interacts with the transmitter or impacts of multiuser scenarios like cooperation among users. Nevertheless, this mode is a rather convenient starting point for development and is a favorable way to analyze nonidealities like RF impairments and their cancellation.

In the second mode, the so-called *online mode*, the whole processing is done in real time, so it will allow us to study the system behavior in multiuser scenarios (see Figure 39.3) like ad hoc networks, infrastructured networks, and point-to-point links with interferers, and also point-to-point links with transmission adaptation by feeding back information. Also the cooperation among multiple users requires real-time processing and can be studied within this mode.

In order to assist a step-by-step development of such a real-time system, we introduce a *hybrid or partly-online mode* which is strongly related to system debugging. In this intermediate mode, memory modules, acting as independent buffers, can be connected with almost any stage of the system. They allow data record or data playback in real time. For example, the memory modules can be placed directly after the ADC stage to log the data, to store them for later analysis, or for later playback by feeding the data directly into the FPGA stage. Alternatively, the modules can be placed after the FPGA stage, if, for example, the synchronization has already been validated. Again, the resulting data stream can be recorded for succeeding offline processing and analysis.

39.2.3. Technical data

The major technical details of STARS are pointed out in Table 39.1.

The possible MIMO topologies mainly depend on the used analog interface to the RF front ends. If an intermediate frequency (IF) is used, only one ADC (or

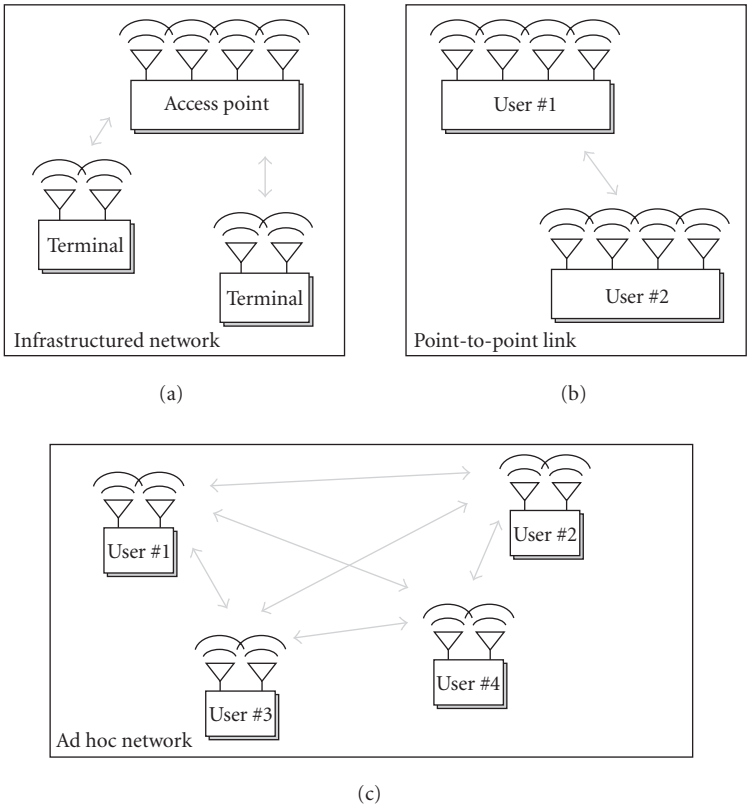

Figure 39.3. Network topologies.

DAC) per antenna path is required, which gives from the hardware point of view the possibility to double the number of antennas on the cost of additional digital processing. In case of zero-IF modulation/demodulation, two ADCs (or DACs) are required per antenna path, because the inphase (I) and quadrature (Q) signals have to be converted. It is therefore called in the following I/Q interface.

In general, additional mechanical constraints (space, number of bus connectors, and so on) give further constraints to the possible number of antennas.

Table 39.2 highlights the possible number of systems assuming an I/Q interface depending on the number of receive antennas, number of transmit antennas, and occupied signal processing resources.

39.3. Hardware platform

39.3.1. Hardware for baseband processing

STARS baseband processing hardware consists of modules mounted on so-called carrier boards and manufactured by Sundance Ltd. The modules are interconnected using over-the-air cabling and carrier-board connections allowing flexible,

Table 39.1. STARS technical data.

ADC/DAC	
Overall number of channels	24/24-2/2 per module
ADC/DAC	
DAC	
Conversion rate	Up to 160 MSPS/400 MSPS (interp.)
Resolution	16 bit
Baseband processing	
Front end	
Processing device	Xilinx Virtex-II 4000-5
Overall system gate count	4×4 M = 16 M + FPGAs on DAQ/DSP modules
External memory	8 MB (ZBTRAM)
Back end	
Processing devices	TI TMS320C6416@600 MHz TI TMS320C6713@225 MHz
Overall calculation power, peak	28 800 MIPS (fixed-point DSPs) 8100 MFLOPS (floating-point DSPs)
Overall DSP memory (internal/external)	7 824 kB/816 MB
Independent memory modules	
Capacity	4×1 GB
Maximum data rate	100 MHz $\times$ 32 bit
Operating modes	Real-time logging, real-time playback

Table 39.2. STARS possible MIMO configurations.

Number of systems		Receive antennas					
		1	2	3	4	5	6
Transmit antennas	1	4	4	4	3(4)	2(3)	2(3)
	2	4	4	4	2(3)	2	2
	3	4	4	d	2	2	2
	4	3(4)	3	2	1(2)	1(2)	1(2)
	5	3	3	2	1(2)	1	1
	6	3	3	2	1(2)	1	1

scalable, and powerful processing architectures. The carrier boards provide access to the PCI bus of the host PC and can carry up to four Sundance modules (based on Texas Instruments Module (TIM) specifications). Changing the host bus to other bus standards, for example, cPCI or VME, is possible by exchanging the carrier boards.

Four categories of modules are employed by STARS:

(i) ADC and DAC modules;

(ii) FPGA modules;

(iii) DSP modules;
(iv) memory modules.

All modules, except for the FPGA modules, employ a supplementary FPGA to provide external and internal interfaces and the modules own firmware. Both types of interfaces will be pointed out within the next section. Typically, these supplementary FPGAs are not fully occupied by the present firmware, so that the programmer can incorporate his own functions to some extent.

The DAQ modules offer two-channel ADC and DAC. The ADC (2x AD6645) allows a resolution of 14 bit and a maximum sampling frequency of 105 MHz. The data are gripped by the Sundance high-speed bus connector (SHB) and forwarded by this bus to the targeted module. The DAC (AD9777) shows a 16-bit resolution at an input rate of 160 megasamples per second (MSPS). It also features an interpolation filter to achieve the DACs maximum rate of 400 MSPS. The DAC data are allocated by a second SHB connector. The on-module Xilinx Virtex-II FPGA (loaded from PROM or JTAG) provides further firmware allowing, beside communication interfaces, complete control of all ADC/DAC features and system debugging facilities. Additional user pins are provided for extra connections, for example, automatic gain control (AGC). The module provides 50Ω single-ended analog inputs and outputs, external triggers, and external clocks, which can be deployed on behalf of the internal ones.

The pure FPGA modules make use of a Xilinx Virtex-II XC2V4000-5, with 4 million system gates as reconfigurable hardware resource and provide 2 MB of external zero bus turnaround (ZBT-)random access memory (RAM). Four SHB connectors are available for module interconnection. The programming is done over a communication link to a DSP module or can be done using JTAG.

The DSP modules use either one TI TMS320C6416 (fixed-point) clocked with 600 MHz or two TI TMS320C6713 (floating-point) clocked with 225 MHz. Flash memory on the DSP modules can be used to store programs and configurations especially for the on-board Xilinx Virtex-II XC2V2000-4 FPGA also existent on the DSP modules. The TMS320C6416 module provides 8 MB of external ZBT-RAM and around 1 MB of internal memory. Two SHB connectors can be deployed for module interconnection. The dual TMS320C6713 module shows 128 MB of external memory and 256 kB of internal memory per DSP. It offers two SHB connectors (one per DSP) and one direct SHB connection between the two DSPs.

The memory modules exploit a Virtex-II Pro XC2VP7 and offer 1 GB memory to store numerous snapshots of data even at 100 MHz sampling frequency. The firmware also facilitates playback of stored data in real time. It can also be interconnected with all other modules offering SHB connectors.

39.3.2. Platform interfaces

For a modular rapid prototyping platform like STARS, the interfacing plays a rather important role. Such a platform must provide different kinds of interfaces for internal high-speed data transfer, interfaces for internal communication, and interfaces for control and setup of external peripherals (e.g., RF front ends, host).

Aim of this section is to give an overview of the most relevant interfaces and to point out the facilities to add further interfaces. Full knowledge of all specifications (including the source code of interface cores) is needed for future interface modifications or improvements.

Internal interfaces. The internal interfaces of the platform are mainly dedicated for communication between the involved Sundance TIM modules and for setup purposes. The interfaces are managed by the TIM's FPGA firmware, which can be reprogrammed for customizing the interfaces if required. Sundance therefore grants access to the interface sources codes on request.

(i) The *communication port* (CP) can connect two TIMs together to provide a bidirectional 8-bit wide path for exchanging streams of 32-bit values at about 20 MBps. This is the basic communication method for all TIMs and is usually used to load programs into processor TIMs and configuration of TIMs offering A/D, D/A, memory, and others.

(ii) The *Sundance digital bus* (SDB) is a 16-bit parallel data link that allows transfer at up to 200 MBps using a ground interlaced signal cable. Like the CP, the SDB is accessed as 32- bit interface, which is presented at the connector as pairs of two 16-bit accesses.

(iii) The *Sundance high-speed bus* (SHB) is the second generation of the Sundance digital bus (SDB). The SHB can be used as a custom-design 60-way I/O port from the FPGA or can be configured as 2×16-bit SDB ports, 1×8-bit and 1×32-bit or 5×8-bit ports. The maximum speed for the SHB is rated up to 200 MHz (800 MBps) using Virtex-2 FPGAs fitted on the module sites. Between DSP modules and others, typically a 2×16-bit port or a 1×32-bit port rated at 100 MHz is used, which leads to a transfer rate of about 400 MBps.

For all mentioned interfaces there are usually no restrictions on the direction of transfer, as the hardware device will automatically switch from reading to writing as necessary. By using the FPGA firmware, all communication devices appear as operating on 32-bit values—so a virtual 32-bit interface is used. In case of the DSP, a communication device is a set of memory-mapped status, control, and data registers, which the DSP reads and writes to access the communication resource. The firmware implementation determines how these bits are presented on physical interface—the connector. This may involve a conversion process, for example the CP interface takes the 32 bits of the virtual interface and transmits them to the CP connectors in four sequential lumps of eight bits.

External interfaces. Thanks to the mixed approach of DSP and FPGA, several interfaces can be used to control or communicate with external peripherals or the host PC. The TI DSPs of the C6000 family know several communication standards off the shelf (e.g., SPI, GPIO[1]) which are accessible on I/O pin headers of the TIM modules. The FPGA modules also provide beside JTAG access over a pin header some user I/O pins on the SHB connectors. In general, it is thereby possible to create specialized and fast interfaces using the signals presented on the SHB

[1]General-purpose input/output.

connectors. In addition, an external buffered CP and a JTAG connector for external debugging are present on the carrier boards. Interfacing to the host PC is done using the global bus (32-bit wide), which interconnects a TIM module to the PCI-bus of the host PC. Usually this is the root DSP module. Data transfer rate to the host PC is 60–100 MBps, which is directly supported by the Sundance software tools and the 3L Diamond real-time operating system (RTOS).

39.3.3. RF front end

ATMEL's AT86RF240 is a fully integrated, low-cost RF 2.4 GHz IEEE 802.11b standard direct-conversion transceiver for wireless LAN applications. It combines excellent RF performance at small size and current consumption. The transceiver combines low noise amplifiers (LNAs), receiver (Rx) I/Q mixers, transmitter (Tx) up-converters, Rx and Tx filters, power amplifier (PA) driver, voltage controlled oscillator (VCO), synthesizer, and autonomous automatic gain control (AGC), which also includes antenna diversity, all fully digital controlled. The number of necessary external devices is limited to only a few devices.

The transceiver is able to operate with nearly every baseband (BB) and medium access controller (MAC) combination existing in the market. The circuit contains four main blocks: receiver, transmitter, synthesizer, and periphery.

Transceiver control. Configuration registers serve as control elements for the analog circuit blocks. The registers are able to set currents and voltages controlling transceiver modes, timing, frequencies, and gain levels. A SPI 4-wire bus is able to write/read the registers. Before the transceiver is able to work, certain initializations are necessary. After power on, a device initialization takes place and loads the registers according to a predefined table. Then the transceiver can be set to the following

(i) *Sleep mode* (all circuit blocks are powered down).
(ii) *Standby mode* (only bias system and internal clock reference block are active).
(iii) *Filter calibration mode* (automatic filter calibration, tunes filters to desired filter behavior independently from process parameter spread).
(iv) *Synthesizer mode* (VCO and PLL synthesizer are powered up and channel setting is done).
(v) *Tx mode* (synthesizer mode and all Tx path circuits switched on).
(vi) *Rx mode* (synthesizer mode and all Rx path circuits switched on); this mode also contains different AGC modes:
  (1) *AGC control* (automatic (successive approximation) or manual gain setting (gain map table) via SPI of all Rx blocks);
  (2) *antenna diversity* (enabling or disabling).

Receive chain. The receive chain consists of LNA, I/Q mixer, lowpass filter (LPF), and several AGC amplifiers. All circuit blocks are based on differential architecture.

The transceiver covers the whole 2.4 GHz band. The Rx path exhibits a total gain range of 10 dB–100 dB, with coarse gain tuning in 6 dB steps and fine gain

tuning in 0.376 dB steps. The sensitivity is −84 dBm for 11 Mbp/s complementary code keying (CCK) signals. The noise figure and 1 dB compression point are 3.5 dB and −5 dBm, respectively. The LNA shows four gain modes: 0 dB, 6 dB, 12 dB, and 18 dB. In the high-gain operation, inductive emitter degeneration is used. This topology also provides low input impedance, good noise behavior, and a good linearity. In the lower gain modes, resistive emitter degeneration is used. The core cell consists of differential modified common emitter with cascaded transistors providing high isolation between LNA input and output.

The external LNA input impedance shows 50Ω differential. An external balun transfers 50Ω single-ended board impedance to this differential input port impedance. The I/Q mixer is a doubly balanced Gilbert-cell-type mixer. The gain control for the gain modes 4 dB, 10 dB, 16 dB, and 22 dB is realized by switching between different gain-mode input transistor pair configurations and their bias currents in both frequency modes. The DC feedback amplifiers are used to remove any undesired differential DC offsets from the output, which is essential in direct-conversion receiver topology. In addition to compensating bias current change due to gain mode switching, a constant current control loop is introduced. Its purpose is to maintain constant load bias current in order to have fixed output RC pole. The process variations over the output RC pole are compensated via the 5-bit controlled CDAC. The I/Q output of the mixer is DC coupled to the following LPF stages.

The Rx lowpass filter is a 6th-order active leapfrog structure with Butterworth characteristic. The corner frequency is 5.5 MHz. Each stage contains an operational amplifier. RC calibration circuit, described under periphery, tunes the corner frequency independently of temperature and process variations.

Three succeeding AGC amplifiers level up the Rx signal. Each is switchable in 6 dB gain steps. The first amplifier is adjustable at 3 dB, 9 dB, 15 dB, and 21 dB, while the second and the third amplifier realize gains at 0 dB, 6 dB, 12 dB, and 18 dB. The amplifier chain is completed by the fine gain stage. To match the needs of different BBs, an output buffer is added delivering a nominal I and Q output voltage of 1 Vpp differential at 0 dB gain setting. The output voltage can be adjusted in a range of −9 dB to 2.25 dB in steps of 0.76 dB.

The main advantages of direct-conversion receivers—lower number of necessary circuit blocks, easy to integrate lowpass filter, and use of operational amplifier with relatively low upper frequency corner—show at least one essential drawback: DC offsets at Rx path output would be converted into a frequency offset in the BB which results in higher error vector magnitude of the desired signal. The DC feedback circuit reduces the different offset sources in a direct-conversion receiver. DC feedback offset compensation is distributed over the gain stages.

Transmit chain. The transmit path consists of fine-gain amplifier, followed by Tx low pass filter, I/Q up-converter, and PA driver.

While the fine-gain amplifier serves as level shifter and gain matching circuit, the following lowpass filter behaves similar to the Rx filter: the same Butterworth filter type but only of 5th order with a corner frequency of 8.25 MHz. The same RC

calibration circuit, described under Receive chain, tunes the corner frequency independently of temperature and process variations. The complex filtered baseband signal is up-converted with an I/Q up-converter. The differential voltage is converted into a differential current. This allows to maximize the input voltage swing and a direct drive of the up-conversion mixer. The power amplifier control block based on the Gilbert cell architecture controls the output power of the following PA driver by more than 30 dB in 1 dB steps. The PA driver delivers 5 dBm power at 50Ω differential output impedance. An external balun transfers 50Ω single-ended board impedance to this differential output port impedance.

Synthesizer. The main parts of the synthesizer are VCO and fractional N PLL. The VCO is a differential 5 GHz LC oscillator with a fully integrated resonator. The VCO is serving the 2.4 GHz band. Dividing by two and following the quadrature generator provide the necessary differential I/Q local oscillator (LO) input signal for the I/Q mixer stages. Coarse and fine tuning elements have been used to cover the wide frequency range and to fulfill a high-frequency resolution. The main reason using a combined analog and digital hybrid operating phase-locked loop (Hybrid PLL) is to overcome tolerance, noise, and integration problems in the VCO. The coarse tuning is realized by switching on and off parts of a capacitor array, which also compensates technology variations; it gets the digital frequency information directly from the digital PLL. The fine tuning is realized by a varactor, which compensates frequency drifts due to temperature change too; it gets the analog voltage from the analog PLL that adjusts the small frequency offset.

Periphery. Several supporting circuits are necessary to setup the right functionality of the transceiver. The most important circuits have been described below. The crystal oscillator delivers the time base for all time-dependent transceiver functions. The complete oscillator has been integrated into the transceiver. Only the 22 MHz crystal and two additional load capacitances has to be added externally. The RC calibration circuit tunes the integrated receive path lowpass filter, which uses on-chip RC components to define the corner frequency. The time constant must be calibrated because of the strong process dependence of the absolute RC values (30%–40%). The transceiver is programmable via a 4-wire SPI bus conform interface. The SPI of the transceiver operates only in slave mode. So data have been transferred between transceiver and BB/MAC via radio's registers.

Antennas. The STARS platform is equipped with omnidirectional, stacked half-wave dipole antennas with a frequency range of 2350–2500 MHz and 7 dBi gain.

39.3.4. Interfacing the RF front end's

Two connections to each RF module have to be realized: first the analog signal path with a bandwidth of 10 MHz on each I and Q path, and second, a digital connection to control the RF module itself.

For the analog path the RF module provides a so-called *differential signal design* interface for the Tx and Rx signals at each I and Q path. With this, two signal

lines run from each signal source to the interface connector and to the connected external component. The signal itself is included in the voltage-level difference between these lines. Any common voltage of both lines is removed. This interfacing design is used for maximum noise rejection, whereas Sundance ADC and DAC modules were delivered in single-ended signal design, when the signal is between one line and module ground. This design is sensitive to noise error, because it picks up environmental electrical activity.

So a single-ended-to-differential conversion has to be done at the transmitter side and the opposite conversion at the receiver side. These conversions are realized by wideband, single-ended-to-differential line drivers and differential-to-single-ended line receiver. Such general-purpose converters are available on the market as integrated circuits. Less external components are required for making use of them.

For the digital control of the registers inside the RF modules, a 4-wire serial peripheral interface (SPI) is applied. In order to interface up to four RF modules to be controlled by one STARS DSP module, a SPI master controller is required. A Texas Instruments TMS320C6713 DSP is assigned for this task. It is equipped with one accessible multichannel buffered serial ports (McBSPs), which is configured as the SPI master. It operates with a 440 kHz SPI clock frequency. The RF modules act as SPI slaves. A resource-saving external microcontroller to transparently interface up to four radio modules is under development.

39.4. Software platform

Among the hardware platform and its components, a rich set of software tools is required to develop DSP- and/or FPGA-based applications in an efficient and fast way. This section therefore points out the software platform and tools used within the STARS project, including additional project support software like revision control for developed software.

39.4.1. DSP development tools

For a single processor system, TI's Code Composer Studio (CCS) for the C6000 family of TI's DSPs gives all tools needed for developing, analyzing, and debugging DSP algorithms in an integrated development environment (IDE). It provides a rich set of tools to profile and optimize the code. Together with TI development starter kits (DSKs), we use the CCS for evaluating computational complexity of single algorithms in a predevelopment process. The RTOS provides tools for development of multiprocessor DSP-based STARS platform. Compilation, linking, and debugging are still done using TI's CCS, to which the RTOS adds a comprehensive framework for multiprocessor software development. The RTOS also supports networks of mixed C6000 types and provides access to host services, C standard I/O, and Windows GUI, from all DSPs in the system. It provides a multiprocessor, multithreading microkernel with preemptive, priority-based real-time scheduling and a context switch time around 500 nanoseconds (200 MHz CPU).

The transparent, deadlock-free communication between DSPs is independent of network topology, which is configured in a single configuration file. It is thereby possible to develop task-structured multiprocessor software on a single-processor hardware and then later deploy the tasks on a multiprocessor hardware without code changes, recompilation, or relinking. Data can be transferred between the host and any DSP in the system over high-speed interprocessor links, leaving the slow JTAG chain free for debugging. It also allows effortless parallelization of sequential code and hassle-free control of on-chip resources, like DMA channels, host PC interaction, and peripheral interface.

39.4.2. FPGA development tools

For FPGA development, several design suites are offered by the market. Targeting at Xilinx's Virtex-II family, three major players are well-known: Xilinx Corporation with its integrated software environment (ISE), Mentor Graphics Corporation with its FPGA advantage suite, and synplicity Inc. with its synthesis and verification solutions.

Typically, they all support up to three most common hardware description languages (HDLs): VHDL, Verilog, and advanced boolean equation language (ABEL). VHDL stands for VHSIC (very high speed integrated circuit) hardware description language. It is a language that describes a logic circuit by functions, data flow behavior, and/or structure. The VHDL programming syntax is similar to the ADA (similar Pascal) programming language, where the Verilog language is similar to the C programming language. ABEL is simpler than VHDL and is especially used in low-complexity designs. Within the STARS project the in Europe widely spread VHDL is used for FPGA programming.

A VHDL design begins with a so-called ENTITY block that describes the interface of the design. The interface defines the input and output logic signals of the circuit. The ENTITY block is followed by an ARCHITECTURE block which describes the operation of a design entity by specifying its interconnection with other design entities, by its behavior, or by a mixture of both. The VHDL language groups the constants and the subprograms into a PACKAGE block. For customizing generic descriptions of design entities, CONFIGURATION blocks are used. VHDL also supports libraries and contains constructs for accessing packages, designs entities, or configurations from various libraries.

The VHDL language is related to other programming languages like ADA or C. It has also the sequential statement like a loop or if-then-else enquiry. The VHDL code is not a construct of a program which runs in a process but a function which describes the logic block and is realized in a programmable logic device (PLD). It provides several concurrent constructs that relate more closely to real hardware design. The program for example written with C is executed sequentially, which means that the next expression runs after the previous one, while the VHDL code highlights the concurrency. Since in an actual digital system, all small or large elements of the system are active simultaneously and perform their tasks concurrently, the concurrency aspect of VHDL is heavily emphasized. In a

hardware description language, concurrency means that transfer statements, descriptions of components, and instances of gates of logical units are all executed such that in the end they appear to have been executed simultaneously. Meanwhile the VHDL language requirements also specify the need for software-like sequential control which describes the internal operational details of the components or subsections by sequential programming language constructs such as case, if-then-else, and loop statements.

After the design is created by VHDL programming language it can be simulated and synthesized to check its logical operation. SIMULATION is a base bones type of test to see if the basic logic works according to design and concept. SYNTHESIS allows timing factors and other influences of actual FPGA devices to effect the simulation thereby doing a more thorough type of check before the design is committed to the FPGA or a similar device.

The FPGA programming of the STARS platform is mainly assisted using software tools offered by Xilinx Corporation, which are centralized in Xilinx's ISE Foundation software. The VHDL files and the schematic design files will be used. The FPGA programming starts from writing different small blocks with VHDL programming language. In the *Project Navigator* interface of the ISE, these VHDL files can be converted into schematic symbols. By interconnecting all these small schematic symbols and adding corresponding user constraints, the top schematic file can be built.

The functionality of the sources can be verified by the ISE by using integrated simulation capabilities, including ModelSim Xilinx edition and the HDL Bencher test bench generator. HDL sources can be synthesized by using the Xilinx Synthesis Technology (XST) as well as partner synthesis engines used standalone or integrated into ISE. The Xilinx implementation tools continue the process into a placed and routed FPGA or fitted CPLD, and finally produce a bitstream file *.bit for the device configuration. This bitstream file is the exact configuration file that can be downloaded into the FPGA and implement the desired design into the FPGA.

39.4.3. Simulink-based development of DSP & FPGA processing

Rapid application development (RAD) tools for fast prototyping are getting very popular, because they are promising reduced learning time and project time. This is done by integrating a system-based and block-oriented development, which is hiding the high effort in programming of complex hardware and their interfaces. RAD tools give also the possibility of hardware and software codesign by putting simulation in software and real hardware together. A typical application is for example the study of bit resolution effects in digital systems. RAD tools can therefore help to evaluate an approach, without getting deep into programming details, which get necessary when tuning is required.

For DSP-based signal processing, Mathworks offers with Simulink and the Real-Time Workshop (RTW) a seamless RAD tool for fast prototyping in DSP-based systems. This approach also offers the possibility of hardware-in-the-loop

simulation, where parts of the application may run on the target DSP and others run on the PC. With the SMT6050, Sundance integrates this Simulink/RTW approach to the Sundance platform concept. It is a software tool, which allows even novice users to develop an entire application targeting Sundance hardware within the Simulink environment and then to automatically generate target DSP code in C programming language. Therefore, the SMT6050 includes a blockset for Simulink providing an optimized library of routines supporting specific Sundance interfaces for communication between DSPs, ADCs, and DACs present in the system.

In Simulink, a model of the application could be developed and simulated on the host computer. The application can consist of components running on the DSP system, and/or components running on the host system. The part running on the DSP platform could be for an embedded application and does not communicate with the host at all. On the other hand, the DSP application could exchange data with Matlab running on the host and benefit from its powerful graphical and functional resources or communicate with a host application also developed under Simulink.

Following a similar approach for FPGA-based development with help of Simulink, Sundance provides the SMT6040 hardware development tool, which gives Simulink the capability of describing digital hardware circuits and systems. The SMT6040 can generate VHDL code from Simulink diagrams and allows accurate and fast cosimulation of the hardware subsystem interacting with associated software subsystems and, when existing, with external devices and systems. This gives the ability to describe, simulate, tune, debug and optimize hardware systems, and eventually programming the FPGA board accordingly, in a straightforward and transparent way. Therefore, an extended hardware blockset is supplied with SMT6040, which supports (in hardware) most blocks from the basic Simulink blockset and the full range of Sundance communication interfaces.

39.4.4. Project and revision control

Once multiple developers are sharing their code and work together on one or more different projects or subprojects, it becomes obligatory to track the changes in software and hardware. Revision software control is done by using the open-source tool CVS (www.cvshome.org), which provides, combined with a graphical user interface like WinCVS (www.wincvs.org) or TortoiseCVS (www.tortoisecvs.org), a powerful and advanced framework for software development and revision of documentation. Hardware changes are tracked within a logbook file, which could also be tracked using CVS. As pointed out in the Five-Ones approach (see, e.g., [1]), a rapid prototyping team requires diverse experts, which are willing to share their specific knowledge in a single team. The knowledge of our team members covers advanced MIMO algorithms as well as hardware and software for DSP and FPGA implementations. The ease-of-use platform is provided by using the Matlab graphical user interface (GUI) facilities and binary file format to exchange and store the configuration data and auxiliary information beside the transmitted or

received data in one file. Revision control, documentation, and ease of use of hard- and software are also the basics for international cooperation in research and development using such a platform.

39.5. System debugging

In the previous sections, the conceptual design of the STARS platform and the used hardware and software components are presented. With setting up the MIMO platform, several challenges must be met to produce and verify the expected behavior of the platform.

In this section, we therefore like to point out some of these challenges and their relation to system debugging:

(i) common clock for radio frequency and sampling;
(ii) automatic gain control issues;
(iii) measurements of usable analog system bandwidth;
(iv) insight to the on-air signal.

39.5.1. Providing a common clock

The RF front ends are equipped with a frequency synthesizer for the up-/down-converter. The reference of the frequency synthesizer is a 22 MHz clock signal. In order to synchronize multiple RF front ends, the same 22 MHz reference clock is applied to all front ends on transmitter side or receiver side, respectively. Therefore, it is ensured that a common radio frequency is used for transmitting or receiving. For system debugging reasons, it is also possible to provide the same 22 MHz reference clock to the transmitter and receiver, thereby a transmission chain with a negligible frequency offset is produced.

Basically the same is required for the ADC/DAC modules. Since each of the used ADC/DAC modules consists of two already synchronized channels, all of the used ADC/DAC modules are supplied with a common synchronized clock. This ensures a synchronous conversion by each of the ADCs/DACs used. In addition, a common trigger is used to obtain a fully synchronized data flow from/to the ADCs/DACs.

39.5.2. Controlling the automatic gain control (AGC)

Usually an AGC is used to ensure that the analog signals are within the dynamic range of the ADCs. In addition, multiple gain-controlled stages can be found within the RF front end to prevent any of its components from being overstrained. The AGC of the used RF transceiver chips are designed for single antenna operation and can run independently and autonomously of baseband processing. The transceiver chip allows to digitally read back the state of AGC, to switch off the AGC, and allows also fully digital control of gain stages by baseband processes.

In principle, two concepts of AGC in case of MIMO can be investigated.

(i) Each antenna path has its own AGC running independently of all other paths. Benefit is that the dynamic range of each ADC is optimized, but for later MIMO processing, the gain in each path is required. Therefore it is mandatory to have the ability to read back the state of each AGC.

(ii) The required gain of each antenna path is acquired and some kind of gain controller decides for a gain setting to be used in all antenna branches. For example, the strongest antenna path determines this setting. In MIMO processing, no additional information is thereby required. One drawback of this method is that dynamic range of all ADCs will not be fully exploited in all cases.

For system debugging purposes, the AGC is switched off and the gain settings are then optimized by hand regarding the currently incoming signals seen on oscilloscopes. This method is of course only useful in case of system debugging. In all other cases, the AGC have to react very fast to lock the currently received signal power and hold this state until one frame is completely received.

39.5.3. Measurement of the usable analog system bandwidth

The usable RF bandwidth of every platform is limited due to several band limiting filters like Rx and Tx filters in the RF front end. To determine the total usable bandwidth, a digital sine wave signal with constant magnitude and sweeping frequency is generated offline, loaded into the memory of the DAC module of the platform, and transmitted using the offline mode of the platform. The received signal, affected by all filters in the transmit-receive chain, is logged by the receiver for later offline analysis. The total transfer function is obtained by analyzing the received signal offline and determining the spectral components in the frequency domain. Since the transmitted signal consists in the frequency domain of a sweeping impulse with constant magnitude, the received signal also consists in the frequency domain of a sweeping impulse but with damped magnitude due to the total transfer function such that the total transfer function can be determined step by step.

39.5.4. Insight to the on-air signal

By simply connecting an antenna to the input of an adequate spectrum analyzer, the on-air signal's spectrum can be viewed. This method allows verifying the occupied signal bandwidth and is giving insight to possible distortions, interferes, nonlinearities, and signal power situations. This convenient approach helps for system debugging by probing the on-air signal in different positions.

In order to verify the on-air signals in the time-domain, a digital storage oscilloscope can be exploited in the same way, providing sufficient analog bandwidth, sampling rate, and memory to store snapshots of signals for later analysis.

39.6. Evaluation of real-time requirements

One of the major challenges of STARS results from the real-time requirements. On the one hand, a sufficient degree of flexibility can be achieved only by rather slow

DSP implementations, on the other hand, high-speed algorithms have to be implemented by programming-intensive FPGAs. The following two sections highlight some basic aspects and show some first results for an IEEE 802.11a transceiver.

39.6.1. Real-time requirements of DSP

The response time (latency and execution time) for processing an OFDM symbol according to IEEE 802.11a standard is 4 microseconds. On the DSP TMS320C6416 @600 MHz, 4 microseconds translates to 2400 cycle count. Designing the transceiver with this constraint is necessary to avoid dropped data or noise in the output that will decrease the targeted performance. One conventional way to develop real-time transceivers is to distribute bitwise (serial) software (SW) processing tasks on a multiprocessor environment. However, the need for more than one DSP and the interconnecting hardware (HW) significantly increase the development cost. Consequently, a new real-time transceiver based on blockwise parallel SW architecture is developed, which operates efficiently in a single processor environment.

39.6.2. Real-time transceiver performance of DSP

The implementation of a bitwise processing SW for the transceiver gives the expected poor performance. A significant speedup comes from unrolling the loops. However, this contributes a little towards satisfying the real-time requirement. A spectacular speedup comes from the blockwise parallel processing. The blockwise parallel SW architecture splits input data into 16-bit or 32-bit sliding window, depending on the processing block, and processes the bits within each window in parallel. The blockwise parallel SW architecture thus allows minimum cycle count per bit, minimizes memory access, and maximizes first-level cache hit ratio. The overall result is a dramatic speedup in cycle count per OFDM symbol for various data rates as shown in Table 39.3. As can be seen, the highly optimized bitwise SW for various data rates are 1.6 to 3.5 orders of magnitude slower than the corresponding parallel SW.

The required number of DSPs for the two SW architectures per OFDM symbol is also presented for comparison. It shows that at least three DSPs and the interconnecting HW are required for the serial SW to operate in real time while the parallel SW algorithm requires only one DSP. To extend the developed real-time transceiver for real-time MIMO-OFDM, we propose to implement computation intensive tasks such as the interleaver, FFT, IFFT, and frequency and timing synchronization on the FPGA module. This is expected to free the DSP for other primitive control requirements and further improve the overall performance of a target real-time MIMO-OFDM transceiver.

39.6.3. Implementation opportunities on FPGA

As mentioned earlier, the high-speed requirements for data processing motivate the employment of FPGAs in order to accelerate the overall execution in the digital

Table 39.3. Cycle count per OFDM symbol for different rates.

Data rate (Mbps)	Modulation	Coding rate	Cycle count for the serial SW architecture	Required DSP(s) for the serial SW in real time	Cycle count for the parallel SW architecture	Required DSP(s) for the parallel SW in real time
6	BPSK	1/2	1927	1	1176	1
9	BPSK	3/4	2109	1	1263	1
12	QPSK	1/2	2759	2	1472	1
18	QPSK	3/4	3006	2	1550	1
24	16-QAM	1/2	3744	2	1425	1
36	16-QAM	3/4	4533	2	1650	1
48	64-QAM	2/3	6001	3	1860	1
54	64-QAM	3/4	6169	3	1942	1

front end. With a high data-rate operation, most of front-end algorithms for correcting RF impairments, filtering, channel equalization, and IFFT/FFTs, among others, can be suitably implemented at the desired data rate.

In MIMO scenarios, the parallelism delivered by FPGAs is convenient for processing signals arriving from different antenna branches. Thus, the overall system throughput is improved by either replicating hardware structures for each receiving antenna, by using multiplexing techniques for the data acquired in each branch, or by pipelining the data paths while making use of the high board clock speeds.

Internally, FPGAs are provided with logic resources that can be configured as registers and memory banks, which help for queuing and intermediate storage; logic and arithmetic functions; and dedicated digital multipliers distributed over the chip area. The amount of resources available makes it feasible to synthesize customized digital signal processing algorithms that execute in a concurrent model. In addition, the high number of input/output pins (configurable for working at different I/O standards, like CMOS, LVTTL, and so forth, with programmable I/O impedance) enables the interfacing to external hardware elements like analog-to-digital and digital-to-analog converters, digital signal processors, and even transmission lines, building up complex high-performance systems. In such an approach, the FPGA can run parallel algorithms in hardware that relieve other processing cores, like DSPs, from computational burden, leaving it for more complex, control-oriented execution. For this, commercial off-the-shelf (COTS) and intellectual property (IP) blocks developed by different manufacturers or providers are thoroughfully tested and ready to synthesize which will improve the development time.

Moreover, FPGA solutions are provided with facilities for generating highly accurate and stable internal and external digital clock managers, which implement

functions like digital locked loops, frequency synthesis, and clock distribution, among others. With the help of these, common clocks can be generated to synchronize MIMO components during testing and eventually in a final design, for example, ADCs and DACs, reducing the complexity of synchronization algorithms.

Among others, algorithms for solving signal impairments, like I/Q mismatch, DC and frequency offset, power amplifier, and analog filters nonlinearities, introduced in the analog radio front ends, are strong candidates for being implemented in FPGAs. They produce unwanted negative effects, like the increase of the bit error rate, interchannel and intersymbol interference, out-of-band emissions, and performance degradation. Hence, the calibration of the RF part must be performed in the digital front end of a communication system in order to improve the system performance, before delivering the received data for further processing. Other applications that are suitable for implementation in a pure hardware approach include fast Fourier transformations, digital filtering, and synchronization tasks.

As first test case and for gaining experience in FPGA development we decided to start implementing the synchronization unit as shown in Section 39.7.3. The required COordinate Rotation DIgital Computer (CORDIC) is a class of hardware-efficient iterative solutions for calculating arithmetic, trigonometric, hyperbolic, exponential, and their inverse functions.

The CORDIC algorithm can be used in general for tasks like channel estimation and equalization, digital modulation and demodulation, and frequency synchronization for fixed-point arithmetics. The algorithm uses elementary operations like addition, subtraction, and shifts to perform its task.

There are a number of ways to synthesize a CORDIC processor. The implementation depends on the speed versus computational complexity tradeoffs in hardware. An iterative architecture is a direct translation from the CORDIC equations, it can be obtained simply by mapping each of the CORDIC equations in hardware. Its disadvantage is that if implemented, it will require several layers of logic and the result is a slow design that uses a large number of logic cells. A result is produced only after all the iterations are completed.

The iteration process can be unrolled so that each of the processing elements always performs the same iteration. The unrolled processor is easily pipelined by inserting registers between the adder-subtractors. This results in a considerably faster CORDIC processor but the need for FPGA resources increases.

The iterative parallel architecture can be seen in Figure 39.4. The schematic contains 3 adder-subtractors, one for each equation, 2 variable-shift shifters, a ROM, a counter, 2-bit inverters, some registers, and a controller that multiplexes between the original inputs and the iterated values according to a control signal generated by the counter. A clock input synchronizes the whole process.

Table 39.4 gives a summary of the device utilization. The target FPGA is a XC2v4000-6-ff1152 Virtex 2 device. The whole implementation process was carried out with help of Xilinx ISE (see Section 39.4.2).

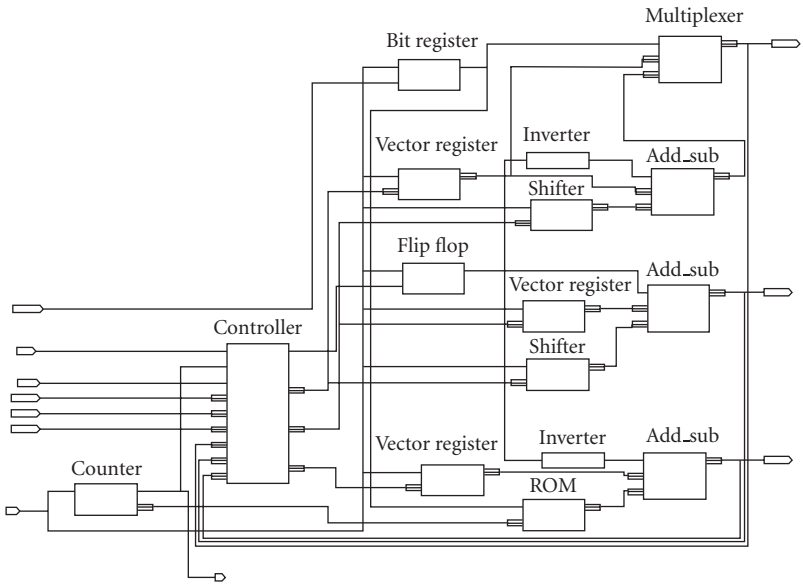

FIGURE 39.4. Parallel iterative CORDIC architecture.

TABLE 39.4. Device utilisation summary.

Selected device		XC2v4000-6-ff1152		
Number of slices	563	out of	23040	2%
Number of slice flip flops	316	out of	46080	0%
Number of 4 input LUTs	1019	out of	46080	2%
Maximum achieved frequency		123.84 MHz		

39.7. An algorithm example

As a test case of the STARS platform, this section presents baseband processing algorithms, which can be used at the receiver to recover the transmitted information. In order to have a common notation, first a mathematical transmission model is introduced.

39.7.1. SIMO OFDM system model

We consider a $1 \times Q$ SIMO transmission. In OFDM, data is transmitted blockwise. An N-point inverse fast Fourier transform (IFFT) of N_u modulated subcarriers $s_n(k)$ of the kth block is performed:

$$x_i(k) = \sum_{n=-N_u/2}^{N_u/2-1} s_n(k) e^{j(2\pi/N)in}, \quad 0 \le i \le N-1. \tag{39.1}$$

To combat interblock interference (IBI), a cyclic prefix of length N_g is preceded before the signal is digitally filtered and D/A converted. In a baseband model, the signal is sent via the baseband radio propagation channel to the qth receive antenna and filtered with the receive pulse shaping filter. Combining transmit filter, channel, and receive filter yields the overall time-variant impulse response

$$h^q(\tau, t) = \sum_{l=1}^{L_c^q} h_l^q(t)\delta(\tau - \tau_l^q), \tag{39.2}$$

where L_c^q is the number of relevant paths between the transmit and the qth receive antenna.

After A/D conversion, the cyclic prefixes are removed and a fast Fourier transform (FFT) is performed to demodulate the signals. In case of perfect synchronization, the signal on the nth subcarrier is given by

$$d_n^q(k) = \sum_{i=0}^{N-1} r_i(k)\mathrm{e}^{-\mathrm{j}(2\pi/N)in} + \nu_n^q(k) = H_n^q(k)s_n^q(k) + \nu_n^q(k) \tag{39.3}$$

with $r_i(k)$ denoting the received samples of the kth block and qth antenna and $H_n^q(k)$ being the channel transfer factor on the qth receive antenna and nth tone. $\nu_n^q(k)$ is assumed to be additive white Gaussian noise. For our testbed, the following system parameters are used concordant with the IEEE 802.11a standard: $N = 64$, $N_u = 52$, $N_g = 16$, and $Q = 2$.

39.7.2. Synchronization algorithm

Synchronization in time is essential in any communication system. However, OFDM-based systems make an additional demand on the synchronization unit as even frequency rather than timing synchronization is more critical. In case of carrier frequency offsets (CFOs) which are caused by mismatches between transmitter and receiver oscillators or Doppler effects, and also of sampling frequency offsets (SFOs) between D/A and A/D converters, the fundamental principle of OFDM, named the orthogonality between subcarriers, is destroyed. Hence, it is indispensable for a properly running system to estimate and compensate for carrier and sampling frequency offsets. Also one major effect of oscillator phase noise—the so-called common phase error (CPE)—must be eliminated.

Time synchronization involves finding the optimal position of the DFT window for demodulation. Usually, the cyclic prefix length is designed to be larger than the channel impulse response length. Due to this margin, the performance requirements are relaxed. If the OFDM block start is found to be within this margin, an imperfect DFT window position start causes only a constant phase rotation for all subcarrier symbols. The phase shift cannot be distinguished from the channel influence and is estimated and compensated for by the channel estimation and equalization unit.

In principle, synchronization algorithms for SISO systems can be extended to SIMO scenarios without major changes. Mostly, data-aided approaches are based on the correlation between repeated signal parts which are provided by the IEEE 802.11a training structure and the cyclic prefixes. For the STARS platform, we adopt the preamble of the IEEE 802.11a standard consisting of ten short and two long training symbols [2].The synchronization procedure that we have chosen is performed in several steps.

39.7.2.1. Coarse timing acquisition

Coarse timing synchronization is found by maximizing the metric (similar to [3])

$$\hat{m}_1 = \arg\max_m \left| \sum_{q=1}^{Q} \frac{R^q(m)}{E^q(m)} \right|^2, \tag{39.4}$$

where $R^q(m)$ denotes the complex correlation sum and $E^q(m)$ the signal energy on each antenna branch. $R^q(m)$ and $E^q(m)$ are composed as the running sums:

$$R^q(m) = \sum_{i=m}^{m+N_\mathrm{p}} \left(r_i^q\right)^* r_{i+N_\mathrm{p}}^q \tag{39.5}$$

$$E^q(m) = \frac{1}{2}\left(\sum_{i=m}^{m+N_\mathrm{p}} \left| r_i^q \right|^2 + \left| r_{i+N_\mathrm{p}}^q \right|^2 \right), \tag{39.6}$$

with r_i^q being the ith received signal sample at antenna q including all nonidealities and $N_\mathrm{p} = 16$ for the short training symbols. Since the metric turns out to form a plateau, we detect the frame start on the falling slope of this plateau. The timing on all branches is assumed to be the same such that diversity is used to increase the estimation accuracy.

39.7.2.2. Carrier frequency synchronization

Since all receive antennas share a common oscillator, respectively, only one CFO must be estimated and compensated. In the SISO case, most algorithms are based upon the observation that CFOs only cause linear phase shifts of the received time-domain symbols. Hence, frequency offsets can be estimated by "measuring" the phase rotation. If there is only one CFO in SIMO, still this signal property can be exploited. The effect of a CFO on the received signal $r_i^q(k)$ for the ith time-domain sample and kth block can be expressed as

$$\tilde{r}_i^q(k) = \mathrm{e}^{\mathrm{j}(2\pi/N)(k(N+N_\mathrm{g})+i)f_\varepsilon} r_i^q(k), \tag{39.7}$$

where f_ε is the (relative) frequency offset normalized to the subcarrier spacing $\Delta f = 312.5\,\mathrm{kHz}$.

When the symbol timing is found, the CFO is estimated by (see [4, 5])

$$\widehat{f}_{\varepsilon} = \frac{1}{2\pi}\frac{N}{N_{\mathrm{p}}}\angle\left(\sum_{q=1}^{Q} R^{q}(\widehat{m}_{1})\right). \tag{39.8}$$

Due to the limited acquisition range of $|\widehat{f}_{\varepsilon,\max}| = N/(2N_{\mathrm{p}})$ in (39.8), the estimate for the frequency offset is found in two steps.

Step 1 (finding coarse estimate $\widehat{f}_{\varepsilon,1}$). Assuming for the short training symbols that, for example, $N = 64$, $N_{\mathrm{p}} = 16$, and a subcarrier spacing of $\Delta f = 312.5\,\mathrm{kHz}$, frequency offsets in the range from $-625\,\mathrm{kHz}$ to $625\,\mathrm{kHz}$ can be uniquely estimated. This large range satisfies usual constraints. For many applications, the accuracy of local oscillators is much higher. As the preamble offers ten identical symbols, we average the estimates from as many symbols as are not distorted from the AGC unit. Typically, half of them can be utilized. Once the coarse estimate is found, all subsequent incoming symbols are multiplied by $\exp(-\mathrm{j}2\pi\widehat{f}_{\varepsilon,1}i/N)$ to remove the CFO.

Step 2 (finding fine estimate $\widehat{f}_{\varepsilon,2}$). Next, since the CFO is significantly reduced by Step 1, we can use the long training symbols to improve the estimation performance. The acquisition range for the long training symbols ($N_{\mathrm{p}} = 64$) is $[-162.5, 162.5]\,\mathrm{kHz}$. Again, we multiply by $\exp(-\mathrm{j}2\pi\widehat{f}_{\varepsilon,2}i/N)$ to further reduce the frequency offset.

The same estimator can be applied to the signal repetition due to the cyclic prefix to track the CFO [6]. However, for our testbed, the CFO does not change significantly during one burst and hence, only post-FFT processing (see Section 39.7.2.4) to track the blockwise phase rotation is necessary.

39.7.2.3. Fine timing acquisition

If needed, a fine symbol timing acquisition can be achieved by cross-correlating the received symbols with the transmitted long training symbols $t_{\mathrm{L},m}$:

$$R_{2}(m) = \sum_{q=1}^{Q}\sum_{m=i}^{i+N_{\mathrm{p}}}\frac{t_{\mathrm{L},m}\left(r_{m}^{q}\right)^{*}}{\left|t_{\mathrm{L},m}\right|^{2}}, \tag{39.9}$$

and finding the maximum of $|R_2|$ for m. For complexity reasons, the cross-correlation is only computed a few samples around the coarse timing estimate.

39.7.2.4. Tracking

At the acquisition stage, the CFO was compensated such that it virtually produces no intercarrier interference. However, a residual frequency offset δf_{ε} still remains

and rotates the phase linearly with time. Moreover, oscillator phase noise induces intercarrier interference that cannot be eliminated with reasonable effort and—which can be compensated—a common phase error constant for all subcarriers and changing on a symbol-by-symbol basis [7]. Finally, imperfect sampling synchronization between Tx and Rx clock generators affects the phase in a similar fashion as CFOs. But the difference is that the phase increases linearly also with the subcarrier index n:

$$\tilde{d}_n^q(k) \approx \mathrm{e}^{\mathrm{j}\Phi_{\mathrm{CPE}}(k)} \mathrm{e}^{\mathrm{j}(2\pi/N)k(N+N_{\mathrm{g}})(\delta f_\varepsilon + n f_{\mathrm{s},\varepsilon})} d_n^q(k), \tag{39.10}$$

where $\Phi_{\mathrm{CPE}}(k)$ and $f_{\mathrm{s},\varepsilon}$ denote the CPE of the kth block and the SFO, respectively.

As a conclusion, the phase must be tracked by post-FFT processing. On the four pilot subcarriers p which are embedded in the OFDM block structure, the phase rotation from block to block is estimated by

$$\Delta\hat{\Phi}_p^q(k) = \angle \frac{d_p^q(k+1)s_p(k)}{s_p(k+1)d_p^q(k)} \quad \forall\, p \in [-21, -7, 7, 21], \tag{39.11}$$

and eliminated in a phase-locked loop (PLL) fashion.[2] Here, we used $d_p^q(k) = H_p^q s_p(k)$ implying that the channel is constant over several blocks. $s_p(k)$ are the known transmitted training symbols and $d_p^q(k)$ the received symbols on the pilot subcarriers. The phase rotation for other subcarriers is found by linearly interpolating between the equally spaced pilot subcarriers to account for the SFO.

In spite of negligible ICI, SFO reduces the bit error ratio significantly if not further considered. The SFO continuously shifts the position of the FFT window. Once the FFT window start has left the undisturbed part of the cyclic prefix, interblock interference occurs. Therefore, we estimate the SFO from (39.10), feed this information back, and eliminate the SFO in the time domain by interpolation. A less complex alternative would be to regularly correct the FFT window position according to the estimated SFO.

39.7.3. Implementation of synchronization unit

Equation (39.4), which provides the coarse timing acquisition, is a continuously running sample-based calculation that makes use of the diversity obtained from each receive antenna branch. In each of these branches, the terms in (39.5) and (39.6) need to be calculated; for both terms, in each receive branch, the procedure described below needs to be performed.

The received signal in each antenna needs to be delayed by N_{p} samples in order to be able to correlate the complex samples of the repeated signal parts. This delaying can be implemented efficiently with RAM memories, and such structures will be dominant over other components in terms of hardware size. Note that the separation by N_{p} will be different when correlating the samples from the short training

[2] The estimated phase rotation can be filtered to reduce estimation errors. However, note that this measure also filters out the contribution of the common phase error.

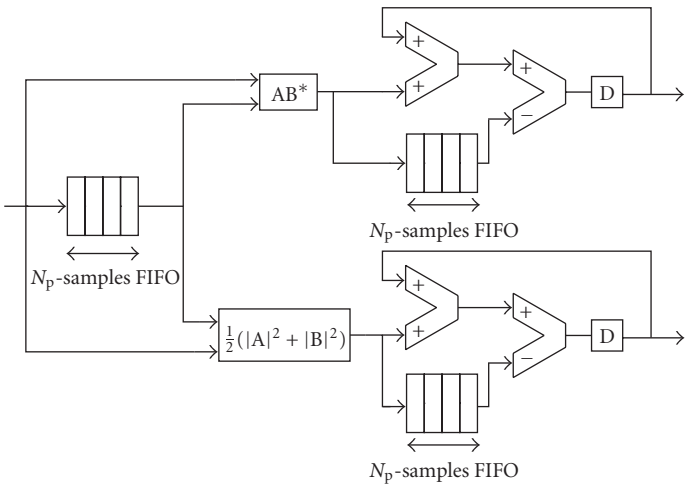

FIGURE 39.5. Metric calculation structure per antenna branch.

symbol and from the long training symbol. Both cases can be implemented in the same memory, if it has the size of the longest training sequence extension and if it is provided with a selectable output. If the in-phase and quadrature components of the samples are represented by B bits, the total storage required for delaying the samples for Q receivers will be $Q \times N_p \times 2 \times B$ bits. Assuming a 1×2 SIMO transmission, $N_p = 64$ and 16- bits samples for in-phase and quadrature parts, the whole delaying memory size will be 4096 bits.

Once the samples are delayed, they will be correlated and their energies will be calculated by means of multipliers, according to the metrics in (39.5) and (39.6). The correlation term, which is a complex value that contains the phase information for estimating the CFO, will be summed up over the last N_p samples; the same is done for the energy term, which will be a real value. Both cases of running sums require buffering of length N_p per antenna branch, containing either complex-valued samples (see (39.5)) or real-valued samples, what can be implemented with the RAM memories described before. The running sums and the metric calculation structure is represented in Figure 39.5.

Hence, the metric for calculating the coarse time acquisition will require 3 buffers per antenna branch. As the number of receiving antennas increases, the whole storage will increase linearly.

At each sample period, (39.4) is calculated. In order to avoid false detections of the preamble, this value is continuously compared with a threshold appropriately chosen. Once above the threshold, the maximum of (39.4) is searched for by comparing each new calculation with the previously recorded maximum, and updating the maximum when required.

Once the frame start has been found, (39.8) can be used for estimating the carrier frequency offset. On fixed-point format, the phase calculation is properly

realized by a CORDIC system. Since the frequency offset is common for all transmitters and receivers, only one estimation needs to be performed. The frequency offset can be compensated for all the samples arriving from this instant on. The correction takes place by multiplying the new arriving samples from each receive branch by $\exp(-j2\pi \widehat{f}_\varepsilon i/N)$. This can be achieved by calculating the real and imaginary parts (cosine and sine) of the argument and using complex multipliers at each receive branch. The same CORDIC used before can be employed for correcting the incoming samples from all the antenna branches from just one sine and cosine calculation; thus, the complexity is not considerably increased as the number of the receive antennas grows.

With the preamble structure of the IEEE 802.11a standard, coarse and fine carrier frequency offsets estimation can be performed. By use of appropriate control signals, the same hardware construction can be used for performing this task. A state machine will be necessary to keep track of the preamble under consideration.

39.7.4. Channel estimation

It is well known that the overall system performance highly depends on the quality of the channel estimation. Therefore, a relatively high amount of data must be reserved for training symbols. As already mentioned, the same frame structure as in IEEE 802.11a is used in the STARS testbed (for SIMO transmission). The preamble is designed to assist an initial channel estimation. BPSK modulated symbols on four pilot subcarriers, which are equally spaced on fixed positions in the frequency grid, serve to track the channel. We consider the SIMO transmission model introduced in the previous chapter. The channel is estimated on each antenna branch q and subcarrier n, separately. The estimation approach to minimize the least square error yields

$$\widehat{H}_n^q = d_n^q / t_{\mathrm{L},n} \quad \forall n, q \tag{39.12}$$

with $t_{\mathrm{L},n}$ denoting the training symbols in the frequency domain. Note that we average the result over the two long training symbols. Taking into account the limited maximum allowed burst duration of 4096 blocks in IEEE 802.11a and the fact that the channel changes slowly with time in indoor scenarios (Doppler frequencies $f_\mathrm{D} < 5\,\mathrm{Hz}$), it is sufficient to track the channel only each several hundred OFDM blocks (on the pilot subcarriers). Depending on the available processing complexity and the availability of the channel statistics, different kinds of interpolating techniques (such as Wiener filtering) in time and frequency directions can be used. Note that the phase rotation is estimated each block anyway.

39.7.5. Equalization

One major advantage of OFDM is the simple receiver structure, especially the equalization unit. As the broadband channel (20 MHz bandwidth) is split into 64

almost flat subchannels (312.5 kHz bandwidth), the equalization in OFDM turns to a simple division per subcarrier (zero forcing):

$$\hat{s}_n^q(k) = \left[\hat{H}_n^q(k)\right]^{-1} d_n^q(k) \quad \forall n, q. \tag{39.13}$$

To exploit spatial diversity in SIMO systems, three possible strategies can be applied: selection combining (SC), equal-gain combining (EGC), and maximum-ratio combining (MRC). In SC, only the strongest (in terms of the highest SNR) branch signal passes. In EGC, antenna signals are averaged. In MRC, all antenna signals are utilized advantageously such that signals with higher SNR are emphasized, which leads to a superior performance in all situations. The receive signals $r_n^{(1)}(k)$ and $r_n^{(2)}(k)$ are weighted with $w_n^{(1)}$ and $w_n^{(2)}$:

$$\hat{s}_n(k) = w_n^{(1)}\hat{s}_n^{(1)}(k) + w_n^{(2)}\hat{s}_n^{(2)}(k) \tag{39.14}$$

with $w_n^{(1)} = 0$ (or $w_n^{(2)} = 0$) for SC, $w_n^{(1)} = w_n^{(2)}$ for EGC, and $w_n^q \propto \sqrt{\mathrm{SNR}_n^q}$ for MRC.

If the noise power is the same for all antenna branches, it follows $\sqrt{\mathrm{SNR}_n^q} \propto |H_n^q|$.

39.8. First measurements with STARS

In the following, first measurement results of a SIMO transmission gained from the STARS testbed are presented. QPSK and 16-QAM modulated symbols embedded into several successive frames (with idle periods of 100 samples in between) are transmitted over air. One transmitted frame consists of 1 000 OFDM blocks—the frame structure used for this transmission is in agreement with the IEEE 802.11a standard. Two receive antennas are used to improve the system performance by spatial diversity.

39.8.1. Synchronization

The synchronization procedure is carried out as described in Section 39.7.2. An example for the metric of the coarse timing versus the sampling instants m is depicted in Figure 39.6.

Clearly, as almost close to the noise-free result, the detection of the frame as well as of the exact position of the frame start can be performed already very precisely such that fine timing synchronization is not needed. However, if the coherence bandwidth of the radio propagation channel becomes less, also fine timing synchronization may be required. After estimating and correcting the CFO up to less than a few kHz, the cyclic prefix is removed and the signals are demodulated blockwise by the FFT. In order to account for the low Doppler frequencies in indoor scenarios and to save demanding computations, the channel estimation is carried out only at the frame start. Nevertheless, the effects of the residual

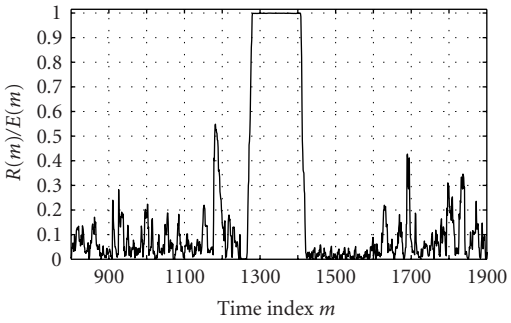

FIGURE 39.6. Metric of coarse timing synchronization.

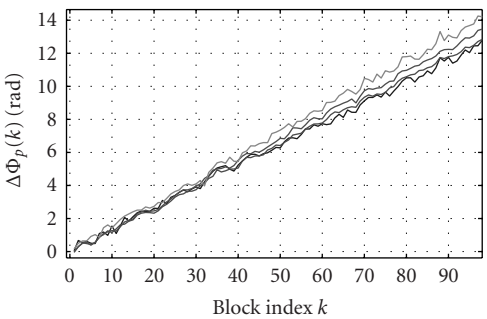

FIGURE 39.7. Estimated phase rotation $\Delta\Phi_p(k)$.

synchronization imperfections, mainly causing phase shifts, must be taken into consideration block by block. The estimated phase rotation of the symbols on the four pilot subcarriers in the frequency domain versus the block index k is shown in Figure 39.7. Three effects can be seen: a linear increase of the phase (caused by the residual CFO), a different slope (caused by the SFO), and random fluctuations (caused by the CPE and estimation errors). In a PLL structure, the phase is derotated blockwise. However, from the estimated phase shift, a very precise estimate of the residual CFO (here, 5.3 kHz) and the SFO (here, 1.2 kHz) can be obtained and fed back to the pre-FFT processing unit. Here, the estimated residual CFO can be compensated (if the error is higher than that of the (limited) bit resolution) for the next incoming symbols. Moreover, the SFO can be corrected via interpolation or by continuously shifting the FFT starting position.

39.8.2. Equalization

The channel estimates $\hat{H}_n^q$ for both receive antennas and all subcarriers are estimated by the use of the long training symbols according to the algorithm which was presented in the last section. The estimates for the two different long training symbols are averaged to decrease the estimation variance. With the estimates H_n^q,

Table 39.5. Properties and parameters of educational testbed.

Conversion	
number of A/D & D/A channels	2 (each)
A/D sampling rate	48 kHz
D/A conversion rate	48 kSPS
Up-/Down-conversion	
Performed	Digitally
Carrier	8 kHz
Bandwidth	Approx. 4 kHz
Rx/Tx Filtering	RRC with roll-off factor $\alpha = 0.22$
Signal processing devices	2x TI DSK TMS320C6713@225 MHz with 16 MB SDRAM (external), with AIC23 audio codec, and with USB interface to host
Loudspeaker	2x active PC speakers with amplifier
Microphones	2x SONY F-V120 (60-12.000 Hz)
Testbed modes	Offline mode (pre- and postprocessing on host using Matlab) Real-time (under development)

the equalized symbols are obtained by zero forcing. Figure 39.8 shows a constellation diagram example of demodulated QPSK symbols on each branch, separately and combined. Obviously, by combining the information of both antenna signals (here MRC is used), a better result from the exploited diversity is achieved.

Another example of a constellation diagram for a 16-QAM transmission is given in Figure 39.9, already the maximum-ratio combined symbols are displayed. Note that here the raw BER without coding is presented. The BERs are significantly decreased by coding, which is required in any OFDM system (coded OFDM—COFDM).

39.9. Educational project

STARS is accompanied by an educational project for our undergraduate students in order to attract and inspire them for technology-based MIMO research.

The project is denoted as STARS "little brother" (Figure 39.10). Based on TI's DSKs for TMS320C6713 and its included audio codec, we built up an audio transmission link facilitating the hardware access by students. Because the right and left stereo channels can be deployed independently, a 2×2 MIMO system is implemented, opening a wide range for studying basic MIMO algorithms. Transmission can be done alternatively over cable, by using an audio equalizer to adjust frequency selectivity, or over air by using two loudspeakers and two microphones. The basic properties and parameters of the educational testbed are shown in Table 39.5. The system setup is pointed out in Figures 39.11 and 39.12.

Measurements have shown that the used hardware elements (microphones, loudspeaker) introduce severe frequency selectivity. The channel transfer function

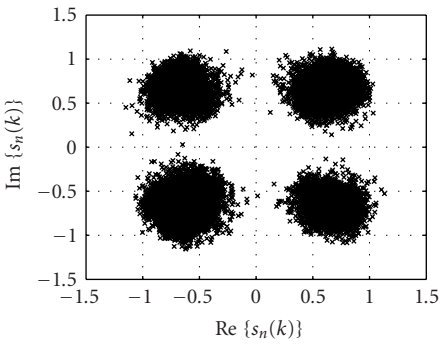

(a)

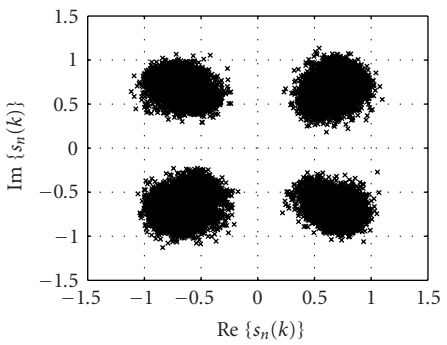

(b)

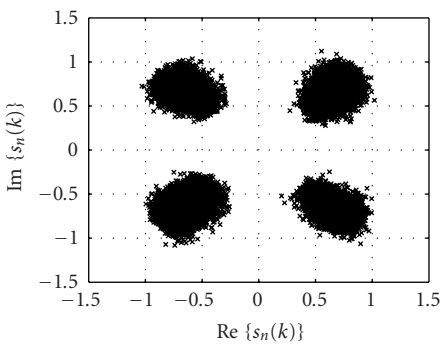

(c)

FIGURE 39.8. Constellation diagrams of demodulated QPSK symbols, BER = 0 (without coding). (a) Antenna signal 1. (b) Antenna signal 2. (c) Signal after combination.

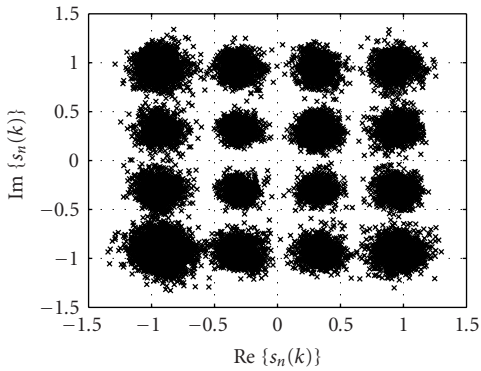

FIGURE 39.9. Constellation diagram of demodulated 16-QAM symbols, BER $\approx 10^{-3}$ (without coding).

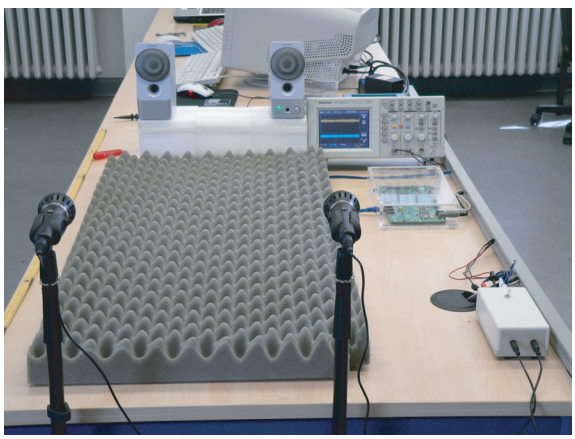

FIGURE 39.10. Educational 2×2 MIMO testbed.

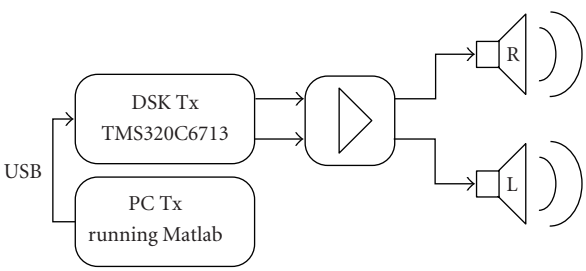

FIGURE 39.11. Educational testbed transmitter.

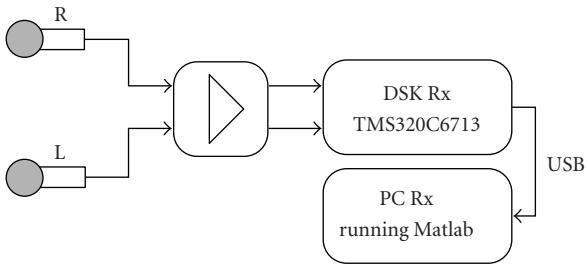

Figure 39.12. Educational testbed receiver.

seen by the baseband processing can be measured with help of the so-called Chu sequences [8], which are defined for an even sequence length N as

$$a_n = e^{j\pi(n^2/N)}, \quad n \in \{0, 1, \ldots, N-1\}. \tag{39.15}$$

Chu sequences have been designed to show up almost perfect autocorrelation properties (single peak). For channel measurement, it is beneficial that they exhibit a constant envelope in time domain and that the magnitude of their frequency transform is also constant over all frequencies. Thereby frequency selectivity of the effective channel of the testbed can be easily measured by transmitting these sequences. Fine timing synchronization is not required if the sequence is repeated multiple times and only an FFT window of the length of sequence is used. The position of the FFT window is thereby irrelevant; it must only be placed within the detected frame. A different position of the FFT window only results in a phase shift very similar to OFDM systems employing cyclic extension. A power delay profile can be obtained by transmitting a single, but long, Chu sequence and using a matched filter to it. Here the good autocorrelation properties of the Chu sequence can be exploited. Sample measurements of the frequency selectivity seen by the baseband processing are given in Figure 39.13.

Open-loop space-time diversity transmission system was implemented first as a MIMO/MISO demonstration for our educational testbed. It uses the offline-mode of the system, so all pre- and postprocessing of data is done on the host PCs with help of Matlab. Transmitter and receiver are fully independent to each other, so all synchronization tasks (frame detection, fine timing, and frequency offset estimation) have to be done.

In contrast to STARS, where special emphasize is given to IEEE 802.11a, we here focus on a CDMA system as given in 3GPP TS 25.213 Release 5, but all system parameters are properly downscaled to meet the requirements of the testbed. The relevant parameters are given in Table 39.6. Space-time encoding and decoding follow the ideas given in [9].

The frame detection and initial synchronization are achieved by using a preamble and a common matched filter approach. A RAKE receiver structure is used to equalize the received signals. The channel estimation is done by exploiting the *primary Common PIlot CHannel* (pCPICH) and the *secondary Common PIlot*

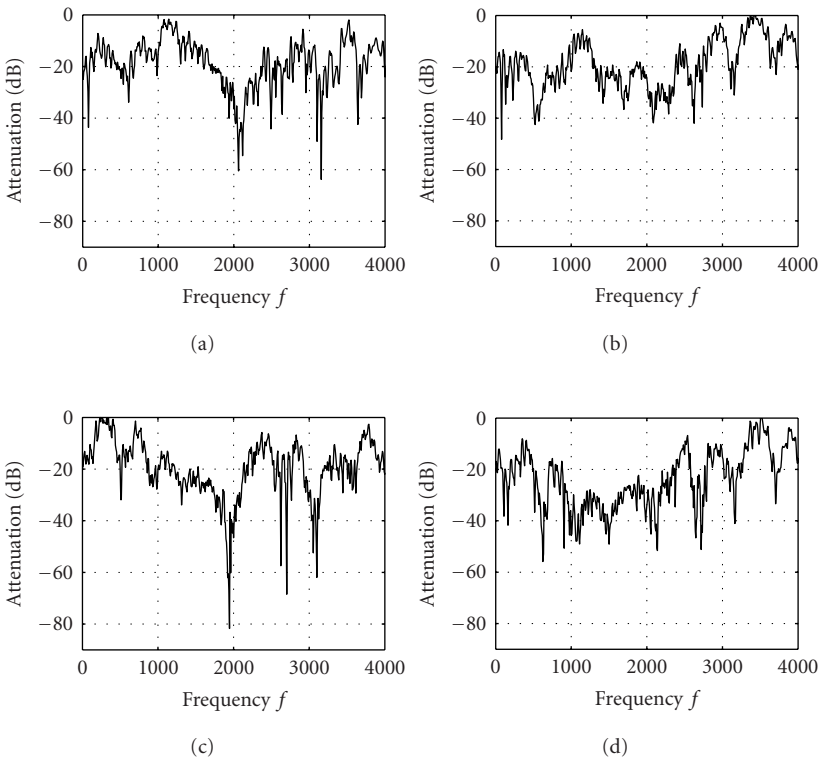

FIGURE 39.13. Baseband channel attenuation—transmitter's (Tx) left (L) and right (R) audio channel to receiver's (Rx) left (L) and right (R) audio channel. (a) Tx R ≥ Rx R. (b) Tx R ≥ Rx L. (c) Tx L ≥ Rx R. (d) Tx L ≥ Rx L.

TABLE 39.6. Signaling parameters of MISO/MIMO demonstration.

Signaling method	Direct sequence spread spectrum (DS-SS) based on 3GPP TS 25.213 and 25.211 Release 5
Equalizer	RAKE receiver
Data modulation	QPSK
Chip rate	4 kchips/s
Spreading factor (SF)	16
Channel estimation	Based on pCPICH and sCPICH
Synchronization	Preamble (Gold sequence)
MIMO/MISO technique deployed	Alamouti coding with/without MRC

CHannel (sCPICH) as given in the specification 3GPP TS 25.211 Release 5. Both provide permanent phase references and allow to distinguish between the two transmit sources (loudspeakers). With help of this phase reference, the frequency

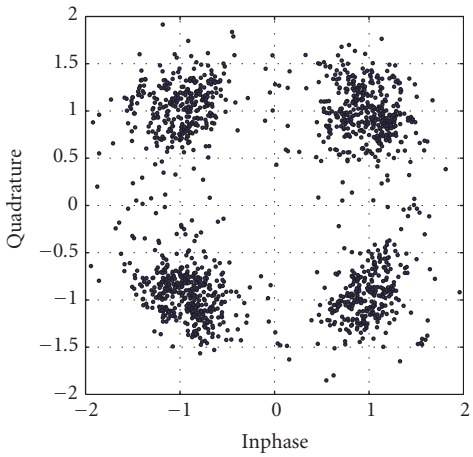

Figure 39.14. Constellation diagram for MISO Alamouti, measured received SNR = 24.41 dB.

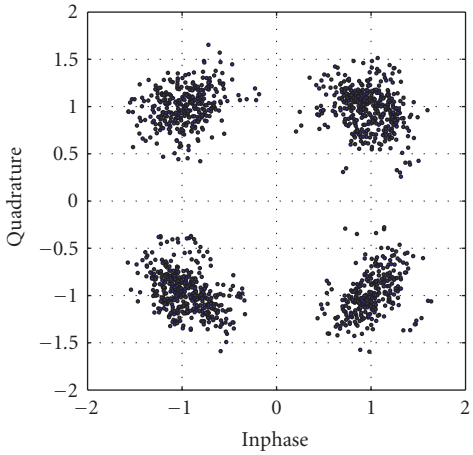

Figure 39.15. Constellation diagram for MISO Alamouti, measured received SNR = 29.81 dB.

offset is estimated and compensated by phase derotation. All operations are done in a frame-by-frame manner.

Sample received constellation diagrams for MISO Alamouti and MIMO Alamouti are given in Figures 39.14 and 39.15. The measured received SNRs indicate a significant edge of MIMO Alamouti over MISO Alamouti of 5.4 dB. The distance between transmitter and receiver was 200 cm. The transmissions take place in a typical office environment with line-of-sight (LOS). For simplicity, only the dominant LOS path is assigned to a single RAKE finger of the RAKE receiver. The same receive data set was used for decoding MISO and MIMO. In case of MISO,

only one of the received signals was decoded. In the MIMO case, both received signals were decoded and maximum-ratio combining (MRC) was exploited to gain performance from the receive diversity.

39.10. Conclusions and outlook

Aims of this contribution were to demonstrate a general concept for a flexible and multiuser capable MIMO testbed, to explain the essential requirements, to illustrate the most useful tools, to exemplary derive necessary algorithms, to underpin its educational value by the "little brother," and finally to show first results.

After dealing with the baseband architecture, the role of DSPs and FPGAs and their splitting inside the STARS were pointed out. Next, the most relevant technical data of STARS, the analog front end and its possible MIMO configurations, were illustrated. The succeeding section covers the system equipment and the measurement setup. Synchronization of STARS has been explained afterwards. Finally, some results are shown under real-world conditions. In conclusion, this chapter can be seen as an introductory construction manual targeted to engineers and scientists who are planning to set up their own MIMO testbed.

Abbreviations

3G	Third generation
3GPP TS	Third Generation Partnership Project Technical Specification
4G	Fourth generation
A/D	Analog-to-digital
ABEL	Advanced boolean equation language
ADC	Analog digital converter
AGC	Automatic gain control
BB	Baseband
BER	Bit error rate
BPSK	Binary phase-shift keying
CCS	Code composer studio
CCK	Complementary code keying
CDMA	Code division multiple access
CFO	Carrier frequency offset
CMOS	Complementary metal-oxide-semiconductor
COFDM	Coded OFDM
CORDIC	Coordinate rotation digital computer
COTS	Commercial off-the-shelf
CP	Communication port
CPE	Common phase error
CPLD	Complex programmable logic device
cPCI	Compact peripheral component interconnect
CVS	Concurrent versions system
D/A	Digital-to-analog
DAC	Digital-to-analog conversion
DAQ	Data aquisition

DC	Direct current
DFT	Digital Fourier transform
DMA	Direct memory access
DSK	Development starter kit
DS-SS	Direct-sequence spread spectrum
DSP	Digital signal processor
EGC	Equal-gain combining
EUSIPCO	European Signal Processing Conference
FFT	Fast Fourier transform
FIFO	First-in first-out
FPGA	Field programmable gate array
GPIO	General purpose input/output
GUI	Graphical user interface
HDL	Hardware description language
HW	Hardware
IEEE	Institute of Electrical and Electronics Engineers
I	Inphase
I/O	Input output
IBI	Interblock interference
ICI	Intercarrier interference
IDE	Integrated development enviroment
IF	Intermediate frequency
IFFT	Inverse fast Fourier transform
IP	Intellectual property
ISE	Integrated synthesis environment
JTAG	Joint test action group interface
kSPS	Kilosample per second
LAN	Local area network
LNA	Low-noise amplifier
LOS	Line of sight
LPF	Lowpass filter
LVTTL	Low-voltage transistor-transistor logic
MAC	Medium access controller
McBSP	Multichannel buffered serial port
MFLOPS	Mega floating-point operations
MIMO	Multiple-input multiple-output
MIPS	Mega instructions per second
MISO	Multiple-input single-output
MSPS	Megasamples per second
OFDM	Orthogonal frequency-division multiplex
PA	Power amplifier
PC	Personal computer
PCI	Peripheral component interconnect
pCPICH	Primary common pilot channel
PLD	Programmable logic device
PLL	Phase-locked Loop
PROM	Programmable read-only memory
Q	Quadrature
QAM	Quadrature amplitude modulation

QPSK	Quadrature phase-shift keying
RAD	Rapid application development
RAM	Random access memory
RF	Radio frequency
RRC	Root raised cosine
RTOS	Real-time operating system
RTW	Real-time workshop
Rx	Receiver
SC	Selection combing
sCPICH	Secondary common pilot channel
SDB	Sundance digital bus
SDK	Software development kit
SFO	Sampling frequency offset
SHB	Sundance high-speed bus
SIMO	Single-input multiple-output
SISO	Single-input single-output
SmART	Smart Antenna Research Team, Duisburg
SNR	Signal-to-noise ratio
SPI	Serial peripheral interface
STARS	SmarT Antenna Real-time System
SW	Software
TCP/IP	Transmission Control Protocol/Internet Protocol
TIM	Texas instruments module
TTL	Transistor-transistor logic
Tx	Transmitter
UMTS	Universal Mobile Telecommunication System
USB	Universal serial bus
VCO	Voltage controlled oscillator
VHDL	VHSIC hardware description language
VHSIC	Very-high-speed integrated circuit
WLAN	Wireless local area network
WMAN	Wireless metropolitan area network
ZBTRAM	Zero bus turnaround random access memory

Bibliography

[1] T. Kaiser, A. Wilzeck, M. Berentsen, and M. Rupp, "Prototyping for MIMO-systems: an overview (invited)," in *Proc. 12th European Signal Processing Conference (EUSIPCO '04)*, Vienna, Austria, September 2004.

[2] Institute of Electrical and Electronics Engineers, "Telecommunications and information exchange between systems—Local and metropolitan area networks—Specific requirements—Part 11: wireless LAN medium access control (MAC) and physical layer (PHY) specifications—Amendment 1: High-speed physical layer in the 5 GHz band," IEEE Standard for Information Technology, 1999.

[3] T. M. Schmidl and D. C. Cox, "Robust frequency and timing synchronization for OFDM," *IEEE Trans. Commun.*, vol. 45, no. 12, pp. 1613–1621, 1997.

[4] P. H. Moose, "A technique for orthogonal frequency division multiplexing frequency offset correction," *IEEE Trans. Commun.*, vol. 42, no. 10, pp. 2908–2914, 1994.

[5] T. C. W. Schenk and A. van Zelst, "Frequency synchronization for MIMO OFDM wireless LAN systems," in *Proc. IEEE 58th Vehicular Technology Conference (VTC '03-Fall)*, vol. 2, pp. 781–785, Orlando, Fla, USA, October 2003.

[6] J. J. van de Beek, M. Sandell, and P. O. Börjesson, "ML estimation of time and frequency offset in OFDM systems," *IEEE Trans. Signal Processing*, vol. 45, no. 7, pp. 1800–1805, 1997.
[7] A. G. Armada and M. Calvo, "Phase noise and sub-carrier spacing effects on the performance of an OFDM communication system," *IEEE Commun. Lett.*, vol. 2, no. 1, pp. 11–13, 1998.
[8] D. C. Chu, "Polyphase codes with good periodic correlation properties (corresp.)," *IEEE Trans. Inform. Theory*, vol. 18, no. 4, pp. 531–532, 1972.
[9] S. Alamouti, "A simple transmit diversity technique for wireless communications," *IEEE J. Select. Areas Commun.*, vol. 16, no. 8, pp. 1451–1458, 1998.

T. Kaiser: Smart Antenna Research Team (SmART), Duisburg, Germany
Email: thomas.kaiser@uni-duisburg.de

A. Wilzeck: Smart Antenna Research Team (SmART), Duisburg, Germany
Email: andreas.wilzeck@uni-due.de

M. Berentsen: Smart Antenna Research Team (SmART), Duisburg, Germany
Email: berentsen@nts.uni-duisburg.de

A. Camargo: Smart Antenna Research Team (SmART), Duisburg, Germany
Email: camargo@nts.uni-duisburg.de

X. Peng: Smart Antenna Research Team (SmART), Duisburg, Germany
Email: xiqunpeng@yahoo.com

L. Häring: Smart Antenna Research Team (SmART), Duisburg, Germany
Email: haering@nts.uni-duisburg.de

S. Bieder: Smart Antenna Research Team (SmART), Duisburg, Germany
Email: bieder@nts.uni-duisburg.de

D. Omoke: Smart Antenna Research Team (SmART), Duisburg, Germany
Email: damoke@hotmail.com

A. Kani: Smart Antenna Research Team (SmART), Duisburg, Germany
Email: ayhan.kani@t-online.de

O. Lazar: Smart Antenna Research Team (SmART), Duisburg, Germany
Email: lazar@uni-duisburg.de

R. Tempel: ATMEL Duisburg GmbH, 47057 Duisburg, Germany
Email: rtempel@atmel-du.de

F. Ancona: Sundance Italia S.r.l, 16040 S. Salvatore di Cogorno(GE), Italy
Email: fabio.a@sundance.com

40 Real-time prototyping of broadband MIMO WLAN systems

Maryse Wouters and Tom Huybrechts

40.1. Introduction

Algorithmic research on multiple-input multiple-output transmission schemes has proven that impressive capacity or diversity gains can be achieved compared to single-antenna systems. The analytical performances of these algorithms are well known. However, they are still based on models of the channel. Mostly these models do not include the front-end impairments such as phase noise and amplifier nonlinearity. A prototype can be built to ensure the designers of the performance of their algorithms in a real-world environment. The prototyping of a wireless system gives a better understanding of the key tradeoffs between the analog and digital architecture designs in order to come to the best combination of digital compensation techniques and low-cost front-end implementations. In this chapter, a generic platform is presented that enables real-time wireless MIMO transmission for indoor applications. The chapter is organized as follows. Section 40.1 is the introduction. In Section 40.2, a multiple-antenna application scenario is described that is used as a driving example for the definition of the platform hardware and software concepts. In Section 40.3, the architecture of the platform is proposed. Section 40.4 outlines the board library that is developed for real-time broadband WLAN demonstration. The prototyping of a single-antenna WLAN system is given in Section 40.5. Section 40.6 describes the prototyping of a broadband MIMO WLAN system composed of a 2-antenna base station with transmit processing and of single-antenna user terminals. The know-how that is gained from the characterization of the single antenna terminal is reused for the implementation of the 2-antenna base station. The impact of certain front-end radio effects, adjustments, and compensation techniques are described in Section 40.7. Section 40.8 gives an insight of the future research for wireless systems.

40.2. Focus on MIMO-OFDM WLAN application scenario

The third-generation WLAN standards (IEEE 802.11a [1] and ETSI HIPERLAN/2 [2]) define data transmission rates ranging from 6 Mbps to 54 Mbps in a 20 MHz

band for an indoor environment with a cell radius of 100 meter. It is based on coded orthogonal frequency-division multiplexing (OFDM) because of its good performance for frequency-selective channels. The WLAN standards evolve and change quickly steered by the demands of new services, advanced functionality, and new features. Spatial multiplexing on top of the time-frequency slots is an attractive technique to increase the spectral efficiency for next-generation WLAN systems. The most important requirements for the MIMO-OFDM WLAN application scenario are as follows: (1) the product should not disturb other WLAN systems and should be operational with existing single-antenna WLAN systems, (2) the product should give an increase in capacity or in link quality, (3) the product should be attractive for the service provider and the user, and (4) the product should include quality-of-service (QoS) management to target multimedia and high-speed internet access at low power. The first requirement is covered by the standardization and regulation committees who define the frequency bands of operation, the limitation on transmission power, and the transmission spectral mask. The cooperation of multiple antenna with existing single-antenna systems offers a smooth migration from SISO to MIMO systems, for example, base stations can be upgraded while (legacy) user terminals can still be operational in the system. The three other requirements are important from business point of view. They show that multiple antenna gives additional system capacity and robustness. As an application scenario, the upgrade of a single-antenna base station towards a multiple antenna base station is chosen. A 2-antenna base station is prototyped, using the space-division multiple-access (SDMA) technique to enhance the link capacity by serving several single-antenna users at the same time and in the same bandwidth (Figure 40.1). This implementation doubles the downlink capacity with a maximum capacity of 2 times 54 Mbps. Besides SDMA processing, the prototype base station incorporates maximum ratio combining (MRC) to enhance the downlink quality. The broadcast channel is done in SISO mode. The medium access controller (MAC) guarantees an optimal mode selection, trading off cost (power consumption) and performance (rate, latency). In this broadband MIMO-OFDM WLAN system implementation, the spatial multiplexing and the spatial diversity processing techniques are all located in the transmitter of the base station. This has the benefit that the user terminal can remain at (1) low complexity, (2) low cost, (3) low power, and (4) small size. The capabilities of the system are demonstrated by running demanding applications. The chosen scenario uses the HIPERLAN/2 standard which through its centrally controlled operation and QoS is suitable for SDMA and multimedia applications. The communication rules of the HIPERLAN/2 protocol are used to implement, for example, the allocation of network resources to mobile terminals based on the link quality and on the application requests of the user.

40.3. Platform concepts

The major challenges in the design of a SISO/MIMO-OFDM prototyping platform are (1) flexibility, (2) the availability of hardware resources to implement

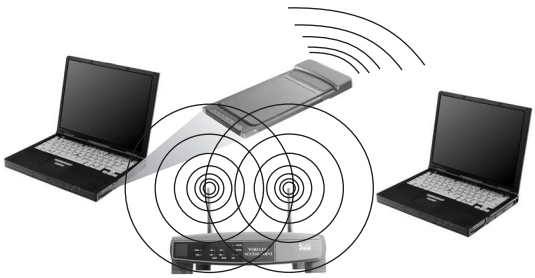

FIGURE 40.1. Application scenario: MIMO-OFDM with transmit processing.

the complex algorithms, and (3) the availability of real-time high-data-rate communication links between components and between boards. The platform should exhibit large flexibility to fulfil these needs: (a) FPGA for programmable intellectual property (IP) core connectivity and for application implementation, (b) easy ASIC and PCB integration, (c) dedicated high-speed interboard data communication links, (d) on-board master or slaved clock and local oscillator selection, and (e) debug logic. The development time for the prototyping of current and next-generation WLAN system can be shortened by defining platform concepts that enables reuse. These concepts should raise the abstraction level of the hardware and software design and makes in this way the platform more accessible to the application engineers. The platform should also comply with a standard PC family bus interface. By doing this, a robust prototyping system can be built by plugging several boards in a standard chassis available from many suppliers. The system can be extended with off-the-shelf PC add-on boards, like video adaptors and digital signal processor (DSP) boards. Imec vzw has developed a platform for real-time prototyping of current and next-generation WLAN systems. It is called PICARD [3]: "Platform for Integrated Communication Applications, Research and Demonstration". Existing platforms do not support real-time prototyping of high-speed telecom systems. For example, [4] proposes a multiboard, multiprocessor prototyping framework with the PCI bus to exchange data between the boards. However, the PCI bus is not appropriate to transfer real-time high-data-rate payload data. Other platforms are single board and are either tuned for emulation and integration of IP cores on small daughter boards (see http://www.chipit.de) or are tuned for system-on-chip verification with multiple field programmable gate arrays (FPGAs) (see http://www.aptix.com). Existing MIMO demonstrators are focusing on spatial diversity techniques at the receiver side to enhance the capacity and on space-time block codes to exploit spatial diversity [5].

40.4. Achieving modular board design for MIMO-OFDM systems

To prototype the SISO-OFDM WLAN system, two boards are designed following the PICARD modular board concepts. Both PCBs are derived from the same basic schematic netlist and contain a common part which includes the central FPGA,

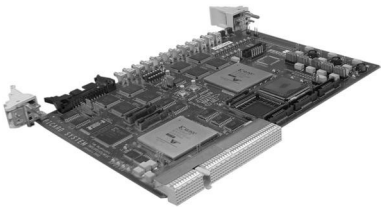

FIGURE 40.2. General-purpose digital board.

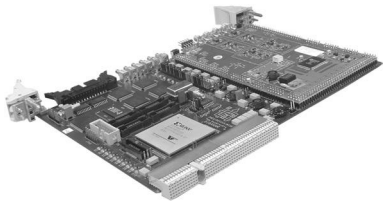

FIGURE 40.3. General-purpose front-end board.

the cPCI connector, the power unit, the clock unit, and the serial high-speed data links. The central FPGA is connected to all inputs and outputs of the application-specific IP cores and contains the communication management unit. The first board is a general-purpose digital board (Figure 40.2) which contains as IP cores a second FPGA, a commercial Viterbi decoder, an in-house developed low-power turbo codec [6], and a 2×4 Mb fast SRAM memory. The second board is a general-purpose front-end board (Figure 40.3) with a socket for a daughter board. The two boards are general in the sense that both contain configurable hardware (max 2 Xilinx XC2V6000 FPGAs at http://www.xilinx.com) for the implementation of the digital part of the SISO/MIMO-OFDM modem and that one board has a socket to plug in a daughter board with the antenna array RF front end. A complete system can be prototyped on the platform using one or more boards. The platform concepts foresee dedicated high-speed data links (1.4 Gbps per link) between the boards to transfer the payload data with low latency. The shared cPCI bus [7] is used for initialization of the boards and for fast DMA transfers (1 Gbps). The number of boards depends on the required system processing power and the level of integration of the antenna array. For example, the antenna array can be built as a set of single-antenna RF boards or can be integrated in one system in package module. An in-house developed 5 GHz superheterodyne WLAN transceiver designed with discrete components can be used in a single-antenna system or in a multiple-antenna system. The platform has the connections to synchronize the ADC and DAC sampling clocks of the antenna branches to a common clock and to steer the phase-locked loops of the RF and IF synthesizers, with the same reference clock. In this way, the antenna branches are synchronized in time and in phase.

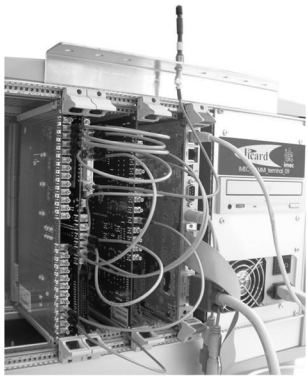

Figure 40.4. Prototyping of OFDM-SISO terminal on PICARD platform.

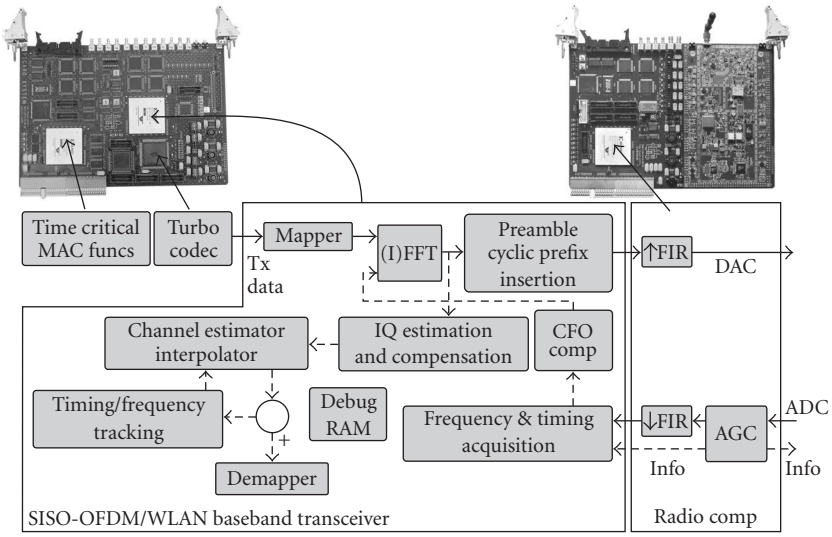

Figure 40.5. Block diagram of SISO-OFDM terminal.

40.5. SISO-OFDM prototyping

The complete SISO-OFDM terminal consists of four boards (Figure 40.4): a general-purpose digital board, a general-purpose front-end board, a clock board, and a host processor. The SISO-OFDM baseband transceiver, turbo codec, and the soft MAC processor core are integrated on the general-purpose digital board (Figure 40.5). The 5 GHz superheterodyne front end and its digital filters and automatic gain control (AGC) are integrated on the general-purpose front-end board.

40.5.1. SISO-OFDM transceiver modem with digital front end compensation

The block diagram of the SISO-OFDM transceiver is shown in Figure 40.5. In transmission mode, the coded payload data enters through a 6-bit parallel interface transceiver and is mapped on either BPSK, QPSK, 16-QAM, or 64-QAM symbols. A complex value weights each subcarrier, allowing for transmitter preemphasis and phase predistortion. The data is converted to time domain by IFFT. The preamble and cyclic prefix are added to format the burst. The preamble serves as reference sequence for synchronization and channel estimation. It is composed of two sections. The first section contains ten known short training sequences (STSs) with a total duration of 8 microseconds. The second section consists of two long training sequences (LTSs), which are two OFDM symbols of normal length (3.2 microseconds), preceded by a cyclic prefix which is a copy of the last 32 samples of the LTS. The cyclic prefix are inserted in front of each symbol to avoid intersymbol interference. In reception mode, the AGC [8] adjusts the front-end gains in order to put the incoming data stream within the dynamic range of the AD converter. The AGC converges within 4 microseconds. The time and frequency offset acquisition and compensation are done in a feed-forward way before the FFT. The start of a burst is detected by combined coarse autocorrelation peak detection on the STS and fine cross-correlation peak detection on the LTS on which the carrier frequency is [9] removed. The frequency offset is determined by autocorrelation on the LTS. The I/Q imbalance estimation [10] is calculated after the FFT in the frequency domain on the second LTS. The algorithm minimizes the square error between two successive subcarriers of the channel estimation. The I/Q estimation is made robust for large carrier frequency offsets and the compensation takes place before the equalizer. This gives that the equalizer remains a simple one-tap equalizer per subcarrier. In our implementation the equalizer is further improved by adaptive interpolation to mitigate time-variant channels, rotations due to slow-varying oscillator phases (common phase noise), and remaining frequency offset. Resource sharing between the transmitter and receiver chain is exploited for the (I)FFT. The implementation figures on the XC2V6000 are given in Table 40.1. The 44 multipliers of the adaptive interpolator in the equalizer are mapped on slices and this gives an increase of 17% in usage of slices compared when the dedicated multipliers of the FPGA are used. Extra memory is allocated to store debug data and channel measurements. For example, an OFDM burst of 819 microseconds and the data on the internal busses can be stored in memory. The data in the memory is processed offline by the cPCI processor for analysis calculations and the results are displayed on screen. In this way, measurements like constellation plots and channel estimation can be visualized on the platform at run time. The AGC unit and up- and down-sampling filters are mapped on the central FPGA of the general-purpose front-end board. The up- and down-sampling filters are implemented as a 41-tap square root raised cosine (SRRC) filter. The implementation is optimized towards FPGA by using the canonical signed digit representation of the coefficients and by expanding the multiplications in add/shift operations. The

Table 40.1. FPGA key features of SISO-OFDM transceiver.

FPGA	XC2V6000
Internal main clock	20 MHz
Slices	25 033 = 74% usage
of which acquisition	2949 = 11.8%
of which equalizer	9162 = 36%
of which FFT	1963 = 7.8%
of which I/Q estimation & compensation	3390 = 13.5%
Multipliers	144 = 100% usage
of which in equalizer	56 = 39%
of which in fft	8 = 5.6%
of which in I/Q estimation & compensation	44 = 30.6%

AGC unit calculates the power of the incoming signal and selects based on threshold comparisons the optimal front-end gain settings that are stored in lookup tables. The AGC unit and filters are mapped on a XC2V3000. It takes 59% of the slices from which 2.5% are used for the AGC at a 80 MHz clock.

40.5.2. The QoS MAC architecture

The MAC layer coordinates the access of the terminals to the common air interface and includes quality-of-service enhancements. The non-timing-critical functions such as association and authentication exchanges or data frame preparation run on the host processor. The time critical functions require the MAC to act within microseconds of an event or at precise intervals. For this purpose, Imec vzw designed a soft processor core with an optimized architecture and instruction set for fast data shuffling. The MAC processor core has three busses for input/output (Figure 40.6). One bus communicates with the dual-port RAM. This RAM contains the firmware and specific MAC data. The host processor writes at startup data for the processor core to the RAM. The configuration bus is used to control the system behavior such as setting up registers and data routing. The third bus is an extension bus that houses different functional units that support the functioning of the processor core. Examples of these units are timers and interrupt controllers. The MAC processor core is integrated in the communication management unit on the central FPGA. The communication management unit has two busses: the configuration bus and the payload data bus. The payload data flow is handled and executed by an arbiter leaving the MAC processor tasks reduced to the control of the data flow directions. The arbiter is based on a round-robin system. It supports every clock cycle a data transfer requested by another component on the shared payload bus. The programming of the data flow directions by the MAC processor has the benefit that a system can be gradually built by adding new communication links without changing the content of the central FPGA. The MAC processor does

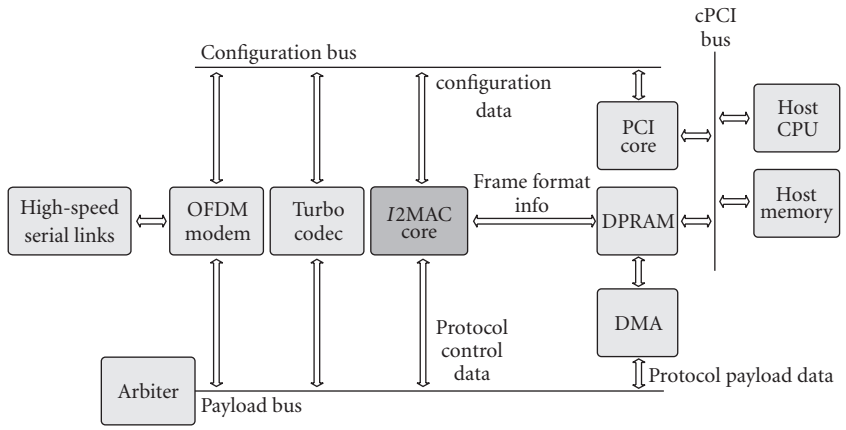

FIGURE 40.6. Communication busses between MAC processor and IP cores.

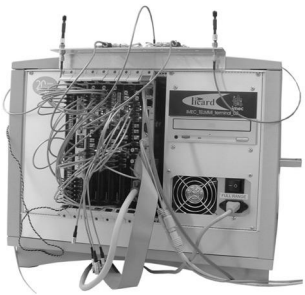

FIGURE 40.7. Prototyping of MIMO-OFDM base station on PICARD platform.

not have to take care of the data formatting of the entire transmission and reception bursts. This is self-controlled in the baseband transceiver. The transceiver only requires initial programming of parameters and a trigger from the MAC processor to start transmission and reception. The transceiver delivers to the MAC processor measures for QoS enhancement like channel state information and received signal strength. Based on this information the MAC will schedule the priority of the transmitted queus and will determine the error coding rate and the used constellation scheme. For example, video streaming requires different error coding than packet-based messages.

40.6. Two antenna MIMO-OFDM base station prototyping

The 2-antenna base station using transmit processing including special front-end techniques for the exploitation of channel reciprocity is prototyped on the platform on eight boards (Figure 40.7): two general-purpose digital boards to implement the baseband modem, two general-purpose front-end boards to implement

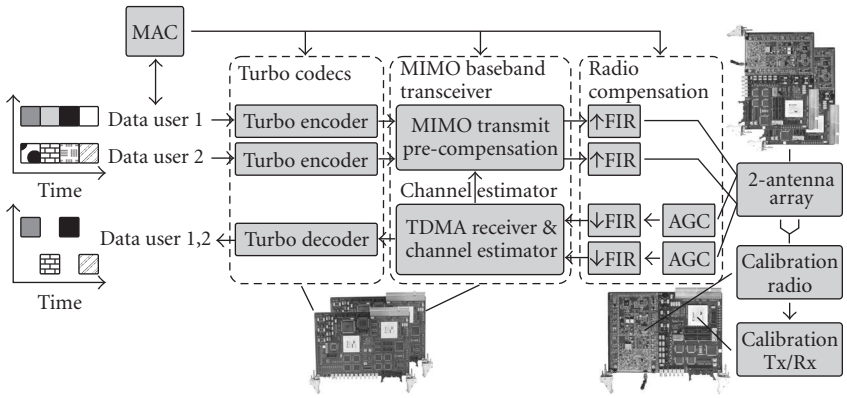

FIGURE 40.8. Block diagram of 2-antenna base station with MIMO transmit compensation and online calibration.

the antenna array, a general-purpose front-end board to calibrate the base station antennas, a clock board, a common local oscillator board, and a host processor. The MIMO transmit processing is more difficult to implement compared with MIMO receive processing because of the lack of instantaneous channel information at the transmitter. In our implementation (Figure 40.8), the channel information is retrieved from the uplink where TDMA is used as an access technique. The channel is composed of the propagation channel between the antennas, the front ends themselves, and the digital filter circuits. To precompensate the channel, the base station receive and transmit front ends should be reciprocal in amplitude and phase for the entire bandwidth [11]. Nonreciprocity causes extra multiuser interference which gives link degradation. The front-end matching accuracy in the base station must be below 0.04 dB and 0.25 degrees to obtain a degradation loss smaller than 1 dB for uncoded 64-QAM at BER of 10^{-3}. These tight overall manufacturing and time-variation matching of the RF and analog circuits between the transmitter and receiver are practically not realizable. Therefore, an online calibration loop is implemented that measures the product $D_{\text{Tx,BS}} \cdot D_{\text{Rx,BS}}^{-1}$ at the base station so that the mismatches between transmitter and receiver can be compensated digitally in the downlink. $D_{\text{Tx,BS}}$ and $D_{\text{Rx,BS}}$ are diagonal matrices representing the multiple-antenna transmit and receive front-end frequency responses.

40.6.1. The SDMA transceiver architecture

In the downlink, the two user streams are first turbo encoded before entering the MIMO transmit precompensation unit. The MIMO transmit precompensation unit (Figure 40.9) maps the 2 streams on BPSK, QPSK, 16-QAM, or 64-QAM symbols. The preamble and cyclic prefix to format the burst are added in the frequency domain before the MIMO transmit compensation. The MIMO transmit compensation is a linear prefilter that is achieved by a multiplication of the

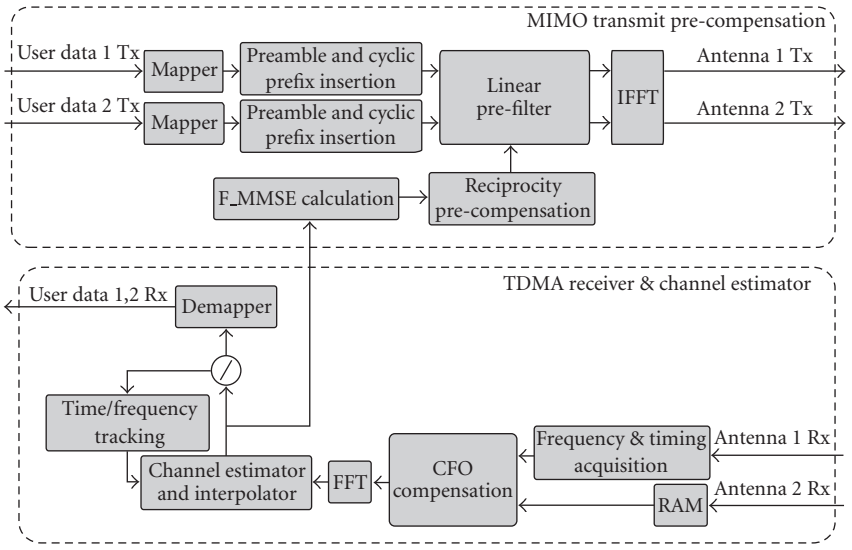

FIGURE 40.9. Detailed block diagram of SDMA transceiver.

transmit symbol vector by a matrix as follows:

$$y^{\mathrm{DL}} = H^{\mathrm{DL}} \cdot F \cdot x^{\mathrm{DL}} + n, \tag{40.1}$$

where x^{DL} is the column vector of the 2 symbols transmitted simultaneously by the base station, y^{DL} is the column vector of the signal received by the 2 user terminals, H^{DL} is the composite downlink channel, and F is the linear prefilter. The dependency of the subcarrier is dropped in the equation for clarity. For the calculation of the prefilter matrix F, it is assumed that the downlink channel is the transpose of the uplink channel. We have implemented an MMSE prefilter that trades off noise and multiuser interference. The MMSE prefilter is given by

$$F_{\mathrm{MMSE}} = \left(H^{\mathrm{DL}}\right)^{H} \cdot \left(H^{\mathrm{DL}} \cdot \left(H^{\mathrm{DL}}\right)^{H} + \sigma^2 \cdot I_{UxU}\right)^{-1}. \tag{40.2}$$

The F_{MMSE} filter coefficients are multiplied with the front end reciprocity compensation values. The data streams are linearly prefiltered and converted to the time domain by IFFT. In the uplink, the users are assigned to separate time slots (TDMA). The user data is received at the base station on the 2 antennas. The AGC at each front end puts the incoming stream within the range of the AD converter. In the uplink TDMA receiver, the timing and the carrier frequency offset is estimated on the preamble of one antenna and the compensation is done on the streams of both antennas. The channel is estimated on the preambles for each antenna and for each user in the uplink time slot. These channel estimations are used as input to the F_{MMSE} coefficients calculation. The remainder of the uplink burst contains the user payload data and is in the receiver further demodulated, turbo

Table 40.2. FPGA key features of 2-antenna MIMO transmit precompensation unit.

FPGA	XC2V6000
Internal main clock	40 MHz
Slices	17 000 = 50% usage
of which F_{MMSE} calculation	5200 = 30%
of which linear prefilter	1200 = 7%
of which IFFT	2600 = 15%
of which reciprocity precompensation	2100 = 12%
Multipliers	86 = 59% usage
of which F_{MMSE} calculation	46 = 53%
of which linear prefilter	8 = 9%
of which IFFT	8 = 9%
of which reciprocity precompensation	12 = 13%
Block RAM	17 = 12% usage

decoded, and passed to the MAC layer. Two general-purpose digital boards are used to integrate the turbo codecs, the MIMO baseband transceiver, and the soft MAC processor. The MIMO transmit precompensation unit is mapped on one XC2V6000. The implementation figures are listed in Table 40.2. The TDMA receiver is the SISO-OFDM baseband transceiver extended with memory to capture the burst on the second antenna. It is mapped on one XC2V6000 of the second general-purpose digital board.

40.6.2. Multiple antenna and calibration transceiver architecture

On the platform, the 2-antenna array is build from two single-antenna 5 GHz superheterodyne front-end boards. The AGC unit and up- and down-sampling filters are reused from the SISO-OFDM terminal and are mapped on the FPGA belonging to the front end. For online calibration purposes, a calibration transceiver with 5 GHz superheterodyne front end is added in the base station. This is a reference front end to measure the transmit and receive transfer functions of the front-end array. It is connected to the 2 antenna branches with combiner, splitters, and cables. The 2 antenna branches on the platform are slaved to the same local oscillators and the same ADC and DAC sampling clocks. In this way, phase noise impairments and synchronization mismatches between the antennas are avoided during calibration. Synchronization offsets result in a phase slope across the frequency response in case of timing offset differences or in a phase shift in case of carrier frequency offset differences. It is also required that the transfer function measurements are done simultaneously over all branches so that the impact of phase noise is identical on all branches. Therefore, calibration sequences on nonoverlapping subcarriers with low PAPR have to be defined (e.g., even subcarriers for antenna 1, odd subcarriers for antenna 2). The calibration is done in three steps. In a first step, the transfer functions of the 2-antenna array receivers are measured for all AGC settings. The reference front end is the transmitter. In a second step, the transfer functions of the 2-antenna array transmitters are measured for all transmit power

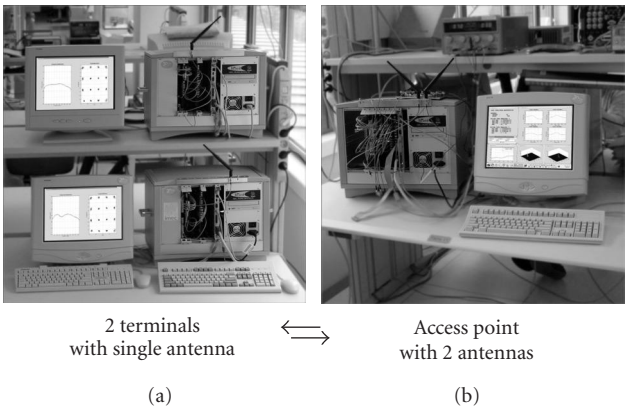

FIGURE 40.10. MIMO demonstrator set-up: (a) 2 terminals with single-antenna, (b) access point with 2 antennas.

settings. The reference front end is the receiver. The calculation of the transfer functions is done in software. In a third step, the reciprocity precompensation values, that is, the ratio of the transmitter frequency responses and receiver frequency responses, are calculated on the host processor and stored on the host memory.

40.6.3. MIMO MAC architecture

Besides allocating network resources for uplink and downlink transmissions, the MAC processor also programs the MIMO baseband transceiver with the reciprocity precompensation value that corresponds to the AGC couple of the uplink transmission link of a user. The MAC soft processor core is present on each transceiver board to control the shuffling of the data and to program the transceiver settings. In the SDMA application, three MAC soft processor cores are used. Each MAC soft processor core has a timer counter on which the actions of the three cores are synchronized. The non-time-critical functions are executed on the host processor.

40.6.4. Wireless MIMO-OFDM demonstrator

The picture in Figure 40.10 shows the composition of the MIMO setup. On the left Figure 40.10a, the 2-user terminals with a single antenna are shown, on the right Figure 40.10b a base station with 2 antennas. Two demonstrators are implemented. The first one is an experimental research demonstrator. The user can select between SDMA or MRC as MIMO schemes, can (des-)activate the reciprocity compensation, and can choose the modulation scheme. On the screens of the user terminal and the base station, the constellation diagram, the channel estimation, BER, and PER are plotted. This wireless demonstrator proves that capacity increase is possible with transmit processing only and proves that reciprocity of the base

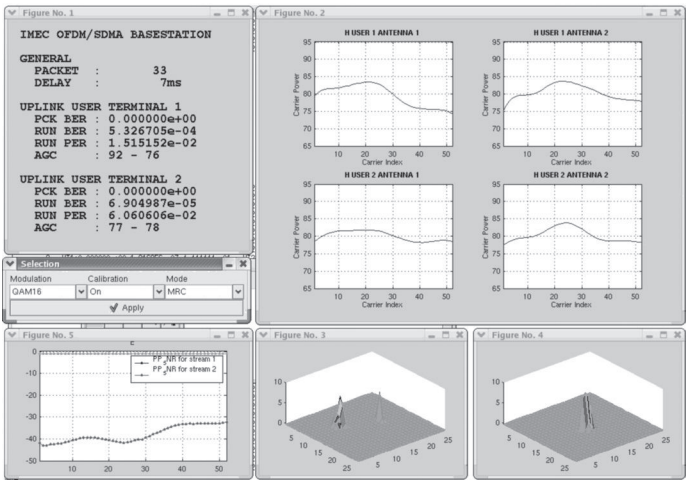

Figure 40.11. Screenshot of base station.

station front end is necessary. In the downlink, two streams of uncoded 16-QAM are transmitted simultaneously to the two user terminals. The channel seen by the user terminal does not vary in time and reflects the ratio of the front-end transfer function of the user terminal and the front end transfer function of the reference front end. This proves that the base station transmit processing compensates the wireless channel. When only compensation of the AGC values is done, this means no compensation of the nonreciprocity of the base station front ends is done, the downlink quality decreases with 5 dB. Calibration and digital compensation of the nonreciprocity between transmit and receive front ends at the base station are required. A detailed view of the screen of the base station is shown in Figure 40.11. The uplink channel estimations in frequency domain are plotted for each user and for each antenna (top right). The wireless channels represent (deep) fades. In the left bottom corner, the product of the F_{MMSE} matrix with the channel estimations H^{DL} is shown. The X-axis represents the subcarrier, the Y-axis the values of the 2×2 matrix expressed in dB. The plot shows that the multiuser interference is reduced below -30 dB due to transmit processing at the base station. The second demonstrator includes the MAC layer. In real-time, multimedia applications are served to the two user terminals in the same time slot and bandwidth.

40.7. Digital front-end compensation and adjustments techniques

The RF circuits introduce phase noise, I/Q imbalance, nonlinear gain, and saturation. These imperfections are measured on the platform by applying an RF signal at the receive antenna via cable and by capturing the data after the AD converter. The RF signal can come from a signal generator or from a transmitter front end. The post processing to extract the front-end characteristics is done

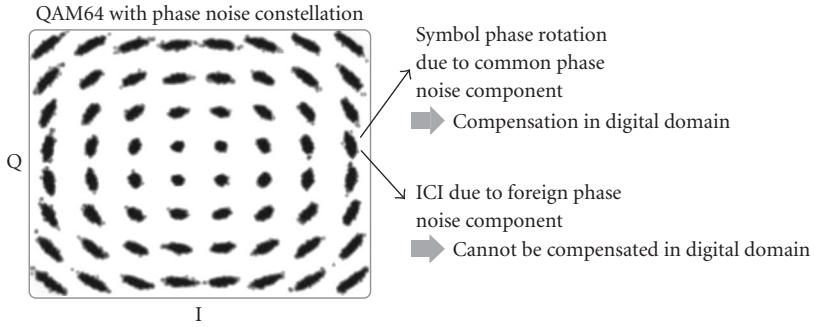

Figure 40.12. Impact of phase noise on the constellation.

in floating point. The measured characteristics are then fed back into the algorithmic model to verify the performance for this front-end realization. Two examples are described: phase noise characterization and AGC characterization.

40.7.1. Example 1: phase noise

Phase noise can be very destructive for OFDM symbols. It reflects as common phase noise on all subcarriers that can be compensated (close-in phase noise, for frequencies below 20 kHz) and as far-end phase noise that increases the noise level by intercarrier interference. Figure 40.12 shows the effect of the phase noise of the superheterodyne front end on the constellation plot. To measure the phase noise a single-carrier QPSK signal is applied at the transmitter (Figure 40.13). The transmitter and receiver front ends are programmed to work in their linear operation range at high signal-to-noise ratio. The captured data at the output of the AD converter represents the time-domain phase noise and the jitter of the AD converter. We have done the measurement on a 5 GHz superheterodyne front end and have compared the power spectrum density (PSD) profile with the measurement on a spectrum analyzer. Both PSD profiles match. The data captured on the platform gives extra information on the phase and amplitude jumps. The performance of the algorithms can be simulated in the high-level system model by multiplying the transmitted burst with the time-domain measured phase noise.

40.7.2. Example 2: AGC characterization

Characterization of the receiver front end for all incoming power levels has to be done to determine the control settings of the attenuators in the front end. An automatic AGC characterization loop is implemented on the platform (see Figure 40.14). During characterization, a software programmable attenuator is placed in the transmission path to regulate the receive input power between -90 dBm and -20 dBm in steps of 1 dB. For each incoming RF power, the Pareto

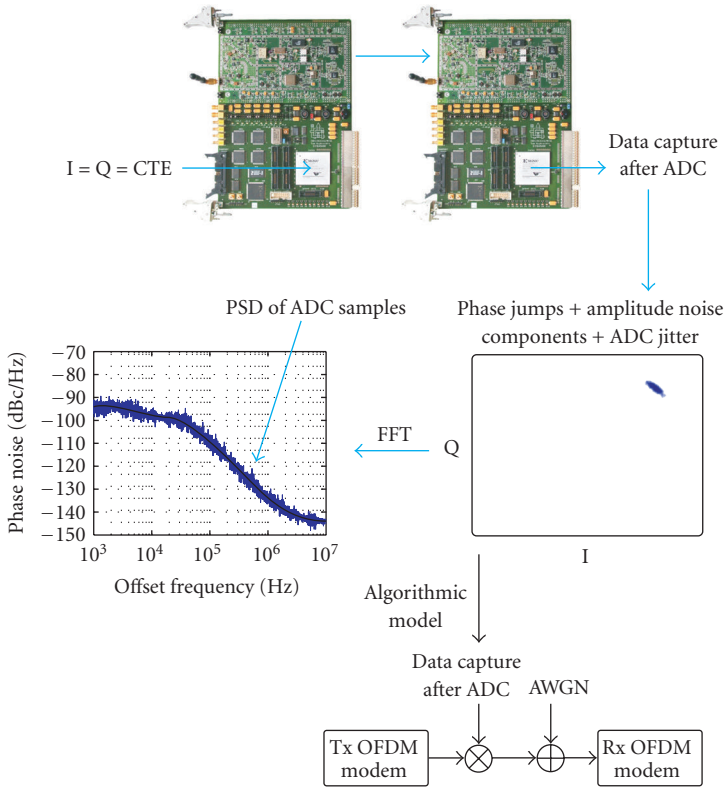

Figure 40.13. Phase noise measurement on PICARD.

optimal front-end settings are calculated (right bottom plot in the figure). They correspond to maximum signal-to-noise-and-distortion ratio (SINAD) and with the desired baseband input power or dynamic range (left bottom plot in the figure). These front-end control settings are programmed in a lookup table. In receive operation, the front-end control settings corresponding with the incoming power are programmed during AGC.

40.8. Future work

Further research will investigate the combined transmit-receive processing, and SDMA separation of MIMO terminals in which a multiple-antenna transmitter sends to several multiple-antenna receivers. This smart MIMO technology is a building block for future multimode terminal implementation. This smart MIMO technology combined with a flexible air interface will enable multimode terminals that can seamlessly switch between different communication types, such as WLAN and cellular communications.

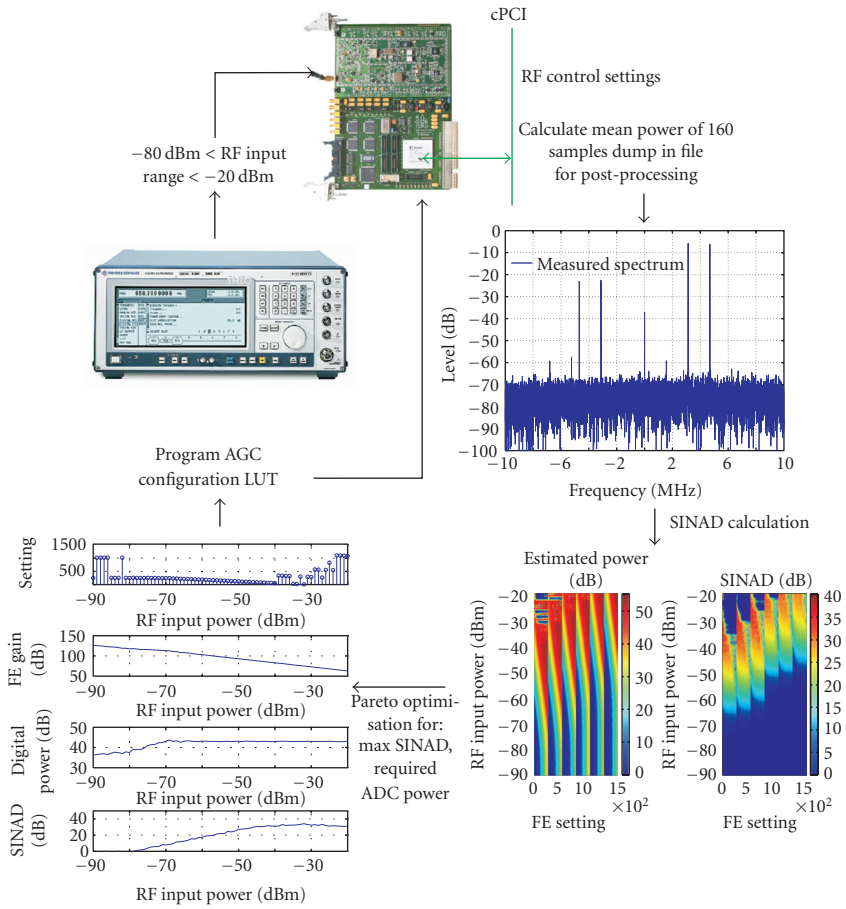

FIGURE 40.14. Automated characterization of the receive front end on PICARD.

Acknowledgment

We would like to thank the Sitex Group and Wireless Group of the Desics Division of IMEC for their contributions and support.

Abbreviations

ADC	Analog digital converter
AGC	Automatic gain control
ASIC	Application specific integrated circuit
BPSK	Binary phase-shift keying
DAC	Digital analog converter
DMA	Direct memory access

DSP	Digital signal processor
FFT	Fast Fourier transform
FPGA	Field programmable gate array
IFFT	Inverse fast Fourier transform
LTS	Long training sequence
MAC	Medium access controller
MIMO	Multiple-input multiple-output
MMSE	Minimum mean square error
MRC	Maximum ratio combining
OFDM	Orthogonal frequency division multiplexing
PAPR	Peak-to-average power ratio
PCB	Printed circuit board
QAM	Quadrature amplitude modulation
QoS	Quality-of-service
QPSK	Quadrature phase-shift keying
RF	Radio frequency
SDMA	Space-division multiple access
SINAD	Signal-to-noise-and-distortion-ratio
SISO	Single-input single-output
STS	Short training sequence
SRRC	Square root raised cosine
TDMA	Time-division multiple access
WLAN	Wireless local area network

Bibliography

[1] "IEEE Std 802.11a Supplement to IEEE Std Part 11: WLAN MAC and PHY specifications: High-speed Physical Layer in the 5 GHz Band," IEEE, September 1999.

[2] "Broadband Radio Access Networks; HIPERLAN Type 2; Physical (PHY) Layer," Technical specification, April 2000, ETSI TS 101 475.

[3] M. Wouters, T. Huybrechts, R. Huys, S. De Rore, S. Sanders, and E. Uman, "PICARD: platform concepts for prototyping and demonstration of high speed communication systems," in *Proc. 13th IEEE International Workshop on Rapid System Prototyping (RSP '02)*, pp. 166–170, Darmstadt, Germany, July 2002.

[4] N. Busa, G. Alkadi, M. Verberne, R. P. Llopis, and S. Ramanathan, "RAPIDO: a modular, multi-board, heterogeneous multi-processor, PCI bus based prototyping framework for the validation of SoC VLSI designs," in *Proc. 13th IEEE International Workshop on Rapid System Prototyping (RSP '02)*, pp. 159–165, Darmstadt, Germany, July 2002.

[5] P. Murphy, F. Lou, and P. Frantz, "A hardware testbed for the implementation and evaluation of MIMO algorithms," in *Proc. 5th IEEE International Conference on Mobile and Wireless Communications Networks (MWCN '03)*, Singapore, October 2003.

[6] A. Giulietti, B. Bougard, V. Derudder, S. Dupont, J.-W. Weijers, and L. Van der Perre, "A 80 Mb/s low-power scalable turbo codec core," in *Proc. IEEE Custom Integrated Circuits Conference (CICC '02)*, pp. 389–392, Orlando, Fla, USA, May 2002.

[7] PCI Industrial Computers Manufacturers Group (PICMG), Compact PCI Specification, revision 2.0R3.1, 1999 Conger, S.; Loch, K.: Ethics and computer use. Com. of ACM 38, 12.

[8] W. Eberle, J. Tubbax, B. Côme, S. Donnay, H. De Man, and G. Gielen, "OFDM-WLAN receiver performance improvement using digital compensation techniques," in *Proc. IEEE Radio and Wireless Conference (RAWCON '02)*, pp. 111–114, Boston, Mass, USA, August 2002.

[9] A. Fort, J.-W. Weijers, V. Derudder, W. Eberle, and A. Bourdoux, "A performance and complexity comparison of auto-correlation and cross-correlation for OFDM burst synchronization," in *Proc. IEEE International Conference on Acoustics, Speech, and Signal Processing (ICASSP '03)*, vol. 2, pp. 341–344, Hong Kong, China, April 2003.

[10] J. Tubbax, B. Côme, L. Van der Perre, et al., "Joint compensation of IQ imbalance and frequency offset in OFDM systems," in *Proc. IEEE Radio and Wireless Conference (RAWCON '03)*, pp. 39–42, Boston, Mass, USA, August 2003.

[11] A. Bourdoux, B. Côme, and N. Khaled, "Non-reciprocal transceivers in OFDM/SDMA systems: Impact and mitigation," in *Proc. IEEE Radio and Wireless Conference (RAWCON '03)*, pp. 183–186, Boston, Mass, USA, August 2003.

Maryse Wouters: Interuniversity MicroElectronics Center (IMEC), 3001 Leuven, Belgium
Email: maryse.wouters@imec.be

Tom Huybrechts: Interuniversity MicroElectronics Center (IMEC), 3001 Leuven, Belgium
Email: huybrech@imec.be

Index